Airplane Design

Part VI: Preliminary Calculation of Aerodynamic, Thrust and Power Characteristics

Dr. Jan Roskam
Ackers Distinguished Professor of Aerospace Engineering
The University of Kansas, Lawrence

2004

DARcorporation
Design • Analysis • Research

1440 Wakarusa Drive, Suite 500 • Lawrence, Kansas 66049, U.S.A.

PUBLISHED BY
Design, Analysis and Research Corporation (*DARcorporation*)
1440 Wakarusa Drive, Suite 500
Lawrence, Kansas 66049
U.S.A.
Phone: (785) 832-0434
Fax: (785) 832-0524
e-mail: info@darcorp.com
http://www.darcorp.com

Library of Congress Catalog Card Number: 97-68580

ISBN 1-884885-52-7

In all countries, sold and distributed by
Design, Analysis and Research Corporation
1440 Wakarusa Drive, Suite 500
Lawrence, Kansas 66049
U.S.A.

Printed in the United States of America
First Printing, 1987
Second Printing, 1990
Third Printing, 2000
Fourth Printing, 2004

TABLE OF CONTENTS
==========

DARPA-NASA-USAF FUTURE APPLICATIONS COMMITTEE

TABLE OF SYMBOLS

The Table of Symbols is organized as follows:

1. GENERAL SYMBOLS

Symbol	Definition	Dimension
a	speed of sound	fps
a.c.	aerodynamic center	-----
$A = b^2/S$	Wing aspect ratio	-----
$A_c = b_c^2/S_c$	Canard aspect ratio	-----
$A_v = b_h^2/S_h$	Vert.tail aspect ratio	-----
A_∞	Inlet capture area	ft^2
A_c	Inlet area	ft^2
$\bar{A_c}$	Cowl cross section area at $\bar{d}_c$	ft^2
A_e	Nozzle (exit) area	ft^2
A_f	Internal area	ft^2
A_m	Cowl cross section area at d_m	ft^2
A_t	Nozzle throat area	ft^2
b	wing span	ft
b_c	canard span	ft
b_{f_i}	inboard flap span, p.89	ft

b_{f_o}	outboard flap span, p.89	ft
b_t	tire width	ft
b_v	vertical tail span, see p.387	ft
B	Compressible sweep correction factor, see Eqn.(10.64)	-----
c	chord	ft
c'	chord with flap extended	ft
$\bar{c}$	mean geometric chord	ft
c_b	control surface overhang, see p.471	ft
c_{d_c}	crossflow drag coeff	-----
c_e	elevator chord	ft
c_{δ_c}	canardvator chord	ft
c_f	flap chord	ft
c_h	two-dim. hingemoment coeff. about control surf. h.l.	-----
$c^t{}_h$	two-dim. hingemoment coeff. about tab h.l.	-----
$c^*{}_l$	airfoil lift coefficient at α^*	-----
$c_{m_{ac}}$	airfoil pitching moment coefficient about a.c.	-----
c_{m_o}	airfoil zero-lift pitching moment coeff.	-----
c_p	wing chord at wing pivot also: engine sfs	ft lbs/shp/hr
c_t, c_T	tip chord	ft
	c_t in Ch.10 also stands for tab chord, see p.473	ft
c_r, c_R	root chord	ft
$\bar{c}_{w_e}$	mean geometric chord of exposed wing	ft
C_D	Airplane drag coeff.	-----
C_{D_A}, $C_{D_{N_2}}$	wave drag coefficients see p.49 and 52	-----

$C_{D_{A(NC)}}$	interference drag coeff. see p.52	-----
C_{D_b}	base drag coefficient	-----
$C_{D_{L_i}}$	Drag due to lift coeff	-----
$C_{D_{L_v}}$	Viscous drag due to lift coefficient	-----
$C_{D_{min}}$	Drag coefficient at $C_{L_{min}}$	-----
$C_{D_{min_w}}$	Wing minimum drag coeff.	-----
$C_{D_{i_w}}$	Wing induced drag coeff.	-----
C_{D_o}	Zero-lift drag coeff.	-----
C_{D_p}	Profile drag coefficient	-----
C_f	turbulent flat plate friction coefficient	-----
C_{f_w}	turbulent flat plate friction coefficient of the wing	-----
C_h	Three-dim. hingemoment coeff. about contr. surf. h.l.	-----
C^t_h	Three-dim. hingemoment coeff. about tab h.l.	-----
c_l	airfoil lift coefficient	-----
c_{l_α}	airfoil lift curve slope	-----
$(c_{l_\alpha})_\delta$	section lift curve slope with the flaps down	1/deg, 1/rad
c_{l_δ}	derivative of airfoil lift coeff. with flap deflect.	-----
C_l	aerodynamic rolling moment coefficient	-----
$C_L = W/\bar{q}S$	Airplane lift coefficient	-----
C_{L_B}	Lift coefficient where drag rise due to separation begins	-----
C_{L_c}	Canard lift coefficient	-----
C_{L_h}	Hor. tail lift coeff.	-----

C_{L_o}	Lift coefficient for zero angle of attack	-----
$C_{L_{min}}$	Lift coefficient at minimum viscous drag due to lift	-----
C_{L_w}	Wing lift coefficient	-----
C_{L_α}	Airplane lift curve slope	1/deg, 1/rad
$C_{L_{\alpha_w}}$	Wing lift-curve slope	1/deg, 1/rad
C_m	Aerodynamic pitching moment coefficient	-----
c_{m_o}	Airfoil pitching moment coefficient at zero lift coefficient	-----
C_n	Aerodynamic yawing moment coefficient	-----
C_{p_b}	base pressure coeff., p.52	-----
C_R	Ram recovery factor	-----
C_y	Aerodynamic side force coefficient	-----
d_b	equivalent base diameter	-----
$\bar{d}_c$	cowl diameter at inlet area	ft
d_{exhnoz}	diam. of exhaust nozzle	in
d_{exhst}	exhaust stack diameter	in
d_f	equivalent fuselage diameter	--
d_{inl}	max. inlet diameter	ft
d_m	max. cowl diameter	ft
d_n	maximum nacelle (equivalent) diameter	ft
d_T	distance of thrustline to center of gravity, see Figure 8.126	ft
D	Drag	lbs
D_p	Propeller diameter	ft
D_t	Max. tire diameter	ft
e	span efficiency factor	-----

	(Also called Oswald's eff. factor)	
f	equivalent parasite area	ft^2
F_t	Factor in Eqn.(6.51)	-----
Δf	incremental eq. par. area	ft^2
F_{A_y}	Aerodynamic side force	lbs
i	incidence angle	deg
I_{xx}	Rolling moment of inertia in body axes	$slugft^2$
I_{xz}	XZ Product of inertia in body axes	$slugft^2$
I_{yy}	Piching moment of inertia in body axes	$slugft^2$
I_{zz}	Yawing moment of inertia in body axes	$slugft^2$
k	ratio of airfoil lift-curve slope to 2π, also:	-----
	equivalent sand roughness	-----
k'	correction factor for non-linear effects	-----
k_{cw}, k_{wc} and k_{wh}	interference factors, see pages 277, 278	-----
K	empirical constant, see p.86	--
K'	factor in Eqn.(3.6)	-----
K''	factor in Eqn.(3.6)	-----
K_B	factor in Eqn.(3.8)	-----
K_Λ	flap span factor for swept wings, p.313	-----
K_p	flap span factor, p.313	-----
K_t	constant in Eqn.(6.50)	-----
K_{wf}	wing-fuselage interference factor: see Eqn.(8.44)	
l	reference length	ft
l_f	fuselage length	ft
l_p	distance in Fig.10.34	ft
l_v	distance in Fig.10.27	ft
L	Lift	lbs
L'	Airfoil thickness location parameter	-----
L/D	Lift-to-drag ratio	-----

L_A	Aerodynamic rolling mom.	lbs
$\dot{m}_a$	engine massflow	slugs/sec
$\dot{m}_{bleed}$	bleed air massflow	slugs/sec
$\dot{m}_{comb}$	combustion massflow	slugs/sec
$\dot{m}_{cool}$	cooling air massflow	slugs/sec
M	Free stream Mach number	-----
M_A	Aerodynamic pitching moment	ftlbs
M_c	Crossflow Mach number	-----
M_{CR}, M_{crit}	Critical Mach number	-----
M_{DD}	Drag divergence Mach number	---
$n=W/\bar{q}S$	airplane load factor	-----
n_p	no. of blades per prop.	-----
N_A	Aerodynamic yawing moment	ftlbs
p	local static pressure	psf
	also: planform shape parameter, p.40	-----
p_{tot}	total pressure	psf
P_t	Factor in Eqn.(6.51)	-----
P_{av}	Power available	hp
P_{el}	Extracted electr. power	hp
P_{extr}	Extracted power	
P_{fp}	Extr. fuel pump power	hp
P_{hydr}	Extr. hydr. pump power	hp
P_{mech}	Extr. mechanical power	hp
P_{other}	Extr. other power	hp
P_{pneum}	Extr. pneumatic power	hp
P_{reqd}	Power required	hp

$\bar{q}$	free stream dyn. pressure	psf
R_N, R_l	Reynold's number	-----
R_{LS}	Lifting surface correction factor	-----
R_{wf}	Wing/fuselage interference factor	-----
S	Wing planform (ref) area	ft^2
$S_{b_{fus}}$	Fuselage base area	ft^2
S_{fus}	Max. fuselage cross section area	ft^2
S_c	Canard area	ft^2
S_{can}	Max. frontal area of canopy	ft^2
S_{cf}	Flapped canard area	ft^2
S_{ef}	Flapped hor.tail area	ft^2
S_{B_s}	Fuselage side area as defined in Fig.10.28	ft^2
S_{wf}	Flapped wing area	ft^2
S_h	Horiz.tail area	ft^2
S_n	Max. frontal area of nacelle	ft^2
S_v	Vertical tail area, see p.387	ft^2
S_{noz}	Nozzle cross section area	ft^2
S_{wet}	Total wetted area	ft^2
$S_{wet_{fus}}$	Wetted area of fuselage	ft^2
$S_{wet_{lam}}$	Wetted area with laminar flow	ft^2
$S_{wet_{turb}}$	Wetted area with turbulent flow	ft^2
S_{wet_w}	Wetted area of wing	ft^2

t/c	thickness ratio (at $\bar{c}$)	-----
T	Temperature of air	deg F
T_{av}	Thrust available	lbs
T_r	Remnant thrust	lbs
T_{reqd}	Thrust required	lbs
U_1 or U	Steady state airspeed	ft/sec
v	induced drag factor due to twist	-----
V_∞	Velocity at sta. A_∞	fps
V_c	Velocity at sta. A_c	fps
$\bar{V}_c$	Canard volume coefficient, see Eqn.(10.74)	-----
$\bar{V}_h$	Hor. tail volume coefficient, see Eqn.(10.23)	-----
VA_{plp}	Required electrical power	hp
$\dot{V}_{hydr}$	Hydr. fluid flow rate	gpm
V_{noz}	Average nozzle flow velocity	fps
w	zero-lift drag factor due to twist	-----
w_f	max. fuselage width	ft
W	Airplane weight	lbs
x_{ac}	position of a.c. on wing mgc,	ft
$\bar{x}_{ac}=x_{ac}/\bar{c}$	position of aerodynamic center on wing mgc, fr.$\bar{c}$	-----
x_{ac_h}	position of hor. tail a.c. on wing mgc	ft
$\bar{x}_{ac_h}=x_{ac_h}/\bar{c}$	position of hor. tail a.c. on wing mgc, fr.$\bar{c}$	-----
x_{cp}	position of wing center of pressure on wing mgc	ft
x_{ref}	position of reference point on wing mgc	ft

$\bar{x}_{ref}=x_{ref}/\bar{c}$	position of reference point on wing mgc, fr.$\bar{c}$	-----
NOTE: see Figure 8.114 for illustration!		
x_w	distance of wing quarter chord mgc to c.g., see Fig.10.39	----
y	spanwise coordinate	ft
z_f	vertical height of fuselage at wing root chord	ft
z_p	distance in Fig.10.34	ft
z_v	distance in Fig.10.27	ft
z_w	wing distance to fuselage centerline, see Fig.(10.9)	ft

2. STABILITY, CONTROL AND HINGEMOMENT DERIVATIVES

NOTE: All derivatives are presented in the airplane stability axes system. See pages 371 and 372 for a definition of axes.

STABILITY DERIVATIVES

Symbol	Definition	Dimension
C_{D_u}	$\partial C_D/\partial(u/U_1)$	-----
C_{L_u}	$\partial C_L/\partial(u/U_1)$	-----
C_{m_u}	$\partial C_m/\partial(u/U_1)$	-----
$C_{T_{x_u}}$	$\partial C_{T_x}/\partial(u/U_1)$	-----
$C_{m_{T_u}}$	$\partial C_{m_T}/\partial(u/U_1)$	-----
C_{D_α}	$\partial C_D/\partial\alpha$	rad^{-1}
C_{L_α}	$\partial C_L/\partial\alpha$	rad^{-1}
C_{m_α}	$\partial C_m/\partial\alpha$	rad^{-1}
$C_{m_{T_\alpha}}$	$\partial C_{m_T}/\partial\alpha$	rad^{-1}
$C_{D_{\dot\alpha}}$	$\partial C_D/\partial(\dot\alpha\bar{c}/2U_1)$	rad^{-1}
$C_{L_{\dot\alpha}}$	$\partial C_L/\partial(\dot\alpha\bar{c}/2U_1)$	rad^{-1}
$C_{m_{\dot\alpha}}$	$\partial C_m/\partial(\dot\alpha\bar{c}/2U_1)$	rad^{-1}

C_{Y_β}	$\partial C_Y/\partial\beta$	rad^{-1}
C_{l_β}	$\partial C_l/\partial\beta$	rad^{-1}
C_{n_β}	$\partial C_n/\partial\beta$	rad^{-1}
$C_{n_{T_\beta}}$	$\partial C_{n_T}/\partial\beta$	rad^{-1}
$C_{Y_{\dot\beta}}$	$\partial C_Y/\partial(\dot\beta b/2U_1)$	rad^{-1}
$C_{l_{\dot\beta}}$	$\partial C_l/\partial(\dot\beta b/2U_1)$	rad^{-1}
$C_{n_{\dot\beta}}$	$\partial C_n/\partial(\dot\beta b/2U_1)$	rad^{-1}
C_{Y_p}	$\partial C_Y/\partial(pb/2U_1)$	rad^{-1}
C_{l_p}	$\partial C_l/\partial(pb/2U_1)$	rad^{-1}
C_{n_p}	$\partial C_n/\partial(pb/2U_1)$	rad^{-1}
C_{D_q}	$\partial C_D/\partial(q\bar{c}/2U_1)$	rad^{-1}
C_{L_q}	$\partial C_L/\partial(q\bar{c}/2U_1)$	rad^{-1}
C_{m_q}	$\partial C_m/\partial(q\bar{c}/2U_1)$	rad^{-1}
C_{Y_r}	$\partial C_Y/\partial(rb/2U_1)$	rad^{-1}
C_{l_r}	$\partial C_l/\partial(rb/2U_1)$	rad^{-1}
C_{n_r}	$\partial C_n/\partial(rb/2U_1)$	rad^{-1}

CONTROL DERIVATIVES

$C_{D_{i_h}}$	$\partial C_D/\partial i_h$	rad^{-1}
$C_{L_{i_h}}$	$\partial C_l/\partial i_h$	rad^{-1}
$C_{m_{i_h}}$	$\partial C_m/\partial i_h$	rad^{-1}
$C_{D_{\delta_e}}$	$\partial C_D/\partial\delta_e$	rad^{-1}

$C_{L_{\delta_e}}$	$\partial C_L / \partial \delta_e$	rad^{-1}
$C_{m_{\delta_e}}$	$\partial C_m / \partial \delta_e$	rad^{-1}
$C_{D_{i_c}}$	$\partial C_D / \partial i_c$	rad^{-1}
$C_{L_{i_c}}$	$\partial C_L / \partial i_c$	rad^{-1}
$C_{m_{i_c}}$	$\partial C_m / \partial i_c$	rad^{-1}
$C_{D_{\delta_c}}$	$\partial C_D / \partial \delta_c$	rad^{-1}
$C_{L_{\delta_c}}$	$\partial C_L / \partial \delta_c$	rad^{-1}
$C_{m_{\delta_c}}$	$\partial C_m / \partial \delta_c$	rad^{-1}
$C_{y_{\delta_a}}$	$\partial C_y / \partial \delta_a$	rad^{-1}
$C_{l_{\delta_a}}$	$\partial C_l / \partial \delta_a$	rad^{-1}
$C_{n_{\delta_a}}$	$\partial C_n / \partial \delta_a$	rad^{-1}
$C_{y_{\delta_s}}$	$\partial C_y / \partial \delta_s$	rad^{-1}
$C_{l_{\delta_s}}$	$\partial C_l / \partial \delta_s$	rad^{-1}
$C_{n_{\delta_s}}$	$\partial C_n / \partial \delta_s$	rad^{-1}
$C_{y_{i_h}}$	$\partial C_y / \partial i_h$	rad^{-1}
$C_{l_{i_h}}$	$\partial C_l / \partial i_h$	rad^{-1}

$C_{n_{i_h}}$	$\partial C_n / \partial i_h$	rad^{-1}
$C_{y_{\delta_r}}$	$\partial C_y / \partial \delta_r$	rad^{-1}
$C_{l_{\delta_r}}$	$\partial C_l / \partial \delta_r$	rad^{-1}
$C_{n_{\delta_r}}$	$\partial C_n / \partial \delta_r$	rad^{-1}

HINGEMOMENT DERIVATIVES

Two-Dimensional Hingemoment Derivatives

Symbol	Definition	Dimension
c_{h_o}	zero-angle-of-attack, zero-control-surface-deflection, zero-tab-angle-deflection hingemoment coefficient	-----
c_{h_α}	$\partial c_h / \partial \alpha$	rad^{-1}
$c_{h_\delta} = c_{h_{\alpha_{bal}}}$	$\partial c_h / \partial \delta$	rad^{-1}
$c_{h_{\delta_t}}$	$\partial c_{h_t} / \partial \delta_t$	rad^{-1}

Three-Dimensional Hingemoment Derivatives

Symbol	Definition	Dimension
C_{h_o}	zero-angle-of-attack, zero-control-surface-deflection, zero-tab-angle-deflection hingemoment coefficient	-----
C_{h_α}	$\partial C_h / \partial \alpha$	rad^{-1}
C_{h_δ}	$\partial C_h / \partial \delta$	rad^{-1}
$C_{h_{\delta_t}}$	$\partial C_h / \partial \delta_t$	rad^{-1}

NOTE: Control surface hingemoment derivatives defined sofar, are taken about the control surface hingeline. Tab hingemoment derivatives taken about the tab hingeline are defined in a similar manner but carry the superscript 't' as in $c^t_{h_x}$ and $C^t_{h_x}$

3. GREEK SYMBOLS

Symbol	Definition	Dimension
α	airfoil angle of attack	deg, rad
α	airplane angle of attack with subscript w, h or c, the symbol indicates the angle of attack of that component	deg, rad
α^*	linear range of α	deg, rad
α_{o_l}	airfoil zero-lift angle of attack	deg, rad
α_{o_L}	airplane zero-lift angle of attack	deg, rad
α_δ	derivative of angle of attack w.r.t. surface deflection angle	-----
β	$(1 - M^2)^{1/2}$	-----
	also: sideslip angle	deg, rad
γ	flight path angle	deg, rad
Γ	dihedral angle	deg, rad
δ	pressure ratio,	-----
	also: flap or control surface deflection	deg, rad
δ_f	flap defl. angle	deg, rad
Δ	increment	depends
$\Delta\alpha_g$	change in angle of attack due to ground effect	deg, rad
$\Delta\alpha_{w/c}$	difference in stall angle of attack between wing and canard, see p.280	deg, rad
Δc_l	incremental airfoil lift coefficient due to flaps	-----
ΔC_L	incremental airplane lift coefficient due to flaps	-----
ΔC_{L_c}	incremental canard lift coefficient to trim, based on wing area, S	-----
ΔC_{L_h}	incremental tail lift coefficient to trim, based on wing area, S	-----
Δc_m	incremental airfoil pitching moment coefficient due to flaps	-----
ΔC_m	incremental airplane piching moment coefficient due to flaps	-----
$\Delta\varepsilon_f$	change in tail downwash angle due to flaps	deg, rad
Δp_{hydr}	hydraulic pressure differential	psi

$\Delta\bar{x}_{ac_f}$	shift in aerodynamic center due to the fuselage, fr.$\bar{c}$	-----
Δy	leading edge shape parameter	-----
ε	downwash angle at the horizontal tail	deg, rad
ε_c	upwash angle at the canard	deg, rad
ε_t	wing twist angle	deg, rad
η	span fraction, or see p.46	-----
η_c	ratio of canard to wing dynamic pressure	-----
η_{diff}	pressure recovery through diffuser	-----
η_{fp}	fuel pump efficiency	-----
η_{gear}	gearbox efficiency	-----
η_{gen}	generator efficiency	-----
η_h	ratio of hor.tail to wing dynamic pressure	-----
η_{hp}	hydr. pump efficiency	-----
η_{inl}	inlet pressure recovery	-----
$\eta_{inl/com}$	inlet pressure recovery, compressible	-----
$\eta_{inl/inc}$	inlet pressure recovery, incompressible	-----
η_p	propeller efficiency	-----
η_{shock}	pressure recovery through shock	-----
$\Lambda_{c/2}$	semi-chord sweep angle	deg, rad
$\Lambda_{c/4}$	quarter chord sweep angle	deg, rad
Λ_{LE}	leading edge sweep angle	deg, rad
λ	taper ratio	-----
μ	coefficient of viscosity for air	-----
μ_{inl}	area ratio A_c/A_∞	-----
π	3.14	-----
ρ	air density	slug/ft^3

σ	sidewash angle	deg, rad
$\bar{\Phi}$	effective turning angle	deg, rad
Φ_{te}	trailing edge angle	deg, rad

4. SUBSCRIPTS

1	steady state
a	aileron
av	available
A	Airplane
b	base
bal	balance
bw	basic wing
c	canard
can	canopy
cg	center of gravity
co	cut-off
cool	cooling
cw	canopy/windshield
e	elevator
eff	effective
emp	empennage
f	friction, sometimes: flap
flap	flap
fus	fuselage
g	ground effect
gear	landing gear
h	horizontal tail
int	interference
kf	krueger flap
lam	laminar
lef	leading edge flap
L	landing
LE, le	leading edge
max	maximum
misc	miscellaneous
M	(at a given) Mach Number
n	nacelle
np	nacelle/pylon
p	pylon
plf	planform
prof	profile
r	rudder
rated	rated, usually SHP
ref	reference, usually the wing, or a point on the wing
reqd	required
s	slat(ted)
sf	split flap
sp	spoiler (speedbrake)

std	standard
store	store(s)
T	thrust or power effect
TE, te	trailing edge
TL	thrustline offset effect
TS	propeller slipstream effect
turb	turbulent
TO	take-off
trim	trim
w	wing
wave	wave (drag)
wb	wing-body (same as wing-fuselage)
wet	wetted
wf	wing-fuselage (same as wing-body)
wing	wing
wmprop	windmilling propeller
ws	windshield

5. ACRONYMS

AEO	All engines operating
APU	Auxiliary power unit
AWACS	Airborne warning and control system
b.l.	boundary layer
BPR	Bypass ratio
CBR	California Bearing Ratio
c.g.	center of gravity
FRP	Fuselage Reference Plane
hl or h.l.	hingeline
i.e.	id est (that is)
l.e.	leading edge
mgc or m.g.c.	mean geometric chord
OEI	one engine inoperative
RAT	Ram air turbine
SHP	Shaft Horsepower
t.e.	trailing edge
W.R.P.	Wing Reference Plane
w.r.t	with respect to

ACKNOWLEDGEMENT

Writing a book on airplane design is impossible without the supply of a large amount of data. The author is grateful to the following companies for supplying data on airplane drag and on airplane stability and control characteristics:

Cessna Aircraft Company	Beech Aircraft Corporation
The Boeing Company	McDonnell Douglas Corp.
Lockheed Aircraft Corp.	Gates Learjet Corporation
Northrop Corporation	SIAI Marchetti

A significant amount of airplane design information has been accumulated by the author over many years from the following magazines:

Interavia (Swiss, monthly)
Flight International (British, weekly)
Business and Commercial Aviation (USA, monthly)
Aviation Week and Space Technology (USA, weekly)
Journal of Aircraft (USA, AIAA, monthly)

The author wishes to acknowledge the important role played by these magazines in his own development as an aeronautical engineer. Aeronautical engineering students and graduates should read these magazines regularly.

This part of the Airplane Design series presents rapid methods for estimating drag, lift, pitching moment, installed thrust and power data as well as stability, control and hingemoment derivatives. In preparing this part much use has been made of the USAF DATCOM, a most impressive and useful document which should be available in all aeronautical engineering design offices and libraries.

FOKKER D.XXI
COURTESY: FOKKER

1. INTRODUCTION

The purpose of this series of books on Airplane Design is to familiarize aerospace engineering students with the design methodology and design decision making involved in the process of designing airplanes.

The series of books is organized as follows:

PART I:	PRELIMINARY SIZING OF AIRPLANES
PART II:	PRELIMINARY CONFIGURATION DESIGN AND INTEGRATION OF THE PROPULSION SYSTEM
PART III:	LAYOUT DESIGN OF COCKPIT, FUSELAGE, WING AND EMPENNAGE: CUTAWAYS AND INBOARD PROFILES
PART IV:	LAYOUT DESIGN OF LANDING GEAR AND SYSTEMS
PART V:	COMPONENT WEIGHT ESTIMATION
PART VI:	PRELIMINARY CALCULATION OF AERODYNAMIC, THRUST AND POWER CHARACTERISTICS
PART VII:	DETERMINATION OF STABILITY, CONTROL AND PERFORMANCE CHARACTERISTICS: FAR AND MILITARY REQUIREMENTS
PART VIII:	AIRPLANE COST ESTIMATION: DESIGN, DEVELOPMENT, MANUFACTURING AND OPERATING

The purpose of PART VI is to present a systematic approach to the prediction of drag, installed power and thrust, lift, pitching moment and other important stability and control data needed in preliminary design.

The methods presented in this volume are meant to be used in conjunction with Preliminary Design Sequence II as outlined in Chapter 2 of Part II of this series. For that reason these methods are sometimes referred to as Class II methods. The preceeding Class I methods are covered in Part I and Part II of this series and are meant to be used with Preliminary Design Sequence I as outlined also in Chapter 2 of Part II.

In Chapter 2 some important definitions relating to flight regime and reference geometries are discussed.

Chapter 3 presents different ways by which airplane drag polars can be represented by simple mathematical models. Several examples are given.

Chapter 4 presents a method to predict the component drag breakdown and the total drag of airplanes. Example drag data are given in Chapter 5.

Methods for predicting installed thrust and power characteristics are presented in Chapter 6. Example thrust and power data are given in Chapter 7.

Chapter 8 contains methods for predicting lift and pitching moment characteristics of airplanes with and without (mechanical) flaps. Example data are given in Chapter 9.

Prediction methods for stability, control and hinge moment derivatives are presented in Chapter 10 with example data provided in Chapter 11.

To make the use of this book easy on students, a USER's GUIDE is presented in Chapter 12. Aeronautical engineering students should use this guide to prevent wasting a lot of time chasing non-existing problems.

Appendix A contains data on the atmosphere.

Appendix B contains data needed in the estimation of areas and volumes.

2. IMPORTANT DEFINITIONS

In this text frequent use is made of:

2.1 Flow regimes defined in terms of Mach number
2.2 Reference geometries defined in terms of areas and lengths

The purpose of this chapter is to define the physical and the mathematical meaning of these terms.

2.1 FLOW REGIME DEFINITIONS

In this text the following flow regimes are used:

2.1.1 Subsonic Flow Regime
2.1.2 Transonic Flow Regime
2.1.3 Supersonic Flow Regime

2.1.1 Subsonic Flow Regime

In terms of Mach number the subsonic flow regime is defined as:

SUBSONIC: $0 < M < 0.60$

It is assumed that in this flow regime all compressibility effects are negligible. The reader should keep in mind that whether or not compressibility effects are negligible depends not just on the free stream Mach number but also on thickness and on angle of attack.

Where the subsonic flow regime ends depends on the values of critical and drag divergence Mach numbers:

The critical Mach number is that free stream Mach number for which a condition of M=1 is first reached somewhere on the airplane.

Figure 2.1 shows how the critical Mach number varies with airfoil shape and with airfoil lift coefficient (or angle of attack).

The drag divergence Mach number is that free stream Mach number for which:

> Boeing definition: the drag coefficient first reaches a value of 0.0020 above that in the subsonic flow regime.

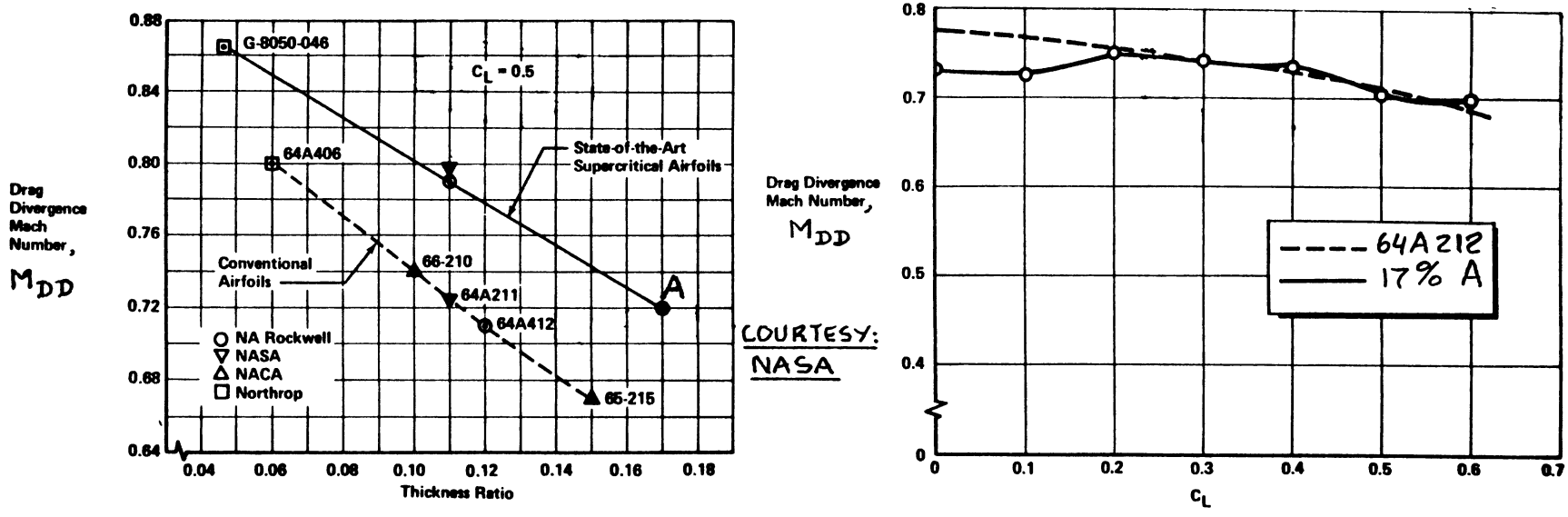

Figure 2.1 Effect of Airfoil Shape and Lift Coefficient on Drag Divergence Mach Number

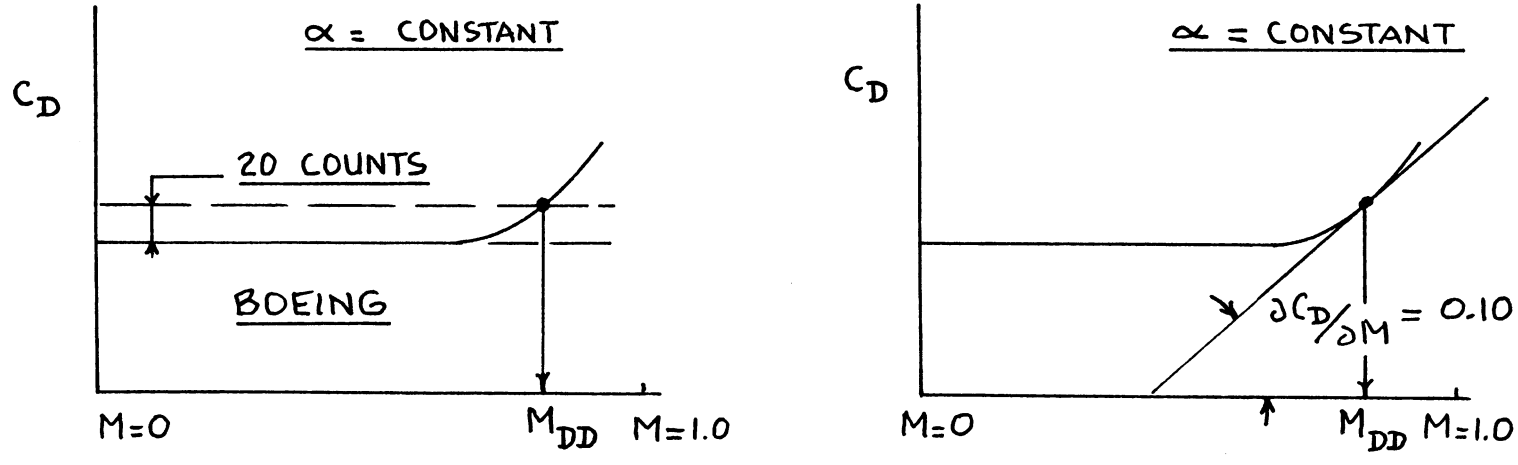

Figure 2.2 Boeing and Douglas Definitions for Drag Divergence Mach Number

Douglas definition: the slope of the drag coefficient versus Mach number first reaches the value of 0.10.

Figure 2.2 depicts these definitions graphically. Experience shows that there is no significant difference between these definitions.

The following equations may be used to estimate the drag divergence Mach number for airfoils:

For modern (aft-loaded) airfoils:

$$M_{DD} = 0.95 - (t/c)_{max} - c_l/10 \qquad (2.1)$$

For NACA airfoils:

$$M_{DD} = 0.90 - (t/c)_{max} - c_l/10 \qquad (2.2)$$

Figures 2.3 may be used to estimate the drag divergence Mach number of uncambered wings. For wings with camber, determine the lift coefficient for zero angle of attack, C_{L_o}. Then use Figures 2.3 with:

$$C_L = C_{L_{actual}} + C_{L_o} \qquad (2.3)$$

Reference 8 contains a wealth of information on the effect of the geometry of fuselages and wings on critical and on drag divergence Mach number.

2.1.2 Transonic Flow Regime

In terms of Mach number the transonic flow regime is defined as:

TRANSONIC: $0.60 < M < 1.2$

Mathematically speaking, the transonic flow regime starts at the critical Mach number.

Physically speaking, the transonic flow regime starts at the drag divergence Mach number.

In the transonic flow regime compressibility effects cannot be neglected. The reader should keep in mind that compressibility effects in this flow regime are a strong function of thickness ratio (for lifting surfaces such as wings, pylons and tails) and of cross sectional area distributions. The sweep angle of lifting surfaces is also an important parameter.

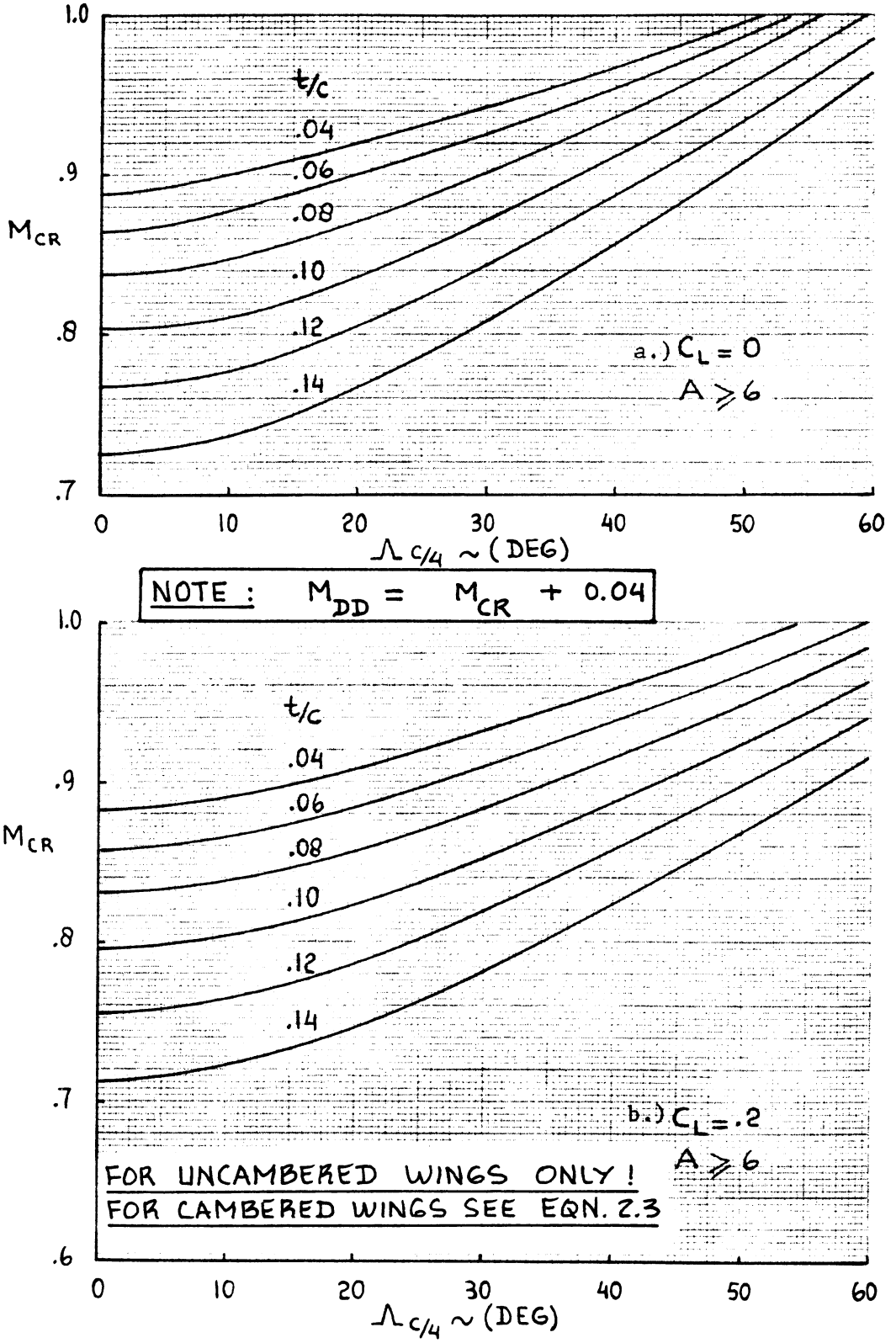

Figure 2.3 Effect of Thickness Ratio, Sweep Angle, Aspect Ratio and Lift Coefficient on the Drag Divergence Mach Number of Wings

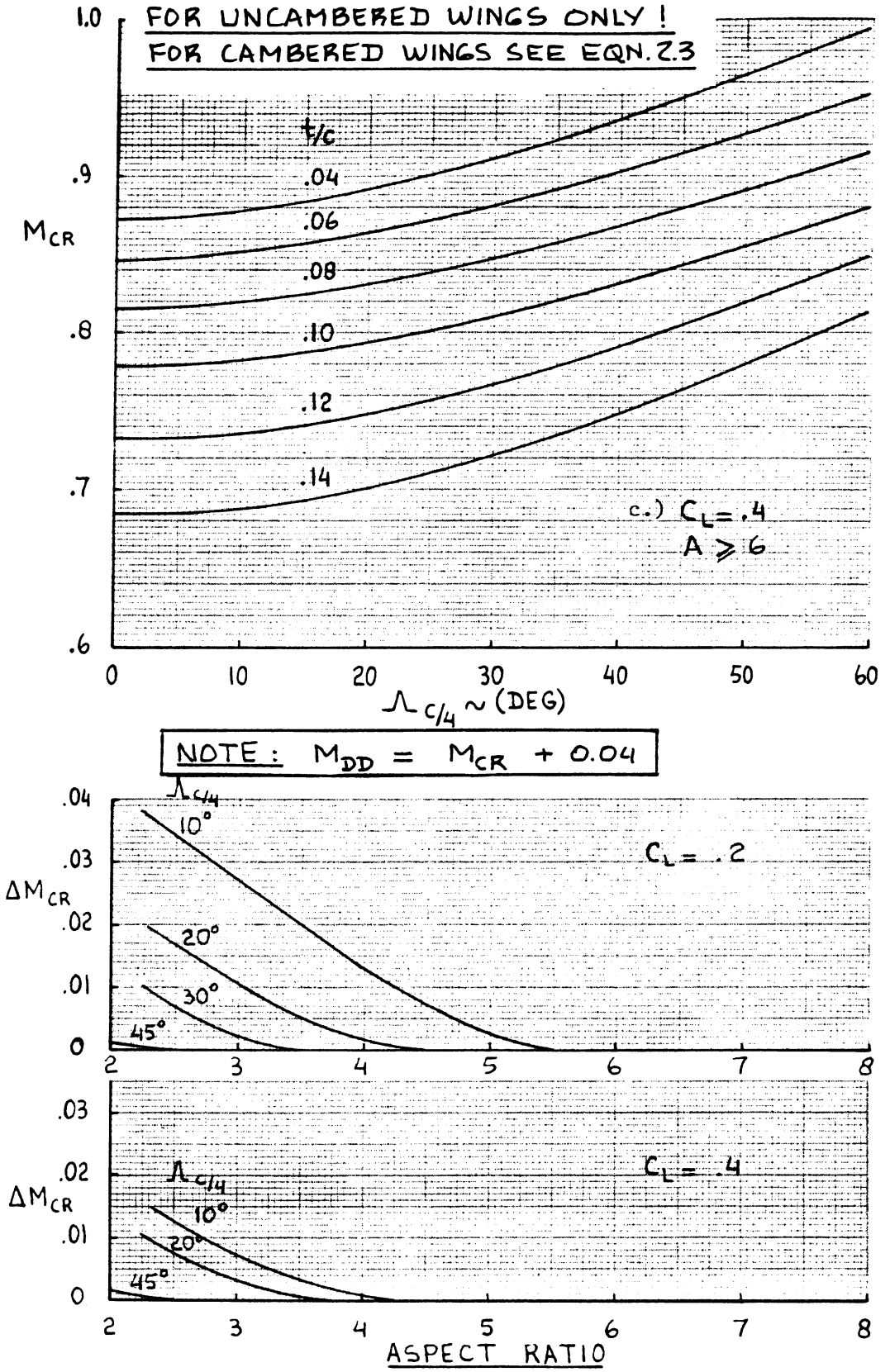

Figure 2.3 (Cont'd) Effect of Thickness Ratio, Sweep Angle, Aspect Ratio and Lift Coefficient on the Drag Divergence Mach Number of Wings

To reduce drag in the transonic flow regime the concept of area ruling plays an important role.

Reference 8 contains information on the variation of drag with Mach number in the transonic speed regime below M=1. Reference 9 should be used for the estimation of drag in the transonic flow regime above M=1.

For applications of the area rule concept, ref.10 should be consulted.

2.1.3 Supersonic Flow Regime

In terms of Mach number the supersonic flow regime is defined as:

SUPERSONIC: $1.2 < M < 3.0$

The aerodynamic behavior of airplanes in this flow regime depends strongly on the location of Mach lines relative to the airplane geometry. In particular whether or not the wing has a subsonic, supersonic or mixed flow leading edge has important consequences.

Figure 2.4 illustrates what is meant by subsonic/ supersonic leading edges.

Reference 9 contains methods for estimating drag in this flow regime.

Note: Reference 11 is strongly recommended as a general text on the effect of Mach number and of angle of attack on the drag and lift characteristics of airplanes.

2.2 IMPORTANT GEOMETRIC DEFINITIONS

2.2.1 Wing Planform Geometries

In this text, all aerodynamic characteristics of airplanes are referred to so-called reference geometries. This is accomplished through the introduction of dimensionless coefficients for drag, lift, pitching moment, side force, rolling moment and yawing moment in the following manner:

For drag: $D = C_D \bar{q} S$ (2.4)

For lift: $L = C_L \bar{q} S$ (2.5)

For pitching moment: $M_A = C_m \bar{q} S \bar{c}$ (2.6)

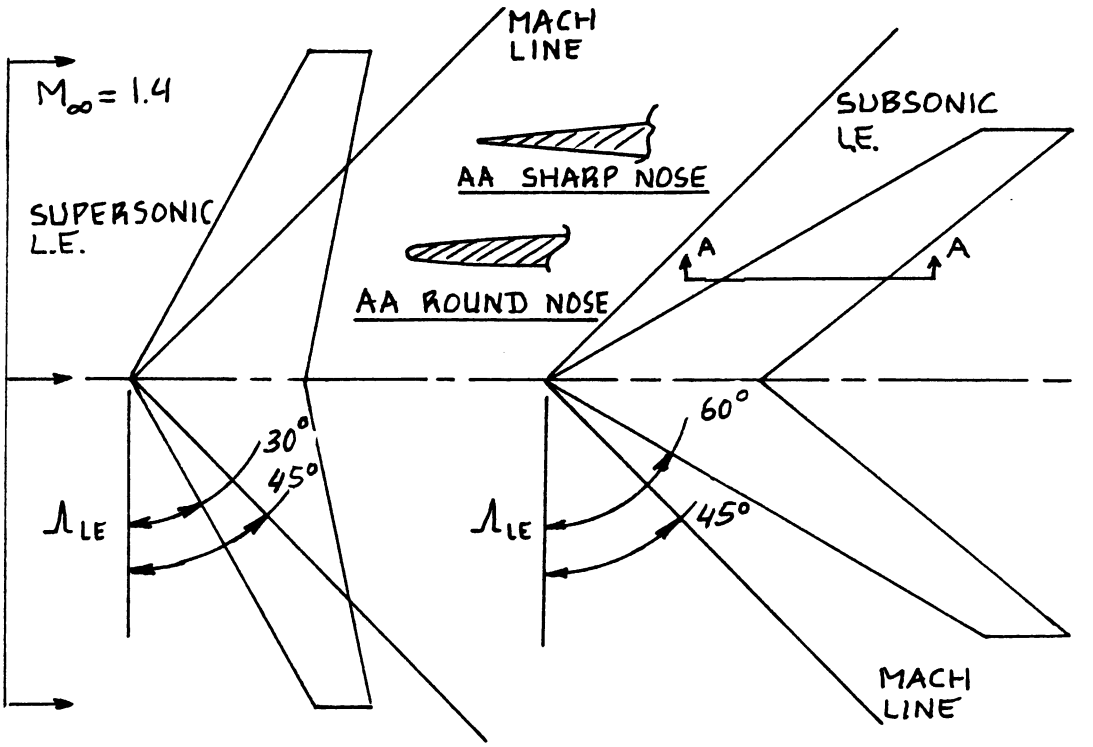

Figure 2.4 Subsonic and Supersonic Leading Edges

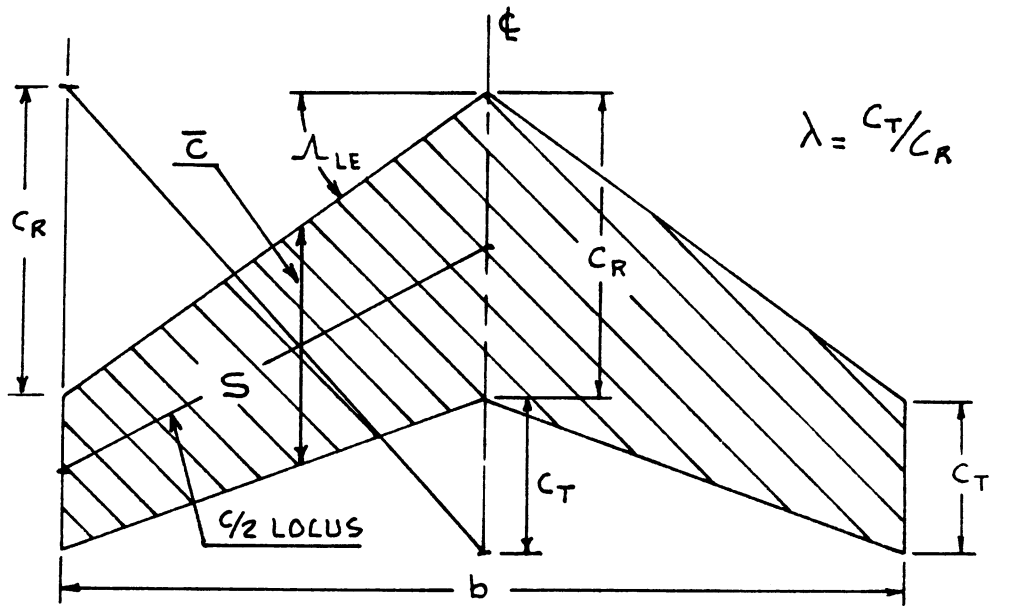

Figure 2.5 Reference Geometry for Straight, Tapered Wings

For side force: $F_{A_y} = C_y \bar{q} S$ (2.7)

For rolling moment: $L_A = C_l \bar{q} S b$ (2.8)

For yawing moment: $N_A = C_n \bar{q} S b$ (2.9)

The reference geometries in Equations (2.4) through (2.9) are S, $\bar{c}$ and b respectively. These reference geometries are normally based on the wing planform. For a straight, tapered wing these parameters are defined in Figure 2.5.

Most wings cannot be classified as straight, tapered wings. Leading edges and trailing edges are often broken or curved to achieve certain aerodynamic, structural or configurational objectives. Figure 2.6 shows how the parameters S, $\bar{c}$ and b are defined for non straight, tapered wings. Note that a so-called equivalent wing is defined for these planforms. This equivalent wing definition is found by 'averaging' areas.

In some airplanes the wings have very rapid changes in leading edge shape and/or trailing edge shape. Examples are shown in Figure 2.7. The definitions of S, $\bar{c}$ and b for such wings are also given in Figure 2.7.

Although the definition of airplane reference geometries is in principle arbitrary, the reader should not deviate too far from the definitions used here. The reason is that in the aerodynamic literature cited in this text the reference geometries are those defined here.

In addition to the parameters S, $\bar{c}$ and b, quantities such as taper ratio and sweep angle play an important role. Figures 2.5 and 2.6 also define these quantities.

2.2.2 Empennage Planform Geometries

To determine the contributions of empennage surfaces (horizontal tail, canard and/or vertical tail) to the aerodynamic characteristics of airplanes it is necessary to define their planform geometries. Figure 2.8 does this for horizontal tails and for canards. Figure 2.9 does this for vertical tails.

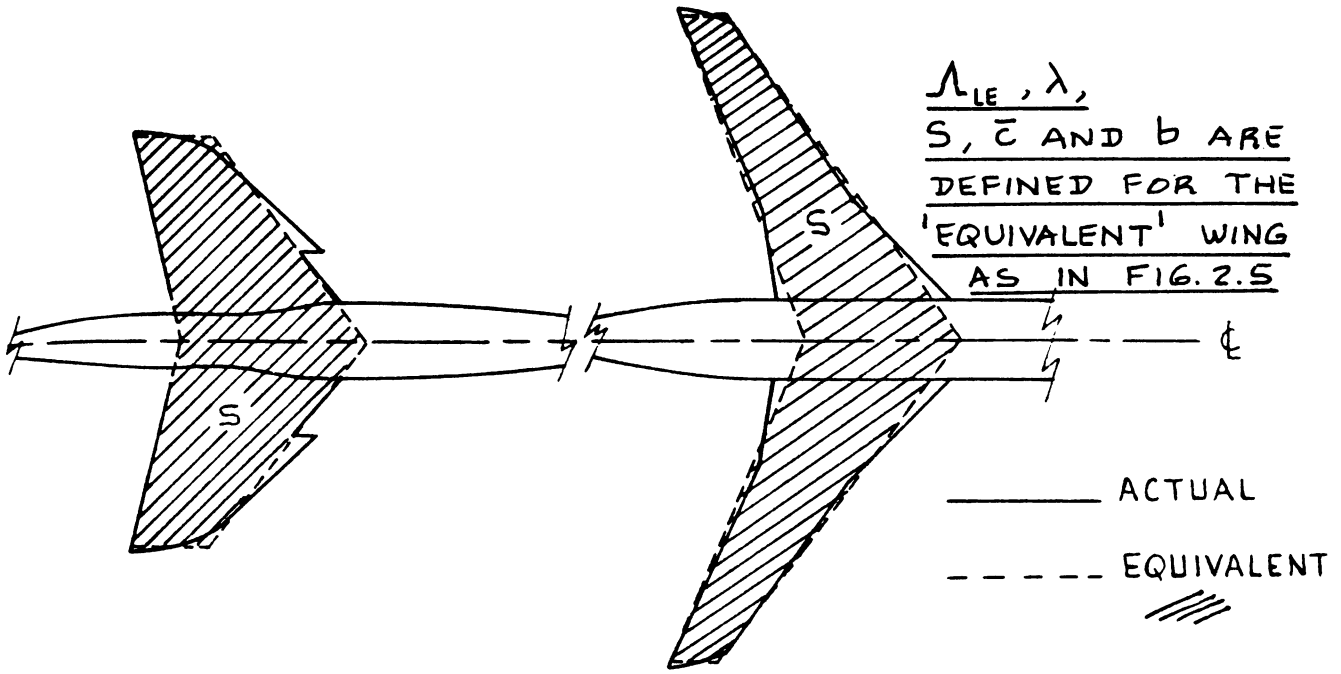

Figure 2.6 Reference Geometry and Equivalent Planform for Non Straight, Tapered Wings

$$y_{\bar{c}} = \frac{2}{S}\int_{0}^{b/2} y\,c(y)\,dy \qquad x_{LE_{\bar{c}}} = \frac{1}{S}\int_{-b/2}^{+b/2} x_{LE}(y)\,c(y)\,dy$$

$$S = \int_{-b/2}^{b/2} c(y)\,dy \qquad \bar{c} = \frac{1}{S}\int_{-b/2}^{+b/2} c^2(y)\,dy$$

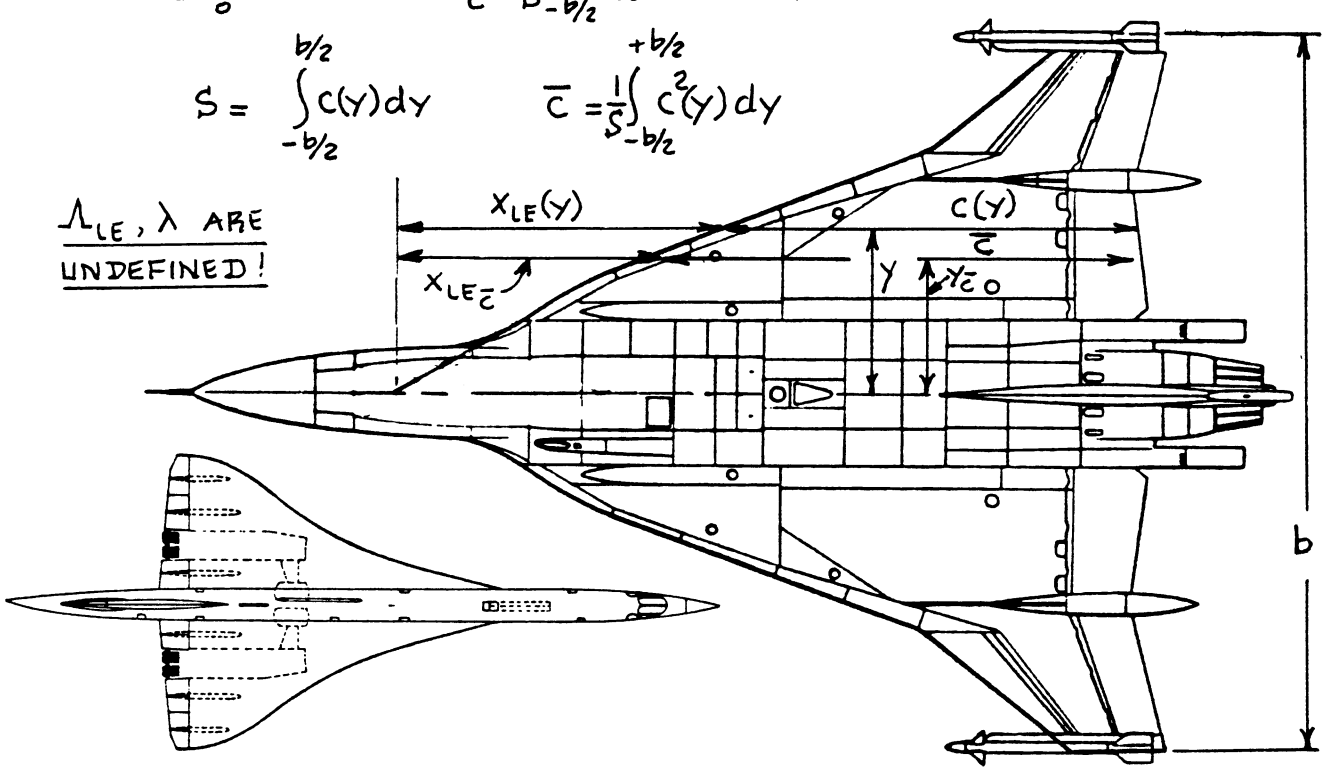

Figure 2.7 Reference Geometry for Arbitrary Wings

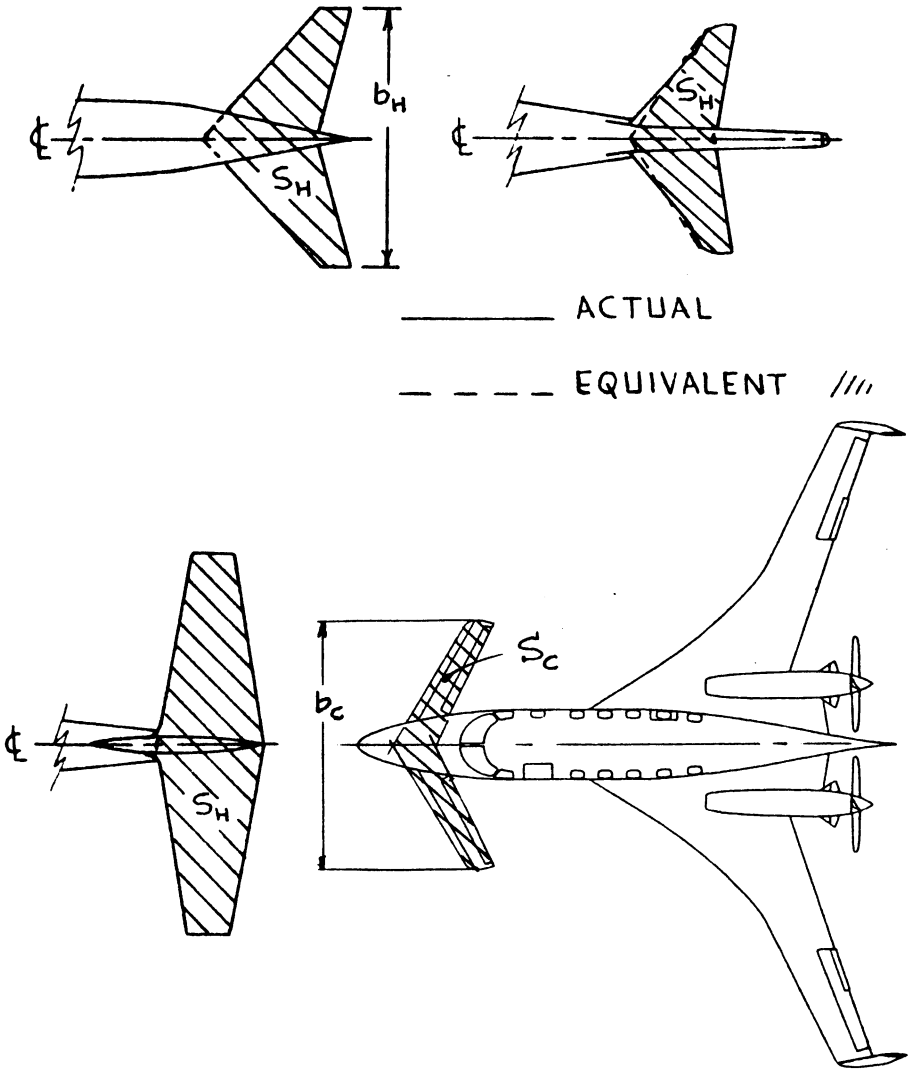

Figure 2.8 Reference Geometries for Horizontal Tails and for Canards

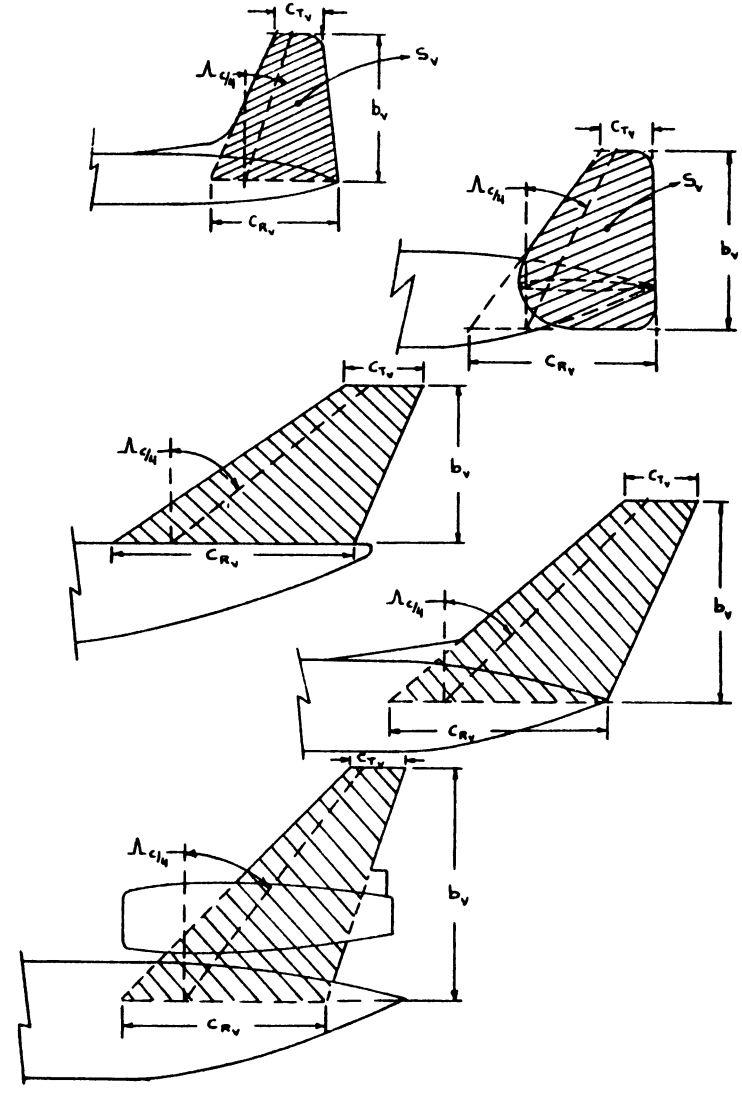

Figure 2.9 Reference Geometries for Vertical Tails

3. SUMMARY OF DRAG CAUSES AND DRAG MODELLING

The purpose of this chapter is to summarize the physical causes of drag, to present ways of breaking down drag and to discuss frequently used methods of modelling drag for use in airplane performance calculations.

For a more detailed study of drag, drag causes and drag computation methods the reader should consult references 8-15.

3.1 PHYSICAL CAUSES OF DRAG

Total drag is defined as the sum of zero-lift drag and induced drag (or drag due to lift):

$$\text{Total Drag} = \text{Zero-lift Drag} + \text{Drag-due-to-lift} \qquad (3.1)$$

This basic breakdown for will be used in all three speed ranges used in this text:

1. Subsonic speed range: $0 < M < 0.6$
2. Transonic speed range: $0.6 < M < 1.2$
3. Supersonic speed range: $1.2 < M < 3.0$

The zero-lift drag of an airplane is considered to be the sum of skin friction drag and pressure drag:

$$\text{Zero-lift Drag} = \text{Skin-friction Drag} + \text{Pressure Drag} \qquad (3.2)$$

Skin-friction drag is caused by the shearing stresses within the thin layer of air adjacent to the skin. This layer of air is called the boundary layer. It arises as a result of the viscosity of the air which resists a body passing through it.

The magnitude of this viscous resistance depends on whether the flow in the boundary layer is laminar or turbulent. Whether the boundary layer is laminar or turbulent depends on the Reynolds Number, on the pressure distribution and on the roughness of the skin (surface).

Pressure drag is caused by the displacement thickness of the boundary layer, which prevents full pressure recovery at the trailing edge. As long as the boundary layer remains attached, pressure drag tends to be small in subsonic flight. However, in transonic and in supersonic flight pressure drag is identified with wave drag and then becomes very significant.

When the boundary layer becomes separated and/or when bluntness is significant, pressure drag can be large in any speed regime.

Drag-due-to-lift is considered to be the sum of induced drag and viscous drag-due-to-lift:

$$\text{Drag-due-to-lift} = \text{Induced Drag} + \text{Viscous Drag-due-to-lift} \qquad (3.3)$$

The induced drag, also called trailing edge vortex drag (or simply vortex drag) depends on the spanwise distribution of lift. It is proportional to the square of the lift coefficient.

The viscous drag due to lift results from the change in the boundary layer development as a result of lift. The upper surface boundary layer thickness increases with increasing angle of attack. This in turn results in an increase in the so-called profile drag which itself is the sum of skin-friction drag and pressure drag.

Figure 3.1 illustrates a drag breakdown according to these physical causes. Intermediate drag types such as induced drag, form drag and profile drag are indicated also in Figure 3.1.

A major problem is that the basic drag causes in Equations (3.1)-(3.3) are interdependent. The flow regime in which the airplane is operating: Mach number, Reynold's number and angle of attack all influence the basic drag causes.

In predicting total airplane drag some 'book-keeping' procedures must be adopted. One 'book-keeping' decision which needs to be made is that which splits drag from thrust. In this text the position is taken that flow phenomena outside the airplane are associated with the generation of drag. Flow phenomena inside the airplane which are not associated with the production of thrust, are also considered to produce drag. An example of this is cooling air flow around a piston engine.

On the other hand, flow phenomena inside engine(s) (and/or nacelles) are associated with the production of thrust (or power).

Chapters 4 and 5 deal with airplane drag. Chapters 6 and 7 deal with airplane thrust (or power).

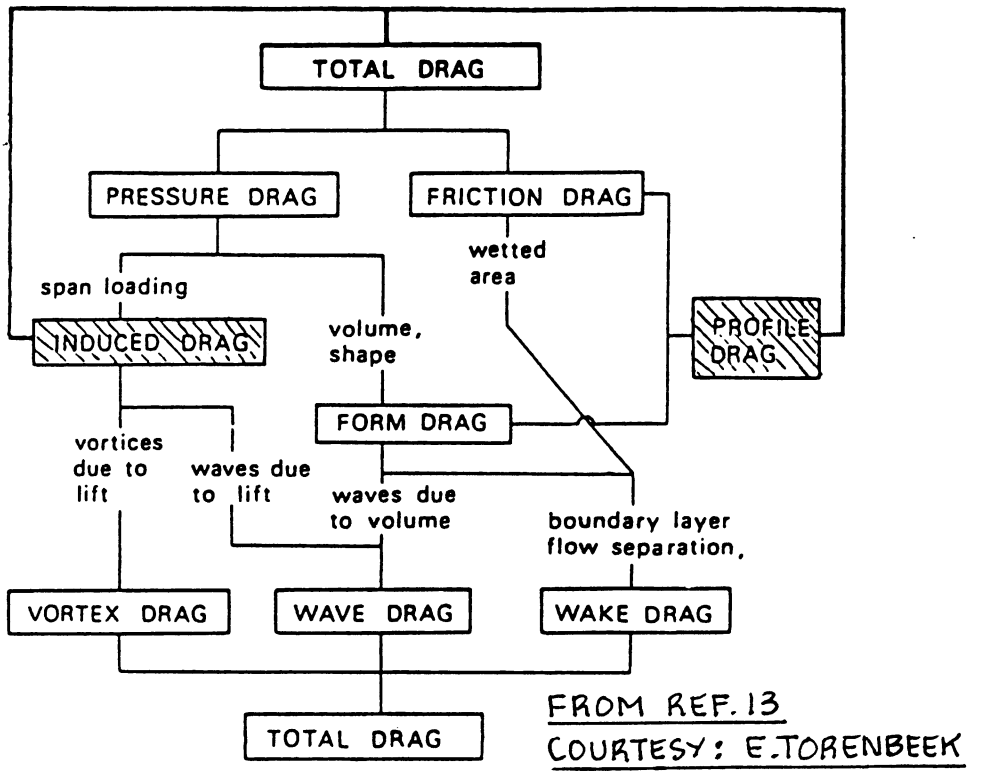

Figure 3.1 Drag Breakdown According to Physical Causes

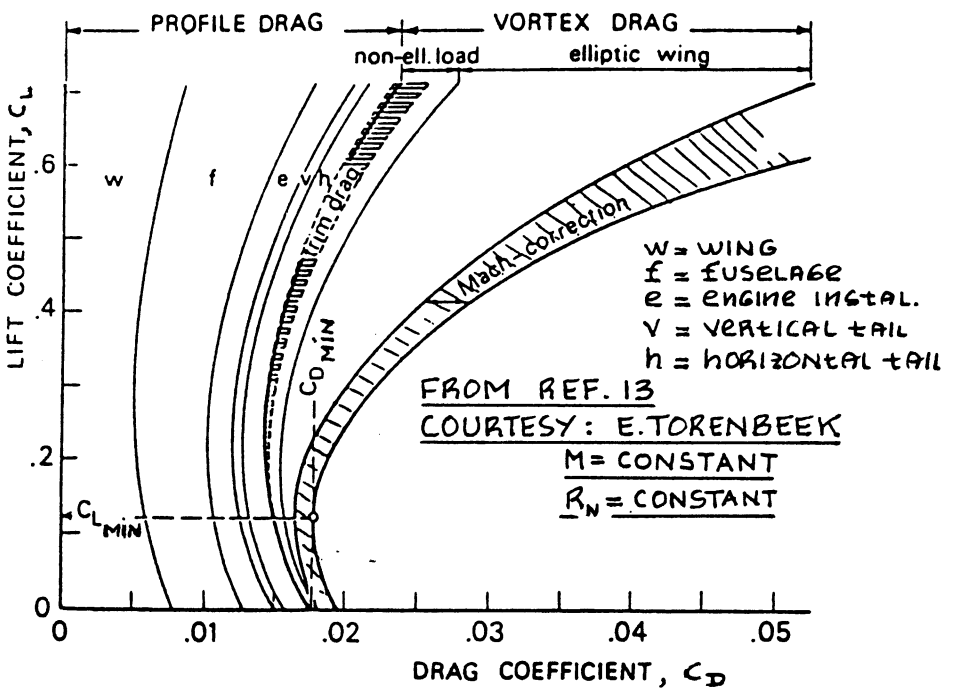

Figure 3.2 Typical Drag Breakdown for a Transport Jet

3.2 DRAG BREAKDOWN METHOD

It is useful to break down the drag of an airplane into that caused by its components. Figure 3.2 shows a typical drag breakdown for a transport operating at a high subsonic Mach number.

The drag breakdown method used in this text considers total airplane drag to be the sum of component drag contributions according to:

Airplane Drag = Component drag of (Wing + Fuselage + + Empennage + Nacelle/Pylon + Flap + + Landing Gear + Canopy/Windshield + + Store + Trim + Interference + + Miscellaneous) (3.4)

Chapter 4 presents a method for computing component drag for subsonic, transonic and supersonic flight.

3.3 DRAG MODELLING FOR PERFORMANCE CALCULATIONS

To enable the rapid calculation of airplane performance (discussed in Part VII), it is useful to represent airplane drag polars by simple mathematical models.

In addition, it is necessary to assume that the airplane can be held in a 'trimmed' state: no moments are acting on the airplane and the pilot does not have to exert a force on the cockpit controls. Requirements for trim are discussed in detail in Ref.16. Part VII contains methods for predicting trimmability.

To trim an airplane usually causes extra drag: trim drag. Eqn.(3.4) includes a term which accounts for trim drag. All drag polars used in performance calculations are assumed to be 'trimmed' drag polars.

For essentially uncambered airplanes in subsonic flight, the drag polar may be modelled as:

$$C_D = C_{D_o} + (C_L)^2/\pi Ae \qquad (3.5)$$

Note that the minimum drag occurs at $C_L = 0$.

The F4C fighter airplane is an example of an essentially uncambered airplane. Figure 3.3 shows its drag polar. It is very well represented by Eqn.(3.5).

For cambered airplanes, the minimum value of drag

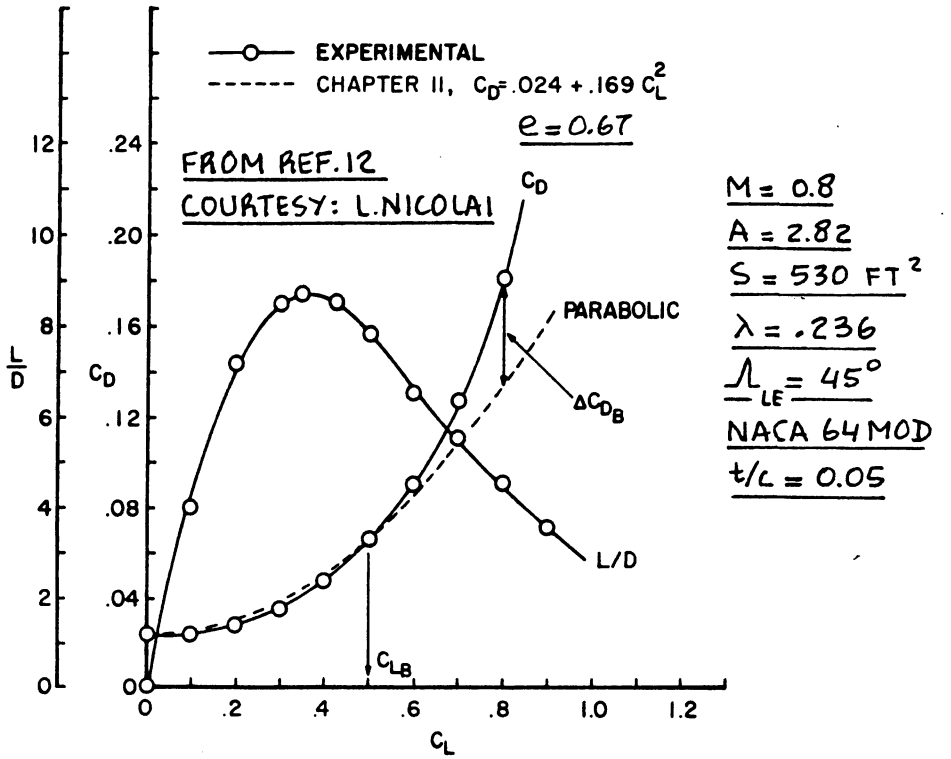

Figure 3.3 Drag Polar for the McDonnell-Douglas F4C

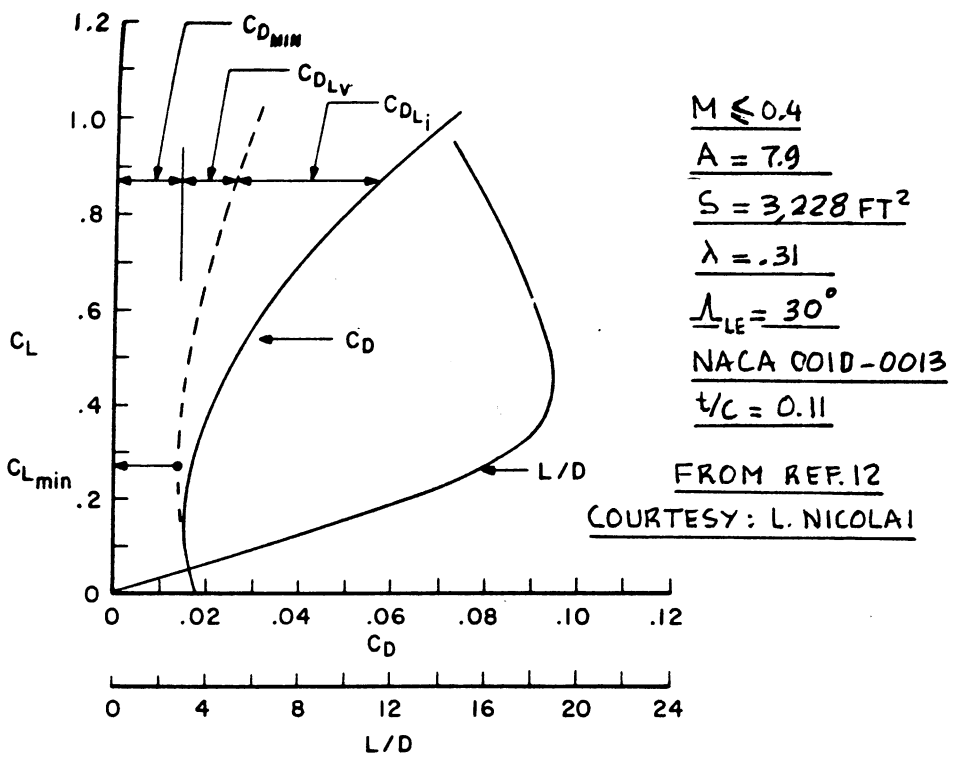

Figure 3.4 Drag Polar for the Lockheed C-141

does not occur at $C_L = 0$ and it becomes necessary to represent the drag polar as:

$$C_D = C_{D_{min}} + K''(C_L - C_{L_{min}})^2 + K'C_L^2 \qquad (3.6)$$

Note that minimum drag in this case occurs at a lift coefficient of $C_L = \{K''/(K''+K')\}C_{L_{min}}$.

The Lockheed C-141 Starlifter is a cambered airplane despite the fact that its wing uses symmetrical airfoil sections (average section is NACA 0011). Since the wing is installed at an incidence angle of 3.2 degrees the airplane acts like it is cambered. Figure 3.4 shows the C-141 low speed drag polar. Note that: $C_{D_{min}} = 0.0140$, which occurs at $C_{L_{min}} = 0.27$.

Note, that for an uncambered airplane Eqn.(3.6) reduces to Eqn.(3.5) since in that case: $C_{L_{min}} = 0$ and:

$$K'' + K' = 1/\pi Ae \text{ (no camber only!)} \qquad (3.7)$$

For airplanes flying at relatively high angles of attack, the drag polars deviate significantly from the parabolic shape. This is caused by flow separation resulting in a steep rise in pressure drag. In that case the polar is modelled as:

$$C_D = C_{D_{min}} + K''(C_L - C_{L_{min}})^2 + K'C_L^2 + K_B(C_L - C_{L_B})^2 \qquad (3.8)$$

Figure 3.5 illustrates a drag polar with this type of behavior.

C_{L_B} is the lift coefficient for which the steep drag rise due to separation begins. The factor K_B is called the break drag-due-to-lift factor and is defined as:

$$K_B = 0 \text{ for } C_L < C_{L_B}$$
$$K_B > 0 \text{ for } C_L > C_{L_B} \qquad (3.9)$$

Table 3.1 presents a summary of important lift-to-drag ratios based on the drag polar models of Eqns 3.5 and 3.6. These lift-to-drag ratios and the lift coefficients at which they occur are used in the performance calculations presented in Part VII.

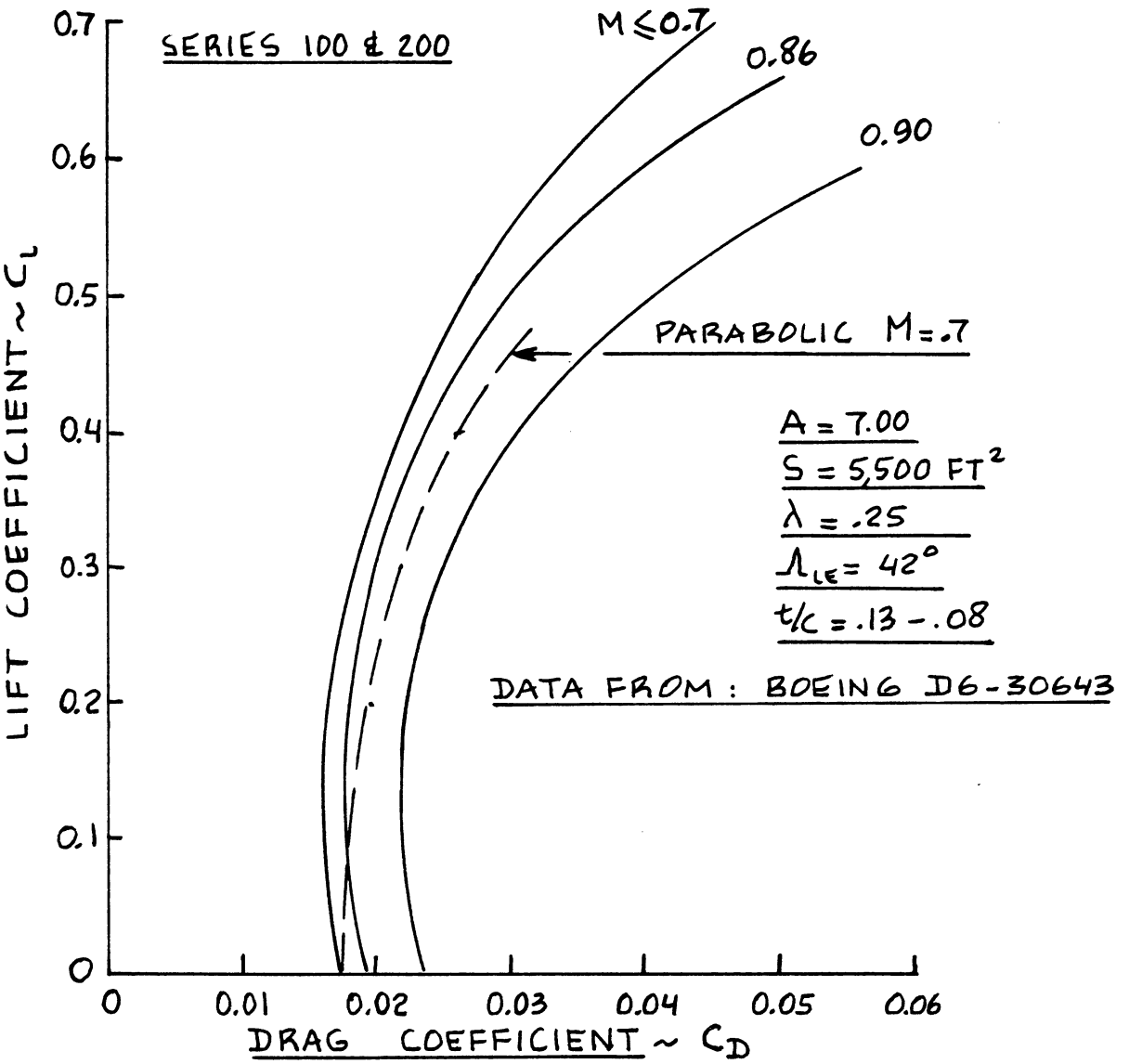

Figure 3.5 Drag Polars for the Boeing 747

Table 3.1 Maximum Lift-to-Drag Ratios and Corresponding Lift Coefficients

Drag Polar According to Eqn.(3.5)

$$(L/D)_{max} = 0.5/(KC_{D_o})^{1/2} \quad (3.10)$$

$$C_{L_{(L/D)_{max}}} = (C_{D_o}/K)^{1/2} \quad (3.11)$$

where: $K = 1/\pi Ae$ (3.12)

Drag Polar According to Eqn.(3.6)

$$(L/D)_{max} = (P^{1/2})/[C_{D_{min}} + K''\{(P^{1/2}) - C_{L_{min}}\}^2 + K'P] \quad (3.13)$$

where: $P = \{C_{D_{min}} + K''(C_{L_{min}})^2\}/(K' + K'')$ (3.14)

$$C_{L_{(L/D)_{max}}} = (P)^{1/2} \quad (3.15)$$

Note that equations (3.13) and (3.15) reduce to equations (3.10) and (3.11) for the case of $K''=0$ and $C_{D_{min}} = C_{D_o}$. In that case, $K' = K$.

4. DRAG POLAR PREDICTION METHODS

A Class I method for drag polar prediction was presented in Part I (Ch. 3). The purpose of this chapter is to present a Class II method for predicting drag polars of airplanes during the preliminary design phase. The method is based on Reference 9 and applies to airplanes with essentially straight, tapered wings. For other wing planforms, see Reference 9.

4.1 DRAG BREAKDOWN PROCEDURE

Total airplane drag in lbs is written as:

$$D = C_D \bar{q} S \tag{4.1}$$

where: C_D = the total airplane drag coefficient

$$\bar{q} = 0.5\rho(U_1)^2 = 1482\delta M^2, \text{ also called} \tag{4.2}$$

free stream dynamic pressure, with:

ρ = air density: see Appendix A.

U_1 = steady state airspeed

δ = pressure ratio: see Appendix A.

$$M = U_1/a = \text{Mach number} \tag{4.3}$$

a = speed of sound: see Appendix A.

S = the wing planform or reference area. Figures 2.5-2.7 define how this area is normally defined for a range of wing designs.

The total airplane drag coefficient is normally broken down into the following components:

$$C_D = C_{D_{wing}} + C_{D_{fus}} + C_{D_{emp}} + C_{D_{np}} + C_{D_{flap}} + C_{D_{gear}} + C_{D_{cw}} + C_{D_{store}} + C_{D_{trim}} + C_{D_{int}} + C_{D_{misc}} \tag{4.4}$$

where: $C_{D_{wing}}$ = wing drag coefficient: Section 4.2

$C_{D_{fus}}$ = fuselage drag coefficient: Section 4.3

$C_{D_{emp}}$ = empennage drag coefficient: Section 4.4

$C_{D_{np}}$ = nacelle/pylon drag coefficient, including cooling drag: Section 4.5

$C_{D_{flap}}$ = leading/trailing edge flap drag coefficient: Section 4.6

$C_{D_{gear}}$ = landing gear drag coefficient: Section 4.7

$C_{D_{cw}}$ = canopy/windshield drag coefficient: Section 4.8

$C_{D_{store}}$ = store(s) drag coefficient: Section 4.9

$C_{D_{trim}}$ = trim drag coefficient: Section 4.10

$C_{D_{int}}$ = interference drag coefficient: Section 4.11

$C_{D_{misc}}$ = miscellaneous drag coefficient, typically caused by such things as: speed brakes, struts, inlet drag, antennas, gaps and surface roughnesses: Section 4.12

Sections 4.2 through 4.12 present methods for predicting the drag coefficient components in Eqn.(4.2). Numerical examples of drag breakdowns and examples of airplane drag polars are presented in Chapter 5.

Important Notes: 1.) The drag prediction methods of Sections 4.2 through 4.5 apply only to flight cases where the boundary layer is mostly turbulent. If extensive laminar flow runs are present (for example because of use of natural laminar flow airfoils or because of use of 'forced' laminar flow by suction), Section 4.13 may be used to obtain the necessary drag corrections.

2.) The drag prediction methods of Sections 4.2 through 4.5 apply only to 'smooth' surfaces. If surface roughness is present, the procedure of Sub-section 4.12.2 should be used in conjunction with the methods of Sections 4.2 through 4.5.

4.2 WING DRAG COEFFICIENT PREDICTION

4.2.1 Subsonic Wing Drag Coefficient

The subsonic wing drag coefficient is found from:

$$C_{D_{wing}} = C_{D_{o_w}} + C_{D_{L_w}} \qquad (4.5)$$

where: $C_{D_{o_w}}$ = wing zero-lift drag coefficient, see 4.2.1.1.

$C_{D_{L_w}}$ = wing drag coefficient due to lift, see 4.2.1.2.

4.2.1.1 Wing zero-lift drag coefficient

The subsonic wing zero-lift drag coefficient may be computed from:

$$C_{D_{o_w}} = (R_{wf})(R_{LS})(C_{f_w})\{1 + L'(t/c) + 100(t/c)^4\}S_{wet_w}/S \qquad (4.6)$$

where: R_{wf} = wing/fuselage interference factor: see Figure 4.1. For a flying wing: $R_{wf} = 1.0$.

R_{LS} = lifting surface correction factor found from Figure 4.2.

C_{f_w} = turbulent flat plate friction coefficient of the wing.

The general turbulent, flat plate friction coefficient, C_f is shown in Figure 4.3 as a function of Mach number and of Reynolds number, R_N.

For the wing, use: $R_{N_w} = \rho U_1 \bar{c}_{w_e}/\mu \qquad (4.7)$

where: $\bar{c}_{w_e}$ = exposed wing m.g.c. (= wing m.g.c. for a flying wing)

μ = coefficient of viscosity of air: see Appendix A.

L' = airfoil thickness location parameter: see Figure 4.4.

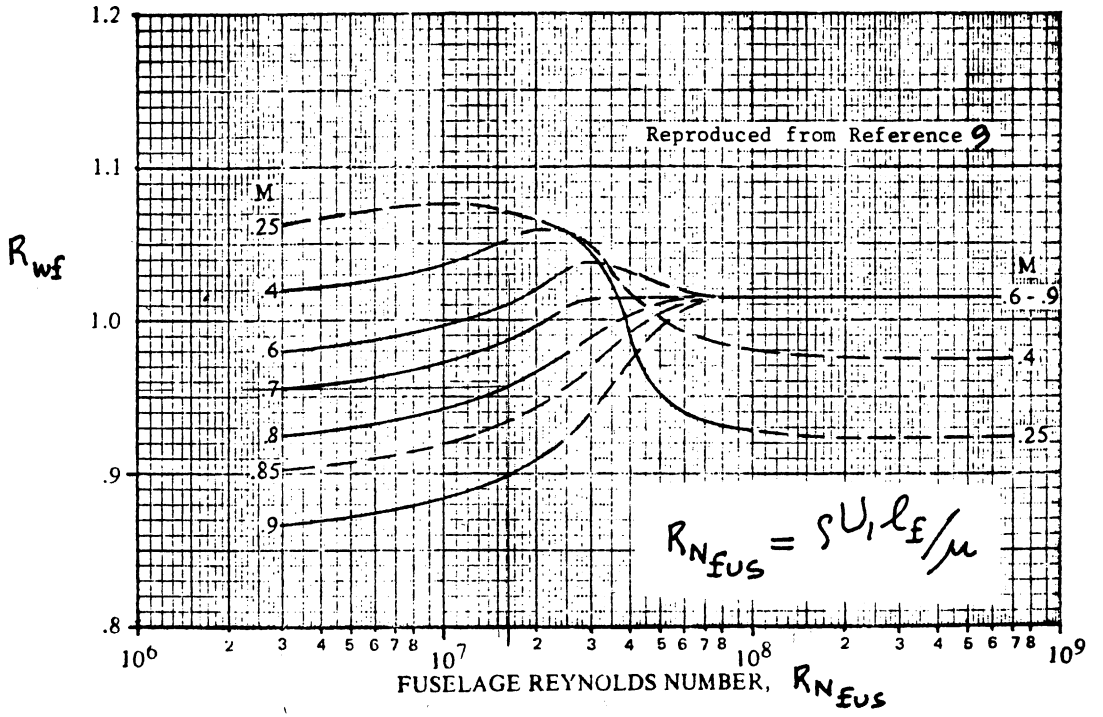

Figure 4.1 Wing Fuselage Interference Factor

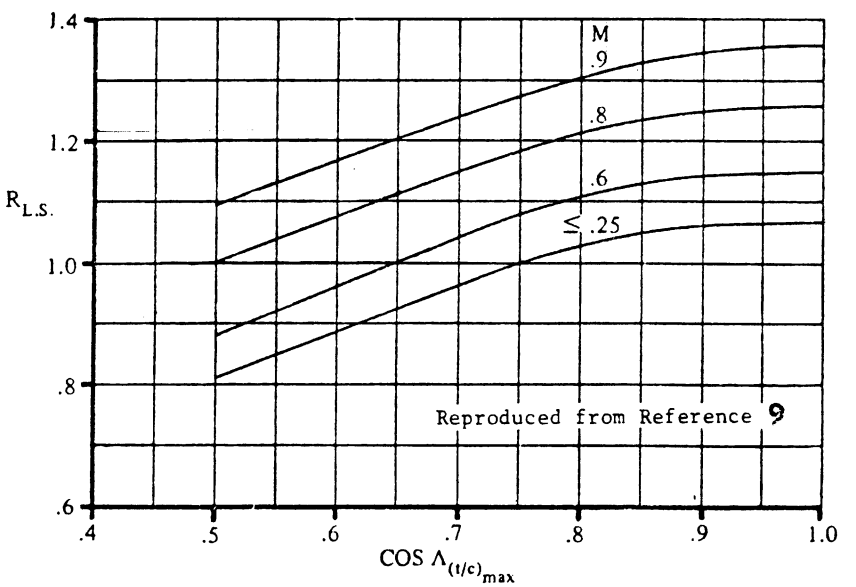

Figure 4.2 Lifting Surface Correction Factor

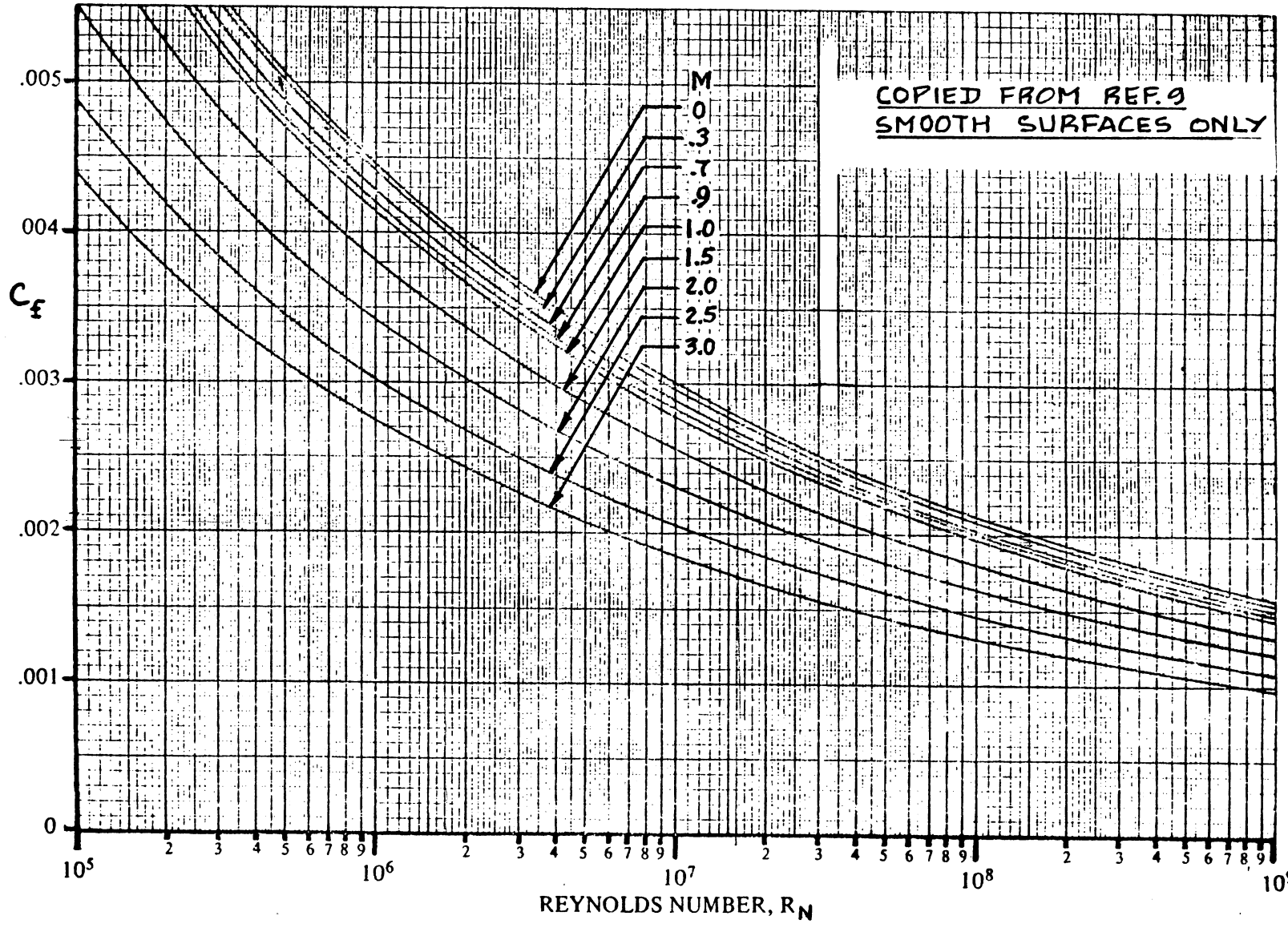

Figure 4.3 Turbulent Mean Skin-Friction Coefficient

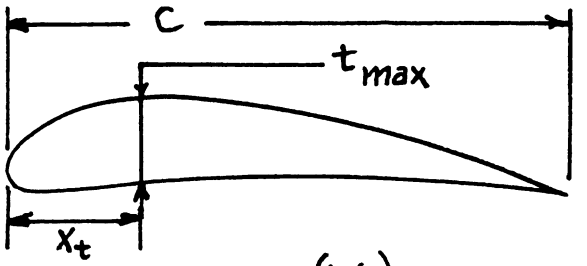

$L' = 1.2$ FOR $(t/c)_{max}$ AT $X_t \geq 0.30C$

$L' = 2.0$ FOR $(t/c)_{max}$ AT $X_t < 0.30C$

Figure 4.4 Airfoil Thickness Location Parameter

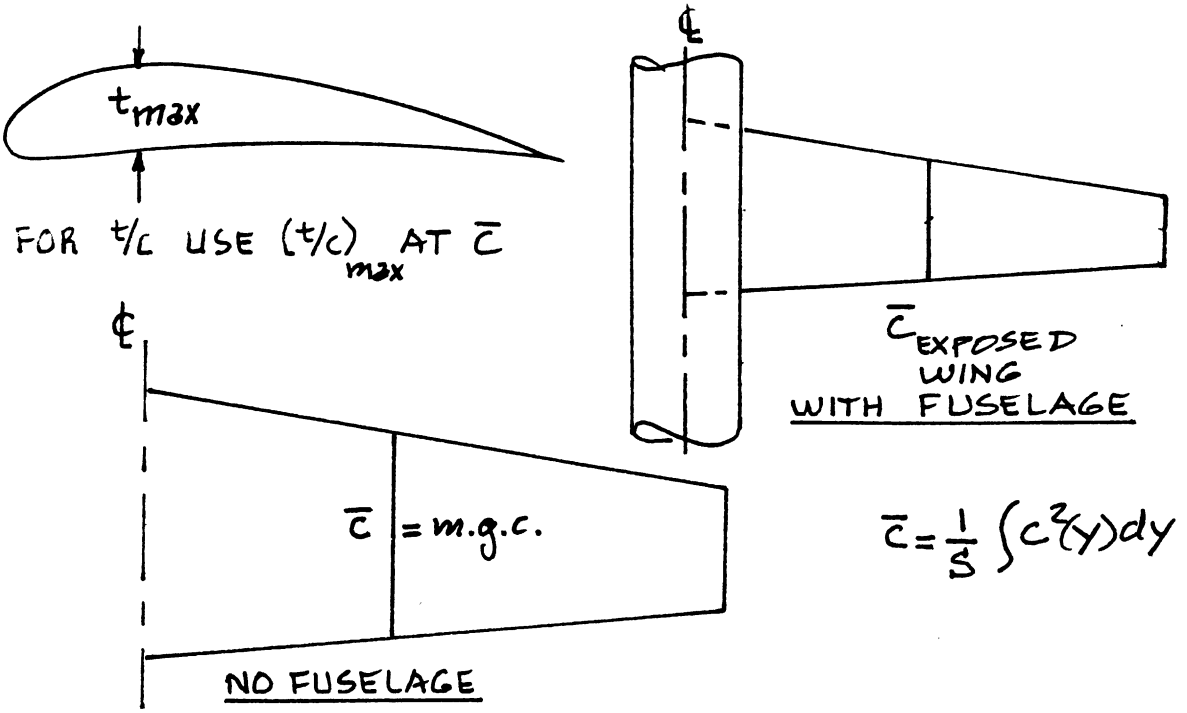

Figure 4.5 Definition of Thickness Ratio for a Wing

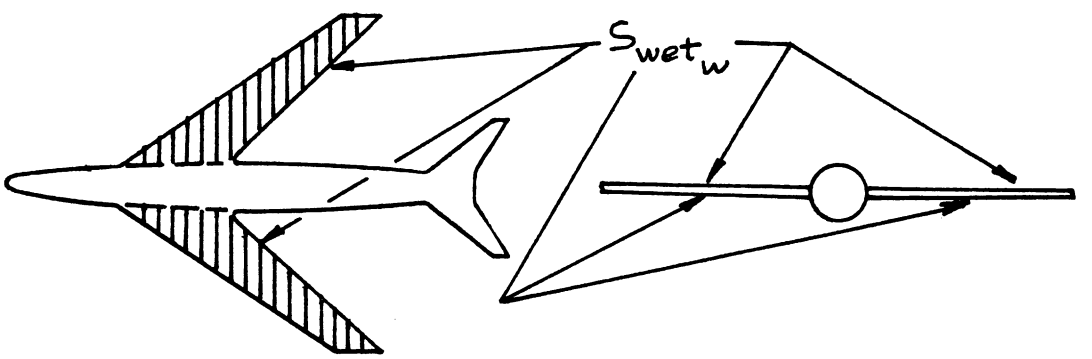

Figure 4.6 Definition of Wing Wetted Area

t/c = thickness ratio defined at the mean geometric chord of the wing: see Figure 4.5.

S_{wet_w} = wetted area of the wing: see Figure 4.6 and Appendix B.

S = wing or reference area. This is normally the wing planform area: see Figs 2.5-2.7.

4.2.1.2 Wing drag coefficient due to lift

The wing drag coefficient due to lift is found from:

$$C_{D_{L_w}} = (C_{L_w})^2/\pi Ae + 2\pi C_{L_w}\varepsilon_t v + 4\pi^2(\varepsilon_t)^2 w \qquad (4.8)$$

where: C_{L_w} = wing lift coefficient, defined as:

$$C_{L_w} = C_L - C_{L_c}S_c/S - C_{L_h}S_h/S \qquad (4.9)$$

where: $C_L = W/\bar{q}S$ (4.10)

The canard and horizontal tail lift coefficients, C_{L_c} and C_{L_h} respectively, are determined from trim considerations. Their values depend on the center of gravity location. To determine these empennage lift coefficients a trim calculation must be performed. This is done with the help of a trim diagram. Part VII contains a method for constructing a trim diagram.

In early preliminary design it is sufficiently accurate to set:

$$C_{L_w} = 1.05C_L \qquad (4.11)$$

A = wing aspect ratio = b^2/S, where:
b = wing span: see Figures 2.5 - 2.7.

e = span efficiency factor, defined as:

$$e = 1.1(C_{L_{\alpha_w}}/A)/\{R(C_{L_{\alpha_w}}/A) + (1 - R)\pi\} \qquad (4.12)$$

where: $C_{L_{\alpha_w}}$ is the wing lift-curve slope which can be found with the help of Chapter 10.

R = leading edge suction parameter as defined in Figure 4.7.

ε_t = wing twist angle, positive for wash-in, negative for wash-out, see Figure 4.8.

v = induced drag factor due to linear twist, see Figures 4.9.

w = zero-lift drag factor due to linear twist, see Figures 4.10.

Note: this method for determining C_{L_w} applies only for $C_{L_w} < C_{L_B}$, the value of lift coefficient where the flow begins to separate.

4.2.2 Transonic Wing Drag Coefficient

The transonic wing drag coefficient is found from:

$$C_{D_{wing}} = C_{D_{o_w}} + C_{D_{L_w}} \qquad (4.13)$$

where: $C_{D_{o_w}}$ = wing zero-lift drag coefficient, see 4.2.2.1.

$C_{D_{L_w}}$ = wing drag coefficient due to lift, see 4.2.2.2.

4.2.2.1 Wing zero-lift drag coefficient

In the transonic speed range the wing zero-lift drag coefficient is found from:

$$C_{D_{o_w}} = C_{D_{o_w}\ \text{at } M=0.6} + C_{D_{w_{wave}}} \qquad (4.14)$$

where: $C_{D_{o_w}\ \text{at } M=0.6}$ = the drag coefficent due to friction. It is found from Eqn.(4.6) and is assumed to stay constant with Mach number in the entire transonic speed range.

$C_{D_{w_{wave}}}$ = the wing wave drag coefficient which depends on the wing sweep angle, $\Lambda_{c/4}$.

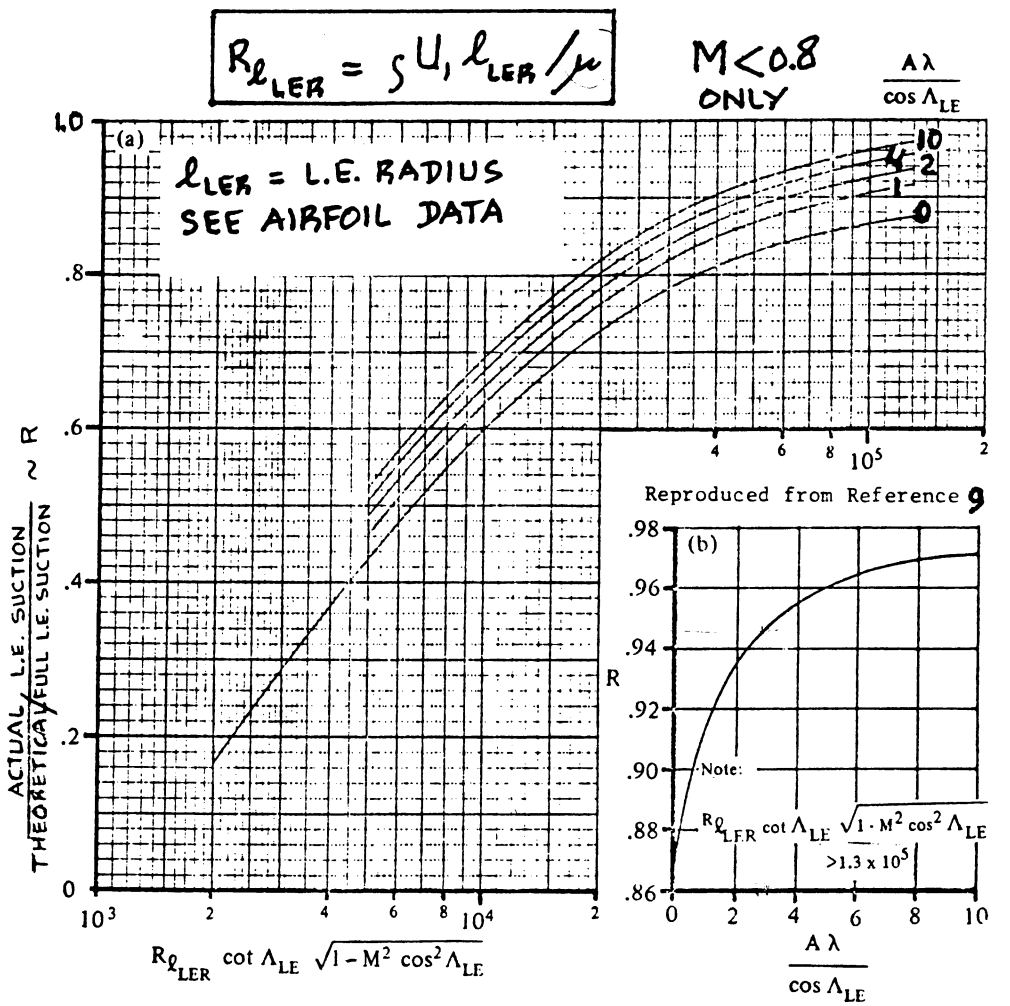

Figure 4.7 Leading Edge Suction Parameter

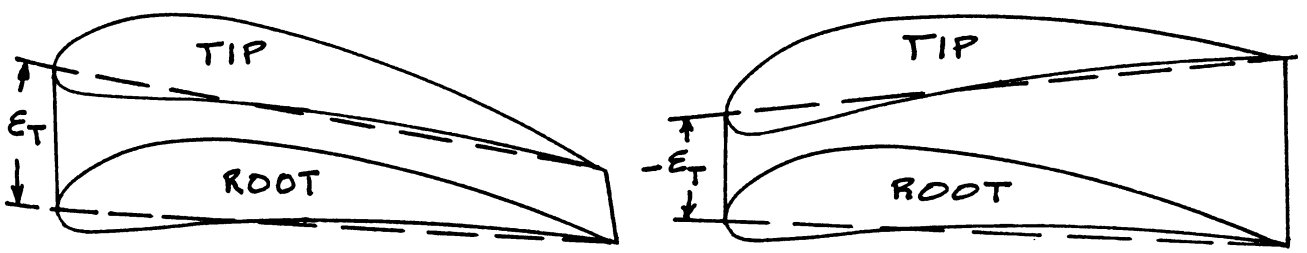

Figure 4.8 Definition of Wing Twist Angle

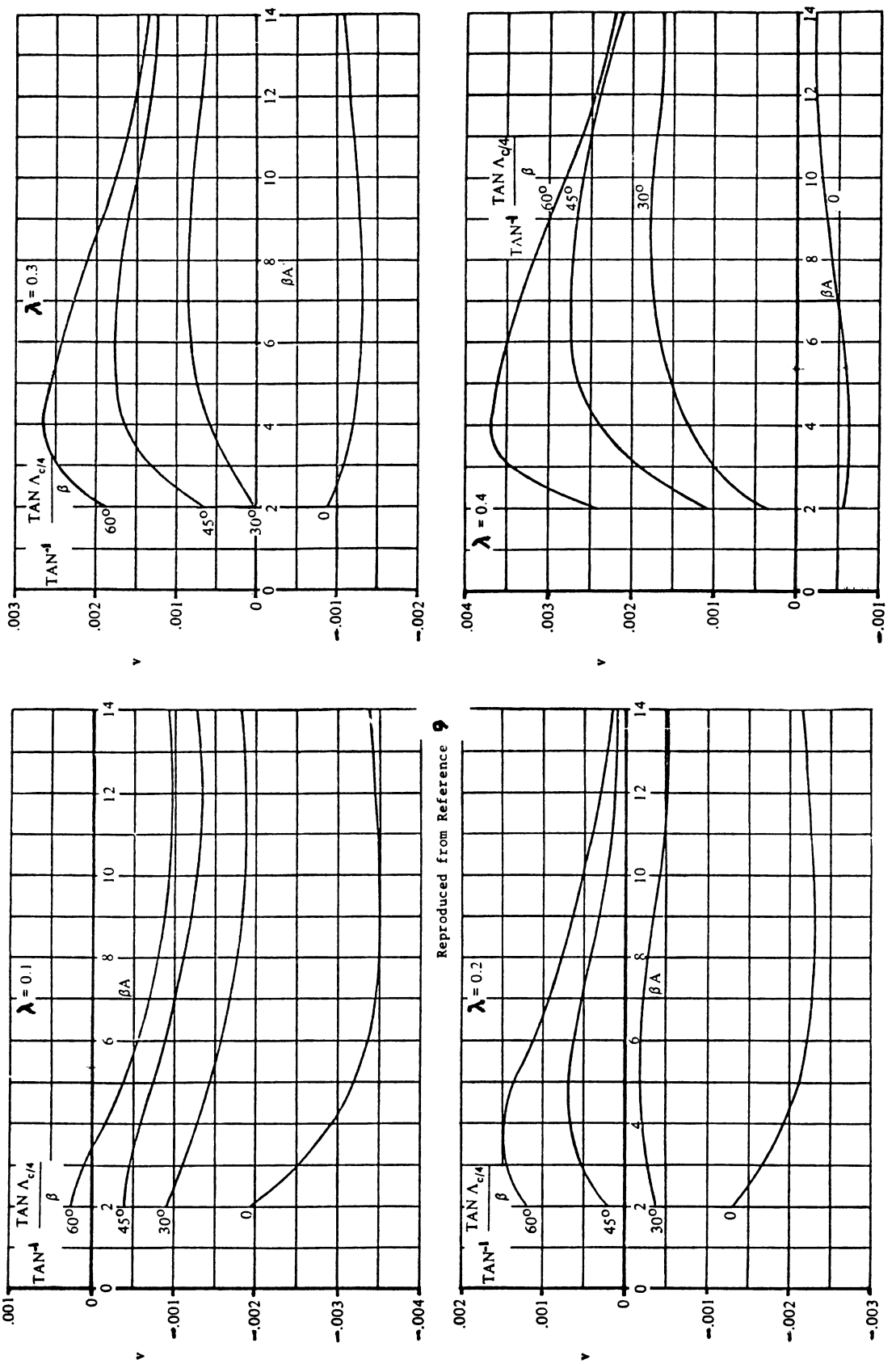

Figure 4.9a Induced Drag Factor due to Linear Twist

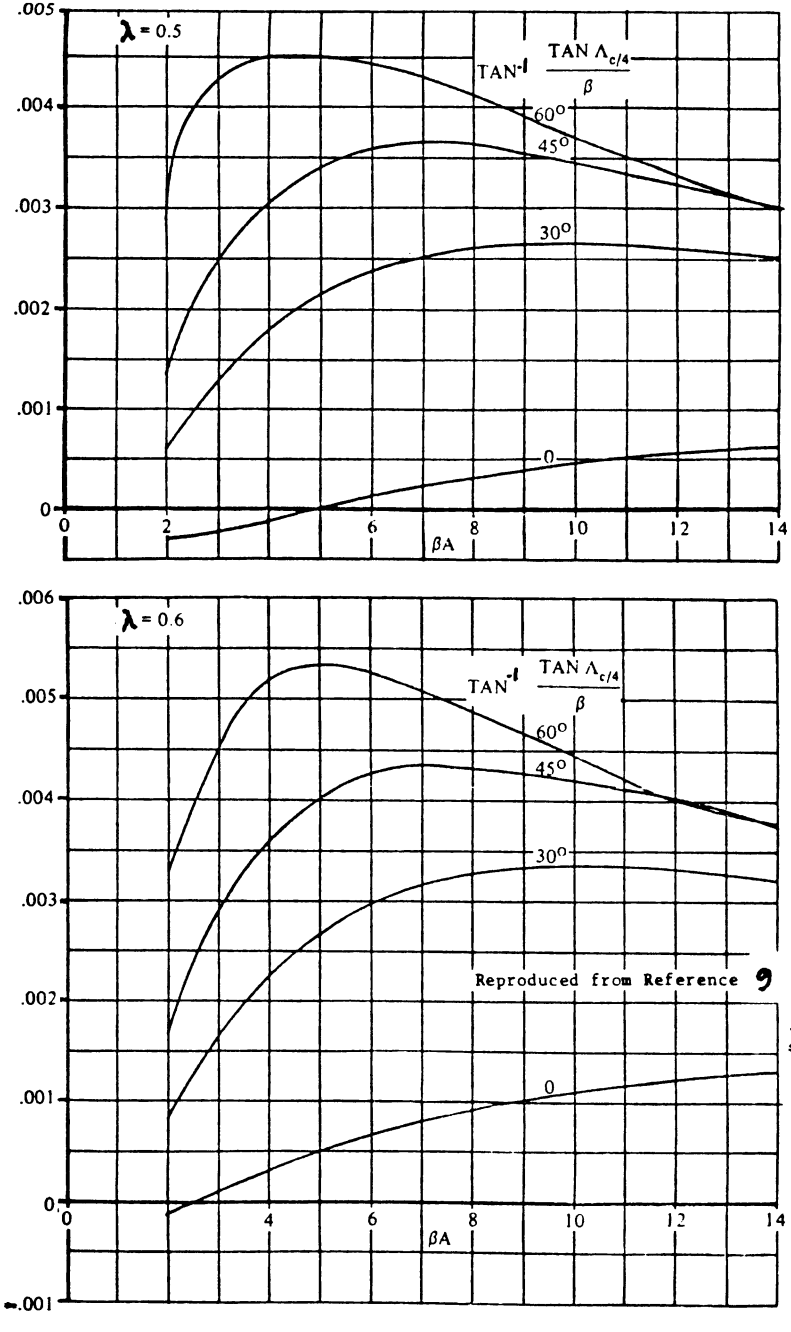

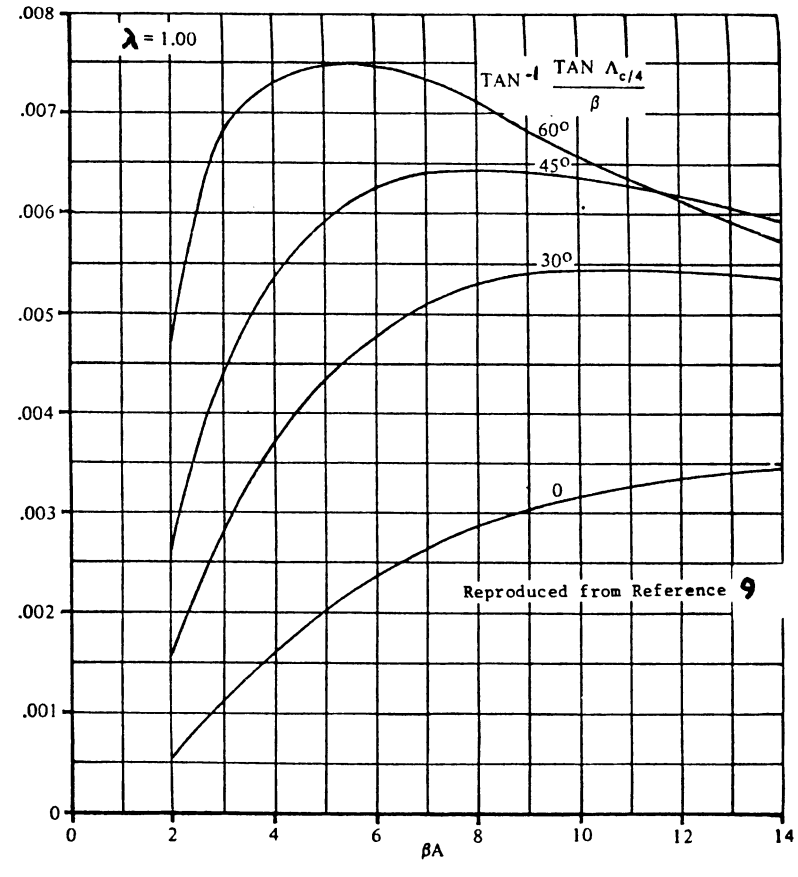

Figure 4.9b Induced Drag Factor due to Linear Twist

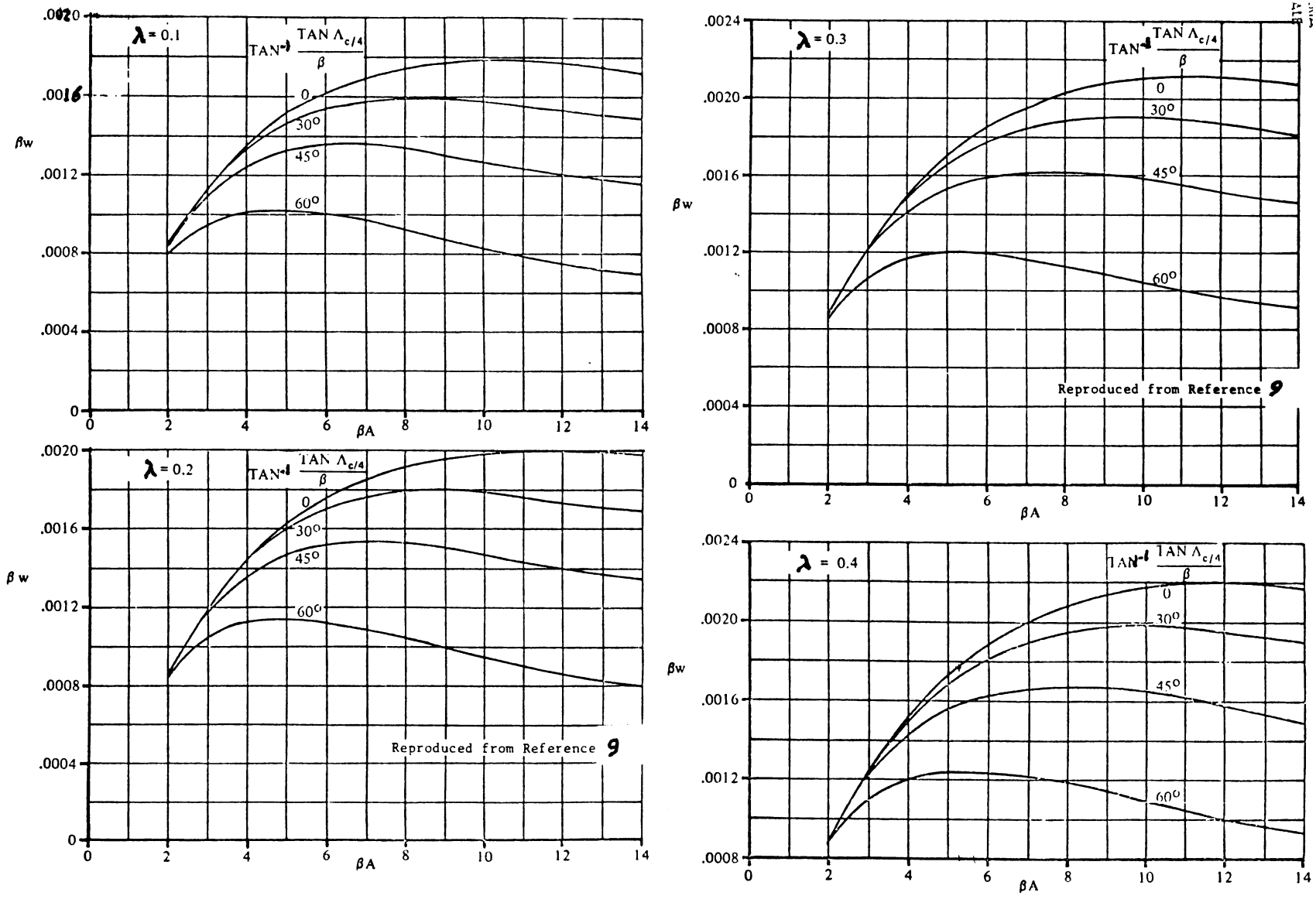

Figure 4.10a Zero-Lift Drag Factor due to Linear Twist

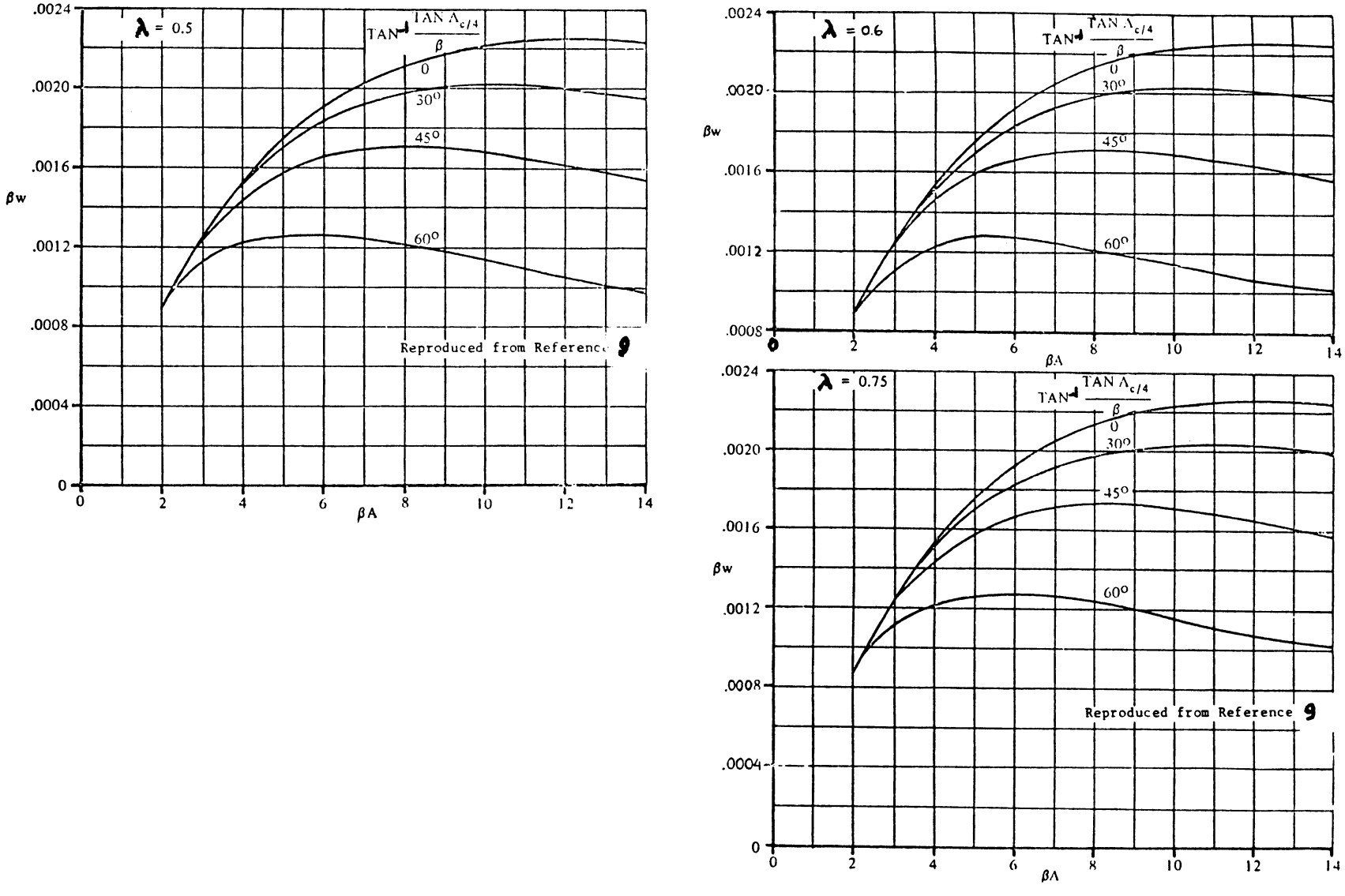

Figure 4.10b Zero-Lift Drag Factor due to Linear Twist

Unswept wings:

The wave drag coefficient, $C_{D_{w_{wave}}}$ for an unswept wing follows from Figure 4.11. This wave drag coefficient should be plotted against the Mach number in the transonic speed range.

Swept wings:

For a swept wing, proceed as follows:

From a plot of $C_{D_{w_{wave}}}$ versus M for the unswept wing of the same aspect ratio, and thickness ratio, read the following values:

M_{DD}, $C_{D_{w_{wave_{peak}}}}$ and $M_{at\ C_{D_{w_{wave_{peak}}}}}$.

Correct these values for sweep angle as follows:

$$M_{DD_{\Lambda_{c/4}}} = M_{DD}/(\cos\Lambda_{c/4})^{1/2} \qquad (4.15)$$

$$C_{D_{wave_{peak_{\Lambda_{c/4}}}}} = C_{D_{wave_{peak}}} (\cos\Lambda_{c/4})^{2.5} \qquad (4.16)$$

$$M_{at\ C_{D_{wave_{peak_{\Lambda_{c/4}}}}}} = \{M_{at\ C_{D_{wave_{peak}}}}\}/(\cos\Lambda_{c/4})^{1/2} \qquad (4.17)$$

Draw in the line of $C_{D_{w_{wave_{\Lambda_{c/4}}}}}$ versus Mach number in the transonic speed range. A typical result is illustrated in Figure 4.12.

4.2.2.2 Wing drag coefficient due to lift

The transonic wing drag coefficient due to lift is written as:

$$C_{D_{L_w}} = (C_{D_L}/C_L^{\,2})C_L^{\,2} \qquad (4.18)$$

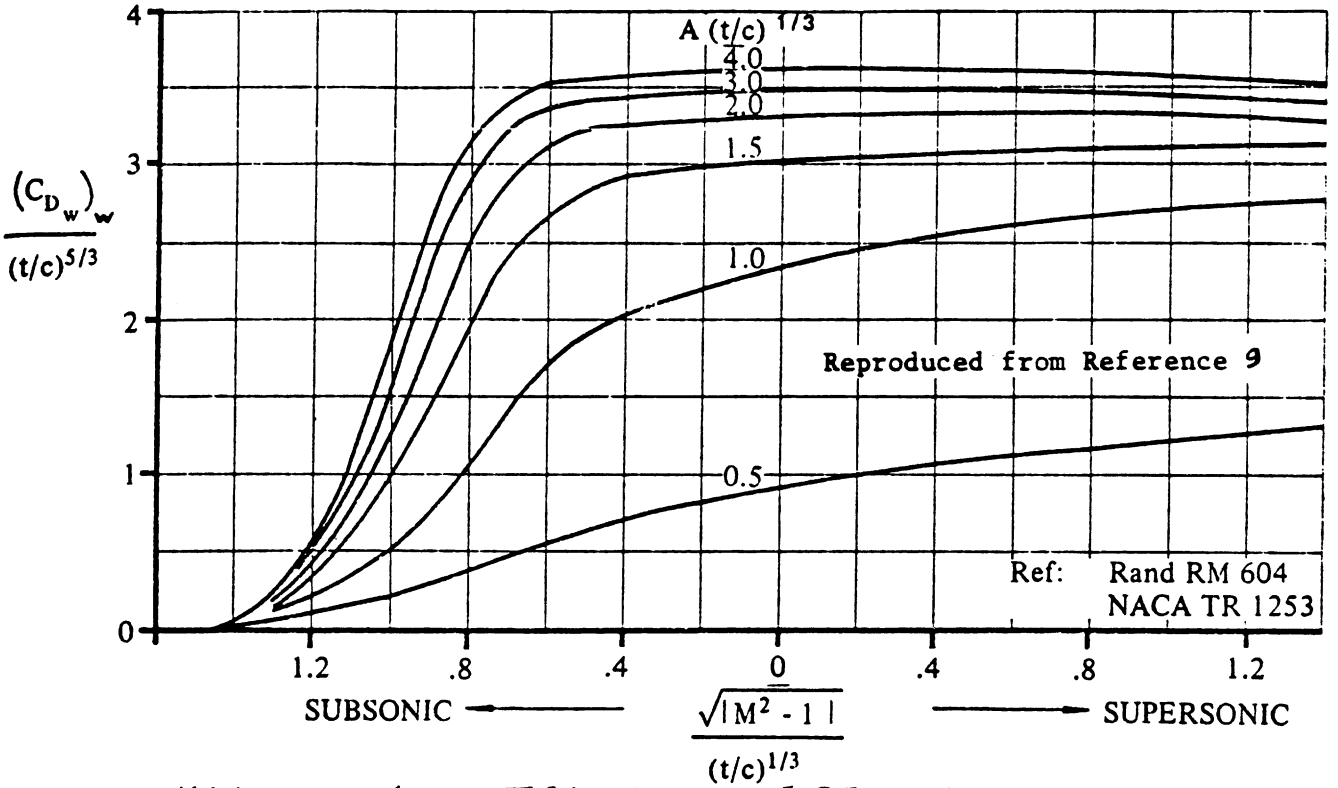

VALID ONLY AT TRANSONIC SPEEDS
VALID ONLY FOR UNSWEPT, ROUNDNOSE AIRFOILS

Figure 4.11 Zero-Lift Wave Drag Coefficient

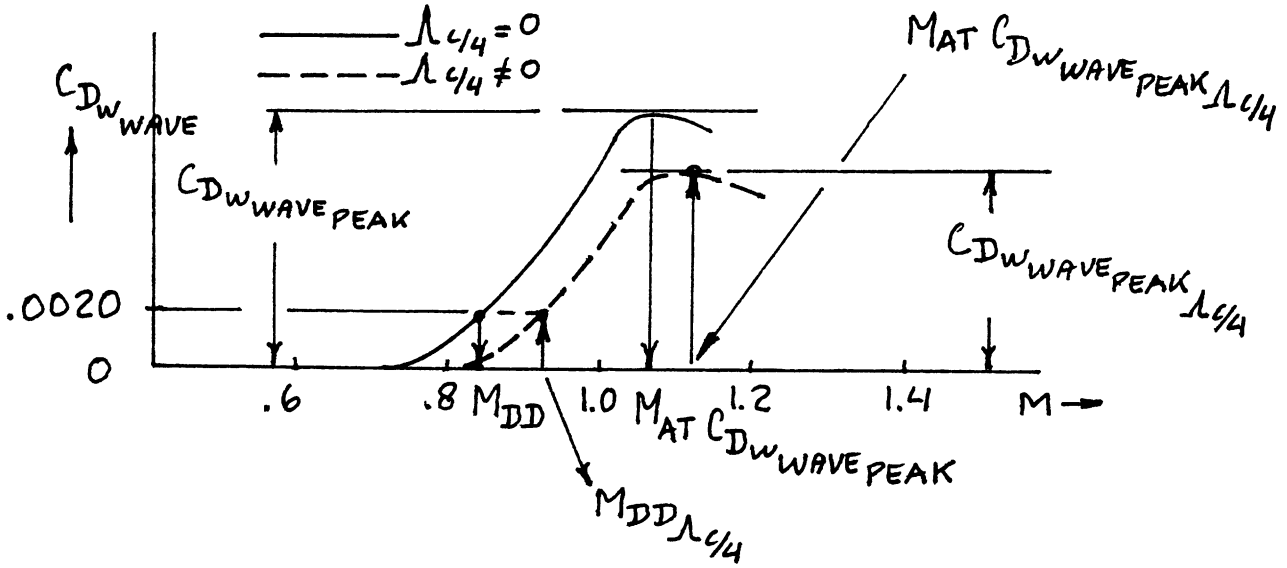

Figure 4.12 Transonic Fairing of Zero-Lift Wave Drag

The induced drag parameter (C_{D_L}/C_L^2) may be found as a function of transonic similarity parameters which are defined in Figures 4.13.

4.2.3 Supersonic Wing Drag Coefficient

The supersonic wing drag coefficient is found from:

$$C_{D_{wing}} = C_{D_{o_w}} + C_{D_{L_w}} \qquad (4.19)$$

where: $C_{D_{o_w}}$ = wing zero-lift drag coefficient, see 4.2.3.1.

$C_{D_{L_w}}$ = wing drag coefficient due to lift, see 4.2.3.2.

4.2.3.1 Wing zero-lift drag coefficient

The supersonic wing zero-lift drag coefficient follows from:

$$C_{D_{o_w}} = C_{D_{w_f}} + C_{D_{w_{wave}}} \qquad (4.20)$$

where: $C_{D_{w_f}}$ = the supersonic skin-friction drag coefficient, found from:

$$C_{D_{w_f}} = C_{f_w} S_{wet}/S \qquad (4.21)$$

where: C_{f_w} may be found from Figure 4.3.

$C_{D_{w_{wave}}}$ = the wing wave drag coefficient which depends on the leading edge radius and on whether the wing has a subsonic or a supersonic leading edge: see Fig.2.4 for definitions. For wings with sharp nose airfoils, see Ref.9. For wings with round nose airfoils:

For wings with a supersonic leading edge:

$$C_{D_{w_{wave}}} = C_{D_{LE}} + (16/3\beta)\{(t/c)_{eff}\}^2 S_{bw}/S \qquad (4.22)$$

For wings with a subsonic leading edge:

$$C_{D_{w_{wave}}} = C_{D_{LE}} + (16/3)\cot\Lambda_{LE_{bw}}\{(t/c)_{eff}\}^2 S_{bw}/S \qquad (4.23)$$

COPIED FROM REF. 9

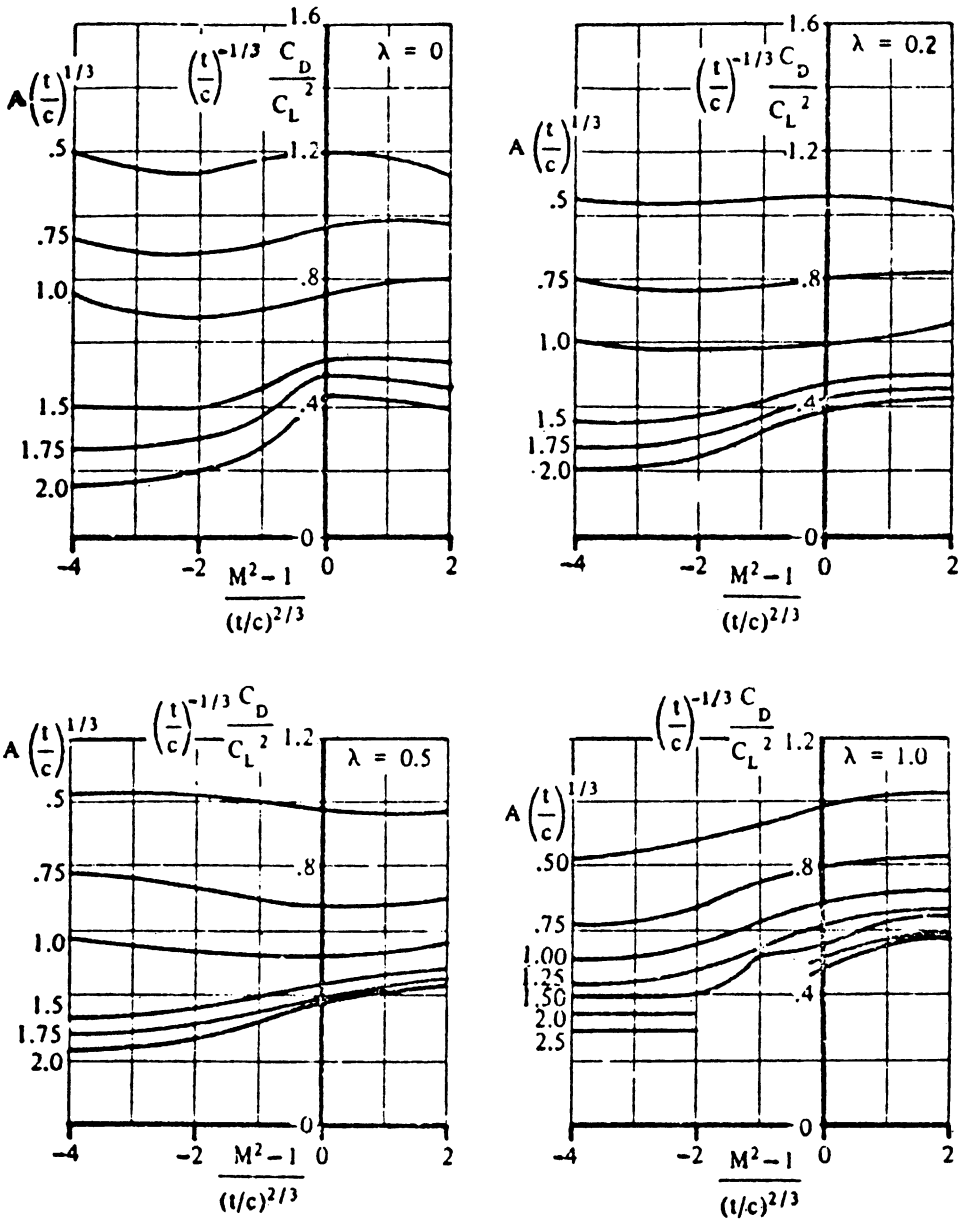

NOTE: $A \tan \Lambda_{LE} = 0$

Figure 4.13a Transonic Drag due to Lift

COPIED FROM REF.9

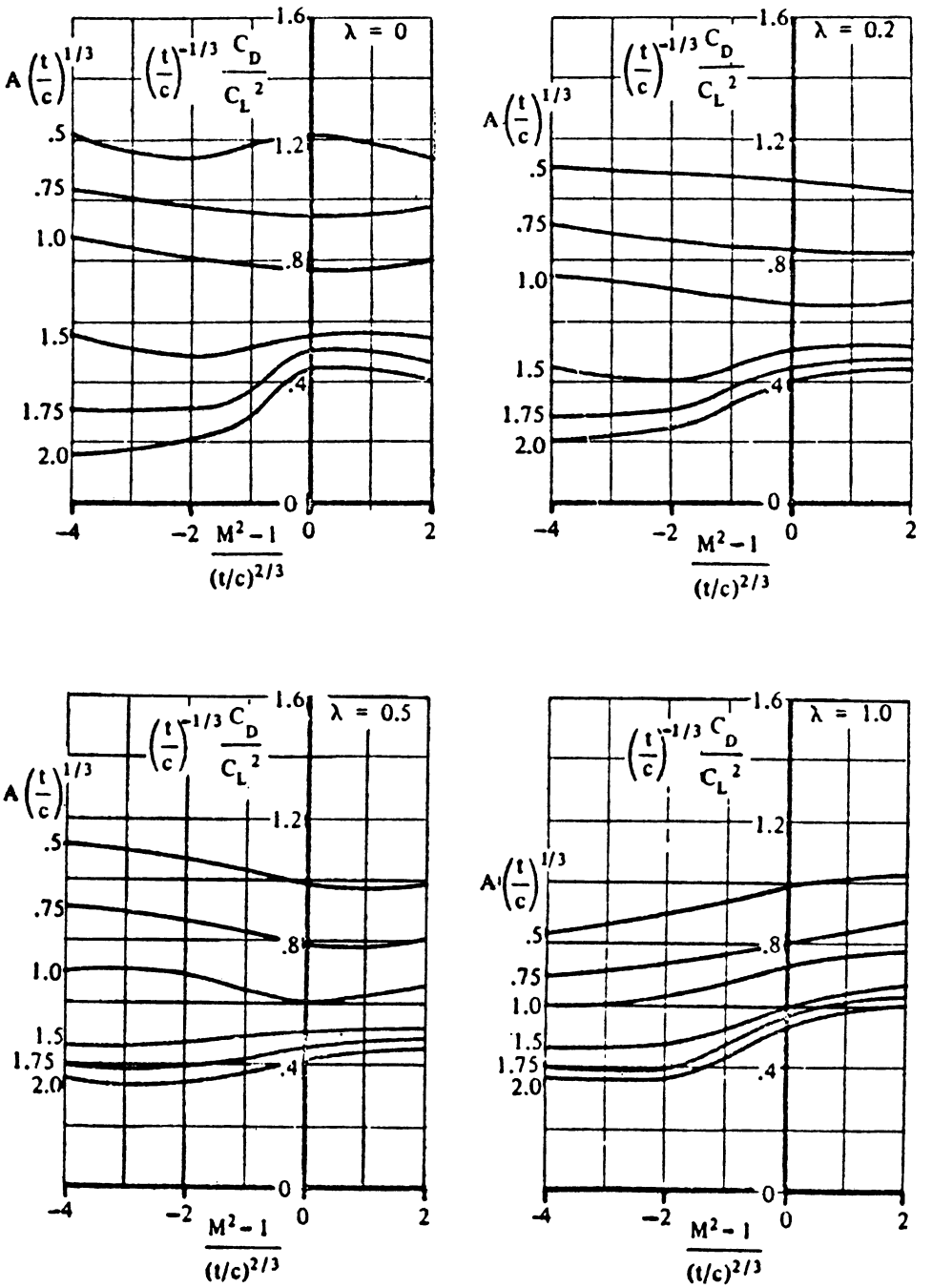

NOTE: $A\tan\Lambda_{LE} = 3$

Figure 4.13b Transonic Drag due to Lift

COPIED FROM REF. 9

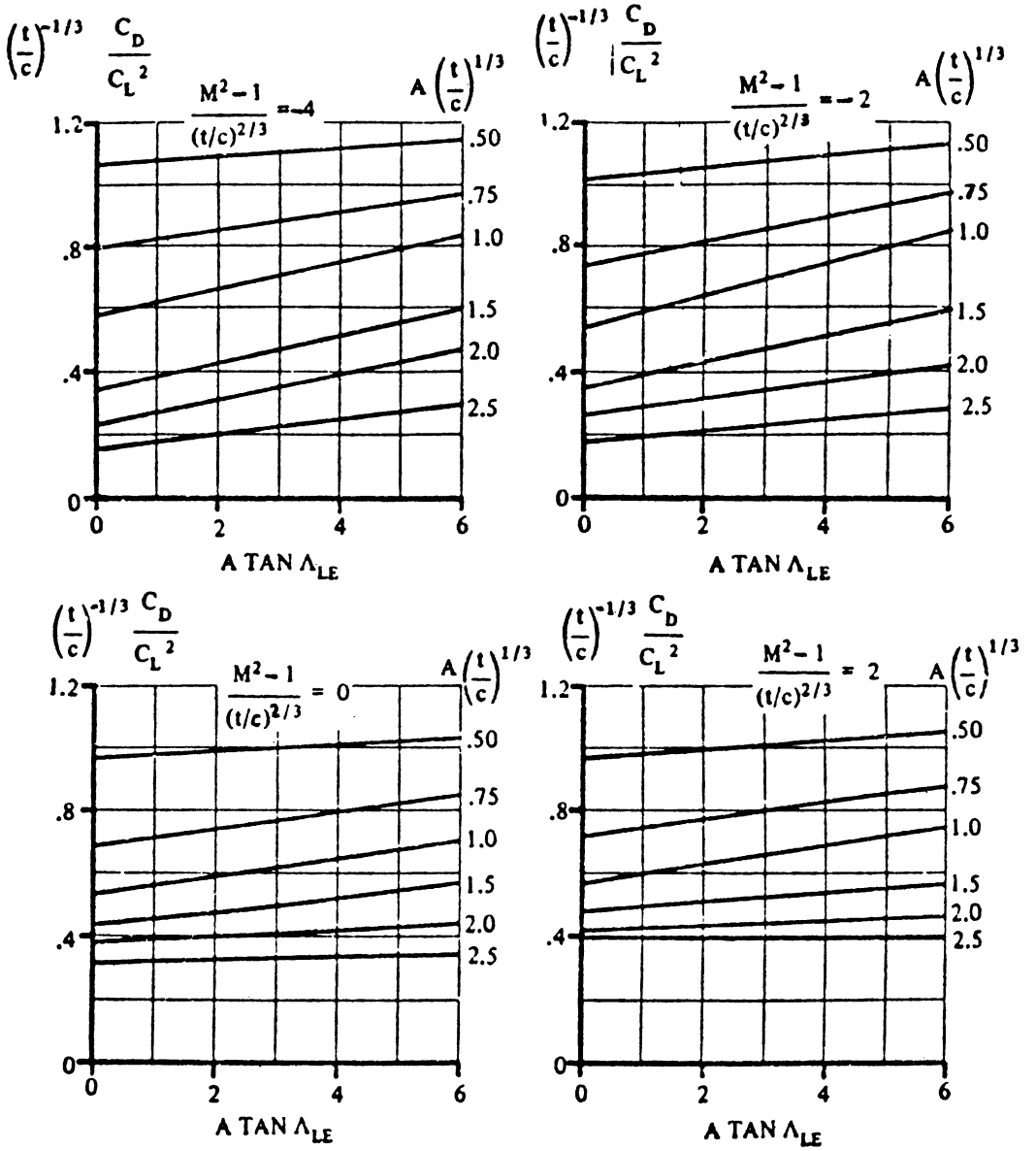

NOTE: $\lambda = 0.5$

Figure 4.13c Transonic Drag due to Lift

The value of the pressure drag coefficient, $C_{D_{LE}}$ follows from Figures 4.14.

Figure 4.15 defines the meaning of basic wing area, S_{bw} for several types of planform. The basic planform leading edge sweep angle, $\Lambda_{LE_{bw}}$ is also defined. Observe, that for a straight tapered wing: $S_{bw} = S$.

The term $(t/c)_{eff}$ in Eqns (4.22) and (4.23) is defined as follows:

$$(t/c)_{eff} = \{\int_0^{b/2} (t/c)^2 c_{bw} dy\}^{1/2} / (S_{bw}/2)^{1/2} \qquad (4.24)$$

4.2.3.2 Wing drag coefficient due to lift

The wing drag coefficient due to lift is found from:

$$C_{D_{L_w}} = (C_{D_L}/C_L^2) C_L^2 \qquad (4.25)$$

To compute the slope (C_{D_L}/C_L^2), proceed as follows:

1.) calculate two wing planform parameters:

planform shape parameter, $p = S/bc_r$

planform slenderness parameter, $b/2c_r$ (4.26)

Figure 4.15 illustrates the meaning of the quantities in Eqns (4.26) for some wing planforms.

2.) at the appropriate value of $\beta b/2c_r$, obtain the value of $\{(\pi A)(C_{D_L}/C_L^2)p/(p+1)\}$ from Fig.4.16. The symbol β is defined as:

$$\beta = (1 - M^2)^{1/2} \qquad (4.27)$$

3.) calculate the value of (C_{D_L}/C_L^2) from:

$$(C_{D_L}/C_L^2) = \{(\pi A)(C_{D_L}/C_L^2)p/(p+1)\}(1/\pi A)(1+p)/p \qquad (4.28)$$

COPIED FROM REF. 9

$$C_{D_{LE}}\left[\frac{S_{ref}}{2r_{LE_{bw}}\left(\frac{b_{bw}}{\cos\Lambda_{LE_{bw}}}\right)}\right] = 1.28\,\frac{M^3\cos^6\Lambda_{LE_{bw}}}{1+M^3\cos^3\Lambda_{LE_{bw}}}$$

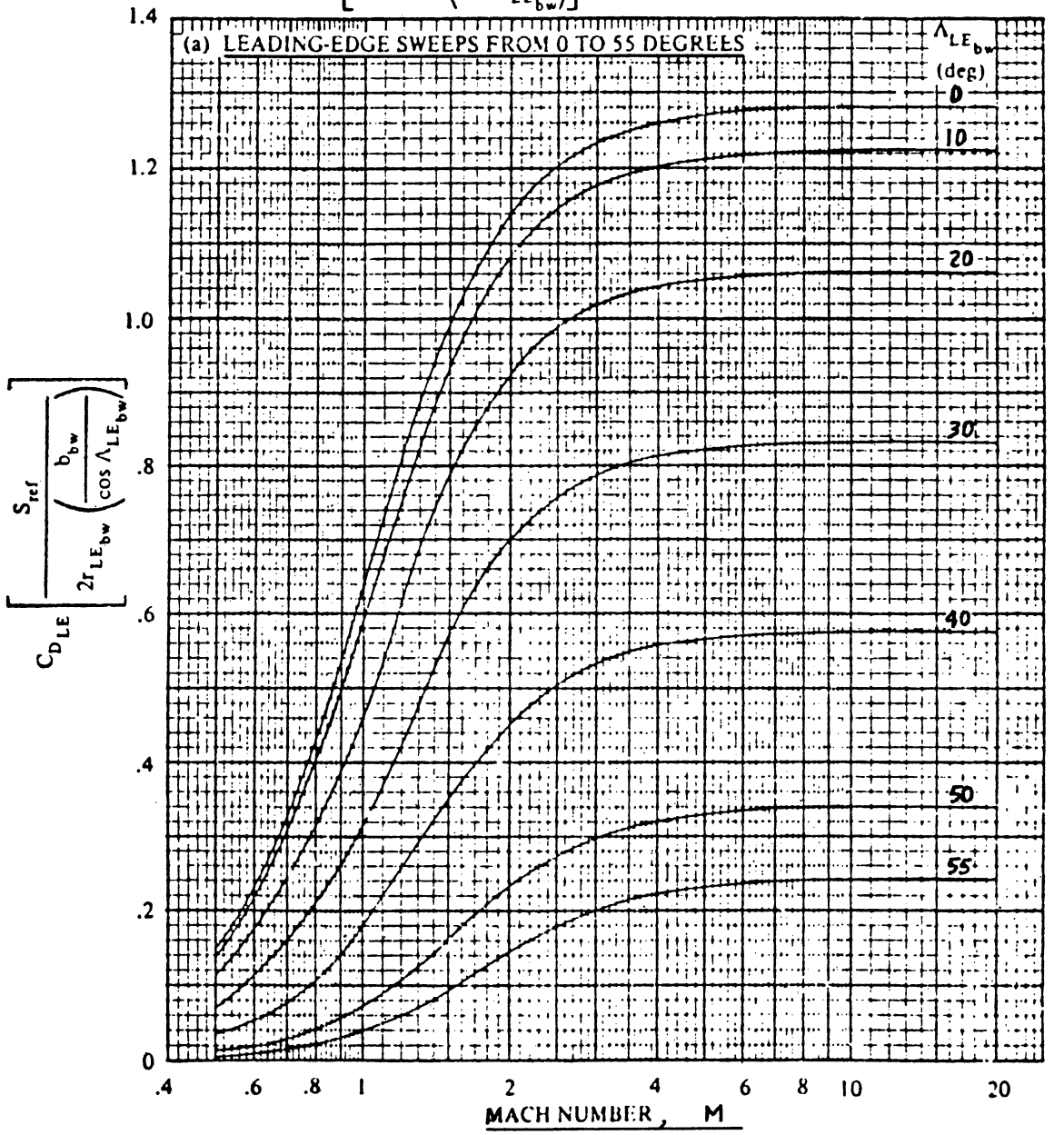

$r_{LE_{bw}}$ = BASIC WING L.E. RADIUS

Figure 4.14a Leading Edge Pressure Drag Coefficient

COPIED FROM REF. 9

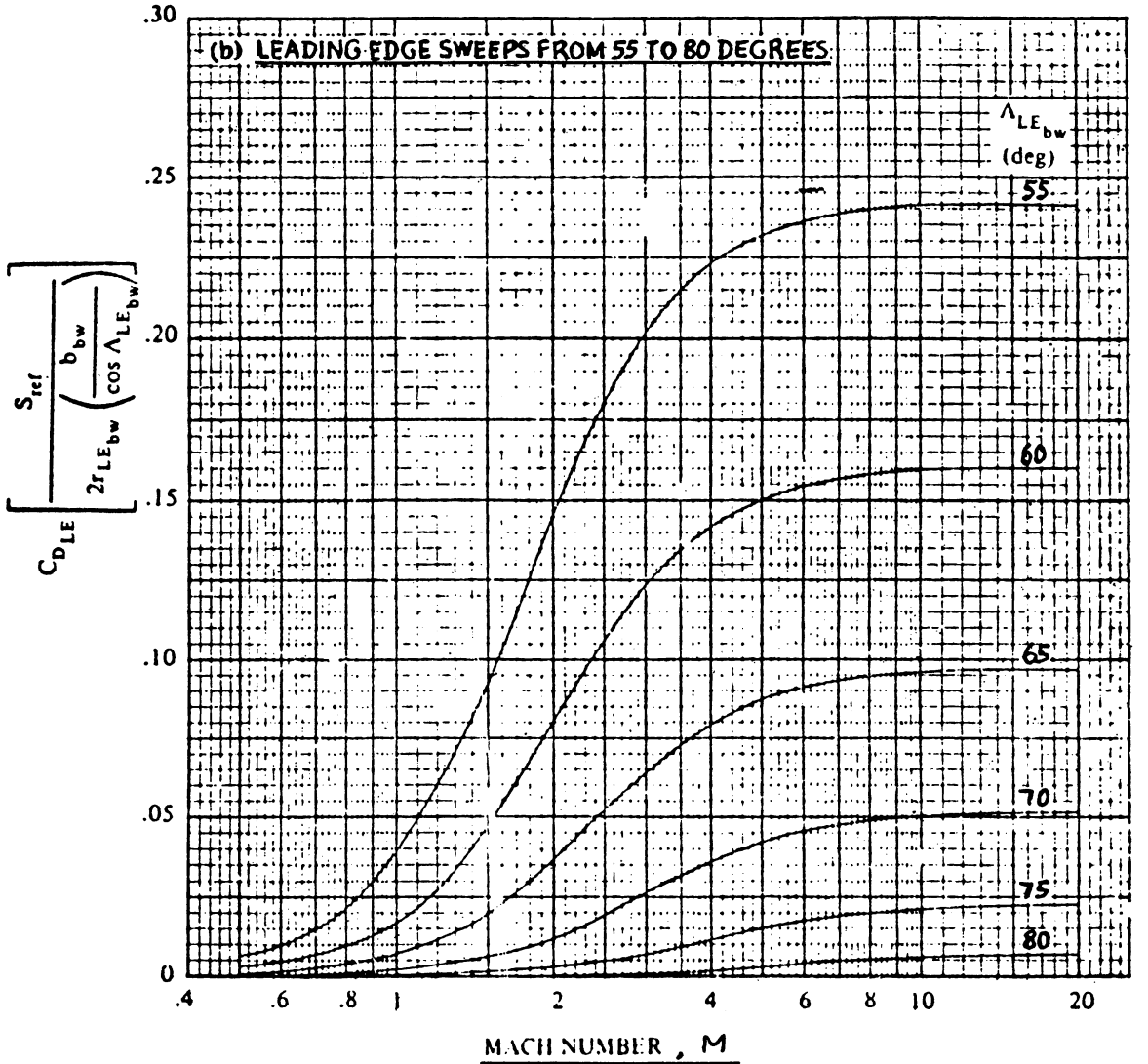

$r_{LE_{bw}}$ = BASIC WING L.E. RADIUS

Figure 4.14b Leading Edge Pressure Drag Coefficient

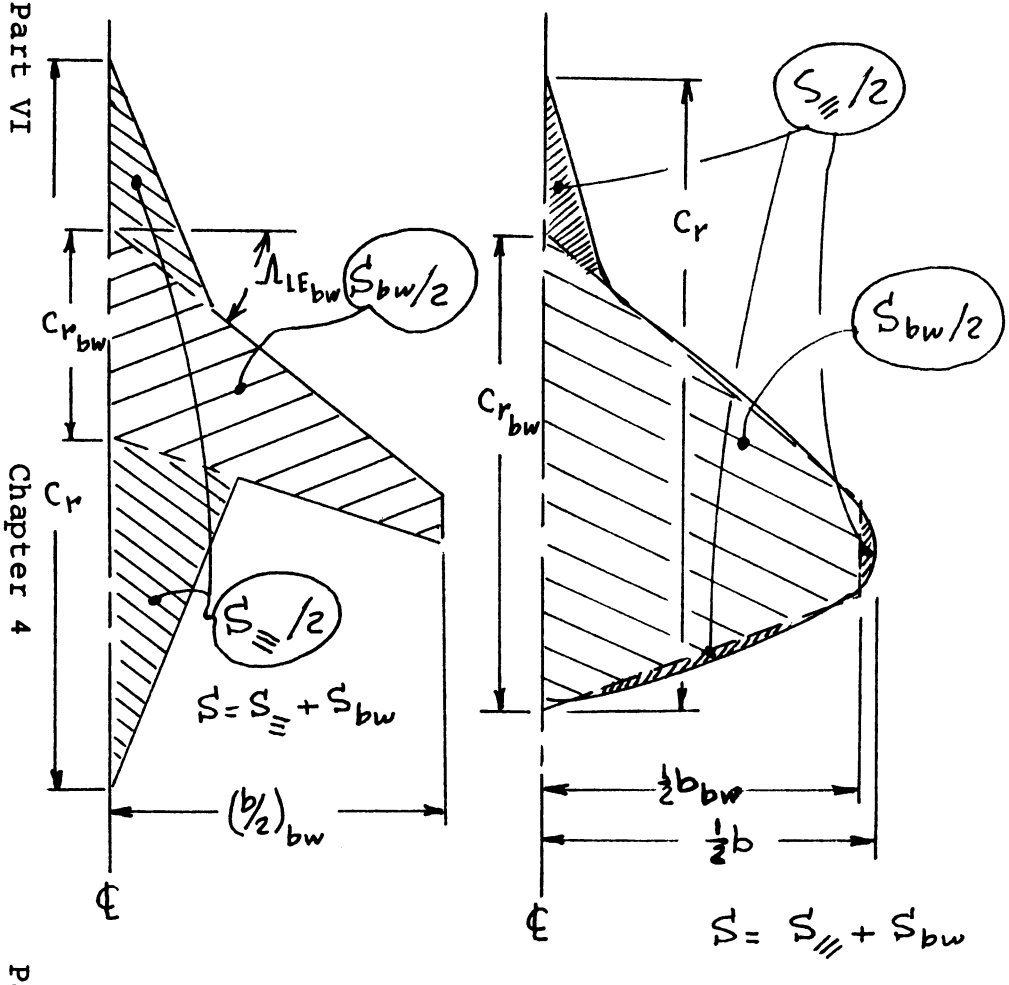

Figure 4.15 Basic Wing and Actual Wing Geometry

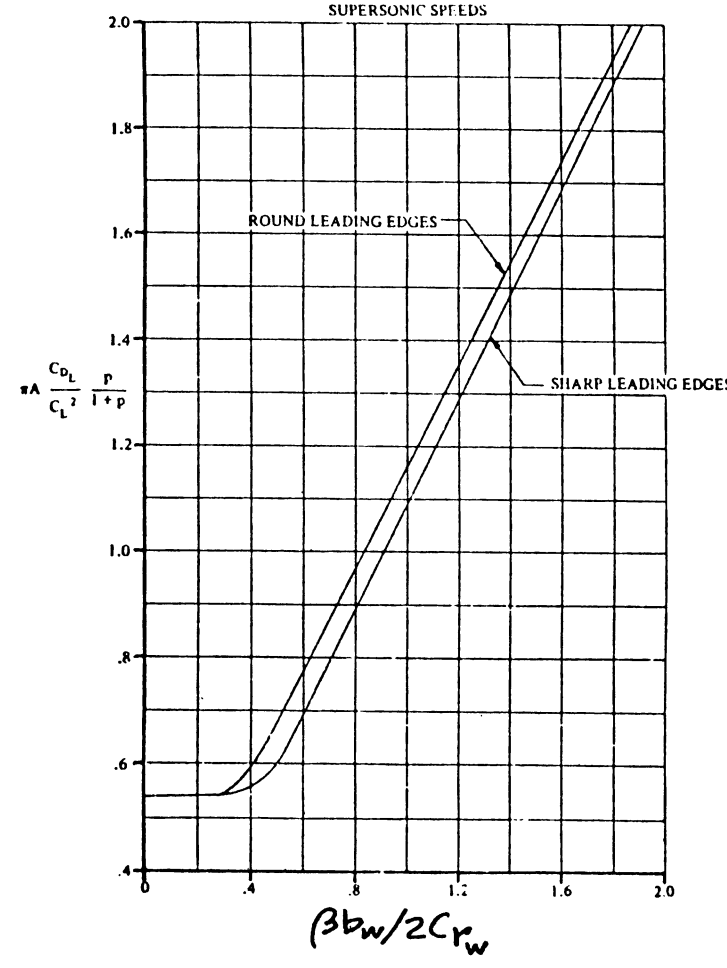

COPIED FROM REF. 9

Figure 4.16 Supersonic Drag due to Lift

4.3 FUSELAGE DRAG COEFFICIENT PREDICTION

4.3.1 Subsonic Fuselage Drag Coefficient

The subsonic fuselage drag coefficient is found from:

$$C_{D_{fus}} = C_{D_{o_{fus}}} + C_{D_{L_{fus}}} \qquad (4.29)$$

where: $C_{D_{o_{fus}}}$ = fuselage zero-lift drag coefficient, see 4.3.1.1.

$C_{D_{L_{fus}}}$ = fuselage drag coefficient due to lift, see 4.3.1.2.

4.3.1.1 Fuselage zero-lift drag coefficient

The subsonic fuselage zero-lift drag coefficient is found from:

$$C_{D_{o_{fus}}} = R_{wf} C_{f_{fus}} \{1 + 60/(l_f/d_f)^3 + 0.0025(l_f/d_f)\} S_{wet_{fus}}/S + C_{D_{b_{fus}}} \qquad (4.30)$$

where: R_{wf} = wing/fuselage interference factor, see Figure 4.1. Note: for a fuselage alone, use $R_{wf} = 1.0$.

$C_{f_{fus}}$ = turbulent flat plate skin-friction coefficient of the fuselage.

The general, turbulent, flat plate friction coefficient C_f is shown in Fig.4.3

as a function of Mach number and of Reynolds number, R_N.

For the fuselage, use:

$$R_{N_{fus}} = \rho U_1 l_f / \mu \qquad (4.31)$$

l_f = fuselage length as shown in Figure 4.17.

d_f = maximum fuselage diameter (equivalent diameter for fuselages with non-circular cross section, see Figure 4.17).

$S_{wet_{fus}}$ = wetted area of the fuselage. See Figure 4.17 and Appendix B.

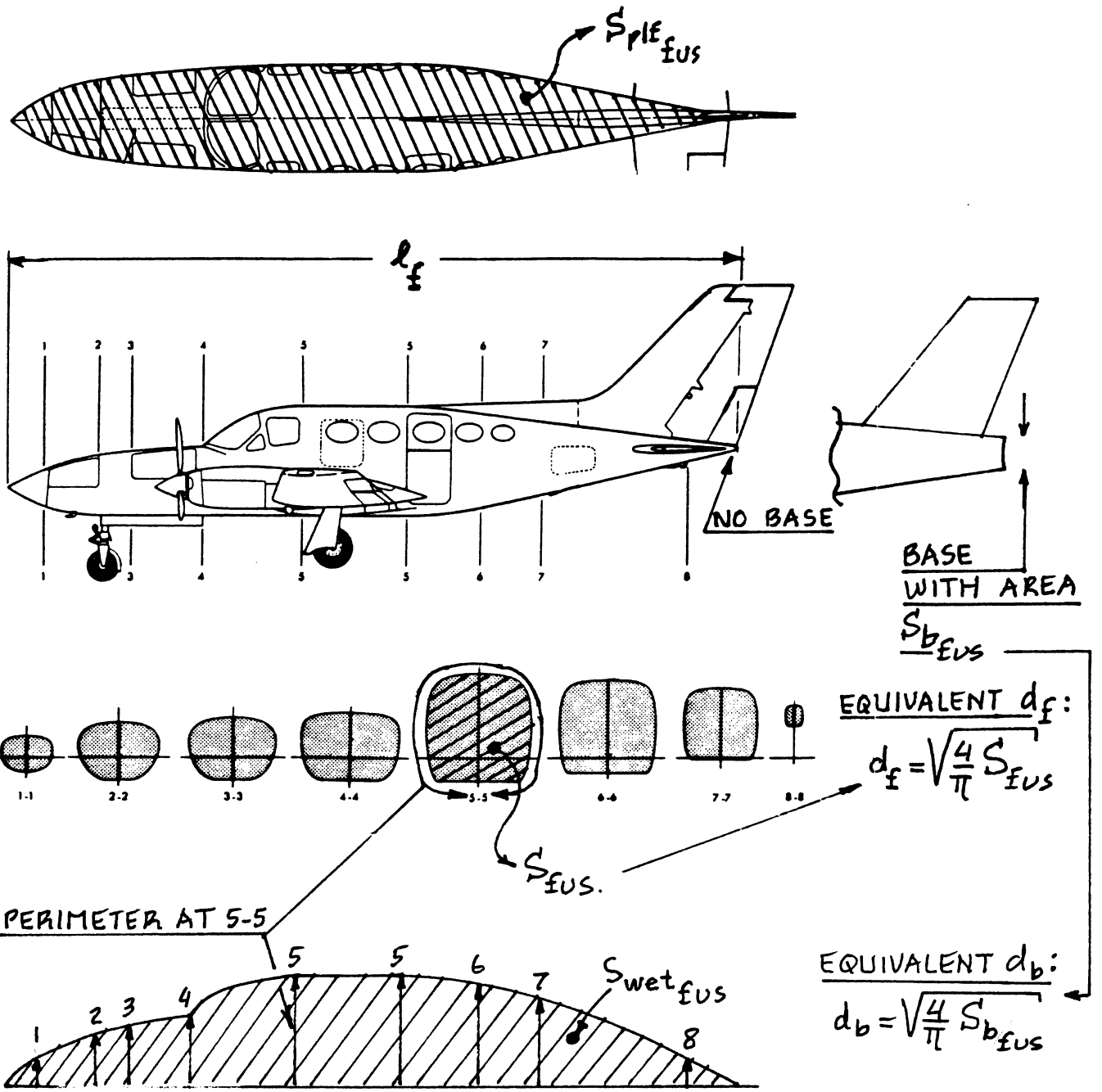

Figure 4.17 Definition of Fuselage Parameters

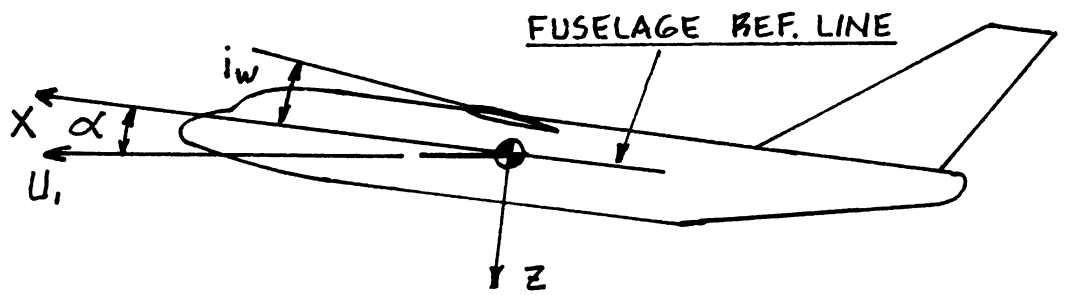

Figure 4.18 Defition of Fuselage Angle of Attack

$C_{D_{b_{fus}}}$ = fuselage base-drag coefficient, given by:

$$C_{D_{b_{fus}}} = [0.029(d_b/d_f)^3/\{C_{D_{o_{fus-base}}}(S/S_{fus})\}^{1/2}](S_{fus}/S) \quad (4.32)$$

where: d_b = fuselage base diameter, defined in Figure 4.17.

$C_{D_{o_{fus-base}}}$ = zero-lift drag coefficient of the fuselage exclusive of the base (see Figure 4.17) as determined from the first term on the right hand side in Eqn.(4.30).

S_{fus} = fuselage maximum frontal area as defined in Figure 4.17.

4.3.1.2 Fuselage drag coefficient due to lift

The fuselage drag coefficient due to lift is found from:

$$C_{D_{L_{fus}}} = 2\alpha^2 S_{b_{fus}}/S + \eta c_{d_c} |\alpha|^3 S_{plf_{fus}}/S \quad (4.33)$$

where: α is the fuselage angle of attack in radians, which is the same as the airplane angle of attack as seen in Figure 4.18.

The airplane angle of attack can be estimated as follows:

$$\alpha = \{(W/\bar{q}S) - C_{L_o}\}/C_{L_\alpha} \quad (4.34)$$

where: C_{L_o} = airplane zero-angle-of-attack lift coefficient, see Chapter 10.

C_{L_α} = airplane lift-curve slope, see Chapter 10.

$S_{b_{fus}}$ = fuselage base area defined in Fig.4.17.

η = ratio of the drag of a finite cylinder to the drag of an infinite cylinder, see Figure 4.19.

c_{d_c} = experimental steady state cross-flow drag coefficient of a circular cylinder, obtained from Figure 4.20.

$S_{plf_{fus}}$ = fuselage planform area, illustrated in Figure 4.17.

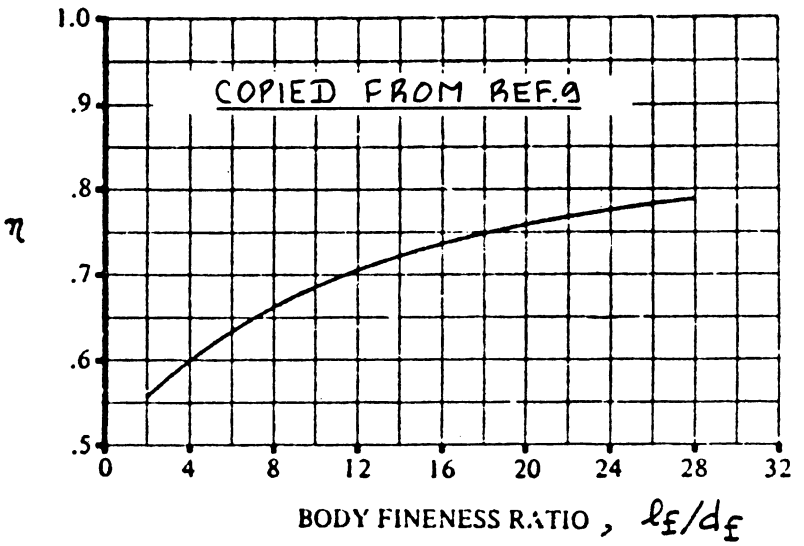

Figure 4.19 Ratio of the Drag Coefficient of a Circular Cylinder of Finite Length to that of a Cylinder of Infinite Length

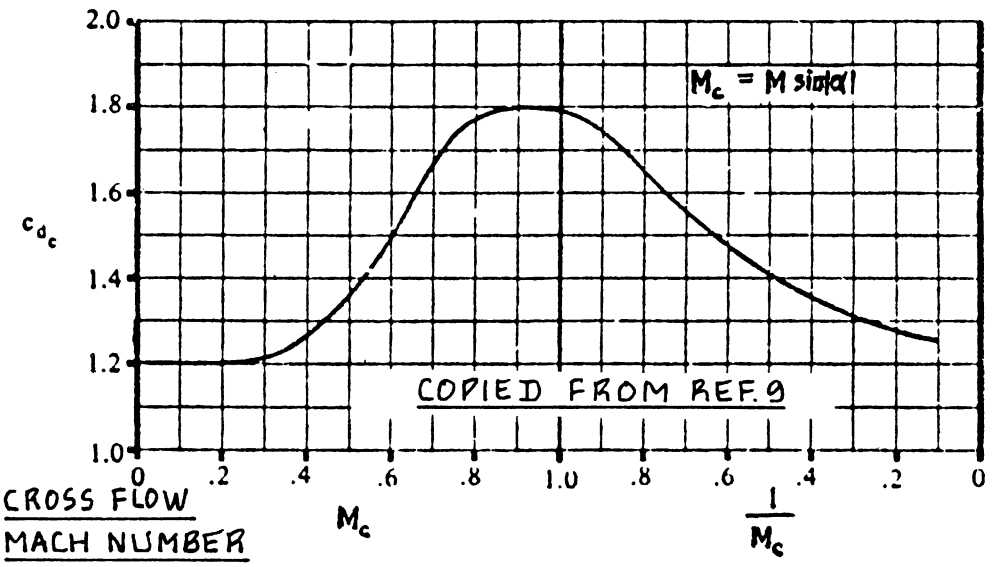

Figure 4.20 Steady State Cross-Flow Drag Coefficient for Two-Dimensional Circular Cylinders

4.3.2 Transonic Fuselage Drag Coefficient

The transonic fuselage drag coefficient is found from:

$$C_{D_{fus}} = C_{D_{o_{fus}}} + C_{D_{L_{fus}}} \qquad (4.35)$$

where: $C_{D_{o_{fus}}}$ = fuselage zero-lift drag coefficient, see 4.3.2.1.

$C_{D_{L_{fus}}}$ = fuselage drag coefficient due to lift, see 4.3.2.2.

4.3.2.1 Fuselage zero-lift drag coefficient

The transonic fuselage zero-lift drag coefficient is found from:

$$C_{D_{o_{fus}}} = R_{wf}(C_{D_{f_{fus}}} + C_{D_{p_{fus}}}) + C_{D_{b_{fus}}} + (C_{D_{wave_{fus}}})S_{fus}/S \qquad (4.36)$$

where: R_{wf} may be obtained from Figure 4.1 up to M=0.9.

For the remainder of the transonic speed range, R_{wf} = 1.0 should be used.

$C_{D_{f_{fus}}} = C_{f_{fus}}(S_{wet_{fus}})/S,$ (4.37)

the fuselage skin-friction drag coefficient at M = 0.6 which is assumed to stay constant in the entire transonic range. The value of $C_{f_{fus}}$ follows from Fig.4.3.

$$C_{D_{p_{fus}}} = (C_{f_{fus}})_{at\ M=0.6}\{60/(l_f/d_f)^3 + 0.0025(l_f/d_f)\}(S_{wet_{fus}})/S, \qquad (4.38)$$

the fuselage pressure drag coefficient. This drag component is assumed to stay constant from M=0.6 to M=1.0 and then decrease linearly to zero at M=1.2.

$C_{D_{b_{fus}}}$ = the fuselage base drag coefficient as given by Eqn.(4.32) at M=0.6. From 0.6 > M < 1.2 this drag coefficient

may be determined by extrapolation, using the 'fairing lines' shown in Figure 4.21.

$C_{D_{wave_{fus}}}$ = the fuselage wave drag coefficient which follows from Figure 4.22.

Figure 4.23 illustrates how the transonic fuselage zero-lift drag coefficient is built up in this manner.

NOTE WELL: The wave drag component of zero lift drag can be much higher than predicted here if the cross sectional area distribution of the wing/fuselage combination is not 'smooth'. Sub-section 4.3.4 defines what is meant by 'smooth' cross sectional area distributions.

4.3.2.2 Fuselage drag coefficient due to lift

The transonic fuselage drag coefficient due to lift is found from:

$$C_{D_{L_{fus}}} = \alpha^2 S_{b_{fus}}/S \qquad (4.39)$$

with the angle of attack in radians.

4.3.3 Supersonic Fuselage Drag Coefficient

The supersonic fuselage drag coefficient is given as:

$$C_{D_{fus}} = C_{D_{o_{fus}}} + C_{D_{L_{fus}}} \qquad (4.40)$$

where: $C_{D_{o_{fus}}}$ = fuselage zero-lift drag coefficient, see 4.3.3.1.

$C_{D_{L_{fus}}}$ = fuselage drag coefficient due to lift, see 4.3.3.2.

4.3.3.1 Fuselage zero-lift drag coefficient

The supersonic fuselage zero-lift drag coefficient follows from:

$$C_{D_{o_{fus}}} = \{C_{f_{fus}}(S_{wet_{fus}})/S_{fus} + C_{D_{N_2}} + C_{D_A} + C_{D_{A(NC)}} + C_{D_{b_{fus}}}\}(S_{fus})/S \qquad (4.41)$$

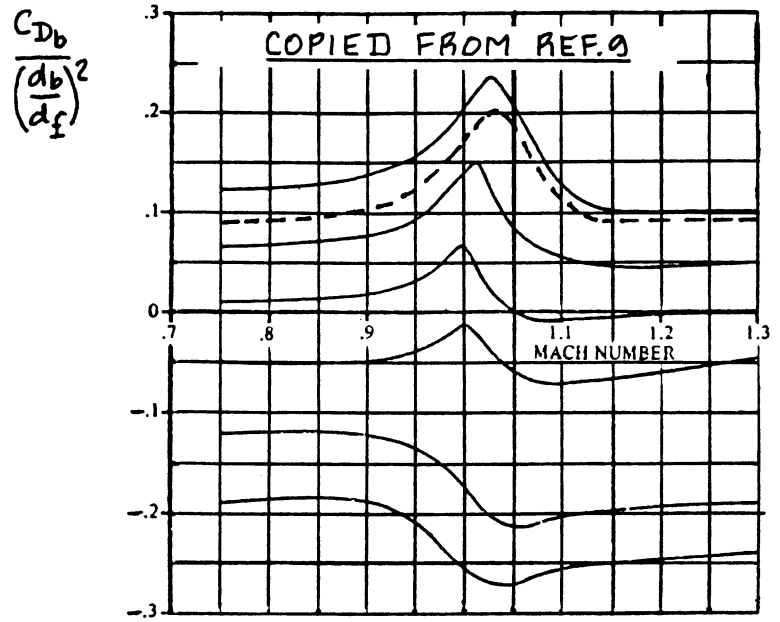

EXAMPLE:

ASSUME

$C_{D_b}/(d_b/d_f)^2 = .09$

THE PROPER FAIRING LINE TO BE USED IS ____

Figure 4.21 Transonic Fairing for Fuselage Base Drag Coefficient

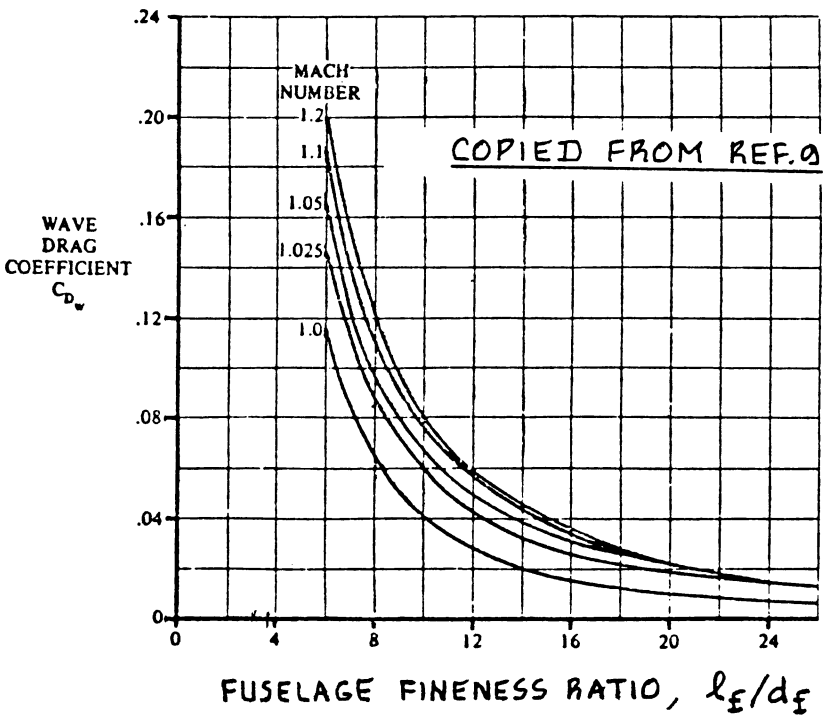

Figure 4.22 Wave Drag Coefficient for Parabolic Fuselages

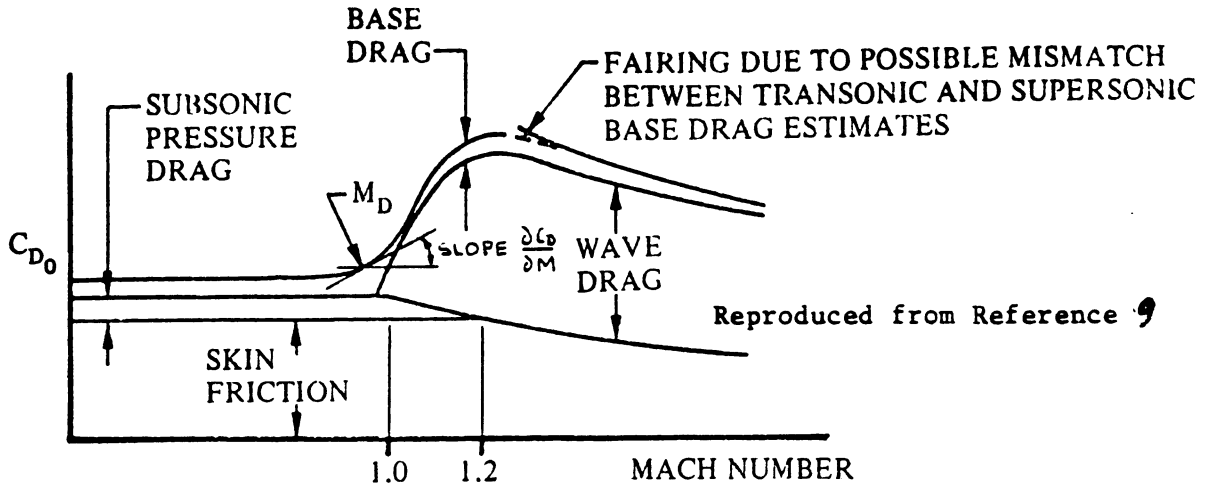

Figure 4.23 Build-up of Transonic Fuselage Drag

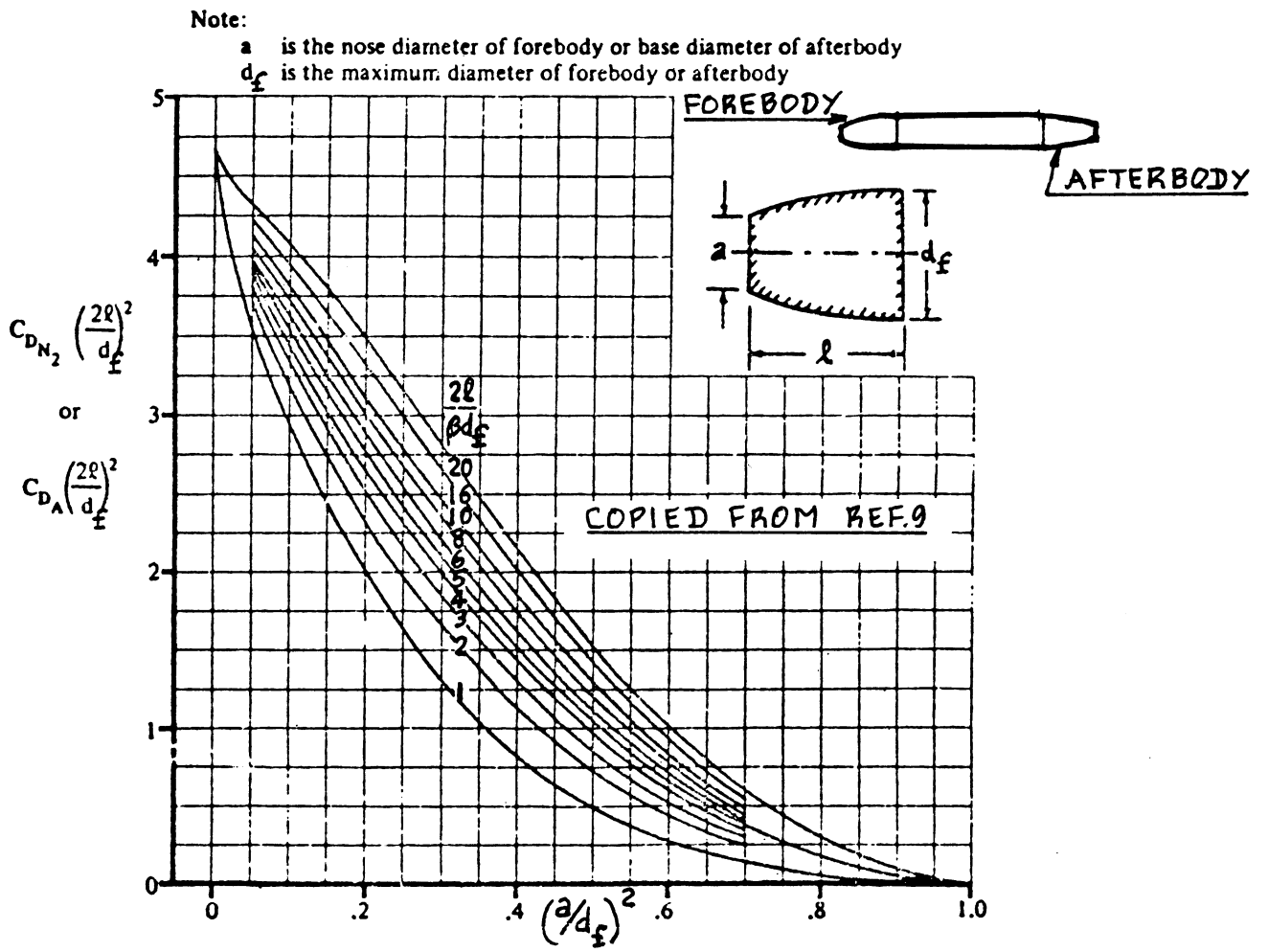

Figure 4.24 Drag of Slender Forebodies or Afterbodies of Parabolic Profile

where: $C_{f_{fus}}$ = turbulent flat plate skin-friction coefficient of the fuselage, determined as described under Eqn.(4.30).

$C_{D_{N_2}}$ and C_{D_A} are the wave drag coefficients of the fuselage nose and afterbody respectively.

These wave drag coefficients may be determined from Figures 4.24 and 4.25 respectively. If the fuselage does not have a circular cross section, the respective equivalent diameters should be used when using Figures 4.24 and 4.25.

NOTE WELL: The wave drag components of zero lift drag can be much higher than predicted here if the cross sectional area distribution of the wing/fuselage combination is not 'smooth'. Sub-section 4.3.4 defines what is meant by 'smooth' cross sectional area distributions.

$C_{D_{A(NC)}}$ = interference drag coefficient acting on the aft-fuselage due to the center-fuselage. This coefficient may be found in Figures 4.26 or 4.27.

$C_{D_{b_{fus}}}$ = fuselage base drag coefficient. For fuselages with an approximate circular cross section this coefficient may be read from Figure 4.28, provided the fuselage has no appreciable base area.

Note: if the fuselage has an appreciable base area (and this almost always is the case in fighter airplanes), the value for the fuselage base drag coefficient may be obtained from:

$$C_{D_{b_{fus}}} = -C_{p_b}(d_b/d_f)^2 \qquad (4.42)$$

where the base pressure coefficient, C_{p_b} follows from Figures 4.29.

4.3.3.2 Fuselage drag coefficient due to lift

The supersonic fuselage drag coefficient due to lift depends strongly on the fuselage cross section:

$$C_{D_{L_{fus}}} = F\{(2\alpha^2)S_{b_{fus}}/S + c_{d_c}(S_{plf_{fus}}/S)|\alpha|^3\} \qquad (4.43)$$

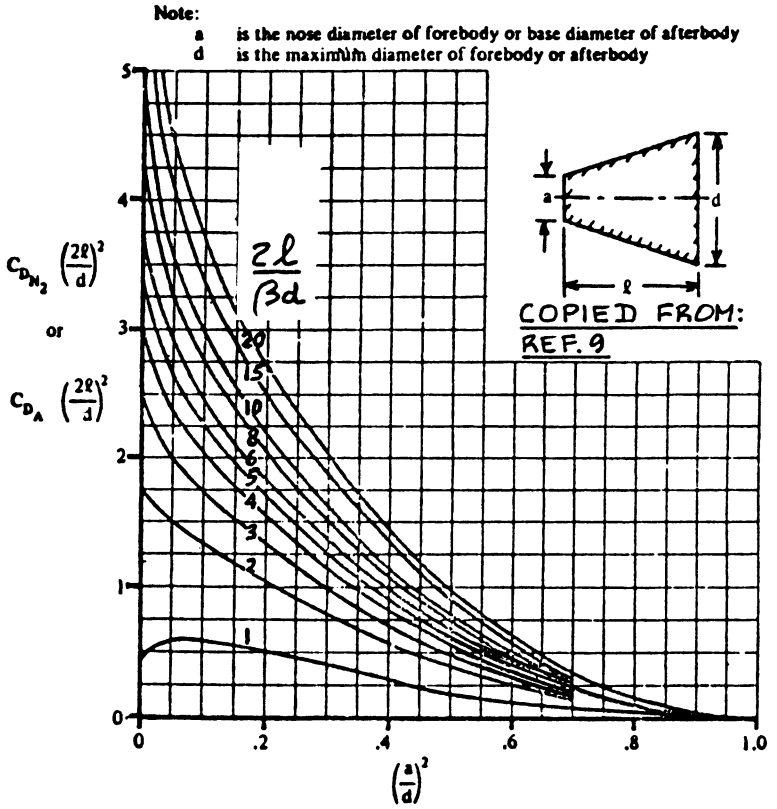

Figure 4.25 Drag of Slender, Conical Forebodies and Afterbodies

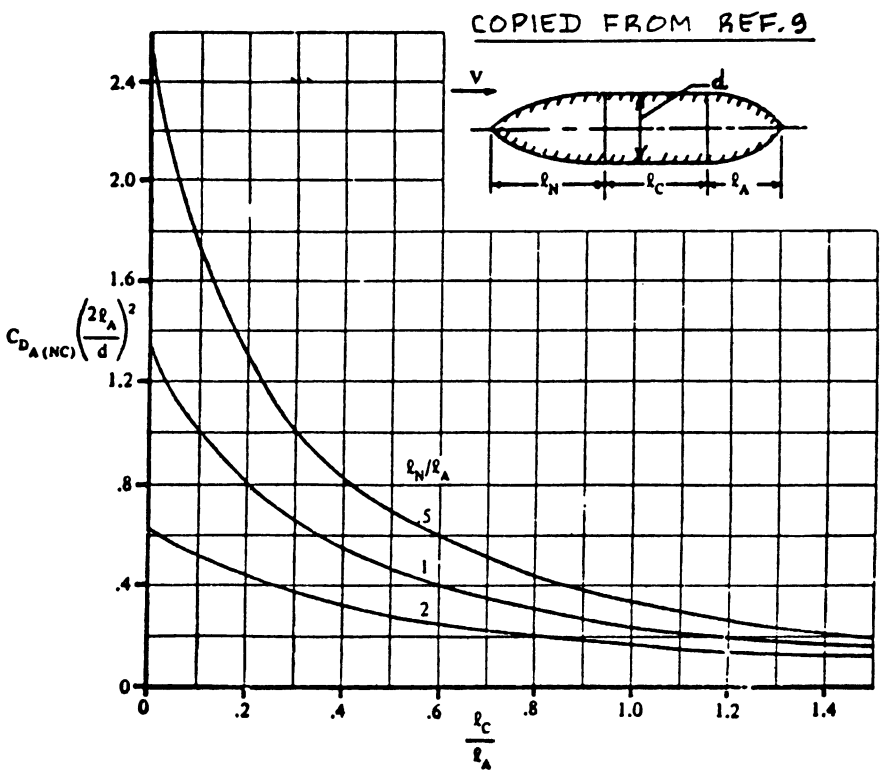

Figure 4.26 Interference Drag for Parabolic Bodies

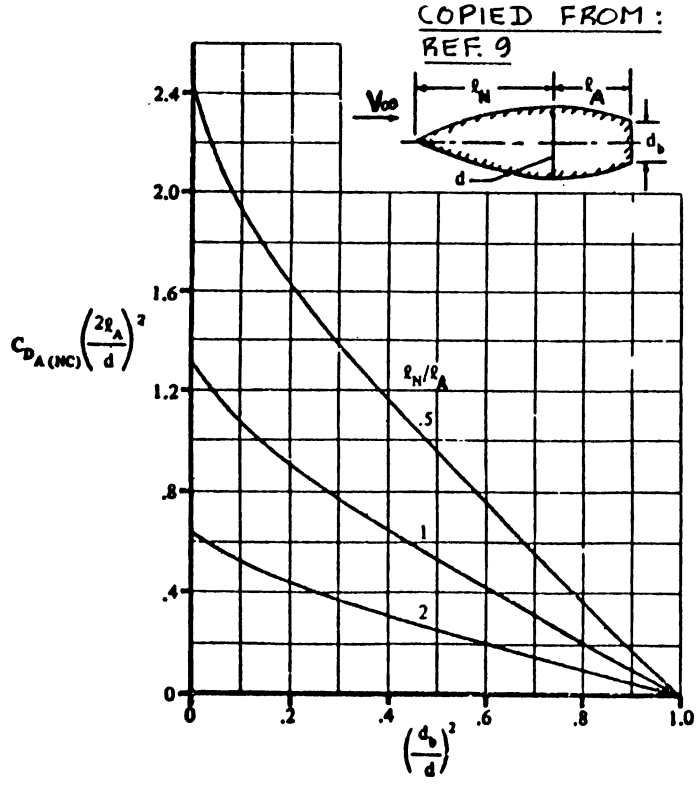

Figure 4.27 Interference Drag of Truncated Afterbodies Behind Parabolic Forebody with no Constant Centersection

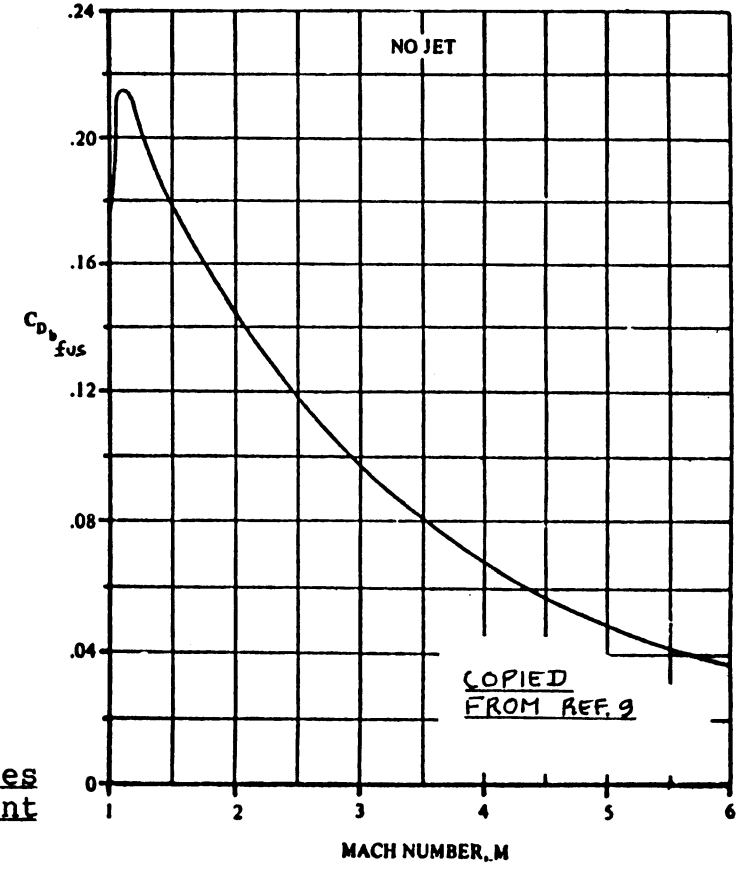

Figure 4.28 Base Drag Coefficient for Bodies of Revolution with no Boattail

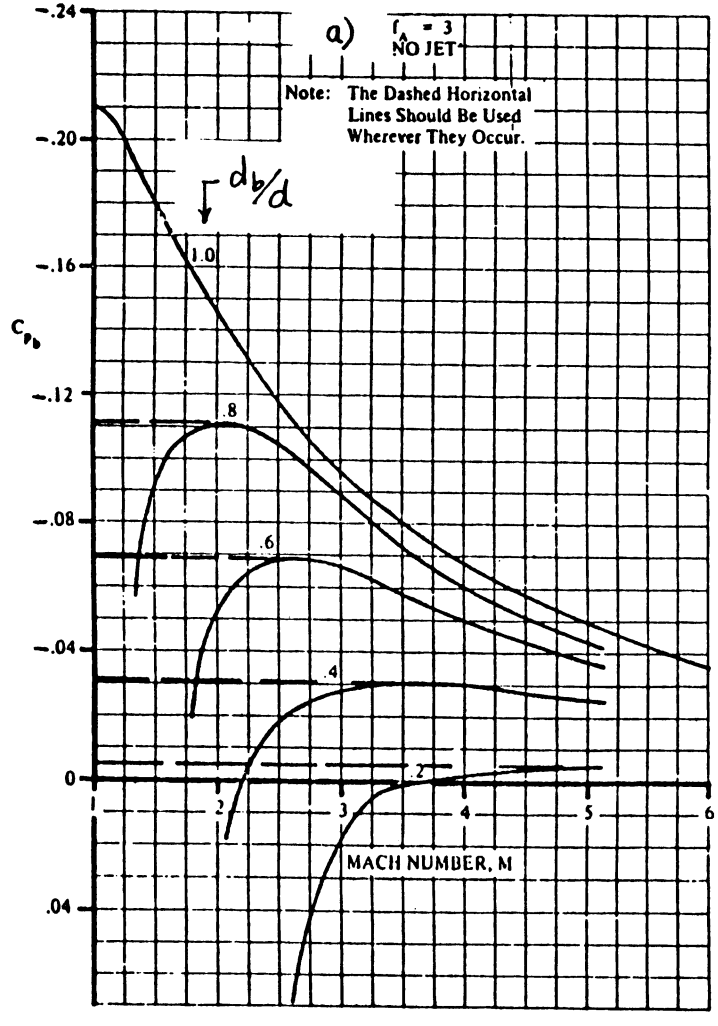

COPIED FROM : REF. 9

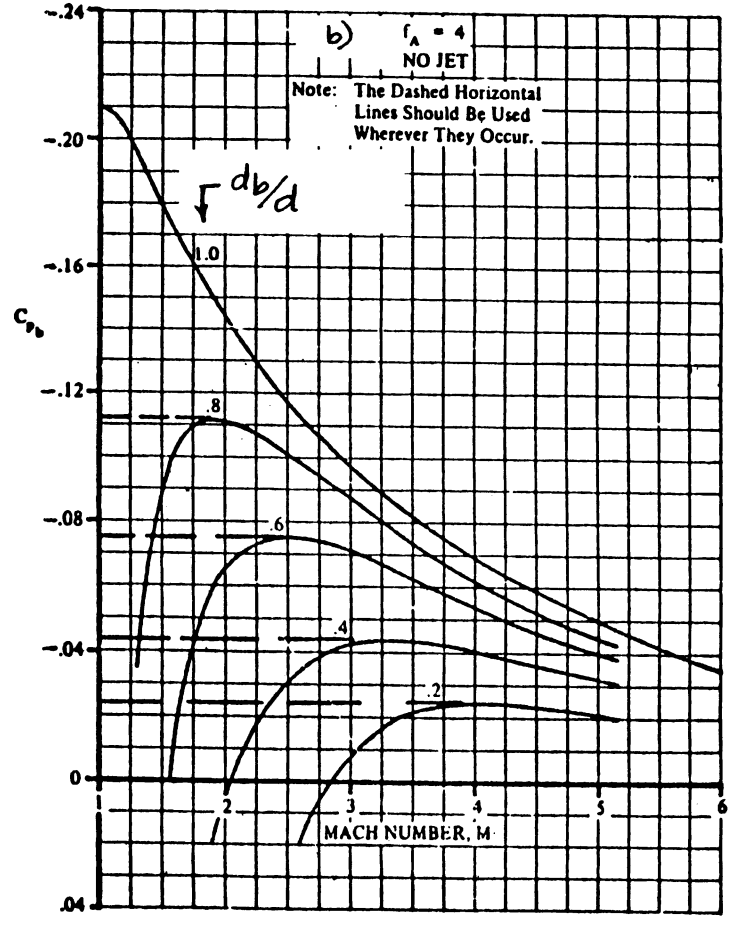

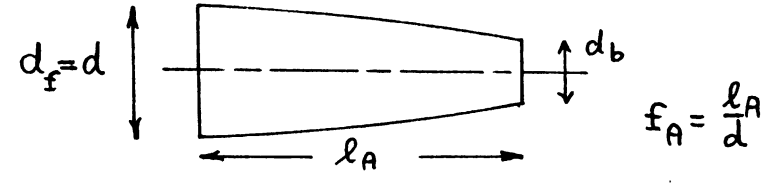

Figure 4.29 Base Pressure Coefficient for Boattails of Approximate Conical Shape

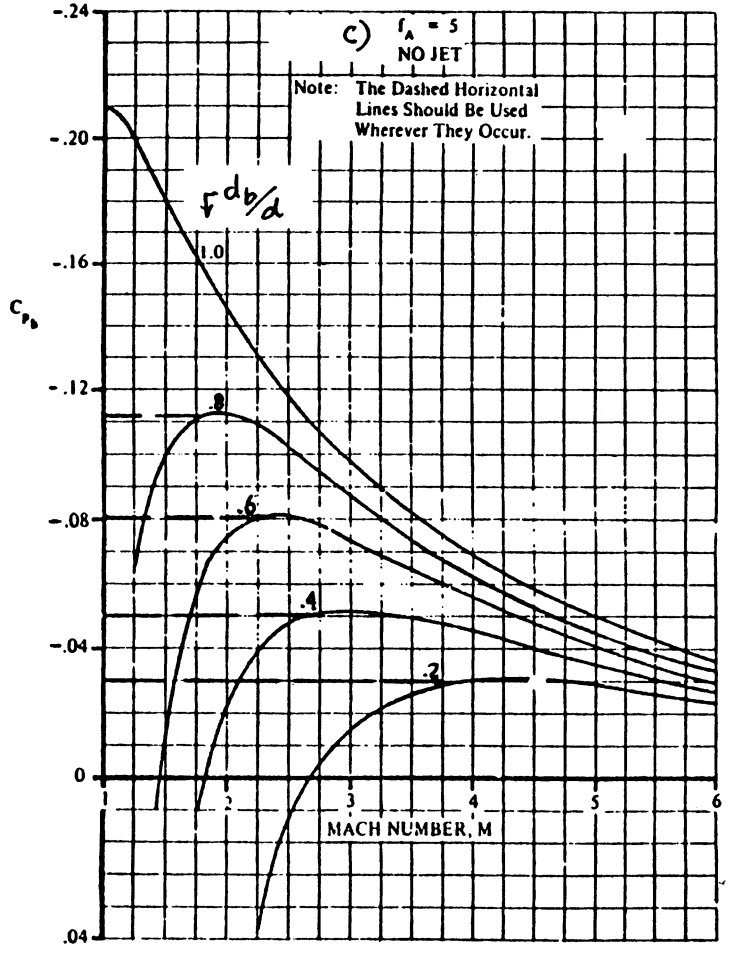

COPIED FROM: REF. 9

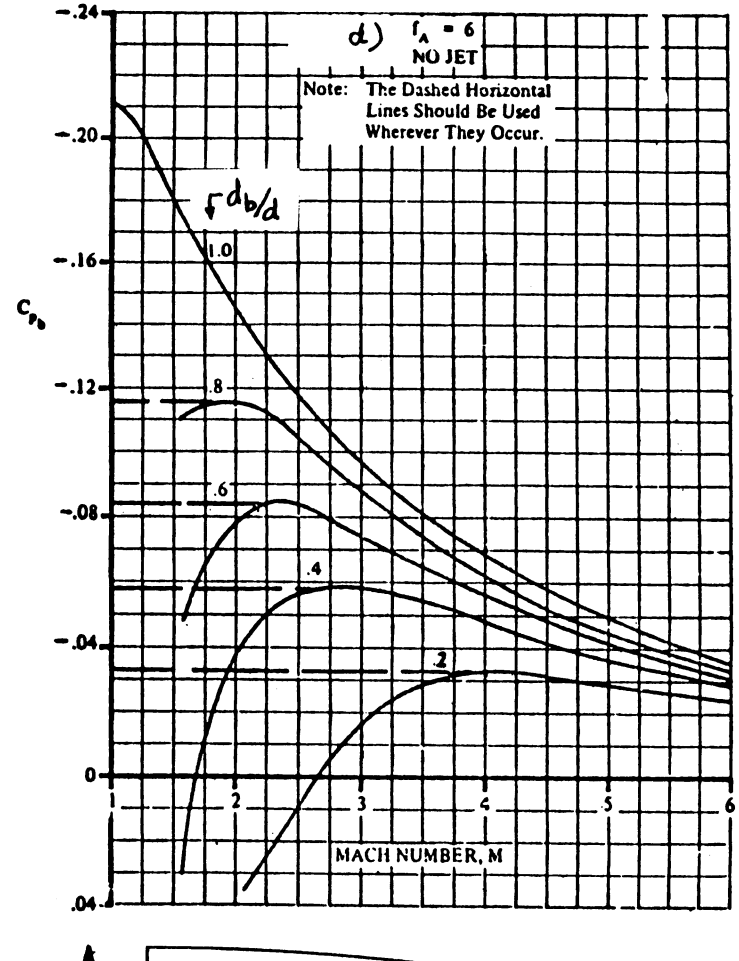

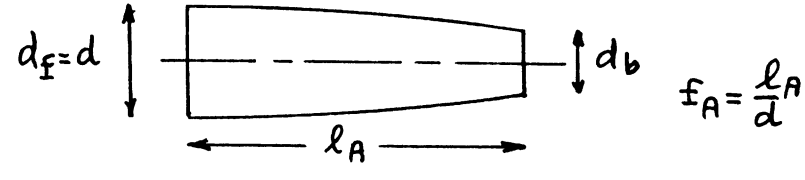

Figure 4.29 Base pressure Coefficient for Boattails of Approximate Conical Shape

For a fuselage with circular cross section: F = 1.0

For a fuselage with elliptical cross section:

$$F = \{(a/b)(\cos\omega)^2 + (b/a)(\sin\omega)^2\} \qquad (4.44)$$

where: a is the major axis of the elliptical cross section.

b is the minor axis of the elliptical cross section.

ω = 0 with the major axis horizontal.
ω = 90 deg. with the minor axis horizontal.

Values for c_{d_c} are found in Figure 4.20.

4.3.4 The Area Rule Concept

The methods for predicting wave drag in Sub-sections 4.3.2 and 4.3.3 are valid only if the wing/fuselage/empennage combination has a 'smooth' cross sectional area distribution. Figure 4.30 illustrates how a cross sectional area distribution of an airplane is obtained.

Whitcomb showed in Reference 17 that the wave drag of an airplane in the transonic speed range is roughly equal to the wave drag of its 'equivalent body of revolution. Figure 4.30 also shows the equivalent body of revolution for the same airplane. Note the irregularities in the equivalent body of revolution.

Minimum wave drag can be achieved by designing the wing/fuselage/empennage cross sectional area distribution in such a way that its equivalent body of revolution approximates the so-called Sears-Haack bodies. This design concept (due to Whitcomb) is referred to as area ruling.

Three types of Sears-Haack bodies are depicted in Figure 4.31:

Type I: used to minimize wave drag for a given length and volume.

Type II: used to minimize wave drag for a given length and diameter.

Type III: used to minimize wave drag for a given diameter and volume.

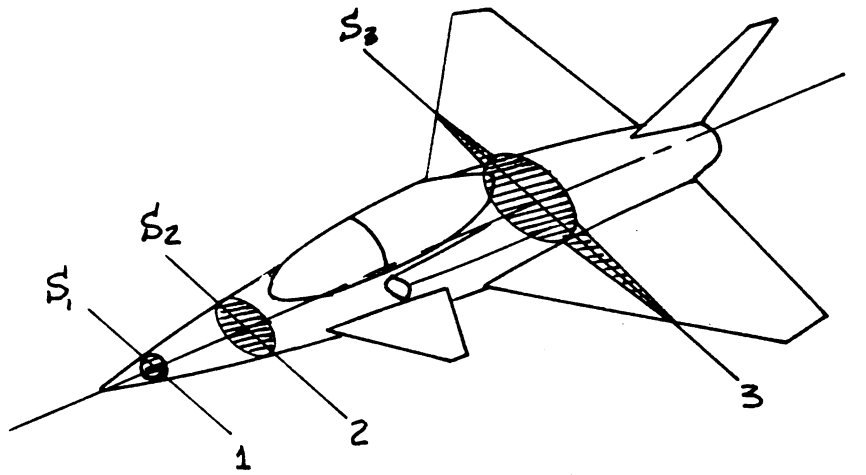

CONSTRUCT 'EQUIVALENT' BODY OF REVOLUTION SO THAT $S_{i\,AIRPLANE} = S_{i\,EQ.}$

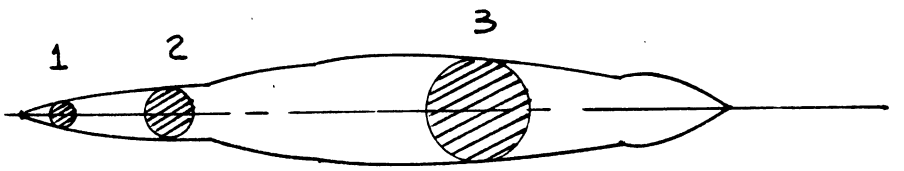

Figure 4.30 Development of a Cross Sectional Area Distribution and its Equivalent Body of Revolution

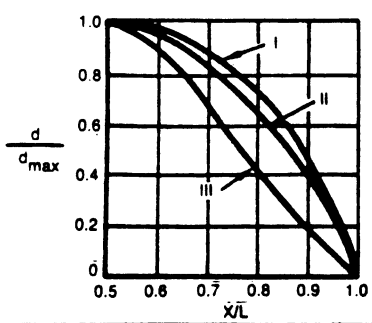

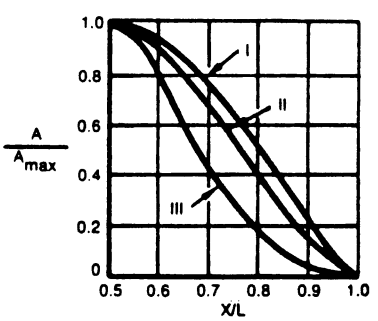

COPIED FROM: REF. 18. COURTESY: B. NELSON, NORTHROP

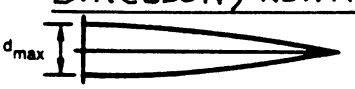

MINIMUM PRESSURE DRAG			VOL = $C_{p_n} \times A_{max} \times L$
TYPE I	$C_D = \frac{9}{8}\pi^2\left(\frac{d}{L}\right)^2$	GIVEN LENGTH & VOL	$C_{P_I} = 0.59$
TYPE II	$C_D = \pi^2\left(\frac{d}{L}\right)^2$	LENGTH & DIA	$C_{P_{II}} = 0.519$
TYPE III	$C_D = 3/2\,\pi^2\left(\frac{d}{L}\right)^2$	DIA & VOL	$C_{P_{III}} = 0.392$

Figure 4.31 Sears Haack Bodies and Drag Coefficients

The wave drag coefficients and volumes for the three Sears-Haack bodies are also given in Figure 4.31.

Note: these wave drag coefficients apply to supersonic Mach numbers only! To a first order of approximation these supersonic wave drag coefficients are independent of Mach number.

It is clear that to minimize wave drag it is essential to distribute any given volume over as much length as possible. However, in airplane layout design several constraints are encountered. Typical constraints are:

a) the airplane may not exceed a given length: this constraint is nearly always encountered in carrier based airplanes. Supersonic transports may encounter length limitations for reasons of ground maneuvering, gate space restrictions and hangar size limits.

b) the airplane must have a minimum total volume: this constraint comes about because of the need to carry fuel, payload, fixed equipment, landing gear and engines. Even airplane structures need a minimum amount of volume.

c) the airplane must have a minimum outside diameter: this constraint arises because of the need for cabin volume, engine size and/or payload size.

Because of these constraints on length, volume and diameter it may be necessary to strike a compromise in the layout design of transonic and supersonic airplanes.

From the previous discussion it is obvious that early knowledge of volume requirements inside the airplane is essential. The airplane layout design procedures of Chapters 4-9 in Part II must be augmented with the following step-by-step procedure:

Step 1: Tabulate preliminary volume requirements as indicated in Table 4.1.

Tables 4.2 give data for the volumetric requirements of the elements listed in Table 4.1. It is essential that the 'critical' (= minimum required) length for all elements is identified. The reader should use judgement in deciding where element critical lengths may overlap.

Step 2: Prepare a preliminary airplane layout which includes all elements listed in Step 1. Do not forget to cross-check with the design layout procedures of Chapters 4-9 of Pt.II.

Table 4.1 Critical Volume and Length Requirements

Airplane Element	Critical Volume (ft^3)	Critical Length (ft)
Forebody: radome, avionics, cockpit, nose gear		
Mid section: gun or weapons bay, main gear, avionics, control runs, body fuel, fixed equipment, wing sweep mechanism, inlets		
Aft body: engine bay(s), tail-pipes, nozzles, afterburners, body fuel, empennage carry-through		
Wing: total wing volume outside the body.		
Refuelling system: if required, this normally resides in the for-ward part of the fuselage.		
Empennage: total empennage volume outside the body.		
Streamtube: that volume taken up by the inlet, engines, tail-pipes, afterburners and nozzles.		
Inlet stream tube: that volume taken up by the inlet up to the engine compressor faces.		

Note: This table can be completed only after a preliminary layout of the airplane has been prepared. Chapters 4-9 in Part II provide step-by-step procedures for preparing such a layout. Tables 4.2a and 4.2b should be consulted for preliminary data on volumetric requirements of airplane elements.

Table 4.2a Critical Volume, Cross Section and Length Data

Notes: 1. Data given are minimum data for fighters. For transports the volume needs follow from layout design results of Chapters 4-9 in Part II.
2. All data refer to 'installed' volumes, not to actual volumes. Data based on Reference 18.

Element		Volume (ft^3)	Cross Section (ft^2)	Length (ft)
Radome:		$0.22(d_{rad} + 0.33)^4$	$(\pi/4)(d_{rad})^2$	
Cockpit:	today	70.0	14.0 upright	
	future	50.0	11.0 upright	
			7.0 semi-supine	
Nose gear:		15.0	3.0 (fighters only!)	
Weapons:	see Part IV, Chapter 3 for dimensioned data on weapons and stores. Some statistical data are:			
conformal carriage:		1.5 ft^3/1,000 lbs		3.0
internal bay:				
	tube launch:	20 ft^3/1,000 lbs		weapon
	ejector launch:	33 ft^3/1,000 lbs		weapon
Guns:	Mk61 20 mm	14.0		gun + 2
	Oerlikon 30 mm	4.8		gun + 2
Ammunition:	20 mm	0.013 ft^3/round		
	30 mm	0.052 ft^3/round		

Main Gear: $\{9 + 10^{-6}(2.56CBR - 4.86)W_{TO}(1.924CBR)^{-0.158}$

For CBR (California Bearing Ratio) definitions and its relation to airfield type, see Ref.19.

For fighters: CBR = 3.0 - 5.0 For transports: CBR = 12

Arresting gear: 4.0

Hydr./pneum. systems: $0.00046W_{TO}$

Electrical systems: 4.0 (for fighters only)

Armor: 1.0

Environmental system: 15.0 (for fighters only)

Table 4.2b Critical Volume, Cross Section and Length Data

Element	Volume (ft^3)	Cross Section (ft^2)	Length (ft)
Oxygen system:	6.0 per crew member for fighters		
Auxiliary gear:	$0.00005W_{TO}$		
Control runs:		1.0 ft^2 between the cockpit and empennage	
Fuselage structure:	$0.13(l_f/d_f)S_{wet_{fus}}$		

Wing: volume outside the body, computed from the wing layout drawing of Step 6.13 in Part II.

Wing sweep mechanism: $0.4(c_p)^2(t/c)_{max}w_f$, c_p= chord at pivot

Body fuel: use a volumetric efficiency of 85 percent for fuselage tanks.

Refuelling system: 2 ft^3, normally in the forebody

Empennage: volume outside the body, computed from the empennage layout drawing of Step 8.7, Part II.

Streamtube: that volume taken up by inlets, engines, tailpipes, afterburners and nozzles.

Wasted volume: it is not possible to package a fuselage without wasted volume. Many system components require accessibility: this adds volume. The following equation is suggested for computing wasted volume:

$$V_{waste} = 0.212\{3(Vol._{fus}/l_f) + 2.7(Vol_{fus}l_f)^{1/2}\}$$

where: Vol_{fus} = sum of all previous volume requirements.

l_f is the overall fuselage length

Total volume: = $Vol_{fus} + V_{waste}$.

Inlet stream tube: that volume taken up by the inlet up to the engine compressor faces. This volume is subtracted from the total volume in arriving at the net cross-sectional area distribution.

Step 3: Translate the preliminary airplane layout into a cross sectional area plot as shown in Figure 4.32. Make certain that all volumetric and critical length requirements of Step 1 are satisfied.

Step 4: Decide which of the Sears-Haack bodies of Figure 4.31 best fit the cross sectional area plot of Step 3. Overlay the selected Sears-Haack cross sectional area plots.

Step 5: Adjust the fuselage geometry until the airplane cross sectional area plot MINUS its inlet capture area conforms to the selected Sears-Haack shapes.

Figure 4.33 shows an example of a cross sectional area distribution of a fighter airplane. Figure 4.34 shows several critical cross sections.

Note that the 'bump' in the area distribution due to the canopy are eliminated by indenting the local fuselage cross section. The Dassault Rafale is an example of a fighter airplane where this has also been done.

Note that the 'bump' in the area distribution due to the wing has been eliminated also by indenting the local fuselage cross section. The result is a 'coke-bottle' shape. Further examples of this coke-bottling are shown in Figures 3.54 - 3.56 in Part II.

Airplanes which fly at high subsonic Mach numbers may require so-called 'local' area ruling. Examples of 'local' area ruling are found in the Boeing 737-300 wing/nacelle region, in the Northrop F-5 wing/tiptank region and in the DC-10 center-engine/vertical tail region.

In using 'local' area ruling, only local cross sectional area distributions are constructed. When these local cross sectional area distributions are 'smooth', no major problems in dragrise at high subsonic Mach numbers should be expected.

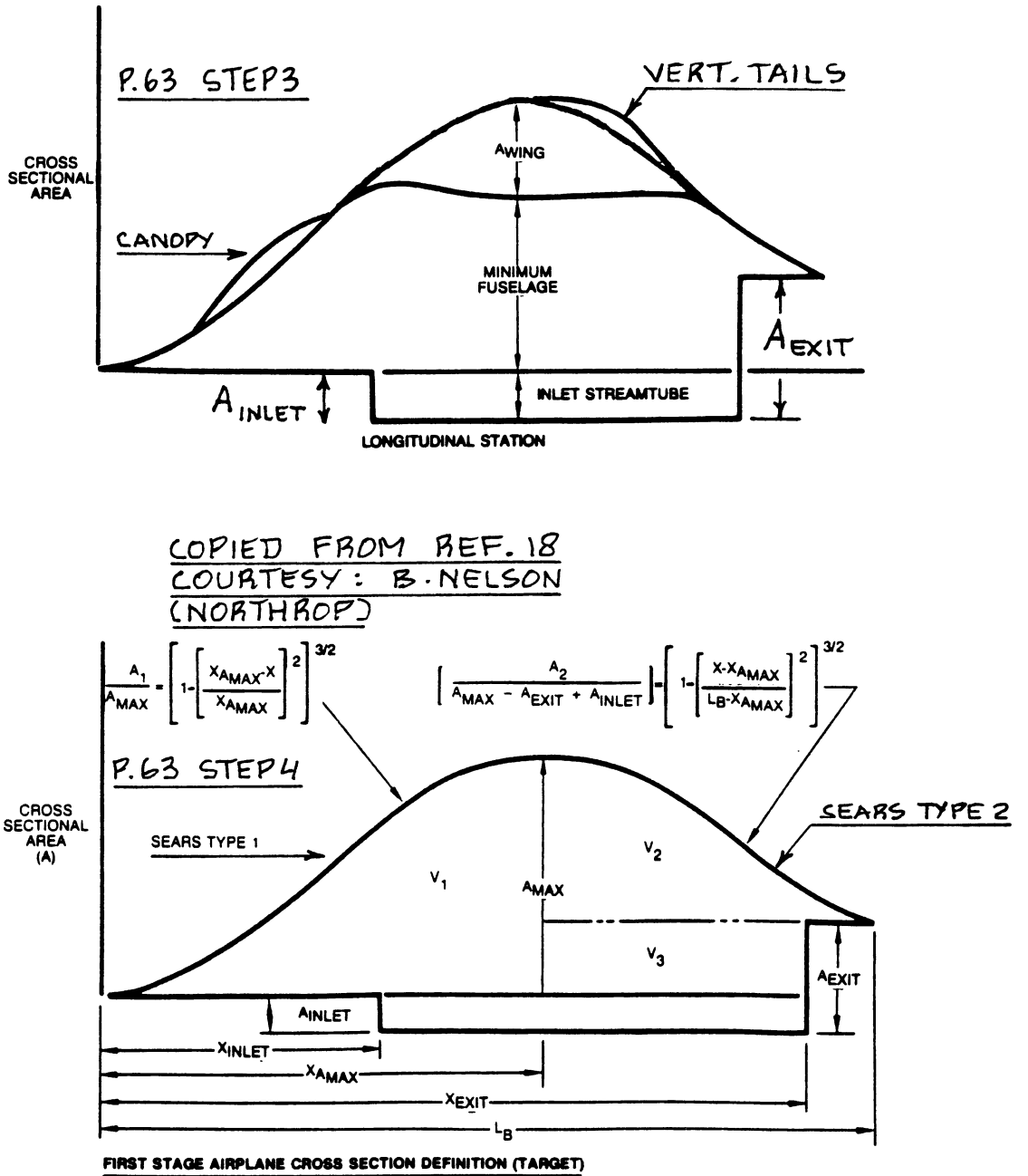

Figure 4.32 Development of a Cross Sectional Area Distribution from Volumetric Requirements

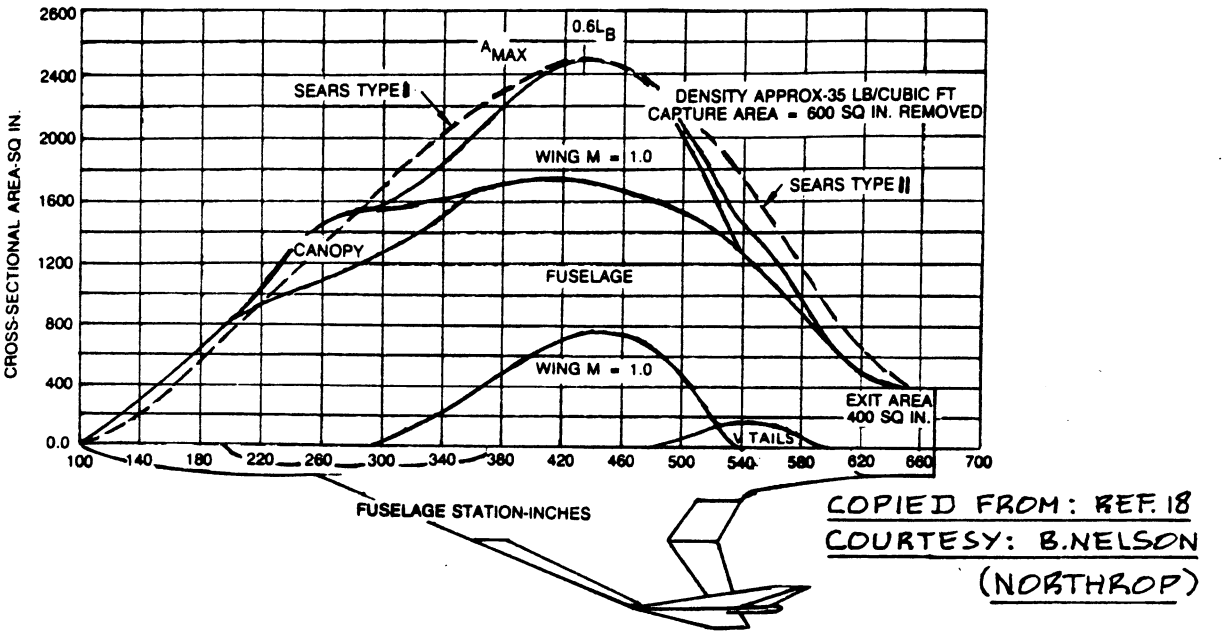

Figure 4.33 Example Cross Sectional Area Distribution

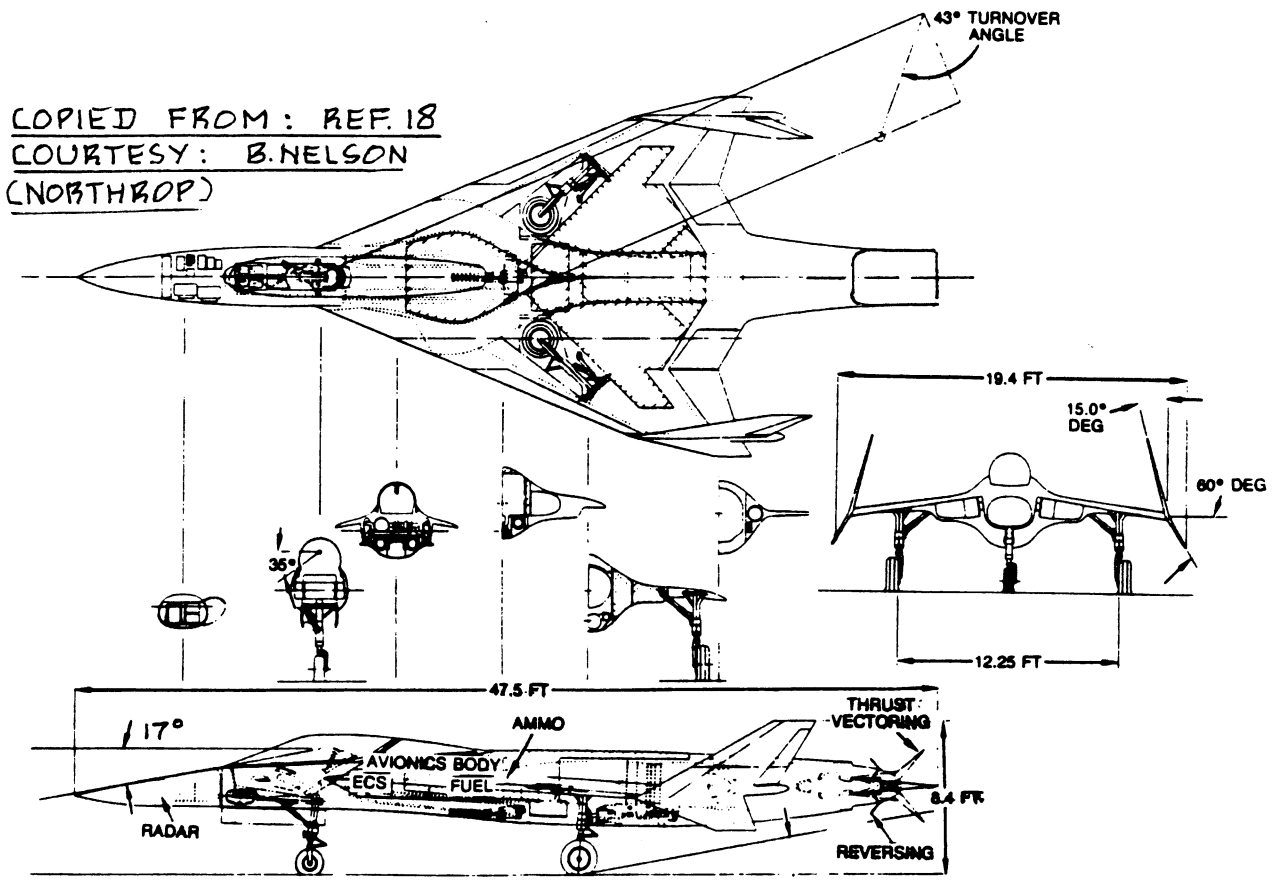

Figure 4.34 Critical Cross Sections for Figure 4.33

4.4 EMPENNAGE DRAG COEFFICIENT PREDICTION

4.4.1 Subsonic Empennage Drag Coefficient

The subsonic empennage drag coefficient is found from:

$$C_{D_{emp}} = SUM_i \{ (C_{D_{o_{emp}}})_i + (C_{D_{L_{emp}}})_i \} \qquad (4.45)$$

where: $(C_{D_{o_{emp}}})_i$ = empennage zero-lift drag coefficient of the number i empennage surface, see 4.4.1.1.

$(C_{D_{L_{emp}}})_i$ = empennage drag coefficient due to lift of the number i empennage surface, see 4.4.1.2.

4.4.1.1 Empennage zero-lift drag coefficient

The empennage zero-lift drag coefficient, $(C_{D_{o_{emp}}})_i$ may be computed with Equation (4.6) after replacing the appropriate wing parameters with those for the empennage.

It is assumed here that any airplane may have the following empennage surfaces:

* horizontal tail surface(s),
* canard surface(s) and
* vertical tail surface(s)

How many of these surfaces an airplane has and where they are located depends strongly on the configuration of the airplane. Chapter 3 of Part II presents more than 150 airplane configurations with different approaches to empennage layout design. Chapter 8 of Part II as well as Chapter V of Part III contain methods and examples for the sizing of empennage surfaces.

NOTE: For each of these empennage surfaces Eqn.(4.6) must be used with the following substitutions:

$S_{wet_w} = (S_{wet_{emp}})_i$

$R_{wf} = 1.0$

R_{LS} = as determined from Figure 4.2, but using the individual empennage surface sweep angle.

$C_{f_w} = C_{f_{emp}}$ which follows from Figure 4.3 at the appropriate empennage Reynolds number computed with as characteristic length, $\bar{c}_{emp_e}$, the exposed mean geometric chord for each empennage surface.

L' = as determined from Figure 4.4, using the maximum thickness location associated with each empennage airfoil.

(t/c) = maximum thickness ratio associated with each empennage airfoil, taken at its exposed mean geometric chord.

The empennage wetted area, $(S_{wet_{emp}})_i$ will normally be different for each empennage surface.

4.4.1.2 Empennage drag coefficient due to lift

The empennage drag coefficient due to lift, $(C_{D_{L_{emp}}})_i$ may be computed with the following method:

Horizontal Tail(s) and Canard(s)

Most canard and horizontal tail surfaces develop lift in a steady state flight condition. This lift causes induced drag.

In this text, the lift carried by empennage surfaces is split into two components:

1. Lift caused by the reference incidence setting of any empennage surface: the induced drag caused by this lift is accounted for in this paragraph.

2. Lift caused by the requirement to 'trim' the airplane at a particular center of gravity location: the induced drag caused by this lift is referred to as 'trim' drag: see Section 4.10.

If the empennage employs the so-called butterfly arrangement, the projection method of page 206 in Part II may be used to arrive at the 'equivalent horizontal' and the 'equivalent vertical' tail surface.

The amount of lift on a horizontal tail surface can

be computed from:

$$C_{L_h} = C_{L_{\alpha_h}} (\alpha_h - \alpha_{o_{L_h}}) \quad (4.46)$$

with: $\alpha_h = \alpha(1 - d\varepsilon/d\alpha) + i_h \quad (4.47)$

The amount of lift on a canard surface can be computed from:

$$C_{L_c} = C_{L_{\alpha_c}} (\alpha_c - \alpha_{o_{L_c}}) \quad (4.48)$$

with: $\alpha_c = \alpha(1 + d\varepsilon_c/d\alpha) + i_c \quad (4.49)$

Methods for predicting downwash ε, upwash ε_c and the zero lift angles of attack, $\alpha_{o_{L_h}}$ and $\alpha_{o_{L_c}}$, are presented in Chapter 10.

In airplanes with a fixed horizontal tailplane, i_h is usually zero. In airplanes with a fixed canard, i_c is normally set to assure that the canard stalls before the wing. In preliminary design it is acceptable to set:

$$i_c = \alpha_{stall_c} - \alpha_{stall_w} + i_w + 3 \quad (4.50)$$

where the values for α_{stall_c} and α_{stall_w} are taken as the airfoil stall angles of attack at the m.g.c. of their respective surfaces and where the wing incidence angle, i_w may be found from Tables 6.7 in Part II or from page 197 in Part III.

Since horizontal tails and canards are normally not twisted, their drag-due-to-lift may be computed from Eqn.(4.8) with ε_t=0, to yield:

$$C_{D_{L_{emp}}} = \{(C_{L_h})^2/\pi A_h e_h\} S_h/S + \{(C_{L_c})^2/\pi A_c e_c\} S_c/S \quad (4.51)$$

This equation applies to an airplane equipped with one horizontal tail and with one canard. If more empennage surfaces are present, they must be accounted for in a manner analogous to Eqn.(4.51).

Values for C_{L_h} and C_{L_c} follow from Eqns (4.46) and (4.48) respectively.

Values for A_h, A_c, S_h and S_c follow from airplane threeviews as developed in Chapter 13 of Part II.

For the Oswald efficiencies e_h and e_c the following values are suggested:

e_h = 0.5 for fuselage mounted tails

= 0.75 for T-tails

e_c = 0.5

Vertical Tail Surface(s)

Vertical tails are normally installed symmetrically so that the vertical tail drag contribution due to lift is usually zero. If the airplane is sideslipping over an angle β, this angle β should be considered as the angle of attack of the vertical tail. A modified version of Eqn.(4.51) may then be used to calculate the drag due to lift (in sideslip) of the vertical tail.

4.4.2 Transonic Empennage Drag Coefficient

The transonic empennage drag coefficient may be found from:

$$C_{D_{emp}} = SUM_i\{(C_{D_{o_{emp}}})_i + (C_{D_{L_{emp}}})_i\} \qquad (4.52)$$

where: $(C_{D_{o_{emp}}})_i$ = empennage zero-lift drag coefficient of the number i empennage surface, see 4.4.2.1.

$(C_{D_{L_{emp}}})_i$ = empennage drag coefficient due to lift of the number i empennage surface, see 4.4.2.2.

4.4.2.1 Empennage zero-lift drag coefficient

In the transonic speed range the empennage zero-lift drag coefficient is found from:

$$(C_{D_{o_{emp}}})_i = (C_{D_{o_{emp}}})_i + (C_{D_{emp_{wave}}})_i (S_{emp})_i / S \quad (4.53)$$

at M=0.6

where: $(C_{D_{o_{emp}}})_i$ at M=0.6 = empennage drag coefficient due to friction of the number i empennage surface at M=0.6. It is obtained from Eqn.(4.6) with the same substitutions as noted in 4.4.1.1.

$(C_{D_{emp_{wave}}})_i$ = empennage zero-lift wave drag coefficient obtained with the procedure of 4.2.2.1 but with the appropriate substitution of empennage (emp) parameters for wing (w) parameters.

To achieve acceptable wave drag characteristics, the entire configuration, including its empennage surfaces must be 'area-ruled'. A procedure for 'area-ruling' any configuration is given in Sub-section 4.3.4.

4.4.2.2 Empennage drag coefficient due to lift

The transonic empennage drag coefficient due to lift, $(C_{D_{L_{emp}}})_i$ may be computed from Eqn.(4.18), as long as the following substitutions are used:

To find $(C_{D_L}/C_L^2)_{emp_i}$ from Figures 4.13, use the appropriate transonic similarity parameters for the number i empennage surface.

For C_{L_i} use either C_{L_h} or C_{L_c} as in Equations (4.46) or (4.48).

4.4.3 Supersonic Empennage Drag Coefficient

The supersonic empennage drag coefficient is found from:

$$C_{D_{emp}} = SUM_i \{(C_{D_{o_{emp}}})_i + (C_{D_{L_{emp}}})_i\} \quad (4.54)$$

where: $(C_{D_{o_{emp}}})_i$ = zero lift drag coefficient of the number i empennage surface, see 4.4.3.1.

$(C_{D_{L_{emp}}})_i$ = drag coefficient due to lift of the number i empennage surface, see 4.4.3.2.

4.4.3.1 Empennage zero-lift drag coefficient

The supersonic empennage zero lift drag coefficient is found from:

$$(C_{D_{o_{emp}}})_i = (C_{D_{emp_f}})_i + (C_{D_{emp_{wave}}})_i \quad (4.55)$$

where: $$(C_{D_{emp_f}})_i = (C_{f_{emp}})_i (S_{wet_{emp}})_i / S \quad (4.56)$$

where: $(C_{f_{emp}})_i$ may be found from Fig.4.3 at the appropriate empennage Reynolds number computed with as characteristic length, $\bar{c}_{emp_e}$, the exposed mean geometric chord of each empennage surface.

$(C_{D_{emp_{wave}}})_i$ = wave drag coefficient of the number i empennage surface. This wave drag coefficient may be determined with the method of 4.2.3.1 as long as the appropriate empennage parameters are substituted for their wing counterparts.

4.4.3.2 Empennage drag coefficient due to lift

The supersonic empennage drag coefficient due to lift is found from:

$$(C_{D_{L_{emp}}})_i = (C_{D_L}/C_L^2)_{emp_i} (C_{L_{emp}}^2)_i \quad (4.57)$$

Values for $(C_{D_L}/C_L^2)_{empi}$ may be obtained from the method of 4.2.3.2, as long as the appropriate parameter substitutions are made.

Values for $(C_{L_{emp}})_i$ follow from either Eqn.(4.46) or from Eqn.(4.48).

4.5 NACELLE/PYLON DRAG COEFFICIENT PREDICTION

Methods for predicting nacelle/pylon drag are presented as follows:

4.5.1 Isolated Nacelle/Pylon Drag Coefficient

This method is applicable in all speed regimes considered in this text.

4.5.2 Installed Nacelle/Pylon Drag Coefficient Increment

This method applies only in the subsonic speed regime and provides the 'interference' drag increment due to nacelle/pylon installations.

It is assumed that this 'interference' drag increment is independent of Mach number as long as the appropriate area ruling is used in the transonic and supersonic speed ranges. See Sub-section 4.3.4 for details on area ruling.

4.5.3 Windmilling Drag and Propeller Drag Coefficients

This method provides the drag increase caused by engine and/or propeller stoppage.

These methods should be applied as follows:

Step 1: Determine the subsonic installed drag increment due to the nacelle or the nacelle/pylon combination from Sub-section 4.5.2. Again: this drag increment represents the interference drag of the installation.

Step 2: Determine the drag increments due to transonic and supersonic operations from Sub-section 4.5.1 which assumes the nacelle/pylon to be isolated.

Step 3: Add the transonic and/or supersonic increments from Step 2 to the nacelle/pylon interference drag obtained in Step 1.

Step 4: For windmilling and/or propeller drag increments use Sub-section 4.5.3. Add this drag increment to the drag obtained in Step 3.

4.5.1 Isolated Nacelle/Pylon Drag Coefficient

The nacelle/pylon drag coefficient may be computed from:

$$C_{D_{np}} = C_{D_n} + C_{D_p} \tag{4.58}$$

where: C_{D_n} = nacelle drag coefficient, see 4.5.1.1.

C_{D_p} = pylon drag coefficient, see 4.5.1.2.

4.5.1.1 Nacelle drag coefficient

Engine operating:

The nacelle drag coefficient is found from:

$$C_{D_n} = SUM_i (C_{D_n})_i \tag{4.59}$$

The number i equals the number of nacelles on the airplane. Each nacelle drag coefficient, $(C_{D_n})_i$ is computed with the method of Section 4.3. This assumes that a nacelle can be treated as if it is a (small) fuselage.

Note: nacelles will generate lift when placed at an angle of attack. Local nacelle angle of attack should be expressed as:

$$\alpha_n = \alpha_w + i_n + \varepsilon_n \tag{4.60}$$

where: α_w = wing angle of attack

i_n = nacelle incidence angle, see Figure 4.35.

ε_n = nacelle upwash and downwash angle. This depends on where the nacelle is intalled on the airplane. Figure 4.36 illustrates two possibilities. $\varepsilon_n > 0$ for upwash and $\varepsilon_n < 0$ for downwash.

The nacelle up- or downwash angle follows from:

$$\varepsilon_n = (d\varepsilon_n/d\alpha)\alpha \tag{4.61}$$

where: $d\varepsilon_n/d\alpha$ is computed with the methods described in Chapter 8.

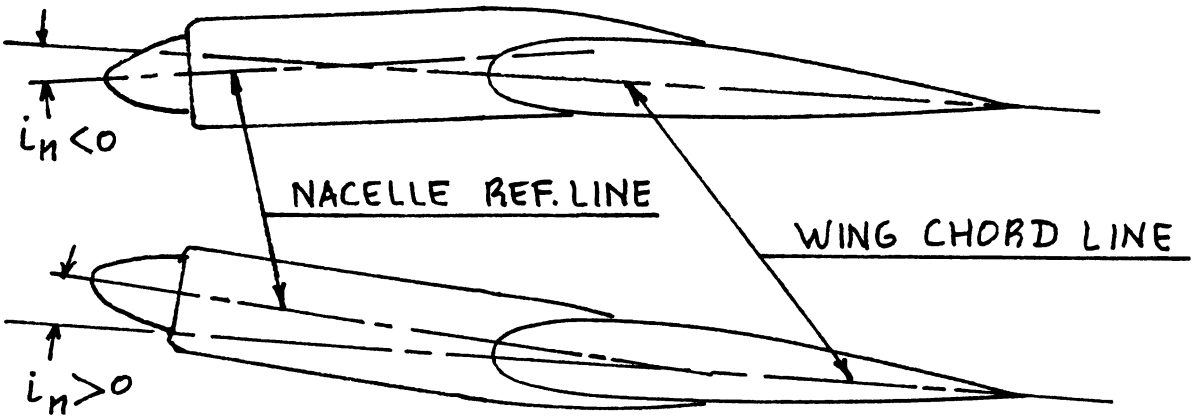

Figure 4.35 Definition of Nacelle Incidence Angle

a) NACELLE ON WING

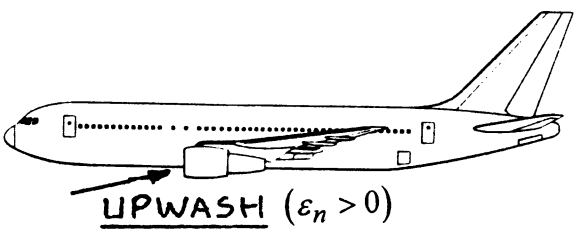

b) NACELLE ON FUSELAGE

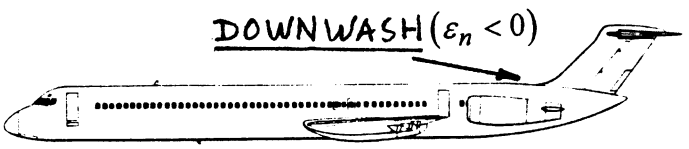

Figure 4.36 Examples for Nacelle Upwash and Downwash

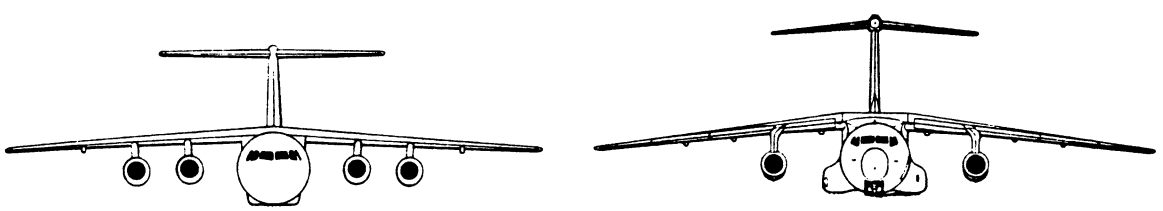

Figure 4.37 Examples of Vertically Installed Pylons

Engine Inoperative:

In addition to the drag given by Eqn.(4.59) there will be extra drag caused by engine or propeller windmilling. If a propeller is stopped, there will be extra drag due to that.

Sub-section 4.5.3 deals with such cases.

4.5.1.2 Pylon drag coefficient

The pylon drag coefficient may be found from:

$$C_{D_p} = SUM_i \ (C_{D_p})_i \qquad (4.62)$$

It will be assumed here that the drag behavior of a pylon can be modelled as that of an empennage. For this reason, values for $(C_{D_p})_i$ may be obtained by using the method of Section 4.4.

For vertically installed pylons (see Figure 4.37), the pylon should be treated as a vertical tail: the drag prediction method of Section 4.4 may be used.

For horizontally installed pylons (see Figure 4.38) the pylon should be treated as a horizontal tail or as a canard: use the drag prediction method of Section 4.4.

NOTA BENE 1: Nacelles installed in the proximity of wings (see Figure 4.37a) must be installed so that they are at zero local sideslip angle in the local flowfield. This results in the need for 'toe-in' for nacelles such as in the Boeing 747 series airplanes: see Figure 4.39.

NOTA BENE 2: The methods of 4.5.1.1 and 4.5.1.2 apply to all speed regimes. However, in the transonic and supersonic speed regimes the method is valid only as long as the nacelle/pylon combination is included in the area-ruling process described in Sub-section 4.3.3. Note: the nacelle stream tube should not be included in this area ruling process.

4.5.2 Installed Nacelle/Pylon Drag Coefficient Increment

Sub-section 4.5.1 provides a method for predicting the drag coefficient, $C_{D_{np}}$ due to isolated nacelle/pylon combinations.

In the following, a method for computing the interference drag increment caused by a nacelle/pylon

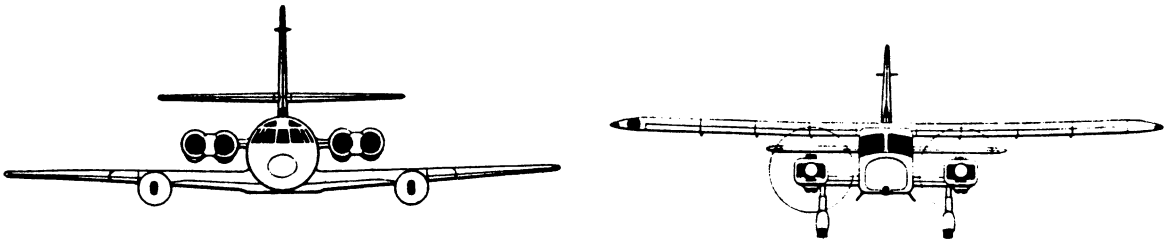

Figure 4.38 Examples of Horizontally Installed Pylons

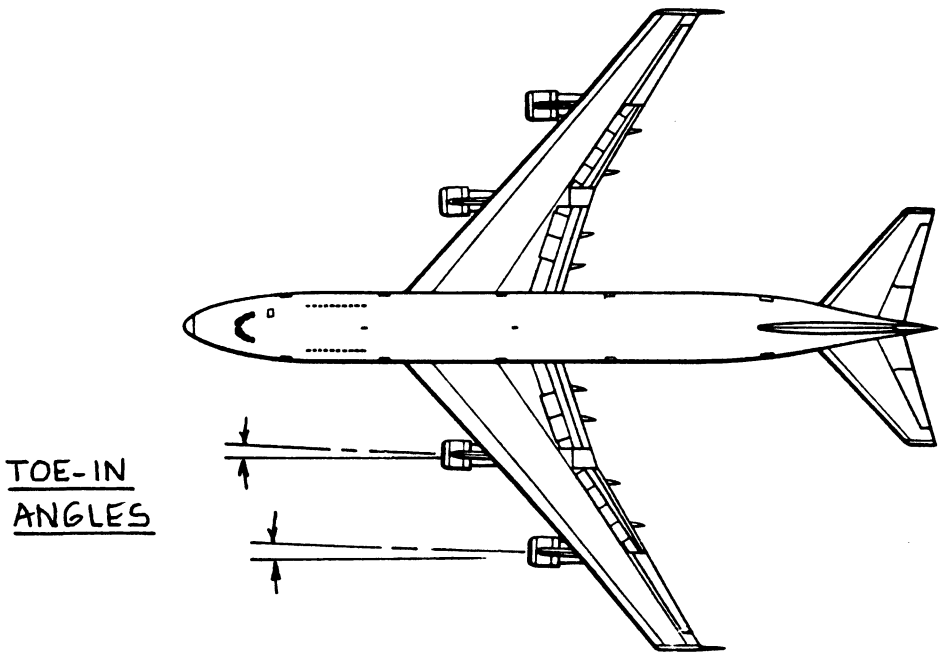

Figure 4.39 Example of Nacelles with Toe-in

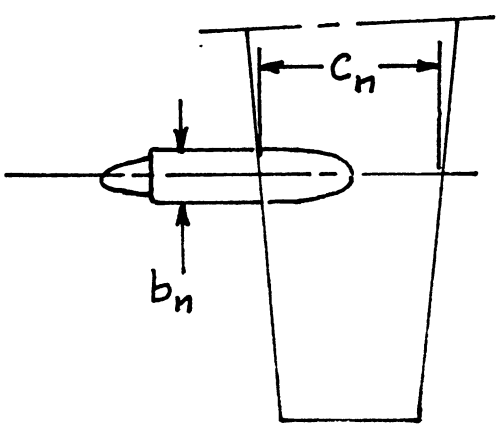

Figure 4.40 Definition of Nacelle Parameters

installation is presented. The method is broken down into three parts:

4.5.2.1 Wing/nacelle interference drag coefficient
4.5.2.2 Fuselage/nacelle interference drag coefficient
4.5.2.3 Cooling drag coefficient increment

Which drag increment should be accounted for depends on the airplane configuration.

4.5.2.1 Wing/nacelle interference drag coefficient

For turboprop and for piston-prop nacelle/wing installations the interference drag coefficient is found from:

$$C_{D_{n_{int}}} = 0.036\,(c_n b_n/S)(\Delta c_{l_1} + \Delta c_{l_2})^2 \qquad (4.63)$$

where: c_n and b_n are defined in Figure 4.40.

Δc_{l_1} = 0.2 for a nacelle on top of the wing

= -0.3 for a nacelle below the wing

$\Delta c_{l_2} = 0.056(i_n)$ (i_n is in degrees)

i_n = nacelle incidence angle defined in Figure 4.35.

For jet-driven airplanes the wing/nacelle interference drag coefficient is found from:

$$C_{D_{n_{int}}} = F_{a_1}(\Delta C_{D_n}/C_{D_n})C_{D_n} \qquad (4.64)$$

where: $(\Delta C_{D_n}/C_{D_n})$ follows from Figure 4.41 at the Mach numbers indicated.

C_{D_n} = nacelle drag coefficient as determined in 4.5.1.1.

F_{a_1} = 1.0 for M < 0.5

1.0 for M > 0.5 and no local area ruling of the nacelle/pylon/wing intersection.

0.5 for M > 0.5 and a locally area ruled nacelle/pylon/wing intersection.

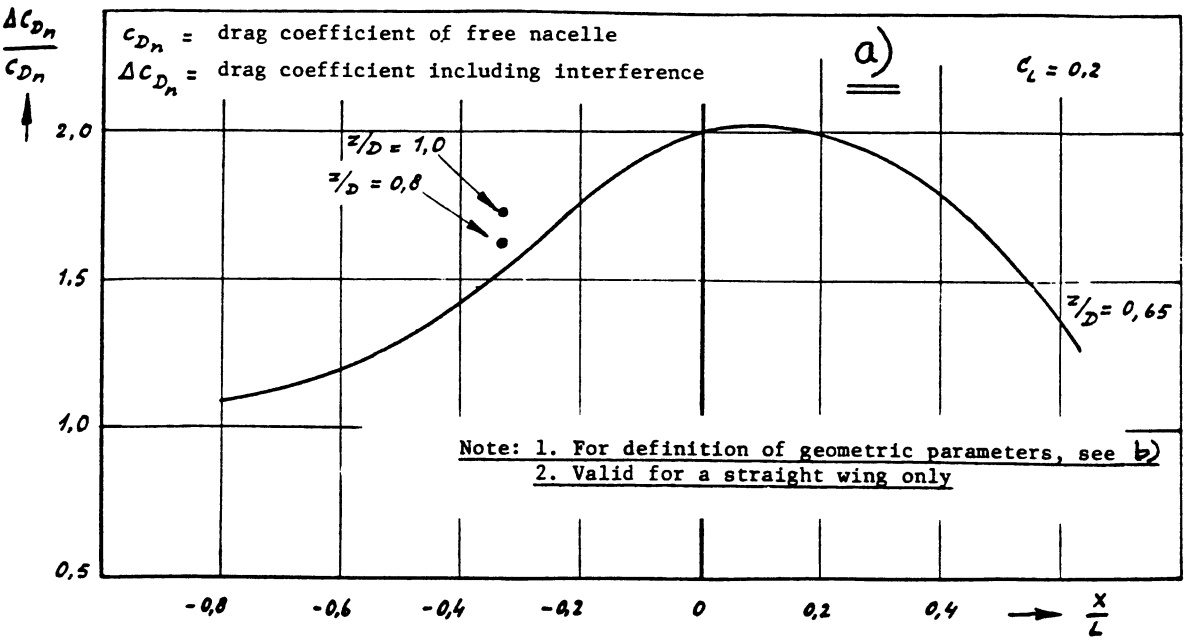

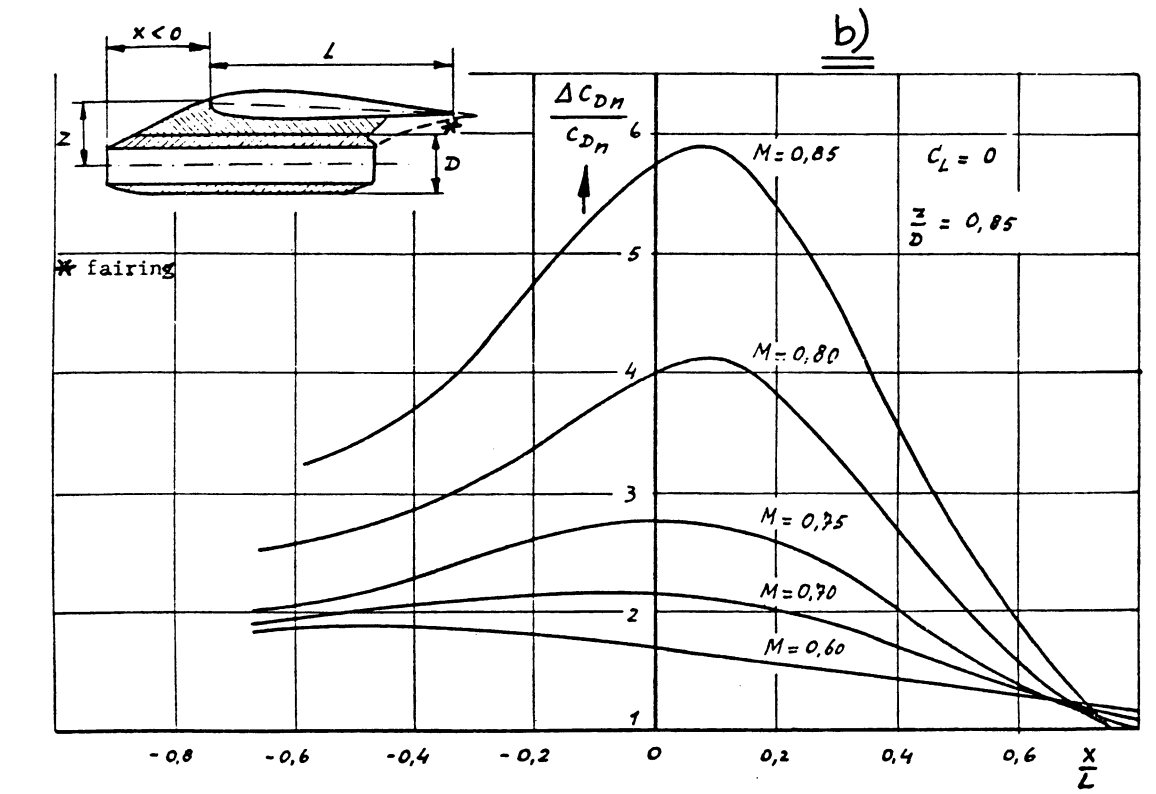

Note: Valid for swept wings only

COPIED FROM: REF. 21

Figure 4.41 Wing-Nacelle Drag Interference Factor

4.5.2.2 Fuselage/nacelle interference drag coefficient

The fuselage/nacelle interference drag coefficient may be found from:

$$C_{D_{n_{int}}} = F_{a_2}\{(C_{D_n})' - 0.05\}(S_n/S) \quad (4.65)$$

where: $(C_{D_n})'$ is found from Figure 4.42

S_n = maximum frontal area of the nacelle, excluding the pylon: see Figure 4.38.

F_{a_2} = 1.0 for fuselage/nacelle intersections without local area ruling

= 0.5 for fuselage/nacelle intersections with local area ruling.

4.5.2.3 Cooling drag coefficient increment

The cooling drag coefficient increment for radial air-cooled engine installations may be estimated from:

$$C_{D_{n_{cool}}} = (\Delta C_{D_{cool}})\{\pi(d_n)^2/4S\} \quad (4.66)$$

where: $\Delta C_{D_{cool}}$ follows from Figure 4.43.

d_n = the maximum nacelle diameter as shown in Figure 4.38.

4.5.3 Windmilling Drag and Propeller Drag Coefficients

The following cases should be considered:

1.) Windmilling drag coefficient due to jet engines: see 4.5.3.1.

2.) Windmilling drag coefficient due to propellers: see 4.5.3.2.

3.) Drag coefficient due to a stopped propeller: see 4.5.3.3.

4.5.3.1 Windmilling drag coefficient due to jet engines

The incremental drag coefficient due to a windmilling jet engine may be estimated from:

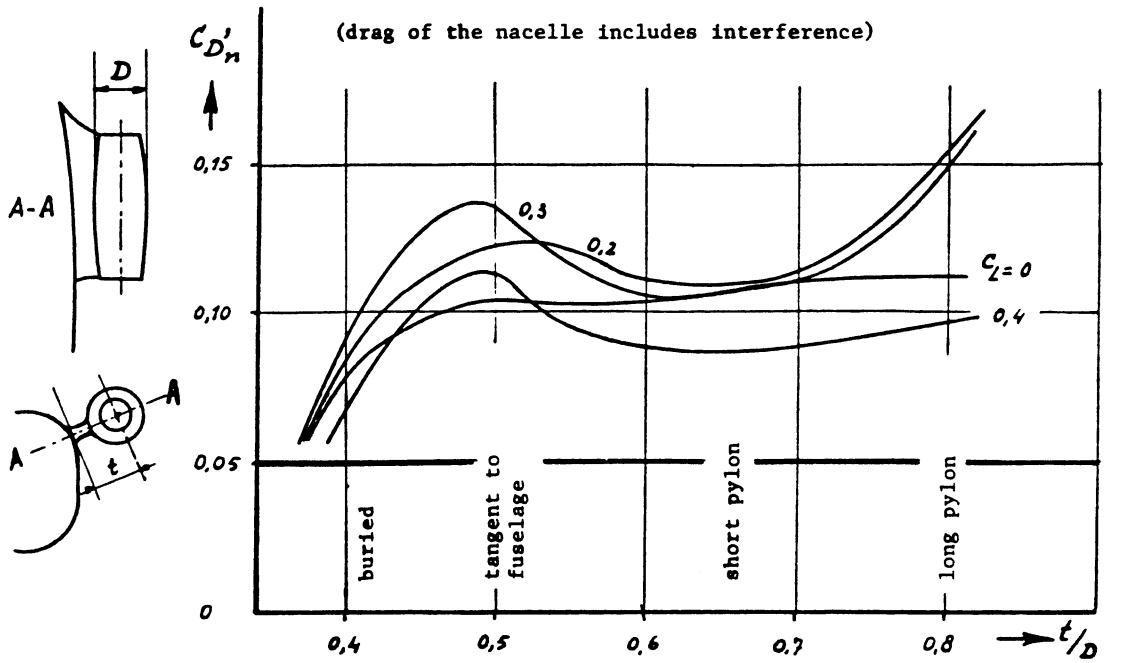

COPIED FROM: REF. 21

Note: 1. C_{D_n} is based on maximum nacelle frontal area

2. drag coefficient of the free nacelle is 0.05

Figure 4.42 Fuselage-Nacelle Drag Interference Factor

①	②	③	④	⑤	⑥	⑦	⑧
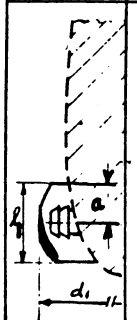							
$\frac{d_1}{l_1} = 1,78$	1,78	1,62	1,5	1,63	1,63	1,63	3,62
$\frac{a}{l_1} = 0,59$	0,59	0,59	0,63	0,66	0,66	0,66	0,16
$\Delta C_D^* = 0,16$	0,075	0,10	0,07	0,06	0,088	0,212	0,152

*) ΔC_D BASED ON: $\frac{\pi}{4} d_1^2$

COPIED FROM REF. 21

Figure 4.43 Cooling Drag Coefficient Increment

$$\Delta C_{D_{wmj}} = 0.0785(d_{inl}^2)/S +$$

$$+ \{2/(1 + 0.16M^2)\}(V_{noz}/U_1)(1 - V_{noz}/U_1)S_{noz}/S \quad (4.67)$$

where: d_{inl} = engine inlet diameter

S_{noz} = nozzle cross section area

V_{noz}/U_1 = ratio of average flow velocity in the nozzle to the steady state flight speed The following values are suggested for this ratio:

V_{noz}/U_1 = 0.25 for turbojets and turboprops

= 0.42 for low by-pass ratio jet engines

= 0.12 for the primary airflow of high by-pass jet engines

= 0.92 for the fan airflow of high bypass jet engines

4.5.3.2 Windmilling drag coefficient due to propellers

Reference 20 provides a method for estimating the windmilling drag due to a propeller. In absence of that reference it is suggested to use:

$$\Delta C_{D_{wmprop}} = 33(1/\bar{q}S)SHP_{rated}/U_1 \quad (4.68)$$

where: SHP_{rated} = maximum rated shaft horsepower of the engine in the flight condition being considered. Note: use hp!

U_1 = steady state flight speed, in fps.

4.5.3.3 Drag coefficient due to a stopped propeller

The incremental drag coefficient due to a stopped propeller may be estimated from:

$$\Delta C_{D_{prop}} = 0.00125n_p(D_p)^2/S \quad (4.69)$$

where: n_p = number of blades per propeller

D_p = diameter of the propeller

4.6 FLAP DRAG PREDICTION

The assumption is made that flaps will be deployed only in the subsonic speed regime. For the effect of flap drag at high speed the reader should consult reference 9.

The drag coefficient due to flap deflection may be estimated from:

$$C_{D_{flap}} = \Delta C_{D_{prof_{flap}}} + \Delta C_{D_{i_{flap}}} + \Delta C_{D_{int_{flap}}} \quad (4.70)$$

where: $\Delta C_{D_{prof_{flap}}}$ = the flap profile drag increment, see 4.6.1.

$\Delta C_{D_{i_{flap}}}$ = the induced drag increment due to the flap, see 4.6.2.

$\Delta C_{D_{int_{flap}}}$ = the interference drag increment due to the flap, see 4.6.3.

4.6.1 Flap Profile Drag Increment

The following method applies to wings with sweep angles up to 40 degrees. For higher sweep angles the reader should consult Reference 9.

The flap profile drag increment may be found from:

$$\Delta C_{D_{prof_{flap}}} = (\Delta C_{d_{p_{\Lambda_{c/4}=0}}})(\cos\Lambda_{c/4})S_{wf}/S \quad (4.71)$$

where: $\Delta C_{d_{p_{\Lambda_{c/4}=0}}}$ = the two-dimensional profile drag increment due to flaps.

This increment depends on the type of flaps used:

For <u>plain</u> flaps: use Figure 4.44.

For <u>split</u> flaps, use Figure 4.45.

For <u>single slotted</u> flaps, use Figure 4.46.

For <u>double slotted</u> flaps: use Figure 4.47.

For <u>Fowler</u> flaps: use Figure 4.48.

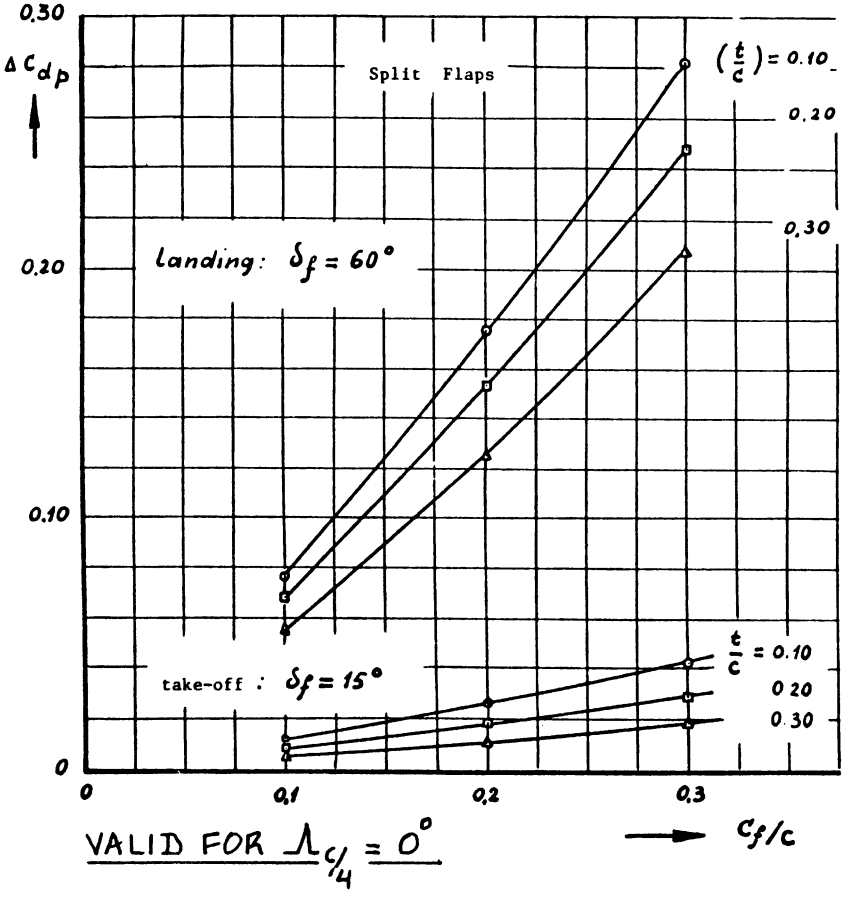

Figure 4.45 Profile Drag Increment: Split Flaps

COPIED FROM REF. 21

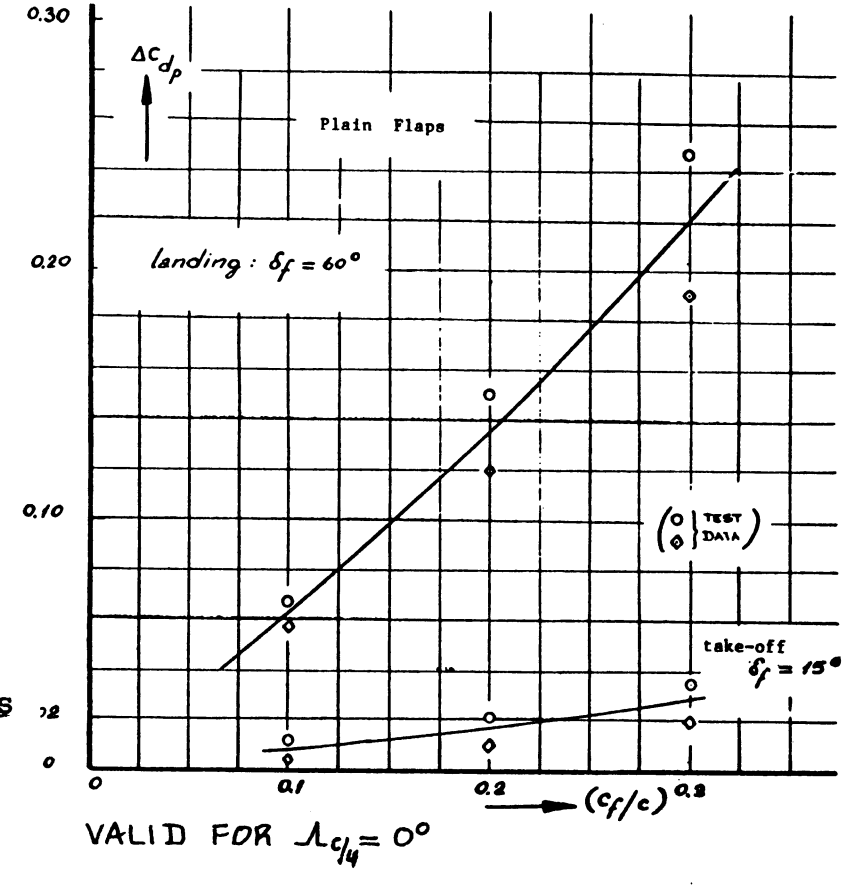

Figure 4.44 Profile Drag Increment: Plain Flaps

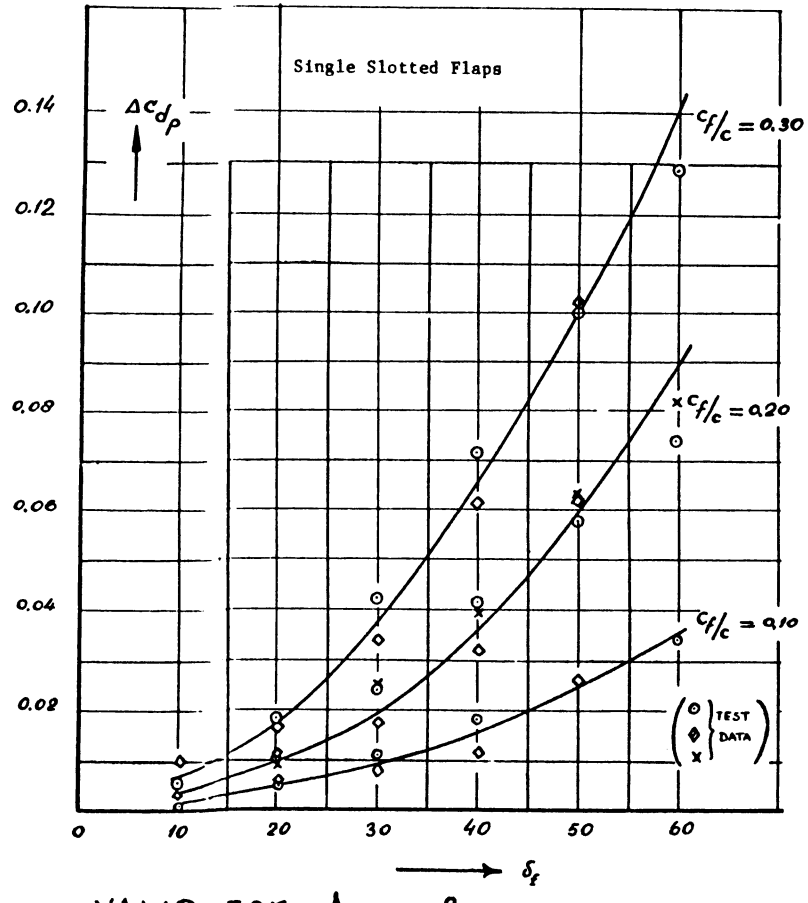

Figure 4.46 Profile Drag Increment: Single Slotted Flaps

COPIED FROM REF. 21

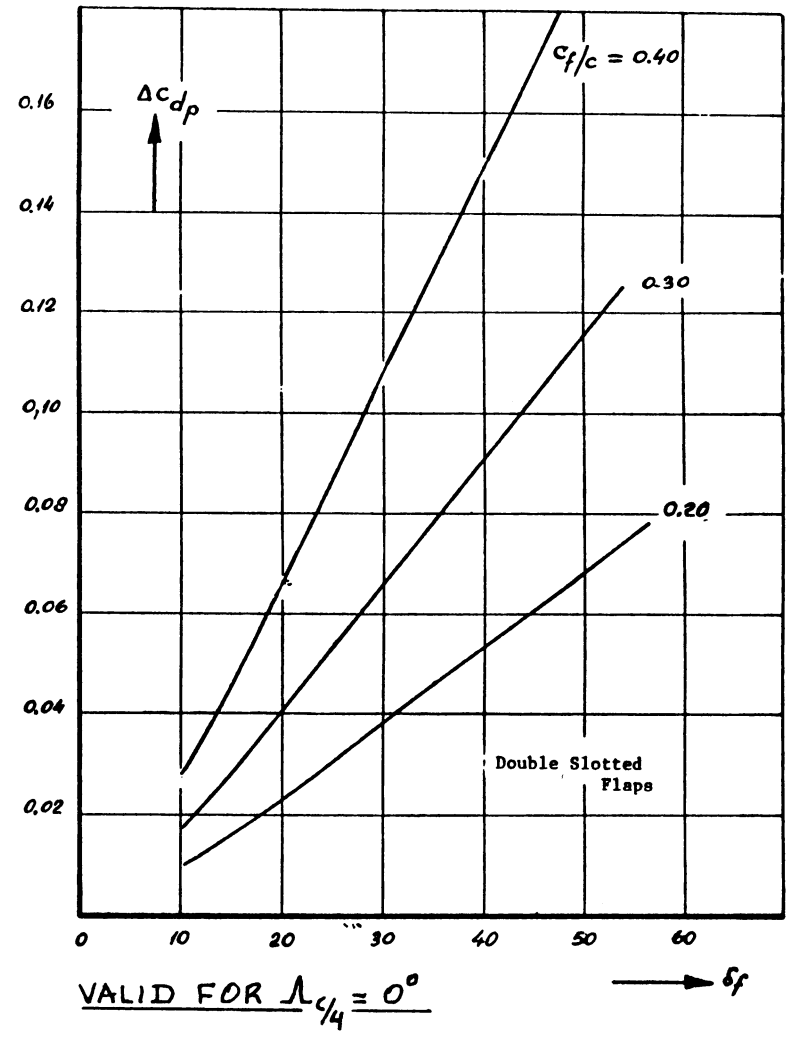

Figure 4.47 Profile Drag Increment: Double Slotted Flaps

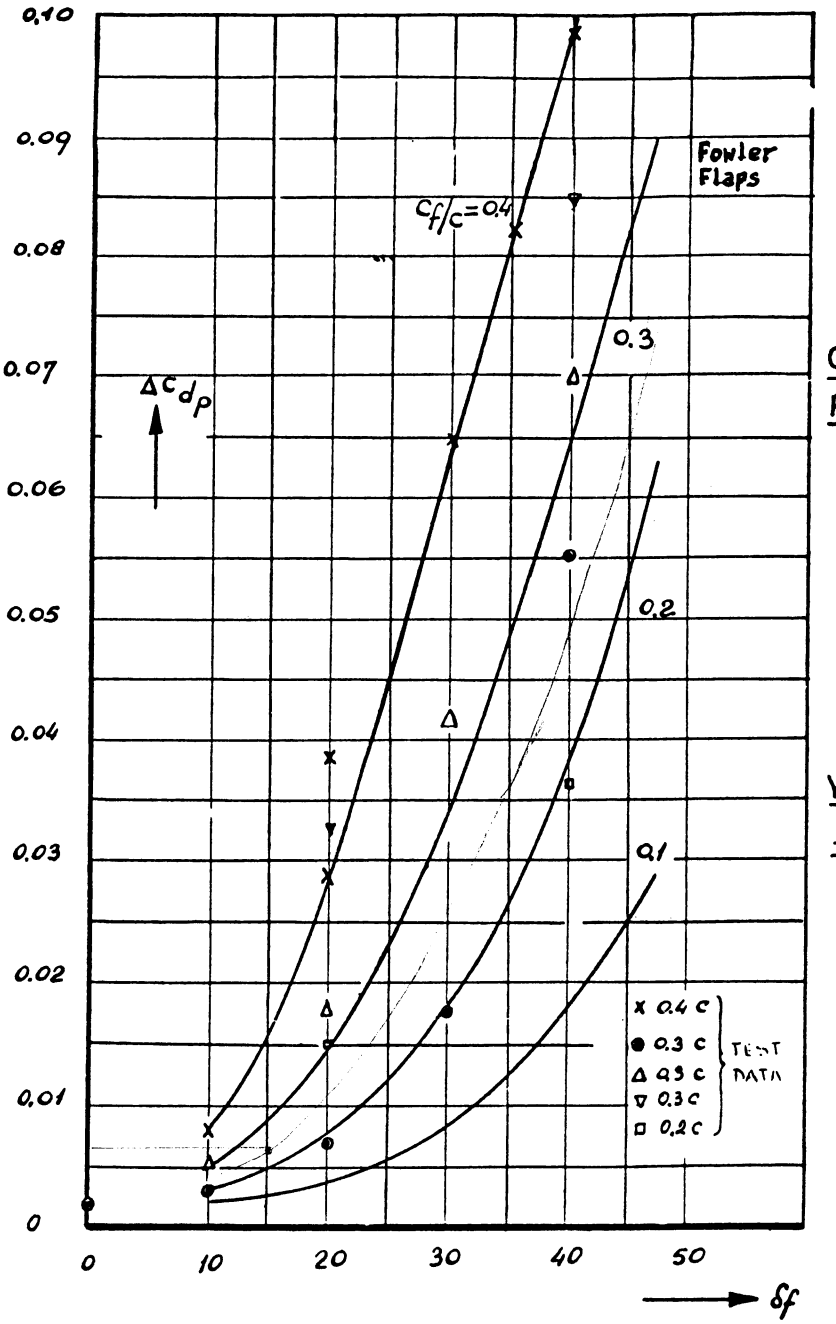

Figure 4.48 Profile Drag Increment: Fowler Flaps

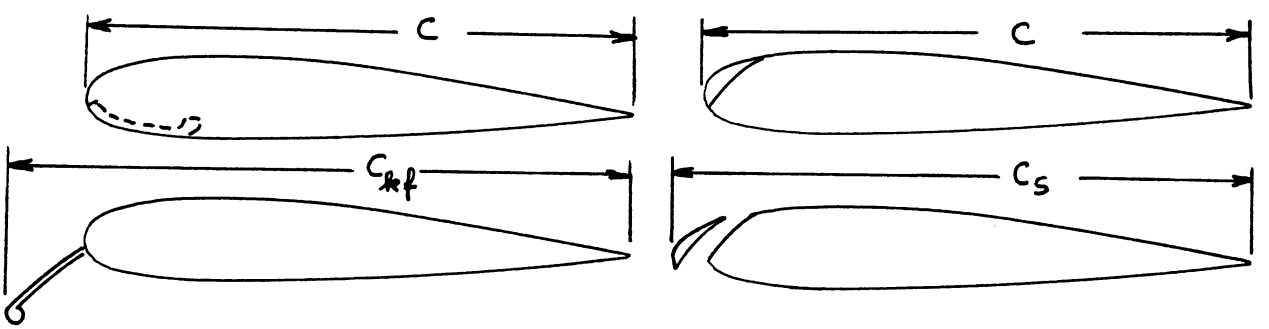

Figure 4.49 Definition of Flap Chords

For Krueger flaps, use:

$$\Delta C_{d_{p_{\Lambda_{c/4}=0}}} = C_{D_{o_w}} (c_{kf}/c) \qquad (4.72)$$

where: $C_{D_{o_w}}$ is obtained from Eqn.(4.6).

c_{kf}/c = ratio of wing chord with Krueger flap extended to that of the wing with the Krueger flap retracted: see Figure 4.49.

For slats, use:

$$\Delta C_{d_{p_{\Lambda c/4}=0}} = C_{D_{o_w}} (c_s/c) \qquad (4.73)$$

where: c_s/c = ratio of wing chord with slats extended to that of the wing with the slats retracted: See Figure 4.49.

Figure 4.50 illustrates these various flap types.

$\Lambda_{c/4}$ = wing quarter chord sweep angle.

S_{wf} = the flapped wing area: see Figure 4.50.

4.6.2 Induced Drag Increment due to Flaps

The induced drag increment due to flaps may be estimated from:

$$\Delta C_{D_{i_{flap}}} = K^2 (\Delta C_{L_{flap}})^2 \cos\Lambda_{c/4} \qquad (4.74)$$

where: $\Delta C_{L_{flap}}$ = the incremental lift coefficient due to the flap. This quantity follows from comparing a flaps-up with a flaps-down C_L-versus-α curve: see Figure 4.51.

Chapter 8 presents a method for constructing Fig.4.51.

K = an empirical constant which follows from Figures 4.52 and 4.53.

4.6.3 Interference Drag Increment due to Flaps

The interference drag increment due to flaps may be estimated from:

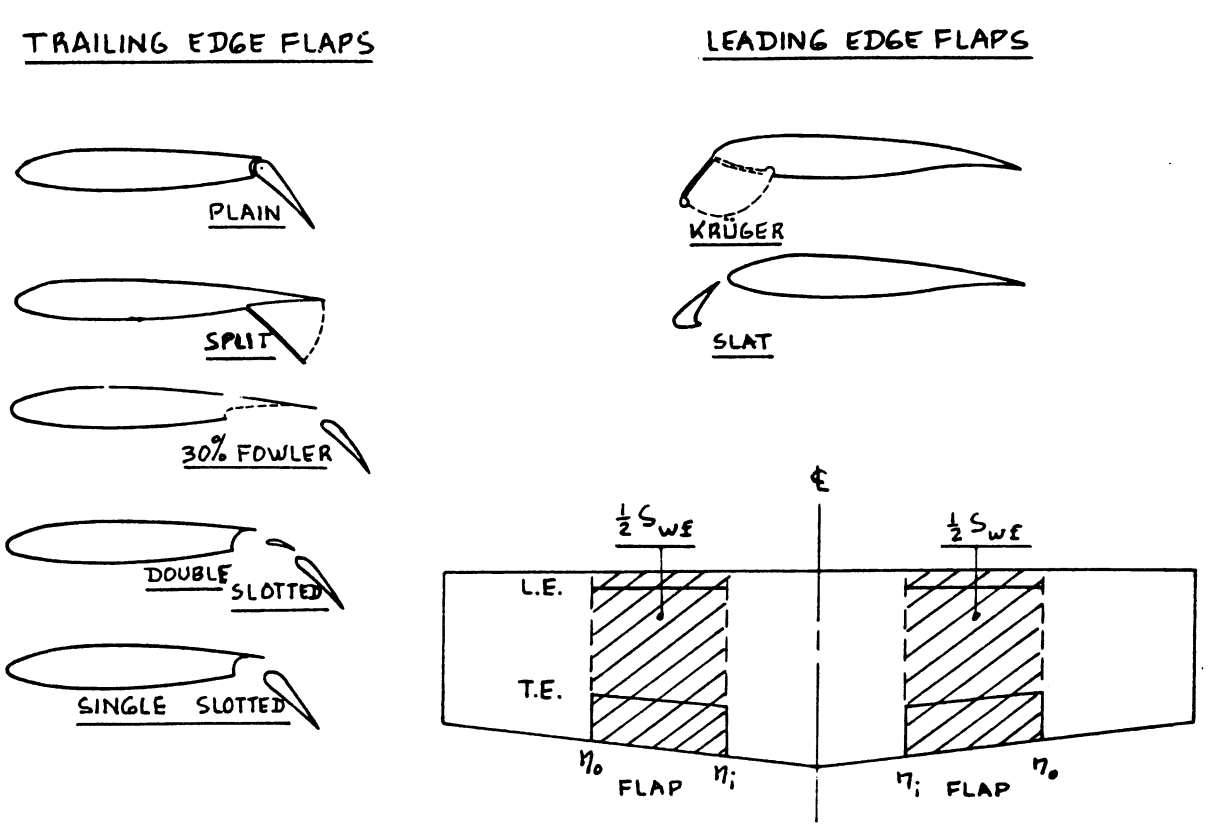

Figure 4.50 Typical Flap Types for Figures 4.44 - 4.48

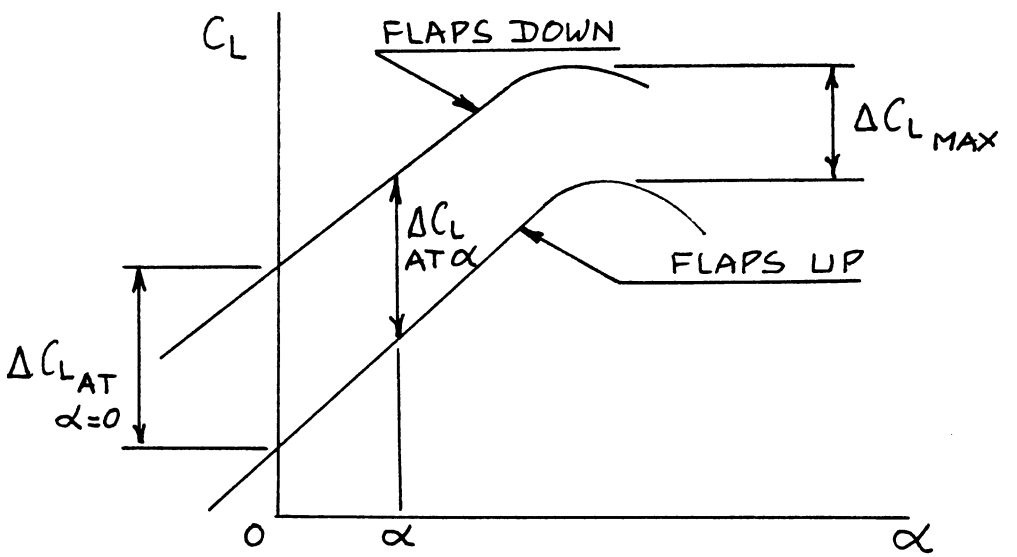

Figure 4.51 Example of Flaps-up and Flaps-down Lift Coefficient Versus Angle-of-Attack Behavior

$$\Delta C_{D_{int_{flap}}} = K_{int} \Delta C_{D_{prof_{flap}}} \quad (4.75)$$

where: $\Delta C_{D_{prof_{flap}}}$ follows Sub-section 4.6.1.

K_{int} = - 0.15 for split flaps

= 0 for plain flaps

= + 0.40 for slotted flaps

= + 0.25 for Fowler flaps

= + 0.10 for slats and for Kruegers

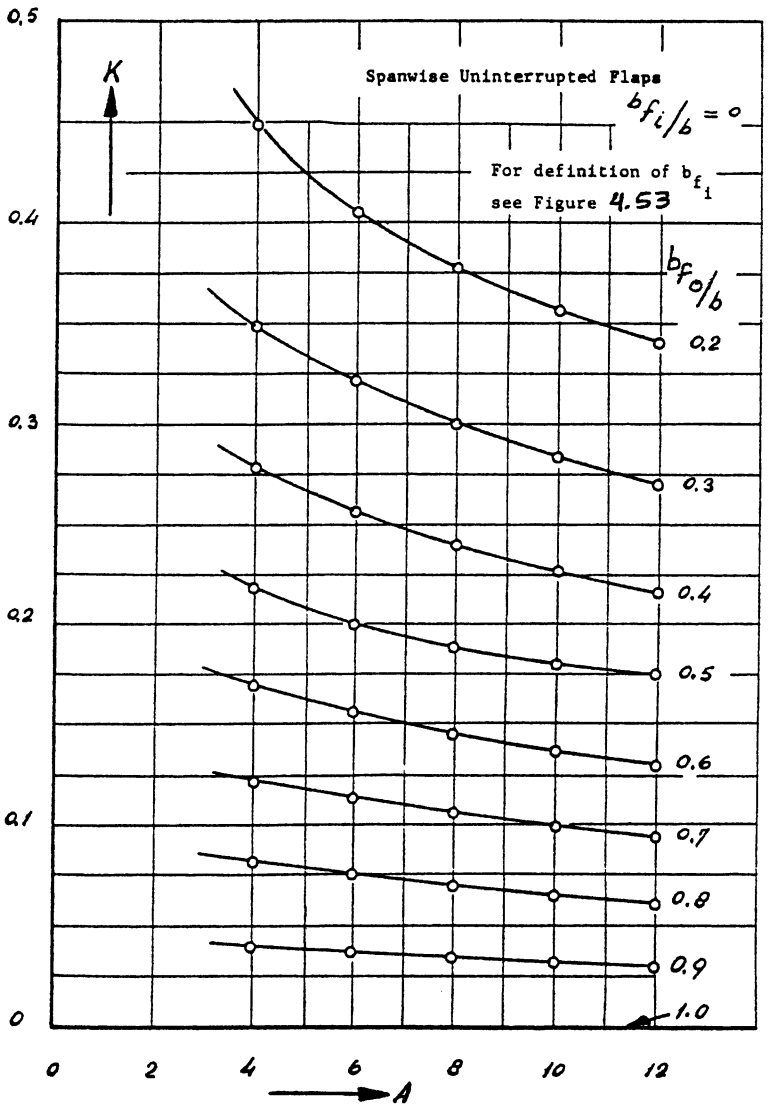

COPIED FROM: REF. 21

Figure 4.52 Induced Drag Factor for Uninterrupted Flaps

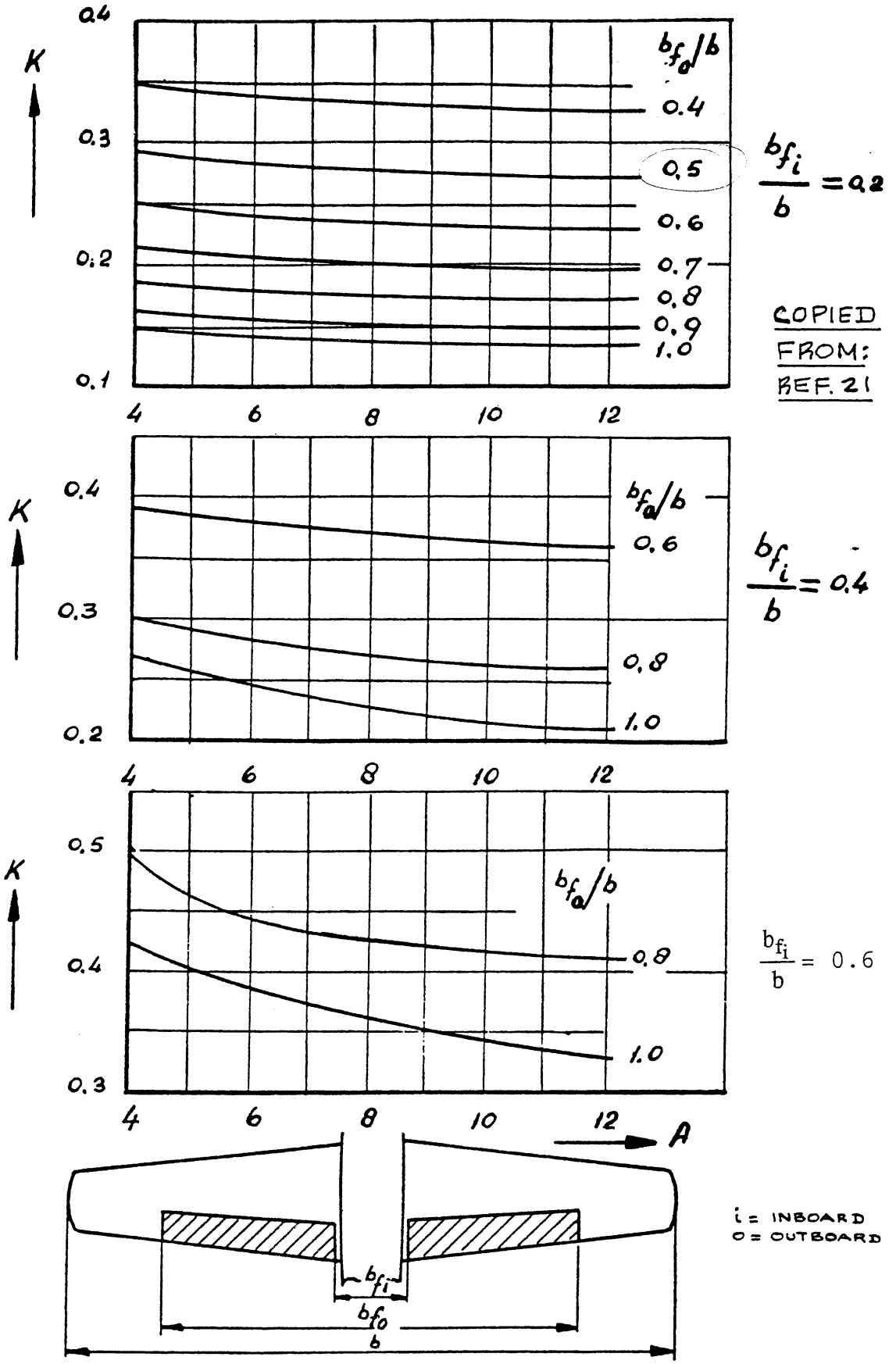

COPIED FROM: REF. 21

Figure 4.53 Induced Drag Factor for Interrupted Flaps

4.7 LANDING GEAR DRAG PREDICTION

The assumption is made that landing gear deployment will occur only in the subsonic speed regime. The method presented here applies only at low speed.

The landing gear drag coefficient for an airplane with i landing gears may be computed from:

$$C_{D_{gear}} = SUM_i[\{(C_{D_{gear_{C_L=0}}})_i + p_i C_L\}(S_{gear})_i/S] \qquad (4.76)$$

where: $C_{D_{gear_{C_L=0}}}$ = the zero-lift drag coefficient of the landing gear based on its own reference area, S_{gear}. Figures 4.54 through 4.60 provide data from which the zero-lift drag coefficient of the landing gear may be determined.

S_{gear} = reference area for the zero-lift gear drag coefficient. This reference area is defined in Figures 4.54-4.60. For most landing gear types: $S_{gear} = b_t x D_t$, where b_t is the tire width and D_t is the tire diameter.

p = a factor which accounts for the variation of gear drag with lift. Figure 4.61 gives a method for determining this factor p.

Airplanes can have a number of different types of landing gear. The summation over i landing gears in Eqn.(4.76) indicates this.

Figures 4.54 - 4.60 should be used as follows:

For fixed landing gears: Figures 4.54 and 4.55 apply to non-retractable (= fixed) landing gears attached to wing or fuselage. Note that these drag coefficients are based on: $S_{gear} = b_t x D_t$.

Figure 4.56 applies to non-retractable (= fixed) landing gears attached to nacelles. These drag coefficients are based on: $S_{gear} = b_t x D_t$.

Important note: The data in Figures 4.54 - 4.56 apply to the entire main gear which is assumed to consist of two of the legs shown in these figures.

Note: 1. All C_D values are referenced to $b_t x D_t$ and are valid for $C_L=0$

2. All landing gears shown in this figure are assumed to have streamlined tires such as shown in Figure 4.57

TYPE 1

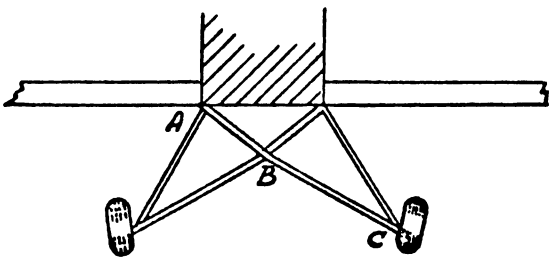

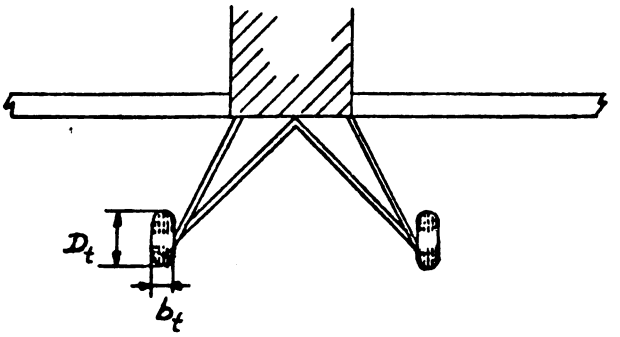

Effect of streamlining

Non streamlined struts	: $C_D=2.56$
Streamlined struts	: $C_D=1.11$
Struts also streamlined at intersections A and B	: $C_D=0.93$
Struts also streamlined at intersections A, B and C	: $C_D=0.85$

Effect of wheel fairings as shown in Figure 4.57

Fairing type A	: $C_D=1.15$
Fairing type B	: $C_D=1.05$
Fairing type C	: $C_D=0.71$

COPIED FROM REF. 21

TYPE 2

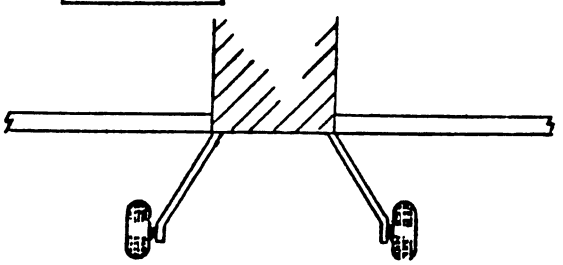

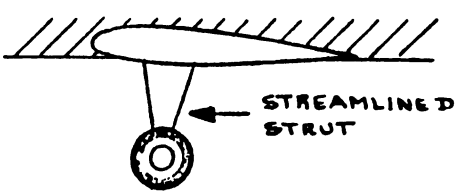

Without wheel fairing	: $C_D=0.565$
With fairing type B	: $C_D=0.54$
With fairing type C	: $C_D=0.49$

as shown in Figure 4.57

Figure 4.54 Gear Drag Increment: Non-retractable Gears Attached to Wing or Fuselage, Types 1-2

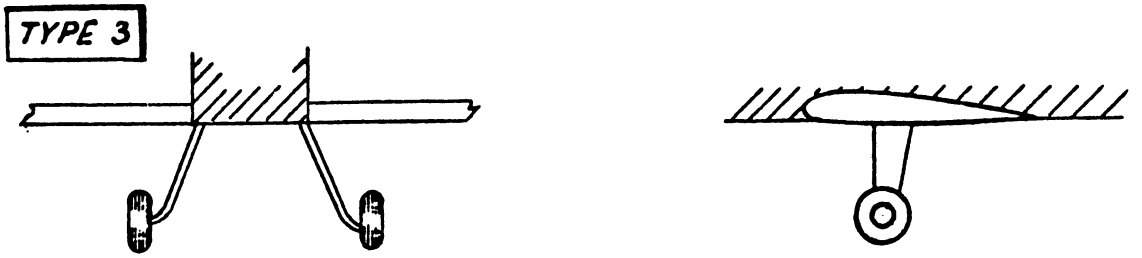

Without wheel fairing : C_D=0.62

With fairing type A : C_D=0.46
as shown in Figure 4.57

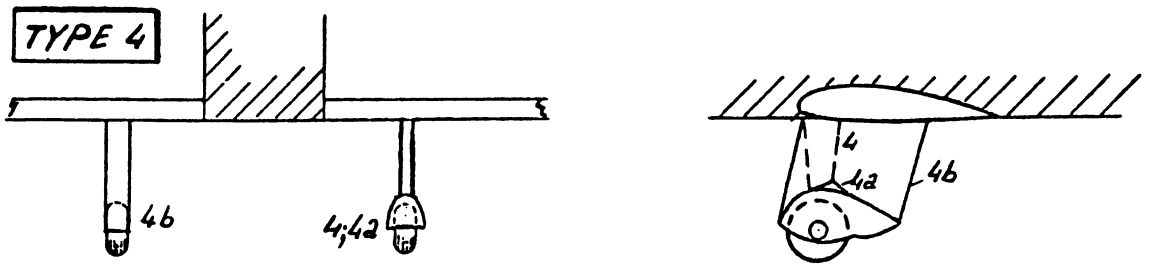

Type 4, narrow strut, no fairing : C_D=0.52

Type 4a, Narrow strut, small fairing : C_D=0.34

Type 4b, strut and wheel faired completely : C_D=0.34

COPIED FROM REF. 21

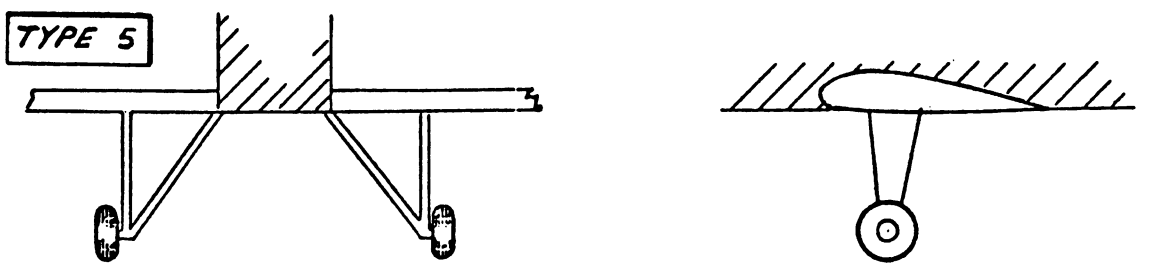

With wheel fairing type C, according to Figure 4.57 : C_D= .68

Without wheel fairing : C_D=1.05

Figure 4.55 Gear Drag Increment: Non-retractable Gears Attached to Wing or Fuselage, Types 3-5

Note: All C_D values are referenced to $b_t \times D_t$ of one wheel, but apply to the entire landing gear, including interference drag

COPIED FROM REF. 21

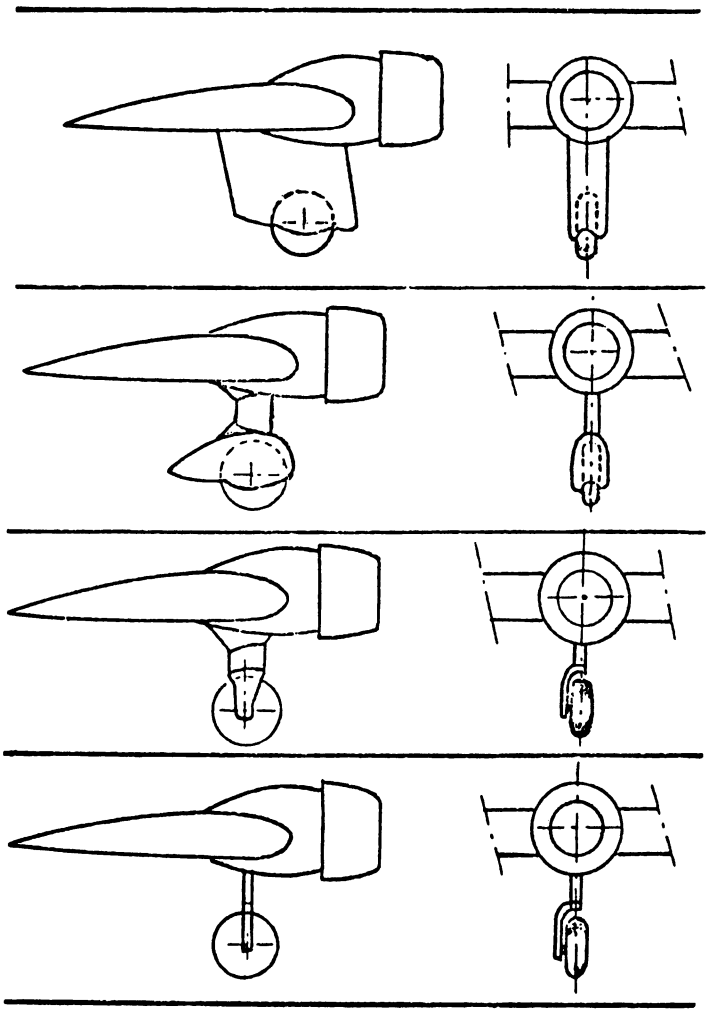

C_D = 0,45 - 0,74

C_D = 0,45 - 0,60

C_D = 0,60 - 0,90

C_D = 1,85 - 2,10

Valid for C_L=0 only

Figure 4.56 Gear Drag Increment: Non-retractable Gears Attached to Nacelles

For landing gear wheels alone: Figure 4.57 applies to wheels with and without streamline caps (fairings). Note that these drag coefficients are based on: $S_{gear} = b_t x D_t$.

For nose gears: Figure 4.58 applies to nose gears with closed nosewheel doors. Note that the reference area is again: $S_{gear} = b_t x D_t$.

For retractable landing gears: Figure 4.59 provides the data. Nota bene: these data are based on the reference area: (axb) as defined in Figure 4.59. The drag coefficients again apply to the entire gear which is assumed to consist of two legs.

For landing gears with more than one wheel per bogey: Figure 4.61 shows a relationship between Δf_{gear} and W_{TO} for different types of landing gear. From these data:

$$C_{D_{gear}} = \Delta f_{gear}/S \qquad (4.77)$$

Many airplane configurations employ 'landing-gear-bulge-fairings'. Many examples of this are depicted in Chapter 3 of Part II. The extra drag created by these bulge fairings should be accounted for in the the estimation of fuselage drag: see Section 4.3. Note that a bulge fairing will add to the cross sectional area of the fuselage and therefore will reduce the 'effective' fuselage slenderness ratio parameter l_f/d_f. This causes an increase in fuselage drag as given by Eqn.(4.30).

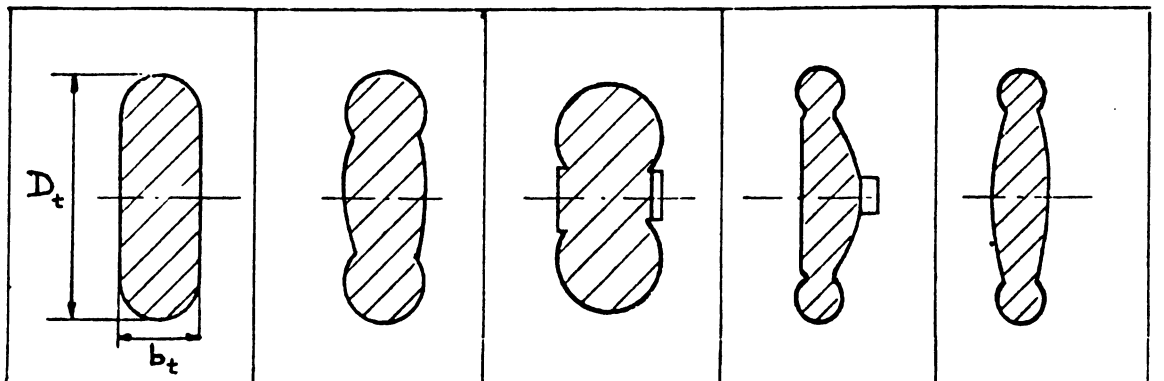

Streamlined Tire	Low Pressure Tire	Very Low Pressure Tire	High Pressure Tire	Standard Tire
$D_t.b_t$=27x9 1/4"	$D_t.b_t$=25x8½"	$D_t.b_t$=19,5x9"	$D_t.b_t$=26x5"	$D_t.b_t$=20x4"
C_D = 0,18	C_D = 0,25	C_D = 0,18	C_D = 0,30	C_D = 0,25

Drag Coefficients of Wheels

COPIED FROM REF. 21

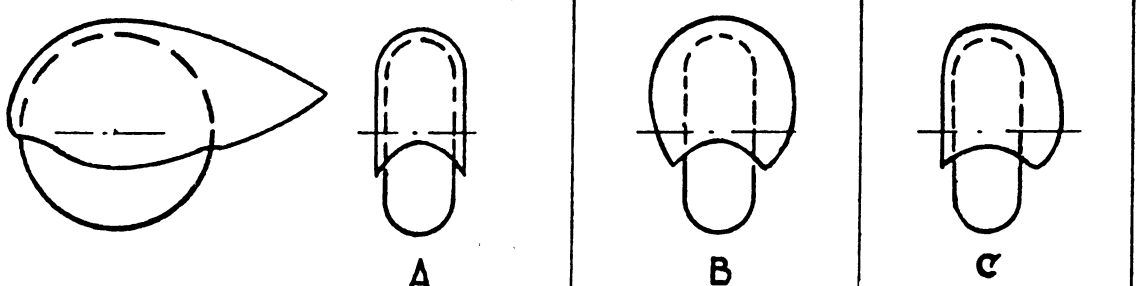

		A	B	C
Wheel without fairing	: C_D = 0,24		0,24	0,24
Wheel with fairing	: C_D= 0,12 - 0,14		0,22	0,19

Drag Coefficients of Wheels With Fairings

Figure 4.57 Wheel Drag Increments

COPIED FROM: REF.21

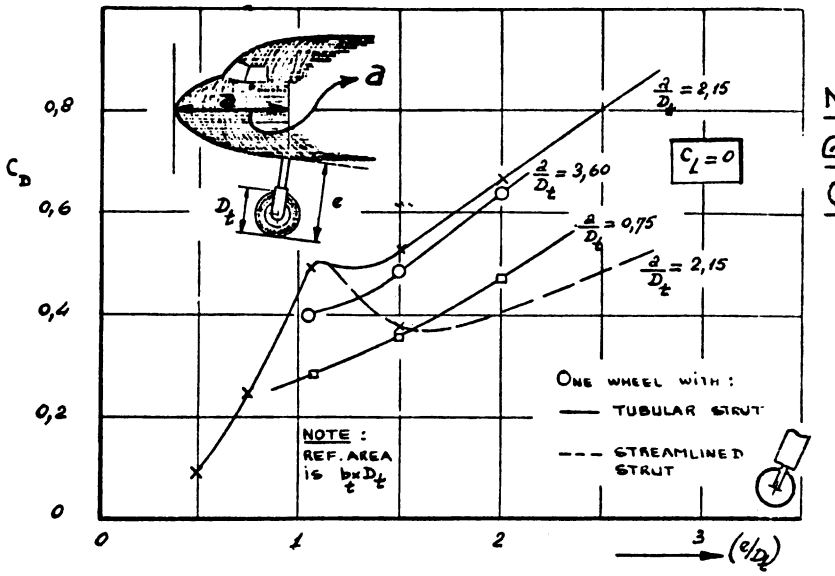

NOTE:
GEAR CAVITY
CLOSED!

Figure 4.58 Nosegear Drag Increments

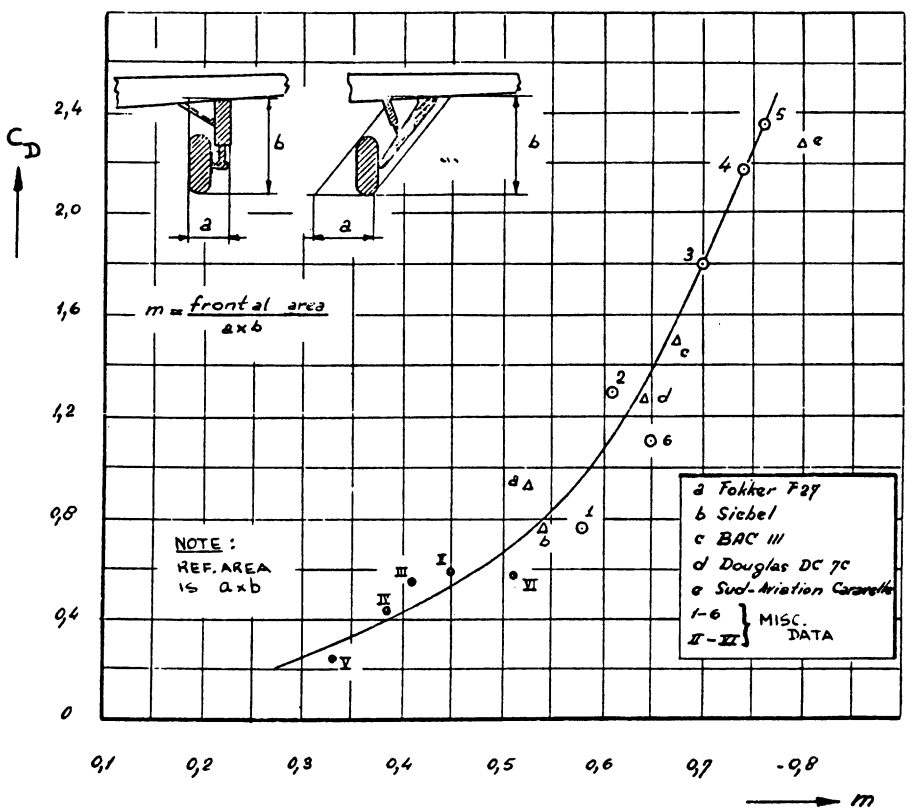

NOTE:
GEAR CAVITY
OPEN!

COPIED
FROM:
REF. 21

Note: All C_D values are referenced to axb of one gear, but apply to the entire landing gear, including interference drag

Figure 4.59 Gear Drag Increments: Retractable Gears

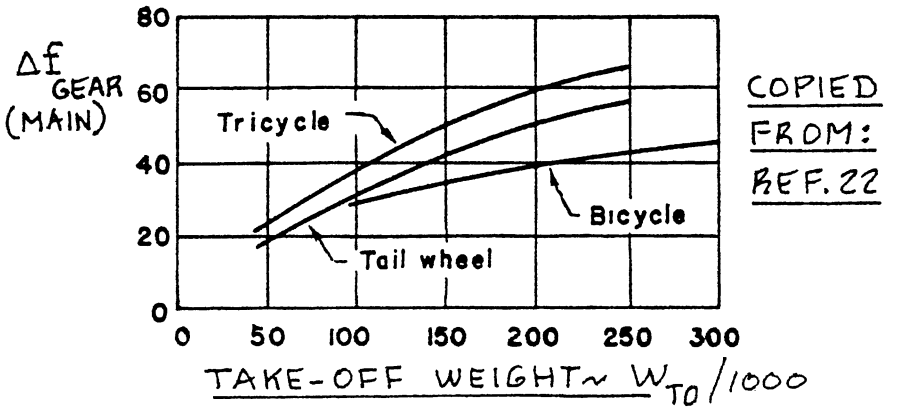

Figure 4.60 Equivalent Parasite Area Increment for Gears with Multiple Wheel Bogies

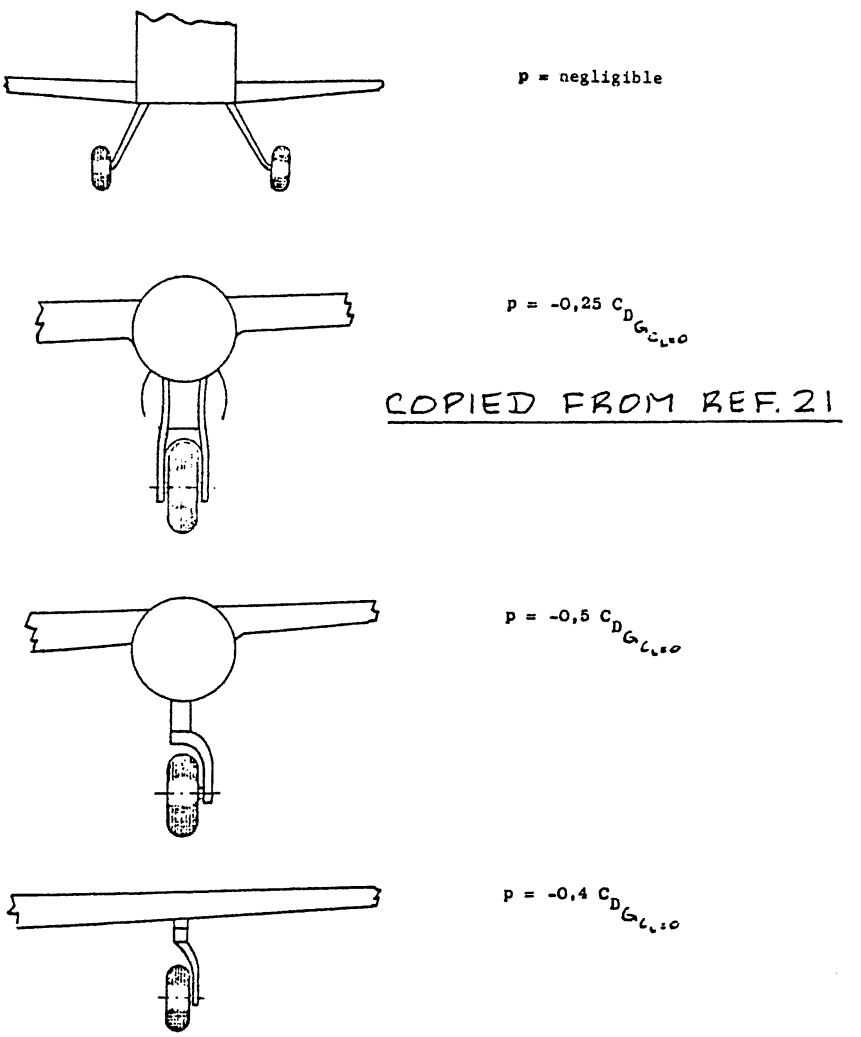

Figure 4.61 Landing Gear Induced Drag Factor

4.8 CANOPY/WINDSHIELD DRAG PREDICTION

The following method applies in the subsonic speed range. In the transonic and supersonic speed ranges the wave drag generated by canopies and windshields can be significant. In these speed ranges it will be necessary to employ area-ruling to cut wave drag to a minimum. Sub-section 4.3.4 presents a discussion on area-ruling.

The drag coefficient due to a canopy and/or a windshield may be found from:

$$C_{D_{cw}} = C_{D_{can}} + C_{D_{ws}} \qquad (4.78)$$

where: $C_{D_{can}}$ = drag coefficient due to a canopy, see 4.8.1.

$C_{D_{ws}}$ = drag coefficient due to a windshield, see 4.8.2.

4.8.1 Canopy Drag Prediction

The drag coefficient due to a canopy may be estimated from:

$$C_{D_{can}} = (\Delta C_{D_{can}})S_{can}/S \qquad (4.79)$$

where: $\Delta C_{D_{can}}$ = the incremental drag coefficient due to the canopy. Figures 4.62 through 4.67 provide data from which this increment may be found. Note from Figure 4.67, that this increment varies with Mach number in the subsonic speed range!

S_{can} = the maximum frontal area of the canopy as shown in Figure 4.62.

4.8.2 Windshield Drag Prediction

The drag coefficient due to a windshield may be determined from:

$$C_{D_{ws}} = (\Delta C_{D_{ws}})S_{fus}/S \qquad (4.80)$$

where: $\Delta C_{D_{ws}}$ = incremental drag coefficient due to a windshield: see Figure 4.68.

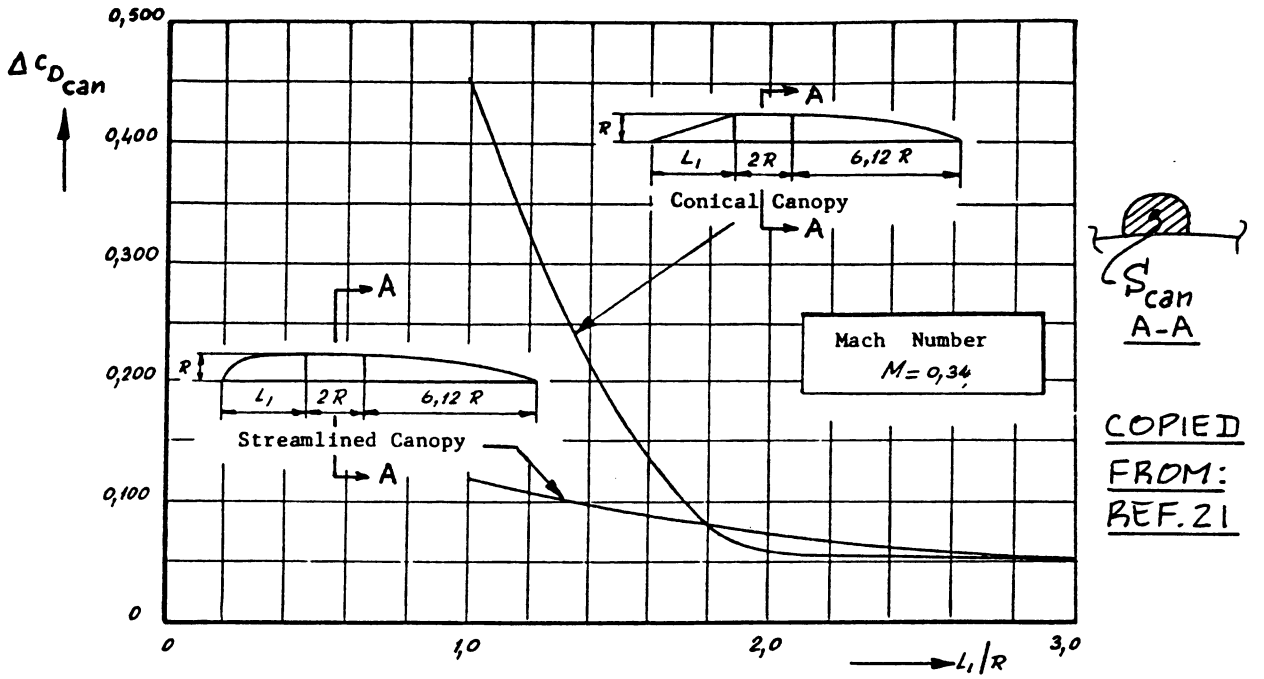

$\Delta C_{D_{can}}$ = Canopy Drag Coefficient Referenced to Frontal Area of Canopy, S_{can}

Figure 4.62 Effect of L_1 on Canopy Drag

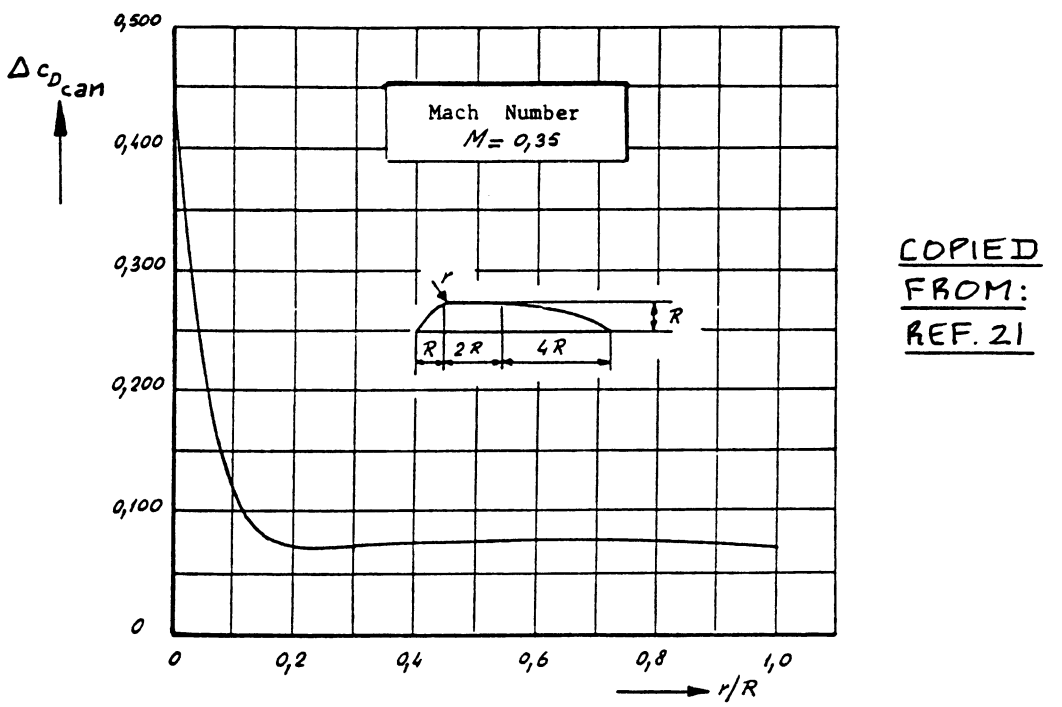

$\Delta C_{D_{can}}$ = Canopy Drag Coefficient Referenced to Frontal Area of Canopy, S_{can}

Figure 4.63 Effect of 'r' on Canopy Drag

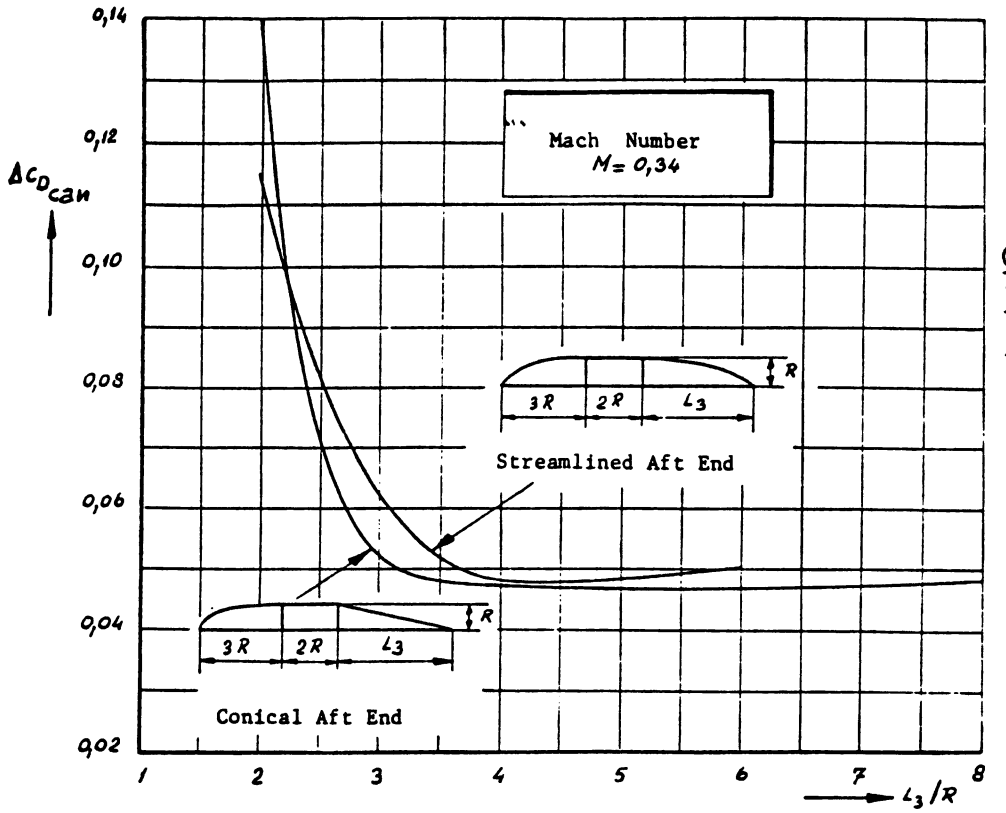

COPIED FROM: REF. 21

$\Delta C_{D_{can}}$ = Canopy Drag Coefficient Referenced to Frontal Area of Canopy, S_{can}

Figure 4.64 Effect of L_3 on Canopy Drag

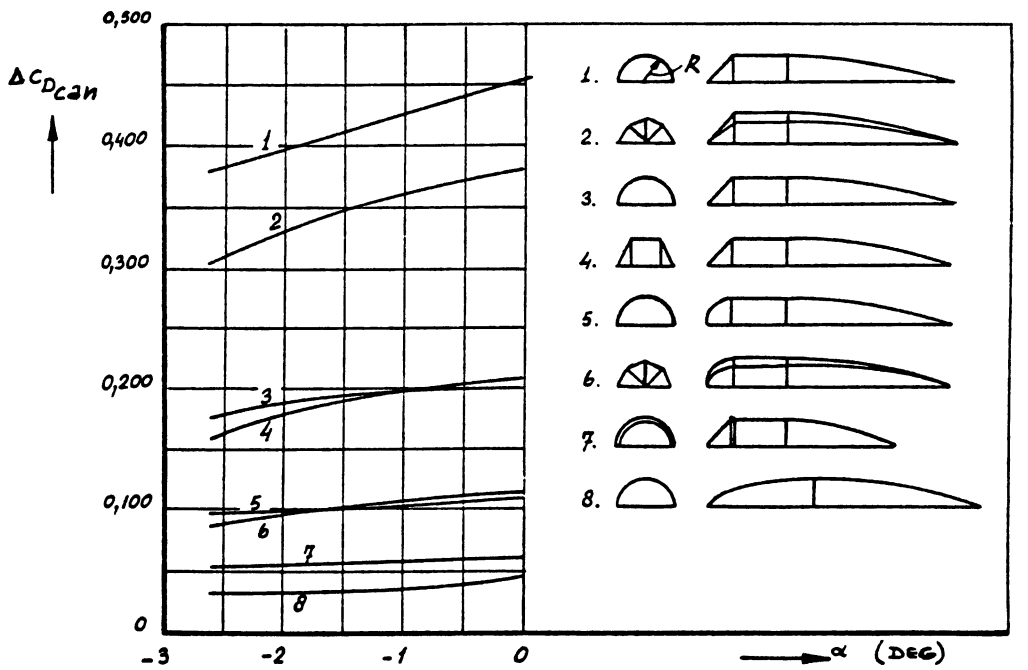

COPIED FROM: REF. 21

α = Fuselage Angle of Attack

$\Delta C_{D_{can}}$ = Canopy Drag Coefficient Referenced to Frontal Area of Canopy, S_{can}

Figure 4.65 Effect of Cross Section on Canopy Drag

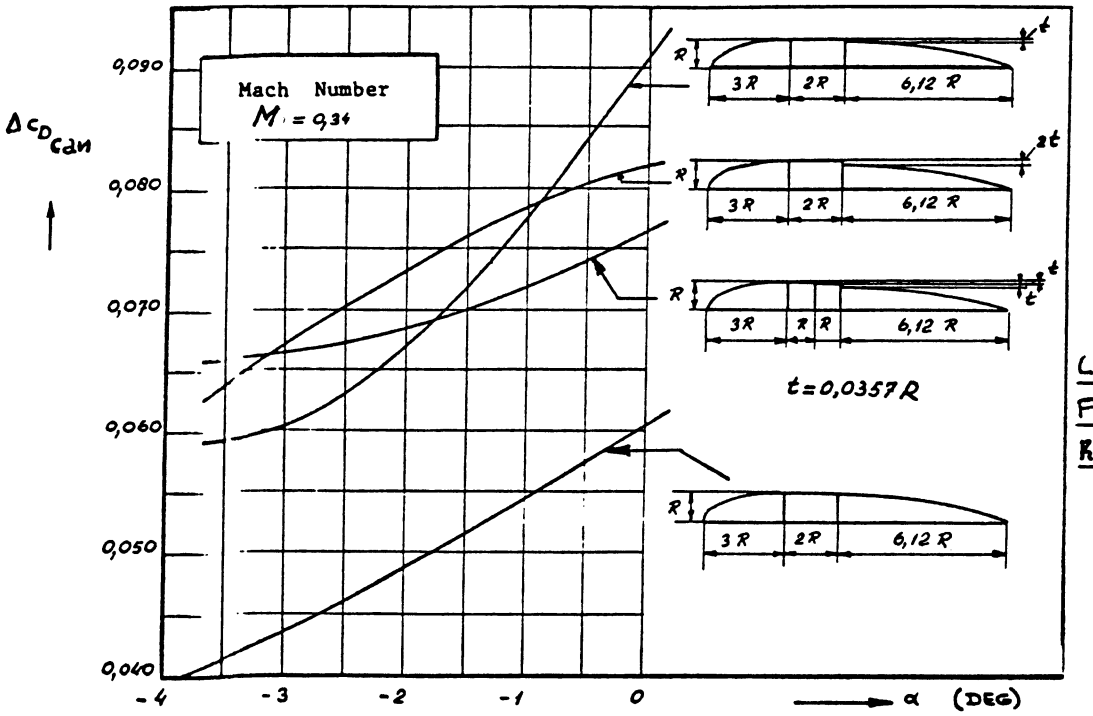

COPIED FROM: REF. 21

α = Fuselage Angle of Attack

$\Delta C_{D_{can}}$ = Canopy Drag Coefficient Referenced to Frontal Area of Canopy, S_{can}

Figure 4.66 Effect of Irregularities on Canopy Drag

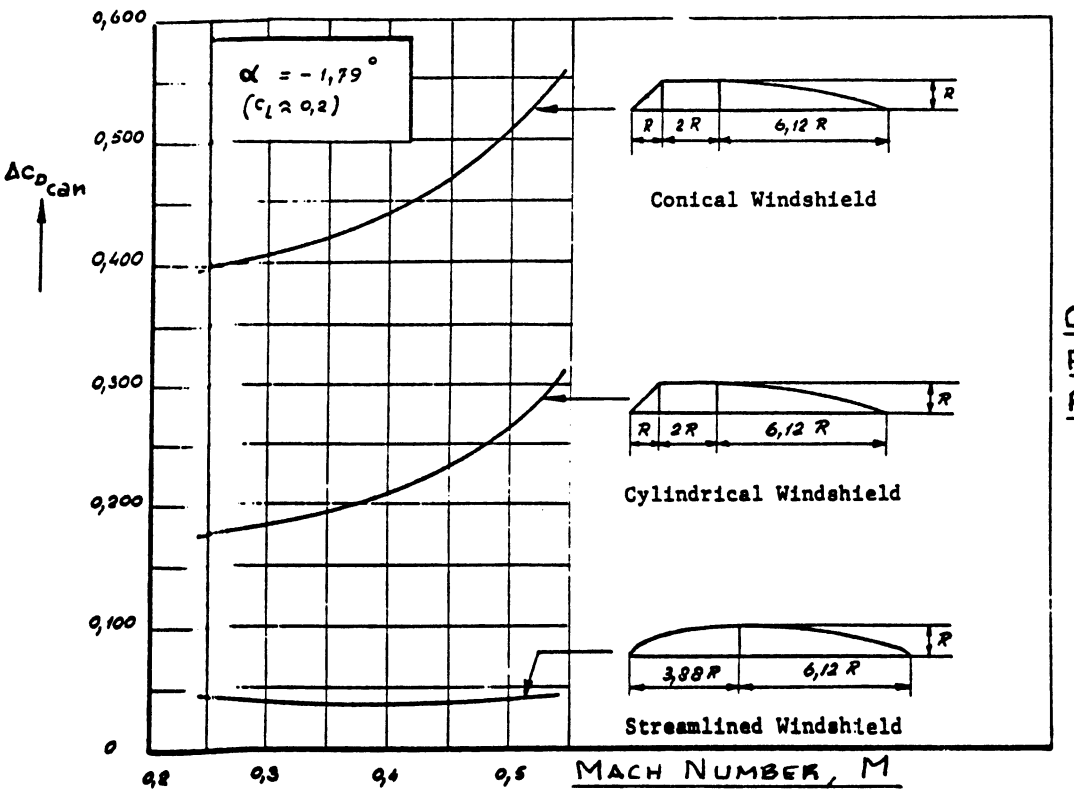

COPIED FROM: REF. 21

$\Delta C_{D_{can}}$ = Canopy Drag Coefficient Referenced to Frontal Area of Canopy, S_{can}

Figure 4.67 Effect of Mach Number on Canopy Drag

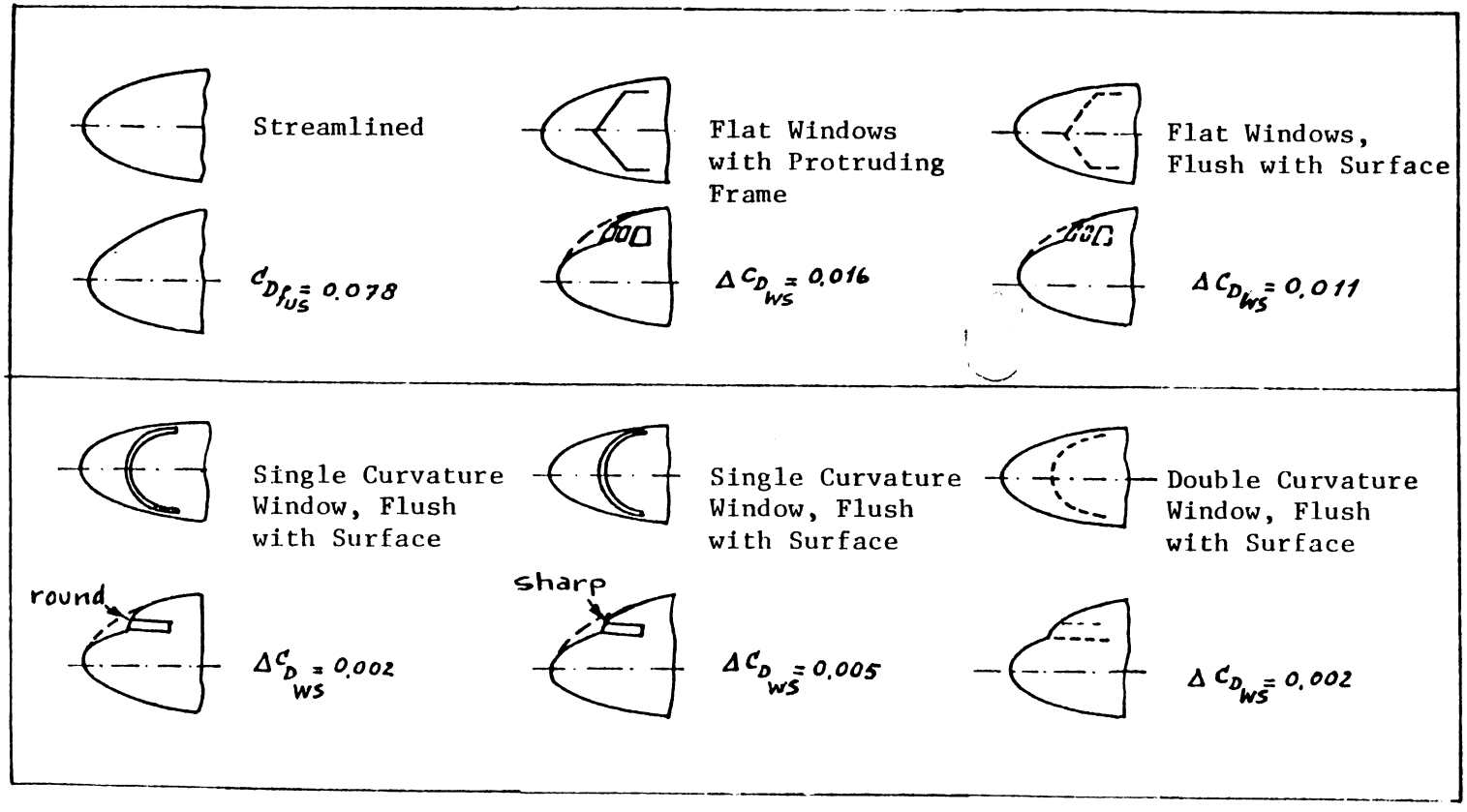

$C_{D_{fus}}$ = Fuselage Drag Coefficient Referenced to the Frontal Area of the Fuselage

$\Delta C_{D_{ws}}$ = Drag Coefficient of the Windshield Referenced to the Frontal Area of the Fuselage, S_{fus}

Figure 4.68 Effect of Windshield Configuration on Drag

4.9 STORE DRAG PREDICTION

Reference 9 provides detailed methods for estimating the drag due to many external store arrangements. Lacking that reference it is suggested to proceed as follows:

Step 1: Determine the isolated store drag coefficient, $(C_{D_{store}})_i$ for each store from the method of Section 4.3 by considering each isolated store to be like a fuselage.

Step 2: Compute the total store drag coefficient from:

$$C_{D_{store}} = SUM_i\{(K_{store})_i (C_{D_{store}})_i\} \qquad (4.81)$$

where: $(K_{store})_i$ = store interference factor:

For semi-submerged stores as shown in Figure 4.69: $K_{store} = 0.7$

For external stores as shown in Figure 4.70: $K_{store} = 1.3$

$(C_{D_{store}})_i$ = drag coefficient of the isolated store, see Step 1.

Additional data on the drag of various externally carried stores may be found in Reference 8.

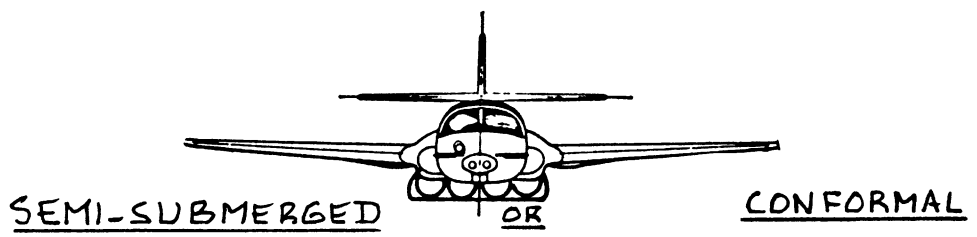

Figure 4.69 Example of Semi-submerged (Conformal) Stores

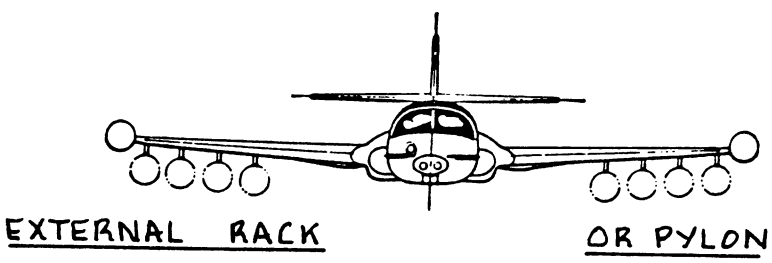

Figure 4.70 Example of External Stores

4.10 TRIM DRAG PREDICTION

Trim drag is caused by lift generated on a horizontal tail and/or a canard as a result of the requirement to 'moment trim' an airplane. Figure 4.71 illustrates two types of trim forces to be considered here. These trim force requirements result in two types of drag:

1. Trim drag due-to-lift generated on the trimming surface
2. Profile drag generated on the trimming surface as due to a control surface or a flap deflection.

The total trim drag coefficient may be found from:

$$C_{D_{trim}} = \Delta C_{D_{trim_{lift}}} + \Delta C_{D_{trim_{prof}}} \qquad (4.82)$$

where: $\Delta C_{D_{trim_{lift}}}$ = the induced drag coefficient increment due to the need for generating trim lift: see 4.10.1.

$\Delta C_{D_{trim_{prof}}}$ = the profile drag coefficient increment due to the need for generating trim lift: see 4.10.2.

4.10.1 Trim Drag Due to Lift

The trim drag due-to-lift increment, $\Delta C_{D_{trim_{lift}}}$ may be estimated from:

$$\Delta C_{D_{trim_{lift}}} = \{(\Delta C_{L_h})^2/\pi A_h e_h\} S/S_h + \{(\Delta C_{L_c})^2/\pi A_c e_c\} S/S_c \qquad (4.83)$$

where: ΔC_{L_h} = the horizontal tail incremental lift coefficient required for trim: see Section 8.3.

ΔC_{L_c} = the canard incremental lift coefficient required for trim: see Section 8.3.

A_h and A_c follow from the airplane threeview as developed in Chapter 13 of Part II.

e_h and e_c are defined on page 68.

4.10.2 Trim Drag Due to Profile Drag

The trim drag increment due to profile drag, is caused by the need to deflect an elevator, a canardvator or a canard flap for purposes of trimming an airplane. The following equation assumes that trim is accomplished by a combination of elevator deflection and canard flap deflection:

$$\Delta C_{D_{trim_{prof}}} = \Delta C_{D_{p_{\Lambda_{c/4_h}=0}}} \cos\Lambda_{c/4_h} (S_{ef}/S_h)(S_h/S) + \Delta C_{D_{p_{\Lambda_{c/4_c}=0}}} \cos\Lambda_{c/4_c} (S_{cf}/S_c)(S_c/S) \quad (4.84)$$

where: $\Delta C_{D_{p_{\Lambda_{c/4}=0}}}$ = the profile drag coefficient due to an elevator and/or a canard control surface. It may be found with the method of Section 4.6, but with the following substitutions:

Elevator and/or canardvator: these should be considered to be plain flaps. Elevator deflection, δ_e and/or canardvator deflection, δ_{cv} are used instead of the flap deflection, δ_f.

Canard flap: if trimming is accomplished with a canard flap then it must be determined what type of flap the canard flap resembles most. The data of Sub-section 4.6.1 can be used to estimate the profile drag due to trim by a canard flap.

S_{ef} = flapped horizontal tail area, see Fig.4.72

S_{cf} = flapped canard area, see Fig.4.72

S_h and S_c are the canard and horizontal tail areas respectively.

Note: trim can be accomplished also with a variable incidence stabilizer or with an elevator trim tab. It is left up to the user to make the required modifications in Equations (4.83) and (4.84) to account for such cases.

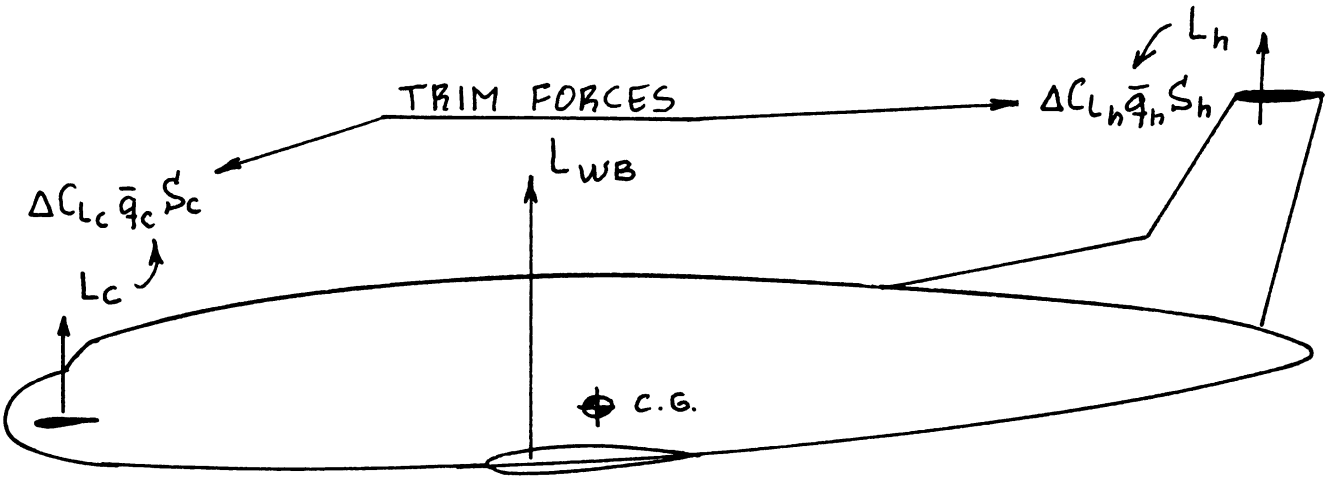

Figure 4.71 Example of Trim Force Requirements

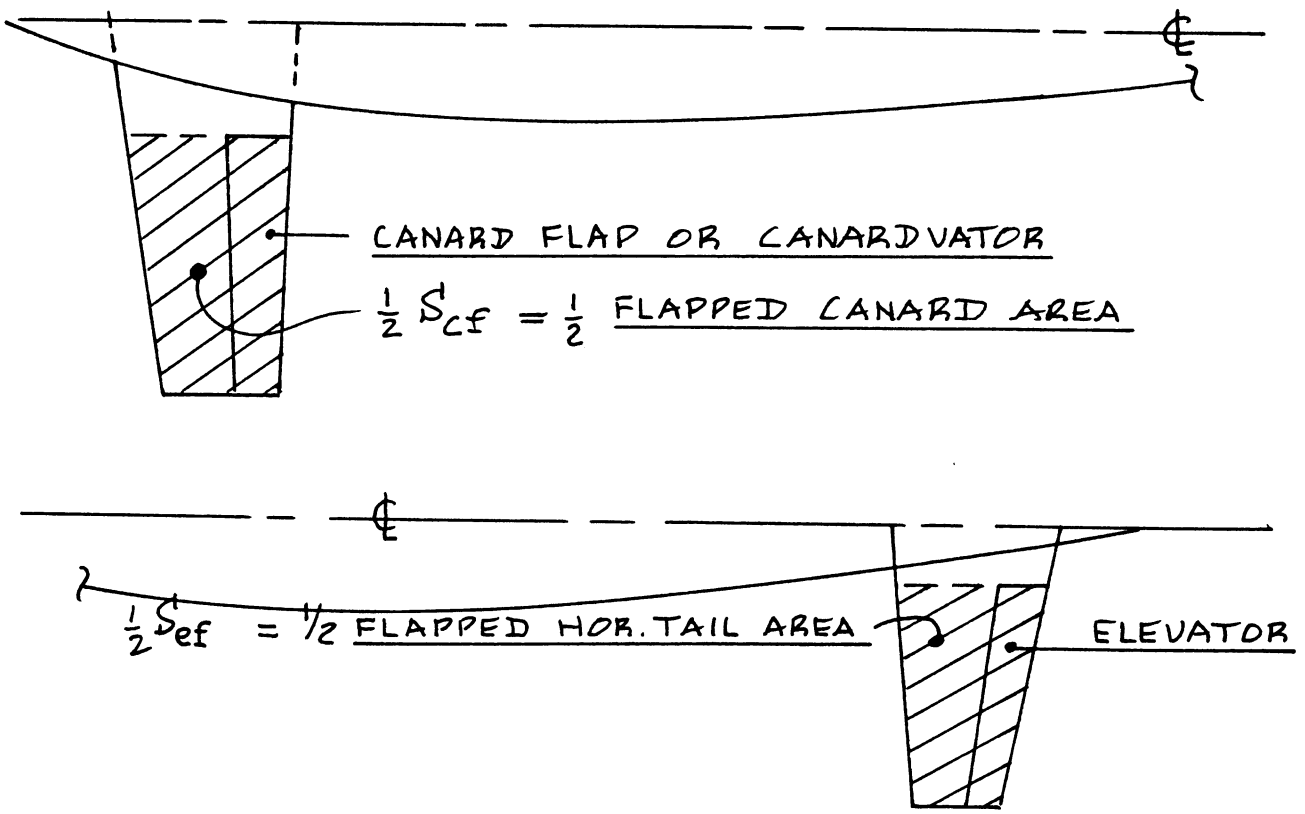

Figure 4.72 Definition of Flapped Areas

4.11 INTERFERENCE DRAG PREDICTION

Interference drag is a type of drag which is not yet fully understood. Its effect is that the total drag of two or more airplane components when integrated in a configuration is always larger than the sum of the individual component drags.

Several interference drag factors were already accounted for in Sections 4.2, 4.3, 4.5, 4.6 and 4.9. In addition to interference drag accounted for by these factors, extra interference drag may be caused by:

1. Wing struts meeting a wing and/or a fuselage at 'sharp' angles. Figure 4.73 shows such a case.

2. Empennage surfaces meeting each other or a fuselage at 'sharp' angles. Figure 4.74 illustrates several cases.

3. Low or high wing airplanes tend to have more interference drag than midwing airplanes: in the midwing configuration, the 'venturi' effect is absent. Figure 4.75 shows examples.

4. Wing/nacelle installations can have significantly greater interference drag than suggested by the the methods of 4.5.2.1 and 4.5.2.2.

In many instances it is possible to decrease interference drag by the use of so-called 'fairings'. Figures 4.73 - 4.75 show typical fairings.

The reader should carefully examine his configuration for additional causes of interference drag. To estimate their effect, the interference drag data base presented in Reference 8 should be used.

4.12 MISCELLANEOUS DRAG PREDICTION

The following drag items will be considered as miscellaneous drag contributions:

4.12.1 Drag due to spoilers (or speed brakes)
4.12.2 Drag due to surface roughness
4.12.3 Drag due to other causes

4.12.1 Drag Due to Spoilers (or Speed Brakes)

The incremental drag coefficient due to spoilers may be estimated from:

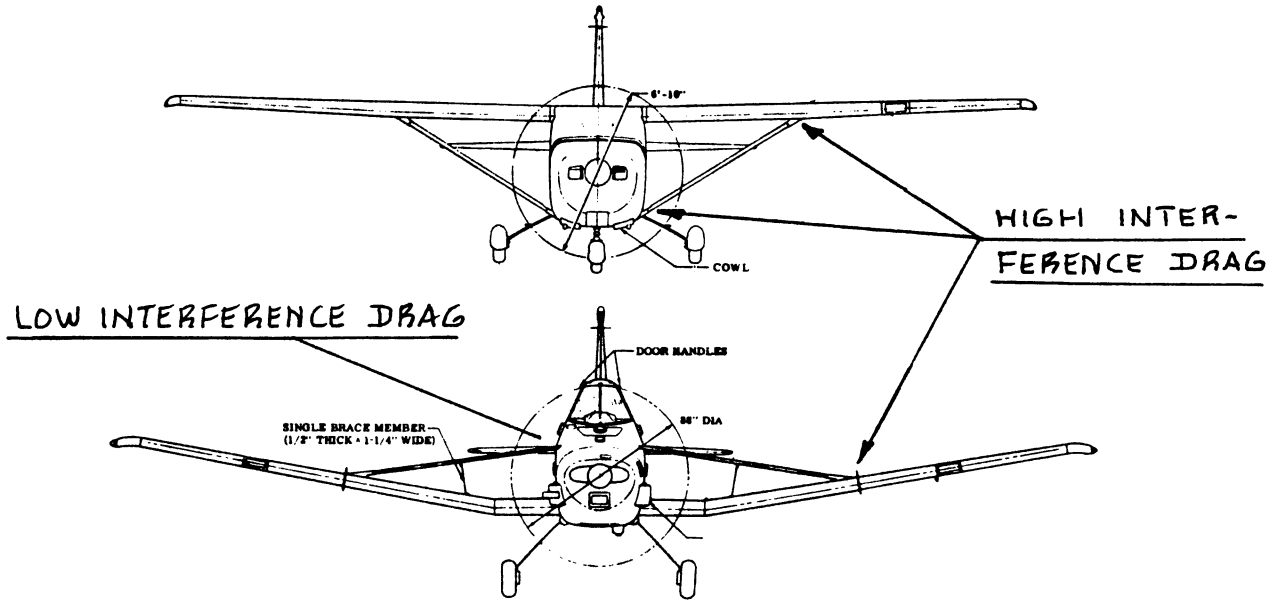

Figure 4.73 Wing Strut Arrangements With High and Low Interference Drag

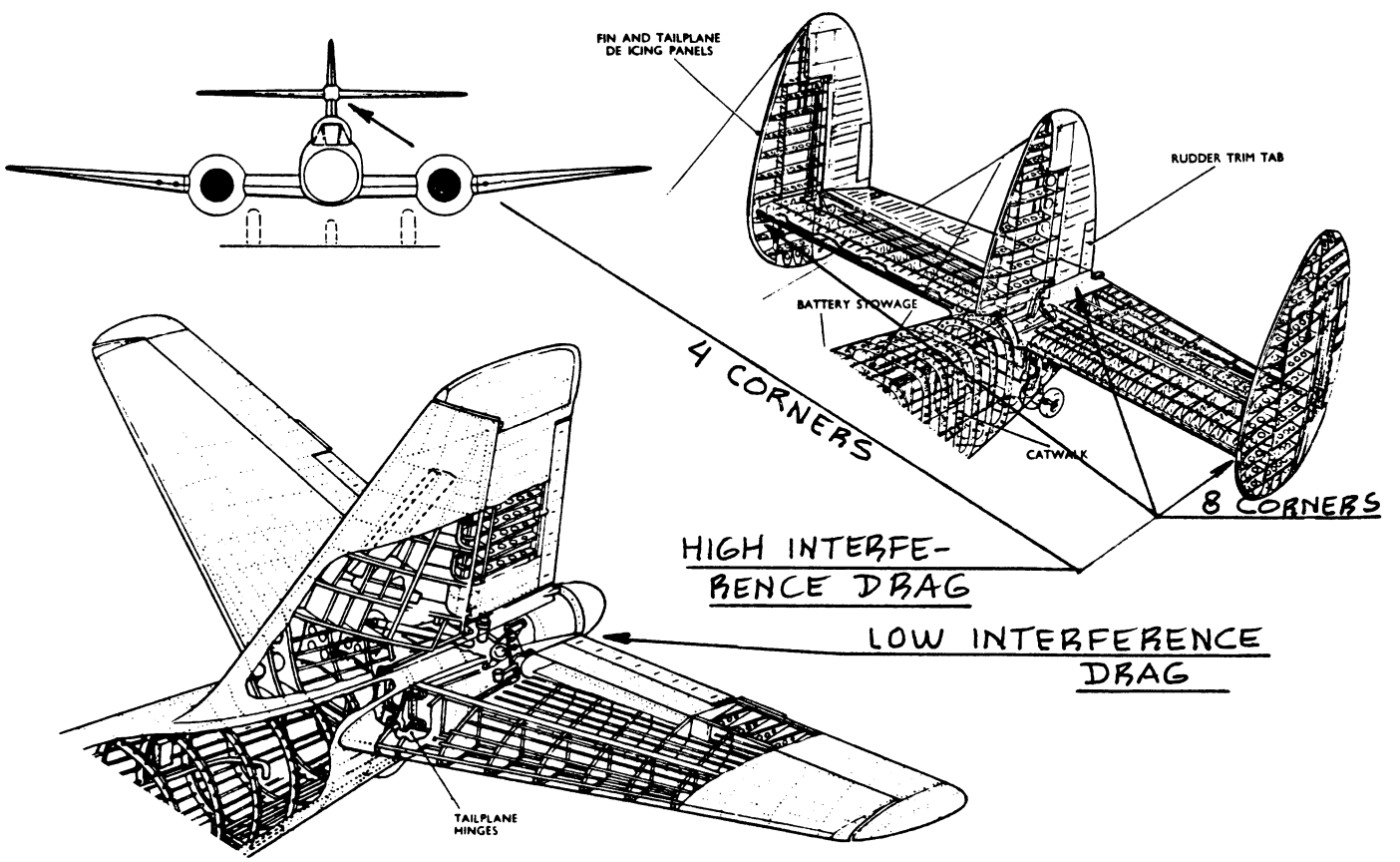

Figure 4.74 Empennage Arrangements with High and Low Interference Drag

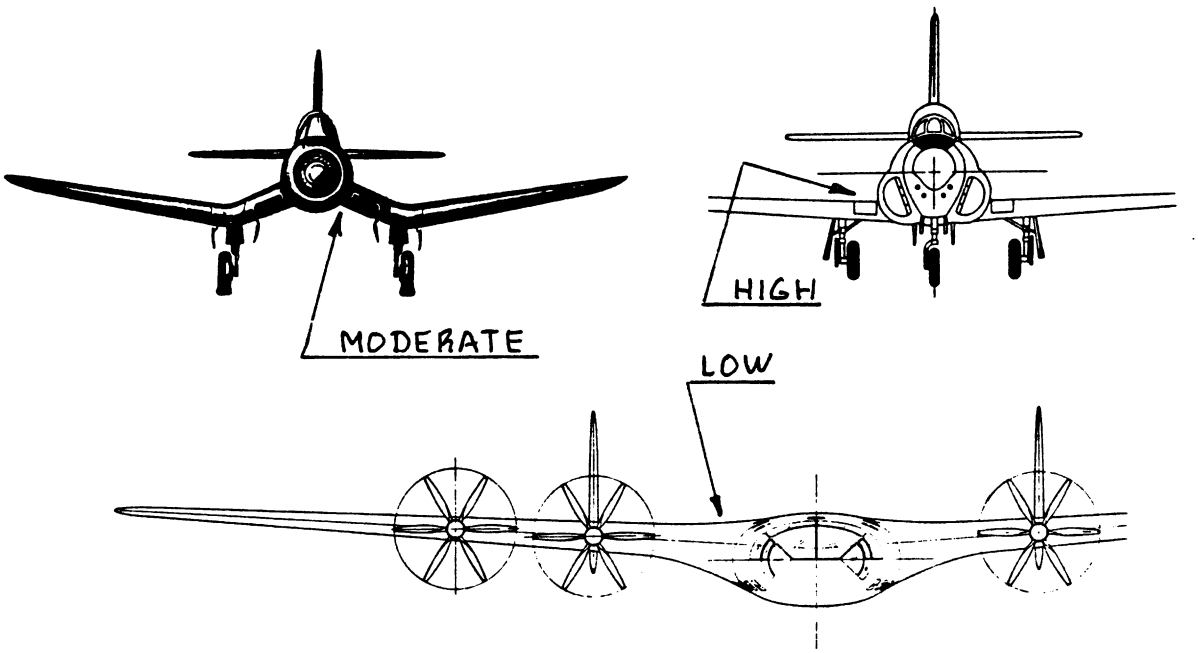

Figure 4.75 Wing/Fuselage Arrangements with High and Low Interference Drag

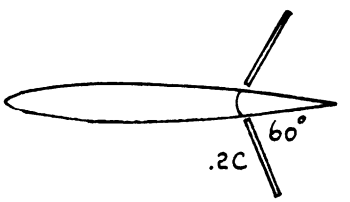

SOLID PLATES

$\Delta C_{D_{sp}}$ = 0.63

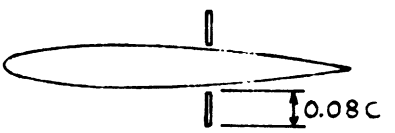

SHOWN AT .60 C

NACA 2412

$\Delta C_{D_{sp}}$ = 1.60 AT .60 C

1.25 AT 1.00 C

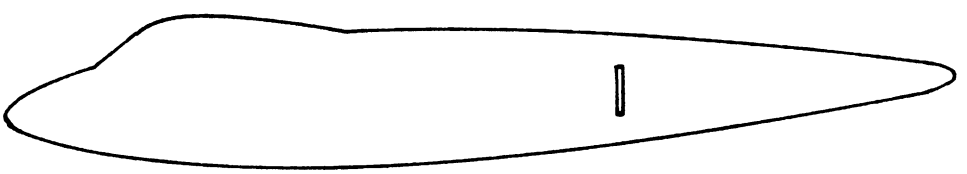

FLAT PLATE DEFLECTED PERPENDICULAR TO FUSELAGE ΔC_D = 1.0

Note: All coefficients are based on the area of the speed brake *or spoiler*

Figure 4.76 Drag Due to Spoilers and Speed Brakes

$$\Delta C_{D_{sp}} = \text{Sum}_i\{(\Delta C_{D_{sp_i}})(S_{sp_i}/S)\} \quad (4.85)$$

where: $C_{D_{sp_i}}$ is found from Figure 4.76 for several spoiler locations.

S_{sp_i} is the flat plate area of each spoiler.

4.12.2 Drag Due to Surface Roughness

The methods for estimating friction and profile drag of wings and fuselages as discussed in Sections 4.2 and 4.3 apply only to 'smooth' surfaces. If a surface is 'rough', additional drag is created.

The actual level of turbulent boundary layer friction drag of 'rough' surfaces may be estimated with the following procedure:

Step 1: Determine the reference length l: this is $\bar{c}_{w_e}$ in the case of a wing and l_f in the case of a fuselage.

Step 2: Compute the parameter l/k, where k is determined from the following table:

Type of Surface	Equivalent Sand Roughness, k, in ft
Aerodynamically smooth	0.0
Polished metal or polished wood	0.00000167 to 0.00000667
Natural sheet metal	0.00001333
Smooth matte paint, carefully applied	0.00002083
Standard camouflage paint, average application	0.00003333
Camouflage paint, mass-production spray	0.0001
Dip-galvanized metal surface	0.0005
Natural surface of cast iron	0.00083

As a practical matter, use this information as follows:

For light airplanes with standard sheet metal manufacturing methods: use k = 0.00001333 ft.

For business jets and jet transports with sheet metal manufacturing methods but polished surfaces: use k = 0.000005 ft.

For airplanes made of composites and polished surfaces: use k = 0.00000167 ft.

For military airplanes with camouflage paint applied in the factory: use k = 0.00002083 ft.

For military airplanes with camouflage paint applied in the field: use k = 0.0001 ft.

Step 3: Determine the 'cut-off Reynolds number', $R_{N_{cut\text{-}off}}$ with the help of Figure 4.77.

Step 4: Determine the actual Reynolds number with Equation (4.7) or Equation (4.31).

Step 5: If $R_{N_{cut\text{-}off}} > R_N$ find C_f from Figure 4.3 at the actual Reynolds number.

If $R_{N_{cut\text{-}off}} < R_N$ find C_f from Figure 4.3 at the 'cut-off' Reynolds number.

Step 6: Substitute the appropriate value of C_f for C_{f_w} in Eqn.(4.6) or for $C_{f_{fus}}$ in Eqn.(4.30) and proceed with the determination of the desired zero-lift drag coefficients as indicated in Sections 4.2 and 4.3.

4.12.3 Drag Due to Other Causes

Other causes for drag may be items such as: struts, antennas, surface gaps, extra drag caused by inlet air spillage and by exhaust nozzle integration. Strut and antenna drag may be estimated by assuming these to be like small wings. For surface gap drag the reader should consult Ref. 8. For estimation of extra inlet drag the method of Sub-section 6.2.4 may be used. For estimation of drag due to exhaust nozzles, see Section 6.3.

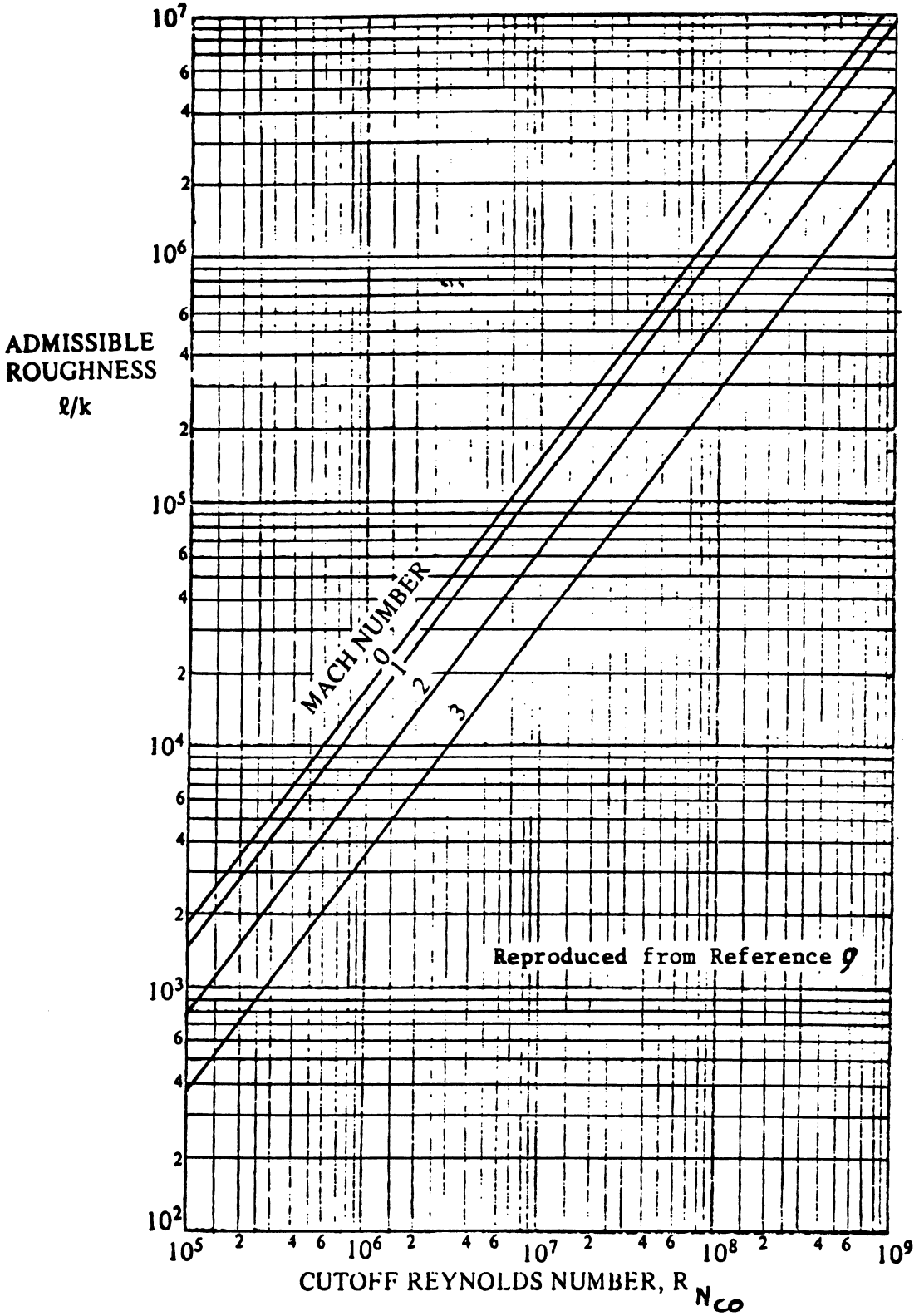

Figure 4.77 Effect of Mach Number on the Relation Between Cut-off Reynolds Number and Roughness

4.13 DRAG ADJUSTMENTS FOR LAMINAR FLOW

During the 70's and the 80's it has become increasingly evident that natural laminar boundary layer flow (instead of turbulent boundary layer flow) is practical in many instances. The resulting reduction in friction drag is very significant and should be accounted for in any realistic drag prediction procedure.

The methods presented in Sections 4.3 through 4.12 assume that the boundary layer is turbulent. To adjust the airplane zero-lift drag coefficient downward due to the existence of laminar flow, the following procedure is recommended:

If laminar flow is expected to occur naturally (natural laminar flow, also called NLF) start at Step 1.

If laminar flow is being forced, by suction or by blowing, start at Step 2.

Step 1: Determine which components of the airplane are likely to experience NLF.

In preliminary design the following criteria for the existence of NLF may be used:

$M < 0.65$ $\qquad$ $\Lambda_{LE} < 15$ degrees

$C_{L_{design}} < 0.65$ $\qquad$ $R_N < 10^7$

Note: by careful design it is possible to extend these criteria. Use of advanced airfoil design codes is recommended to verify that NLF is practical.

Step 2: Divide the surface area of all airplane components which according to Step 1 will have a certain amount of NLF in two parts: $S_{wet_{lam}}$ and $S_{wet_{turb}}$.

Figure 4.78 shows how these wetted areas are defined for a wing and for a fuselage respectively.

Step 3: For a wing or for an empennage surface, use Equation (4.6), but replace the term:

$\{(C_{f_w})S_{wet_w}/S\}$ by: (4.86)

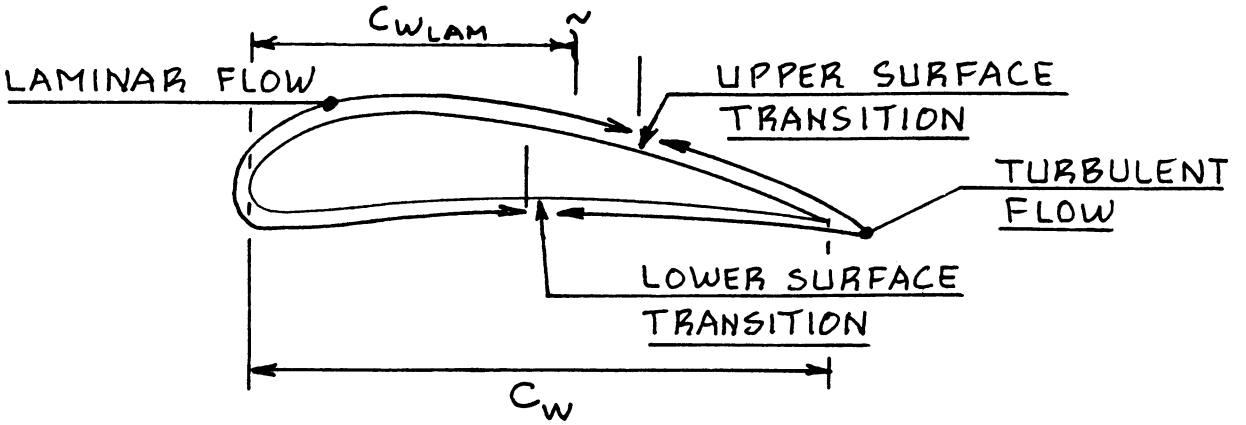

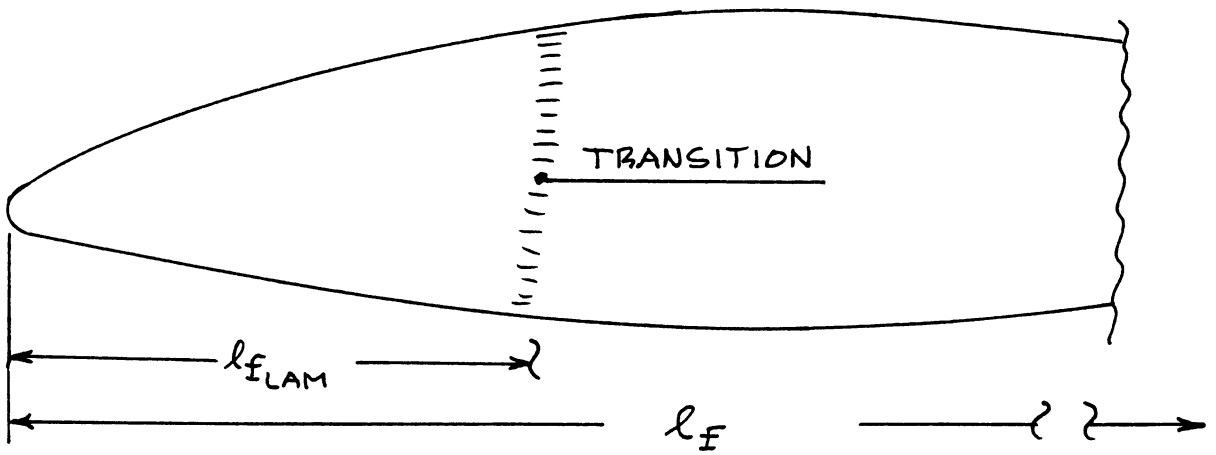

$S_{WET_{W_{LAM}}}$ = WETTED AREA OF THE WING IN THE LAMINAR FLOW REGION

$S_{WET_{FUS_{LAM}}}$ = WETTED AREA OF THE FUSELAGE IN THE LAMINAR FLOW REGION

Figure 4.78 Definition of Laminar and Turbulent Reference Lengths and Reference Areas

$$\{(C_{f_{w_{lam}}} - C_{f_{w_{tur}}})S_{wet_{w_{lam}}} + (C_{f_{w_{tur}}})S_{wet_{w}}\}/S$$

For a fuselage or for a body similar to a fuselage, use Equation (4.30), but replace the term:

$\{(C_{f_{fus}})S_{wet_{fus}}/S\}$ by: (4.87)

$$\{(C_{f_{fus_{lam}}} - C_{f_{fus_{tur}}})S_{wet_{fus_{lam}}} + (C_{f_{fus_{tur}}})S_{wet_{fus}}\}/S$$

where: $C_{f_{w_{tur}}}$ is the turbulent wing skin friction coefficient as found on p.23 of this text.

$$C_{f_{w_{lam}}} = 1.328/R_{N_{w_{lam}}}^{1/2}, \quad (4.88)$$

with: $$R_{N_{w_{lam}}} = \rho U_1 c_{w_{lam}}/\mu \quad (4.89)$$

$c_{w_{lam}}$ is the wing reference length of the laminar part of the wing: see Figure 4.78.

$S_{wet_{w_{lam}}}$ = the wing wetted area part exposed to laminar flow, see Figure 4.78.

$C_{f_{fus_{tur}}}$ is the turbulent fuselage skin friction coefficient as found on p.44 of this text.

$$C_{f_{fus_{lam}}} = 1.328/(R_{N_{fus_{lam}}})^{1/2}, \quad (4.90)$$

with: $$R_{N_{fus_{lam}}} = \rho U_1 l_{f_{lam}}/\mu \quad (4.91)$$

$l_{f_{lam}}$ is the fuselage reference length of the laminar part of the fuselage: see Figure 4.78.

$S_{wet_{fus_{lam}}}$ = the fuselage wetted area part exposed to laminar flow, see Figure 4.78.

NOTES: 1. This procedure applies in the subsonic speed range only!

2. This procedure applies only as long as any surface irregularities (steps, waviness and roughness) are within the limits defined in Reference 23.

By using laminar flow control (sucking and/or blowing) it is possible to achieve laminar flow under conditions where natural laminar flow cannot be maintained. References 24 - 26 provide some data on the types of systems needed to achieve controlled laminar flow and on a number of operational considerations.

Once such systems are in place, the procedure given above for the adjustment of friction drag would apply except for the need to account for compressibility on the equations for skin friction coefficient. Reference 27 should be consulted for replacement of Eqns (4.88) and (4.90) by equations which account for compressibility effects in the transonic speed range below M=1.0

This text does not provide a method for accounting for laminar flow in the transonic speed range above M=1.0 nor for the supersonic flow regimes. This does not mean that laminar flow in these speed ranges is not feasible. Research in progress at NASA Langley indicates that in particular in the supersonic flow range extensive laminar flow may be possible. The conditions for which this can be achieved have not yet been firmly established.

References 28-30 provide some data on the design of fuselage shapes which are conducive to NLF. Design details such as inspection covers, doors and windshields must receive very careful attention, if laminar flow capability is to be retained after the airplane has been in service for some time!

5. AIRPLANE DRAG DATA

The purpose of this chapter is to present a range of actual airplane drag data. These data are given in the form of:

5.1 Drag polars
5.2 Equivalent parasite areas
5.3 Oswald's efficiency factors
5.4 Wetted area breakdown examples

Finally, once drag data for a new airplane have been computed, they should always be 'verified' by comparison against known drag data for similar airplanes. A method for verifying drag polar predictions is given in:

5.5 Verification of realism of computed drag polars

5.1 DRAG POLARS

Figures 5.1 through 5.19 present examples of actual airplane drag polars. The information is organized in the following manner:

Figure 5.1 Cessna 177: includes flap drag
Figure 5.2 Cessna 310: includes gear and flap drag
Figure 5.3 Gulfstream I: includes gear drag, flap drag and drag due to a feathered engine
Figure 5.4 SAAB 340
Figure 5.5 Fokker F-27: includes gear and flap drag
Figure 5.6 Lockheed C-130H: includes ground effect and compressibility data
Figure 5.7 SIAI-M S-211: includes gear and flap drag
Figure 5.8 NAA T2C: includes compressibility data
Figure 5.9 Convair F-106: includes supersonic drag
Figure 5.10 McDD AV8B: includes compressibility data
Figure 5.11 Learjet M25: includes compressibility data
Figure 5.12 Boeing 727-100: includes compressibility data
Figure 5.13 Boeing 707-320B: incl. compressibility data
Figure 5.14 Boeing 747-200: includes compressibility data
Figure 5.15 Boeing B-47B: includes compressibility data
Figure 5.16 Boeing B-52A: includes compressibility data
Figure 5.17 Lockheed C-141B: incl. compressibility data
Figure 5.18 Lockheed C-5A: includes compressibility data
Figure 5.19 Boeing SST Design: includes supersonic data

The reader should note that the wing (or reference) area, S, upon which the drag and lift coefficient data are based, is indicated on all Figures 5.1 through 5.19.

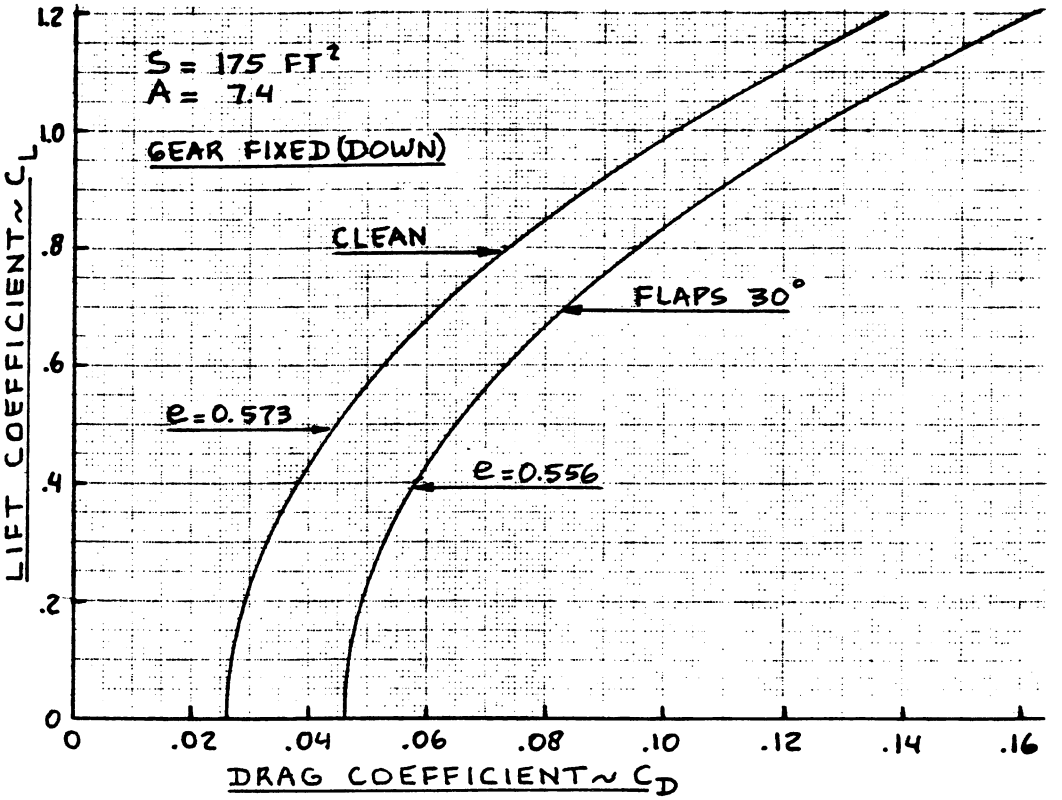

Figure 5.1 Drag Polars: Cessna 177

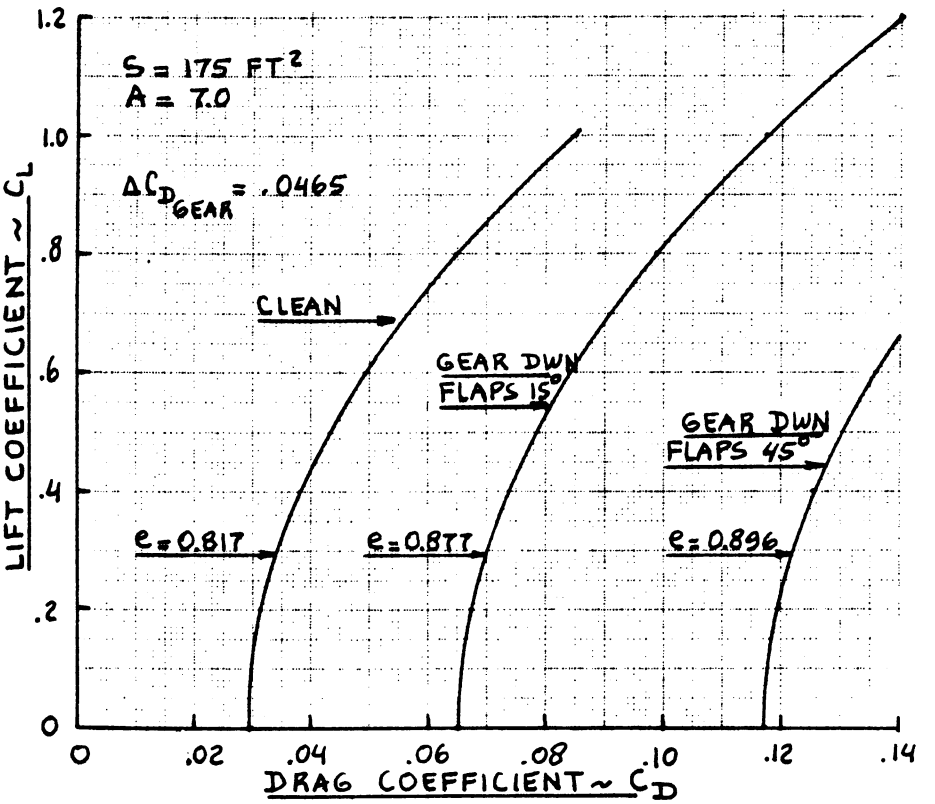

Figure 5.2 Drag Polars: Cessna 310

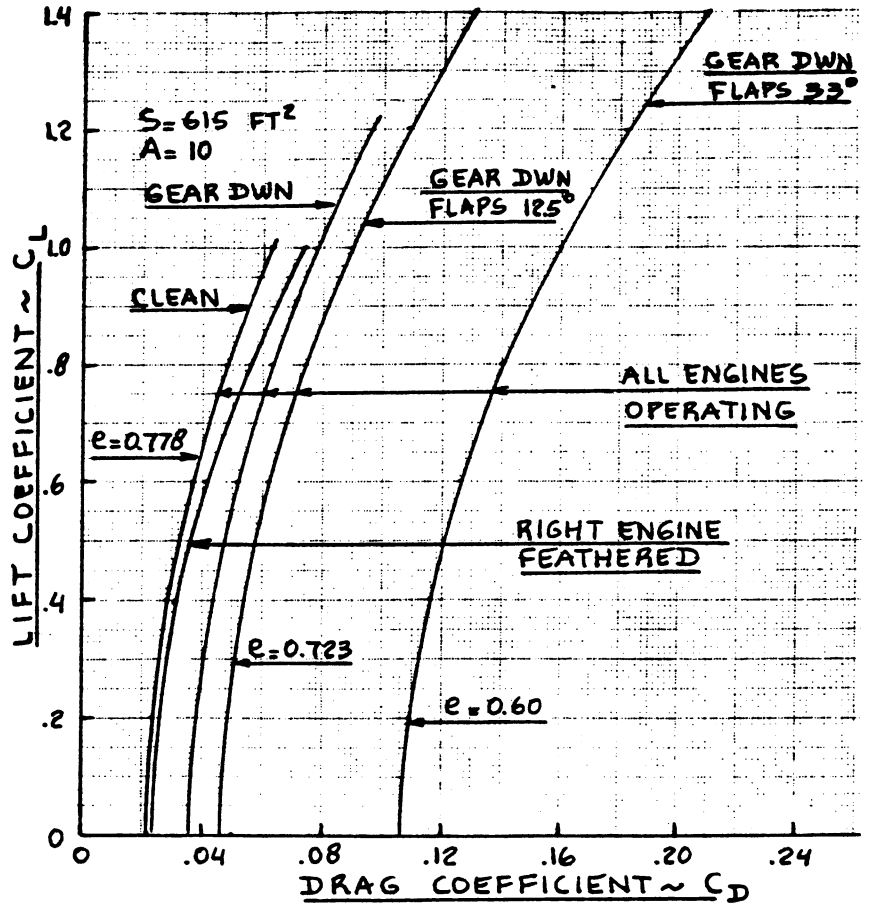

Figure 5.3 Drag Polars: Gulfstream I

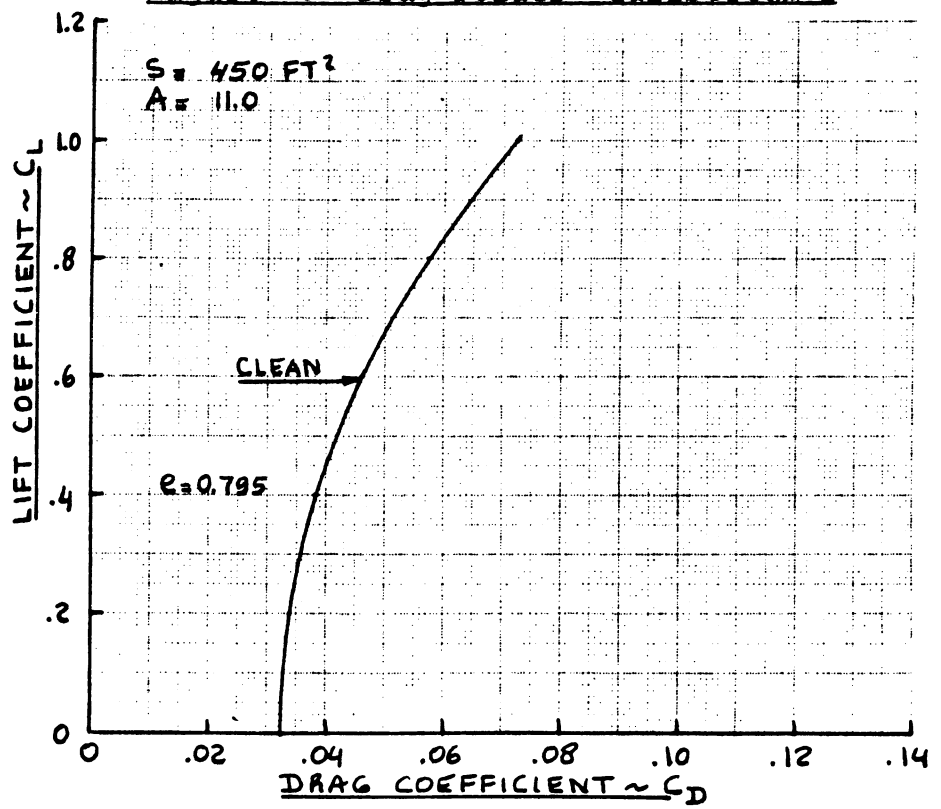

Figure 5.4 Drag Polar: SAAB 340

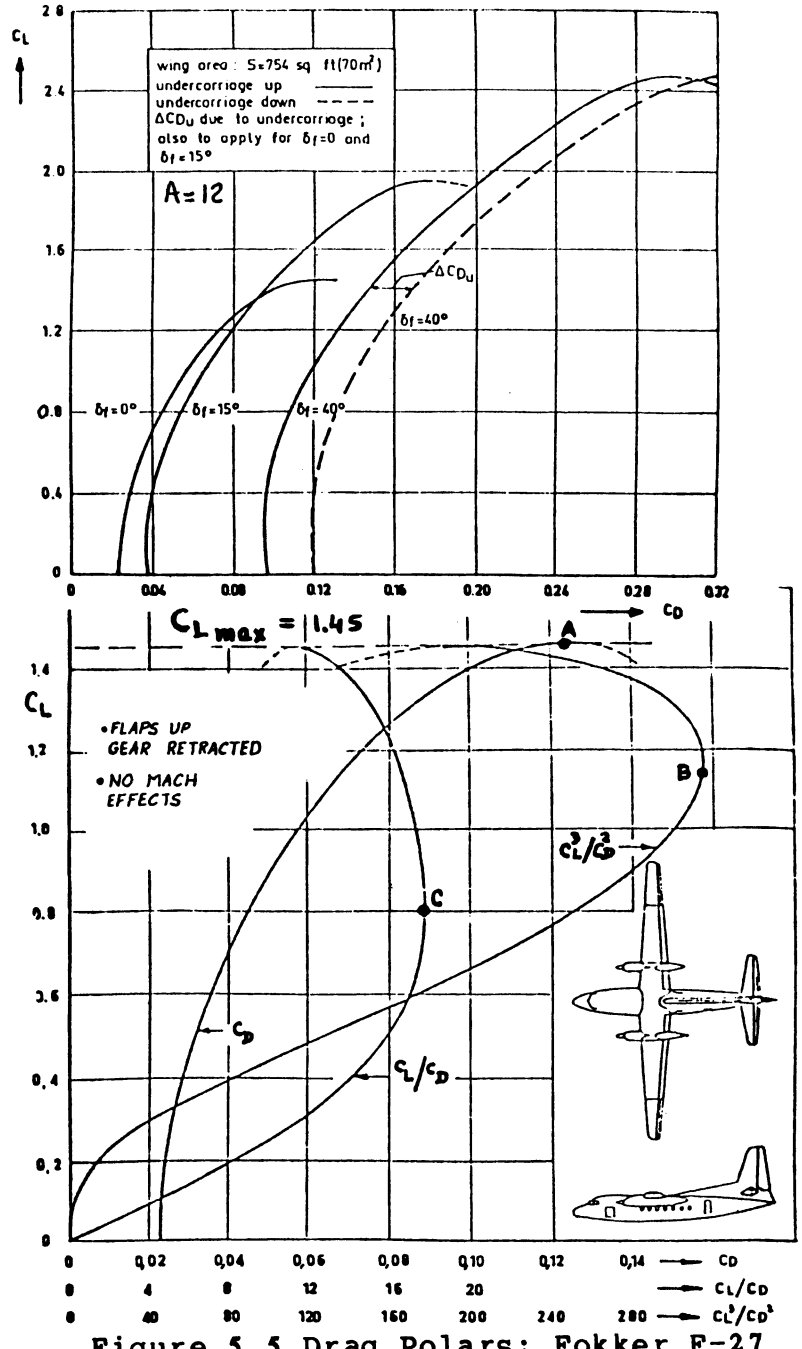

Figure 5.5 Drag Polars: Fokker F-27

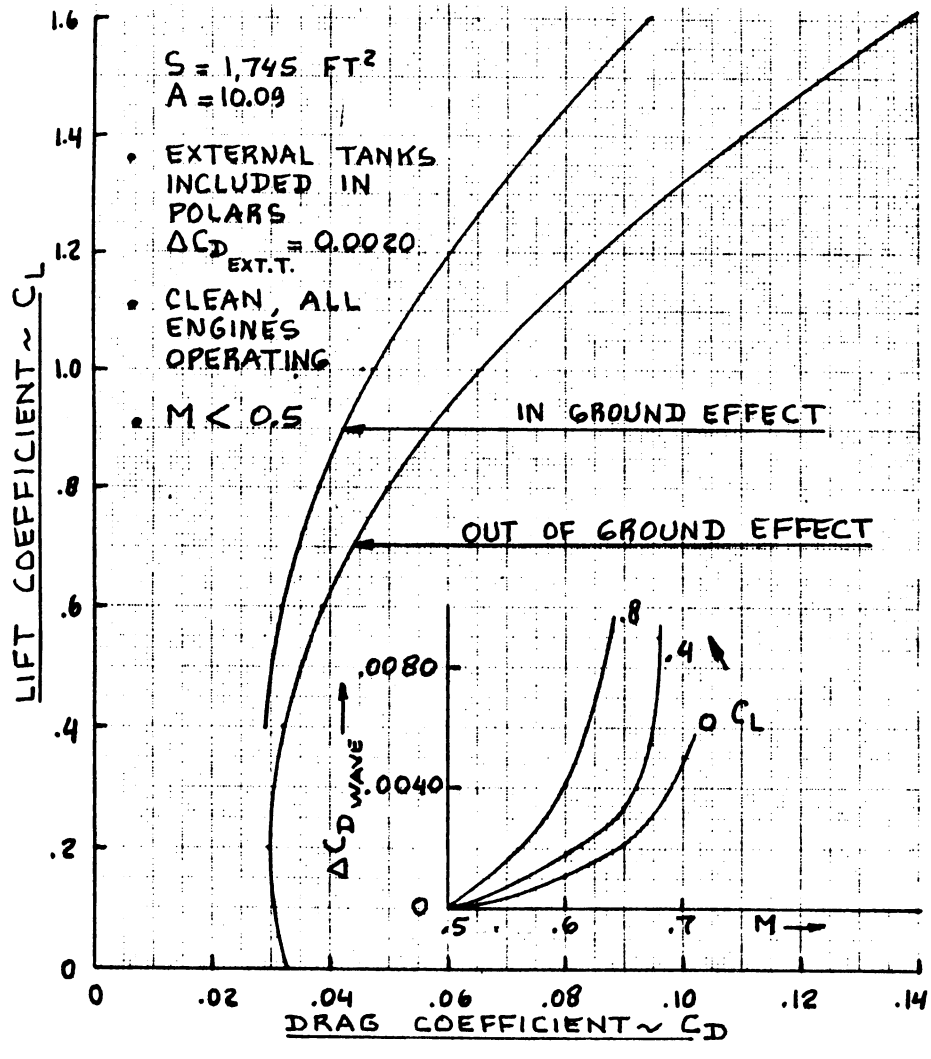

Figure 5.6 Drag Polars: Lockheed C-130H

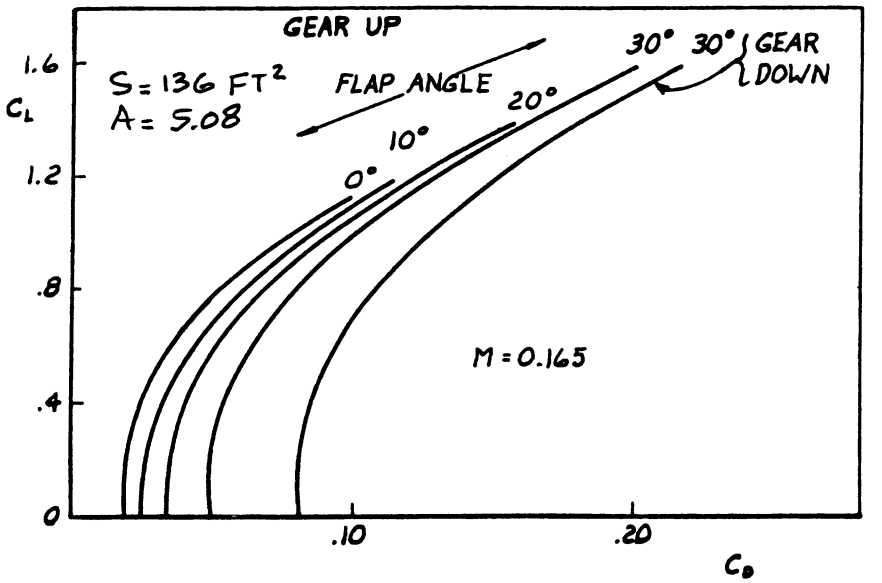

Figure 5.7 Drag Polars: SIAI-Marchetti S-211

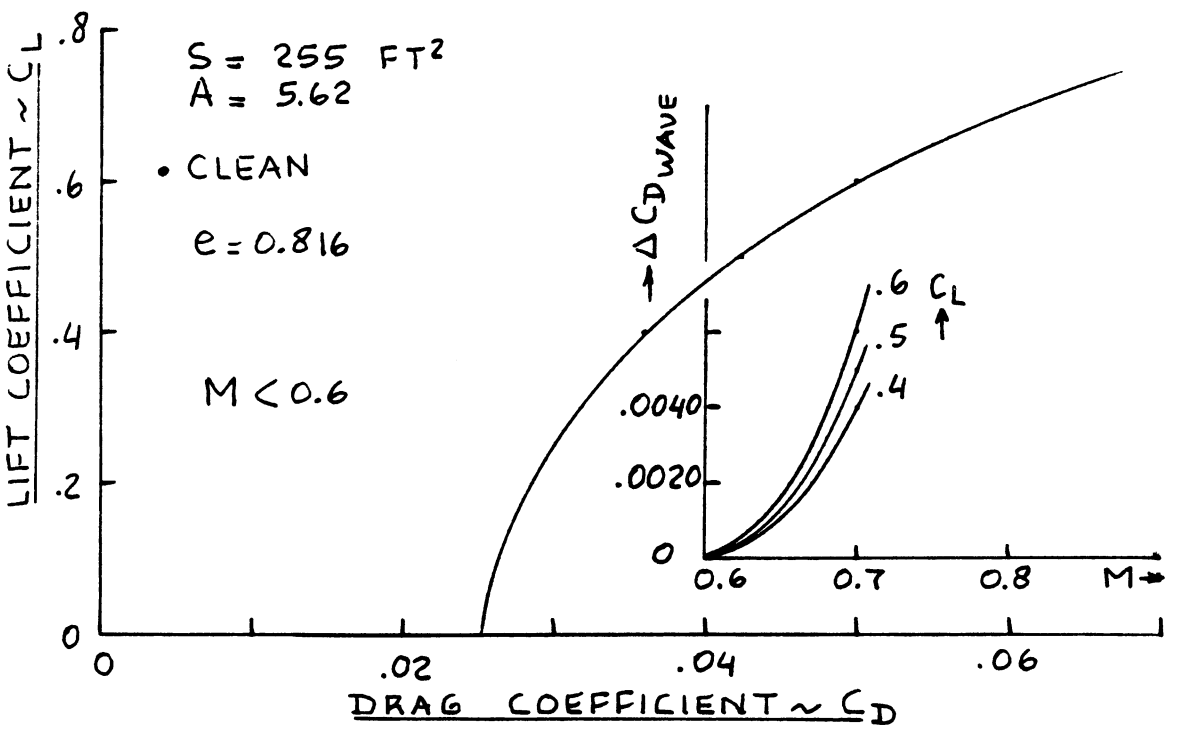

Figure 5.8 Drag Polars: NAA Rockwell T2C

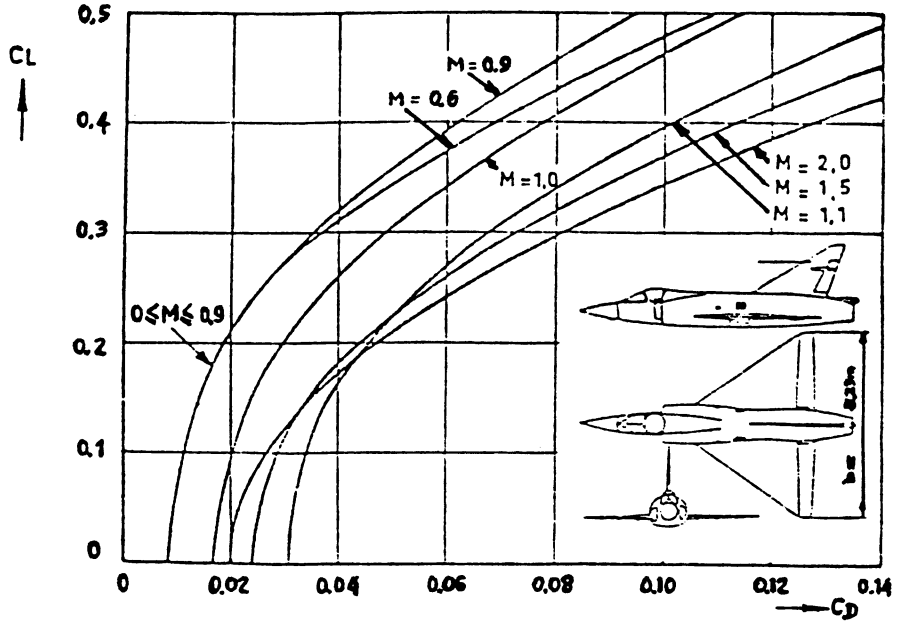

Figure 5.9 Drag Polars: Convair F-106

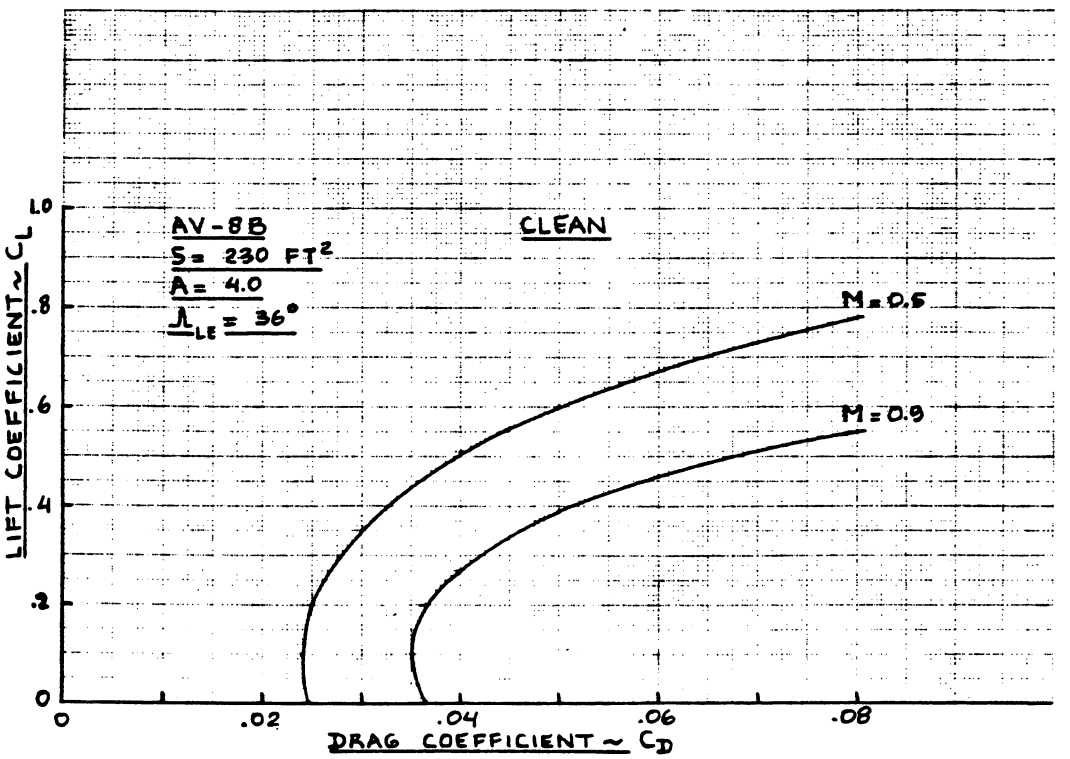

Figure 5.10 Drag Polars: McDonnell Douglas AV8B

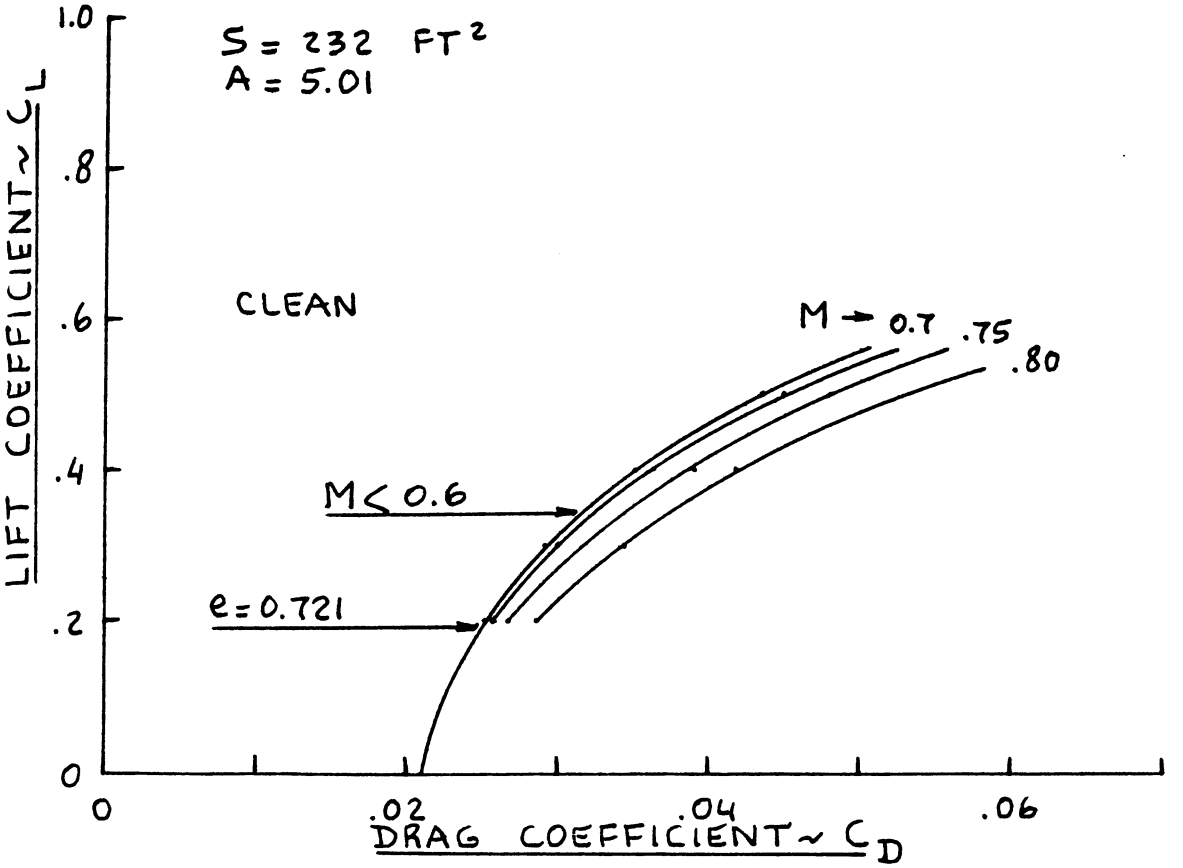

Figure 5.11 Drag Polars: Learjet M25

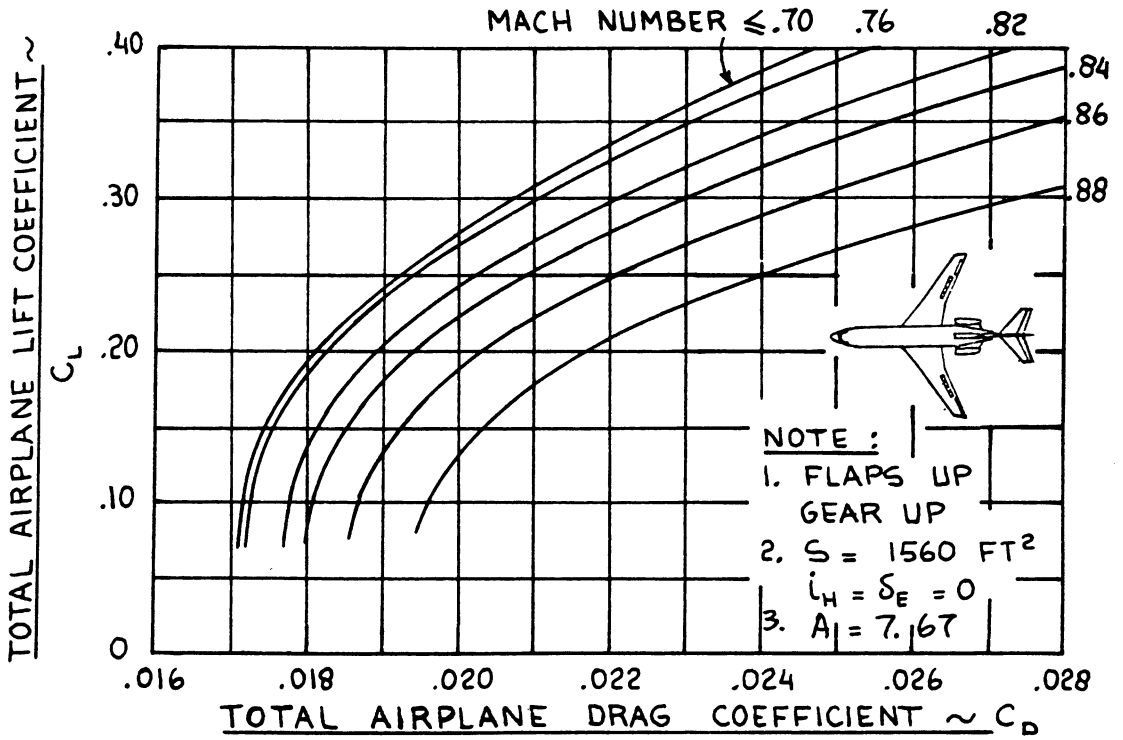

Figure 5.12 Drag Polars: Boeing 727-100

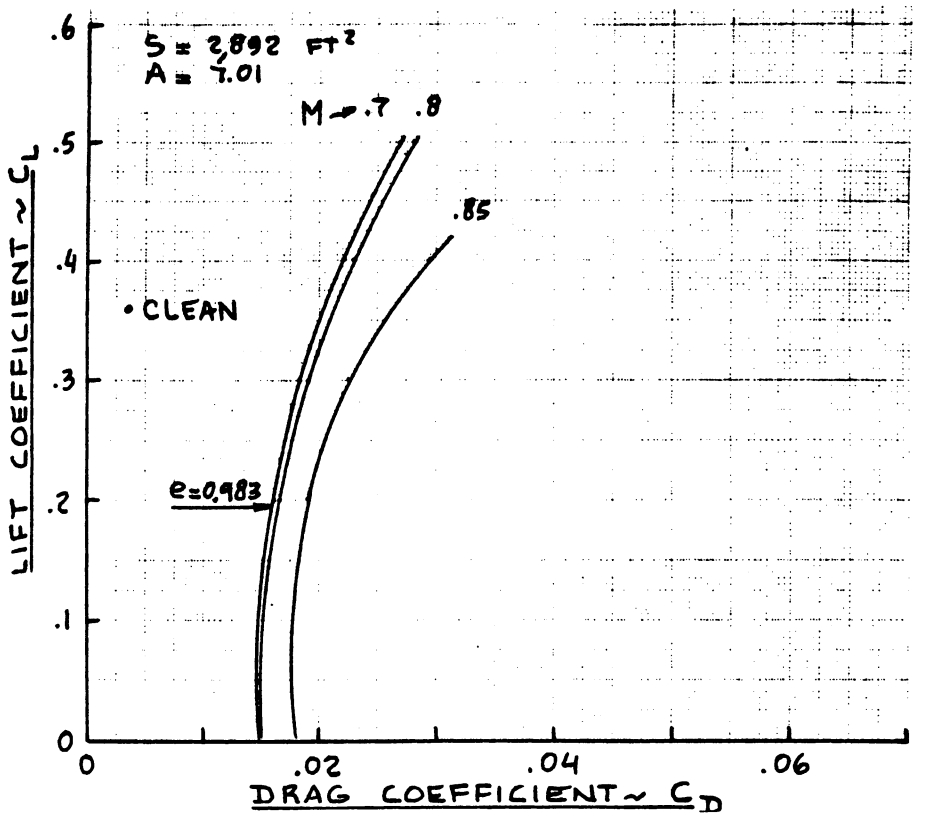

Figure 5.13 Drag Polars: Boeing 707-320B

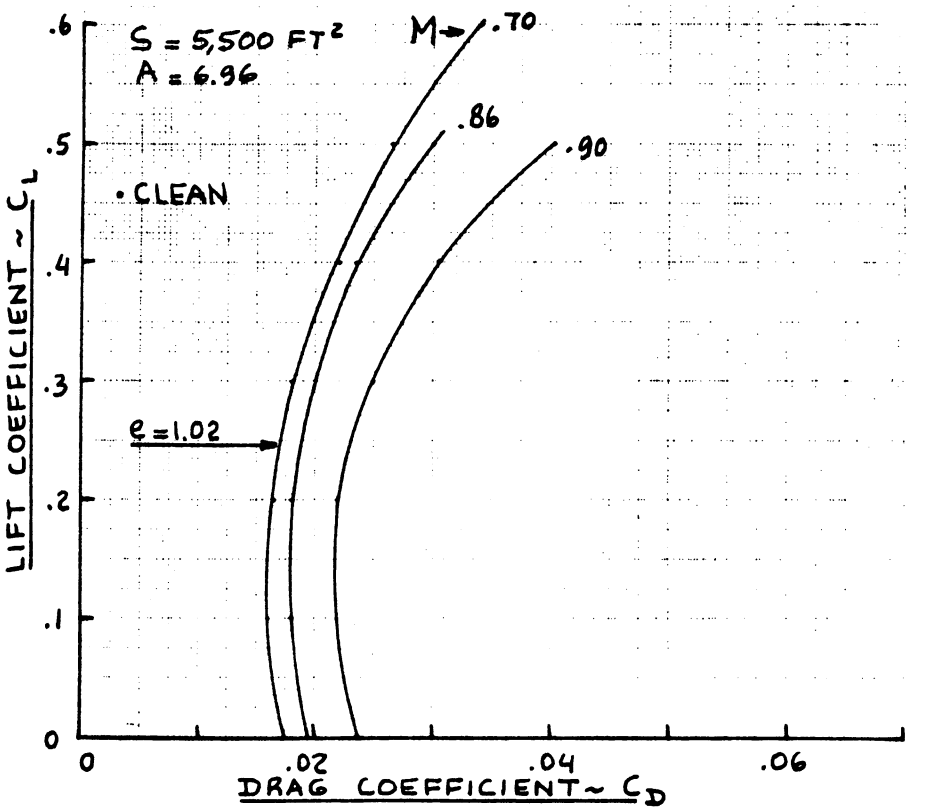

Figure 5.14 Drag Polars: Boeing 747-200

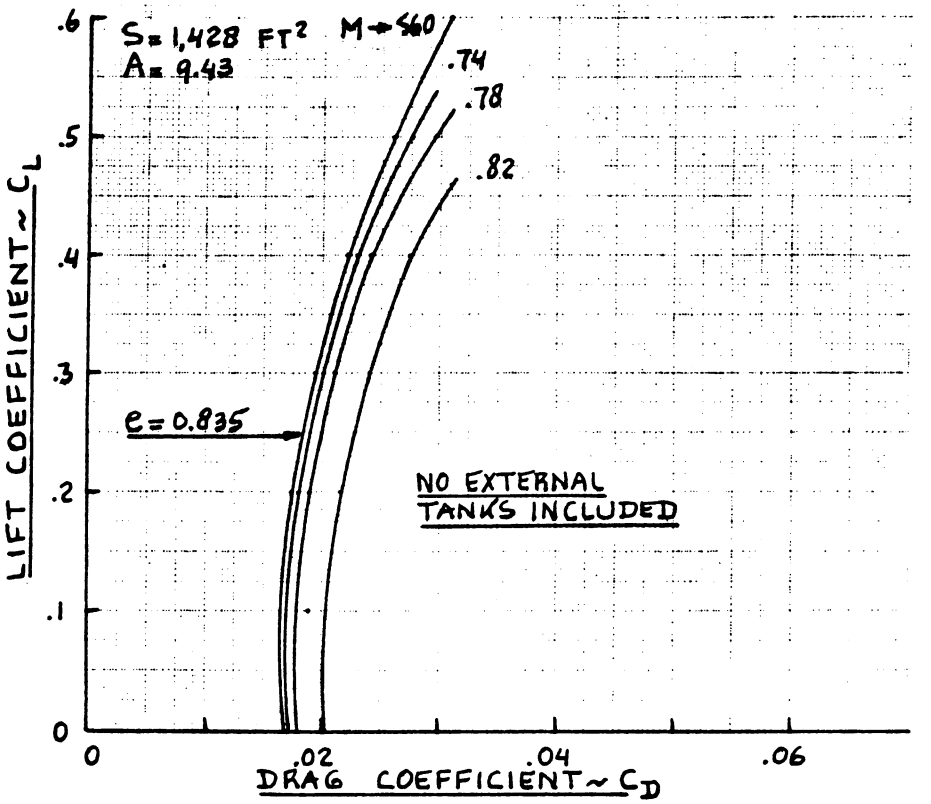

Figure 5.15 Drag Polars: Boeing B-47B

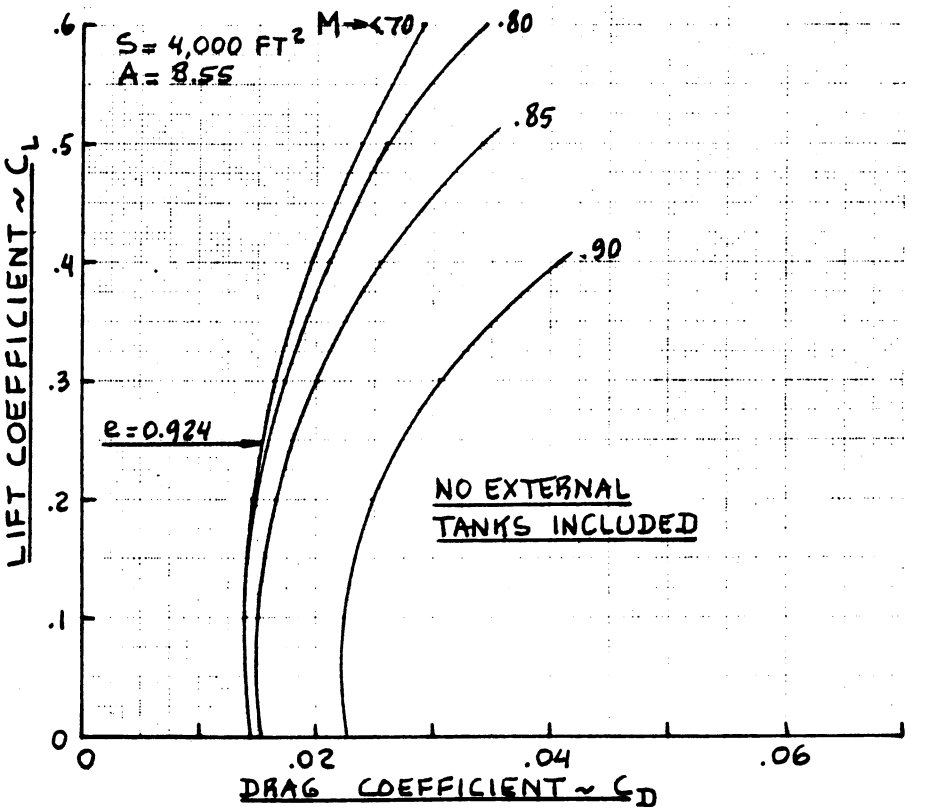

Figure 5.16 Drag Polars: Boeing B-52A

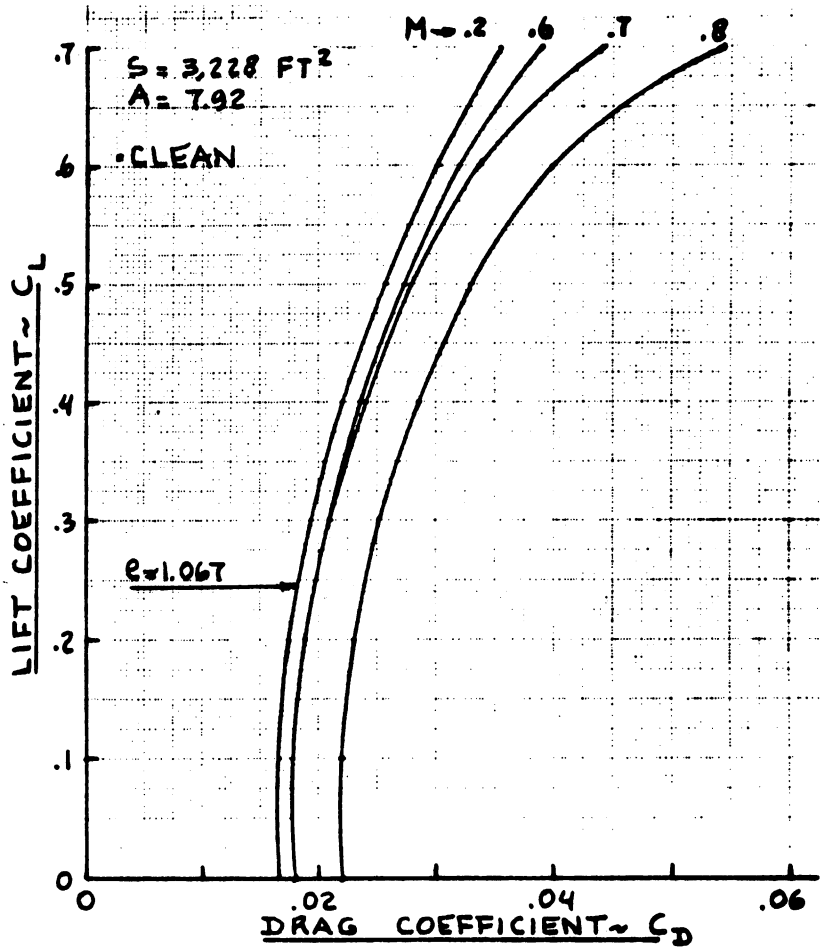

Figure 5.17 Drag Polars: Lockheed C-141B

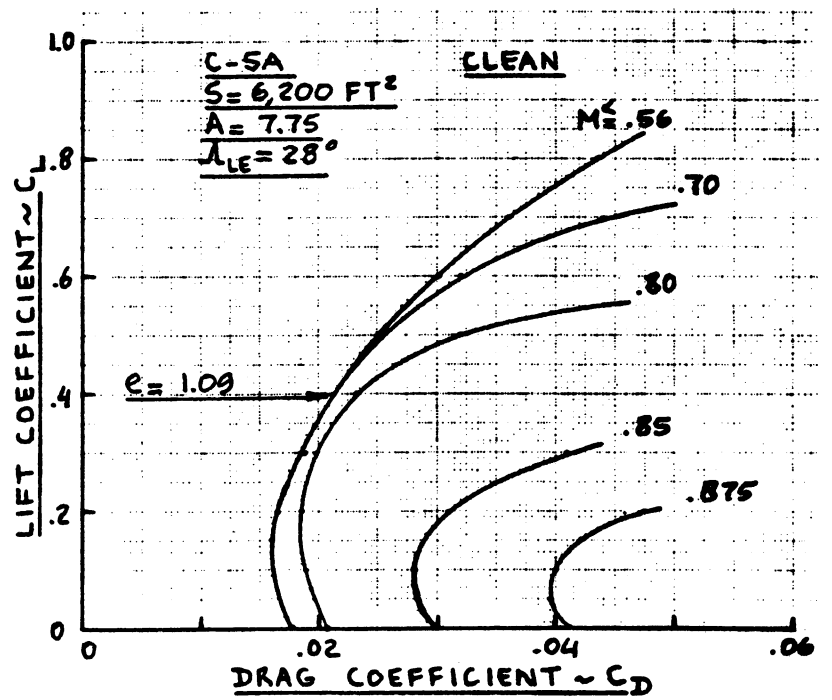

Figure 5.18 Drag Polars: Lockheed C-5A

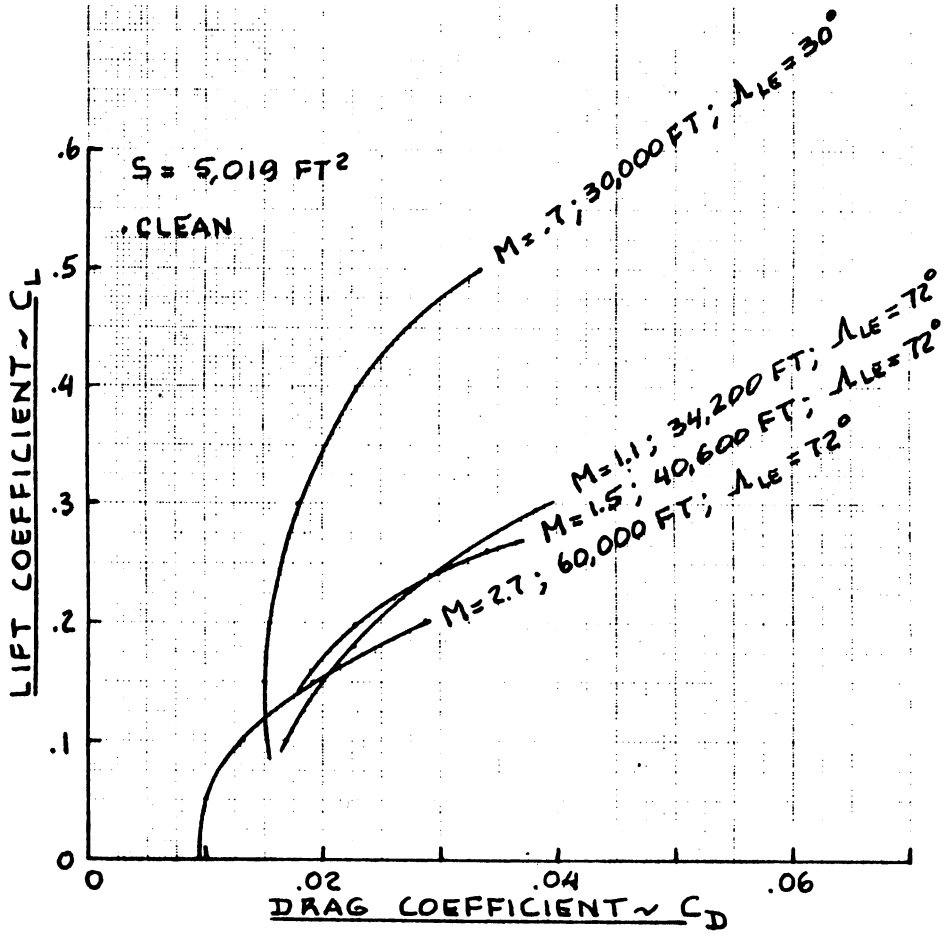

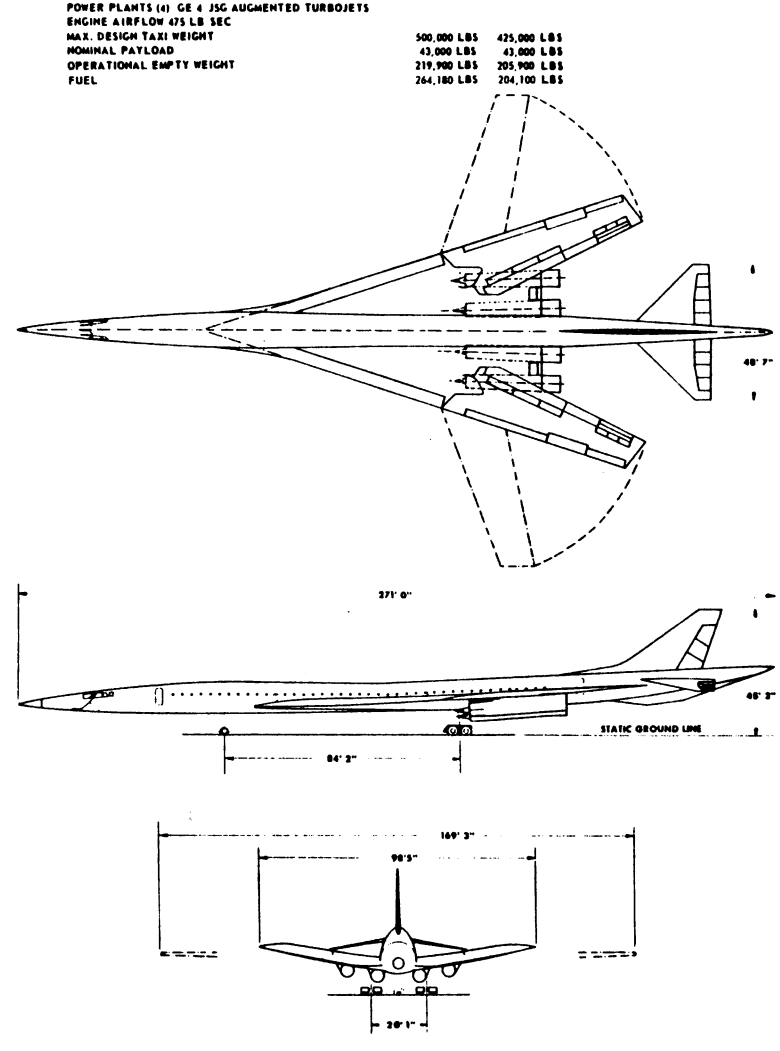

Figure 5.19 Drag Polars: Boeing SST Design

5.2 EQUIVALENT PARASITE AREAS

Figures 5.20 through 5.22 provide data on the relationship between total airplane equivalent parasite area, 'f', the equivalent skin friction coefficient, C_f and the total airplane wetted area, S_{wet}. The zero-lift airplane drag coefficient C_{D_o} is related to the equivalent parasite area, 'f' and to airplane wing area, S by:

$$C_{D_o} = f/S \qquad (5.1)$$

The airplanes for which data are included in Figures 5.20-5.22 are described in some detail in various issues of Reference 31. Wing areas, S, are also given in Reference 31,

5.3 OSWALD'S EFFICIENCY FACTORS

Table 5.1 provides data for Oswald's efficiency factor 'e' in the simplified airplane drag polar equation:

$$C_D = C_{D_o} + (C_L^2)/\pi Ae \qquad (5.2)$$

Note that high values of 'e' are rare, but they do occur. The reader may 'reconstruct' a value for 'e' from any drag polar by matching the polar to Equation 5.2.

5.4 EXAMPLES OF WETTED AREA BREAKDOWNS

Tables 5.2 and 5.3 present example data for wetted area breakdowns of fighters, commuters, transports and a business jet. Table 5.3 also includes data on the breakdown of equivalent parasite area with the corresponding value of average skin friction coefficient.

The reader should always verify any computed wetted area breakdown with known breakdowns for similar airplanes. Any significant differences should be explained!

The reader is also reminded of the correlations between total airplane wetted area and airplane take-off weight, provided in Chapter 3 of Part I. These data should be regarded as a source of comparative information.

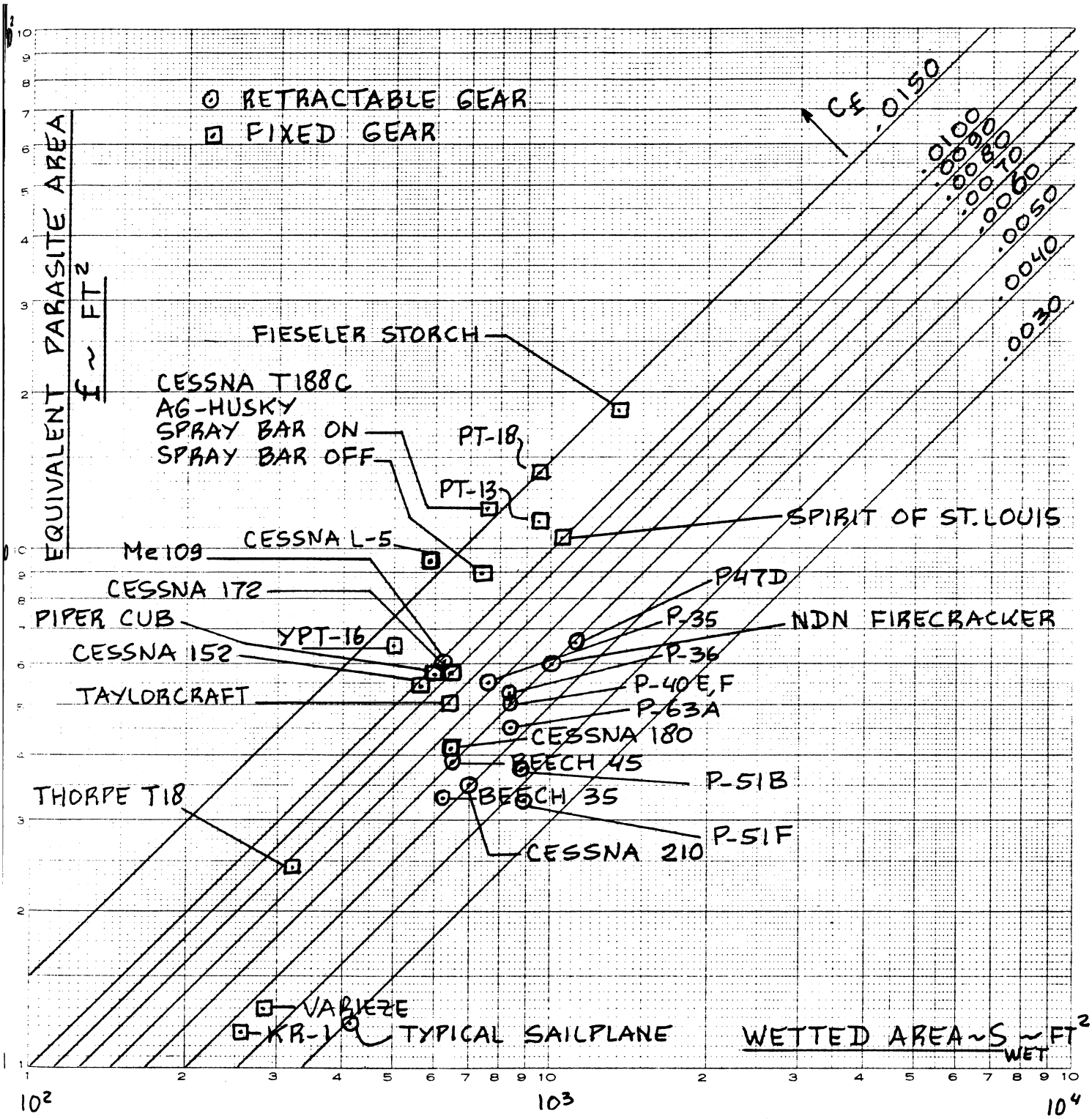

Figure 5.20 Relation Between Equivalent Parasite Area, Equivalent Skin Friction and Wetted Area for Single Engine Propeller Driven Airplanes

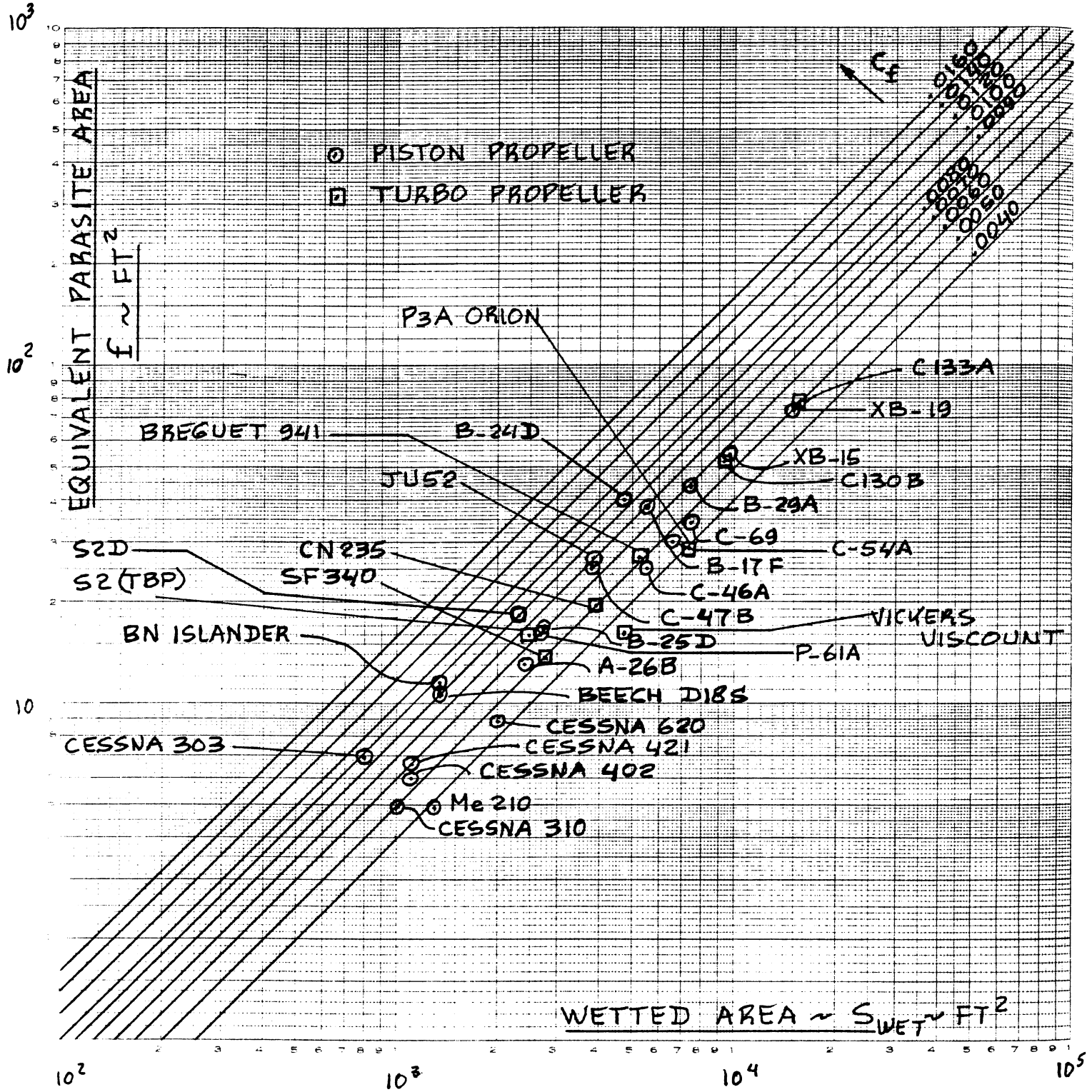

Figure 5.21 Relation Between Equivalent Parasite Area, Equivalent Skin Friction and Wetted Area for Multi-engine Propeller Driven Airplanes

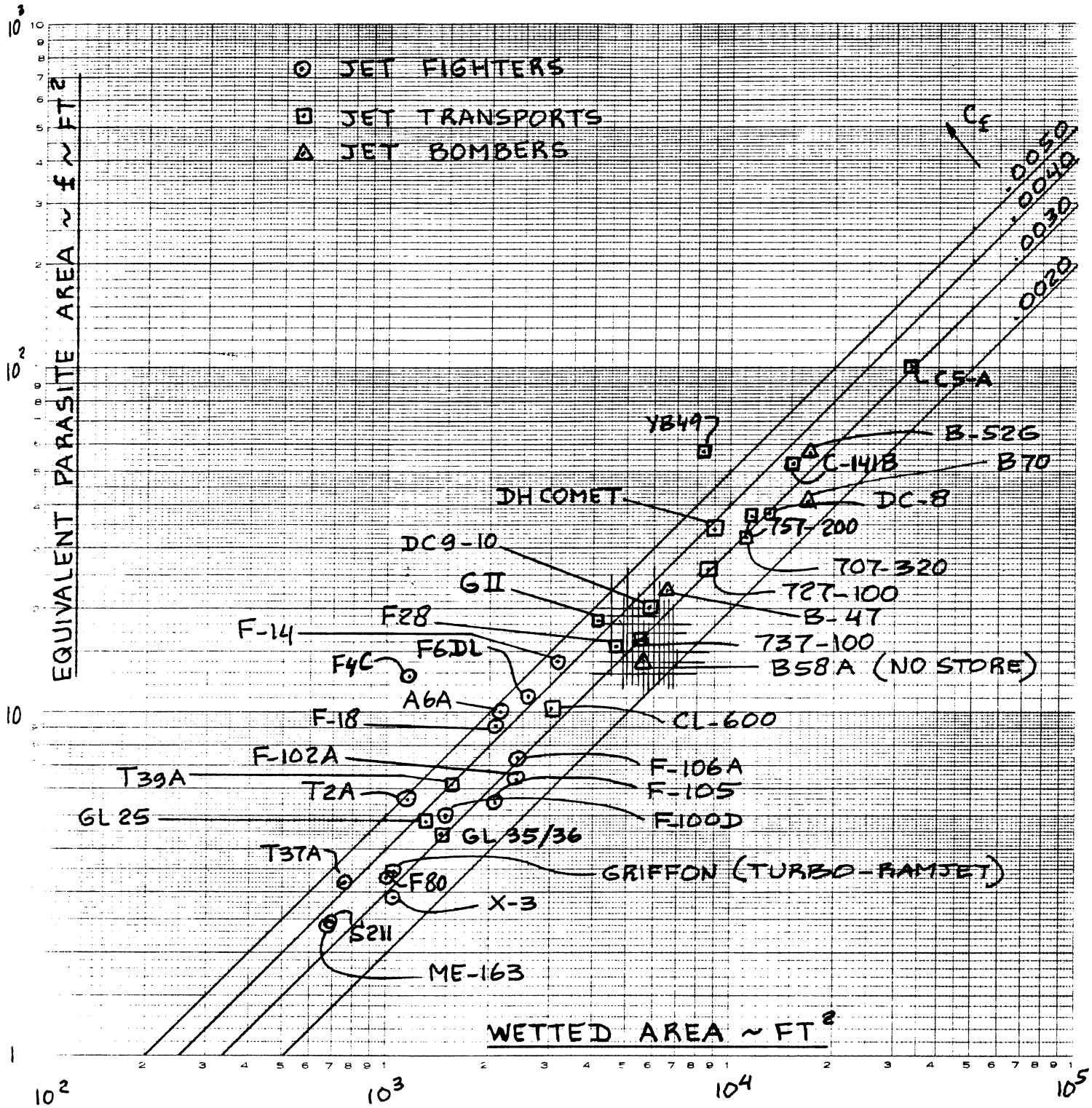

Figure 5.22 Relation between Equivalent Parasite Area, Equivalent Skin Friction and Wetted Area for Jets: Fighters, Bombers and Transports

Table 5.1 Oswald's Efficiency Factor 'e' for Several Airplanes

Single Engine Propeller	'e'		'e'	Four Engine Prop.	'e'
PT-18	0.75	Cessna 150	0.77	C-54A	0.81
AT-7	0.74	Cessna 172	0.77	C-60A	0.63
AT-8	0.61	Cessna 182	0.84	C-64	0.97
Cessna L-5	1.02	Cessna 185	0.86	C-69	0.82
O-46A	0.80	Cessna 177	0.57	XB-19	0.76
OE-2	0.70			B-24D	0.78
Cessna 180	0.75			B-24G	0.84
Beech 35	0.82			B-29A,B	0.94

Prop. Fighters	'e'	Jet Fighter/Trainers	'e'
P-38J	0.76	P-63A	0.86
P-40F	0.70	T-37	0.78
P-47D	1.02	NAA T2C	0.816
P-49	0.80		
P-51B	0.86	Jet Bombers	
P-51F	0.80		'e'
XP-60C	0.66	Boeing B-47B	0.84
P-61A	0.86	Boeing B-52A	0.924

Twin Engine Prop.	'e'	Jet Transports	'e'
A-26B	0.79	Learjet M 25	0.721
C-46A	0.88	Gulfstr.GII	0.950
C-47B	0.89	F-28-2000	0.818
B-25D	0.78	B 707-320B	0.983
B-26F	0.76	L C-141B	1.067
Cessna 310	0.73	L C-5A	1.091
Gulfstream GI	0.78		
SAAB SF 340	0.80		

Table 5.2 Wetted Area Breakdowns for Fighters, Commuters and Transports

Type:	AV-8B	F-4E	F-15C	F/A-18A	SDS330	SC7	F-27
Wing area, S, ft^2	230	530	608	400	453	373	754
Wing aspect ratio, A	4.0	2.82	3.0	3.5	12.3	11.0	12.0
Wetted Areas (ft^2):							
Wing	379	730	691	562	788	477	1,507
Wing strake/LEX				210			
Fuselage	597	1,124	1,468	890	1,543	1,034	1,614
Horizontal tail	86	154	216	176	98	98	344
Vertical tail	56	116	257	208	173	155	387
Nacelles					163	115	in fus.
Ventral	11						
Miscellaneous	45 (outriggers)				114	81 (wing struts)	
					45	48 (stub wings)	
					126 (gear fairing)		
TOTALS	1,174	2,123	2,632	2,046	3,049	2,008	3,852

Type:	B-757	F-28 1000	F-28 4000	VFW 614	GL M26
Wing area, S, ft^2	1,951	822	850	689	253
Wing aspect ratio, A	7.95	7.3	7.96	7.21	5.74
Wetted areas (ft^2)					
Wing	3,358	1,334	1,399	1,077	402
Fuselage	5,601	2,217	2,453	1,682	520
Horizontal tail	893	430	430	342	108
Vertical tail	762	269	269	202	75
Nacelles	662	323	323	77	140
Pylons	127	75	75	74	25
Flap tracks	225			87	11 (ventral)
Miscellaneous			(antennas) 5		132 (tiptanks)
TOTALS	11,588	4,648	4,950	3,547	1,413

Table 5.3 Wetted Area and Parasite Area Breakdowns for Jet Transports (ft^2)

Type:	B-47B			B-52A			KC-135		
Component:	S_{wet}	c_f	f	S_{wet}	c_f	f	S_{wet}	c_f	f
Fuselage	2,611	.00167	5.552	4,260	.00168	8.489	3,830	.00169	7.976
Wing	2,580	.00229	7.953	7,710	.00224	23.594	4,332	.00224	13.819
Horiz. tail	508	.00243	1.617	1,650	.00232	4.831	875	.00236	2.655
Vert. tail	450	.00229	1.356	930	.00235	2.755	622	.00230	1.842
Trim			.170			1.000			.380
Nacelles	782	.00223	4.510	1,320	.00235	8.437	632	.00231	3.640
Nac. interf.			.541						
Pylons	139	.00232	.376	310	.00234	.843	304	.00227	.803
Aircon. noz.									.650
Roughness			.438			1.029			.658
Miscellaneous							refuel boom:		1.250
TOTALS	7,070		22.513	16,180		50.978	10,595		33.673

Type:	720			707-320B			727-100		
Component	S_{wet}	c_f	f	S_{wet}	c_f	f	S_{wet}	c_f	f
Fuselage	3,971	.00171	8.453	4,590	.00165	9.400	3,838	.00167	8.080
Wing	4,451	.00226	14.693	5,463	.00222	17.246	2,800	.00223	9.490
Horiz. tail	875	.00239	2.685	1,050	.00236	3.186	720	.00233	2.170
Vert. tail	684	.00235	2.066	684	.00234	2.057	685	.00210	1.860
Trim			.380			.550			.200
Nacelles	660	.00234	4.301	368	.00265	2.696	432	.00219	2.270
						center:	130	.00226	.700
Nacelle interf.			.308			.572			.150
Noise suppr.	140	.00311	.435						
Thrust rev.			1.063						
Pylons	304	.00230	.813	304	.00230	.813	108	.00219	.290
Aircond. nozzle			1.300			.350			.250
Roughness			.700			.765			.530
Miscellaneous				scrubbing drag:		4.238	fl.track fair.:		1.000
TOTALS	11,085		37.197	12,459		41.873	8,713		26.990

5.5 VERIFICATION OF REALISM OF COMPUTED DRAG POLARS

After estimating the drag polar of a new airplane with the methods of Chapter 4, the following procedure should always be followed to verify that the computed drag data are indeed 'in-the-ball-park':

Step 1: Determine for which flight condition and for which external configuration the drag polars need to be determined.

The reader should recognize the fact that airplane drag polars depend upon the following factors:

A) Flight condition:

Mach Number, altitude, lift coefficient (or angle of attack) and Reynold's number which also depends on a characteristic length.

B) External configuration:

The external airplane configuration may be influenced by:

1) flap deflection (take-off, climb, cruise, landing or maneuvering
2) landing gear position: up or down (gear well doors open or not?)
3) speed brake position: open or closed
4) external store disposition
5) loading door position: open or closed
6) weapons door position: open or closed
7) cooling flap position: open for take-off, open for climb, or closed
8) propeller control position: feathered, windmilling or normal
9) jet engine condition: windmilling or normal
10) inlet configuration: blow-down doors, ramps, spikes, bleed- and bypass doors
11) control surface deflection for trim (trim drag), with AEO or OEI

Drag polars can differ significantly depending on how these factors are selected for any given airplane in any given flight condition.

Step 2: Plot the C_D versus α data from the calculations performed with Chapter 4.

Step 3: Plot the C_L versus α data for the airplane with the method of Chapter 10.

Step 4: From steps 2 and 3 crossplot the C_D versus C_L polar.

Figure 5.23 shows an example of how Steps 2, 3 and 4 are carried out.

Step 5: A) From step 4, determine C_{D_o} and compute:

$$f = C_{D_o} S \qquad (5.3)$$

B) Determine the wetted area of your airplane. The data for doing this are already available from the drag polar calculations performed in Chapter 4.

'Verify' the computed wetted area breakdown with the data of Tables 5.2 or 5.3. Also check the total wetted area against the trend data of Figures 3.22 in Part I.

C) Plot the 'f' and S_{wet} data on one of the graphs in Figures 5.20-5.22, whichever is applicable. Determine the C_f value for the airplane and judge whether or not the value of C_f is a reasonable one from an 'aerodynamics technology' viewpoint. This is done by comparison to other airplanes in the same figure.

Step 6: Plot $(C_L)^2$ versus C_D, and determine $dC_D/d(C_L)^2$ as indicated in Figure 5.23.

Compute: $e = \{\pi A(dC_D/dC_L)^2 \qquad (5.4)$

Compare this value of 'e' with that for similar airplanes in Table 5.1. If there is a large difference, check the calculations or explain why the airplane might be different!

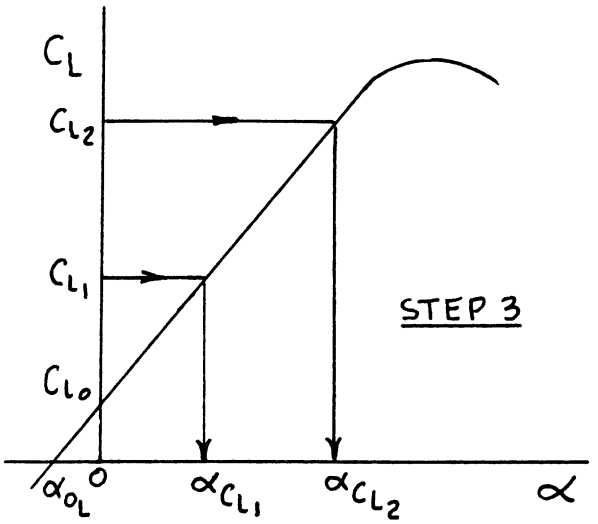

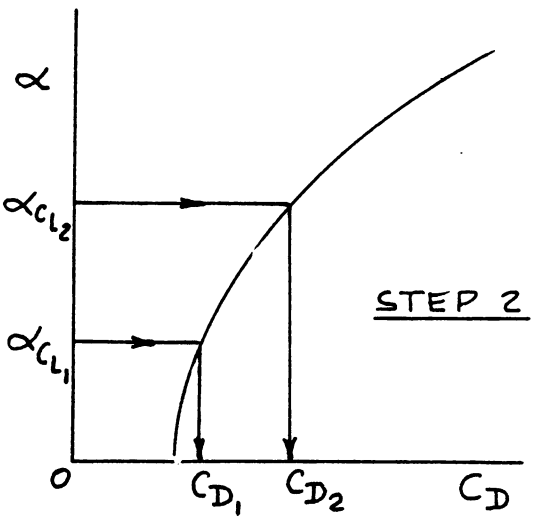

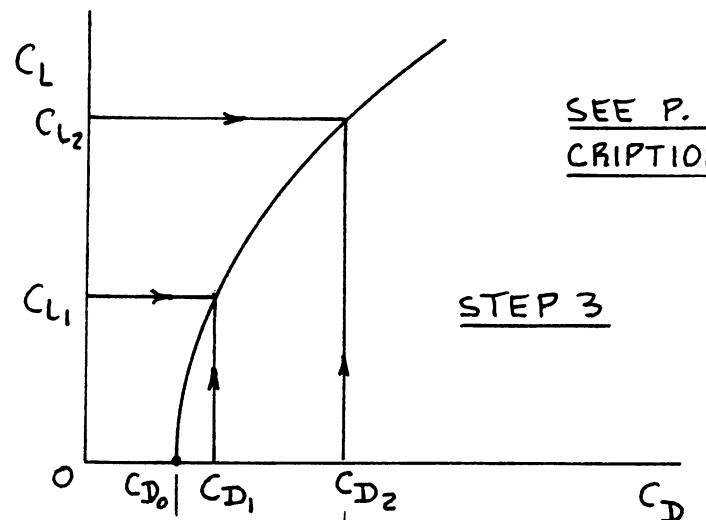

SEE P. 136 FOR DESCRIPTION OF STEPS

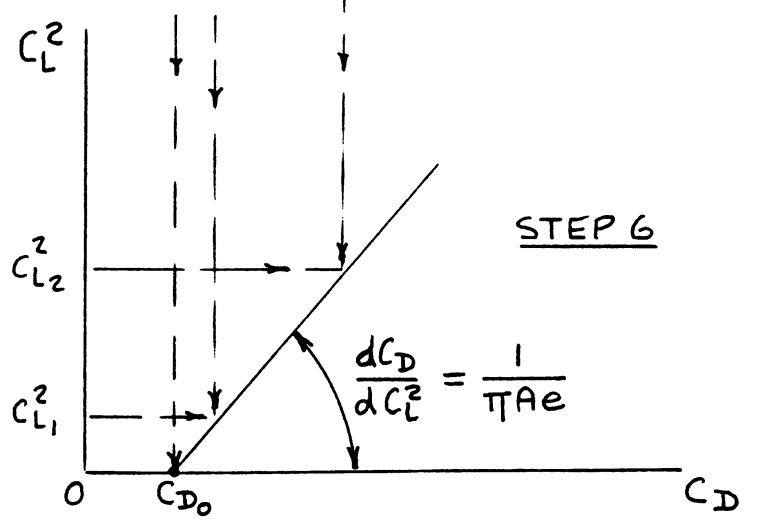

Figure 5.23 Drag Polar Construction from Lift and Drag Data with Angle of Attack

AV-8B Harrier II

MCDONNELL DOUGLAS

The United States Marine Corps AV-8B Harrier II V/STOL Light Attack aircraft built by the McDonnell Douglas Corporation is a vastly improved derivative of the British Aerospace AV-8A Harrier currently in service with the USMC. The Marines have, with ten years of operational experience in the AV-8A, proven the effectiveness advantages of V/STOL for the close air support mission. With the AV-8B Harrier II, the Marines will have a V/STOL aircraft with payload/radius capability comparable to any modern, conventional, light attack aircraft.

The AV-8B will provide:

- Double the payload/radius,
- Accurate, first pass weapon delivery,
- Improved VTO and STO capability,
- Greatly reduced pilot workload,

and will be

- More reliable and more maintainable.

The key to the V/STOL capability of the AV-8B is found in the vectored, 21,180 lb thrust Rolls-Royce Pegasus 11 engine. The pilot can control the direction of engine thrust by positioning the four exhaust nozzles; aft for wingborne flight, down for vertical flight and at intermediate positions for short takeoff and short landing. Aircraft attitude control during V/STOL and hover is accomplished through the reaction control system which directs engine bleed air through reaction nozzles located at the wing tips, the nose and the tail.

Performance Tropical Day (90°F)

- STO distance at max TOGW ..... 1,200 ft
- VTO Weight ..... 19,185 lb
- VL Weight ..... 17,500 lb
- Vmax at altitude ..... 0.91 M
- Vmax at sea level ..... 585 Kts
- Load factor ..... +7 g, −3 g

Interdiction Mission Hi-Lo-Hi

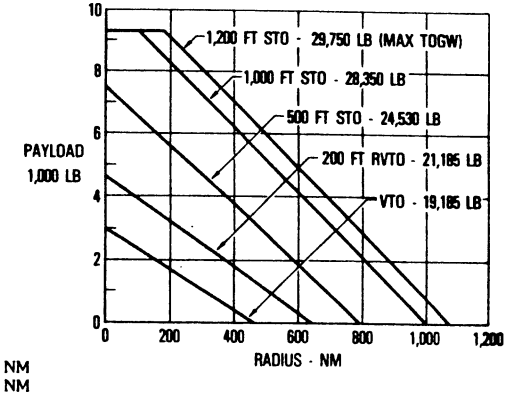

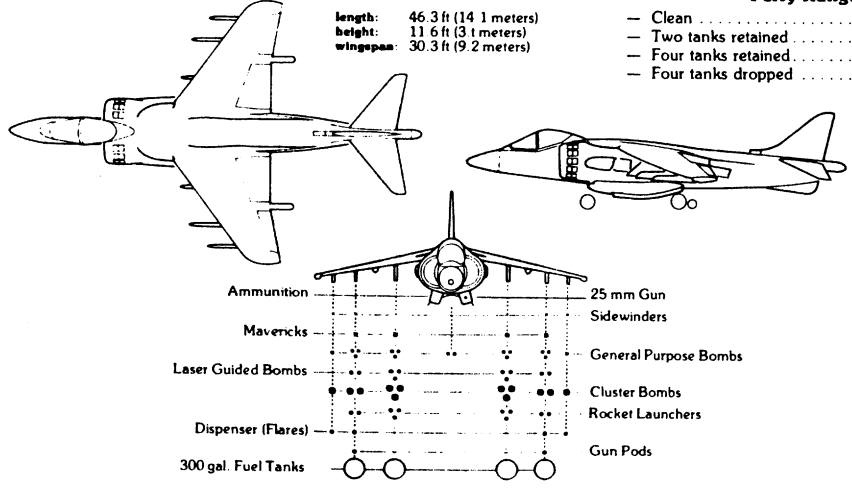

Ferry Ranges

- Clean ..... 1500+ NM
- Two tanks retained ..... 1800+ NM
- Four tanks retained ..... 2000+ NM
- Four tanks dropped ..... 2400+ NM

Weights

- Max design TOGW ..... 29,750 lb
- Operating weight empty ..... 12,750 lb
- Internal fuel ..... 7,500 lb
- Internal and external fuel ..... 15,829 lb
- Max external load ..... 9,200 lb

Major AV-8B Changes from the AV-8A

- Supercritical/composite material wing
- Lift improvement devices
- Large, positive circulation flaps
- Narrowed outrigger tread
- High recovery engine inlets
- Raised, high visibility cockpit
- Stability augmentation and attitude hold system
- Angle rate bombing set
- Inertial navigation set
- Integrated crew station
- Onboard oxygen generation system
- Zero scarf front engine nozzles
- Lengthened aft fuselage

6. INSTALLED POWER AND THRUST PREDICTION METHODS

The purpose of this chapter is to present rapid methods for the prediction of installed power and/or thrust in airplanes. The assumption will be made that the following characteristics of the engine are known:

1. For piston engines: manufacturers shaft horsepower data for a range of altitudes and throttle settings.

2. For gas generators: manufacturers shaft horsepower and thrust data for a range of altitudes, Mach numbers and throttle settings.

3. For jet engines: manufacturers thrust data for a range of altitudes, Mach numbers and throttle settings.

These engine manufacturers data (also called uninstalled data) are based on ideal (teststand) conditions and do <u>not</u> normally include the following effects:

A. Effect of the inlet (air induction system) on pressure recovery, on drag and therefore on engine performance.

   <u>Note:</u> A bellmouth inlet system, assuring very high inlet pressure recovery, is frequently used to determine engine manufacturers data. Fig.6.1 shows a typical teststand arrangement.

B. Effect of power extraction (needed to run essential airplane services) on engine performance.

   <u>Note:</u> Power extraction to run essential engine services ARE normally included in engine manufacturers data.

C. Effect of the exhaust or nozzle configuration on drag and on engine performance.

   <u>Note:</u> The engine manufacturer uses a nozzle configuration which is usually different from that preferred by the airframer. See Figure 6.1.

The methods presented in this chapter are organized as follows:

6.1 Power extraction requirements

6.2 Inlet sizing and integration

6.3 Exhaust or nozzle sizing and integration

6.4 Prediction of installed power and thrust

For a detailed and concise methodology of inlet design and analysis the reader should consult Reference 32. For considerations of design and analysis of inlet and exhaust systems both, Reference 33 is recommended.

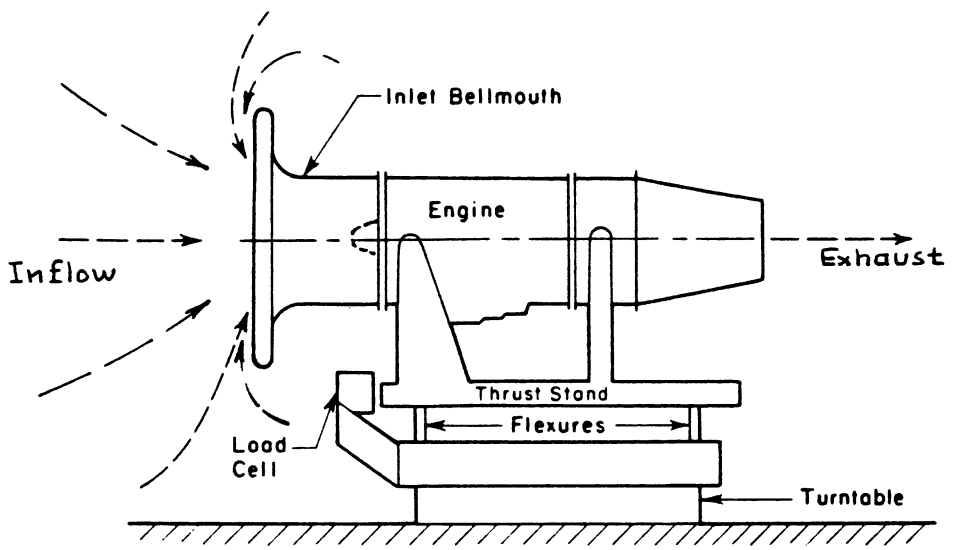

Figure 6.1 Engine Test Stand with Bellmouth Inlet

6.1 POWER EXTRACTION REQUIREMENTS

To operate an airplane in any phase of its mission a certain amount of electrical, mechanical and pneumatic power may be required. These power requirements are normally satisfied by the engines. For that reason they are referred to as power extraction requirements. In some cases power sources other than the propulsion system (for example an APU) are used.

The magnitude of power extraction requirements differs from one airplane to another and from one mission phase to another.

In this section a rapid method for estimating power extraction requirements is presented for:

6.1.1 Piston-propeller driven airplanes

6.1.2 Turbopropeller and jet driven airplanes

6.1.1 Piston-propeller Driven Airplanes

In this type of airplane the following power extraction requirements may be present:

$$P_{extr} = P_{el} + P_{mech} \qquad (6.1)$$

where: P_{el} = the electrical power extraction in shp

P_{mech} = the mechanical power extraction in shp

Electrical power extraction requirements, P_{el} follow from the essential electrical services which are required during any given mission phase. To determine electrical power requirements, an 'electric power load profile' must be prepared. Using p.320 of Part IV as an example, the reader should prepare an electric power load profile for his airplane.

From this electric power load profile the electrical power extraction requirement, P_{el} is determined as:

$$P_{el} = .00134(VA_{plp})/\eta_{gen} \text{ in shp} \qquad (6.2)$$

where: VA_{plp} = the maximum required electrical power in Volt-amperes as obtained from the electric power load profile.

η_{gen} = 0.9 is the efficiency of the electric power generator(s) which are assumed to be driven off the engine accessory drive pad. Modern generators can achieve efficiencies of 0.90 to 0.95.

Lacking a detailed electric power load profile, the P_{el} values suggested in Table 6.1 may be used. The reader should also consult Chapter 7 in Part IV for more information on electrical system power capabilities.

Mechanical power extraction requirements, P_{mech} depend on the systems which are required for the operation of the airplane in a given mission phase. Examples of such system may be:

fuel pumps, hydraulic pumps, cooling fans, heating/airconditioning system, pressurization system, spray system (in agricultural airplanes).

The reader should prepare a list of those systems which require the generation of mechanical power. The total mechanical power required can be written as:

$$P_{mech} = P_{fp} + P_{hydr} + P_{other} \qquad (6.3)$$

where: P_{fp} = the mechanical power required to drive the fuel pumps. This may be found from:

$$P_{fp} = 0.00014(c_p)(SHP)/\eta_{fp} \qquad (6.4)$$

where: c_p is the engine sfc in lbs/shp/hr

SHP is the engine shaft horsepower required in the flight condition being analyzed

η_{fp} = 0.65 is the fuel pump efficiency.

The assumption has been made here that the fuel pumps are operating on a pressure differential of 50 psi. Information on pumps may be found in Ref.34. Data on fuel systems is provided in Chapter 5 of Part IV.

Note: power required to drive electric fuel pumps should be included in P_{el}.

P_{hydr} = the mechanical power required to drive

the hydraulic pumps. The magnitude of P_{hydr} depends on the hydraulic flow and pressure differential needs of the airplane hydraulic system. Section 6.2 of Part IV contains a discussion on the sizing of hydraulic systems. As indicated in Part IV, a hydraulic system load analysis must be performed to find the total hydraulic fluid flow which is required. Having also selected the hydraulic system operating pressure (Part IV, Ch.6), the hydraulic system shaft horsepower requirements are found from:

$$P_{hydr} = 0.0006(\Delta p_{hydr})(\dot{V}_{hydr})/\eta_{hp} \qquad (6.5)$$

where: Δp_{hydr} = the pressure differential (psi), over which the hydraulic system operates. This is roughly equal to the system operating pressure which ranges from 1,500 to 5000 psi. See Chapter 6 in Part IV.

$\dot{V}_{hydr}$ = the hydraulic fluid flow rate in gallons/min (gpm). Page 308 in Part IV provides some guidance for estimating hydraulic fluid flow rates.

η_{hp} = the hydraulic pump(s) operating efficiency. This may be taken to be 0.75 in modern systems.

Note: the power required for electrically driven hydraulic pumps should be included in P_{el}.

P_{other} = the sum of all 'other' mechanical power extraction requirements. Determination of these 'other' mechanical power extraction needs is left to the reader. The best way to proceed is to make a complete list of all 'other' mechanical power requirements for on-board systems. By using appropriate efficiency values, the required value of 'to be extracted' engine shaft horsepower, P_{other} can then be estimated. Ref.34 is a good source for general mechanical system data. Part IV contains discussions of various 'other' types of

system which may be required in airplanes.

Lacking a detailed listing of mechanical power extraction requirements, the values suggested for P_{mech} in Table 6.1 may be used.

The effect of P_{extr} as determined from Eqn. 6.1 on installed engine performance is discussed in Section 6.4.

Table 6.1 Summary of Power Extraction Requirements

Power Extraction Type:	Electrical shp, P_{el}	Mechanical shp, P_{mech}	Pneumatic Bleed slugs/sec
Airplane Type:			
Piston Propeller Driven:			
Single engine, light airplanes	1-2	1-2	0
Single engine, military trainers	2-4	2-4	0
Twin engine, light airplanes	4-6	5-10	0
Multi-engine transports	20-40	30-50	0
Turboprop and Jet Airplanes:			
Single engine, light airplanes	2-4	3-5	$0.01\dot{m}_a$
Single engine, military trainers	5-7	6-10	$0.015\dot{m}_a$
Twin engine turboprops	6-8	7-9	$0.015\dot{m}_a$
Twin engine turbojets or fans	8-10	9-11	$0.025\dot{m}_a$
Twin jet military trainers	10-15	15-20	$0.03\dot{m}_a$
Jet Fighters, air-superiority	50-100	50-100	$0.03\dot{m}_a$
Jet Fighters, attack	100-200	100-200	$0.04\dot{m}_a$
Jet Transports, civil	$0.00070W_{TO}$	$0.00060W_{TO}$	$0.03\dot{m}_a$
Jet Transports, military	$0.00100W_{TO}$	$0.00080W_{TO}$	$0.04\dot{m}_a$

6.1.2 Turbopropeller and Jet Driven Airplanes

For this class of airplanes the power extraction requirements may be determined from:

$$P_{extr} = P_{el} + P_{mech} + P_{pneum} \qquad (6.6)$$

where: P_{el} = the electrical power extraction in shp

P_{mech} = the mechanical power extraction in shp

P_{pneum} = the pneumatic (also called bleed air) power extraction in shp

Electrical power extraction requirements, P_{el} may be determined with the method of Sub-section 6.1.1, via preparation of an electric power load profile as shown on p.320 of Part IV. Lacking such detailed information the P_{el} values suggested in Table 6.1 may be used.

Some airplanes may require extensive radar and electronic warfare equipment. Examples are the Boeing E-3A, the Boeing E-6, the Grumman E-2C and the Lockheed P3V. In those cases large electrical power requirements may exist: 600 kVA in the case of the Boeing E-6!

Normally, these power requirements are satisfied by the installation of directly driven generators on the propulsion installation. If these power requirements cannot be satisfied by power extraction from the regular propulsion system separate power sources may have to be installed.

Mechanical power extraction requirements, P_{mech} may be determined with the method of Sub-section 6.1.1, via a listing of all required mechanical services. Lacking a detailed power extraction calculation, the values suggested in Table 6.1 may be used.

Pneumatic power extraction requirements, P_{pneum} are determined by those systems which are driven by bleed air form the main engines. Typical of such services are:

de-icing and anti-icing systems, heating and airconditioning systems, engine starting systems (for ground start and for air restart), pressurization of fuel tanks, for flap deployment (For example, the B-747 leading edge devices) and for water system pressurization.

A list of airplane services which require bleed air as the source of power must be prepared. Next, the required bleed airflows, $\dot{m}_{bleed}$ (in slugs/sec) must be estimated for each flight situation. From this the total engine bleed airflow can be computed. As a general rule, engine bleed airflow should not exceed 5 percent of the total engine massflow requirement in any given flight condition, $\dot{m}_a$, or major degradation of thrust will occur:

$$\dot{m}_{bleed} < 0.05\dot{m}_a \text{ in slugs/sec} \qquad (6.7)$$

Lacking a detailed evaluation of bleedair requirements, the data of Table 6.1 may be used.

As long as Eqn.(6.7) is satisfied, a first order estimate for P_{pneum} is:

$$P_{pneum} = (\dot{m}_{bleed}/\dot{m}_a)P_{reqd} \text{ for turboprops} \qquad (6.8)$$

and:

$$P_{pneum} = (\dot{m}_{bleed}/\dot{m}_a)(T_{reqd}U_1/550) \text{ for jets} \qquad (6.9)$$

where: P_{reqd} = power required in some flight condition

T_{reqd} = thrust required in some flight condition.

Methods for estimating the power required, P_{reqd} or the thrust required, T_{reqd} are discussed in Part VII.

The effect of P_{extr} as determined from Eqn.(6.6) on installed power or thrust is discussed in Section 6.4.

6.2 INLET SIZING AND INTEGRATION

In preliminary design the process of inlet sizing consists of the determination of the inlet area and the shaping of the duct leading from the inlet area to the engine compressor face.

The inlet must be sized in such a way that it is 'matched' to the airflow requirements of the engine. Figure 6.2 shows a generalized inlet flow situation. Note the following important areas:

A_∞: streamtube cross section at infinity, also called the inlet capture area

A_c: streamtube cross section at the inlet, also called inlet area or cowl capture area

A_f: streamtube cross section at the engine station, also called internal area (note that this cross section is determined by the maximum cross section of the engine plus tolerances for cooling and for installation)

A_e: streamtube cross section at the exit or exhaust, also called the nozzle area

Inlet operation is often characterized by the inlet flow ratio, A_∞/A_c.

During static ground operation, the inlet flow ratio is infinite. Inlet lip flow separation is a major problem in such a case. Figure 6.3a shows such a situation. Frequently an auxiliary inlet is required to allow enough air into the inlet. This is done with a variable inlet geometry feature. Figure 6.3a shows several options.

In the design cruise condition, the inlet is normally matched so that the flow ratio is in the range of 0.5 to 0.8. The inlet operates at its peak performance (high pressure recovery). Figure 6.3b shows this situation.

In some inlets, external surface area is present at points ahead of the inlet: see Figure 6.3c. If external surface area exists ahead of the inlet, the flow ratio is selected to be closer to 1.0 to prevent inlet separation. If no wetted surface area exists ahead of the inlet, the flow ratio is in the 0.5 - 0.8 range.

In a climb, the inlet delivers more air than the engine requires, excess air will be spilled, resulting in

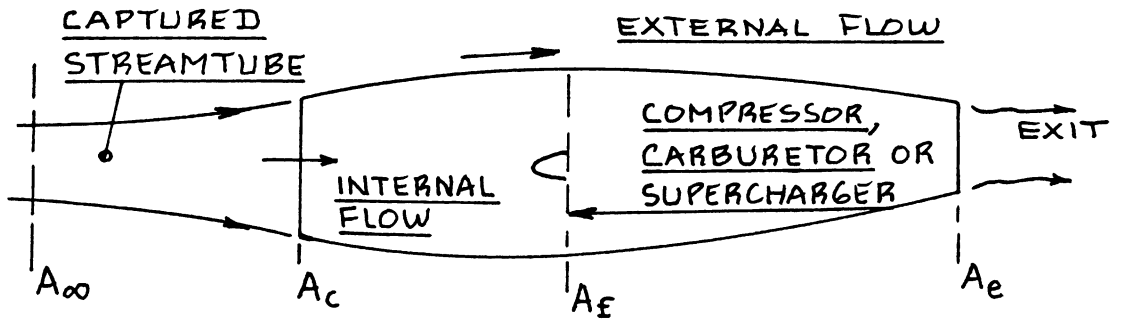

Figure 6.2 Generalized Engine Flow Stations

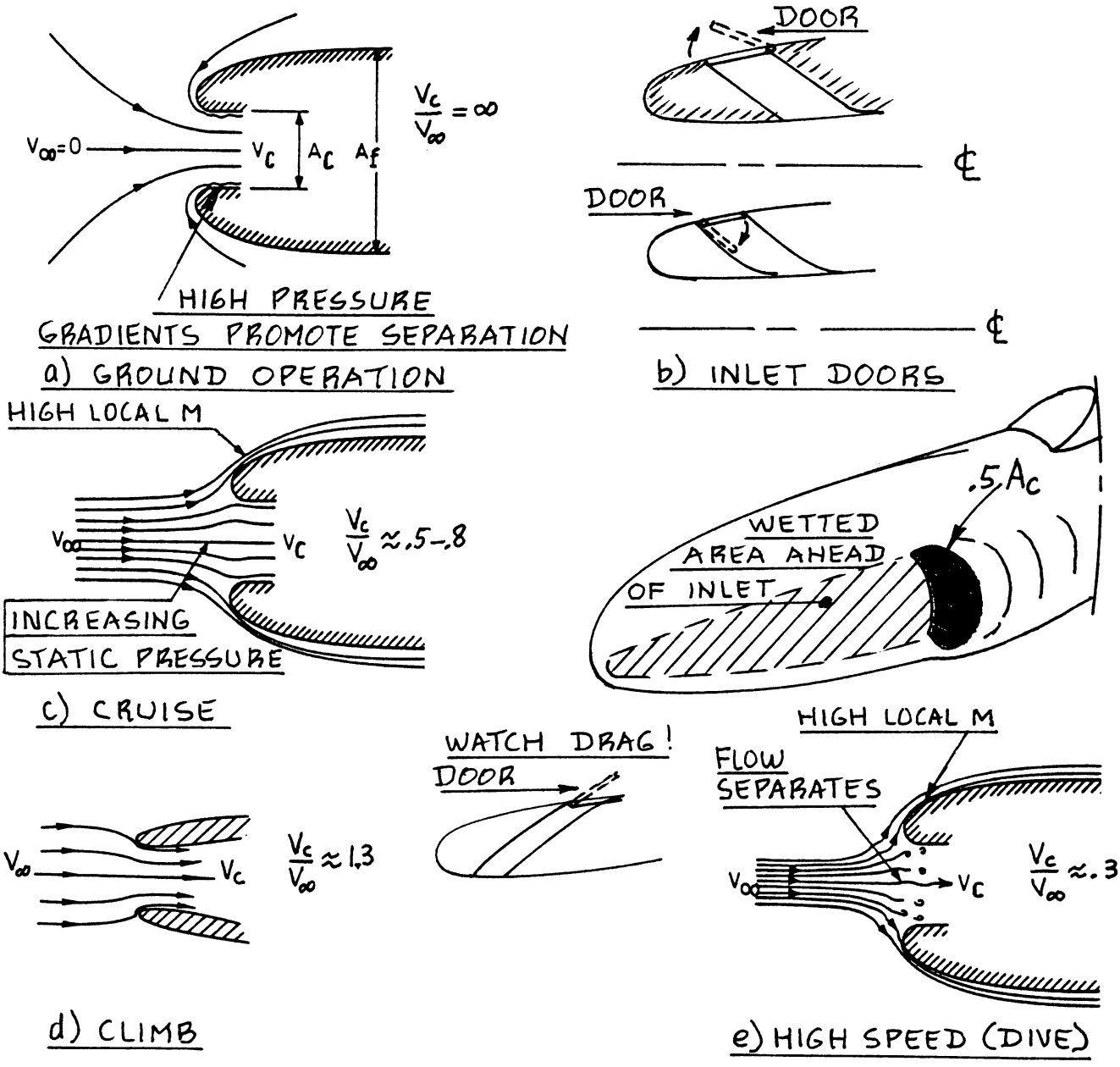

Figure 6.3 Flow Conditions for Subsonic Inlets

extra drag. The flow ratio is in excess of 1.0. Such a situation is shown in Figure 6.3d. If spillage drag becomes too high, bleedair doors may be required: Fig.6.3d shows one such option.

At very high speeds, such as occur in a high speed dive, the flow ratio is much smaller than 1.0. Such low flow ratios, particularly in the presence of large wetted areas in front of the inlet can lead to inlet flow separation resulting in compressor surge. Figure 6.3e shows such a situation.

If an inlet is undersized (such that it does not deliver enough air to the engine), unsatisfactory engine operation may result, causing deficiencies in thrust and/or power.

The objective of an inlet is to deliver air to the engine such that:

1. The correct amount of airflow is delivered to the engine

2. Pressure losses are minimized: pressure losses reduce thrust

3. Inlet flow distortion is minimized (i.e. as much as possible uniform flow is realized)

4. Inlet flow swirl is minimized or matched to the compressor requirements

Fundamentally, two types of inlets exist:

1. Straight through inlets: see Figure 6.4a
   This inlet type is used for engines with axial flow compressors, one-sided centrifugal flow compressors and supercharged piston engines.

2. Plenum chamber inlets: see Figure 6.4b
   This inlet type is used for engines with two-sided centrifugal flow compressors and with normally aspirated piston engines.

The detailed design of inlets is a strong function of how the engine (s) is (are) being integrated into the airframe.

The following subjects will be discussed:

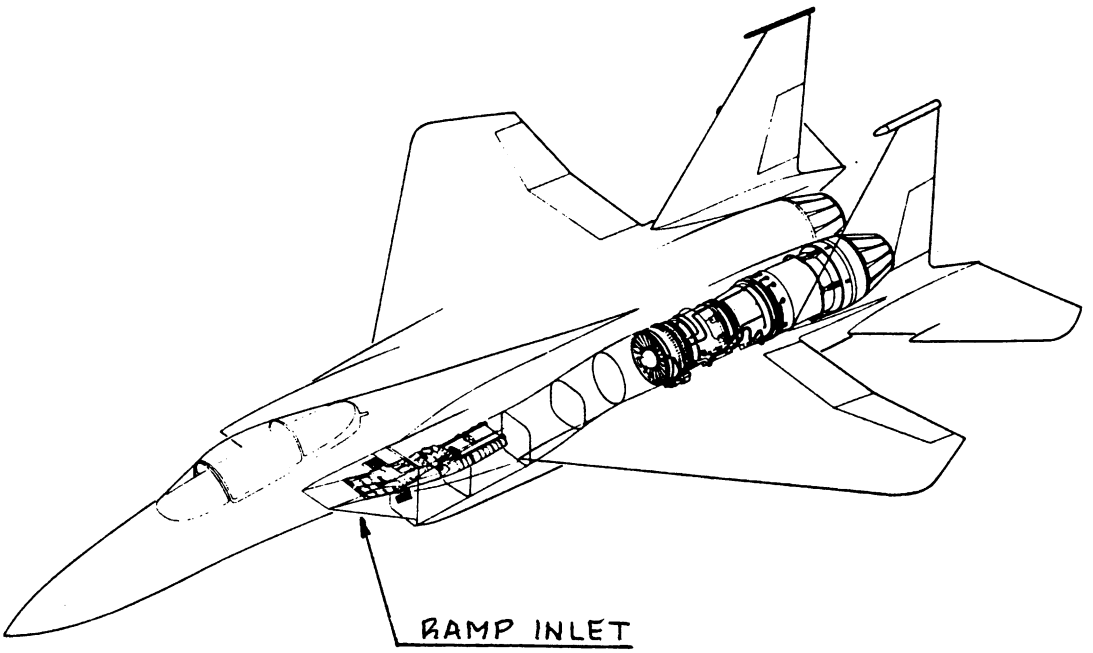

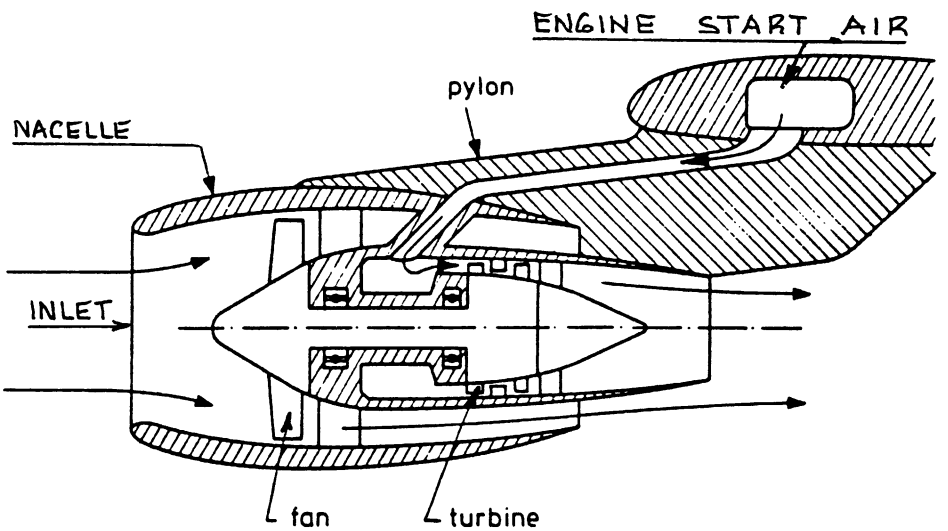

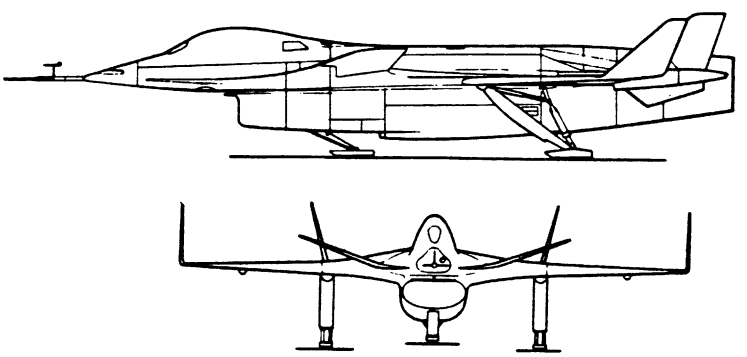

Figure 6.4a Examples of Straight Through Inlets

6.2.1 General inlet arrangements: presents a discussion of different types of inlet arrangement

6.2.2 Inlet sizing: presents a rapid method for estimating the required inlet area, A_c

6.2.3 Inlet pressure loss estimation: presents a rapid method for estimating inlet pressure losses

6.2.4 Inlet drag estimation: presents a rapid method for estimating inlet drag

Selection of the correct type of inlet and the associated inlet geometry has important consequences to the realism of any proposed airplane design. For that reason, inlet design should receive considerable attention in the early design phases of an airplane.

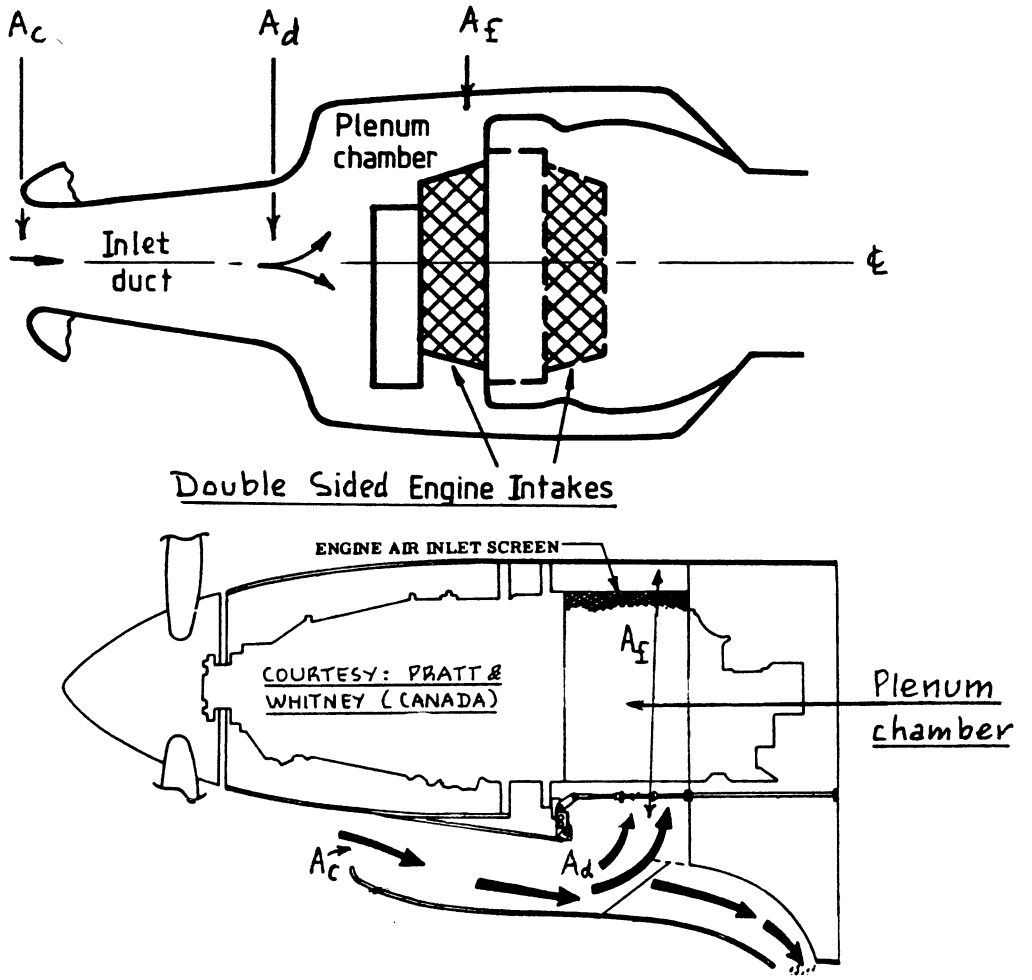

Figure 6.4b Examples of Plenum Inlets

6.2.1 General Inlet Arrangements

The purpose of this sub-section is to present a number of example inlet arrangements as well as comments regarding their applications.

The information is organized as follows:

6.2.1.1 Piston engine inlets
6.2.1.2 Turbopropeller inlets
6.2.1.3 Jet engine inlets: subsonic
6.2.1.4 Jet engine inlets: supersonic

6.2.1.1 Piston engine inlets

Figures 6.5a and 6.5b show several examples of piston engine inlet arrangements.

Figures 6.5a show that inlets for normally aspirated piston engines are of the plenum type. Most plenum installations do not completely seal off all air: cooling air must be routed to those engine components which need cooling for proper operation. After taking care of the cooling function the air is dumped overboard, preferably such that drag is not increased.

Engines with turbochargers tend to have straight through type inlets as shown in Figures 6.5b.

6.2.1.2 Turbopropeller inlets

Figure 6.6 shows several examples of turbopropeller engine (gas generator) inlets. Those shown are all of the straight through type. An example of a plenum type inlet for a turbopropeller installation was shown in Figure 6.4b.

The pressure recovery of the so-called concentric inlet (Figure 6.6d) can be strongly influenced by the design of the propeller airfoils which are in front of the inlet. Icing of such inlets is a major problem and requires detailed attention in the development of inlet anti- and de-icing systems. See Part IV, Chapter 10 for a general discussion of the icing problem.

6.2.1.3 Jet engine inlets: subsonic

Figures 6.7 show several example inlets for subsonic jet engine installations. Note the following types:

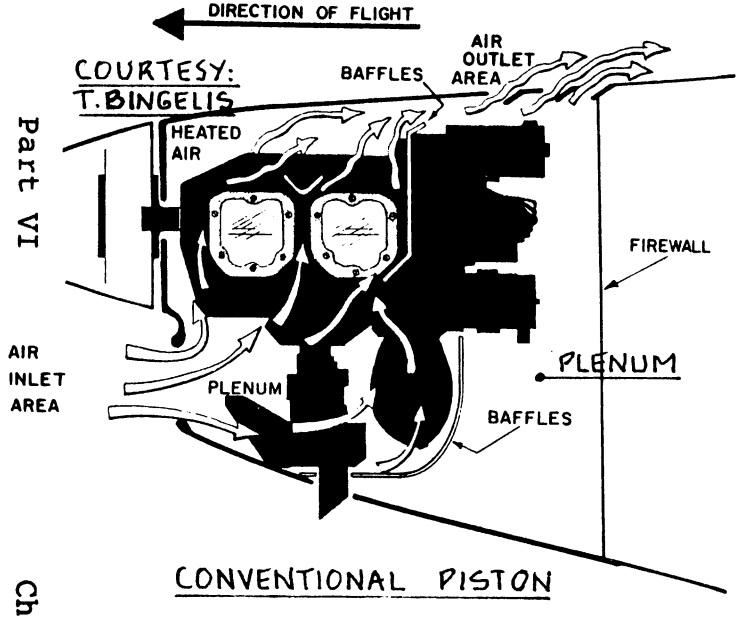

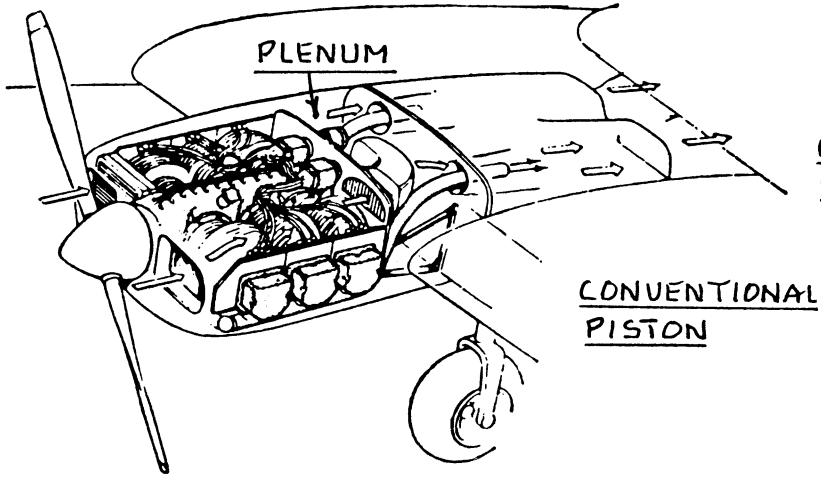

Figure 6.5a Inlets for Normally Aspirated Piston Engines

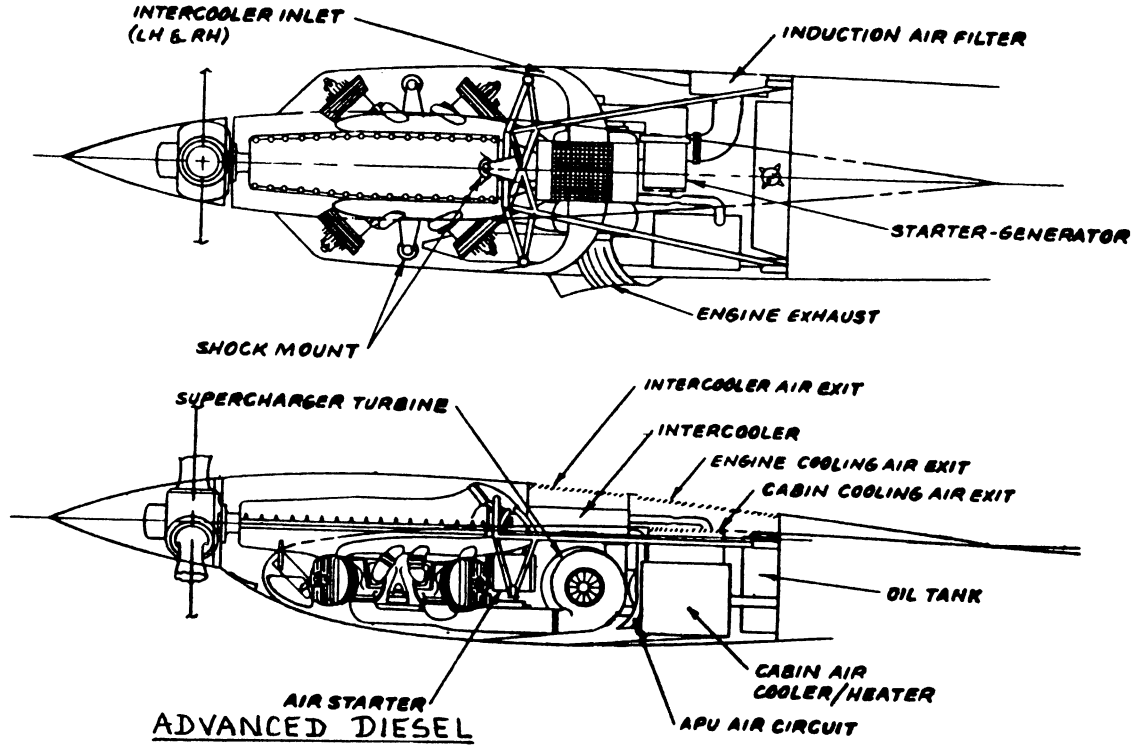

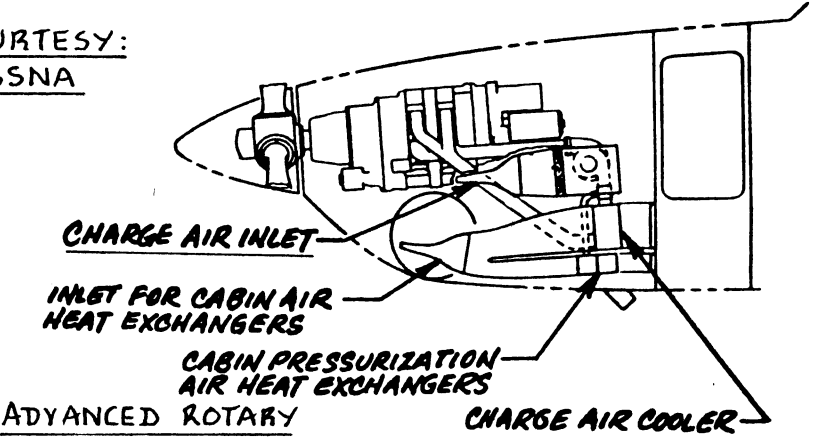

Figure 6.5b Inlets for Supercharged Piston Engines

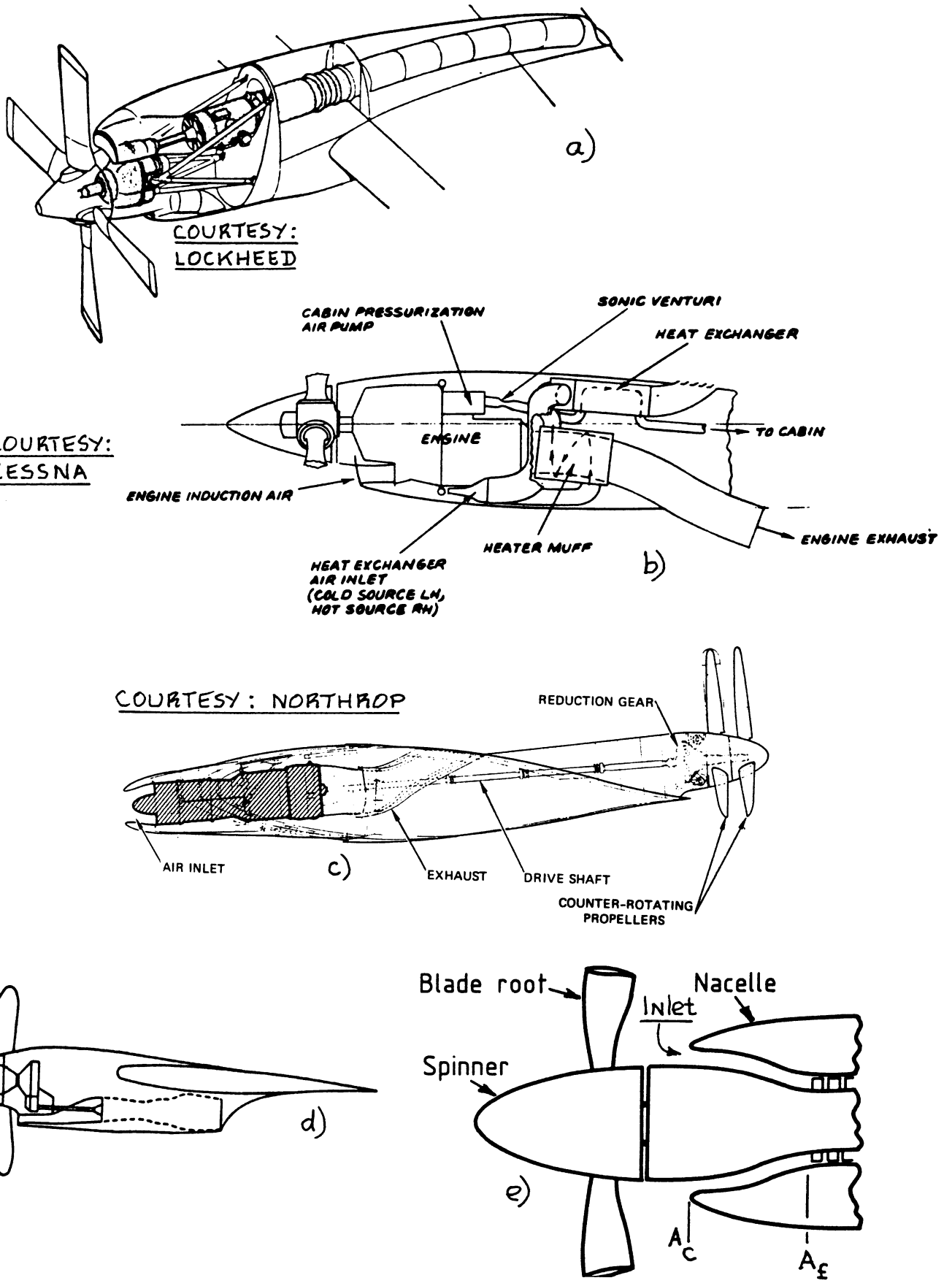

Figure 6.6 Inlets for Turbopropeller Engines

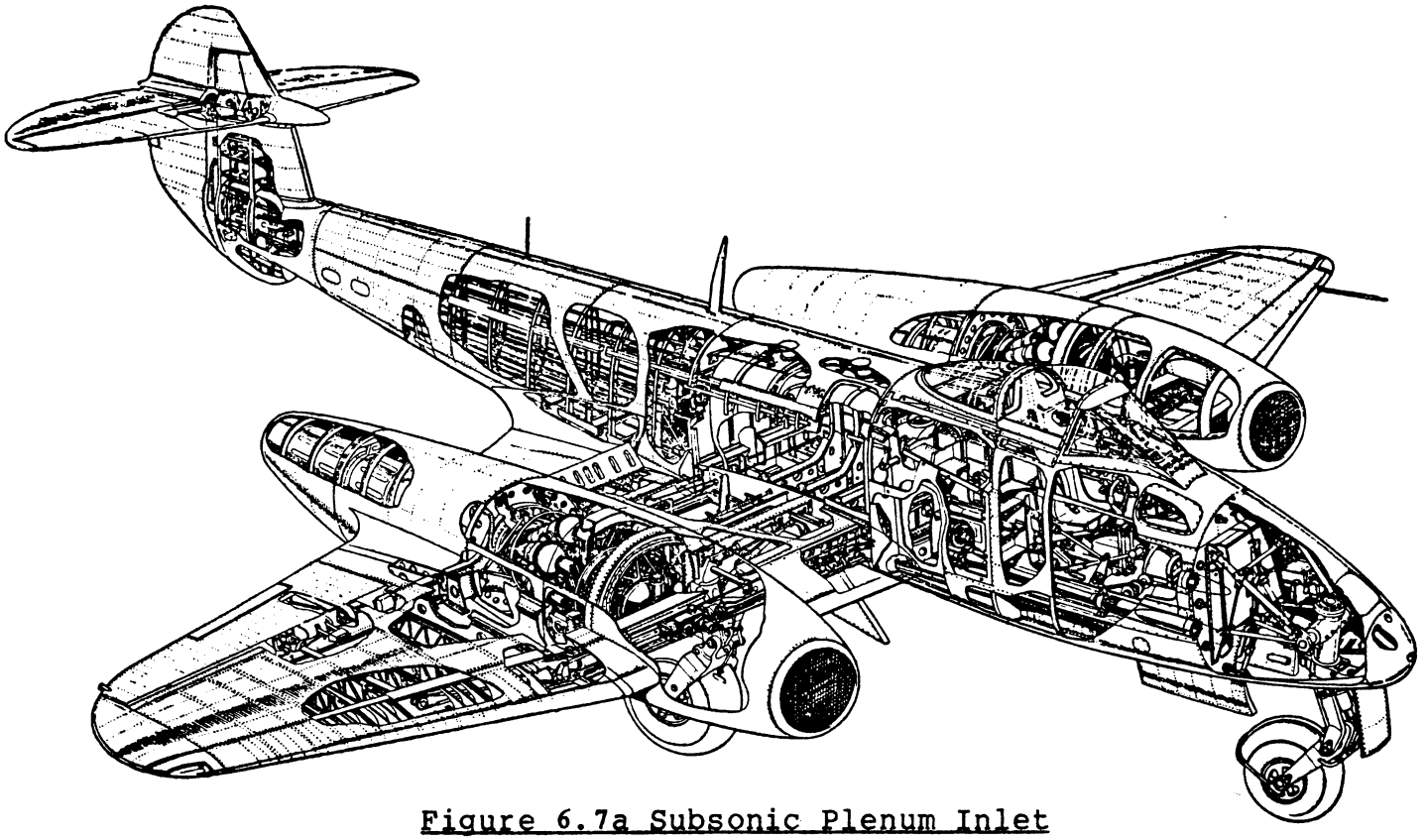

Figure 6.7a Subsonic Plenum Inlet

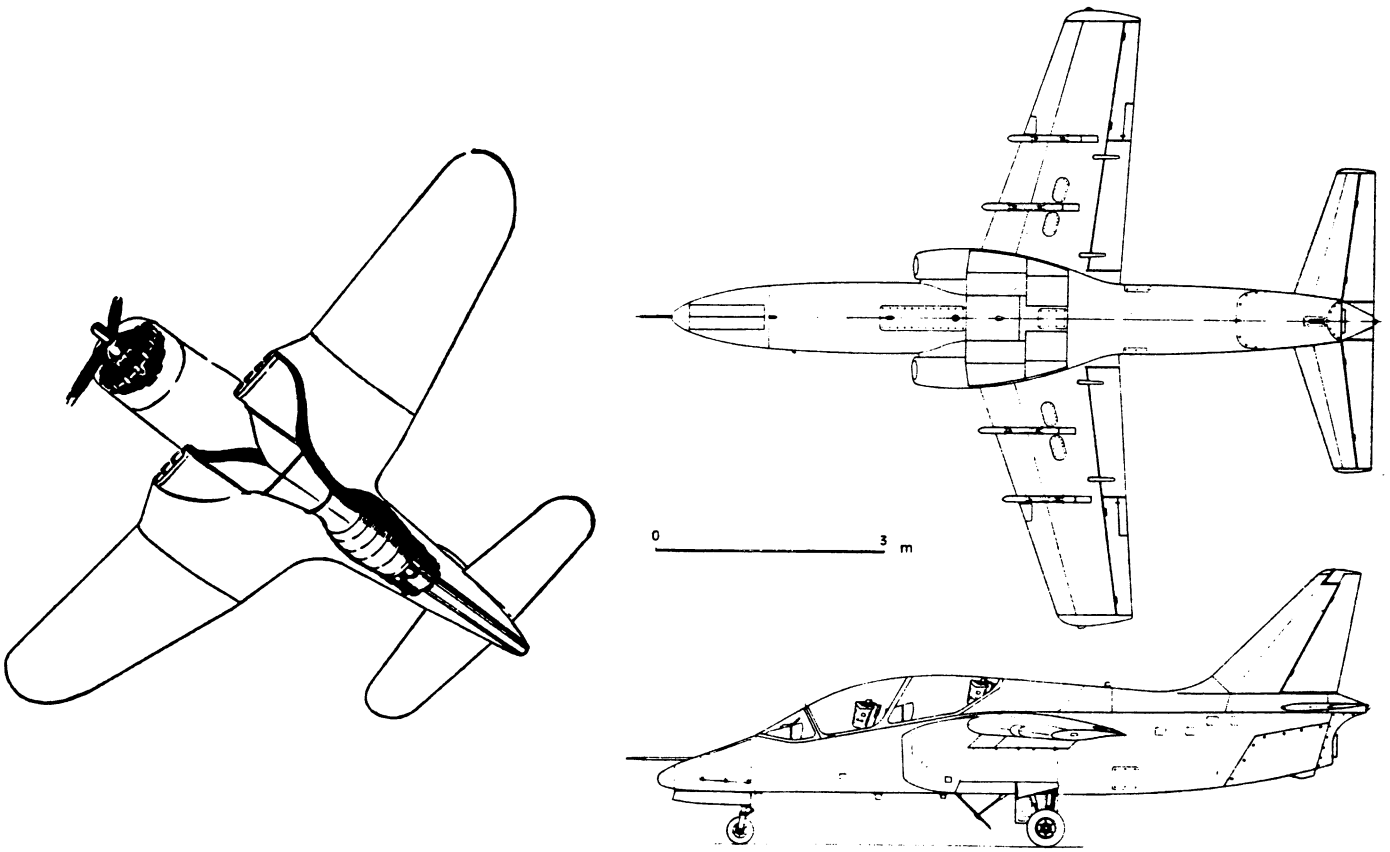

Figure 6.7b Subsonic Bifurcated Inlet

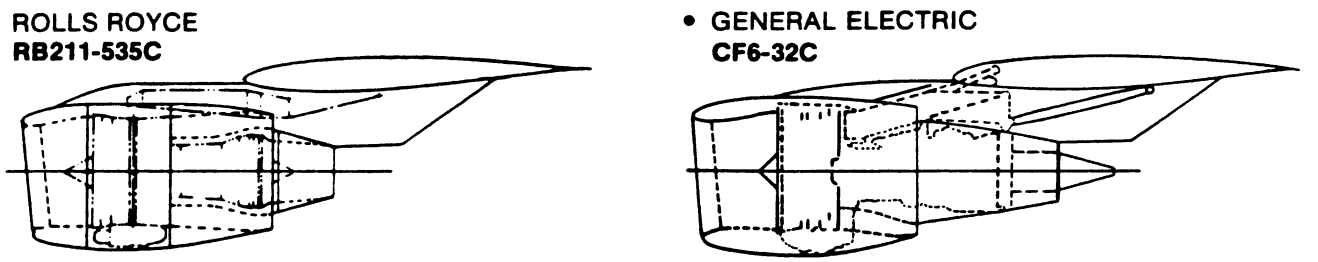

Figure 6.7c Subsonic Podded Nacelle Inlet

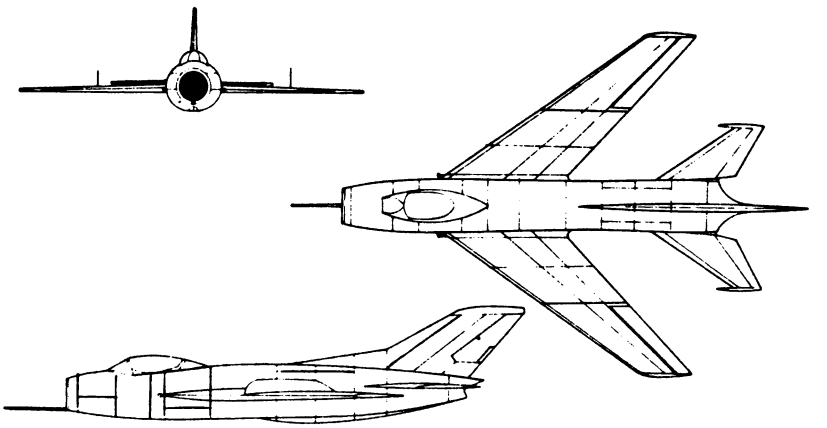

Figure 6.7d Subsonic Pitot Inlet

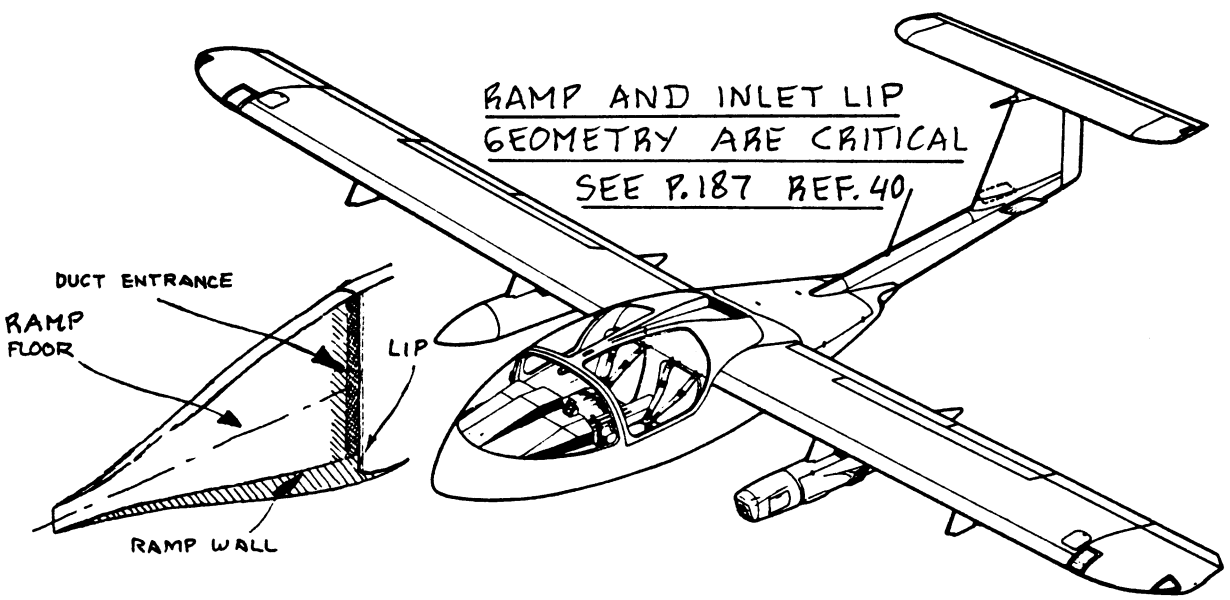

Figure 6.7e Subsonic NACA Submerged Inlet

Figure 6.7a: plenum inlet
Figure 6.7b: bifurcated, straight through inlet
Figure 6.7c: podded nacelle inlet
Figure 6.7d: pitot inlet
Figure 6.7e: NACA submerged inlet

Plenum inlets (Figure 6.7a) are used mainly in combination with double-sided centrifugal flow compressors.

Bifurcated inlets (Figure 6.7b) are used primarily in single engine installations with side inlets. Flow characteristics of bifurcated inlets are complicated, especially at high sideslip angles: inlet buzz and reversed flow on one side are phenomena which need to be 'designed out' of such inlets. Ref.32 contains more information.

Podded nacelle type inlets (Figure 6.7c) have become popular because of easy engine access. When using wing mounted engine pods there is an additional wing weight advantage due to inertial relief.

Pitot type inlets (Figure 6.7d) have been applied to many fighter airplanes. They are not influenced by the flowfield of other airplane components. However, they require very long ducts which causes extra weight and loss in pressure recovery.

The NACA submerged type inlet shown in Figure 6.7e is not very efficient for use with propulsion installations. However, when used for inlets of auxiliary systems (APU, heating and avionics bay cooling) they are quite acceptable and frequently used.

Important Note: Except for pitot and podded nacelle type inlets, all jet engine inlets must be equipped with so-called boundary layer diverters (or b.l. splitters). Figure 6.8 shows two b.l. diverter installations in some detail. If such boundary layer diverters are not used, large pressure recovery losses (thus losses in thrust) will be incurred.

A major consideration in jet fighter inlet design is the behavior of the inlet at very high angles of attack and sideslip. Compressor stall and engine surging are easily induced in such conditions. Ref.32 should be consulted for data on high angle of attack operation.

In subsonic installations it is usually best to keep the inlet as short as possible: long ducts translate into weight and pressure recovery losses. In jet fighters and in jet trainers long ducts cannot always be avoided.

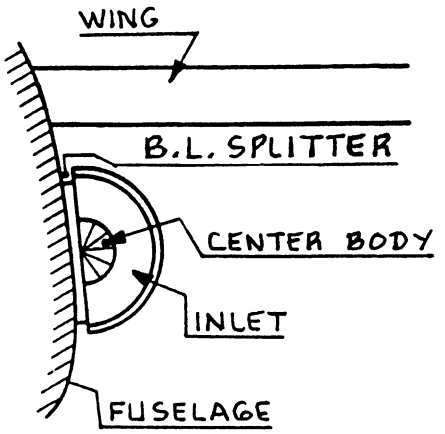

SEE REF. 32 FOR DETAILS ON B.L. SPLITTERS (DIVERTERS)

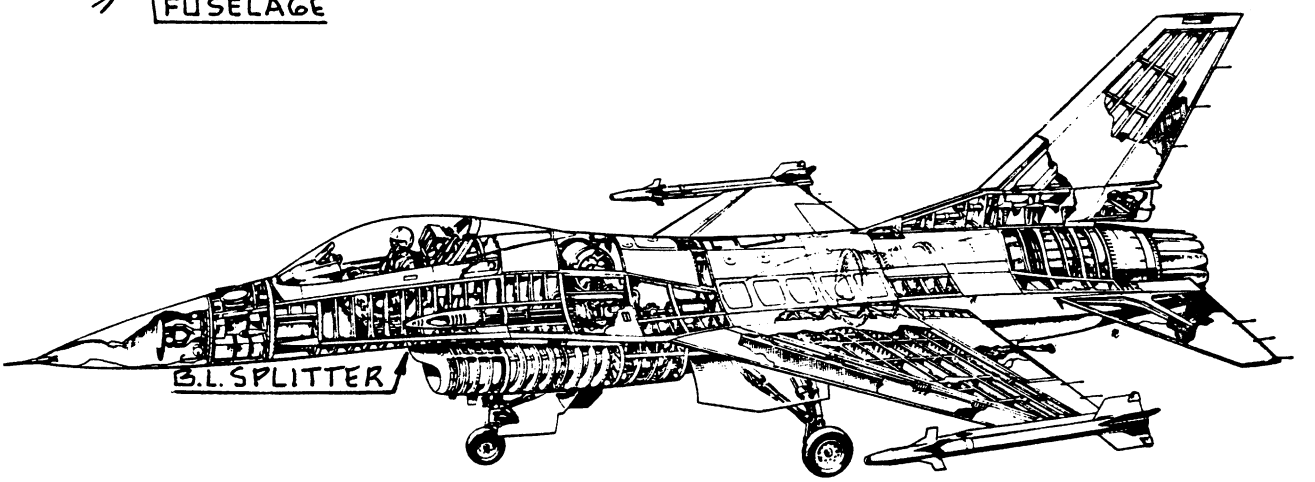

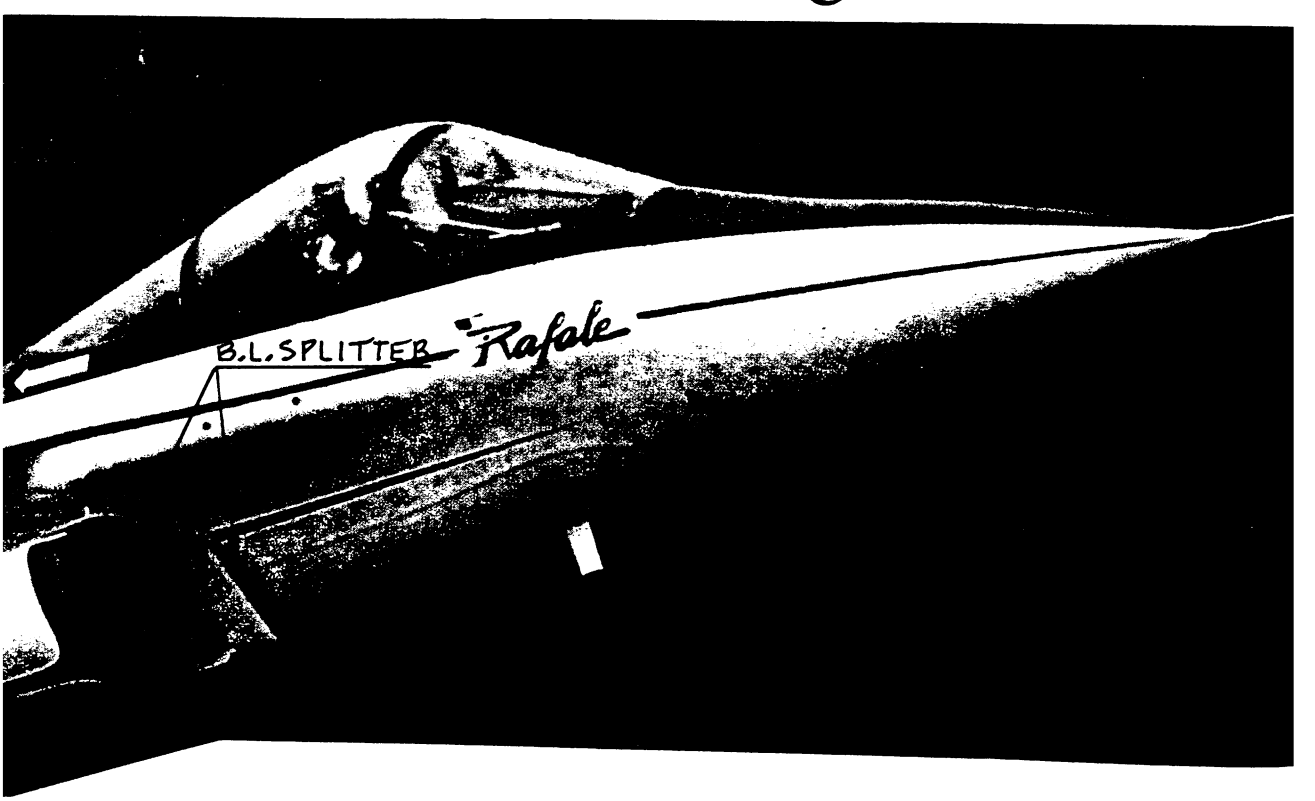

Figure 6.8 Boundary Layer Diverter Examples

6.2.1.4 Jet engine inlets: supersonic

Figures 6.9 show various types of supersonic inlets. Note the boundary layer splitters!

Figure 6.10 shows three fundamentally different types of supersonic inlet:

Fig.6.10a Pitot inlet
Fig.6.10b External compression inlet
Fig.6.10c Mixed (or external/internal) compression inlet

Pressure recovery in supersonic inlets is a strong function of the number and types of shock employed. The theoretical pressure recovery attainable with oblique and with conical shocks are shown in Figure 6.11.

Proper inlet design is extremely critical to supersonic installations as illustrated in Figure 6.12. Note that the inlet is responsible for 75 percent of the total installed thrust! A long inlet duct in supersonic engine installations is often needed to assure smooth flow deceleration (to around M=0.4 at the compressor face) and to assure full use of the favorable pressure distribution in the inlet duct. Figure 6.13 shows the effect of Mach number on thrust distribution. Note that at subsonic speeds, the engine itself (including a convergent nozzle) produces virtually all the thrust. Note also, that at supersonic Mach numbers the engine contribution itself can become negative!

Supersonic inlets frequently require a considerable amount of variable geometry devices. Examples are shown in Figures 6.13. For more information on the operation of such inlets, see References 12 and 32.

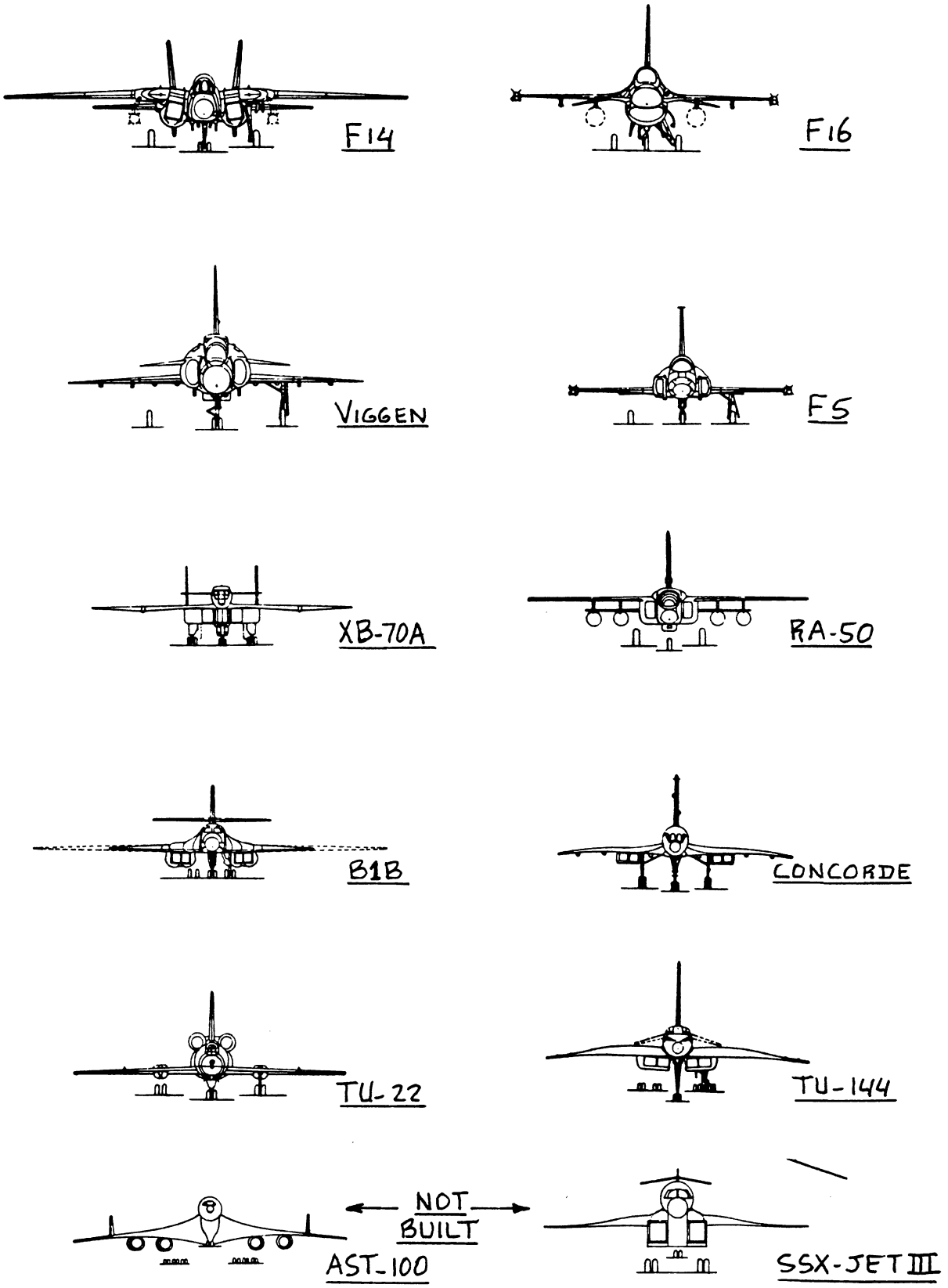

Figure 6.9 Supersonic Inlet Examples

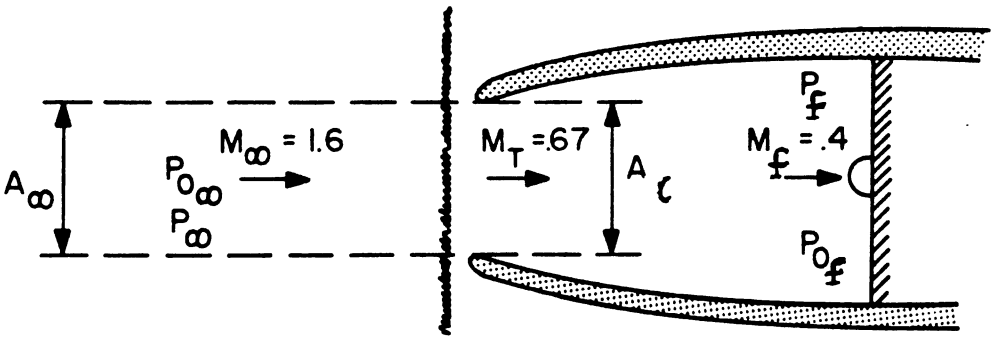

Figure 6.10a Supersonic Pitot Inlet

COPIED FROM REF. 12, COURTESY: L. NICOLAI

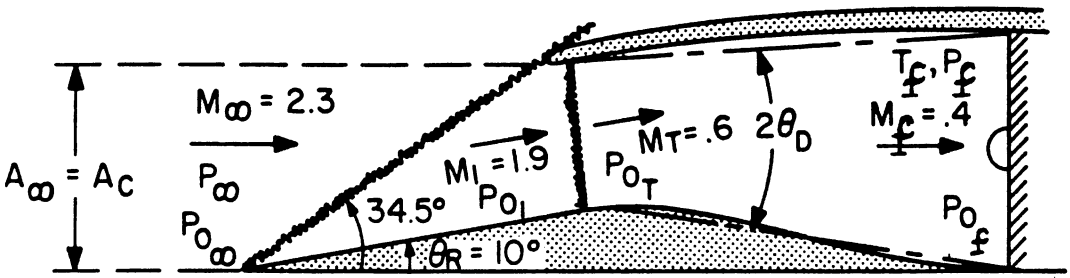

Figure 6.10b Supersonic External Compression Inlet

COPIED FROM REF. 12, COURTESY: L. NICOLAI

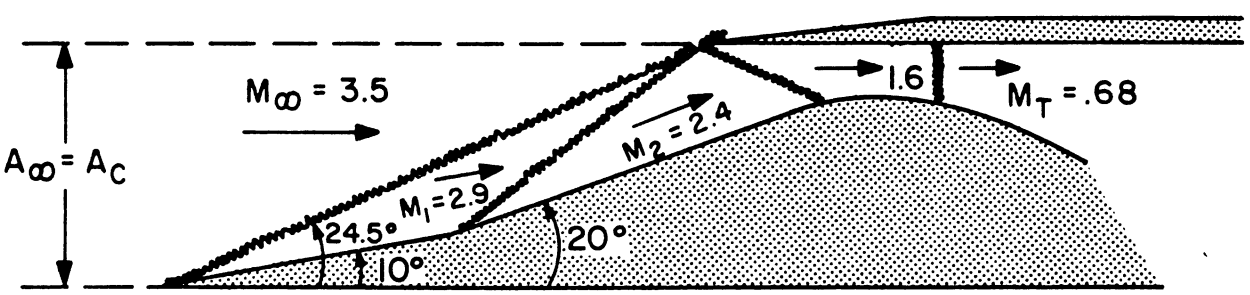

Figure 6.10c Supersonic Mixed Compression Inlet

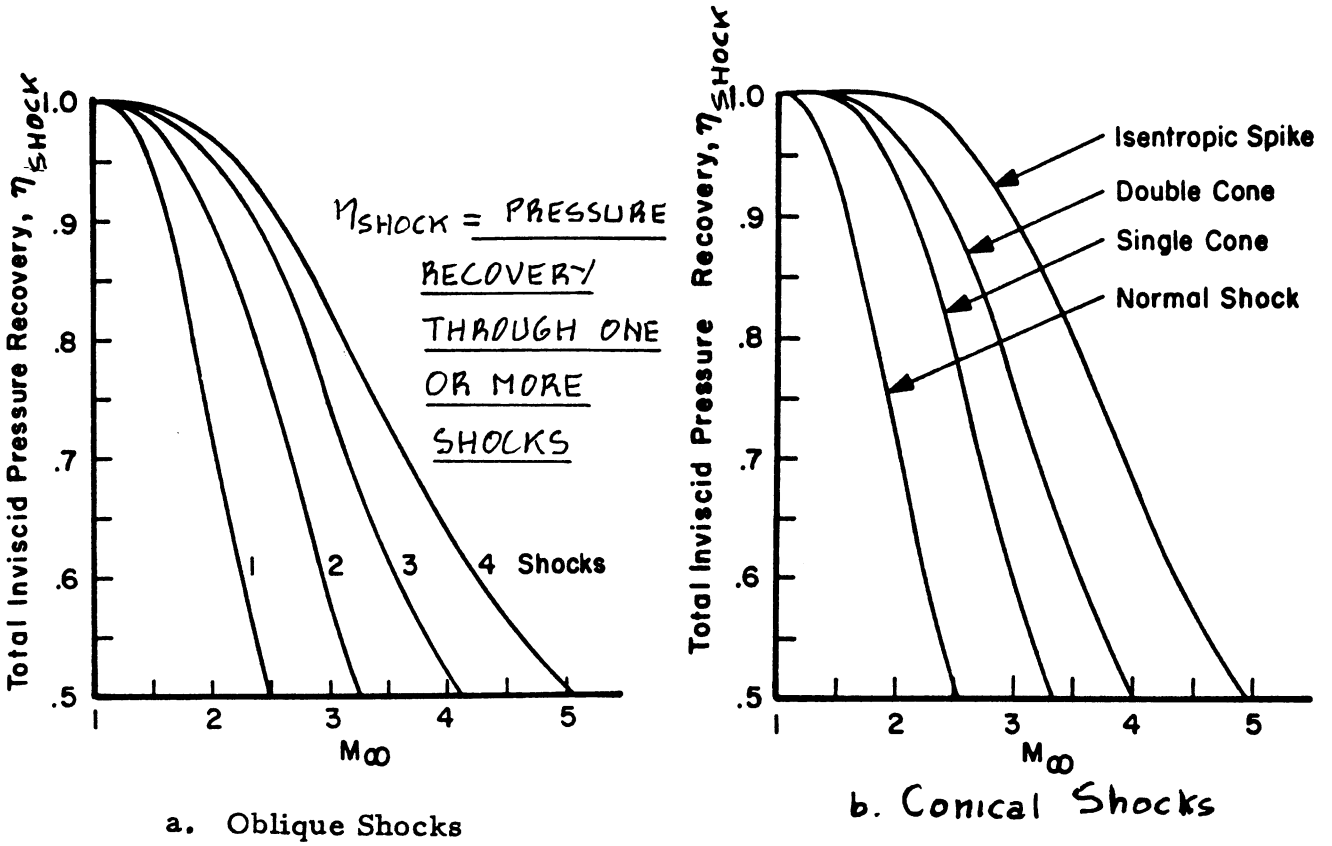

a. Oblique Shocks

b. Conical Shocks

COPIED FROM REF. 12, COURTESY: L. NICOLAI

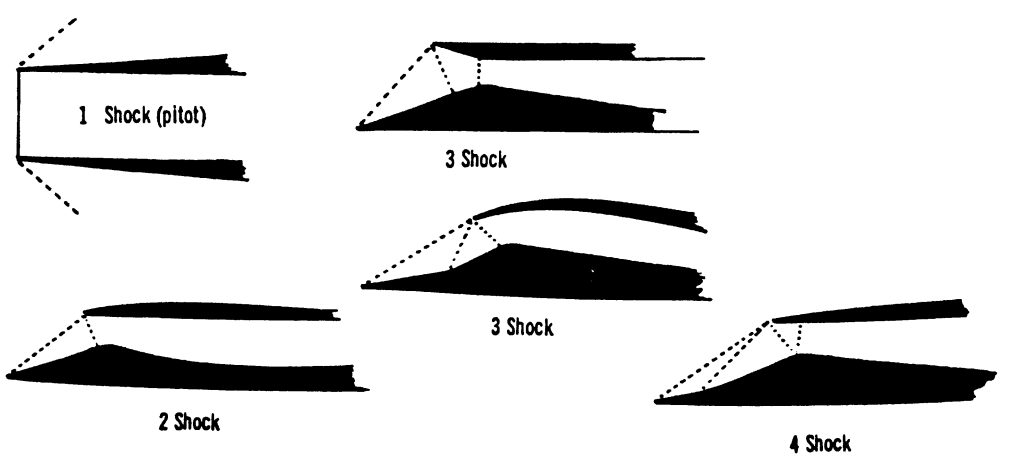

Figure 6.11 Ideal Pressure Recoveries for Oblique and for Conical Shocks

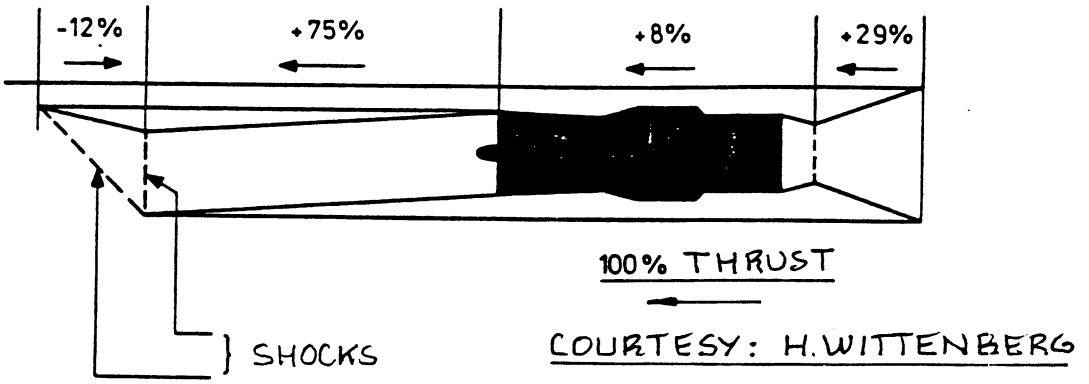

Figure 6.12 Example of the Thrust Distribution over a Supersonic Engine Installation at M=2.2

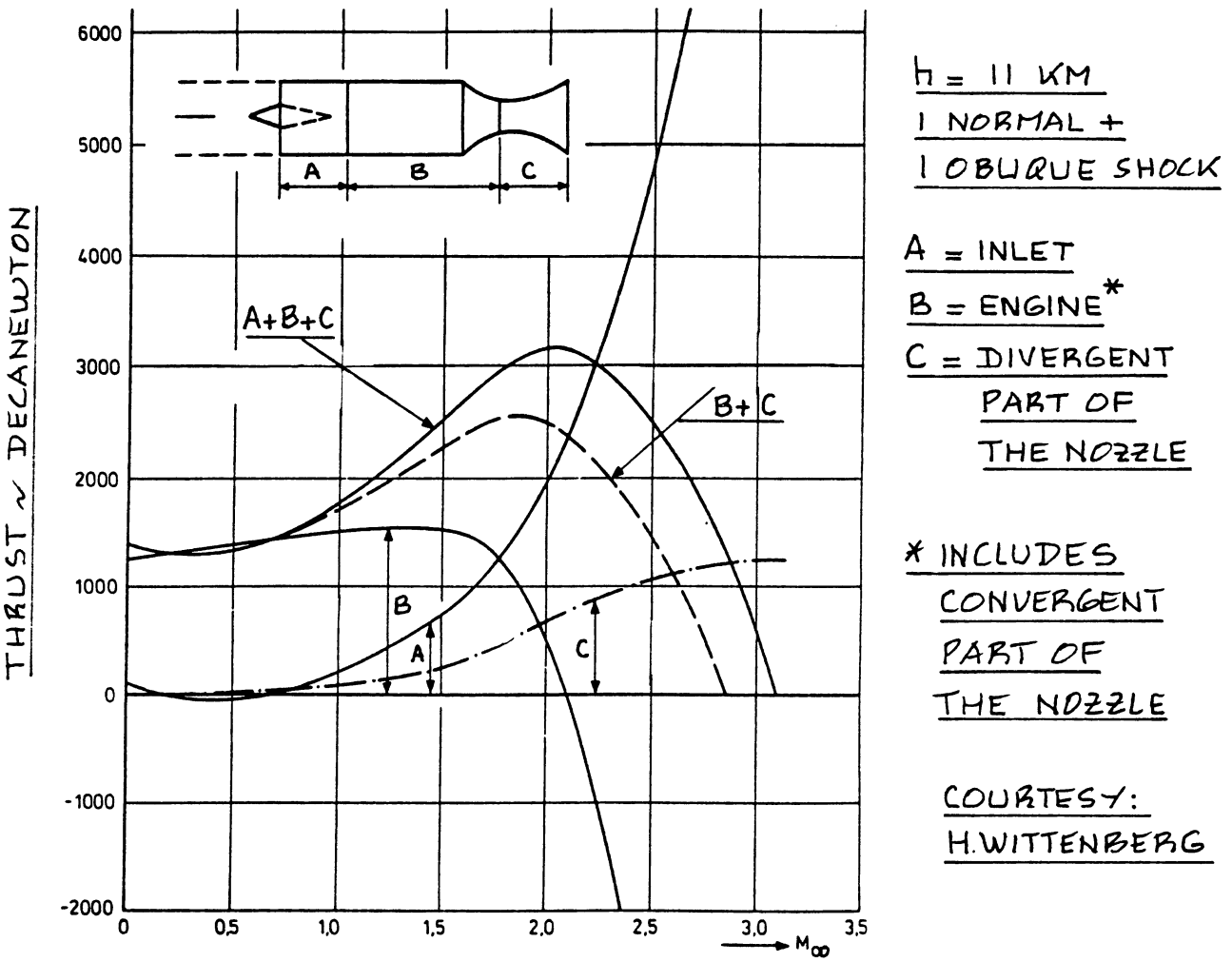

Figure 6.13 Effect of Mach Number on Thrust Distribution of a Supersonic Engine Installation

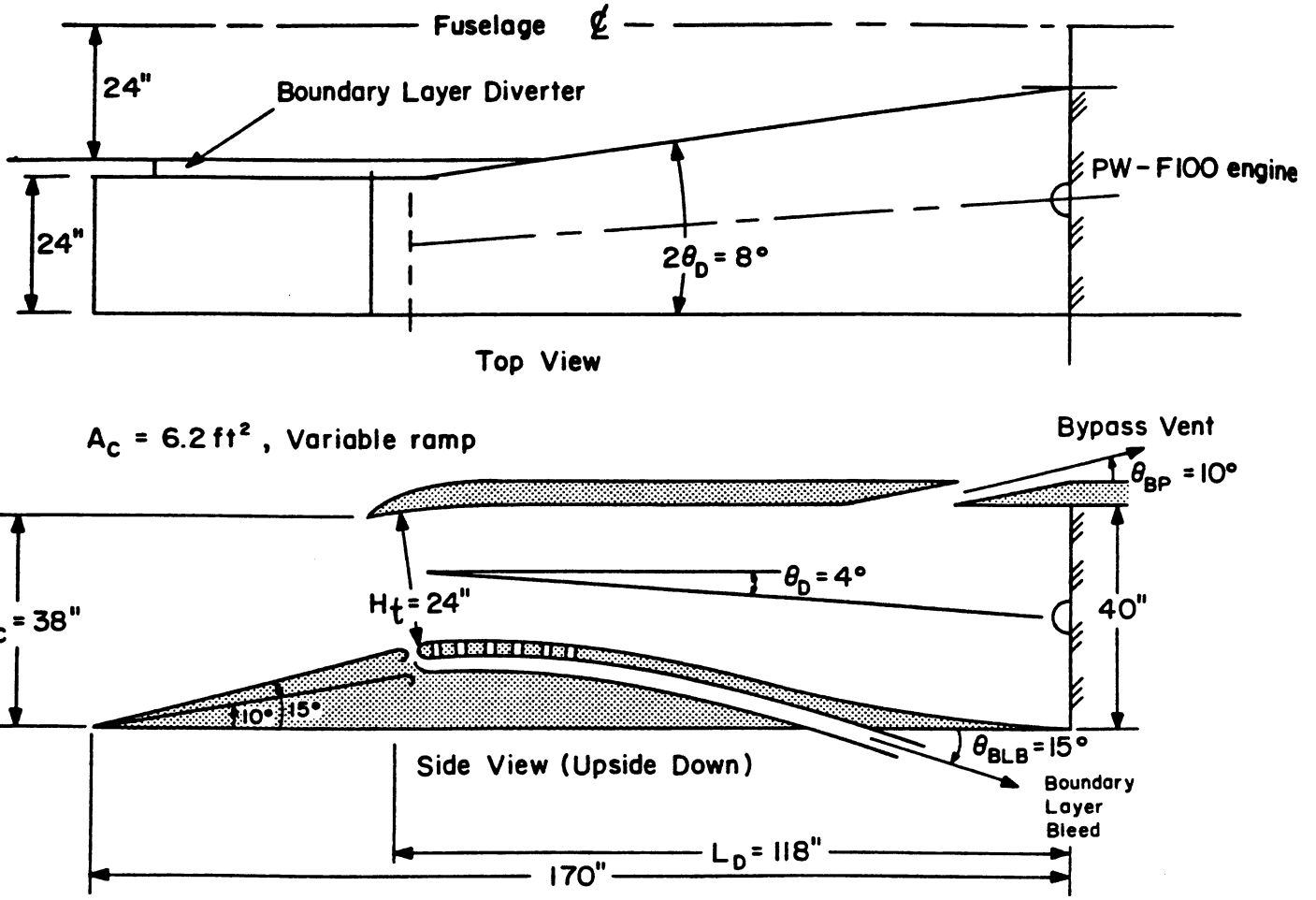

Mach 2.3 Two-Dimensional External Compression Inlet

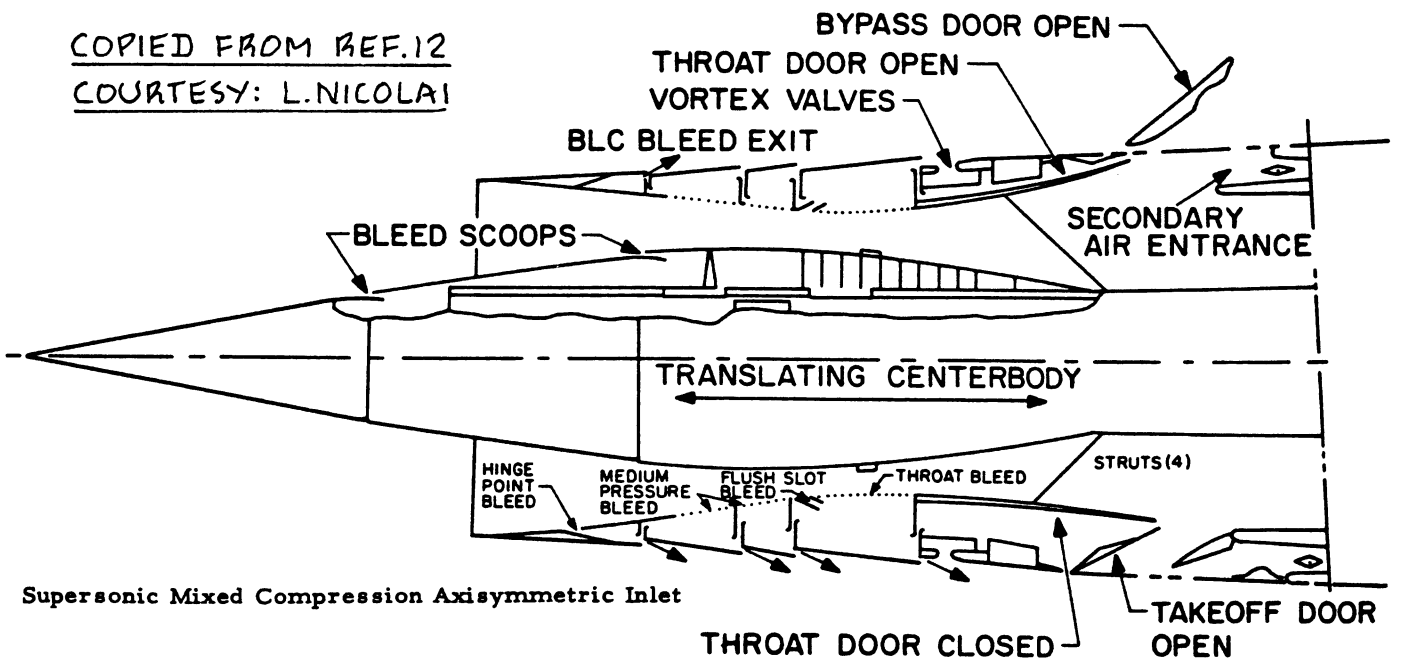

Supersonic Mixed Compression Axisymmetric Inlet

Figure 6.14 Examples of Variable Geometry in Supersonic Engine Installations

6.2.2 Inlet Sizing

The purpose of this sub-section is to present inlet sizing methods for:

6.2.2.1 Piston engine installations
6.2.2.2 Turbopropeller installations
6.2.2.3 Jet engine installations: subsonic
6.2.2.4 Jet engine installations: supersonic

For each of these inlet installations, the general flow picture of Figure 6.2 will be used to identify the required inlet area, A_c.

6.2.2.1 Piston engine installations

Figure 6.5 shows typical inlet configurations for piston engine installations. To determine the required inlet area, A_c it is first required that the engine air flow requirements be determined.

Inlet air for piston engines is required for:

1. Combustion 2. Cooling

The mass flow rate required for a piston engine may be estimated as follows:

$$\dot{m}_a = \dot{m}_{comb} + \dot{m}_{cool} \quad \text{(in slugs/sec)} \tag{6.10}$$

where: $\dot{m}_{comb}$ = the mass flow rate required for combustion. It may be estimated from:

$$\dot{m}_{comb} = (0.000062)(SHP)_{reqd} \tag{6.11}$$

where: $$(SHP)_{reqd} = P_{reqd}/\eta_p \tag{6.12}$$

where: P_{reqd} is the horsepower required for the flight condition being analyzed. Part VII contains methods for determining P_{reqd} for a variety of flight conditions.

η_p is the propeller efficiency.

Section 6.4 and Ref.15 show how to obtain data for

propeller efficiency. In preliminary design, first approximations are:

η_p = 0.85 for cruise
0.80 for climb
0.70 for take-off

In Equation (6.11) it is assumed that:

1. that the engine efficiency in converting chemical energy in the fuel to shafthorsepower (SHP) is 30 percent.
2. that the fuel/air ratio used is the stochiometrically required value.

$\dot{m}_{cool}$ = the mass flow rate required for cooling.

Its magnitude depends on the type of engine:

For aircooled airplane engines the mass flow rate required for engine cooling may be estimated from:

$$\dot{m}_{cool} = 0.00056(SHP)_{reqd} \quad \text{in slugs/sec} \qquad (6.13)$$

where: $(SHP)_{reqd}$ follows from Eqn.(6.12).

In preliminary design, SHP_{TO} may be used for $(SHP)_{reqd}$.

Detailed methods for estimating $\dot{m}_{cool}$ for aircooled engines are given in References 35 and 36.

For liquid cooled airplane engines the required mass flow rate for the radiator depends strongly on the type of liquid cooling used. Chapter 9 in Reference 8 and Reference 37 should be consulted.

For preliminary design purposes it is suggested to use Eqn.(6.10) for liquid cooled engines also.

Considerable experience with liquid cooled engine installations was obtained in WWII. In many cases it proved possible to design the radiator system in such a way that negligible losses were incurred. However, this was achieved at a considerable increase in weight and complexity.

Knowing the total air mass flow rate, the size of the required inlet area may be estimated from:

$$A_c = \dot{m}_a / \rho U_1 \qquad (6.14)$$

where: $\dot{m}_a$ follows from Eqn.(6.10),

ρ is the air density in slugs/ft^3 and

U_1 is the steady state airspeed in fps.

Note: Eqn.(6.14) is valid for incompressible flow!

The reader must determine which conditions for air density, ρ and airspeed, U_1, yield the largest value for inlet area, A_c. Since zero airspeed represents an anomalie, lift-off speed or climbout speeds are normally used. Extra inlet doors (or cowl flaps) may be required for prolonged static and taxi operations.

To minimize the drag caused by momentum loss in the cooling air, careful design of the ducting leading from the inlet to the overboard dumping point is required. References 8 and 38 should be consulted for more details. Reference 39 contains example calculations for inlet area sizing for piston engines.

6.2.2.2 Turbopropeller installations

Figure 6.6 shows typical inlet configurations for turbopropeller engines.

To determine the required inlet area, A_c it is first necessary to determine the engine air flow requirements.

Inlet air for turbopropeller engines (also called: gas generators) is required for:

1. combustion and mass flow
2. cooling

The mass flow rate for turbopropeller engines may be estimated from:

$$\dot{m}_a = \dot{m}_{gas} + \dot{m}_{cool} \qquad (6.15)$$

where: $\dot{m}_{gas}$ = the air flow rate required by the engine for combustion and for mass flow. In a gas generator the mass flow rate is much larger than the air flow required for combustion. Manufacturers engine data normally include the maximum mass flow rate. Reference 31 also lists required mass flow rates for gas generators. Tables 6.6 and 6.7 in Part III list take-off mass flow rates in lbs/sec for a range of turbopropeller engines.

In preliminary design, a good approximation is:

$$\dot{m}_{gas} = (0.00028)(SHP)_{reqd} \quad \text{(in slugs/sec)} \qquad (6.16)$$

where: $(SHP)_{reqd}$ is given by Eqn.(6.12).

$\dot{m}_{cool}$ = the mass flow rate needed for cooling.

For gasgenerators this may be taken as 5 percent of $\dot{m}_{gas}$ for most turboprop installations:

$$\dot{m}_{cool} = 0.05\dot{m}_{gas} \qquad (6.17)$$

The required inlet area may be estimated from:

$$A_c = \dot{m}_a/\rho U_1 \qquad (6.18)$$

where: $\dot{m}_a$ is found from Eqn.(6.15).

Note: Eqn.(6.18) is valid for incompressible flow!

The reader must determine which conditions for air density, ρ and airspeed, U_1 yield the largest value for inlet area A_c.

Since zero airspeed represents an anomalie, lift-off speed or climbout speeds are normally used. Extra inlet doors (variable inlet geometry) may be needed for prolonged static and taxi operations.

6.2.2.3 Jet engine installations: subsonic

Figure 6.7 shows examples of subsonic jet engine inlets.

To determine the required inlet area, A_c it is first

necessary to determine the engine airflow requirements.

Inlet air for jet engines is required for:

1. combustion and mass flow 2. cooling

The mass flow rate required for a subsonic jet engine installation may be found from:

$$\dot{m}_a = \dot{m}_{gas} + \dot{m}_{cool} \qquad (6.19)$$

where: $\dot{m}_{gas}$ = the air flow rate required for the engine.

In jet engines the flow rate required for combustion is much less than that needed for mass flow. Manufacturers engine data normally include the maximum mass flow $\dot{m}_{gas}$ required by the engine.

Reference 31 also lists those flow rates. Tables 6.8 - 6.11 in Part III list take-off mass flows for a range of jet engines. In preliminary design the following approximation may be used:

$$\dot{m}_{gas} = k_{gas} T_{TO} \qquad (6.20)$$

where: k_{gas} = 0.0003 for BPR values of 0 to 1.0

= 0.0007 for BPR values of 1.0 to 2.0

= 0.0009 for BPR values of 2.0 to 4.0

= 0.0011 for BPR values of 4.0 to 6.0

$\dot{m}_{cool}$ = the air flow rate needed for cooling.

In preliminary design it may be assumed that:

$$\dot{m}_{cool} = 0.06\dot{m}_{gas} \qquad (6.21)$$

The required inlet area, A_c may be estimated from:

$$A_c = \dot{m}_a/\rho U_1 \qquad (6.22)$$

where: $\dot{m}_a$ is found from Eqn.(6.19)

ρ and U_1 are determined by the flight condition.

Note: Eqn.(6.22) is valid for compressible flow.

The inlet size for most subsonic airplanes is dictated by low speed requirements. For that reason, Eqn.(6.22) is applicable to preliminary inlet sizing for subsonic jets.

6.2.2.4 Jet engine installations: supersonic

Figures 6.9 and 6.10 show examples of supersonic jet engine inlet installations.

Inlet air for jet engines in supersonic installations is required for:

1. combustion and mass flow
2. cooling
3. inlet boundary layer bleed

The mass flow rate required for a jet engine in a supersonic installation may be estimated from:

$$\dot{m}_a = \dot{m}_{gas} + \dot{m}_{cool} + \dot{m}_{blb} \qquad (6.23)$$

where: $\dot{m}_{gas}$ = the air flow rate required for the engine.

In jet engines the air flow rate required for combustion is much less than that for mass flow. Manufacturers engine data normally include the maximum mass flow, $\dot{m}_{gas}$ required by the engine.

Reference 31 also lists those flow rates. Tables 6.8*- 6.11* list mass flow rate values for a range of engines. Since most supersonic inlets must also operate at subsonic speeds, the take-off mass flow rates normally size the inlet area. For this reason, Eqn.(6.20) may be used for computing $\dot{m}_{gas}$.

$\dot{m}_{cool}$ = the air flow rate needed for cooling.

In preliminary design it is acceptable to use:

$$\dot{m}_{cool} = 0.08\dot{m}_{gas} \qquad (6.24)$$

$\dot{m}_{blb}$ = the air flow rate needed for boundary layer bleed in the inlet. Because of the fact that supersonic installations require fairly long inlets, the resulting build-up of boundary layer air must be bled away before it reaches the compressor. Figure 6.14 shows such a boundary layer bleed system. The need for boundary layer bleed

*see Part III

translates into a need for extra inlet capture area as shown in Eqn.(6.25).

The inlet area, A_c for a supersonic inlet is as defined in Figure 6.15. The required inlet area, A_c for a supersonic jet engine installation may be estimated from:

$$A_c = (1.08\dot{m}_a / \rho U_1)\{1 + k_{bl}(M_1 - 0.8)\} \qquad (6.25)$$

where: $\dot{m}_a$ follows from Eqn.(6.19)

ρ and U_1 are determined by the flight condition which in the case of a supersonic installation is taken to be the design supersonic cruise condition or the take-off condition. If the latter results in a larger inlet area than the former, the possibility of using extra inlet doors for subsonic operation must be weighed against 'oversizing' the inlet for supersonic conditions.

$$M_1 = U_1/a \qquad (6.26)$$

where: a is the speed of sound in the design cruise flight condition

k_{bl} is a constant which depends on the type of inlet used:

k_{bl} = 0 for pitot inlets and for $M_1 < 0.8$

k_{bl} = 0.028 for external compression inlets

k_{bl} = 0.041 for mixed external/internal compression inlets

The inlet throat area, A_{throat} in Figure 6.15 must be carefully sized to assure that it can handle the required engine mass flow rate. References 12 and 32 contain methods for determining the throat size.

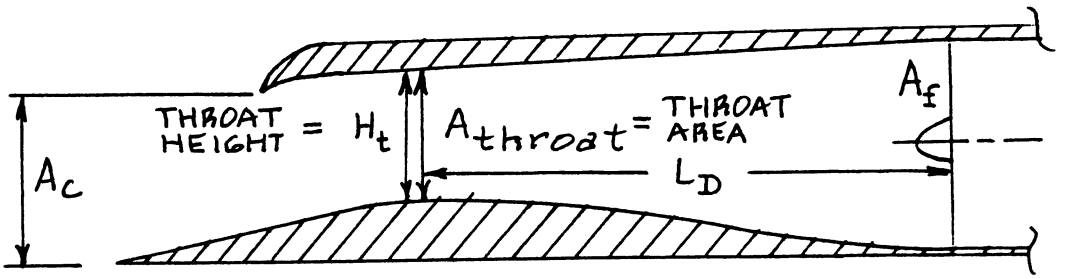

Figure 6.15 Geometry Definition for a Supersonic Inlet

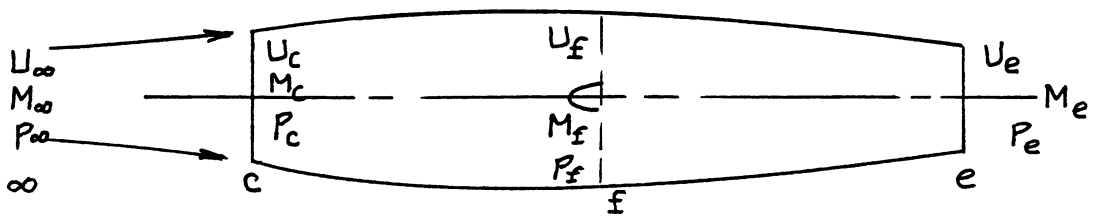

Figure 6.16 Definition of Flow Parameters for Figure 2

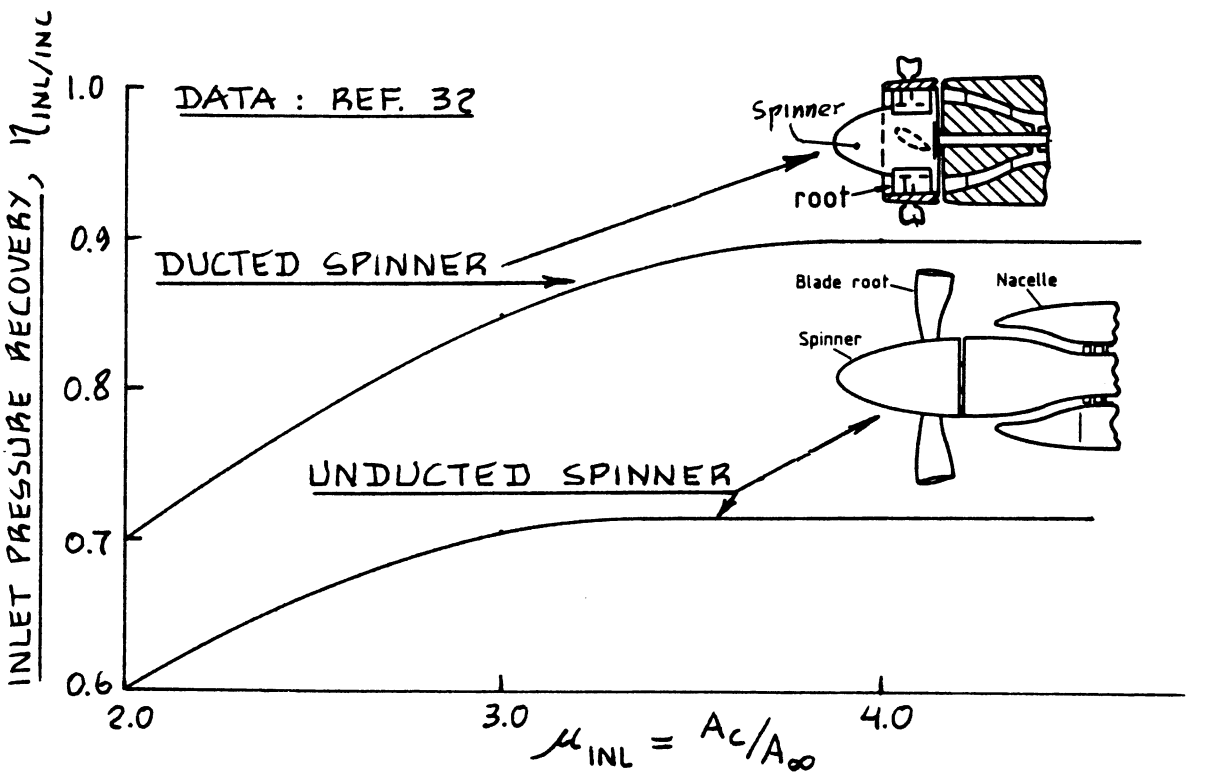

Figure 6.17 Pressure Recovery for Turbopropeller Inlets

6.2.3 Inlet Pressure Loss Estimation

The generalized flow situation shown in Figure 6.2 is repeated in Figure 6.16 with the addition of speed, U, Mach number, M and static pressure, p at each station.

The total pressure at each station is defined as:

$$p_{tot} = p + 0.5\rho U^2 = p + \bar{q} \qquad (6.27)$$

where: p is the local static pressure,

ρ is the local air density and

U is the local air velocity.

The inlet pressure loss is defined as:

$$\Delta p_{inl} = p_{tot_\infty} - p_{tot_f} \qquad (6.28)$$

Inlet pressure loss is frequently compared to free stream dynamic pressure or to free stream total pressure, in which cases it is referred to as the inlet efficiency or inlet pressure recovery, η_{inl}:

For incompressible flow:

$$\eta_{inl/inc} = (p_{tot_f} - p_\infty)/\bar{q}_\infty \qquad (6.29)$$

which can be written as:

$$\eta_{inl/inc} = 1 - \Delta p_{inl}/\bar{q}_\infty \qquad (6.30)$$

For compressible flow:

$$\eta_{inl/com} = p_{tot_f}/p_{tot_\infty} \qquad (6.31)$$

which can be written as:

$$\eta_{inl/com} = 1 - \Delta p_{inl}/p_{tot_\infty} \qquad (6.32)$$

The purpose of this sub-section is to present rapid methods for the calculation of inlet pressure losses in terms of either Δp_{inl} or η_{inl}.

Inlet pressure losses in turn have a detrimental effect on installed engine power or thrust. Methods for determining the effect of inlet pressure losses on installed power or thrust are presented in Section 6.4.

The information is organized as follows:

6.2.3.1 Piston engine inlets
6.2.3.2 Turbopropeller inlets
6.2.3.3 Jet engine inlets: subsonic
6.2.3.4 Jet engine inlets: supersonic

6.2.3.1 Piston engine inlets

For plenum inlets:

Figure 6.5a shows plenum inlets for piston engines.

In well designed piston engine plenum installations, the inlet losses may be held to less than 2 percent. For preliminary design purposes it is acceptable to use:

$$\eta_{inl/inc} = 0.98 \qquad (6.33)$$

For 'straight through' inlets:

Figure 6.5b shows 'straight through' inlets for piston engine applications. The method of 6.2.3.3 for subsonic jet inlets may be used to estimate pressure losses.

6.2.3.2 Turbopropeller inlets

For plenum inlets:

For turbopropellers with plenum inlet installations (See Figure 6.6), the pressure losses may be estimated with the plenum inlet method of 6.2.3.3.

For 'straight through' inlets:

As shown in Figure 6.6, many turbopropeller installations utilize 'straight through' inlets. For such inlets the pressure recovery may be estimated from:

$$\eta_{inl/inc} = f(\mu_{inl}) \qquad (6.34)$$

where: $f(\mu_{inl})$ is established in Figure 6.17 for inlets with unducted spinners as well as ducted spinners.

$$\mu_{inl} = A_c/A_\infty \qquad (6.35)$$

Note that μ_{inl} is the inverse of the inlet flow ratio as defined on page 147.

6.2.3.3 Jet engine inlets: subsonic

For plenum inlets:

Figure 6.7a shows a plenum inlet for a subsonic jet. Pressure losses may be estimated from:

$$\Delta p_{inl}/\bar{q}_\infty = \{1/(\mu_{inl}^2)\}(A_c/A_d)^2(1 - A_d/A_f)^2 \quad (6.36)$$

where: A_c, A_d and A_f for a plenum installation are as defined in Figure 6.18. Ref. 32 should be consulted for more details on jet engine plenum inlets.

For straight through inlets:

Figures 6.7b-d show subsonic, 'straight through' jet inlet examples. The pressure loss in such inlets is a strong function of the absence or presence of boundary layer diverters. Figure 6.8 shows examples of boundary layer diverters.

Without a boundary layer diverter, the pressure loss of a subsonic jet engine inlet may be estimated from:

$$\Delta p_{tot}/\bar{q}_\infty = IC_{Fd}/(\mu_{inl})^2 + HC_{Fa}\mu_{inl} \quad (6.37)$$

where: I is the so-called duct integral, defined as:

$$I = \int_{l_c}^{l_f} (A_c/A)^2 (per_A/A)dl \quad (6.38)$$

where: A is the duct area at station 1,

per_A is the duct perimeter at station 1

l_c is the duct station at the inlet area, A_c: see Figure 6.19

l_f is the duct station at the engine compressor face: see Figure 6.19.

$$C_{Fd} = fC_f \quad (6.39)$$

where: the factor f is given in Figure 6.20

C_f is the equivalent flat plate friction coefficient based on the duct Reynold's Number with the characteristic length taken as $(l_f - l_c)$. Figure 4.3 may

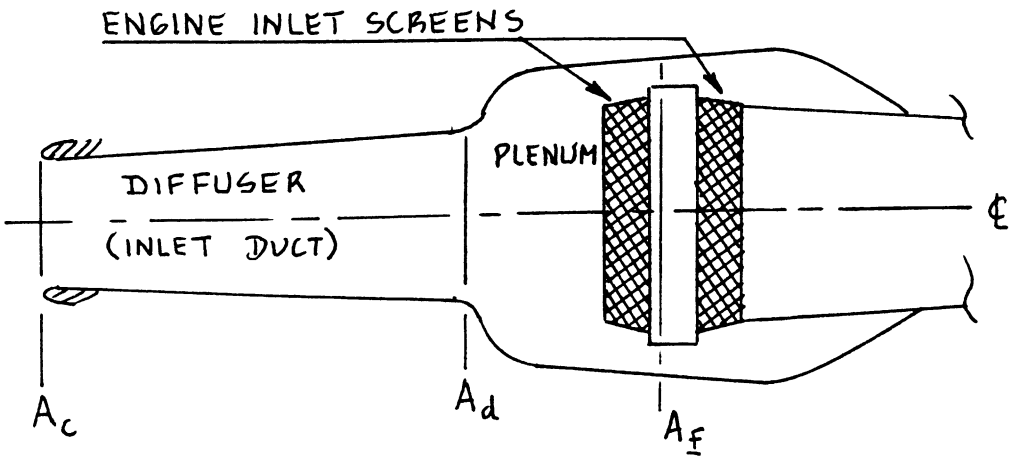

Figure 6.18 Geometry Definition for a Plenum Inlet

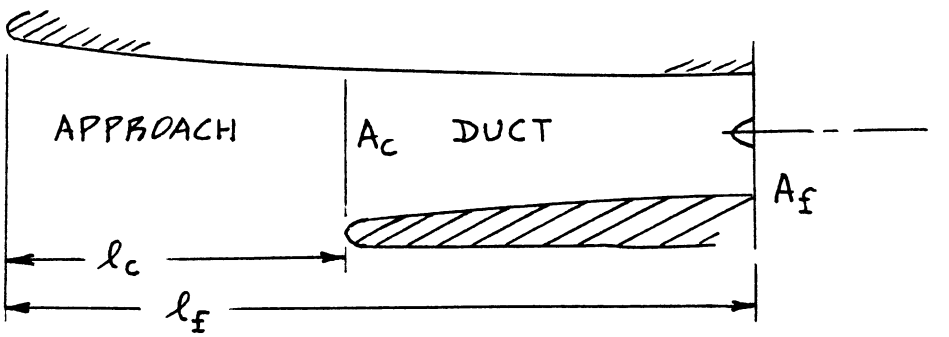

Figure 6.19 Duct Geometry with External Wetted Area

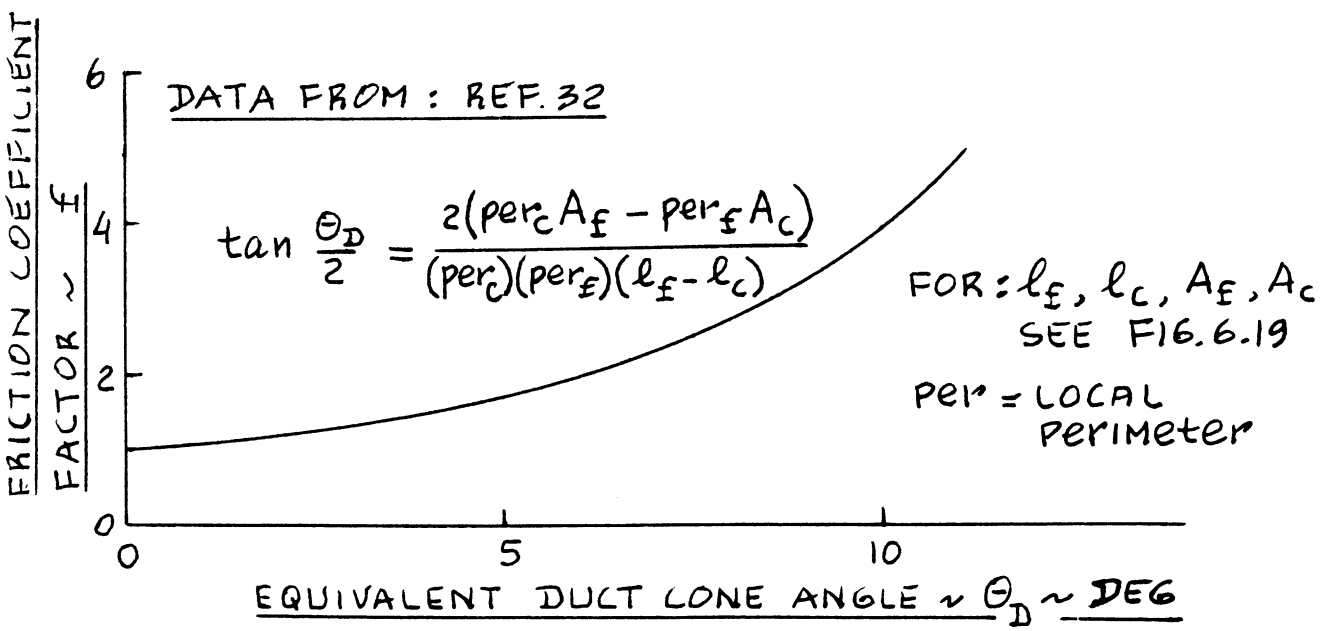

Figure 6.20 Friction Coefficient Factor for Inlet Ducts

be used to find C_f.

μ_{inl} is defined in Eqn.(6.35)

H is the corrected position ratio, defined as:

$$H = (0.8S_{wet\ appr})/A_c \qquad (6.40)$$

where: $S_{wet\ appr}$ is the wetted area of the inlet 'approach' as indicated by the cross-hatched area in Figure 6.21. Observe that for podded nacelle inlets and for pitot inlets: $S_{wet\ appr} = 0$!

C_{Fa} is the overall approach friction coefficient.

It may be set equal to the flat plate friction coefficient corresponding to a Reynolds Number based on l_{appr} as the characteristic length.

Figure 6.21 shows how l_{appr} is defined. Note that $l_{appr} = 0$ for podded nacelle inlets and for pitot inlets!

With a boundary layer diverter, the pressure loss of a subsonic jet engine inlet may be estimated from Eqn.(6.37) by setting H = 0.

The reader should consult Reference 32 for further details.

6.2.3.4 Jet engine inlets: supersonic

Figures 6.9, 6.10 and 6.14 give examples of supersonic inlet configurations. Note that all are of the so-called 'straight through' type. The pressure recovery of a supersonic inlet system is defined as:

$$\eta_{inl/com} = (\eta_{shock})(\eta_{diff}) \qquad (6.41)$$

where: η_{shock} is the pressure recovery through the inlet shock system. It is found from Fig.6.11 depending on the type of inlet.

η_{diff} is the pressure recovery through the subsonic diffuser which follows the system of shocks in the inlet. It may be found from:

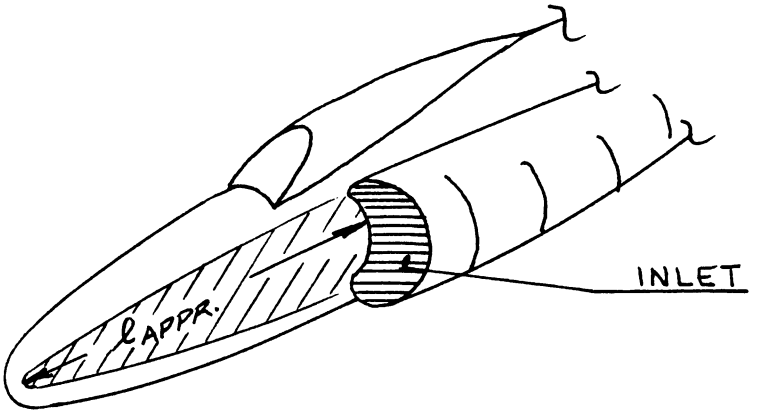

Figure 6.21 Definition of Approach Length

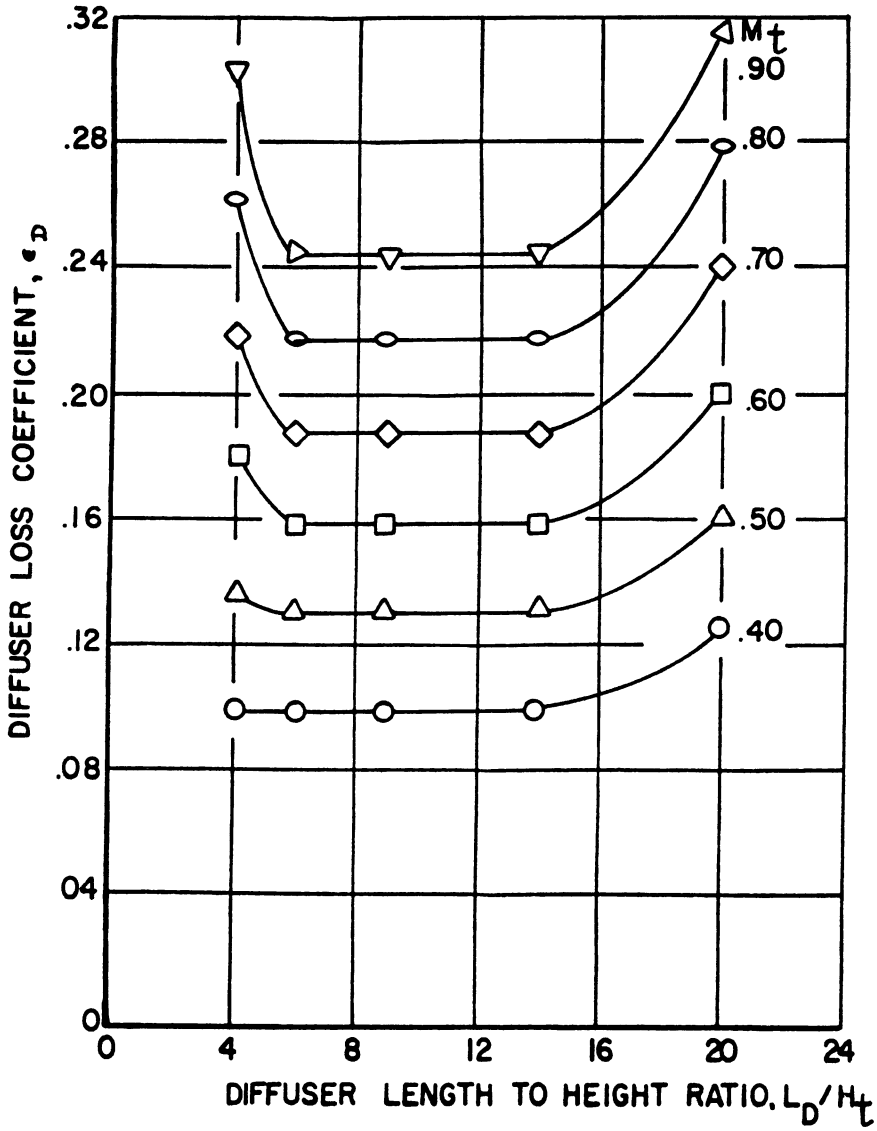

COPIED FROM:
REF. 12
COURTESY:
L. NICOLAI

SEE FIG. 6.15
FOR L_D AND H_t

Figure 6.22a Effect of Diffuser Geometry on Diffuser Loss Coefficient (Shock Ahead of Entrance)

$$\eta_{diff} = 1 - \varepsilon_D\{1 - (1 + 0.2M_T^2)^{-3.5}\} \qquad (6.42)$$

where: ε_D is the diffuser loss coefficient found from Figure 6.22. It depends on the subsonic diffuser geometry!

M_T is the diffuser entry Mach number. This Mach number is equal to the Mach number of the flow through the last shock in the inlet shock system. It can range from 0.4 to 0.9 in practical applications. Usually a number of 0.6 to 0.7 is found in such inlets. In preliminary design it is suggested to 'pick' a suitable number in this range.

M_T must be computed from the system of shocks. A method for doing this may be found in Appendix D of Ref.12.

Methods for determining the effect of inlet pressure losses on installed engine power or thrust are presented in Section 6.4.

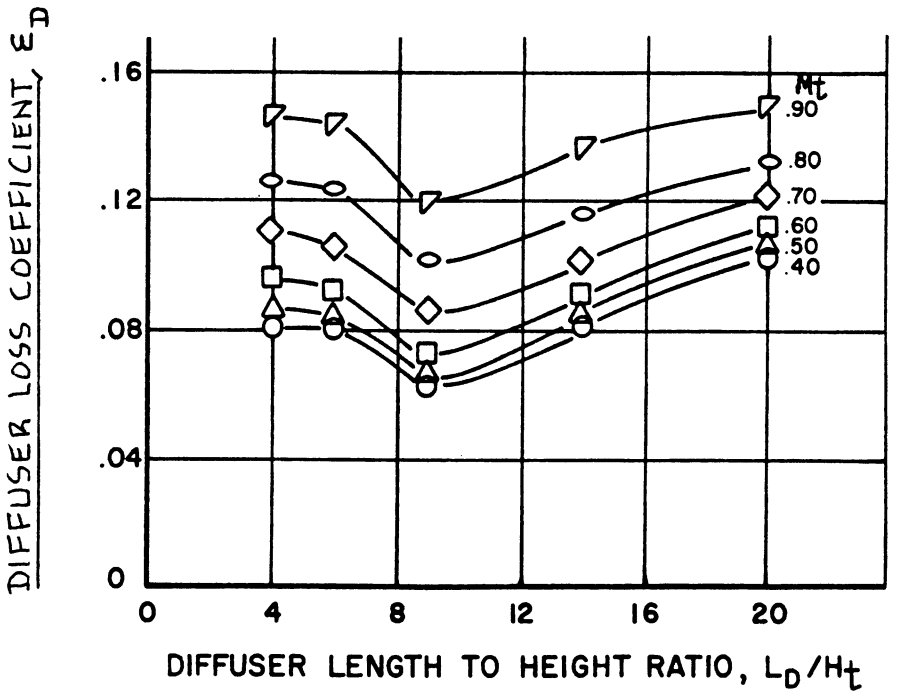

COPIED FROM:
REF. 12
COURTESY:
L. NICOLAI

SEE FIG. 6.15
FOR L_D AND H_t

Figure 6.22b Effect of Diffuser Geometry on Diffuser Loss Coefficient (Subsonic Entrance)

6.2.4 Inlet Extra Drag Estimation

The purpose of this sub-section is to present rapid methods for estimation of the so-called inlet extra drag, $C_{D_{inlextra}}$, which was considered a part of $C_{D_{misc}}$ in Sub-section 4.12.3. The inlet extra drag considered here is that contribution of inlet drag not accounted for in Ch.4 as a result of wetted areas or as a result of cross sectional area distribution.

Inlet pressure recovery and any associated loss in inlet pressure have been discussed in Sub-section 6.2.3. The effect of these losses on installed power and thrust is discussed in Section 6.4.

The extra inlet drag discussion is organized as in the following manner:

6.2.4.1 Piston engine inlets
6.2.4.2 Turbopropeller inlets
6.2.4.3 Jet engine inlets: subsonic
6.2.4.4 Jet engine inlets: supersonic

6.2.4.1 Piston engine inlet extra drag

In well designed piston engine installations, the inlet extra drag should be negligible. If the inlet is undersized, spillage drag may result. Estimation of inlet spillage drag is discussed in 6.2.4.3.

6.2.4.2 Turbopropeller inlet extra drag

In properly designed turbopropeller inlets the inlet extra drag should be negligible. If the inlet is undersized, spillage drag may result. Estimation of inlet spillage drag is discussed in 6.2.4.3.

6.2.4.3 Jet engine inlet extra drag: subsonic

For properly designed subsonic jet inlets the inlet extra drag should be negligible. However, if the inlet is undersized for some flight condition, spillage drag may result. The inlet extra drag due to spillage may be estimated from:

$$C_{D_{inlextra}} = C_f[1 + 0.33\{(d_m - \bar{d}_c)/l_{mc}\}F_{inl}]^{1.667}\left(\frac{\bar{A}_c}{S}\right) \quad (6.43)$$

with:

$$F_{inl} = 1 + 1.75\{(\mu_{inl} - 1)/[\mu_{inl}\{(A_m/\bar{A}_c) - 1\}]\} \qquad (6.44)$$

where: C_f is the equivalent flat plate friction coefficient at a Reynold's Number based on a characteristic length equal to l_{mc}: see Figure 6.23.

d_m is the maximum cowl diameter for the inlet

$\bar{d}_c$ is the cowl diameter at the inlet area position

A_m is the cowl cross section area at d_m

$\bar{A}_c$ is the cowl cross section area at $\bar{d}_c$

μ_{inl} is defined in Eqn.(6.35).

Equation (6.43) applies up to the critical Mach number. To reduce inlet drag above M_{crit}, it is necessary to shape the inlet lips so that they in fact have properties similar to high speed airfoils. Reference 32 contains discussions on inlet lip design at high subsonic Mach numbers.

6.2.4.4 Jet engine inlet extra drag: supersonic

In the supersonic case there are three sources for extra inlet drag:

1. Spillage drag (called additive drag)
2. Bypass drag
3. Boundary layer diverter drag
4. Boundary layer bleed drag

Figure 6.24 shows where these drag types are caused in a supersonic inlet. All three drag types depend on the state of the shock systems in the inlet. Detailed presentations of methods for estimating these drag contributions are beyond the scope of this text. Ref.12 contains methods for estimating these drag increments. Since Ref.12 uses A_c as the inlet drag reference area, all results must be multiplied by A_c/S.

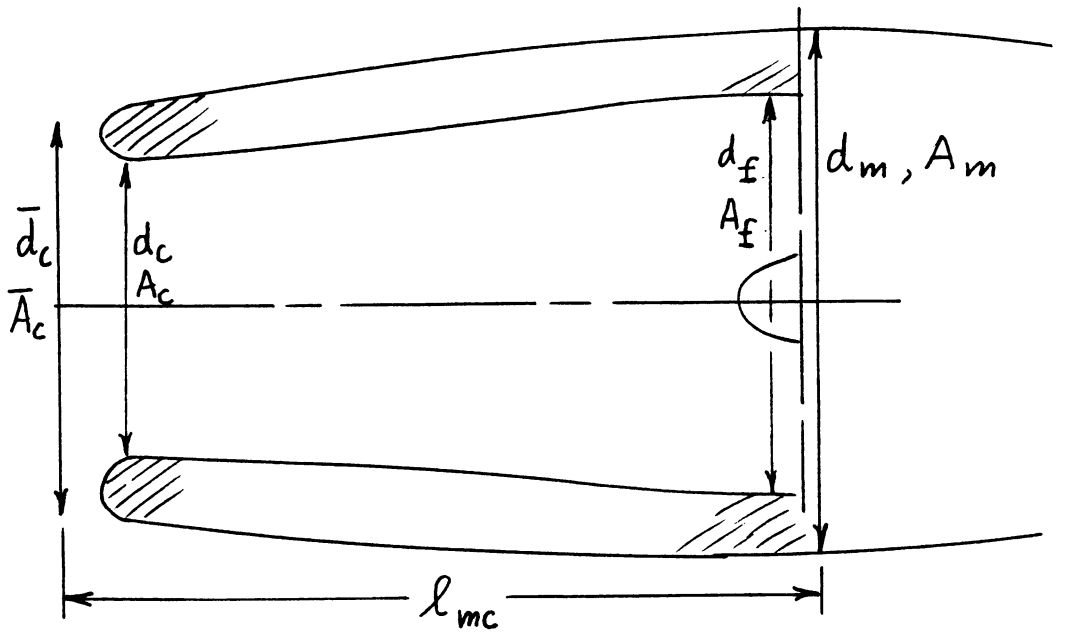

Figure 6.23 Duct Geometry for Inlet Extra Drag Evaluation

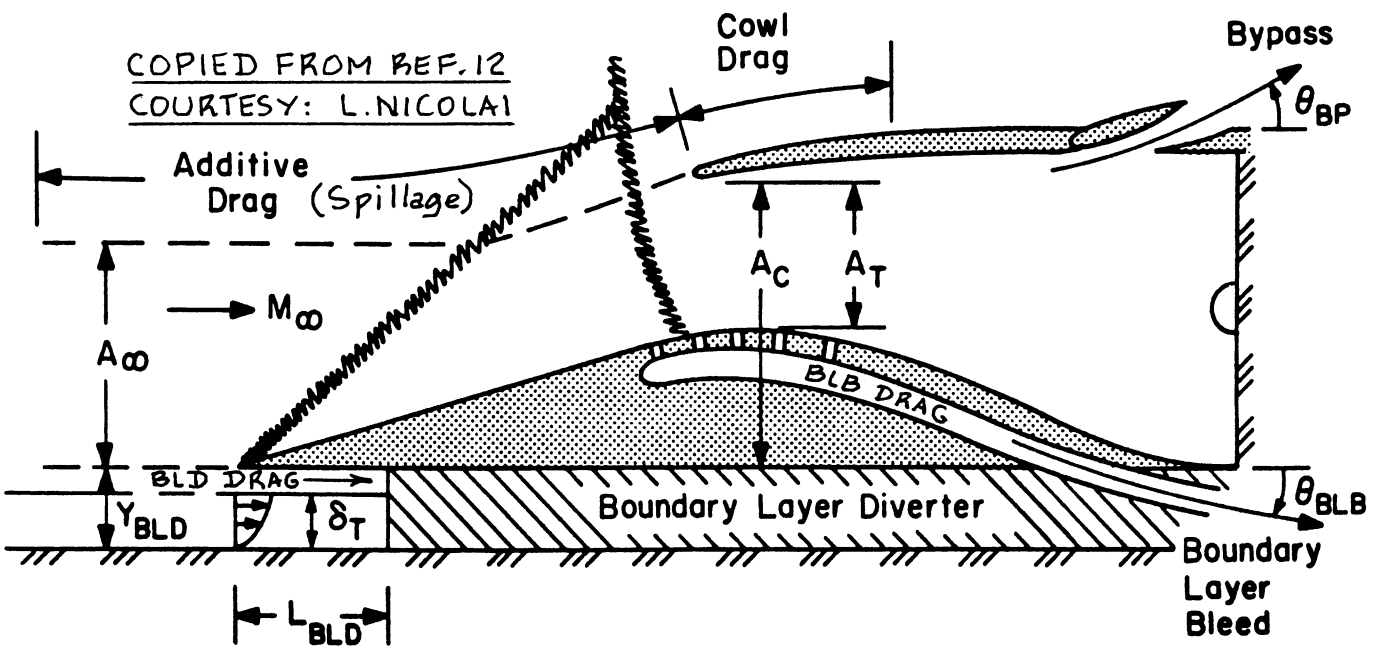

Figure 6.24 Visualization of Extra Drag Types in a Supersonic Inlet

6.3 EXHAUST OR NOZZLE SIZING AND INTEGRATION

In preliminary design the process of exhaust or nozzle sizing and integration consists of:

1. the determination of exhaust and/or nozzle areas

2. the integration of the exhausts and/or nozzles into the airplane

Figure 6.2 defines the nozzle exit area, A_e. Note from Fig.6.77 in Part III that in turbofan engines the nozzle area consists of two concentric areas, located at different longitudinal stations.

Integration of exhausts and/or nozzles into the airplane configuration must be done with care! Without such care, major increases in drag can be the result.

The information in this section is presented as:

6.3.1 General exhaust/nozzle arrangements

6.3.2 Exhaust/nozzle sizing

6.3.3 Estimation of exhaust/nozzle extra drag

The reader should also refer to Part III, Chapter 6 for examples of engine exhaust/nozzle installations.

6.3.1 General Exhaust/Nozzle Arrangements

The purpose of this sub-section is to present examples of exhaust/nozzle configurations which are being used in a number of airplanes.

The information is organized as follows:

6.3.1.1 Piston engine exhausts
6.3.1.2 Turbopropeller exhausts
6.3.1.3 Jet engine nozzles: subsonic
6.3.1.4 Jet engine nozzles: supersonic

6.3.1.1 Piston engine exhausts

Figure 6.5 shows several examples of piston engine exhaust configurations. In many older installations the engine exhaust is 'dumped' overboard in the manner shown in the 'upper' Figure 6.5a: this is very inefficient and causes extra drag. A lower drag installation is the one

shown in the 'lower' Figure 6.5a. Figure 6.25 shows the difference between a 'low drag' and 'high drag' case.

The reader must keep in mind that lowering drag is not always good. If the lower drag is obtained at the cost of increased weight and complexity, a 'design trade study must provide the information on basis of which the decision is made to proceed one way or the other.

The installations of Figures 6.5b represent modern concepts which take maximum advantage of the momentum exchange between inlet, combustion process, cooling requirements and exhaust.

6.3.1.2 Turbopropeller nozzles

Figure 6.6 shows several examples of turbopropeller engine (gas generator) exhaust installations. Note the trend toward exhausting 'parallel' to the local stream.

In many contemporary installations the exhaust pipes are arranged as shown in Figure 6.26. This creates much extra drag. The 'design trade study' comments made under 6.3.1.1 also apply here!

6.3.1.3 Jet engine nozzles: subsonic

Figure 6.7 shows several example of nozzle installations for subsonic jet engines. Note that all nozzles are of the convergent type. In subsonic flow, convergent nozzles are the only efficient nozzle configuration.

6.3.1.4 Jet engine nozzles: supersonic

Figure 6.27 shows a typical supersonic exhaust configuration. Depending on the flight Mach number of the airplane the nozzle should have a different geometry. Figure 6.28 illustrates the effect of flight condition on desired nozzle configuration. Note the convergent/divergent shape of nozzles at supersonic speeds.

The integration of nozzles into the after body of a supersonic airplane is particularly critical to drag. Figure 6.29 shows a number of nozzle/airframe integration concepts with commentary about the effect on drag. Here also, the consequence of weight, cost and complexity must be weighed against aerodynamic efficiency.

6.3.2 Exhaust/Nozzle Sizing

The purpose of this sub-section is to present rapid

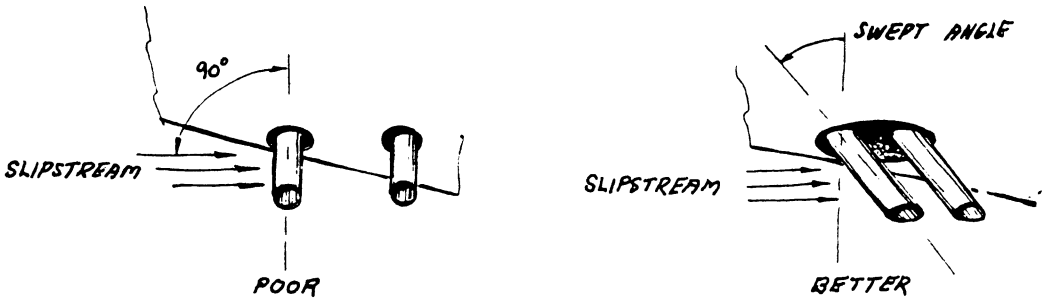

COPIED FROM REF. 38 COURTESY: T.BINGELIS

Figure 6.25 Example of High Drag and Lower Drag Exhaust Stack Installation

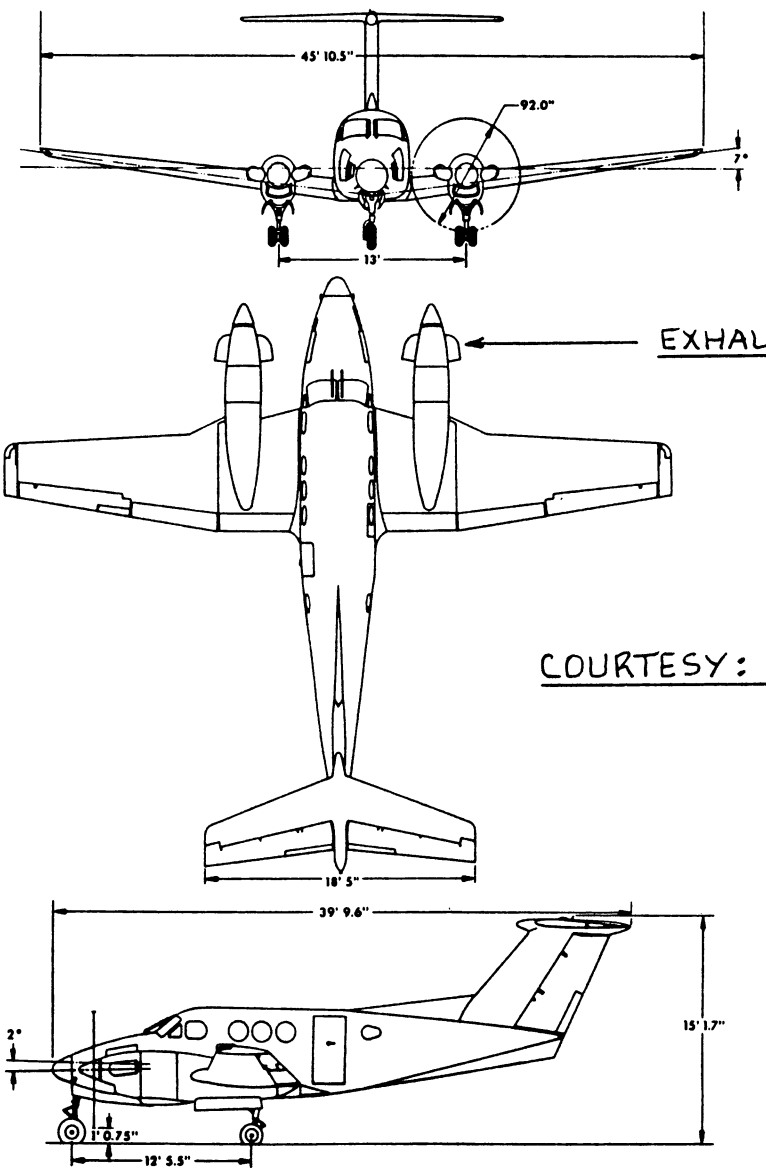

COURTESY: BEECH

Figure 6.26 Example of a High Drag Exhaust Installation as Seen on Contemporary Turboprops

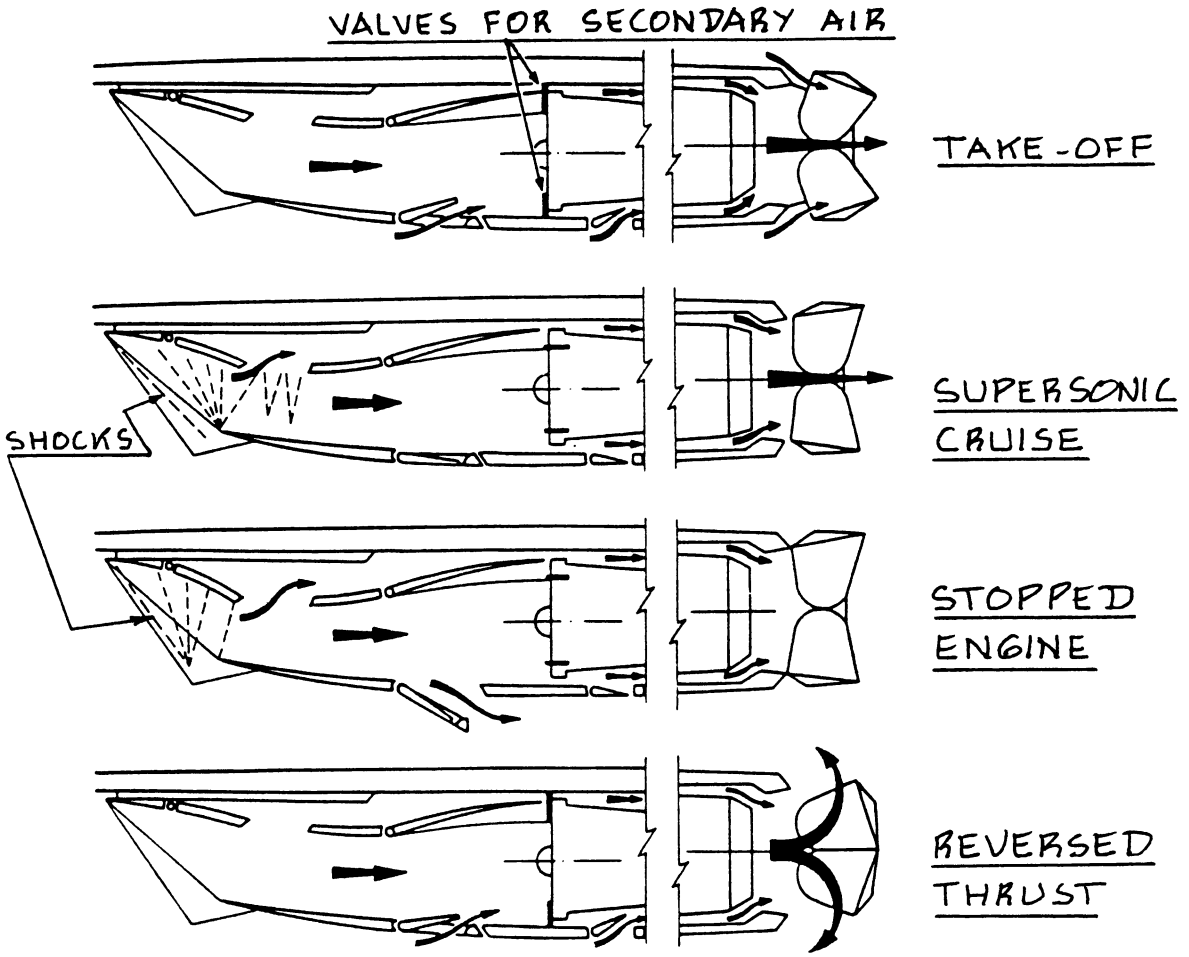

Figure 6.27 Examples of Supersonic Exhaust Configurations

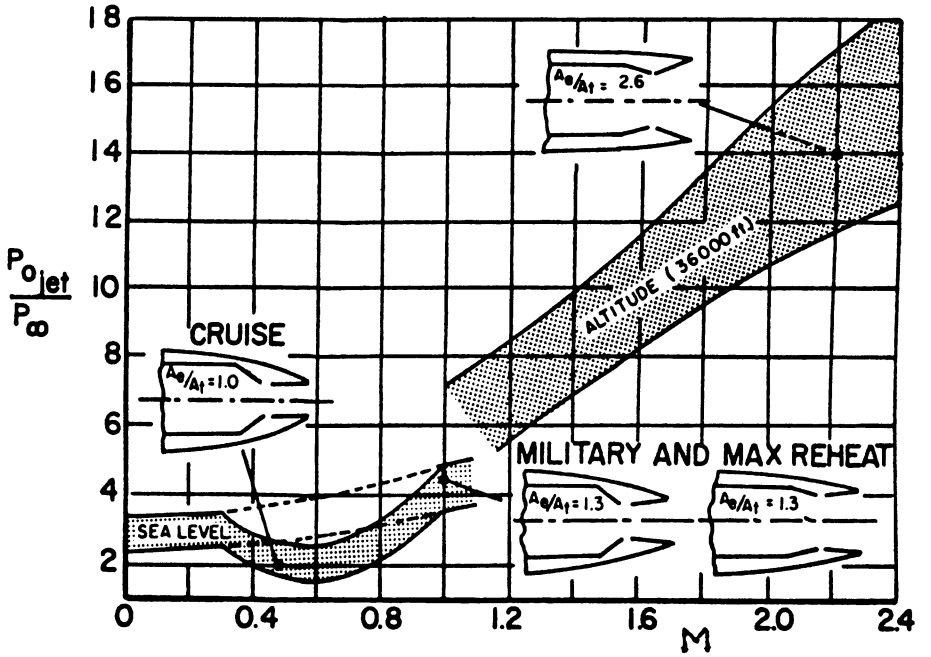

COPIED FROM REF. 12 COURTESY: L. NICOLAI

SEE FIG. 6.30 FOR A_e AND A_t DEFINITION

Figure 6.28 Variation of Nozzle Geometry with Mach Number

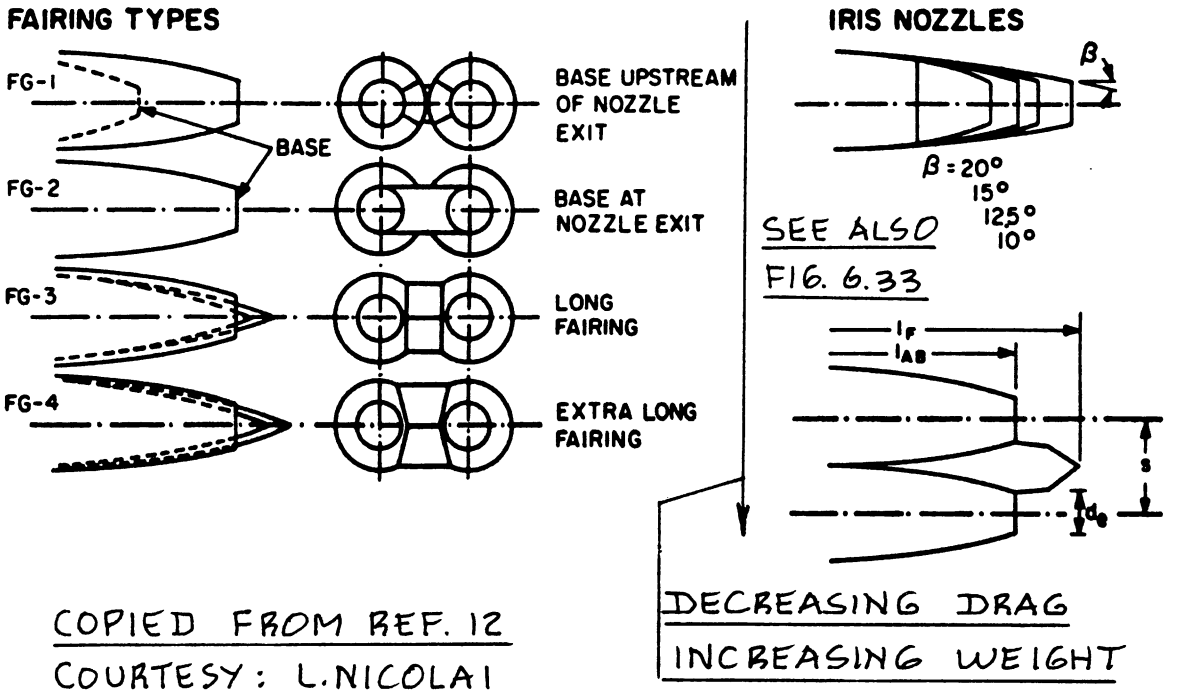

Figure 6.29 Examples of Nozzle/Airframe Integration

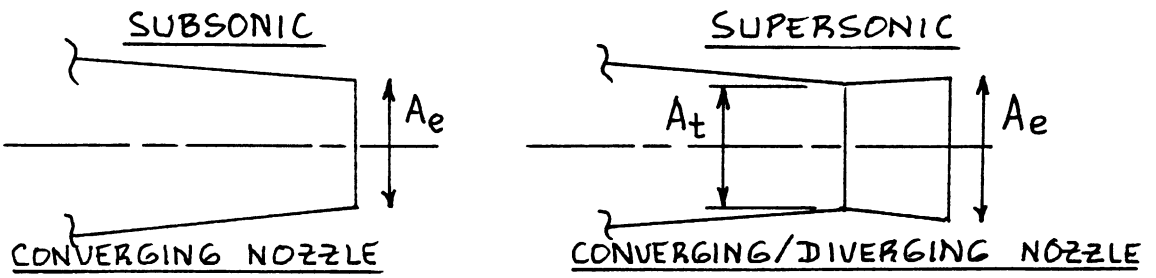

Figure 6.30 Definition of Nozzle Exit and Throat Areas

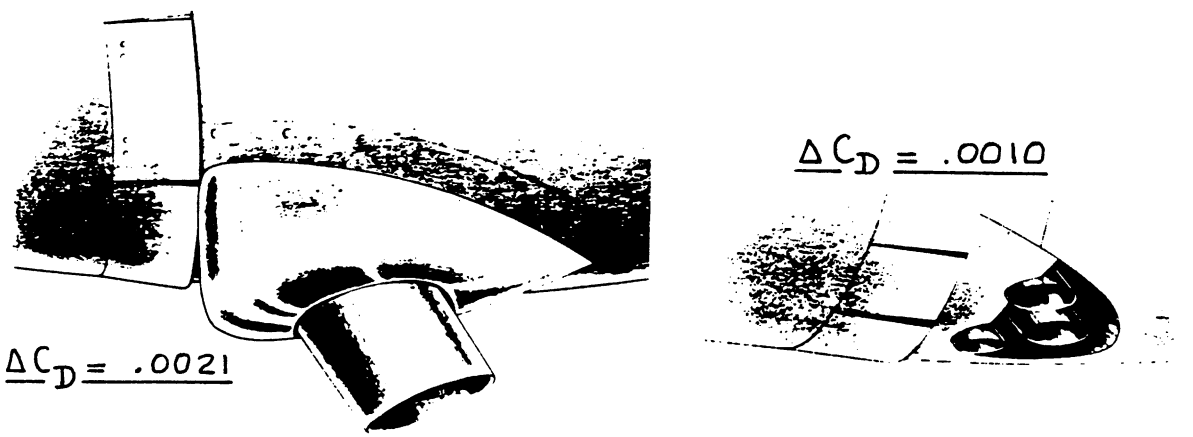

Figure 6.31 Effect of Exhaust Stack Configuration on Drag

methods for the 'sizing' of exhausts and/or nozzle exit areas. Figure 6.30 shows the definition of important nozzle exit and throat areas.

The material in this sub-section is presented as:

6.3.2.1 Piston engine exhausts
6.3.2.2 Turbopropeller nozzles
6.3.2.3 Jet engine nozzles: subsonic
6.3.2.4 Jet engine nozzles: supersonic

6.3.2.1 Piston engine exhausts

The exit size of piston engine exhausts is normally defined by the engine manufacturer. The exit area of the exhaust(s) are dependent on the cross sectional areas of the engine exhaust valve ports. Reference 37 contains detailed descriptions of this aspect of engine design.

The airframer may wish to use the exhaust manifold for purposes of heat extraction (by routing cabin air through a heat exchanger which is wrapped around the exhaust manifold). The airframer may also add noise suppressors and/or ejectors to the exhaust stack(s).

Refs 38 and 40 as well as Section 6.9 in Part III should be consulted for more details on piston engine exhaust configurations.

As a first approximation to the sizing of the total exit area, it is suggested to use an exhaust stack diameter given by:

$$d_{exhst} = (0.0038)SHP_{TO} \text{ in inches} \qquad (6.45)$$

If this diameter becomes too large, it is best to split the exhaust manifold into two or more small stacks.

6.3.2.2 Turbopropeller nozzles

Because turbopropellers are used only in subsonic flight conditions, the nozzles are always of the convergent type as seen in Figure 6.28.

As a first approximation to the sizing of the nozzle exit area, it is suggested to use:

$$d_{exhnoz} = (0.016)SHP_{TO} \text{ in inches} \qquad (6.46)$$

In many turboprop engines the nozzle area is divided over two exhausts. Engine manufacturers specify the ex-

haust area on the basis of their performance guarantees.

6.3.2.3 Jet engine nozzles: subsonic

In subsonic applications the exhaust nozzle is nearly always of the convergent type as shown in Figure 6.28.

The exhaust nozzle size and its configuration depend strongly on the following factors:

1. maximum take-off thrust
2. by-pass ratio
3. need for afterburning
4. design Mach number

The reader should use engine manufacturers data for exhaust nozzle areas. References 12, 33 and 41 provide more details on the subject of nozzle design.

6.3.2.4 Jet engine nozzles: supersonic

The exhaust nozzle size and its configuration depend strongly on the following factors:

1. maximum take-off thrust
2. by-pass ratio
3. need for afterburning
4. design Mach number

The usual nozzle configuration employs variable geometry: convergent for subsonic flight and convergent/divergent for supersonic flight: see Fig.6.28.

Engine manufacturers data should be used to find the size of the subsonic nozzle exit area. Figure 6.28 can be used to estimate the required exit area of the divergent part of the nozzle in its supersonic position.

Sizing of the length of the convergent part of the nozzle is not critical as long as it is not too short: a length of twice the entry diameter should be sufficient.

Sizing of the length of the diverging part of the nozzle is critical if separation is to be prevented. In preliminary design, a length of at least three times the nozzle throat diameter should be adequate.

References 12, 33 and 41 provide more details on the subject of nozzle design.

6.3.3 Estimation of Exhaust/Nozzle Extra Drag

In this sub-section rapid methods for estimating the extra drag caused by exhaust and/or nozzle installations. The material is organized as follows:

6.3.3.1 Piston engines
6.3.3.2 Turbopropeller engines
6.3.3.3 Jet engines: subsonic
6.3.3.4 Jet engines: supersonic

6.3.3.1 Piston engines

Figure 6.31 illustrates the drag increments associated with two piston engine exhaust configurations. In preliminary design it is suggested to use drag increments on the basis of similarity of the proposed installation with those of Figure 6.31.

6.3.3.2 Turbopropeller engines

If the exhaust configuration of a turbopropeller is similar to the one shown in Figure 6.26, the drag increments of 6.3.3.1 may be used as a guide.

If the exhaust configuration is similar to those of Figure 6.6, the additional drag penalty caused by the exhaust may be negligible.

6.3.3.3 Jet engines: subsonic

For engines mounted in nacelle pods, no additional drag increment is incurred: the nacelle drag is accounted for separately.

For engines mounted in a fuselage and exhausting in the rear, extra drag may be incurred. Figure 6.32 shows several nozzle concepts used for subsonic applications. Each concept has a drag penalty associated with it. The drag penalty may be found with the help of Table 6.2.

The airplane drag increment due to the nozzle may be found from:

$$\Delta C_{D_{noz}} = (\Delta C_{D_{noztype}}) S_{fus}/S \qquad (6.47)$$

Note: Eqn.(6.47) assumes that only ONE nozzle is at the rear of the fuselage. If more are present, the drag increases accordingly.

S_{fus} = fuselage maximum frontal area as defined in Figure 4.17.

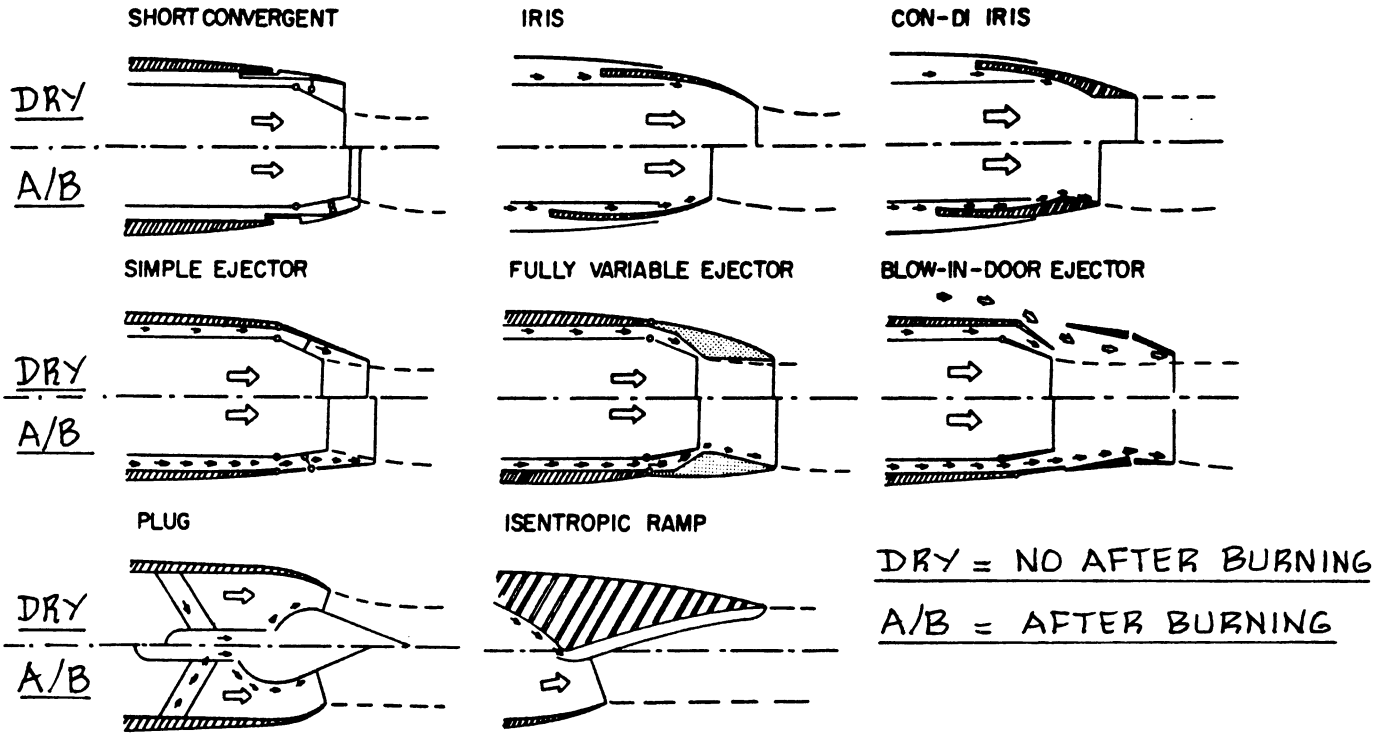

COPIED FROM REF. 12, COURTESY: L. NICOLAI

Figure 6.32 Typical Subsonic Nozzle Concepts

Table 6.2 Drag Penalties for Nozzles Mounted in the Rear of a Fuselage, for Subsonic Flight

Nozzle Type	Drag Increment $\Delta C_{D_{noztype}}$
Short convergent	0.036 - 0.042
Blow-in-door ejector	0.025 - 0.035
Plug	0.015 - 0.020
Fully variable ejector	0.010 - 0.020
Iris	0.010 - 0.020
Ramp	0.010

Notes: 1. these data apply in the M = 0.8 - 0.95 range
2. these data apply to nozzle pressure ratios of 2.5 to 3.0

If more than one engine exhausts at the rear of the fuselage, a difficult 'aerodynamic fairing' problem between the engines can arise. Figure 6.33 shows a number of possibilities. The drag increments due to such 'faired' nozzle arrangements may be estimated from Fig.6.33. Note that longer fairings reduce the drag of the installation. However: a longer fairing also implies a weight increase: as usual, a trade study must be performed to arrive at the correct decision.

6.3.3.4 Jet engines: supersonic

The supersonic drag increment of nozzles is strongly dependent on the method used to 'fair' the rear end of the airplane, especially in the area of the variable geometry nozzle. No simple method can be given for the estimation of nozzle drag increment. References 9, 12, 33 and 41 should be consulted for details.

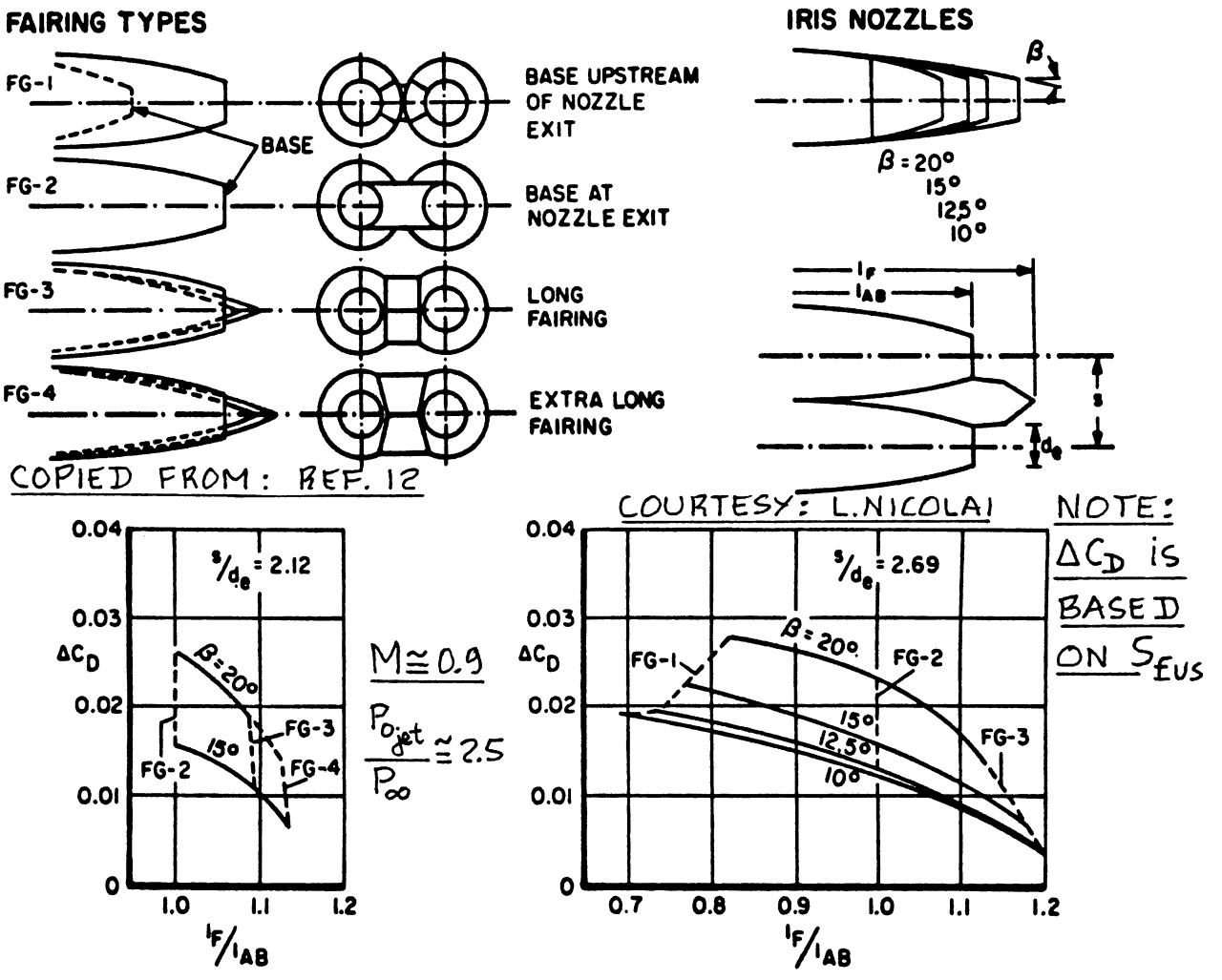

Figure 6.33 Effect of Nozzle Fairing Concept on Drag

6.4 PREDICTION OF INSTALLED POWER AND THRUST

The purpose of this section is to present rapid methods for estimating the installed performance of engines in airplanes. The material is presented as follows:

6.4.1 Propeller Driven Airplanes
6.4.2 Jet Driven Airplanes

6.4.1 Propeller Driven Airplanes

Propeller driven airplanes can use different methods for driving the propeller. In this text the following possibilities will be presented:

6.4.1.1 Piston propeller driven airplanes
6.4.1.2 Turbopropeller driven airplanes

6.4.1.1 Piston propeller driven airplanes

The installed performance of piston engines is normally stated in terms of available, installed power, P_{av}.

In some applications, the static thrust obtainable from a propeller may be important. Methods for finding static propeller thrust for a given amount of available shaft-horse-power are given in Reference 15.

The following step-by-step procedure is suggested for finding available, installed power, P_{av}.

Step 1: Determine the flight conditions for which the installed power available calculation is to be made. This consists of the selection of altitude, temperature and airspeed.

Step 2: From engine manufacturers data determine the available shaft horse power, SHP_{av} for each flight condition. Figure 6.34 shows a typical example of such data.

Step 3: Find the installed, available power, P_{av} from:

$$P_{av} = \{(\eta_{inl/inc} SHP_{av} - P_{extr})\eta_p\}\,\eta_{gear} \qquad (6.48)$$

where: SHP_{av} follows from Step 2,

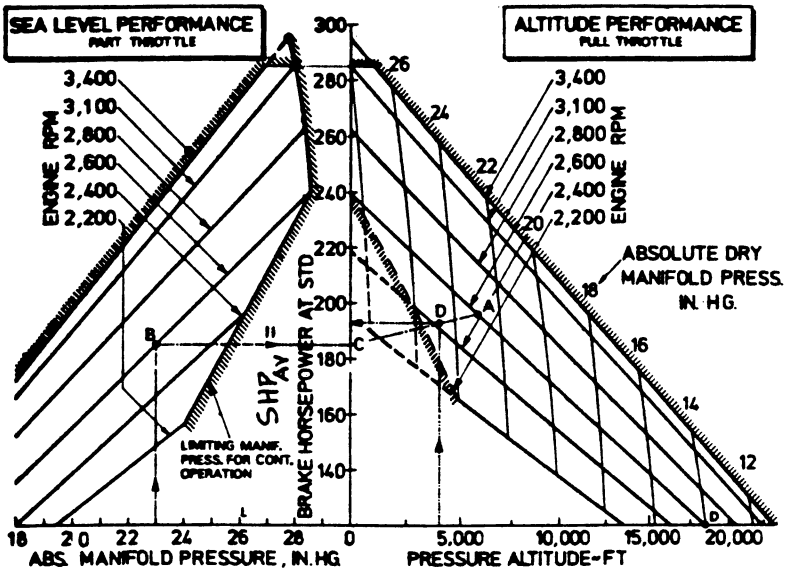

NOTE:

To find the actual horsepower from altitude, rpm, manifold pressure and air inlet temperature:

1. Locate A on full throttle altitude curve for given rpm and manifold pressure
2. Locate B on sea level curve for rpm and manifold pressure and transfer to C
3. Connect A and C by a straight line and read horsepower at given altitude: D
4. Modify horsepower at D for variation of air inlet temperature T from standard altitude temperature T_S by the formula:

Actual hp = hp at D x $\sqrt{\frac{T_s}{T}}$

where T and T_s are absolute temperatures

NORMALLY ASPIRATED

SUPERCHARGED

COPIED FROM REF. 13
COURTESY: E. TORENBEEK

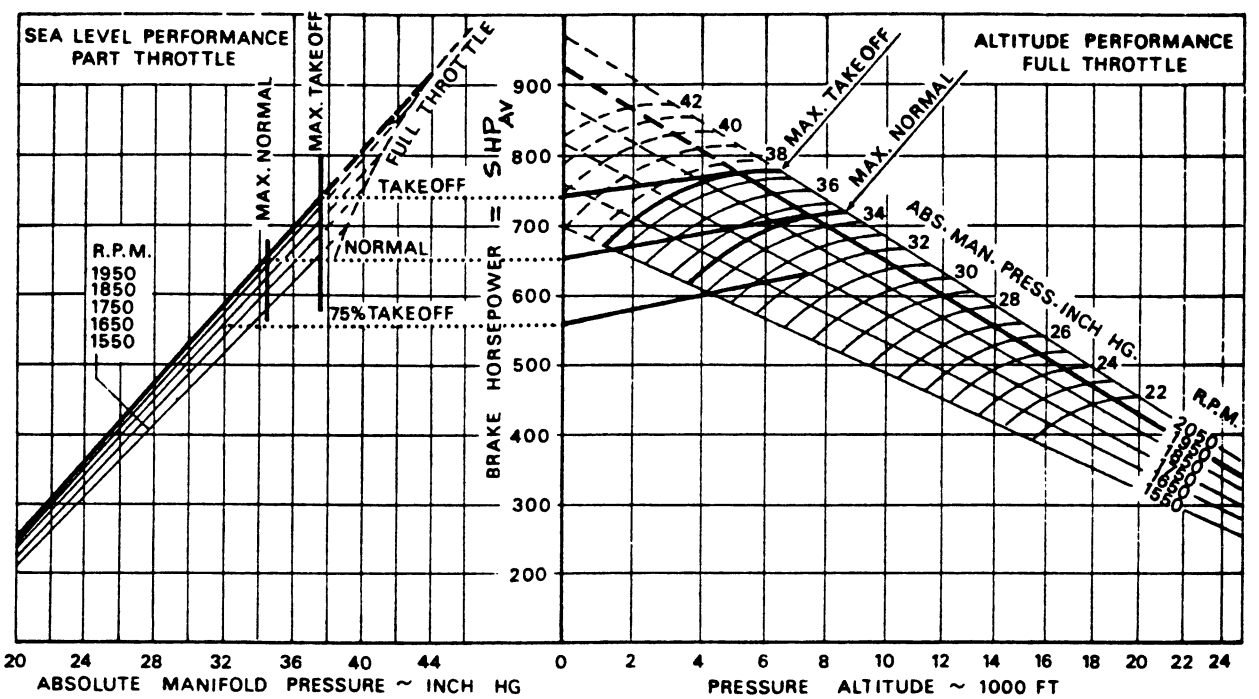

Figure 6.34 Example of Manufacturers Uninstalled Engine Performance Data for a Piston Engine

P_{extr} follows from sub-section 6.1.1.

η_p, the propeller efficiency, may be found from propeller data. Methods to compute propeller efficiency for conventional propellers are provided in References 15, 42, 43, 44 and 45.

NOTE: a rapid method for the determination of the diameter of propellers was given in Chapter 5 of Part II. External noise considerations were not a part of that method. To assure that a propeller meets FAR 36 noise requirements, the method of References 46, 47 and 48 may be used. For preliminary design purposes, as long as the propeller tip speed is kept below a Mach number of 0.85, noise certification should not be a problem.

η_{gear} is the gearbox efficiency.

For direct drive installations use:

$\eta_{gear} = 1.0$

For geared installations with a well designed gearbox, use:

$\eta_{gear} = 0.98$

Step 4: Plot P_{av} versus speed and altitude. Refer to Figure 7.1 in Chapter 7 for an example.

6.4.1.2 Turbopropeller driven airplanes

Installed turbopropeller performance is presented in terms of installed, available power P_{av}.

Most turboprops also deliver a remnant thrust, T_r which varies with the flight condition. For performance calculations this remnant thrust is usually converted to power. This will be done in this text also.

For some applications it is necessary to know the static thrust available from a turboprop installation. For such cases the static remnant thrust is added to the static propeller thrust. Methods for determining static propeller thrust are given in Reference 15.

The following step-by-step procedure is suggested to find

installed, available power, P_{av}:

Step 1: Determine the flight conditions for which the calculation of available installed power and thrust is to be made. This consists of the selection of altitude, temperature and airspeed.

Step 2: From engine manufacturers data determine the available shaft horsepower, SHP_{av} as well as the available remnant thrust, T_r for each flight condition. An example of such data is shown in Figure 6.35.

Step 3: Find the available, installed power, P_{av} from:

$$P_{av} = (\eta_{inl/inc} SHP_{av} - P_{extr})\eta_p \eta_{gear} + (\eta_{inl/inc}) T_r U_1/550 \quad (6.49)$$

where: $\eta_{inl/inc}$ follows from 6.2.3.2

SHP_{av} and T_r follow from Step 2

P_{extr} follows from sub-section 6.1.2

η_p, the propeller efficiency follows from Step 3 in 6.4.1.1.

Note 1: Eqn.(6.49) assumes that T_r is not affected by power extraction. Actually, this is not correct. Because the contribution of T_r to total available power is usually very small, the error made by this assumption is negligible.

Note 2: Eqn.(6.49) is not valid for $U_1 = 0$.

Note 3: Most turbopropeller engines already have a gearbox installed. The engine manufacturers data include the gearbox losses.

Step 4: Plot P_{av} versus speed and altitude. Refer to Figure 7.2 in Chapter 7 for an example.

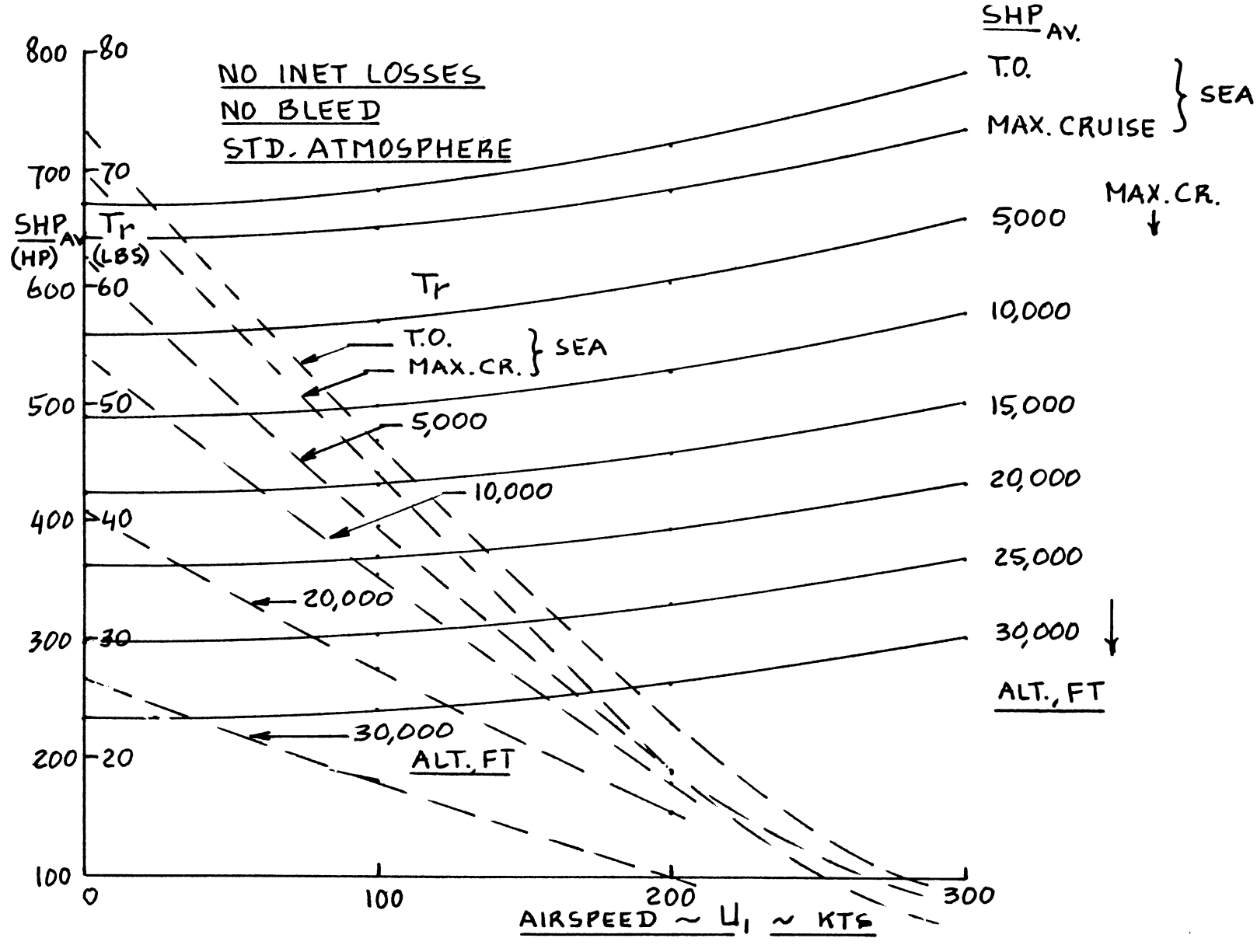

Figure 6.35 Example of Manufacturers Uninstalled Engine Performance Data for a Turboprop Engine

6.4.2 Jet Driven Airplanes

For jet driven airplanes, engine performance is given in terms of available, installed thrust, T_{av}.

Step-by-step procedures for determining T_{av} are presented as follows:

6.4.2.1 Subsonic operations
6.4.2.2 Supersonic operations

6.4.2.1 Subsonic operations:

Step 1: Determine the flight condition for which the installed thrust must be determined. This consists of the selection of altitude, temperature and airspeed.

Step 2: From engine manufacturers data, determine the available uninstalled thrust, $T_{tst/av}$.

Figure 6.36 shows an example of such data.

Step 3: Find the available installed thrust from:

$$T_{av} = \quad (6.50)$$

$$[(T_{tst/av})\{1 - 0.35K_tM_1(1 - \eta_{inl/inc})\} - 550(P_{extr}/U_1)]$$

where: $T_{tst/av}$ follows from Step 2

M_1 is the flight Mach number

$\eta_{inl/inc}$ may be found from 6.2.3.3

P_{extr} follows from Sub-section 6.1.2

K_t is determined from Figure 6.37

Step 4: Plot T_{av} versus speed and altitude. Refer to Figure 7.3 in Chapter 7 for an example.

6.4.2.2 Supersonic operations:

Step 1: Determine the flight conditions for which the available thrust, T_{av} must be found.

This consists of the selection of altitude, temperature and airspeed.

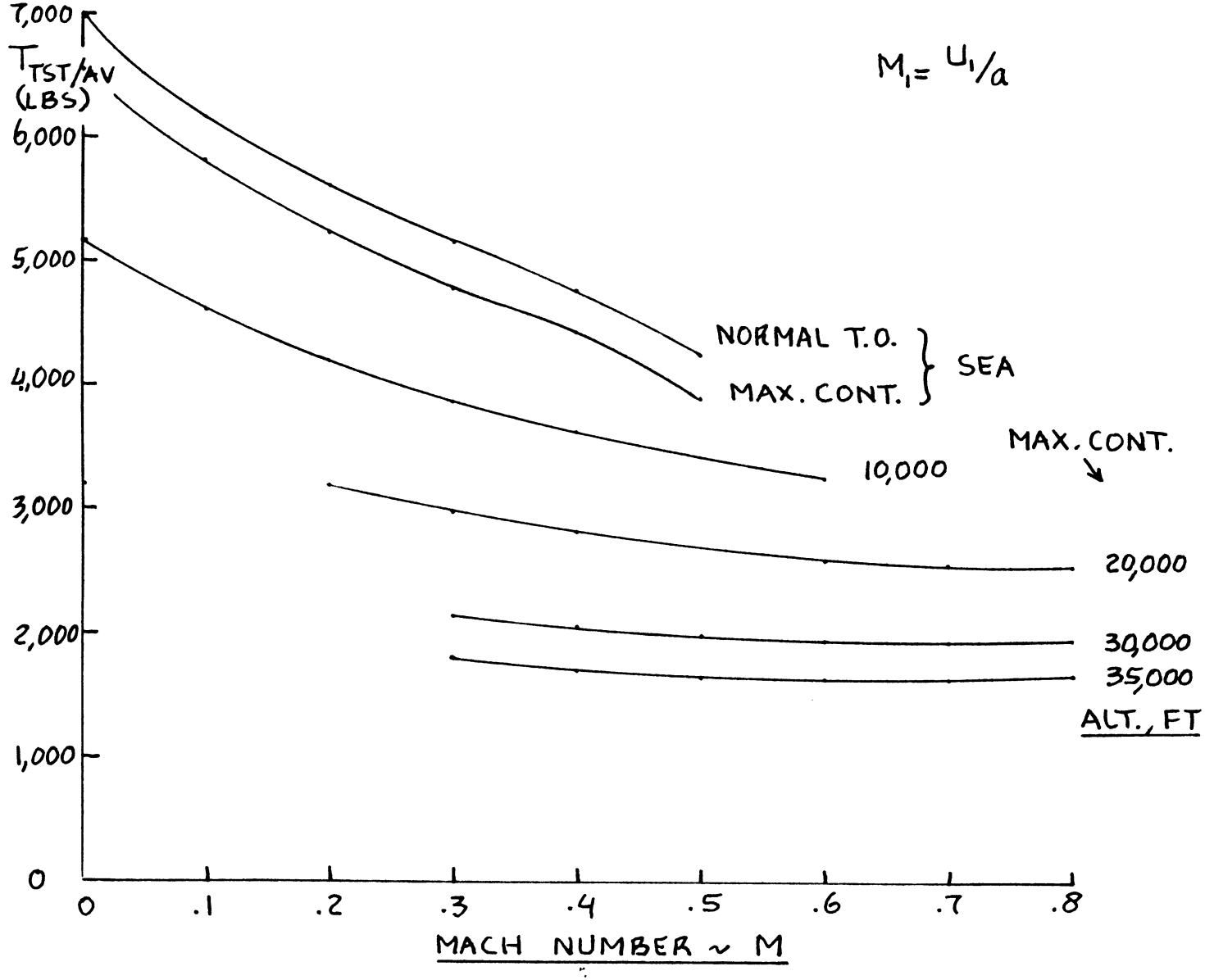

Figure 6.36 Example of Manufacturers Uninstalled Engine Performance Data for a Subsonic Turbofan

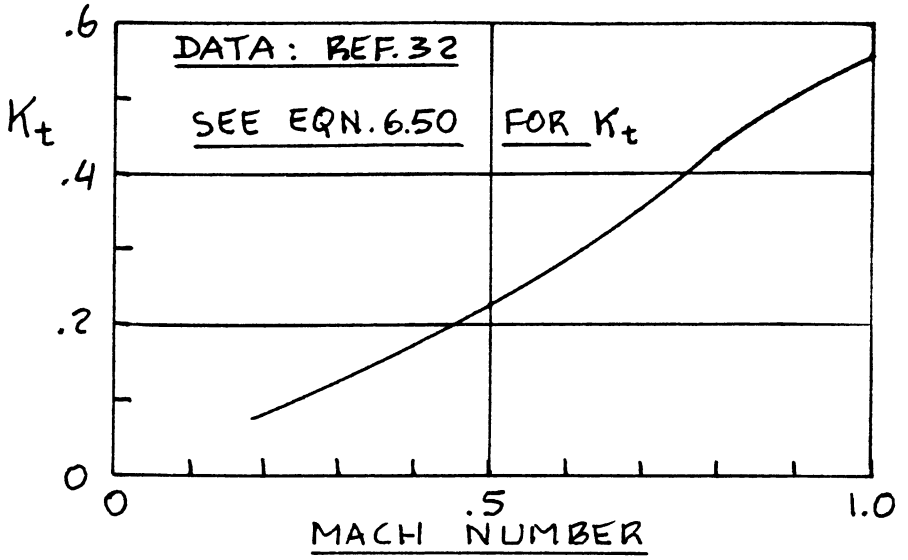

Figure 6.37 Effect of Mach Number on K_t

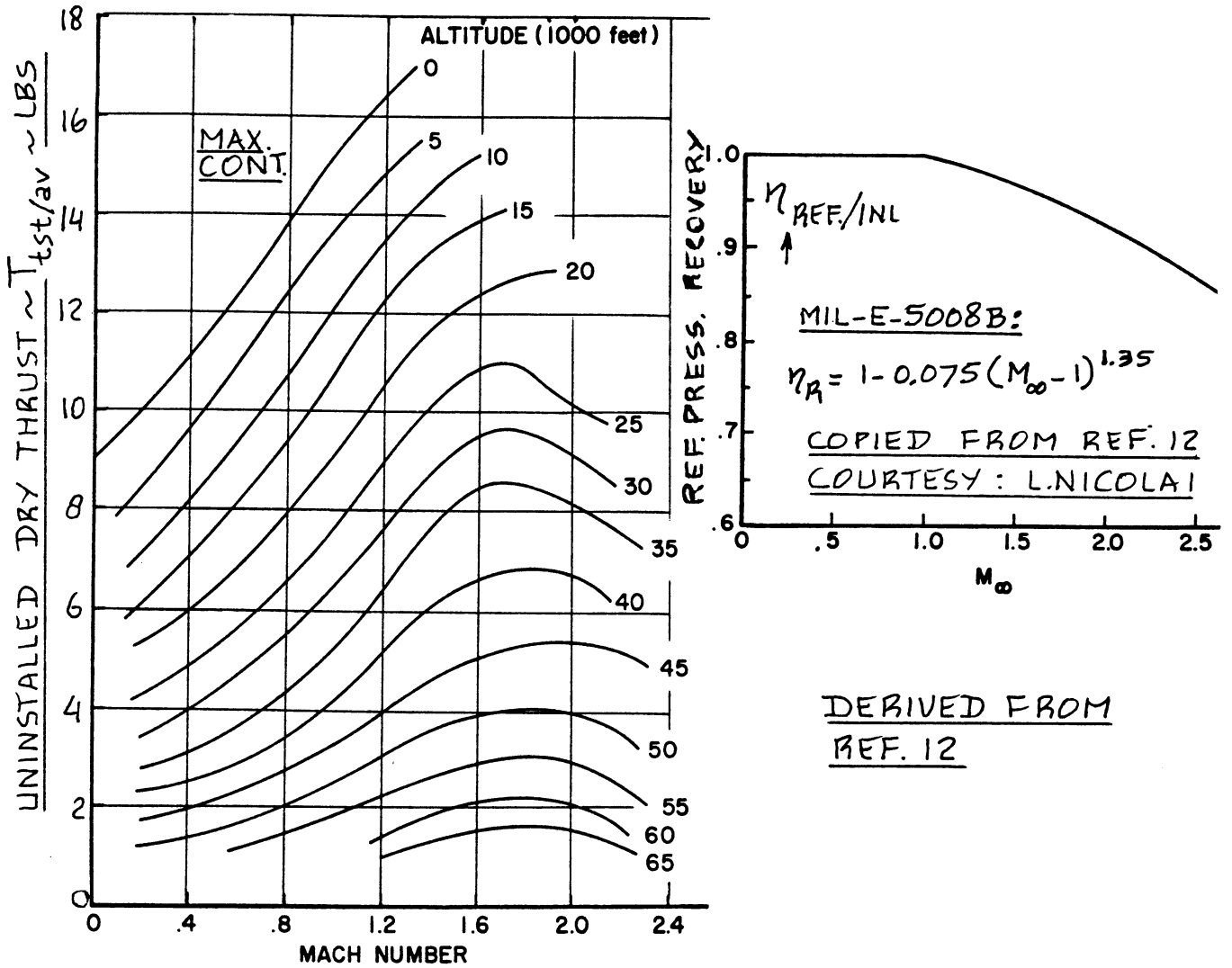

Figure 6.38 Example of Manufacturers Uninstalled Engine Performance Data for a Supersonic Turbofan

Step 2: From engine manufacturers data find the uninstalled, available thrust, $T_{tst/av}$.

Figure 6.38 gives an example of such data.

Note: These data are normally given for an assumed pressure recovery schedule with free stream Mach number: $\eta_{ref/inl}$. Figure 6.38 shows a typical pressure recovery schedule used by engine manufacturers for military engines.

Step 3: Compute the installed, available thrust, T_{av} from:

$$T_{av} = T_{tst/av}(1 - F_t - P_t) - 550P_{extr}/U_1 \qquad (6.51)$$

where: F_t accounts for actual inlet pressure recoveries and is found from:

$$F_t = C_R(\eta_{ref/inl} - \eta_{inl/com}) \qquad (6.52)$$

with: C_R is the ram recovery correction factor found from Figure 6.39.

$\eta_{inl/com}$ is the actual inlet pressure recovery which may be determined from Eqn.(6.41).

$\eta_{ref/inl}$ is found either from Fig.6.38 or from engine manufacturers data

$$P_t = 2\dot{m}_{bleed}/\dot{m}_a \qquad (6.53)$$

with: $\dot{m}_{bleed}$ found from Eqn.(6.7)

$\dot{m}_a$ determined from engine manufacturers data

P_{extr} follows from Sub-section 6.1.2

NOTE: The installed, available thrust, T_{av} is the

total thrust available from the entire installation. In other words, the effect of the thrust distribution over the various installation components as shown in Fig.6.12 has already been accounted for in the uninstalled engine manufacturers data albeit based on a reference pressure recovery and a reference nozzle.

Step 4: Plot T_{av} versus speed and altitude. Refer to Figure 7.5 in Chapter 7 for an example.

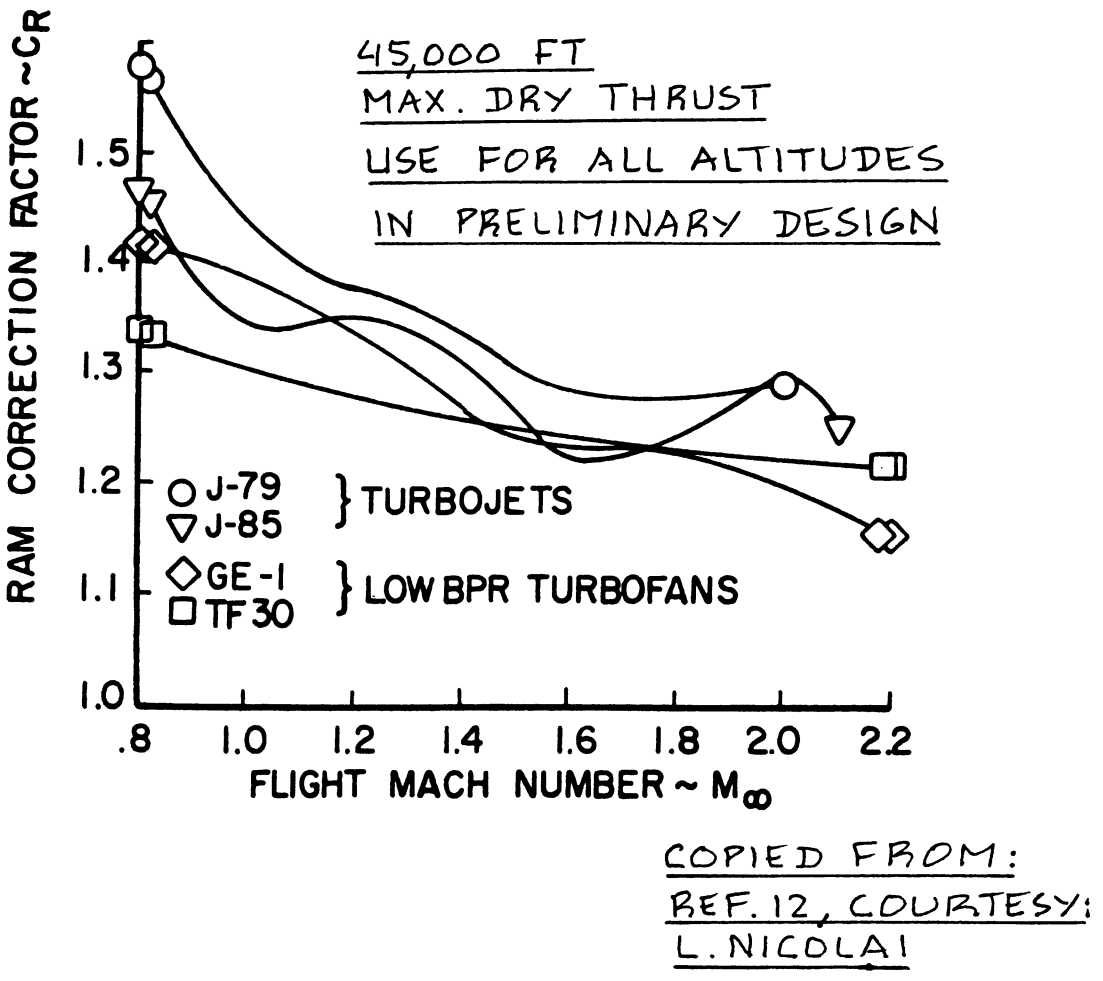

Figure 6.39 Effect of Mach Number on the Ram Recovery Factor of Several Jet Engines

7. INSTALLED POWER AND THRUST DATA

The purpose of this chapter is to present example data for installed power and thrust. The information is presented as follows:

7.1 Propeller driven airplanes
7.2 Jet driven airplanes

7.1 PROPELLER DRIVEN AIRPLANES

In this section, two examples will be given for the determination of installed power data for propeller driven airplanes:

7.1.1 Piston propeller driven airplanes
7.1.2 Turbopropeller driven airplanes

7.1.1 Piston Propeller Driven Airplanes

The step-by-step procedure of 6.4.1.1 will be used.

Step 1: It will be assumed that installed, available power data must be provided for the following flight conditions:

altitude:	0 - 20,000 ft in increments of 5,000 ft
speed:	from 0 - 200 kts
temperature:	standard atmosphere

Note: the flight condition range must be compatible with the stated mission objectives of the airplane. Such mission objectives are normally defined in the airplane mission specification. Examples of airplane mission specifications are discussed in Part I.

The airplane used in this example is assumed to be a single engine airplane. It has an engine with the uninstalled characteristics of Figure 6.34.

Step 2: Figure 6.34 provides typical engine manufacturers data for a small piston engine. Notice that the data are given in terms of SHP_{av} for various altitudes, engine rpm (throttle) and inlet manifold pressure.

Step 3: The following input information is required before Eqn.(6.48) can be used:

P_{extr}, $\eta_{inl/inc}$, η_{gear} and η_p

This input information must be determined for each individual installation. In preliminary design the methods suggested in 6.4.1.1 may be used.

For the current example the following data will be assumed:

$P_{extr} = 4$ hp $\qquad \eta_{inl/inc} = 0.98$

$\eta_{gear} = 1.0$ (direct drive) $\qquad \eta_p = 0.88$

Warning: propeller efficiency for a fixed pitch propeller can be this high for only one flight condition. In this example a variable pitch propeller has been used.

Step 4: The determination of P_{av} now proceeds as follows:

For a given altitude and engine rpm, Figure 6.34 is used to find the SHP_{av}. Using Equation (6.48) it is then possible to compute P_{av} for each flight condition.

Figure 7.1 shows the results of these calculations for the required range of altitudes and flight speeds.

Note: for the effect of atmospheric temperature on engine performance, engine manufacturers data should be consulted. In the absence of such data, the following approximation may be used:

$$SHP_{av_{at\ T}} = SHP_{av_{at\ std\ T}} (T_{std}/T)^{1/2} \qquad (7.1)$$

7.1.2 Turbopropeller Driven Airplanes

The step-by-step procedure of 6.4.1.2 will be used.

Step 1: It will be assumed that installed, available power data must be provided for the following flight conditions:

altitude:	0 - 40,000 ft in increments of 10,000 ft
speed:	0 - 400 kts
temperature:	standard sealevel

Note: the flight condition range must be compatible

The data in this Figure were arrived at with the assumptions listed in Sub-section 7.1.1.

Eqn.(6.48):

$$P_{av} = (\eta_{inl/inc} SHP_{av} - P_{extr})\eta_p \eta_{gear}$$

$$= (SHP_{av}(0.98) - 4)(0.88)(1.0)$$

<From Fig.6.34> <from Step 3, p.203/204>

3,400 RPM, max. allow.	Sea	5K	10K	15K	20K
SHP_{av}	285	248	206	172	140
$\eta_{inl/inc} SHP_{av}$	279	243	202	169	137
$- P_{extr}$	275	239	198	165	133
P_{av}	242	210	174	145	117

Note that P_{av} is not a function of speed in these calculations. The reason is: propeller efficiency was assumed to be constant. This is not always the case!

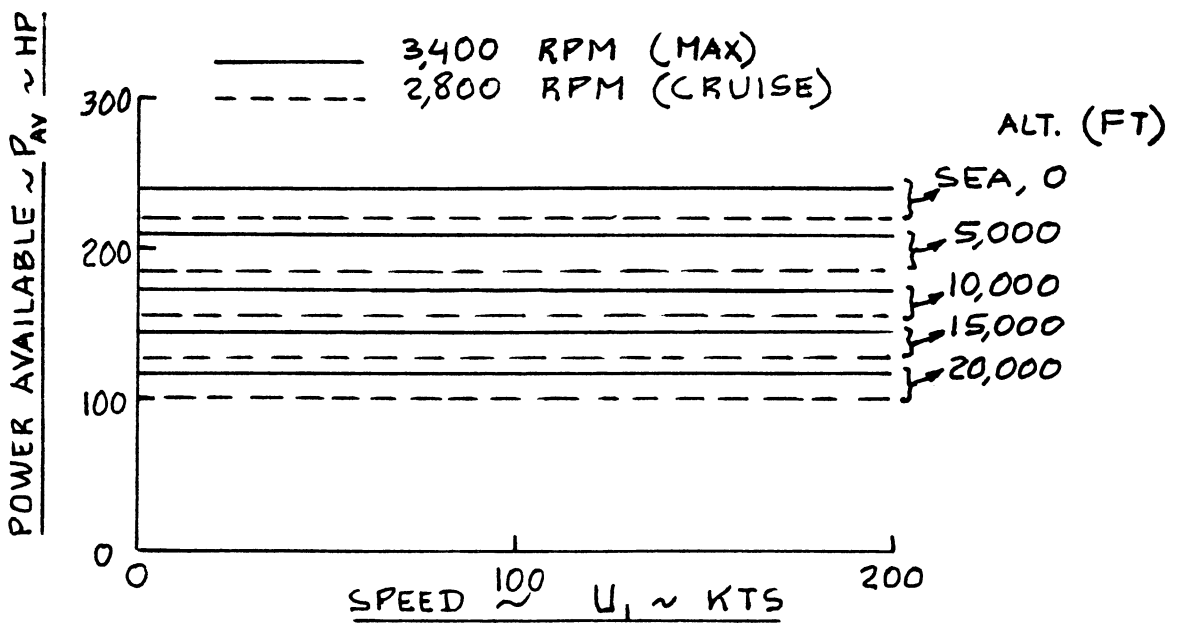

Figure 7.1 Installed Available Horsepower Data for a Single Engine Piston Propeller Airplane

with the stated mission objectives of the airplane. Such mission objectives are normally defined in the airplane mission specification. Examples of airplane mission specifications are discussed in Part I.

The airplane used in this example is assumed to be a twin engine turbopropeller driven airplane. The engines have the uninstalled characteristics of Figure 6.35.

Step 2: Figure 6.35 defines the engine manufacturers data for this example calculation. Note that these data are given in terms of SHP_{av} and T_r.

Step 3: The following input information is required before Equation (6.49) can be used:

P_{extr}, $\eta_{inl/inc}$, U_1 and η_p

This input information must be determined for each individual installation. In preliminary design the methods suggested in 6.4.1.2 may be used.

For the current example the following data will be assumed:

$P_{extr} = 10$ shp

Plenum inlet with bypass duct: $\eta_{inl/inc} = 0.89$

$\eta_p = 0.92$

U_1 is selected in increments of kts airspeed

Warning: propeller efficiency varies considerably with Mach number. The assumption has been made here that the propeller blades have supercritical airfoil sections and that a propeller pitch angle schedule is used which allows the propeller efficiency to be optimized at all speeds.

Step 4: The determination of installed, available power, P_{av} proceeds as follows:

For any given altitude, Figure 6.35 is used to find SHP_{av} and T_r. Using Equation (6.49) it is now possible to compute P_{av} for each flight condition. Figure 7.2 shows the installed engine performance for the airplane with both engines operating.

Note: for the effect of atmospheric temperature on engine performance, engine manufacturers data should be consulted. In the absence of such data, the following approximation may be used for sealevel performance:

$$SHP_{av_{at\ T}} = SHP_{av_{at\ std\ T}} - 2.33(T - T_{std}) \qquad (7.2)$$

where: T is the actual atmospheric temperature in degrees F.

T_{std} is the atmospheric temperature in the standard atmosphere in degrees F.

Observe that Eqn.(7.2) implies that for each degree of temperature increase above standard, 2.33 hp will be lost!

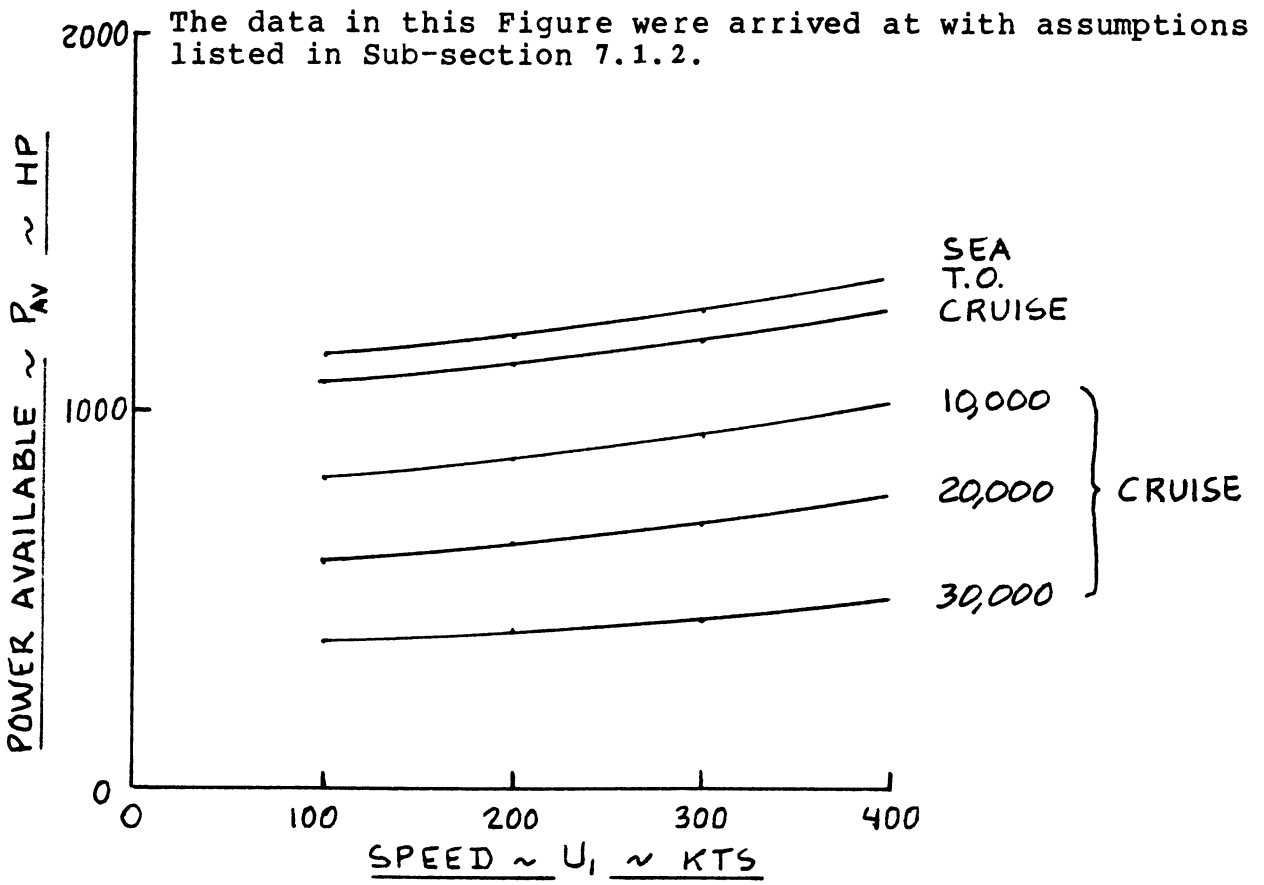

Figure 7.2 Installed Available Horsepower Data for a Twin Engine Turbopropeller Airplane

7.2 JET DRIVEN AIRPLANES

In this section, two examples will be given for the determination of installed thrust for jet driven airplanes:

7.2.1 Subsonic operations

7.2.2 Supersonic operations

7.2.1 Subsonic Operations

The step-by-step procedure of 6.4.2.1 will be used.

Step 1: It will be assumed that installed, available thrust data must be provided for the following flight conditions:

altitude:	0 - 50,000 ft in increments of 10,000 ft
speed:	0 - 500 kts
temperature:	standard atmosphere

Note: the flight condition range must be compatible with the stated mission objectives of the airplane. Such mission objectives are normally defined in the airplane mission specification. Examples of airplane mission specifications are discussed in Part I.

The airplane used in this example is assumed to be a twin engine airplane. It has engines with the uninstalled characteristics of Figure 6.36.

The airplane will be assumed to have a straight-through inlet.

Step 2: Figure 6.36 defines the engine manufacturers data for this example calculation. Note that these data are in terms of $T_{tst/av}$ for a range of flight conditions.

Step 3: The following input information is required before Eqn.(6.50) can be used:

K_t, M_1, $\eta_{inl/inc}$, P_{extr} and U_1

This input information must be determined for each individual installation. In preliminary design the methods suggested in 6.4.2.1 may be used.

For the current example, the following data will be assumed:

K_t from Figure 6.37 at each value of M_1

M_1 follows from the speed and altitude for which the calculations are made.

$\eta_{inl/inc}$ follows from Eqns (6.30) and (6.37).

Note: the inlet geometry must be available before the inlet pressure recovery can be computed! In this example it will be assumed that $\eta_{inl/inc} = 0.95$.

P_{extr} follows from Sub-section 6.1.2. In this example it will be assumed that $P_{extr} = 60$ hp.

U_1 is selected in increments of kts airspeed.

Step 4: The determination of T_{av} now proceeds as follows:

For each speed and altitude combination, Eqn.(6.50) is now used to determine T_{av}. This information is then plotted as in Figure 7.3.

Note: for the effect of atmospheric temperature on engine performance, engine manufacturers data should be consulted.

7.2.2 Supersonic Operations

The step-by-step procedure of 6.4.2.2 will be used.

Step 1: It will be assumed that installed, available thrust must be provided for the following range of flight conditions:

altitude:	0 - 60,000 ft in increments of 10,000 ft
speed:	M = 0 to 2.5
temperature:	standard atmosphere

Note: the flight condition range must be compatible with the stated mission objectives of the airplane. Such mission objectives are normally defined in the airplane mission specification. Examples of airplane mission specifications are discussed in Part I.

The airplane used in this example is assumed to be a

The data in this Figure were arrived at with assumptions listed in Sub-section 7.1.3.

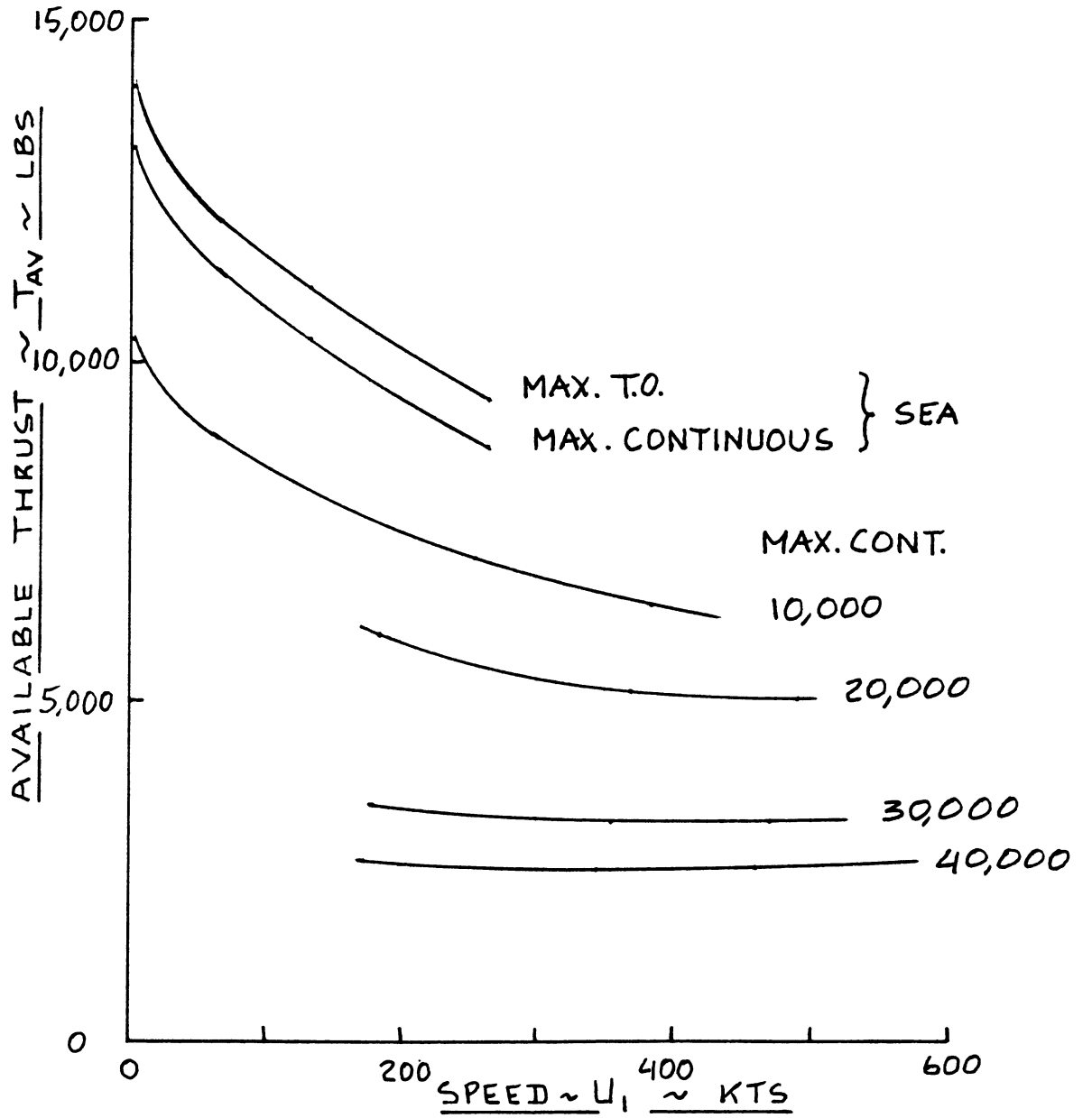

Figure 7.3 Installed Available Thrust Data for a Subsonic Twin Engine Jet Transport

twin engined, supersonic business jet. The inlets are assumed to be of the mixed compression type (Fig.6.10c) with four shocks.

The uninstalled engine performance characteristics are assumed to be those of Figure 6.38.

Step 2: Figure 6.38 defines the engine manufacturers data for this installation in terms of $T_{tst/av}$. Note the reference pressure recovery schedule.

Step 3: The following input information is required before Eqn.(6.51) can be used:

F_t: which depends on C_R, $\eta_{inl/com}$ and $\eta_{ref/inl}$,

P_t: which depends on $\dot{m}_{bleed}$ and $\dot{m}_a$,

P_{extr} and U_1

For the current example it will be assumed that F_t has been determined to vary with Mach number as shown in Figure 7.4, that $P_t = 0.07$ and that $P_{extr} = 20$ hp

Step 4: The determination of T_{av} now proceeds as follows:

For any given speed and altitude, Eqn.(6.51) is used to compute T_{av}. The result is plotted in Figure 7.5.

Note: for the effect of atmospheric temperature on engine performance, engine manufacturers data should be consulted.

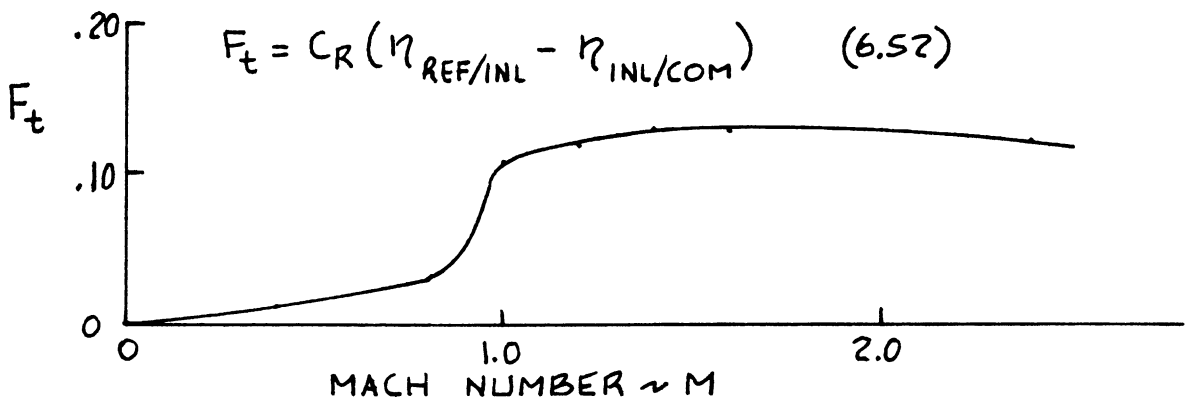

Figure 7.4 Effect of Mach Number on F_t for an Example Supersonic Twin Engine Business Jet

The data in this Figure were arrived at with assumptions listed in Sub-section 7.1.4 and the F_t data of Fig.7.4.

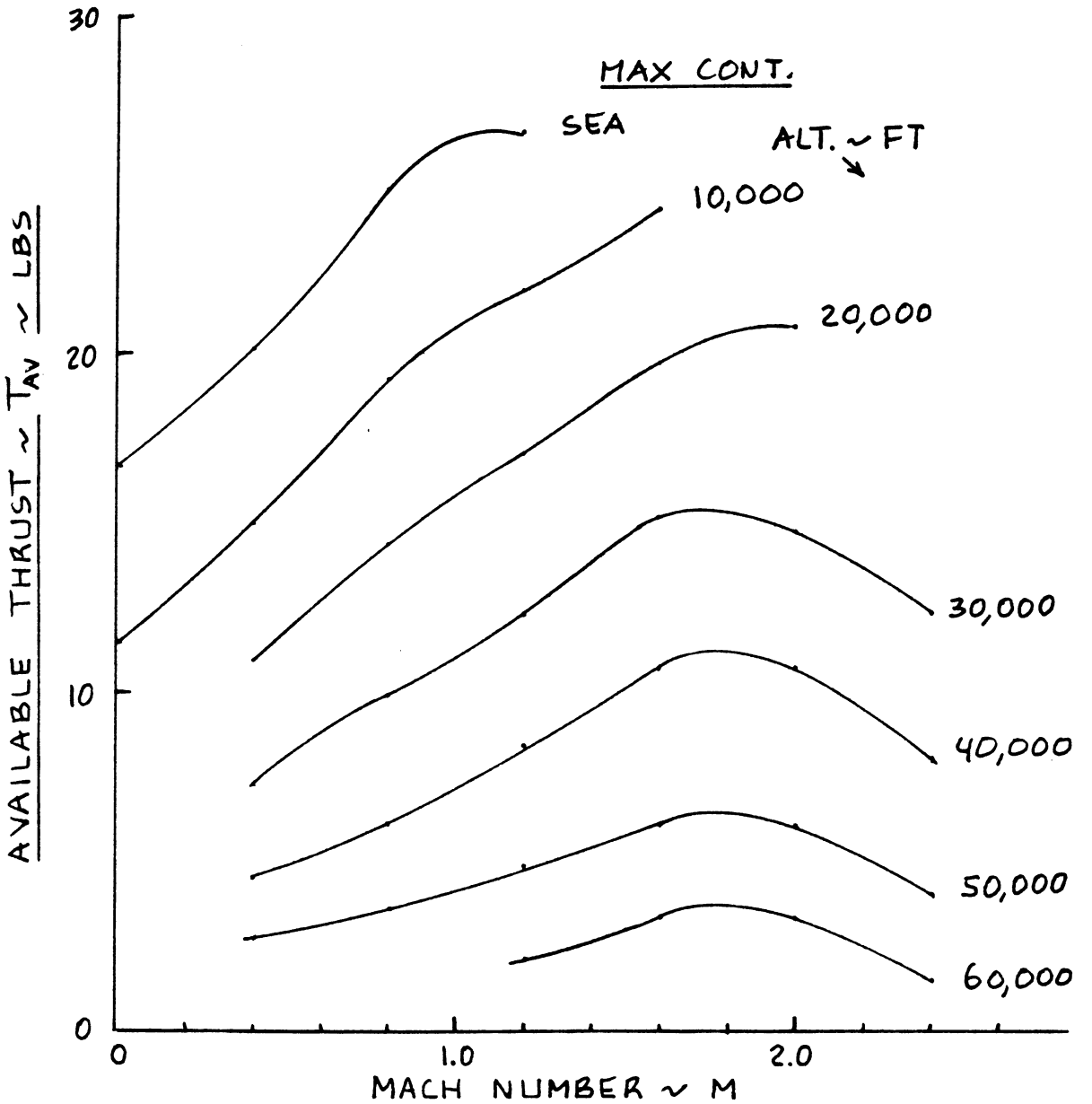

Figure 7.5 Installed Available Thrust Data for a Supersonic Twin Engine Business Jet

8. LIFT AND PITCHING MOMENT PREDICTION METHODS

The purpose of this chapter is to present rapid methods for the prediction of lift and pitching moment characteristics of airplanes. These characteristics are expressed in terms of the following relationships:

*Lift coefficient versus angle of attack

*Pitching moment coefficient versus lift coefficient

The reason for combining these relationships is the fact that unless an airplane can be trimmed (i.e. flown at zero pitching moment coefficient), it is not useful.

Figure 8.1 shows the fundamental C_L-α and C_m-C_L relationships which must be determined for any new design. Note the following maximum lift coefficients:

Clean airplane (flaps up): $C_{L_{max}}$

Flaps down: take-off: $C_{L_{max_{TO}}}$

landing: $C_{L_{max_L}}$

} Trimmed with: $\bar{x}_{cg} = \bar{x}_{ref}$

Methods for determining the magnitude of these maximum lift coefficients required to satisfy performance objectives are discussed in Part I as part of the overall sizing process of airplanes.

Class I methods for determining whether or not any given airplane design can achieve certain required maximum lift coefficients are given in Chapter 7 of Part II. The reader must take note of the fact that the effect of trim requirements was accounted for in Ch.7 of Pt.II by subtracting a 'token' increment from the untrimmed maximum lift coefficients. In this chapter Class II methods for estimating trimmed lift coefficients and trimmed maximum lift coefficients are presented. The material is organized as follows:

8.1 Prediction of lift coefficient versus angle of attack
8.2 Prediction of pitching moment versus lift coefficient
8.3 Prediction of trimmed lift and trimmed maximum lift coefficient

The methods are presented for the subsonic flow range. The reader is referred to specific sections of Ref.9 for those transonic and supersonic effects which are considered beyond the scope of this text.

8.1 PREDICTION OF LIFT COEFFICIENT VERSUS ANGLE OF ATTACK

In this section methods for predicting the variation of lift coefficient with angle of attack will be presented as follows:

8.1.1 Airfoil lift and maximum lift: flaps up
8.1.2 Airfoil lift and maximum lift: flaps down
8.1.3 Wing lift and maximum lift: flaps up
8.1.4 Wing lift and maximum lift: flaps down
8.1.5 Airplane lift and maximum lift: flaps up
8.1.6 Airplane lift and maximum lift: flaps down
8.1.7 Airplane lift in ground effect
8.1.8 Power effects on airplane lift

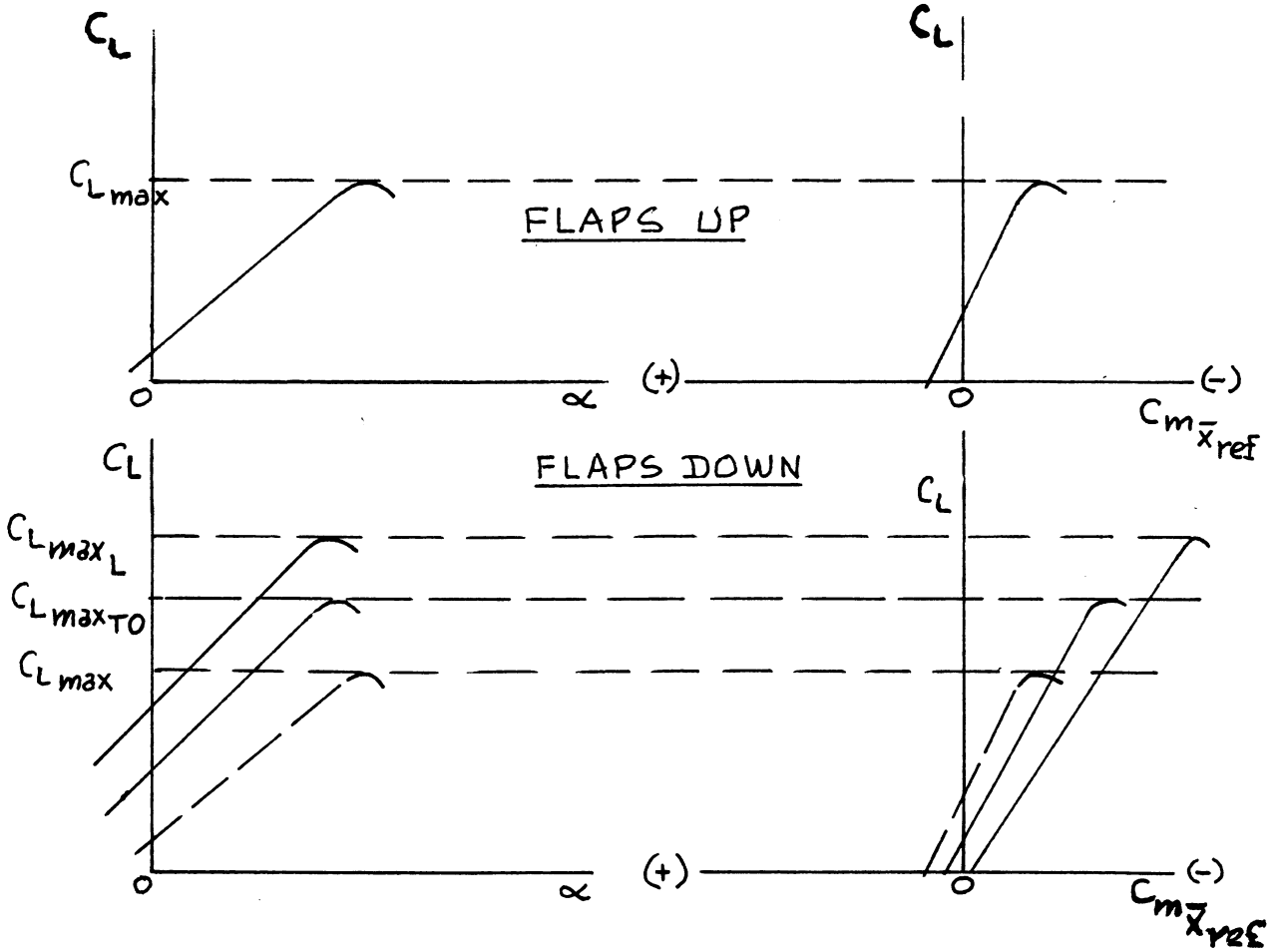

Figure 8.1 Fundamental Airplane Lift and Pitching Moment Characteristics

8.1.1 Airfoil Lift and Maximum Lift: Flaps Up

Figure 8.2 shows the relationship between airfoil lift coefficient and airfoil angle of attack which must be be determined with the methods to be presented in this Section. Key quantities needed in the construction of the airfoil c_l versus α curve are listed, with an indication of where methods for their estimation may be found.

8.1.1.1 Airfoil zero-lift angle of attack: α_{0_l}

Table 8.1 provides a summary of basic airfoil data from which α_{0_l} may be determined. Whenever possible, actual airfoil data should be used.

The airfoil zero-lift angle of attack may be estimated from Ref.9 (4.1.1.1) for arbitrary airfoils.

Experience shows that the airfoil zero-lift angle of attack is NOT a function of Reynold's number or Mach number in the subsonic speed range.

8.1.1.2 Airfoil lift curve slope: c_{l_α}

Table 8.1 provides a summary of basic airfoil data from which c_{l_α} may be determined. Whenever possible, actual airfoil data should be used.

The airfoil lift curve slope may be estimated from Ref.9 (4.1.1.2) for arbitrary airfoils.

Experience shows that the airfoil lift curve slope is dependent on Mach number in accordance with the Prandt-Glauert transformation:

For subsonic speeds:

$$c_{l_\alpha}\ \text{at M} = (c_{l_\alpha}\ \text{at M=0})/(1 - M^2)^{1/2} \qquad (8.1)$$

For supersonic speeds:

$$c_{l_\alpha}\ \text{at M} = 4/(M^2 - 1)^{1/2} \qquad (8.2)$$

For transonic speeds: use tunnel data.

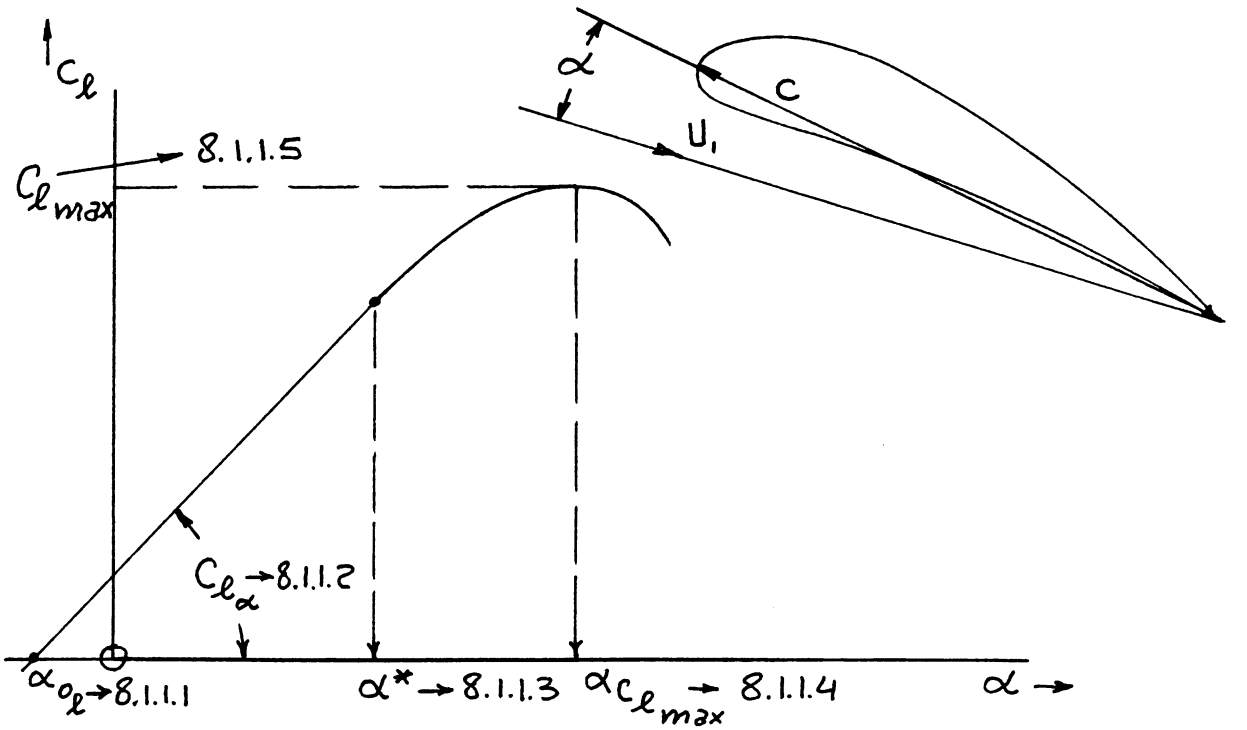

Figure 8.2 Airfoil Lift Coefficient Versus Angle of Attack Curve

Table 8.1a Experimental Low Speed Data for 4- and 5- Digit NACA Airfoils with a Smooth Leading Edge and for $R_N = 9 \times 10^6$ (Ref.16)

Airfoil	α_{o_ℓ} (deg)	c_{m_o}	c_{l_α} (deg^{-1})	a.c. (tenths c)	$\alpha_{c_{l_{max}}}$ (deg)	$c_{l_{max}}$	α^* (deg)
0006	0	0	.108	.250	9.0	.92	9.0
0009	0	0	.109	.250	13.4	1.32	11.4
1408	0.8	-.023	.109	.250	14.0	1.35	10.0
1410	-1.0	-.020	.108	.247	14.3	1.50	11.0
1412	-1.1	-.025	.108	.252	15.2	1.58	12.0
2412	-2.0	-.047	.105	.247	16.8	1.68	9.5
2415	-2.0	-.049	.106	.246	16.4	1.63	10.0
2418	-2.3	-.050	.103	.241	14.0	1.47	10.0
2421	-1.8	-.040	.103	.241	16.0	1.47	8.0
2424	-1.8	-.040	.098	.231	16.0	1.29	8.4
4412	-3.8	-.093	.105	.247	14.0	1.67	7.5
4415	-4.3	-.093	.105	.245	15.0	1.64	8.0
4418	-3.8	-.088	.105	.242	14.0	1.53	7.2
4421	-3.8	-.085	.103	.238	16.0	1.47	6.0
4424	-3.8	-.082	.100	.239	16.0	1.38	4.8
23012	-1.4	-.014	.107	.247	18.0	1.79	12.0
23015	-1.0	-.007	.107	.243	18.0	1.72	10.0
23018	-1.2	-.005	.104	.243	16.0	1.60	11.8
23021	-1.2	0	.103	.238	15.0	1.50	10.3
23024	-0.8	0	.097	.231	15.0	1.40	9.7

Table 8.1b Experimental Low Speed Data for 6- Digit NACA Airfoils with a Smooth Leading Edge and for $R_N = 9 \times 10^6$ (Ref.16)

Airfoil	α_{o_ℓ} (deg)	c_{m_o}	c_{l_α} (deg^{-1})	a.c. (tenths c)	$\alpha_{c_{l_{max}}}$ (deg)	$c_{l_{max}}$	α^* (deg)
63-006	0	.005	.112	.258	10.0	.87	7.7
63-009	0	0	.111	.258	11.0	1.15	10.7
63-206	-1.9	-.037	.112	.254	10.5	1.06	6.0
63-209	-1.4	-.032	.110	.262	12.0	1.40	10.8
63-210	-1.2	-.035	.113	.261	14.5	1.56	9.6
63_1-012	0	0	.116	.265	14.0	1.45	12.8
63_1-212	-2.0	-.035	.114	.263	14.5	1.63	11.4
63_1-412	-2.8	-.075	.117	.271	15.0	1.77	9.6
64-006	0	0	.109	.256	9.0	.8	7.2
64-009	0	0	.110	.262	11.0	1.17	10.0
64-206	-1.0	-.040	.110	.253	12.0	1.03	8.0
64-209	-1.5	-.040	.107	.261	13.0	1.40	8.9
64-210	-1.6	-.040	.110	.258	14.0	1.45	10.8
64_1-012	0	0	.111	.262	14.5	1.45	11.0
64_1-212	-1.3	-.027	.113	.262	15.0	1.55	11.0
64_1-412	-2.6	-.065	.112	.267	15.0	1.67	8.0

Table 8.1c Experimental Low Speed Data for 6- Digit NACA Airfoils with a Smooth Leading Edge and for $R_N = 9 \times 10^6$ (Ref.16)

Airfoil	α_{o_ℓ} (deg)	c_{m_o}	c_{l_α} (deg^{-1})	a.c. (tenths c)	$\alpha_{c_{l_{max}}}$ (deg)	$c_{l_{max}}$	α^* (deg)
65-006	0	0	.105	.258	12.0	.92	7.6
65-009	0	0	.107	.264	11.0	1.08	9.8
65-206	-1.6	-.031	.105	.257	12.0	1.03	6.0
65-209	-1.2	-.031	.106	.259	12.0	1.30	10.0
65-210	-1.6	-.034	.108	.262	13.0	1.40	9.6
65_1-012	0	0	.110	.261	14.0	1.36	10.0
65_1-212	-1.0	-.032	.108	.261	14.0	1.47	9.4
65_1-412	-3.0	-.070	.111	.265	15.5	1.66	10.5
63A010	0	.005	.105	.254	13.0	1.20	10.0
63A210	-1.5	-.040	.103	.257	14.0	1.43	10.0
64A010	0	0	.110	.253	12.0	1.23	10.0
64A210	-1.5	-.040	.105	.251	13.0	1.44	10.0
64A410	-3.0	-.080	.100	.254	15.0	1.61	10.0
64_1A212	-2.0	-.040	.100	.252	14.0	1.54	11.0
64_2A215	-2.0	-.040	.095	.252	15.0	1.50	12.0

8.1.1.3 Airfoil linear range angle of attack: α^*

Table 8.1 provides a summary of basic airfoil data from which α^* may be determined. Whenever possible, actual airfoil data should be used.

The airfoil linear range angle of attack may also be estimated from Ref.9 (4.1.1.3) for existing airfoils.

8.1.1.4 Airfoil angle of attack for maximum lift: $\alpha_{c_{l_{max}}}$

Table 8.1 provides a summary of basic airfoil data from which $\alpha_{c_{l_{max}}}$ may be determined. Whenever possible, actual airfoil data should be used.

The airfoil angle of attack for maximum lift may be estimated from Ref.9 (4.1.1.4) for existing airfoils.

8.1.1.5 Airfoil maximum lift coefficient: $c_{l_{max}}$

It has been found that airfoil maximum lift coefficient, $c_{l_{max}}$ depends upon the following parameters:

1. Leading edge shape as quantified by the so-called Δy parameter.
2. Maximum thickness and position of maximum thickness.
3. Maximum camber and position of maximum camber.
4. Reynold's number: $\rho c U_1 / \mu$
5. Mach number.

Figure 8.3 defines these parameters for an arbitrary airfoil.

The method is valid for a 'base Reynold's number' of 9×10^6 and for Mach numbers below 0.2. The effect of variations in Reynold's number and Mach number relative to this 'base' is accounted for in the method.

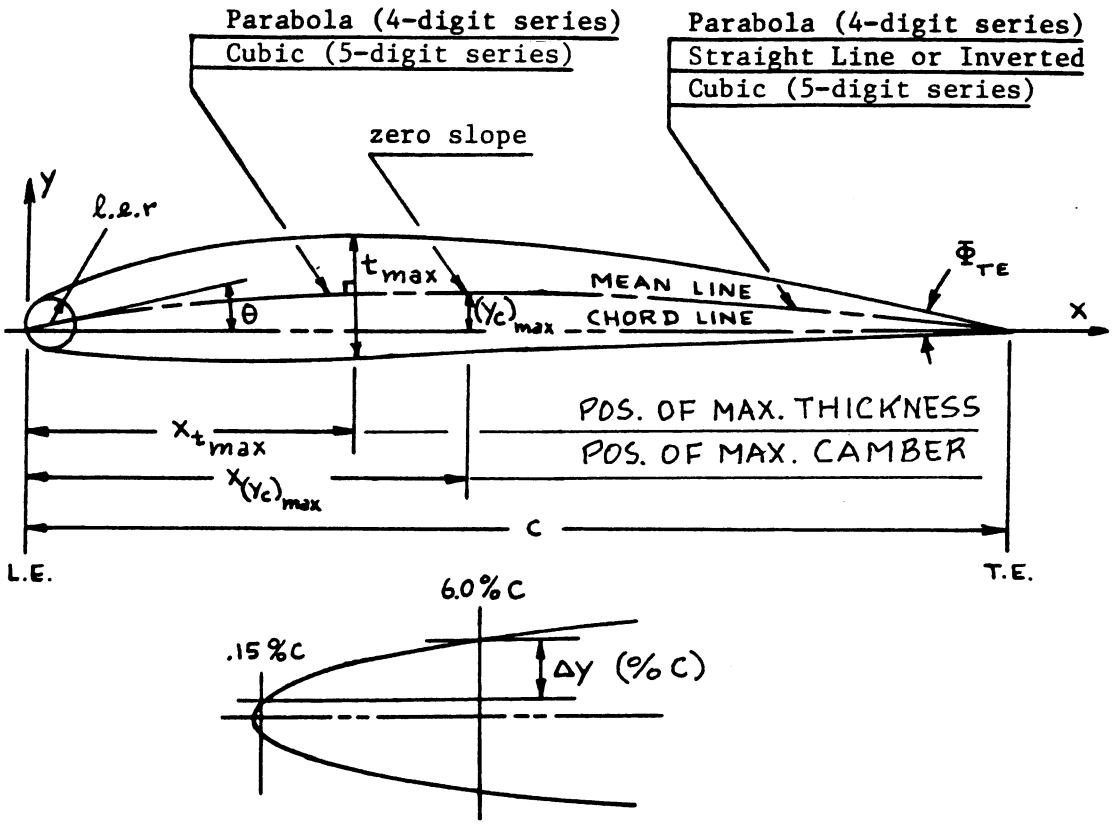

Figure 8.3 Airfoil Geometric Characteristics

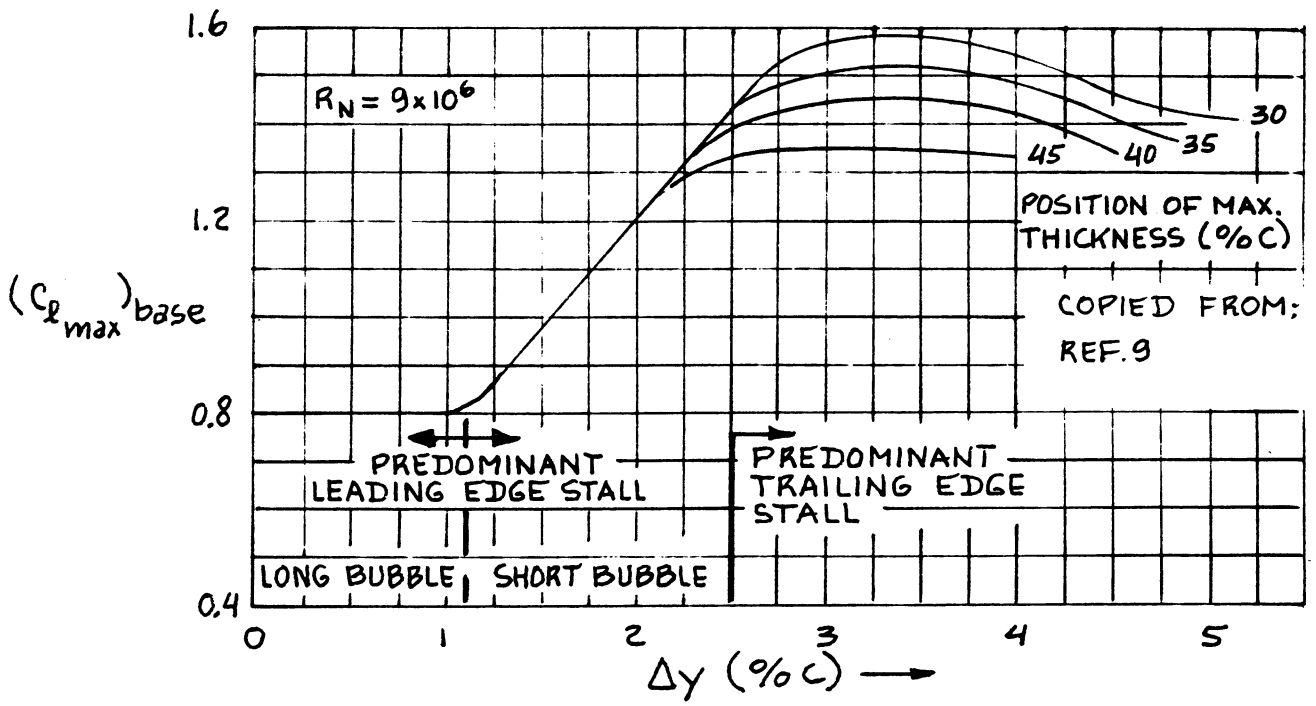

Figure 8.4 Basic Airfoil Maximum Lift Coefficient for Uncambered Airfoils

The maximum lift coefficient of an airfoil may be estimated from:

$$c_{l_{max}} = (c_{l_{max}})_{base} + \Delta_1 c_{l_{max}} + \Delta_2 c_{l_{max}} + \Delta_3 c_{l_{max}} + \Delta_3 c_{l_{max}} + \Delta_4 c_{l_{max}} + \Delta_5 c_{l_{max}} \quad (8.3)$$

where: $(c_{l_{max}})_{base}$ is the basic airfoil maximum lift coefficient, found from Figure 8.4 as a function of airfoil geometry. The parameter Δy in Figure 8.4 is defined in Figure 8.3. Table 8.2 lists example data for Δy.

$\Delta_1 c_{l_{max}}$ is the airfoil maximum lift increment due to camber and due to position of maximum camber. See Figure 8.5.

$\Delta_2 c_{l_{max}}$ is the airfoil maximum lift increment due position of maximum thickness. This increment is obtained from Figure 8.6. NOTE: when the position of maximum thickness is at 30 percent chord, this increment is ZERO.

$\Delta_3 c_{l_{max}}$ is the airfoil maximum lift increment due to Reynold's number: see Figure 8.7.

$\Delta_4 c_{l_{max}}$ is the airfoil maximum lift increment due to airfoil roughness. The basic roughness used is the so-called standard NACA roughness of 0.011 inch grit applied over the first 8 percent chord. Actual airplane roughness is much less severe. For airplanes with 'smooth' and 'clean' leading edges this increment is ZERO. Figure 8.8 provides data for finding this increment.

$\Delta_5 c_{l_{max}}$ is the section maximum lift increment due to Mach number (compressibility) Fig. 8.9 gives data for finding this increment

Whenever possible, actual data should be used. References 49, 50 and 51 should be consulted for specific data on airfoil maximum lift coefficients.

Table 8.1 contains $c_{l_{max}}$ data for a range of airfoils at the base Reynold's number of 9×10^6.

Table 8.2 Example Data for the Leading Edge Δy Parameter

Airfoil NACA	Position of max t/c perc. of c	Camber perc. of c	Position of max camber perc. of c	Δy perc. of c
0009	30	0	not appl.	2.35
1410	30	1.0	40	2.60
2415	30	2.0	40	3.80
4412	30	4.0	40	3.08
4315	30	4.0	30	3.30
4321	30	4.0	30	5.24
23012	30	1.8	13	3.03
23021	30	1.8	15	5.24
43012	30	3.7	15	3.08
63012	30	5.5	15	3.08
63-009	35	0	not appl.	2.00
63-209	35	1.1	50	2.00
63_1-012	35	0	not appl.	2.65
63_1-212	35	1.1	50	2.65
63_1-412	35	2.2	50	2.65
63_1-018	35	0	not appl.	3.95
63_1-618	35	3.3	40	3.95
64-108	40	0.55	50	1.70
64_1-112	40	0.55	50	2.52
64_3-013	40	0	not appl.	3.75
64_3-412	40	2.2	50	3.75
66-009	45	0	not appl.	1.65
66-205	45	1.1	50	1.65
66_2-018	45	0	not appl.	3.30
66_2-416	45	3.2	50	3.30

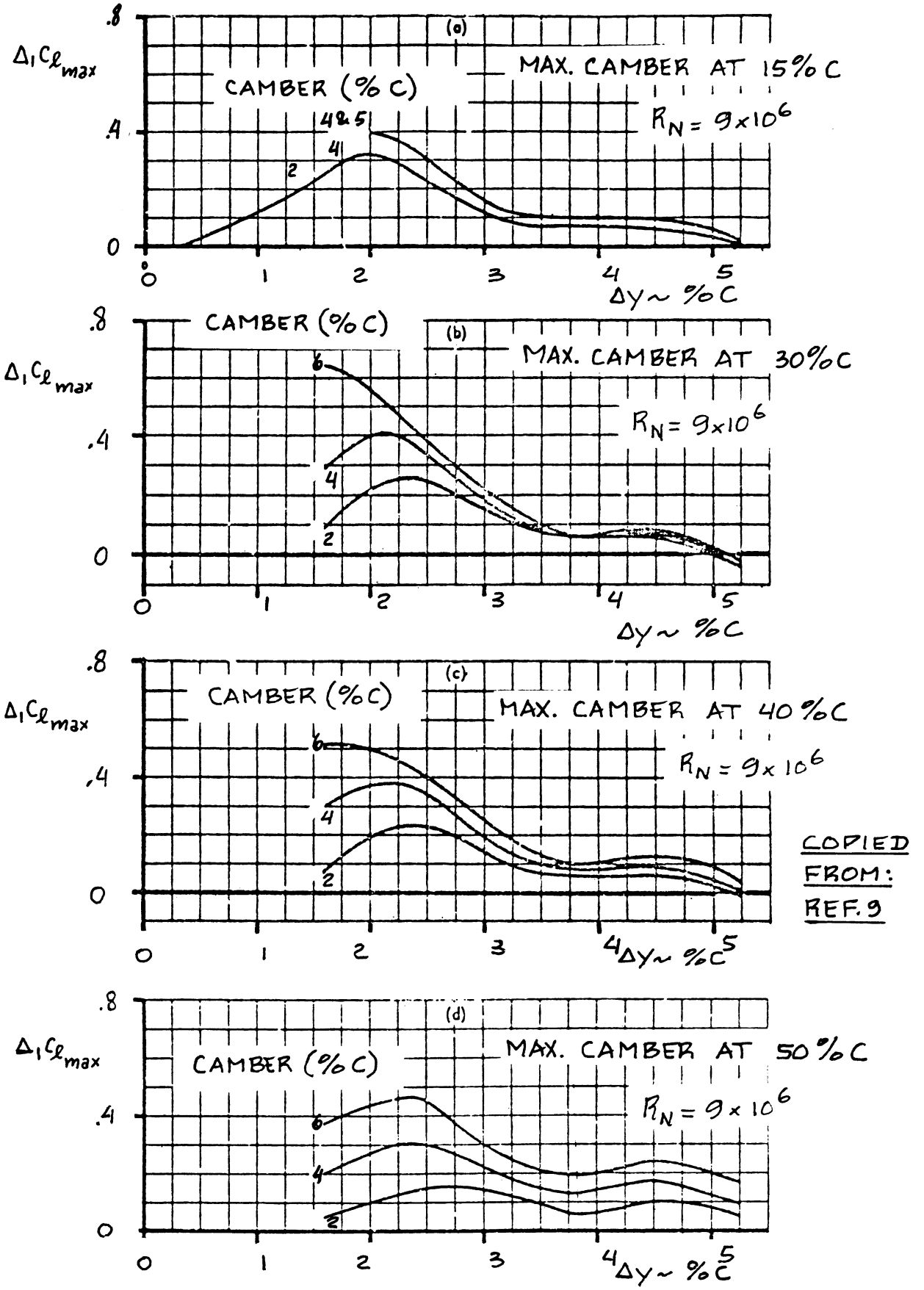

COPIED FROM: REF. 9

Figure 8.5 Effect of Camber on Maximum lift

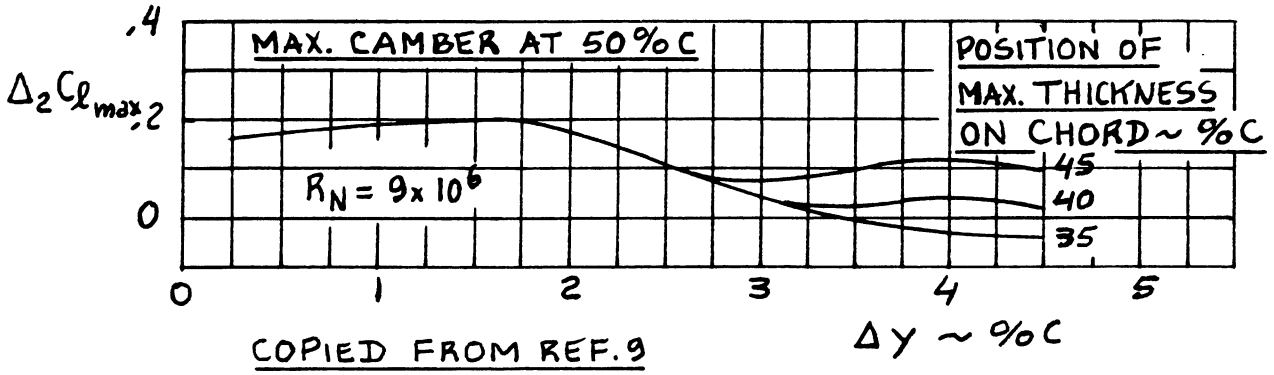

Figure 8.6 Effect of Maximum Thickness Position on Maximum Lift

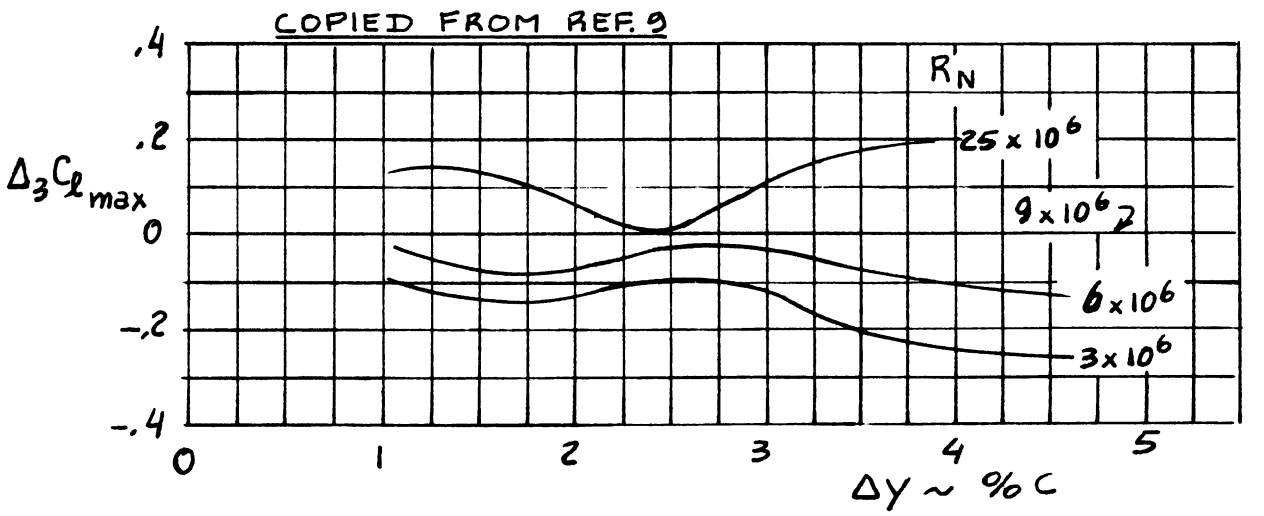

Figure 8.7 Effect of Reynold's Number on Maximum Lift

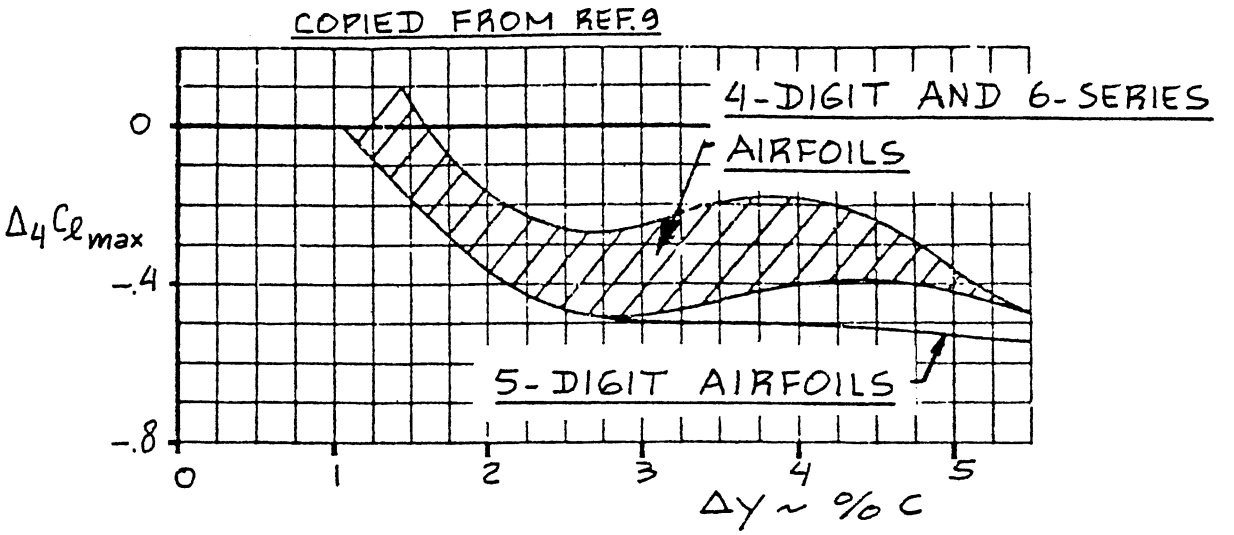

Figure 8.8 Effect of Surface Roughness on Maximum Lift

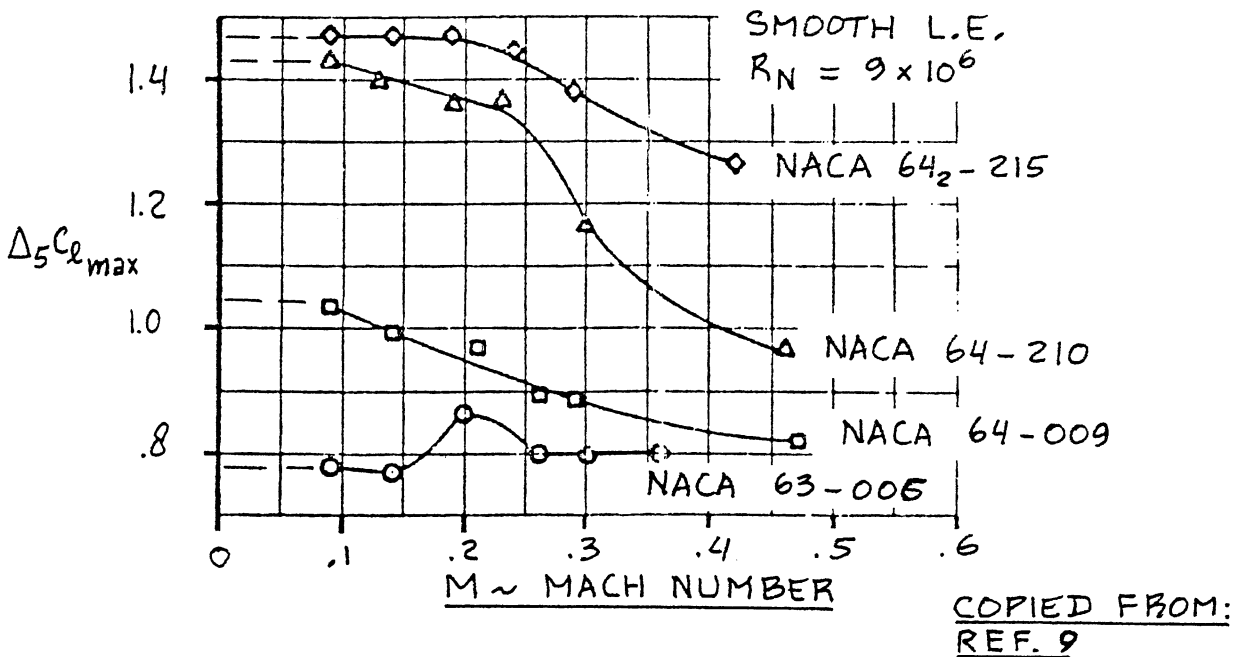

Figure 8.9 Effect of Mach Number on Maximum Lift

8.1.1.6 Construction of airfoil lift curve: flaps up

All ingredients needed to construct the flaps-up airfoil c_l versus α curve are now available. The flaps-up curve in Figure 8.2 can therefore be constructed. Figure 8.10 shows how this is done in a step-by-step manner. The fairing between α^* and $\alpha_{c_{l_{max}}}$ is done with the help of a french curve. The behavior of the lift curve just before and just after stall depends on Reynold's number. Reference 49 and Ref.9 (4.1.1.3) contain more information.

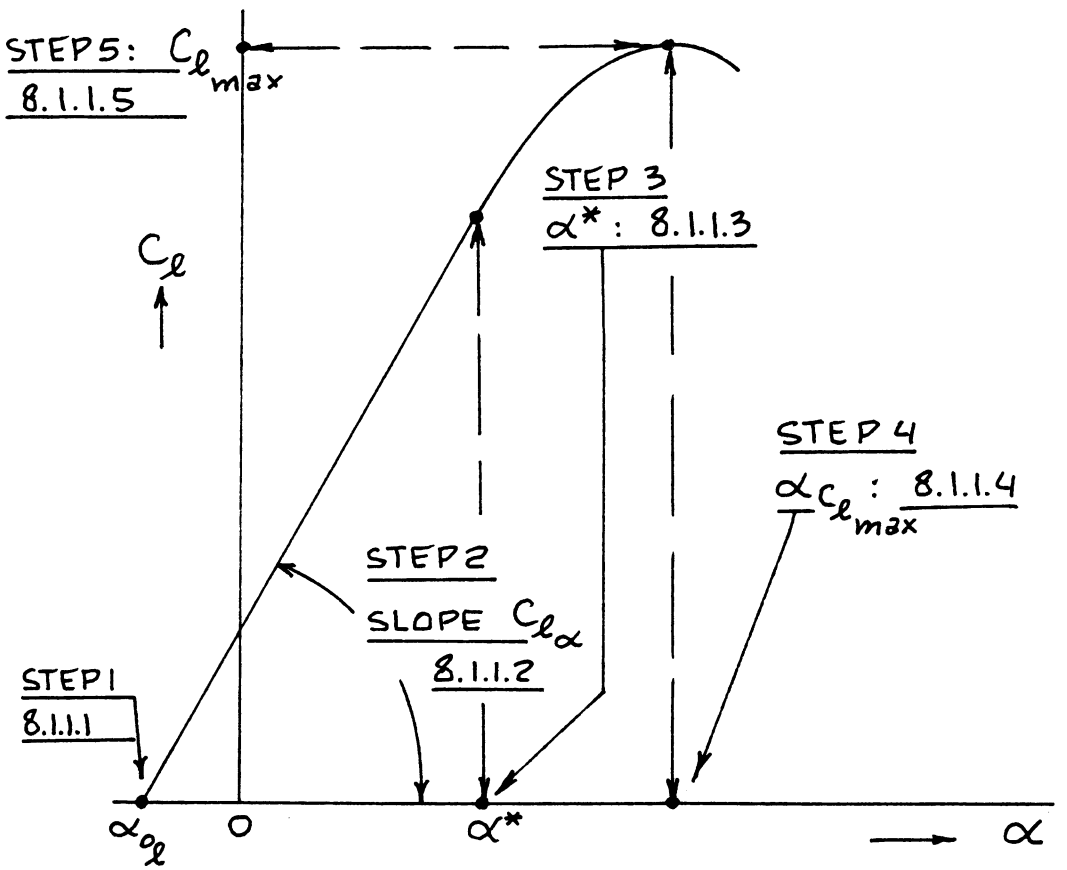

Figure 8.10 Construction of Airfoil Lift Versus α Curve

8.1.2 Airfoil Lift and Maximum Lift: Flaps Down

Figure 8.11 shows the comparison between flaps-up and flaps-down airfoil lift characteristics. Key quantities which are required to determine the flaps-down airfoil lift characteristics are listed with an indication of where methods for their estimation may be found.

8.1.2.1 Airfoil lift increment due to flaps: Δc_l

The airfoil incremental lift coefficient increment due to flaps, Δc_l depends on the type of flaps used.

Methods are presented for the following flap types:

A) Trailing Edge Flaps

a) Plain flaps
b) Single-slotted flaps
c) Fowler flaps
d) Double slotted flaps
e) Split flaps

B) Leading Edge Flaps

a) Nose flaps
b) Krueger flaps
c) Leading edge slats
d) Spoilers

Note: If a wing is equipped with any combination of flaps as defined under A) or B) it is acceptable in preliminary design to add the increments due to each individual flap type. The reader should be aware that this can result in over-prediction of high lift capability!

A) Trailing Edge Flaps

a) Plain flaps

Figure 8.12 defines the geometry of a plain flap. The airfoil incremental lift coefficient due to a plain flap deflection with a sealed gap is given by:

$$\Delta c_l = (\delta_f)\{c_{l_\delta} / (c_{l_\delta})_{theory}\}(c_{l_\delta})_{theory} k' \qquad (8.4)$$

where: k' is a correction factor which accounts for non-linearities at high flap deflections: see Figure 8.13.

$(c_{l_\delta})_{theory}$ is found from Figure 8.14. It accounts for flap size and for thickness ratio.

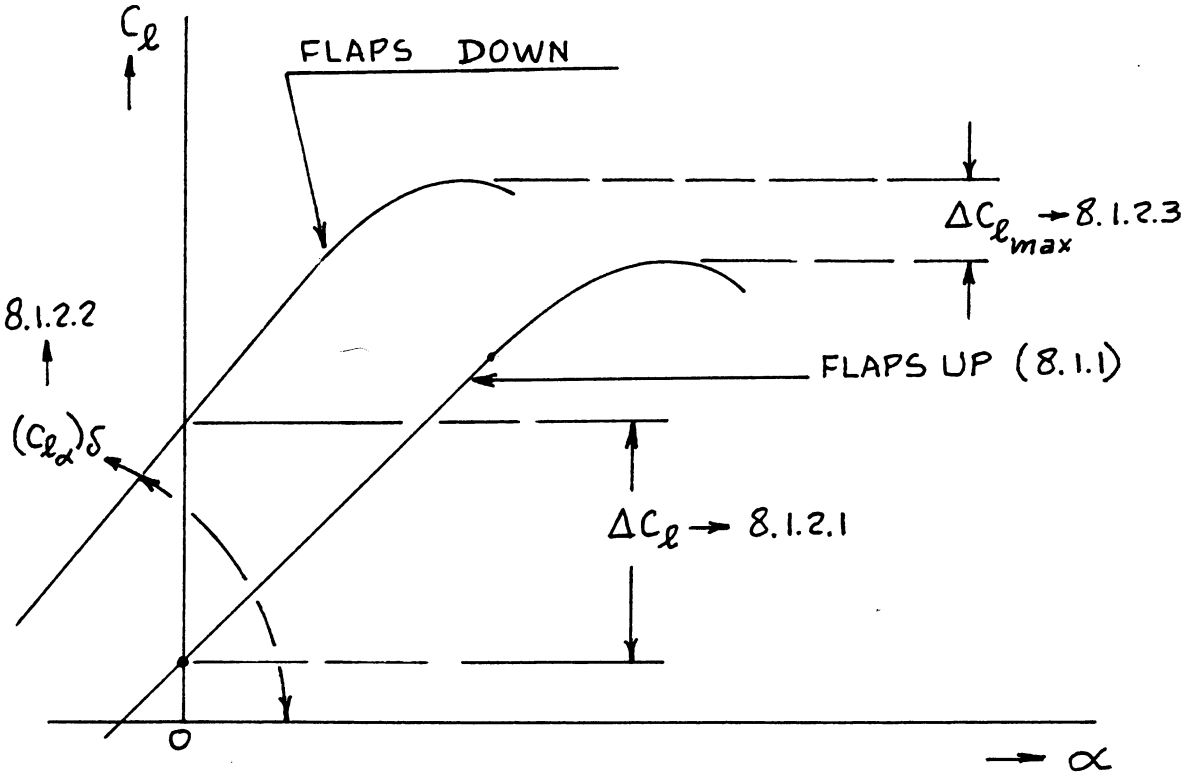

Figure 8.11 Fundamental Airfoil Lift Versus α Curve with the Flaps Down

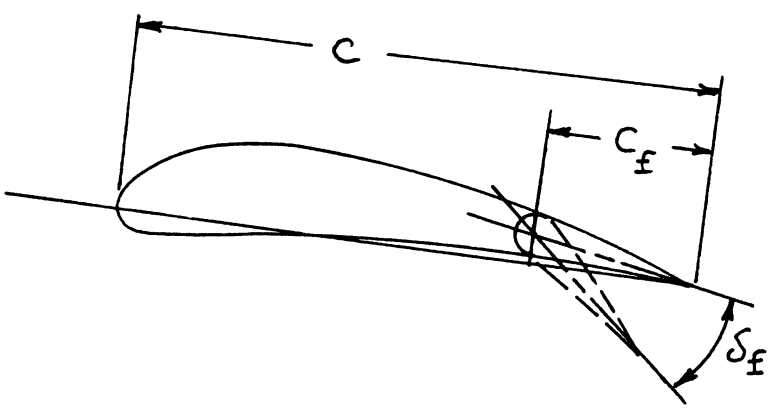

Figure 8.12 Plain Flap Geometry

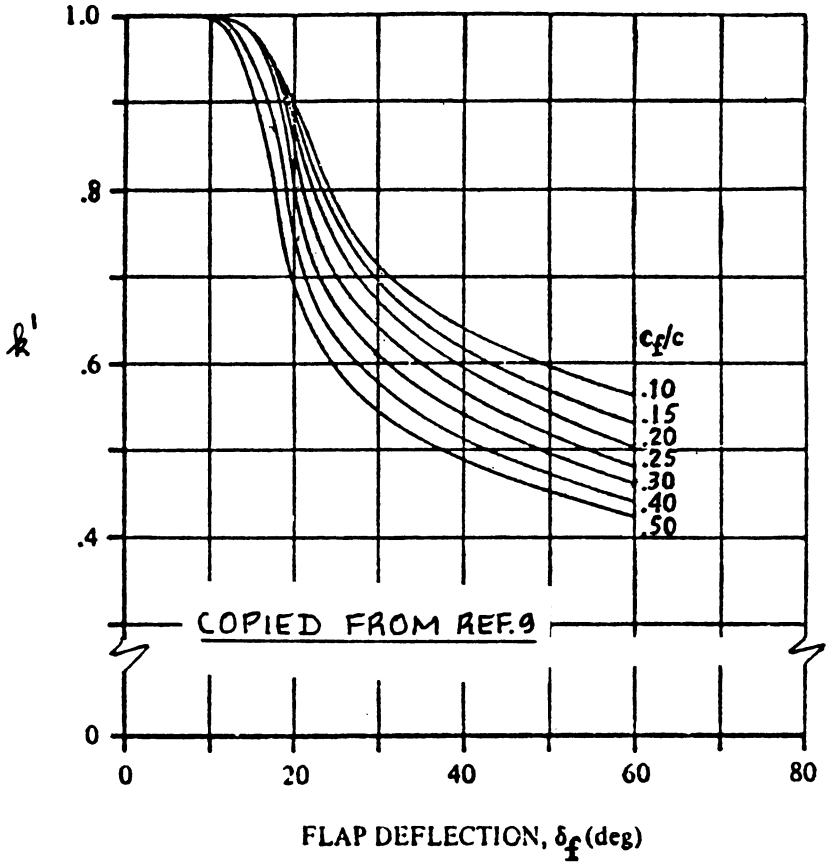

Figure 8.13 Correction Factor for Nonlinear Lift Behavior of Plain Flaps

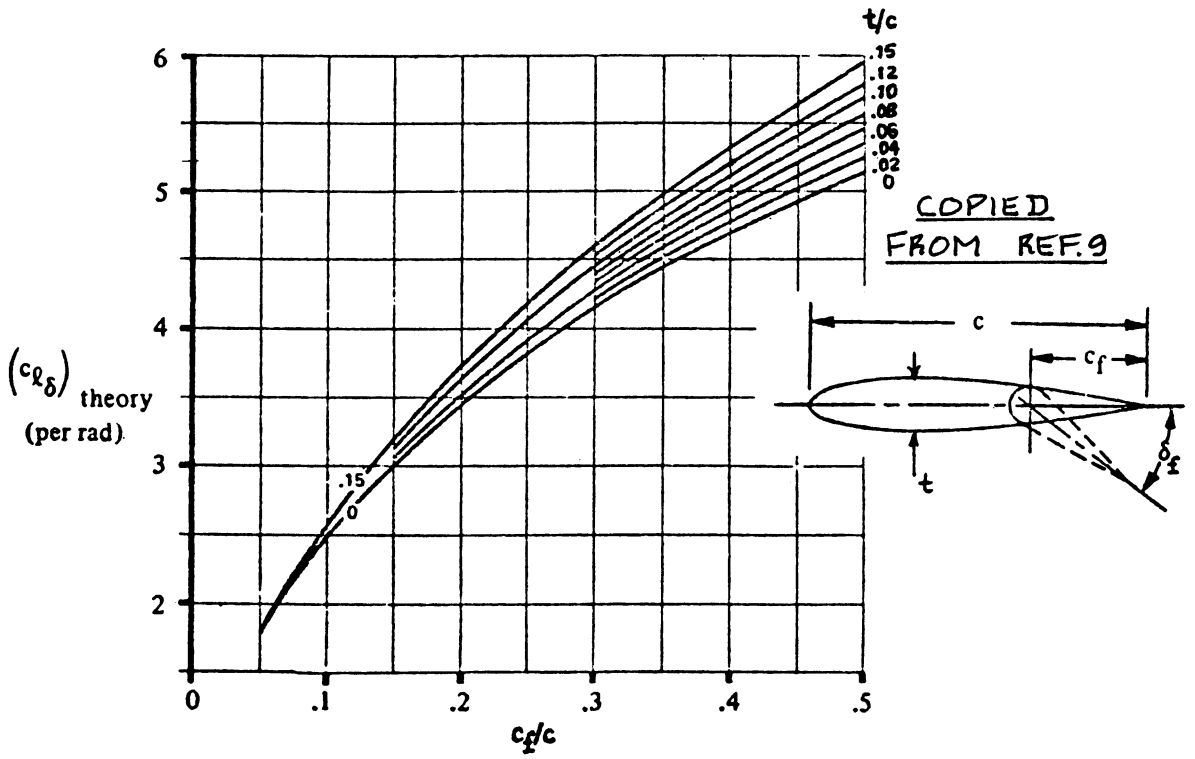

Figure 8.14 Lift Effectiveness of a Plain Flap

$\{c_{l_\delta}/(c_{l_\delta})_{theory}$ is found from Figure 8.15.

δ_f is the flap deflection in rad.

Note: for plain flaps with open gaps (not sealed) Reference 49 should be consulted.

b) Single-slotted flaps

Figure 8.16 defines the geometry of a single-slotted flap. The airfoil incremental lift coefficient due to a single-slotted flap deflection is given by:

$$\Delta c_l = (c_{l_\alpha})(\alpha_\delta)(\delta_f) \qquad (8.5)$$

where: c_{l_α} is the airfoil lift-curve-slope with the flaps up. It is found from 8.1.1.2.

α_δ is the airfoil lift effectiveness parameter found from Figure 8.17.

c) Fowler flaps

Figure 8.18 defines the geometry of a Fowler flap. The airfoil incremental lift coefficient due to a Fowler flap deflection is given by:

$$\Delta c_l = (c_{l_\alpha})(\alpha_\delta)(c'/c)(\delta_f) \qquad (8.6)$$

where: (c'/c) is defined in Figure 8.18. All other quantities in Eqn.(8.6) are those listed under b) Single-slotted flaps.

d) Double slotted flaps

Figure 8.19 defines the geometry of double slotted flaps: Types I and II.

Type I:

The airfoil incremental lift coefficient due to a Type I double slotted flap deflection is given by:

$$\Delta c_l = \eta_1 (c_{l_{\delta_{f_1}}})(\delta_{f_1})\{(c + c_1)/c\} + \eta_2 (c_{l_{\delta_{f_2}}})(\delta_{f_2})(c'/c) \qquad (8.7)$$

where: η_1 and η_2 are found from Figure 8.20 using c_1/c

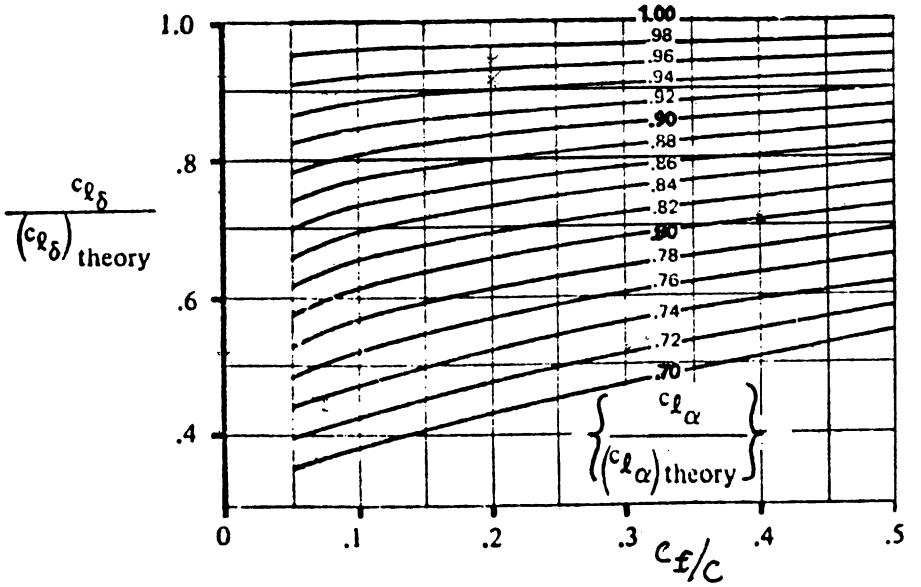

Figure 8.15 Correction Factor for Plain Flap Lift

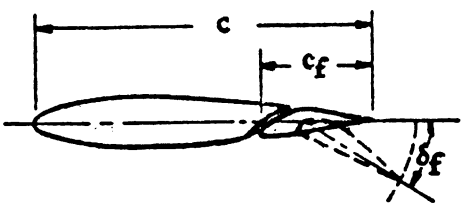

Figure 8.16 Single Slotted Flap Geometry

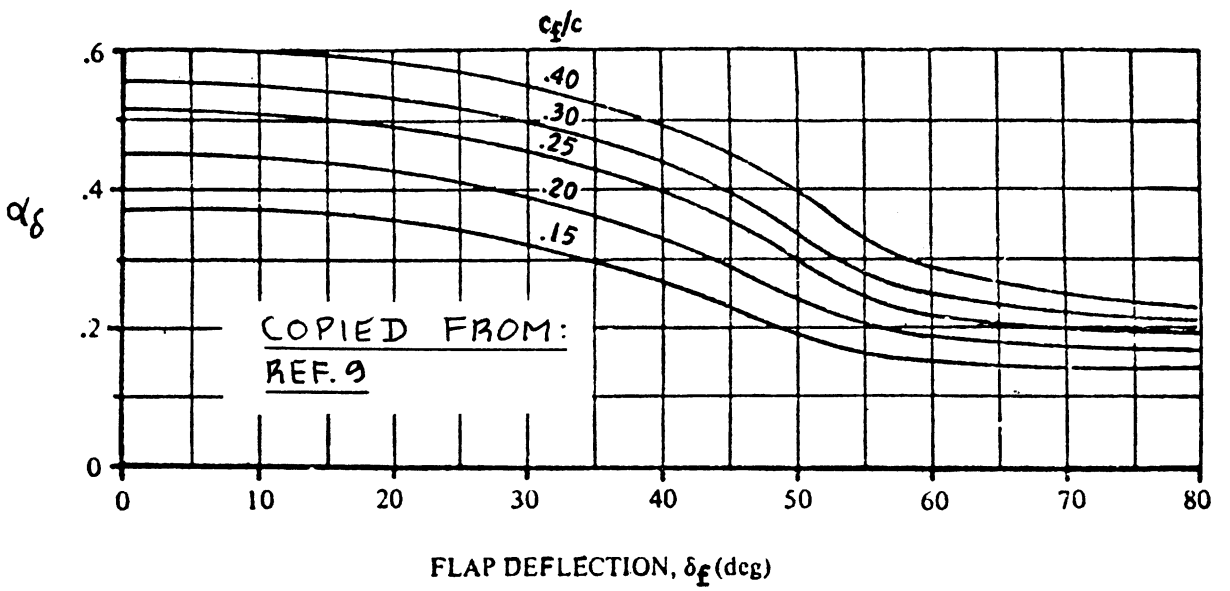

Figure 8.17 Lift Effectiveness of a Single Slotted Flap

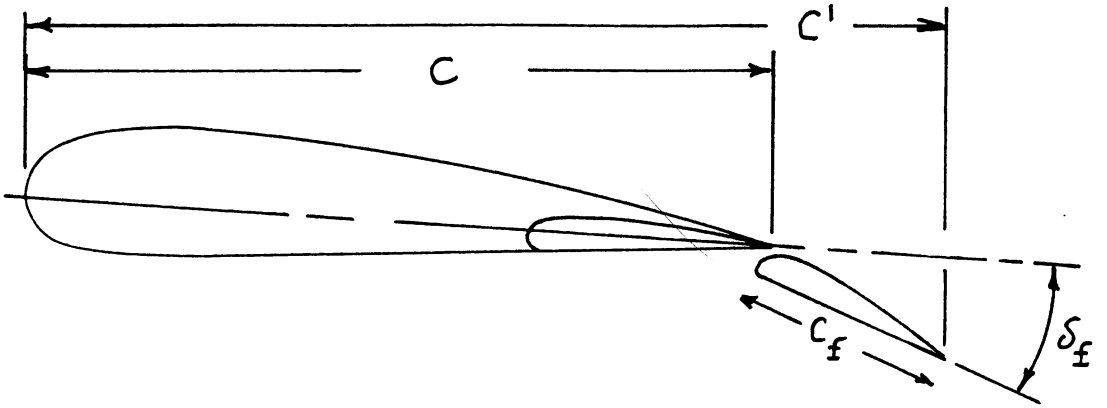

Figure 8.18 Fowler Flap Geometry

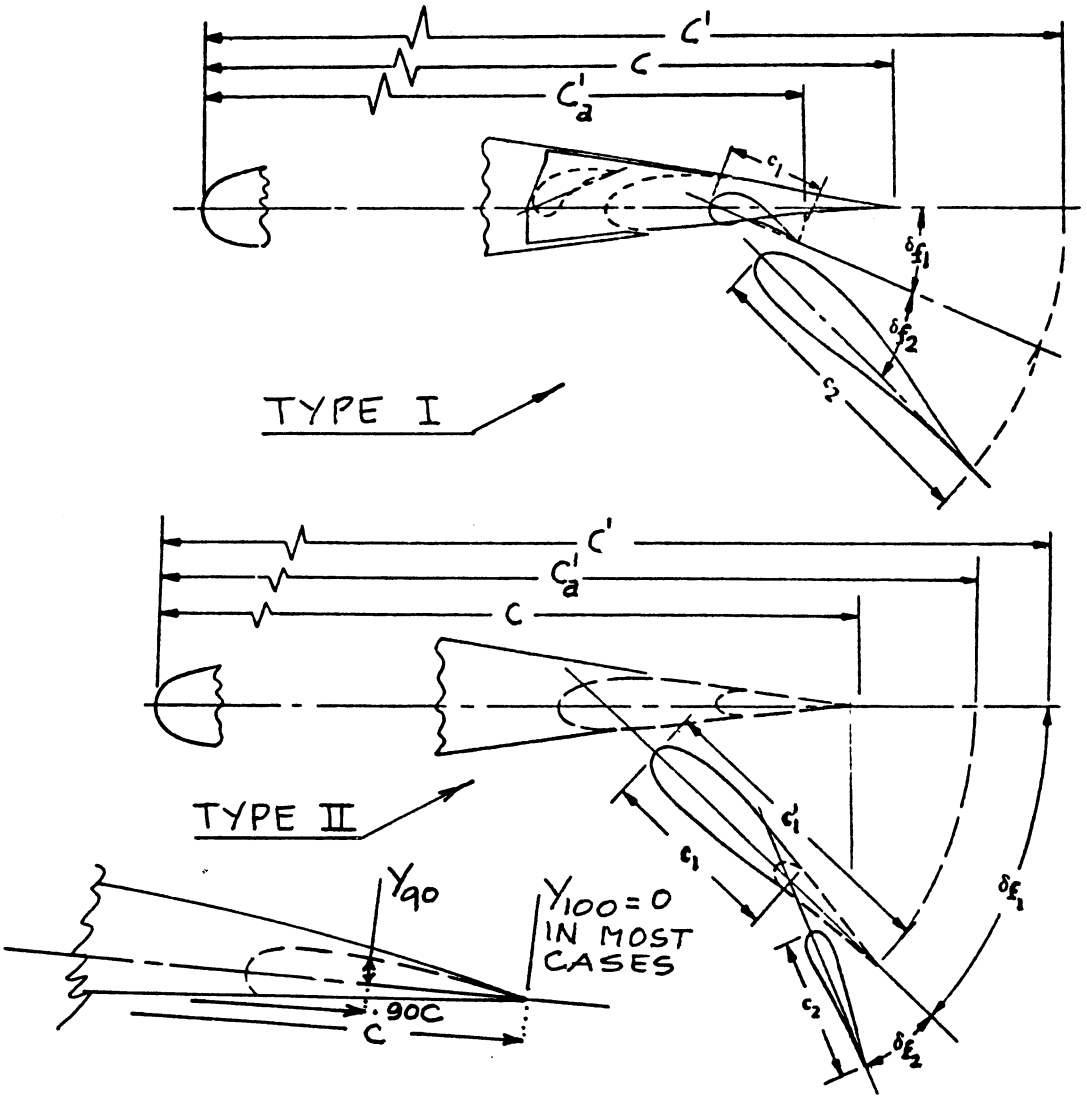

Figure 8.19 Double Slotted Flap Geometry

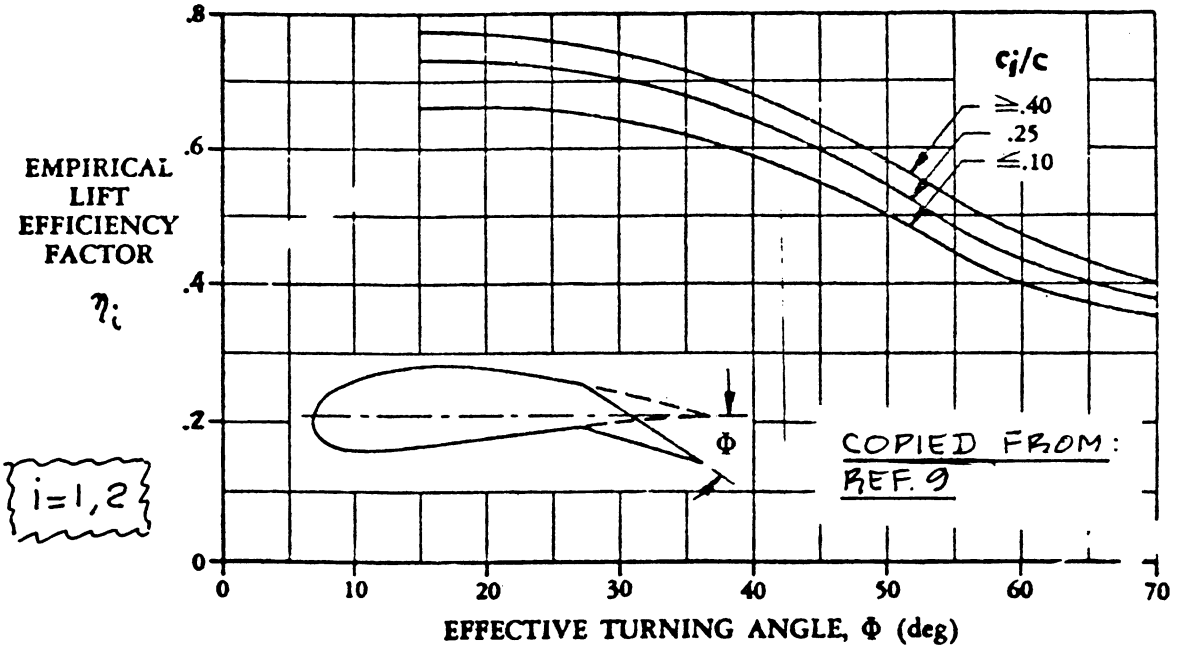

Figure 8.20 Lift Effectiveness for Slotted Flaps

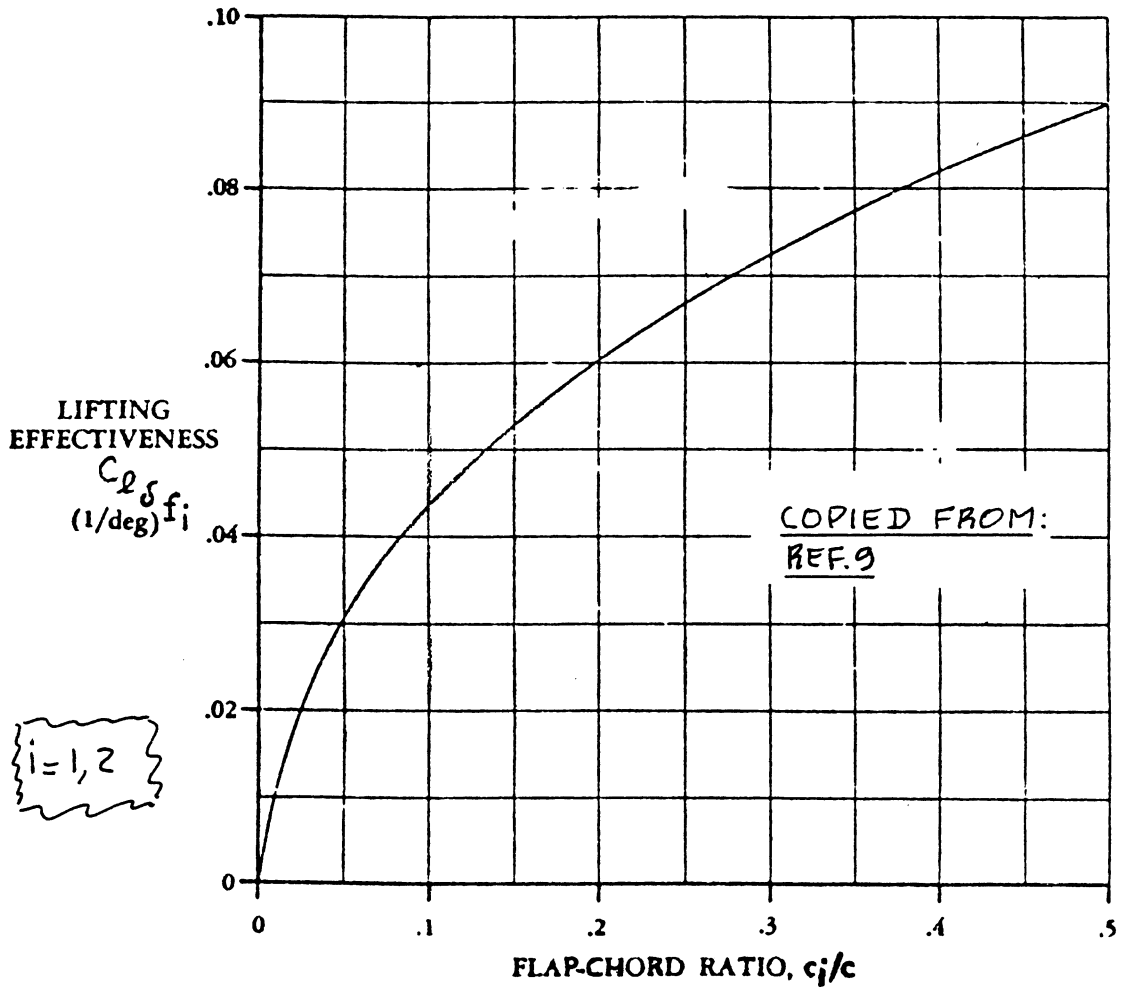

Figure 8.21 Lift Effectiveness for Trailing Edge Flaps

and c_2/c respectively. The effective turning angle, Φ is defined as:

for vane: $$\Phi = \delta_{f_1} + \Phi_{TE_{upper}} \quad (8.8)$$

for flap segment: $$\Phi = \delta_{f_1} + \delta_{f_2} + \Phi_{TE_{upper}} \quad (8.9)$$

with: $$\Phi_{TE_{upper}} = \arctan\{(10)(y_{90} - y_{100})/c\} \quad (8.10)$$

where: y_{90} and y_{100} are also defined in Figure 8.19.

$c_{l_{\delta_{f_1}}}$ and $c_{l_{\delta_{f_2}}}$ are found from Figure 8.21 for c_1/c and c_2/c respectively.

Type II:

The incremental lift coefficient due to a Type II double-slotted flap is given by:

$$\Delta c_l = \eta_1 (c_{l_{\delta_{f_1}}})(\delta_{f_1})(c_a'/c) + \eta_2 \eta_t (c_{l_{\delta_{f_2}}})(\delta_{f_2})\{1 + (c'-c_a')/c\} \quad (8.11)$$

where: η_t is found from Figure 8.22.

c' and c_a' are defined in Figure 8.19.

all other quantities are defined under Type I.

e) Split flaps

Figure 8.23 defines the geometry for a split flap. The incremental lift coefficient due to a split flap is given by:

$$\Delta c_l = (c_{l_\alpha})(\alpha_{\delta_{sf}})(\delta_f) \quad (8.12)$$

where: c_{l_α} is found from 8.1.1.2.

$\alpha_{\delta_{sf}}$ is found from Figure 8.24.

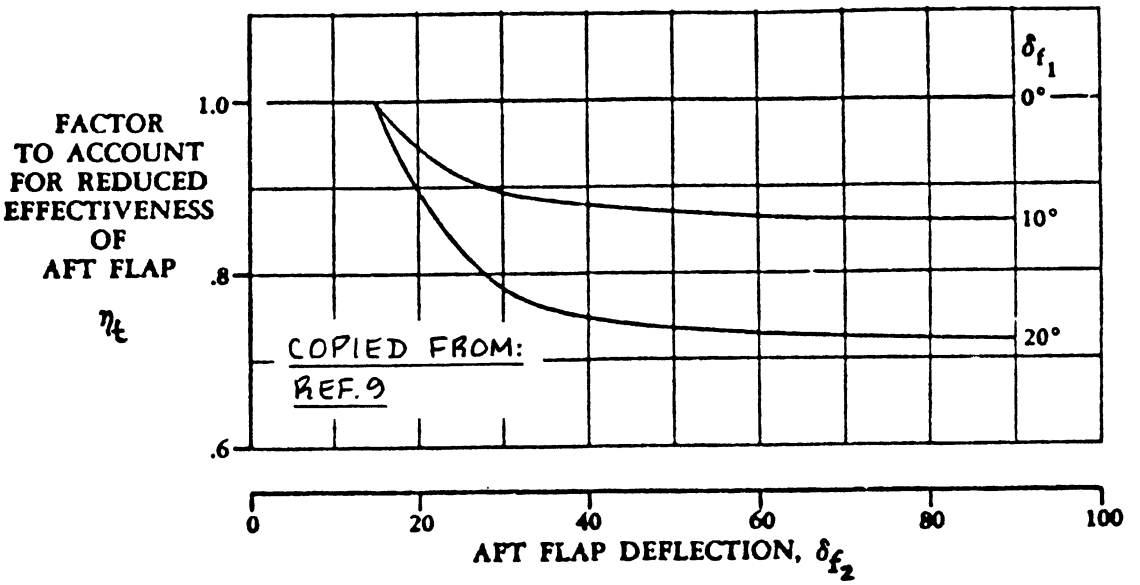

Figure 8.22 Correction Factor for Aft Flap

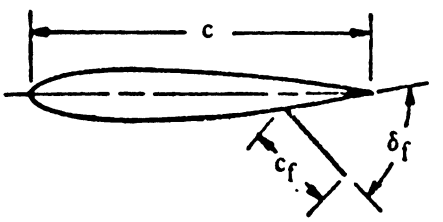

Figure 8.23 Split Flap Geometry

Figure 8.24 Lift Effectiveness of a Split Flap

B) Leading Edge Flaps

a) Nose flaps

Figure 8.25 defines the geometry for a nose flap. The airfoil incremental lift coefficient due to a nose flap deflection is given by:

$$\Delta c_l = c_{l_\delta} \delta_f \qquad (8.13)$$

where: c_{l_δ} is the leading edge flap effectiveness parameter for a nose flap: see Figure 8.26. Use c_f/c as the flap-chord to wing-chord ratio.

δ_f is the nose flap deflection in degrees as defined in Figure 8.25.

b) Krueger Flaps

Figure 8.27 defines the geometry for a Krueger flap. The airfoil incremental lift coefficient due to a Krueger flap is given by:

$$\Delta c_l = c_{l_\delta} \delta_f (c'/c) \qquad (8.14)$$

where: c_{l_δ} is the leading edge flap effectiveness parameter for a Krueger flap: see Figure 8.26. Use c_f/c' as the flap-chord to wing-chord ratio.

δ_f is the Krueger flap deflection in degrees as defined in Figure 8.27.

c'/c is as defined in Figure 8.27.

c) Leading Edge Slats

Figure 8.28 defines the geometry of a leading edge slat. The airfoil incremental lift coefficient due to a leading edge slat is given by:

$$\Delta c_l = c_{l_\delta} \delta_f (c'/c) \qquad (8.15)$$

where: c_{l_δ} is the leading edge flap effectiveness parameter for a leading edge slat as found from Figure 8.26 by using c_f/c' as the leading-edge-slat-chord to wing-chord ratio.

δ_f is the slat deflection in deg.: see Fig. 8.28.

c'/c is as defined in Figure 8.28.

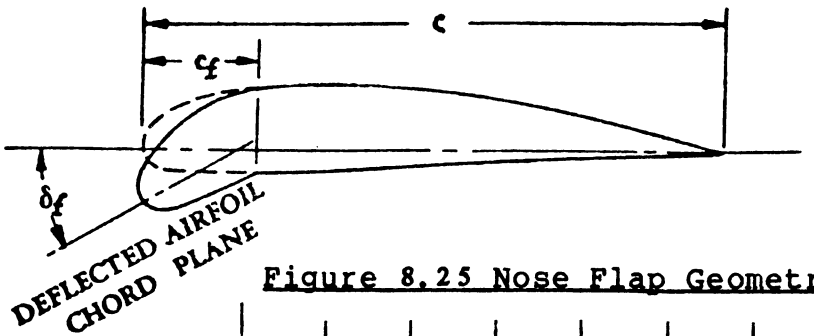

Figure 8.25 Nose Flap Geometry

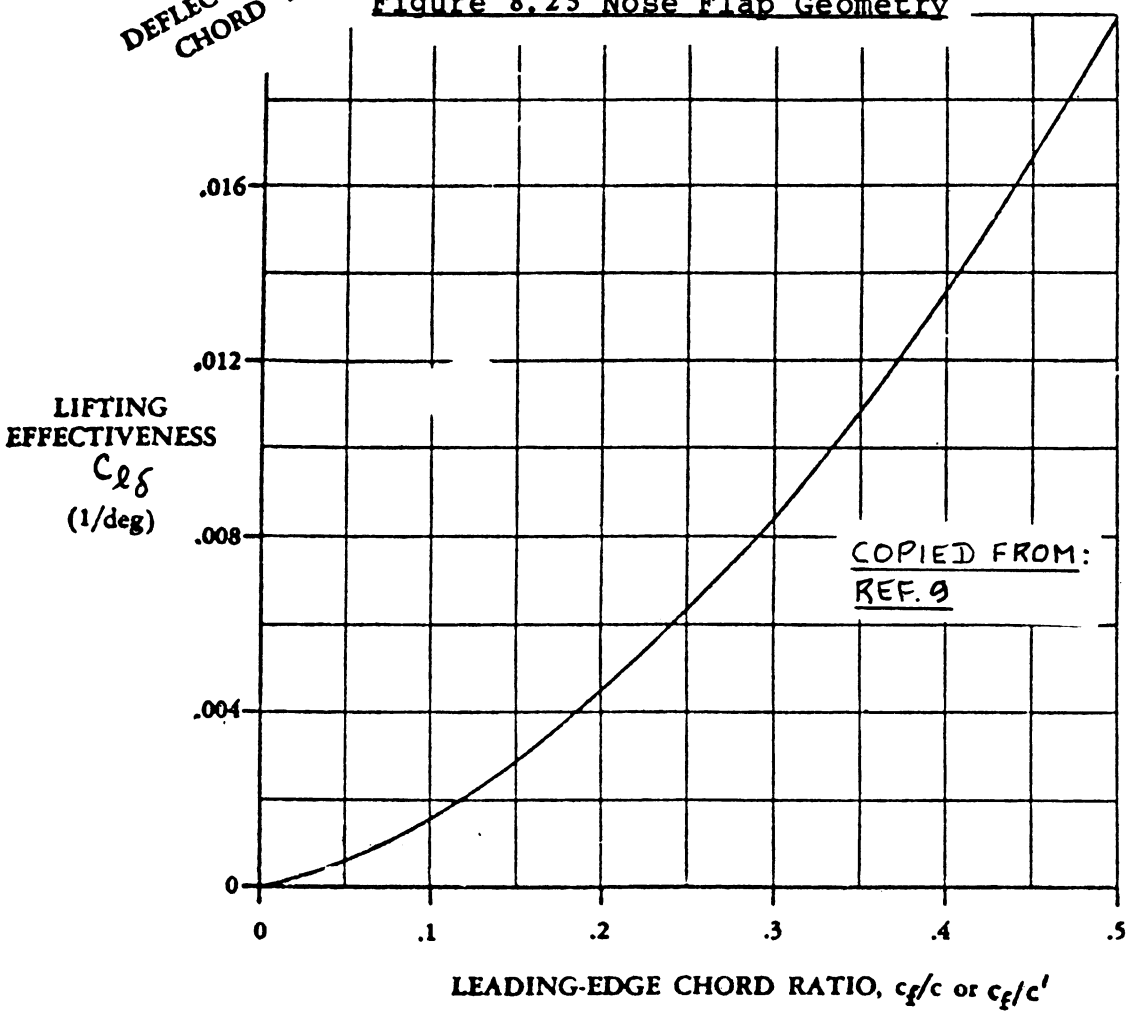

Figure 8.26 Lift Effectiveness of a Leading Edge Flap

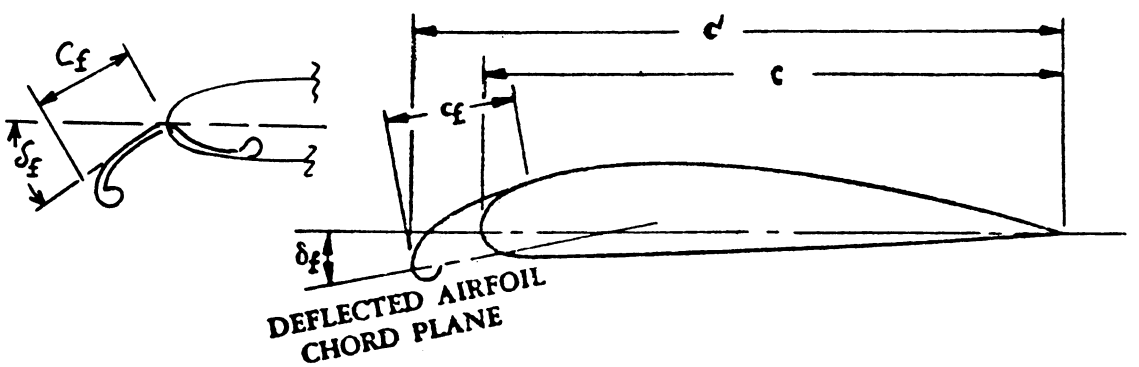

Figure 8.27 Krueger Flap Geometry

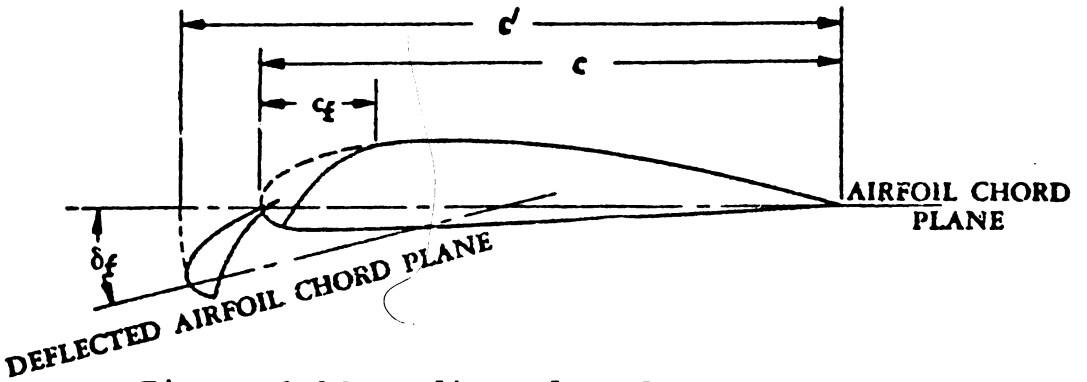

Figure 8.28 Leading Edge Slat Geometry

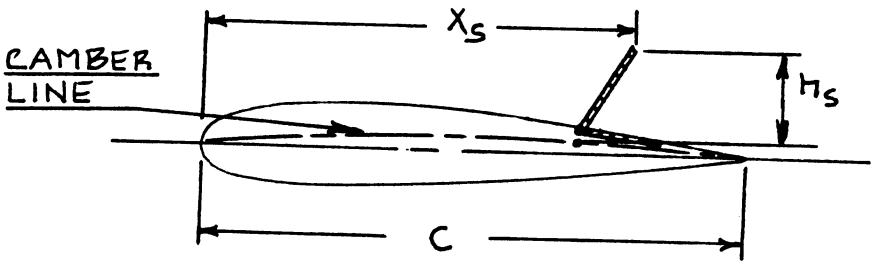

Figure 8.29 Spoiler Geometry

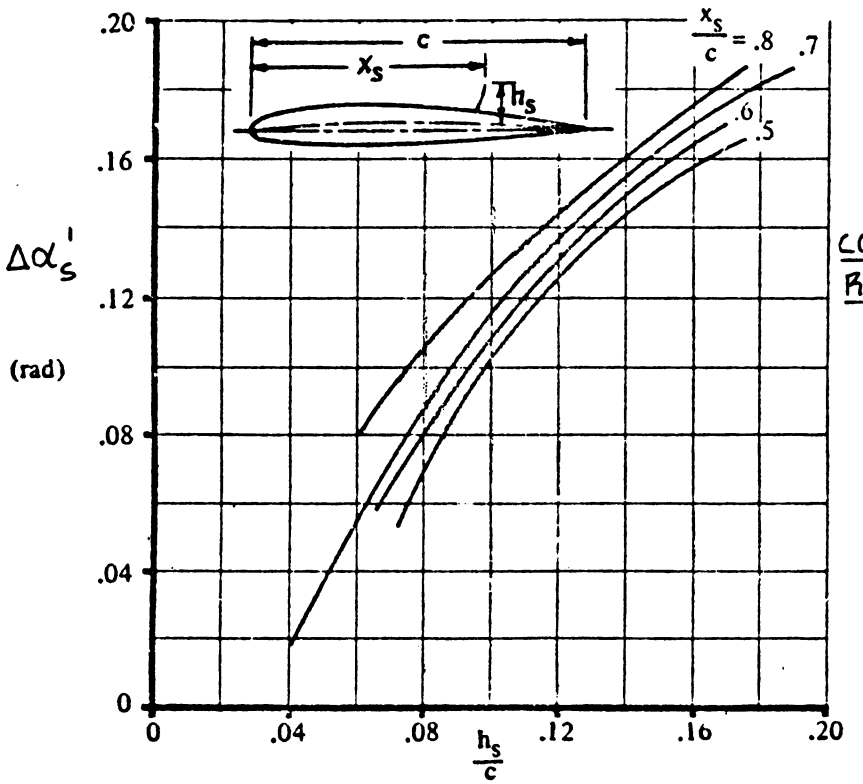

COPIED FROM: REF. 9

Figure 8.30 Lift Effectiveness of a Spoiler

d) Spoilers

Figure 8.29 defines the geometry of a spoiler. Observe that the spoiler is defined by chord position and by vertical position of the spoiler trailing edge. The location of the spoiler hinge line is not important.

The airfoil incremental lift coefficient due to a spoiler deflection is given by:

$$\Delta c_l = -c_{l_\alpha} \Delta\alpha_s' \qquad (8.16)$$

where: c_{l_α} is the unflapped airfoil lift curve slope as found from 8.1.1.2

$\Delta\alpha_s'$ is the spoiler lift effectiveness parameter as found from Figure 8.30.

8.1.2.2 Airfoil lift curve slope due to flaps: $(c_{l_\alpha})_\delta$

As long as the chord length of a flapped airfoil does not change, its lift curve slope does not change either. However, as seen from Figures 8.12, 8.16, 8.19, 8.23, 8.27, 8.28 and 8.29 the flapped airfoil chord is normally larger than the unflapped airfoil chord. For that reason, the flapped airfoil lift curve slope is given by:

$$(c_{l_\alpha})_\delta = (c'/c)c_{l_\alpha} \qquad (8.17)$$

where: c is the chord of the unflapped airfoil

c' is the chord of the flapped airfoil as defined in Figs 8.12, 8.16, 8.23, 8.27, 8.28 or 8.30.

c_{l_α} is the unflapped airfoil lift curve slope as found from 8.1.1.2.

Note: spoiler deflections will be assumed not to alter the lift curve slope of an airfoil.

8.1.2.3 Airfoil maximum lift increment due to flaps: $\Delta c_{l_{max}}$

The magnitude of the maximum lift increment due to flaps depends on the type of flaps used. Methods are presented for trailing edge flaps as well as for leading edge flaps.

A. Trailing Edge Flaps

The airfoil incremental, maximum lift coefficient due to trailing edge flaps is given by:

$$\Delta c_{l_{max}} = k_1 k_2 k_3 (\Delta c_{l_{max}})_{base} \qquad (8.18)$$

where: $(\Delta c_{l_{max}})_{base}$ is the airfoil incremental, maximum lift coefficient due to flaps as determined from Figure 8.31. Note that the data in Figure 8.31 are based on a 25 percent reference flap-chord to airfoil chord ratio AND on a reference flap deflection angle defined in Figure 8.33.

k_1 is a factor which accounts for flap-chord to airfoil chord ratios different from 25 percent. It can be found from Figure 8.32.

k_2 is a factor which accounts for flap angles different from the reference flap angle. It can be found from Figure 8.33.

k_3 is a factor which accounts for flap motion as a function of flap deflection. It can be found from Figure 8.34.

B) Leading Edge Flaps

The airfoil incremental, maximum lift coefficient due to leading edge flaps is given by:

$$\Delta c_{l_{max}} = (c_{l_{\delta_{max}}}) \eta_{max} \delta_f (c'/c) \qquad (8.19)$$

where: $c_{l_{\delta_{max}}}$ is the theoretical maximum lifting effectiveness as found from Figure 8.35.

η_{max} is an empirical factor which accounts for the ratio of airfoil leading edge radius to airfoil thickness of the unflapped airfoil. It is obtained from Figure 8.36.

η_δ is an empirical factor which accounts for the difference between the actual leading edge flap deflection and the reference deflection. It is found from Figure 8.37.

δ_f is the leading edge flap deflection angle in

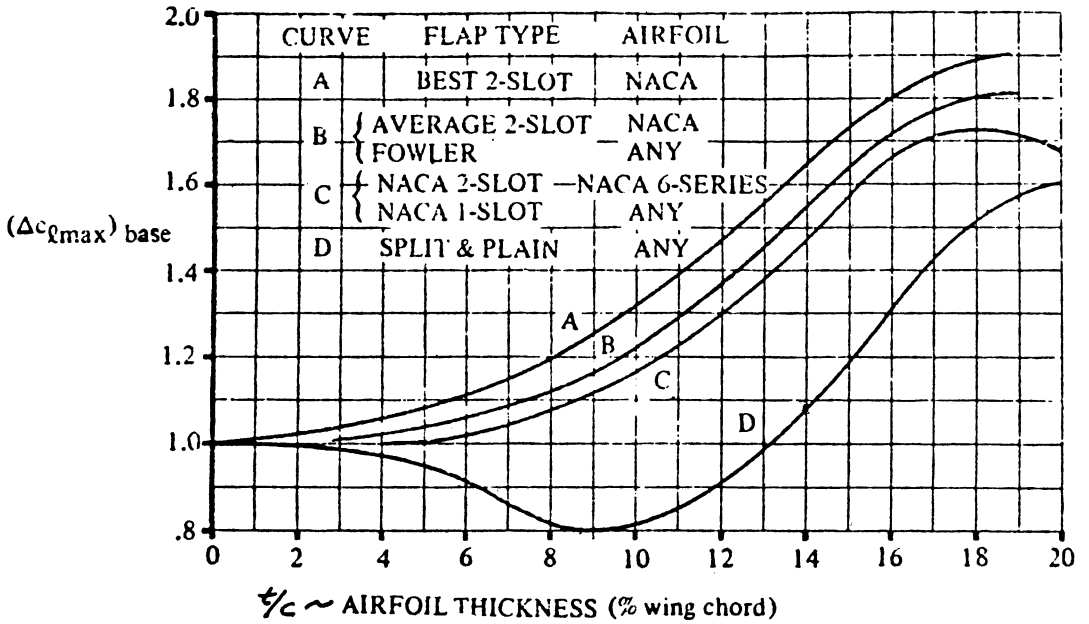

COPIED FROM REF.9

Figure 8.31 Basic Airfoil Maximum Lift Increment due to Trailing Edge Flaps

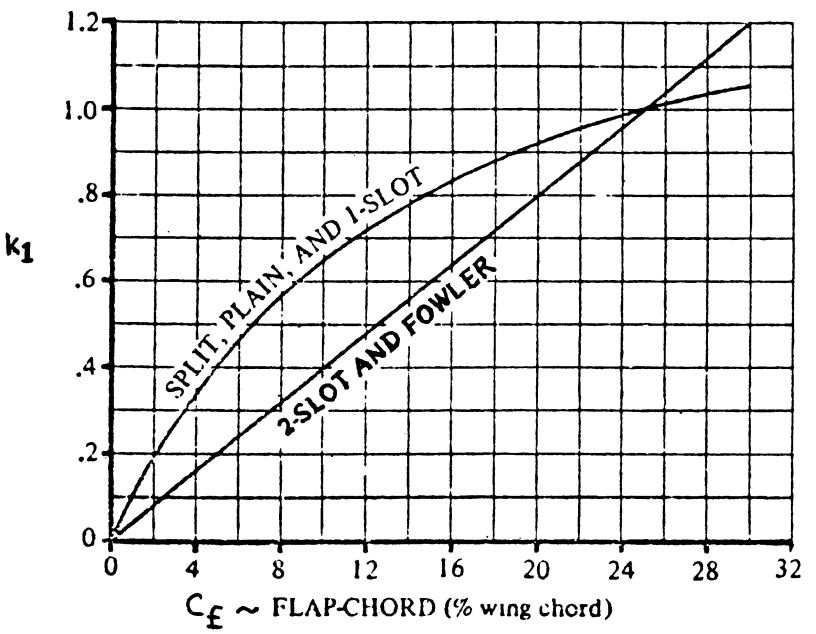

COPIED FROM: REF.9

Figure 8.32 Flap Chord Correction Factor

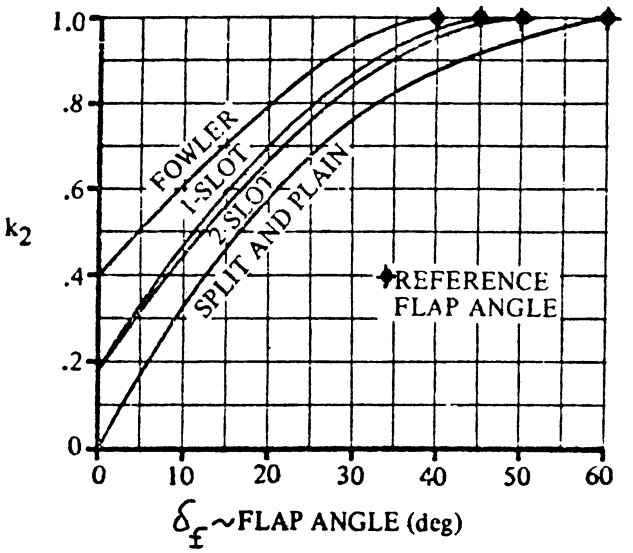

Figure 8.33 Flap Angle Correction Factor

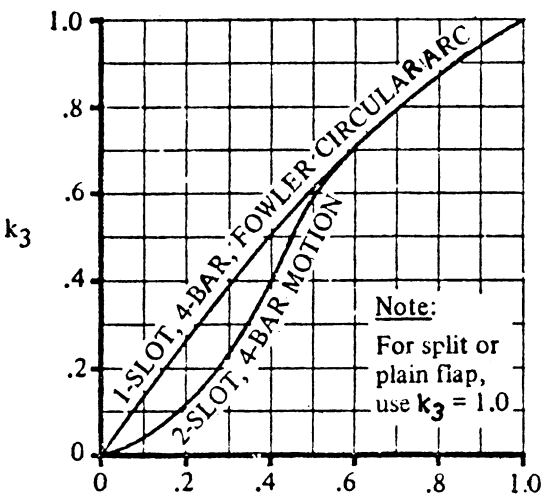

COPIED FROM:
REF. 9

Figure 8.34 Flap Motion Correction Factor

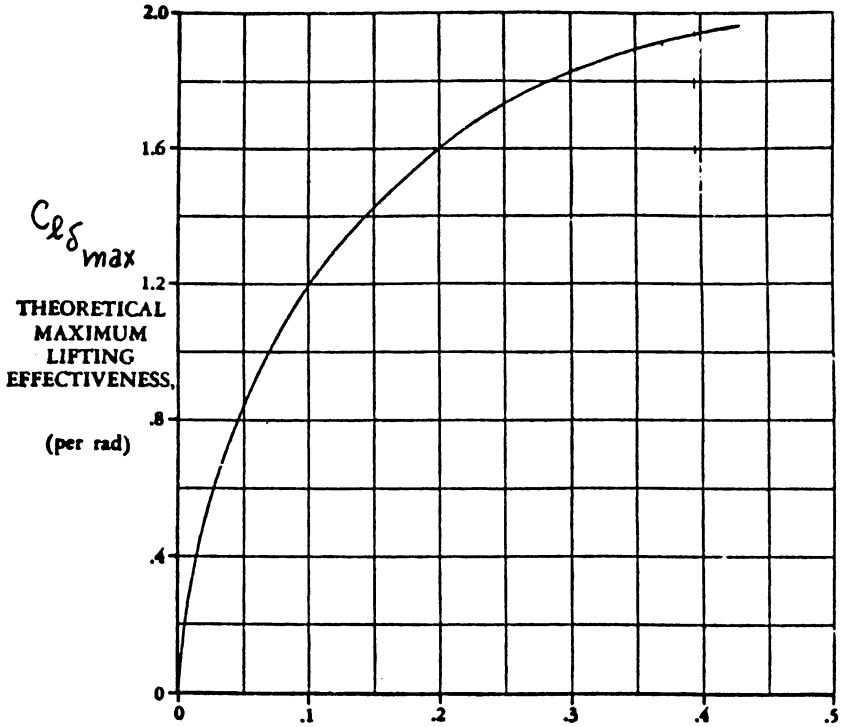

COPIED FROM: REF. 9

Figure 8.35 Maximum Lift Effectiveness for Leading Edge Flaps

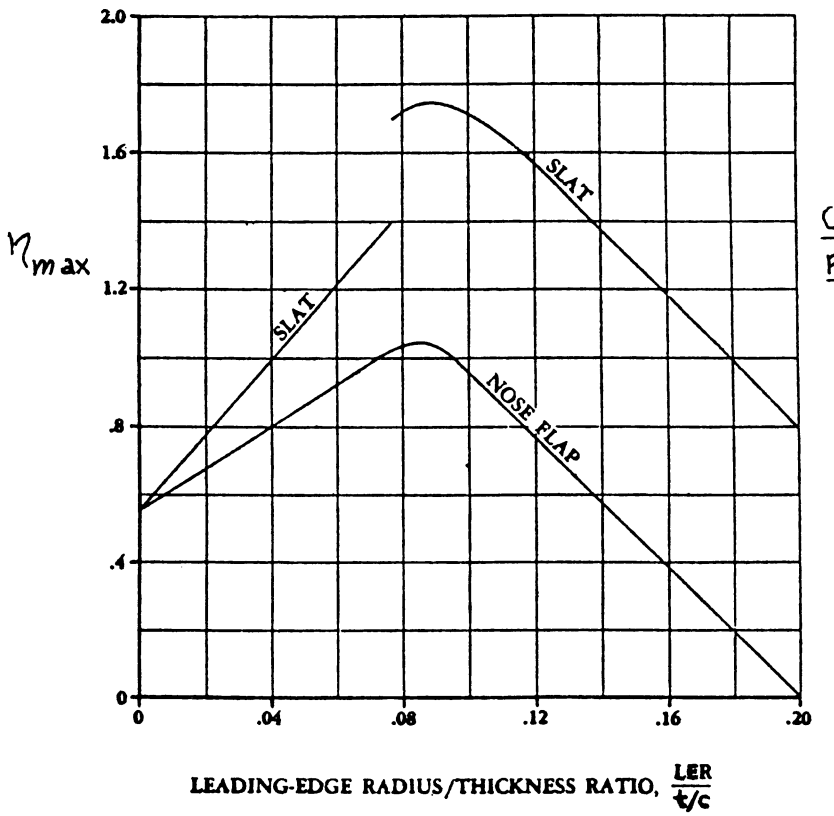

COPIED FROM: REF. 9

Figure 8.36 Effect of Leading Edge Radius and Thickness Ratio on Maximum Lift of Leading Edge Flaps

radians as shown in Figure 8.25, 8.27 or 8.28.

c'/c is the ratio of the airfoil chord with leading edge flaps extended to the basic airfoil chord.

8.1.2.4 Construction of airfoil lift curve: flaps down

All ingredients needed to construct the flaps-down airfoil c_l versus α curve are now available. The flaps-down curve in Figure 8.2 can therefore be constructed. Figure 8.38 shows how this is done in a step-by-step manner. Since no empirical method for the determination of α^* has been presented, the fairing between the linear range and the maximum lift point must be done by guestimation.

The following groundrules are useful:

Trailing edge flaps: the angle of attack for maximum lift with trailing edge flaps down is normally below that for the basic airfoil.

Leading edge flaps: the angle of attack for maximum lift with leading edge flaps down is normally above that for the basic airfoil.

All flaps: the flap deflection angle beyond which the flap lift increment Δc_l ceases to be linear depends on detailed attention paid to flap contour and flap gap design. Table 8.3 provides some guidelines for flap deflection ranges for which linear behavior is expected.

Table 8.3 Linear Flap Effectiveness Range at Low Angles of Attack for Trailing Edge Flaps

Flap Type	δ_f (deg)	
	Poor Design	Good Design
Plain	0 to 10	0 to 20
Single Slotted and Fowler	0 to 20	0 to 30
Double Slotted	0 to 30	0 to 60
Split	0 to 30 or 45	

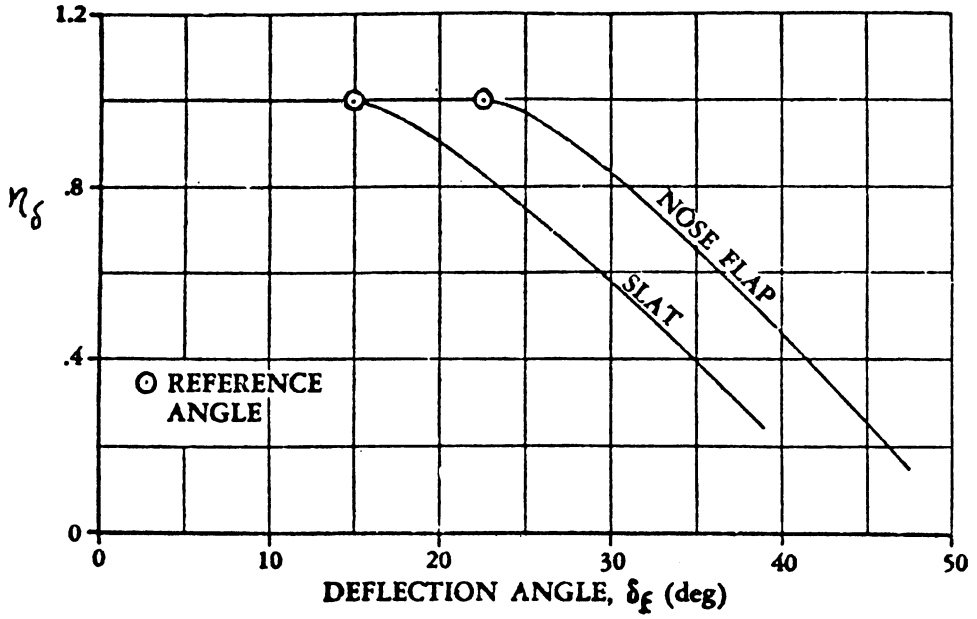

Figure 8.37 Effect of Leading Edge Flap Deflection on Maximum Lift

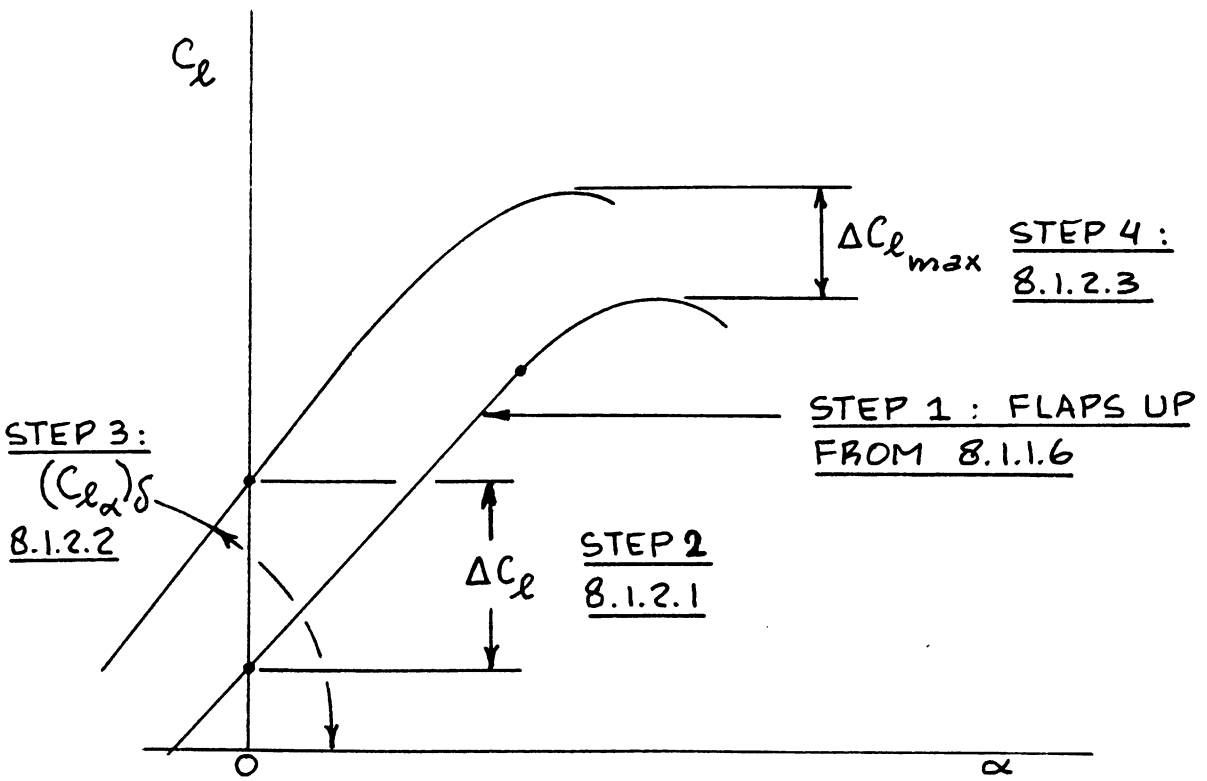

Figure 8.38 Construction of Flaps Down Airfoil Lift Versus α Curve

8.1.3 Wing Lift and Maximum Lift: Flaps Up

Figure 8.39 shows the relationship between wing lift coefficient and wing angle of attack which must be determined with the methods to be presented in this section. Key quantities needed in the construction of the wing C_{L_w} versus α_w curve are listed, with an indication of where methods for their estimation may be found.

8.1.3.1 Wing zero-lift angle of attack: $\alpha_{o_{L_w}}$

The wing angle of attack, α_w is defined as follows:

$$\alpha_w = \alpha + i_w \qquad (8.20)$$

where: α is the airplane angle of attack and

i_w is the wing incidence angle

Figure 8.40 shows how these quantities relate to each other on an airplane. Criteria for the selection of the wing incidence angle, i_w are discussed in Part III, p.195.

For subsonic speeds:

For wings with constant airfoil sections and linear twist distributions the wing zero-lift angle of attack may be estimated from:

$$\alpha_{o_{L_w}} =$$

$$= \{\alpha_{o_l} + (\Delta\alpha_o/\varepsilon_t)\varepsilon_t\}\{(\alpha_{o_l})_{\text{at } M}\}/\{(\alpha_{o_l})_{\text{at } M=0.3}\} \qquad (8.21)$$

where: α_{o_l} is found from 8.1.1.1

$(\Delta\alpha_o/\varepsilon_t)$ is the change in wing zero-lift angle of attack per degree of linear wing twist: See Figure 8.41.

ε_t is the wing twist angle: see Figure 8.41. Criteria for the selection of wing twist angle are presented in Part III, p.193.

$\{(\alpha_{o_l})_{\text{at } M}\}\{(\alpha_{o_l})_{\text{at } M=0.3}\}$ is found from Fig.8.42.

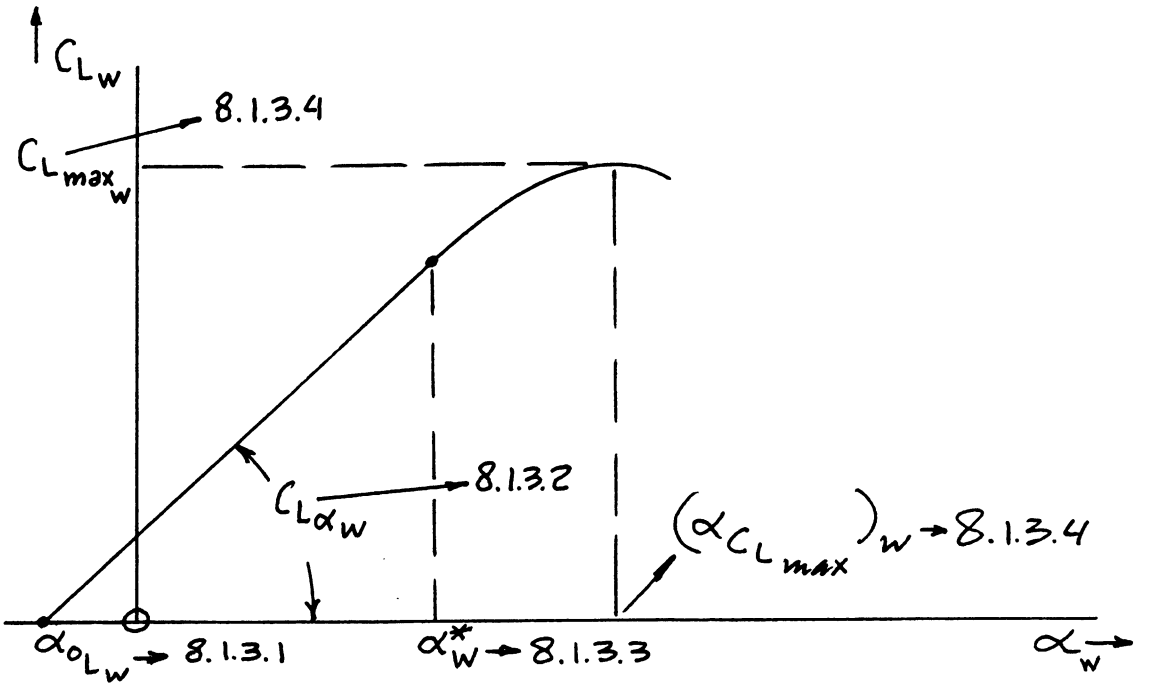

Figure 8.39 Wing Lift Coefficient Versus Angle of Attack Curve

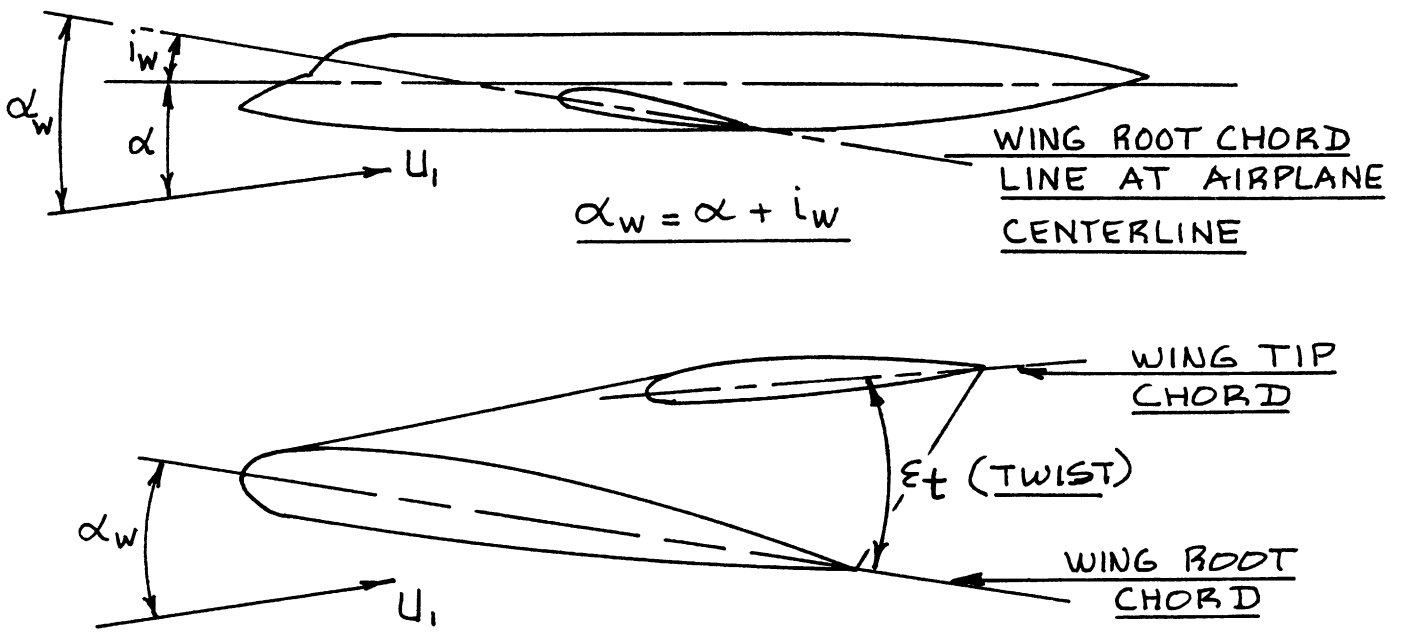

Figure 8.40 Relationship Between Wing Incidence, Wing Angle of Attack and Airplane Angle of Attack

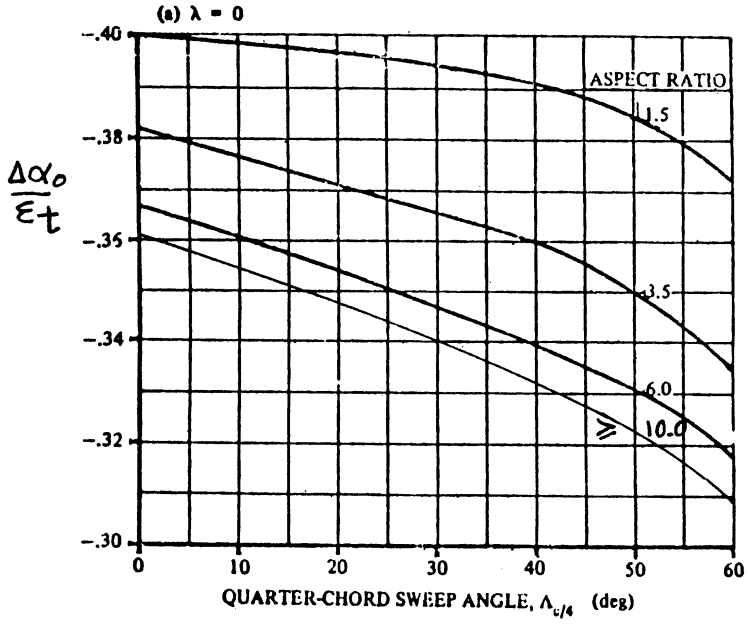

COPIED FROM REF. 9

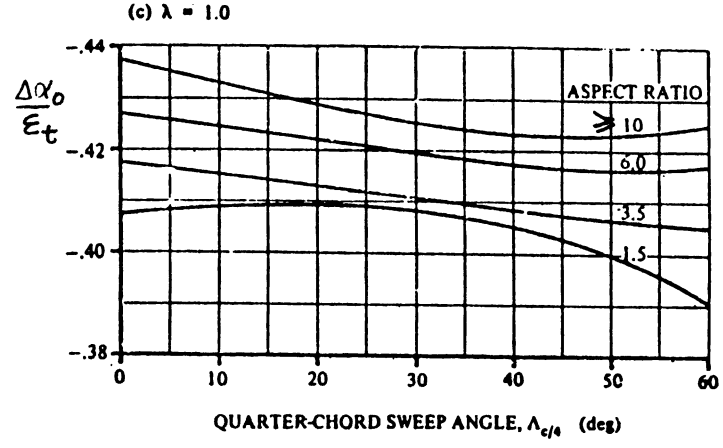

Figure 8.41 Effect of Linear Twist on Wing Angle of Attack for Zero Lift

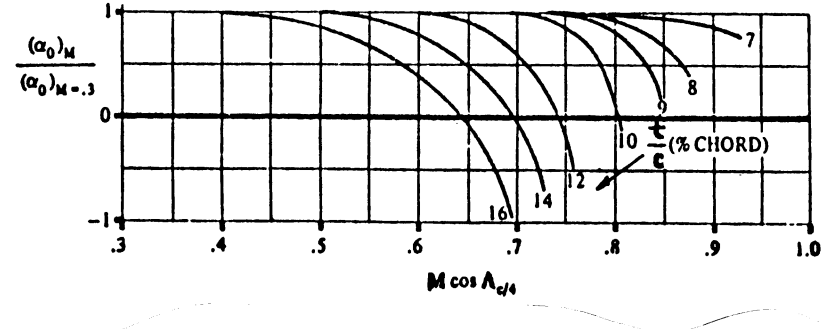

Figure 8.42 Mach Number Correction for Zero-Lift Angle of Attack of Cambered Airfoils

For transonic and supersonic speeds:

In the transonic and supersonic speed ranges experimental data should be used.

8.1.3.2 Wing lift curve slope: $C_{L_{\alpha_W}}$

For subsonic speeds:

For conventional, straight tapered wings, with 'moderate' sweep angles, the lift curve slope may be estimated from Figures 8.43 or from:

$$C_{L_{\alpha_W}} = \qquad (8.22)$$

$$2\pi A/[2 + \{(A^2\beta^2/k^2)(1 + \tan^2\Lambda_{c/2}/\beta^2) + 4\}^{1/2}]$$

where: $A = b^2/S$ is the wing aspect ratio (8.23)

Wing aspect ratio may have to be computed for the so-called 'equivalent' wing planform: See Figure 8.44.

$$\beta = (1 - M^2)^{1/2} \qquad (8.24)$$

$$k = (c_{l_\alpha})_{\text{at } M}/(2\pi/\beta) \qquad (8.25)$$

where $(c_{l_\alpha})_{\text{at } M}$ follows from Eqn.(8.1).

$\Lambda_{c/2}$ is the semi-chord sweep angle. Relations between semi-chord, quarter-chord and leading edge sweep angles are defined in Figures 8.45 and 8.46.

For transonic speeds: see Reference 9.

For supersonic speeds: See Figures 8.47. Note: these figures apply only for low angles of attack.

Methods for estimating wing lift curve slopes for arbitrary wing planforms are presented in Reference 9.

8.1.3.3 Wing linear range of angle of attack: α_W^*

In preliminary design it is acceptable to use:

$\alpha_W^* = \alpha^*$ as found from 8.1.1.3.

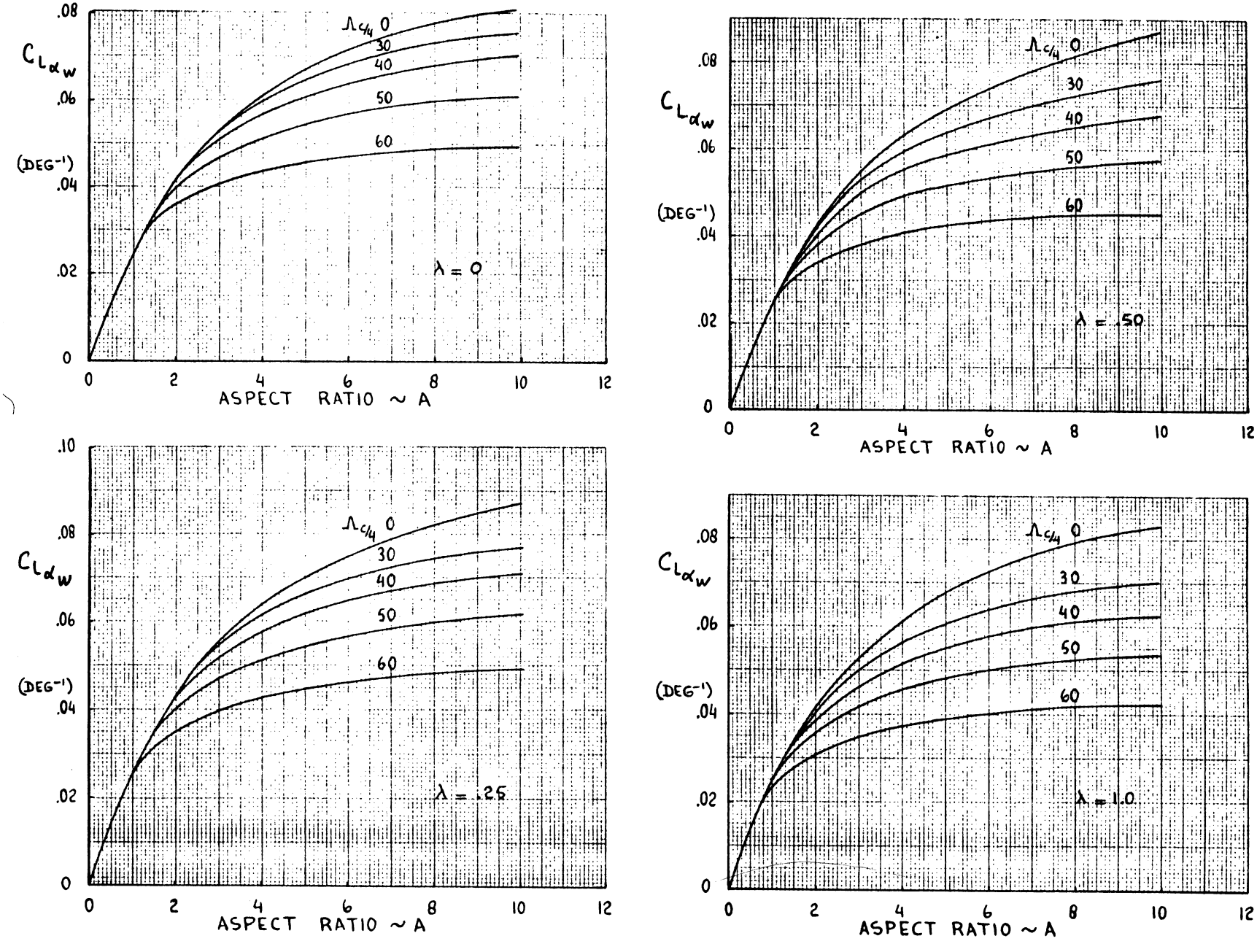

Figure 8.43 Wing Lift Curve Slope at Low Mach Numbers

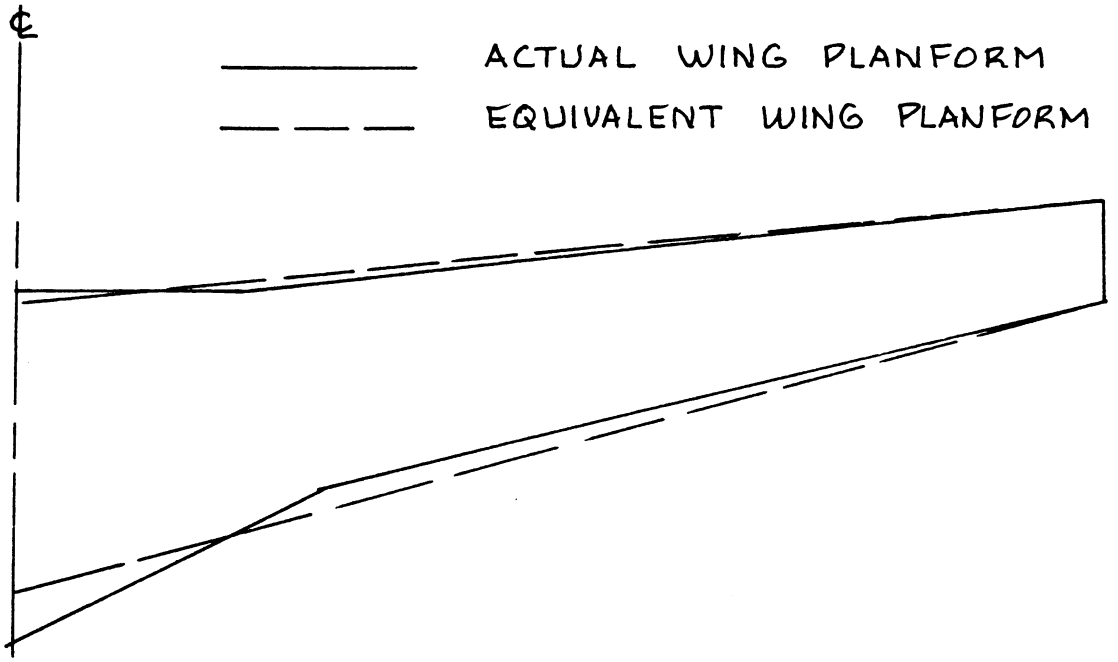

Figure 8.44 Example of an Equivalent Wing Planform

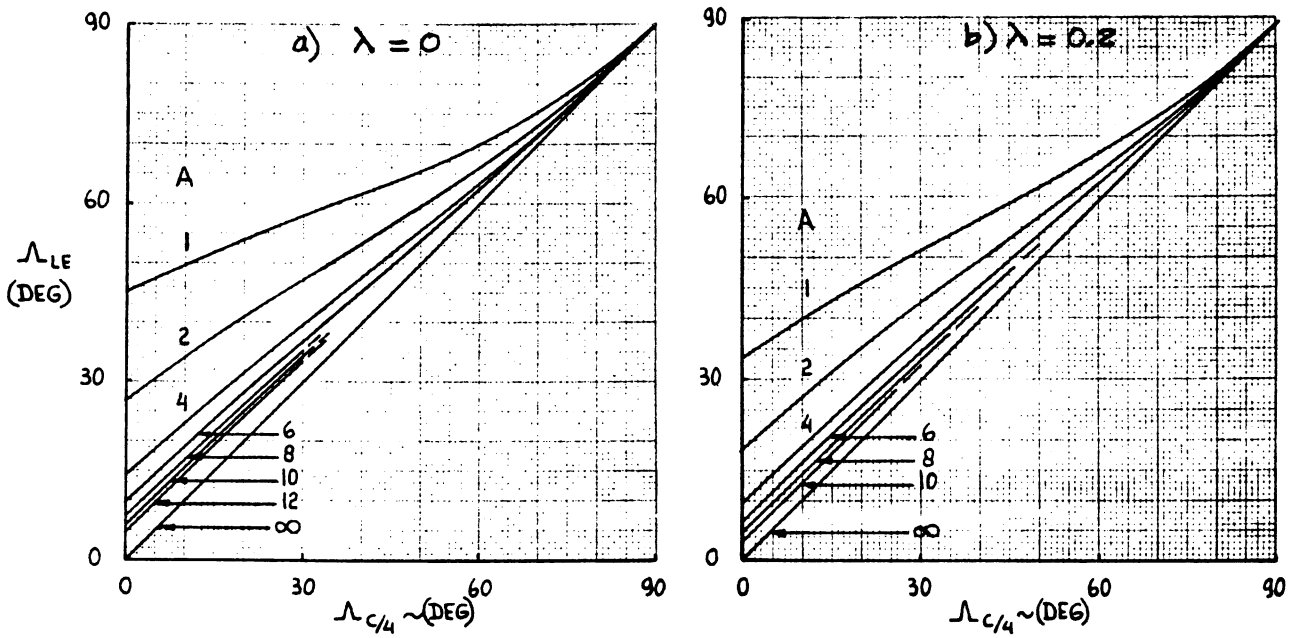

Figure 8.45 Leading Edge Sweep Angle Versus Quarter Chord Sweep Angle for Straight Tapered Wings

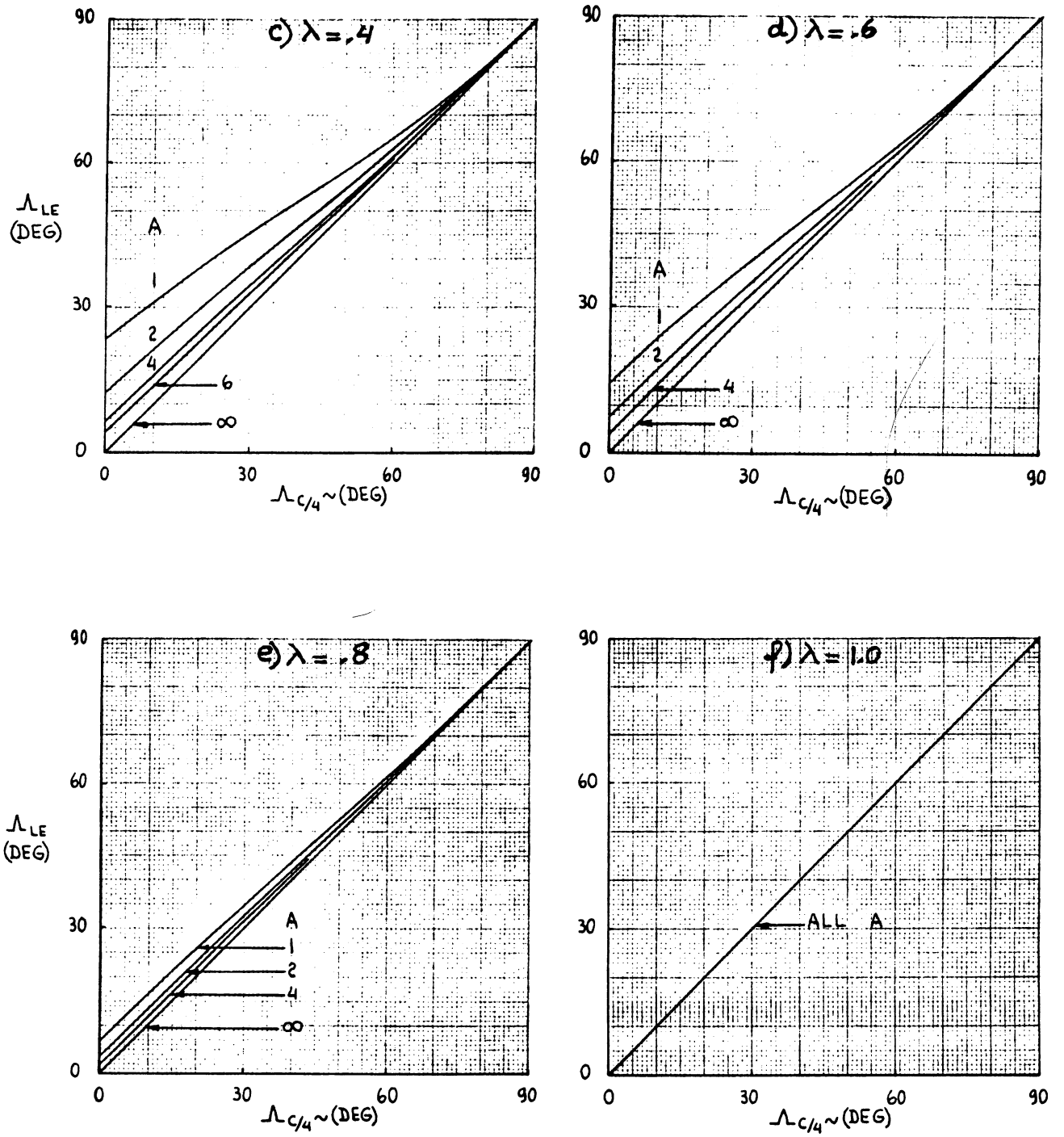

Figure 8.45 (Cont'd) Leading Edge Sweep Angle Versus Quarter Chord Sweep Angle for Straight Tapered Wings

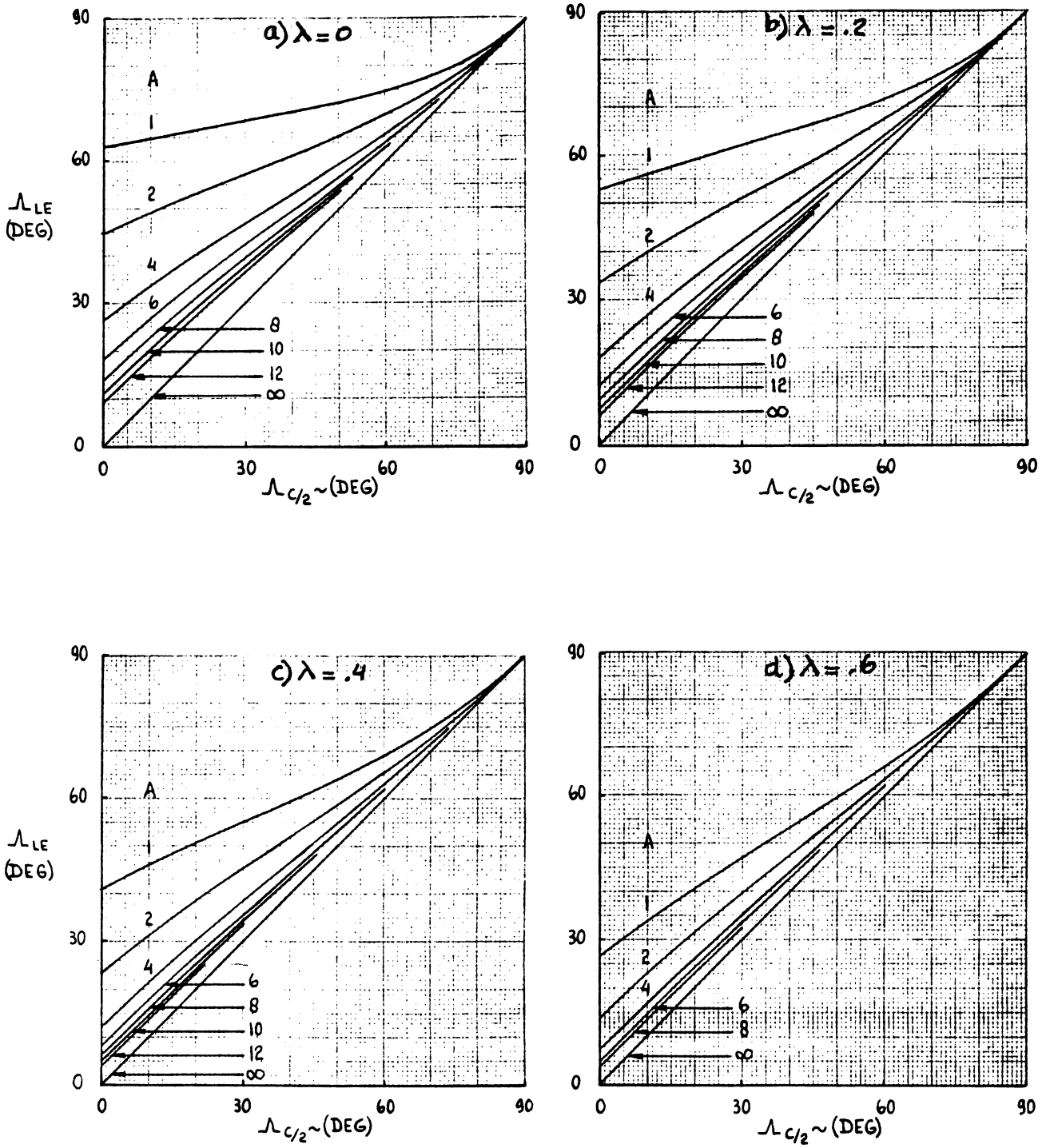

Figure 8.46 Leading Edge Sweep Angle Versus Semi-chord Sweep Angle for Straight Tapered Wings

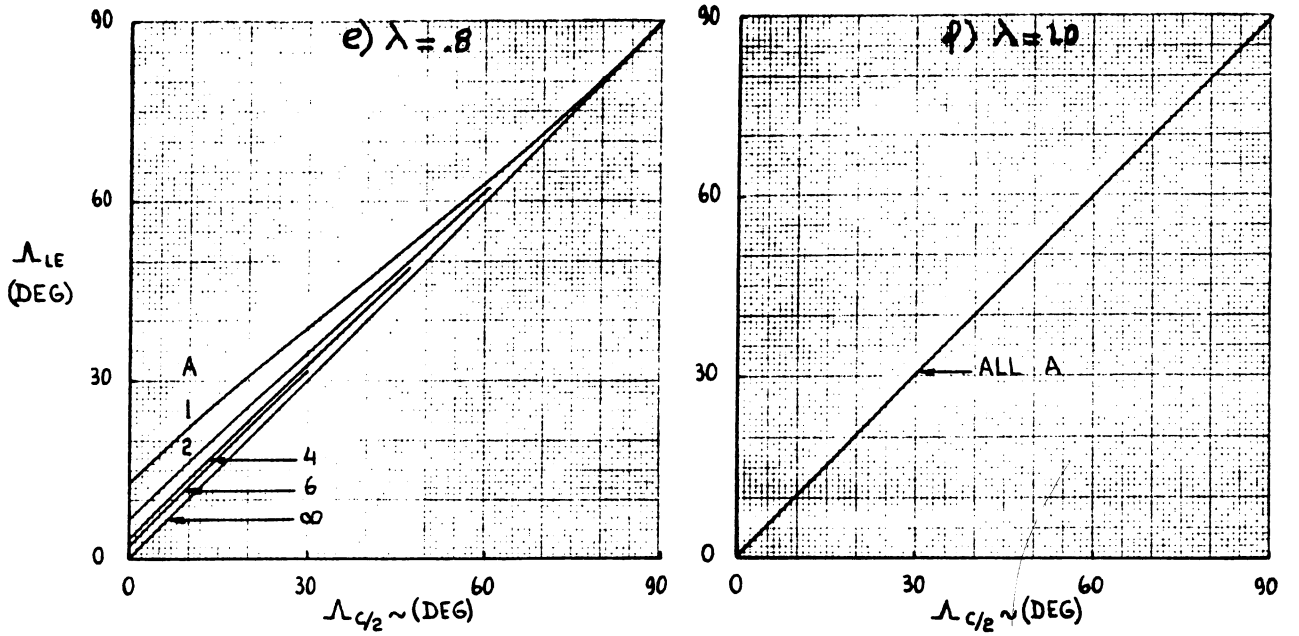

Figure 8.46 (Cont'd) Leading Edge Sweep Angle Versus Semi-chord Sweep Angle for Straight Tapered Wings

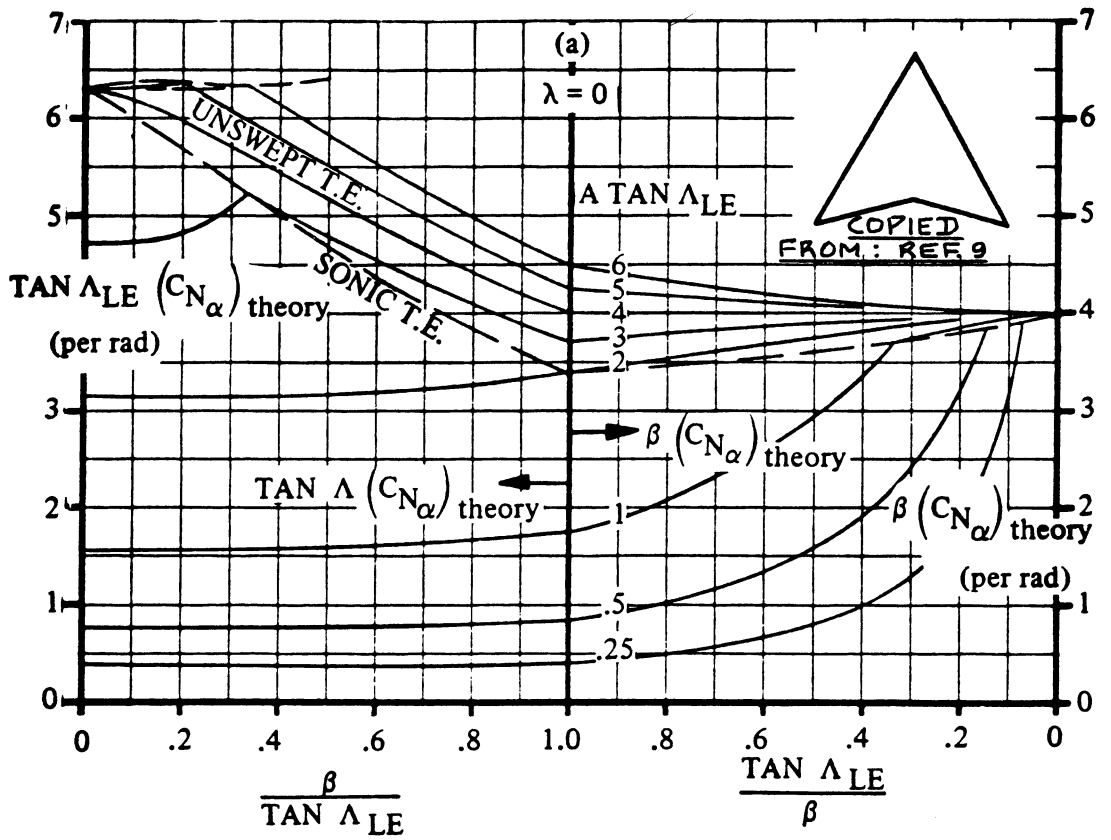

Figure 8.47a Wing Lift Curve Slope for Supersonic Mach Numbers and Low Angle of Attack

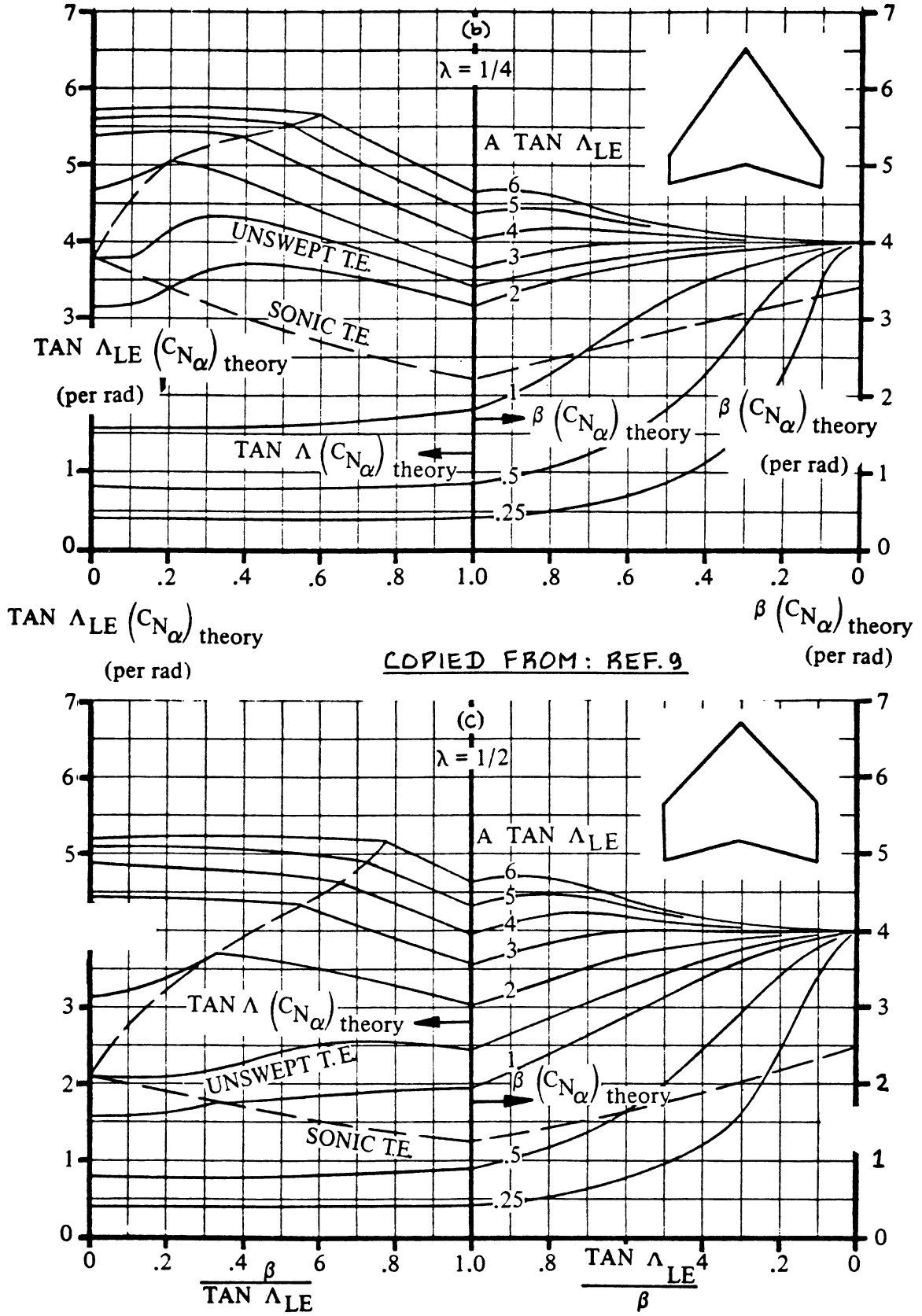

COPIED FROM: REF. 9

Figure 8.47b Wing Lift Curve Slope for Supersonic Mach Numbers and Low Angle of Attack

HINTS FOR USING FIGURES 8.47 a, b, AND c:

Note: for low angles of attack:

$$C_{L_\alpha} = C_{N_\alpha}$$

Note: $C_{N_\alpha} = (C_{N_\alpha})_{theory}\{(C_{N_\alpha})/(C_{N_\alpha})_{theory}\}$,

where: $(C_{N_\alpha})_{theory}$ follows from Figures 8.47a or 8.47b

$\{(C_{N_\alpha})/(C_{N_\alpha})_{theory}\}$ follows from Figure 8.47c

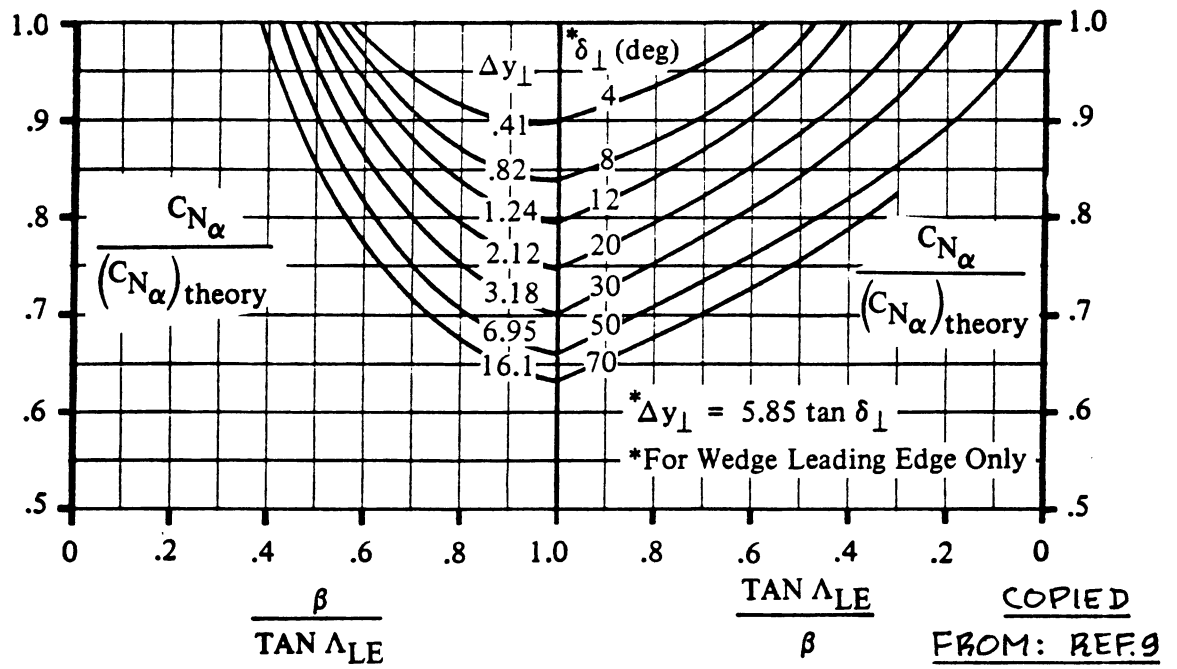

Figure 8.47c Wing Lift Curve Slope Correction Factor for Wings with Sonic Leading Edge Regions

8.1.3.4 Wing maximum lift coefficient: $C_{L_{max_w}}$ and wing angle of attack for maximum lift: $(\alpha_{C_{L_{max}}})_w$

In this section, the assumption is made that the reader has available a computer program for the calculation of the spanwise lift coefficient distribution for a given wing angle of attack, α_w as defined by Eqn.(8.20).

Methods for finding spanwise distributions of lift coefficient with angle of attack can be found in:

Reference 49: Chapter 1: this method applies to unswept wings at subsonic Mach numbers. However, by using the cosine rule, this method will work for sweep angles up to 35 degrees.

Reference 52: this method applies to arbitrary wing planforms at subsonic speeds.

To estimate the maximum wing (flaps-up) lift coefficient, the following step-by-step procedure is suggested:

Step 1: Determine the spanwise distribution of section maximum lift coefficient. Plot this as shown in Figure 8.48. Note: the section maximum lift coefficient at each spanwise station is found from Section 8.1.1.5 or from airfoil data.

NOTE: at each spanwise station the Reynold's number will be different!

Step 2: With the help of either Ref.49, Ref.52 or with the help of a spanwise-lift computer program, plot the spanwise variation in local section lift coefficient for increasing values of wing angle of attack. Note that at some value of α_w the spanwise plot of

of c_l is tangent to the spanwise plot of

$c_{l_{max}}$ as obtained from Step 1. That value of wing angle of attack is: $(\alpha_{C_{L_{max}}})_w$.

Fig.8.48 also shows the resulting plot(s).

Step 3: Calculate the wing maximum lift coefficient from:

$$C_{L_{max_w}} = (1/S)\int_0^{1.0} bc(c_{l_{w_{stall}}})d\eta \qquad (8.26)$$

where $c_{l_{w_{stall}}}$ is the spanwise value of the local section lift coefficient at:

$$\alpha_w = (\alpha_{C_{L_{max}}})_w$$

Important note: the magnitude of $C_{L_{max_w}}$ is always below that of the magnitude of $c_{l_{max}}$ of any wing airfoil.

8.1.3.5 Construction of wing lift curve: flaps up

All ingredients for constructing the wing lift curve are now available. Figure 8.49 shows how this can be done in a stepwise manner.

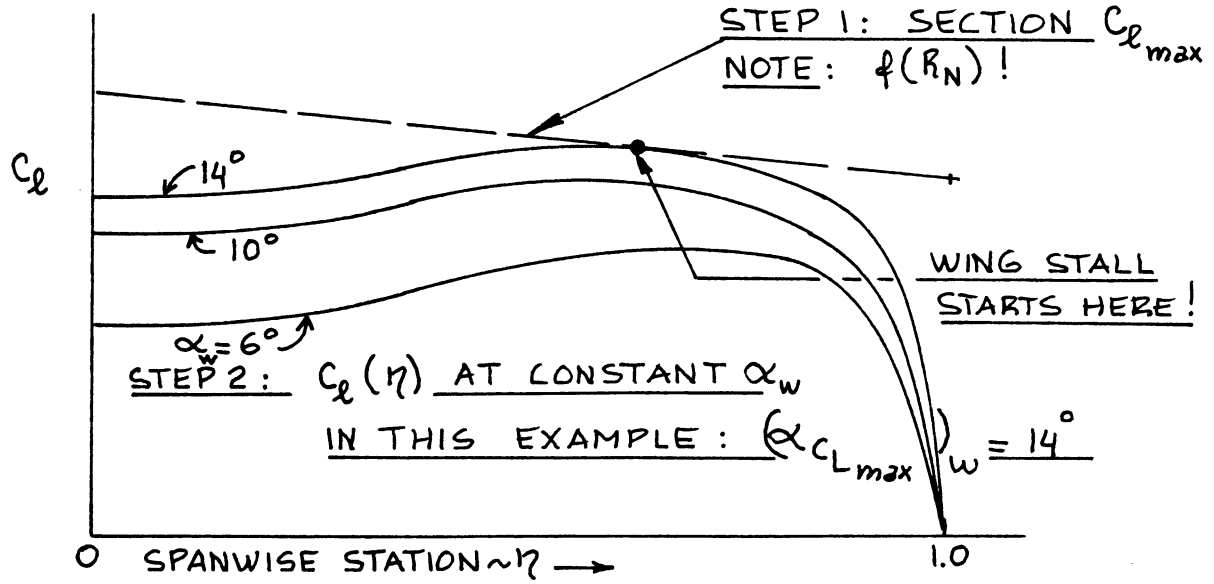

Figure 8.48 Section Maximum Lift Coefficient and Section Lift Coefficient at a Given Angle of Attack Versus Spanwise Position on a Wing

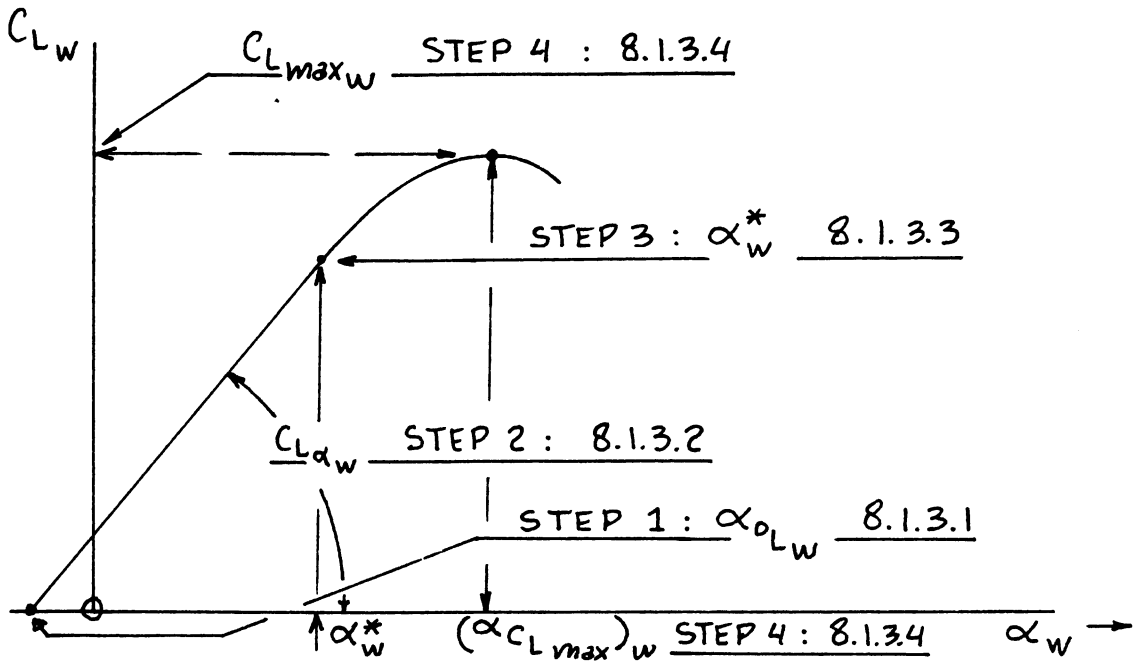

Figure 8.49 Construction of Flaps Up Wing Lift Versus Angle of Attack Curve

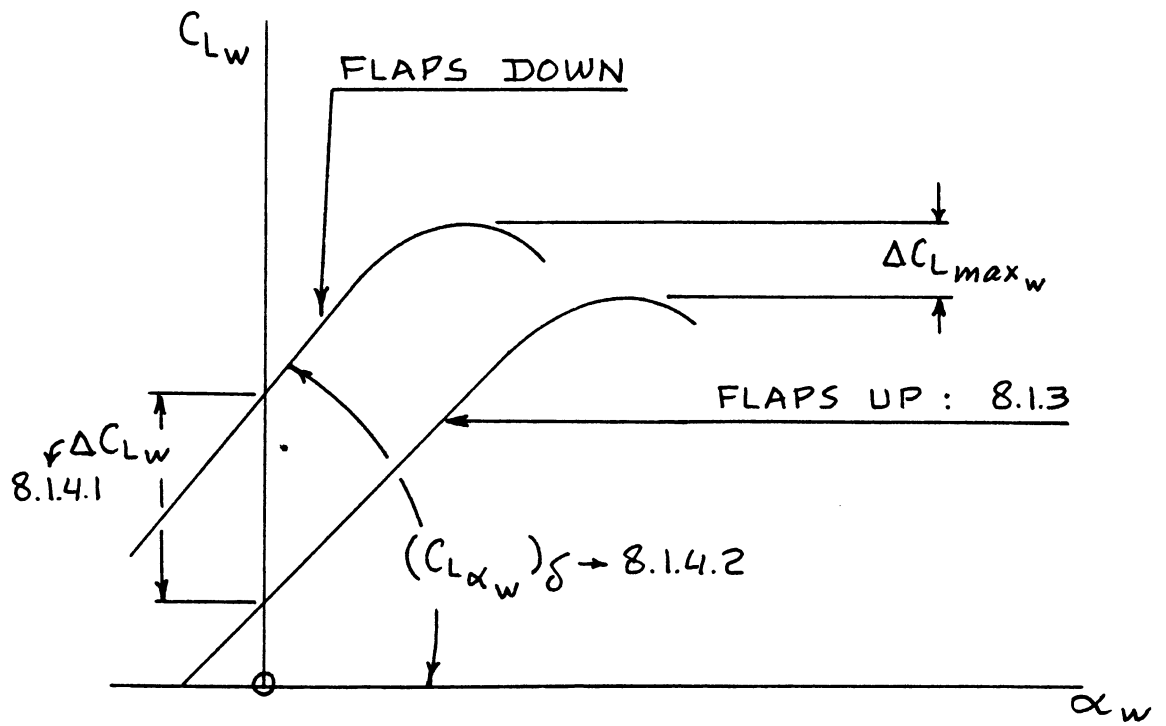

Figure 8.50 Fundamental Wing Lift Versus α Curve with the Flaps Down

8.1.4 Wing Lift and Maximum Lift: Flaps Down

Figure 8.50 shows the relationship between flaps up and flaps down wing lift characteristics. Key quantities needed in the construction of the flaps down wing C_{L_w} versus α_w curve are listed, with an indication of where methods for their estimation may be found.

8.1.4.1 Wing lift increment due to flaps: ΔC_{L_w}

The wing lift increment due to trailing edge and/or leading edge flaps may be estimated from:

$$\Delta C_{L_w} = K_b(\Delta c_l)(C_{L_{\alpha_w}}/c_{l_\alpha})\,[\{(\alpha_\delta)_{C_L}\}/\{(\alpha_\delta)_{c_l}\}] \qquad (8.27)$$

where: K_b is the flap-span factor as obtained from the procedure suggested in Figure 8.51 but with the data from Figure 8.52.

Δc_l is the airfoil lift increment due to flaps as obtained from 8.1.2.1.

$C_{L_{\alpha_w}}$ is the wing lift curve slope as obtained from 8.1.3.2.

c_{l_α} is the wing airfoil lift curve slope as obtained from 8.1.1.2.

$\frac{(\alpha_\delta)_{C_L}}{(\alpha_\delta)_{c_l}}$ is the ratio of the three-dimensional flap-effectiveness parameter to the two-dimensional flap-effectiveness parameter as found in Figure 8.53.

Note: If a mechanical high lift system consists of a combination of leading and trailing edge high lift devices, the method should be applied to each type of device separately. The resulting increments in lift coefficients can then be added.

8.1.4.2 Wing lift curve slope due to flaps: $(C_{L_{\alpha_w}})_\delta$

Wings with NON-TRANSLATING flap systems:

For wings with NON-TRANSLATING flap systems (such as split flaps, plain flaps and nose flaps), the wing lift curve slope flaps-down is considered to be the same as

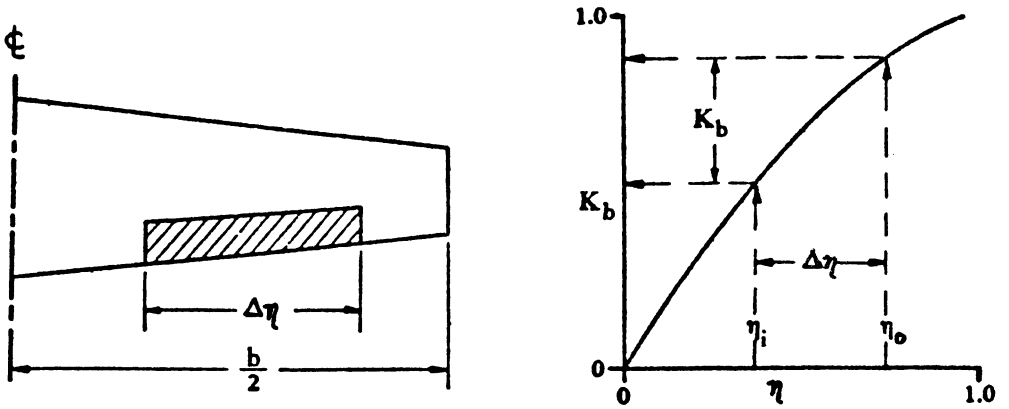

Figure 8.51 Procedure for Estimating K_b

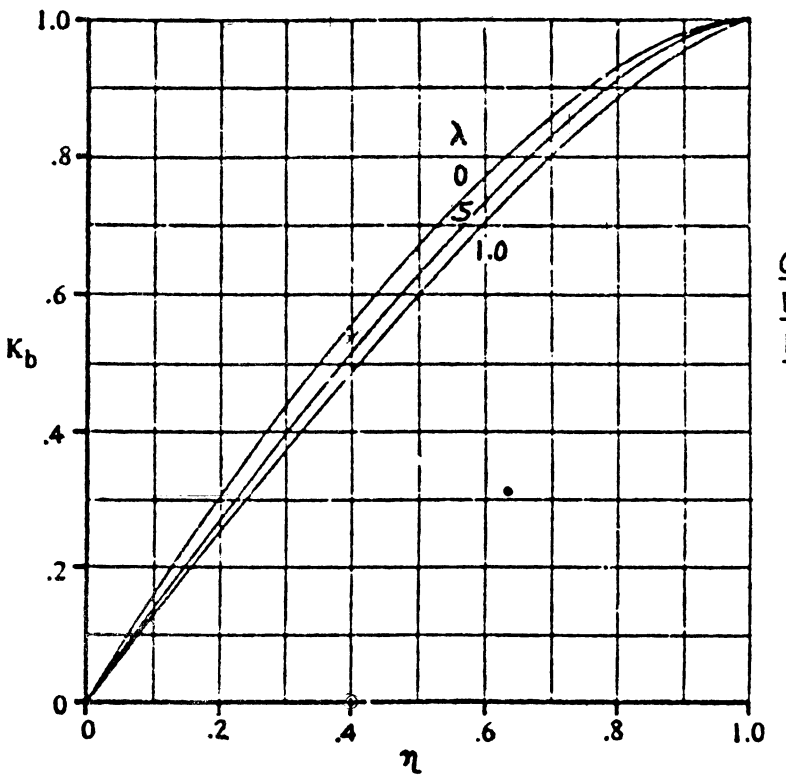

COPIED FROM: REF. 9

Figure 8.52 Effect of Taper Ratio and Flap Span on K_b

COPIED FROM: REF. 9

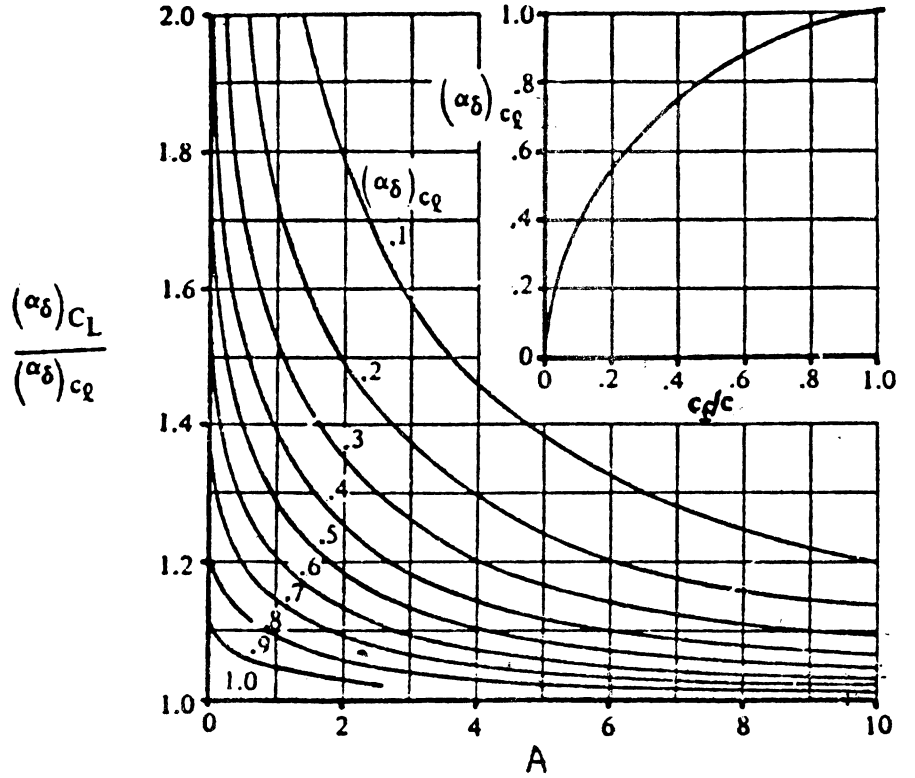

Figure 8.53 Effect of Aspect Ratio and Flap-Chord Ratio on the Three-Dimensional Flap Effectiviness

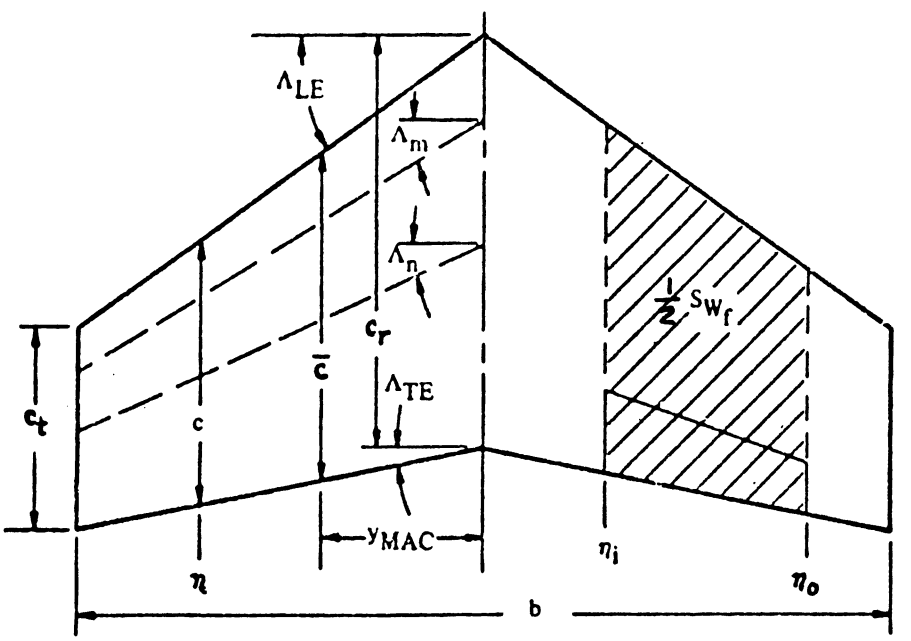

Figure 8.54 Definition of 'Flapped' Wing Area

that for the flaps-up: the method of 8.1.4.1 may be used.

Wings with TRANSLATING flap systems:

For wings with translating flaps (such as Fowler flaps, most slotted flaps, slats and Krueger flaps), the flaps-down lift curve slope may be estimated from:

$$(C_{L_{\alpha_W}})_\delta = C_{L_{\alpha_W}} \{1 + (c'/c - 1)(S_{W_f}/S)\} \qquad (8.28)$$

where: $C_{L_{\alpha_W}}$ is found from 8.1.4.1

c'/c is the ratio of extended wing chord to the chord of the flaps-up wing. Figures 8.18, 8.19 and 8.27 show definitions for these chords depending on the type of flap used.

S_{W_f}/S is the ratio of the 'flapped' wing area to that of the area of the flaps-up wing. Figure 8.54 shows how this is defined.

8.1.4.3 Wing maximum lift increment due to flaps: $\Delta C_{L_{max_W}}$

A) Trailing Edge Flaps

The maximum wing incremental lift coefficient due to trailing edge flaps is found from:

$$\Delta C_{L_{max_W}} = (\Delta c_{l_{max}})(S_{W_f}/S)K_\Delta \qquad (8.29)$$

where: $(\Delta c_{l_{max}})$ is the airfoil incremental lift coefficient due to trailing edge flaps as found from 8.1.2.3.

S_{W_f}/S is defined in Figure 8.54

K_Δ is a planform correction factor found from Figure 8.55.

B) Leading Edge Flaps

The maximum wing incremental lift coefficient due to leading edge flaps (slats and/or Kruegers) is found from:

$$\Delta C_{L_{max_W}} = 7.11(c_f/c)(b_{lef}/b_e)^2 \cos^2 \Lambda_{c/4} \qquad (8.30)$$

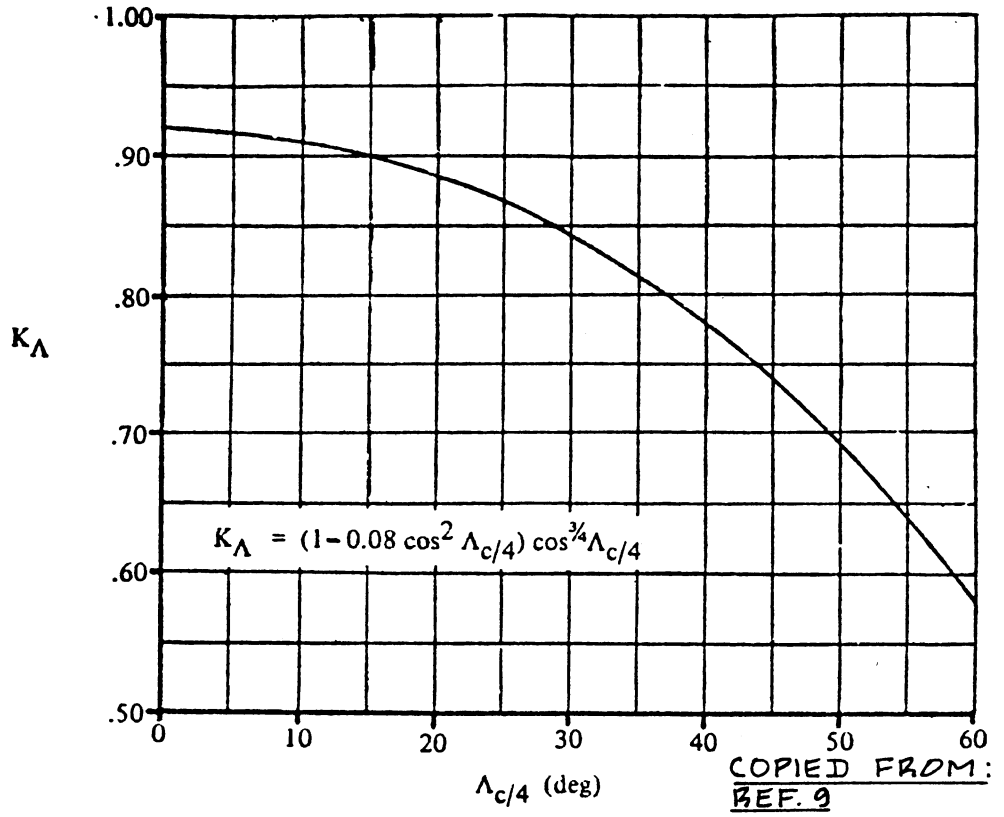

Figure 8.55 Effect of Sweep on Planform Correction Factor

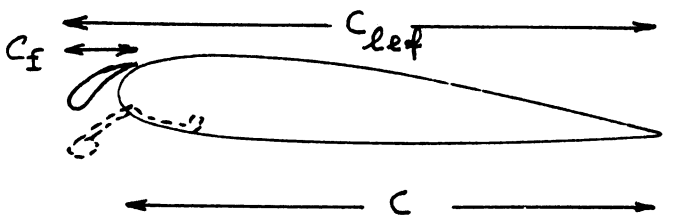

Figure 8.56 Definition of Leading Edge Flap Chord Ratio

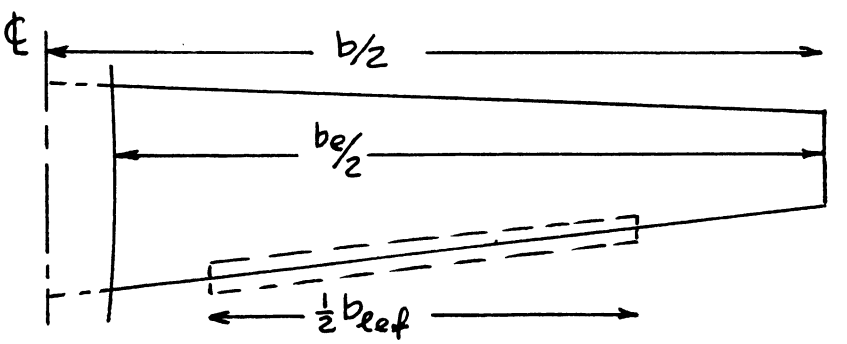

Figure 8.57 Definition of Leading Edge Flap Span Ratio

where: c_{lef}/c is defined in Figure 8.56.

b_{lef}/b_e is defined in Figure 8.57.

8.1.4.4 Construction of the wing lift curve: flaps down

All ingredients necessary to construct the flaps down wing lift curve are now available. Figure 8.58 shows the step-by-step manner in which this can be done.

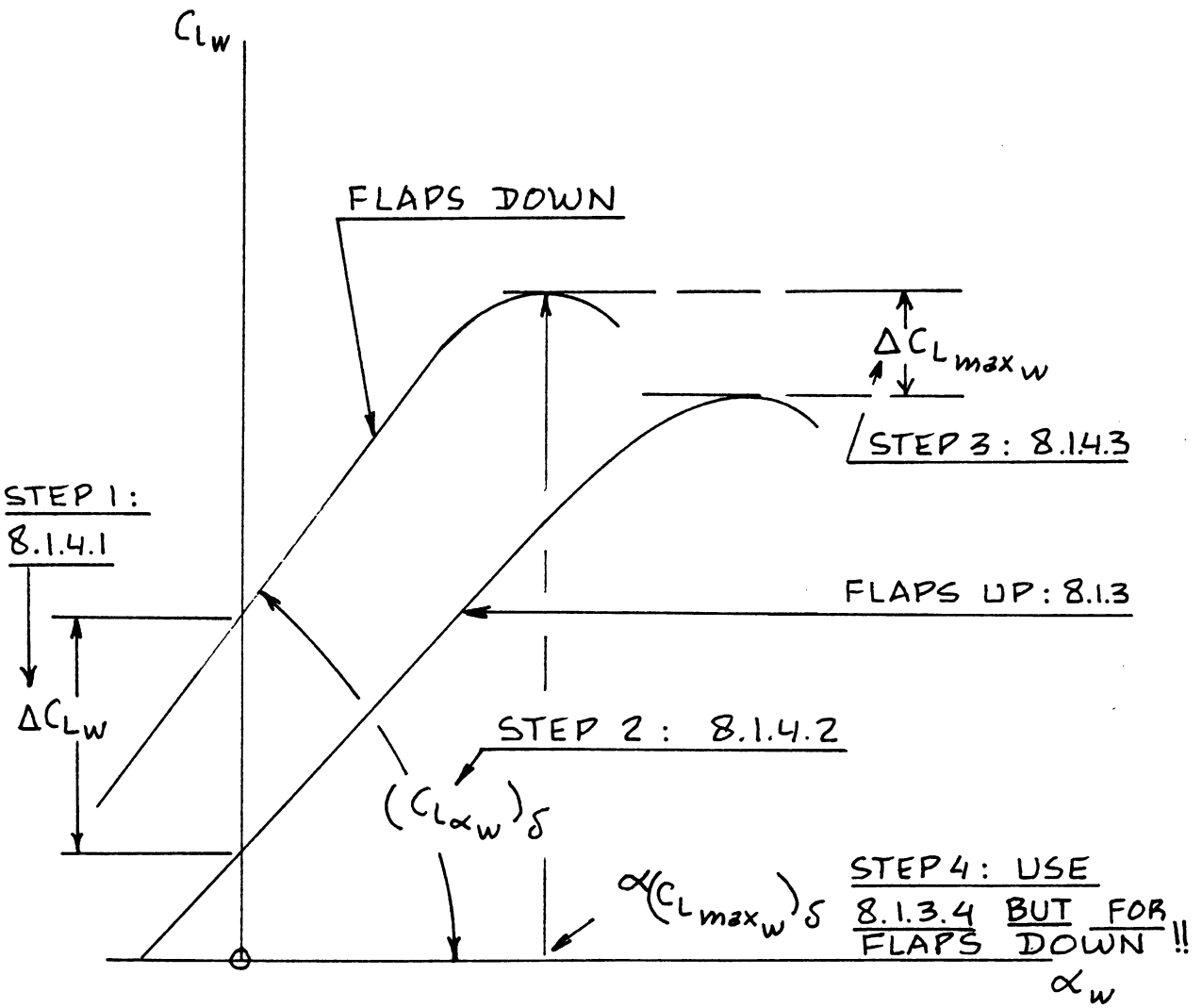

Figure 8.58 Construction of Flaps Down Wing Lift Versus Angle of Attack Curve

8.1.5 Airplane Lift and Maximum Lift: Flaps Up

Figure 8.59 shows the relationship between airplane lift coefficient and airplane angle of attack which must be determined with the methods to be presented in this section. Key quantities needed in the construction of airplane C_L versus α curve are listed, with an indication of where methods for their estimation may be found.

The assumption will be made, that an airplane can be considered to consist of three components:

a) wing + fuselage b) horizontal tail c) canard

Figure 8.60 shows the relative arrangement of these three major components. If an airplane is equipped with pylon mounted nacelles (such as the B-727 and the DC-9), the pylon + nacelle combination should be 'counted' as an additional horizontal tail. Figure 8.61 indicates the 'equivalent' geometries which should then be used.

Figure 8.62 shows a number of important geometric parameters which are used in the calculation of overall airplane lift characteristics.

IMPORTANT CONSIDERATIONS:

In this chapter the following incidence angles are accounted for:

Canard: i_c Wing: i_w Horizontal Tail: i_h

These incidence angle are defined in Figure 8.60. In this sub-section, these incidence angles are assumed to be CONSTANT. The effect of trim requirements is considered in Section 8.3.

A horizontal tail and a canard may be equipped with a trailing edge control surface:

Horizontal tail with elevator, deflection: δ_e

Canard with canardvator, deflection: δ_c

In this sub-section, the assumption will be made that all control surface deflection angles are ZERO. The effect of trim requirements which would cause these control surface deflections to be non-zero is considered in Section 8.3.

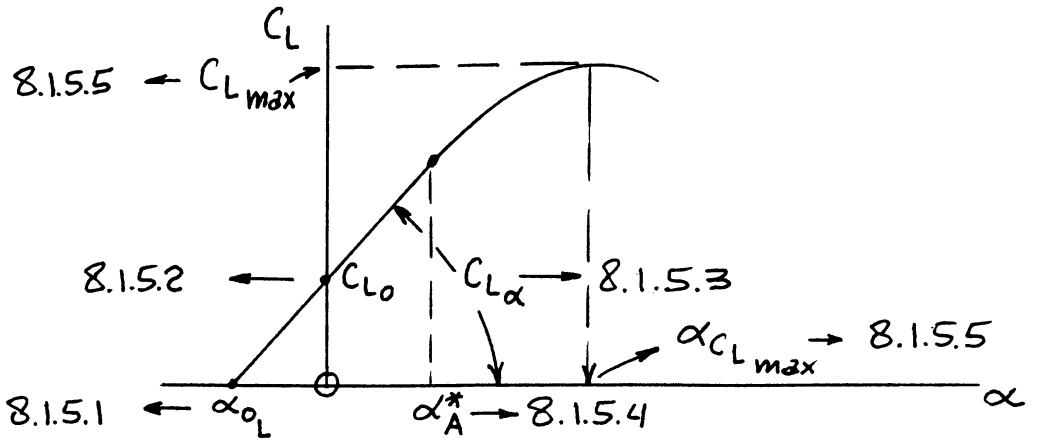

Figure 8.59 Airplane Lift Coefficient Versus Angle of Attack Curve

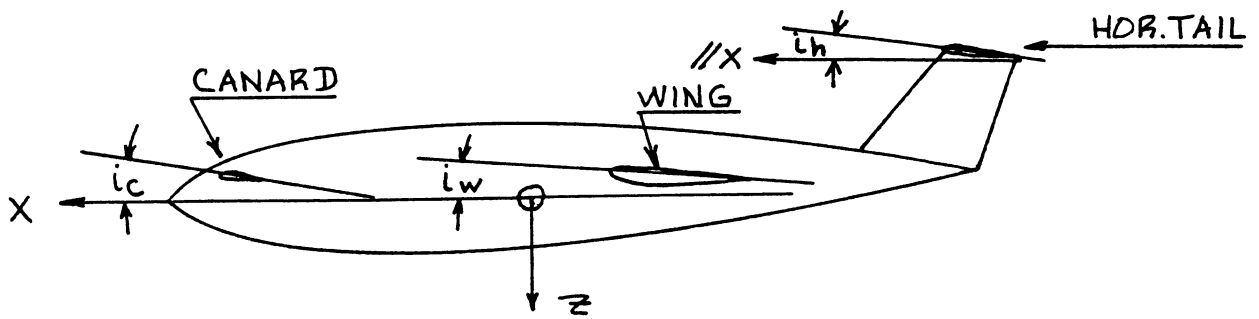

Figure 8.60 Relative Arrangement of Canard, Wing and Horizontal Tail

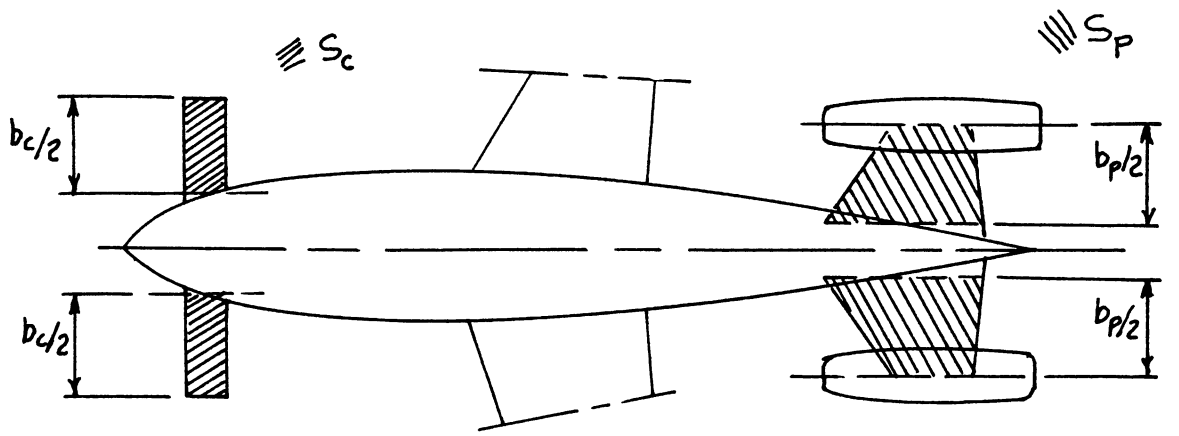

Figure 8.61 Equivalent Geometries for Pylon Engine Mounts

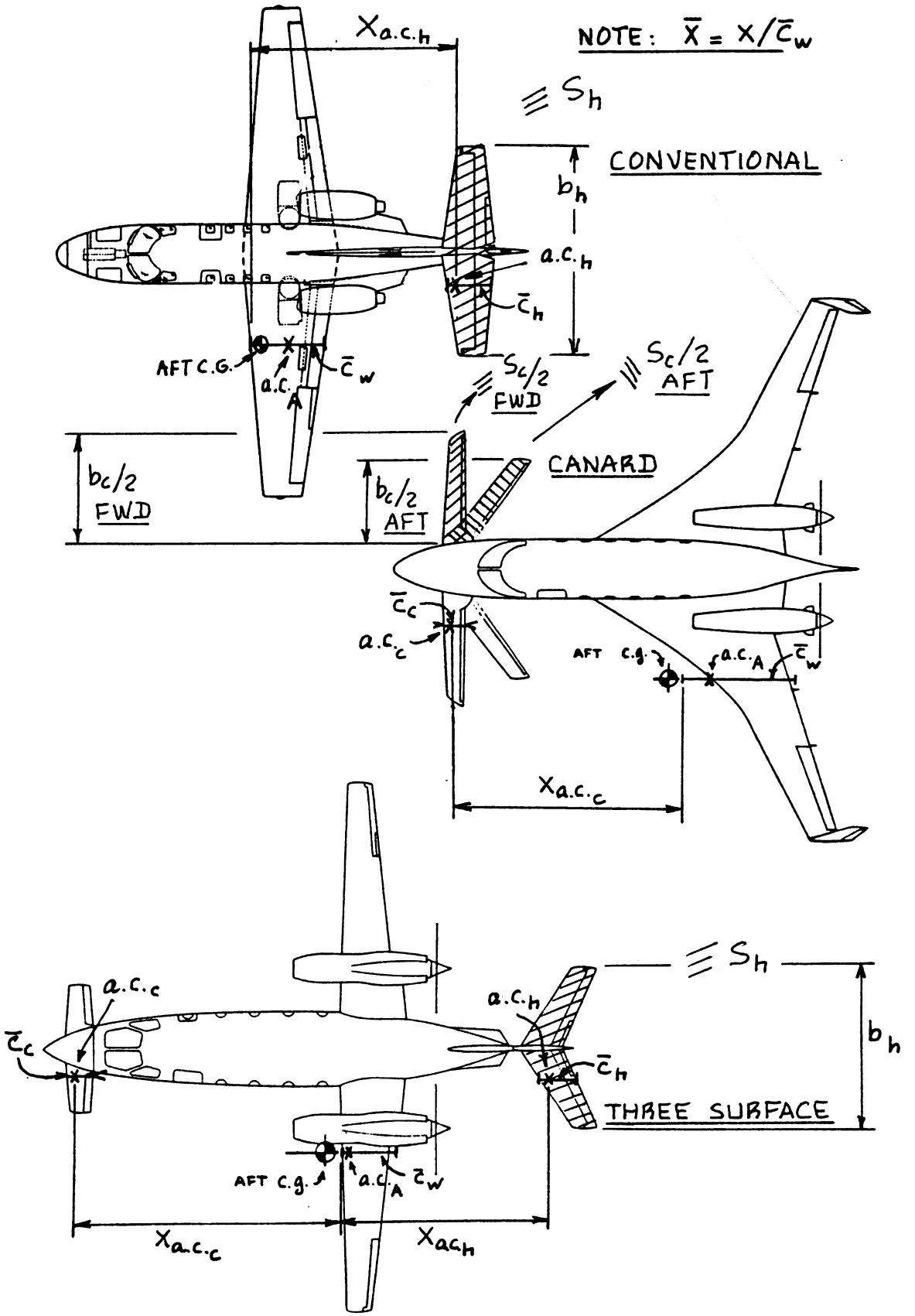

Figure 8.62 Geometric Parameters Required for Computing Overall Airplane Lift

8.1.5.1 Airplane zero-lift angle of attack: α_{o_L}

The airplane zero-lift angle of attack may be estimated from:

$$\alpha_{o_L} = (-C_{L_o})/C_{L_\alpha} \qquad (8.31)$$

where: C_{L_o} is the zero-angle-of-attack lift coefficient which is found from 8.1.5.2.

C_{L_α} is the airplane lift curve slope which may be found from 8.1.5.3.

8.1.5.2 Airplane zero-angle-of-attack lift coefficient: C_{L_o}

The airplane zero-angle-of-attack lift coefficient may be estimated from:

$$C_{L_o} = C_{L_{o_{wf}}} + C_{L_{\alpha_h}} \eta_h (S_h/S)(-\alpha_{o_{L_h}} - \varepsilon_{o_h}) +$$

$$+ C_{L_{\alpha_c}} \eta_c (S_c/S)(-\alpha_{o_{L_c}} + \varepsilon_{o_c}) \qquad (8.32)$$

where: $C_{L_{o_{wf}}}$ is the zero-angle-of-attack lift coefficient of the wing-fuselage combination. Unless the fuselage is severely cambered:

$$C_{L_{o_{wf}}} = \{i_w - \alpha_{o_{L_w}}\} C_{L_{\alpha_{wf}}} \qquad (8.33)$$

where: $\alpha_{o_{L_w}}$ is the wing zero-lift angle of attack found from 8.1.3.1.

$C_{L_{\alpha_{wf}}}$ is the wing-fuselage lift curve slope as found from 8.1.5.3.

Note: the subscripts wf (wing-fuselage) and wb (wing-body) are interchangeable.

$C_{L_{\alpha_h}}$ is the horizontal tail lift curve slope as found from 8.1.3.2 with appropriate substitution of tail parameters for wing parameters.

$C_{L_{\alpha_c}}$ is the canard lift curve slope as found from 8.1.3.2 with appropriate substitution of canard parameters for wing parameters.

NOTE: Figure 8.62 defines the necessary geometric parameters needed to compute horizontal tail and canard lift curve slopes.

$$\eta_h = \bar{q}_h/\bar{q} \tag{8.34}$$

$$\eta_c = \bar{q}_c/\bar{q} \tag{8.35}$$

The dynamic pressures $\bar{q}_h$ and $\bar{q}_c$ seen by a horizontal tail and a canard differ from the free stream dynamic pressure $\bar{q}$ for the following reasons:

a) as the air passes over a wing-fuselage combination it gradually looses some of its kinetic energy. This energy loss is proportional to the friction drag of the wing-fuselage.

b) when a horizontal tail or a canard surface are placed in the slipstream of a propeller, the local dynamic pressure depends on the power absorbed by the propeller and on the distance of the surface from the propeller.

In preliminary design it is acceptable to use:

For jet airplanes:

$$\eta_c = 1.0 \tag{8.36}$$

$$\eta_h = \tag{8.37}$$

$$[1 - \{\cos^2(\pi z_h/2z_w)\}\{2.42(C_{D_{o_w}})^{1/2}\}/(x_h/\bar{c} + 0.30)]$$

where: $z_h = a\sin(\gamma_h + \varepsilon_{cl} - \alpha_w)$ (8.38)

$x_h = a\cos(\gamma_h + \varepsilon_{cl} - \alpha_w)$

with a, γ_h, ε_{cl} and α_w shown in Fig. 8.63.

$$\varepsilon_{cl} = 1.62C_{L_w}/\pi A \tag{8.39}$$

$$z_w = 0.68\bar{c}\{C_{D_{o_w}}(x_h/\bar{c} + 0.15)\}^{1/2} \tag{8.40}$$

$C_{D_{o_w}}$ is the wing zero-lift drag coefficient as found from 4.2.1.1.

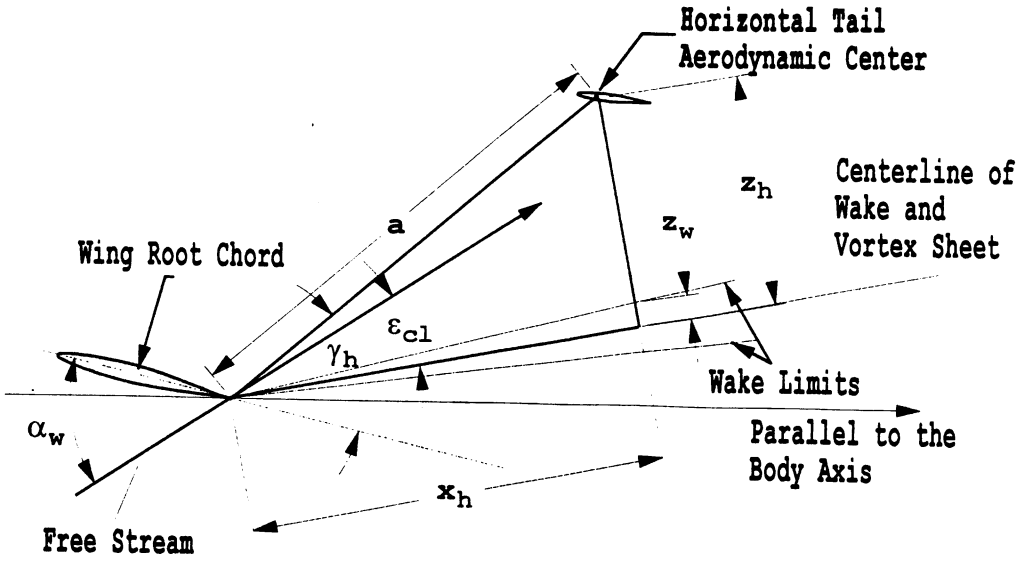

Figure 8.63 Geometric Parameters Required for Computing Dynamic Pressure Ratios

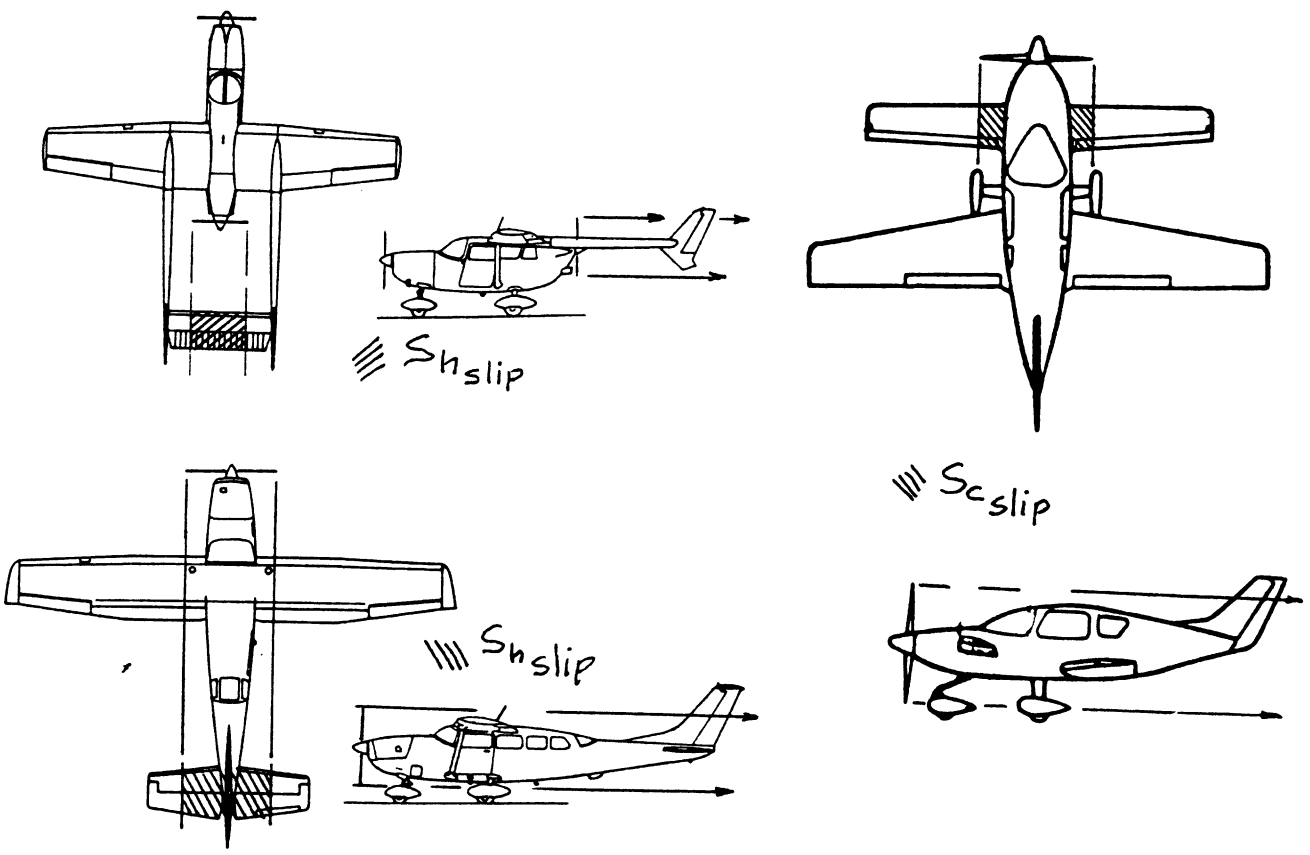

Figure 8.64 Definition of Canard and Tail Areas which are Submerged in Propeller Slipstream

For propeller driven airplanes:

The dynamic pressure ratios depend on where the canard and/or the horizontal tail are located relative to the propeller. The following approximation is suggested:

$$\eta_{h \text{ or } c} = 1 + \{(S_{h \text{ or } c})_{slip}/(S_{h \text{ or } c})\}x$$

$$x[(2200P_{av})/\{\bar{q}U_1\pi(D_p)^2\}] \qquad (8.41)$$

where: $(S_{h \text{ or } c})_{slip}$ is the area of the tail or canard which is submerged in the propeller slipstream: see Figure 8.64.

U_1 is the steady state speed of the airplane

P_{av} is the available horsepower, see Section 6.4.

D_p is the propeller diameter in ft

S_h is the horizontal tail area: see Figure 8.62.

S_c is the canard area: see Figure 8.62.

ε_{o_h} is the horizontal tail downwash angle for zero airplane angle of attack

ε_{o_c} is the canard upwash angle for zero airplane angle of attack

NOTE: the magnitudes of tail downwash angle and canard upwash angle at zero airplane angle of attack are dependent on the wing lift distribution at zero airplane angle of attack. For most airplanes (flaps up) it is acceptable to use: $\varepsilon_{o_h} = \varepsilon_{o_c} = 0$.

In Section 8.1.6 it is seen that with the flaps down this approximation is not valid. In that case, an incremental downwash angle, $\Delta\varepsilon_f$ must be accounted for.

$\alpha_{o_{L_h}}$ is the horizontal tail zero-lift angle of attack as found from 8.1.3.1 with appropriate substitution of tail parameters for wing parameters.

$\alpha_{o_{L_c}}$ is the canard zero-lift angle of attack as found from 8.1.3.1 with appropriate substitution of canard parameters for wing parameters.

8.1.5.3 Airplane lift curve slope: C_{L_α}

The airplane lift curve slope may be estimated from:

$$C_{L_\alpha} = C_{L_{\alpha_{wf}}} + C_{L_{\alpha_h}} \eta_h (S_h/S)(1 - d\varepsilon/d\alpha) + C_{L_{\alpha_c}} \eta_c (S_c/S)(1 + d\varepsilon_c/d\alpha) \quad (8.42)$$

where: $C_{L_{\alpha_{wf}}}$ is the wing-fuselage (wing-body) lift curve slope, given by:

$$C_{L_{\alpha_{wf}}} = K_{wf} C_{L_{\alpha_w}} \quad (8.43)$$

where: K_{wf} is the wing-fuselage interference factor given by:

$$K_{wf} = 1 + 0.025(d_f/b) - 0.25(d_f/b)^2 \quad (8.44)$$

$C_{L_{\alpha_w}}$ is found from 8.1.3.2.

$d\varepsilon/d\alpha$ = downwash gradient at the horizontal tail =

$$4.44[\{K_A K_\lambda K_h (\cos\Lambda_{c/4})^{1/2}\}^{1.19}]x \{(C_{L_{\alpha_w}})_{at\ M}\}/\{(C_{L_{\alpha_w}})_{at\ M=0}\} \quad (8.45)$$

where: $K_A = (1/A) - 1/(1 + A^{1.7})$ (8.46)

as shown in Figure 8.65a.

$K_\lambda = (10 - 3\lambda)/7$ (8.47)

as shown in Figure 8.65b.

$K_h = (1 - |h_h/b|)/(2l_h/b)^{1/3}$ (8.48)

as shown in Figure 8.65c with the parameters h_h, l_h defined in Fig. 8.66.

$d\varepsilon_c/d\alpha$ is the upwash gradient at the canard. It may be found from Figure 8.67 for wings of quarter chord sweep angles up to 35 deg.

All other quantities in Eqn. (8.42) are defined in 8.1.5.2.

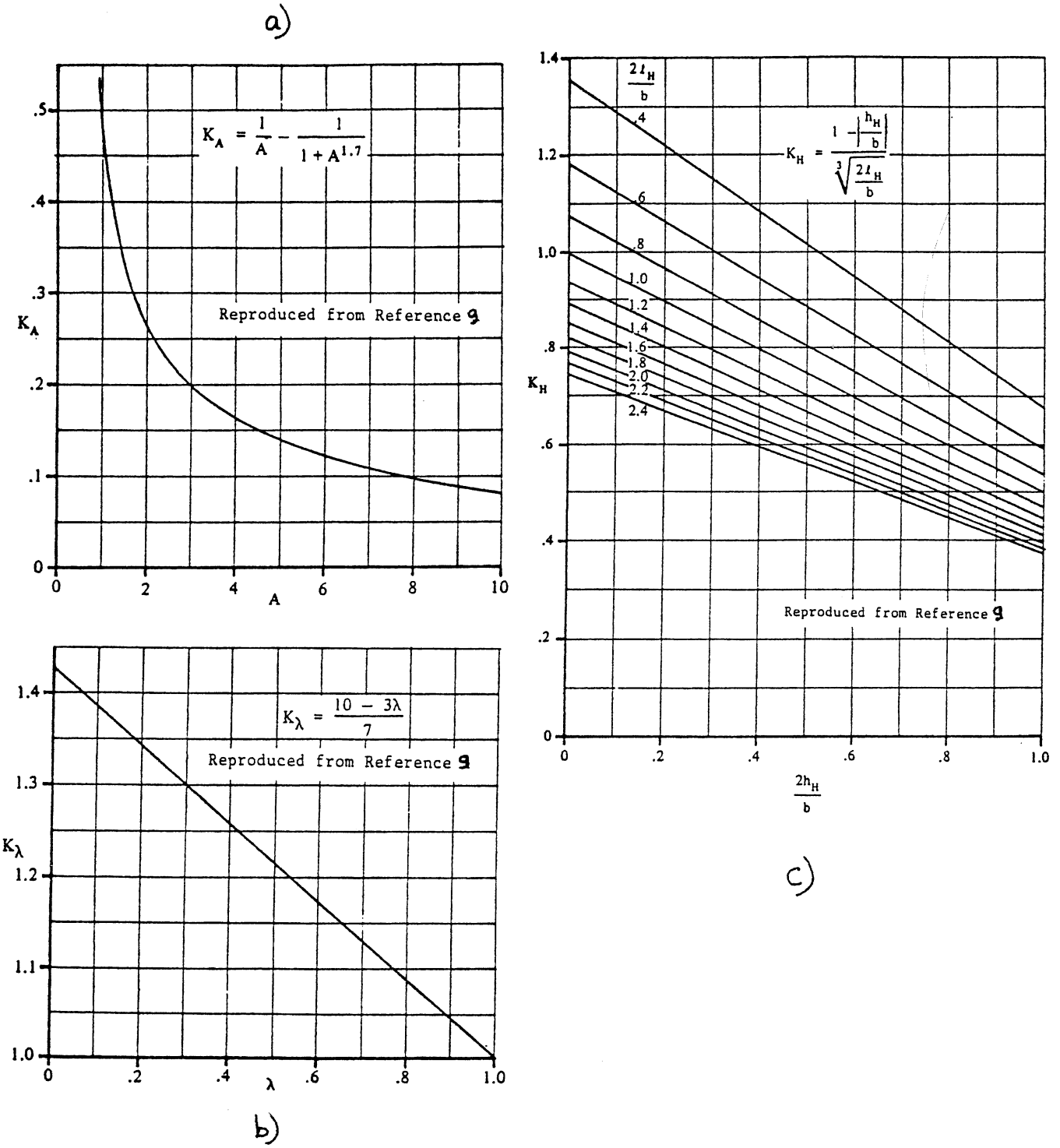

Figure 8.65 Factors for Computing Downwash

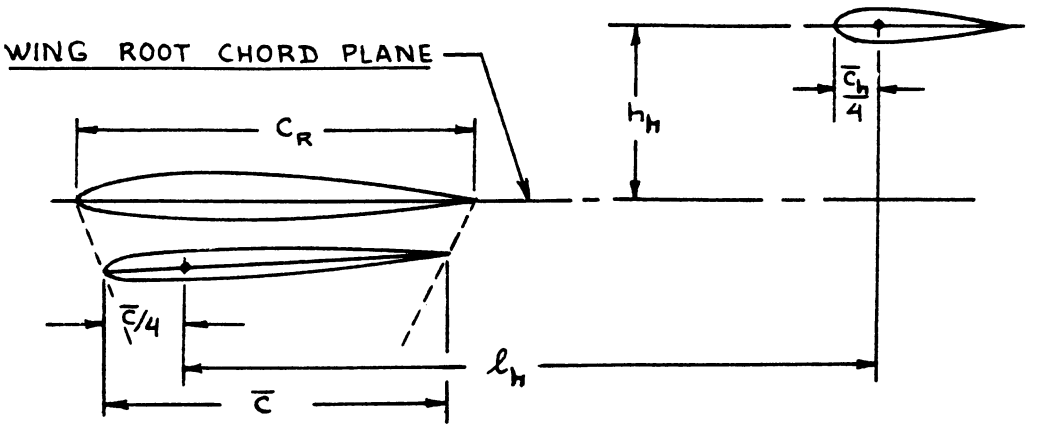

Figure 8.66 Geometric Parameters for Horizontal Tail Location

COPIED FROM: REF. 9

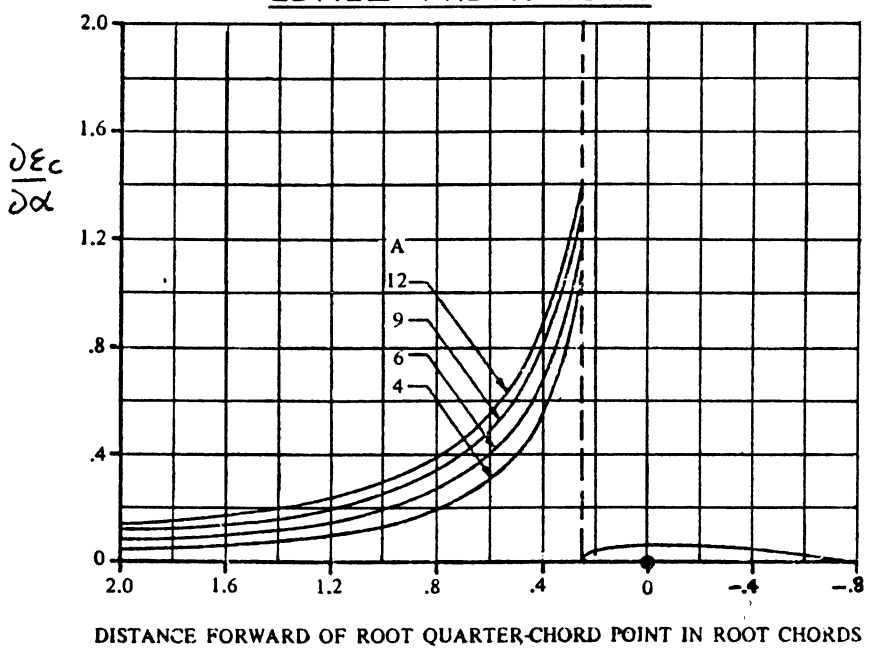

Figure 8.67 Wing Upwash Gradient

8.1.5.4 Airplane linear range of angle of attack: α_A^*

In preliminary design it is acceptable to use:

$$\alpha_A^* = \alpha_w^* - i_w \qquad (8.49)$$

where: α_w^* is found from 8.1.3.3.

8.1.5.5 Airplane maximum lift coefficient: $C_{L_{max}}$ and airplane angle of attack for maximum lift: $\alpha_{C_{L_{max}}}$

The airplane maximum lift coefficient is found from:

$$C_{L_{max}} = C_{L_{max_w}} - (C_{L_{\alpha_{wf}}})\Delta\alpha_{w/c} + \qquad (8.50)$$

$$+ (C_{L_{\alpha_h}})(S_h/S)\{(\alpha_{C_{L_{max}}})(1 - d\varepsilon/d\alpha) - \varepsilon_{o_h} + i_h\} +$$

$$+ (C_{L_{\alpha_c}})(S_c/S)\{(\alpha_{C_{L_{max}}})(1 + d\varepsilon_c/d\alpha) + \varepsilon_{o_c} + i_c\}$$

where: $C_{L_{max_w}}$ is found from 8.1.3.4.

$C_{L_{\alpha_{wf}}}$ is found from Eqn.(8.43)

$\Delta\alpha_{w/c}$ is the difference between the airplane angles of attack for canard stall and for wing stall. In a canard airplane, the canard must always stall before the wing! In preliminary design it is suggested to use: $\Delta\alpha_{w/c} = 3$ deg.

$$\alpha_{C_{L_{max}}} = \alpha_{C_{L_{max_w}}} - i_w - \Delta\alpha_{w/c} \qquad (8.51)$$

where: $\alpha_{C_{L_{max_w}}}$ is found from 8.1.3.4.

All other quantities are defined in 8.1.5.2.

8.1.5.6 Construction of airplane lift curve: flaps-up

All ingredients necessary to construct the airplane C_L versus α curve are now available. Figure 8.68 shows how this can be done in a step-by-step manner.

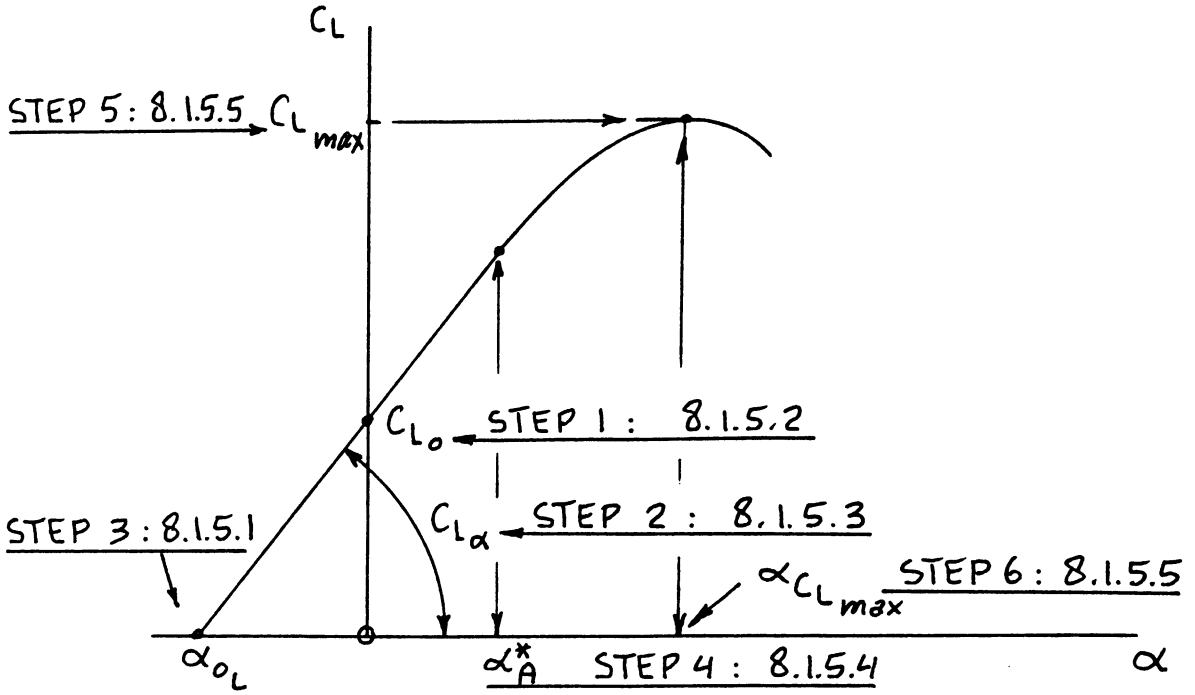

Figure 8.68 Construction of Airplane Lift Versus α Curve

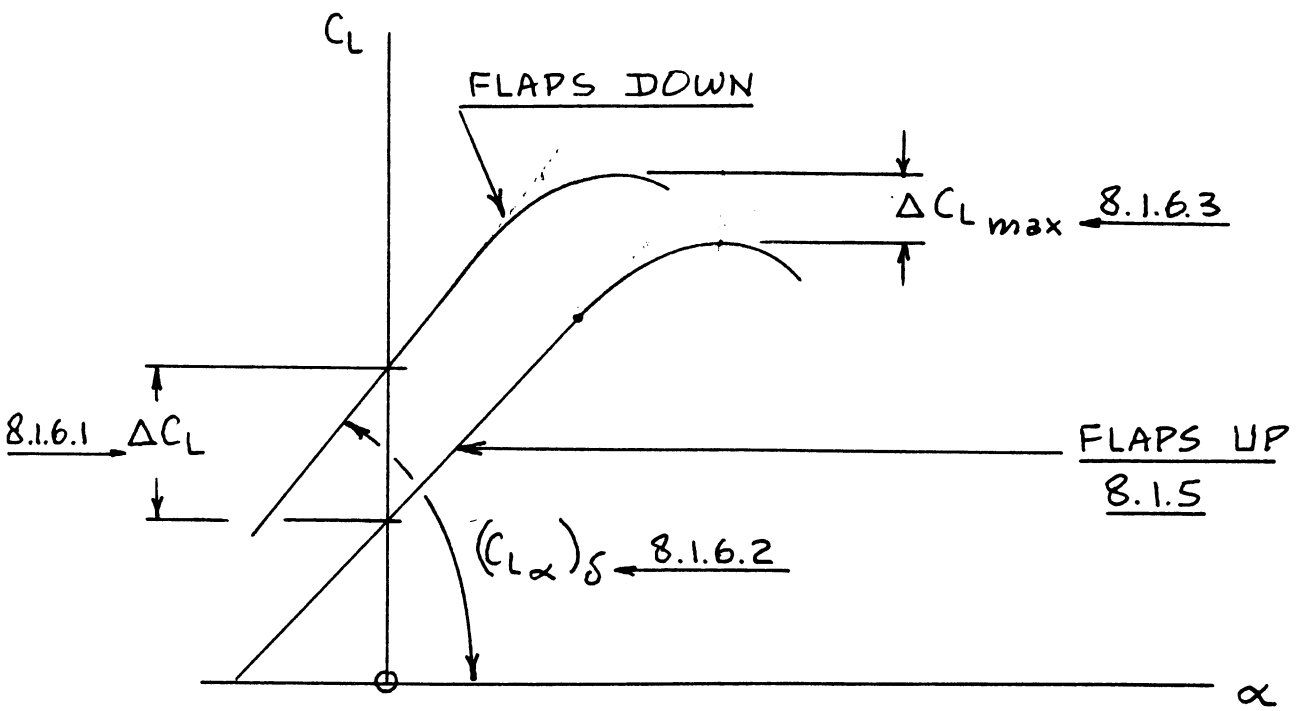

Figure 8.69 Fundamental Airplane Lift Versus α Curve with the Flaps Down

8.1.6 Airplane Lift and Maximum Lift: Flaps Down

Figure 8.69 shows the relationship between airplane lift coefficient in the flaps down configuration and airplane angle of attack which must be determined with the methods to be presented in this section. Key quantities needed in the construction of the flaps down airplane C_L versus α curve are listed, with an indication of where methods for their estimation may be found.

8.1.6.1 Airplane lift increment due to flaps: ΔC_L

The airplane lift increment due to flaps may be estimated from:

$$\Delta C_L = k_{cw}\Delta C_{L_w} + k_{wc}(S_c/S)\Delta C_{L_c} + \quad (8.52)$$

$$+ k_{wh}(S_h/S)\Delta C_{L_h} - C_{L_{\alpha_h}}\eta_h(S_h/S)\Delta\varepsilon_f$$

where: ΔC_{L_w} is found from 8.1.4.1

k_{cw} is a canard-on-wing interference factor. If the canard is small relative to the wing and if the canard is far enough forward of the wing, $k_{cw} = 1.0$ may be used in early design.

Whenever one or both of these conditions are not met, a finite element aerodynamic analysis of the canard-on-wing effect is needed. Such methods are beyond the scope of this text.

k_{wc} is the wing-on-canard interference factor. It is similar to (albeit not the same as) k_{cw}.

In early design it is acceptable to use: $k_{wc} = 1.0$.

S_c is the canard area: see Figure 8.62.

ΔC_{L_c} is found from 8.1.4.1 with appropriate substitution of canard parameters for wing parameters. If a canardvator deflection is present, it should be treated as a plain flap and its lift increment must be added.

Note: In airplanes such as the Piaggio P 180 Avanti, the canard is equipped with a Fowler

flap which is geared to the wing flap. The effect of such a flap must be accounted for! A detailed treatment of such a system is beyond the scope of this text.

k_{wh} is the wing-on-horizontal-tail interference factor. It is similar to (albeit not the same as) k_{cw}. In early design it is acceptable to use: $k_{wh} = 1.0$.

S_h is the horizontal tail area: see Figure 8.62.

ΔC_{L_h} is found from 8.1.4.1 with appropriate substitution of horizontal tail parameters for wing parameters. If an elevator is present, its deflection can be accounted for by considering the elevator to be a plain flap.

$C_{L_{\alpha_h}}$ is the horizontal tail lift-curve-slope which may be found from Eqn. (8.22) with appropriate substitution of horizontal tail parameters for wing parameters.

$\Delta\varepsilon_f$ is the increase in tail downwash angle due to wing flap deflection. It may be estimated from Figure 8.70.

<u>8.1.6.2 Airplane lift curve slope due to flaps:</u> $(C_{L_\alpha})_\delta$

The airplane lift curve slope with the flaps down may be estimated from:

$$(C_{L_\alpha})_\delta = K_{wf}(C_{L_{\alpha_w}})_\delta + C_{L_{\alpha_h}}\eta_h(S_h/S)\{1 - (d\varepsilon/d\alpha)_\delta\} + C_{L_{\alpha_c}}\eta_c(S_c/S)\{1 - (d\varepsilon_c/d\alpha)_\delta\} \qquad (8.53)$$

where: $(C_{L_{\alpha_w}})_\delta$ is the wing lift-curve-slope with the flaps down. It is found from Eqn. (8.28).

where: $(d\varepsilon/d\alpha)_\delta$ is the flaps-down downwash gradient at the horizontal tail.

$(d\varepsilon_c/d\alpha)_\delta$ is the flaps-down upwash gradient at the canard.

<u>Note:</u> in preliminary design it is acceptable to set these flaps-down downwash and upwash gradients equal to those with the flaps up. The latter may be determined

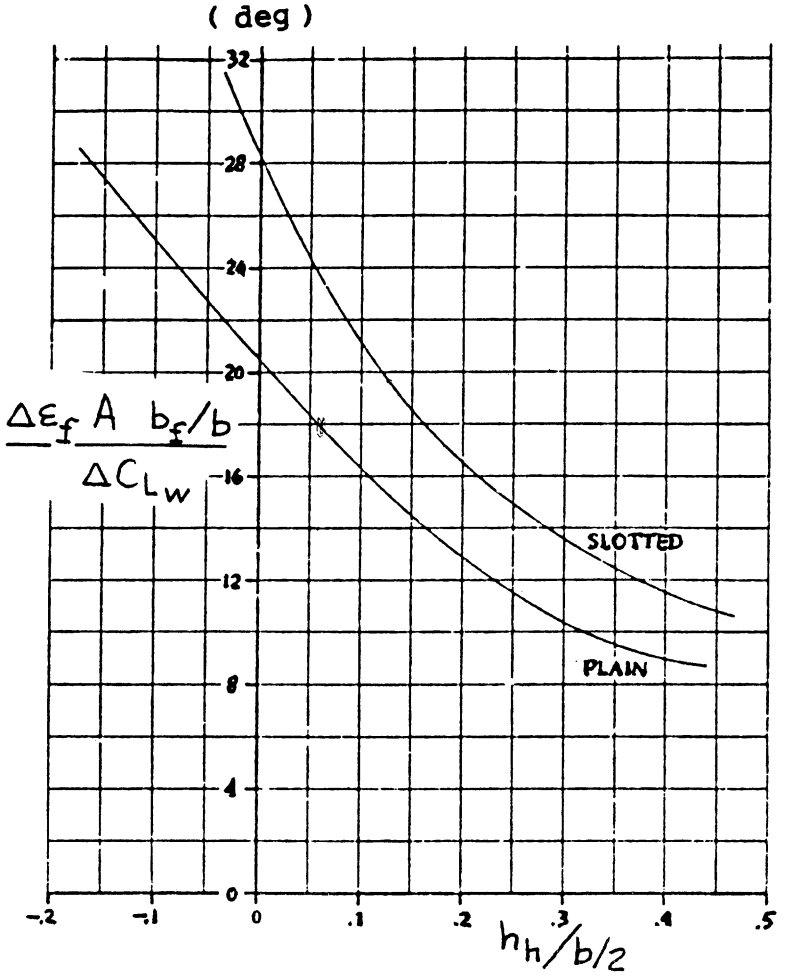

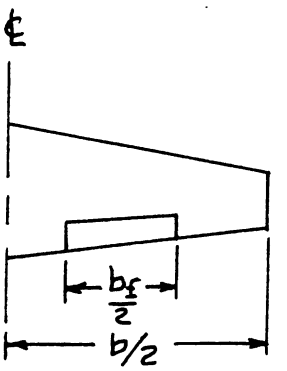

COPIED FROM: REF. 9

FOR h_h SEE FIG. 8.66

Figure 8.70 Incremental Downwash Angle at the Horizontal Tail due to Flaps

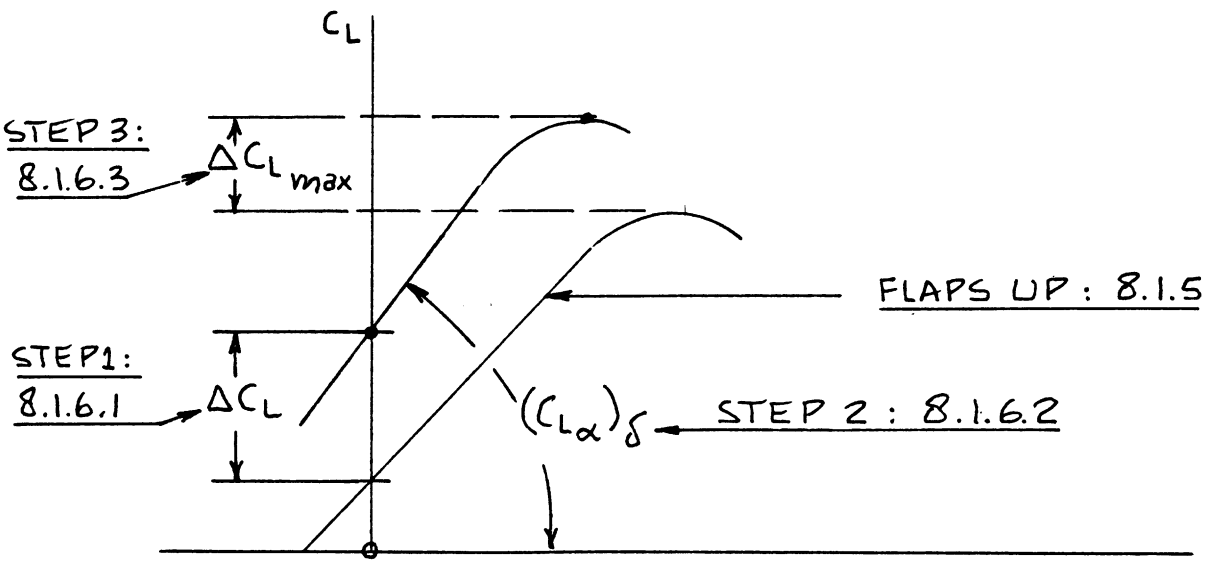

Figure 8.71 Construction of Airplane Lift Versus α Curve with the Flaps Down

from 8.1.5.3.

All other quantities were defined in 8.1.5.2 and 8.1.5.3.

8.1.6.3 Airplane maximum lift increment due to flaps: $\Delta C_{L_{max}}$

The airplane maximum lift increment due to flaps may be estimated from:

$$\Delta C_{L_{max}} = k_{cw}\Delta C_{L_{max_w}} - (C_{L_{\alpha_w}})_{\delta}\Delta\alpha_{w/c} + (S_c/S)\Delta C_{L_{max_c}} + (S_h/S)C_{L_{\alpha_h}}\{-\Delta\varepsilon_f\} \quad (8.54)$$

where: k_{cw} is the canard-on-wing interference factor. If the canard is small relative to the wing and if the canard is far enough forward of the wing, $k_{cw} = 1.0$ may be used in early design.

Whenever one or both of these conditions are not met, a finite element aerodynamic analysis of the canard-on-wing effect is needed. Such methods are beyond the scope of this text.

$\Delta\alpha_{w/c}$ is the difference between the airplane angles of attack for canard stall and for wing stall. In a canard airplane, the canard must always stall before the wing! In In preliminary design, use: $\Delta\alpha_{w/c} = 3$ deg.

$\Delta\varepsilon_f$ is the increase in tail downwash angle due to flaps. It may be found from Figure 8.70.

All other quantities in Eqn.(8.51) are defined in 8.1.6.1 and 8.1.6.2.

8.1.6.4 Construction of airplane lift curve: flaps down

All ingredients necessary to construct the flaps down airplane lift curve are now available. Figure 8.71 shows the step-by-step manner in which this can be done.

8.1.7 Airplane Lift in Ground Effect

When an airplane operates close to the ground, the downwash and the upwash patterns around its lifting surfaces change. References 9 and 14 contain physical explanations for these effects. In this section, the position is taken that the effect of the ground on the C_L versus α behavior of an airplane is a change in angle of attack at constant lift coefficient (or, vice versa, a change in lift coefficient at constant angle of attack). Figure 8.72 shows this in terms of the ground induced change in angle of attack at constant lift coefficient: $\Delta\alpha_g$. Note the difference in ground effect on high and on low aspect ratio configurations. This difference is accounted for as follows:

8.1.7.1 High aspect ratio configurations: transports
8.1.7.2 Low aspect ratio configurations: fighters

NOTE: it will be assumed that the effect of the ground on tail downwash and canard upwash can be neglected as far as overall airplane lift is concerned. The effect of the ground on tail downwash does alter tail lift and because of that the airplane pitching moment is affected: this is accounted for in Section 8.2.

8.1.7.1 High aspect ratio configurations: transports

Figure 8.72a shows the ground induced change in angle of attack at constant lift coefficient: $\Delta\alpha_g$.

For high aspect ratio configurations the change in angle of attack at constant lift coefficient in ground effect may be found from:

$$\Delta\alpha_g = -F_{tv}\{(9.12/A) + 7.16(c_r/b)\}(C_{L_{wf}}) + \qquad (8.55)$$

$$- \{A/(2C_{L_{\alpha_{wf}}})\}(c_r/b)\{(L/L_o) - 1\}(C_{L_{wf}})r_g +$$

$$- \{(\delta_f/50)^2/(C_{L_{\alpha_{wf}}})\}\Delta(\Delta C_L)_f$$

where: F_{tv} is a factor which accounts for the effect on lift due to the image trailing vortex. It is found from Figure 8.73.

A is the wing aspect ratio

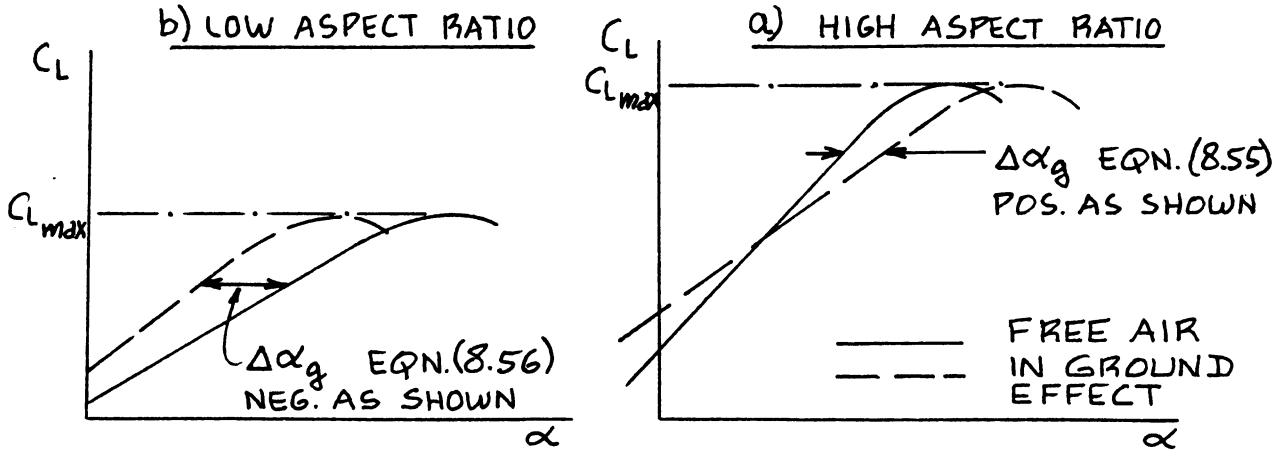

Figure 8.72 Ground Effect on Lift Curves

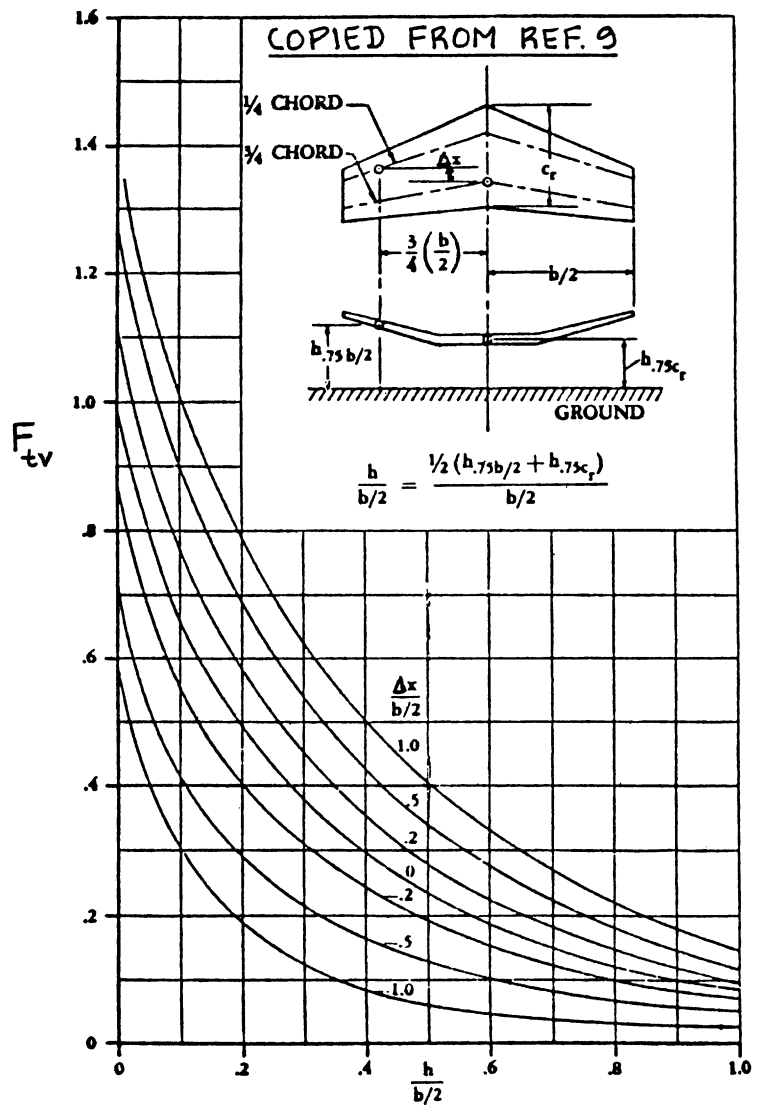

Figure 8.73 Factor Due to Image Trailing Vortex

c_r/b is the ratio of wing root chord to wing span

$C_{L_{wf}}$ is the wing-fuselage lift coefficient out of ground effect. This is found from Section 8.1.5 or from Section 8.1.6 (depending on the flap deflection) by setting $S_h = S_c = 0$.

$C_{L_{\alpha_{wf}}}$ is the wing-fuselage lift-curve-slope as determined from Eqn.(8.43), in 1/deg.

$(L/L_o - 1)$ accounts for the effect on lift due to the image bound vortex. It is found from Figure 8.74.

r_g is a factor which accounts for the effect of finite span. It may be found from Figure 8.75.

δ_f is the flap deflection in degrees

$\Delta(\Delta C_L)_f$ is a factor which accounts for the effect of flaps in ground effect. It is found from Figure 8.76.

Equation (8.55) is used to estimate $\Delta\alpha_g$ for two values of $C_{L_{wf}}$ after which the airplane C_L versus α curve is modified as indicated in Figure 8.72a. This procedure neglects the effect of the horizontal tail and the canard on airplane lift in ground effect. In Section 8.2.7 it will be seen that the effect of the horizontal tail and the canard on airplane pitching moment in ground effect is NOT neglected.

8.1.7.2 Low aspect ratio configurations: fighters

Figure 8.72b shows the ground induced change in angle of attack at constant lift coefficient: $\Delta\alpha_g$. For low aspect ratio configurations, this quantity follows from:

$$\Delta\alpha_g = -18.24(C_{L_{wf}})\sigma_g/A + r_g T_g (C_{L_{wf}})^2/57.3(C_{L_\alpha})_{wf} - r_g B_g \qquad (8.56)$$

where: $C_{L_{wf}}$ is the wing-fuselage lift coefficient in free air. This follows from Section 8.1.5 or from Section 8.1.6 (depending on the flap state) by setting $S_h = S_c = 0$.

BOTH COPIED FROM REF. 9

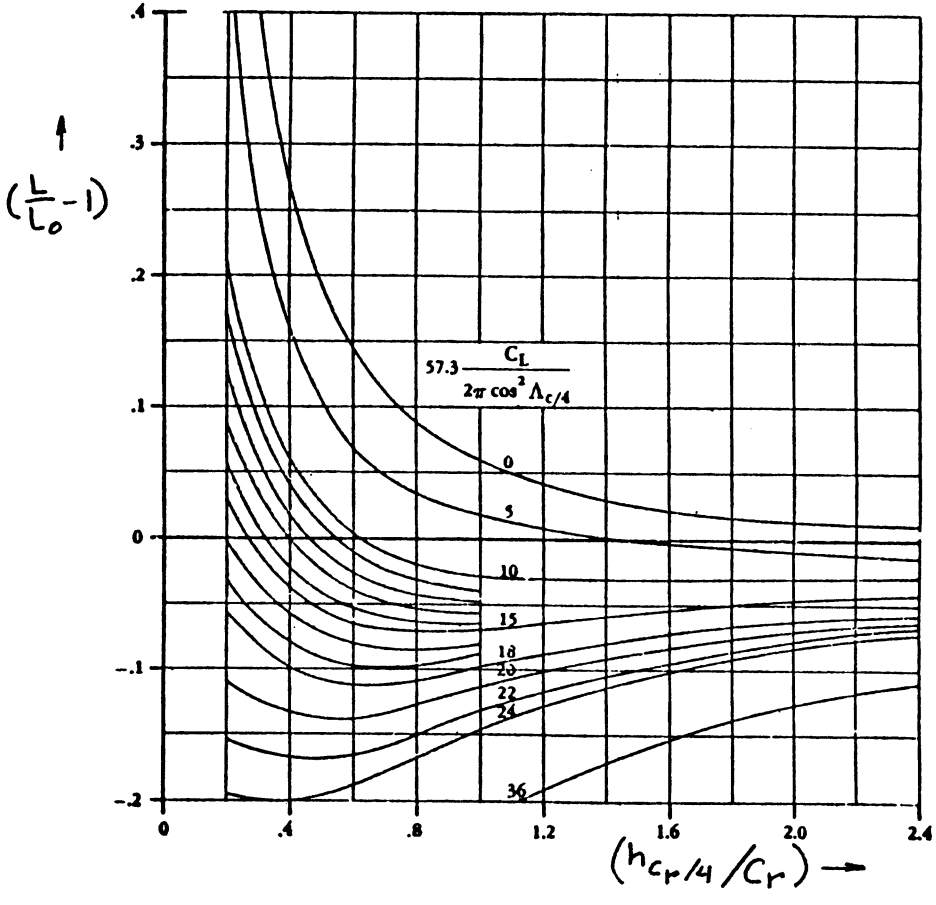

Figure 8.74 Factor Due to Image Bound Vortex

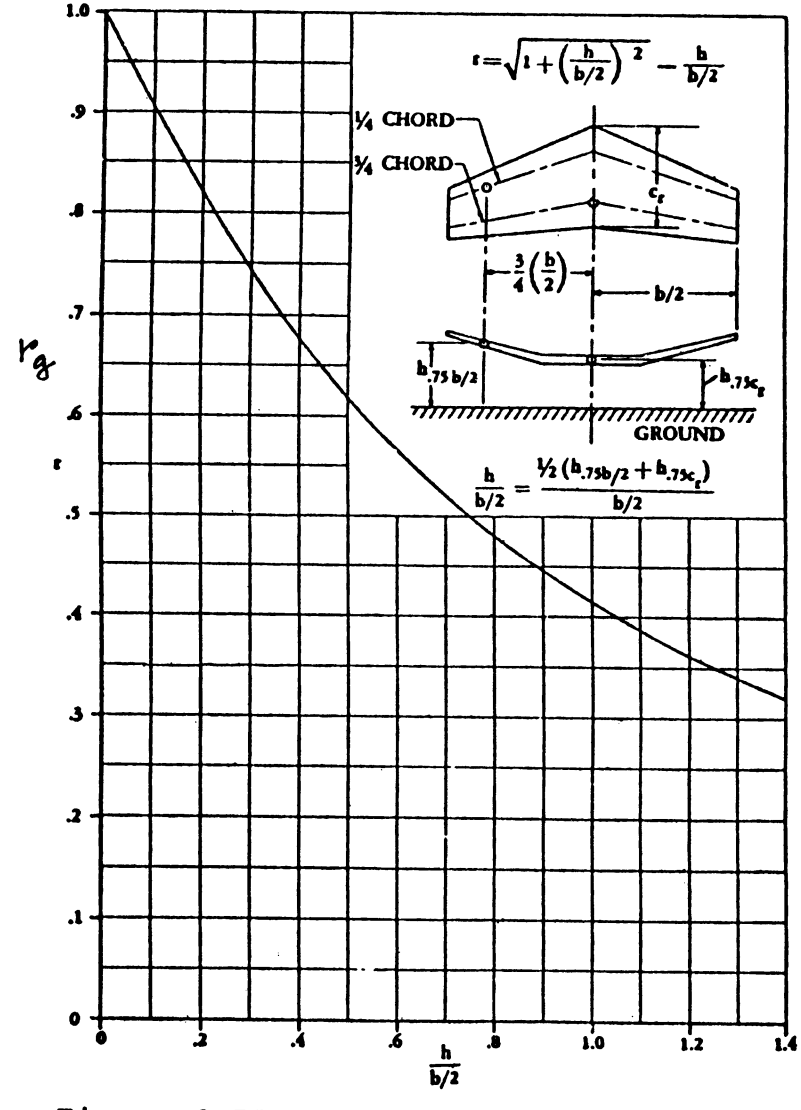

Figure 8.75 Factor Due to Finite Span

BOTH COPIED FROM REF. 9

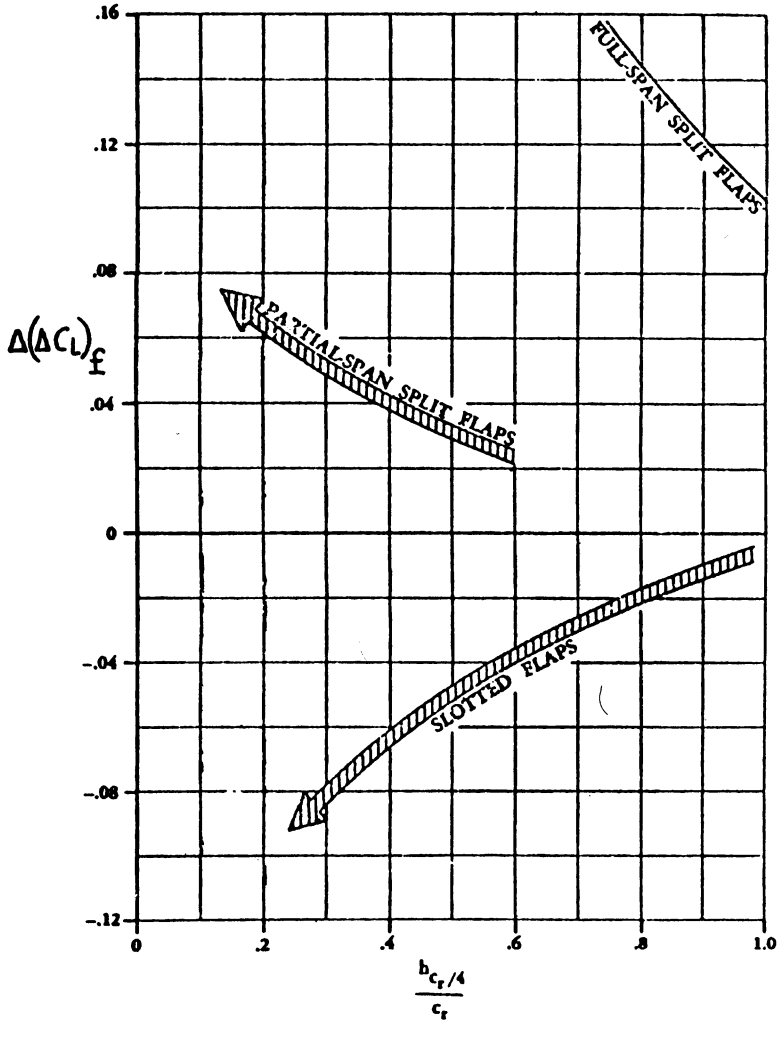

Figure 8.76 Ground Effect on Lift Due to Flaps

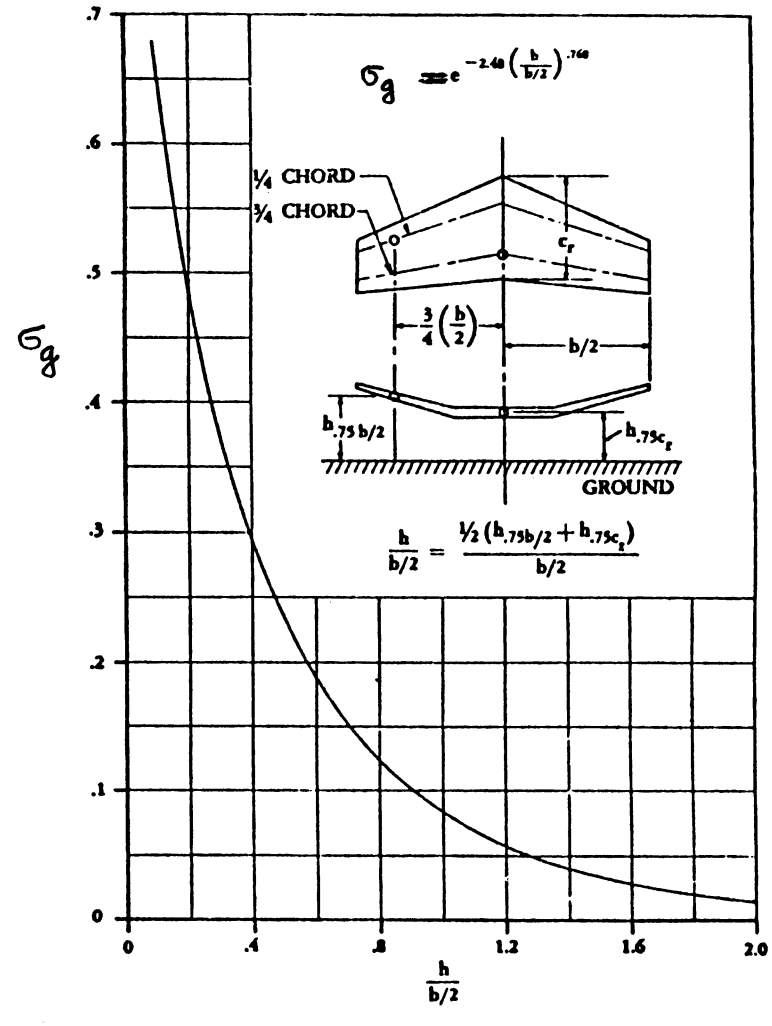

Figure 8.77 Factor Due to Vertical Induced Velocity

σ_g is found from Figure 8.77.

A is the wing aspect ratio.

r_g is found from Figure 8.75.

T_g is found from Figure 8.78.

$(C_{L_\alpha})_{wf}$ is found from Eqn.(8.43), in 1/deg.

B_g is found from Figure 8.79.

Equation (8.56) neglects the effect of wing thickness which is small except for very thick wings close to the ground.

Equation (8.56) is used to estimate $\Delta\alpha_g$ for two values of $C_{L_{wf}}$ after which the airplane C_L versus α curve is modified as indicated in Figure 8.72b. This procedure neglects the effect of the horizontal tail and the canard on airplane lift in ground effect. In Section 8.2.7 it will be seen that the effect of the horizontal tail and the canard on airplane pitching moment in ground effect is NOT neglected.

8.1.8 Power Effects on Airplane Lift

The only power effect on lift which will be considered here is that due to propeller slipstream acting on a wing. Figure 8.80 shows the basic propeller-on-wing geometry. The effect of the propeller is to increase the dynamic pressure over the wing behind the propeller. In turn, this causes an increase in wing lift (and thus in airplane lift) which may be estimated from:

$$\Delta C_{L_w} = \text{Sum}_{i=1}^{i=n}\left[(S_{p_i}/S)(C_{L_w})\left[(2200P_{av_i})/\{\bar{q}U_1\pi(D_{p_i})^2\}\right]\right] \qquad (8.57)$$

where: S_{p_i} is the wing area affected by the slipstream, see Figure 8.80.

C_{L_w} is the lift coefficient at which the wing is operating. It follows from Sub-sections 8.1.3 or 8.1.4.

BOTH COPIED FROM REF. 9

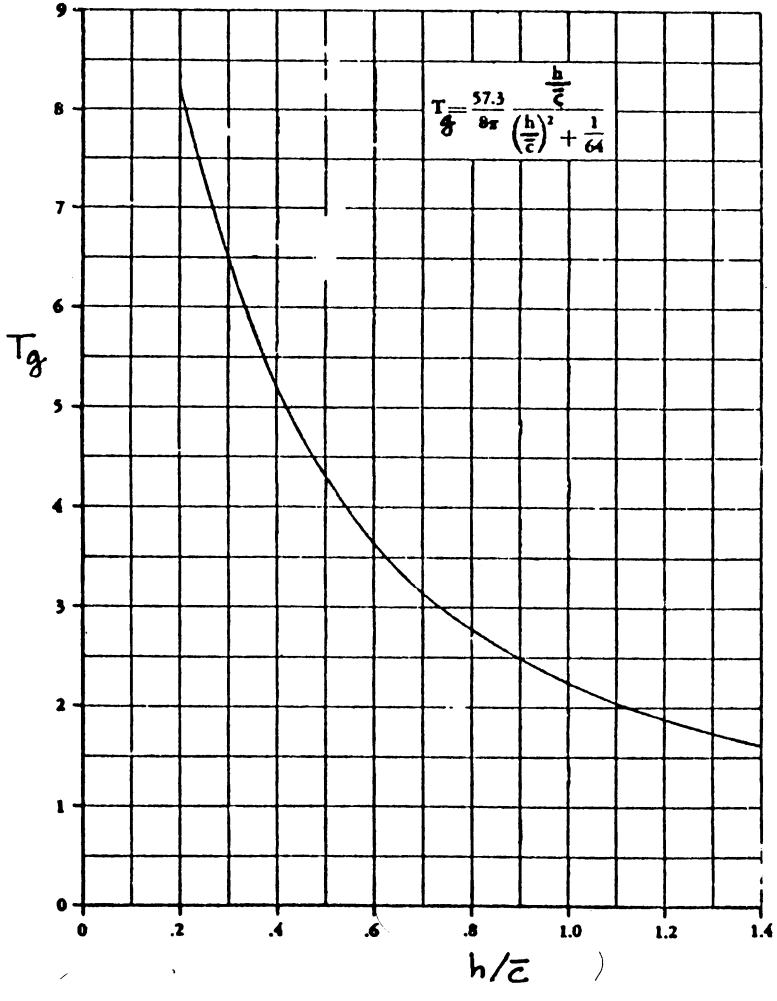

Figure 8.78 Factor Due to Horizontal Induced Velocity

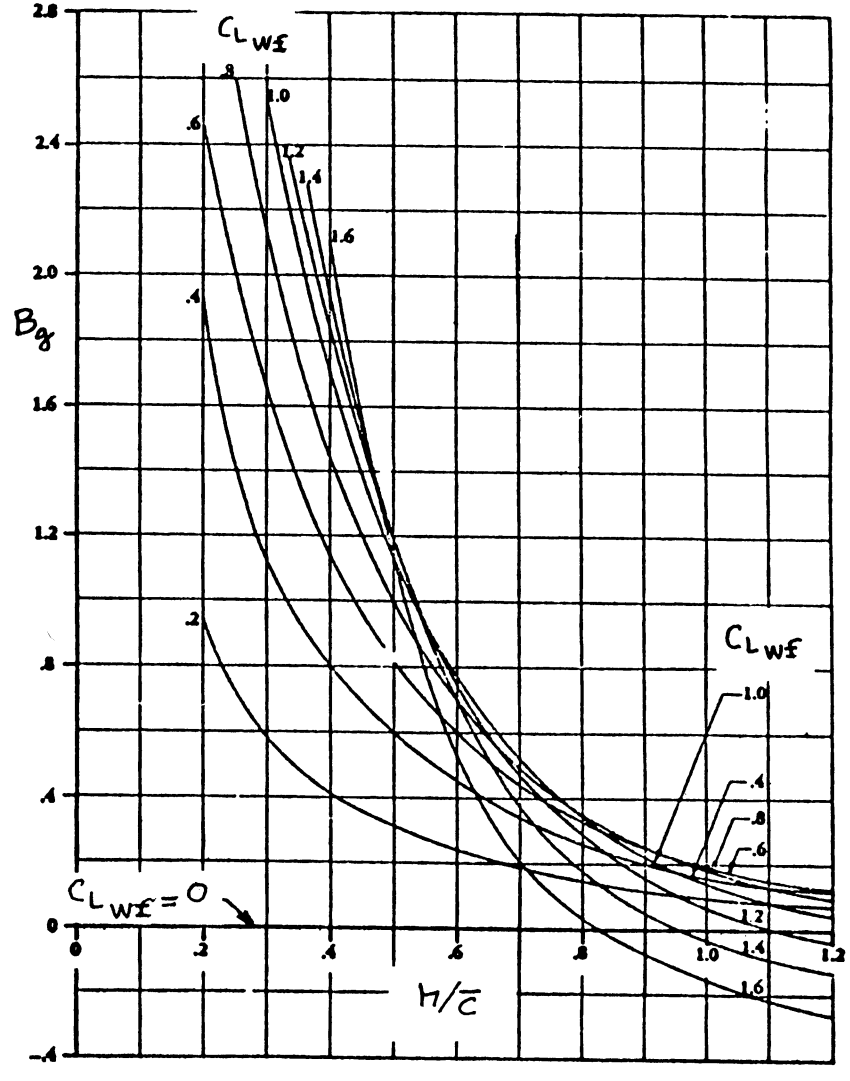

Figure 8.79 Factor Due to Circulation Change

P_{av_i} is the available horsepower, see Section 6.4.

U_1 is the steady state speed of the airplane

D_{p_i} is the propeller diameter in ft.

A more detailed treatment of power effects on lift is considered beyond the scope of this text. Reference 9 addresses this topic.

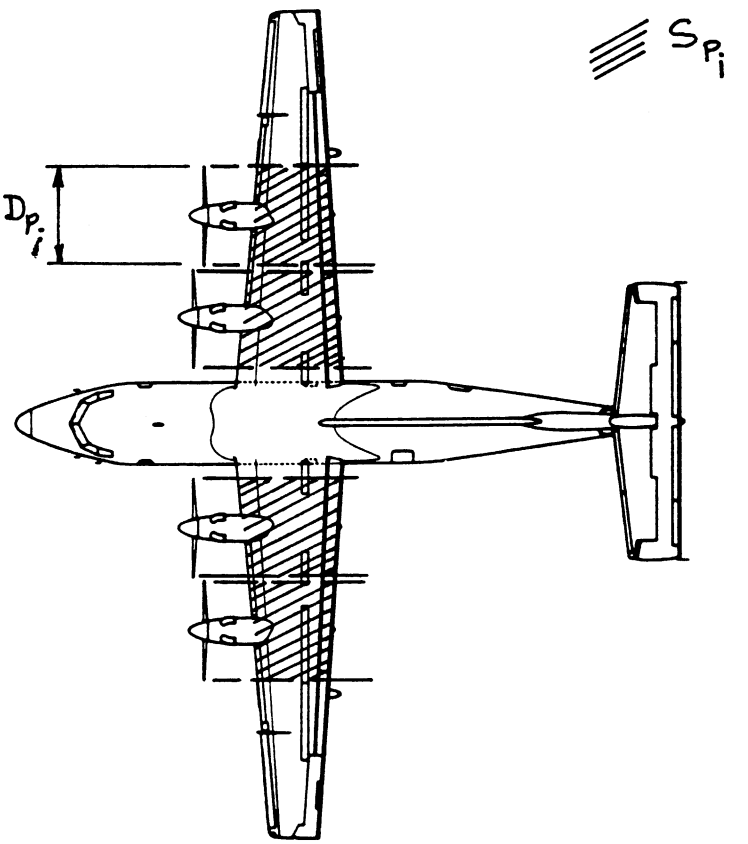

Figure 8.80 Wing Area Affected by Propeller Slipstream

8.2. PREDICTION OF PITCHING MOMENT COEFFICIENT VERSUS LIFT COEFFICIENT

In this section methods for predicting the variation of pitching moment coefficient with lift coefficient will be presented as follows:

8.2.1 Airfoil pitching moment: flaps up
8.2.2 Airfoil pitching moment: flaps down
8.2.3 Wing pitching moment: flaps up
8.2.4 Wing pitching moment: flaps down
8.2.5 Airplane pitching moment: flaps up
8.2.6 Airplane pitching moment: flaps down
8.2.7 Airplane pitching moment in ground effect
8.2.8 Power effects on airplane pitching moment

8.2.1 Airfoil Pitching Moment: Flaps Up

Figure 8.81 shows the relationship between airfoil pitching moment coefficient and airfoil lift coefficient which must be determined with the methods presented in this Section. Key quantities needed in the construction of the airfoil c_m versus c_l curve are listed, with an indication of where methods for their estimation are found. Note that c_m has meaning only when taken about a known reference point. The location of this reference point is defined in 8.2.1.3.

8.2.1.1 Airfoil zero-lift pitching moment coefficient: c_{m_o}

IMPORTANT NOTES:

1. In Chapter 4 the subscript 'o' indicates a drag coefficient at zero lift coefficient.

2. In Section 8.1 the subscript 'o' indicates a lift coefficient at zero angle of attack.

3. In this section (8.2) the subscript 'o' indicates a pitching moment coefficient at zero lift coefficient.

Reference 49 contains a large data base for finding c_{m_o} for many airfoils. This data base applies to the so-called NACA airfoils.

Table 8.1 (p.216-217) provides a summary of airfoil

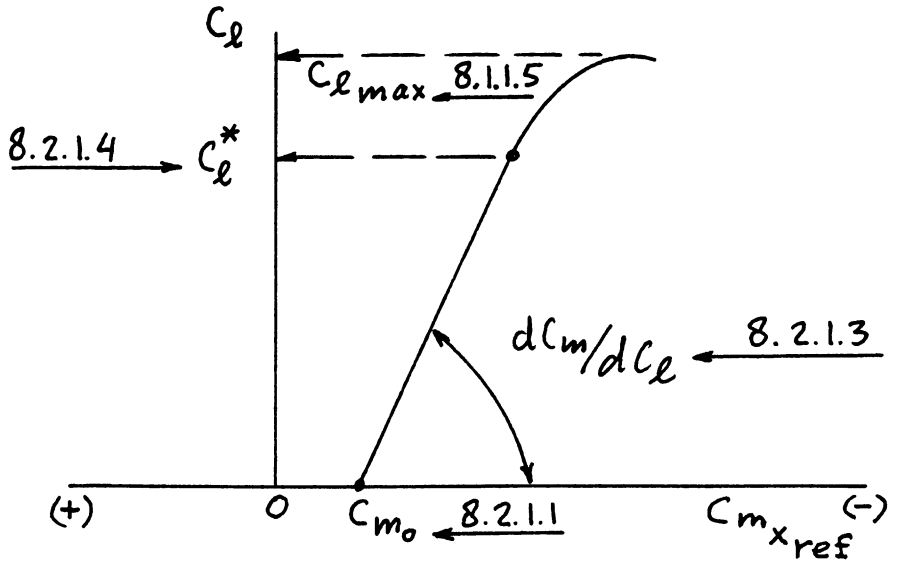

Figure 8.81 Airfoil Pitching Moment Coefficient Versus Lift Coefficient

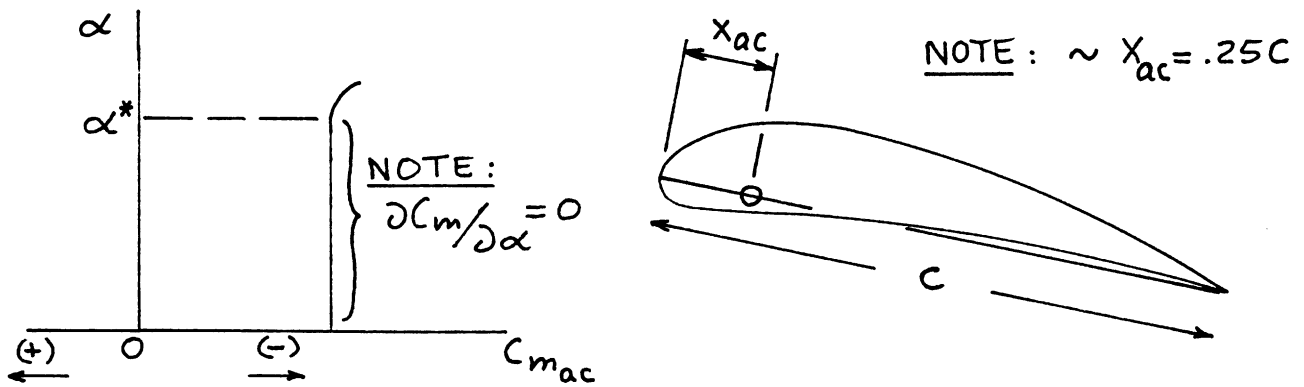

Figure 8.82 Location of Airfoil Aerodynamic Center

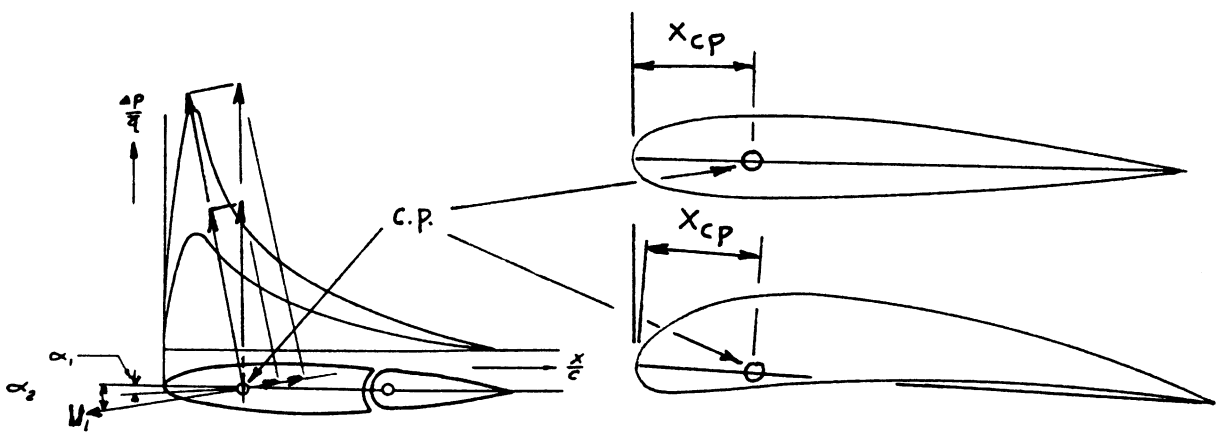

Figure 8.83 Airfoil Center of Pressure: Origin and Location

data from which c_{m_o} may be determined. Where possible, actual airfoil data should be used. Such data may be obtained either from windtunnel data or from theoretical predictions obtained with a modern airfoil code.

Note from Table 8.1 that these c_{m_o} values are zero for symmetrical sections and negative (i.e. nose-down!) for positively cambered airfoils. This will have important consequences to airplane trim!

8.2.1.2 Airfoil aerodynamic center: x_{ac} and airfoil center of pressure: x_{cp}

Definition: The aerodynamic center is that point about which the variation of pitching moment coefficient with angle of attack is zero.

Figure 8.82 shows how the aerodynamic center for an airfoil is located.

Note that this concept implies also that the variation of pitching moment coefficient with lift coefficient is zero, when:

$$\alpha < \alpha^* \tag{8.58}$$

Definition: The center of pressure is that point where the resultant force caused by the pressure distribution acts.

Figure 8.83 shows how the center of pressure arises from the airfoil pressure distribution and how the center of pressure is located.

Evidently, there are two methods to represent forces and moments acting on an airfoil. Figure 8.84 shows both methods. The following relationship exists between the two methods:

$$x_{cp} = x_{ac} - (c_{m_{ac}})c/c_l \tag{8.59}$$

This can also be written as:

$$c_{m_{ac}} = -c_l(x_{cp} - x_{ac})/c \tag{8.60}$$

Note from this that:

$$c_{m_{ac}} = c_{m_o} \tag{8.61}$$

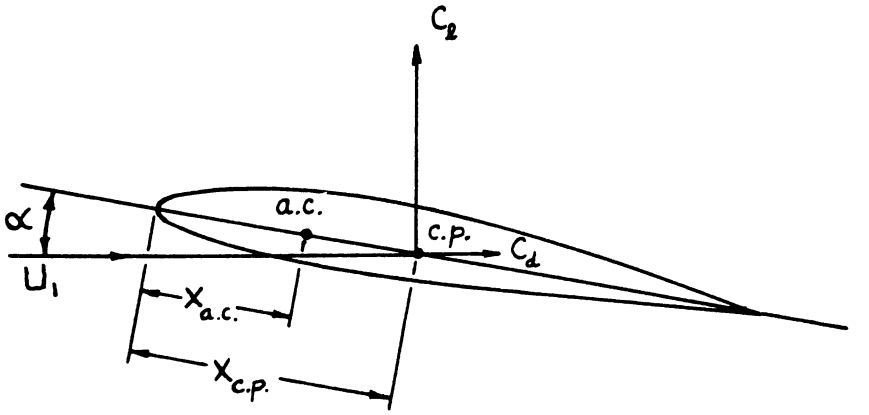

a. Forces at the Center of Pressure

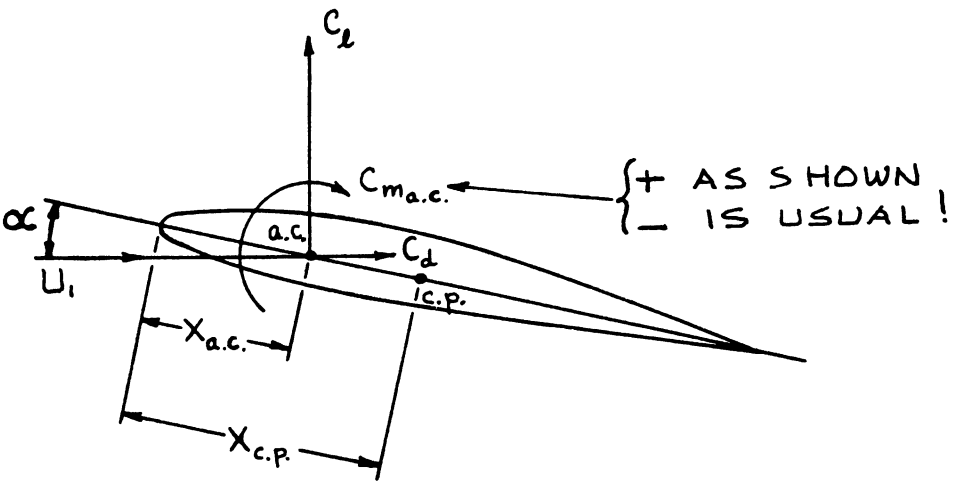

b. Forces at the Aerodynamic Center

Figure 8.84 Methods for Resolving Airfoil Forces and Moments

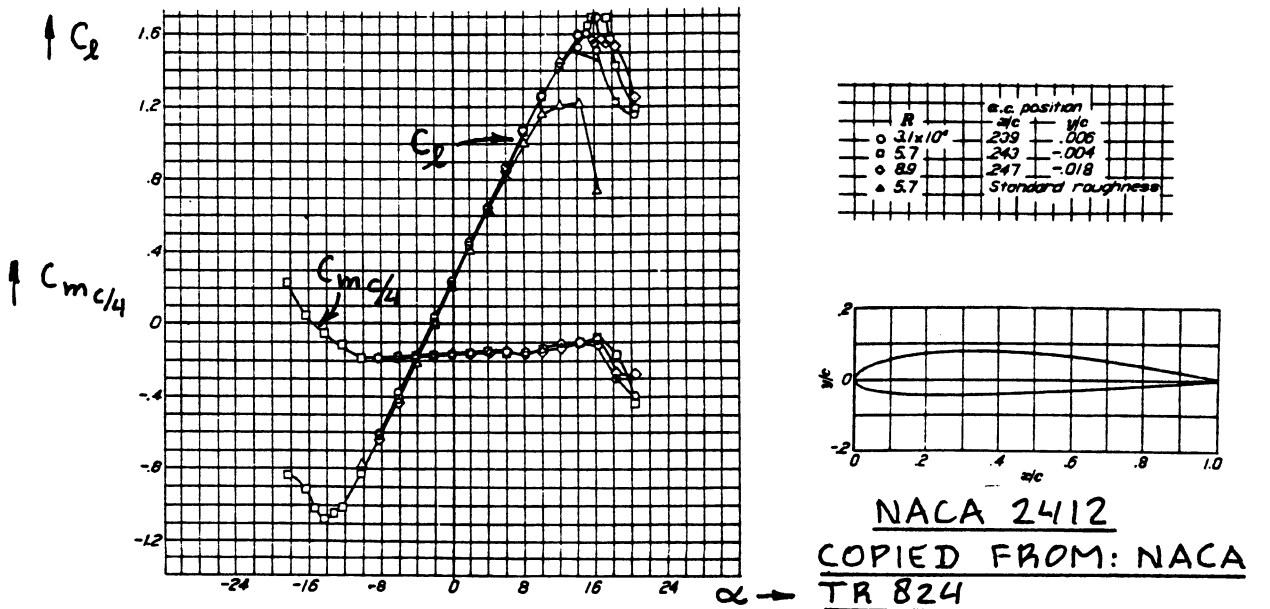

Figure 8.85 Typical Airfoil Lift and Pitching Moment Behavior at Subsonic Speeds

Subsonic:

Figure 8.85 shows typical variations of airfoil pitching moment coefficient with airfoil lift coefficient and with airfoil angle of attack in the subsonic flow range. Such data may be obtained from Reference 49.

Modern airfoil theory is capable of estimating airfoil lift, drag and pitching moment data very accurately. In the absence of experimental data, such theoretically obtained airfoil data may be used.

Table 8.1 (p.216-217) lists values for x_{ac} for several airfoils. Fig.8.86 shows how airfoil a.c. location changes with the thickness ratio, t/c and with the trailing edge angle, ϕ_{te}.

Transonic:

Airfoil pitching moment behavior changes markedly above the so-called critical Mach number. Experimental data or data obtained from modern airfoil codes should be used to predict the airfoil pitching moment behavior above M_{crit}. The critical Mach number of an airfoil at any lift coefficient may be estimated from:

For NACA airfoils:

$$M_{crit} = 0.86 - 0.1c_l - t/c \qquad (8.62)$$

For supercritical airfoils:

$$M_{crit} = 0.91 - 0.1c_l - t/c \qquad (8.63)$$

Supersonic:

Theoretically, for very thin airfoils at low lift coefficients, the center of pressure moves toward the 50 percent chord point. Figure 8.87 indicates how the centers of pressure vary with thickness ratio, t/c and with angle of attack for symmetrical airfoils. For symmetrical airfoils it is noted that: $x_{cp} = x_{ac}$!

Note: this aft shift of the center of pressure in the supersonic speed range has very significant implications to airplane trim and drag in this speed range!

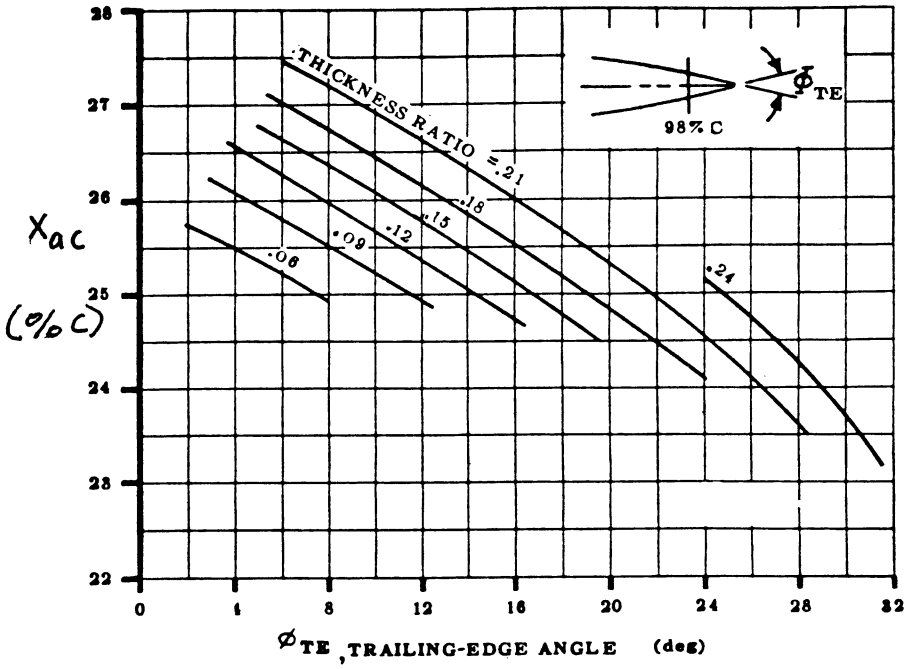

COPIED FROM: REF. 9

Figure 8.86 Effect of Trailing Edge Angle and Thickness Ratio on Airfoil Aerodynamic Center Location at Subsonic Speeds

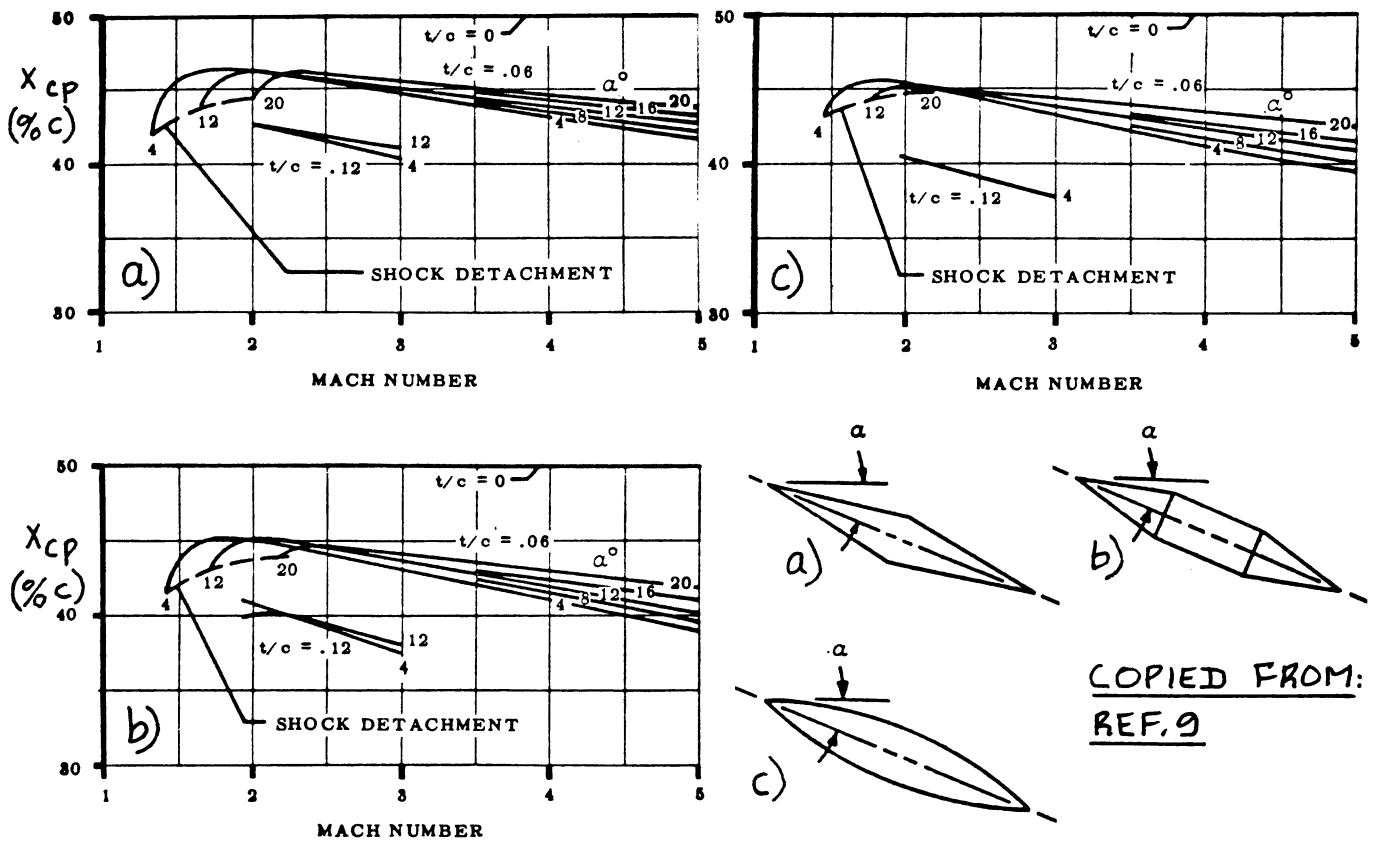

COPIED FROM: REF. 9

Figure 8.87 Effect of Thickness Ratio and Angle of Attack on Airfoil Center of Pressure Location at Supersonic Speeds

8.2.1.3 Airfoil pitching moment variation with lift coefficient: dc_m/dc_l

To determine the variation of airfoil pitching moment coefficient with lift coefficient it is necessary to first select a so-called reference center: Figure 8.88 shows such a reference center. The pitching moment coefficient is defined relative to this reference center:

$$c_m = c_{m_0} + c_l(x_{ref} - x_{ac})/c \qquad (8.64)$$

The variation of pitching moment coefficient with lift coefficient follows by differentiation:

$$dc_m/dc_l = (x_{ref} - x_{ac})/c = \bar{x}_{ref} - \bar{x}_{ac} \qquad (8.65)$$

8.2.1.4 Airfoil linear range for pitching moment: c_l^*

The range of lift coefficients for which the variation of airfoil pitching moment coefficient with lift coefficient is linear follows from:

$$c_l^* = (c_{l_\alpha})(\alpha^* - \alpha_{o_l}) \qquad (8.66)$$

where all quantities are defined in 8.1.1.

8.2.1.5 Construction of airfoil pitching moment curve: flaps up

All ingredients necessary to construct the airfoil pitching moment curve about a reference center x_{ref} are now available. Figure 8.89 shows how this may be done in a step-by-step manner. Whether or not the pitching moment coefficient breaks in a stable or in an unstable manner depends on the separation behavior of the airfoil. Reference 49 contains experimental data which defines the pitching moment 'break' behavior of airfoils. Many (in fact, most) airfoils have stable pitching moment breaks.

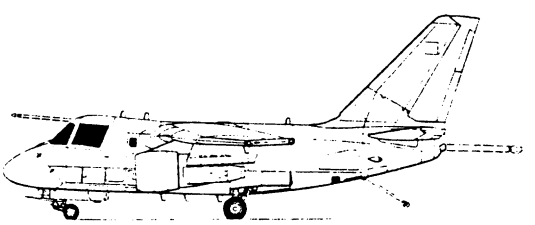

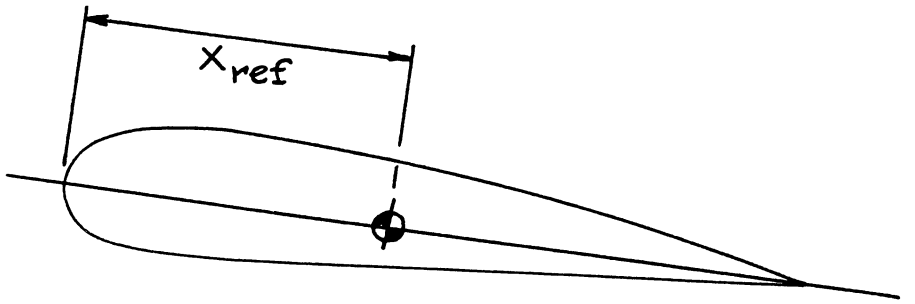

Figure 8.88 Example Location of Reference Center

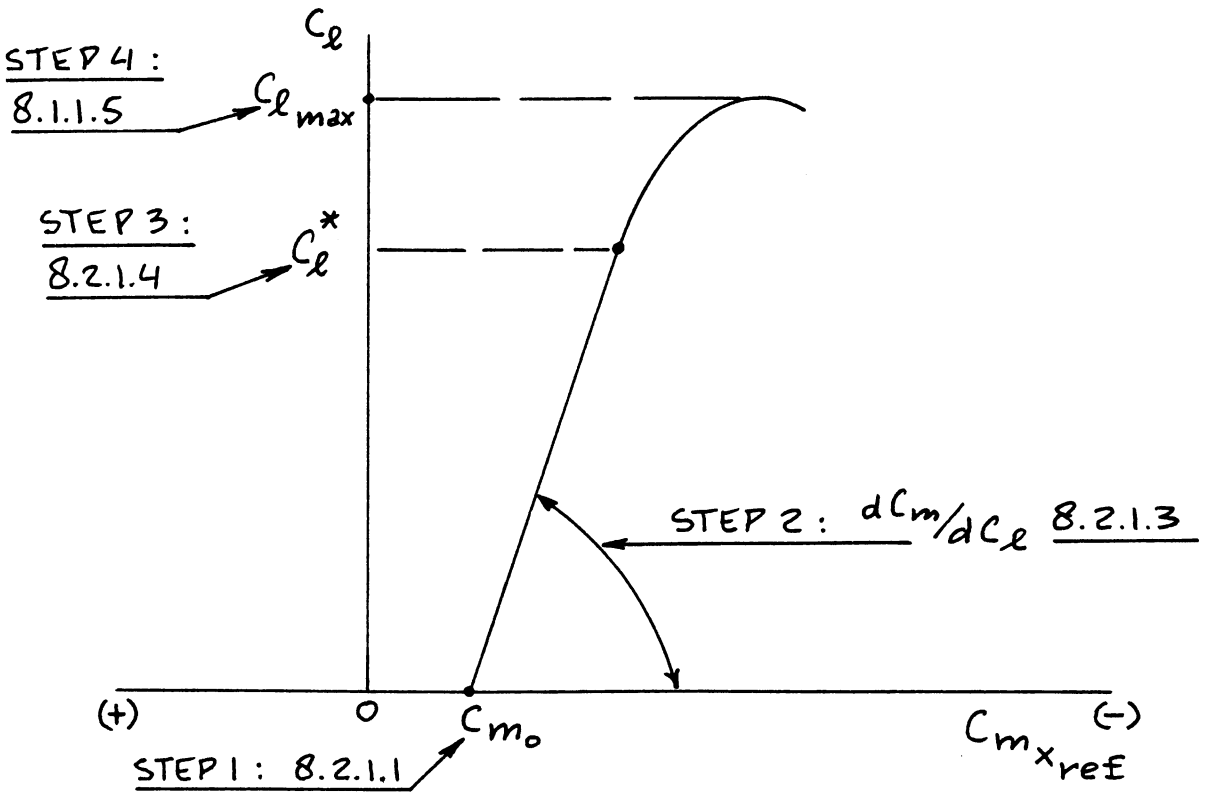

Figure 8.89 Construction of Airfoil Pitching Moment Versus Lift Curve

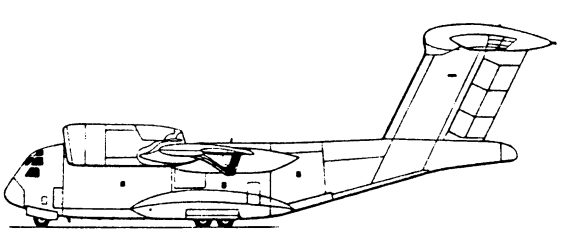

8.2.2 Airfoil Pitching Moment: Flaps Down

Figure 8.90 shows the comparison between flaps-up and flaps-down pitching moment characteristics for an airfoil. Key quantities which are required in the estimation of flap-down behavior are listed with an indication of where methods for their estimation may be found.

Note that the assumption is made that the dc_m/dc_l slope of the airfoil with the flaps down is the same as that for the airfoil with the flaps up. This is reasonable because in the linear angle of attack range, a change in airfoil camber (read flap deflection) has no effect on the c_m-c_l slope.

8.2.2.1 Airfoil pitching moment increment due to flaps: Δc_m

The airfoil incremental pitching moment coefficient due to flaps, Δc_m depends on the type of flaps used.

Methods are presented for trailing edge and for leading edge flaps.

A. Trailing Edge Flaps

For Split, Slotted and Fowler Flaps:

The following method applies to all types of trailing edge flaps, except for plain flaps:

$$\Delta c_m = \Delta c_l \{x_{ref}/c - (x_{cp}/c')(c'/c)\} \qquad (8.67)$$

where: Δc_l is the lift increment due to flaps as found from 8.1.2.

x_{ref} is defined in Figures 8.88 and 8.91.

x_{cp}/c' is found from Figure 8.91.

c' is defined in Figures 8.18 and 8.19. For a split flap and for a plain flap: $c' = c$.

Note: since Δc_l due to flaps as used in Eqn.(8.64) depends on the flap type and on the flap deflection, the latter is inherently accounted for in this method.

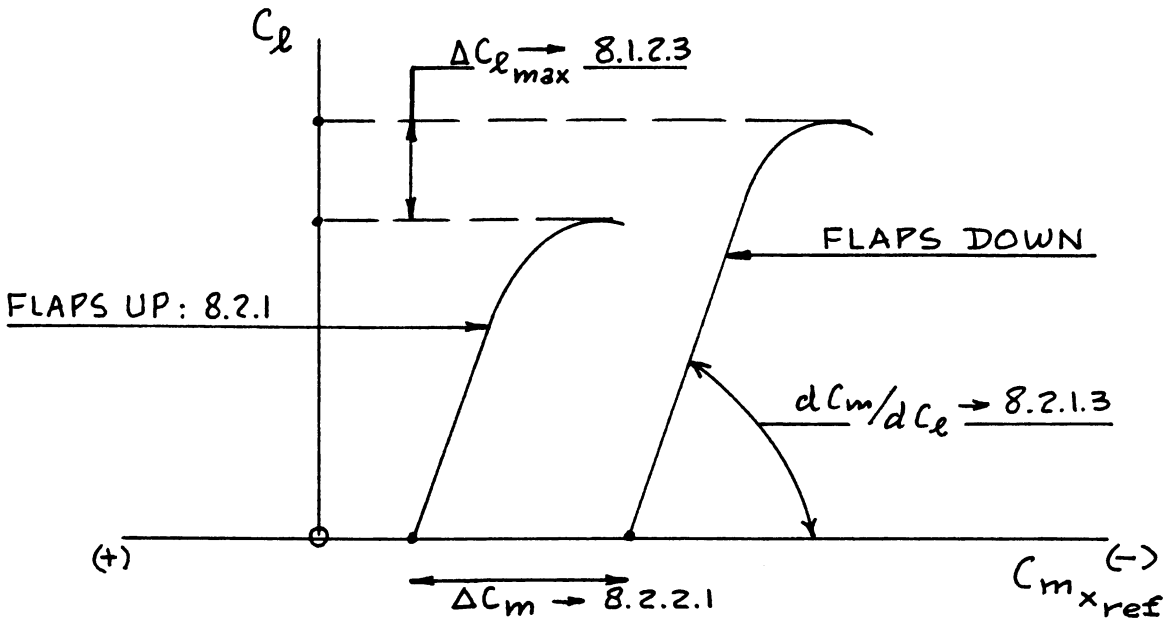

Figure 8.90 Airfoil Pitching Moment Coefficient Versus Lift Coefficient with the Flaps Down

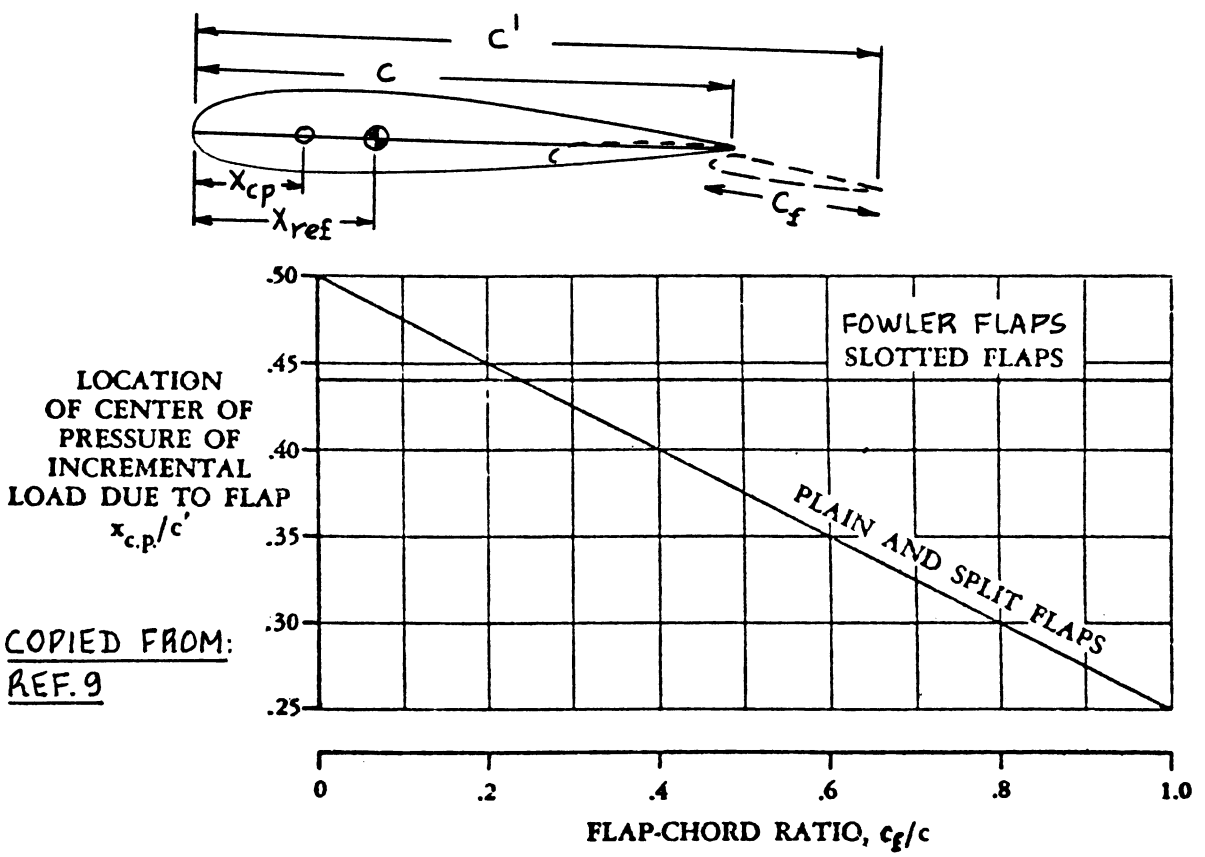

COPIED FROM: REF. 9

Figure 8.91 Location of Center of Pressure due to Incremental Flap Load

For Plain Flaps:

Δc_m is found from Figure 8.92. Observe that this is a pure moment coefficient: its lift dependence is expressed through the plain flap deflection.

B. Leading Edge Flaps:

$$\Delta c_{m_{le}} = (c_{m_{\delta le}})'(c'/c)^2 \delta_{f_{le}} + \{(x_{ref}/c) + (c' - c)/c\}\Delta c_{l_{le}} + c_m\{(c'/c)^2 - 1\} + 0.75c_l(c'/c)\{(c'/c) - 1\} \quad (8.68)$$

where: $(c_{m_{\delta le}})'$ is found from Figure 8.93.

c'/c is defined in Figures 8.27, 8.28 and 8.93.

δ_{fle} is defined in Figures 8.25, 8.27 and 8.28, where it is called δ_f (in deg).

$\Delta c_{l_{le}}$ is the lift coefficient increment due to leading edge flaps as found from 8.1.2.

c_m is the airfoil pitching moment coefficient with the flaps-up, taken about x_{ref} and as found from 8.2.1.

c_l is the airfoil lift coefficient with the flaps-up as determined from the flight condition.

8.2.2.2 Construction of the flaps-down airfoil pitching moment curve

Figure 8.94 shows how the flaps-down pitching moment curve is obtained from the corresponding flaps-up curve.

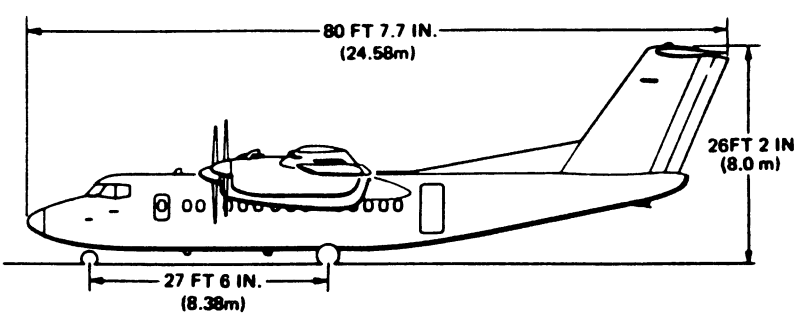

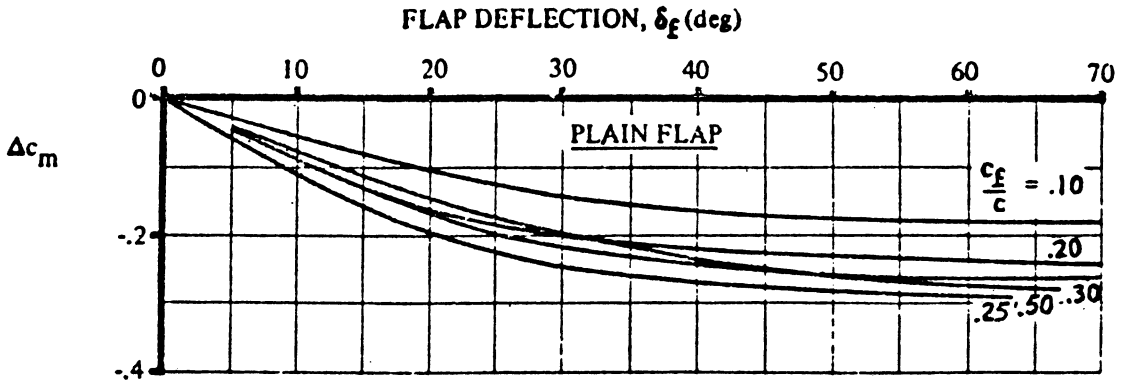

COPIED FROM: REF. 9

Figure 8.92 Incremental Pitching Moment Coefficient due to Plain Flaps

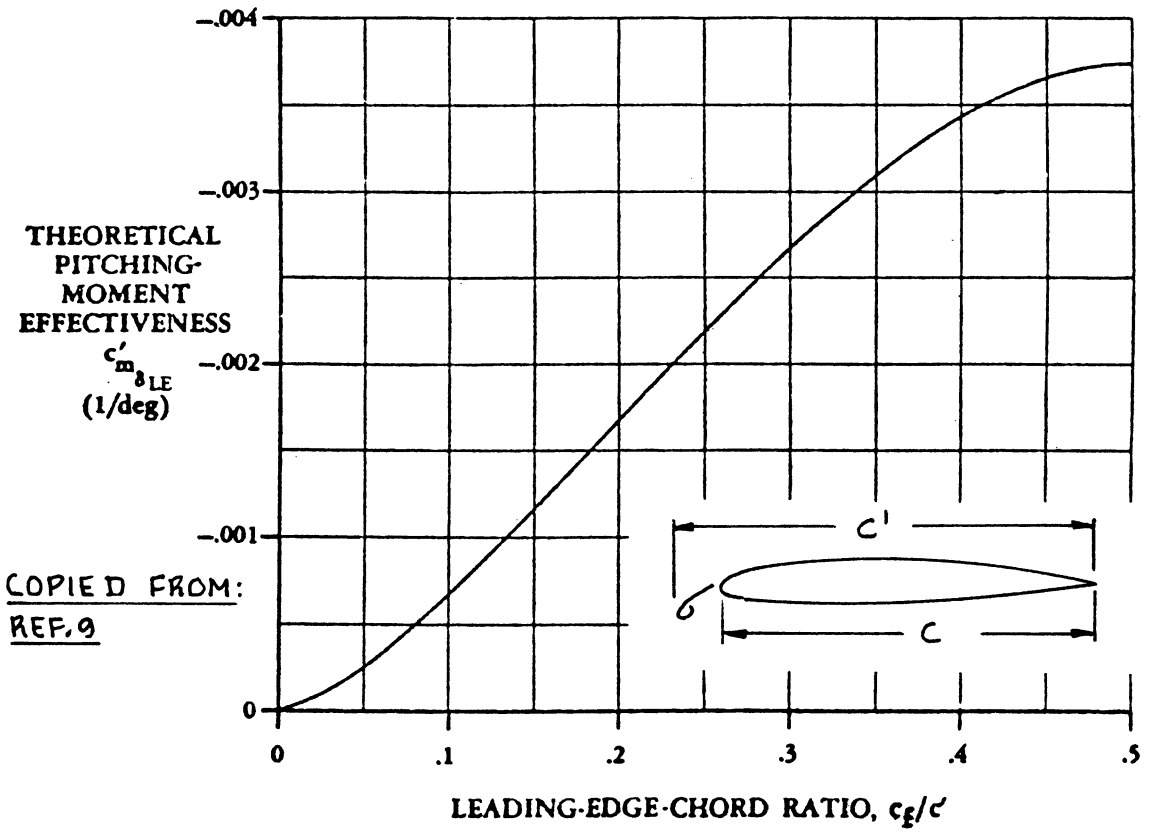

COPIED FROM: REF. 9

Figure 8.93 Pitching Moment Effectiveness due to Leading Edge Flaps

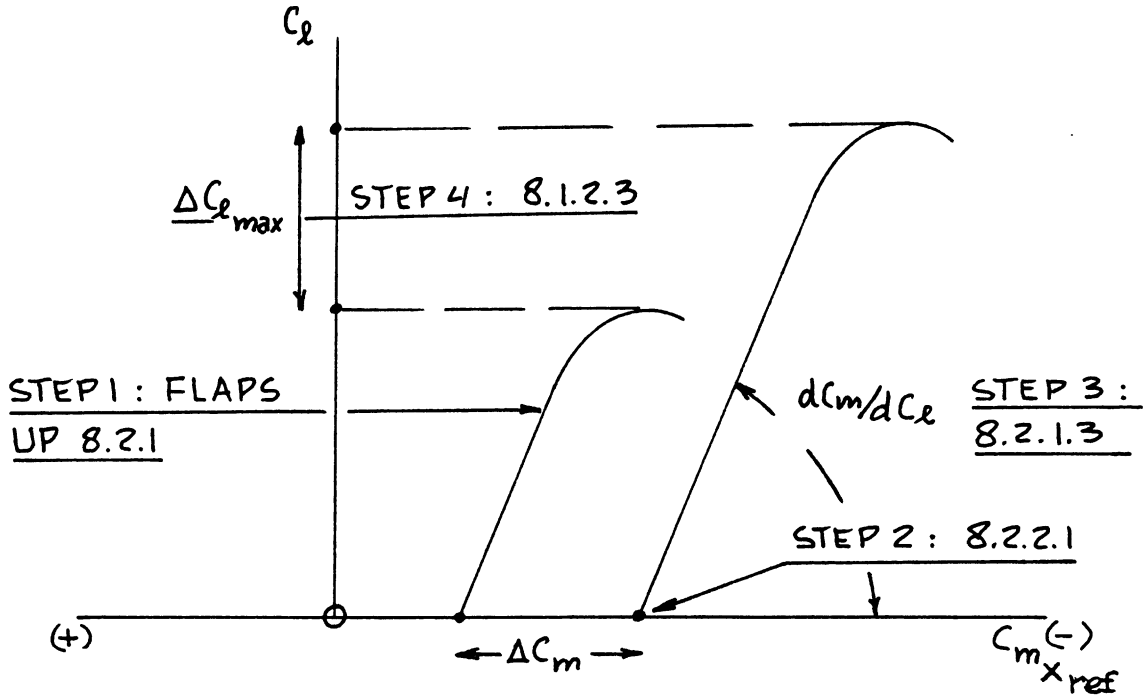

Figure 8.94 Construction of Flaps Down Airfoil Pitching Moment Versus Lift Curve

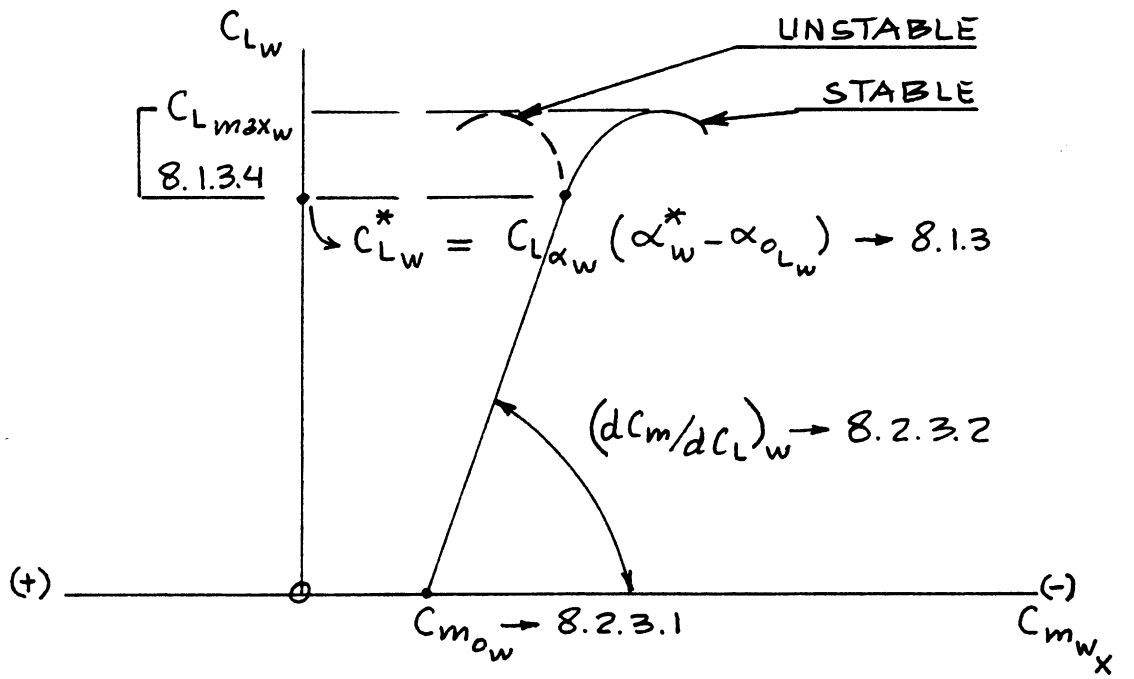

Figure 8.95 Wing Pitching Moment Coefficient Versus Lift Coefficient Curve

8.2.3 Wing Pitching Moment: Flaps-Up

Figure 8.95 shows the flaps-up pitching moment behavior which needs to be predicted with the methods of this section. Key quantities which are required in the estimation of flaps-up behavior are listed with an indication of where methods for their estimation may be found.

A key parameter in estimating wing pitching moment behavior is the mean geometric chord of the wing (mgc), $\bar{c}$ and its location on the planform. Figure 8.96 defines these quantities for two types of straight tapered wing as well as for a more general wing.

Since pitching moments are defined relative to a reference point, it is mandatory to locate such a reference point (also called moment reference center) on the wing planform. Figures 8.97 shows two methods used do this.

Observe that:

$$n_{ref} = x_{ref} + n_{mgc} \qquad (8.69)$$

The method labelled as 2 is the preferred method.

8.2.3.1 Wing zero-lift pitching moment coefficient: $C_{m_{o_w}}$

Subsonic:

$$C_{m_{o_w}} = \{(A\cos^2\Lambda_{c/4})/(A + 2\cos\Lambda_{c/4})\}(c_{m_{o_r}} + c_{m_{o_t}})/2 + (\Delta C_{m_o}/\varepsilon_t)\varepsilon_t \qquad (8.70)$$

where: $c_{m_{o_r}}$ and $c_{m_{o_t}}$ are the zero-lift pitching moment coefficients of the root and tip airfoils respectively. These follow from 8.2.1.1.

$\Delta C_{m_o}/\varepsilon_t$ is found from Figure 8.98.

Note: This method applies to conventional straight tapered wings with sweep angles below 45 degrees and aspect ratios above 2.5. For other wing types, Reference 9 should be consulted.

Transonic:

Up to the critical Mach number, use:

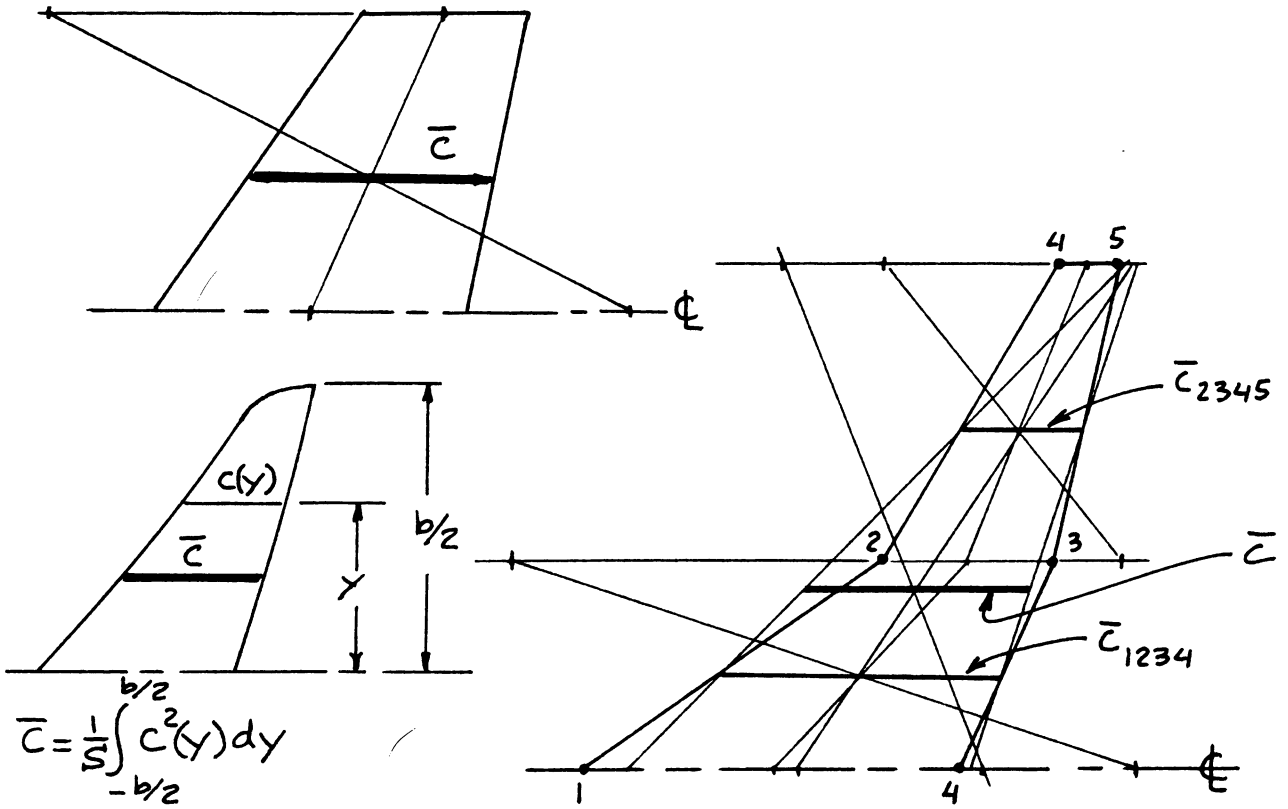

Figure 8.96 Methods for Determining the Wing Mean Geometric Chord

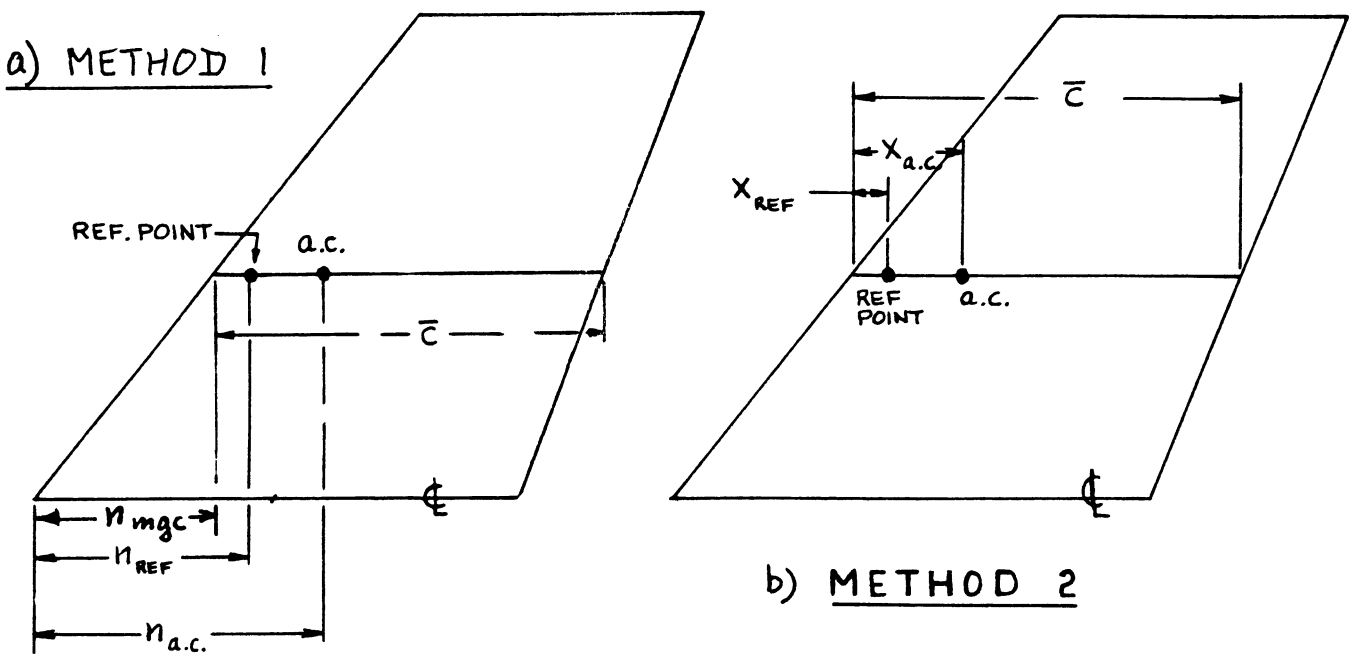

Figure 8.97 Methods for Locating a Wing Reference Point and the Wing Aerodynamic Center

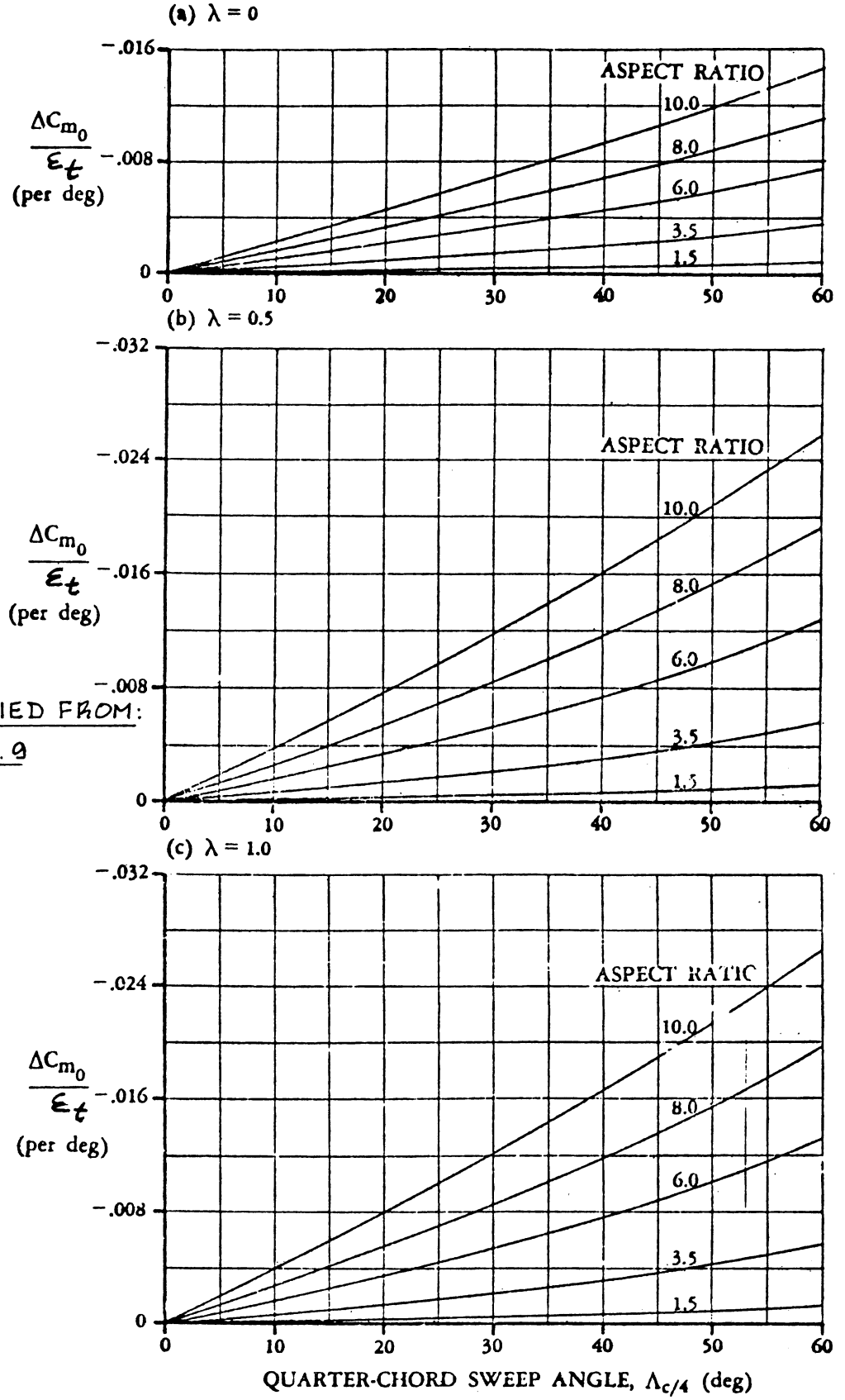

COPIED FROM:
REF. 9

Figure 8.98 Effect of Linear Twist on Wing Zero-lift Pitching Moment Coefficient

$$C_{m_{o_w}}\text{ at M} = C_{m_{o_w}}\text{ at M=0}\ \{(C_{m_o})_M/(C_{m_o})_{M=0}\} \quad (8.71)$$

where: $\{(C_{m_o})_M/(C_{m_o})_{M=0}\}$ is given in Figure 8.99.

$C_{m_{o_w}}$ at M=0 is found from Eqn.(8.70).

Supersonic:

For supersonic Mach numbers it is suggested to use experimental data. Since supersonic wings frequently have little camber, their $C_{m_{o_w}}$ values tend to be small.

8.2.3.2 Slope of the wing pitching moment curve: $(dC_m/dC_L)_w$

The method which follows applies only to straight, tapered planforms. For very highly swept wings and for cranked wings the method of Reference 9 should be used.

Subsonic:

The subsonic slope of the wing pitching moment curve may be found from:

$$(dC_m/dC_L)_w = \{(n_{ref} - n_{ac})/c_r\}(c_r/\bar{c}) \quad (8.72)$$

where: n_{ref} is the location of the moment reference center relative to the wing apex: see Fig.8.97a.

n_{ac} is the location of the wing aerodynamic center relative to the wing apex: see Figure 8.97a.

For wings of aspect ratios above 5 and sweep angles below 35 degrees it is usually acceptable to use:

$$n_{ac} = n_{mgc} + 0.25\bar{c} \quad (8.73)$$

For other wings, Figure 8.100 should be used.

Transonic:

For transonic Mach numbers, see Reference 9.

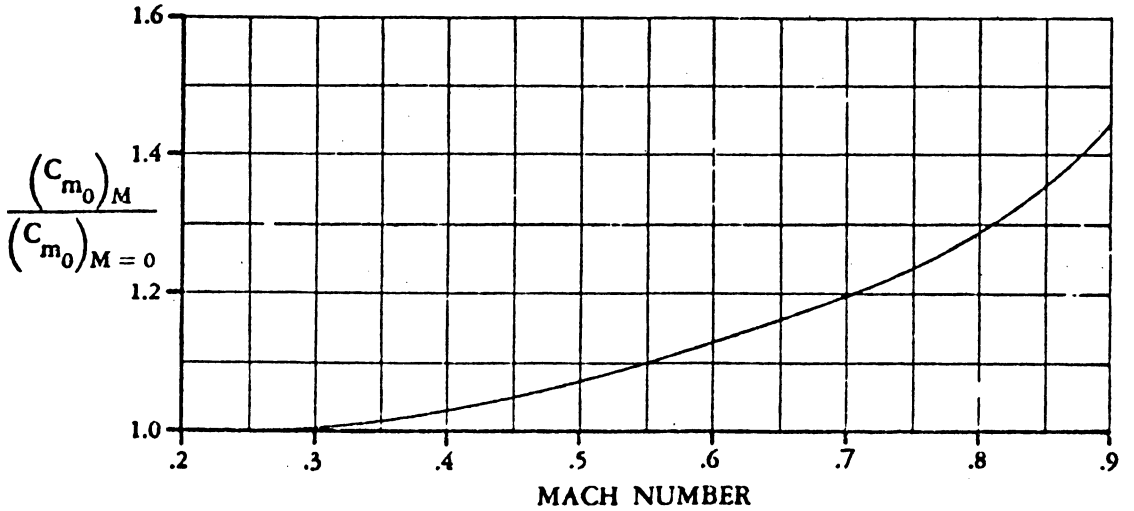

COPIED FROM : REF. 9

Figure 8.99 Effect of Mach Number on Wing Zero-lift Pitching Moment Coefficient

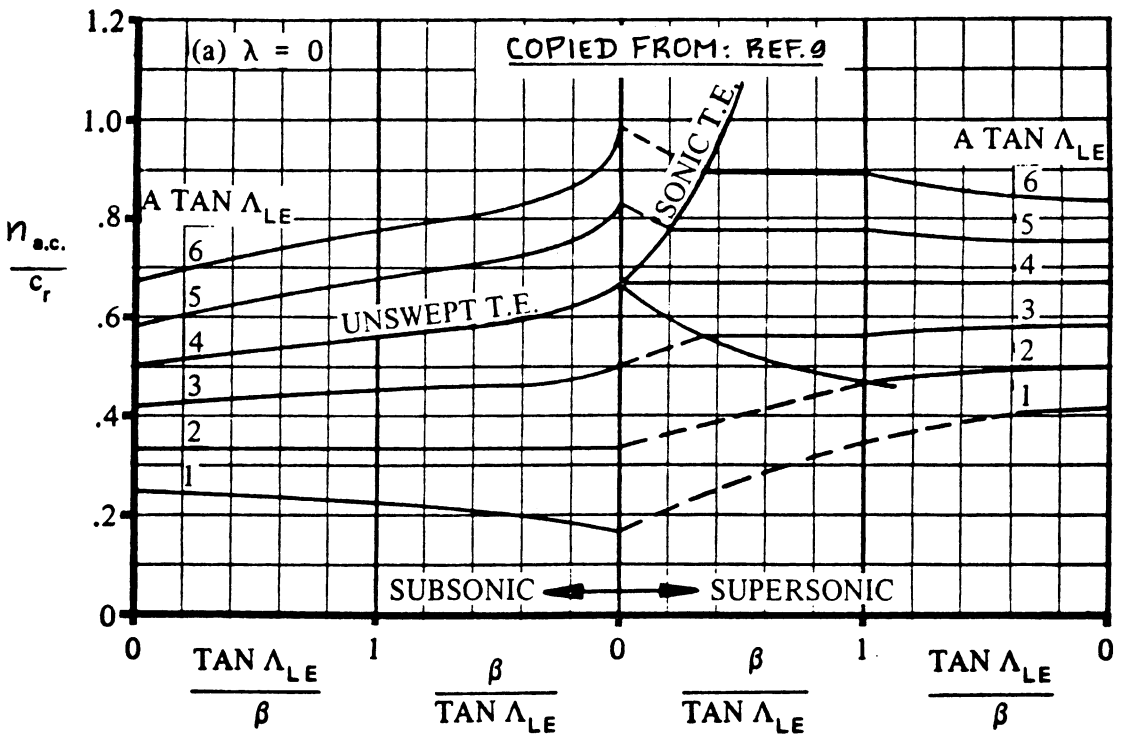

Figure 8.100 Effect of Aspect Ratio, Sweep Angle and Taper Ratio on Wing Aerodynamic Center

COPIED FROM: REF.9

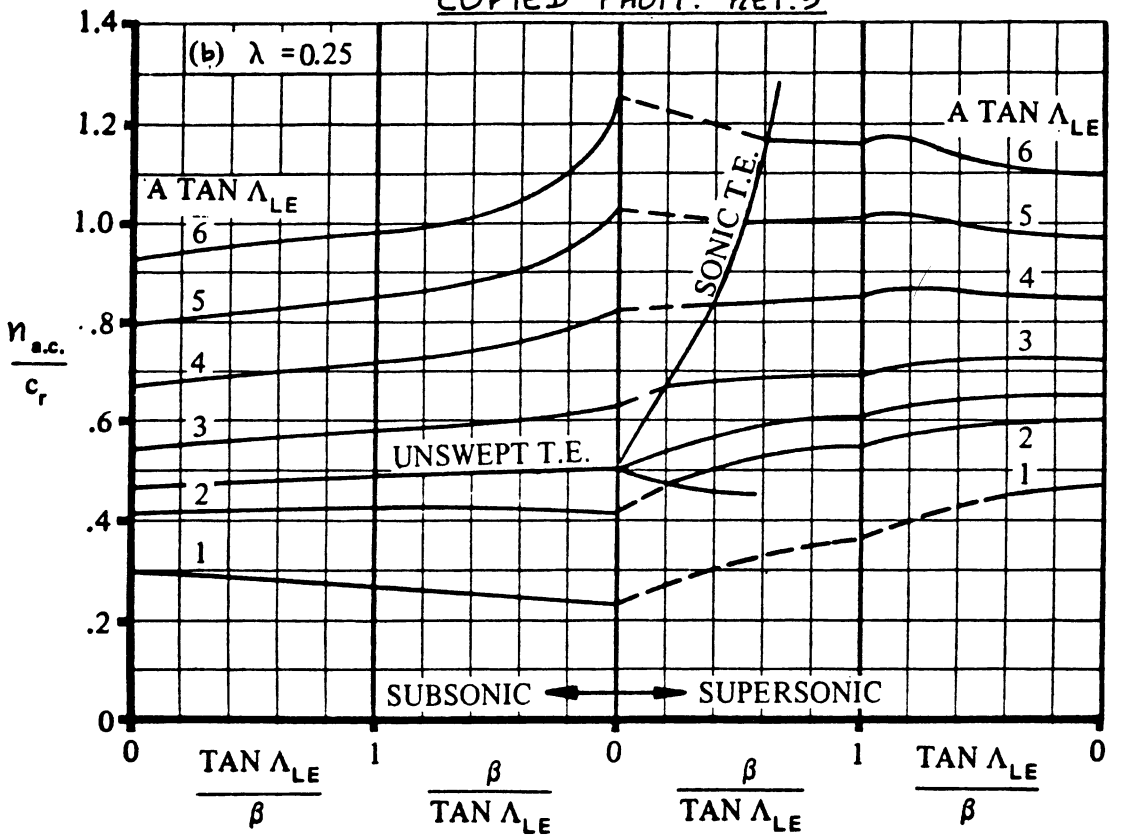

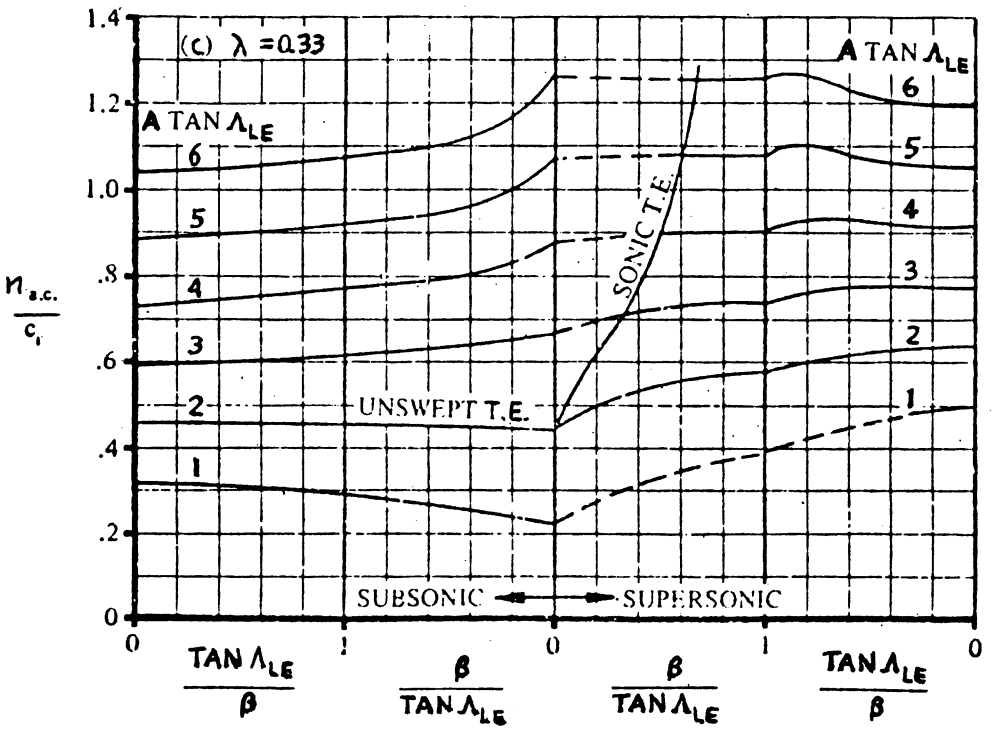

Figure 8.100 (Cont'd) Effect of Aspect ratio, Sweep Angle and Taper Ratio on Wing Aerodynamic Center

COPIED FROM REF.9

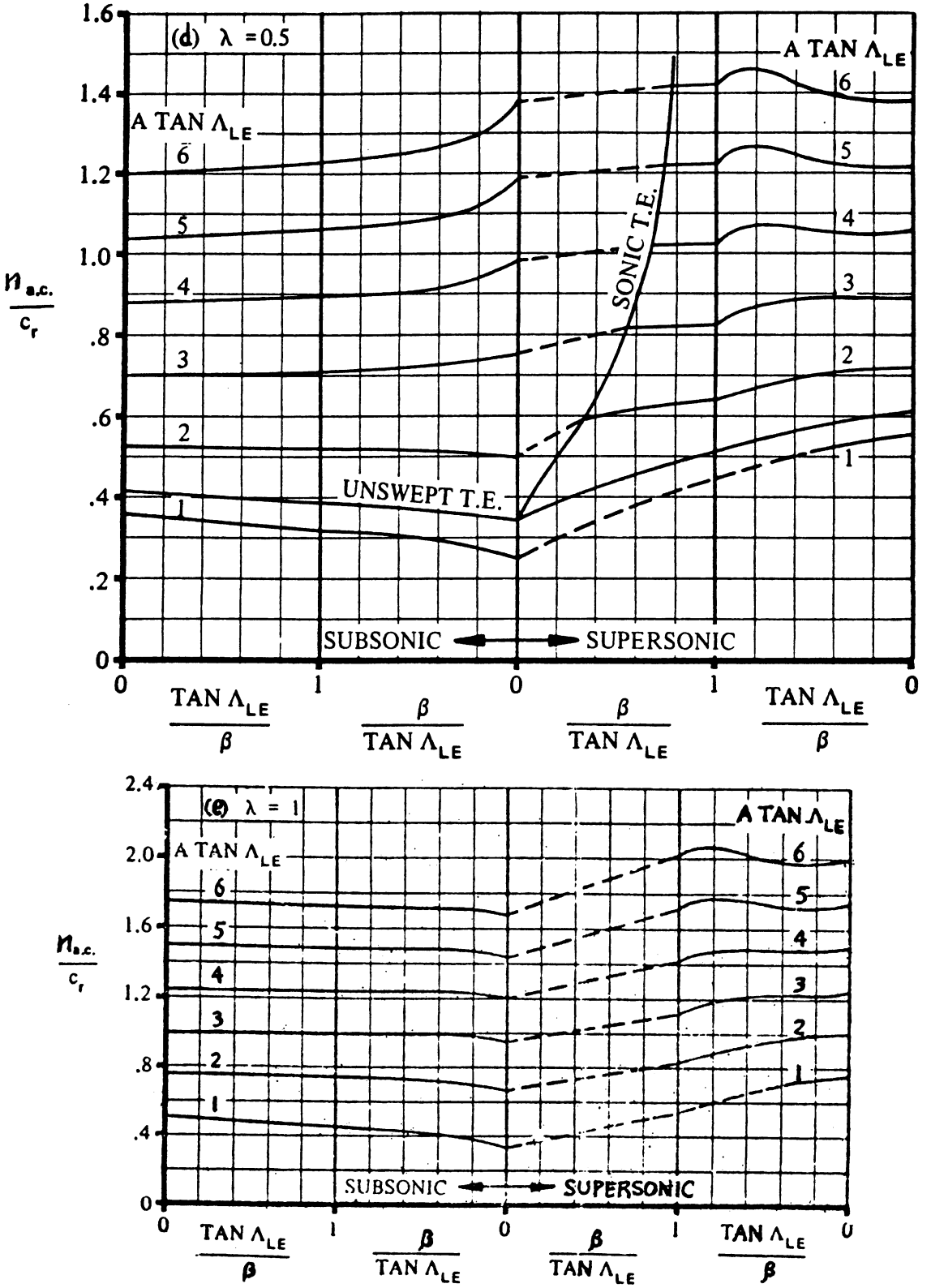

Figure 8.100 (Cont'd) Effect of Aspect Ratio, Sweep Angle and Taper Ratio on Wing Aerodynamic Center

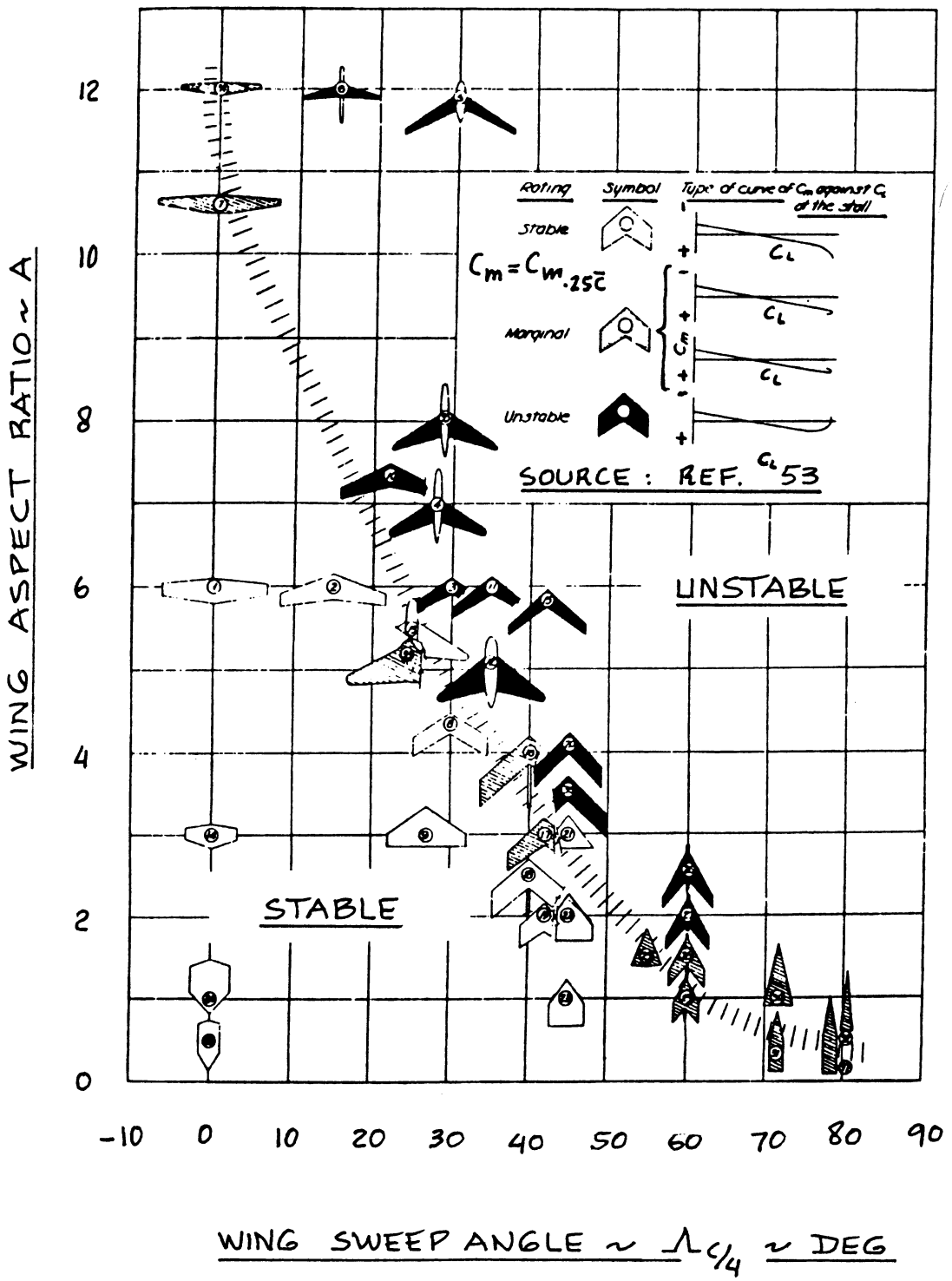

Figure 8.101 Wing Alone Pitch Break Stability Boundary

Supersonic:

For supersonic Mach numbers, see Reference 9.

8.2.3.3 Prediction of stable or unstable pitch break

Whether a wing has stable or unstable pitch break behavior depends on the type of airfoil(s) used as well as on the wing planform. Figure 8.101 may be used as an initial guide in the prediction of pitch break behavior. The reader should refer to Part III, p.266-269 for a more detailed discussion of the pitch break phenomenon. As pointed out in Part IV (p.269) wings with highly swept strakes should be expected to have severely unstable pitch breaks.

8.2.3.4 Construction of the wing pitching moment curve: flaps-up

All ingredients needed for the construction of the flaps-up wing pitching moment curve are now available. Figure 8.102 shows how this can be done in a stepwise manner.

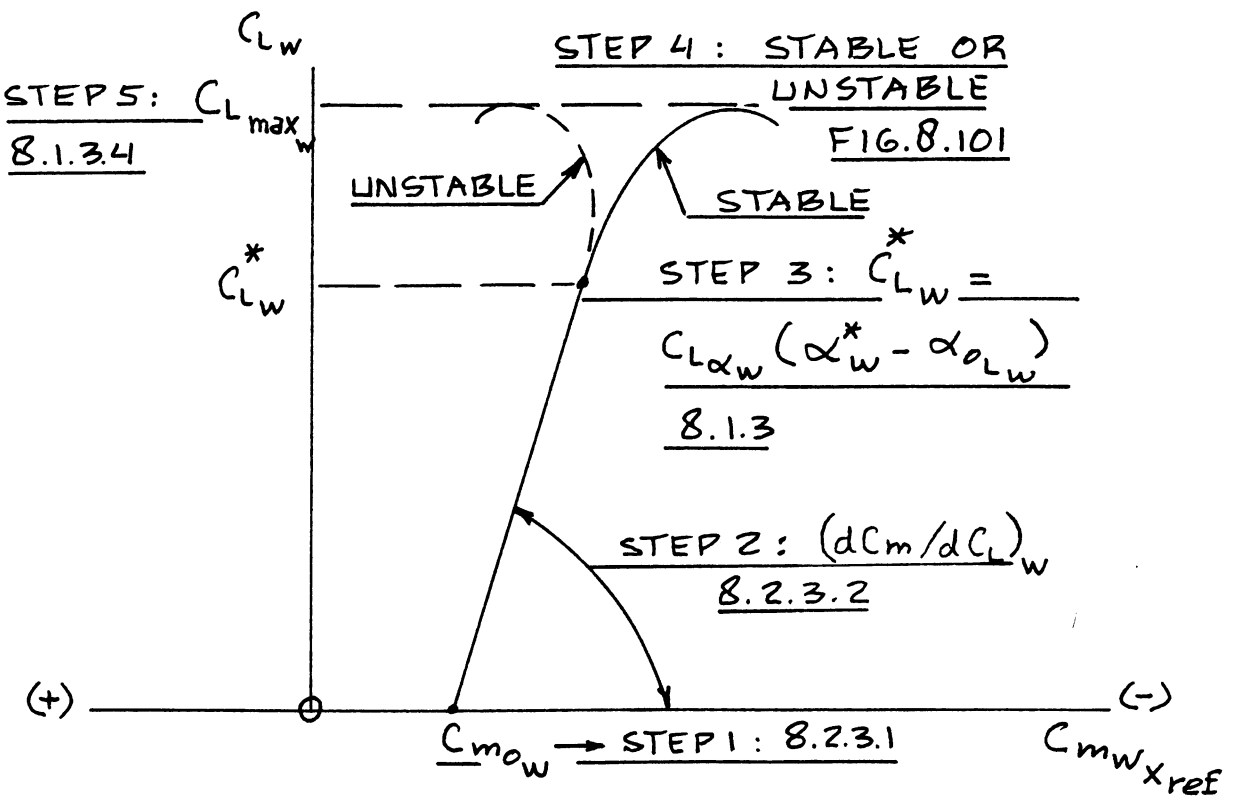

Figure 8.102 Construction of Flaps Up Wing Pitching Moment Versus Lift Curve

8.2.4 Wing Pitching Moment: Flaps-Down

Figure 8.103 shows the flaps-down pitching moment behavior which must be predicted with the methods of this section. Key quantities which are required in the estimation of flaps-down behavior are listed with an indication of where methods for their estimation may be found.

The method given here does not apply to wings with sweep angles in excess of 45 degrees. The method is also not applicable to wings with aspect ratios: A < 2.5.

8.2.4.1 Wing pitching moment increment due to flaps: ΔC_{m_w}

The wing incremental pitching moment coefficient due to flaps depends on the type of flaps used. Methods are presented for trailing edge flaps and for leading edge flaps.

A. Trailing Edge Flaps

In the low angle of attack range, the incremental wing pitching moment coefficient due to trailing edge flaps (taken relative to x_{ref}) may be found from:

$$\Delta C_{m_w} = \tag{8.74}$$

$$(\bar{x}_{ref} - 0.25)\Delta C_{L_w} + K_\Lambda (A/1.5)(\Delta C_{L_{ref_w}})\tan\Lambda_{c/4} +$$

$$+ K_p[(\Delta C'_m/\Delta C_{L_{ref_w}})\Delta C_{L_{ref_w}}(c'/c)^2] +$$

$$- K_p[0.25C_{L_w}\{(c'/c)^2 - (c'/c)\}] + K_p C_{m_w}\{(c'/c)^2 - 1\}$$

where: x_{ref} is defined in Figure 8.97.

$(C_{L_w})_\delta$ is the wing lift coefficient with the flaps down. It follows from 8.1.4.

C_{L_w} is the flaps-up wing lift coefficient as determined from 8.1.3.

ΔC_{L_w} is the wing lift increment due to flaps.

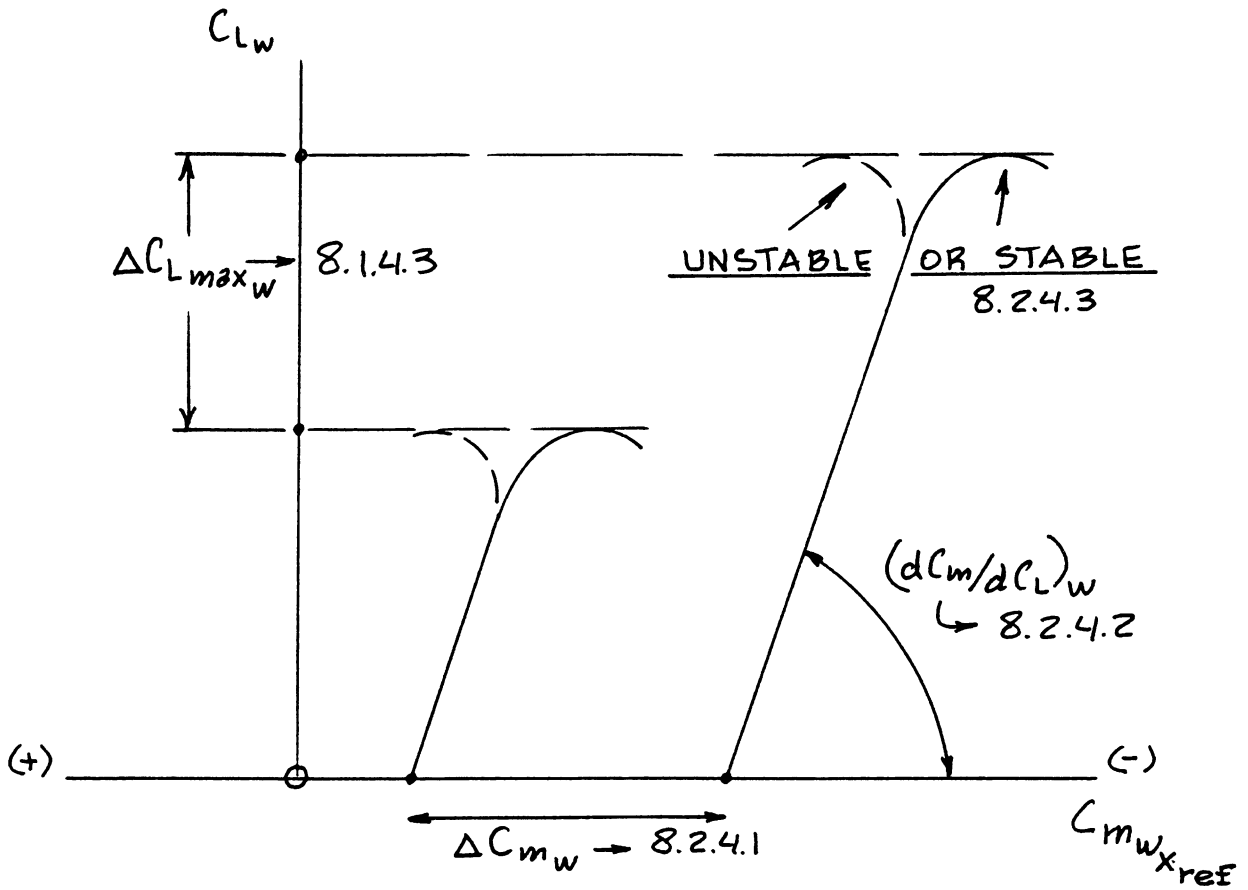

Figure 8.103 Wing Pitching Moment Versus Lift Curve with the Flaps Down

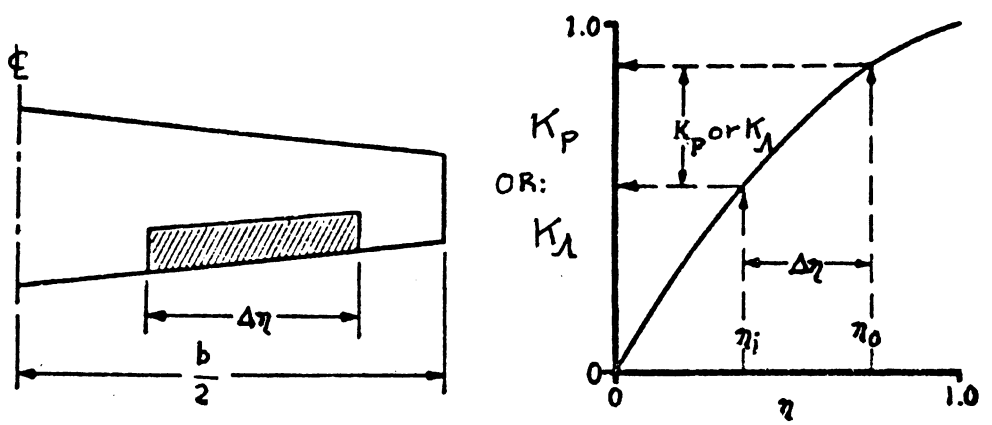

Figure 8.104 Method to Account for Partial Span Flaps

$\Delta C_{L_{ref_w}}$ is the lift increment due to flaps for a reference wing defined by the following geometry:

*full span flap *A = 6 *$\Lambda_{c/2}$ = 0

This quantity can be determined with the methods of 8.1.4.

K_p is the flap span factor which is obtained as shown in Fig. 8.104 with the data of Fig. 8.105.

c'/c is the ratio of the flaps extended wing chord to that with the flaps retracted. Fig. 8.106 shows typical definitions.

$(\Delta C'_m/\Delta C_{L_{ref_w}})$ is obtained from Figure 8.106.

K_Λ is a conversion factor which accounts for a partial-span flap on a swept wing. It is obtained from Fig. 8.107 using the procedure of Figure 8.104.

A is the wing aspect ratio

$\Lambda_{c/4}$ is the wing quarter chord sweep angle.

C_{m_w} is the wing pitching moment coefficient with the flaps retracted as obtained from 8.2.3.

B. Leading Edge Flaps

In the low angle of attack range, the incremental wing pitching moment coefficient due to leading edge flaps (taken relative to $\bar{\eta}_{ref}$) may be found from:

$$\Delta C_{m_w} = \{(c_{m_{\delta le}})'(c'/c) + (\bar{\eta}_{ref} - \bar{\eta}_{le})c_{l_\delta}\}(S_{w_f}/S)\delta_f + \quad (8.75)$$

$$+ [C_{m_w}\{(\bar{c}'/c)^2 - 1\} + 0.75C_{L_w}\{(\bar{c}'/c)(\bar{c}'-c)/c)\}](b_{lef}/b)$$

where: $(c_{m_{\delta le}})'$ is found from Figure 8.93.

$\bar{c}'$ is the mgc of that wing segment affected by the leading edge devices as shown in Figure 8.108.

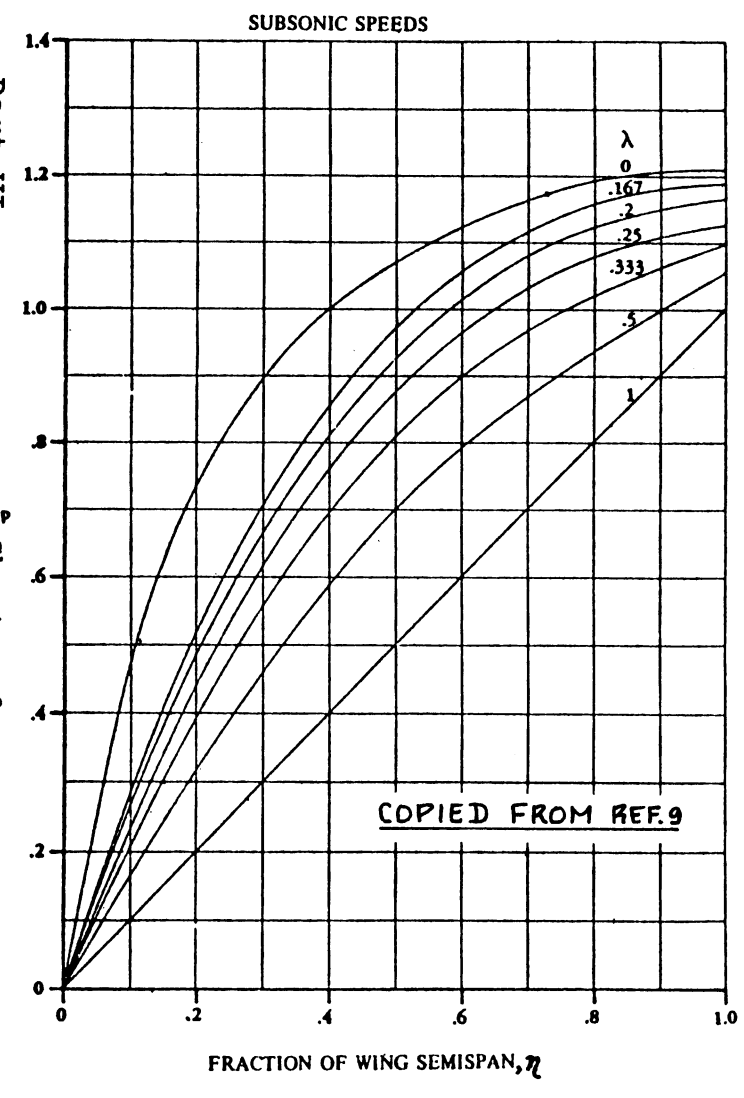

Figure 8.105 Partial Flap Span Factor

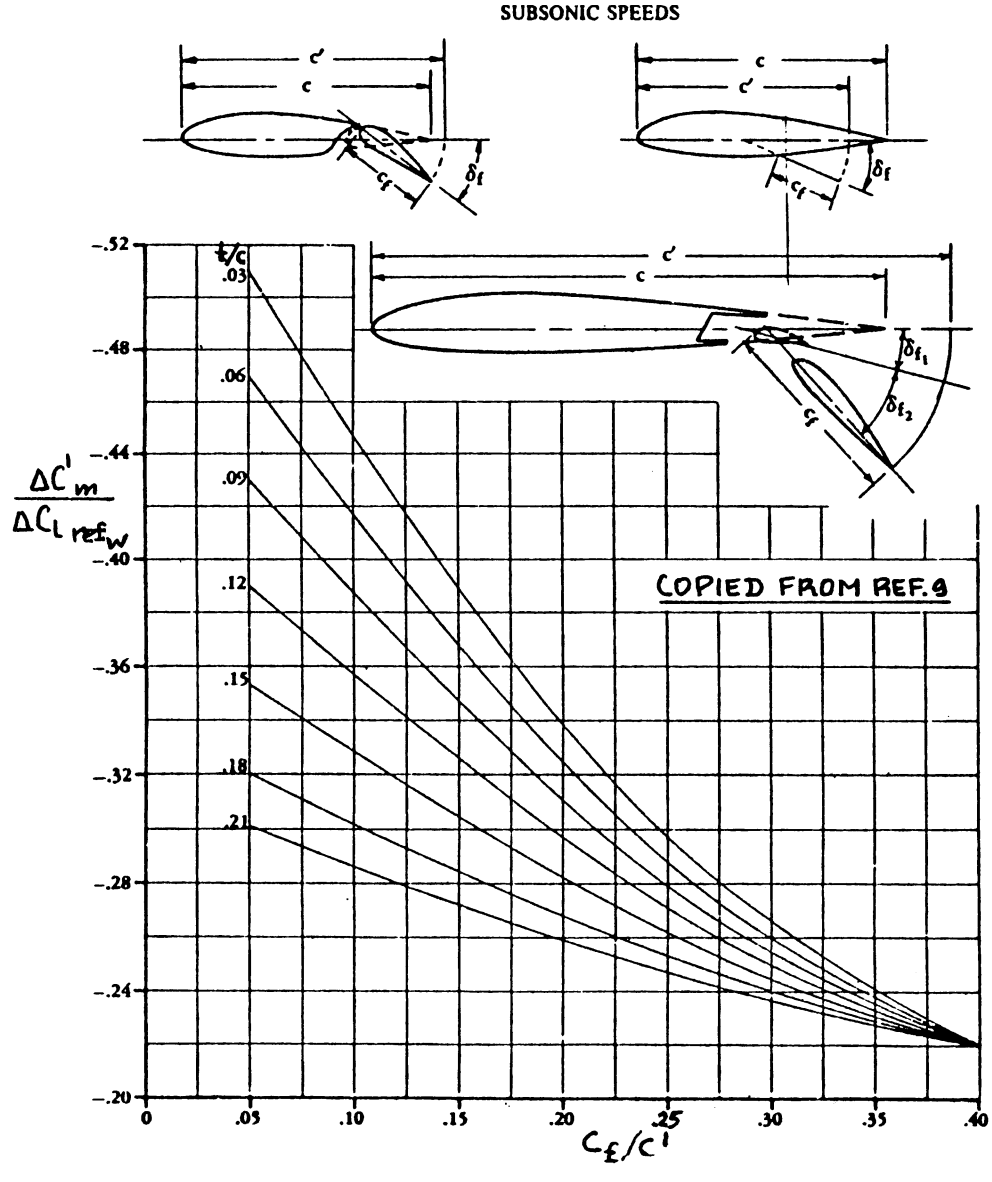

Figure 8.106 Effect of Lift on Pitching Moment for the Reference Wing

COPIED FROM REF. 9

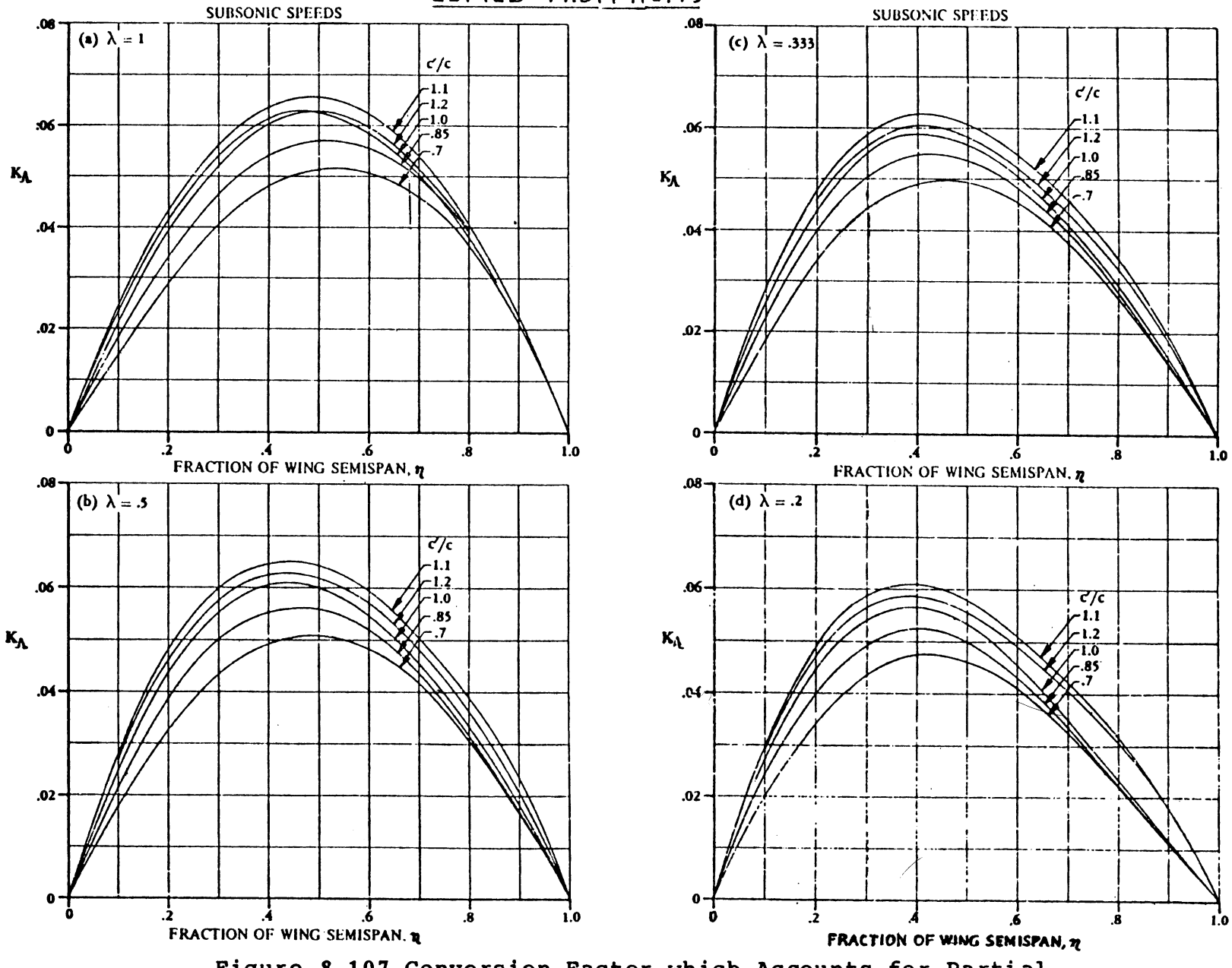

Figure 8.107 Conversion Factor which Accounts for Partial Span Flaps on a Swept Wing

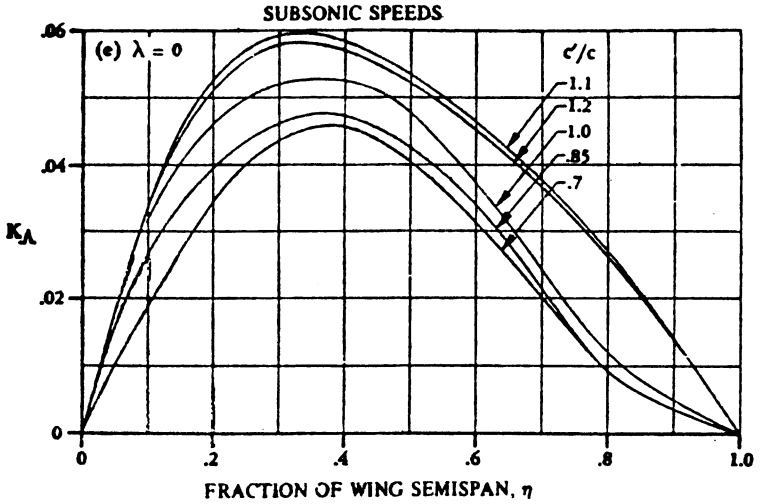

COPIED FROM REF. 9

Figure 8.107 (Cont'd) Conversion Factor which Accounts for Partial Span Flaps on a Swept Wing

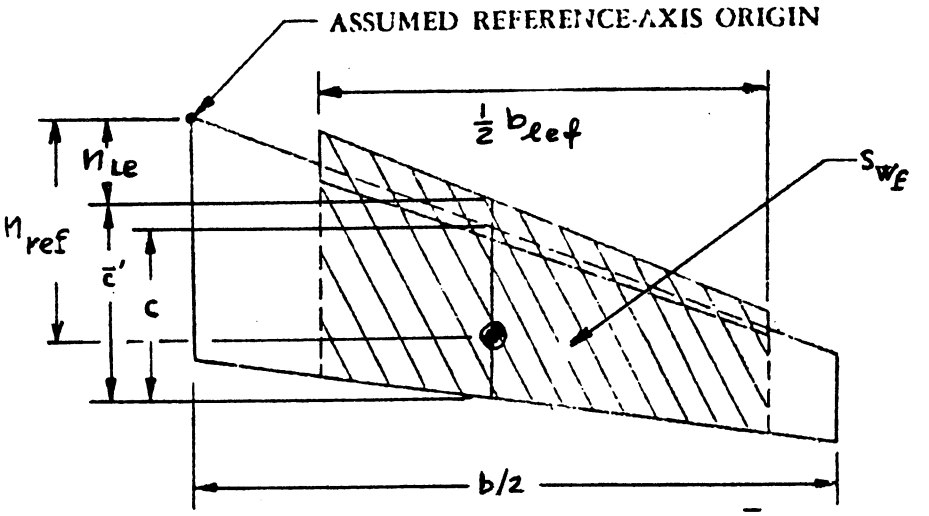

Figure 8.108 Definition of $\bar{c}'$

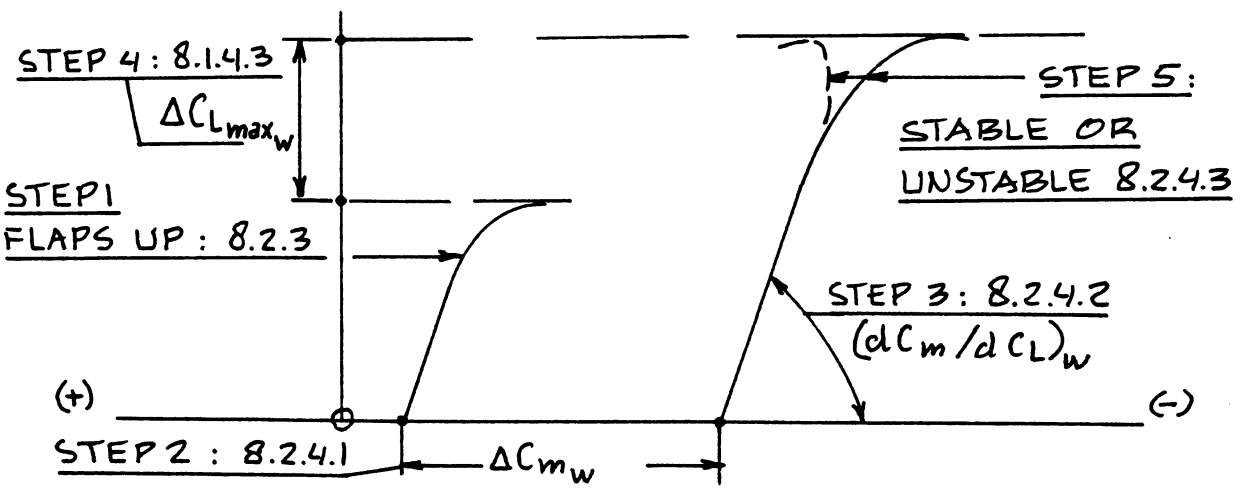

Figure 8.109 Construction of the Flaps Down Wing Pitching Moment Versus Lift Curve

c is the wing chord at $\bar{c}'$, see Figure 8.108.

$\bar{n}_{ref}$ and $\bar{n}_{le}$ are defined in Figure 8.108.

b_{lef} is defined in Figure 8.108.

S_{wf} is the flapped wing area: see Figure 8.108.

C_{m_w} is the wing pitching moment coefficient with the flaps retracted as obtained from 8.2.3.

C_{L_w} is the wing lift coefficient with flaps-up.

8.2.4.2 Slope of the wing pitching moment curve, flaps-down: $(dC_m/dC_L)_{w\delta}$

It may be assumed, that the slope of the wing pitching moment curve with the flaps-down is identical to that with the flaps-up: see 8.2.3.2.

8.2.4.3 Prediction of stable or unstable pitch break: flaps-down

It will be assumed that the pitch break behavior of the wing with the flaps down is similar to that with the flaps up: see 8.2.3.3.

8.2.4.4 Construction of the wing pitching moment curve: flaps-down

All ingredients necessary to construct the flaps-down wing pitching moment curve are now available. Figure 8.109 shows how this may be done in a step-by-step manner.

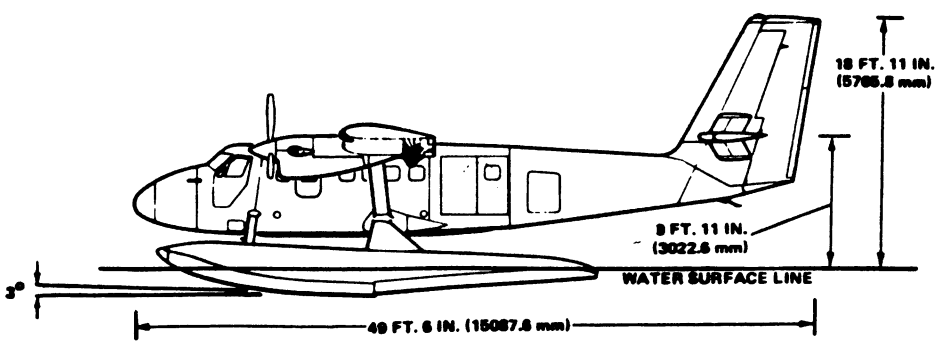

8.2.5 Airplane Pitching Moment: Flaps Up

Figure 8.110 shows the relationship between airplane pitching moment coefficient and airplane lift coefficient which is to be determined with the methods presented in this section. Key quantities needed in the construction of airplane C_m versus C_L curve are listed, with an indication of where methods for their estimation are found.

The assumption will be made, that an airplane can be considered to consist of three components:

a) wing + fuselage b) horizontal tail c) canard

Figure 8.60 shows the relative arrangement of these three major components. If an airplane is equipped with pylon mounted nacelles (such as the B-727 and the DC-9), the pylon + nacelle combination should be 'counted' as an additional horizontal tail. Figure 8.61 indicates the 'equivalent' geometries which should then be used.

Figure 8.62 shows a number of important geometric parameters which are used in the calculation of overall airplane pitching moment characteristics.

IMPORTANT CONSIDERATIONS:

In this chapter the following incidence angles are accounted for:

Canard: i_c Wing: i_w Horizontal Tail: i_h

These incidence angle are defined in Figure 8.60. In this sub-section, these incidence angles are assumed to be CONSTANT. The effect of trim requirements is considered in Section 8.3.

A horizontal tail and a canard may be equipped with a trailing edge control surface:

Horizontal tail with elevator, deflection: δ_e

Canard with canardvator, deflection: δ_c

In this sub-section, the assumption will be made that all control surface deflection angles are ZERO. The effect of trim requirements which would cause these control surface deflections to be non-zero is considered in Section 8.3.

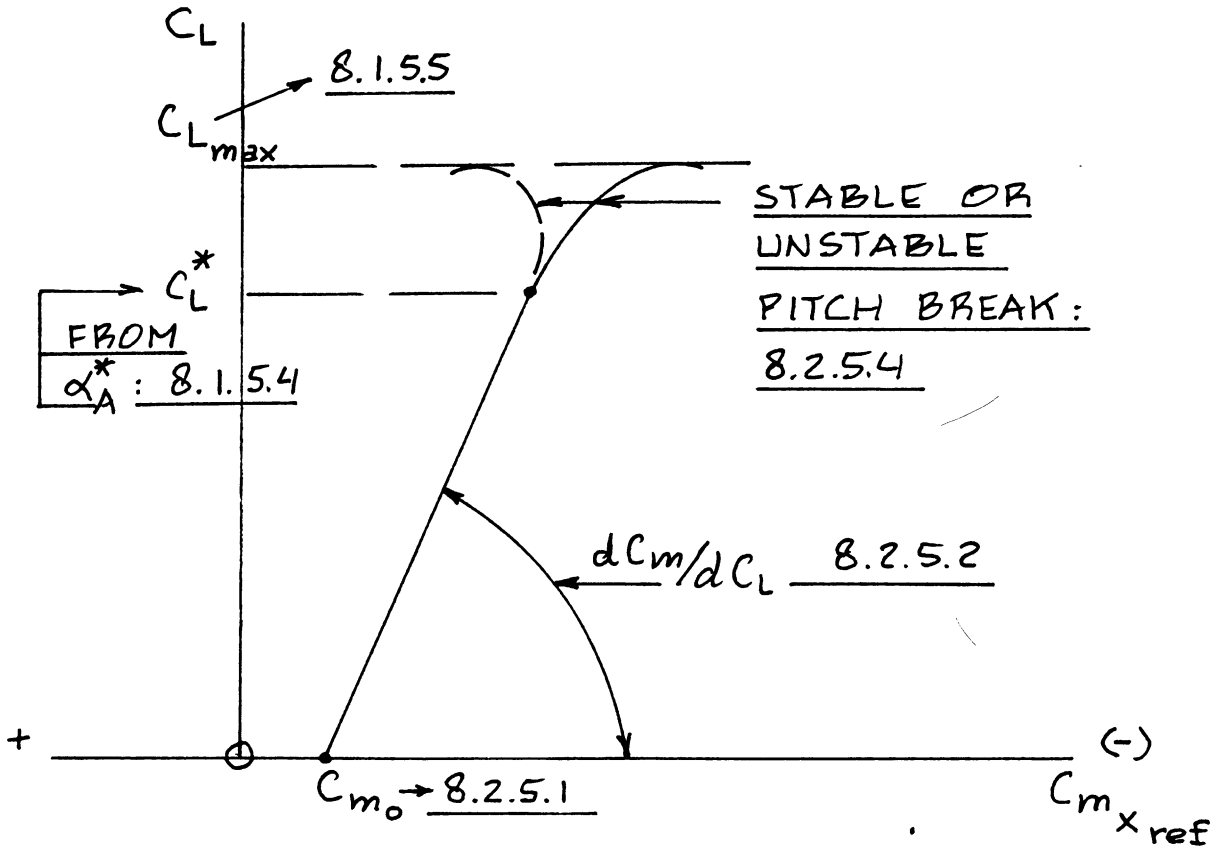

Figure 8.110 Airplane Pitching Moment Versus Lift Curve with the Flaps Up

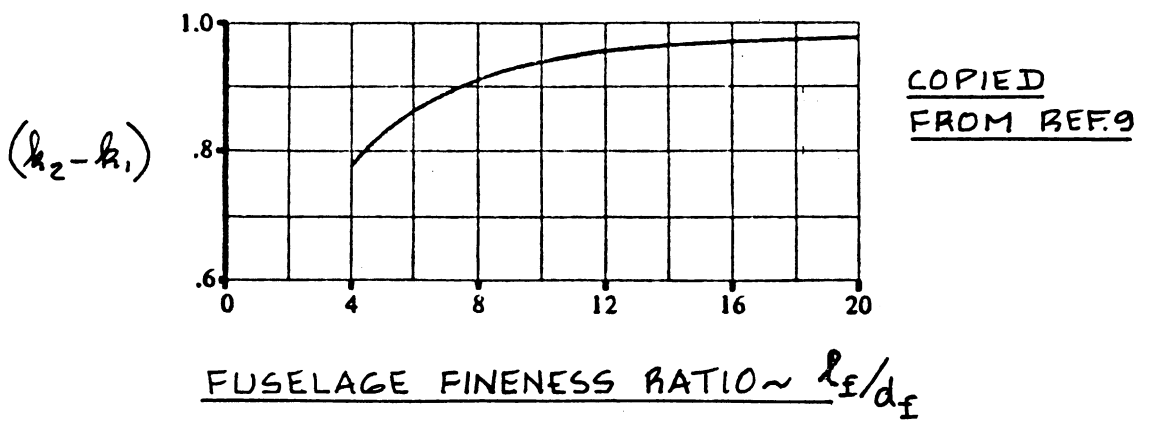

Figure 8.111 Effect of Fuselage Slenderness on the Apparent Mass Factor

8.2.5.1 Airplane zero-lift pitching moment coefficient: C_{m_o}

Subsonic:

The airplane zero-lift pitching moment coefficient may be estimated from:

$$C_{m_o} = C_{m_{o_{wf}}} + C_{m_{o_c}} + C_{m_{o_h}} \quad (8.76)$$

where: $C_{m_{o_{wf}}}$ is the zero-lift pitching moment coefficient of the wing-fuselage combination. It may be computed from:

$$C_{m_{o_{wf}}} = \{(C_{m_{o_w}}) + (C_{m_{o_f}})\}\{(C_{m_o})_M/(C_{m_o})_{M=0}\} \quad (8.77)$$

where: $C_{m_{o_w}}$ is found from Eqn.(8.70)

$$C_{m_{o_f}} = \quad (8.78)$$

$$\{(k_2 - k_1)/36.5\bar{S}c\}[\text{Sum}_{i=1}^{i=13}\{(w_{f_i}^2)(-i_w + \alpha_{o_{L_w}} + i_{cl_f})\Delta x_i\}]$$

where: $(k_2 - k_1)$ is found from Figure 8.111.

w_{f_i} is the average width of a fuselage segment as shown in Figure 8.112.

Δx_i is the length of a fuselage segment as shown in Figure 8.112.

i_w is the wing incidence angle as defined in Figure 8.60.

$\alpha_{o_{L_w}}$ is found from Eqn.(8.21)

i_{cl_f} is the incidence angle of the fuselage camber line RELATIVE to the fuselage reference plane (FRP) at the center of each fuselage increment. The sign convention for this angle is illustrated in Figure 8.112. Note that this angle is NEGATIVE for down-camber at the fuselage nose as well as for up-camber at the fuselage tailcone.

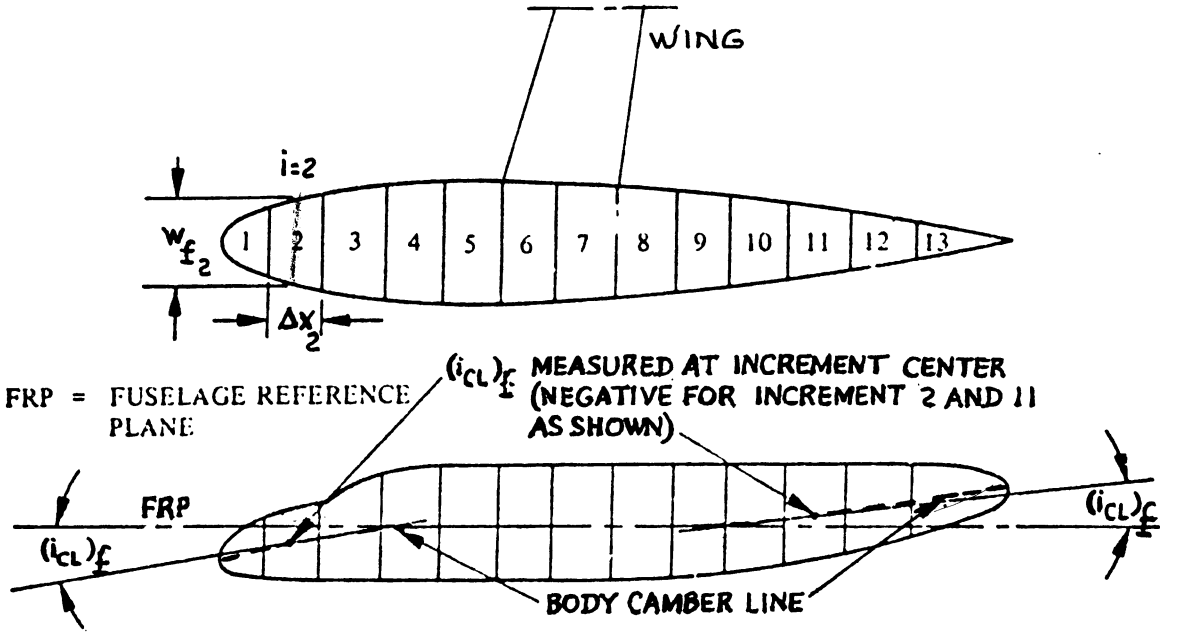

COPIED FROM REF. 9

Figure 8.112 Fuselage Segmentation and Fuselage Camber

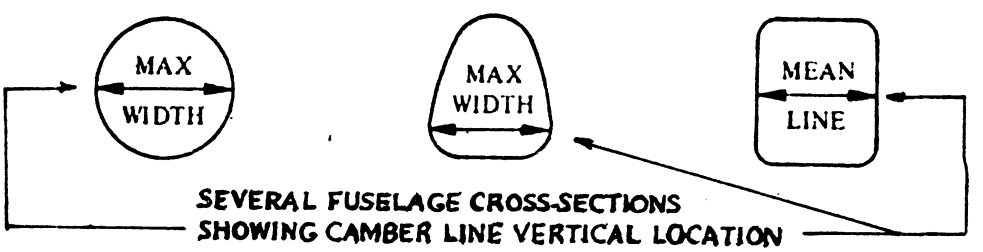

COPIED FROM REF. 9

Figure 8.113 Definition of Maximum Fuselage Width for Several Fuselage Cross Sections

The fuselage camber line is determined in the fuselage sideview by the so-called maximum width locus which in turn arises from the fuselage cross section distribution. It is shown in Figure 8.113 how the maximum fuselage width is defined for three types of fuselage cross sections.

$C_{m_{o_c}}$ and $C_{m_{o_h}}$ are the zero-lift pitching moment coefficient due to the canard and due to the horizontal tail respectively. Their sum may be computed from:

$$C_{m_{o_c}} + C_{m_{o_h}} = (\bar{x}_{ac_c} + \bar{x}_{ref})C_{L_{o_c}} - (\bar{x}_{ac_h} - \bar{x}_{ref})C_{L_{o_h}} \qquad (8.79)$$

where: x_{ac_c} and x_{ac_h} are defined in Figure 8.114, POSITIVE as shown in that Figure! Note that this is an inconsistent sign convention!!

x_{ref} is the reference (or c.g.) location about which the airplane pitching moment is to be determined: see Figures 8.114 and 8.97b. NOTE: this quantity is POSITIVE when behind the leading edge of the wing m.g.c. and NEGATIVE when forward of the leading edge of the wing m.g.c.!

Observe that:
$$\bar{x}_{ref} = (x_{ref})/\bar{c} \qquad (8.80a)$$
$$\bar{x}_{ac_c} = (x_{ac_c})/\bar{c} \qquad (8.80b)$$
$$\bar{x}_{ac_h} = (x_{ac_h})/\bar{c} \qquad (8.80c)$$

NOTE: for the entire airplane, x_{ref} is normally selected to be a c.g. location in between the most forward and the most aft center of gravity location as found from Chapter 10 in Part II.

$C_{L_{o_c}}$ and $C_{L_{o_h}}$ are the lift coefficients at

airplane zero angle of attack of the canard and of the horizontal tail respectively. These quantities are the third and second term respectively in Eqn (8.32).

Transonic:

For Mach numbers between 0.6 and 0.9 the subsonic method may be used. Above M=0.9 experimental data should be employed.

Supersonic:

Experimental methods should be used. For slender configurations such as fighter aircraft, Ref.9 presents a reasonable procedure for estimating C_{m_o}.

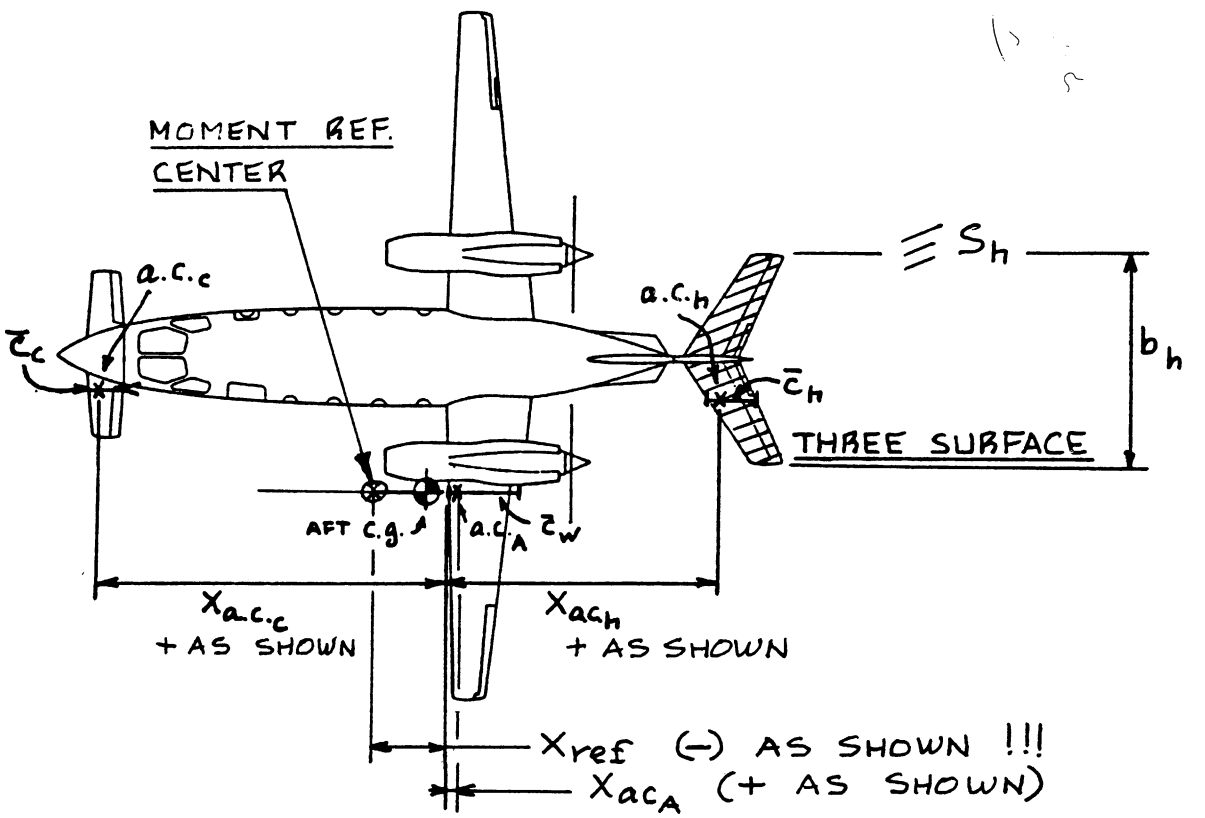

Figure 8.114 Definition of Aerodynamic Center Location Parameters and Moment Reference Center

8.2.5.2 Airplane pitching moment variation with lift coefficient: dC_m/dC_L

Subsonic:

The variation of airplane pitching moment coefficient with lift coefficient may be estimated from:

$$dC_m/dC_L = \bar{x}_{ref} - \bar{x}_{ac_A} \qquad (8.81)$$

where:

$\bar{x}_{ref}$ is the location of the moment reference center in fractions of the m.g.c. It is defined in Figures 8.97b and 8.114.

NOTE: for the entire airplane, x_{ref} is normally selected to be a c.g. location in between the most forward and the most aft center of gravity location as determined from Chapter 10 in Part II.

$\bar{x}_{ac_A}$ is the location of the airplane aerodynamic center in fractions of the m.g.c. Fig. 8.114 defines its location on the m.g.c. The following equation may be used to compute it:

$$\bar{x}_{ac_A} = \qquad (8.82)$$

$$[(\bar{x}_{ac_{wf}})C_{L_{\alpha_{wf}}} + \{\eta_h C_{L_{\alpha_h}} (1 - d\varepsilon/d\alpha)(S_h/S)\bar{x}_{ac_h} + \eta_c C_{L_{\alpha_c}} (1 + d\varepsilon_c/d\alpha)(S_c/S)\bar{x}_{ac_c}\}]/C_{L_\alpha}$$

where: $\bar{x}_{ac_{wf}} = \bar{x}_{ac_w} + \Delta\bar{x}_{ac_f}$, (8.83)

both being given as fractions of the m.g.c. Note that in terms of their actual lengths:

$$x_{ac_w} = n_{ac} - n_{mgc}, \qquad (8.84)$$

both of which are defined in Figure 8.97a.

n_{ac} may be determined from Figure 8.100 or from Eqn. (8.73), depending on the wing type used.

$\Delta\bar{x}_{ac_f}$ is the shift in aerodynamic center caused by adding the fuselage to the wing: it is determined with the method of 8.2.5.3.

η_h and η_c may be found from 8.1.5.2.

$C_{L_{\alpha_{wf}}}$ is found from Eqn.(8.43)

$C_{L_{\alpha_h}}$ and $C_{L_{\alpha_c}}$ are found from Eqn.(8.22) with appropriate substitution of parameters.

$d\varepsilon/d\alpha$ and $d\varepsilon_c/d\alpha$ are found from 8.1.5.3.

C_{L_α} is the total airplane liftcurve slope which follows from Eqn.(8.42).

Transonic:

In the transonic speed range, the airplane undergoes an aft shift in aerodynamic center location. In preliminary design it may be assumed that this aft shift is the same as that due to the wing alone. The latter may be determined from Figure 8.100. Note that this figure applies only to straight tapered wings. For other wings, use Ref.9.

Supersonic:

In the supersonic speed range, the airplane undergoes an aft shift in aerodynamic center location. In preliminary design it may be assumed that this aft shift is the same as that due to the wing alone. The latter can be found from Figure 8.100. Note that this figure applies only to straight tapered wings. For other wings, use Ref.9.

8.2.5.3 Calculation of the aerodynamic center shift due to the fuselage: $\Delta\bar{x}_{ac_f}$

The following method may be used up to a Mach number of 0.9. Beyond this Mach number, the fuselage induced shift in a.c. location is assumed constant throughout the transonic and supersonic speed range.

The method presented here is due to Munk, as reported in Reference 54:

$$\Delta\bar{x}_{ac_f} = -(dM/d\alpha)/(\bar{q}S\bar{c}C_{L_{\alpha_W}}) \qquad (8.85)$$

where: $C_{L_{\alpha_W}}$ is found from Eqn.(8.22) in 1/deg.

$$(dM/d\alpha) = \qquad (8.86)$$

$$(\bar{q}/36.5)(C_{L_{\alpha_W}}/0.08)\left[\text{Sum}_{i=1}^{i=13}\{(w_{f_i})^2(d\bar{\varepsilon}/d\alpha)_i \Delta x_i\}\right]$$

where: w_{f_i} and Δx_i are defined in 8.2.5.1.

$C_{L_{\alpha_W}}$ is found from Eqn.(8.22) in 1/deg.

$(d\bar{\varepsilon}/d\alpha)_i$ takes on values which depend on the fuselage segment under consideration:

for i=1,2,3,4, use curve 1 in Figure 8.115

for i=5 use curve 2 in Figure 8.115.

for i=6,7,8,9,10,11,12,13, use:

$$(d\bar{\varepsilon}/d\alpha)_i = (x_i/x_h)(1 - d\varepsilon/d\alpha) \qquad (8.87)$$

where: x_i and x_h are defined in Fig.8.116,

and $d\varepsilon/d\alpha$ is found from Eqn.(8.45), but with: $h_h = 0$.

IMPORTANT NOTE: if the airplane has wing mounted nacelles forward of the wing or wing mounted stores forward of the wing, this method should be used to compute the additional a.c. shift. In such cases only segments 1-5 need to be accounted for.

8.2.5.4 Prediction of stable or unstable pitch break

Whether or not an entire airplane has an unstable or a stable pitch break depends on the overall configuration as well as on the sequence with which separated wakes arrive from the wing at aft mounted pylon/nacelle combinations and/or at horizontal tails. The reader should con-

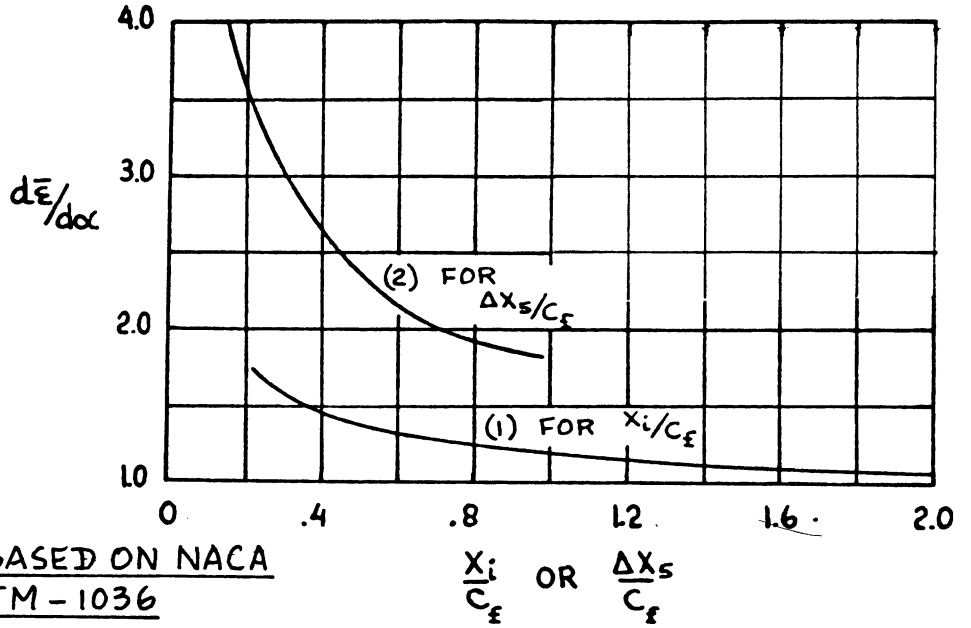

Figure 8.115 Effect of Fuselage (or Nacelle) Segment Location on Upwash Gradient

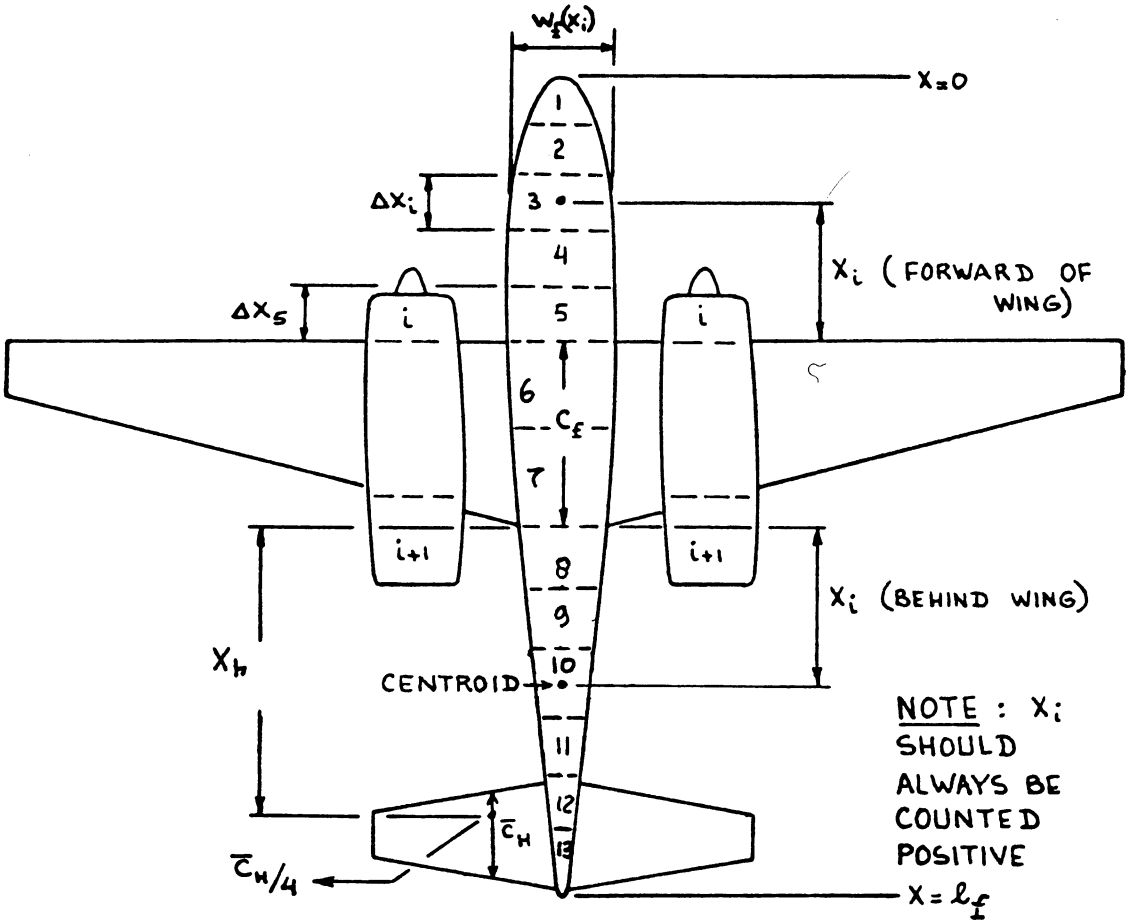

Figure 8.116 Layout for Computing Fuselage and (or) Nacelle Contribution to Airplane Aerodynamic Center Location

sult the discussion of pitch break behavior found in Subsection 5.1.4 of Part III, pages 263-272. As a result of applying this material to a given design, a determination of stable or unstable pitch break behavior can be made.

8.2.5.5 Construction of airplane pitching moment coefficient versus lift coefficient

All ingredients needed to construct the overall airplane C_m versus C_L curve are now available. A step-by-step procedure for doing this is given in Fig. 8.117.

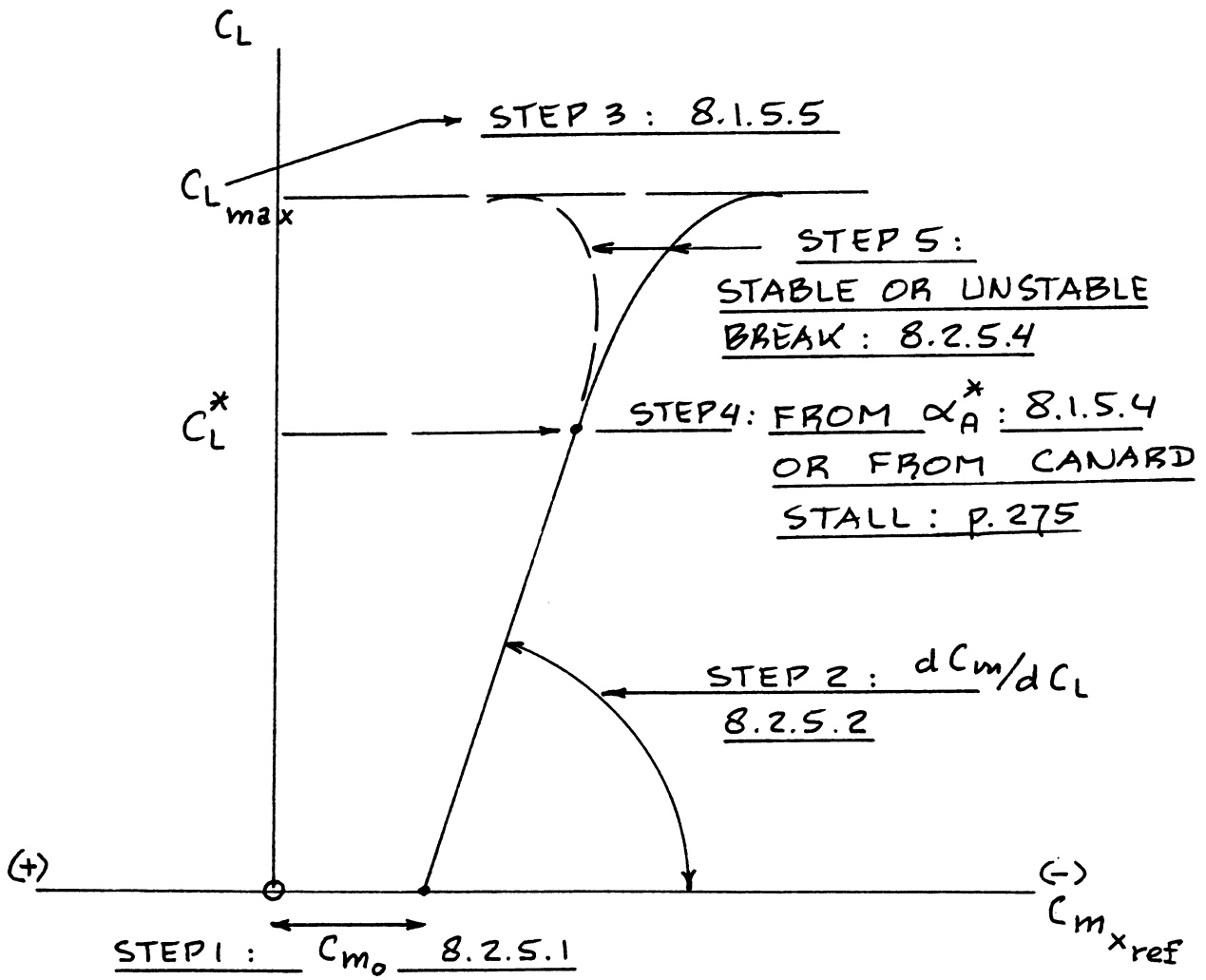

Figure 8.117 Construction of the Flaps Up Airplane Pitching Moment Versus Lift Curve

8.2.6 Airplane Pitching Moment: Flaps Down

Figure 8.118 shows the relationship between airplane pitching moment coefficient and airplane lift coefficient in the flaps down configuration. This relationship will be determined with the methods presented in this section. Key quantities needed in the construction of the airplane C_m versus C_L curve are listed, with an indication of where methods for their estimation are found.

8.2.6.1 Airplane pitching moment coefficient increment due to flaps: ΔC_m

The airplane pitching moment increment due to flaps may be estimated from:

$$\Delta C_m = \Delta C_{m_w} + \Delta C_{m_c} \eta_c (S_c \bar{c}_c / S\bar{c}) + \Delta C_{L_c} (\bar{x}_{ac_c} + \bar{x}_{ref}) +$$

$$+ C_{L_{\alpha_h}} \eta_h (S_h/S)(\bar{x}_{ac_h} - \bar{x}_{ref}) \Delta\varepsilon_f \qquad (8.88)$$

where: ΔC_{m_w} accounts for the pitching moment change due to wing flaps (leading edge and/or trailing edge) and is found from 8.2.4.1

ΔC_{m_c} accounts for the pitching moment change due to canard flaps (usually trailing edge only) and is found from 8.2.4.1 with appropriate substitution of canard parameters for wing parameters. If the canard has no flaps, this quantity is equal to zero.

ΔC_{L_c} is found from 8.1.4.1 with appropriate substitution of canard parameters for wing parameters. The comments made on p.277 apply!

x_{ref}, x_{ac_c} and x_{ac_h} are defined in Figure 8.114.

NOTE: the reader should carefully observe the inconsistent sign convention used for these quantities!

$C_{L_{\alpha_h}}$ is found from 8.1.3.2 with appropriate substitution of horizontal tail parameters for wing parameters.

η_c and η_h are found from 8.1.5.2.

$\Delta\varepsilon_f$ is found from Figure 8.70.

8.2.6.2 Slope of the airplane pitching moment curve flaps down: $(dC_m/dC_L)_\delta$

It may be assumed that the slope of the flaps down pitching moment curve is the same as that of the flaps up pitching moment curve:

$$(dC_m/dC_L)_\delta = dC_m/dC_L \qquad (8.89)$$

8.2.6.3 Prediction of stable or unstable pitch break: flaps down

It will be assumed that the pitch break behavior of the airplane with the flaps down is similar to that with the flaps up. The reader is referred to 8.2.5.4.

8.2.6.4 Construction of the airplane flaps down pitching moment curve

All items needed in the construction of the total airplane pitching moment curve with the flaps down are now available. Figure 8.119 shows a step-by-step procedure to accomplish this.

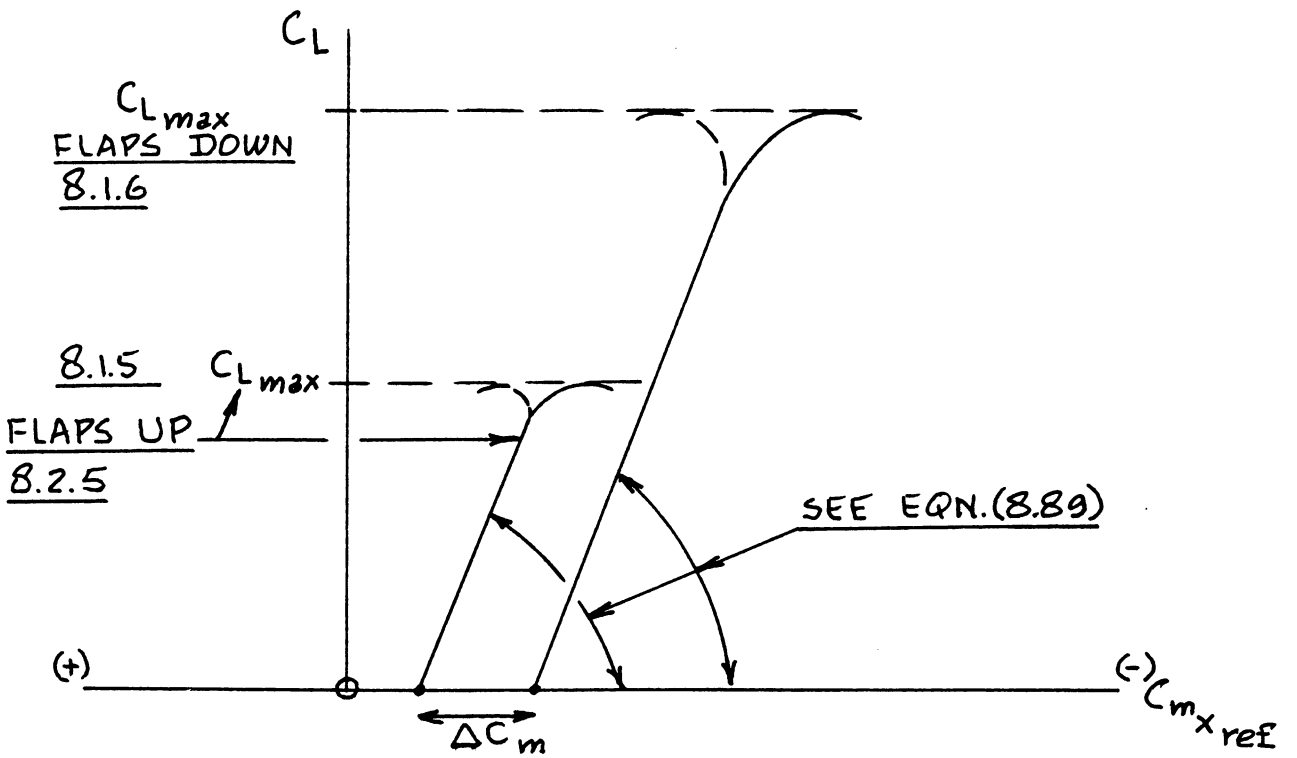

Figure 8.118 Airplane Pitching Moment Versus Lift Curve with the Flaps Down

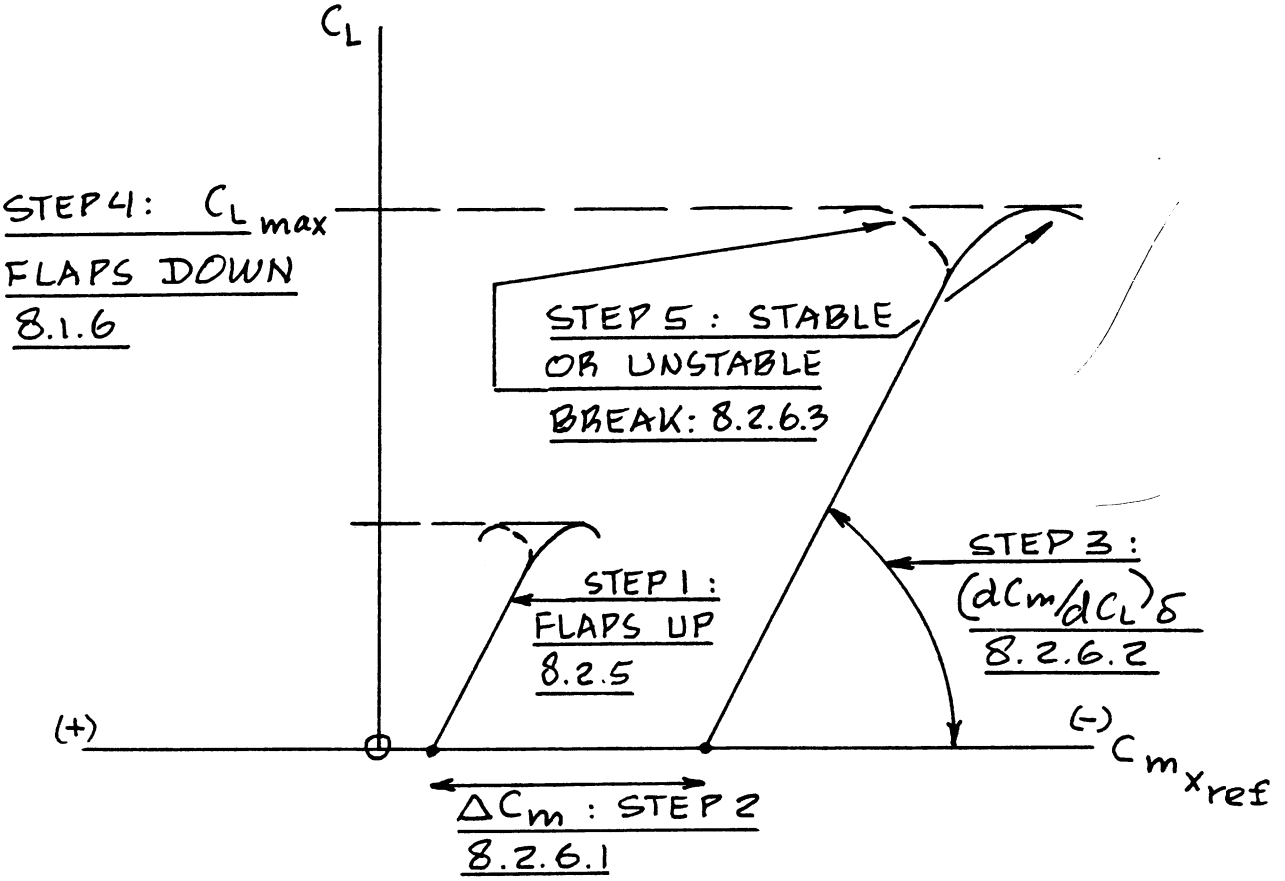

Figure 8.119 Construction of the Flaps Down Airplane Pitching Moment Versus Lift Curve

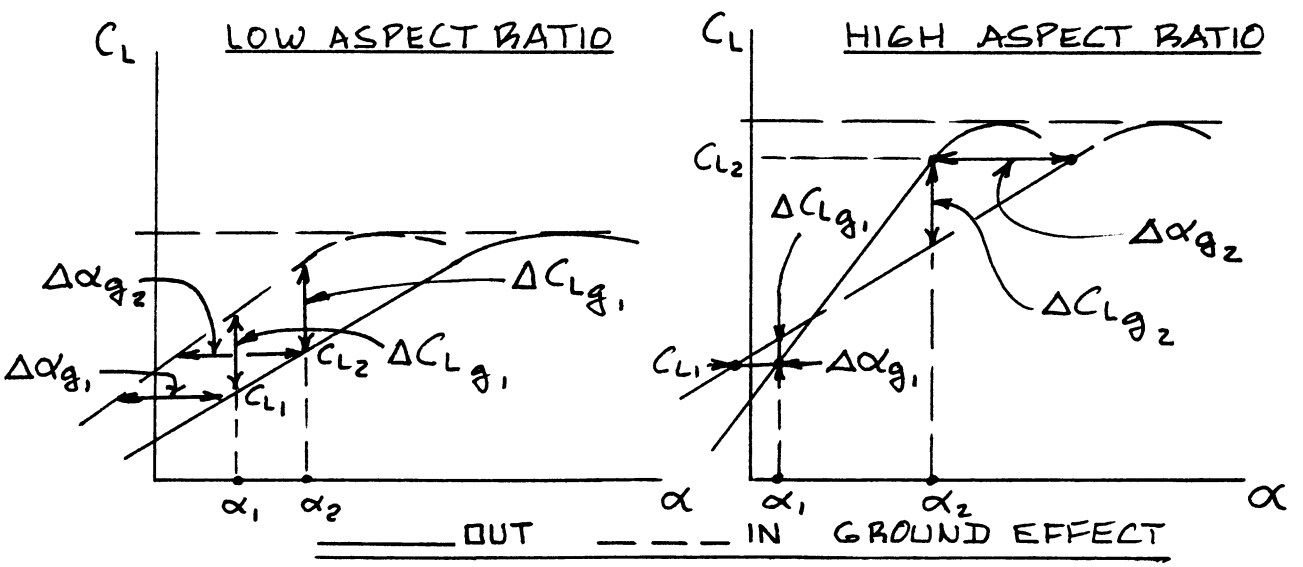

Figure 8.120 Ground Effect on Lift Curves: Revisited

8.2.7 Airplane Pitching Moment in Ground Effect

Figure 8.120 shows a re-interpretation of the airplane lift versus angle of attack curve in and out of ground attack. Figure 8.120 is a different way of looking at Figure 8.72. In Figure 8.72 the assumption was made that the tail lift (and/or the canard lift) do not contribute significantly to airplane lift change due to ground effect. Although this is usually true to a first order of approximation, that does not mean that the pitching moments due to ground induced lift changes on these surfaces are also negligible.

It will be assumed that the aerodynamic center of the airplane does not change due to ground effect. In that case, the pitching moment increment due to ground effect on the entire airplane may be estimated from:

$$(\Delta C_m)_g = \tag{8.90}$$

$$(\Delta C_{m_{wf}})_g + (\Delta C_{m_c})_g + (\Delta C_{m_h})_g$$

where: $$(\Delta C_{m_{wf}})_g = (\bar{x}_{ref} - \bar{x}_{ac_A})(\Delta C_{L_{wf}})_g \tag{8.91}$$

with: x_{ref} and x_{ac_A} defined in Section 8.2.5: observe the inconsistent sign convention!

$(\Delta C_{L_{wf}})_g = (\Delta C_L)_g$ as shown in Figure 8.120.

$(\Delta C_L)_g$ in turn is found at two values of angle of attack, α, from Section 8.1.7 and plotted as shown in Figure 8.120. Note from Section 8.1.7 the difference between high and low aspect ratio configurations!

$$(\Delta C_{m_c})_g = (\Delta C_{L_c})_g \eta_c (\bar{x}_{ac_c} + \bar{x}_{ref}) \tag{8.92}$$

with: x_{ac_c} and x_{ref} defined in Section 8.2.5: observe the inconsistent sign convention!

η_c is found from 8.1.5.2 and:

$$-(\Delta C_{L_c})_g = -C_{L_{\alpha_c}} (S_c/S)(\Delta \varepsilon_c)_g \tag{8.93}$$

where: $C_{L_{\alpha_c}}$ is found from 8.1.3.2 with appropriate substitution of canard parameters for wing parameters.

$(\Delta\varepsilon_c)_g$, the ground induced change in upwash angle at the canard is found from 8.2.7.1.

$$(\Delta C_{m_h})_g = -(\Delta C_{L_h})_g \eta_h (\bar{x}_{ac_h} - \bar{x}_{ref}) \qquad (8.94)$$

with: x_{ac_h} and x_{ref} defined in Section 8.2.5: observe the inconsistent sign convention!

η_h is found from 8.1.5.2 and:

$$(\Delta C_{L_h})_g = -C_{L_{\alpha_h}} (S_h/S)(\Delta\varepsilon)_g \qquad (8.95)$$

where: $C_{L_{\alpha_h}}$ is found from 8.1.3.2 with appropriate substitution of horizontal tail parameters for wing parameters.

$(\Delta\varepsilon)_g$ the ground induced change in tail downwash angle is found from 8.2.7.1.

Equation (8.90) is used to find ΔC_m for two angles of attack. The C_m-C_L curve of the airplane in ground effect can now be replotted as shown in Figure 8.121. Note that this in effect causes a slight change in airplane stability due to ground effect despite the assumption of constant a.c. location which was made in Eqn.(8.91).

8.2.7.1 Ground effect on downwash and on upwash

Ground Effect on Downwash

The decrease in tail downwash due to ground effect may be computed from:

$$(\Delta\varepsilon)_g = \qquad (8.96)$$
$$\varepsilon[\{b_{eff}^2 + 4(H_h - H_w)^2\}/\{b_{eff}^2 + 4(H_h + H_w)^2\}]$$

where: $\varepsilon = \alpha(d\varepsilon/d\alpha) + \varepsilon_{o_h}$ (8.97)

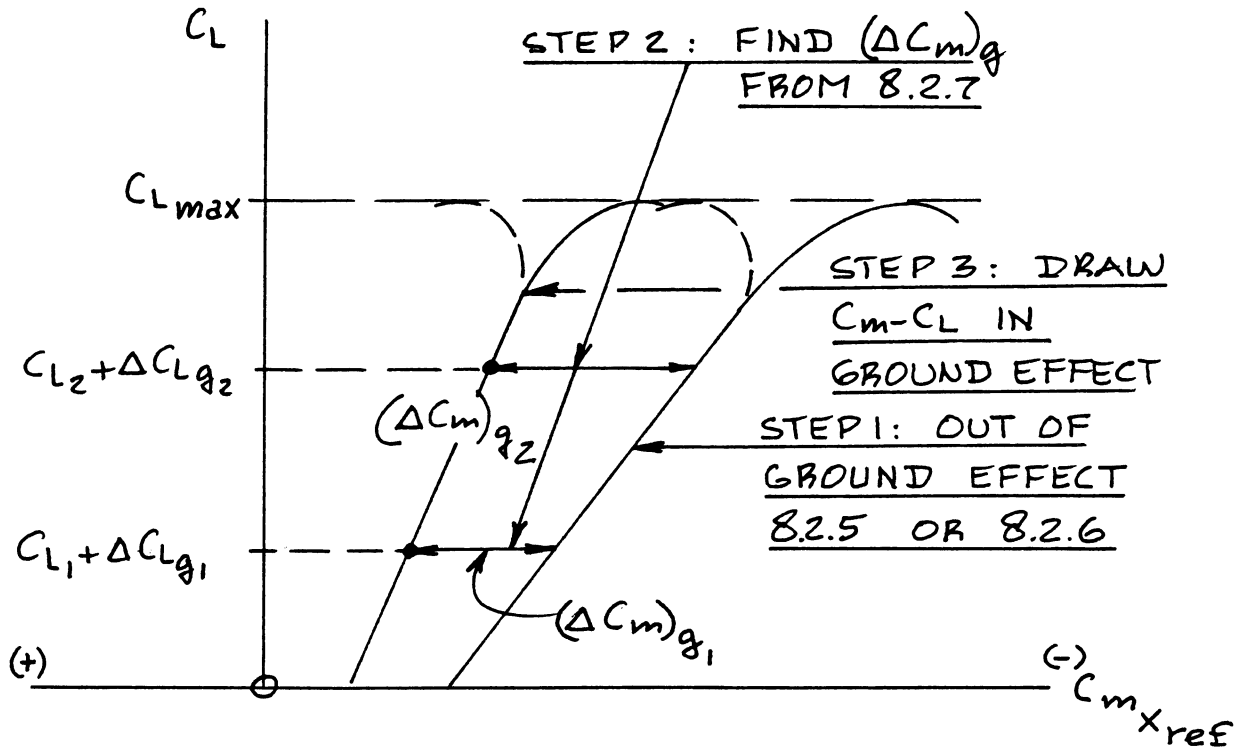

Figure 8.121 Construction of Airplane Pitching Moment Versus Lift Curve in Ground Effect

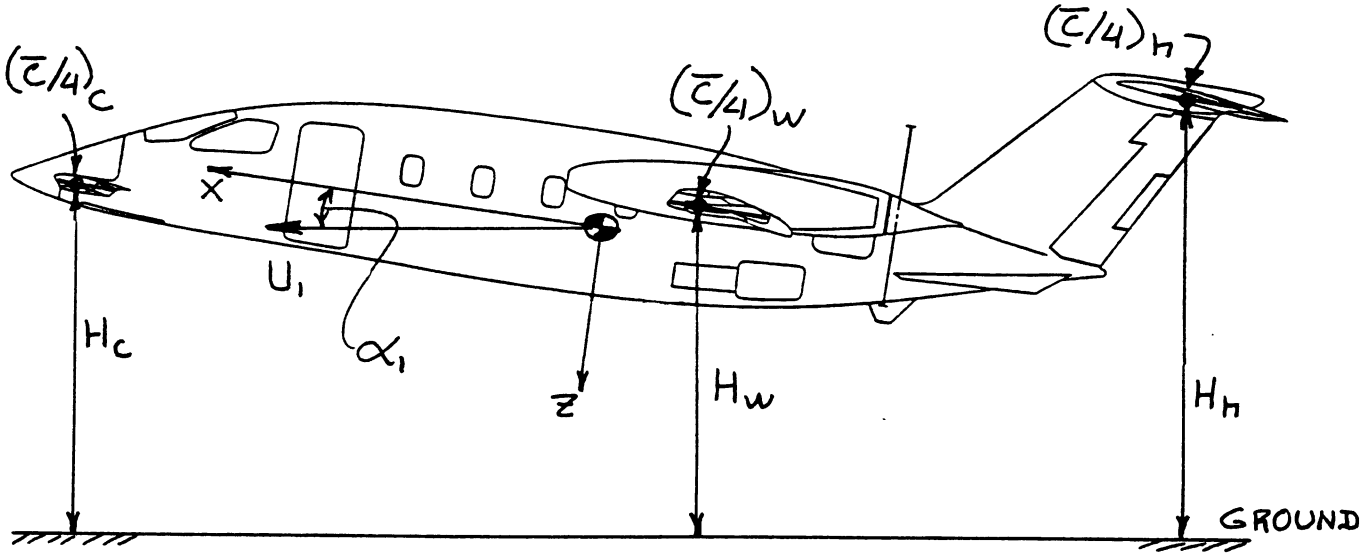

Figure 8.122 Definition of Canard, Wing and Tail Height Above the Ground

with $d\varepsilon/d\alpha$ found from Eqn.(8.45).

ε_{o_h} is the horizontal tail downwash angle for zero airplane angle of attack.

H_h is the height of the horizontal tail $\bar{c}_h/4$ above the ground: see Figure 8.122.

H_w is the height of the wing $\bar{c}/4$ above the ground: see Figure 8.122.

$$b_{eff} = \frac{(C_{L_{wf}} + \Delta C_L)}{\{(C_{L_{wf}}/b'_w) + (\Delta C_L)/b'_f\}} \qquad (8.98a)$$

where: $C_{L_{wf}}$ is the wing-fuselage lift coefficient flaps up, out of ground effect as found from 8.1.5.

ΔC_L is the lift increment due to flaps out of ground effect as found from 8.1.6.

$$b'_w = b(b'_w/b) \qquad (8.98b)$$

with: (b'_w/b) given in Figure 8.123.

$$b'_f = b(b'_f/b'_w)(b'_w/b) \qquad (8.98c)$$

with: (b'_f/b'_w) given in Figure 8.124.

Ground Effect on Upwash

The decrease in canard upwash due to ground effect may be computed from:

$$(\Delta\varepsilon_c)_g = \varepsilon_c\{(H_c - H_w)^2/(H_c + H_w)^2\} \qquad (8.99)$$

where: $$\varepsilon_c = \alpha\,(d\varepsilon_c/d\alpha) + \varepsilon_{o_c} \qquad (8.100)$$

with: α being the airplane angle of attack and

ε_{o_c} being the canard upwash angle for zero airplane angle of attack, while

$d\varepsilon_c/d\alpha$ is found from Figure 8.67

H_c is the height of the canard $\bar{c}_c/4$ above the ground: see Figure 8.122.

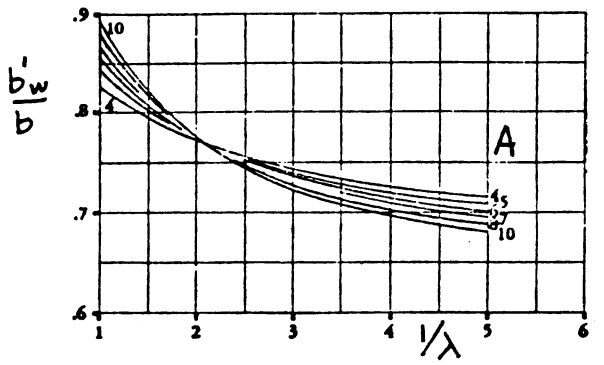

COPIED FROM: REF. 9

Figure 8.123 Effective Wing Span Close to the Ground

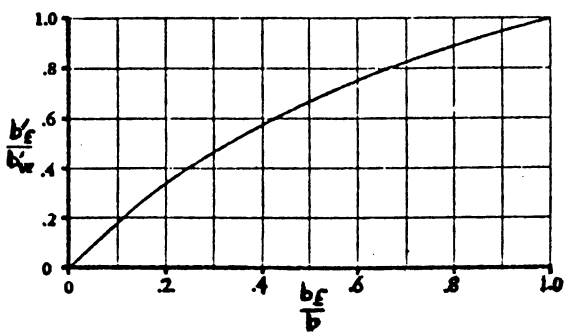

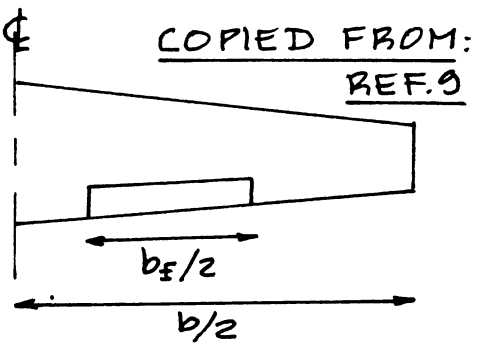

Figure 8.124 Effective Flap Span Close to the Ground

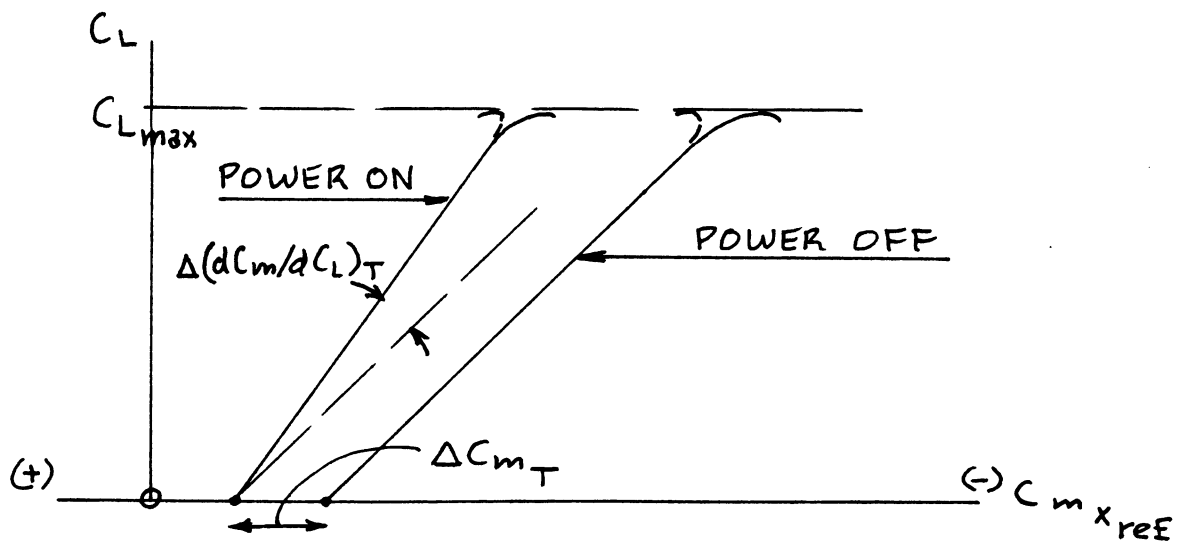

Figure 8.125 Power Effects on Airplane Pitching Moment

8.2.8 Power Effects on Airplane Pitching Moment

For a detailed treatment of power effects on pitching moment the reader should consult Reference 9.

Figure 8.125 shows that two types of power effect on the airplane C_m-C_L curve must be accounted for:

1. A shift in pitching moment at zero lift coefficient: ΔC_{m_T}

   This type of power effect is caused by thrustline offset and/or by the effect of propeller slipstream.

2. A change in slope: $\Delta(dC_m/dC_L)_T$

   The change in slope must be interpreted as a change in apparent static longitudinal stability. This type of power effect is caused by thrustline offset and/or by propeller/inlet normal forces.

These effects are accounted for as follows:

8.2.8.1 Power effect on pitching moment at zero lift coefficient

8.2.8.2 Power effect on longitudinal stability

8.2.8.1 Power effect on pitching moment at zero lift coefficient: ΔC_{m_T}

The effect of power on the pitching moment coefficient at zero lift coefficient may be estimated from:

$$\Delta C_{m_T} = \Delta C_{m_{TL}} + \Delta C_{m_{TS}} \qquad (8.101)$$

where: $\Delta C_{m_{TL}}$ is the pitching moment increment due to thrustline offset

$\Delta C_{m_{TS}}$ is the pitching moment increment due to propeller slipstream

Effect of Thrustline Offset: $\Delta C_{m_{TL}}$

Figure 8.126 illustrates the geometry of thrustline offset as it affects the pitching moment of an airplane.

Since multi-engine airplanes can have the engines

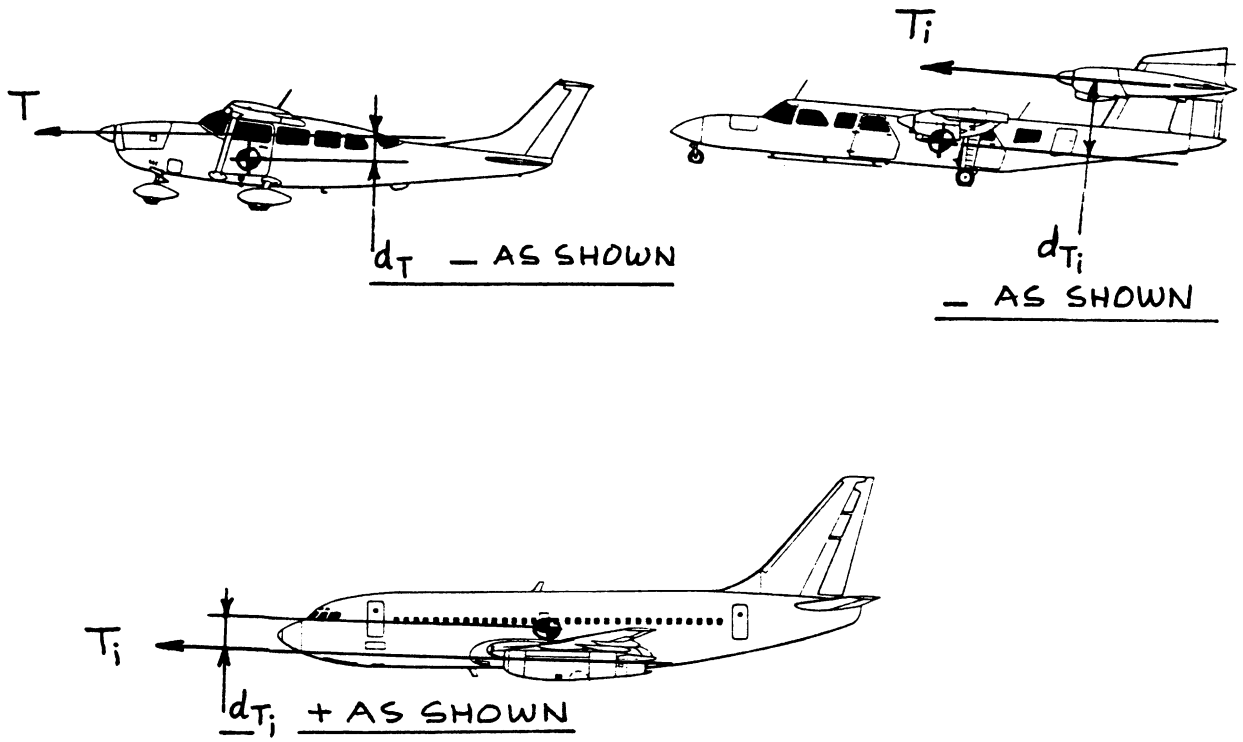

Figure 8.126 Geometry of Thrustline Offset

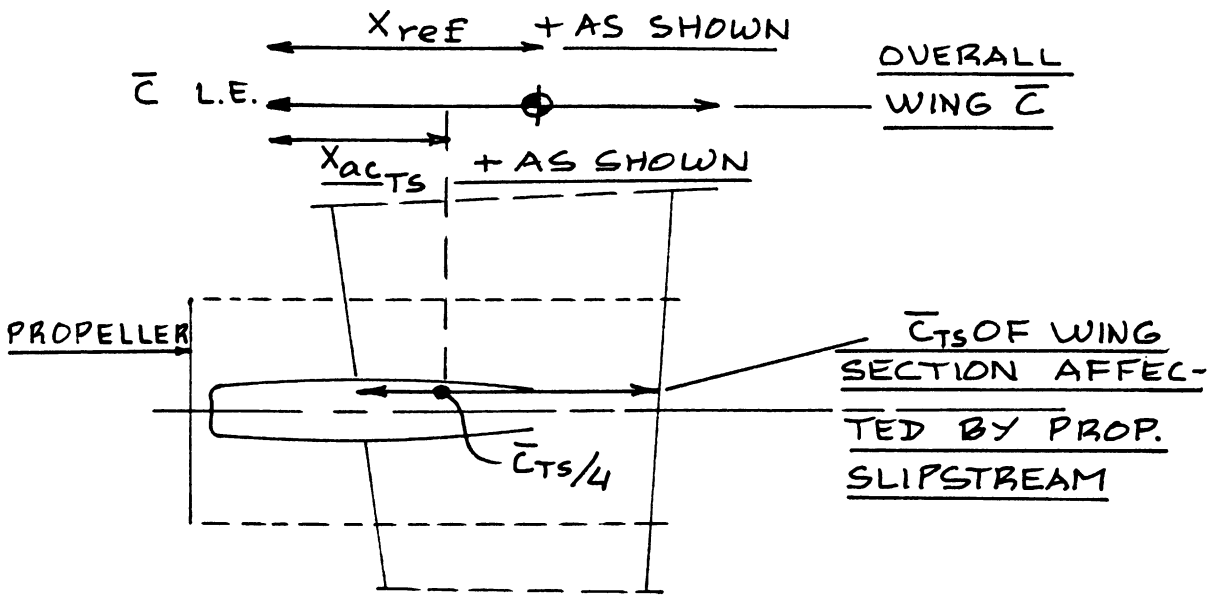

Figure 8.127 Geometric Parameters Affecting Slipstream Effect on a Wing

installed in relationsship to the moment reference point, x_{ref} in a variety of ways, a summation of the effect of individual engines will be required. The incremental pitching moment due to thrustline offset is found from:

$$\Delta C_{m_{TL}} = \sum_{i=1}^{i=n} (T_{av_i} d_{T_i} / \bar{q}\bar{S}\bar{c}) \qquad (8.102)$$

where: T_{av_i} is the available installed thrust from a propeller or from a jet engine

d_{T_i} is the thrustline offset relative to x_{ref}

Note from Figure 8.126, that d_{T_i} is counted as positive if the thrust line is located beneath the reference point.

Effect of Propeller Slipstream:

There are two types of slipstream effect which can alter the pitching moment of an airplane:

1. Effect of slipstream on a canard or on a horizontal tail
2. Effect of slipstream on a wing

1. Effect of slipstream on a canard or on a horizontal tail

The effect of (propeller) slipstream on the local dynamic pressure at the canard or at the horizontal tail has already been accounted for through the dynamic pressure ratios, η_c and η_h as found from 8.1.5.2.

In all previous calculations for pitching moment, the effect of power can be left out by using $\eta_{h \text{ or } c} = 0$.

2. Effect of slipstream on a wing

The effect of propeller slipstream on a wing may be accounted for from:

$$\Delta C_{m_{TS}} = (\bar{x}_{ac_{TS}} - \bar{x}_{ref}) \Delta C_{L_w} \qquad (8.103)$$

where: $x_{ac_{TS}}$ and x_{ref} are defined in Figure 8.127.

ΔC_{L_w} is found from Eqn.(8.57)

8.2.8.2 Power effect on longitudinal stability: $\Delta(dC_m/dC_L)_T$

The following method to account for power effect on stability is adapted from Reference 54:

$$\Delta(dC_m/dC_L)_T = (dC_m/dC_L)_{TL} + (dC_m/dC_L)_N \qquad (8.104)$$

where: $(dC_m/dC_L)_{TL}$ is the effect of thrustline offset on longitudinal stability

$(dC_m/dC_L)_N$ is the effect of propeller or inlet normal force on longitudinal stability

Methods for estimating these stability effects are now given for:

1. Propeller driven airplanes

2. Jet driven airplanes

1. Propeller driven airplanes:

The effect of thrustline offset on longitudinal stability for propeller driven airplanes is:

$$(dC_m/dC_L)_{TL} = \sum_{i=1}^{i=n}[(dT_{c_i}/dC_L)\{2(D_{p_i})^2 d_{T_i}/S\bar{c}\}] \qquad (8.105)$$

where: D_{p_i} is the diameter of propeller i.

d_{T_i} is the thrustline offset for propeller i, see Figure 8.126.

$$dT_{c_i}/dC_L = (3/2)K_{T_i}\eta_{p_i}(C_L)^{1/2} \qquad (8.106)$$

with: η_{p_i} is the efficiency of propeller i, and:

$$K_{T_i} = \{550(SHP_{av_i})(\rho)^{1/2}\}/\{(2W/S)^{3/2}(D_{p_i})^2\} \qquad (8.107)$$

Note: The effect of thrustline offset on longitudinal stability can be used by the designer to obtain minor changes in static margin by tilting the thrustline relative to the c.g. or relative to x_{ref}. Figure 8.128 shows an example of thrustline tilt angle used in a light air-

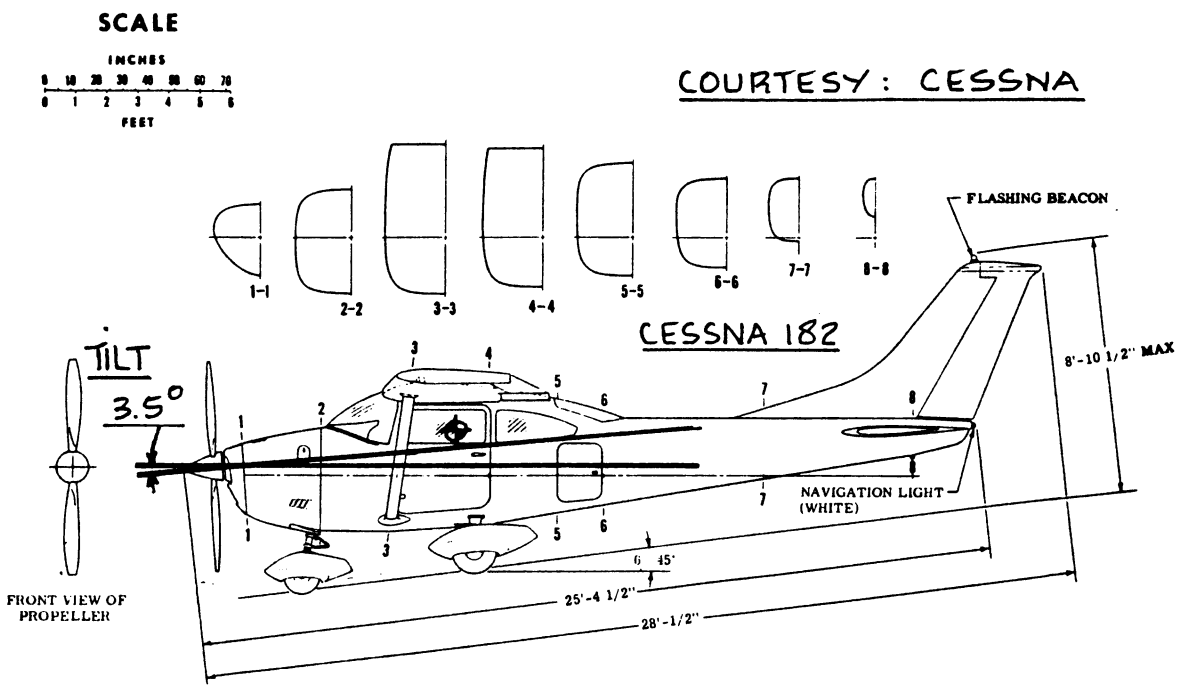

Figure 8.128 Example of Thrustline Tilt

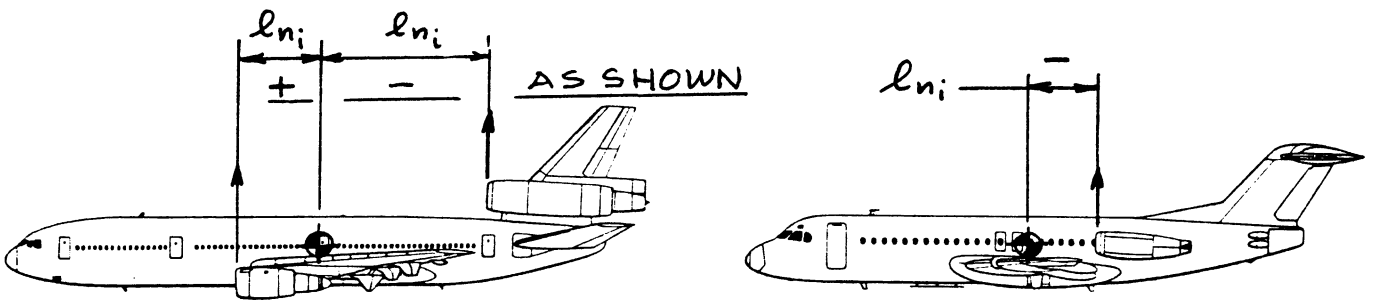

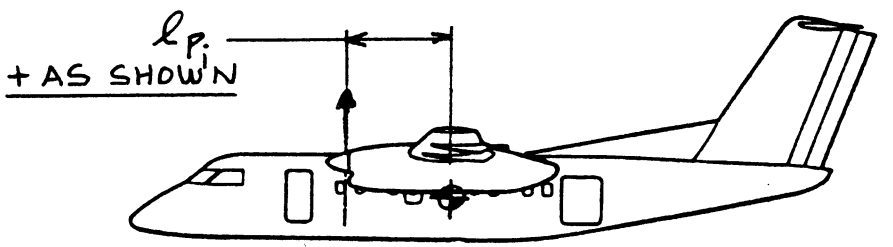

Figure 8.129 Moment Arms for Normal Forces

plane to achieve such an effect.

The effect of propeller normal force on longitudinal stability may be found from:

$$(dC_m/dC_L)_N = \qquad (8.108)$$

$$\text{Sum}_{i=1}^{i=n}\left[\{(dC_N/d\alpha)_{p_i}(d\bar{\varepsilon}_{p_i}/d\alpha)(l_{p_i})(\pi/4)(D_{p_i})^2\}/S\bar{c}C_{L_{\alpha_w}}\right]$$

where: l_{p_i} is the moment arm of the propeller normal force to the reference point: see Fig. 8.129.

$d\bar{\varepsilon}_{p_i}/d\alpha$ is found from Figure 8.115.

$(dC_N/d\alpha)_{p_i}$ is the change in propeller normal force coefficient with angle of attack. It may be computed from:

$$(dC_N/d\alpha)_{p_i} = \qquad (8.109)$$

$$[\{(C_{N_\alpha})_{p_i}\}_{K_{N_i}=80.7}][1 + 0.8\{(K_{N_i}/80.7) - 1\}]$$

with: $\{(C_{N_\alpha})_{p_i}\}_{K_{N_i}=80.7}$ found from Figure 8.130,

and with:

$$K_{N_i} = 262\{(w_{p_i}/R_{p_i})_{0.3R_{p_i}}\} + \qquad (8.110)$$

$$+ 262(w_{p_i}/R_{p_i})_{0.6R_{p_i}} + 135(w_{p_i}/R_{p_i})_{0.9R_{p_i}}$$

where: w_{p_i} is the propeller blade width at the radius station indicated in the subscript

R_{p_i} is the propeller blade radius ($0.5D_{p_i}$)

2. Jet driven airplanes:

The effect of thrustline offset on the longitudinal stability of most jet driven airplanes is negligible. The reason is the relatively small change in thrust with small changes in speed.

The effect of inlet normal force on longitudinal stability of a jet airplane may be estimated from:

$$(dC_m/dC_L)_N = \text{Sum}_{i=1}^{i=n} \left[\frac{\{0.035(\dot{m}_{a_i})(d\bar{\varepsilon}/d\alpha)_i(l_{n_i})\}}{\{Sc\rho U_1(C_{L_{\alpha_w}})\}} \right] \qquad (8.111)$$

where: $\dot{m}_{a_i}$ is the mass flow rate through engine i
This mass flow rate follows from Chapter 6.

$(d\bar{\varepsilon}/d\alpha)_i$ is obtained from Figure 8.115 for inlet i

l_{n_i} is the moment arm of the inlet lip as illustrated in Figure 8.129.

COPIED FROM: REF. 9

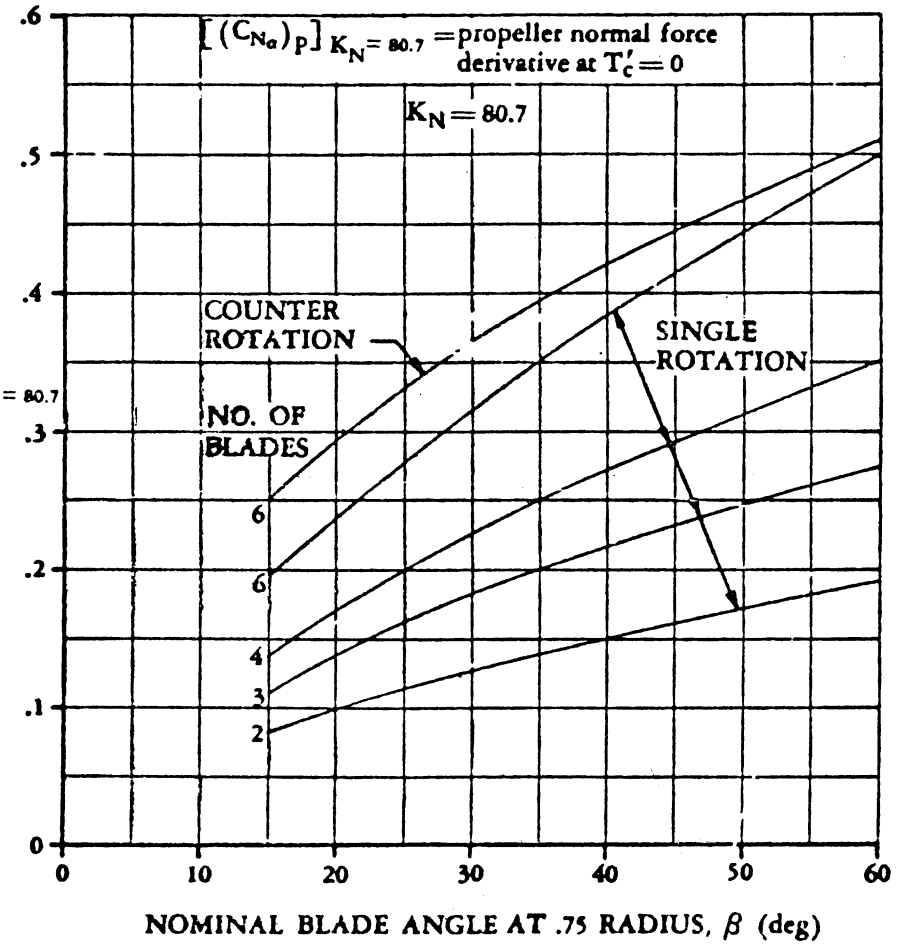

Figure 8.130 Propeller Normal Force Parameter

8.3 PREDICTION OF TRIMMED LIFT AND TRIMMED MAXIMUM LIFT COEFFICIENT

In Sections 8.1 and 8.2 methods are presented for the construction of airplane lift and pitching moment curves. The position was taken that all longitudinal control surface deflections were set at zero.

In any equilibrium flight condition the airplane must also be in moment equilibrium. The effect of pitching moment equilibrium (also known as longitudinal moment trim, or simply: trim) on airplane lift at different center of gravity locations will be accounted for in this section. The following condition must be satisfied in a trimmed flight condition:

$$C_m = 0 \qquad (8.112)$$

The pitching moment coefficient C_m takes on values which depend on:

1. the lift coefficient at which the airplane is flying,
2. the location of the center of gravity and
3. the power setting.

Methods for computing C_m are given in Section 8.2.

The trim condition as expressed by Eqn.(8.112) is achieved by deflection of one or more control surfaces. In this Section, the following control surfaces will be accounted for:

1. Stabilizer incidence, i_h
2. Elevator deflection, δ_e
3. Canard incidence, i_c
4. Canardvator deflection, δ_c

Figure 8.131 shows typical examples of these control surfaces and their typical arrangement on an airplane. Different types of longitudinal controls may be required on certain airplanes. Examples are: elevons on delta wings (as on the F-106) or symmetrically deflected ailerons (as on the Starship). In this section only types 1-4 will be considered.

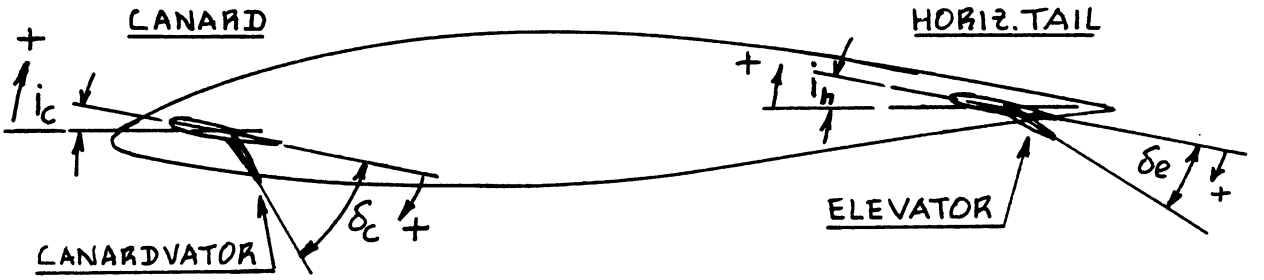

Figure 8.131 Example of Control Surface Arrangements

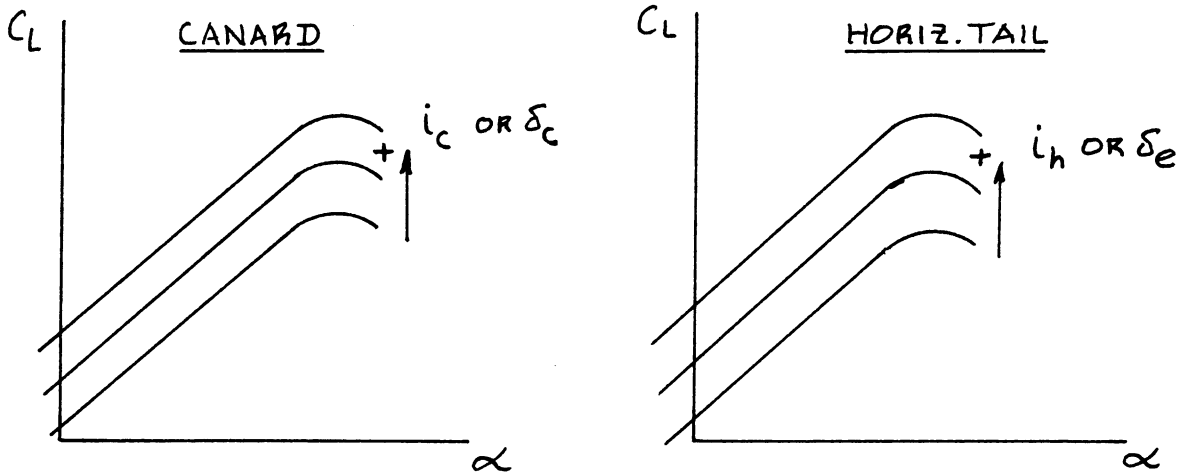

Figure 8.132 Effect of Control Surface Deflection on Airplane Lift

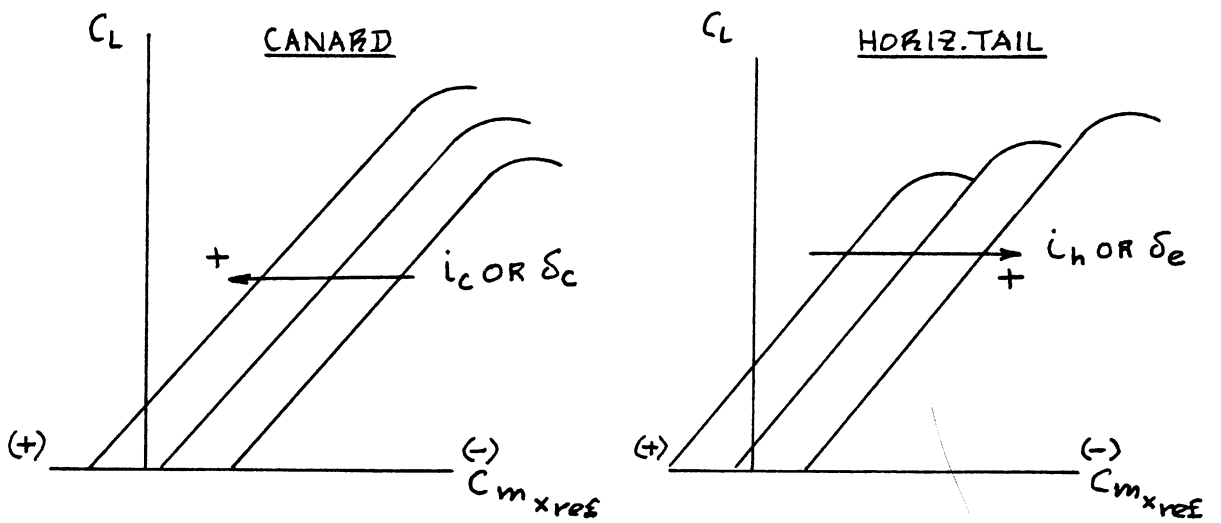

Figure 8.133 Effect of Control Surface Deflection on Airplane Pitching Moment

Deflection of a control surface (which effectively can be thought of as a plain flap) causes changes in airplane lift and in airplane pitching moment in the following ways:

1. Effect of control surface deflection on lift

2. Effect of control surface deflection on pitching moment

1. Effect of Control Surface Deflection on Lift:

$$\Delta C_{L_{ctl}} = \quad (8.113)$$

$$(C_{L_{i_h}})i_h + (C_{L_{\delta_e}})\delta_e + (C_{L_{i_c}})i_c + (C_{L_{\delta_c}})\delta_c$$

where: $C_{L_{i_h}}$, $C_{L_{\delta_e}}$, $C_{L_{i_c}}$ and $C_{L_{\delta_c}}$ are the control surface lift derivatives. They are computed with the methods given in Chapter 10.

Figure 8.132 shows how a control surface deflection affects the airplane lift versus angle of attack curve. Note the control surface sign conventions in Fig. 8.131!

2. Effect of Control Surface Deflection on Pitching Moment:

$$\Delta C_{m_{ctl}} = \quad (8.114)$$

$$(C_{m_{i_h}})i_h + (C_{m_{\delta_e}})\delta_e + (C_{m_{i_c}})i_c + (C_{m_{\delta_c}})\delta_c$$

where: $C_{m_{i_h}}$, $C_{m_{\delta_e}}$, $C_{m_{i_c}}$ and $C_{m_{\delta_c}}$ are the control power derivatives. They may be computed with the methods given in Chapter 10.

Figure 8.133 shows how a control surface deflection affects the airplane pitching moment versus lift curve. Note the control surface sign conventions in Fig. 8.131!

Next, methods are presented for determining the trimmability of airplanes. This is accomplished using so-called trim diagrams.

A method for determining trimmed lift and trimmed maximum lift capability of an airplane is presented for the following cases:

8.3.1 Stable airplane with stable pitchbreak
8.3.2 Unstable airplane with stable pitchbreak
8.3.3 Stable airplane with unstable pitchbreak
8.3.4 Unstable airplane with unstable pitchbreak

In the case of military airplanes with external stores and/or with deployed speedbrakes, significant additional pitching moments may be introduced due to these devices. Such 'drag-induced' pitching moments can be accounted for through a shift of the origin of the C_m-C_L plot. This shift is computed from:

$$\Delta C_{m_{store/speedbrake}} = (\Delta C_{D_{store/speedbrake}}) d_D/\bar{c} \qquad (8.115)$$

where: $\Delta C_{D_{store/speedbrake}}$ is the drag increment due to the store or speedbrake. This increment follows from Section 4.9 or from 4.12.

d_D is the moment arm, positive if the drag increment acts ABOVE the c.g.

8.3.1 Stable Airplane with Stable Pitch Break

Figures 8.134a,b present trim diagrams for a stable airplane with a stable pitch break:

Fig. 8.134a is for a conventional (tail-aft) airplane
Fig. 8.134b is for a canard airplane.

The C_L-α and C_L-C_m curves for ZERO control surface deflections are obtained with the methods of Sections 8.1 and 8.2 respectively. The effect of control surface deflections on these curves is determined with the method indicated in Figures 8.132 and 8.133.

Note that the C_m axis is labelled: $C_{m_{x_{ref}}}$. The location of the moment reference center, x_{ref} is normally selected somewhere between the most forward and the most aft locations of the airplane center of gravity. Methods for determining the center of gravity location of any airplane are discussed in Part II, Chapter 10.

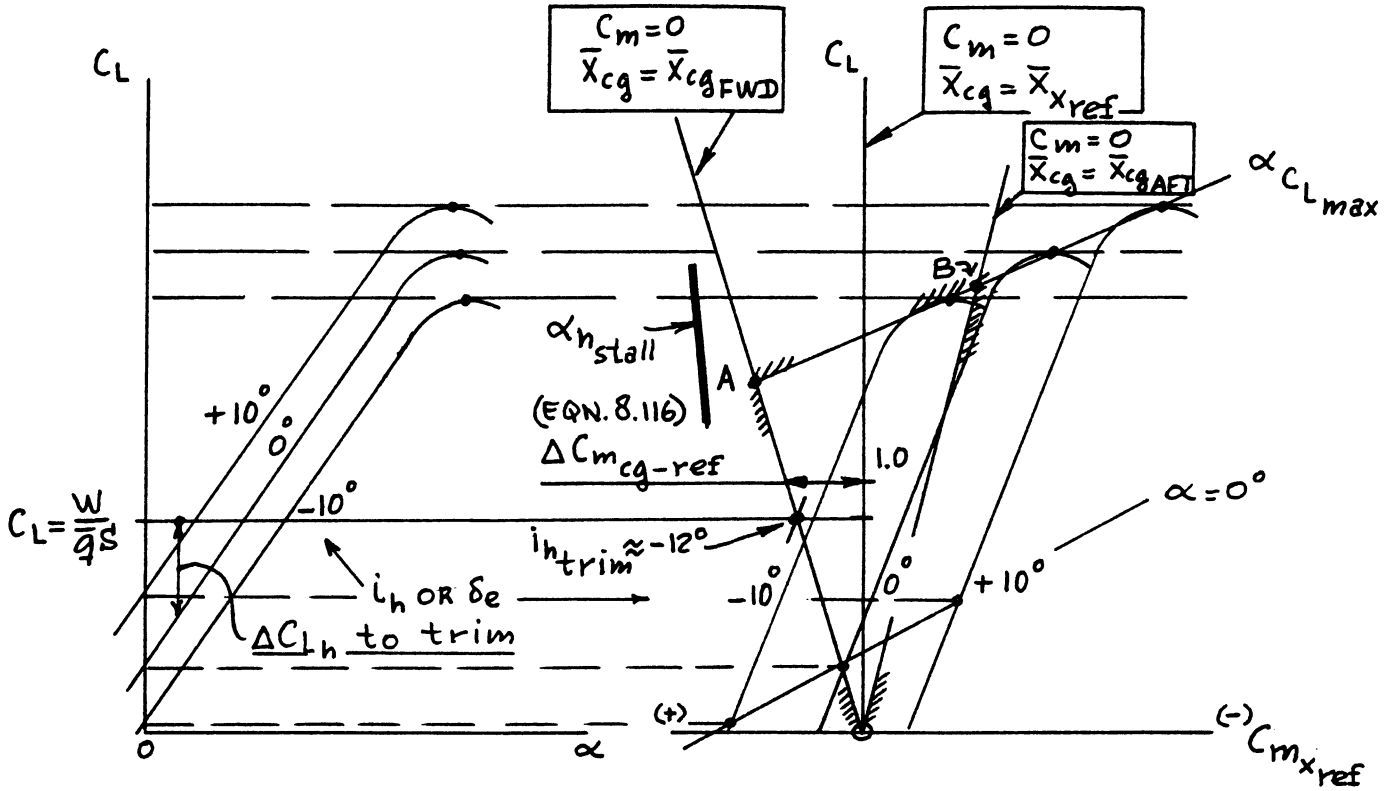

Figure 8.134a Trim Diagram: Stable, Conventional with Stable Pitch Break

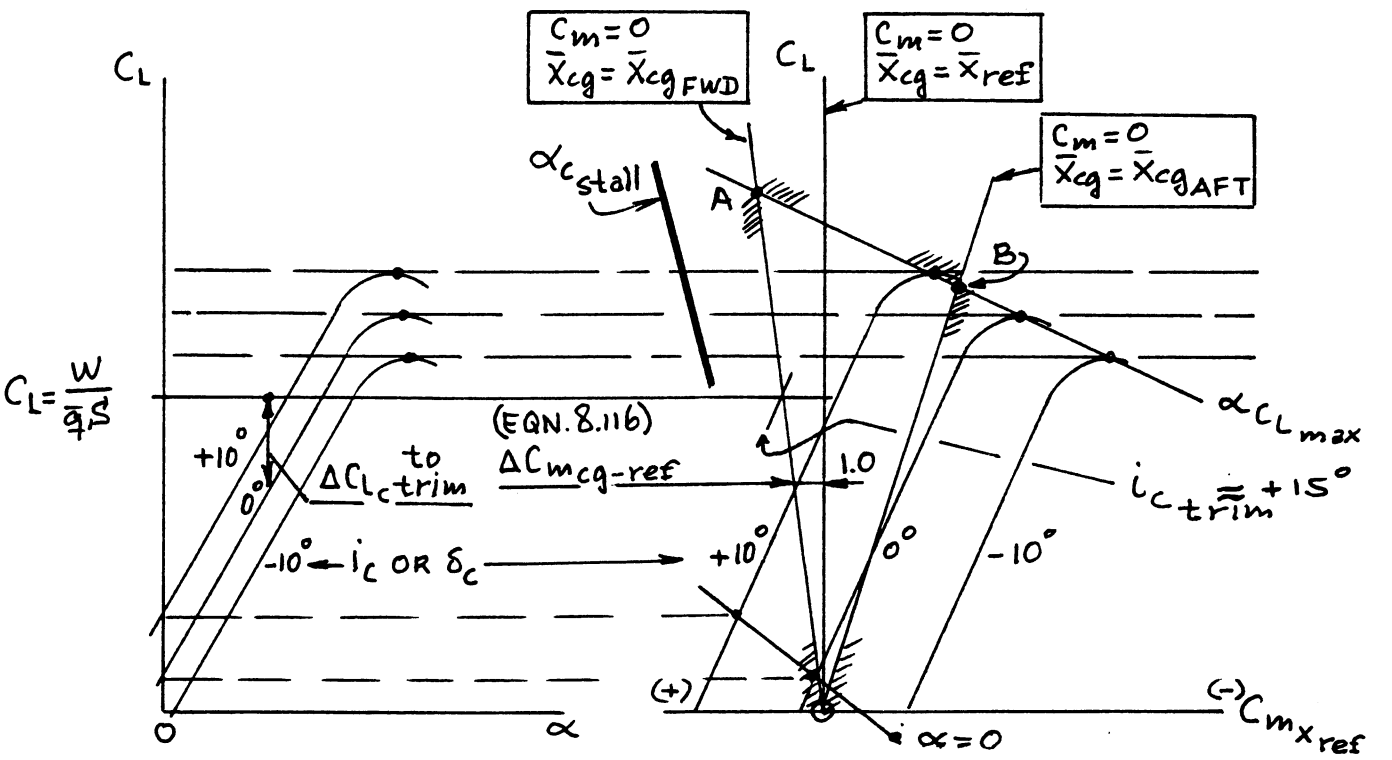

Figure 8.134b Trim Diagram: Stable, Canard with Stable Pitch Break

Observe in Figures 8.134a,b that C_m=0 lines at different centers of gravity have slopes different from that of the C_m=0 line with $x_{cg}=x_{ref}$. These different slopes may be determined with the help of Procedure 1.

==========

PROCEDURE 1: Determination of Slopes of C_m=0 Lines at Different C.G. Locations

1. Determine the most forward and the most aft c.g. locations of the airplane. This is done with the method of Chapter 10 in Part II.
2. Compute $\bar{x}_{cg} - \bar{x}_{ref}$
3. At C_L=1.0 determine:

$$\Delta C_{m_{cg-ref}} = -1.0(\bar{x}_{cg} - \bar{x}_{ref}) \qquad (8.116)$$

4. Plot $\Delta C_{m_{cg-ref}}$ as shown in Figures 8.134a,b and connect that point with the origin. The line so obtained is the C_m = 0 locus for the new c.g. location.

   Note: the proof for this procedure is found in Chapter 5 of Reference 16.

==========

The determination of trimmed lift and maximum lift now proceeds according to Procedure 2.

==========

PROCEDURE 2: Determination of Trimmed Lift and Trimmed Maxiximum Lift

1. Construct the trim diagram as shown in Figures 8.134a or 8.134b. This includes a number of α = constant lines up to α_{stall}
2. Construct the C_m=0 lines for the most aft and for the most forward c.g. locations, with the help of Procedure 1.
3. Identify the trim-triangle: OAB.
4. Draw in the tail or canard stall locus with the

following considerations. For a stalled tail:

$$\alpha_h = \alpha_{h_{stall}} = \alpha + i_h - \varepsilon_{o_h} - \alpha(d\varepsilon/d\alpha) \quad (8.117)$$

where: ε_{o_h} follows from 8.1.5.2

$d\varepsilon/d\alpha$ follows from 8.1.5.3

A value for the tail stall angle, $\alpha_{h_{stall}}$ is found from 8.1.3.4 by substitution of appropriate tail parameters for wing parameters.

For any value of airplane angle of attack, α, Eqn.(8.117) can be used to solve for the corresponding value of i_h which will cause the tail to stall. By repeating this for a range of angles of attack, a tail stall locus can be drawn into Figure 8.134a.

Note: for a canard airplane, the canard stall locus is found in a similar manner by using the following equation:

$$\alpha_c = \alpha_{c_{stall}} = \alpha + i_c + \varepsilon_{o_c} + \alpha_c(d\varepsilon_c/d\alpha) \quad (8.118)$$

where: ε_{o_c} follows from 8.1.5.2

$d\varepsilon_c/d\alpha$ follows from 8.1.5.3

IMPORTANT OBSERVATION: the tail stall and/or the canard stall loci MUST be outside the so-called trim triangle identified in Step 3. If this condition is not satisfied, severe restrictions on the performance of the airplane may result.

5. Compute $C_L = W/\bar{q}S$ for significant points in the airplane flight envelope. Figure 8.135 shows examples of significant trim points in the flight envelope of low and high speed airplanes. These points depend on the mission requirements

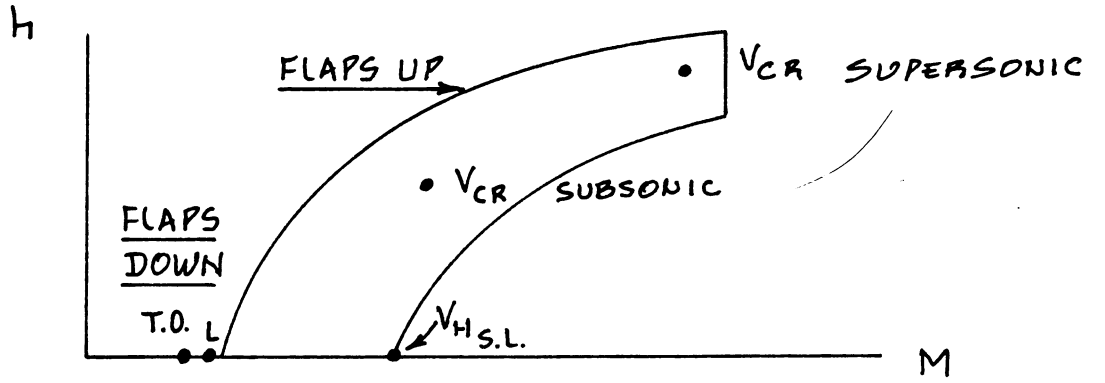

Figure 8.135 Significant Trim Points in Flight Envelope

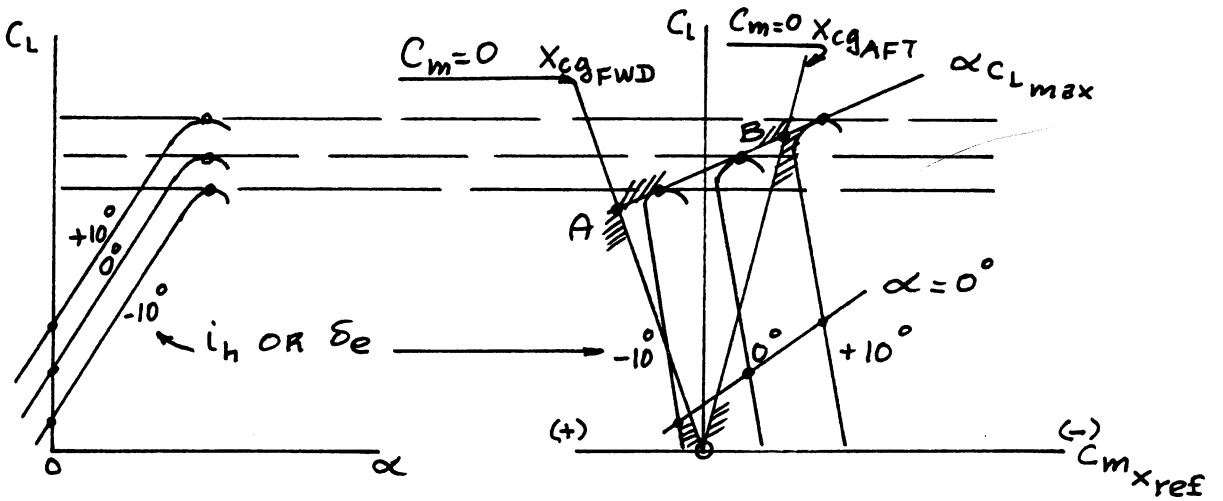

Figure 8.136a Trim Diagram: Unstable, Conventional with Stable Pitch Break

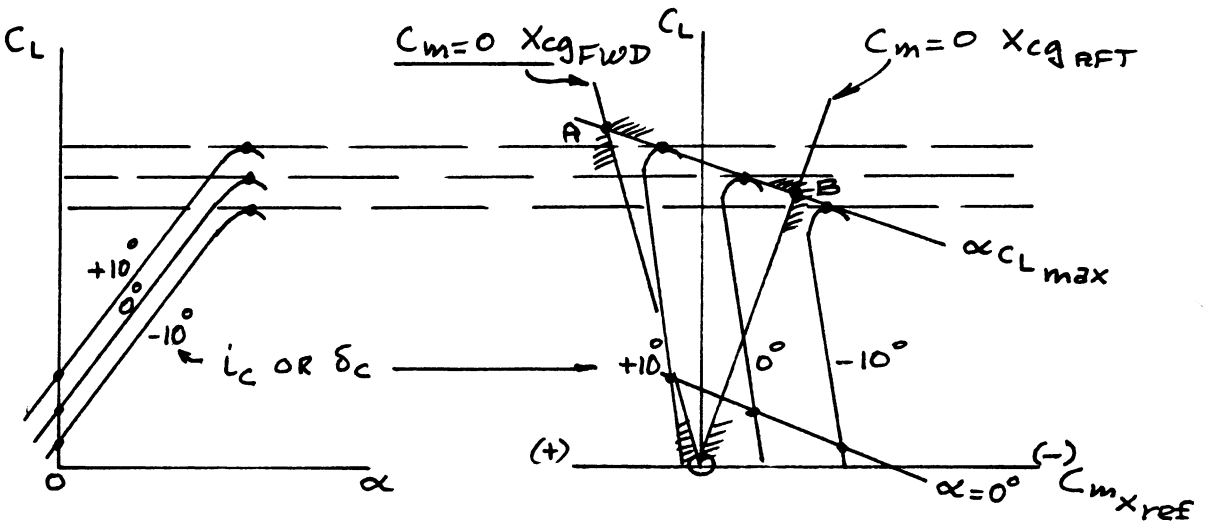

Figure 8.136b Trim Diagram: Unstable, Canard with Stable Pitch Break

placed on the airplane.

6. Determine the c.g. location(s) at which the trim needs to be investigated. Combinations of weight and c.g. locations follow from the weight-c.g. excursion diagram discussed in detail in Ch.10 of Part II.

7. Plot the C_L points on the appropriate C_m=0 line (corresponding to its c.g. location) in Figures 8.134a,b and determine the amount of control surface deflection required to trim. From these control deflections required for trim it is posble to compute the tail or canard lift increments to trim, needed in the trim drag calculations on p.104:

$$\Delta C_{L_{h \text{ or } c}} = (C_{L_{i_{h \text{ or } c}}}) i_{h \text{ or } c} \qquad (8.119)$$

or:

$$\Delta C_{L_{h \text{ or } c}} = (C_{L_{\delta_{e \text{ or } c}}}) \delta_{e \text{ or } c} \qquad (8.120)$$

8. Points A and B in Figures 8.134a,b represent the trimmed maximum lift coefficients at the corresponding c.g. locations of the airplane.

==========

SPECIAL CASE: Three-surface Airplane Trim

In the case of a three surface configuration the designer can choose how to deflect control surfaces on the canard, the wing and the tail in conjunction with each other. Several possible optimization schemes are now possible:

1. Minimize trimmed drag
2. Maximize trimmed maximum lift
3. Maximize maneuvering capability

The construction of a trim diagram for a three surface airplane is left to the reader. The Grumman X-29 and the Piaggio Avanti are examples of three surface airplanes.

8.3.2 Unstable Airplane with Stable Pitch Break

Figures 8.136a,b present example trim diagrams for an unstable airplane with a stable pitch break. The pro-

cedures outlined in 8.3.1 for determining trimmed lift and trimmed maximum lift also apply in this case.

8.3.3 Stable Airplane with Unstable Pitch Break

Figures 8.137a,b present example trim diagrams for a stable airplane with an unstable pitch break. The method of 8.3.1 for determining trimmed lift can be used without modification.

However, to determine the allowable trimmed maximum lift coefficient now is not very straightforward. Depending on the number of pitch curve 'wiggles' and depending on the change in control power at high angle of attack, the trimmed maximum lift coefficient may be limited for reasons other than aerodynamic stall. If handling quality problems or severity of pitch divergence so dictate, the airplane may have to be equipped with stick-shakers and/or with stick-pushers. In such cases the maximum trimmable lift coefficient which can be used in the normal performance envelope of the airplane is predicated on the lift coefficient corresponding to stick-pusher operation. Figures 8.137a,b indicate such an artificial limit.

In the case of airplanes equipped with digital flight control systems a control-limiting scheme may be added to the flight control laws. Such a control limiting scheme may limit the angle of attack which actually can be reached by the airplane. The limiting value of trimmed maximum lift coefficient must then be the one which corresponds to the limit set by the flight control law and not by any inherent aerodynamic limit.

8.3.4 Unstable Airplane with Unstable Pitch Break

Figures 8.138a,b show examples of trim diagrams for an unstable airplane with an unstable pitch break. The comments made under 8.3.2 apply to this case.

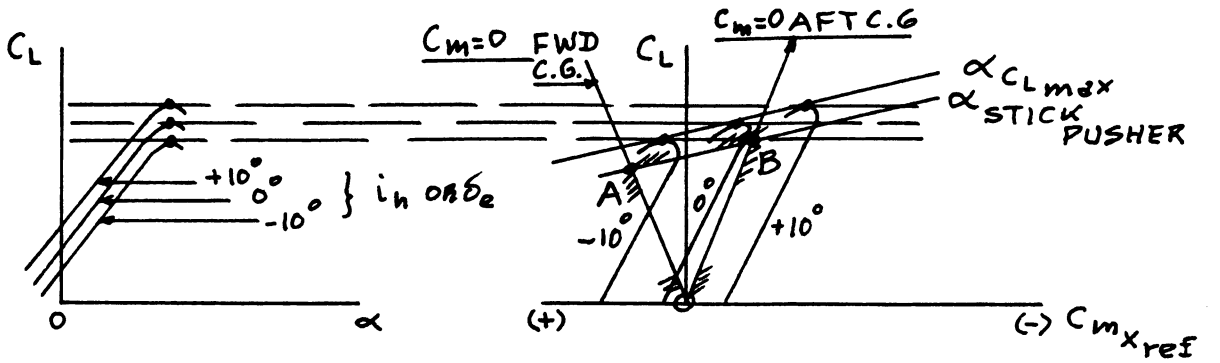

Figure 8.137a Trim Diagram: Stable, Conventional with Unstable Pitch Break

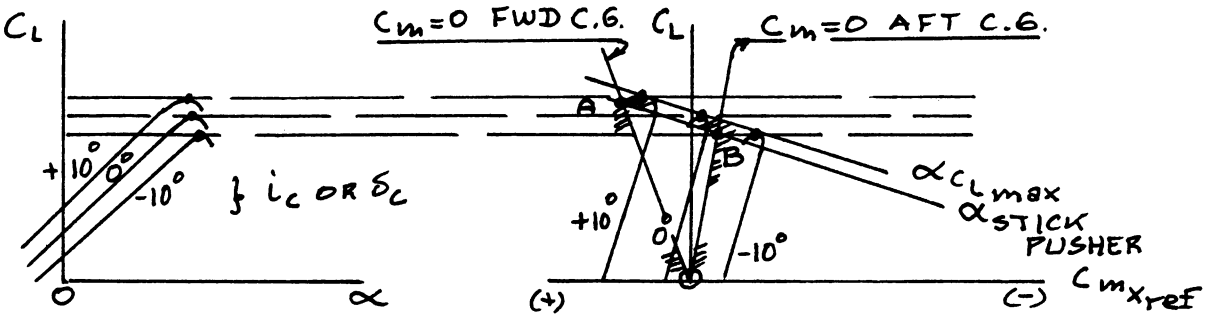

Figure 8.137b Trim Diagram: Stable, Canard with Unstable Pitch Break

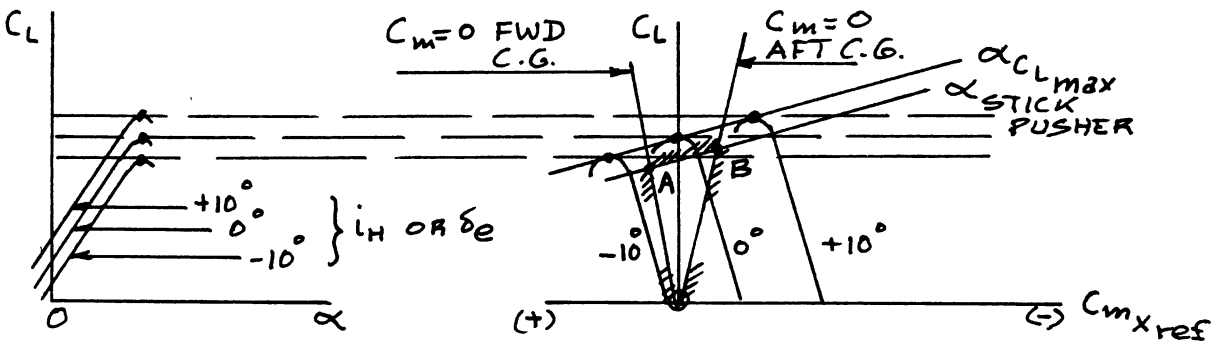

Figure 8.138a Trim Diagram: Unstable, Conventional with Unstable Pitch Break

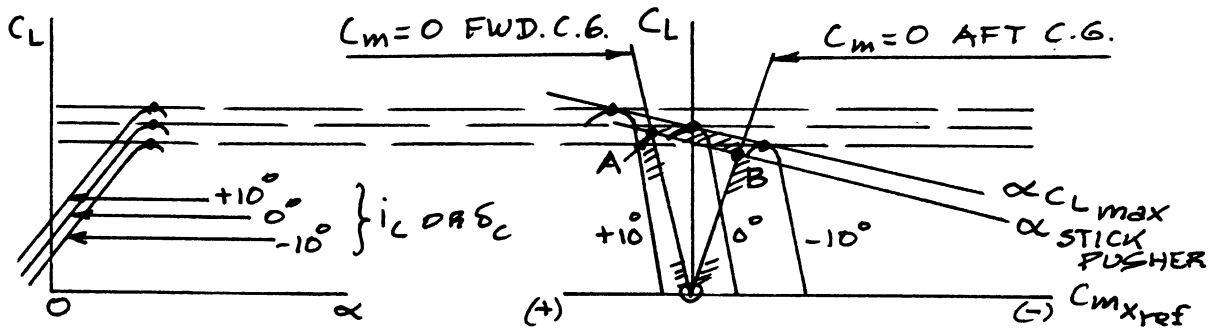

Figure 8.138b Trim Diagram: Unstable, Canard with Unstable Pitch Break

9. AIRPLANE HIGH LIFT DATA

The purpose of this chapter is to present a range of high lift (and some pitching moment) data. These data are presented in the following form:

9.1. Airfoil high lift data: flaps up and down

9.2. Airplane high lift data: flaps up and down

9.3. Mach number effects on high lift

9.1 AIRFOIL HIGH LIFT DATA: FLAPS UP AND FLAPS DOWN

A summary of NACA airfoil high lift and pitching moment data is provided in Table 9.1 for flaps up.

Tables 9.2, 9.3 and 9.4 provide data on airfoil high lift and pitching moment for flaps down.

The reader should carefully note the effect of Reynold's Number on the maximum lift coefficient. This effect must not be neglected in preliminary design. A summary of the effect of Reynold's Number on airfoil maximum lift is provided in Figures 9.1 and 9.2.

References 49 and 51 provide much additional data on airfoil maximum lift and pitching moment as well as on the effect of Reynold's Number.

9.2 AIRPLANE HIGH LIFT DATA: FLAPS UP AND FLAPS DOWN

In this section some examples of actual airplane high lift data are presented.

Tables 9.5 present a summary of airplane trimmed maximum lift coefficient data, flaps up anf flaps down.

Actual airplane high lift versus angle of attack data are presented as follows:

Figure 9.3 N.A.Rockwell T2C
Figure 9.4 N.A.Rockwell S-60 Sabreliner
Figure 9.5 Raisbeck Modification, S-65 Sabreliner
Figure 9.6 Canadair Challenger
Figure 9.7 Learjet M55
Figure 9.8 Boeing 767-300
Figure 9.9 Boeing 737-300

9.3 MACH NUMBER EFFECTS ON HIGH LIFT

At high subsonic Mach numbers the magnitude of maximum lift coefficient tends to decrease as a result of shock induced separations. This decrease in maximum lift manifests itself as buffet (below maximum lift) and as a reduction in maneuvering capability of the airplane. This effect is strongly influenced by:

1. wing sweep angle
2. airfoil thickness
3. airfoil camber

Figure 9.10 shows some early data indicating the effect of planform and Mach number on the maximum lift of wings with a 6 percent thick airfoil.

With modern airfoil design it is possible to achieve significant improvements in high lift at all Mach numbers and do so at much higher airfoil thickness ratios. (This also results in lower structural weights!) Figure 9.11 illustrates this on the Rockwell T2C: the basic airfoil has t/c = 0.12, the modified airfoil has t/c = 0.17.

A penalty which accompanies almost any increase in high lift is an increase in pitching moment. Since this needs to be trimmed out, the net gain in lift is not as high as untrimmed data would indicate. Figure 9.12 shows the effect of airfoil change on the T2C on its pitching moment behavior: note the rather large negative increase in pitching moment.

An example of the buffet boundary ($C_{L_{buffet}} < C_{L_{max}}$) for a modern business jet airplane with an advanced airfoil is given in Figure 9.13.

Most high lift data are obtained for steady state conditions. In flight test such conditions are simulated by accepting high lift data only when the rate of reduction of airspeed is not greater than 1 kt/sec.

In addition to the effect of speed changes on high lift, there are strong effects of rate of change of angle of attack on high lift. The data in Figs 9.14 and 9.15 indicate this! In determining the performance of fighter aircraft these unsteady effects are very important.

Table 9.1 Experimental Low Speed Data for 4- and 5- Digit NACA Airfoils with a Smooth Leading edge and for $R_N = 9 \times 10^6$ (Ref.49)

Airfoil	α_{o_ℓ} (deg)	c_{m_o}	c_{l_α} (deg^{-1})	a.c. (tenths c)	$\alpha_{c_{l_{max}}}$ (deg)	$c_{l_{max}}$	α^* (deg)
0006	0	0	.108	.250	9.0	.92	9.0
0009	0	0	.109	.250	13.4	1.32	11.4
1408	0.8	-.023	.109	.250	14.0	1.35	10.0
1410	-1.0	-.020	.108	.247	14.3	1.50	11.0
1412	-1.1	-.025	.108	.252	15.2	1.58	12.0
2412	-2.0	-.047	.105	.247	16.8	1.68	9.5
2415	-2.0	-.049	.106	.246	16.4	1.63	10.0
2418	-2.3	-.050	.103	.241	14.0	1.47	10.0
2421	-1.8	-.040	.103	.241	16.0	1.47	8.0
2424	-1.8	-.040	.098	.231	16.0	1.29	8.4
4412	-3.8	-.093	.105	.247	14.0	1.67	7.5
4415	-4.3	-.093	.105	.245	15.0	1.64	8.0
4418	-3.8	-.088	.105	.242	14.0	1.53	7.2
4421	-3.8	-.085	.103	.238	16.0	1.47	6.0
4424	-3.8	-.082	.100	.239	16.0	1.38	4.8
23012	-1.4	-.014	.107	.247	18.0	1.79	12.0
23015	-1.0	-.007	.107	.243	18.0	1.72	10.0
23018	-1.2	-.005	.104	.243	16.0	1.60	11.8
23021	-1.2	0	.103	.238	15.0	1.50	10.3
23024	-0.8	0	.097	.231	15.0	1.40	9.7

Airfoil	α_{o_ℓ} (deg)	c_{m_o}	c_{l_α} (deg^{-1})	a.c. (tenths c)	$\alpha_{c_{l_{max}}}$ (deg)	$c_{l_{max}}$	α^* (deg)
63-006	0	.005	.112	.258	10.0	.87	7.7
63-009	0	0	.111	.258	11.0	1.15	10.7
63-206	-1.9	-.037	.112	.254	10.5	1.06	6.0
63-209	-1.4	-.032	.110	.262	12.0	1.40	10.8
63-210	-1.2	-.035	.113	.261	14.5	1.56	9.6
63_1-012	0	0	.116	.265	14.0	1.45	12.8
63_1-212	-2.0	-.035	.114	.263	14.5	1.63	11.4
63_1-412	-2.8	-.075	.117	.271	15.0	1.77	9.6
64-006	0	0	.109	.256	9.0	.8	7.2
64-009	0	0	.110	.262	11.0	1.17	10.0
64-206	-1.0	-.040	.110	.253	12.0	1.03	8.0
64-209	-1.5	-.040	.107	.261	13.0	1.40	8.9
64-210	-1.6	-.040	.110	.258	14.0	1.45	10.8
64_1-012	0	0	.111	.262	14.5	1.45	11.0
64_1-212	-1.3	-.027	.113	.262	15.0	1.55	11.0
64_1-412	-2.6	-.065	.112	.267	15.0	1.67	8.0

Airfoil	α_{o_ℓ} (deg)	c_{m_o}	c_{l_α} (deg^{-1})	a.c. (tenths c)	$\alpha_{c_{l_{max}}}$ (deg)	$c_{l_{max}}$	α^* (deg)
65-006	0	0	.105	.258	12.0	.92	7.6
65-009	0	0	.107	.264	11.0	1.08	9.8
65-206	-1.6	-.031	.105	.257	12.0	1.03	6.0
65-209	-1.2	-.031	.106	.259	12.0	1.30	10.0
65-210	-1.6	-.034	.108	.262	13.0	1.40	9.6
65_1-012	0	0	.110	.261	14.0	1.36	10.0
65_1-212	-1.0	-.032	.108	.261	14.0	1.47	9.4
65_1-412	-3.0	-.070	.111	.265	15.5	1.66	10.5
63A010	0	.005	.105	.254	13.0	1.20	10.0
63A210	-1.5	-.040	.103	.257	14.0	1.43	10.0
64A010	0	0	.110	.253	12.0	1.23	10.0
64A210	-1.5	-.040	.105	.251	13.0	1.44	10.0
64A410	-3.0	-.080	.100	.254	15.0	1.61	10.0
64_1A212	-2.0	-.040	.100	.252	14.0	1.54	11.0
64_2A215	-2.0	-.040	.095	.252	15.0	1.50	12.0

Table 9.2 Effect of Airfoil, Flap Type and Flap Deflection on Drag and on High Lift

ADAPTED FROM REF. 51

FLAP TYPE	FLAP GEOMETRY	NACA AIRFOIL	FLAP CHORD %C	R_N	$C_{l_{max}}$ t.o.	δ_f (DEG) t.o.	C_{d_o} for $C_{l_{max}}$ t.o.	C_{d_o} for δ_f at t.o. with C_l = 1,5	2,0	2,5	$C_{l_{max}}$ LAND.	δ_f (DEG) LAND.	C_{d_o} for $\delta_f=0$	SOURCE:
DOUBLE SLOTTED FLAP		23012	0,1467 0,2500	$3,5.10^6$	3,08	28,65	0,20	—	0,072	0,096	3,35	36,70	0,0088	NACA ARR 3L10
✓	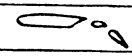	〃	0,2270 0,2566	〃	3,15	30,60	0,17	—	0,055	0,076	3,46	30,70	〃	NACA Rep. 723
✓	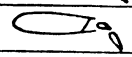	23021	0,1467 0,2566	〃	3,06	20,60	0,28	—	0,148	0,175	3,32	〃	0,0122	NACA ARR L4J05
✓	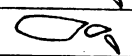	〃	0,2267 0,2566	〃	3,00	20,50	0,18	0,048	0,056	0,075	3,66	30,60	〃	NACA Rep. 723
✓		23020	0,2600 0,2566	〃	3,30	〃	0,22	0,102	0,110	0,122	3,70	40,80	0,0175	〃 〃
✓	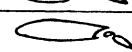	65,3-118	0,309	$6,0.10^6$	2,88	35	0,026	0,009	0,017	0,022	3,40	65	0,0047	NACA ACR 3120
✓		65_3-418	0,29	$1,9.10^6$	2,92	40	—	0,0248	—	—	3,51	〃	0,0061	NACA TN 1071
SINGLE SLOTTED FLAP	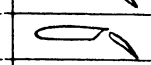	23012	0,40	$3,5.10^6$	2,80	40	0,16	0,018	0,043	0,092	2,91	50	0,0100	NACA TN 715
✓	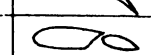	23021	〃	〃	2,62	20	0,13	0,43	0,054	0,075	2,87	〃	0,0140	NACA TN 728
✓	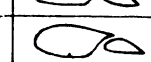	23030	0,40	〃	2,48	〃	0,14	0,082	0,057	—	2,88	〃	0,0230	NACA TN 755
✓	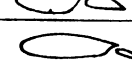	63,4-420	0,28	$6,0.10^6$	2,83	30	0,0297	0,0118	0,0173	0,0232	3,00	40	0,0058	NACA ACR 3121
VANED SLOTTED FLAP		23012	0,25	$3,5.10^6$	2,70	50	0,13	0,076	0,097	0,110	2,70	50	0,0150	NACA TN 699
SLOTTED FLAP+ .05C SPLIT FLAP		〃	0,2566	〃	2,74	30,60	0,12	0,036	0,050	0,074	2,83	40,70	0,0250	NACA Rep. 679
SLOTTED FLAP+ .10C SL. FLAP		〃	〃	〃	2,96	40,60	0,155	—	0,083	0,114	2,99	〃	0,0120	〃 〃
PLAIN FLAP	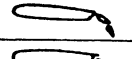	〃	0,20	〃	2,38	60	0,19	0,152	0,154	—	2,40	75	0,0090	NACA Rep. 664
JUNKERS FLAP		〃	0,2667	〃	2,28	30,2	0,095	0,028	0,046	—	2,37	40,5	0,0100	〃 〃
SPLIT FLAP	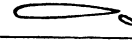	〃	0,20	〃	2,29	30	0,115	0,080	0,083	—	2,54	75	0,0090	〃 〃
FOWLER FLAP	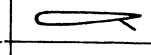	〃	0,30	〃	3,30	40	0,17	〃	0,095	0,113	3,30	40	〃	NACA TN 808
QUAD. SLOTTED FOWLER FLAP	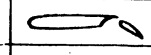 .10C EACH	〃	0,40	〃	3,28	30	0,14	0,028	0,031	0,050	3,60	40,50 50,70	〃	NACA Rep. 689
QUAD SLOTTED FOWLER FLAP	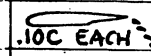 .075C EACH	〃	0,30	〃	3,40	20,30 40,50	0,17	—	0,055	0,070	3,40	20,30 40,50	〃	NACA Rep. 742

Table 9.3 Effect of Flap Type and Flap Deflection on High Lift

ADAPTED FROM REF. 51

FLAP TYPE	FLAP GEOMETRY	AIRFOIL	R_N	FLAP CHORD %C	FLAP ANGLE (DEG)	A	$C_{L_{MAX}}$	$\Delta C_{L_{MAX}}$	(DEG) $\alpha_{AT\ C_{L_{MAX}}}$	SOURCE:
FIXED SLOT	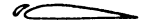	Clark Y	$1{,}03.10^6$	—	—	6	1,77	0,48	24°	TR 427, TR 554
✓	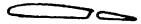	"	"	—	—	"	1,44	0,15	17°	" "
FIXED SLAT	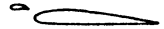	"	"	0,145	0°	"	1,70	0,41	24°	TR 428, TR 554
TRIPLE SLOTTED WING		"	"	—	—	"	1,93	0,64	25°	TR 427, TR 554
HANDLEY PAGE SLAT	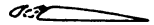	"	"	0,147	—	"	1,84	0,55	28°	TR 400, TR 554 TN 423, TN 443
MAXWELL SLAT	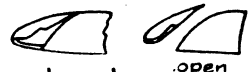	"	$0{,}85.10^6$	—	—	"	2,07	0,82	28°	TN 598, TR 544
PLAIN FLAP + FIXED SLOT	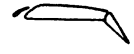	"	$1{,}03.10^6$	0,30	45°	"	2,18	0,89	19°	TR 427, TR 554
✓ (S)	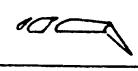	"	"	"	"	"	2,24	0,95	20°	" "
SPLIT FLAP + MAXWELL SLAT	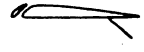	"	$0{,}85.10^6$	0,211	60°	"	2,33	1,28	21,6°	TR 598, TR 544
SLOTTED FLAP+ FIXED SLOT	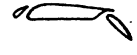	"	$1{,}03.10^6$	0,30	45°	"	2,26	0,97	19°	TR 427, TR 554, TN 702
✓		"	"	"	"	"	2,44	1,15	16°	TR 427, TR 554, TN 702
SLOTTED FLAP+ 2 FIXED SLOTS		"	"	"	"	"	2,60	1,31	20°	TR 427, TR 554

Table 9.4 Effect of Flap Type on High Lift, on Pitching Moment and on Drag

HIGH-LIFT CONFIGURATION	HIGH-LIFT DEVICE TYPE	$\delta^{\circ}_{opt.}$ for $c_{\ell_{max}}$	$\Delta c_{\ell_{max}}$	$\Delta c_{m_{c/4}} / \Delta c_{\ell}$	$\partial c_m / \partial \delta$	$\Delta c_{d_{min}}$ @ δ_{opt}	REYN. NO. OF TEST	REFERENCES.
1 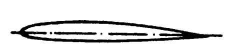	BASIC WING SECTION 64A010	-	$c_{\ell_{max}} = 1.0$ (STANDARD ROUGHNESS)	$c_{m_{c/4}} = 0$	-	$c_{d_{min}} = .009$ (STANDARD ROUGHNESS)	6×10^6	NACA TN. 3007 NACA REP. 824
2 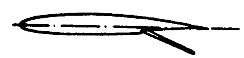	SPLIT FLAP	60	.8	-.275	-.0067	.23	6×10^6	NACA TN. 3007 NACA TN. 4040
3 	ZAP FLAP	45	1.15	-.38		.21		W.S. DIEHL, ENGG. AERO. NACA TN. 422 ASME TRANSACTIONS APRIL 1934
4 	PLAIN FLAP	60	.9	-.275	-.0125	.12	6×10^6	NACA REP. 938 NACA TN. 4040 ARC. R&M. 2622
5 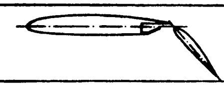	SINGLE SLOTTED FLAP	40	1.18	-.33	-.01	.13	3.5×10^6	NACA REP. 938 NACA TN. 4040 ARC. R&M. 2622
6 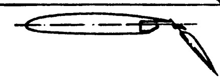	DOUBLE SLOTTED FLAP	30/55	1.4	-.41	-.0125	.23	6×10^6	NACA TN. 3007 NACA TN. 4040
7 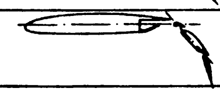	TRIPLE SLOTTED FLAP	30/44/55	1.6	-.44		.23	6×10^6	NACA WR. L-641
8 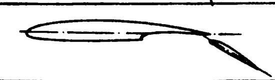	FOWLER FLAP	30	1.67	-.42		.10	$\sim 3.5 \times 10^6$	1ST AS-RAS. INT'L. CONF. 1947, MORGAN ABBOTT-DOENHOFF, THEORY OF WING SECTIONS NACA REP. 664 (K.D. WOOD 1947 ED. P. 170) ARC. R&M. 2622 H.D. FOWLER, THE FOWLER FLAP.
9 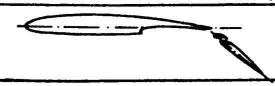	DOUBLE SLOTTED FOWLER FLAP	15/30	2.25	-.44		~.15	$\sim 3.5 \times 10^6$	1ST AS-RAS. INT'L. CONF. 1947, MORGAN
10 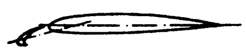	LEADING EDGE SLAT	26 (STRAIGHT WINGS) 30 WITH No. 2 45-60 (SWEPT WINGS)	~.93	+.11		~0	6×10^6	NACA TN. 3007 JOURN. OF AIRCR. NOV.-DEC. 1966 P. 528
11 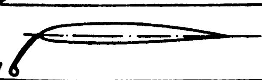	KRUGER FLAP	40-45 (STRAIGHT WINGS) 60 (SWEPT WINGS)	~.5	-.10		~0	8.2×10^5	NACA TM. 1119 JOURN. OF AIRCR. NOV-DEC. 1966
12 	LEADING EDGE FLAP (DROOP NOSE)	30	.55 WITH No. 2&4 .75 WITH No. 4→8	-.09 for δ=10 with No. 1 -.005 w. No. 2 -0 w. No. 4→8		~0	6×10^6	NACA TN. 3007 NACA TN. 2228

NOTE: ALL DATA FOR:

$A = 12 \quad \lambda = 1.0$

$t/c = 0.10$

$\Lambda_{c/4} = 0^{\circ}$

$b_f/b = 1.0$

$c_f/c = 0.30$ T.E.

0.15 L.E.

COPIED FROM: REF. 56

Table 9.5a Experimental Trimmed Maximum Lift Coefficients for Several Airplanes

COPIED FROM: REF. 56

MODEL	A	$\Lambda_{C/4}$	$b_{f/b}$	HLD TYPE	TEST TYPE	$C_{L_{max}}$*		REFERENCE
						CLEAN	ALL HLD	
Grumman A6A	5.0	25	~0.8	Fowler Flaps + LE Flaps	F	1.25	2.00	Flight Manual Data
North Am. A5A	4.0	37.5	.765	Plain Flaps + LE Flaps	F	1.05	1.5	Flight Manual Data
North Am. RA-5C	4.0	37.5	.7	Plain Flaps + Blown Outbd. LE Flaps	F		1.8	AIAA Paper 65-751
Douglas A4D	2.91	33	.57	Split Flaps + LE Autoslats	F	.901	1.45	Flight Manual Data
McDonnell F4	2.78	45	.65	Plain Blown Flaps + Inbd. LE Flaps + Outbd. Blown LE Flaps	F	1.05	1.40	Canad. Aeron & Space Journ. March 1966
Fiat G91	4.5	37	.52	Single Slotted Flaps	F	1.0	1.18	Calculated
Republic F105D	3.18	43	.705	Single Slotted Flaps + LE Flaps	F	1.1	1.38	Pilot Handbk. Data
Lockheed F104G	2.45	18.6	.65	Plain Flaps, Droop Ailerons, LE Flaps	F	.75	1.12	Pilot Handbk. Data
Northrop F5	3.7	25	.55	Single Slotted Flaps + LE Flaps	F	1.0	1.4	Pilot Handbk. Data
Hawker Siddeley Buccaneer	3.58	24	1.00	Blown Plain Flaps + Blown LE	F	.96	2.2	Aviation Week 7 Aug 1961 Flight Int'l 3 Nov 1966
Gen. Dynamics F-111	6.0	13	.665	Blown Plain Flaps + Blown Center & Outer LE Flaps	F	1.55	2.45	NASA 1964 SST Conference
North Am. F-100 A (Exp.)	3.72	45	.8	Blown Plain Flaps + Blown LE Flaps	F	1.2	1.5	NASA TN D-321
Douglas F5D-1 (Tailless, NASA OGEE Wing Mod.)	1.7	46	1.0	Plain Elevons + Partial LE Slats	F	1.0	~1.0	NASA TN D-3071
Lockheed XV-4A	6.0	0	.76	Plain Flaps	Full Scale WT	1.15	1.5	NASA TN D-3725
Boeing 727	7.1	30	.75	Triple Slotted Fowler Flaps + LE Slats Outbd. + Kruger Flaps Inbd.	F		2.62	Journ of Aircr. March 65, The Aeroplane Feb. 21, 1963
Boeing 707-320C	7.0	35	.665	Triple Slotted Fowler Flaps + Split Fillet Flaps + LE Flaps	F		1.9	Journ. of Aircr. Mar - Apr. 1965.
Boeing 707-120	7.0	35	.665	Double Slotted Fowler Flaps + Split Fillet Flaps + LE Flaps	F	~1.37 (WT)	1.75	Journ. of Aircr. Mar-Apr. 1965. NACA RM A58H12
Boeing 707-120 (Exp)	7.0	35	.665	Blown Plain Flaps + LE Flaps	F		2.34	NASA TN D-4804

F = Flight; WT = Wind Tunnel; HLD = High Lift Device(s) Down * TRIMMED, GEAR-UP

Table 9.5b Experimental Trimmed Maximum Lift Coefficients for Several Airplanes

COPIED FROM: REF. 56

MODEL	A	$\Lambda^{\circ}_{C/4}$	$b_{f/b}$	HLD TYPE	TEST TYPE	$C_{L_{max}}$* CLEAN	$C_{L_{max}}$* ALL HLD	REFERENCE
Breguet 941 **	6.52	0	~1.0	Double & Triple-Slotted Flaps (Droop Ailerons)	F	1.15	2.8	Journ. of Aircr. May-June 1968 NASA TN D-2231
Lockheed Electra **	7.5	0	.64	Fowler Flaps	F	1.5	2.5	Journ. of Aircr. May-June 1968 NASA TN D-2231
Sud. Caravelle	8.2	20	.63	Double Slotted Flaps	F	1.5	2.25	Journ. of Aircr. May-June 1968 NASA TN D-2231
Lockheed C5A	8	25	.715	Single Slotted Fowler & LE Slats	WT F	1.2 1.45	2.55 2.60	Aircr. Engg. June 1968 LOCKHEED
			.74	Double Slotted Flaps + LE Kruger Flaps + External Jet Blowing	WT		3.8	NASA TN D-4928
Mitsubishi/Mooney MU-2S **	6.8	~0	.93	Double Slotted Flaps + Droop Ailerons	F	1.77	3.13	Vertic. World July 1968 Flight Magaz. Febr. 1964.
Cessna 177 **	7.4	0	.65	Plain Flaps	F	.95	1.55	SAE Paper 680199
Ryan Model 143 (XV-5A) **	3.42	20/37	1.0	Single-Slotted Flaps + Droop Ailerons	F	1.05	1.63	Ryan UP-108 (1965) (Ryan Rep. 29466-2 Vol. II)
Ryan Model 92 (VZ-3RY) **	4.4	0	1.0	Double-Slotted Flaps (Slipstream Deflection) + Fixed LE Slats	WT	1.15	1.5	NASA TN D-89
Douglas A3D	6.75	35.9	.575	Single-Slotted Flaps + LE Slats	Full Scale WT	1.37	1.9	NACA RM A57A24
Douglas A3D	6.75	35.9	.575	Blown, Single-Slotted Flaps + LE Slats	Full Scale WT	1.37	2.7	NACA RM A57D11
North Am. F-86	4.79	35.2	.50	Plain Flaps + LE Autoslats	Full Scale WT	1.09	1.64	NACA RM A52B05
Dornier Do-27 **	7.4	0	.71	Double-Slotted Flaps (Partial Droop Ailerons) + LE Fixed Slots	F	1.3	2.95	Luftfahrttechnik No. 3, 1962
DeHavilland DHC-4 Caribou **	9.9	~0	1.0	Double-Slotted Flaps (Droop Ailerons)	F	1.37	2.63	Calcul. from Pilot Hdbk. Data
Lockheed 49 Constellation **	9.2	0	.62	Fowler Flaps + Split-Fillet Flap	F		2.88	The Fowler Flap
Boeing B-17 **	7.3	0	.57	Zap Flaps	F		2.95	Neville, Aircr. Designers Data Book
Douglas DC-9	8.5	24	.66	Double-slotted Flaps + LE Slat	F	1.5	3.0	SAE Paper 670846
Piper PA-30-160 **	7.3	0	.62	Plain Flaps	Full Scale WT	1.24	1.6	NASA TN D-4983

F = FLIGHT WT = WINDTUNNEL HLD = HIGH LIFT DEVICES DOWN
* TRIMMED, GEAR UP ** PROPELLER(S) OFF

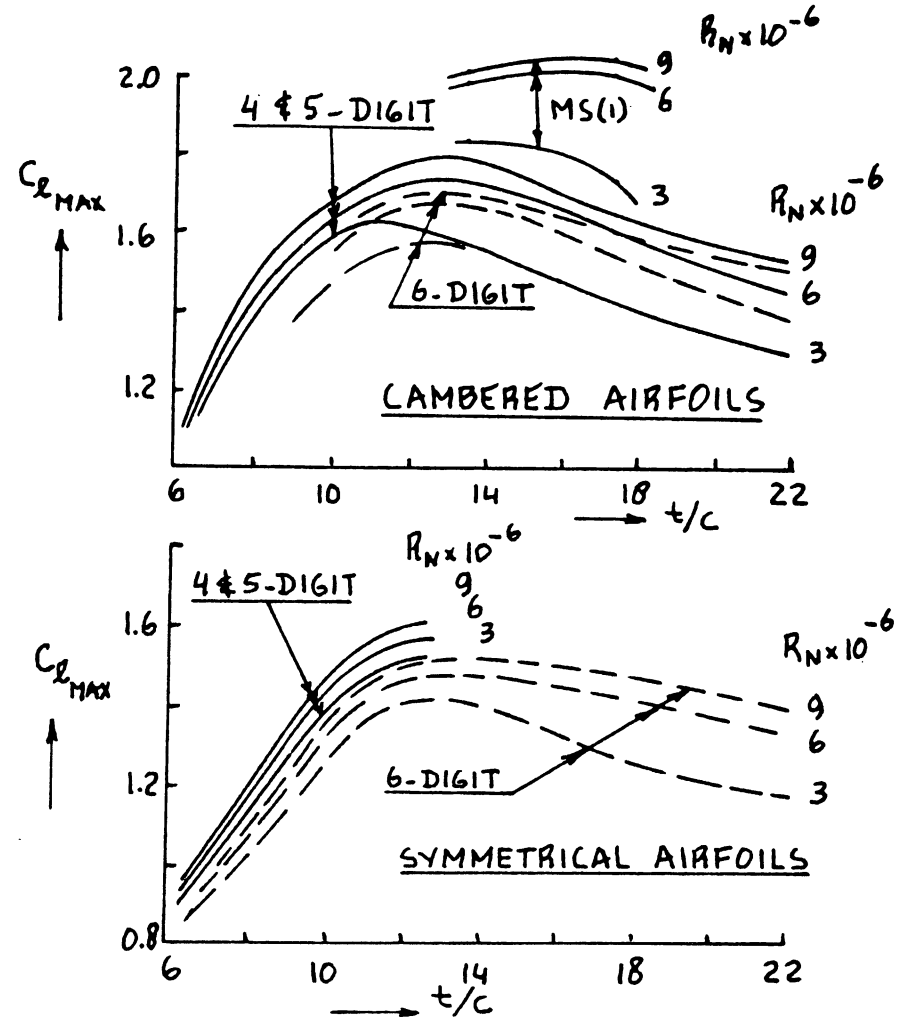

Figure 9.1 Effect of Thickness Ratio and Reynold's Number on NACA Airfoil Maximum Lift Coefficient

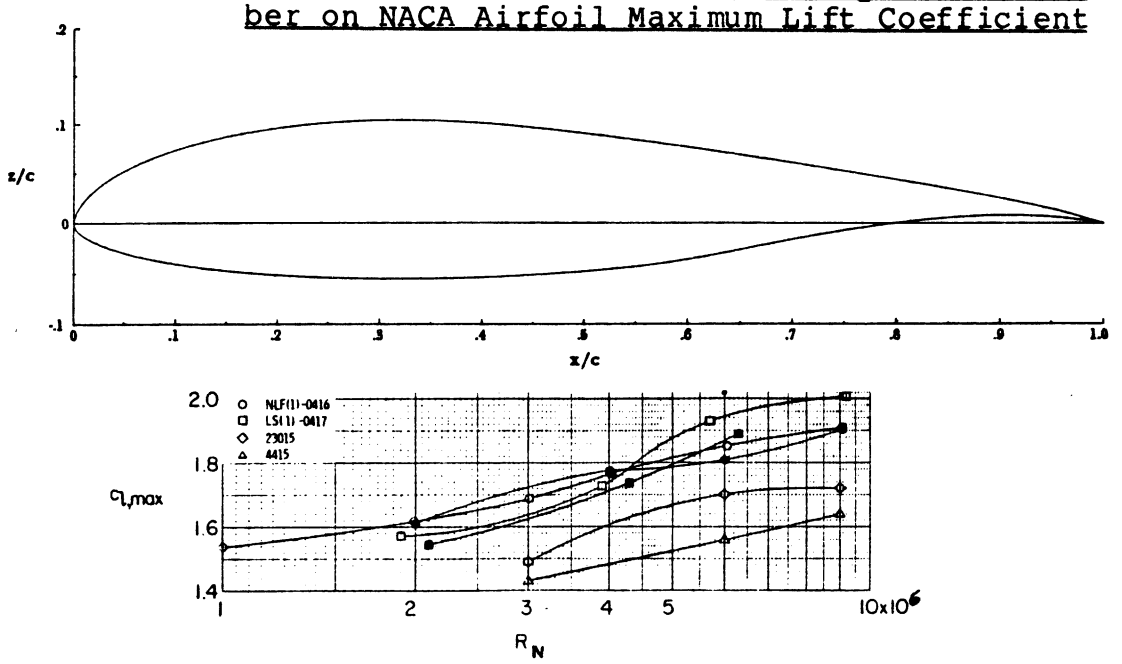

Figure 9.2 Effect of Thickness Ratio and Reynold's Number on Modern Airfoil Maximum Lift Coefficient

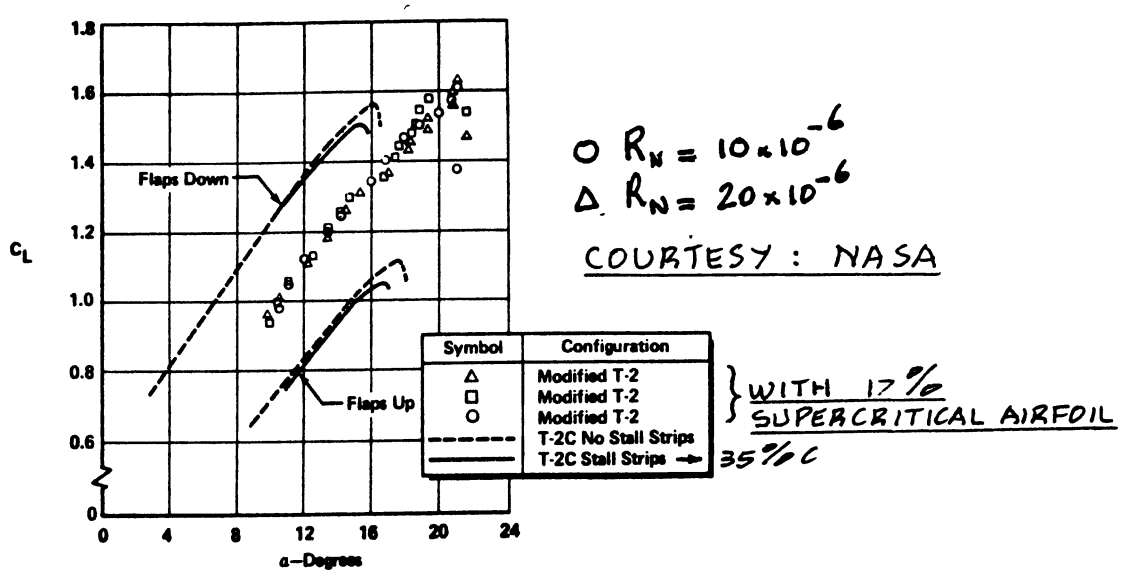

Figure 9.3 Airplane Lift Curve: N.A.Rockwell T2C

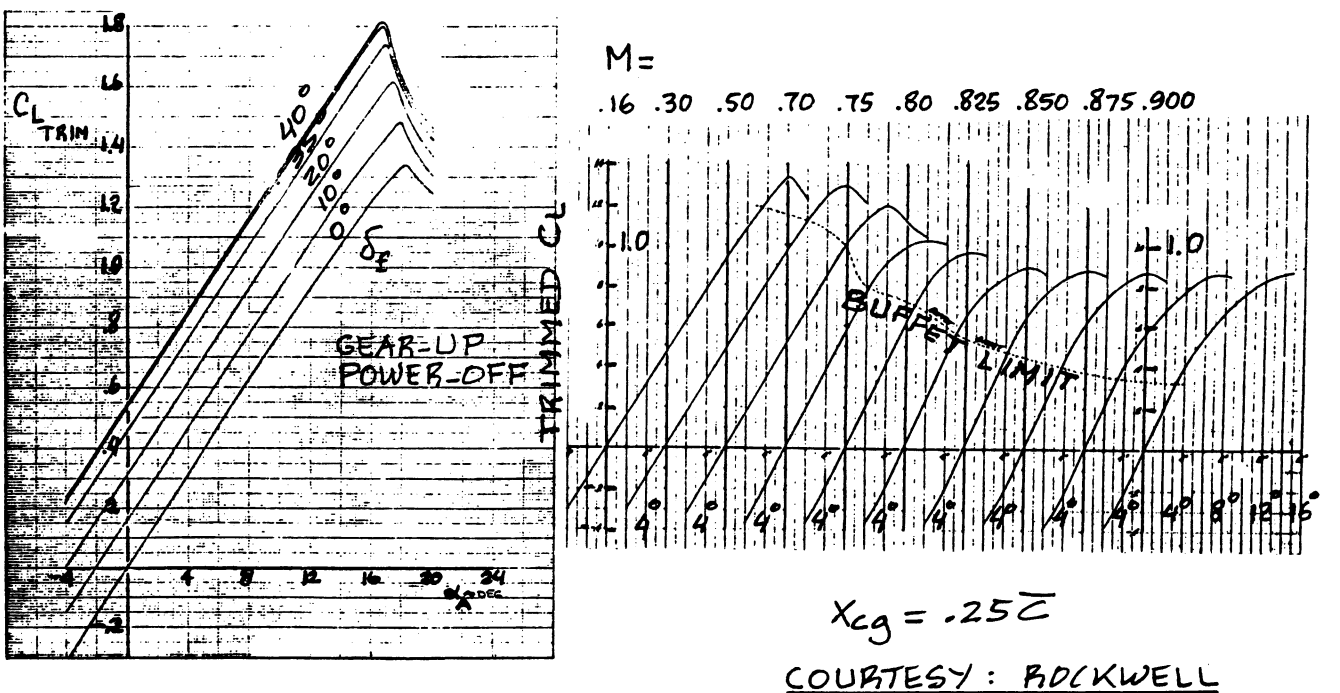

Figure 9.4 Airplane Lift Curve: N.A.Rockwell S-60

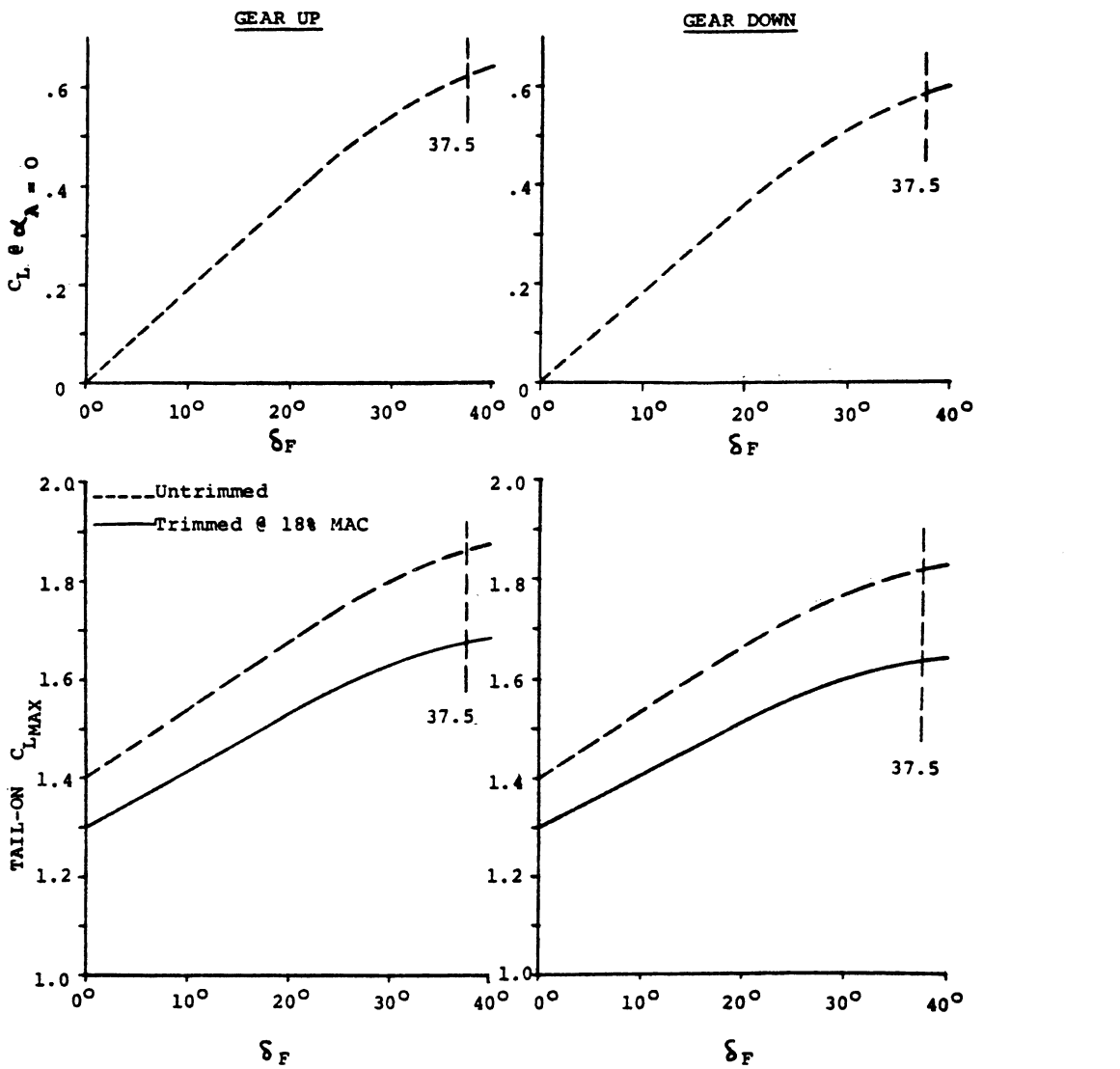

COURTESY: RAISBECK

RAISBECK FOWLER FLAP

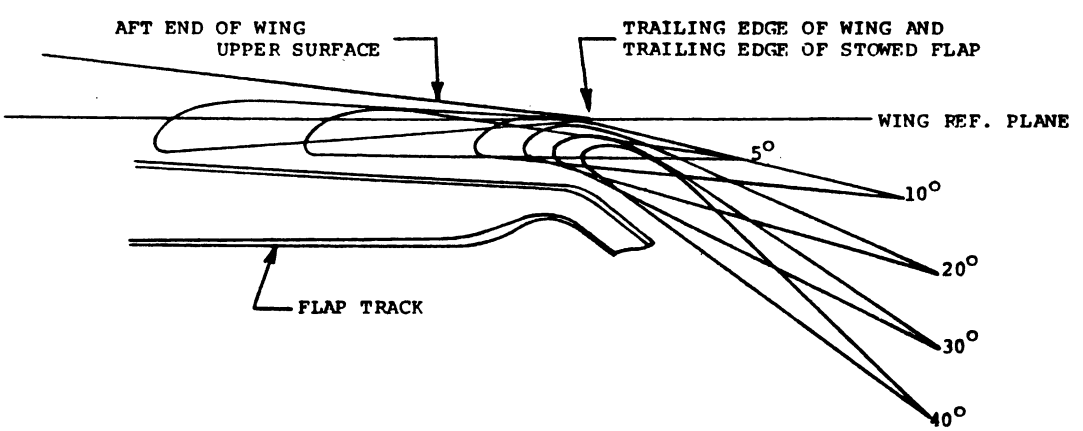

Figure 9.5 Airplane Lift Curve: Raisbeck/Rockwell S-65

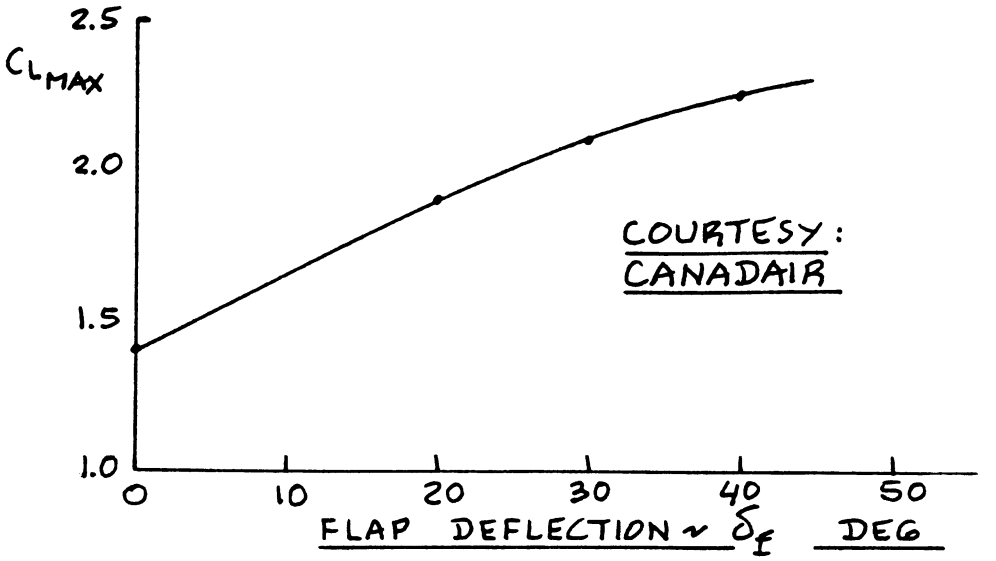

Figure 9.6 Airplane Lift Curve: Canadair Challenger

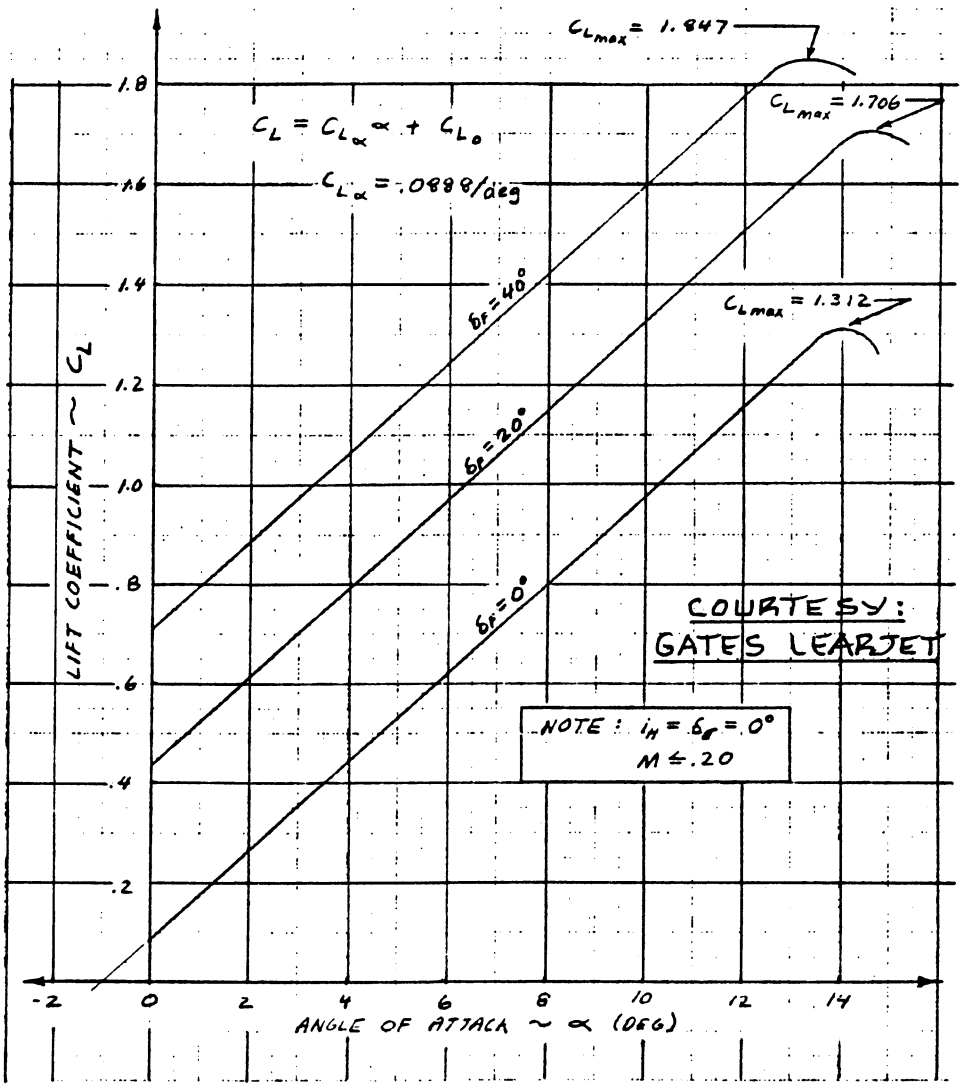

Figure 9.7 Airplane Lift Curve: Gates-Learjet M55

COURTESY: BOEING

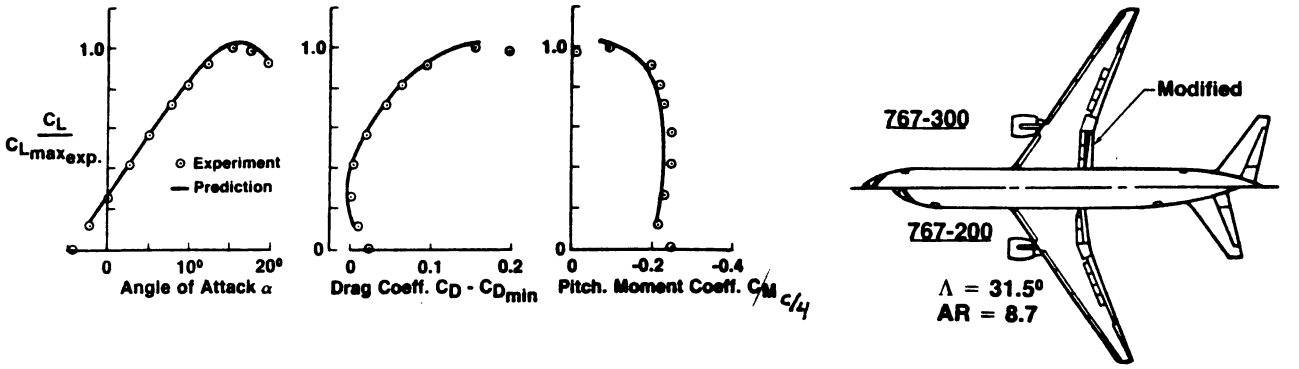

Figure 9.8 Airplane Lift Curve: Boeing 767-300

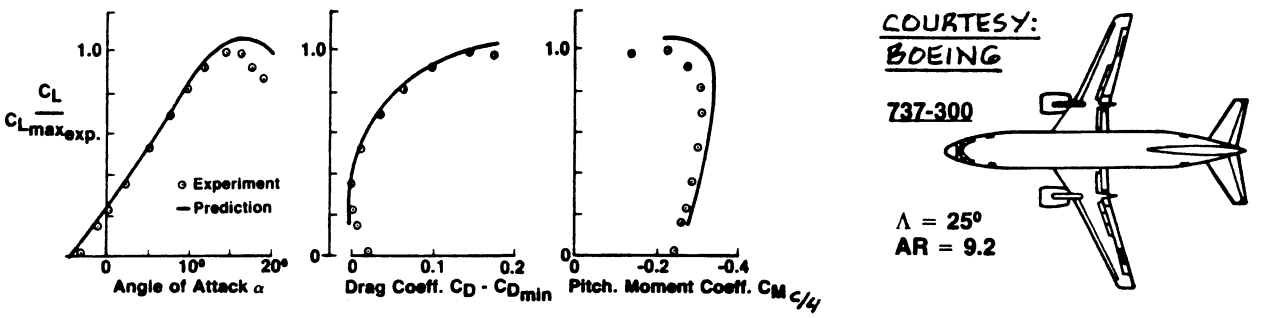

Figure 9.9 Airplane Lift Curve: Boeing 737-300

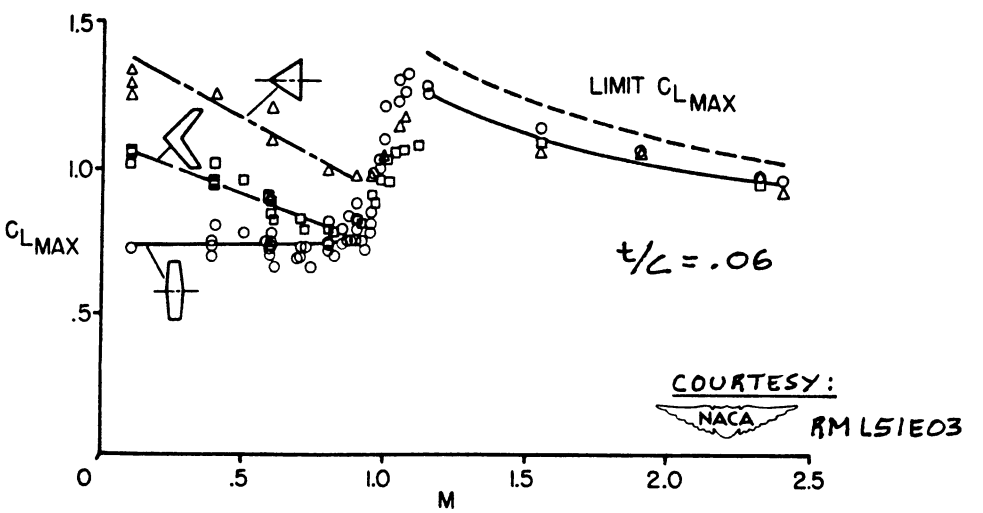

Figure 9.10 Effect of Wing Planform on the Variation of Maximum Lift Coefficient with Mach Number

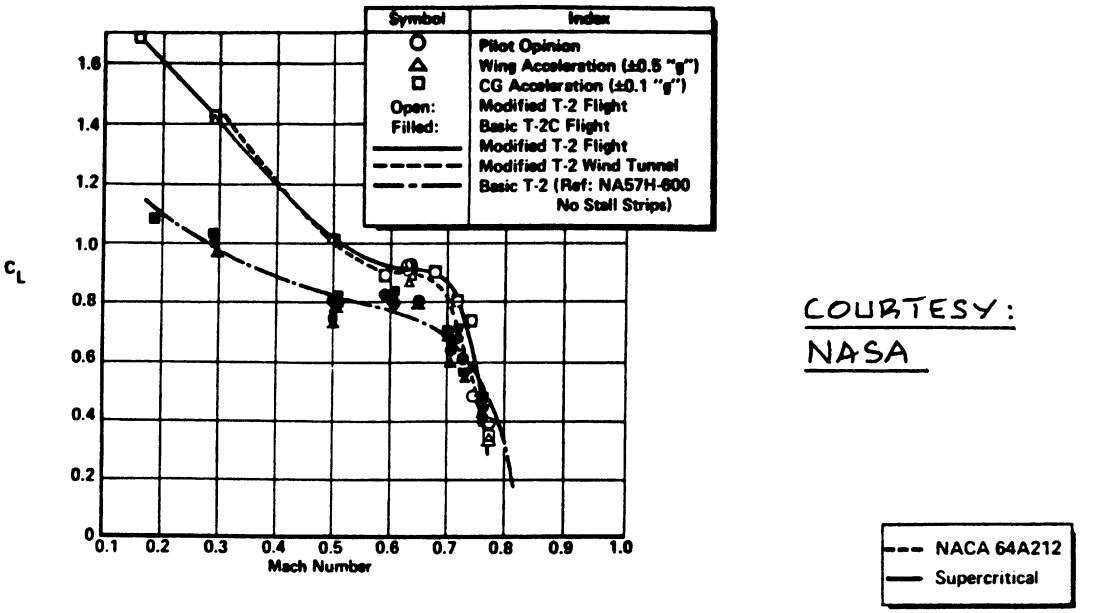

Figure 9.11 Effect of Mach Number on Buffet Onset for a NACA and for and Advanced Airfoil

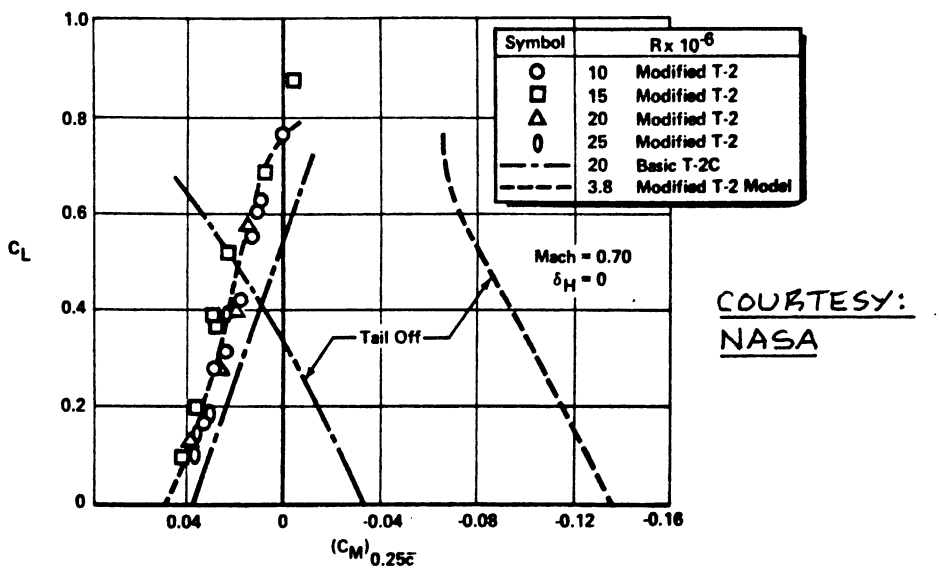

Figure 9.12 Effect of Airfoil Change on Pitching Moment

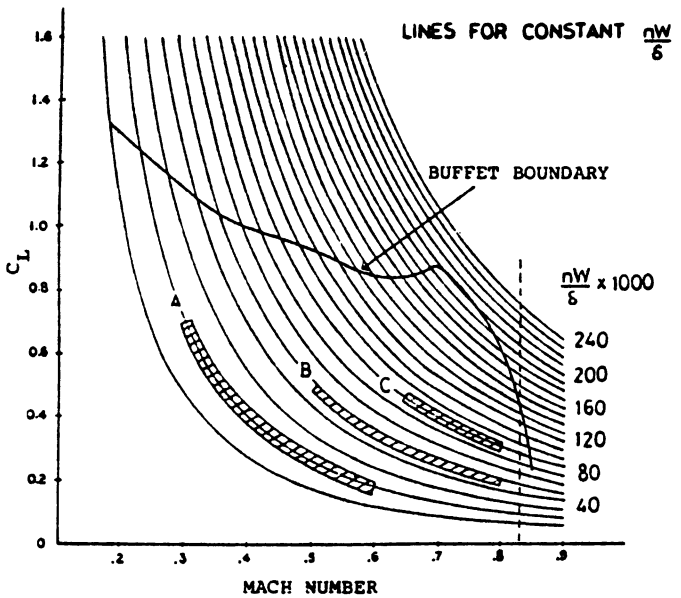

Figure 9.13 Buffet Boundary for the Cessna Citation III

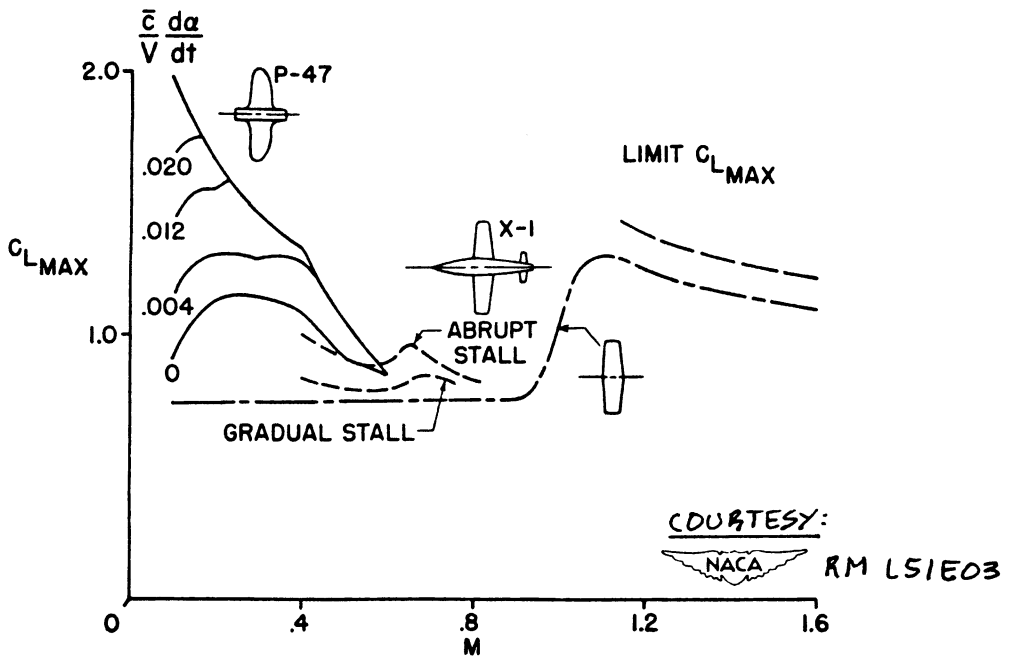

Figure 9.14 Effect of Angle of Attack Rate on the Variation of Maximum Lift with Mach Number

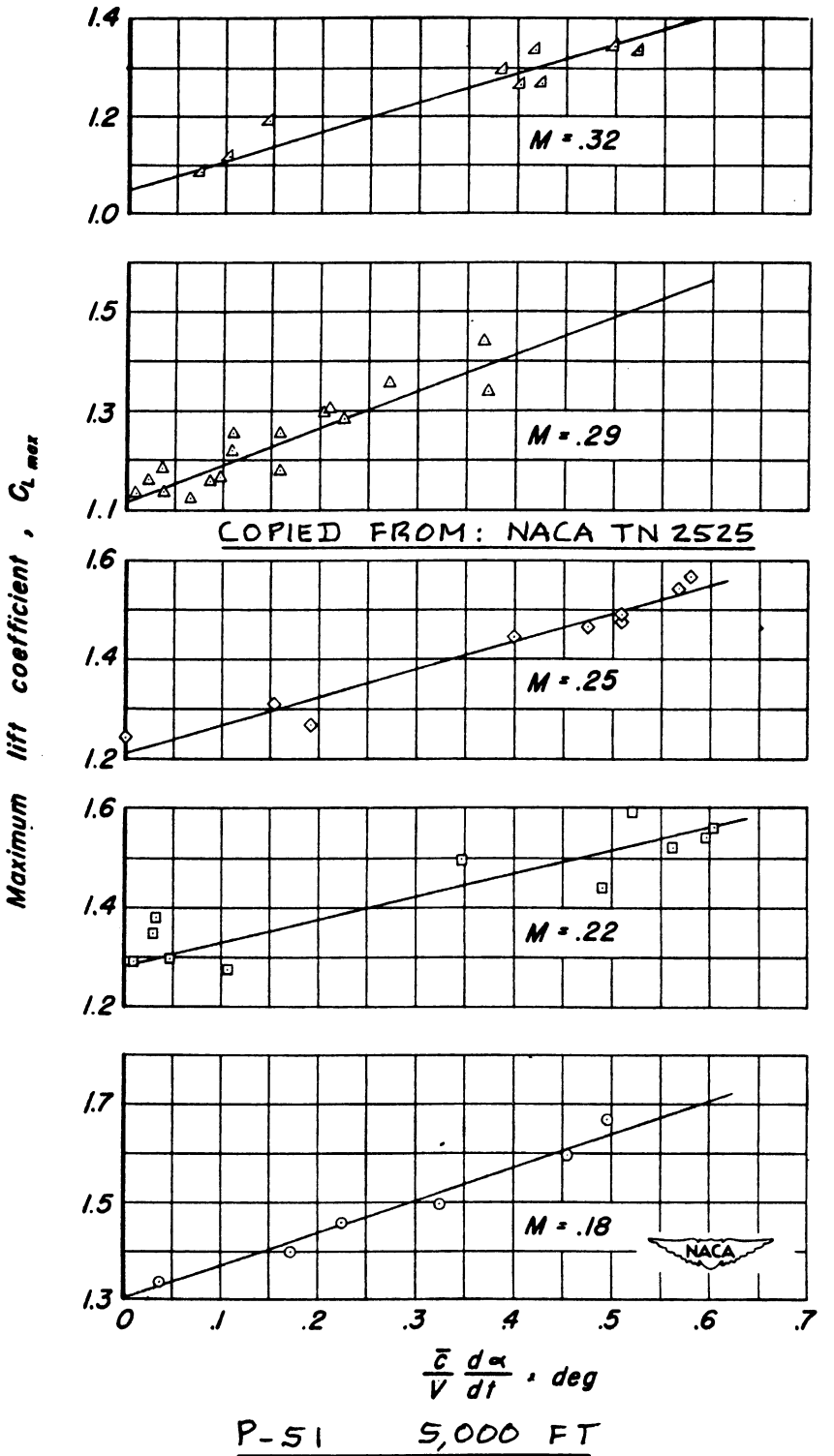

Figure 9.15 Effect of Angle of Attack Rate and Mach Number on Maximum Lift Coefficient

10. STABILITY, CONTROL AND HINGEMOMENT DERIVATIVES

The purpose of this chapter is to present preliminary design methods for the calculation of stability, control and hingemoment derivatives. These derivatives are required as input to the determination of static and dynamic stability and control behavior (handling qualities) of airplanes. Methods for computing static and dynamic stability and control behavior of airplanes are given in Part VII of this text.

Table 10.1 presents the mathematical model used in representing aerodynamic and thrust forces and moments as well as cockpit control forces: Eqns 10.1 through 10.5.

The equations of Table 10.1 are discussed and justified in Chapter 4 of Reference 16. The coefficients and derivatives shown in Table 10.1 may be estimated with the methods of this chapter. These methods are presented in the following manner:

10.1 Steady state coefficients
10.2 Stability Derivatives
10.3 Control derivatives
10.4 Hingemoment Derivatives.

IMPORTANT NOTES:

1.) The methods presented in this chapter apply to rigid airplanes only. Methods which account for aeroelastic effects are discussed in Chapter 8 of Ref.16.

2.) The methods presented in this chapter do not always apply to all speed regimes. Restrictions on applicability to certain speed regimes are given in the text.

3.) All derivatives are in rad^{-1}.

4.) All coefficients and derivatives are defined in the stability axes system, see Table 10.1.

10.1 STEADY STATE COEFFICIENTS

In Table 10.1 there appear a number of steady state coefficients: C_{D_1}, C_{L_1}, C_{m_1}, $C_{T_{x_1}}$ and $C_{m_{T_1}}$.

In the following, definitions are given from which these coefficients may be determined.

Table 10.1a Longitudinal Aerodynamic and Thrust Forces and Moments and Cockpit Control Forces

Forces and Moments

AERODYNAMIC

$$\begin{Bmatrix} \frac{f_{A_x}}{\bar{q}S} \\ \frac{f_{A_z}}{\bar{q}S} \\ \frac{m_A}{\bar{q}S} \end{Bmatrix} = \left[\begin{array}{c|c|c|c|c} -(C_{D_u}+2C_{D_1}) & (-C_{D_\alpha}+C_{L_1}) & -C_{D_{\dot\alpha}} & -C_{D_q} & -C_{D_{\delta_E}} \\ \hline -(C_{L_u}+2C_{L_1}) & (-C_{L_\alpha}-C_{D_1}) & -C_{L_{\dot\alpha}} & -C_{L_q} & -C_{L_{\delta_E}} \\ \hline (C_{m_u}+2C_{m_1}) & C_{m_\alpha} & C_{m_{\dot\alpha}} & C_{m_q} & C_{m_{\delta_E}} \end{array}\right] \begin{Bmatrix} \frac{u}{U_1} \\ \alpha \\ \frac{\dot\alpha \bar{c}}{2U_1} \\ \frac{q\bar{c}}{2U_1} \\ \delta_E \end{Bmatrix} \quad (10.1)$$

(3x1) (3x5) (5x1)

THRUST

$$\begin{Bmatrix} \frac{f_{T_x}}{\bar{q}_1 S} \\ \frac{f_{T_z}}{\bar{q}_1 S} \\ \frac{m_T}{\bar{q}_1 S\bar{c}} \end{Bmatrix} = \left[\begin{array}{c|c} (C_{T_{x_u}} + 2C_{T_{x_1}}) & 0 \\ \hline 0 & 0 \\ \hline (C_{m_{T_u}} + 2C_{m_{T_1}}) & C_{m_{T_\alpha}} \end{array}\right] \begin{Bmatrix} \frac{u}{U_1} \\ \alpha \end{Bmatrix} \quad (10.2)$$

3x1 3x2 2x1

$$F_{S_e} = G_e \cdot HM_e = G_e \cdot \bar{q}_h \cdot S_e \bar{c}_e C_{h_e} \quad (10.3a)$$

$$C_{h_e} = C_{h_0} + C_{h_\alpha}\alpha_h + C_{h_{\delta_e}}\delta_e + C_{h_{\delta_t}}\delta_t \quad (10.3b)$$

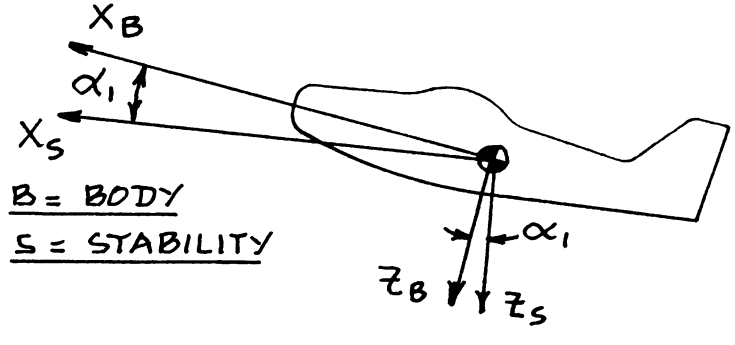

B = BODY

S = STABILITY

Table 10.1b Lateral-Directional Aerodynamic and Thrust Forces and Moments and Cockpit Control Forces

Forces and Moments

$$\begin{Bmatrix} f_{A_y}/\bar{q}S \\ \ell_A/\bar{q}Sb \\ n_A/\bar{q}Sb \end{Bmatrix}_{(3\times1)} = \underbrace{\begin{bmatrix} C_{y_\beta} & C_{y_{\dot\beta}} & C_{y_p} & C_{y_r} & C_{y_{\delta_A}} & C_{y_{\delta_R}} \\ C_{\ell_\beta} & C_{\ell_{\dot\beta}} & C_{\ell_p} & C_{\ell_r} & C_{\ell_{\delta_A}} & C_{\ell_{\delta_R}} \\ C_{n_\beta} & C_{n_{\dot\beta}} & C_{n_p} & C_{n_r} & C_{n_{\delta_A}} & C_{n_{\delta_R}} \end{bmatrix}}_{\text{AERODYNAMIC}\ (3\times6)} \begin{Bmatrix} \beta \\ \dot\beta b/2U_1 \\ pb/2U_1 \\ rb/2U_1 \\ \delta_A \\ \delta_R \end{Bmatrix}_{(6\times1)} \quad (10.4)$$

$$\begin{Bmatrix} f_{T_y}/\bar{q}_1 S \\ \ell_T/\bar{q}_1 Sb \\ n_T/\bar{q}_1 Sb \end{Bmatrix}_{(3\times1)} = \underbrace{\begin{Bmatrix} 0 \\ 0 \\ C_{n_{T_\beta}} \end{Bmatrix}}_{\text{THRUST}\ (3\times1)} \beta \quad (1\times1) \quad (10.5)$$

AILERON

$$F_{s_a} = G_a \cdot HM_a = G_a \bar{q} \cdot S_a \bar{c}_a C_{h_a} \quad (10.3c)$$

$$C_{h_a} = C_{h_{\delta_a}} \delta_a + C_{h_{\delta_{a_t}}} \delta_{a_t} \quad (10.3d)$$

RUDDER

$$F_{s_r} = G_r \cdot HM_r = G \cdot \bar{q}_v \cdot S_r \bar{c}_r C_{h_r} \quad (10.3e)$$

$$C_{h_r} = C_{h_\beta} \beta + C_{h_{\delta_r}} \delta_r + C_{h_{\delta_{r_t}}} \delta_{r_t} \quad (10.3f)$$

C_{D_1} is the airplane steady state drag coefficient. It is found with the methods of Chapter 4 and is tied uniquely to a specific value of the steady state lift coefficient, C_{L_1}. Figure 10.1 illustrates this.

C_{L_1} is the airplane steady state lift coefficient:

$$C_{L_1} = nW/\bar{q}S \tag{10.6}$$

where: n is the airplane load factor. Note that for 1g flight, n=1.

C_{m_1} is the airplane steady state pitching moment coefficient. It is determined with the methods of Chapter 8 (8.2.5 and 8.2.6) and is tied uniquely to a specific value of the steady state lift coefficient, C_{L_1}. Figure 10.2 shows this.

$C_{T_{x_1}}$ is the airplane steady state thrust coefficient component in the direction of the stability X-axis. It is determined from:

$$C_{T_{x_1}} = T_{reqd}/\bar{q}S \tag{10.7}$$

where: T_{reqd} is the thrust required in the steady state. The condition:

$$C_{T_{x_1}} = C_{D_1} \tag{10.8}$$

is normally satisfied in the steady state.

$C_{m_{T_1}}$ is the airplane steady state pitching moment coefficient due to thrust. It is found from:

$C_{m_{T_1}} = \Delta C_{m_{TL}}$, see: Eqn.(8.102)

The trim condition:

$$C_{m_1} = -C_{m_{T_1}} \tag{10.9}$$

is normally satisfied in the steady state.

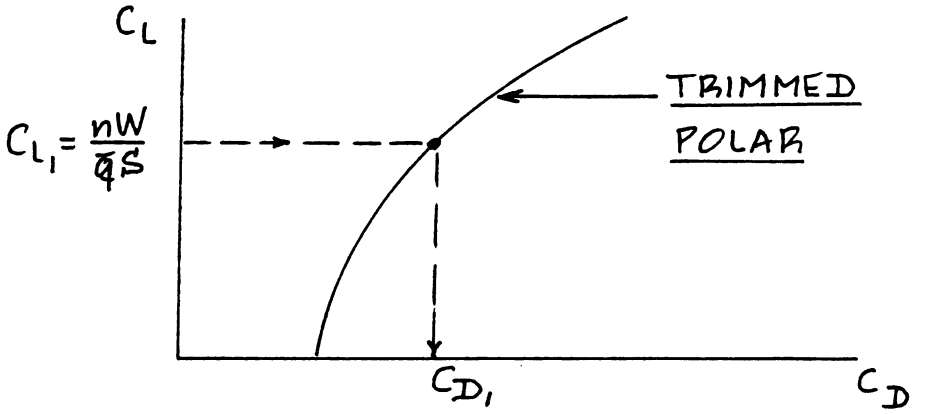

Figure 10.1 Determination of Drag Coefficient from a Known Value of the Lift Coefficient

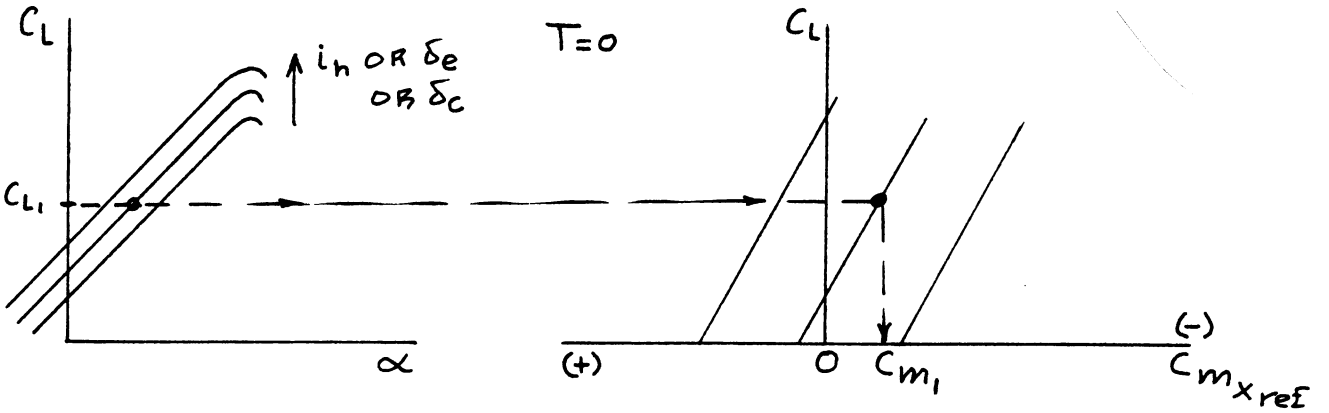

Figure 10.2 Determination of the Value of the Pitching Moment Coefficient

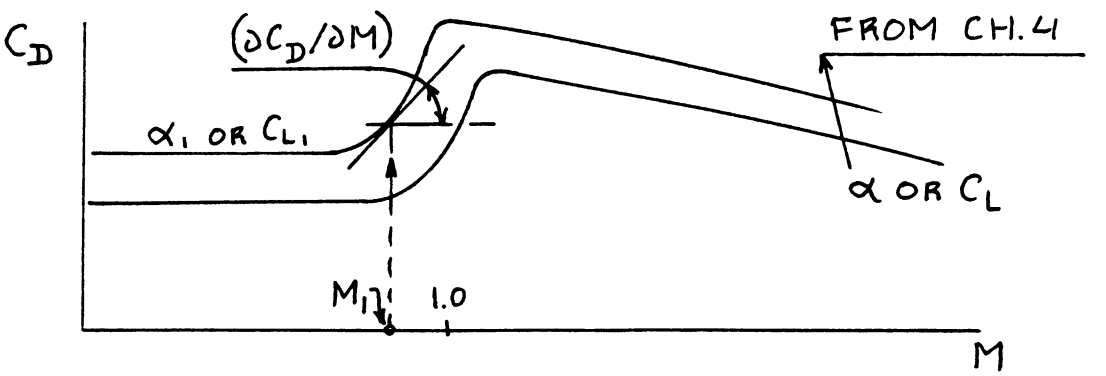

Figure 10.3 Determination of: $\partial C_D/\partial M$

10.2 STABILITY DERIVATIVES

In this section, methods for computing the following stability derivatives will be presented:

10.2.1 Speed derivatives
10.2.2 Angle-of-attack derivatives
10.2.3 Rate of angle-of-attack derivatives
10.2.4 Angle of sideslip derivatives
10.2.5 Rate of angle of sideslip derivatives
10.2.6 Roll rate derivatives
10.2.7 Pitch rate derivatives
10.2.8 Yaw rate derivatives

10.2.1 Speed Derivatives: C_{D_u}, C_{L_u}, C_{m_u}, $C_{T_{x_u}}$ and $C_{m_{T_u}}$

Table 10.1 lists the required speed derivatives: note the existence of aerodynamic as well as thrust derivatives.

10.2.1.1 Aerodynamic speed derivatives: C_{D_u}, C_{L_u} and C_{m_u}

1.) C_{D_u}

The drag-due-to-speed derivative, C_{D_u} may be determined in all speed regimes from:

$$C_{D_u} = M_1(\partial C_D/\partial M) \qquad (10.10)$$

where: M_1 is the Mach number in steady state flight

$\partial C_D/\partial M$ is the derivative of the airplane drag coefficient with respect to Mach number. This derivative is found from Figure 10.3.

2.) C_{L_u}

The lift-due-to-speed derivative, C_{L_u} may be determined as follows:

Subsonic:

$$C_{L_u} = \{M_1^2(\cos\Lambda)^2_{c/4} C_{L_1}\}/\{1 - M_1^2(\cos\Lambda)^2_{c/4}\} \qquad (10.11)$$

Transonic: Fair from M=0.8 to M=1.2 as in Fig.10.4

Supersonic: use Eqn.(10.11) also!

3.) C_{m_u}

The pitching-moment-due-to-speed derivative, C_{m_u} may be determined in all speed regimes from:

$$C_{m_u} = - C_{L_1} (\partial \bar{x}_{ac_A} / \partial M) M \qquad (10.12)$$

where: C_{L_1} is the airplane lift coefficient in the steady state as found from Eqn.(10.6).

$\bar{x}_{ac_A}$ is the location of the airplane aerodynamic center in fractions of the wing m.g.c. as determined from 8.2.5.2.

10.2.1.2 Thrust versus speed derivatives: $C_{T_{x_u}}$ and $C_{m_{T_u}}$

These derivatives are equal to zero in all speed regimes for gliders and for airplanes equipped with rocket powerplants only.

For propeller-driven airplanes and for jet-driven airplanes these derivatives depend on the characteristics of the propulsion installation.

1.) $C_{T_{x_u}}$

The thrust-due-to-speed derivative, $C_{T_{x_u}}$ may be computed in all speed regimes from:

For Propeller Driven Airplanes:

Fixed pitch propellers:

$$C_{T_{x_u}} = (1/\bar{q}S)(\partial P_{reqd} / \partial u) - 3C_{T_{x_1}} \qquad (10.13)$$

where: P_{reqd} is the installed power required for the flight condition being studied: see Ch.6.

Variable pitch (constant speed) propellers:

$$C_{T_{x_u}} = - 3C_{T_{x_1}} \qquad (10.14)$$

For Jet Driven Airplanes:

$$C_{T_{x_u}} = (M_1/\bar{q}S)(\partial T_{reqd} / \partial M) - 2C_{T_{x_1}} \qquad (10.15)$$

where: M_1 is the steady state Mach number

$\partial T_{reqd}/\partial M$ is the derivative of installed thrust required with respect to Mach number. It is determined from plots of installed thrust versus Mach number: see Ch.6.

2.) $C_{m_{T_u}}$

The thrust-moment-due-to-speed derivative, $C_{m_{T_u}}$ may be computed in all speed regimes from:

$$C_{m_{T_u}} = (d_T/\bar{c})C_{T_{x_u}} \qquad (10.16)$$

where: d_T is the thrust moment arm relative to the center of gravity as indicated in Figure 8.126. Note: the sign of d_T depends on the location of the thrust line relative to the c.g.

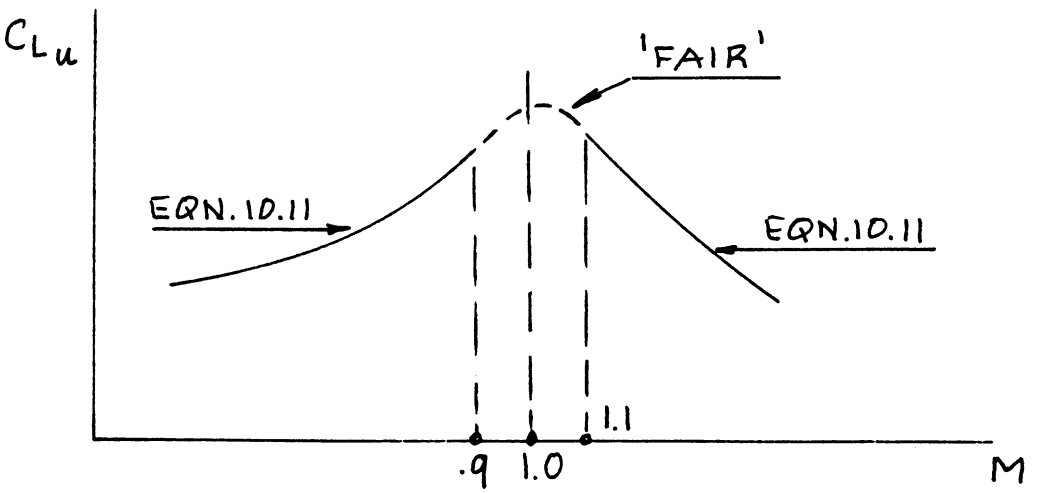

Figure 10.4 Example of Transonic Fairing for: C_{L_u}

10.2.2 Angle-of-Attack Derivatives: C_{D_α}, C_{L_α}, C_{m_α} and $C_{m_{T_\alpha}}$

Table 10.1 identifies the required angle-of-attack derivatives: note that there are aerodynamic as well as thrust derivatives.

10.2.2.1 Aerodynamic angle-of-attack derivatives: C_{D_α}, C_{L_α} and C_{m_α}

1.) C_{D_α}

The drag-due-to-angle-of-attack derivative, C_{D_α} may be found in all speed regimes from:

$$C_{D_\alpha} = (\partial C_D/\partial C_L)C_{L_\alpha} \qquad (10.17)$$

where: $(\partial C_D/\partial C_L)$ is determined as shown in Figure 10.5. Note that this slope must be obtained at the appropriate value of the lift coefficient, C_{L_1} AND at the appropriate value of Mach number, M_1.

C_{L_α} is the overall airplane lift curve slope as found from Eqn.(8.42): see the note of caution under 2.) C_{L_α}.

For airplanes with parabolic drag polars it is often more convenient to use:

$$C_{D_\alpha} = (2C_{L_1}/\pi Ae)C_{L_\alpha} \qquad (10.18)$$

2.) C_{L_α}

The lift-due-to-angle-of-attack derivative (also called lift curve slope), C_{L_α} is found from Eqn.(8.42).

NOTE OF CAUTION: Equation (8.42) applies to all speed regimes, provided the values for upwash and for downwash are valid for the appropriate speed regimes. The method of page 272 for computing downwash is valid only below M=0.9. For the transonic and for the supersonic speed regime Ref.9 must be consulted.

3.) C_{m_α}

The pitching-moment-due-to-angle-of-attack derivati-

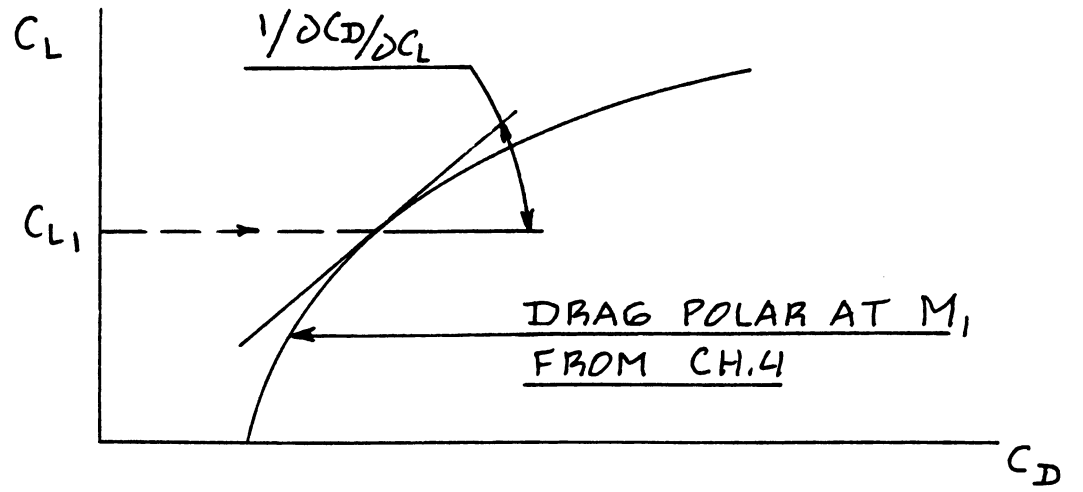

Figure 10.5 Determining $\partial C_D/\partial C_L$ From the Drag Polar

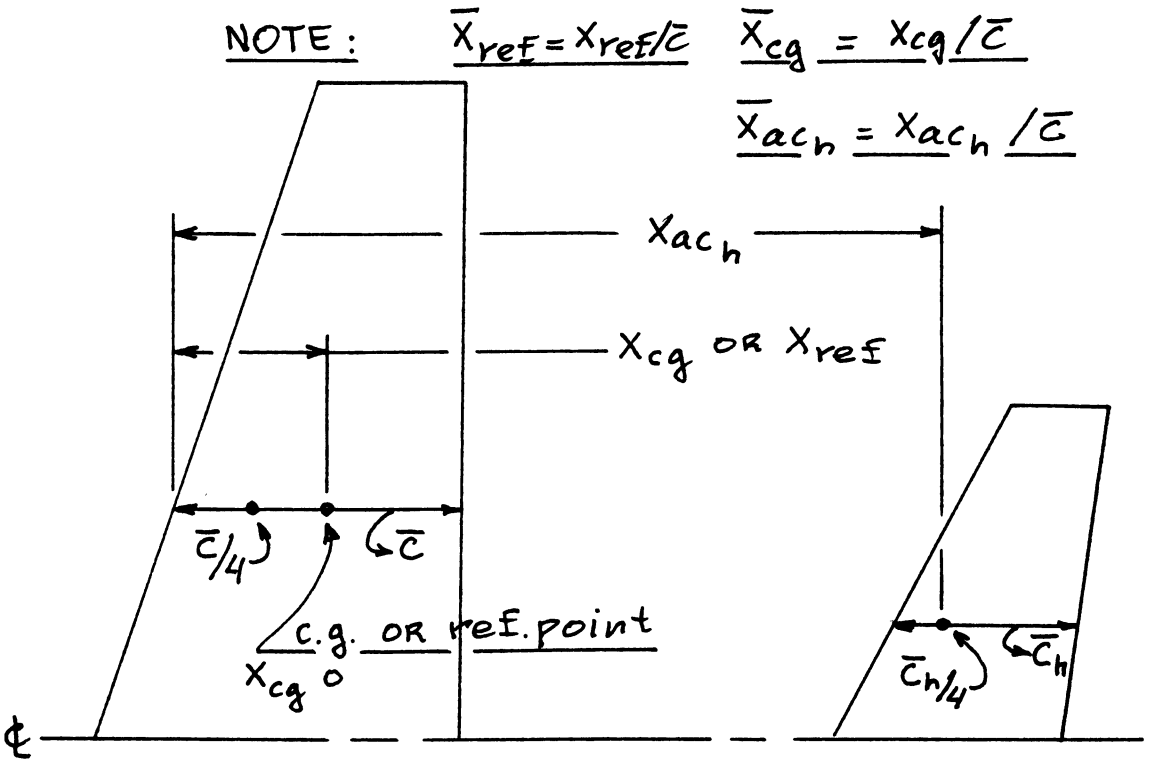

Figure 10.6 Definition of Geometric Parameters for Volume Coefficient

ve (also called static longitudinal stability), C_{m_α} is computed in all speed regimes from:

$$C_{m_\alpha} = (dC_m/dC_L)C_{L_\alpha} \qquad (10.19)$$

where: dC_m/dC_L is found from Eqn.(8.81) with possible corrections for power effects as given in 8.2.8.

C_{L_α} is determined from Eqn.(8.42). The note of caution given before, applies here also!

10.2.2.2 Thrust versus angle-of-attack derivative: $C_{m_{T_\alpha}}$

The only thrust versus angle-of-attack derivative which appears in Table 10.1 is $C_{m_{T_\alpha}}$. This derivative may be found from:

$$C_{m_{T_\alpha}} = \{\Delta(dC_m/dC_L)_T\}C_{L_\alpha} \qquad (10.20)$$

where: $\{\Delta(dC_m/dC_L)_T\}$ is found from Eqn.(8.104).

C_{L_α} is found from Eqn.(8.42). The note of caution given before, applies here also!

10.2.3 Rate of Angle-of-attack Derivatives: $C_{D_{\dot\alpha}}$, $C_{L_{\dot\alpha}}$ and $C_{m_{\dot\alpha}}$

Except for $C_{m_{\dot\alpha}}$, these derivatives are usually not important. The reader should consult Ref.9 for detailed methods covering all speed regimes. The methods given here apply only in the subsonic speed range.

1.) $C_{D_{\dot\alpha}}$

The drag-due-to-rate-of-angle-of-attack derivative, $C_{D_{\dot\alpha}}$ is normally neglected:

$$C_{D_{\dot\alpha}} = 0 \qquad (10.21)$$

2.) $C_{L_{\dot\alpha}}$

The lift-due-to-rate-of-angle-of-attack derivative, $C_{L_{\dot\alpha}}$ may be computed from:

$$C_{L_{\dot\alpha}} = 2(C_{L_{\alpha_h}})\eta_h(\bar{V}_h)(d\varepsilon/d\alpha) \qquad (10.22)$$

where: $C_{L_{\alpha_h}}$ is found from 8.1.3.2 with appropriate substitution of horizontal tail parameters for wing parameters.

η_h is found from 8.1.5.2

$d\varepsilon/d\alpha$ is found from Eqn.(8.45)

$\bar{V}_h$ is the horizontal tail volume coefficient:

$$\bar{V}_h = (\bar{x}_{ac_h} - \bar{x}_{cg})(S_h/S) \qquad (10.23)$$

where: $\bar{x}_{ac_h}$ and $\bar{x}_{cg}$ (or $\bar{x}_{ref}$) are defined in Figure 10.6.

3.) $C_{m_{\dot{\alpha}}}$

The pitching-moment-due-to-rate-of-angle-of-attack, $C_{m_{\dot{\alpha}}}$ may be computed from:

$$C_{m_{\dot{\alpha}}} = -2(C_{L_{\alpha_h}})\eta_h(\bar{V}_h)(\bar{x}_{ac_h} - \bar{x}_{cg})(d\varepsilon/d\alpha) \qquad (10.24)$$

where: all quantities are defined before.

NOTE: the reader will observe that Equations (10.22) and (10.24) are based on the assumption that the contribution of the horizontal tail is the only important contribution to these derivatives. This assumption is frequently satisfied. If not, Ref.9 should be used.

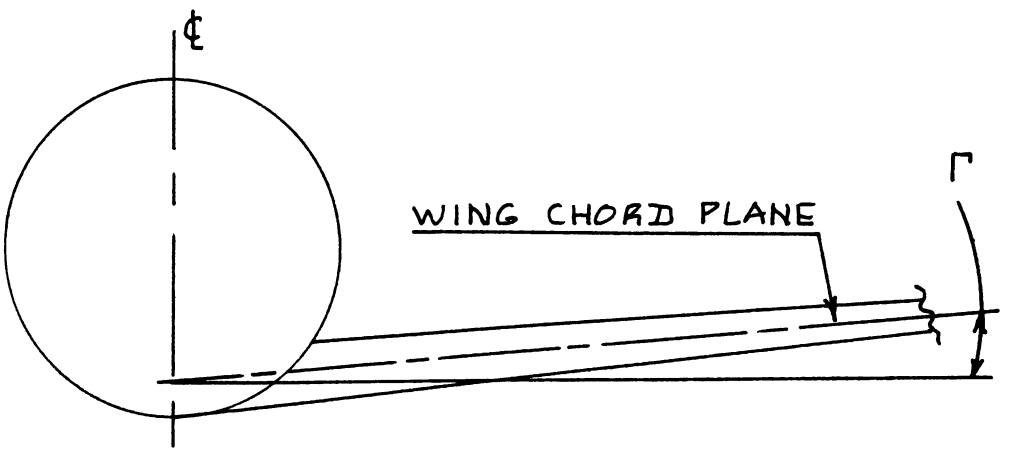

Figure 10.7 Definition of Wing Geometric Dihedral

10.2.4 Angle-of-Sideslip Derivatives: C_{y_β}, C_{l_β}, C_{n_β} and $C_{n_{T_\beta}}$

Table 10.1 identifies the required angle-of-sideslip derivatives: note that there are aerodynamic as well as thrust derivatives.

NOTE: All methods presented for the sideslip derivatives apply to the subsonic speed regime only. For other speed ranges, Ref.9 should be used.

10.2.4.1 Aerodynamic angle-of-sideslip derivatives: C_{y_β}, C_{l_β} and C_{n_β}

1.) C_{y_β}

The sideforce-due-to-sideslip derivative, C_{y_β} may be found from:

$$C_{y_\beta} = C_{y_{\beta_w}} + C_{y_{\beta_f}} + C_{y_{\beta_v}} \qquad (10.25)$$

where: the wing contribution is given by:

$$C_{y_{\beta_w}} = -0.00573(|\Gamma|) \qquad (10.26)$$

with: Γ the wing geometric dihedral angle in deg. Figure 10.7 defines this angle.

the fuselage contribution is given by:

$$C_{y_{\beta_f}} = -2K_i(S_o/S) \qquad (10.27)$$

with: K_i defined in Figure 10.8. The quantities z_w and d_f are defined in Figure 10.9

S_o is the cross-sectional area of the fuselage at station x_o, where the flow ceases to be potential. The distance x_o depends on the distance x_1. The latter is equal to that fuselage station where the derivative dS_x/dx first reaches its maximum negative value: see Figure 10.10. The

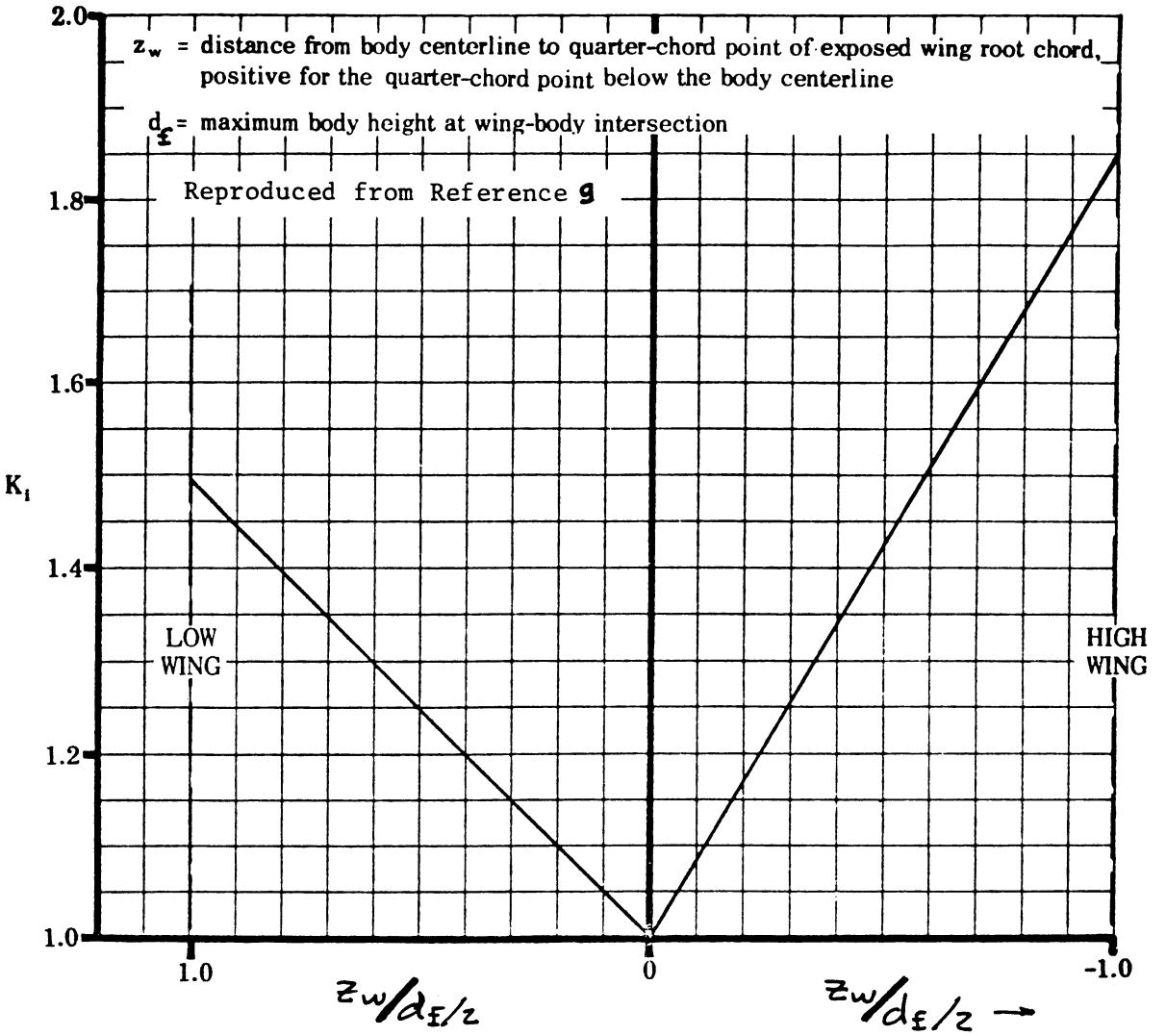

Figure 10.8 Wing-Fuselage Interference Factor, K_i

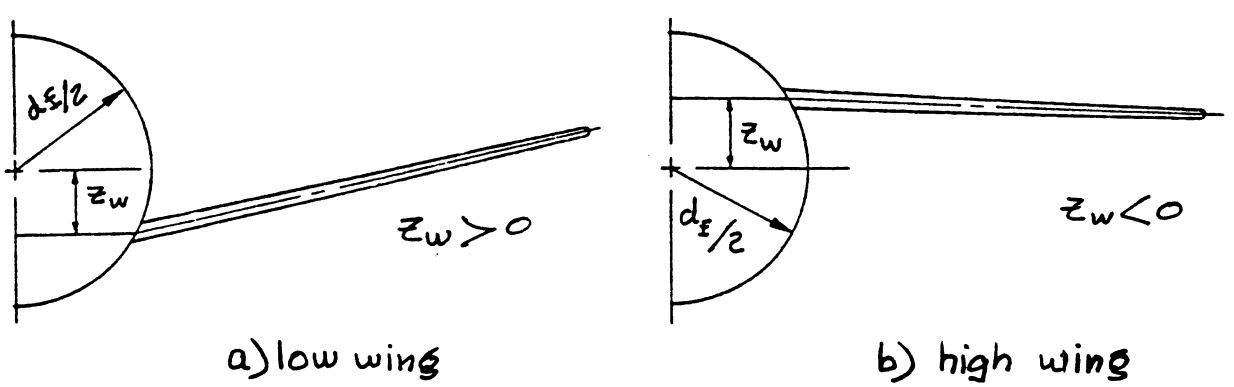

Figure 10.9 Definition of Wing-Fuselage Parameters: z_w and d_f

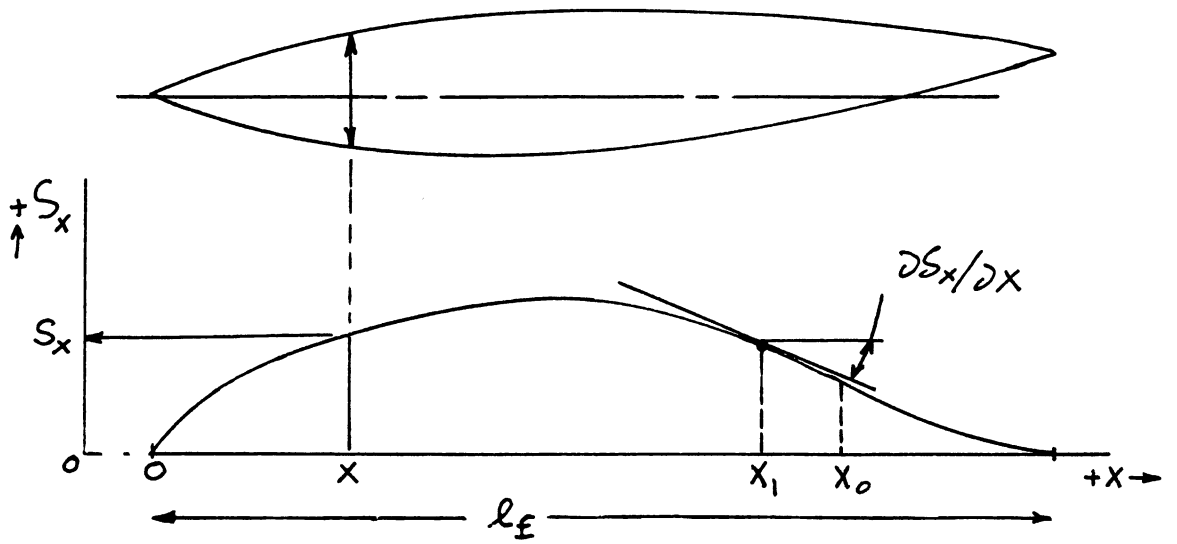

Figure 10.10 Determination of S_o

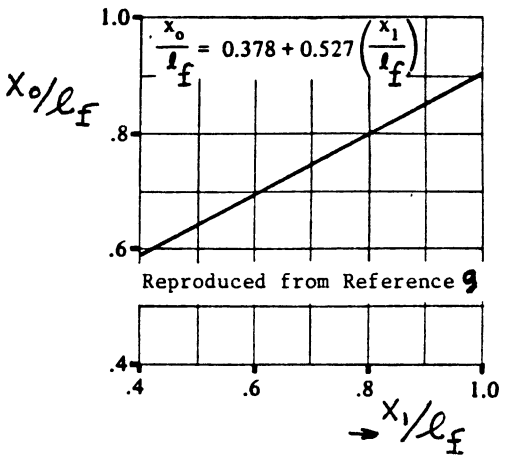

Figure 10.11 Fuselage Station Where Flow Becomes Viscous

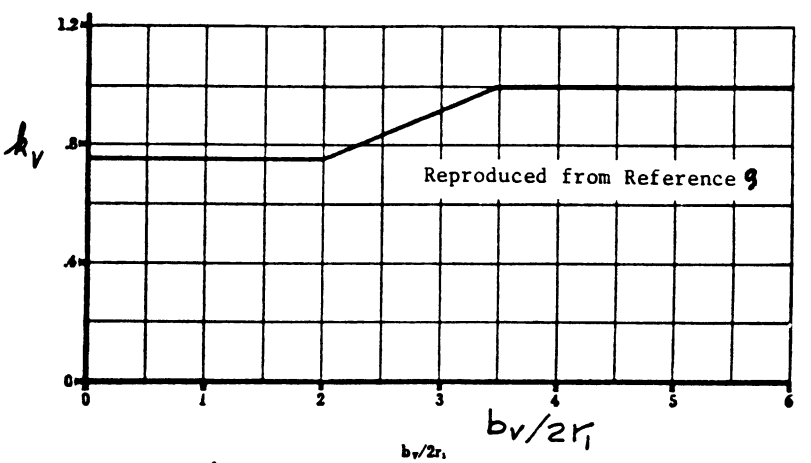

(For definition of $2r_1$ see Figure 10.17)

Figure 10.12 Empirical Factor for Estimating Side-force due to Sideslip of a Single Vertical Tail

distances x_o and x_1 are correlated in Figure 10.11. The fuselage contribution is virtually independent of Mach number.

the vertical tail contribution is given by:

1. For Single Vertical Tails:

$$C_{Y_{\beta_v}} = -k_v(C_{L_{\alpha_v}})(1 + d\sigma/d\beta)\eta_v(S_v/S) \qquad (10.28)$$

with: k_v given by Figure 10.12.

$C_{L_{\alpha_v}}$ found from 8.1.3.2 with appropriate substitution of vertical tail parameters for wing parameters. The vertical tail aspect ratio, $A_{v_{eff}}$ must be substituted for A in the method of 8.1.3.2. The effective aspect ratio of the vertical tail may be estimated from:

$$A_{v_{eff}} = (A_{v(f)}/A_v)A_v\{1 + K_{vh}\{(A_{v(hf)}/A_{v(f)}) - 1\}\} \qquad (10.29)$$

with: $A_v = (b_v)^2/S_v$ (10.30)

where: b_v and S_v depend on the vertical tail configuration as shown in Figure 10.13 for a range of vertical tail configurations.

$(A_{v(f)}/A_v)$ is the ratio of the vertical tail aspect ratio in the presence of the fuselage to that of an isolated vertical tail. This ratio can be determined from Figure 10.14.

$(A_{v(hf)}/A_{v(f)}$ is the ratio of the vertical tail aspect ratio in the presence of the horizontal tail and the fuselage to that in the presence of the fuselage alone. This ratio can be determined from Figure 10.15.

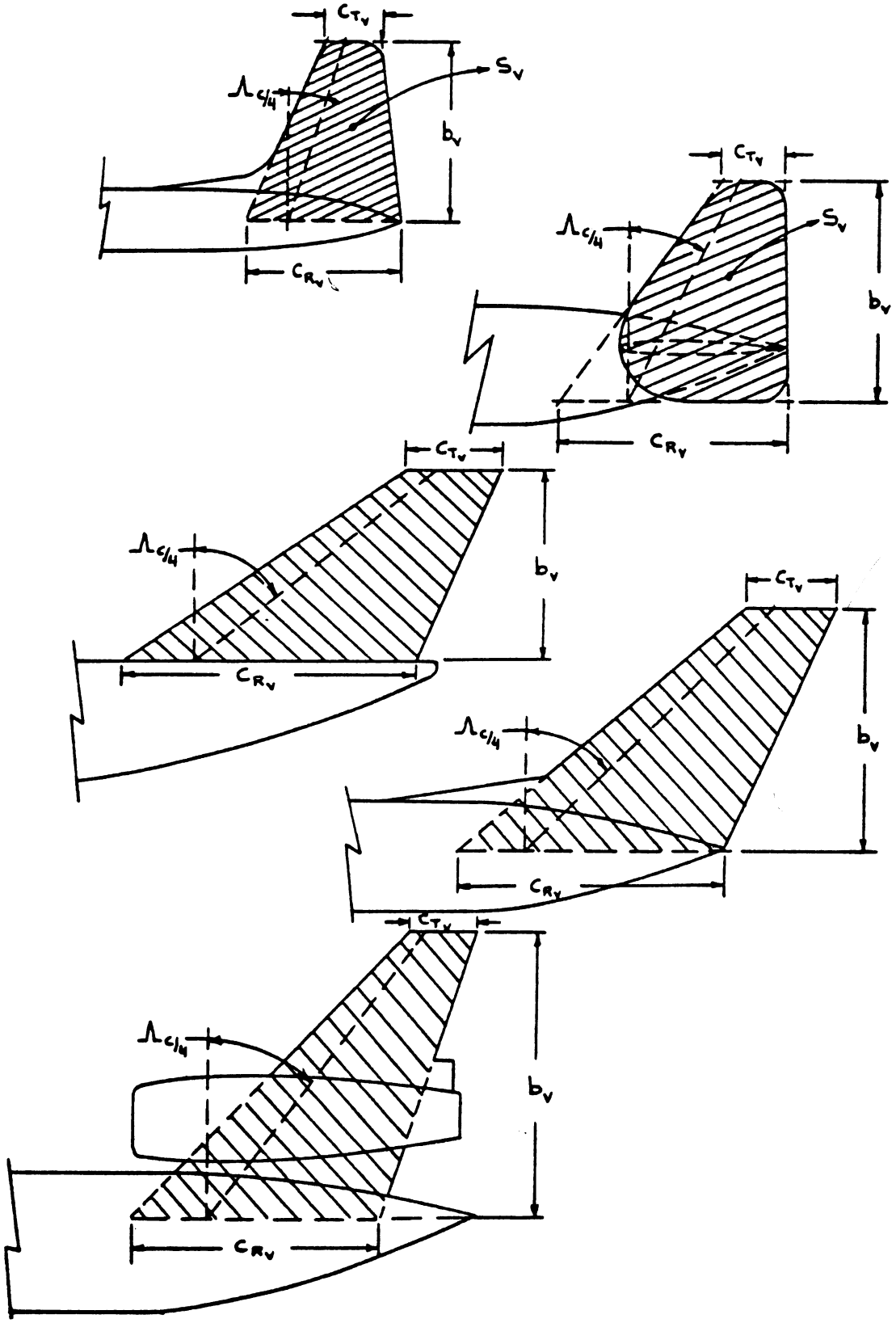

Figure 10.13 Examples of Effective Vertical Tail Geometry

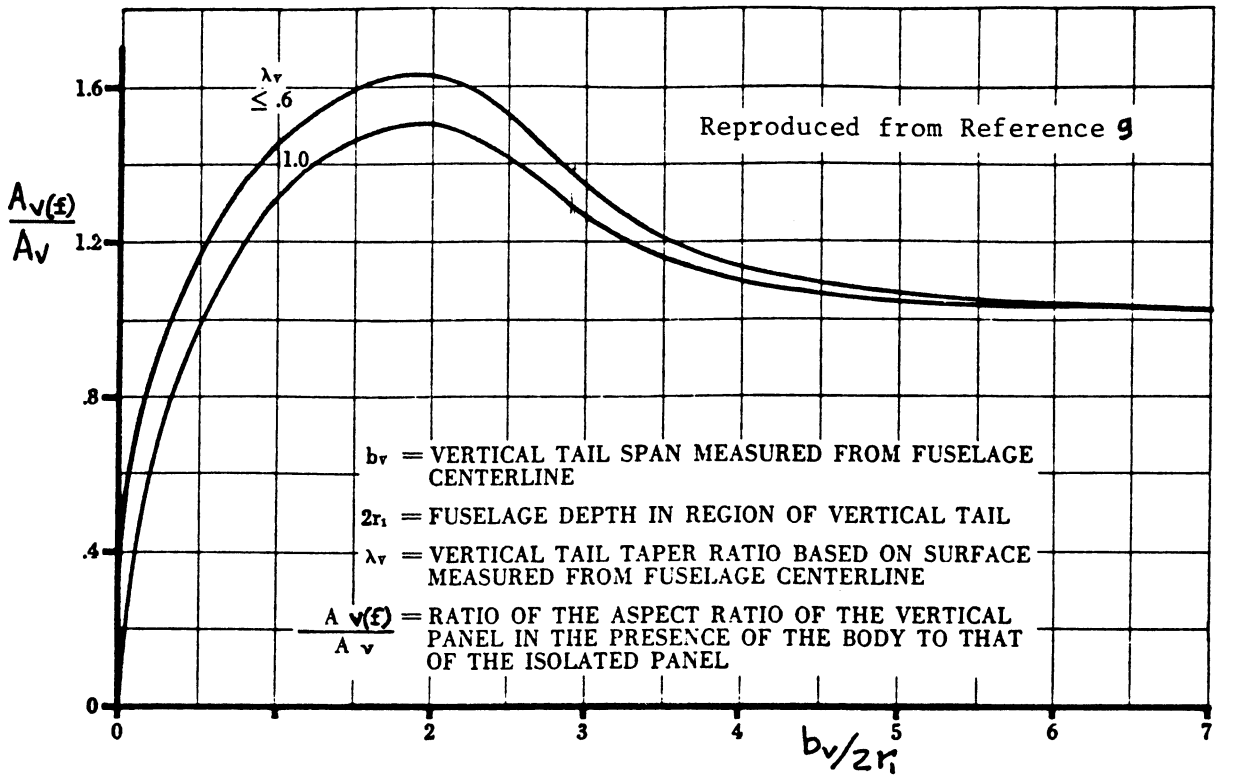

Figure 10.14 Ratio of Vertical Tail Aspect Ratio in Presence of Fuselage to that of Isolated Tail

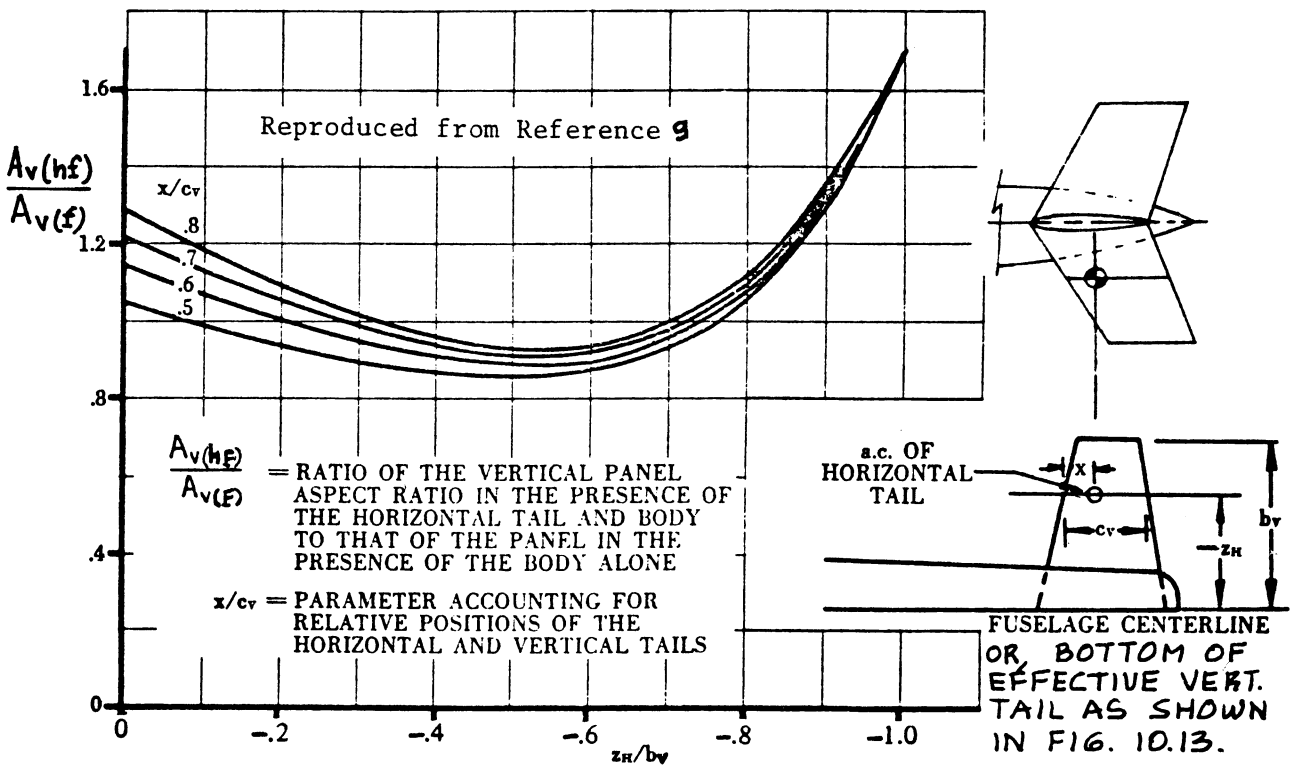

Figure 10.15 Ratio of Vertical Tail Aspect Ratio in Presence of Fuselage and Horizontal Tail to that in Presence of Fuselage Alone

K_{vh} is a factor which accounts for the relative size of the horizontal and the vertical tail. It may be determined from Figure 10.16.

$$(1 + d\sigma/d\beta)\eta_v = \quad (10.31)$$

$$0.724 + 3.06\{(S_v/S)/(1 + \cos\Lambda_{c/4})\} + 0.4z_w/z_f + 0.009A$$

S_v is the effective vertical tail area as defined in Figure 10.13 for several example configurations.

$\Lambda_{c/4}$ is the wing quarter chord sweep angle

A is the wing aspect ratio

z_w is the distance from wing root quarter chord point to the fuselage centerline, positive below fuselage centerline.

z_f is the maximum fuselage depth

2. For Twin Vertical Tails:

$$C_{Y_{\beta_v}} = -2\{C_{Y_{\beta_{v(wfh)}}}/C_{Y_{\beta_{v_{eff}}}}\}(C_{Y_{\beta_{v_{eff}}}})(S_v/S) \quad (10.32)$$

with: $\{C_{Y_{\beta_{v(wfh)}}}/C_{Y_{\beta_{v_{eff}}}}\}$ determined from Figure 10.17.

$C_{Y_{\beta_{v_{eff}}}}$ determined from Figure 10.18 with the corresponding value of $A_{v_{eff}}$ found from Figure 10.19.

S_v is the area of a single vertical tail panel as defined in Figure 10.13.

2.) C_{l_β}

The rolling-moment-due-to-sideslip derivative, C_{l_β} (also called dihedral effect) may be found from:

$$C_{l_\beta} = C_{l_{\beta_{wf}}} + C_{l_{\beta_h}} + C_{l_{\beta_v}} \quad (10.33)$$

where: the wing-fuselage contribution is given by:

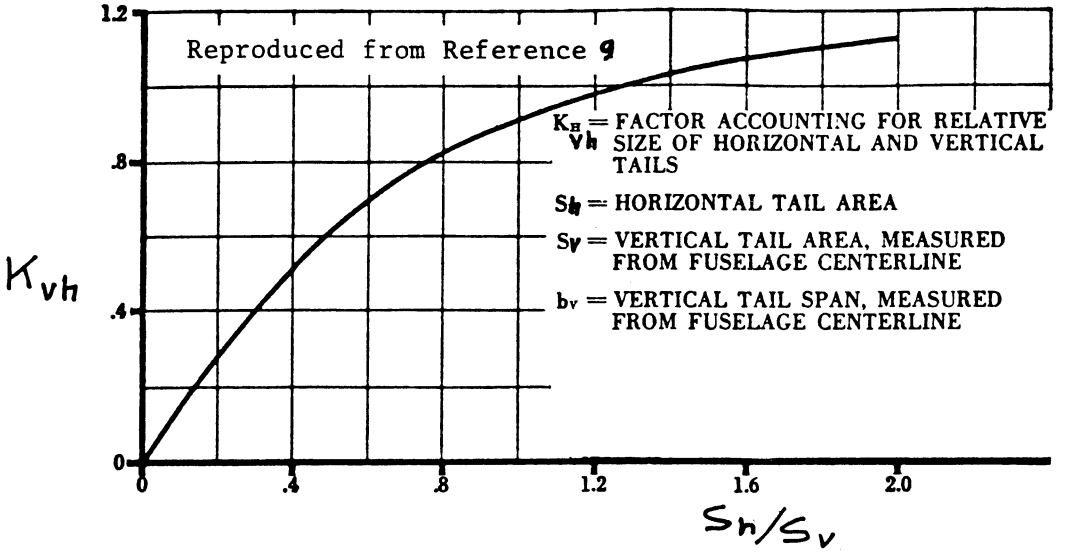

Figure 10.16 Factor which Accounts for Relative Size of Horizontal and Vertical Tail

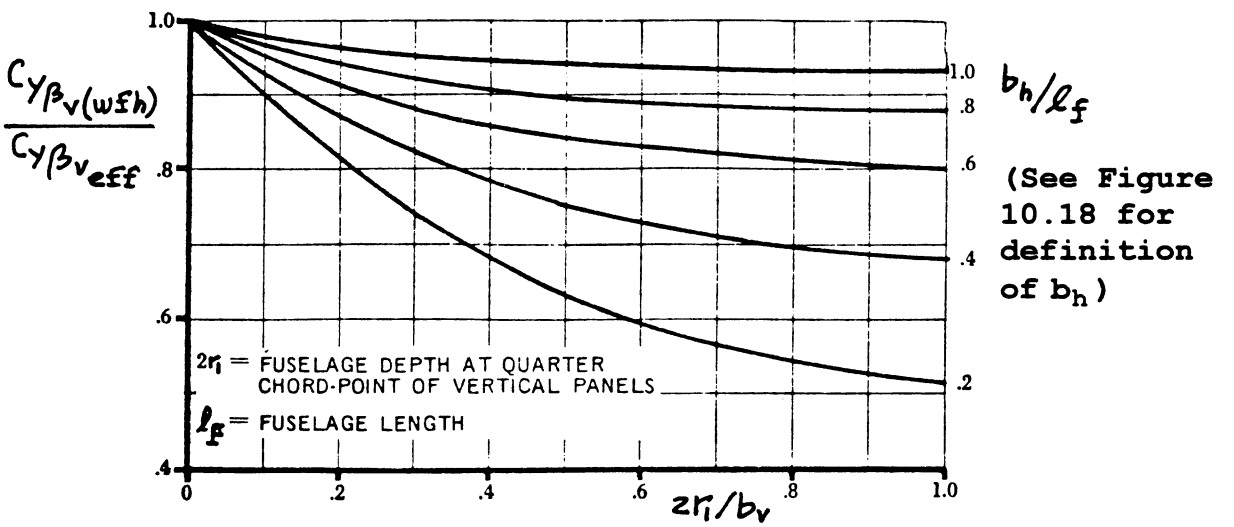

(See Figure 10.18 for definition of b_h)

Reproduced from Reference 9

Figure 10.17 Wing-Fuselage-Horizontal-Tail Interference on Side-force due to Sideslip of Twin Vertical Tails

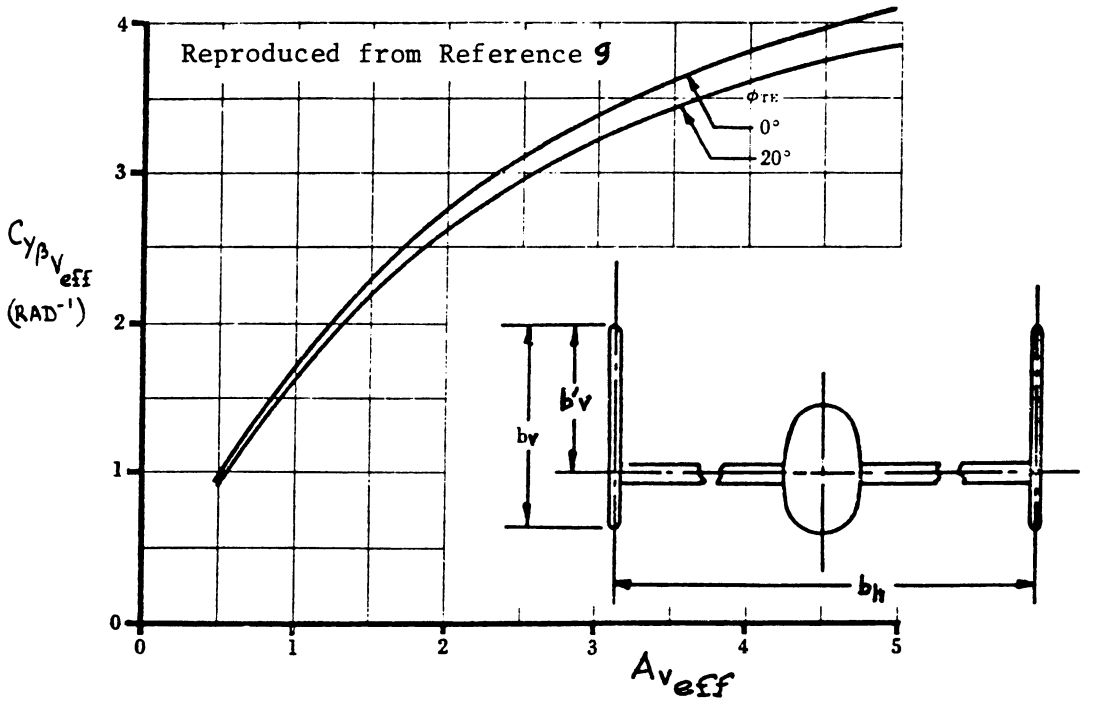

Figure 10.18 Effective Value of the Side-force due to Sideslip Derivative for Twin Vertical Tails

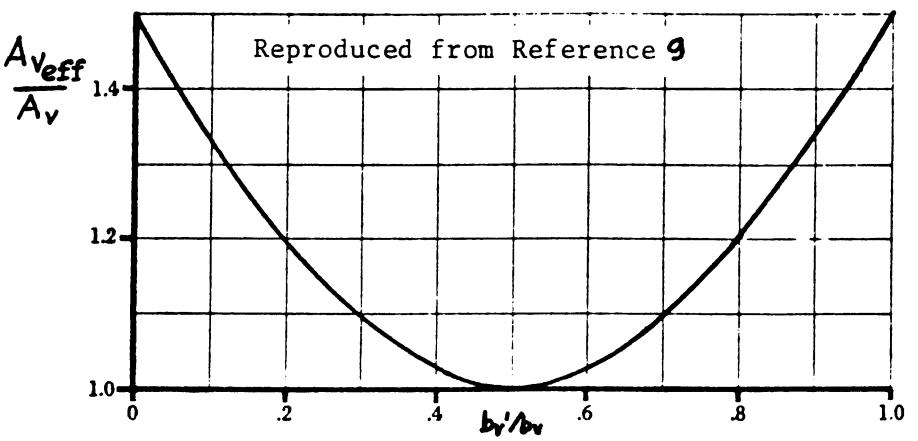

For definition of b'_v see Figure 10.18

Figure 10.19 Effective Value of Vertical Tail Aspect Ratio Used with Figure 10.18

$$C_{l_{\beta_{wf}}} = 57.3[C_{L_{wf}}\{(C_{l_\beta}/C_L)_{\Lambda_{c/2}}(K_{M_\Lambda})(K_f) + (C_{l_\beta}/C_L)_A\} +$$

$$+ \Gamma\{(C_{l_\beta}/\Gamma)K_{M_\Gamma} + (\Delta C_{l_\beta}/\Gamma)\} + (\Delta C_{l_\beta})_{z_w} +$$

$$+ (\varepsilon_t \tan\Lambda_{c/4})\{(\Delta C_{l_\beta})/\varepsilon_t \tan\Lambda_{c/4}\}] \qquad (10.34)$$

with: $C_{L_{wf}}$ is the lift coefficient of the wing-fuselage combination. For any given value of airplane lift coefficient, this may be computed by subtracting the tail and/or the canard lift coefficients (but based on wing area!). For preliminary design purposes it seems acceptable to set: $C_{L_{wf}} = C_{L_1}$.

$(C_{l_\beta}/C_L)_{\Lambda_{c/2}}$ is the wing sweep contribution which may be found from Figure 10.20.

K_{M_Λ} is the compressibility correction to sweep. It is found from Figure 10.21.

K_f is a fuselage correction factor obtained from Figure 10.22.

$\Lambda_{c/2}$ is the wing semi-chord sweep angle

$\Lambda_{c/4}$ is the wing quarter-chord sweep angle

$(C_{l_\beta}/C_L)_A$ is the aspect ratio contribution obtained from Figure 10.23.

Γ is the geometric dihedral angle of the wing as defined in Figure 10.7.

(C_{l_β}/Γ) is the wing dihedral effect found from Figure 10.24.

K_{M_Γ} is the compressibility correction to dihedral as obtained from Figure 10.25.

$(\Delta C_{l_\beta}/\Gamma)$ is the fuselage induced effect on the wing height and is found from:

$$(\Delta C_{l_\beta}/\Gamma) = -0.0005A(d_{f_{ave}}/b)^2 \qquad (10.35)$$

where: A is the wing aspect ratio

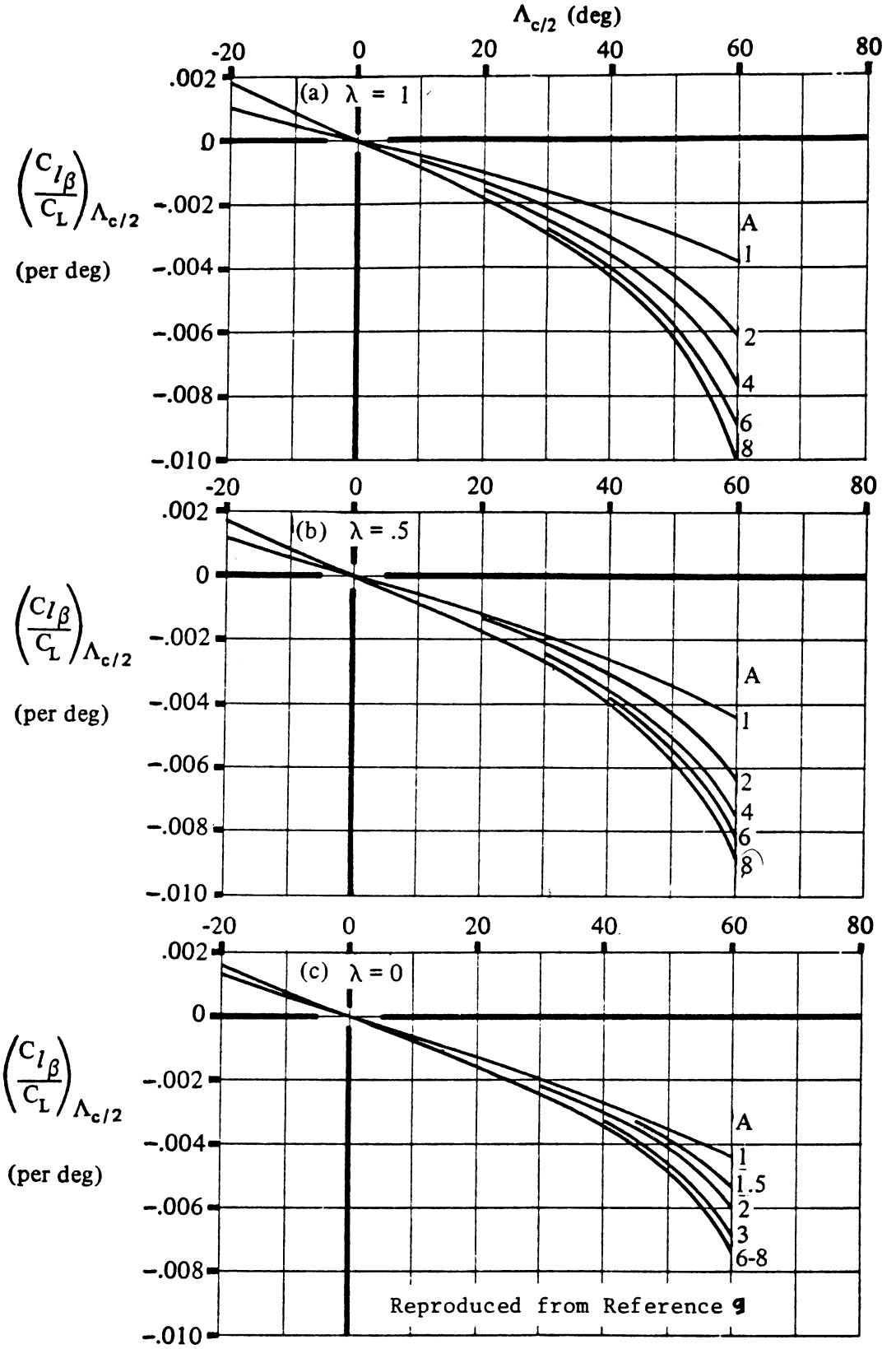

Figure 10.20 Wing Sweep Contribution to Rolling Moment due to Sideslip

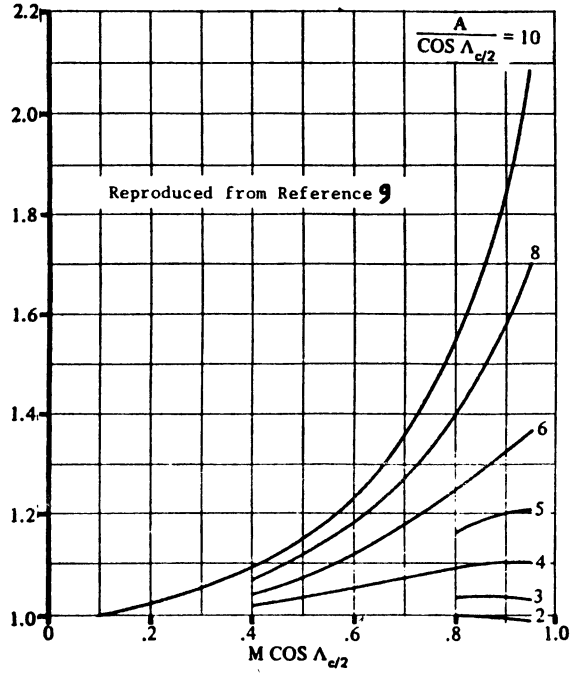

Figure 10.21 Compressibility Correction to Wing Sweep

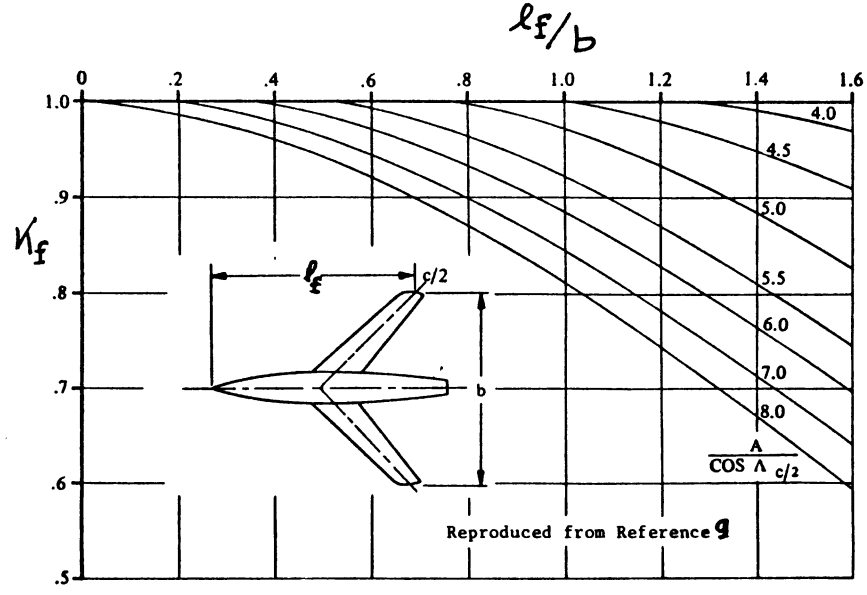

Figure 10.22 Fuselage Correction Factor

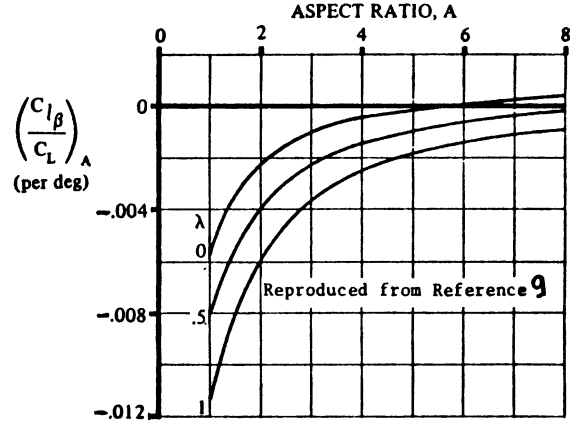

Figure 10.23 Wing Aspect Ratio Contribution to Rolling Moment due to Sideslip

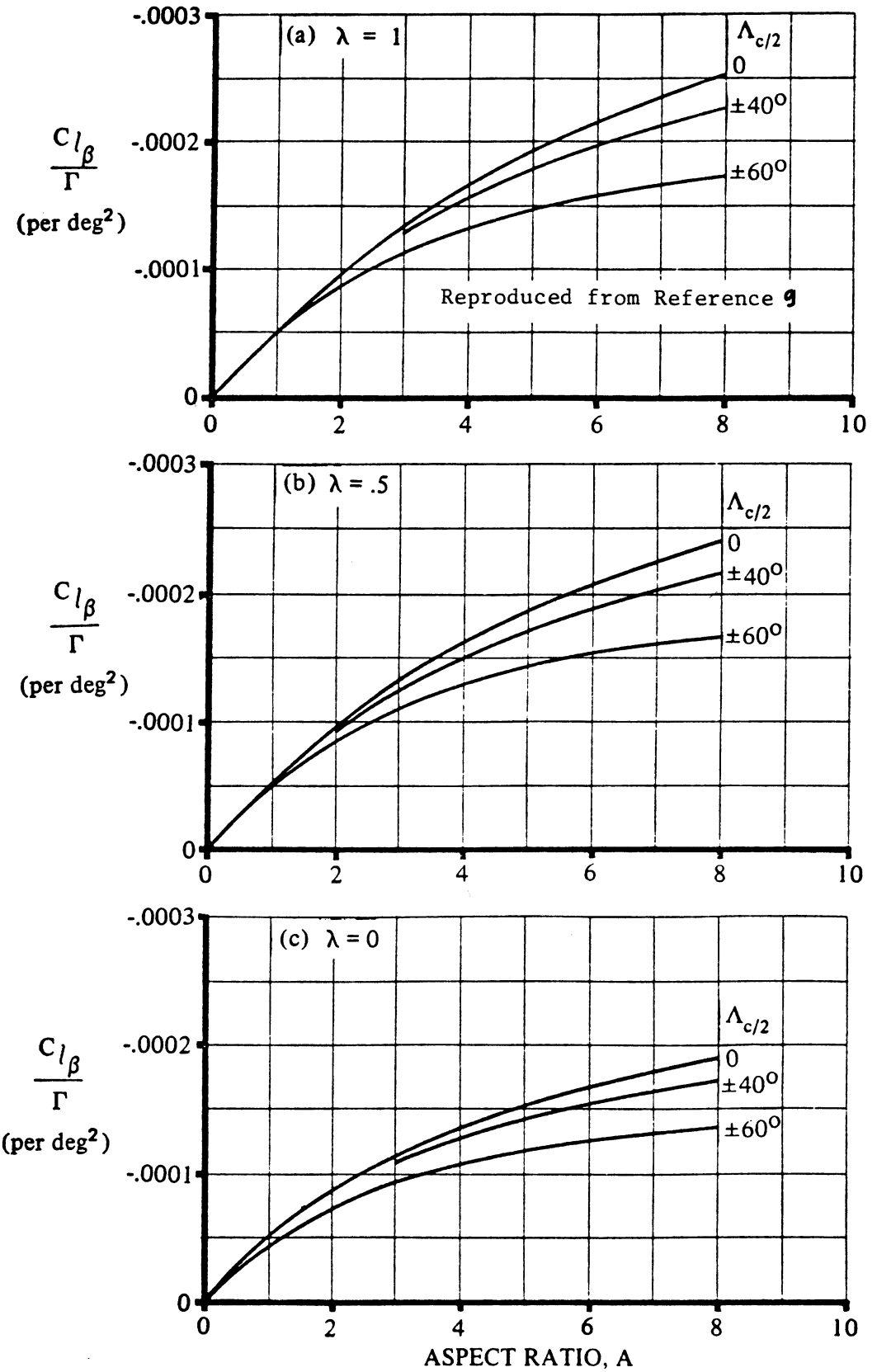

Figure 10.24 Wing Geometric Dihedral Contribution to Rolling Moment due to Sideslip

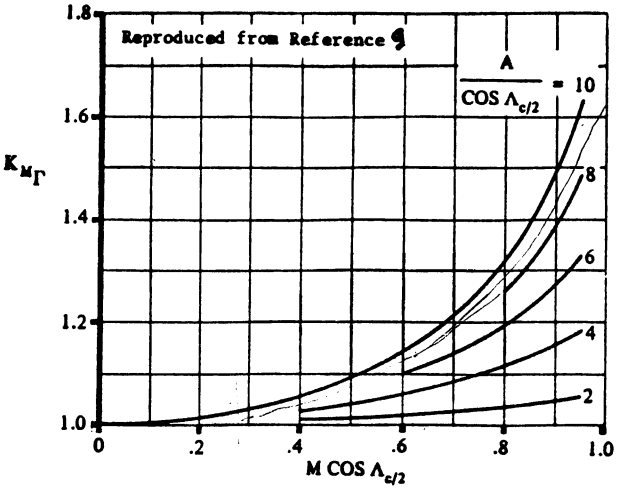

Figure 10.25 Compressibility Correction to Wing Dihedral

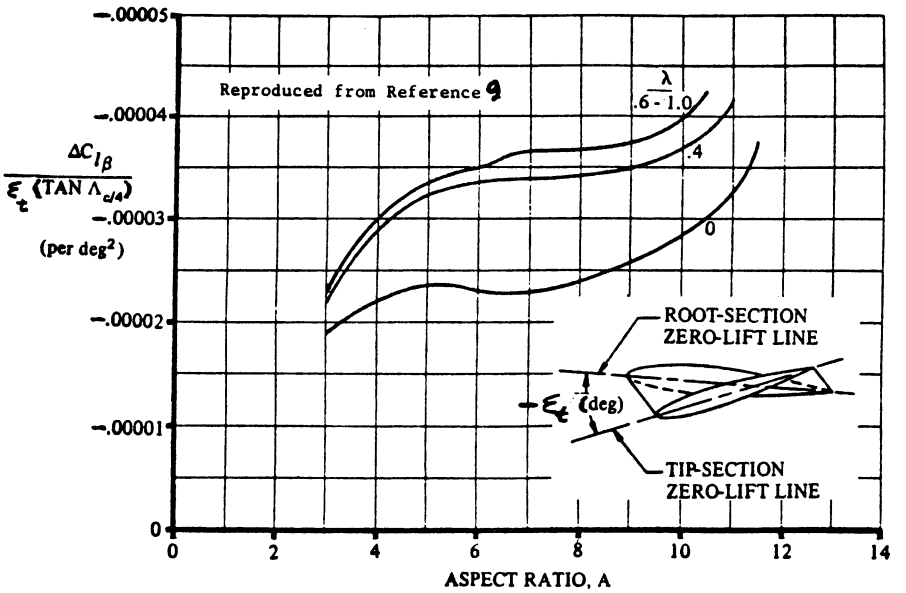

Figure 10.26 Contribution of Wing Twist to Rolling Moment due to Sideslip

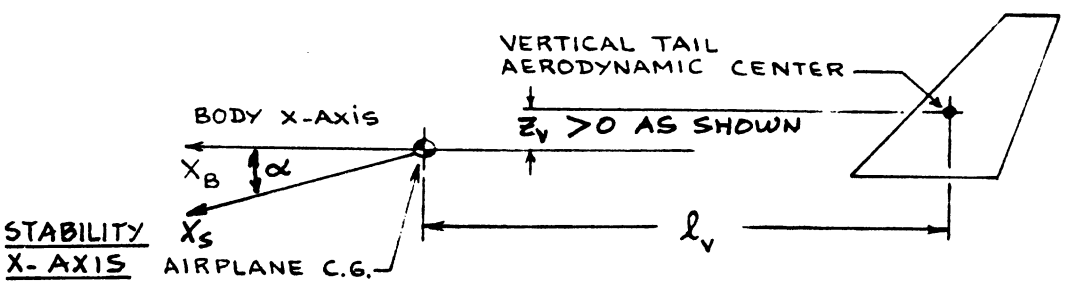

Figure 10.27 Geometry for Locating Vertical Tail(s)

b is the wing span

$$d_{f_{ave}} = \{(\text{ave. fusel. cross-section area})/0.7854\}^{1/2} \quad (10.36)$$

$$(\Delta C_{l_\beta})_{z_w} = 0.042(A)^{1/2}(z_w/b)(d_{f_{ave}}/b) \quad (10.37)$$

where: z_w is defined in Figure 10.9

$d_{f_{ave}}$ is given by Eqn.(10.36)

$\{(\Delta C_{l_\beta})/\varepsilon_t \tan\Lambda_{c/4}\}$ is a wing twist correction factor which is obtained from Fig.10.26.

the horizontal tail contribution is given by:

$$C_{l_{\beta_h}} = (C_{l_{\beta_{hf}}})(S_h b_h/Sb) \quad (10.38)$$

with: $C_{l_{\beta_{hf}}}$ the horizontal tail dihedral effect as computed from Equation (10.34) with appropriate substitution of tail-fuselage for wing-fuselage parameters.

S_h is the horizontal tail area

b_h is the horizontal tail span

the vertical tail contribution is given by:

$$C_{l_{\beta_v}} = (C_{y_{\beta_v}})\{(z_v \cos\alpha - l_v \sin\alpha)/b\} \quad (10.39)$$

with: $C_{y_{\beta_v}}$ given by Eqn.(10.28)

z_v and l_v defined in Figure (10.27)

3.)C_{n_β}

The yawing-moment-due-to-sideslip derivative, C_{n_β} (also called static directional stability) may be computed from:

$$C_{n_\beta} = C_{n_{\beta_w}} + C_{n_{\beta_f}} + C_{n_{\beta_v}} \quad (10.40)$$

where: the wing contribution is important only at high angles of attack. Ref.9 contains a method for estimating this contribution in such cases. For preliminary design purposes:

$$C_{n_{\beta_w}} = 0 \qquad (10.41)$$

the fuselage contribution is found from:

$$C_{n_{\beta_f}} = -57.3 K_N K_{R_l} (S_{B_s} l_f / Sb) \qquad (10.42)$$

with: K_N an empirical factor determined from Figure 10.28

K_{R_l} a factor dependent on Reynold's Number and obtained from Figure 10.29

S_{B_s} and l_f are defined in Figure 10.28.

the vertical tail contribution is found from:

$$C_{n_{\beta_v}} = -(C_{y_{\beta_v}})(l_v \cos\alpha + z_v \sin\alpha)/b \qquad (10.43)$$

where: $C_{y_{\beta_v}}$ is found from Eqn.(10.28)

l_v and z_v are given in Figure 10.27.

10.2.4.2 Thrust versus sideslip derivative: $C_{n_{T_\beta}}$

As suggested in Table 10.1, the only contribution which is of some significance is the yawing-moment-due-to-thrust-in-sideslip derivative, $C_{n_{T_\beta}}$.

For Propeller Driven Airplanes:

$$C_{n_{T_\beta}} = \qquad (10.44)$$

$$-\sum_{i=1}^{i=n} [\{(dC_N/d\alpha)_{p_i}\}(0.79)(D_{p_i})^2 (l_{p_i})\}/Sb]$$

where: all terms are as defined on page 342.

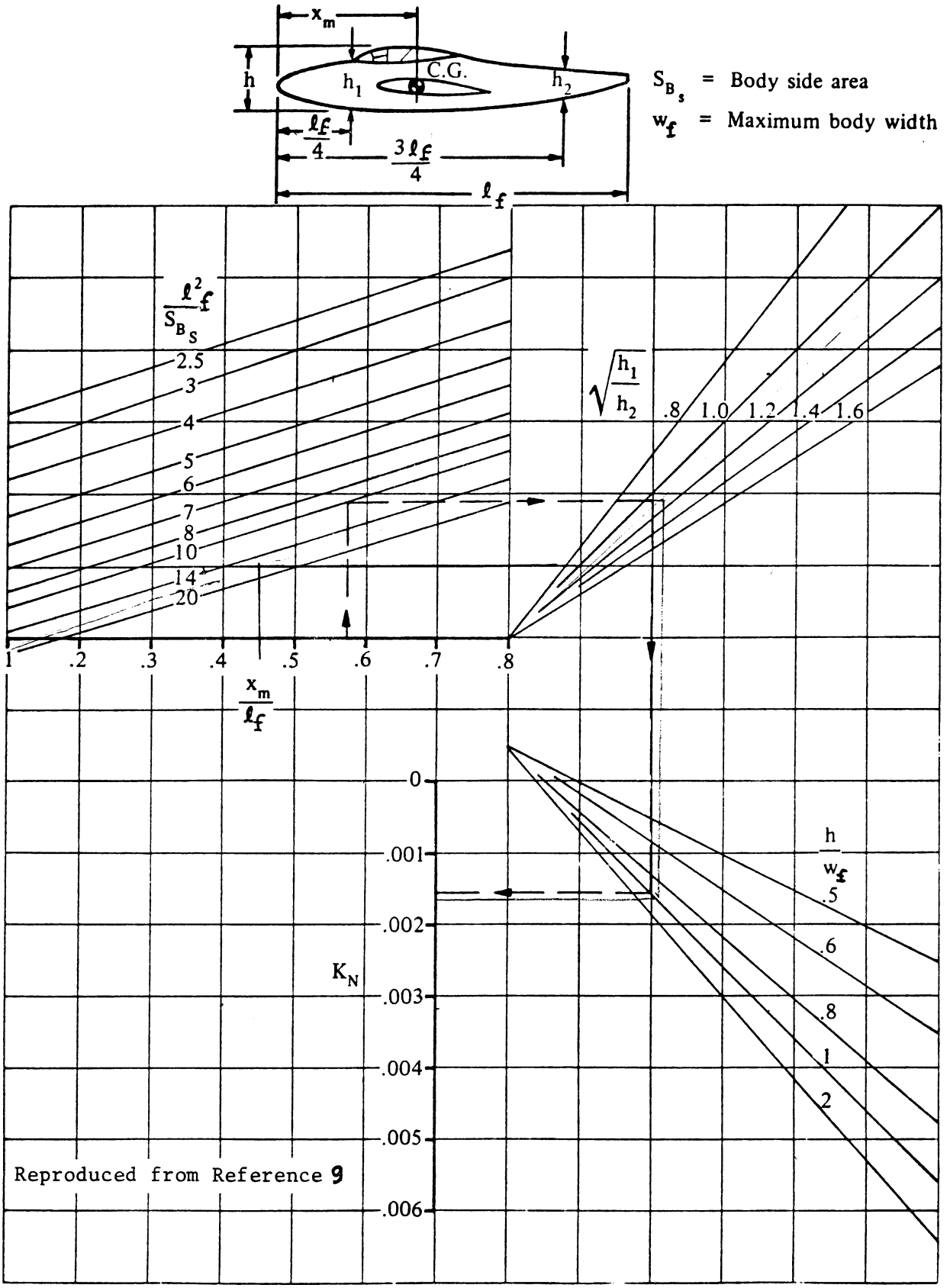

Figure 10.28 Factor Accounting for Wing-Fuselage Interference with Directional Stability

For Jet Driven Airplanes:

$$C_{n_{T_\beta}} = \sum_{i=1}^{i=n} [\{0.035(m_{a_i})(l_{n_i})\}/Sb\rho U_1] \qquad (10.45)$$

where: all terms are as defined on page 343.

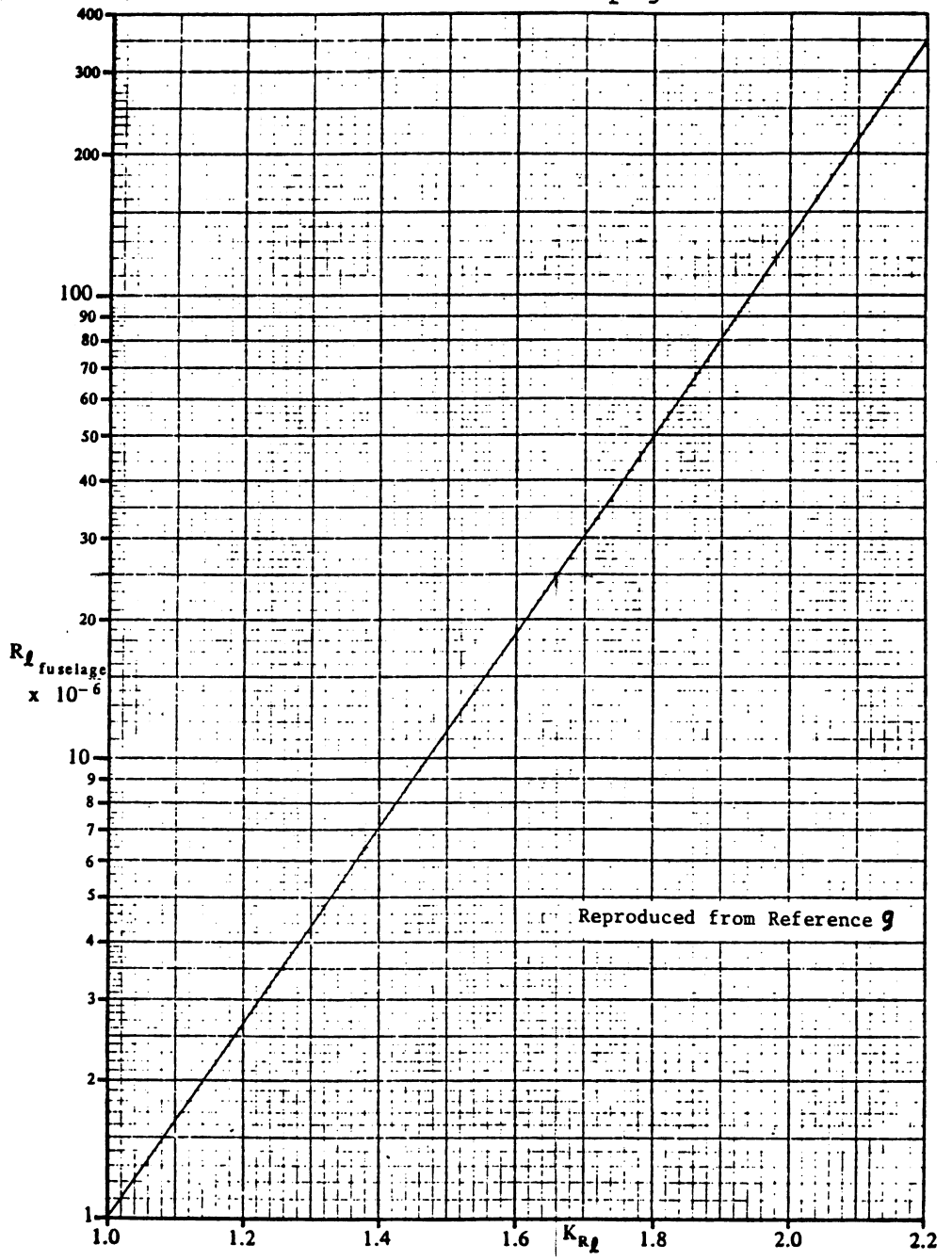

Figure 10.29 Effect of Fuselage Reynold's Number on Wing-Fuselage Directional Stability

10.2.5. Rate of Angle-of-Sideslip Derivatives: $C_{y_{\dot{\beta}}}$, $C_{l_{\dot{\beta}}}$ and $C_{n_{\dot{\beta}}}$

Table 10.1 identifies the required rate-of-angle-of-sideslip derivatives. According to Reference 9, only the vertical tail contributes significantly to these rate derivatives.

NOTE: All methods presented for the rate-of-sideslip derivatives are valid only for the subsonic speed regime. For other speed ranges the reader should consult Ref.9.

1. $C_{y_{\dot{\beta}}}$

The sideforce-due-to-rate-of-sideslip derivative, $C_{y_{\dot{\beta}}}$ may be estimated from:

$$C_{y_{\dot{\beta}}} = \qquad (10.46)$$

$$2(C_{L_{\alpha_v}})(d\sigma/d\beta)(S_v/S)(l_p\cos\alpha_f + z_p\sin\alpha_f)/b$$

where: $C_{L_{\alpha_v}}$ is found with the method indicated under Equation (10.28)

$$d\sigma/d\beta = \qquad (10.47)$$

$$(\sigma_{\beta_\alpha})\alpha_f + (\sigma_{\beta_\Gamma})(\Gamma/57.3) - (\sigma_{\beta_{\varepsilon_t}})\varepsilon_t + (\sigma_{\beta_{wf}})$$

where: σ_{β_α} is the sidewash contribution due to angle of attack. It is found from Figures 10.30.

α_f is the angle of attack of the fuselage

σ_{β_Γ} is the sidewash contribution due to wing dihedral. It is found from Figures 10.31.

Γ is the wing dihedral angle as defined in Figure 10.7.

$\sigma_{\beta_{\varepsilon_t}}$ is the sidewash contribution due to wing twist as obtained from Figures 10.32.

ε_t is the wing twist angle as shown in Figure 10.26.

$\sigma_{\beta_{wf}}$ is the sidewash effect due the fuselage as

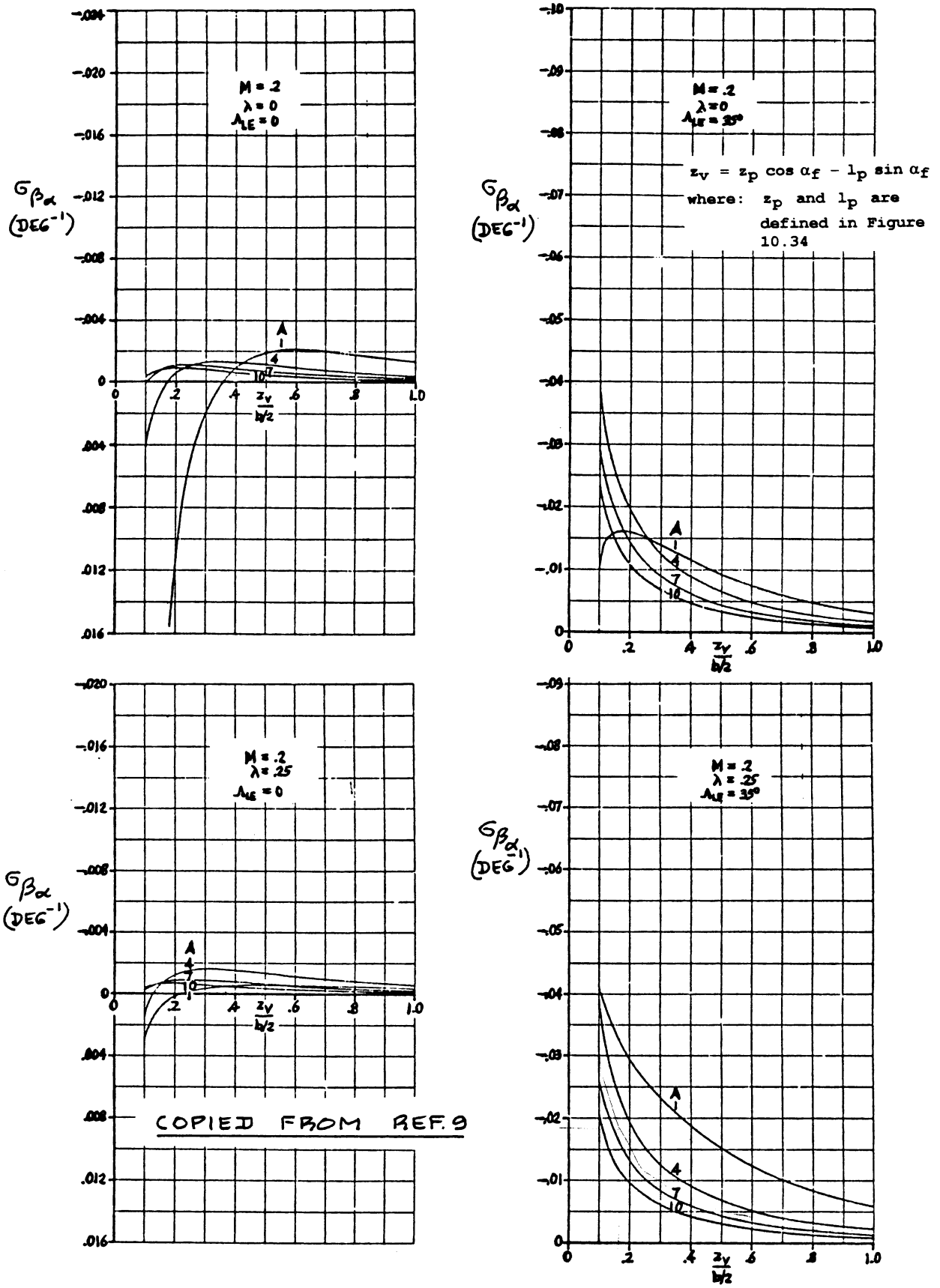

Figure 10.30a Sidewash Contribution due to Angle of Attack

$z_v = z_p \cos \alpha_f - l_p \sin \alpha_f$

where: z_p and l_p are defined in Figure 10.34

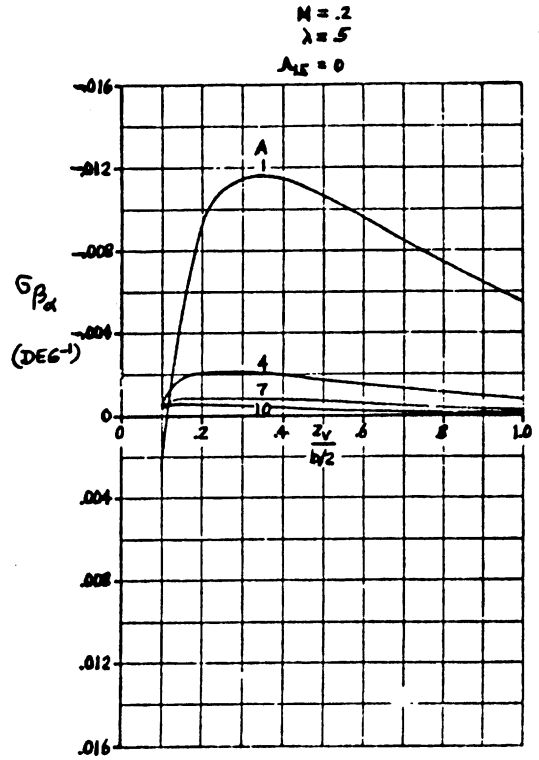

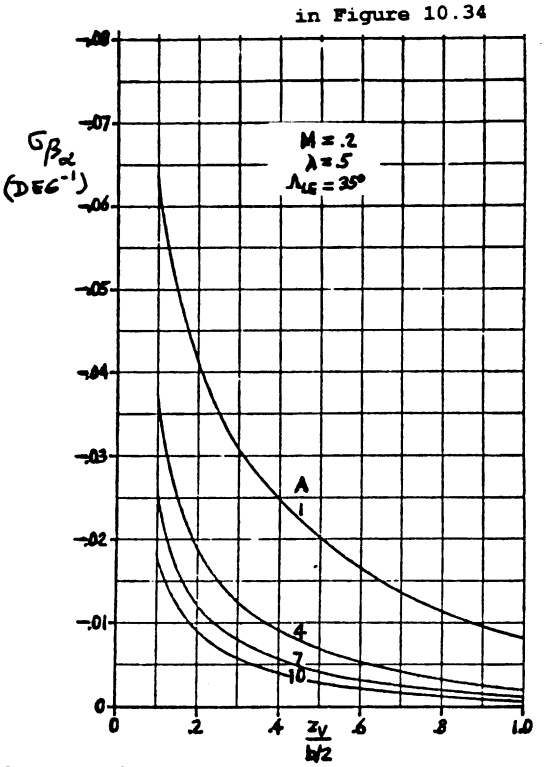

COPIED FROM REF. 9

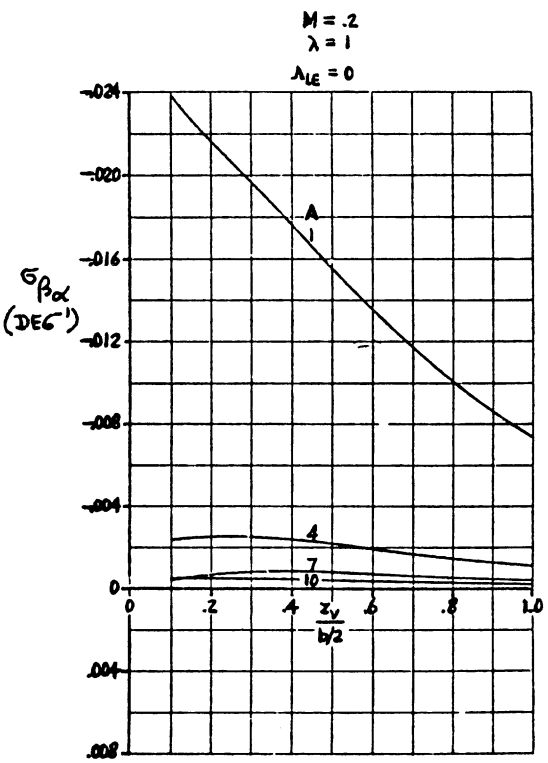

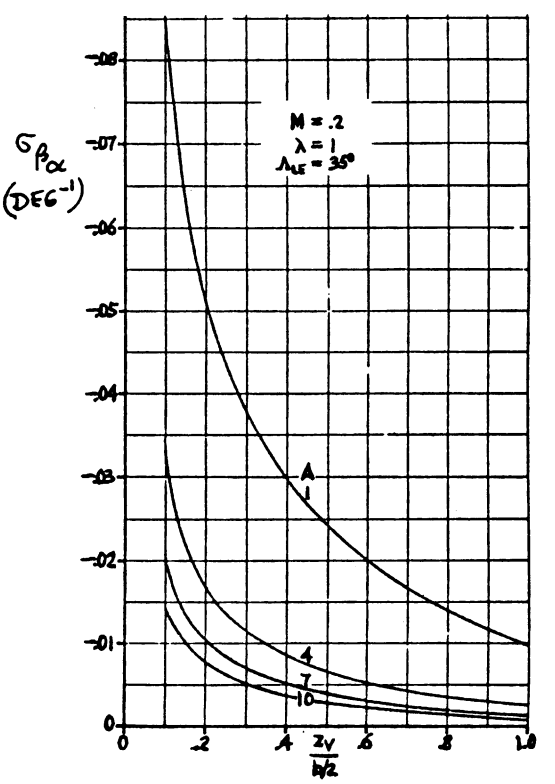

Figure 10.30b Sidewash Contribution due to Angle of Attack

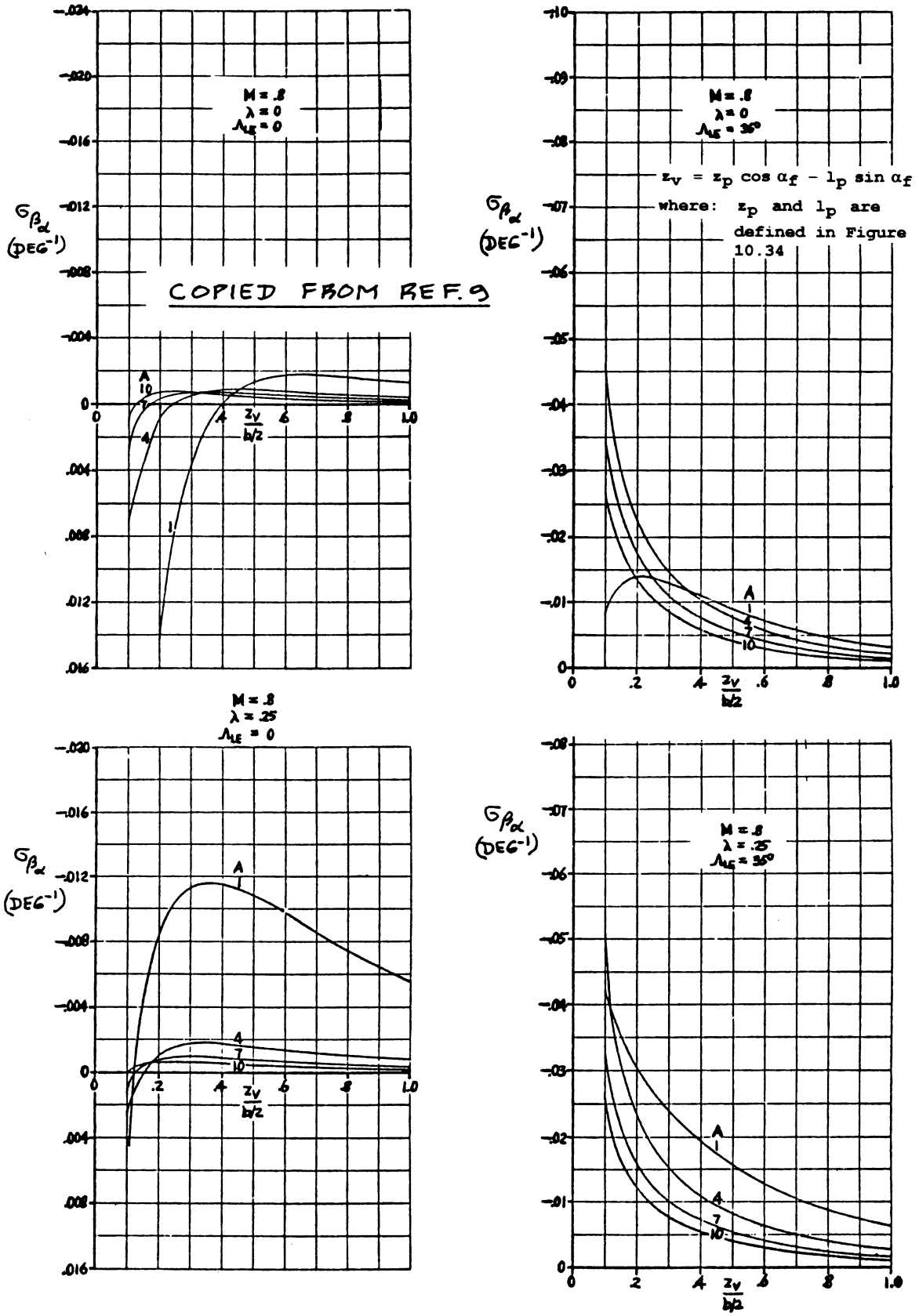

Figure 10.30c Sidewash Contribution due to Angle of Attack

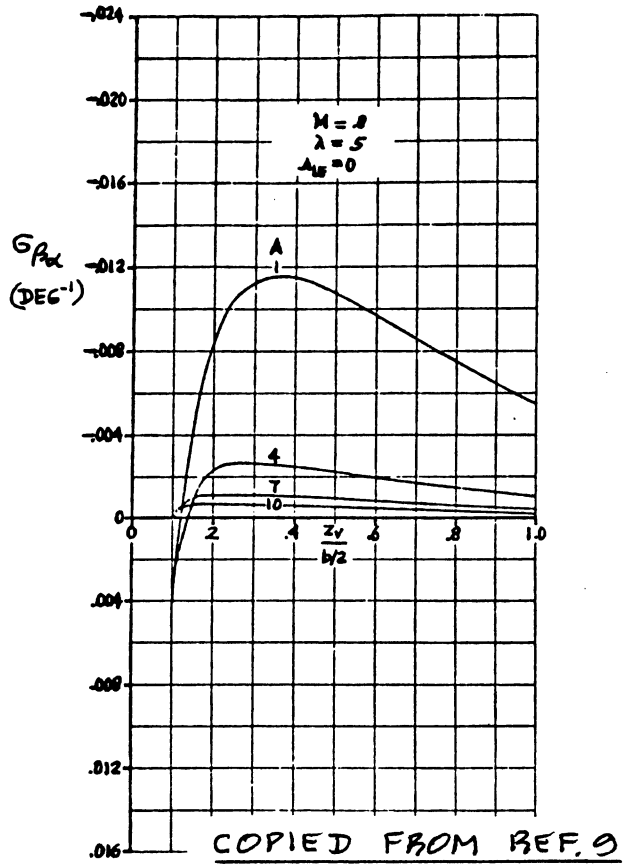

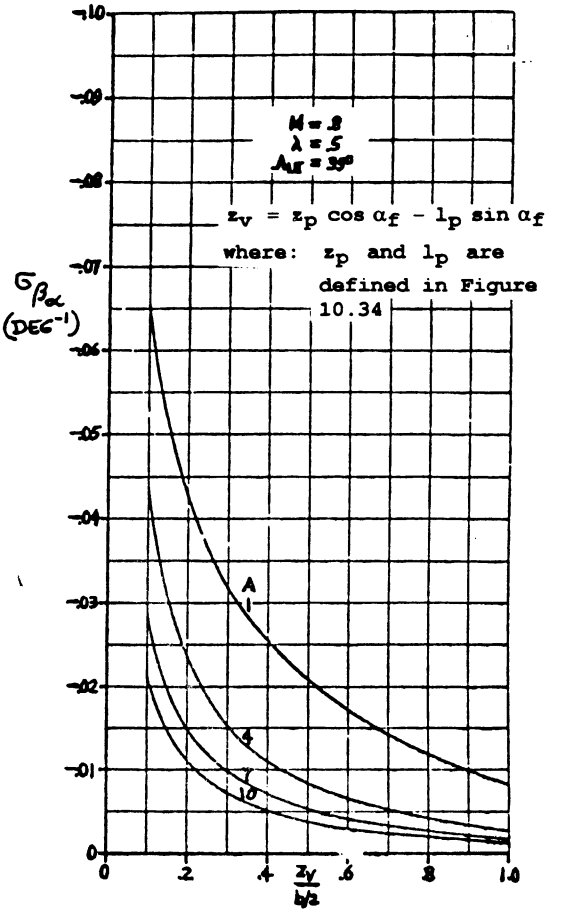

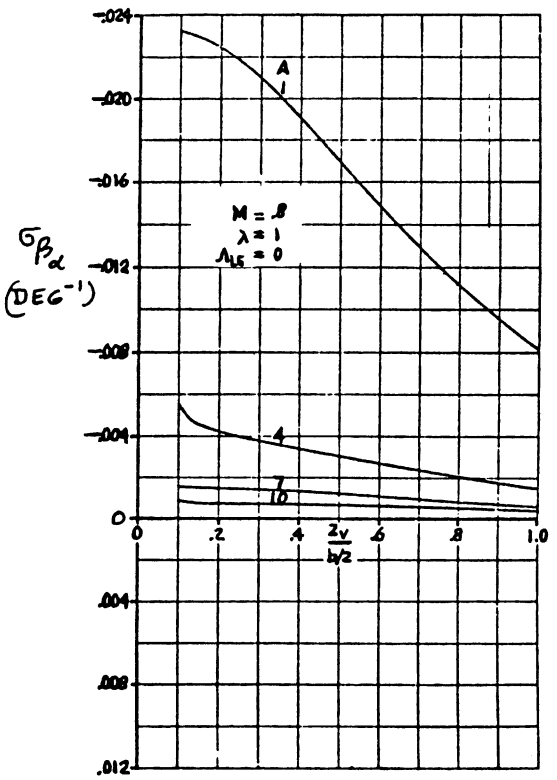

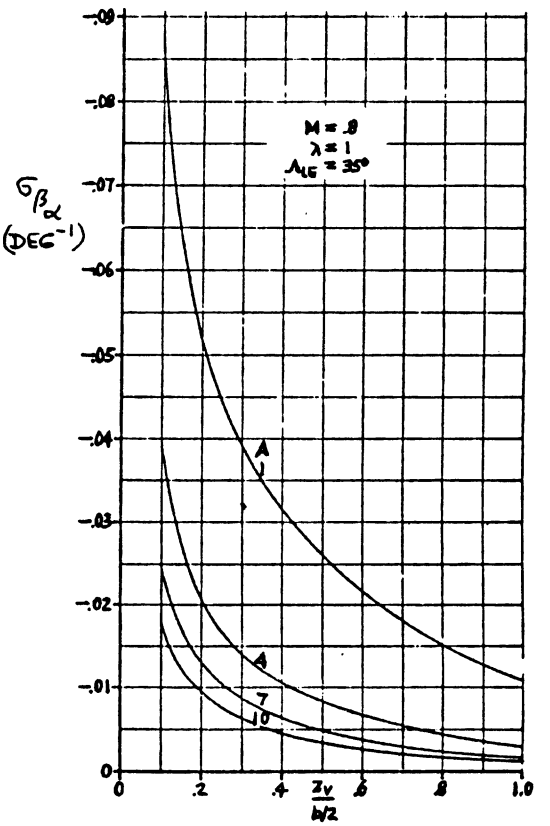

Figure 10.30d Sidewash Contribution due to Angle of Attack

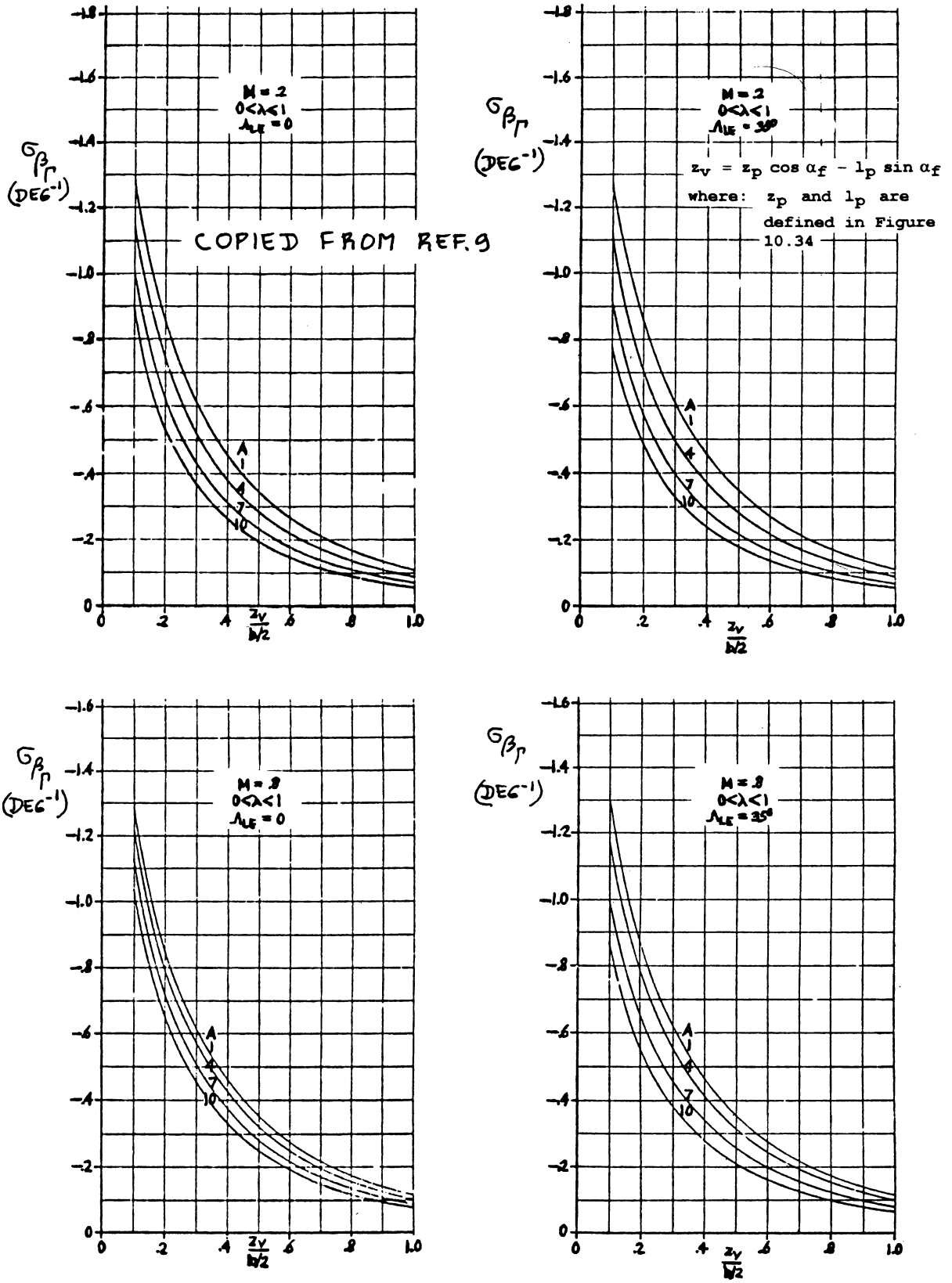

Figure 10.31 Sidewash Contribution due to Wing Dihedral

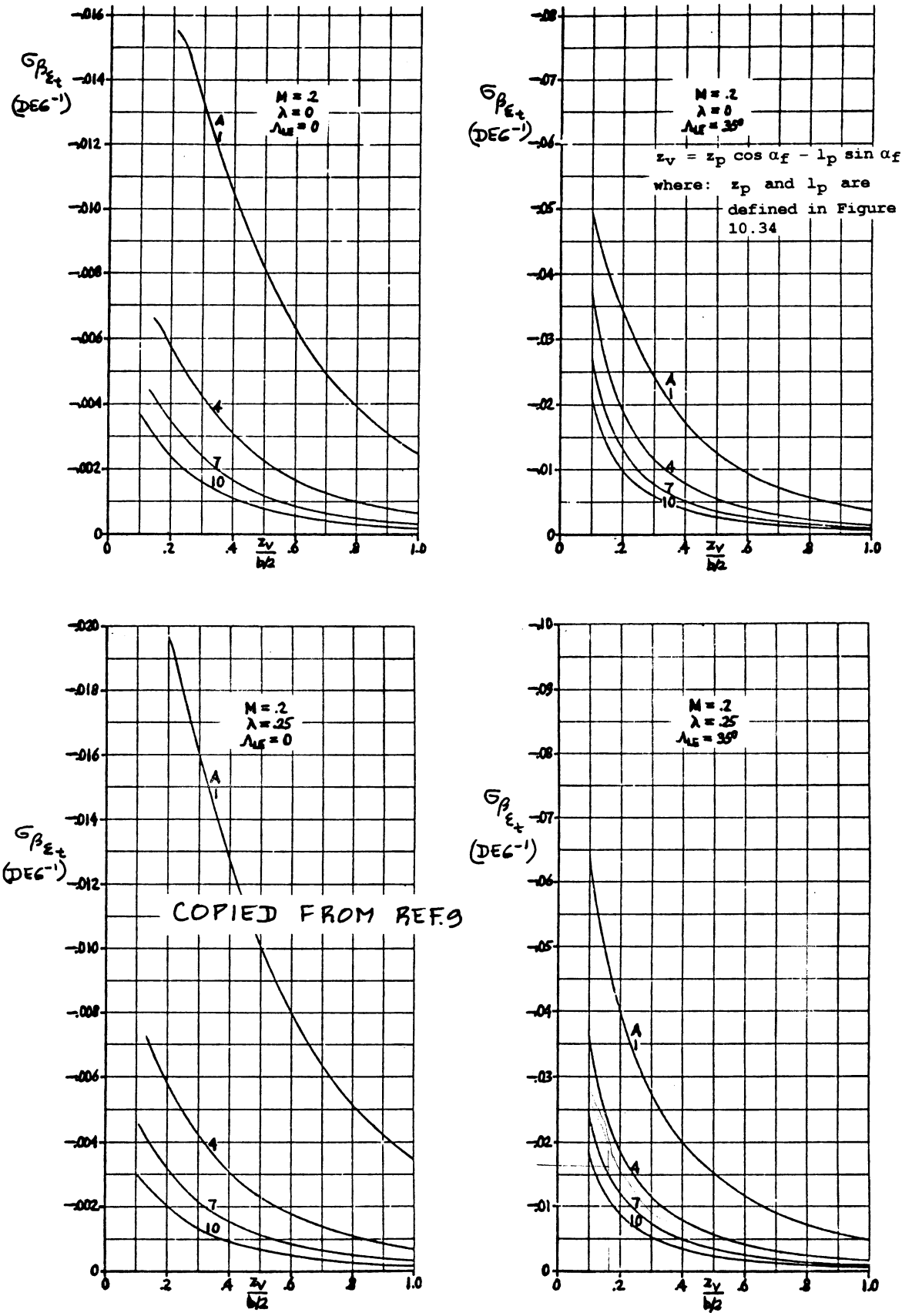

Figure 10.32a Sidewash Contribution due to Wing Twist

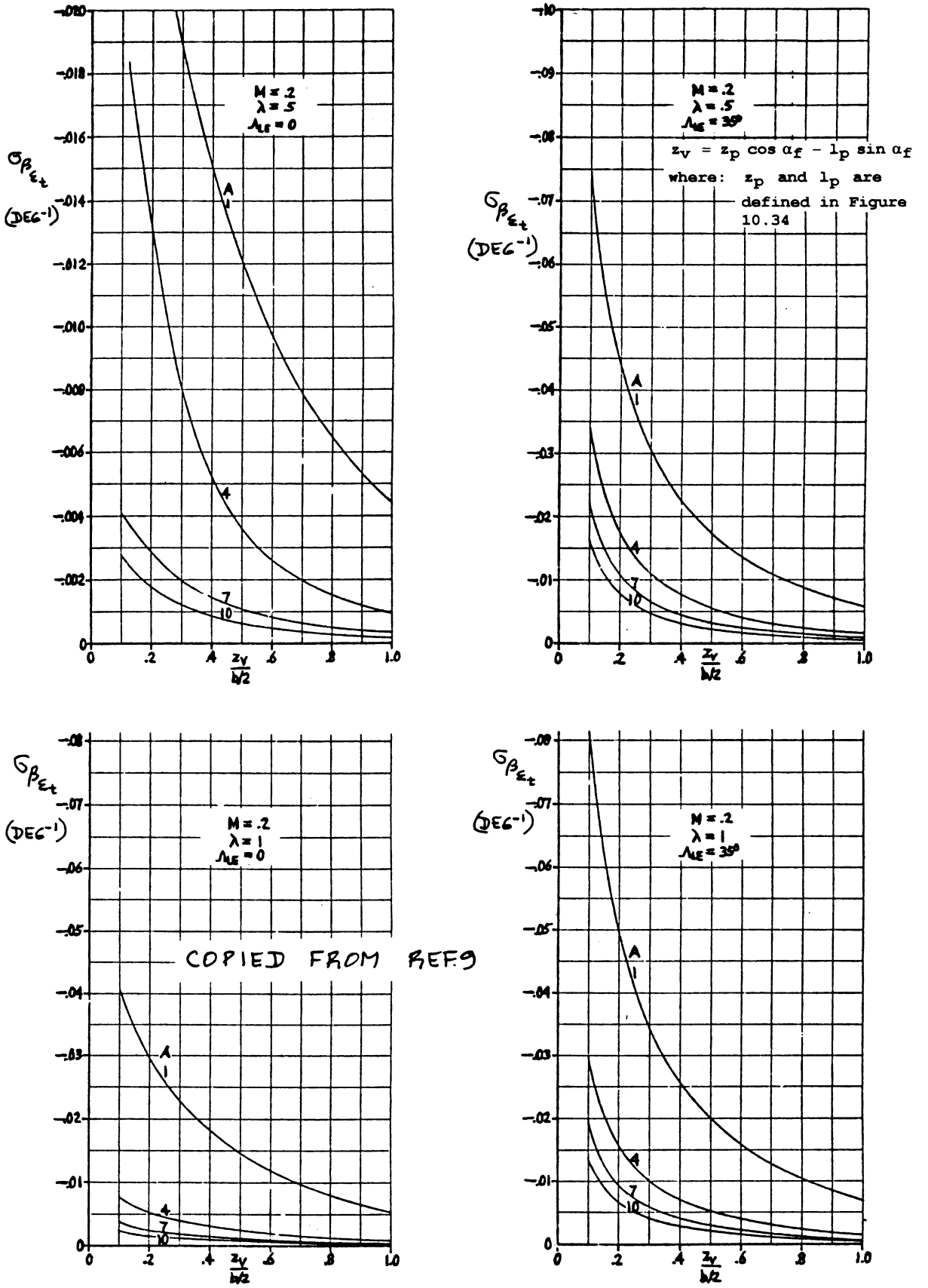

Figure 10.32b Sidewash Contribution due to Wing Twist

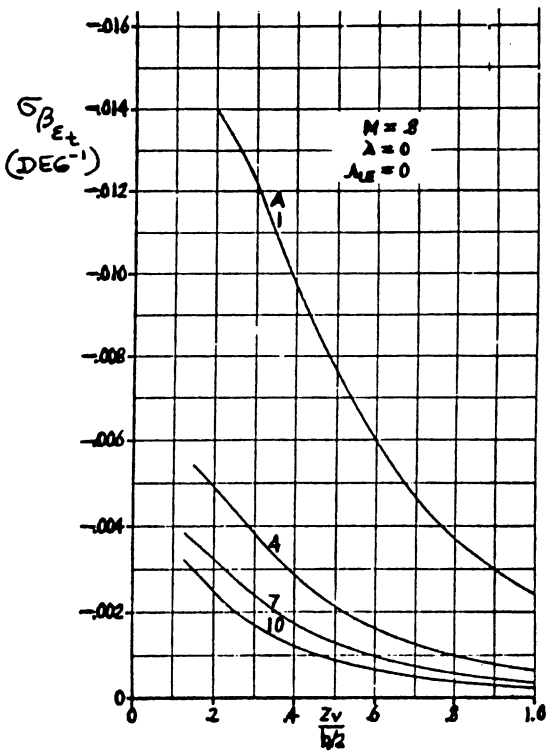

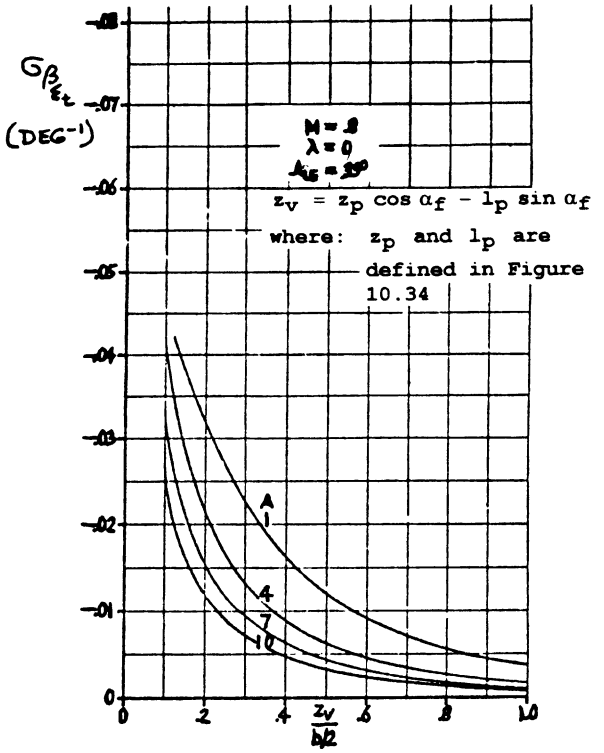

COPIED FROM REF.9

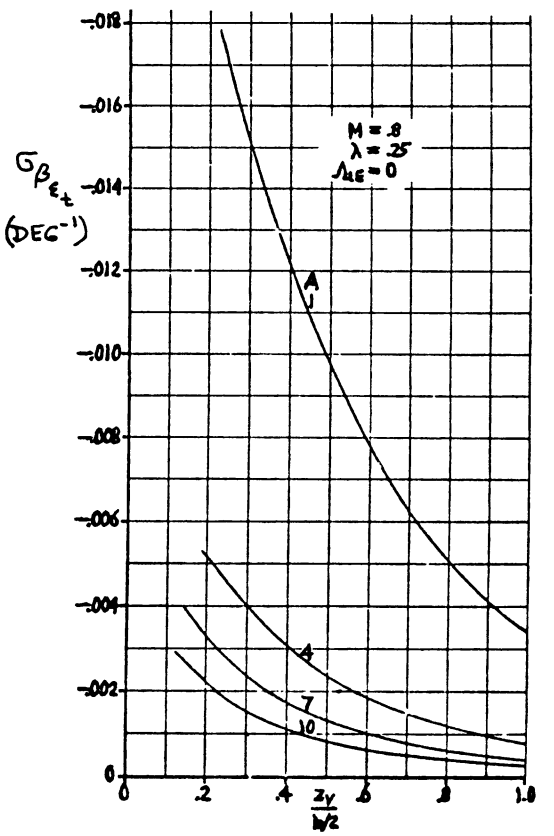

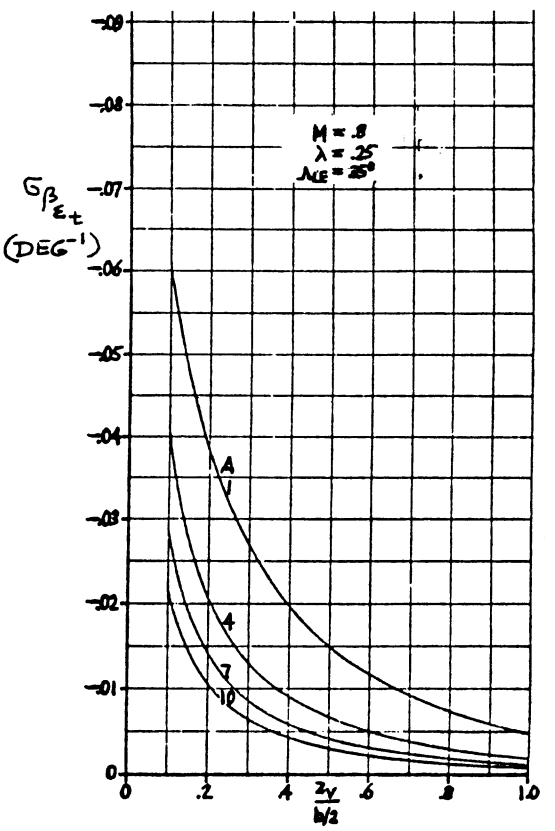

Figure 10.32c Sidewash Contribution due to Wing Twist

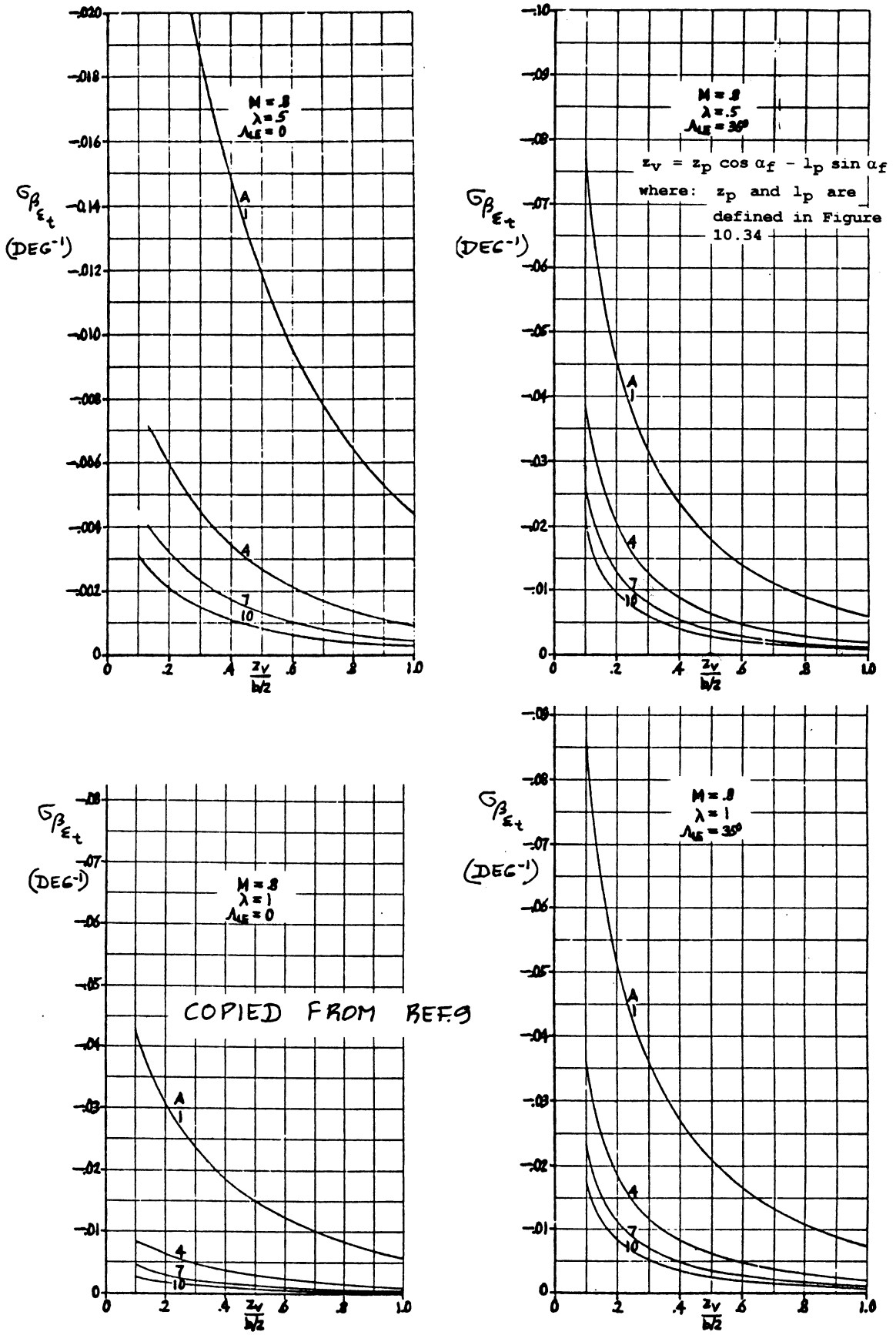

COPIED FROM REF 9

Figure 10.32d Sidewash Contribution due to Wing Twist

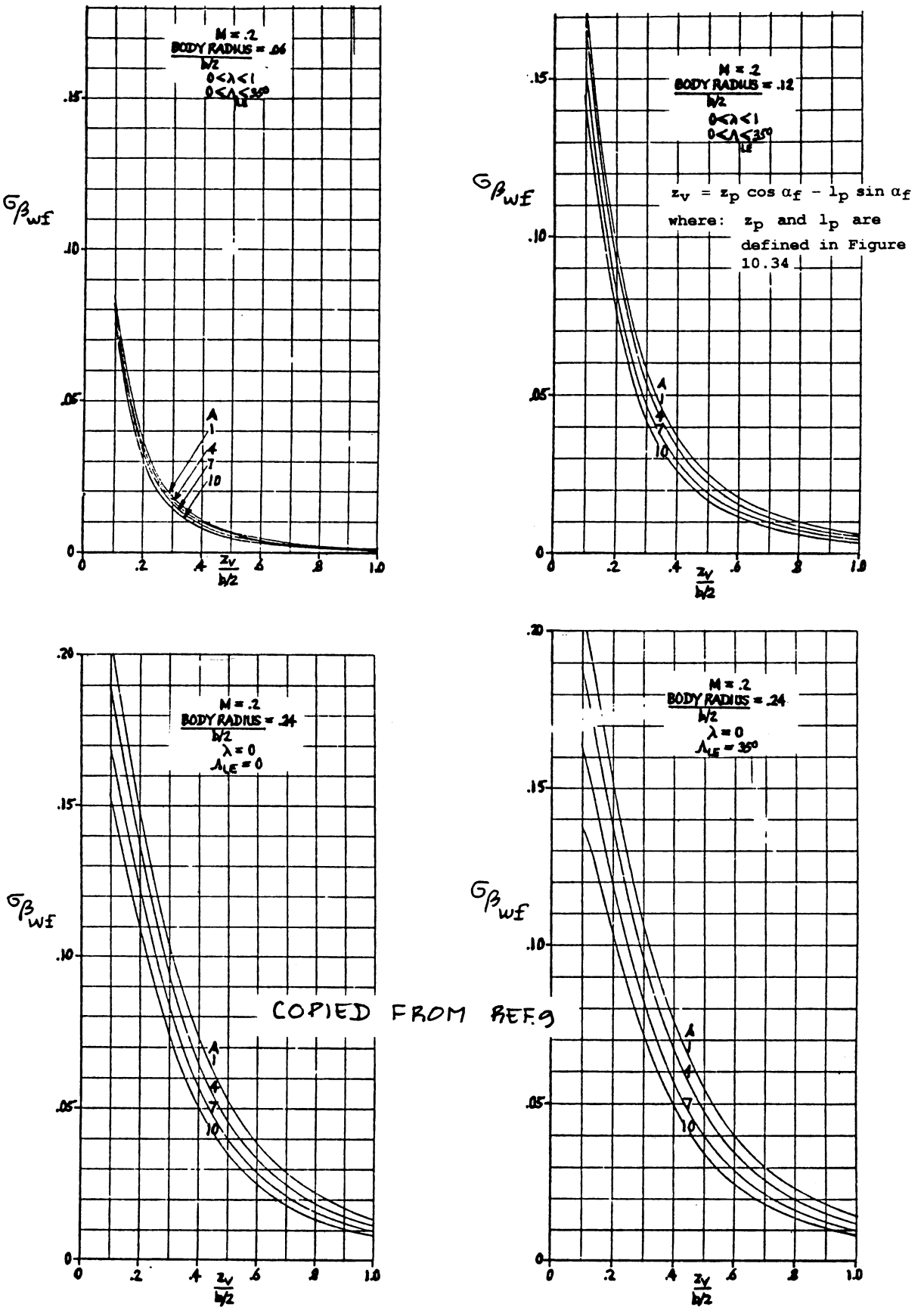

COPIED FROM REF.9

Figure 10.33a Sidewash Contribution due to the Fuselage

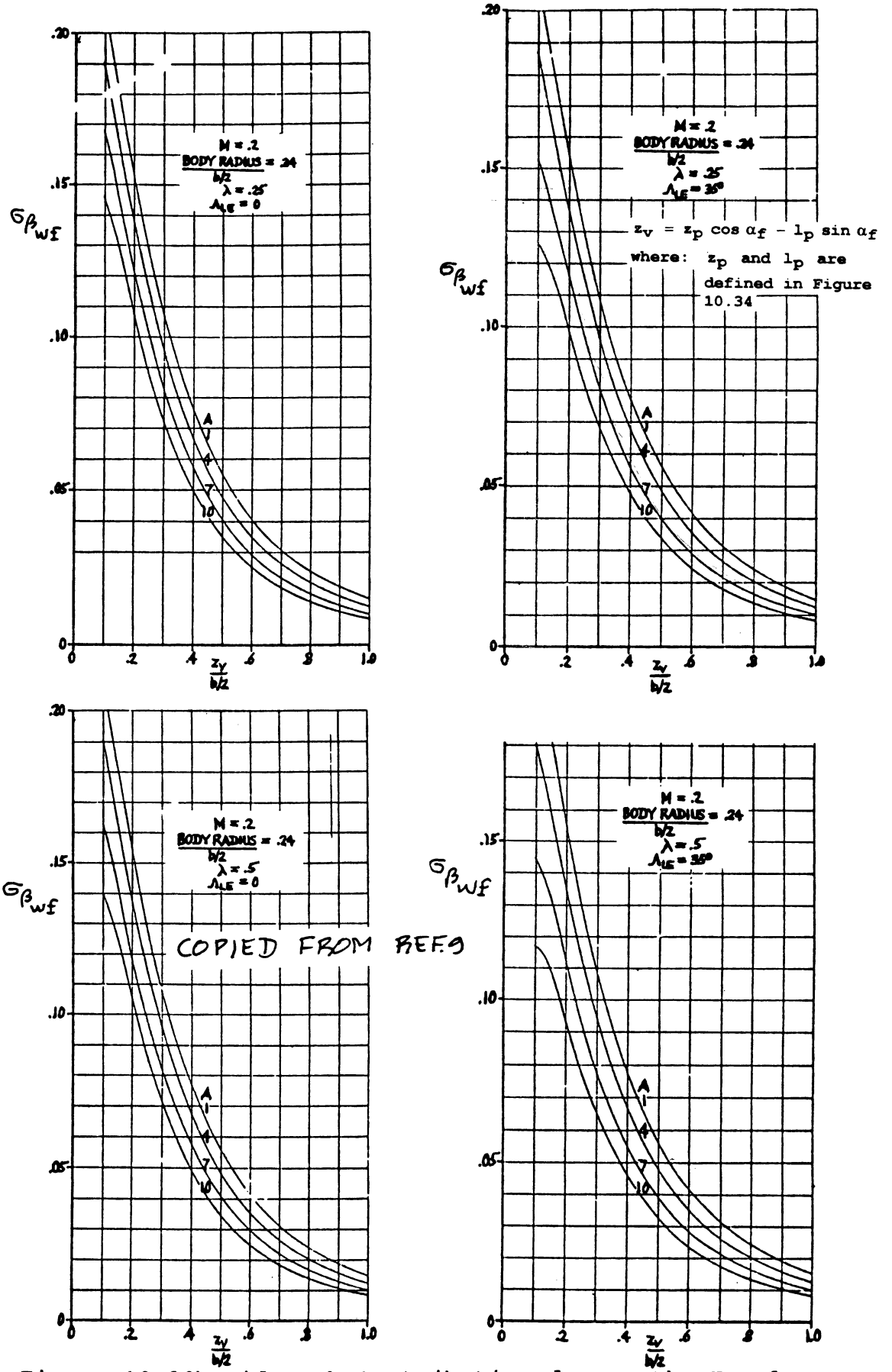

Figure 10.33b Sidewash Contribution due to the Fuselage

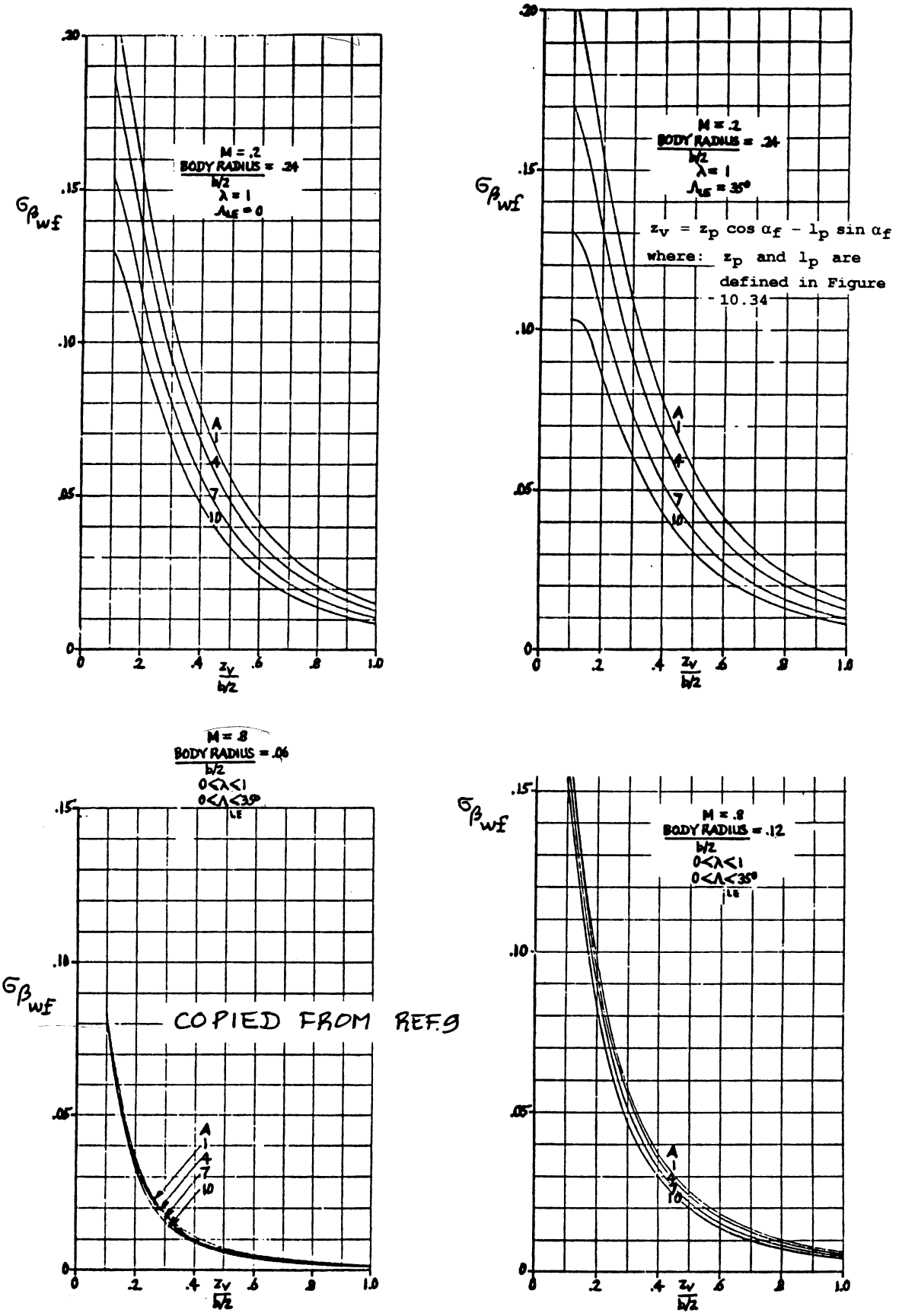

Figure 10.33c Sidewash Contribution due to the Fuselage

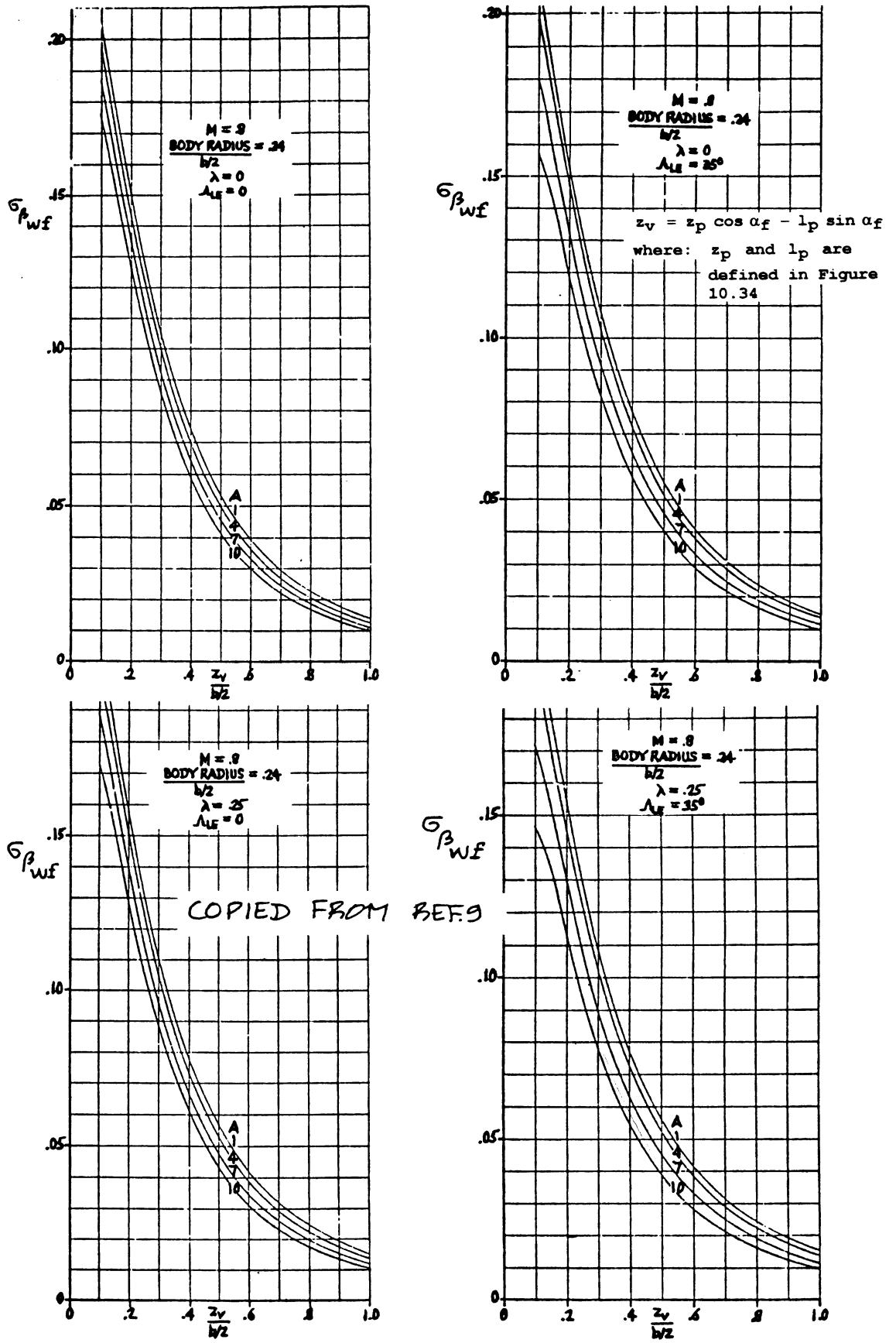

$z_v = z_p \cos \alpha_f - l_p \sin \alpha_f$

where: z_p and l_p are defined in Figure 10.34

COPIED FROM REF. 9

Figure 10.33d Sidewash Contribution due to the Fuselage

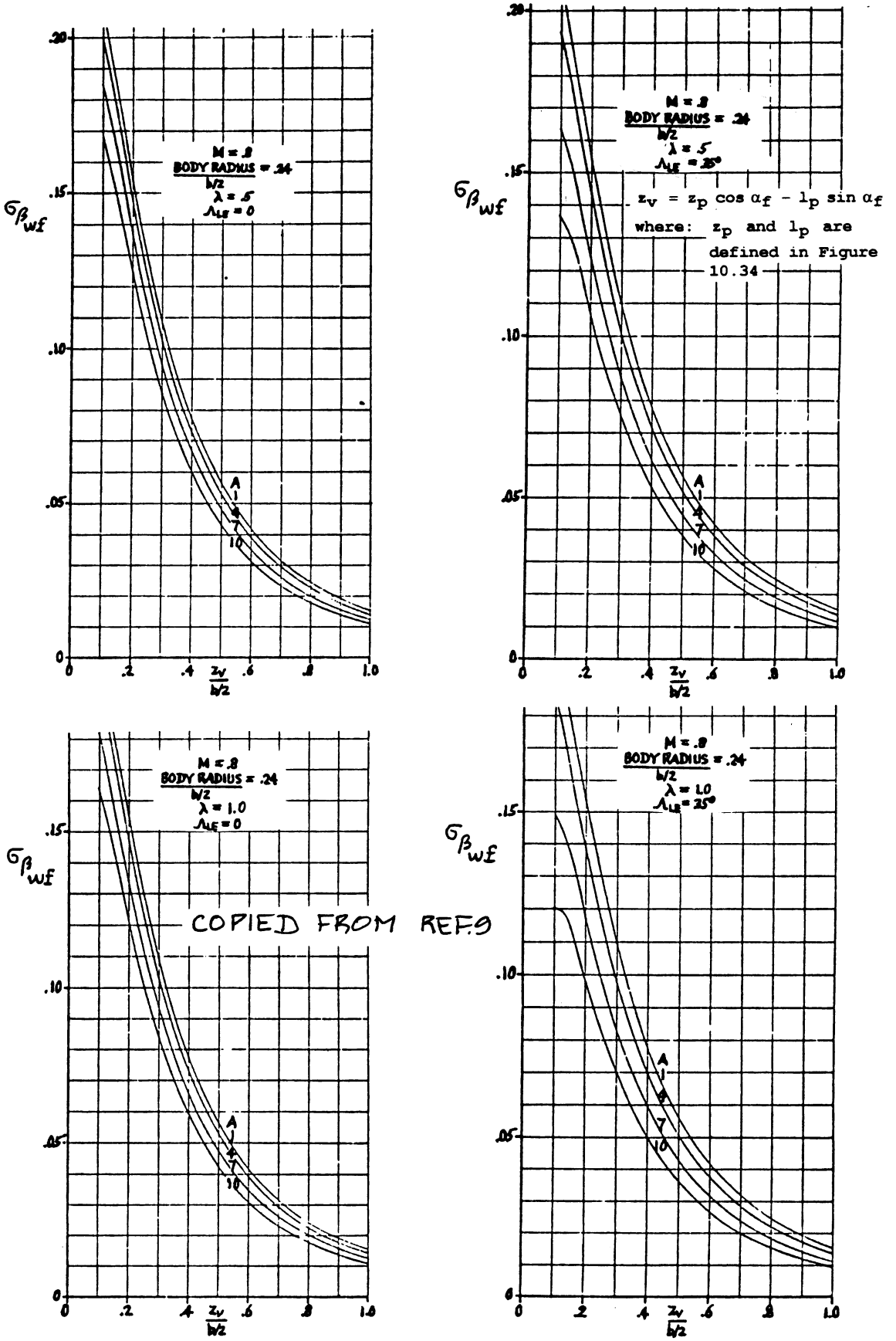

COPIED FROM REF.9

Figure 10.33e Sidewash Contribution due to the Fuselage

obtained from Figures 10.33. Note that the data are presented for a low wing as shown in Figure 10.9a. For a high wing (Fig.10.9b) this term becomes negative because z_w changes sign.

z_p and l_p are defined in Figure 10.34.

2.) $C_{l_{\dot{\beta}}}$

The rolling-moment-due-to-rate-of-sideslip derivative, $C_{l_{\dot{\beta}}}$ may be estimated from:

$$C_{l_{\dot{\beta}}} = C_{y_{\dot{\beta}}}(z_p \cos\alpha_f - l_p \sin\alpha_f)/b \qquad (10.48)$$

where: $C_{y_{\dot{\beta}}}$ is found from Eqn.(10.46)

3.) $C_{n_{\dot{\beta}}}$

The yawing-moment-due-to-rate-of-sideslip derivative, $C_{n_{\dot{\beta}}}$ may be estimated from:

$$C_{n_{\dot{\beta}}} = C_{y_{\dot{\beta}}}(l_p \cos\alpha_f + z_p \sin\alpha_f)/b \qquad (10.49)$$

where: $C_{y_{\dot{\beta}}}$ is found from Eqn.(10.46)

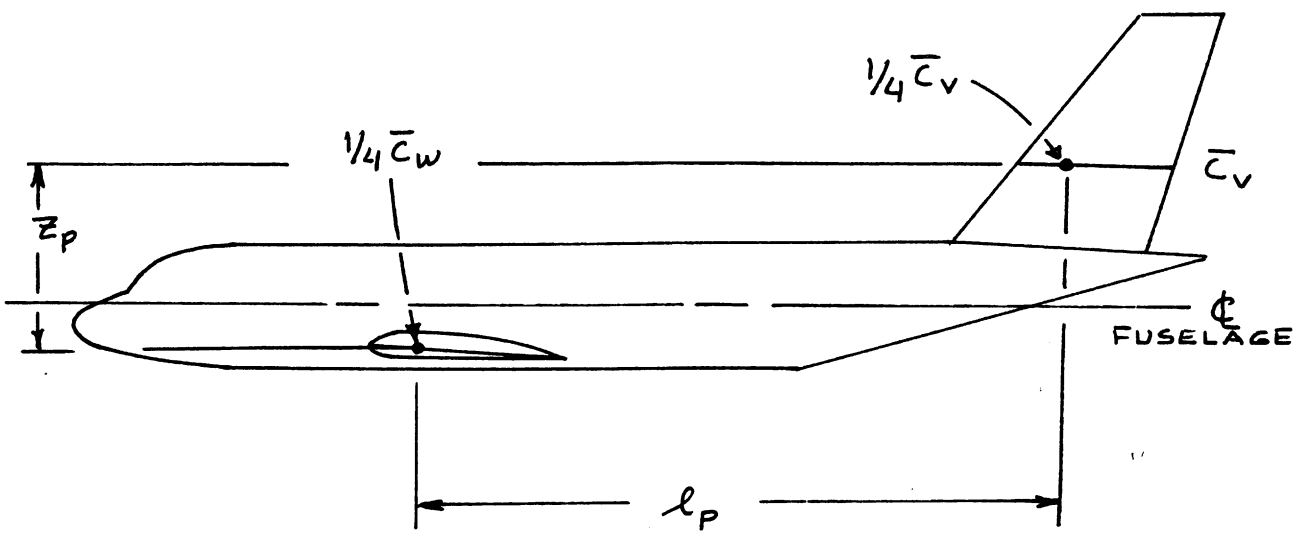

Figure 10.34 Definition of z_p and l_p in Eqn.(10.46)

10.2.6 Roll Rate Derivatives: C_{y_p}, C_{l_p} and C_{n_p}

Table 10.1 identifies the required roll rate derivatives.

NOTE: All methods presented for estimation of the roll rate derivatives apply only in the subsonic speed range. For other speed ranges Ref.9 should be used.

1.) C_{y_p}

The side-force-due-to-roll-rate derivative, C_{y_p} is primarily influenced by the vertical tail and may be determined from:

$$C_{y_p} = 2C_{y\beta_v}\left(z_v \cos\alpha - l_v \sin\alpha - z_v \right) / b + 3\sin\Gamma\left[1 - \left(4z / b \right)\sin\Gamma \right]\left(C_{l_p}\right)_{\substack{\Gamma=0 \\ C_L=0}} \quad (10.50)$$

where: $C_{y\beta_v}$ is found from Eqns (10.28) or (10.32).

z_v and l_v are defined in Figure 10.27.

z is the vertical distance between the airplane center of gravity and the wing root quarter chord point.

$$\left(C_{l_p} \right)_{\substack{\Gamma=0 \\ C_L=0}} = (\kappa / \beta)\left[\left(\beta\, C_{l_p} \right) / \kappa \right]_{C_L=0} \quad (10.50a)$$

2.) C_{l_p}

The rolling-moment-due-to-roll-rate derivative, C_{l_p} (also called the roll damping derivative) may be found from:

$$C_{l_p} = C_{l_{p_w}} + C_{l_{p_h}} + C_{l_{p_v}} \quad (10.51)$$

where: the wing contribution is given by:

$$C_{l_{p_w}} = \left(\beta C_{l_p} / \kappa \right)_{C_L=0} \left(\kappa/\beta \right) * *\left\{ \left(C_{L_{\alpha_w}}\right)_{C_L} / \left(C_{L_{\alpha_w}}\right)_{C_L=0} \right\} * \left\{ \left(C_{l_p}\right)_{\Gamma} / \left(C_{l_p}\right)_{\Gamma=0} \right\} + \left(\Delta C_{l_p}\right)_{drag} \quad (10.52)$$

where: $\left(\beta C_{l_p} / \kappa \right)_{C_L=0}$ is the roll damping parameter at zero lift which is obtained from Figure 10.35

Note: the parameter β in Eqn. (10.52) is NOT sideslip! In this case: $\beta = \left(1 - M^2 \right)^{1/2}$

β : EQN. (10.53)

κ : EQN. (10.54)

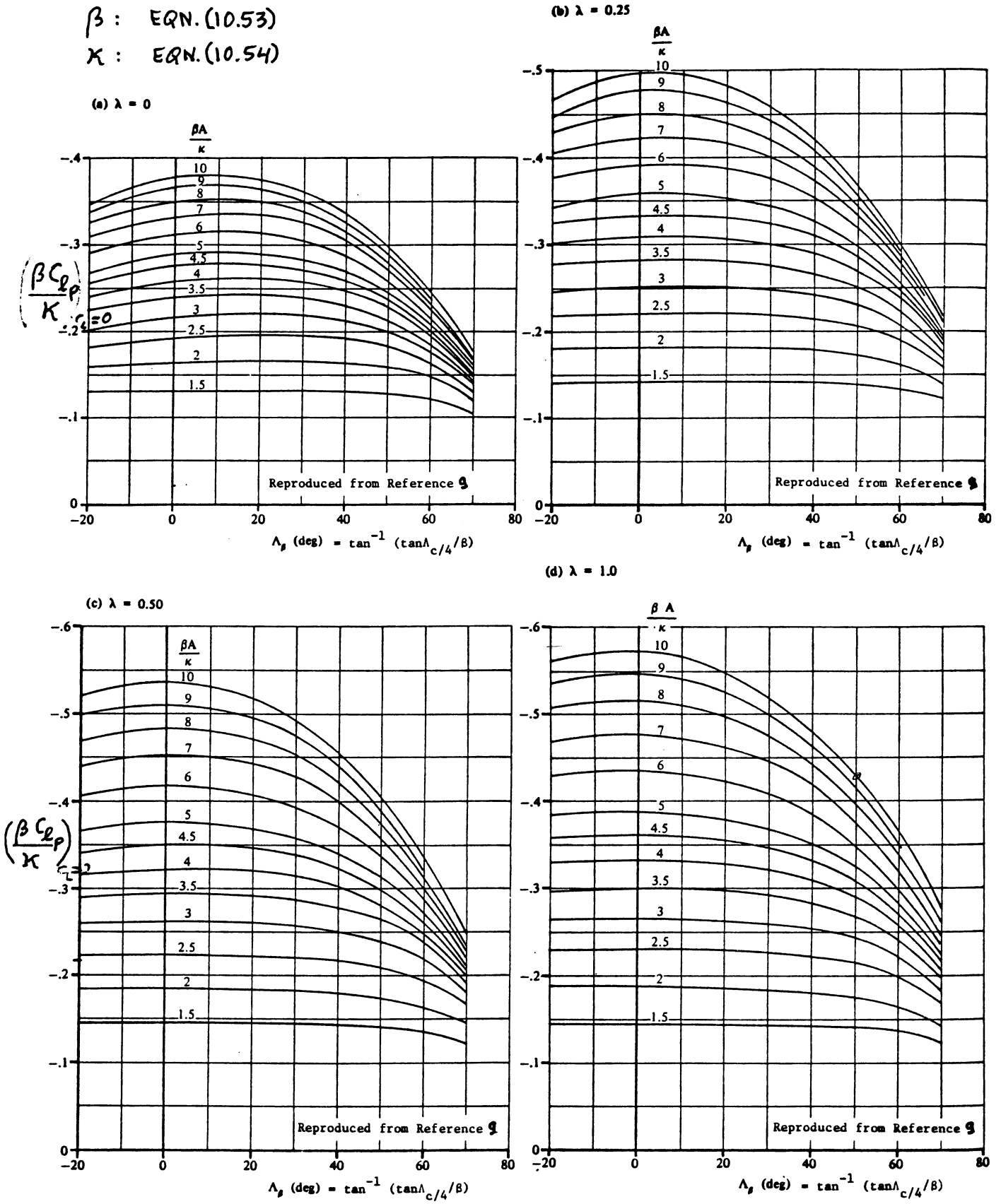

Figure 10.35 Roll Damping Parameter

$$k = (C_{l_\alpha})_M \beta/2\pi \qquad (10.54)$$

$(C_{L_{\alpha_w}})_{C_L=0}$ is the wing lift-curve slope at zero lift as obtained from Equation (8.22).

$(C_{L_\alpha})_{C_L}$ is the wing lift-curve slope at any lift coefficient. It is obtained as the local slope of the wing C_L versus α curve as obtained from 8.1.3.5 or from 8.1.4.4.

$\{(C_{l_p})_\Gamma/(C_{l_p})_{\Gamma=0}\}$ is the dihedral effect parameter which may be obtained from:

$$\{(C_{l_p})_\Gamma/(C_{l_p})_{\Gamma=0}\} =$$

$$\{1 - (4z_w/b)\sin\Gamma + 12(z_w/b)^2(\sin\Gamma)^2\} \qquad (10.55)$$

with: Γ defined in Figure 10.7

z_w defined in Figure 10.9

The wing drag contribution to roll damping is given by:

$$(\Delta C_{l_p})_{drag} = \qquad (10.56)$$

$$\{(C_{l_p})_{C_{D_L}}/(C_{L_w})^2\}(C_{L_w})^2 - 0.125C_{D_{o_w}}$$

with: $\{(C_{l_p})_{C_{D_L}}/(C_L)^2\}$, the drag-due-to-lift roll damping parameter as found from Figure 10.36

C_{L_w} is the wing lift coefficient as obtained from:

$$C_{L_w} = C_{L_1} - C_{L_h} - C_{L_c} \qquad (10.57)$$

In preliminary design it is acceptable to set:

$$C_{L_1} = C_{L_w} \qquad (10.58)$$

$C_{D_{o_w}}$ is the wing zero-lift drag coefficient as obtained from Chapter 4.

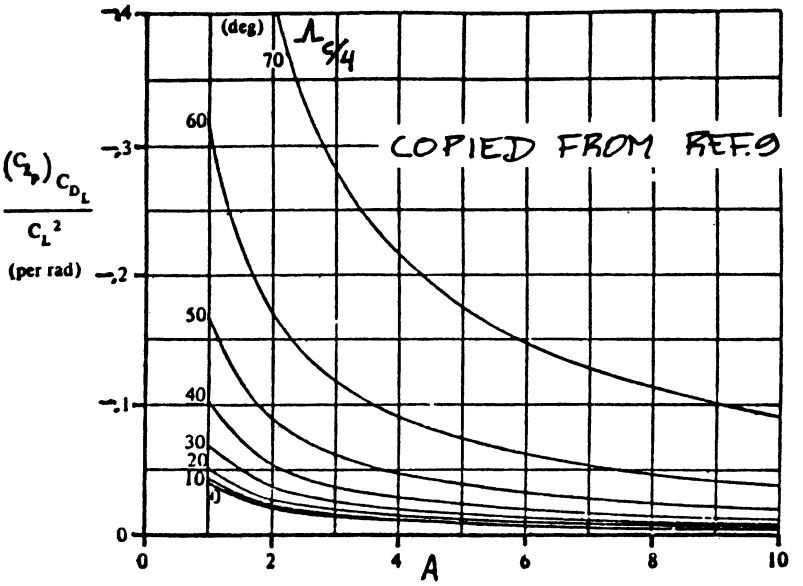

Figure 10.36 Drag-due-to-lift Roll Damping Parameter

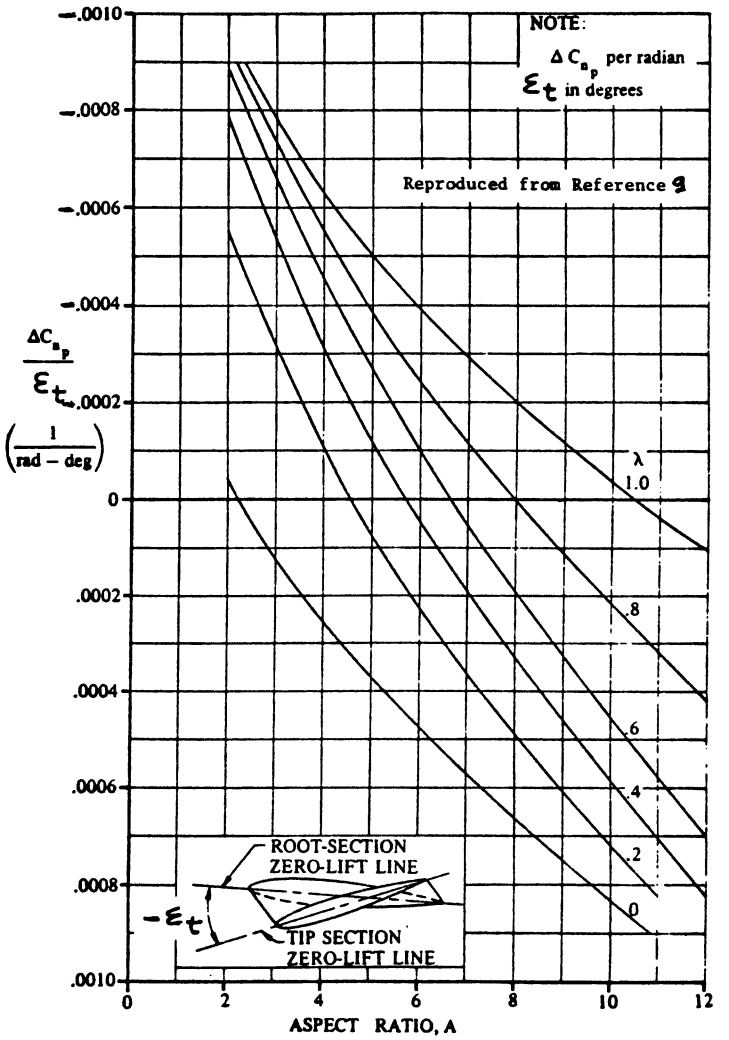

Figure 10.37 Effect of Wing Twist on C_{n_p}

The fuselage contribution to C_{l_p} tends to be negligible for airplanes for which $d_f/b<0.3$. Most airplane configurations satisfy this criterion.

the horizontal tail contribution is given by:

$$C_{l_{p_h}} = 0.5(C_{l_p})_h(S_h/S)(b_h/b)^2 \qquad (10.59)$$

where: $(C_{l_p})_h$ is the roll-damping derivative of the horizontal tail based on its own reference geometry. It is obtained from Eqn.(10.52) with appropriate substitution of horizontal tail parameters for wing parameters.

the vertical tail contribution is given by:

$$C_{l_{p_v}} = \frac{2}{b^2}\left|(z_v\cos\alpha - l_v\sin\alpha)[z_v\cos\alpha - l_v\sin\alpha - z_v]\right| C_{Y_{\beta_v}} \qquad (10.60)$$

where: z_v and l_v are defined in Figure 10.27

$C_{Y_{\beta_v}}$ is found from Eqn.(10.28) or from Eqn.(10.32)

3.) C_{n_p}

The yawing-moment-due-to-roll-rate derivative, C_{n_p} may be determined from:

$$C_{n_p} = C_{n_{p_w}} + C_{n_{p_v}} \qquad (10.61)$$

where: the wing contribution is given by:

$$C_{n_{p_w}} = \{(C_{n_p}/C_L)_{\substack{C_L=0\\M}}\}C_{L_w} + (C_{n_p}/\varepsilon_t)\varepsilon_t + \left[\{\Delta C_{n_p}/\{(\alpha_{\delta_f})(\delta_f)\}\}(\alpha_{\delta_f})\delta_f \right. \qquad (10.62)$$

with:

$$\left(\frac{C_{n_p}}{C_L}\right)_{\substack{C_L=0\\M}} = \left(\frac{A+4\cos\Lambda_{c/4}}{AB+4\cos\Lambda_{c/4}}\right)\left[\frac{AB+\frac{1}{2}(AB+\cos\Lambda_{c/4})\tan^2\Lambda_{c/4}}{A+\frac{1}{2}(A+\cos\Lambda_{c/4})\tan^2\Lambda_{c/4}}\right]\left(\frac{C_{n_p}}{C_L}\right)_{\substack{C_L=0\\M=0}} \qquad (10.63)$$

where: $B = \{1 - M^2(\cos\Lambda_{c/4})^2\}^{1/2}$ (10.64)

and with:

$$\left(\frac{C_{n_p}}{C_L}\right)_{\substack{C_L=0 \\ M=0}} = -\frac{1}{6}\,\frac{A+6(A+\cos\Lambda_{c/4})\left(\frac{\bar{x}}{c}\,\frac{\tan\Lambda_{c/4}}{A} + \frac{\tan^2\Lambda_{c/4}}{12}\right)}{A+4\cos\Lambda_{c/4}} \quad (\text{rad}^{-1}) \qquad (10.65)$$

C_{n_p}/ε_t is the wing twist contribution as given by Figures 10.37.

ε_t is the wing twist angle defined in Fig.10.37.

$(\Delta C_{n_p}/\alpha_{\delta_f}\delta_f)$ is the contribution due to symmetrical flap deflection as found from Figures 10.38.

$$\alpha_{\delta_f} = \Delta c_l/(c_{l_\alpha}\delta_f) \qquad (10.66)$$

with: Δc_l determined from 8.1.2.1 for the type of flap used

c_{l_α} is the airfoil (flaps-up) lift-curve-slope as found from 8.1.1.2

δ_f is the flap deflection employed

<u>the vertical tail contribution</u> is given by:

$$C_{n_{p_v}} = \qquad (10.67)$$

$$-(2/b^2)(l_v\cos\alpha + z_v\sin\alpha)(z_v\cos\alpha - l_v\sin\alpha - z_v)C_{y_{\beta_v}}$$

where: z_v and l_v are defined in Figure 10.27

$C_{y_{\beta_v}}$ is found from Eqns (10.28) or (10.32)

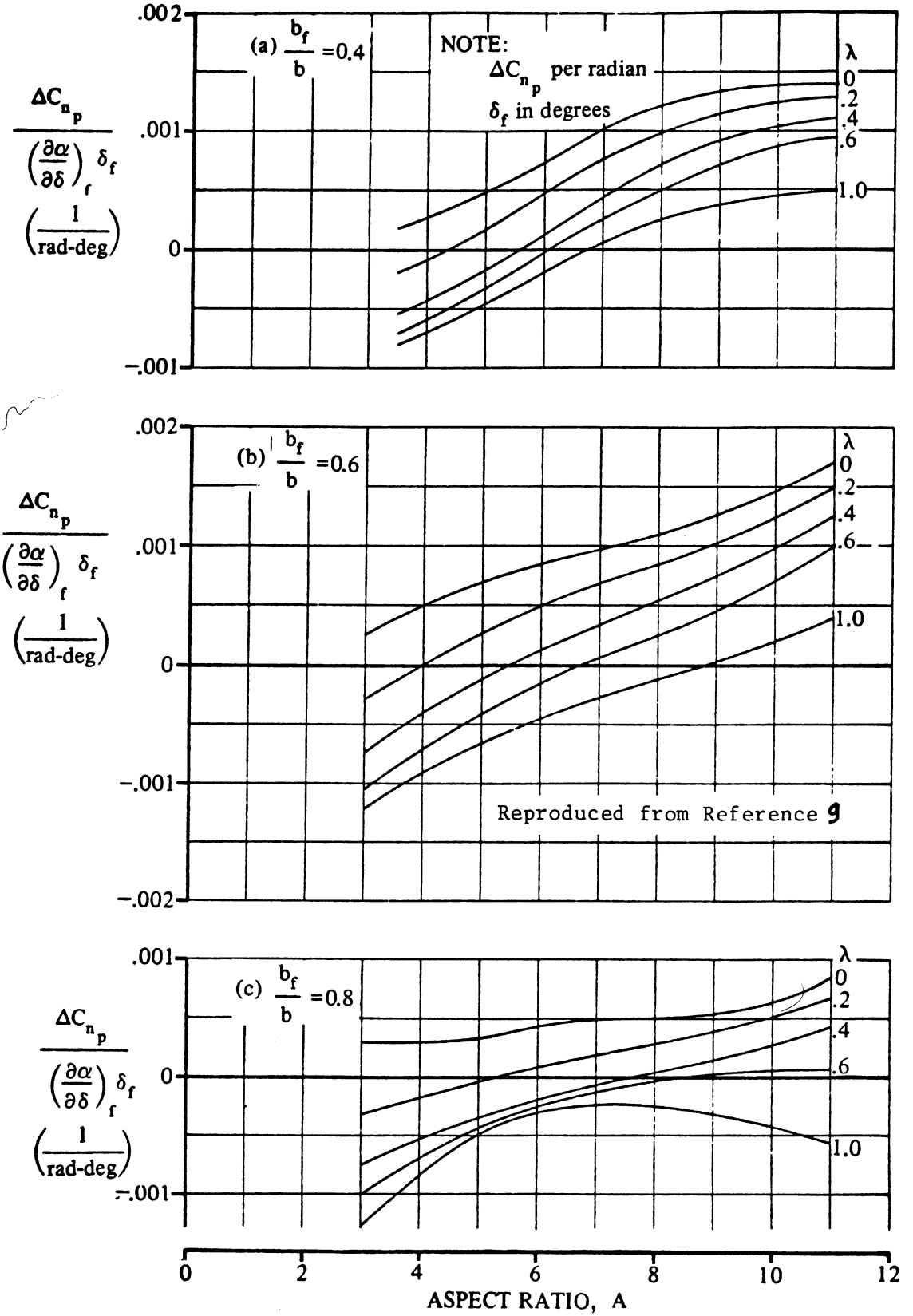

Figure 10.38 Effect of Symmetrical Flap Deflection on C_{n_p}

10.2.7 Pitch Rate Derivatives: C_{D_q}, C_{L_q} and C_{m_q}

Table 10.1 identifies the required pitch rate derivatives.

NOTE: All methods presented for the pitch rate derivatives are valid only for the subsonic speed regime. For other speed ranges the reader should consult Ref.9.

1.) C_{D_q}

The drag-due-to-pitch-rate derivative, C_{D_q} is negligible for almost all airplanes:

$$C_{D_q} = 0 \tag{10.68}$$

2.) C_{L_q}

The lift-due-to-pitch-rate derivative, C_{L_q} may be estimated from:

$$C_{L_q} = C_{L_{q_w}} + C_{L_{q_h}} + C_{L_{q_c}} \tag{10.69}$$

where: the wing contribution is given by:

$$C_{L_{q_w}} = \{(A + 2\cos\Lambda_{c/4})/(AB + 2\cos\Lambda_{c/4})\}(C_{L_{q_w}})_{M=0} \tag{10.70}$$

where: B is given by Eqn.(10.64)

$$(C_{L_{q_w}})_{M=0} = (0.5 + 2x_w/\bar{c})C_{L_{\alpha_w}} \tag{10.71}$$

with: x_w defined in Figure 10.39

$C_{L_{\alpha_w}}$ is the wing lift curve slope as found from Section 8.1.3.2.

the horizontal tail contribution is given by:

$$C_{L_{q_h}} = 2(C_{L_{\alpha_h}})\eta_h \bar{V}_h \qquad (10.72)$$

where: $C_{L_{\alpha_h}}$ is found from Eqn.(8.22) with appropriate substitution of horizontal tail parameters for wing parameters.

η_h is found from 8.1.5.2

$\bar{V}_h$ is found from Eqn.(10.23)

the canard contribution is found from:

$$C_{L_{q_c}} = -2(C_{L_{\alpha_c}})\eta_c \bar{V}_c \qquad (10.73)$$

where: $C_{L_{\alpha_c}}$ is found from Eqn.(8.22) with appropriate substitution of canard parameters for wing parameters.

η_c is found from 8.1.5.2

$$\bar{V}_c = (\bar{x}_{ac_c} + \bar{x}_{cg})S_c/S \qquad (10.74)$$

where: x_{ac_c} and x_{cg} are shown in Fig.10.39. Note that x_{ac_c} is positive, while x_{cg} is negative as shown!!!

3.) C_{m_q}

The pitching-moment-due-to-pitch-rate derivative, C_{m_q} (also called pitch damping derivative) may be estimated from:

$$C_{m_q} = C_{m_{q_w}} + C_{m_{q_h}} + C_{m_{q_c}} \qquad (10.75)$$

where: the wing contribution is found from:

$$C_{m_{q_w}} = C_{m_{q_{w/at\ M=0}}} \left\{\frac{A^3\tan^2\Lambda_{c/4}}{AB + 6\cos\Lambda_{c/4}} + \frac{3}{B}\right\}/\left\{\frac{A^3\tan^2\Lambda_{c/4}}{A + 6\cos\Lambda_{c/4}} + 3\right\} \qquad (10.76)$$

with:

$$(C_{m_{q_w}})_{M=0} = \qquad (10.77)$$

$$= -K_w C_{l_{\alpha_w}} \cos\Lambda_{c/4}\left[\frac{A\{2(x_w/\bar{c})^2 + 0.5(x_w/\bar{c})\}}{(A + 2\cos\Lambda_{c/4})} + \frac{A^3\tan^2\Lambda_{c/4}}{24(A + 6\cos\Lambda_{c/4})} + \frac{1}{8}\right]$$

where: K_w is found from Figure 10.40, x_w from Fig. 10.39.

the horizontal tail contribution is given by:

$$C_{m_{q_h}} = -2(C_{L_{\alpha_h}})\eta_h \bar{V}_h (\bar{x}_{ac_h} - \bar{x}_{cg}) \qquad (10.78)$$

where: x_{ac_h} is defined in Figure 10.39

All other quantities were defined before!

the canard contribution is given by:

$$C_{m_{q_c}} = -2(C_{L_{\alpha_c}})\eta_c \bar{V}_c (\bar{x}_{ac_c} + \bar{x}_{cg}) \qquad (10.79)$$

where: all quantities have been defined before!

NOTE: many airplanes have pylon mounted nacelles. These pylons contribute to the pitch rate derivatives in the same manner as any empennage surface.

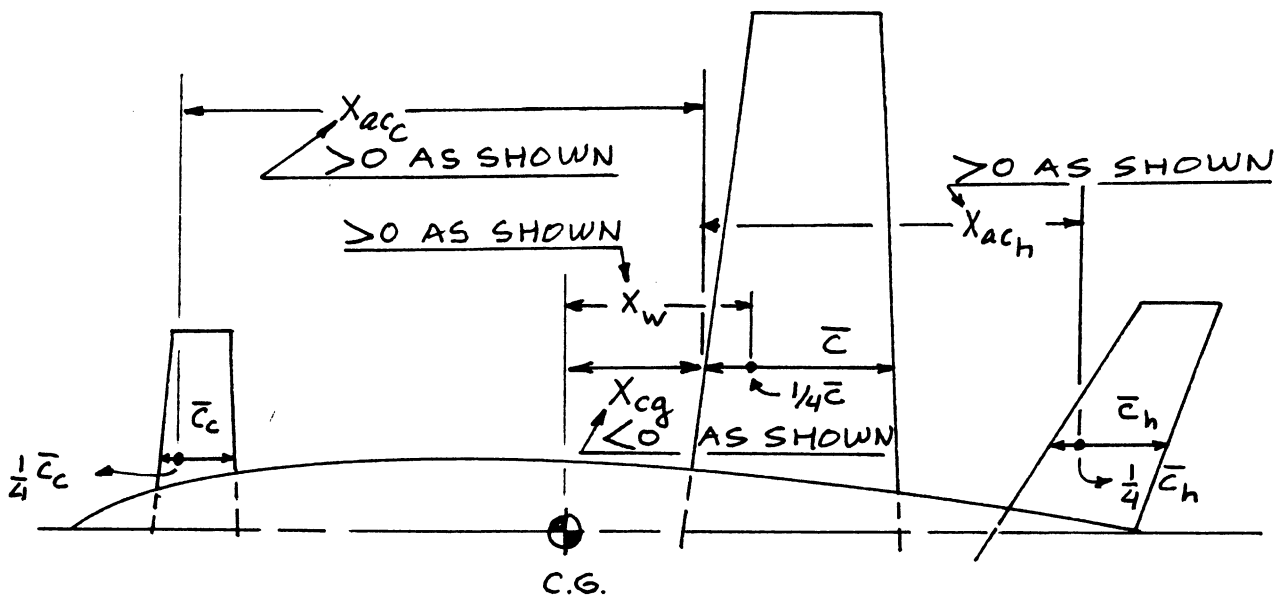

Figure 10.39 Definition of Geometric Parameters

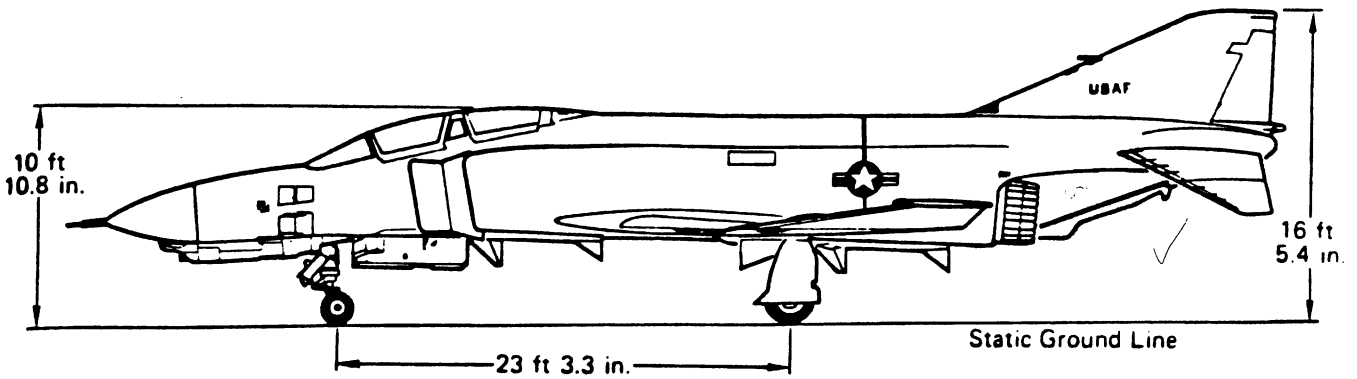

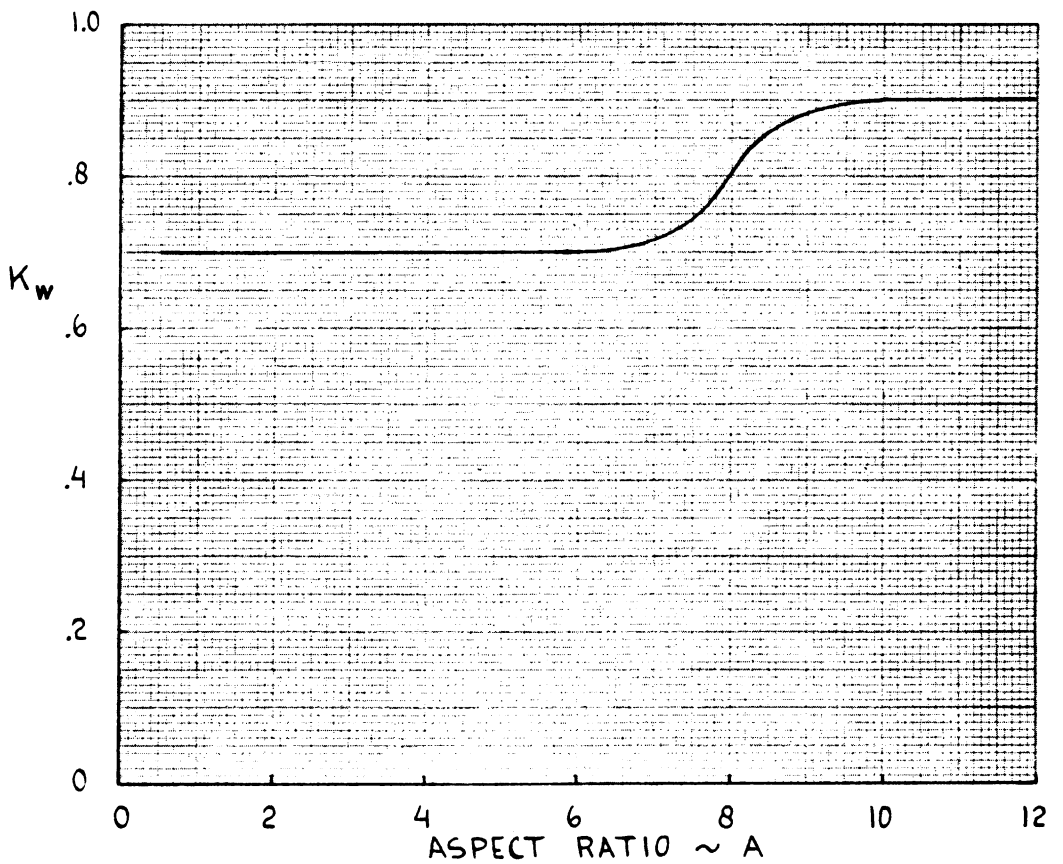

Figure 10.40 Correction Constant for Wing Contribution to Pitch Damping

10.2.8 Yaw Rate Derivatives: C_{y_r}, C_{l_r} and C_{n_r}

Table 10.1 identifies the required yaw rate derivatives.

NOTE: All methods presented for the yaw rate derivatives are valid only for the subsonic speed regime. For other speed ranges the reader should consult Ref.9.

1.) C_{y_r}

The side-force-due-to-yaw-rate derivative, C_{y_r} is primarily influenced by the vertical tail and may be determined from:

$$C_{y_r} = -2(C_{y_{\beta_v}})(l_v \cos\alpha + z_v \sin\alpha)/b \qquad (10.80)$$

where: $C_{y_{\beta_v}}$ is found from Eqns (10.28) or (10.32).

l_v and z_v are defined in Figure 10.27.

2.) C_{l_r}

The rolling-moment-due-to-yaw-rate derivative, C_{l_r} may be estimated from:

$$C_{l_r} = C_{l_{r_w}} + C_{l_{r_v}} \qquad (10.81)$$

where: the wing contribution is found from:

$$C_{l_{r_w}} = (C_{L_w})(C_{l_r}/C_L)_{\substack{C_L=0 \\ M}} + (\Delta C_{l_r}/\Gamma)\Gamma +$$

$$+ (\Delta C_{l_r}/\varepsilon_t)\varepsilon_t + (\Delta C_{l_r}/\alpha_{\delta_f}\delta_f)(\alpha_{\delta_f})\delta_f \qquad (10.82)$$

where: $(C_{l_r})_{\substack{C_L=0 \\ M}}$, the slope of the rolling moment due to roll rate at zero lift is found from:

$$\left(\frac{C_{\ell_r}}{C_L}\right)_{\substack{C_L=0 \\ M}} = \frac{1 + \frac{A(1-B^2)}{2B(AB+2\cos\Lambda_{c/4})} + \frac{AB+2\cos\Lambda_{c/4}}{AB+4\cos\Lambda_{c/4}} \frac{\tan^2\Lambda_{c/4}}{8}}{1 + \frac{A+2\cos\Lambda_{c/4}}{A+4\cos\Lambda_{c/4}} \frac{\tan^2\Lambda_{c/4}}{8}} \left(\frac{C_{\ell_r}}{C_L}\right)_{\substack{C_L=0 \\ M=0}} \qquad (10.83)$$

with B determined by Eqn.(10.64)

and $(C_{l_r}/C_L)_{C_L=0}$ is the slope of the low-speed rolling moment due to yaw rate at zero lift found from Figure 10.41.

C_{L_w} is the wing lift coefficient as in Eqn.(10.57) or (10.58)

$$(\Delta C_{l_r}/\Gamma) = 0.083(\pi A \sin\Lambda_{c/4})/(A + 4\cos\Lambda_{c/4}) \quad (10.84)$$

Γ is defined in Figure 10.7

$\Delta C_{l_r}/\varepsilon_t$ is the increment in C_{l_r} due to twist and may be determined from Figure 10.42

ε_t is the wing twist angle defined in Figure 10.42

$\Delta C_{l_r}/\alpha_{\delta_f}\delta_f$ is the effect of symmetric flap deflection on the rolling moment due to roll rate and is found from Figure 10.43.

α_{δ_f} is found from Eqn.(10.66)

δ_f is the flap deflection used

<u>the vertical tail contribution is found from:</u>

$$C_{l_{r_v}} = \quad (10.85)$$

$$-(2/b^2)(l_v\cos\alpha + z_v\sin\alpha)(z_v\cos\alpha - l_v\sin\alpha)C_{y_{\beta_v}}$$

where: z_v and l_v are defined in Figure 10.27

$C_{y_{\beta_v}}$ is found from Eqn.(10.28) or (10.32)

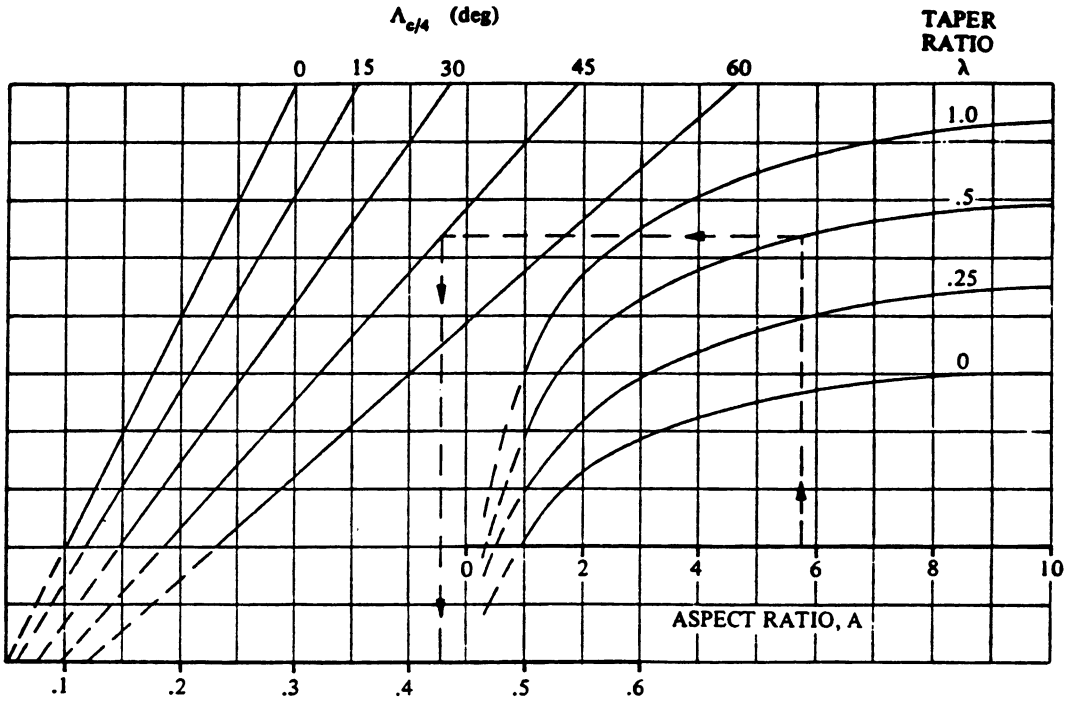

Figure 10.41 Wing Rolling Moment due to Yaw Rate Derivative: Lifting Effect

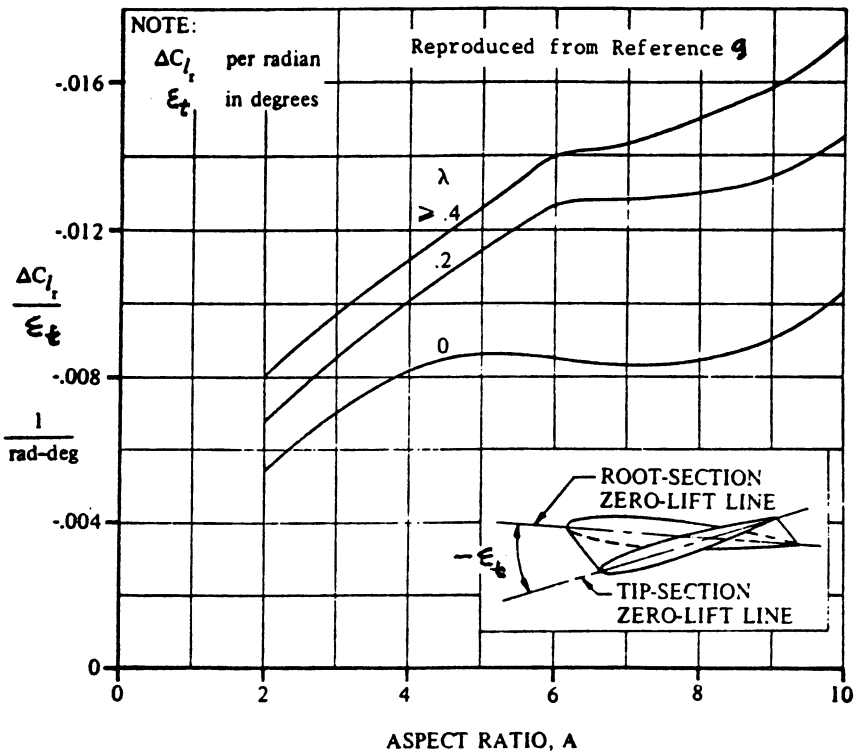

Figure 10.42 Effect of Wing Twist on C_{l_r}

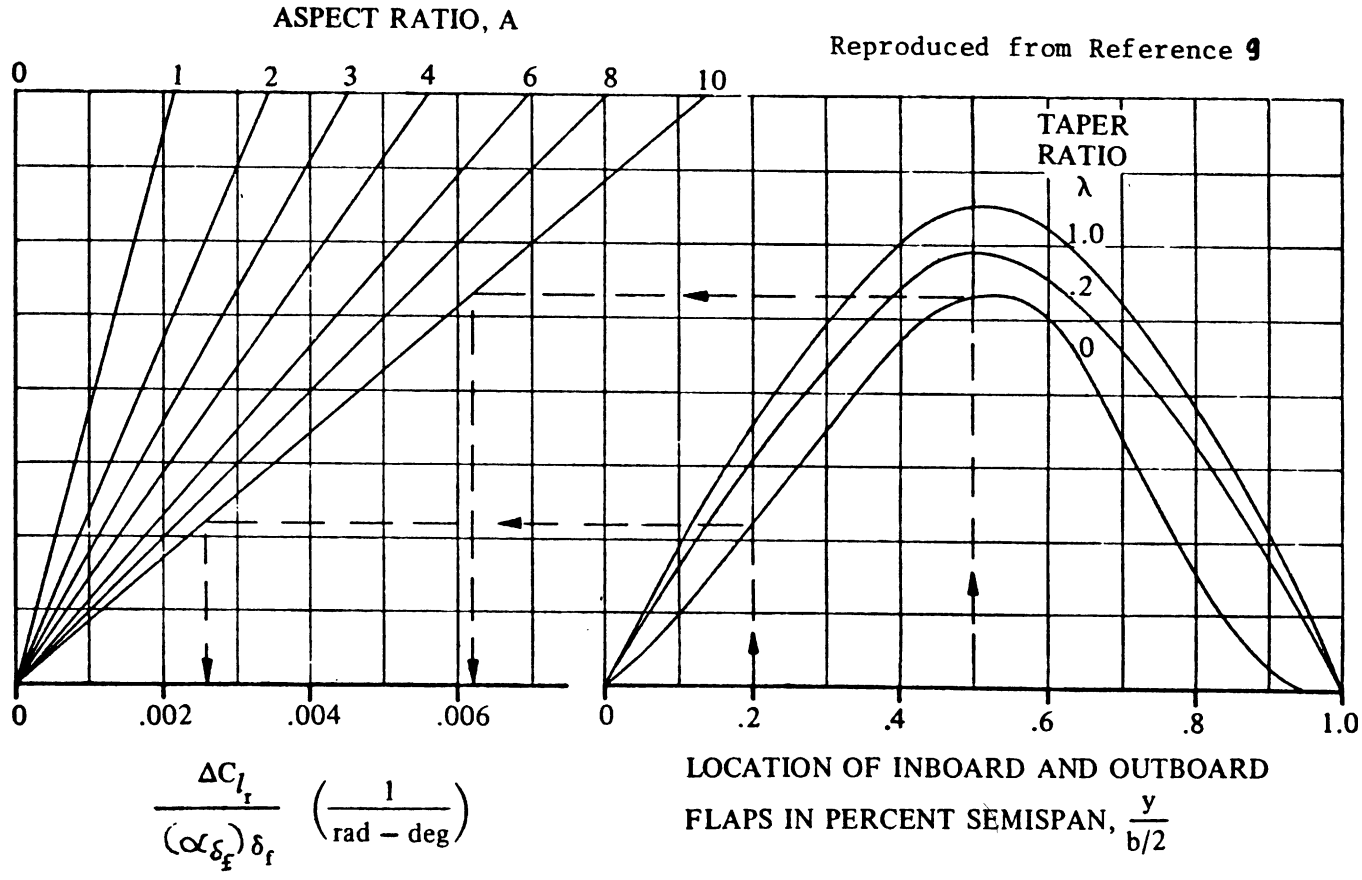

NOTE:

ΔC_{l_r} per radian

δ_f in degrees

NOTE: $\dfrac{\Delta C_{l_r}}{(\alpha_{\delta_f})\,\delta_f} = \left[\dfrac{\Delta C_{l_r}}{(\alpha_{\delta_f})\,\delta_f}\right]_{\text{outboard}} - \left[\dfrac{\Delta C_{l_r}}{(\alpha_{\delta_f})\,\delta_f}\right]_{\text{inboard}}$

Figure 10.43 Effect of Symmetric Flap Deflection on C_{l_r}

3.) C_{n_r}

The yawing-moment-due-to-yaw-rate derivative, C_{n_r} (also called yaw-damping derivative) follows from:

$$C_{n_r} = C_{n_{r_w}} + C_{n_{r_v}} \tag{10.86}$$

where: the wing contribution is found from:

$$C_{n_{r_w}} = \tag{10.87}$$

$$(C_{n_r}/C_L^2)(C_{L_w})^2 + (C_{n_r}/C_{D_o})C_{D_{o_w}}$$

where: (C_{n_r}/C_L^2) follows from Figure 10.44

C_{L_w} is given by Eqn.(10.57) or (10.58)

(C_{n_r}/C_{D_o}) is found from Figure 10.45

$C_{D_{o_w}}$ is the zero-lift drag coefficient of the wing as found from Chapter 4.

the vertical tail contribution is found from:

$$C_{n_{r_v}} = (2/b^2)(l_v\cos\alpha + z_v\sin\alpha)^2 C_{y_{\beta_v}} \tag{10.88}$$

where: l_v and z_v are defined in Figure 10.27

$C_{y_{\beta_v}}$ is found from Eqnn.(10.20) or (10.32)

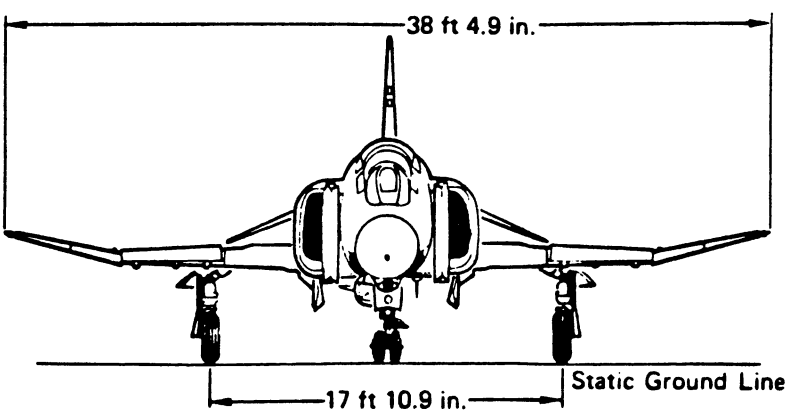

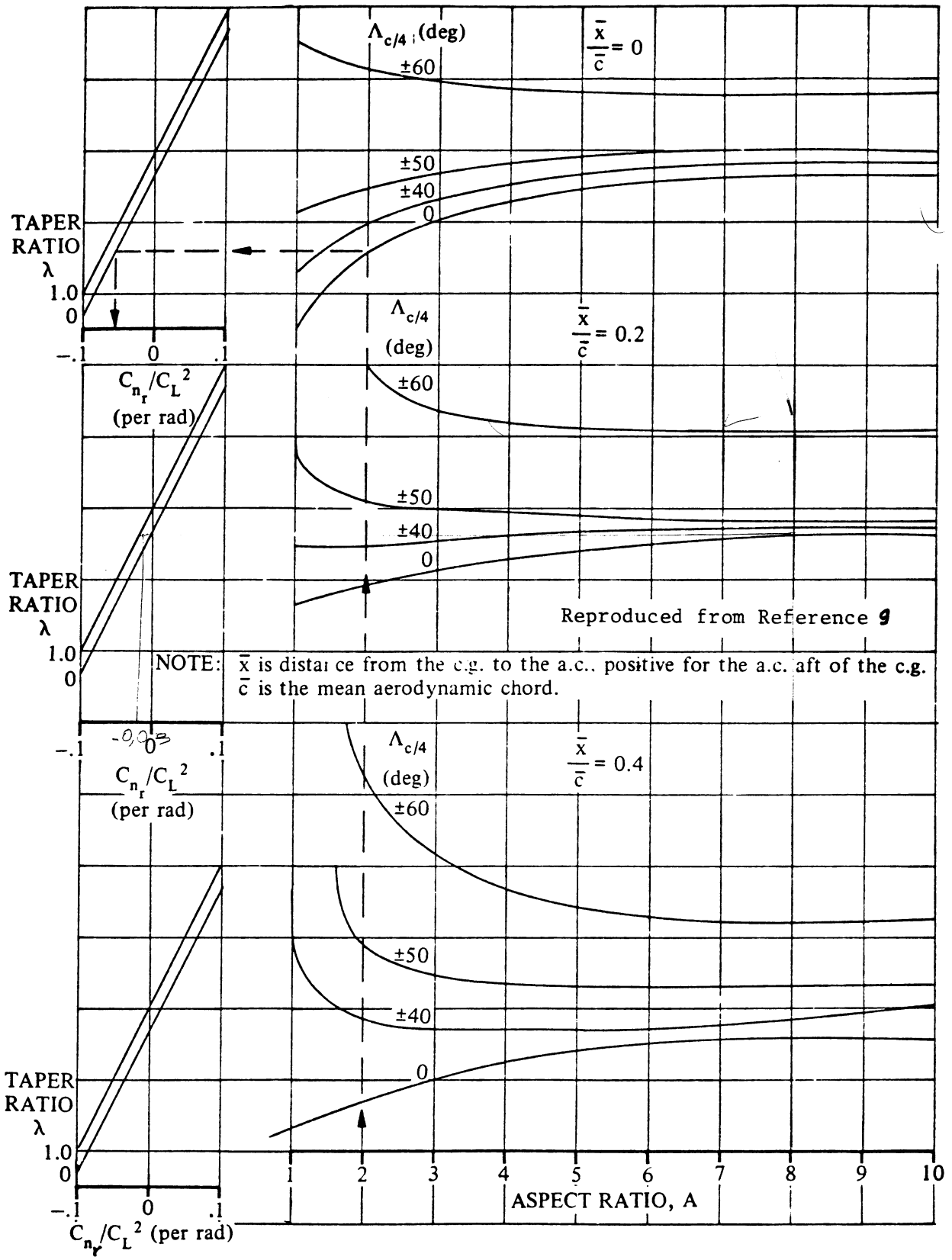

Figure 10.44 Wing Yaw Damping Derivative: Lifting Effect

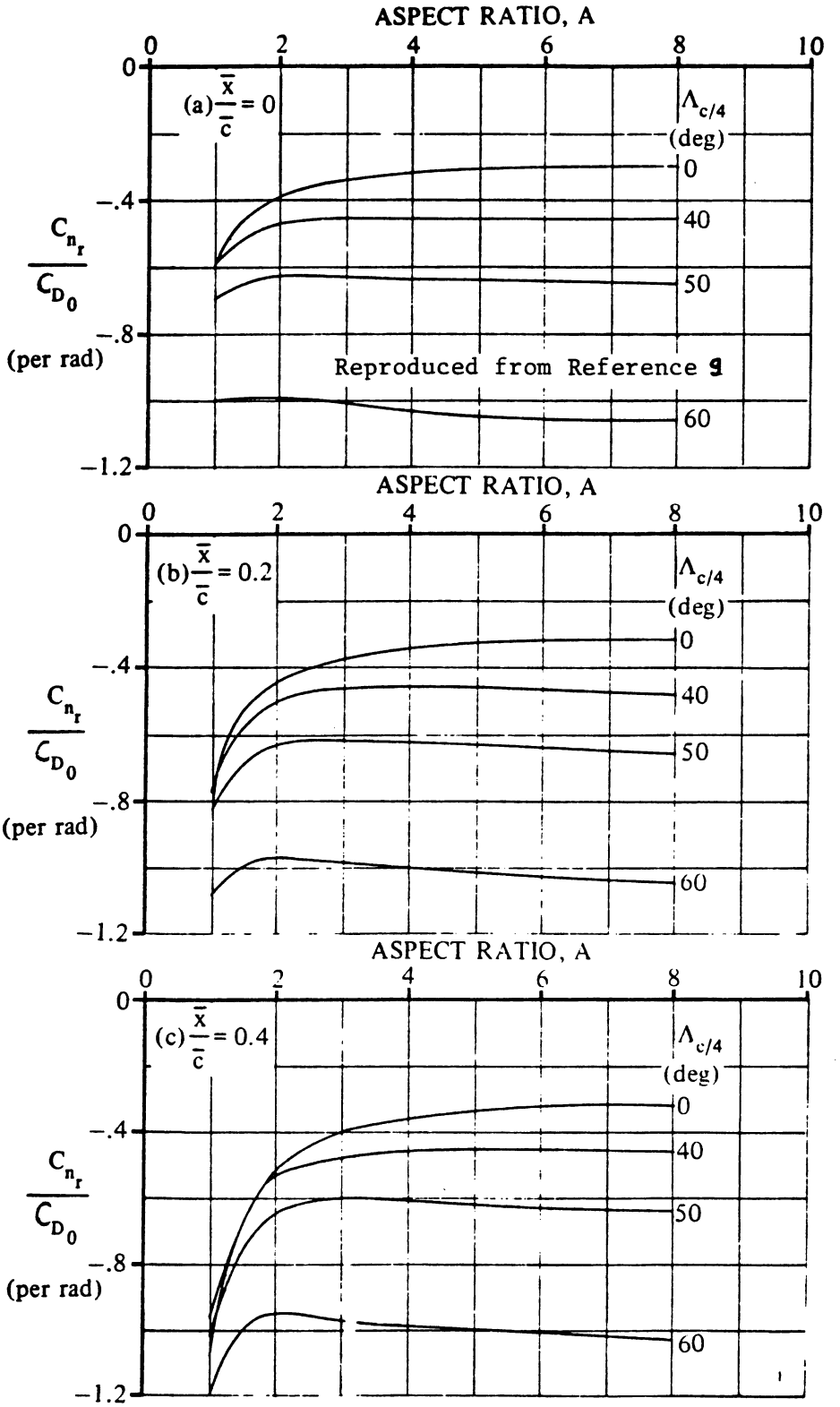

NOTE: $\bar{x}$ is the distance from the c.g. to the a.c., positive for the a.c. aft of the c.g.
$\bar{c}$ is the wing mean aerodynamic chord.

Figure 10.45 Wing Yaw Damping Derivative: Drag Effect

10.3 CONTROL DERIVATIVES

In Table 10.1 the following control derivatives are identified: elevator, aileron and rudder. Because in most airplanes the horizontal stabilizer itself is used as a control device, its derivatives must also be considered. In addition, many recent fighter airplanes and several small commercial airplanes sprout canards, with or without a separate control surface. Many airplanes use spoilers and differential stabilizers as well as ailerons for lateral control.

For these reasons, the following control (power) derivatives are considered in this Section:

10.3.1 Stabilizer Control Derivatives
10.3.2 Elevator Control Derivatives
10.3.3 Canard Control Derivatives
10.3.4 Canardvator Control Derivatives
10.3.5 Aileron Control Derivatives
10.3.6 Spoiler Control Derivatives
10.3.7 Differential Stabilizer Control Derivatives
10.3.8 Rudder Control Derivatives

The methods presented in this section apply only to the subsonic speed regime. For other speed regimes Ref.9 should be consulted.

10.3.1 Stabilizer Control Derivatives: $C_{D_{i_h}}$, $C_{L_{i_h}}$ and $C_{m_{i_h}}$

For a discussion of preliminary sizing of the horizontal stabilizer the reader is referred to Chapters 8 and 11 of Part II.

The methods to be presented apply to cases where the ratio of stabilizer span to local fuselage width is larger than 4.0.

1.) $C_{D_{i_h}}$

The drag-due-to-stabilizer-incidence derivative, $C_{D_{i_h}}$ may be estimated from:

$$C_{D_{i_h}} = 2\{(C_L)/\pi A e\}(C_{L_{\alpha_h}})\eta_h(S_h/S) \qquad (10.89)$$

where: C_L is the airplane lift coefficient follows from

Eqn. (10.90):

$$C_L = (nW)/(\bar{q}S) \qquad (10.90)$$

where: n is the load factor
W is the airplane weight
$\bar{q}$ is the free stream dynamic pressure as described in Section 4.1.
S is the wing area

A is the wing aspect ratio

e is the Oswald' s efficiency factor as found from Section 5.3

$C_{L_{\alpha_h}}$ is found from Eqn.(8.22) with appropriate substitution of horizontal tail parameters for wing parameters

η_h is found from p.269 or p.271.

2.) $C_{L_{i_h}}$

The lift-due-to-stabilizer-incidence derivative may be estimated from:

$$C_{L_{i_h}} = \eta_h (S_h/S) C_{L_{\alpha_h}} \qquad (10.91)$$

where: all quantities have been defined before.

3.) $C_{m_{i_h}}$

The pitching-moment-due-to-stabilizer-incidence derivative, $C_{m_{i_h}}$ (also called stabilizer control power) may be found from:

$$C_{m_{i_h}} = -(C_{L_{\alpha_h}})\eta_h \bar{V}_h \qquad (10.92)$$

where: $\bar{V}_h$ is defined by Eqn.(10.23)

all other quantities were defined before.

10.3.2 Elevator Control Derivatives: $C_{D_{\delta_e}}$, $C_{L_{\delta_e}}$ and $C_{m_{\delta_e}}$

For a discussion of preliminary sizing of the elevator the reader is referred to Chapter 8 of Part II.

Although many airplanes carry approximately full span elevators on the horizontal stabilizer, exceptions do occur. For that reason the elevator should be thought of as a partial span, plain flap.

1.) $C_{D_{\delta_e}}$

The drag-due-to-elevator derivative, $C_{D_{\delta_e}}$ may be estimated from:

$$C_{D_{\delta_e}} = (\alpha_{\delta_e})C_{D_{i_h}} \qquad (10.93)$$

where: $C_{D_{i_h}}$ follows from Eqn. (10.89)

$$(\alpha_{\delta_e}) = \qquad (10.94)$$

$$K_b\{c_{l_\delta}/(c_{l_\delta})_{theory}\}(c_{l_\delta})_{theory}*$$

$$*(k'/c_{l_{\alpha_h}})[\{(\alpha_\delta)_{C_L}\}/\{(\alpha_\delta)_{c_l}\}]$$

where: K_b is the elevator (= plain flap) span factor as obtained from page 259

$\{c_{l_\delta}/(c_{l_\delta})_{theory}\}$ is found from Figure 8.15

$(c_{l_\delta})_{theory}$ is found from Figure 8.14

k' is a correction factor which accounts for nonlinearities at high elevator deflection angles. It is found from Figure 8.13

$[\{(\alpha_\delta)_{C_L}\}/\{(\alpha_\delta)_{c_l}\}]$ is found from Figure 8.53.

Note: in Figs 8.13, 8.14, 8.15 and 8.53 use c_e/c_h for c_f/c

$c_{l_{\alpha_h}}$ is the airfoil lift curve slope of the horizontal stabilizer as obtained from 8.1.1.2.

2.) $C_{L_{\delta_e}}$

The lift-due-to-elevator derivative, $C_{L_{\delta_e}}$ may be found from:

$$C_{L_{\delta_e}} = (\alpha_{\delta_e})C_{L_{i_h}} \qquad (10.95)$$

where: (α_{δ_e}) is found from Eqn.(10.94)

$C_{L_{i_h}}$ is found from Eqn.(10.91)

3.) $C_{m_{\delta_e}}$

The pitching-moment-due-to-elevator derivative, $C_{m_{\delta_e}}$ (also called elevator control power) may be found from:

$$C_{m_{\delta_e}} = (\alpha_{\delta_e})C_{m_{i_h}} \qquad (10.96)$$

where: (α_{δ_e}) is found from Eqn.(10.94)

$C_{m_{i_h}}$ is found from Eqn.(10.92)

10.3.3 Canard Control Derivatives: $C_{D_{i_c}}$, $C_{L_{i_c}}$ and $C_{m_{i_c}}$

For a discussion of preliminary canard sizing the reader is referred to Chapter 11 of Part II.

The methods to be presented apply to cases where the ratio of canard span to local fuselage width is larger than 3.0.

1.) $C_{D_{i_c}}$

The drag-due-to-canard-incidence derivative, $C_{D_{i_c}}$ may be estimated from:

$$C_{D_{i_c}} = 2\{(C_L)/\pi A\, e\}(C_{L_{\alpha_c}})\eta_c(S_c/S) \qquad (10.97)$$

where: C_L is the airplane lift coefficient follows from Eqn. (10.98):

$$C_L = (nW)/(\bar{q}S) \qquad (10.98)$$

where: n is the load factor
W is the airplane weight
$\bar{q}$ is the free stream dynamic pressure as described in Section 4.1.
S is the wing area

A is the wing aspect ratio
e is the Oswald's efficiency factor as found from Section 5.3

$C_{L_{\alpha_c}}$ is found from Eqn.(8.22) with appropriate substitution of canard parameters for wing parameters

η_c is found from p.269 or p.271.

2.) $C_{L_{i_c}}$

The lift-due-to-canard-incidence derivative may be estimated from:

$$C_{L_{i_c}} = \eta_c(S_c/S)C_{L_{\alpha_c}} \qquad (10.99)$$

where: all quantities have been defined before.

3.) $C_{m_{i_c}}$

The pitching-moment-due-to-canard-incidence derivative, $C_{m_{i_c}}$ (also called canard control power) may be found from:

$$C_{m_{i_c}} = (C_{L_{\alpha_c}})\eta_c\bar{V}_c \qquad (10.100)$$

where: $\bar{V}_c$ is defined by Eqn.(10.74)

all other quantities were defined before.

10.3.4 Canardvator Control Derivatives: $C_{D_{\delta_c}}$, $C_{L_{\delta_c}}$ and $C_{m_{\delta_c}}$

Because of a lack of statistical data on canard equipped airplanes, no simple, preliminary design methods are available for the sizing of a canardvator. If the canard is used for trim and control purposes, the trim considerations of Section 8.3 should be used.

Although several canard equipped airplanes carry full span canardvators on the canard, exceptions do occur. For that reason the canardvator should be thought of as a partial span, plain flap.

1.) $C_{D_{\delta_c}}$

The drag-due-to-canardvator derivative, $C_{D_{\delta_c}}$ may be estimated from:

$$C_{D_{\delta_c}} = (\alpha_{\delta_c})C_{D_{i_c}} \qquad (10.101)$$

where: $C_{D_{i_c}}$ follows from Eqn.(10.97)

$$(\alpha_{\delta_c}) = \qquad (10.102)$$

$$K_b\{c_{l_\delta}/(c_{l_\delta})_{theory}\}(c_{l_\delta})_{theory}*$$

$$*(k'/c_{l_{\alpha_c}})[\{(\alpha_\delta)_{C_L}\}/\{(\alpha_\delta)_{c_l}\}]$$

where: K_b is the canardvator (= plain flap) span factor as obtained from page 259

$\{c_{l_\delta}/(c_{l_\delta})_{theory}\}$ is found from Figure 8.15

$(c_{l_\delta})_{theory}$ is found from Figure 8.14

k' is a correction factor which accounts for nonlinearities at high canardvator deflection angles. It is found from Figure 8.13

$[\{(\alpha_\delta)_{C_L}\}/\{(\alpha_\delta)_{c_l}\}]$ is found from Figure 8.53

Note: in Figs 8.13, 8.14, 8.15 and 8.53 use c_{δ_c}/c_c for c_f/c

$c_{l_{\alpha_c}}$ is the airfoil lift curve slope of the canard as obtained from 8.1.1.2.

2.) $C_{L_{\delta_c}}$

The lift-due-to-canardvator derivative, $C_{L_{\delta_c}}$ may be found from:

$$C_{L_{\delta_c}} = (\alpha_{\delta_c})C_{L_{i_c}} \qquad (10.103)$$

where: (α_{δ_c}) is found from Eqn.(10.102)

$C_{L_{i_c}}$ is found from Eqn.(10.99)

3.) $C_{m_{\delta_c}}$

The pitching-moment-due-to-canardvator derivative, $C_{m_{\delta_c}}$ (also called canardvator control power) may be found from:

$$C_{m_{\delta_c}} = (\alpha_{\delta_c})C_{m_{i_c}} \qquad (10.104)$$

where: (α_{δ_c}) is found from Eqn.(10.102)

$C_{m_{i_c}}$ is found from Eqn.(10.100)

10.3.5 Aileron Control Derivatives: $C_{y_{\delta_a}}$, $C_{l_{\delta_a}}$ and $C_{n_{\delta_a}}$

For a discussion of preliminary aileron sizing the reader is referred to Chapter 6 of Part II.

1.) $C_{y_{\delta_a}}$

The side-force-due-to-aileron derivative, $C_{y_{\delta_a}}$ is negligible for most conventional aileron arrangements:

$$C_{y_{\delta_a}} = 0 \qquad (10.105)$$

If ailerons are located in close proximity to a vertical tail (F-106!) a significant side-force due to aileron deflection may arise. Windtunnel data are recommended to determine such aileron induced side forecs.

2.) $C_{l_{\delta_a}}$

The rolling-moment-due-to-aileron derivative, $C_{l_{\delta_a}}$ (also called roll control power) can be estimated with the following procedure:

Step 1: Determine the inboard span location η_i and the outboard span location η_o for the aileron(s) as fractions of the semi-span of the wing. These data follow from the Class I threeview obtained from Chapter 13, Part II.

Step 2: For full chord ailerons ($c_a/c = 1.0$), antisymmetrically deflected, and running from: η=0 to η_i and to η_o respectively, determine the rolling moment effectiveness parameter: $\beta C'_{l_\delta}/k$ from Figures 10.46, with:

β found from Eqn.(10.53)

k found from Eqn.(10.54), where $(c_{l_\alpha})_M$ is

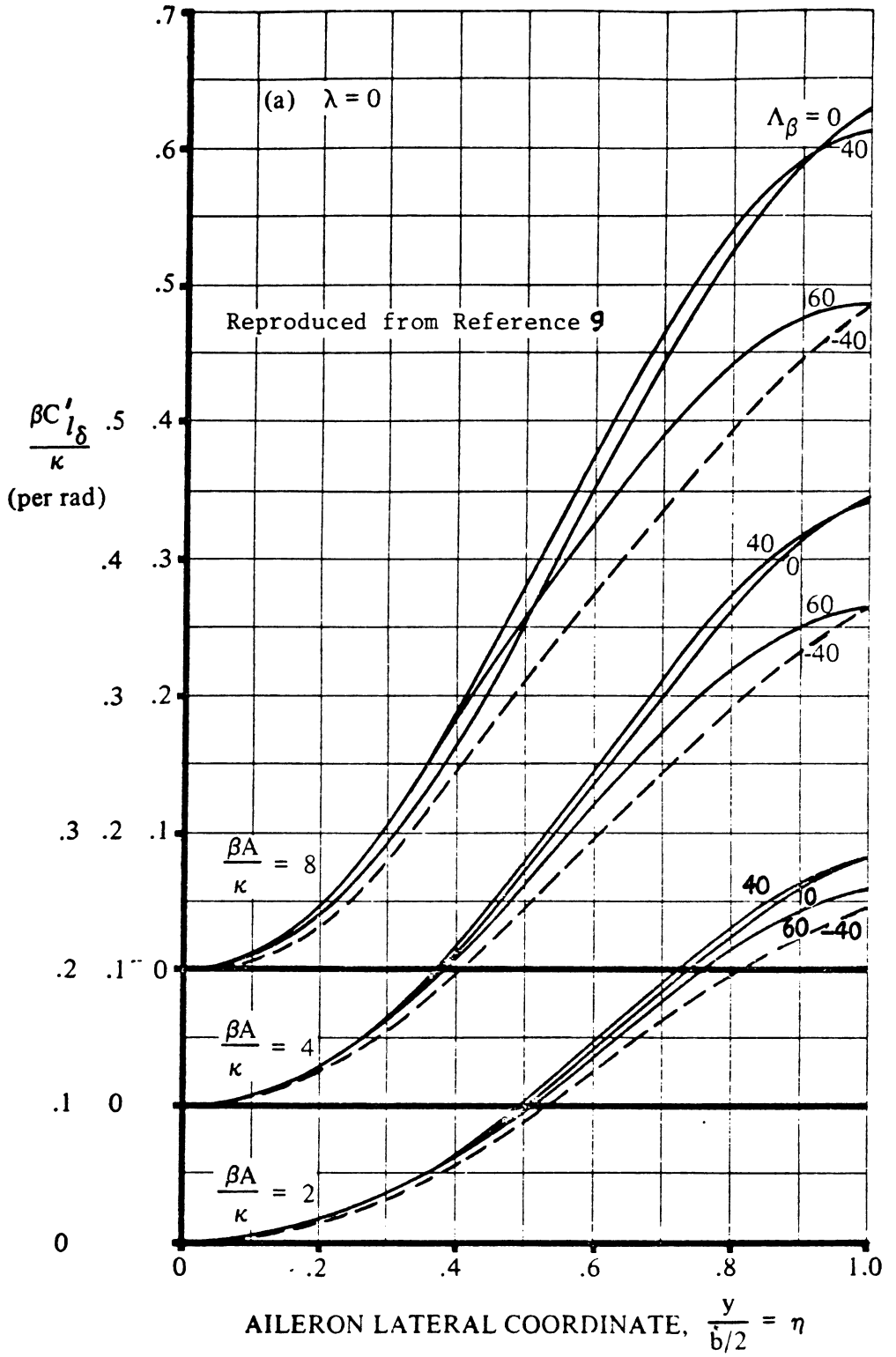

Figure 10.46a Aileron Rolling Moment Parameter

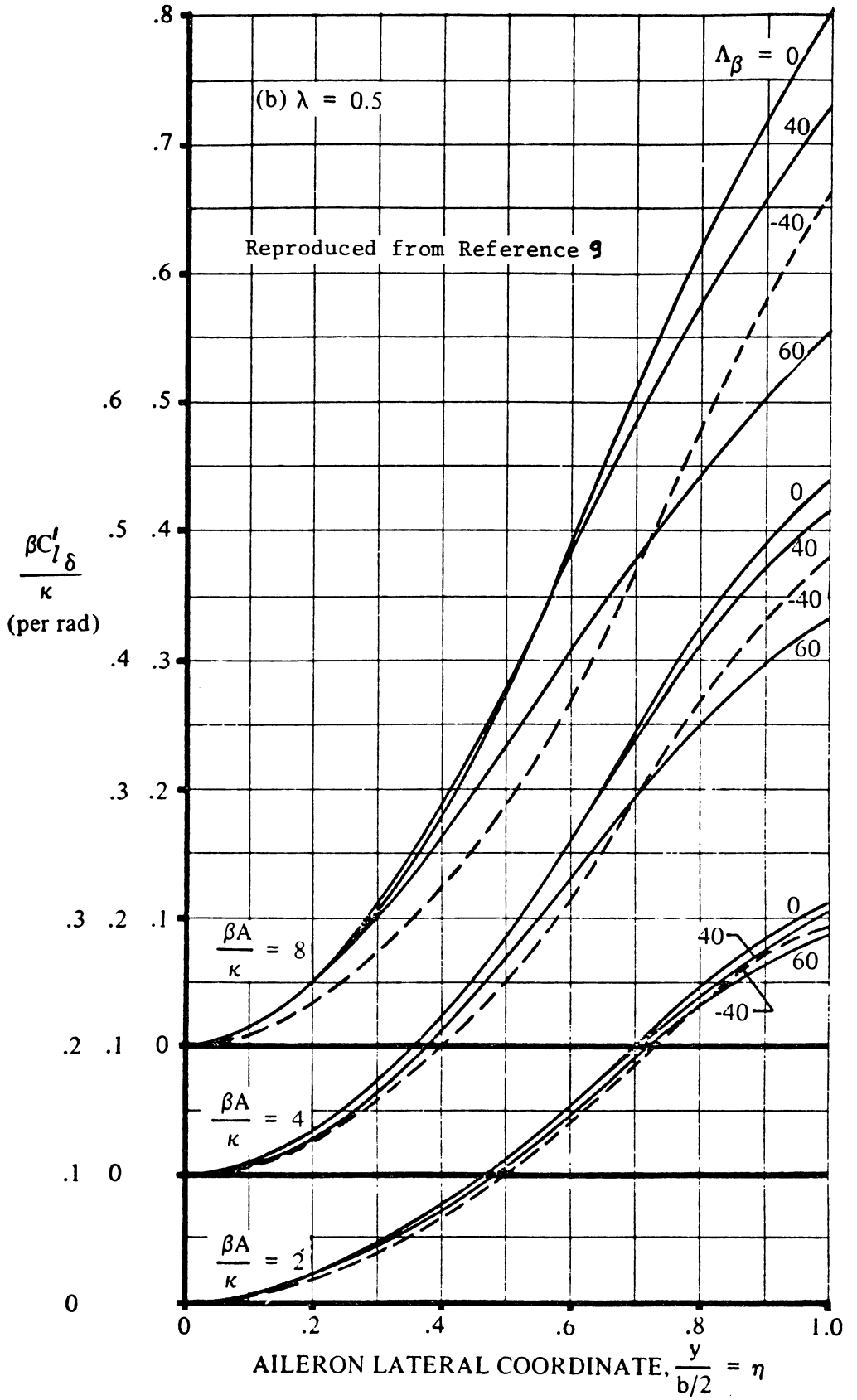

Figure 10.46b Aileron Rolling Moment Parameter

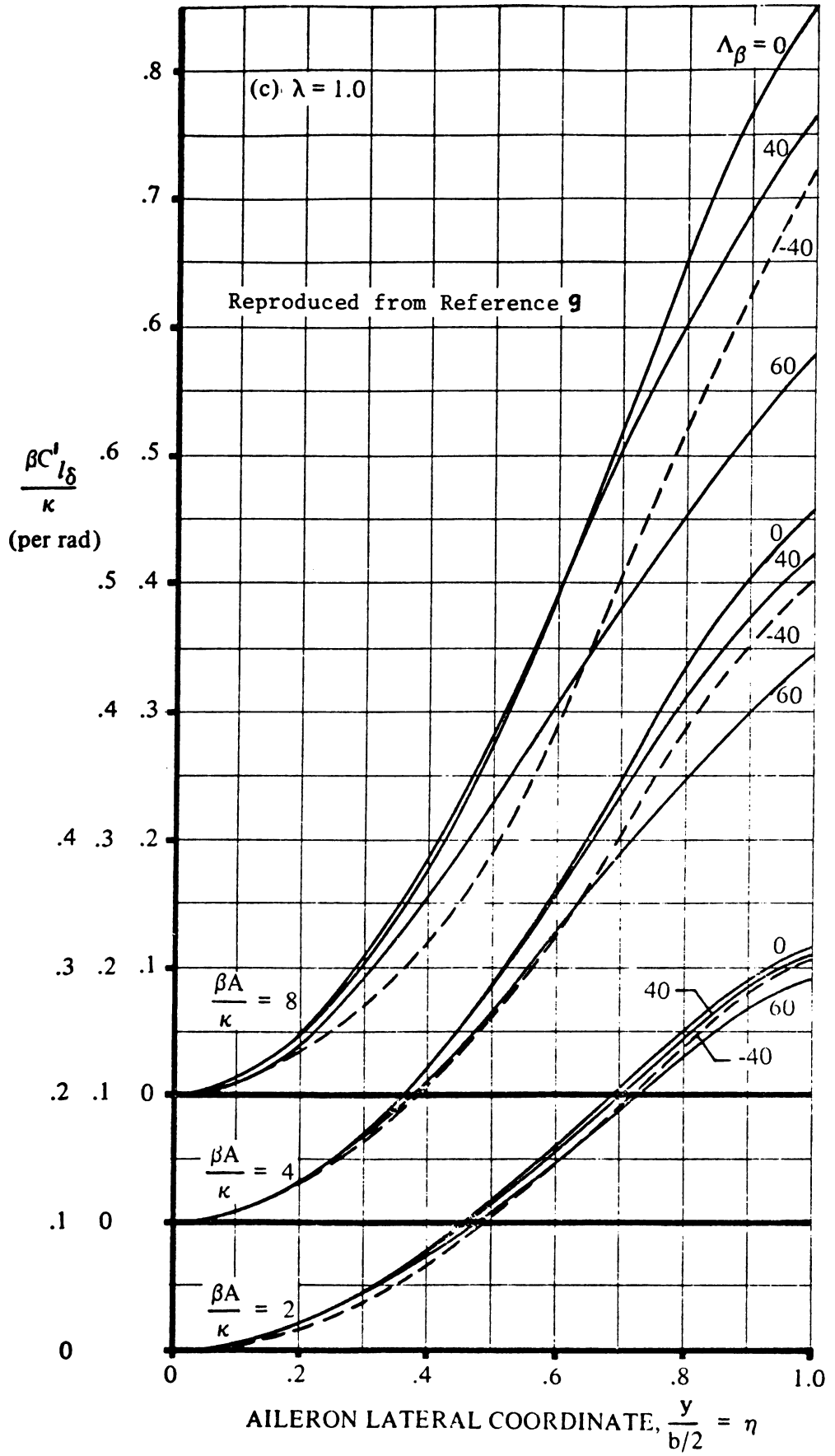

Figure 10.46c Aileron Rolling moment Parameter

determined for the airfoil at the m.g.c of the part of the wing covered by the aileron(s)

A is the wing aspect ratio

$$\Lambda_\beta = \arctan(\tan\Lambda_{c/4}/\beta) \qquad (10.106)$$

Figures 10.46 give the control effectiveness parameter for control spans measured from the plane of symmetry (η=0) to aileron outboard. For partial span controls running from η_i to η_o the actual effectiveness parameter is obtained as the difference between the two full span controls. This is illustrated in Figure 10.47.

Step 3: Determine the rolling effectiveness of two full-chord controls anti-symmetrically deflected by:

$$C'_{l_\delta} = (k/\beta)(\beta C'_{l_\delta}/k) \qquad (10.107)$$

Step 4: Determine the rolling effectiveness of the partial-chord controls ($c_a/c < 1.0$), anti-symmetrically deflected from:

$$C_{l_\delta} = (\alpha_{\delta_a})C'_{l_\delta} \qquad (10.108)$$

where:

$$\alpha_{\delta_a} = c_{l_\delta}/(c_{l_\alpha})_a \qquad (10.109)$$

with: c_{l_δ} =

$$\{c_{l_\delta}/(c_{l_\delta})_{theory}\}(c_{l_\delta})_{theory}k' \qquad (10.110)$$

where: $\{c_{l_\delta}/(c_{l_\delta})_{theory}\}$ is found from Figure 8.15

k' is found from Figure 8.13.

$(c_{l_\delta})_{theory}$ is found from Figure 8.14

Note: in Figures 8.14 and 8.15, use c_a/c for c_f/c

and where: $(c_{l_\alpha})_a$ is the average airfoil lift-curve-slope of that part of the wing covered by the ailerons. The airfoil at the wing span station corresponding to that of the aileron m.g.c. may be used to compute this.

Step 5: The effect of differential aileron control deflection (for an example, see Part IV, pgs 217 and 220) is taken into account by considering C_{l_δ} of each control as ONE-HALF the anti-symmetric value determined with the aid of Eqn(10.108). The total rolling moment coefficient for differential aileron control deflection is found from:

$$C_{l_a} = (C_{l_\delta}/2)_{left}\delta a_{left} + (C_{l_\delta}/2)_{right}\delta a_{right} \qquad (10.111)$$

A positive aileron deflection results in a positive rolling moment. Thus, the deflection is positive for the left aileron with trailing edge down and for right aileron with trailing edge up.

THE aileron deflection, δ_a of the airplane is defined as:

$$\delta_a = 0.5(\delta a_{left} + \delta a_{right}) \qquad (10.112)$$

Step 6: The aileron roll control power derivative now follows from:

$$C_{l_{\delta_a}} = C_{l_a} / \delta_a \qquad (10.113)$$

3.) $C_{n_{\delta_a}}$

The yawing-moment-due-to-aileron derivative, $C_{n_{\delta_a}}$ (also called adverse aileron yaw) may be computed from:

$$C_{n_{\delta_a}} = K_a C_{L_w} C_{l_{\delta_a}} \qquad (10.114)$$

where: K_a **is found from Figure 10.48. Note that it is the difference between the inboard and outboard values**

C_{L_w} is found from Eqns (10.57) or (10.58)

$C_{l_{\delta_a}}$ is given by Eqn.(10.113)

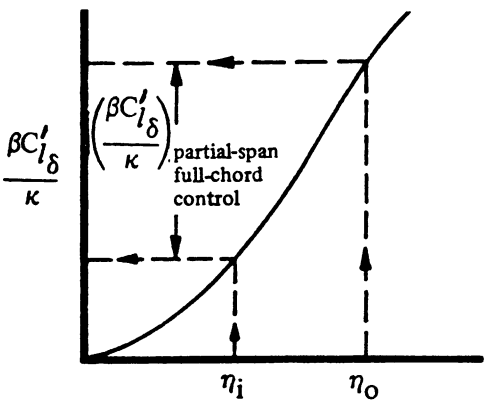

Reproduced from Reference 9

Figure 10.47 Finding the Partial Span Aileron Parameter

Reproduced from Reference 9

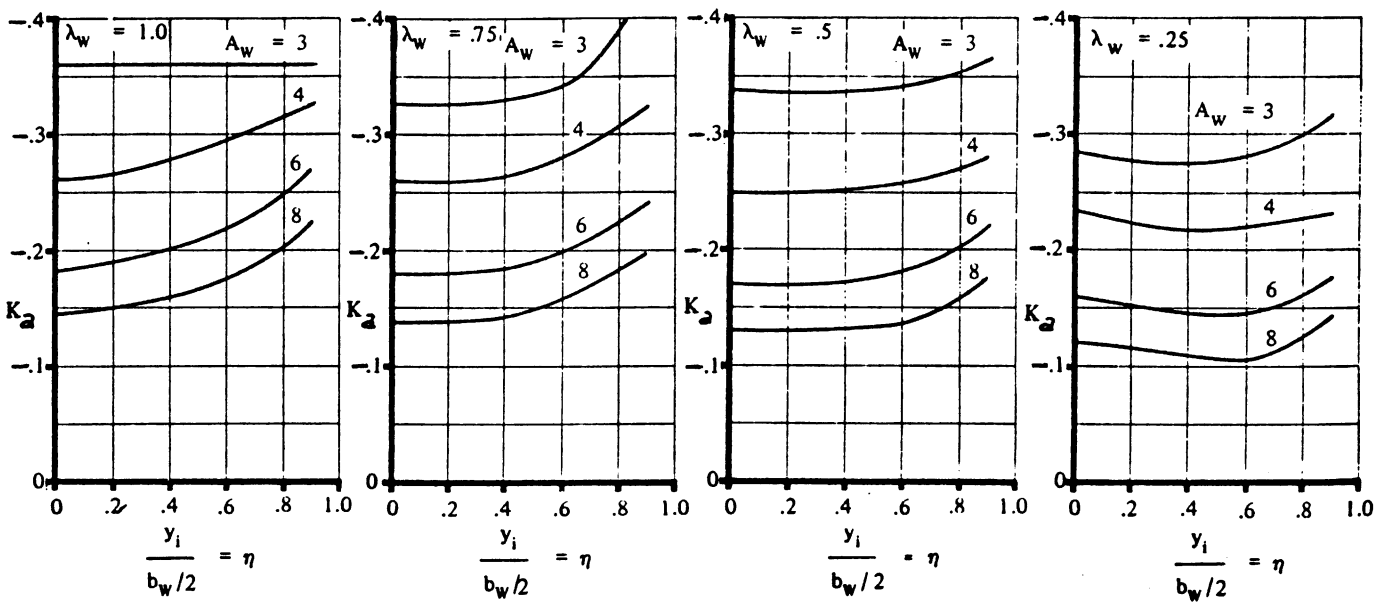

Figure 10.48 Correlation Constant for Yawing Moment due to Aileron Deflection

10.3.6 Spoiler Control Derivatives: $C_{y_{\delta_s}}$, $C_{l_{\delta_s}}$ and $C_{n_{\delta_s}}$

For a discussion of preliminary spoiler sizing the reader is referred to Chapter 6 of Part II.

In this sub-section the following two types of spoilers will be considered:

A) Plug or Flap-Type Spoilers

B) Spoiler-Slot-Deflector Arrangements

Figures 10.49A and B show typical layouts for these spoiler types. Dimensions needed in the determination of spoiler derivatives are also given.

Definition: a positive spoiler deflection is one which results in a positive rolling moment i.e. a roll to the right.

1.) $C_{y_{\delta_s}}$

The side-force-due-to-spoiler derivative, $C_{y_{\delta_s}}$ is negligible for most conventional spoiler arrangements, regardless of spoiler type:

$$C_{y_{\delta_s}} = 0 \qquad (10.115)$$

If spoilers are located in close proximity to a vertical surface a significant side-force due to spoiler deflection may arise. Windtunnel data are recommended to determine such spoiler induced side forces.

2.) $C_{l_{\delta_s}}$

The rolling-moment-due-to-spoiler derivative $C_{l_{\delta_s}}$ (also called spoiler roll control power) depends on the type of spoiler used.

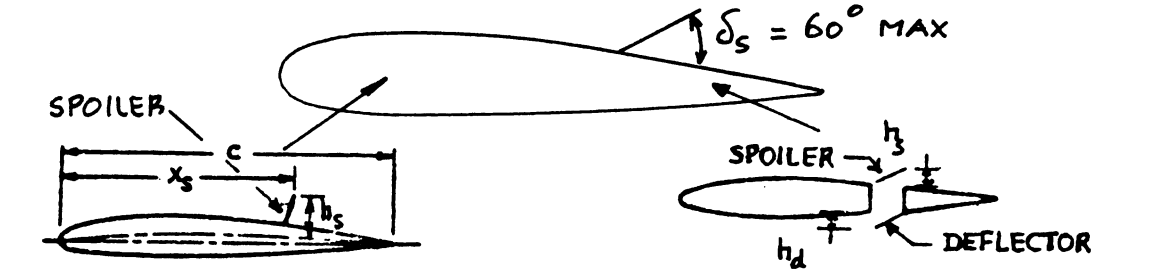

A) PLUG OR FLAP-TYPE

B) SPOILER-SLOT-DEFLECTOR

Figure 10.49 General Arrangement for Two Types of Spoiler

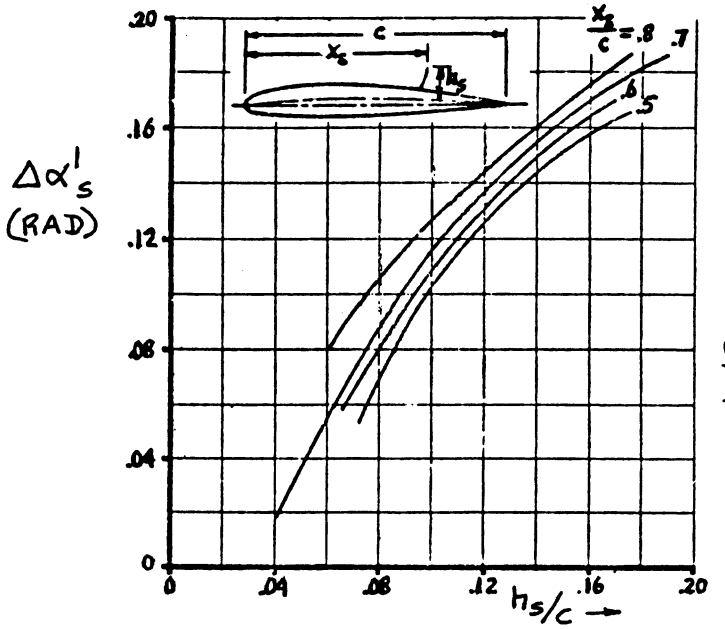

COPIED FROM REF. 9

Figure 10.50 Spoiler Lift Effectiveness

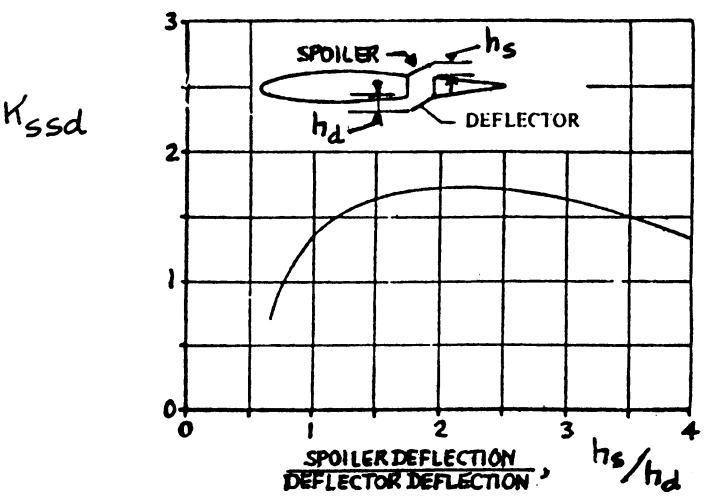

COPIED FROM REF. 9

Figure 10.51 Effect of Spoiler Slot and Deflector on Spoiler Rolling Moment Effectiveness

A) Plug or Flap-Type Spoilers

The rolling-moment-due-to-spoiler derivative, $C_{l_{\delta_s}}$ for a plug or flap-type spoiler can be estimated with the following procedure:

Step 1: Determine the inboard span location η_i and the outboard span location η_o for the spoiler panels as fractions of the semi-span and as fractions of the chord of the wing. These data follow from the Class I three-view obtained from Chapter 13, Part II.

Step 2: Assuming a maximum spoiler plate deflection of 60 degrees, translate the spoiler geometry of Step 1 into one consistent with the spoiler geometry of Figure 10.49A: in other words, determine values for h_s/c and x_s/c.

These quantities may be averaged over the span of the spoiler.

Step 3: From Figure 10.50 find the corresponding value of $\Delta\alpha'_s$.

Step 4: Find the spoiler roll control derivative from:

$$C_{l_{\delta_s}} = (1/120)(C'_{l_\delta})\Delta\alpha'_s \cos\Lambda_{c/4} \quad (1/\text{deg}) \qquad (10.116)$$

where: C'_{l_δ} is the rolling-moment effectiveness parameter for full chord, antisymmetrically deflected controls as obtained from Eqn.(10.107). The inboard and outboard ends of these controls are taken to be the same as the inboard and outboard ends of the hinge line of the spoiler.

$\Lambda_{c/4}$ is the wing quarter chord sweep angle.

NOTE: this method is valid only for sweep angles up to 40 degrees. For higher sweep angles, see the method of Ref.9.

B) Spoiler-Slot Deflector Arrangements

For a spoiler-slot-deflector arrangement the roll control power derivative may be determined from:

$$C_{l_{\delta_{ssd}}} = K_{ssd} C_{l_{\delta_s}} \quad \text{(1/deg)} \qquad (10.117)$$

where: K_{ssd} follows from Figure 10.51 for a given ratio of spoiler angle to deflector angle, δ_s/δ_d

$C_{l_{\delta_s}}$ is determined from Eqn.(10.116).

3.) $C_{n_{\delta_s}}$

The yawing-moment-due-to-spoiler derivative, $C_{n_{\delta_s}}$ (also called proverse yawing moment due to spoiler) also depends on the type of spoiler used.

A) Plug and Flap Type Spoilers

$$C_{n_{\delta_s}} = (1/60) C_{n_s} \quad \text{(1/deg)} \qquad (10.118)$$

where: C_{n_s} is found from Figures 10.52 and 10.53 for straight and for swept wings respectively.

B) Spoiler-Slot-Deflector Arrangements

$$C_{n_{\delta_{ssd}}} = K_{ssd} C_{n_{\delta_s}} \quad \text{(1/deg)} \qquad (10.119)$$

where: K_{ssd} is found from Figure 10.54

$C_{n_{\delta_s}}$ follows from Eqn.(10.118).

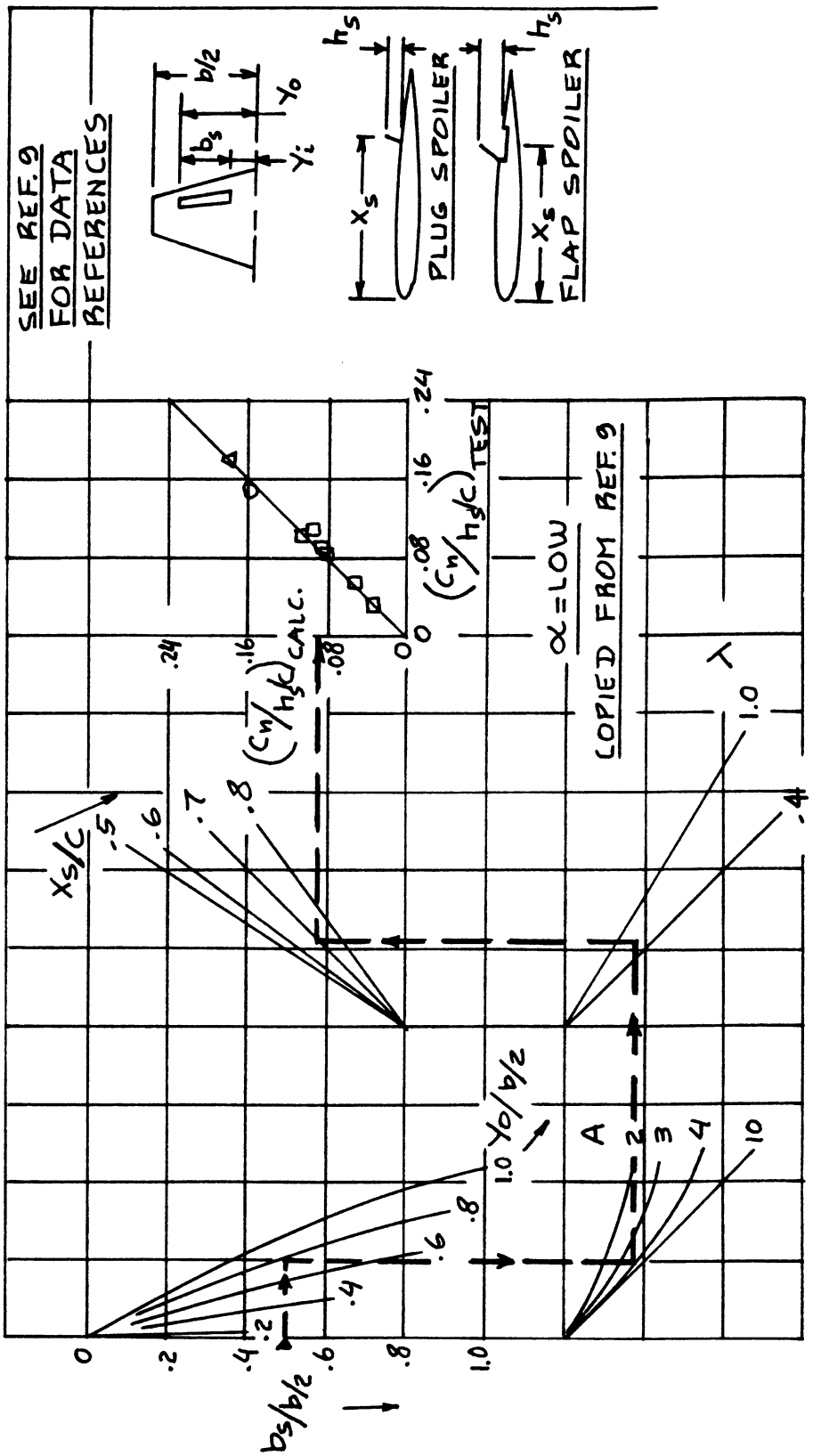

Figure 10.52 Yawing Moment due to Spoiler for Straight Wings at Low Angles of Attack

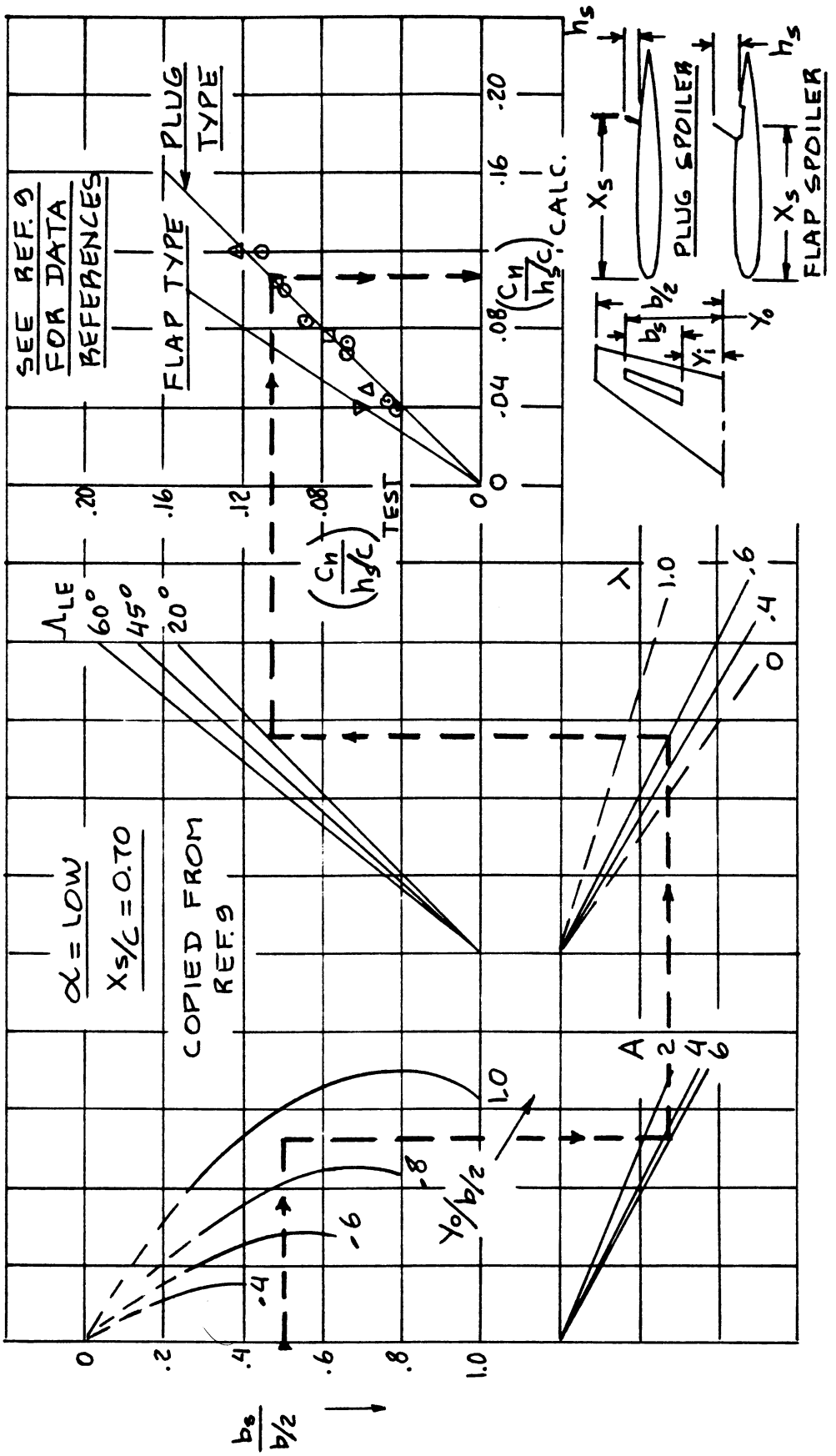

Figure 10.53 Yawing Moment due to Spoiler for Swept Wings at Low Angles of Attack

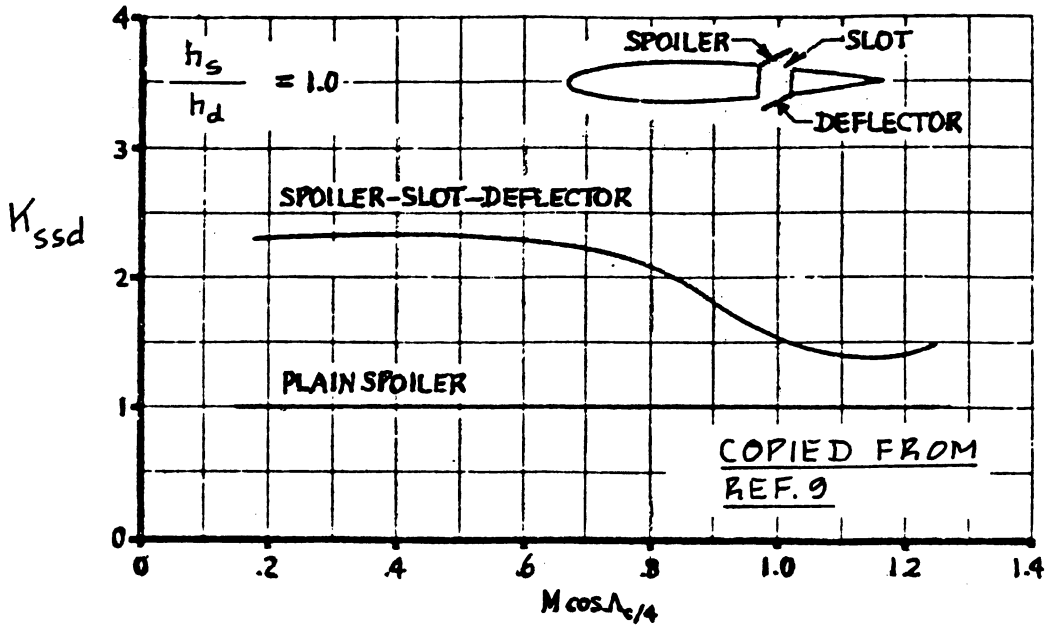

Figure 10.54 Effect of Slot and Deflector on Spoiler Yawing Moment

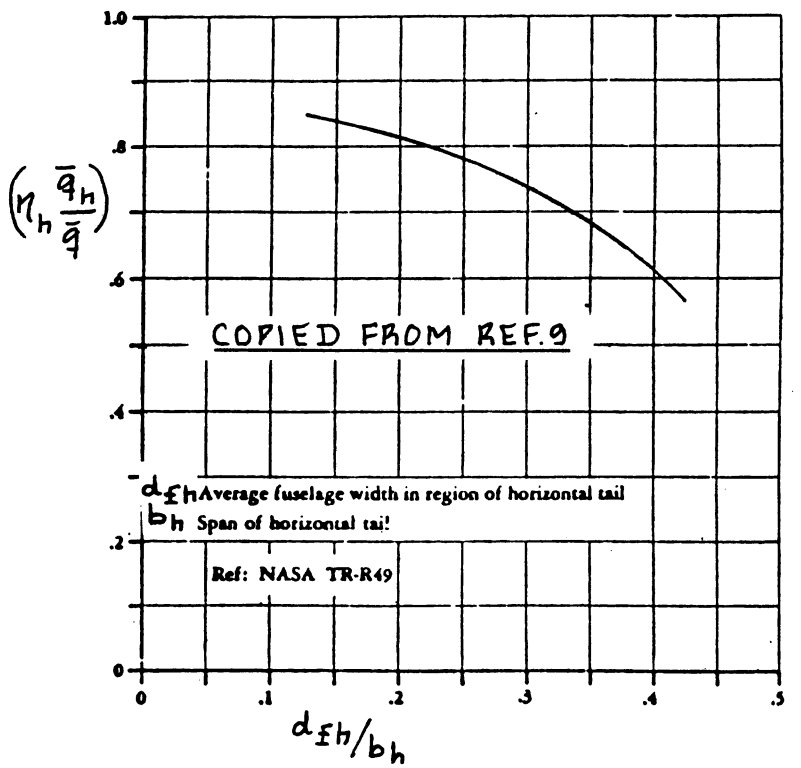

Figure 10.55 Tail Effectiveness Parameter for Fuselage Mounted Horizontal Stabilizers

10.3.7 Differential Stabilizer Control Derivatives: $C_{y_{i_h}}$, $C_{l_{i_h}}$ and $C_{n_{i_h}}$

Many fighter airplanes require so much lateral control power to meet combat roll requirements that differentially controlled horizontal stabilizers are used in addition to wing mounted lateral control devices. The sizing of the horizontal tail (stabilizer) is normally based on requirements for longitudinal stability and control. The reader should refer to Chapter 8 of Part II for preliminary horizontal tail sizing methods.

In this sub-section it will be assumed that the geometry of the horizontal tail surfaces is known.

Definition: a positive differential stabilizer deflection is one resulting in a positive rolling moment: l.e. left stabilizer up AND l.e. right stabilizer down).

1.) $C_{y_{i_h}}$

The side-force-due-to-differential stabilizer derivative, $C_{y_{i_h}}$ is negligible for many airplanes:

$$C_{y_{i_h}} = 0 \qquad (10.120)$$

If the stabilizers are located in close proximity to to a vertical surface a significant side-force due to differential stabilizer deflection may arise. Windtunnel data must be used to determine these side forces.

2.) $C_{l_{i_h}}$

The rolling-moment-due-to-differential stabilizer derivative $C_{l_{i_h}}$ (also called differential stabilizer roll control power) may be found from:

$$C_{l_{i_h}} = 0.5\{1 - (\pi A/57.3)(d\varepsilon/d\alpha)\}(\eta_h \bar{q}_h/\bar{q})* \\ *\{(y_{h_e} S_{h_e})/Sb\}(C_{L_{\alpha_h}})_e \qquad (10.121)$$

where: $d\varepsilon/d\alpha$ is found from Eqn.(8.45)

$(\eta_h \bar{q}_h / \bar{q})$ is found from Figure 10.55)

y_{h_e} is the distance from the exposed stabilizer center of pressure to the airplane centerline, and may be determined from:

$$y_{h_e} = (\eta_{cp} b_{h_e}/2) + r_{fh} \qquad (10.122)$$

where: η_{cp} is found from Figure 10.56. In Figure 10.16, A_{h_e} is the aspect ratio of the exposed horizontal tail

b_{h_e} is the semispan of the exposed horizontal stabilizer

r_{fh} is the radius or one half of the equivalent fuselage width at the point of stabilizer attachment

S_{h_e} is the exposed stabilizer area

$(C_{L_{\alpha_h}})_e$ is the lift-curve slope of the exposed horizontal tail. It is obtained by using the exposed horizontal tail aspect ratio, A_{h_e} in Eqn.(8.22) and substituting other appropriate horizontal tail parameters for wing parameters.

NOTE: This method is valid only for angles of attack below roughly six degrees. At higher angles of attack body shed vortices will interfere with the flow over the horizontal tail A method to account for these vortices is given in Ref.9.

3.) $C_{n_{i_h}}$

No reliable preliminary design methods are available for the estimation of this derivative. The qualitative discussion which follows has been adapted from Ref.9.

Figure 10.57 shows typical relations between aileron and differential tail induced yawing moments. The magnitude of the differential tail induced yawing moment is a strong function of tail height (relative to the vertical tail and relative to the wing): Figure 10.58 illustrates

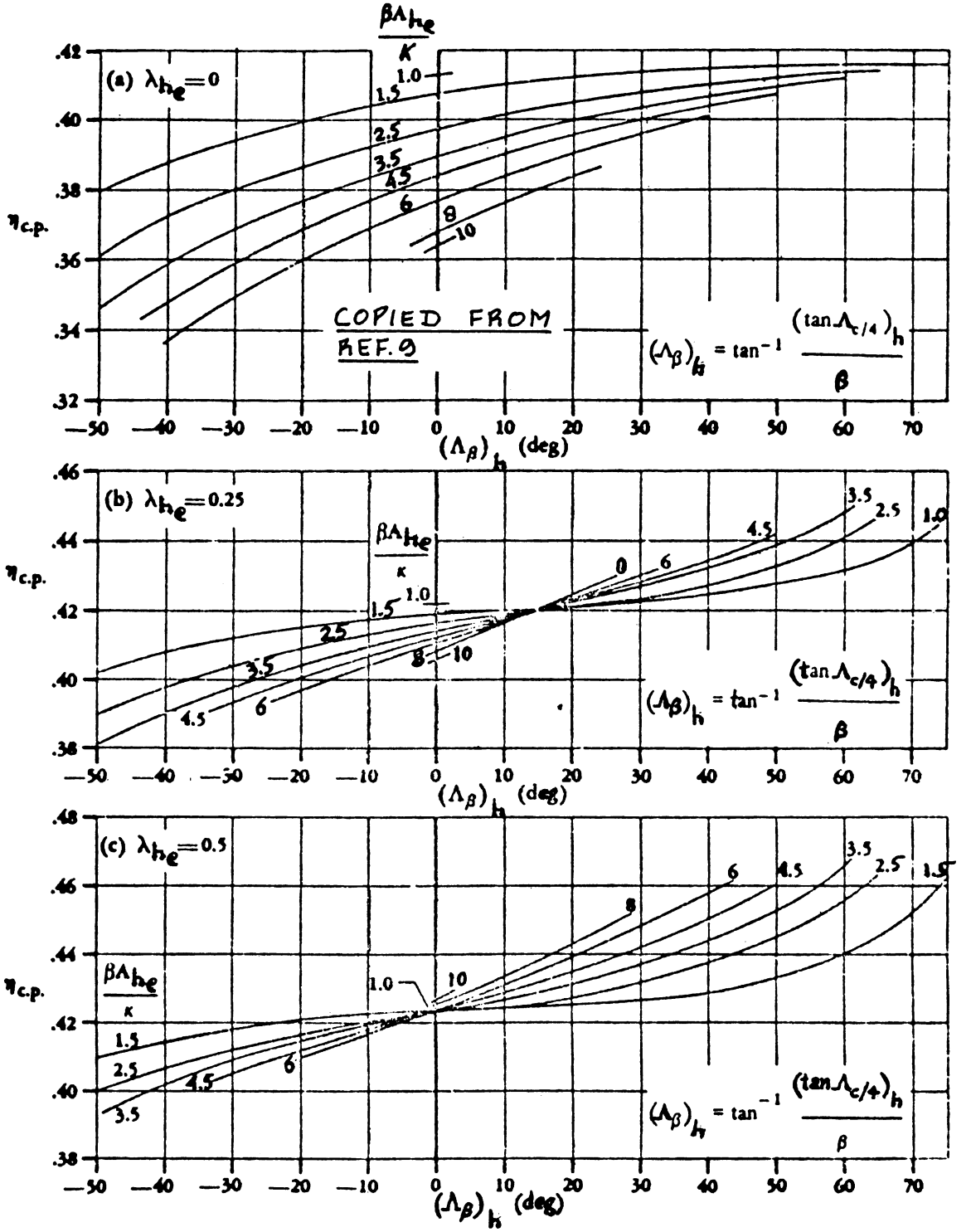

Figure 10.56 Exposed Stabilizer Center of Pressure Location as Affected by Aspect Ratio, Sweep Angle and Taper Ratio

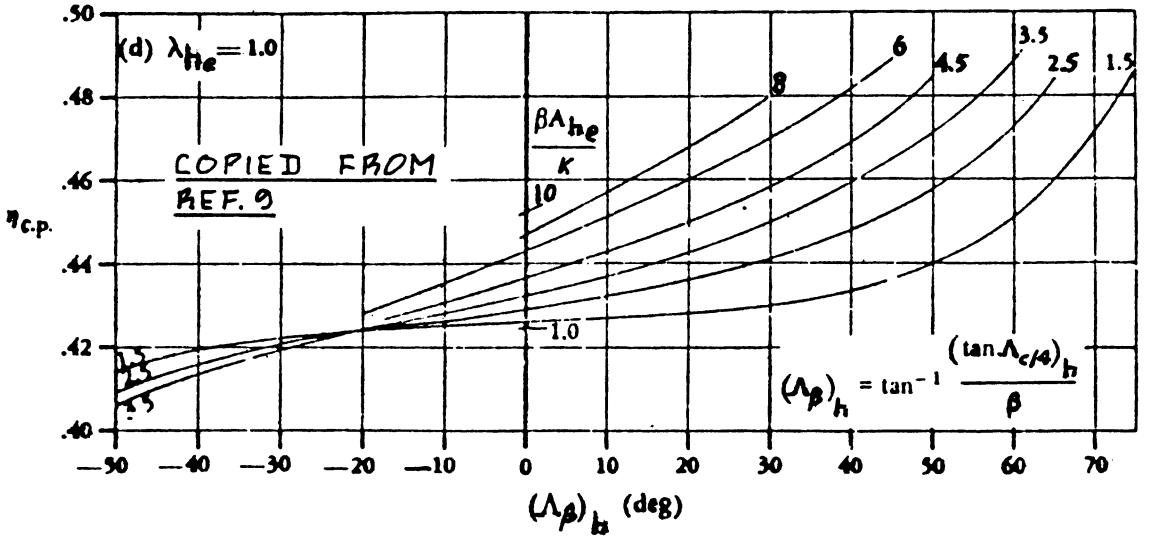

Figure 10.56 (Cont'd) Exposed Stabilizer Center of Pressure Location as Affected by Aspect Ratio, Sweep Angle and Taper Ratio

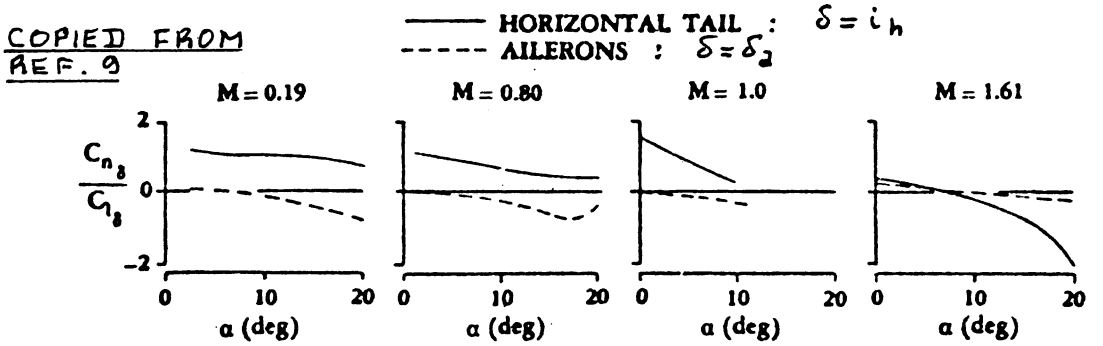

Figure 10.57 Effect of Mach Number on the Yaw-to Roll Ratio of Differential Stabilizers

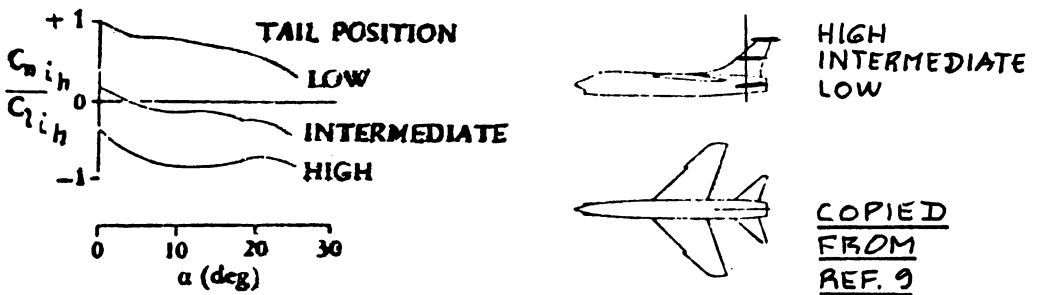

Figure 10.58 Effect of Tail Location on the Yaw-to-Roll Ratio of Differential Stabilizers

typical trends. In addition, the dihedral angle of the horizontal tail can be significant as shown in Fig.10.59.

Finally, the deflection of wing flaps can have significant influence as well. This is shown in Fig.10.60.

For purposes of preliminary design the reader may wish to 'guestimate' a value of $C_{n_{i_h}}/C_{l_{i_h}}$ from Figs 10.57 through 10.60. Where possible windtunnel data should be used.

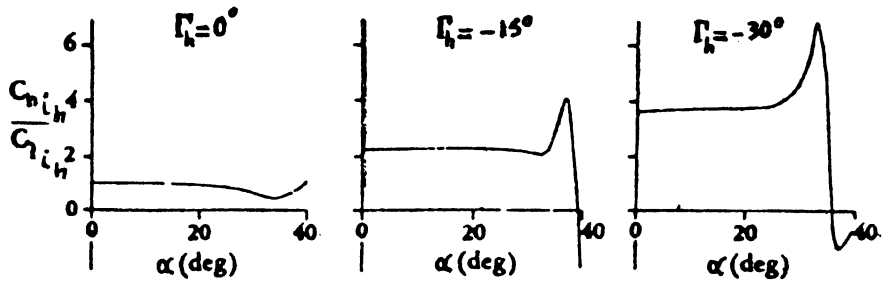

Figure 10.59 Effect of Tail Dihedral on the Yaw-to-Roll Ratio of Differential Stabilizers

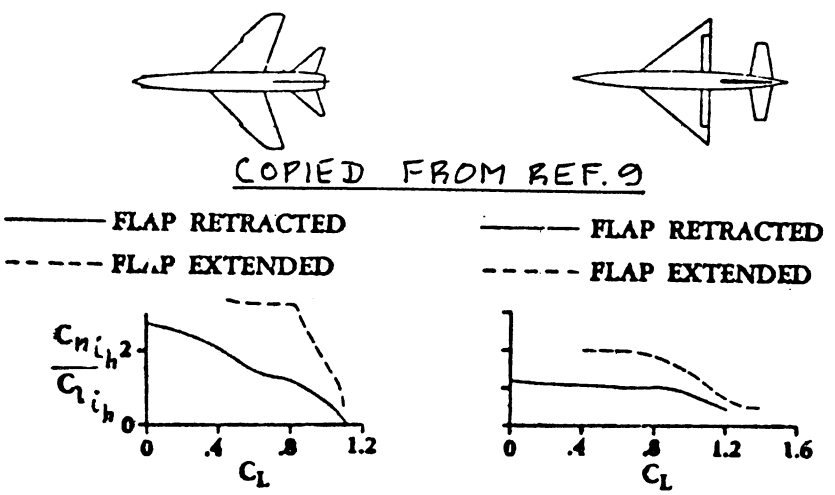

Figure 10.60 Effect of Flaps on the Yaw-to-Roll Ratio of Differential Stabilizers

10.3.8 Rudder Control Derivatives: $C_{y_{\delta_r}}$, $C_{l_{\delta_r}}$ and $C_{n_{\delta_r}}$

For a discussion of vertical tail sizing and rudder sizing the reader is referred to Chapters 8 and 11 in Part II.

Definition: a positive rudder deflection is one resulting in a negative yawing moment (i.e. rudder to the left)

1.) $C_{y_{\delta_r}}$

The side-force-due-to-rudder derivative, $C_{y_{\delta_r}}$ may be computed from:

For single vertical tail:

$$C_{y_{\delta_r}} = (C_{L_{\alpha_v}} / c_{l_{\alpha_v}}) (k' K_b) \{ (\alpha_\delta)_{C_L} / (\alpha_\delta)_{c_l} \} * * (C_{l_\delta} / c_{l_{\delta_{theory}}}) c_{l_{\delta_{theory}}} (S_v / S) \quad (10.123a)$$

where: $C_{L_{\alpha_v}}$ is found from p. 386

$c_{l_{\alpha_v}}$ is found from Section 8.1.1.2

k' is found from Figure 8.13

K_b is found from page 259

$\{ (\alpha_\delta)_{C_L} / (\alpha_\delta)_{c_l} \}$ is found from Figure 8.53

$(C_{l_\delta} / c_{l_{\delta_{theory}}})$ is found from Figure 8.15

$c_{l_{\delta_{theory}}}$ is found from Figure 8.14

S_v is the effective vertical tail area as defined in Figure 10.13

For twin vertical tail:

$$C_{y_{\delta_r}} = 2 (C_{y_{\beta_{v(wfh)}}} / C_{y_{\beta_{v_{eff}}}}) (C_{L_{\alpha_v}} / c_{l_{\alpha_v}}) * * (k' K_b) \{ (\alpha_\delta)_{C_L} / (\alpha_\delta)_{c_l} \} * (C_{l_\delta} / c_{l_{\delta_{theory}}}) c_{l_{\delta_{theory}}} (S_v / S) \quad (10.123b)$$

where: $(C_{y_{\beta_{v(wfh)}}} / C_{y_{\beta_{v_{eff}}}})$ is found from Figure 10.17

2.) $C_{l_{\delta_r}}$

The rolling-moment-due-to-rudder derivative, $C_{l_{\delta_r}}$ is found from:

$$C_{l_{\delta_r}} = \{ (z_v \cos\alpha - l_v \sin\alpha) / b \} C_{y_{\delta_r}} \quad (10.124)$$

where: z_v and l_v are defined in Figure 10.27

$C_{y_{\delta_r}}$ is found from Eqn.(10.123)

3. $C_{n_{\delta_r}}$

The yawing-moment-due-to-rudder derivative, $C_{n_{\delta_r}}$ (also called rudder control power) may be estimated from:

$$C_{n_{\delta_r}} = -C_{y_{\delta_r}} (l_v \cos\alpha + z_v \sin\alpha)/b \qquad (10.125)$$

where: l_v and z_v are defined in Figure 10.27

$C_{y_{\delta_r}}$ is given by Eqn.(10.123).

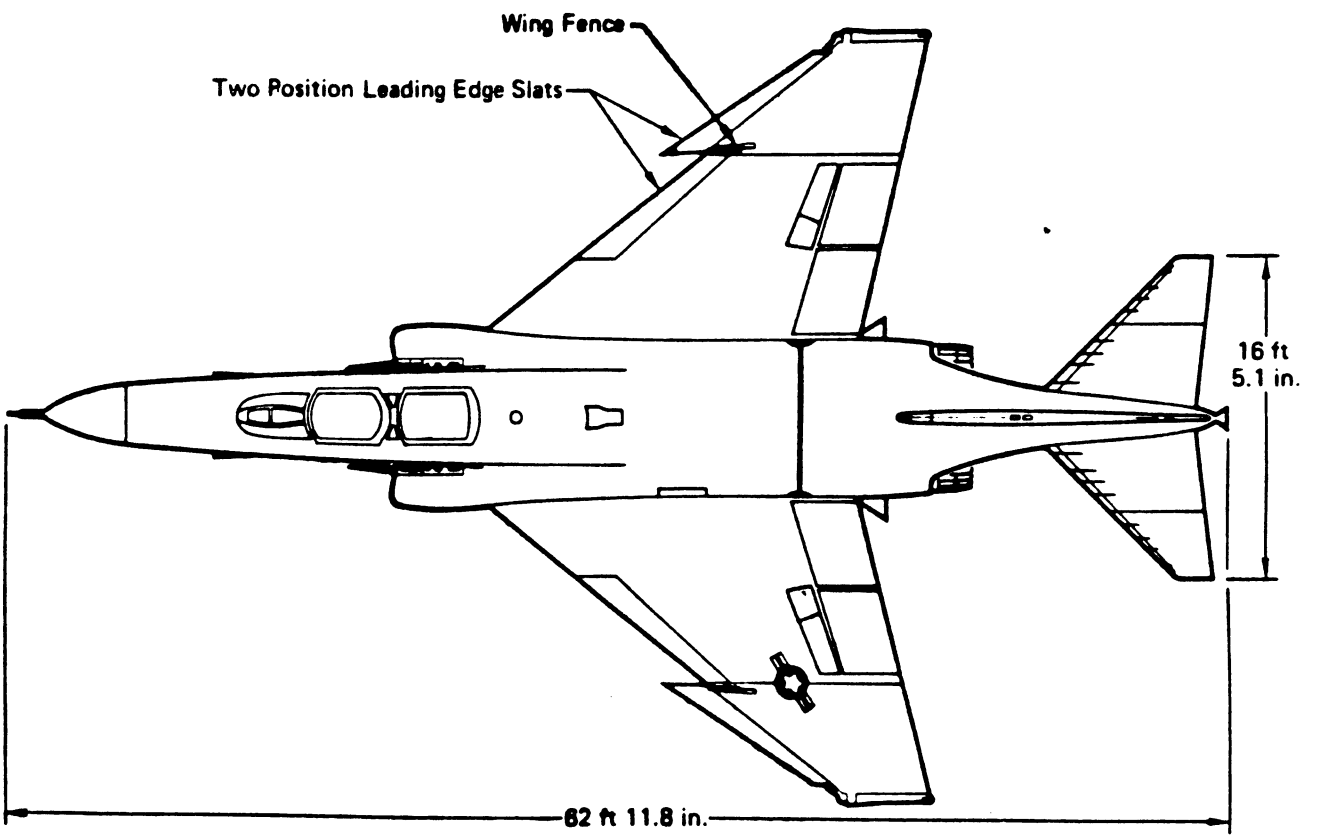

10.4 HINGEMOMENT DERIVATIVES OF CONTROL SURFACES

The purpose of this section is to present rapid methods for the estimation of hingemoment derivatives of control surfaces and tabs in the subsonic speed range. For methods which apply in the transonic and supersonic speed ranges the reader should consult Reference 9.

The methods to be presented apply only in the linear range of control surface deflections (< 20 degrees at best) and in the linear range of angles of attack (roughly 12 degrees). For nonlinear effects the reader should consult Ref.9 and use windtunnel data wherever possible.

Hingemoment derivatives are used for two purposes:

1. Computing stick, wheel and pedal cockpit control forces so they can be checked against airworthiness requirements.

   Part VII contains methods for computing the cockpit control forces as well as methods for checking with airworthiness standards.

2. Computing actuator force levels so that hydraulic or electro-mechanical actuators can be properly sized.

   Chapter 4 in Part IV contains a discussion of actuator sizing criteria.

Figure 10.61 shows a basic control surface and tab arrangement with the necessary geometric parameters identified. Note the use of the following nomenclature: main surface, control surface and tab, shown in Figure 10.61. This nomenclature applies to the following combinations:

1. horizontal tail + elevator + elevator tab

2. canard + canardvator + canardvator tab

3. wing + aileron + aileron tab

4. vertical tail + rudder + rudder tab

For a detailed discussion of the purpose of various combinations of tabs and control surfaces, the reader should consult Chapter 4 of Part IV.

In most cases, hingemoments are taken about the control surface hingeline: corresponding hingemoment coeffi-

cients and derivatives are denoted:

c_h and c_{h_x} respectively.

In some cases, hingemoments need to be considered about the tab hinge line: for example in servo-tab systems. The corresponding hingemoment coefficients and derivatives in that case are denoted:

c^t_h and $c^t_{h_y}$ respectively.

The material in this sub-section is organized as follows:

10.4.1 Two-Dimensional Control Surface and Tab Hingemoment Derivatives about the Control Surface Hingeline

10.4.2 Three-Dimensional Control Surface and Tab Hingemoment Derivatives about the Control Surface Hingeline

10.4.3 Two-Dimensional Tab Hingemoment Derivatives about the Tab Hingeline

10.4.4 Three-Dimensional Tab Hingemoment Derivatives about the Tab Hingeline

The methods apply as long as the airflow over the control surface is attached.

NOTES: 1.) All Two-D hingemoment derivatives are based on c_f^2, where c_f is the plain flap chord defined in Figure 10.61. The plain flap is either the control surface or the tab, depending on the point about which the hingemoments are taken.

2.) All Three-D hingemoment derivatives are based on $(S_{surface})*(\bar{c}_{surface})$, where the area and chord depend on the type of control surface considered: rudder, aileron, elevator, tab, etc.

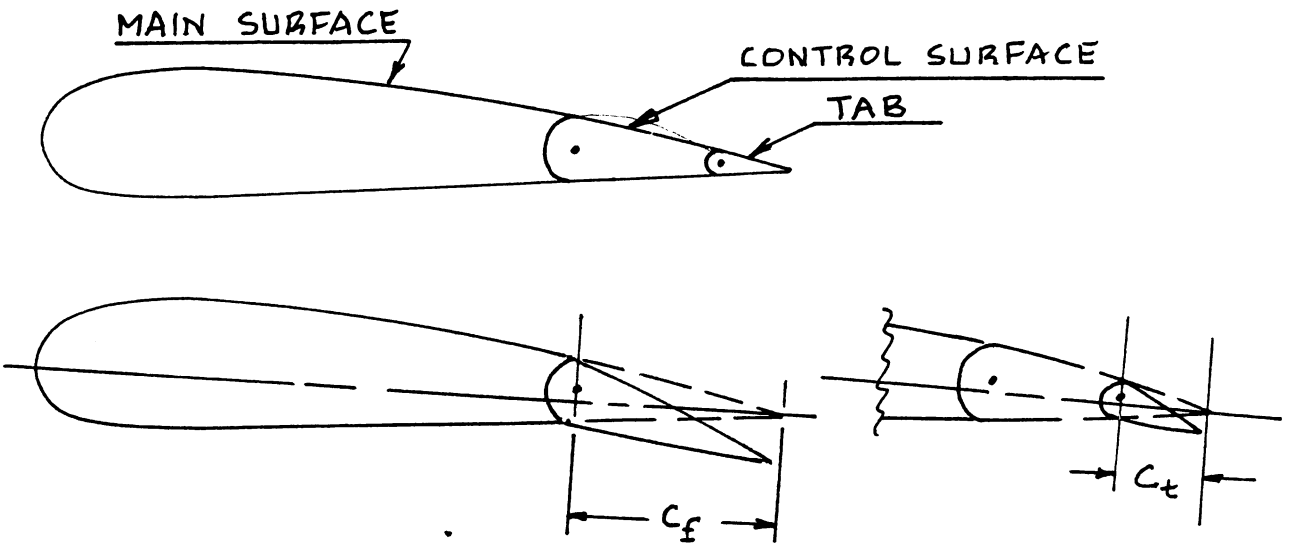

Figure 10.61 Geometry and Nomenclature Used with Control Surfaces and Tabs

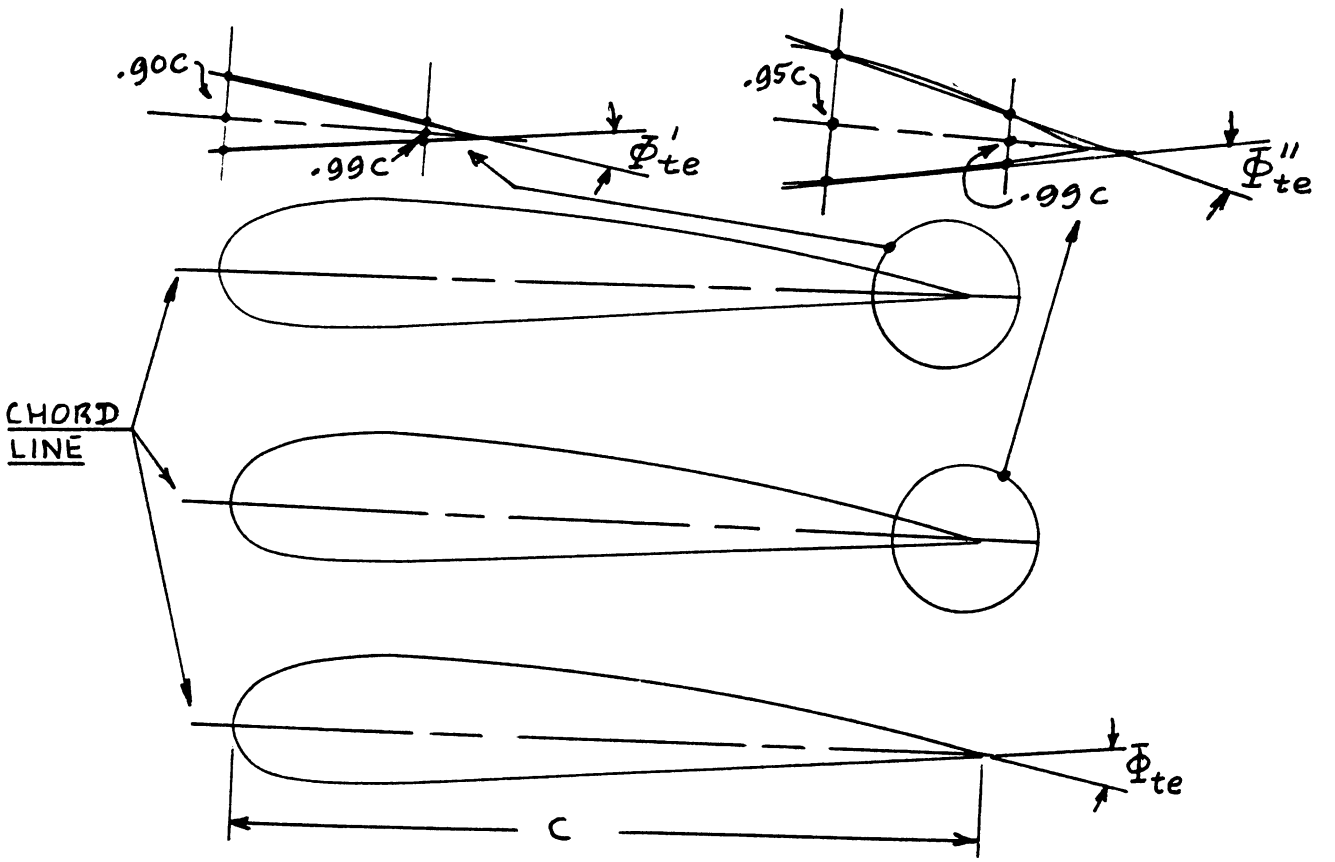

Figure 10.62 Definitions of Trailing Edge Angles

10.4.1 Two-Dimensional Control Surface and Tab Hingemoment Derivatives about the Control Surface Hingeline

The two-dimensional (=airfoil) hingemoment coefficient for a control surface is estimated from:

$$c_h = c_{h_o} + c_{h_\alpha}\alpha + c_{h_\delta}\delta + c_{h_{\delta_t}}\delta_t \qquad (10.126)$$

where: c_{h_o} is the zero-angle-of-attack, zero-control-surface-deflection, zero-tab-angle-deflection hingemoment coefficient. For main surfaces with symmetrical airfoils:

$$c_{h_o} = 0 \qquad (10.127)$$

For main surfaces with cambered airfoils, experimental data should be used.

c_{h_α} is the control surface hingemoment derivative due to angle of attack. It is estimated from 10.4.1.1, where it is called: $c_{h_{\alpha_{bal}}}$

c_{h_δ} is the control surface hingemoment derivative due to control surface deflection. It is obtained from 10.4.1.2

$c_{h_{\delta_t}}$ is the control surface hingemoment derivative due to a tab deflection. It is estimated from 10.4.1.3.

NOTE: The reader should recognize, that depending on the application, the following substitutions must be made in Equation (10.126):

for a wing: $\alpha = \alpha_w$ and $\delta = \delta_a$ or δ_{flap}

for a horizontal tail: $\alpha = \alpha_h$ and $\delta = \delta_e$

for a canard: $\alpha = \alpha_c$ and $\delta = \delta_c$

for a vertical tail: $\alpha = \beta$ and $\delta = \delta_r$

10.4.1.1 Two-D control surface hingemoment derivative due to angle of attack: c_{h_α}

The Two-D control surface hingemoment due to angle of attack derivative, c_{h_α} is determined with the following procedure:

Step 1: Check whether or not the following trailing edge angle condition is satisfied:

$$\tan(\Phi'_{te}/2) = \tan(\Phi''_{te}/2) = \tan(\Phi_{te}/2) = t/c \qquad (10.128)$$

where: Φ'_{te} is the trailing-edge angle defined as the angle between straight lines passing through points at 90 and 99 percent of the chord on the upper and lower airfoil surfaces

Φ''_{te} is the trailing-edge angle defined as the angle between straight lines passing through points at 95 and 99 percent of the chord on the upper and lower airfoil surfaces

Φ_{te} is the trailing-edge angle defined as the angle between tangents to the upper and lower airfoil surfaces at the trailing-edge

Figure 10.62 illustrates these angles.

Condition (10.128) is satisfied whenever the upper and lower surface lines of the control surface are straight.

Step 2: Determine c'_{h_α} from:

$$c'_{h_\alpha} = \qquad (10.129)$$

$$\{c'_{h_\alpha}/(c_{h_\alpha})_{theory}\}(c_{h_\alpha})_{theory}$$

where: $\{c'_{h_\alpha}/(c_{h_\alpha})_{theory}\}$ is found from Fig.10.63a which applies only to radius nose, sealed gap, plain flap type control surfaces

$(c_{h_\alpha})_{theory}$ is found from Figure 10.63b. The parameter $\{c_{l_\alpha}/(c_{l_\alpha})_{theory}\}$ in Fig.10.63a is itself found from Fig.10.64a with the assumption shown in Eqn. (10.128)

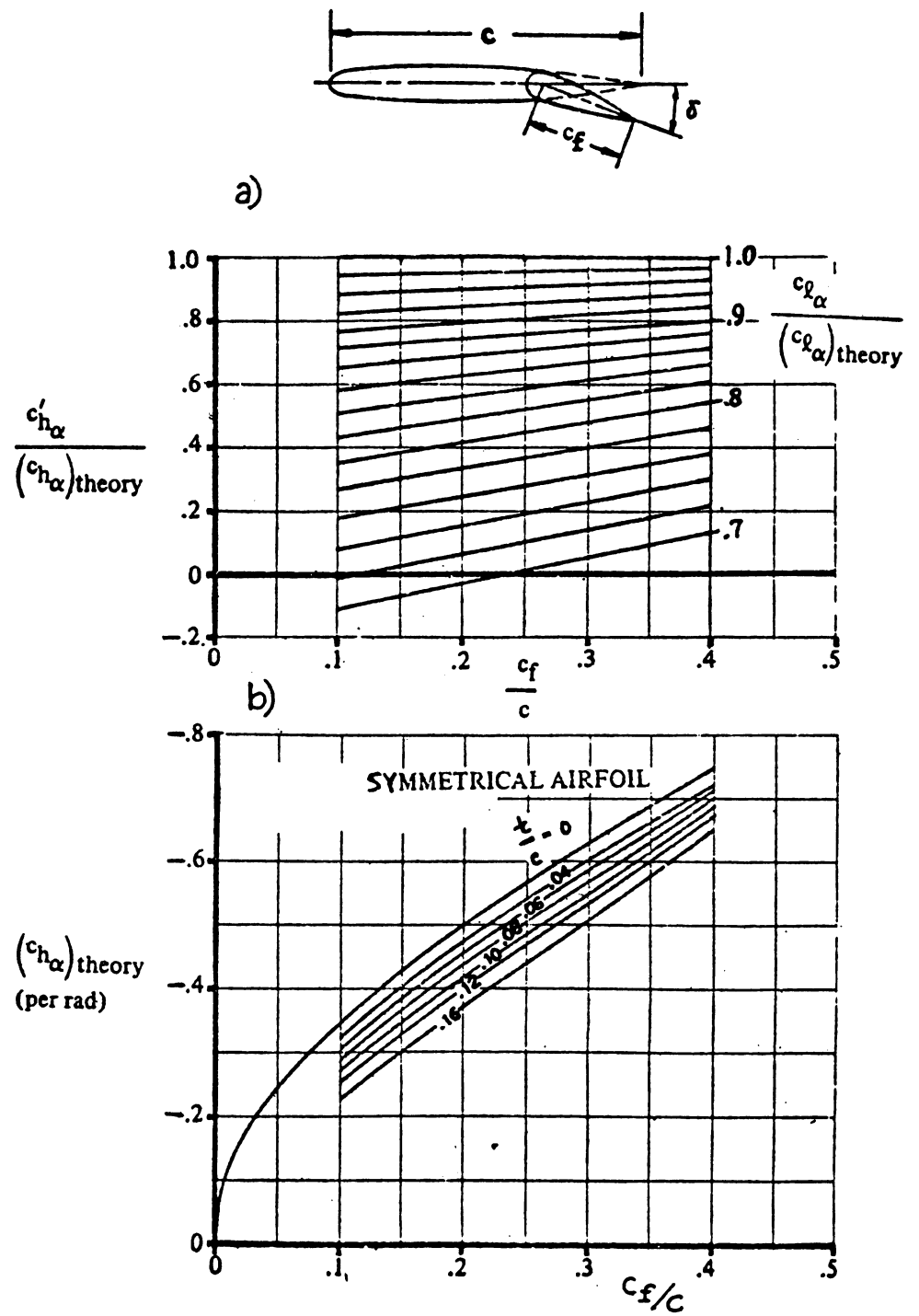

COPIED FROM: REF. 9

Figure 10.63 Two-Dimensional Control Surface Hingemoment Derivative due to Angle of Attack

COPIED FROM REF. 9

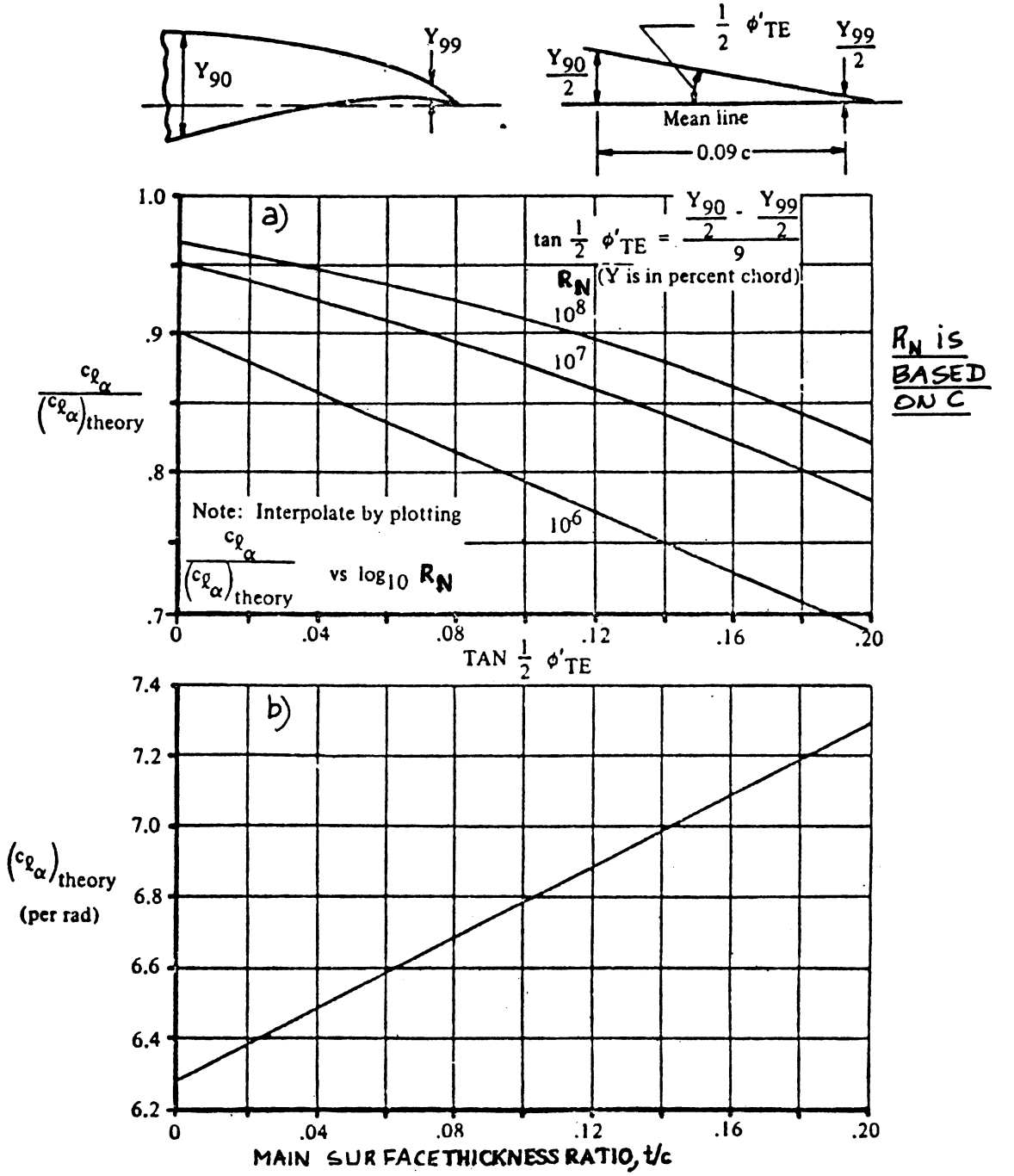

R_N is BASED ON C

Figure 10.64 Effect of Airfoil Thickness and Trailing Edge Angle on Lift Curve Slope

Step 3: If condition (10.128) is not satisfied, compute c''_{h_α} from:

$$c''_{h_\alpha} = (c'_{h_\alpha}) + \qquad (10.130)$$

$$+ 2(c_{l_\alpha})_{theory}[1 - \{c_{l_\alpha}/(c_{l_\alpha})_{theory}\}] *$$

$$*\{\tan(\Phi''_{te}/2) - (t/c)\}$$

where: (c'_{h_α}) is obtained from Eqn. (10.129)

$(c_{l_\alpha})_{theory}$ is obtained from Figure 10.64b at the appropriate thickness ratio, t/c

$\{c_{l_\alpha}/(c_{l_\alpha})_{theory}\}$ is obtained from Figure 10.64a with the assumption shown in Eqn. (10.128)

Φ''_{te} is defined under Step 1.

Note that if condition (10.128) is satisfied, and only in that case:

$$c''_{h_\alpha} = c'_{h_\alpha} \qquad (10.131)$$

Step 4: Since the value for c'_{h_α} or c''_{h_α} as found from either Step 2 or Step 3 applies only to round-nose control surfaces, corrections must be made which account for different nose shapes and for aerodynamic balance.

The corrected value for c_{h_α} is found from:

$$(c_{h_\alpha})_{bal} = \qquad (10.132)$$

$$(c''_{h_\alpha})\{(c_{h_\alpha})_{bal}/c''_{h_\alpha}\}$$

where: c''_{h_α} is obtained from Step 3.

$\{(c_{h_\alpha})_{bal}/c''_{h_\alpha}\}$ is found from Figure 10.65a for various nose shapes and

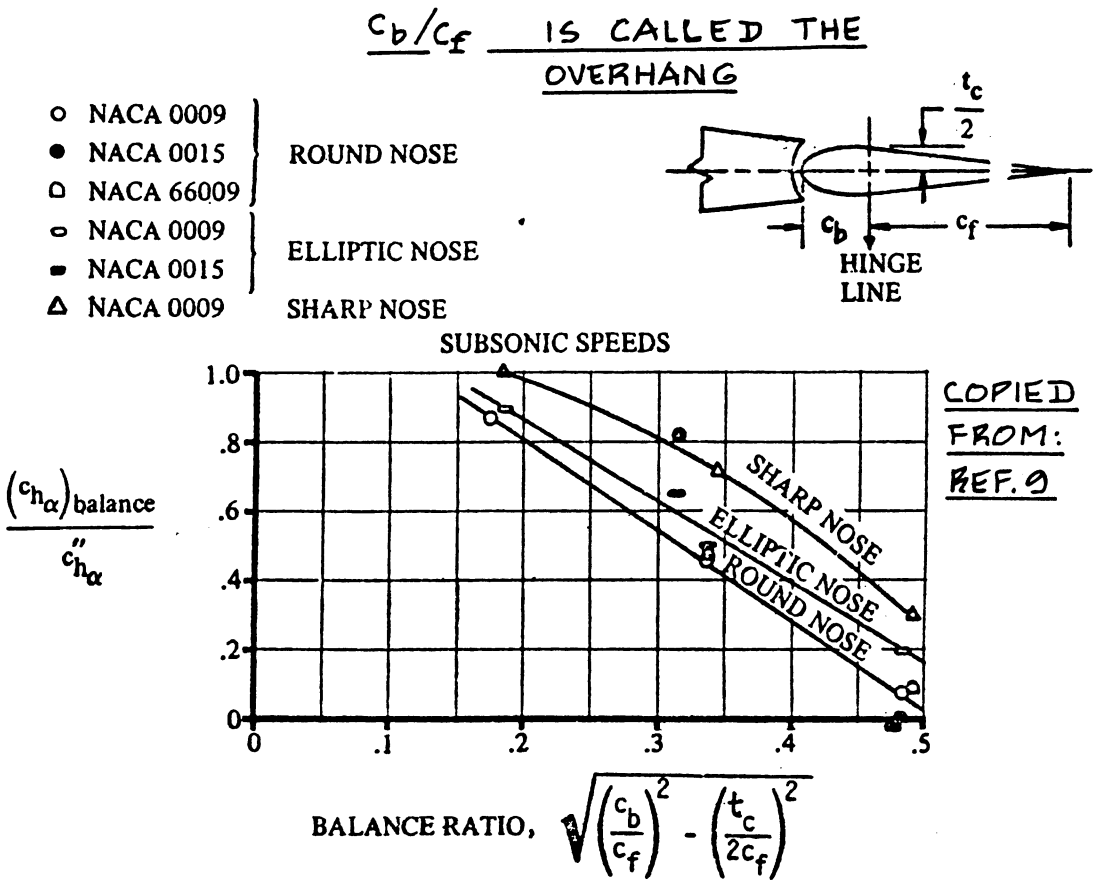

Figure 10.65a Effect of Nose Shape and Balance on the Two-Dimensional Hingemoment Derivative due to Angle of Attack

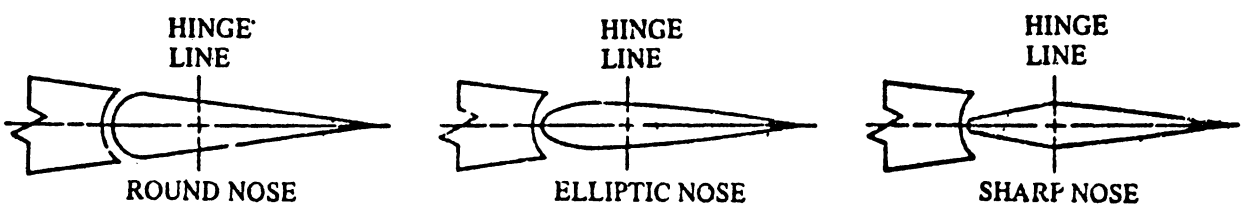

COPIED FROM REF. 9

Figure 10.65b Nose Shape Examples for 35 Percent Balance

at the proper balance ratio. Nose shapes and balance ratio are illustrated and defined in Figure 10.65b.

Step 5: Correct the hingemoment derivative for the effect of Mach Number:

$$(c_{h_\alpha})_M = (c_{h_\alpha})_{bal}/(1 - M^2)^{1/2} \qquad (10.133)$$

Step 6: Hingemoments also depend on whether or not the control surface and/or tab gaps are closed (i.e sealed). Figure 10.66 illustrates the difference between open and closed gaps.

Figure 10.67 may be used to introduce corrections for open gaps, depending on gap-size for the control surface.

Figure 10.68a may be used to correct for the effect of gap-size in the case of an unsealed tab.

NOTE: the Step 6 corrections are applied to $(c_{h_\alpha})_M$ by using ratios obtained from Figures 10.67 or 10.68a as appropriate.

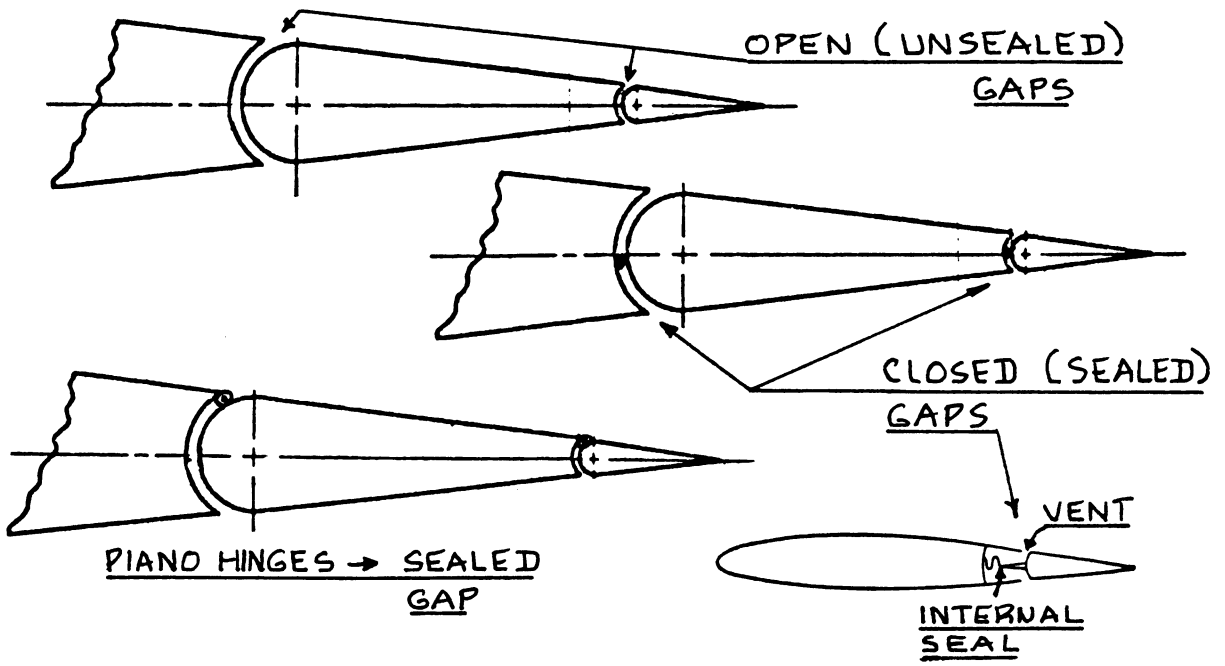

Figure 10.66 Examples of Closed (Sealed) and Open (Unsealed) Control Surface and Tab Gaps

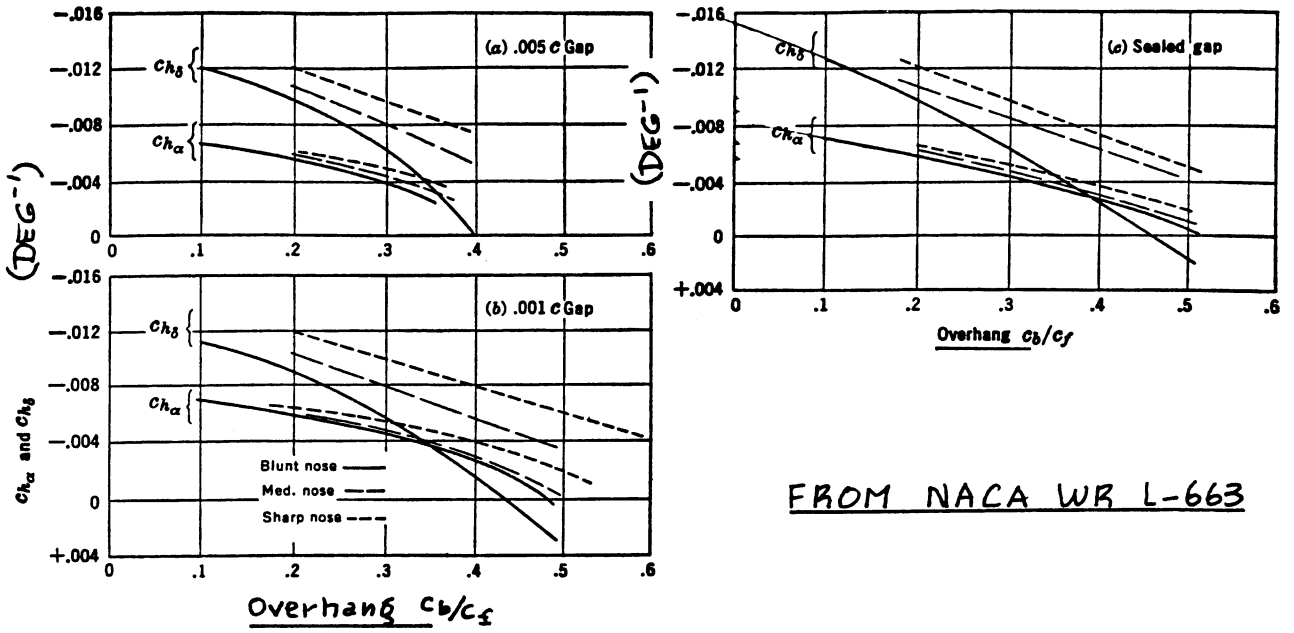

FROM NACA WR L-663

Figure 10.67 Effect of Gap Size and Overhang on Two-Dimensional Hingemoment Derivatives

COPIED FROM REF. 9

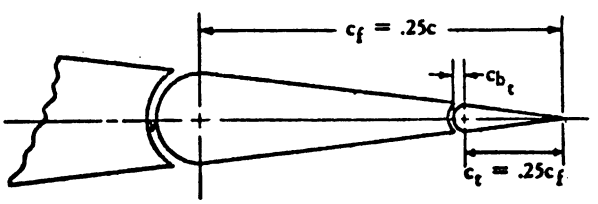

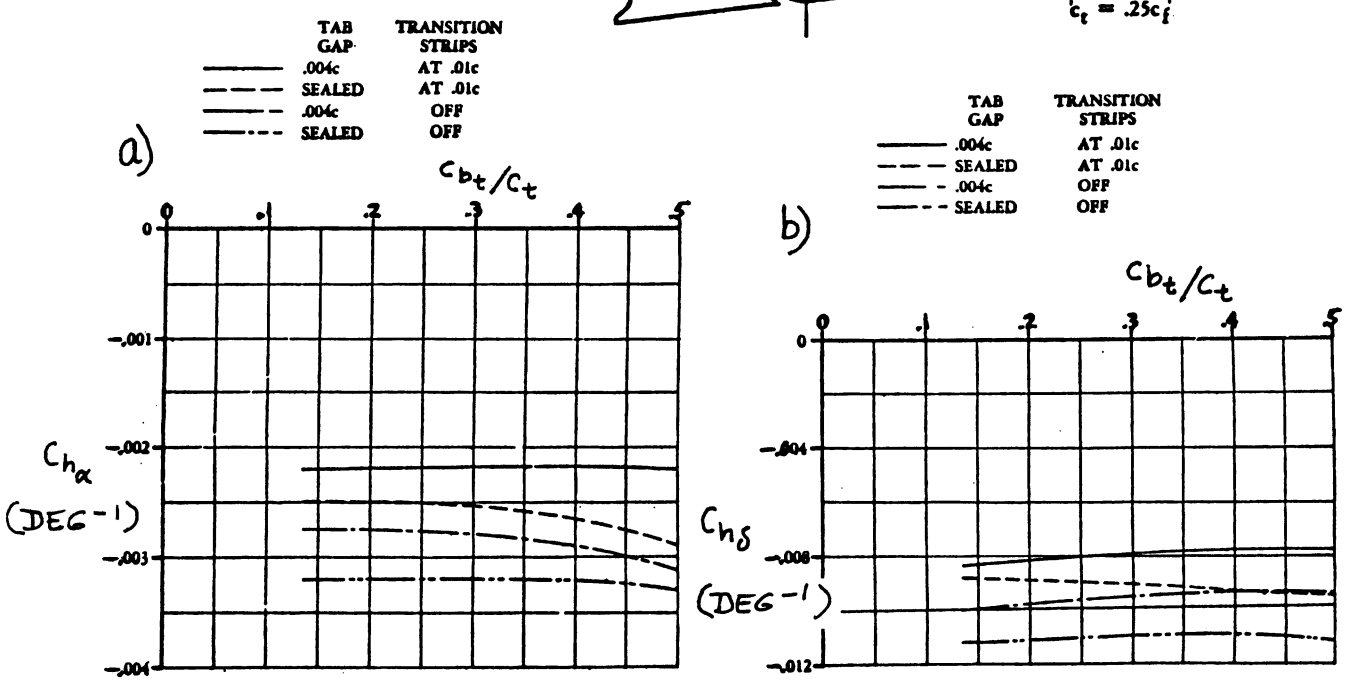

Figure 10.68 Effect of Tab Gap Size and Tab Overhang On Two-Dimensional Hingemoment Derivatives

10.4.1.2 Two-D control surface hingemoment derivative due to control surface deflection: c_{h_δ}

The Two-D control surface hingemoment due to control surface deflection derivative, c_{h_δ} is determined with the following procedure:

Step 1: This is a repeat of Step 1 in 10.4.1.1.

Step 2: Determine c'_{h_δ} from:

$$c'_{h_\delta} = \{c'_{h_\delta}/(c_{h_\delta})_{theory}\}(c_{h_\delta})_{theory} \quad (10.134)$$

where: $\{c'_{h_\delta}/(c_{h_\delta})_{theory}\}$ is found from Fig.10.69a which applies only to radius nose, sealed gap, plain flap type control surfaces

$(c_{h_\delta})_{theory}$ is found from Figure 10.69b. The parameter $\{c_{l_\alpha}/(c_{l_\alpha})_{theory}\}$ in Fig.10.69a is itself found from Figure 10.64a.

Step 3: If condition (10.128) is not satisfied, compute c''_{h_δ} from:

$$c''_{h_\delta} = (c'_{h_\delta}) + 2(c_{l_\delta})_{theory}* \quad (10.135)$$

$$*[1 - \{c_{l_\delta}/(c_{l_\delta})_{theory}\}]\{\tan(\Lambda''_{te}/2) - (t/c)\}$$

where: (c'_{h_δ}) is obtained from Eqn.(10.134)

$(c_{l_\delta})_{theory}$ is obtained from Figure 8.14 at the appropriate thickness ratio, t/c

$\{c_{l_\delta}/(c_{l_\delta})_{theory}\}$ is obtained from Figure 8.15

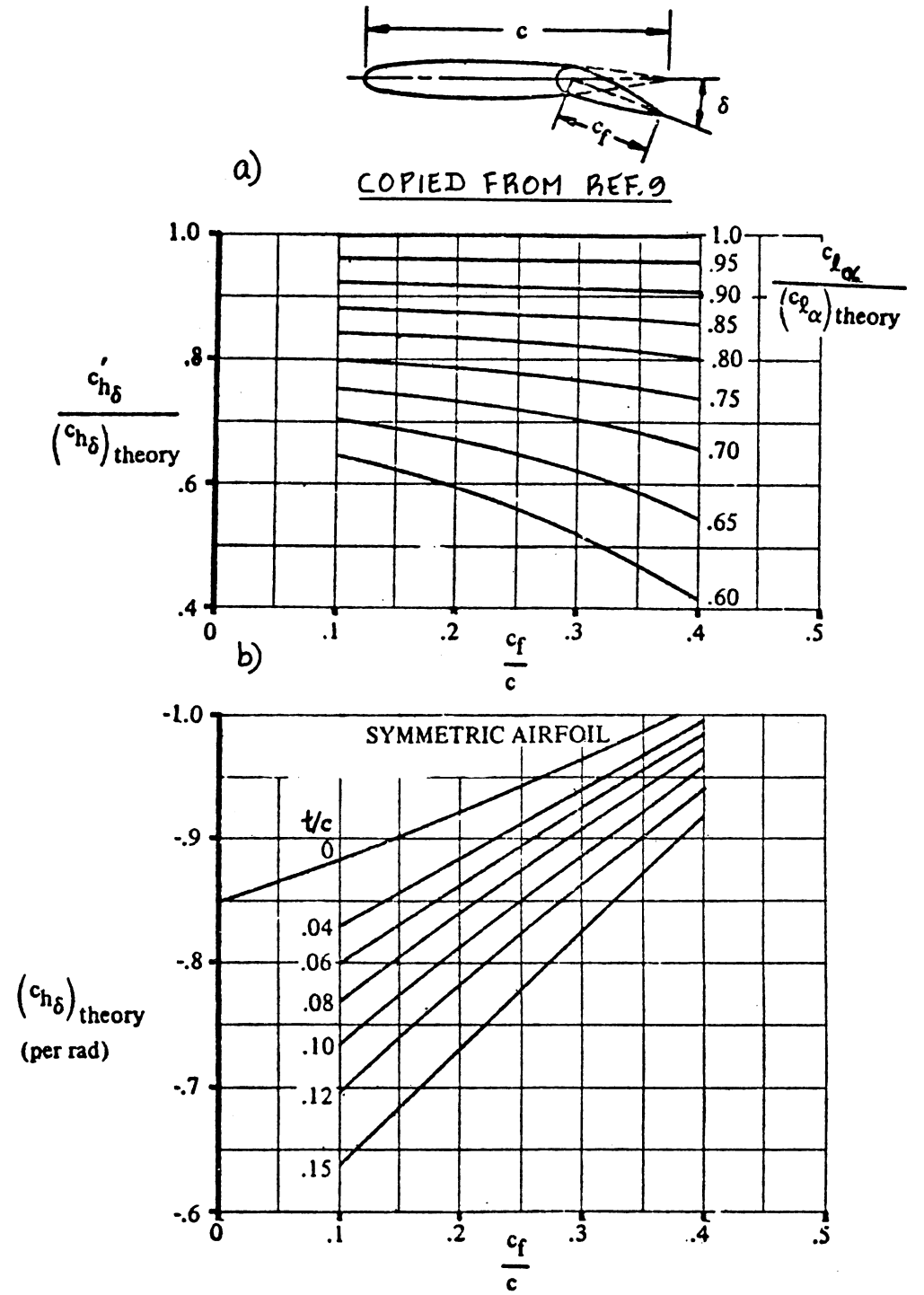

Figure 10.69 Two-Dimensional Control Surface Hingemoment Derivative due to Control Surface Deflection

Φ''_{te} is defined under Step 1 in 10.4.1.1.

NOTE: If the control surface trailing edge is beveled as in Fig.10.70, the value of Φ''_{te} should be set equal to the angle of the bevel!

Note that if condition (10.128) is satisfied, and only in that case:

$$c''_{h_\delta} = c'_{h_\delta} \qquad (10.136)$$

Step 4: Since the value for c_{h_δ} obtained under either Step 2 or Step 3 applies only to round-nose control surfaces, corrections must be made which account for different nose shapes and for aerodynamic balance.

The corrected value for c_{h_δ} is found from:

$$(c_{h_\delta})_{bal} = \qquad (10.137)$$

$$(c''_{h_\delta})\{(c_{h_\delta})_{bal}/c''_{h_\delta}\}$$

where: c''_{h_δ} is obtained from Step 3.

$\{(c_{h_\delta})_{bal}/c''_{h_\delta}\}$ is found from Figure 10.71 for various nose shapes and at the proper balance ratio. Nose shapes and balance ratio are illustrated and defined in Figure 10.65b.

Step 5: Correct the hingemoment derivative for the effect of Mach Number:

$$(c_{h_\delta})_M = (c_{h_\delta})_{bal}/(1 - M^2)^{1/2} \qquad (10.138)$$

Step 6: Hingemoments also depend on whether or not the control surface gaps are closed (i.e. i.e sealed). Figure 10.66 illustrates the the difference between open and closed gaps.

Figures 10.67 and 10.68b may be used to introduce corrections for open gaps, depending on gap size for the control surface and for the tab.

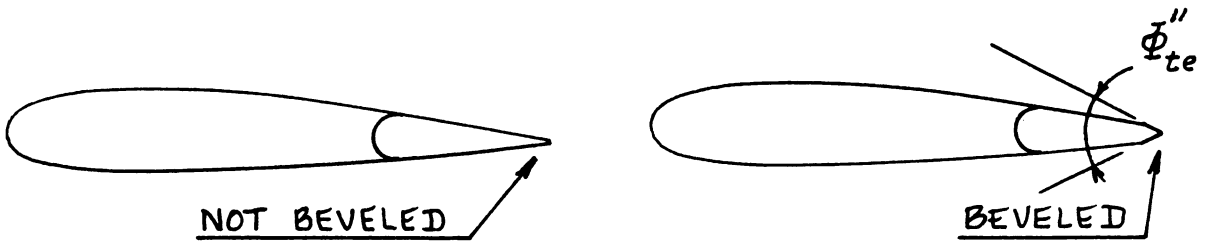

Figure 10.70 Example of Control Surface Beveling

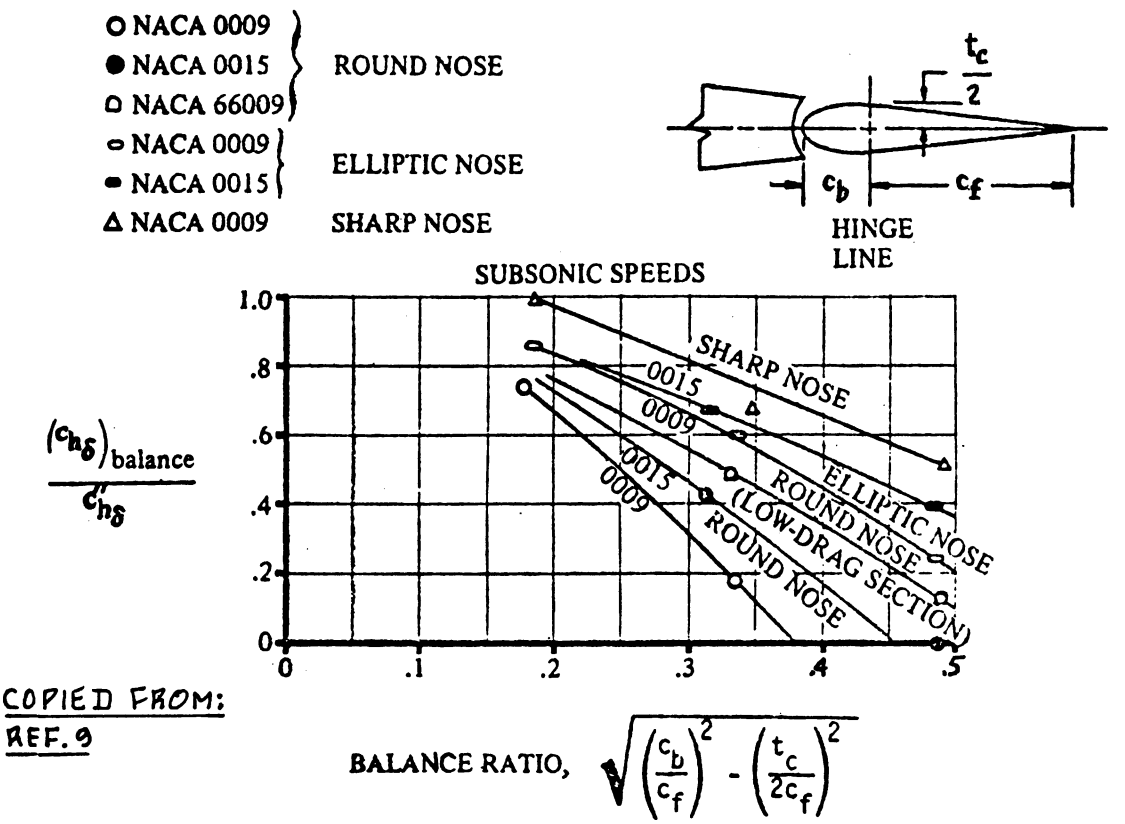

COPIED FROM: REF. 9

Figure 10.71 Effect of Nose Shape and Balance on the Two-Dimensional Control Surface Hingemoment Derivative due to Control Surface Deflection

10.4.1.3 Two-D control surface hingemoment derivative due to tab deflection: $c_{h_{\delta_t}}$

The Two-D control surface hingemoment derivative due to tab deflection, $c_{h_{\delta_t}}$, measured at constant angle of attack and at constant control surface deflection is found from:

$$c_{h_{\delta_t}} = (c_{h_{\delta_t}})_{c_l,\delta} + \quad (10.139)$$

$$- \{(c_{h_{c_l}})_{\delta_t,\delta}\} * \{(c_{l_\alpha})_{\delta_t,\delta}\} * \{(\alpha_{\delta_t})_{c_l,\delta}\}$$

where: $(c_{h_{\delta_t}})_{c_l,\delta}$ is the change in control surface hingemoment coefficient due to tab deflection at constant lift and at constant control surface deflection. It is obtained from Figure 10.72.

$(c_{h_{c_l}})_{\delta_t,\delta}$ is the change in control surface hingemoment due to lift at constant tab deflection and at constant control surface deflection. It is obtained from Figure 10.73.

$(c_{l_\alpha})_{\delta_t,\delta}$ is the airfoil lift curve slope of the main surface to which the control surface is attached. It is found in 8.1.1.2.

$(\alpha_{\delta_t})_{c_l,\delta}$ is the change in angle of attack due to a change in tab deflection. It is found from Figure 10.74.

The derivatives in Equation (10.139) do not account for the effects of tab nose shape and tab gaps: they apply to round nose tabs with sealed gaps only! To account for the effect of differing tab nose shapes and for unsealed tab gaps, the reader should correct $c_{h_{\delta_t}}$ by using appropriate ratios obtained from Figs 10.75 and 10.76.

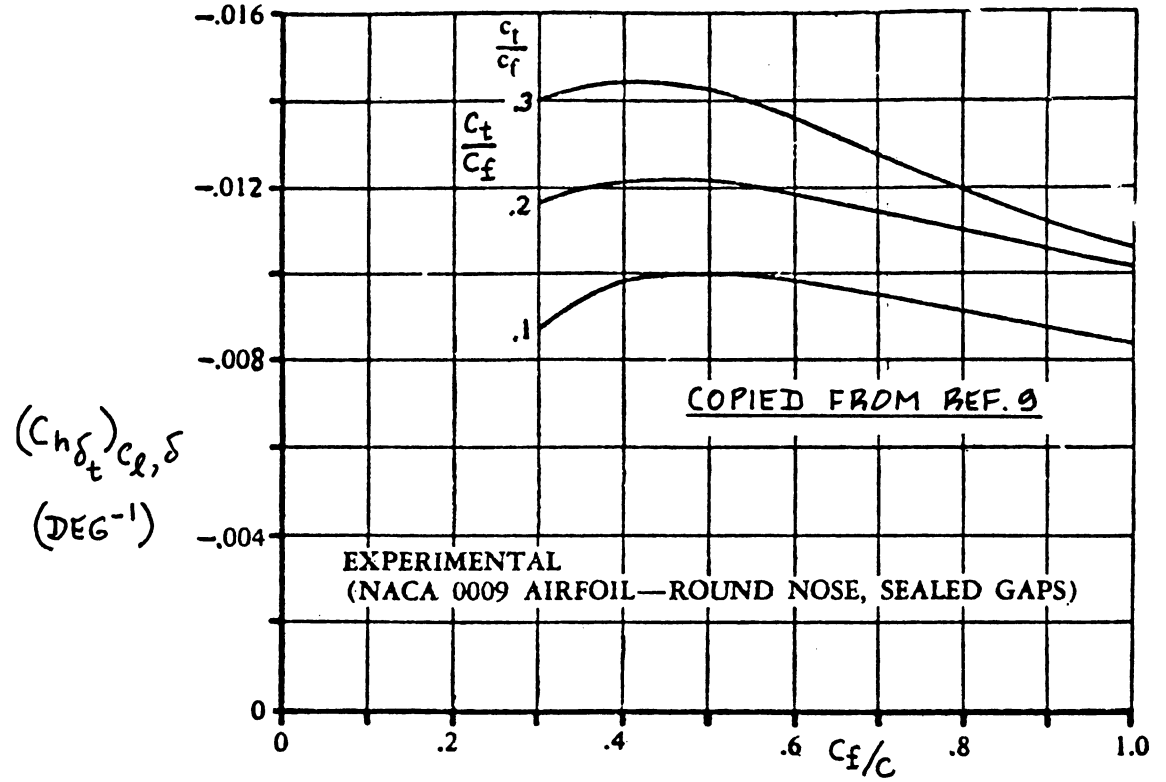

Figure 10.72 Effect of Control Surface Size and Tab Size on the Change in Control Surface Hingemoment Coefficient due to Tab Deflection at Constant Lift Coefficient and at Constant Control Surface Deflection

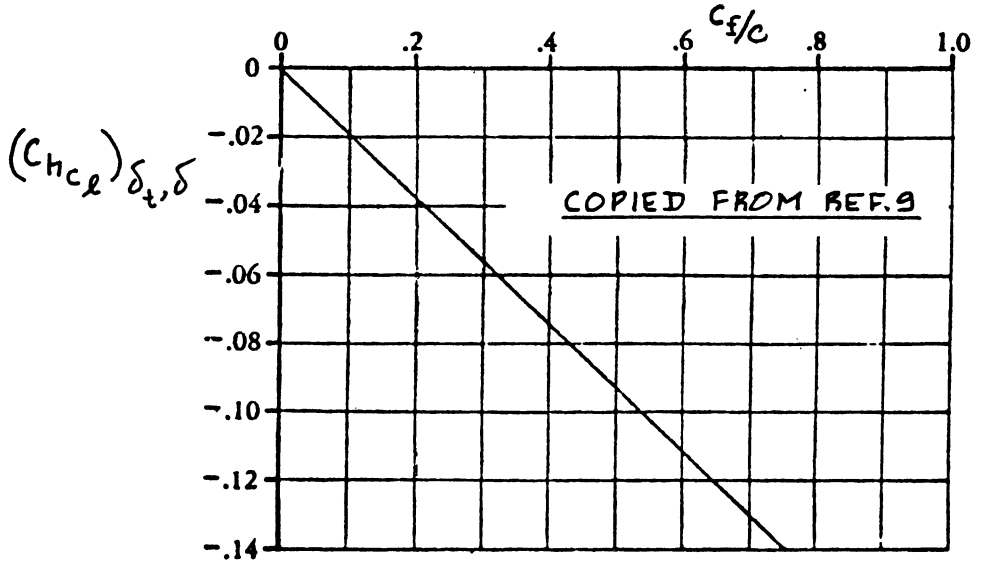

Figure 10.73 Effect of Control Surface Size on the Change in Control Surface Hingemoment due to Lift at Constant Tab Deflection and at Constant Control Surface Deflection

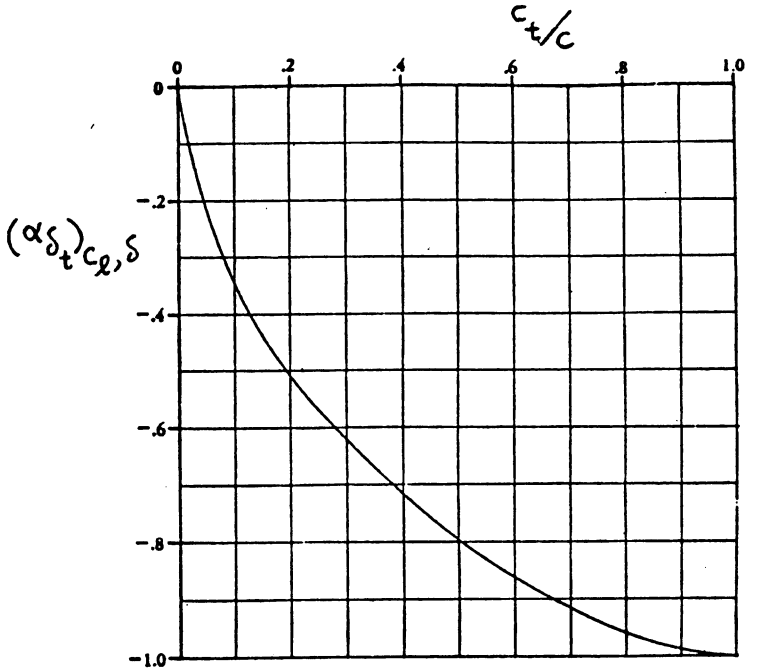

COPIED FROM:
REF. 9

Figure 10.74 Change in Angle of Attack due to a Change in Tab Deflection

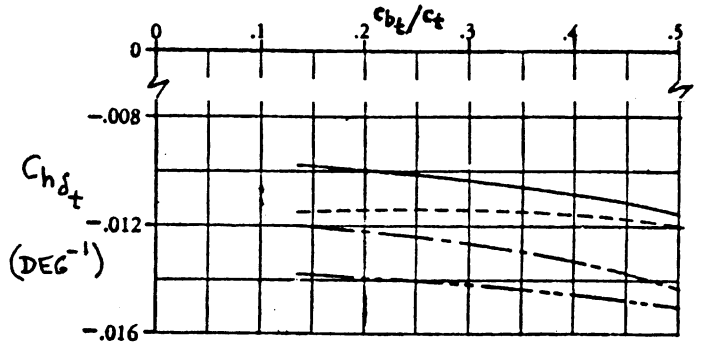

COPIED FROM:
REF. 9

TAB GAP	TRANSITION STRIPS
.004c	AT .01c
SEALED	AT .01c
.004c	OFF
SEALED	OFF

Figure 10.75 Effect of Tab Nose Shape and Tab Overhang on the Control Surface Hingemoment Derivative due to Tab Deflection

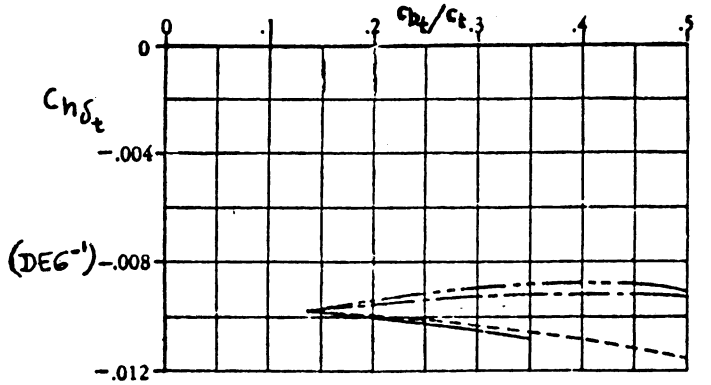

BLUNT
ROUND
ELLIPTICAL
SHARP

COPIED FROM:
REF. 9

Figure 10.76 Effect of Tab Gap Size and Tab Overhang on the Control Surface Hingemoment Derivative due to Tab Deflection

10.4.2 Three-Dimensional Control Surface and Tab Hingemoment Derivatives

The three-dimensional hingemoment coefficient for a control surface is estimated from:

$$C_h = C_{h_o} + C_{h_\alpha}\alpha + C_{h_\delta}\delta + C_{h_{\delta_t}}\delta_t \qquad (10.140)$$

where: C_{h_o} is the zero-angle-of-attack, zero-control-surface-deflection and zero-tab-deflection hingemoment coefficient. For main surfaces with symmetrical airfoils:

$$C_{h_o} = 0 \text{ (symmetrical airfoils only)} \qquad (10.141)$$

For main surfaces with cambered airfoils, experimental data should be used to determine this quantity.

C_{h_α} is the Three-D control surface hingemoment derivative due to angle of attack. It is found from 10.4.2.1

C_{h_δ} is the Three-D control surface hingemoment derivative due to control surface deflection. It is estimated from 10.4.2.2

$C_{h_{\delta_t}}$ is the Three-D control surface hingemoment derivative due to a tab deflection. It is estimated from 10.4.2.3.

10.4.2.1 Three-D control surface hingemoment derivative due to angle of attack: C_{h_α}

The Three-D control surface hingemoment due to angle of attack derivative, C_{h_α} is determined from:

$$C_{h_\alpha} = \qquad (10.142)$$

$$\{(A\cos\Lambda_{c/4})/(A + 2\cos\Lambda_{c/4})\}(c_{h_\alpha})_M + \Delta C_{h_\alpha}$$

where: $(c_{h_\alpha})_M$ is obtained from Eqn. (10.133)

$$\Delta C_{h_\alpha} = \qquad (10.143)$$

$$\{\Delta C_{h_\alpha}/(c_{l_\alpha} B_2 K_\alpha \cos\Lambda_{c/4})\} * (c_{l_\alpha} B_2 K_\alpha \cos\Lambda_{c/4})$$

with: $\{\Delta C_{h_\alpha} / (c_{l_\alpha} B_2 K_\alpha \cos\Lambda_{c/4})\}$ a factor obtained from Figure 10.77a

c_{l_α} is the airfoil lift-curve-slope of the surface to which the control surface is attached. The main surface airfoil at the m.g.c. of the control surface may be used. The method of 8.1.1.2 can be employed to estimate this quantity.

B_2 accounts for control surface and balance chord ratios. It may be determined from Figure 10.77c. The primed values of control surface and balance chord ratios in Figure 10.77c refer to measurements normal to the quarter chord line of the main surface.

K_α accounts for the effect of control surface span. It is found from:

$$K_\alpha = \{(K_\alpha)_{\eta_i}(1 - \eta_i) - (K_\alpha)_{\eta_o}(1 - \eta_o)\}/(\eta_o - \eta_i) \qquad (10.144)$$

where: η_i is the inboard span station of the control surface as a fraction of the main surface semi-span

$(K_\alpha)_{\eta_i}$ is found from Figure 10.77b

η_o is the outboard span station of the control surface as a fraction of the main surface semi-span

$(K_\alpha)_{\eta_o}$ is found from Figure 10.77b

NOTE: Control surface hingemoments are also affected by items such as horns, internal balance plates and various types of tab configurations. A discussion of these items is found in Chapter 3 of Part IV and in Chapter 5 of Reference 16. A detailed treatment of methods for estimating hingemoment derivatives due to these effects is beyond the scope of this text.

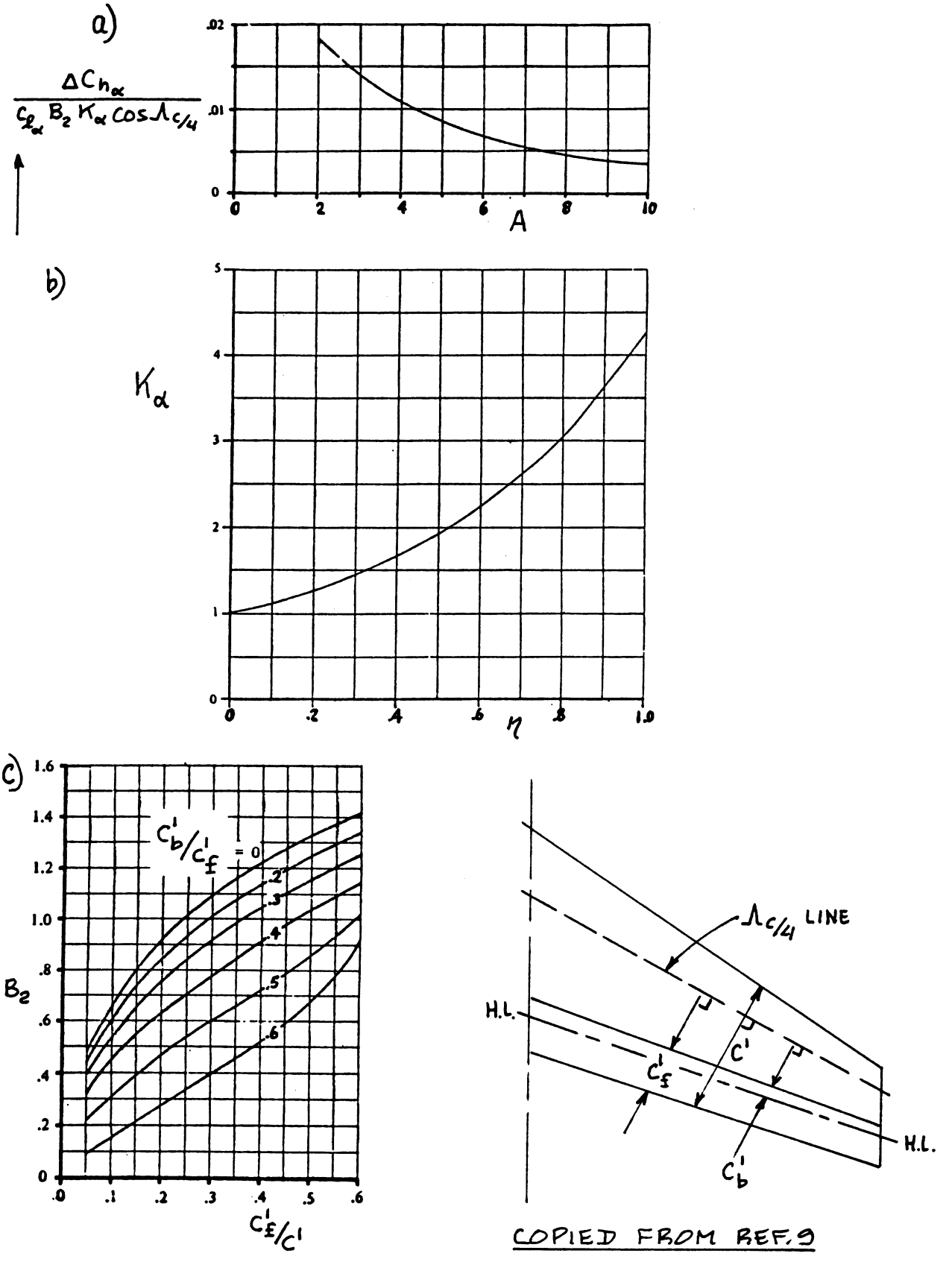

COPIED FROM REF. 9

Figure 10.77 Three-Dimensional Correction Factors for the Control Surface Hingemoment Derivative due to Angle of Attack

10.4.2.2 Three-D control surface hingemoment derivative due to control surface deflection: C_{h_δ}

The Three-D control surface hingemoment due to control surface deflection derivative, C_{h_δ} is found from:

$$C_{h_\delta} = (\cos\Lambda_{c/4})(\cos\Lambda_{hl})^* \qquad (10.145)$$

$$*[(c_{h_\delta})_M - \alpha_\delta (c_{h_\alpha})_M \{(2\cos\Lambda_{c/4})/(A + 2\cos\Lambda_{c/4})\}] + \Delta C_{h_\delta}$$

where: $(c_{h_\alpha})_M$ is found from Equation (10.133)

$(c_{h_\delta})_M$ is found from Equation (10.138)

α_δ is obtained from Figure 8.17

$$\Delta C_{h_\delta} = \qquad (10.146)$$

$$\{\Delta C_{h_\delta}/(c_{l_\delta} B_2 K_\delta \cos\Lambda_{c/4} \cos\Lambda_{hl})\}^* (c_{l_\delta} B_2 K_\delta \cos\Lambda_{c/4} \cos\Lambda_{hl})$$

with: $\{\Delta C_{h_\delta}/(c_{l_\delta} B_2 K_\delta \cos\Lambda_{c/4} \cos\Lambda_{hl})\}$ a factor obtained from Fig.10.78a

c_{l_δ} is found from Figure 8.14

B_2 is found from Figure 10.77c, where the primed values of the control-surface and the balance-chord ratios refer to measurements normal to the quarter chord line

$$K_\delta = \qquad (10.147)$$

$$\{(K_\delta)_{\eta_i}(1 - \eta_i) - (K_\delta)_{\eta_o}(1 - \eta_o)\}/(\eta_o - \eta_i)$$

where: η_i is defined in 10.4.2.1

$(K_\delta)_{\eta_i}$ is found from Figure 10.78b

η_o is defined in 10.4.2.1

$(K_\delta)_{\eta_o}$ is found from Figure 10.78b

The note at the end of 10.4.2.1 applies here also!

10.4.2.3 Three-D control surface hingemoment derivative due to tab deflection: $C_{h_{\delta_t}}$

The Three-D control surface hingemoment due to tab deflection derivative, $C_{h_{\delta_t}}$ is estimated by employing

Equation (10.145) and its sequel with appropriate substitution of tab parameters for control surface parameters.

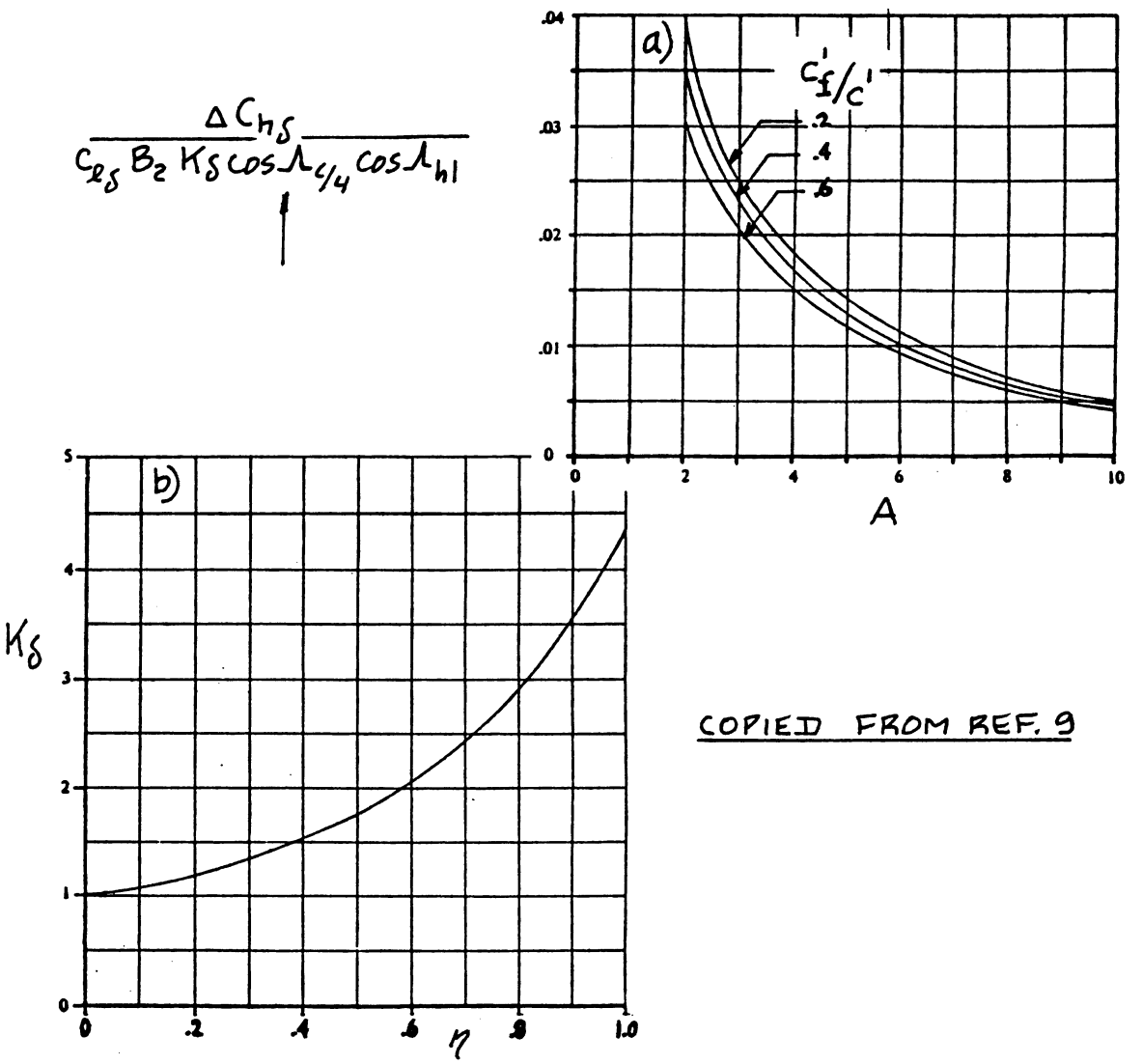

COPIED FROM REF. 9

Figure 10.78 Three Dimensional Correction Factors for the Control Surface Hingemoment Derivative due to Control Surface Deflection

10.4.3 Two-Dimensional Tab Hingemoment Derivatives about the Tab Hingeline

The two-dimensional tab hingemoment coefficient about the tab hingeline can be written as:

$$c^t_h = c^t_{h_o} + c^t_{h_\alpha}\alpha + (c^t_{h_\delta})_{\alpha,\delta_t}\delta + c^t_{h_{\delta_t}}\delta_t \quad (10.148)$$

where: $c^t_{h_o}$ is the zero-angle-of-attack, zero-control-surface-deflection and zero-tab-deflection hingemoment coefficient of the tab about its own hingeline. This quantity is zero for symmetrical airfoils. For cambered airfoils experimental data should be used.

$c^t_{h_\alpha}$ is found from 10.4.1.1 by substitution of tab parameters for control surface parameters

$c^t_{h_{\delta_t}}$ is found from 10.4.1.2 by substitution of tab parameters for control surface parameters

$$(c^t_{h_\delta})_{\alpha,\delta_t} = \quad (10.149)$$

$$(c^t_{h_\delta})_{c_l,\delta_t} - (c^t_{h_{c_l}})_{\delta,\delta_t} * (c_{l_\alpha})_{\delta,\delta_t} * (\alpha_\alpha)_{c_l,\delta_t}$$

with: $(c^t_{h_\delta})_{c_l,\delta_t}$ being the change in tab hingemoment coefficient due to control surface deflection at constant lift and at constant tab deflection. It is found from Figure 10.79a.

$(c^t_{h_{c_l}})_{\delta,\delta_t}$ being the change in tab hingemoment coefficient due to lift at constant control surface deflection and at constant tab deflection. It is found from Figure 10.79b.

$(c_{l_\alpha})_{\delta,\delta_t}$ is the airfoil lift curve slope of the main surface to which the tab (via the control surface) is attached. It is found in 8.1.1.2.

$(\alpha_\delta)_{c_l,\delta_t}$ is the change in angle of attack due to a change in control surface deflection. It is obtained from Figure 10.80 by using the tab-chord to main surface chord ratio.

The derivatives in Equation (10.148) do not account for the effects of tab nose shape and tab gaps: they apply to round nose tabs with sealed gaps only! To account for the effect of differing tab nose shapes and for unsealed tab gaps, the reader should correct $c^t h_y$ by using appropriate ratios obtained from Figs 10.81a,b,c and d.

10.4.4 Three-Dimensional Tab Hingemoment Derivatives about the Tab Hingeline

The three-dimensional tab hingemoment coefficient about the tab hingeline can be determined from:

$$C^t_h = C^t_{h_o} + C^t_{h_\alpha}\alpha + \qquad (10.150)$$

$$(C^t_{h_\delta})_{\alpha,\delta_t}\delta + C^t_{h_{\delta_t}}\delta_t$$

where all coefficients may be determined from their two-dimensional counterparts by using the methods of 10.4.2.1 and 10.4.2.2.

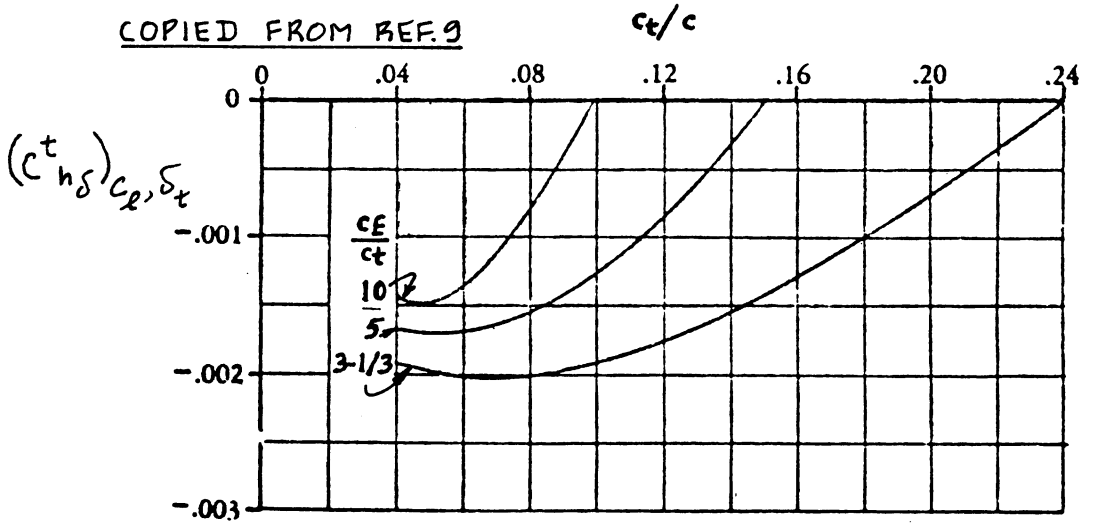

Figure 10.79a Effect of Tab and Control Surface Size on the Change in Tab Hingemoment Coefficient due to Control Surface Deflection at Constant Lift and at Constant Tab Deflection

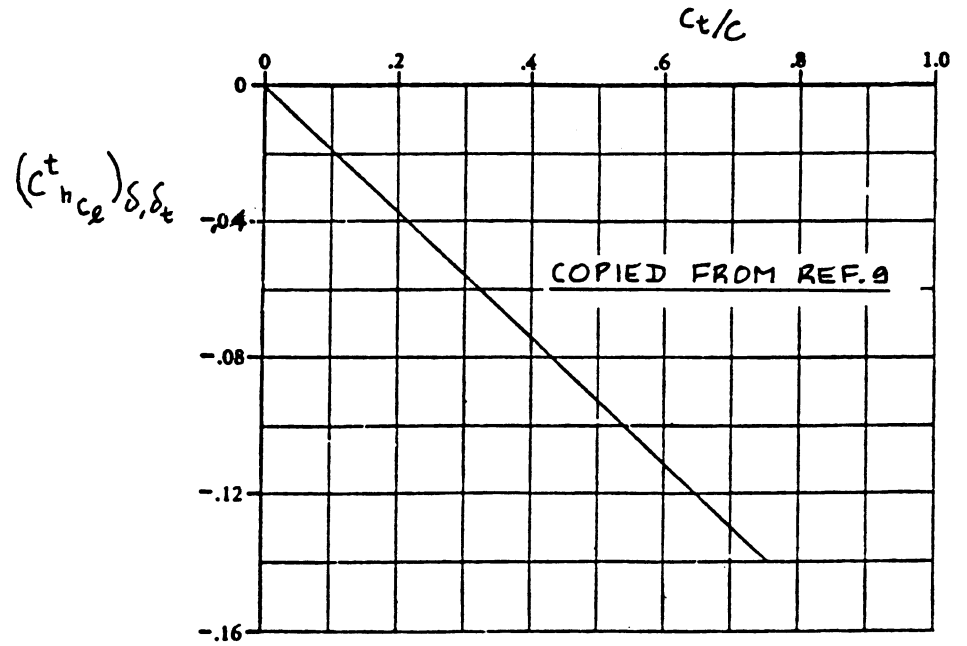

Figure 10.79b Effect of Tab Size on the Change in Tab Hingemoment Coefficient due to Lift at Constant Control Surface Deflection and at Constant Tab Deflection

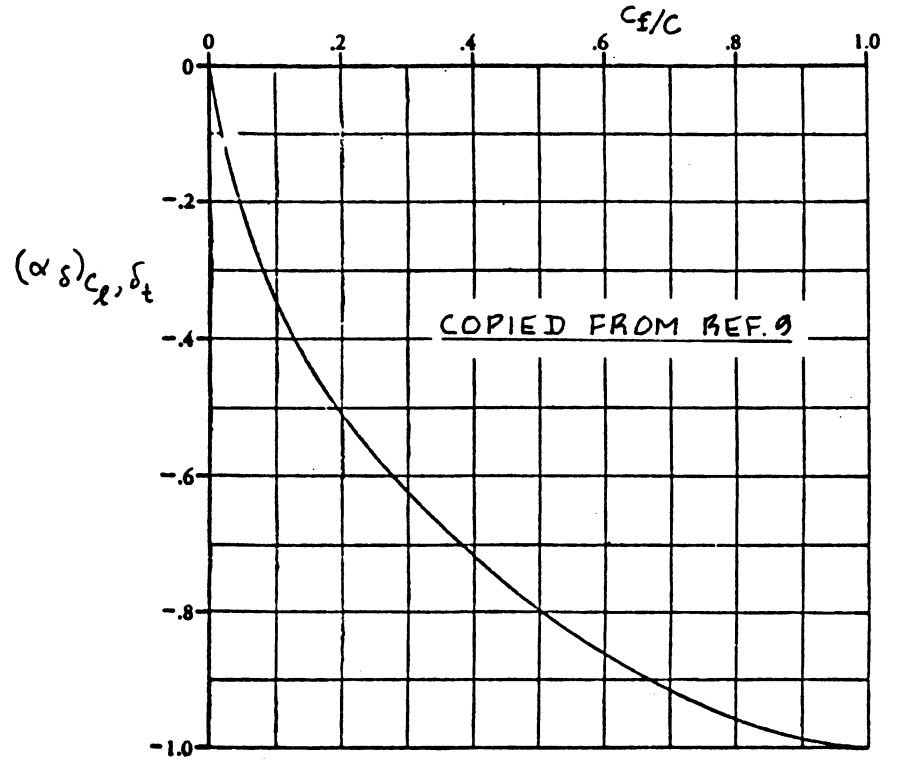

Figure 10.80 Change in Angle of Attack due to a Change in Control Surface Deflection

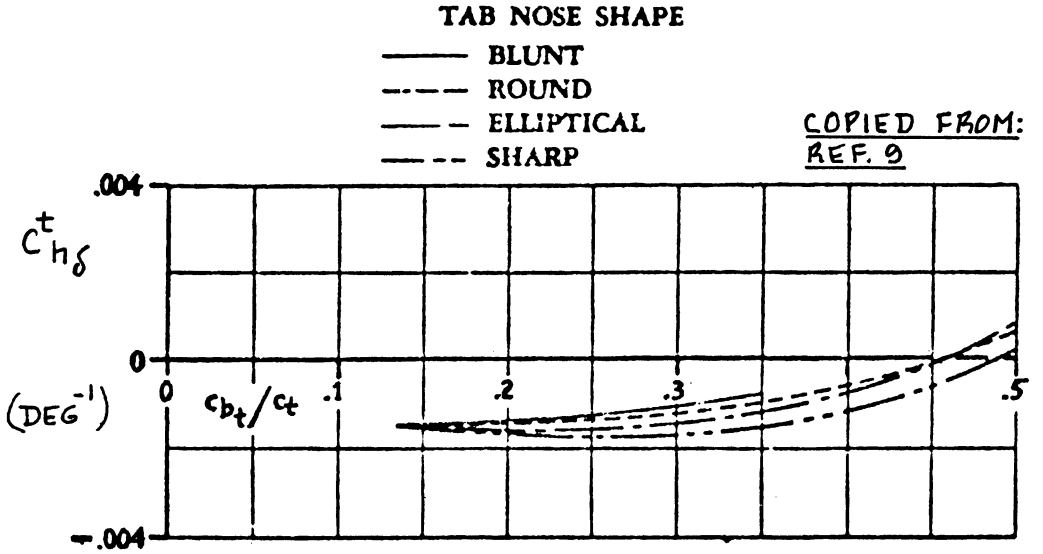

Figure 10.81a Effect of Tab Nose Shape on the Tab Hingemoment Derivative due to Control Surface Deflection

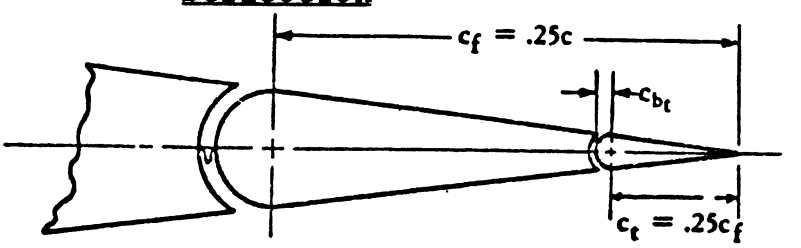

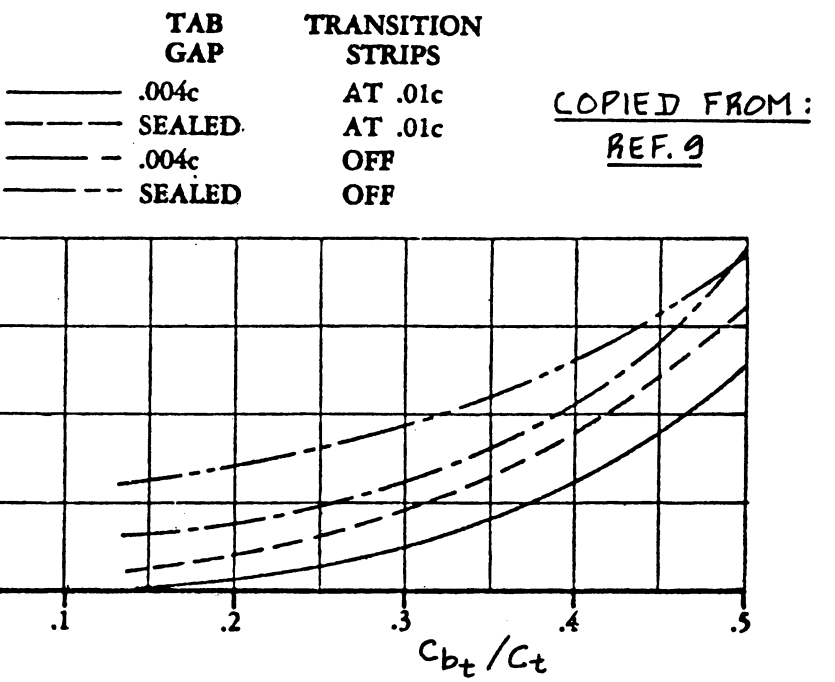

Figure 10.81b Effect of Tab Gap and Tab Size on the Tab Hingemoment Derivative due to Angle of Attack

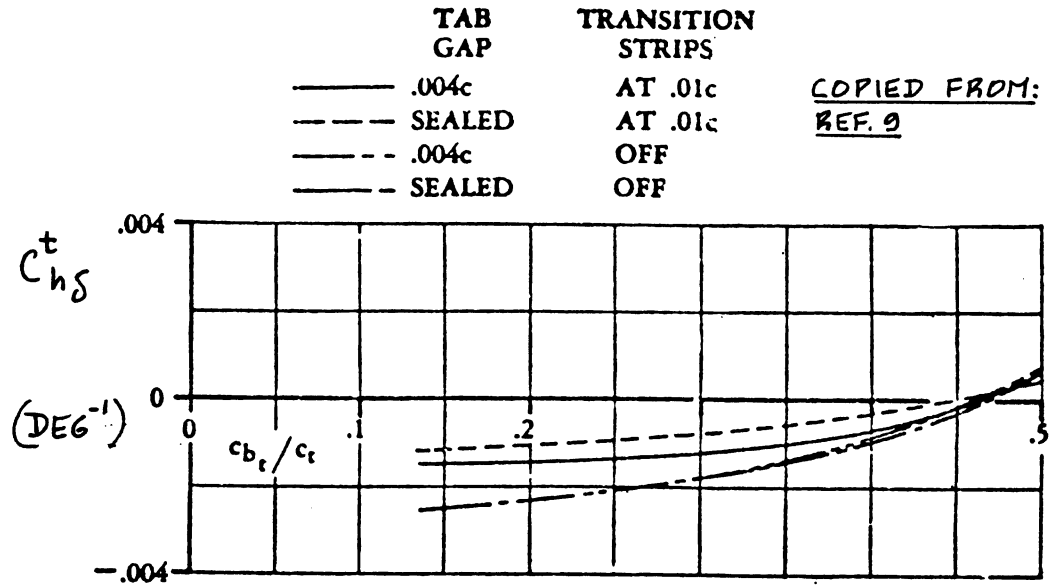

Figure 10.81c Effect of Tab Gap and Tab Size on the Tab Hingemoment Derivative due to Control Surface Deflection

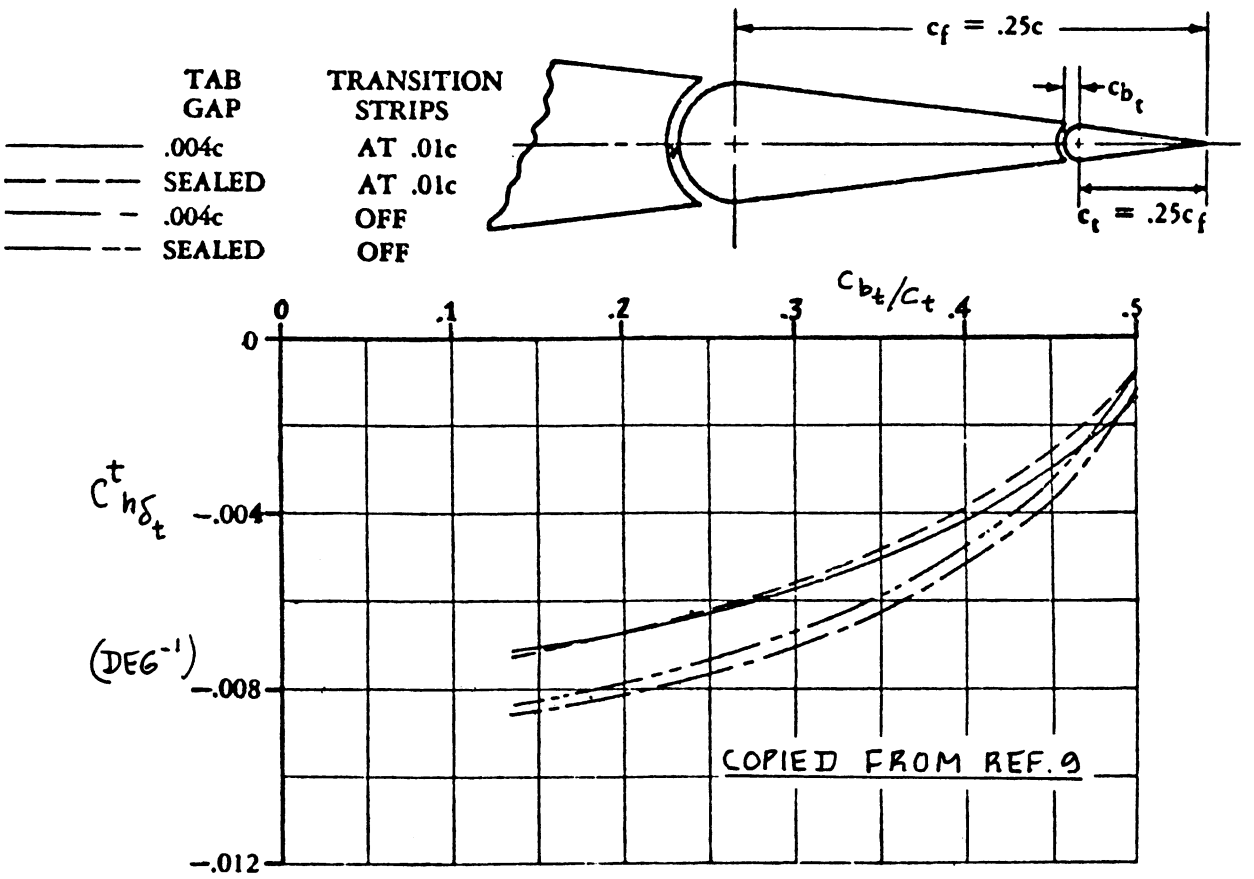

Figure 10.81d Effect of Tab Gap and Tab Size on the Tab Hingemoment Derivative due to Tab Deflection

11. STABILITY AND CONTROL DERIVATIVE DATA

The purpose of this chapter is to provide example data of stability and control derivatives for the following airplanes:

Tables 11.1 Airplane A (representative of a Cessna Model 172 type of airplane)

Tables 11.2 Airplane B (representative of a Beech Model 99 type of airplane)

Tables 11.3 Airplane C (representative of a SIAI-Marchetti S-211 type of airplane)

Tables 11.4 Airplane D (representative of a Gates Learjet Model 24 type of airplane)

Tables 11.5 Airplane E (representative of a McDonnell Douglas F4C type of airplane)

Tables 11.6 Airplane F (representative of a Boeing 747-100 type of airplane)

Except for airplane A, no data were available for hingemoment derivatives. All data are dimensionless.

Table 11.1a Geometry and Derivative Data for Airplane A

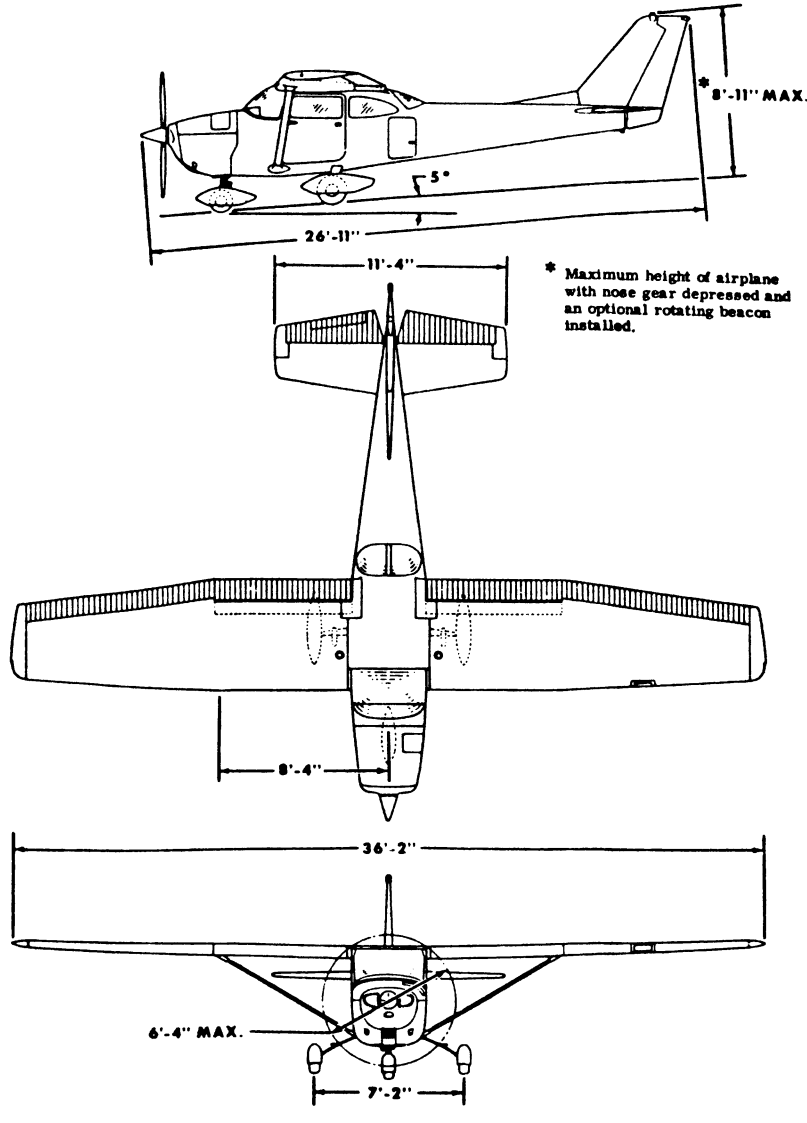

Flight Condition	1
	Cruise
Altitude (ft)	5,000
Air Density (slugs/ft^3)	.002050
Speed (fps)	219
Center of Gravity ($\bar{x}_{cg}$)	.25
Initial Attitude (θ_1 in rad)	0
Geometry and Inertias	
Wing Area (ft^2)	174
Wing Span (ft)	35.8
Wing Mean Geometric Chord (ft)	4.9
Weight (lbs)	2,645
I_{xx} (slug ft^2)	948
I_{yy} (slug ft^2)	1,346
I_{zz} (slug ft^2)	1,967
I_{xz} (slug ft^2)	0
Steady State Coefficients	
C_{L_1}	.31
C_{D_1}	.031
$C_{T_{X_1}}$	.031
C_{m_1}	0
$C_{m_{T_1}}$	0

Table 11.1b Geometry and Derivative Data for Airplane A

Longitudinal Derivatives		Lateral Directional Derivatives	
C_{m_u}	0	C_{ℓ_β}	-.089
C_{m_α}	-.89	C_{ℓ_p}	-.47
$C_{m_{\dot{\alpha}}}$	-5.2	C_{ℓ_r}	.096
C_{m_q}	-12.4	$C_{\ell_{\delta_A}}$	.178
$C_{m_{T_u}}$	0	$C_{\ell_{\delta_R}}$	.0147
$C_{m_{T_\alpha}}$	0	C_{n_β}	.065
C_{L_u}	0	C_{n_p}	-.03
C_{L_α}	4.6	C_{n_r}	-.099
$C_{L_{\dot{\alpha}}}$	1.7	$C_{n_{\delta_A}}$	-.053
C_{L_q}	3.9	$C_{n_{\delta_R}}$	-.0657
C_{D_α}	.13	C_{y_β}	-.31
C_{D_u}	0	C_{y_p}	-.037
$C_{T_{X_u}}$	-.093	C_{y_r}	.21
$C_{L_{\delta_E}}$	.43	$C_{y_{\delta_A}}$	0
$C_{D_{\delta_E}}$	.06	$C_{y_{\delta_R}}$	.187
$C_{m_{\delta_E}}$	-1.28		
C_{h_α}	-.050	$C_{h_{\delta_a}}$	-.010
$C_{h_{\delta_e}}$	-.590	$C_{h_{\delta_r}}$	-.570
		C_{h_β}	+.082

Table 11.2a Geometry and Derivative Data for Airplane B

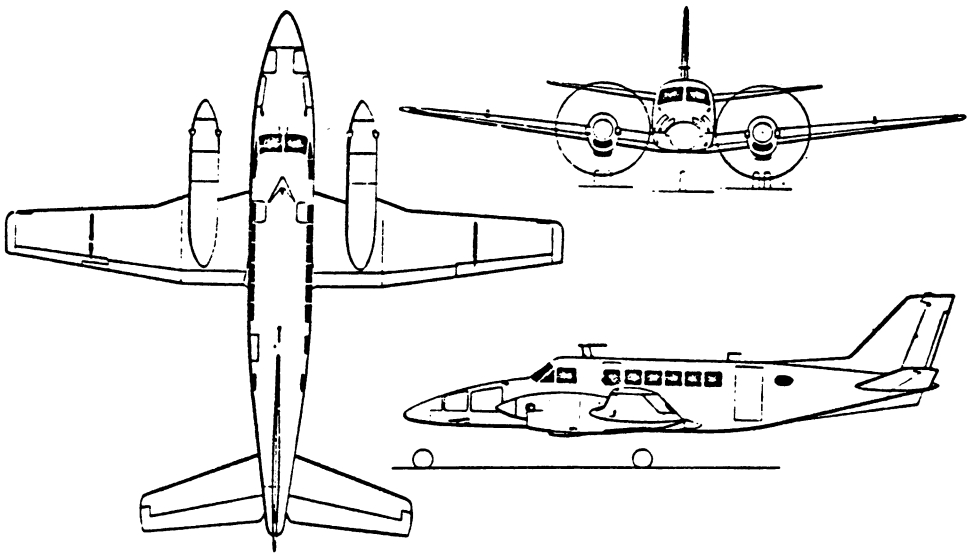

Flight Condition	1	2	3
	Power Approach	Cruise (Low)	Cruise (Normal)
Altitude (ft)	Sealevel	5,000	20,000
Air Density (slugs/ft^3)	.002378	.00205	.001268
Speed (fps)	170	340	450
Center of Gravity ($\bar{x}_{cg}$)	.16	.16	.16
Initial Attitude (θ_1 in rad)	0	0	0
Geometry and Inertias			
Wing Area (ft^2)	280	280	280
Wing Span (ft)	46	46	46
Wing Mean Geometric Chord (ft)	6.5	6.5	6.5
Weight (lbs)	11,000	7,000	11,000
I_{xx} (slug ft^2)	15,189	10,085	15,189
I_{yy} (slug ft^2)	20,250	15,148	20,250
I_{zz} (slug ft^2)	34,141	23,046	34,141
I_{xz} (slug ft^2)	4,371	1,600	4,371
Steady State Coefficients			
C_{L_1}	1.15	.191	.30
C_{D_1}	.162	.0298	.0298
$C_{T_{X_1}}$	.162	.0298	.0298
C_{m_1}	0	0	0
$C_{m_{T_1}}$	0	0	0

Table 11.2b Geometry and Derivative Data for Airplane B

Longitudinal Derivatives	1	2	3
C_{m_u}	0	0	0
C_{m_α}	-2.08	-1.89	-1.89
$C_{m_{\dot{\alpha}}}$	-9.1	-9.1	-9.1
C_{m_q}	-34.0	-34.0	-34.0
$C_{m_{T_u}}$	0	0	0
$C_{m_{T_\alpha}}$	0	0	0
C_{L_u}	.027	.020	.020
C_{L_α}	6.24	5.48	5.48
$C_{L_{\dot{\alpha}}}$	2.7	2.5	2.5
C_{L_q}	8.1	8.1	8.1
C_{D_α}	.933	.131	.131
C_{D_u}	0	0	0
$C_{T_{X_u}}$	-.324	-.0596	-.0596
$C_{L_{\delta_E}}$	.58	.6	.6
$C_{D_{\delta_E}}$	0	0	0
$C_{m_{\delta_E}}$	-1.9	-2.0	-2.0

Lateral-Directional Derivatives	1	2	3
C_{ℓ_β}	-.13	-.13	-.13
C_{ℓ_p}	-.50	-.50	-.50
C_{ℓ_r}	.06	.14	.14
$C_{\ell_{\delta_A}}$	.156	.156	.156
$C_{\ell_{\delta_R}}$	.0087	.0109	.0106
C_{n_β}	.120	.080	.080
C_{n_p}	-.005	.019	.019
C_{n_r}	-.204	-.197	-.197
$C_{n_{\delta_A}}$	-.0012	-.0012	-.0012
$C_{n_{\delta_R}}$	-.0763	-.0772	-.0758
C_{y_β}	-.59	-.59	-.59
C_{y_p}	-.21	-.19	-.19
C_{y_r}	.39	.39	.39
$C_{y_{\delta_A}}$	0	0	0
$C_{y_{\delta_R}}$	.144	.148	.144

Table 11.3a Geometry and Derivative Data for Airplane C

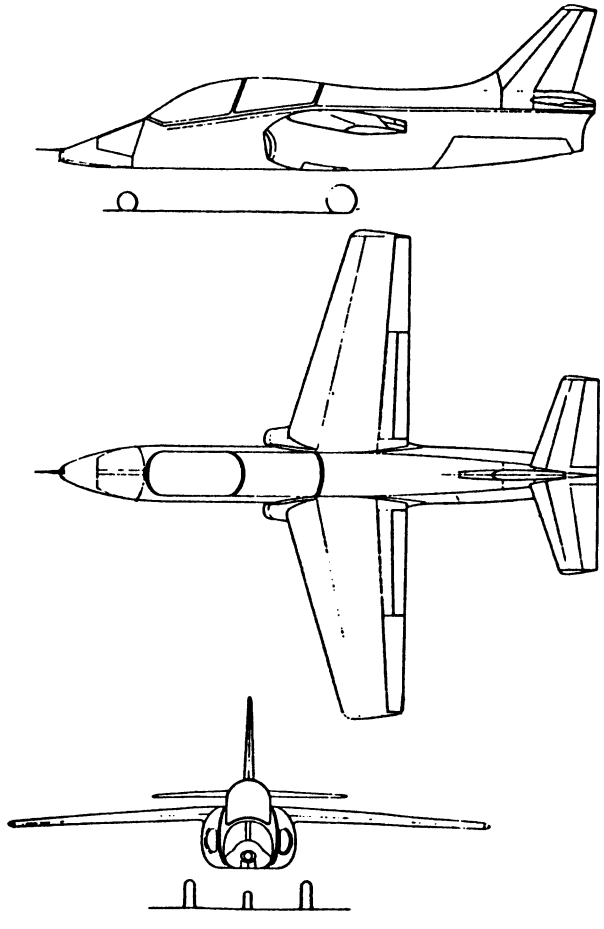

Flight Condition	1	2	3
	Power Approach	Cruise (Normal)	Cruise (High)
Altitude (ft)	Sealevel	25,000	35,000
Air Density (slugs/ft^3)	.002378	.001066	.000739
Speed (fps)	124 ($1.2\ V_{S_{PA}}$)	610 (M = .6)	584 (M = .6)
Center of Gravity ($\bar{x}_{cg}$)	.25 (mid)	.25 (mid)	.25 (mid)
Initial Attitude (θ_1 in rad)	0	0	0
Geometry and Inertias			
Wing Area (ft^2)	136	136	136
Wing Span (ft)	26.3	26.3	26.3
Wing Mean Geometric Chord (ft)	5.4	5.4	5.4
Weight (lbs)	3,500	4,000	4,000
I_{xx} (slug ft^2)	750	800	800
I_{yy} (slug ft^2)	4,800	4,800	4,800
I_{zz} (slug ft^2)	5,000	5,200	5,200
I_{xz} (slug ft^2)	200	200	200
Steady State Coefficients			
C_{L_1}	1.4	.15	.23
C_{D_1}	.21	.022	.025
$C_{T_{X_1}}$	.21	.022	.025
C_{m_1}	0	0	0
$C_{m_{T_1}}$	0	0	0

Table 11.3b Geometry and Derivative Data for Airplane C

Longitudinal Derivatives	1	2	3
C_{m_u}	0	0	0
C_{m_α}	-.6	-.24	-.24
$C_{m_{\dot{\alpha}}}$	-7.0	-9.6	-9.6
C_{m_q}	-15.7	-17.7	-17.7
$C_{m_{T_u}}$	0	0	0
$C_{m_{T_\alpha}}$	0	0	0
C_{L_u}	.071	.084	.132
C_{L_α}	5.0	5.5	5.5
$C_{L_{\dot{\alpha}}}$	3.0	4.2	4.2
C_{L_q}	9.0	10.0	10.0
C_{D_α}	1.14	.12	.17
C_{D_u}	0	0	0
$C_{T_{X_u}}$	0	0	0
$C_{L_{\delta_E}}$	.39	.38	.35
$C_{D_{\delta_E}}$	0	0	0
$C_{m_{\delta_E}}$	-.90	-.88	-.82

Lateral-Directional Derivatives	1	2	3
C_{ℓ_β}	-.140	-.110	-.110
C_{ℓ_p}	-.350	-.390	-.390
C_{ℓ_r}	.560	.280	.310
$C_{\ell_{\delta_A}}$	.110	.100	.100
$C_{\ell_{\delta_R}}$	.030	.050	.050
C_{n_β}	.160	.170	.170
C_{n_p}	-.030	+.090	+.080
C_{n_r}	-.310	-.260	-.260
$C_{n_{\delta_A}}$	-.030	-.003	-.005
$C_{n_{\delta_R}}$	-.110	-.120	-.120
C_{y_β}	-.94	-1.00	-1.00
C_{y_p}	-.010	-.14	-.12
C_{y_r}	.590	.610	.620
$C_{y_{\delta_A}}$	0	0	0
$C_{y_{\delta_R}}$	.260	.280	.280

Table 11.4a Geometry and Derivative Data for Airplane D

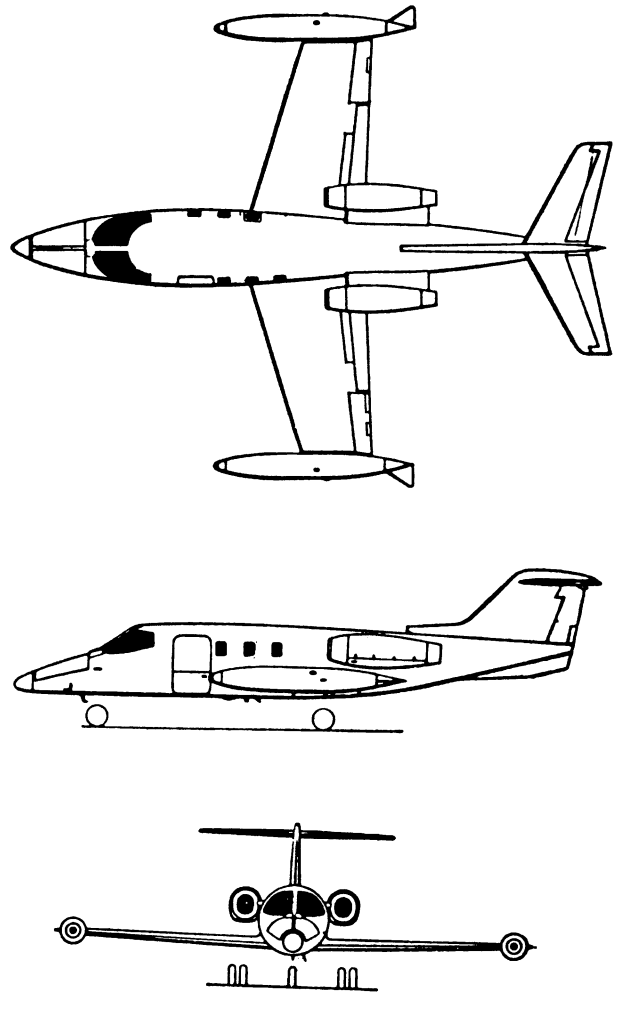

Flight Condition	1	2	3
	Power Approach	Cruise Max. Wht.	Cruise Low Wht.
Altitude (ft)	Sealevel	40,000	40,000
Air Density (slugs/ft^3)	.002378	.000588	.000588
Speed (fps)	170	677 (M = .7)	677 (M = .7)
Center of Gravity ($\bar{x}_{cg}$)	.32 (aft)	.32 (aft)	.32 (aft)
Initial Attitude (deg)	1.8	2.7	1.5
Geometry and Inertias			
Wing Area (ft^2)	230	230	230
Wing Span (ft)	34	34	34
Wing Mean Geometric Chord (ft)	7	7	7
Weight (lbs)	13,000	13,000	9,000
I_{xx_B} (slug ft^2)	28,000	28,000	6,000
I_{yy_B} (slug ft^2)	17,800	18,800	17,800
I_{zz_B} (slug ft^2)	47,000	47,000	25,000
I_{xz_B} (slug ft^2)	1,300	1,300	1,400
Steady State Coefficients			
C_{L_1}	1.64	.41	.28
C_{D_1}	.256	.0335	.0279
$C_{T_{X_1}}$	.256	.0335	.0279
C_{m_1}	0	0	0
$C_{m_{T_1}}$	0	0	0

Table 11.4b Geometry and Derivative Data for Airplane D

Longitudinal Derivatives	1	2	3
C_{m_u}	-.01	.05	.07
C_{m_α}	-.66	-.64	-.64
$C_{m_{\dot{\alpha}}}$	-5.0	-6.7	-6.7
C_{m_q}	-13.5	-15.5	-15.5
$C_{m_{T_u}}$	.006	-.003	-.003
$C_{m_{T_\alpha}}$	0	0	0
C_{L_u}	.04	.40	.28
C_{L_α}	5.04	5.84	5.84
$C_{L_{\dot{\alpha}}}$	1.6	2.2	2.2
C_{L_q}	4.1	4.7	4.7
C_{D_α}	1.06	.30	.22
C_{D_u}	0	.104	.104
$C_{T_{X_u}}$	0	0	0
$C_{L_{\delta_E}}$	.40	.46	.46
$C_{D_{\delta_E}}$	0	0	0
$C_{m_{\delta_E}}$	-.98	-1.24	-1.24

Lateral-Directional Derivatives	1	2	3
C_{ℓ_β}	-.173	-.110	-.100
C_{ℓ_p}	-.39	-.45	-.45
C_{ℓ_r}	.45	.16	.14
$C_{\ell_{\delta_A}}$	.149	.178	.178
$C_{\ell_{\delta_R}}$	.014	.019	.021
C_{n_β}	.150	.127	.124
C_{n_p}	-.13	-.008	-.022
C_{n_r}	-.26	-.20	-.20
$C_{n_{\delta_A}}$	-.05	-.02	-.02
$C_{n_{\delta_R}}$	-.074	-.074	-.074
C_{y_β}	-.73	-.73	-.73
C_{y_p}	0	0	0
C_{y_r}	.4	.4	.4
$C_{y_{\delta_A}}$	0	0	0
$C_{y_{\delta_R}}$	.140	.140	.140

Table 11.5a Geometry and Derivative Data for Airplane E

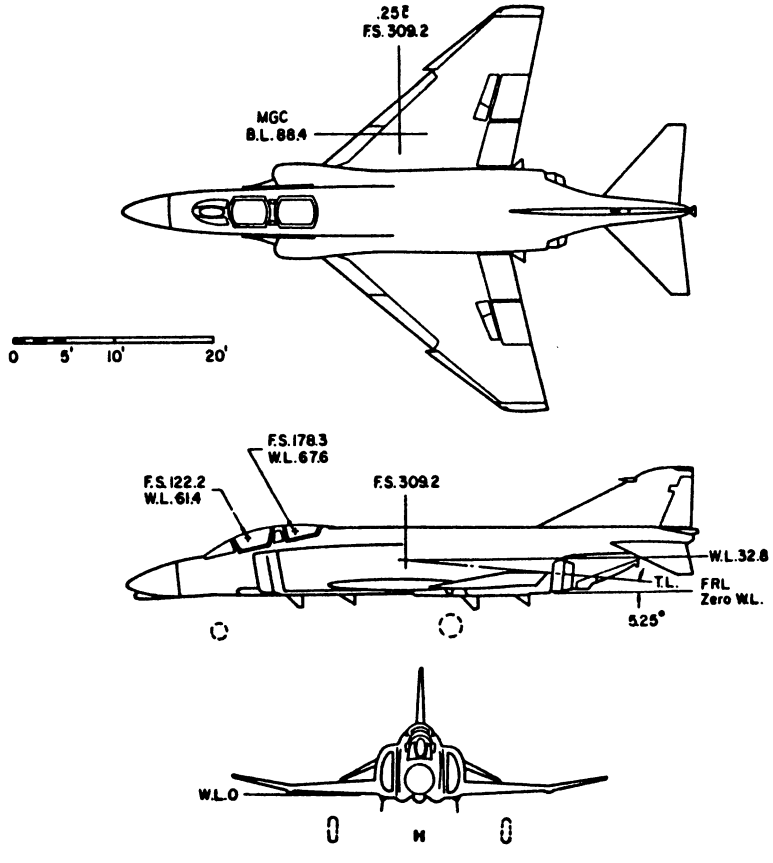

Flight Condition	1	2	3
	Power Approach	Subsonic Cruise	Supersonic Cruise
Altitude (ft)	Sealevel	35,000	55,000
Air Density (slugs/ft^3)	.002378	.000739	.000287
Speed (fps)	230	876	1742
Center of Gravity ($\bar{x}_{cg}$)	.29	.29	.29
Initial Attitude (deg)	11.7	2.6	3.3
Geometry and Inertias			
Wing Area (ft^2)	530	530	530
Wing Span (ft)	38.7	38.7	38.7
Wing Mean Geometric Chord (ft)	16.0	16.0	16.0
Weight (lbs)	33,200	39,000	39,000
I_{xx_B} (slug ft^2)	23,700	25,000	25,000
I_{yy_B} (slug ft^2)	117,500	122,200	122,200
I_{zz_B} (slug ft^2)	133,700	139,800	139,800
I_{xz_B} (slug ft^2)	1,600	2,200	2,200
Steady State Coefficients			
C_{L_1}	1.0	.26	.17
C_{D_1}	.2	.03	.048
$C_{T_{X_1}}$	.2	.03	.048
C_{m_1}	0	0	0
$C_{m_{T_1}}$	0	0	0

Table 11.5b Geometry and Derivative Data for Airplane E

Longitudinal Derivatives	1	2	3
C_{m_u}	0	-.117	+.054
C_{m_α}	-.098	-.40	-.78
$C_{m_{\dot{\alpha}}}$	-.95	-1.3	-.25
C_{m_q}	-2.0	-2.7	-2.0
$C_{m_{T_u}}$	0	0	0
$C_{m_{T_\alpha}}$	0	0	0
C_{L_u}	0	+.27	-.18
C_{L_α}	2.8	3.75	2.8
$C_{L_{\dot{\alpha}}}$	0	0	0
C_{L_q}	0	0	0
C_{D_α}	.555	.3	.4
C_{D_u}	0	+.027	-.054
$C_{T_{X_u}}$	0	0	0
$C_{L_{i_H}}$	.24	.40	.25
$C_{D_{i_H}}$	-.14	-.10	-.15
$C_{m_{i_H}}$	-.322	-.58	-.38

(Note: longitudinal control through stabilizer only)

Lateral-Directional Derivatives	1	2	3
C_{ℓ_β}	-.156	-.080	-.025
C_{ℓ_p}	-.272	-.240	-.200
C_{ℓ_r}	.205	.070	.040
$C_{\ell_{\delta_A}}$	.057	.042	.015
$C_{\ell_{\delta_R}}$	.0009	.0060	.0030
C_{n_β}	.199	.125	.090
C_{n_p}	.013	-.036	0
C_{n_r}	-.320	-.270	-.260
$C_{n_{\delta_A}}$	+.0041	-.0010	-.0009
$C_{n_{\delta_R}}$	-.072	-.066	-.025
C_{y_β}	-.655	-.68	-.70
C_{y_p}	0	0	0
C_{y_r}	0	0	0
$C_{y_{\delta_A}}$	-.0355	-.016	-.010
$C_{y_{\delta_R}}$	.124	.095	.050

Table 11.6a Geometry and Derivative Data for Airplane F

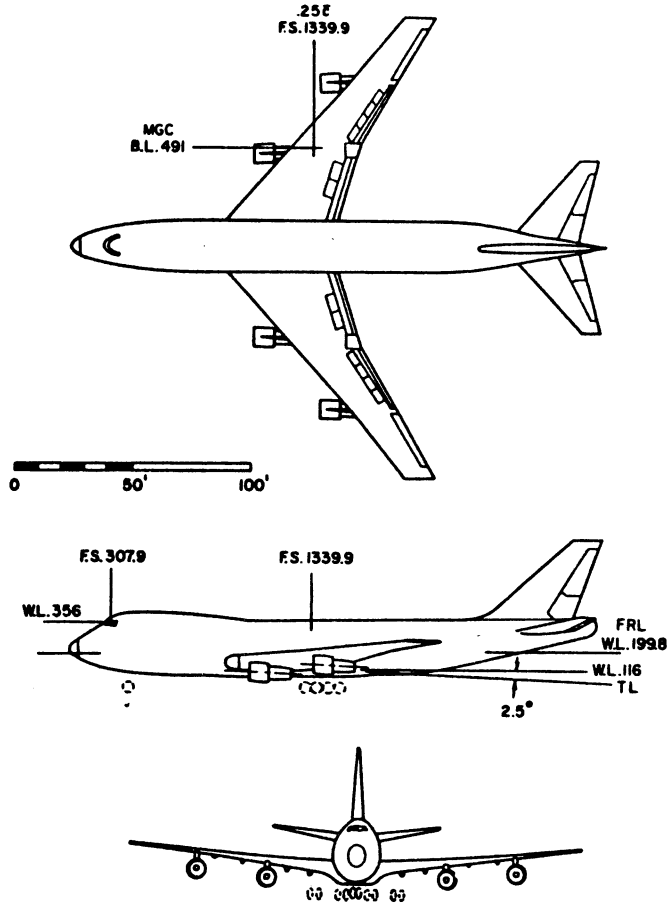

Flight Condition	1	2	3
	Power Approach	Cruise (High)	Cruise (Low)
Altitude (ft)	Sealevel	40,000	20,000
Air Density (slugs/ft^3)	.002389	.000588	.001268
Speed (fps)	221	871	673
Center of Gravity ($\bar{x}_{cg}$)	.25	.25	.25
Initial Attitude (deg)	8.5	2.4	2.5
Geometry and Inertias			
Wing Area (ft^2)	5,500	5,500	5,500
Wing Span (ft)	196	196	196
Wing Mean Geometric Chord (ft)	27.3	27.3	27.3
Weight (lbs)	564,000	636,636	636,636
I_{xx_B} (slug ft^2)	13.7 x 10^6	18.2 x 10^6	18.2 x 10^6
I_{yy_B} (slug ft^2)	30.5 x 10^6	33.1 x 10^6	33.1 x 10^6
I_{zz_B} (slug ft^2)	43.1 x 10^6	49.7 x 10^6	49.7 x 10^6
I_{xz_B} (slug ft^2)	.83 x 10^6	.97 x 10^6	.97 x 10^6
Steady State Coefficients			
C_{L_1}	1.76	.52	.40
C_{D_1}	.263	.045	.025
$C_{T_{X_1}}$	.263	.045	.025
C_{m_1}	0	0	0
$C_{m_{T_1}}$	0	0	0

Table 11.6b Geometry and Derivative Data for Airplane F

Longitudinal Derivatives	1	2	3
C_{m_u}	.071	-.09	+.013
C_{m_α}	-1.45	-1.60	-1.00
$C_{m_{\dot{\alpha}}}$	-3.3	-9.0	-4.0
C_{m_q}	-21.4	-25.5	-20.5
$C_{m_{T_u}}$	0	0	0
$C_{m_{T_\alpha}}$	0	0	0
C_{L_u}	-.22	-.23	+.13
C_{L_α}	5.67	5.5	4.4
$C_{L_{\dot{\alpha}}}$	6.7	8.0	7.0
C_{L_q}	5.65	7.8	6.6
C_{D_α}	1.13	.50	.20
C_{D_u}	0	.22	0
$C_{T_{X_u}}$	0	0	0
$C_{L_{\delta_E}}$	.36	.30	.32
$C_{D_{\delta_E}}$	0	0	0
$C_{m_{\delta_E}}$	-1.40	-1.20	-1.30

Lateral-Directional Derivatives	1	2	3
C_{ℓ_β}	-.281	-.095	-.160
C_{ℓ_p}	-.502	-.320	-.340
C_{ℓ_r}	.195	.200	.130
$C_{\ell_{\delta_A}}$	.053	.014	.013
$C_{\ell_{\delta_R}}$	0	.005	.008
C_{n_β}	.184	.210	.160
C_{n_p}	-.222	+.020	-.026
C_{n_r}	-.36	-.33	-.28
$C_{n_{\delta_A}}$	+.0083	-.0028	+.0018
$C_{n_{\delta_R}}$	-.113	-.095	-.100
C_{y_β}	-1.08	-.90	-.90
C_{y_p}	0	0	0
C_{y_r}	0	0	0
$C_{y_{\delta_A}}$	0	0	0
$C_{y_{\delta_R}}$	.179	.060	.120

SAAB SF-340

COURTESY: SAAB

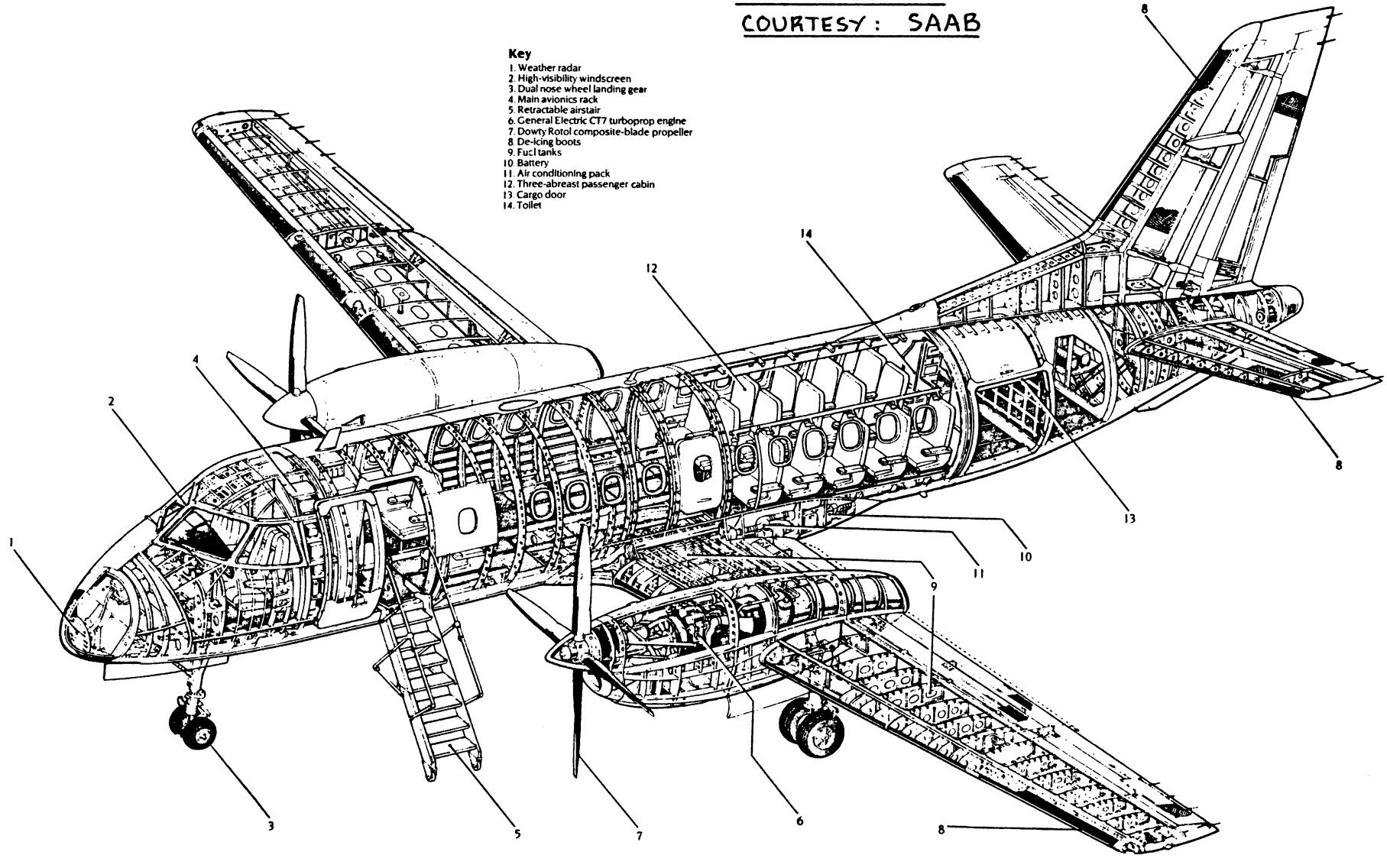

12. USER'S GUIDE

The purpose of this chapter is to present a User's Guide to the prediction methods presented in this part of the eight part series on Airplane Design.

It is assumed that the Preliminary Design Sequence I (see p.11, Part II) has been completed and that the results of the accompanying Class I work have been properly documented. The stage is now set for a more 'in depth' (Class II) analysis of the capabilities of the design. To accomplish this, the following characteristics need to be determined:

1.) Drag polars
2.) Installed thrust or power data
3.) Lift versus angle of attack
4.) Pitching moment versus angle of attack
5.) Stability, control and hingemoment derivatives

The data which are the result of determining items 1.) through 5.) are themselves input data to the calculation and the evaluation of performance, stability, control, handling qualities and airworthiness capabilities of the airplane as outlined in Part VII.

NOTE: The reader should not attempt to perform any of the calculations represented by 1.) through 5.) without a complete geometric definition of the airplane: a dimensioned, Class I threeview MUST be available. This threeview should be of a size large enough so that dimensions needed in predicting items 1.) through 5.) can be 'scaled' directly from this threeview drawing. If a CAD (Computer Aided Design) data base is available for the airplane, so much the better.

12.1 USER'S GUIDE FOR DRAG POLAR DETERMINATION

Step 1: The reader should determine for which conditions drag polars are needed:

Airplane Configuration:
- *Clean
- *Flap position (up, take-off or landing)
- *Landing Gear (up or down)
- *External stores
- *Engine and inlet status

Flight Condition: *Mach Number
*Altitude
*Reynold's Number
*Weight
*Center of Gravity Location

The conditions selected depend on the type of performance calculations which need to be performed with the drag polars. Example of performance capabilities which typically must be determined are:

A) Mission oriented performance such as:

* take-off	* climb	* cruise
* loiter	* descent	* landing
* maneuvering	* high speed dash	* accelerate

B) Airworthiness oriented performance such as:

* climb rate or gradient with failed engine(s)
* balanced fieldlength
* performance following major damage (for example combat damage)

Step 2: Proceed to Chapter 4 to compute the required drag data. Refer to Equation 4.4 and identify which drag components must be determined. Prepare a list of input data needed for the calculation of each drag component.

Plot the results in the form of C_D versus α.

Step 3: Proceed to Section 12.3 and use the resulting C_L versus α plot together with the C_D versus α plot obtained from Step 2 to construct a C_L versus C_D plot (=drag polar).

Step 4: Verify the drag polars with the procedure of Section 5.5, p.135. Also compare the drag polar data with data on similar airplanes: see Section 5.1, p.117.

12.2 USER'S GUIDE FOR DETERMINATION OF INSTALLED THRUST OR POWER

It will be assumed that the Class I powerplant integration has been carried out as indicated in Chapter 5 of Part II. The powerplant installation has therefore been temporarily 'frozen' which means that the following information should be available:

* engine type
* inlet type and inlet size
* number of engines
* exhaust type and nozzle size

Manufacturers uninstalled thrust or power data must also be available at this point.

Finally, it will be assumed that a list of systems required by the airplane including a preliminary determination of the power requirements of these systems, is avalable.

Step 1: Obtain engine manufacturers uninstalled thrust or power data. These data should define uninstalled thrust (or power) as a function of altitude, temperature, airspeed and fuel flow.

If such detailed data are not available, the data in Chapter 6 of Part III may be used to 'guestimate' a set of uninstalled data.

Step 2: Refer to pages 139 and 140 (Chapter 6) and proceed with the preparation of the input data necessary in the calculation of installed thrust or power data.

Step 3: Using the methods of Sections 6.1 through 6.4 estimate the installed power or thrust capabilities of the airplane.

Example data are given in Chapter 7.

12.3 USER'S GUIDE FOR DETERMINATION OF LIFT VERSUS ANGLE OF ATTACK

Step 1: The reader should determine for which flight conditions the lift versus angle of attack data need to be prepared. Refer to Step 1 in Section 12.1 for some guidelines.

Step 2: Proceed to Section 8.1 for the calculation of the required lift versus angle of attack characteristics. Plot the results in the form of C_L versus α.

Step 3: Check the results of Step 2 by comparing with example data on similar airplanes such as given in Chapter 9.

12.4 USER'S GUIDE FOR THE DETERMINATION OF PITCHING MOMENT VERSUS ANGLE OF ATTACK AND THE TRIM DIAGRAM

Step 1: The reader should determine for which flight conditions the pitching moment versus angle of attack data need to be prepared. Refer to Step 1 of Section 12.1 for guidelines.

Step 2: Refer to the weight versus center of gravity diagram (See Chapter 10, Part II) and determine the most forward and aft c.g. location which applies to each flight condition selected in Step 1. Select a suitable c.g. location for use as the reference point in the pitching moment calculations.

Step 3: Proceed to Section 8.2 and determine the pitching moment versus angle of attack characteristics. Plot the results in the form of C_m versus α for the reference point selected in Step 2.

Step 4: Proceed to Section 8.3 and determine the airplane trim diagram in the form of a plot of C_m versus C_L for the reference point selected in Step 2.

Step 5: Verify the results of Step 4 by comparing with data on similar airplanes. Some data are given in Chapter 9.

12.5 USER'S GUIDE FOR THE DETERMINATION OF STABILITY, CONTROL AND HINGEMOMENT DERIVATIVES

Step 1: Determine the flight conditions for which the derivatives need to be determined. Use Step 1 in Section 12.1 for guidelines.

Step 2: Proceed to Chapter 10 and compute the required derivatives.

Step 3: Verify the results of Step 2 by comparing with data on similar airplanes. Example derivative data are given in Chapter 11.

13. REFERENCES

1. Roskam, J., Airplane Design: Part I, Preliminary Sizing of Airplanes.
2. Roskam, J., Airplane Design: Part II, Preliminary Configuration Design and Integration of the Propulsion System.
3. Roskam, J., Airplane Design: Part III, Layout Design of Cockpit, Fuselage, Wing and Empennage: Cutaways and Inboard Profiles.
4. Roskam, J., Airplane Design: Part IV, Layout Design of Landing Gear and Systems.
5. Roskam, J., Airplane Design: Part V, Component Weight Estimation.
6. Roskam, J., Airplane Design: Part VII, Determination of Stability, Control and Performance Characteristics: FAR and Military Requirements.
7. Roskam, J., Airplane Design: Part VIII, Airplane Cost Estimation and Optimization: Design, Development Manufacturing and Operating.

Note: These books are all published by: Design, Analysis and Research Corporation, 1440 Wakarusa Drive, Suite 500, Lawrence, KS, 66049, Tel. (785) 832-0434

8. Hoerner, S.F., Fluid Dynamic Drag, Hoerner Fluid Dynamics, P.O. Box 342, Brick Town, N.J., 08723, '65.
9. Hoak, D.E., et al, USAF Stability and Control Datcom, Flight Control Division, Air Force Flight Dynamics Laboratory, WPAFB, Ohio, 45433-0000, 1978, revised.
10. Nelson and Welsh, Some Examples of the Application of the Transonic and Supersonic Area Rules to the Prediction of Wave Drag, NASA TN D-446, 1960.
11. Kuchemann, D., The Aerodynamic Design of Aircraft, Pergamon Press, England, 1978.
12. Nicolai, L.M., Fundamentals of Aircraft Design, METS Inc., 6520 Kingsland Court, San Jose, CA, 95120.
13. Torenbeek, E., Synthesis of Subsonic Airplane Design, Kluwer Boston inc., Hingham, Maine, 1982.
14. McCormick, B.W., Aerodynamics, Aeronautics and Flight Mechanics, John Wiley and Sons, 1979, N.Y., N.Y.
15. Lan, C.E. and Roskam, J., Airplane Aerodynamics and Performance, Roskam Aviation and Engineering Corp., Route 4, Box 274, Ottawa, Kansas, 66067, 1980.

16. Roskam, J., Airplane Flight Dynamics and Automatic Flight Control Systems, Roskam Aviation and Engineering Corp., Route 4, Box 274, Ottawa, Kansas, 1981.

17. Whitcomb, R.T., A Study of the Zero-lift Drag Rise Characteristics of Wing-Body Combinations Near the Speed of Sound, NACA Report 1273, 1956.

18. Nelson, B.D., Design Scope for Student Supersonic Projects, AIAA Paper 86-2638, Presented at the AIAA/AHS/ASEE Aircraft Systems, Design and Technology Meeting, Dayton, Ohio, 1986.

19. Curry, N.S., Landing Gear Design Handbook, Lockheed Georgia Company, Georgia, 30063, 1982.

20. Royal Aeronautical Society Data Sheets, 1963, London.

21. Anonymous, Aircraft Design, Part III (in Dutch), Dept. of Aeronautical Engineering, Technological University of Delft, Delft, Holland, 1970.

22. Corning, G., Supersonic and Subsonic Airplane Design, Box No.14, College Park, Maryland.

23. Holmes, B.J. et al, Manufacturing Tolerances for Natural Laminar Flow Airframe Surfaces, SAE Paper 850863, 1985.

24. Maddalon, D.V. and McMillin, M.L., Effect of Surface Waviness on a Supercritical Laminar-Flow-Control Airfoil, NASA TM 85705, 1983.

25. Braslow, A.L. and Fischer, M.C., Design Considerations for Application of Laminar Flow Control Systems to Transport Aircraft, Paper presented at the AGARD/FDP VKI Special Course on 'Aircraft Drag Prediction and Reduction', NASA Langley, VA, 1985.

26. Maddalon, D.V. and Wagner, R.D., Operational Considerations for Laminar Flow Aircraft, Paper presented at the NASA/SAE/AIAA/FAA Laminar Flow Aircraft Certification Workshop, Wichita, Kansas, 1985.

27. Schlichting, H., Boundary Layer Theory, Mc Graw-Hill, N.Y., 1955.

28. Vijgen, P.M.H.W., et al, Effects of Compressibility on Design of Subsonic Natural Laminar Flow Fuselages, AIAA Paper 86-1825 CP, 1986.

29. Dodbele, S.S., et al, Shaping of Airplane Fuselages for Minimum Drag, AIAA Paper 86-0316, 1986.

30. Dodbele, S.S. et al, Design of Fuselage Shapes for Natural Laminar Flow, NASA CR-3970, 1986.

31. Taylor, J.W.R., Jane's All The World Aircraft, Published annually by: Jane's Publishing Company' 238 City Road, London EC1V 2PU, England.

32. Seddon, J. and Goldsmith, E.L., Intake Aerodynamics, AIAA Education Series, American Institute of Aeronautics and Astronautics, N.Y., N.Y.

33. Covert, E.E. et al, Thrust and Drag: Its Prediction and Verification, AIAA Education Series, American Institute of Aeronaytics and Astronautics, N.Y., N.Y.

34. Marks, L.S. et al, Mechanical Engineer's Handbook, McGraw Hill Book Company, N.Y., N.Y.

35. Monts, F., The Development of Reciprocating Engine Installation Data for General Aviation Aircraft, SAE Paper 730325, Business Aircraft Meeting, Wichita, Kansas, April, 1973.

36. Corsiglia, V.R. and Katz, J., Full-Scale Study of the Cooling System Aerodynamics of an Operating Piston Engine Installed in a Light Aircraft Wing Panel, SAE Paper 810623, Business Aircraft Meeting, Wichita, Kansas, April, 1981.

37. Taylor, C.F., The Internal Combustion Engine in Theory and Practice, Volumes I and II, MIT Press, 1966.

38. Bingelis, T., Firewall Forward, Engine Installation Methods, Tony Bingelis, 8509 Greenflint Lane, Austin, Texas, 78759, 1974.

39. Thurston, D.B., Design for Flying, McGraw Hill Book Co., N.Y., N.Y., 1978.

40. Bingelis, T., Sportplane Builder, Tony Bingelis, 8509 Greenflint Lane, Austin, Texas, 78759, 1985.

41. Kerrebrock, J.L., Aircraft Engines and Gas Turbines, MIT Press, 1977.

42. Borst, H.V., Propeller Performance and Design as Influenced by the Installation, SAE Paper 810602, Business Aircraft Meeting, Wichita, Kansas, April, 1981.

43. Borst, H.V. et al, Summary of Propeller Design Procedures and Data, Volumes I, II and III, USAAMRL Technical Report 73-34, H.V.Borst Associates, Wayne, Pa, November 1973.

44. McCormick, B.W. et al, The Analysis of Propellers Including Interaction Effects, SAE Paper 790576, Business Aircraft Meeting, Wichita, Kansas, April, 1979.

45. Weick, F.E., Aircraft Propeller Design, McGraw Hill Book Co., N.Y., N.Y., 1930.

46. Smith, M.H., A Prediction Procedure for Propeller Aircraft Flyover Noise Based on Empirical Data, SAE Paper 810604, 1981.

47. Anon., Prediction Procedure for Near-Field and Far-Field Propeller Noise, AIR 1407, SAE Aerospace Information Report, May, 1977.

48. Klatte, R.J., General Aviation Propeller Noise Reduction- Penalties and Potential, SAE Paper 810585, 1981

49. Abbott, I.H. and Von Doenhoff, E., Theory of Wing Sections, Dover Publications, N.Y., 1959.

50. Mueller, T.J. et al, Proceedings of the Conference on Low Reynolds Number Airfoil Aerodynamics, Sponsored by NASA, USNavy and University of Notre Dame, UNDAS CP-77B123, June 1985.

51. Hoerner, S.F. and Borst, H.V., Fluid-Dynamice Lift, Hoerner Fluid Dynamics, Box 342, Brick Town, N.J., 08723, 1975.

52. DeYoung, J., Theoretical Symmetric Span Loading Due To Flap Deflection For Wings Of Arbitrary Planform At Subsonic Speeds, NACA TR 1071, 1952.

53. Shortal, J.A. and Maggin, B., Effect of Sweepback and Aspect Ratio on Longitudinal Stability Characteristics of Wings at Low Speeds, NACA TN 1093, 1946.

54. Perkins, C.D. and Hage, R.E., Airplane Performance, Stability and Control, J.Wiley and Sons, N.Y., 1957.

55. Wittenberg, H., Calculation of Lift and Drag at Low Speeds, Part I: Wing (in Dutch), Technological University Delft, Delft, The Netherlands, 1970.

56. Sanders, K.L., High Lift Devices, A Weight and Performance Trade-off Methodology, T.P.761, Society of Aeronautical Weights Engineers, 1969.

57. Anon., Aeronautical Vestpocket Handbook, United Technologies, Pratt and Whitney Aircraft, PWA Part No. 79500, August 1981.

58. Torenbeek, E., The Computation of Characteristic Areas and Volumes of Major Aircraft Components in Project Design, Memorandum M-189, Delft University of Technology, Dept. of Aerospace Engineering, Delft, The Netherlands, 1973.

14. INDEX

APPENDIX A: STANDARD ATMOSPHERE, SPECIFIC WEIGHTS AND CONVERSION FACTORS

This appendix presents tabulated data for:

The data have been copied from Reference 57.

A1. U.S. STANDARD ATMOSPHERE, 1962

Definition of Standard Atmosphere

A standard atmosphere is a hypothetical vertical distribution of atmospheric temperature, pressure and density which by international or national agreement is taken to be representative of the atmosphere for the purpose of altimeter calibrations, aircraft design, performance calculations, etc. The internationally accepted standard atmosphere is called the International Civil Aeronautical Organization (ICAO) Standard Atmosphere or the International Standard Atmosphere (ISA). The U.S. Standard Atmosphere, 1962 is in agreement with the ICAO Standard Atmosphere up to 65,000 feet altitude. It is ideal air devoid of moisture, water vapor, and dust, and obeys the perfect gas law. It is based upon accepted standard values of sea level air density, temperature and pressure. Other standard atmosphere models, such as MIL-STD-210A, which represents hot and cold ambient temperature extremes, have also been established.

ICAO and U.S. Standard Atmospheres

Standard Values at Sea Level

	British Units	Metric Units
Pressure, P_o	2116.22 lb/ft^2 29.92 in. Hg	1.013250×10^5 N/m^2 760 mm Hg
Temperature, T_o	518.67°R 59.0°F	288.15°K 15.0°C
Acceleration due to gravity, g_o	32.1741 ft/sec^2	9.80665 m/sec^2
Specific weight, $g_o\rho_o$	0.076474 lb/ft^3	1.2250 kg/m^3
Density, ρ_o	0.0023769 lb-sec^2/ft^4	0.12492 kg sec^2/m^4
Kinematic viscosity, ν_o	1.5723×10^{-4} ft^2/sec	1.4607×10^{-5} m^2/sec
Absolute viscosity, μ_o	1.2024×10^{-5} lb/ft sec	1.7894×10^{-5} kg/m sec

Standard Values at Altitude

Isothermal altitude, Z_i	36089 ft	11000 m
Isothermal temperature, t	−69.7°F	−56.5°C
Temperature lapse rate (sea level to isothermal)	−3.57°F/1000 ft	−6.5°C/km

Temperature Conversion Formulas

$t\ (°C) = T(°K) - 273.15$
$t\ (°C) = [T(°R) - 491.67]/1.8$
$t\ (°C) = [t(°F) - 32]/1.8$

$T\ (°R) = 1.8\ T(°K)$
$t\ (°F) = 1.8[T(°K) - 273.15] + 32$
$t\ (°F) = T\ (°R) - 459.67$
$t\ (°F) = 1.8\ t(°C) + 32$

U.S. Standard Atmosphere, 1962
(Geopotential Altitude)

British Units

Altitude feet	Temperature °F	°R	°C	Pressure psia	in. Hg	θ	$\sqrt{\theta}$	δ	σ	$\bar{q}/M^2$ lb/ft²	Sonic Velocity ft/sec	kts
−2000	66.1	525.8	19.0	15.79	32.15	1.0138	1.0069	1.074	1.060	1592.	1124.1	666.0
−1000	62.5	522.2	17.0	15.23	31.02	1.0069	1.0034	1.037	1.030	1536.	1120.2	663.7
0	59.0	518.7	15.0	14.70	29.92	1.0000	1.0000	1.000	1.000	1481.	1116.4	661.5
1000	55.4	515.1	13.0	14.17	28.86	.9932	.9966	.9644	.9710	1429.	1112.6	659.2
2000	51.9	511.6	11.0	13.66	27.82	.9863	.9931	.9298	.9427	1377.	1108.7	656.9
3000	48.3	508.0	9.1	13.17	26.82	.9794	.9897	.8962	.9151	1328.	1104.9	654.6
4000	44.7	504.4	7.1	12.69	25.84	.9725	.9862	.8637	.8881	1279.	1101.0	652.3
5000	41.2	500.9	5.1	12.23	24.90	.9657	.9827	.8321	.8616	1233.	1097.1	650.0
6000	37.6	497.3	3.1	11.78	23.98	.9588	.9792	.8014	.8358	1187.	1093.2	647.7
7000	34.0	493.7	1.1	11.34	23.09	.9519	.9757	.7716	.8106	1143.	1089.2	645.4
8000	30.5	490.2	−0.8	10.92	22.23	.9450	.9721	.7428	.7860	1100.	1085.3	643.0
9000	26.9	486.6	−2.8	10.50	21.39	.9382	.9686	.7148	.7619	1059.	1081.3	640.7
10000	23.3	483.0	−4.8	10.11	20.58	.9313	.9650	.6877	.7385	1019.	1077.4	638.3
11000	19.8	479.5	−6.8	9.720	19.79	.9244	.9615	.6614	.7155	979.8	1073.4	636.0
12000	16.2	475.9	−8.8	9.346	19.03	.9175	.9579	.6360	.6932	942.1	1069.4	633.6
13000	12.6	472.3	−10.7	8.984	18.29	.9107	.9543	.6113	.6713	905.6	1065.4	631.2
14000	9.1	468.8	−12.7	8.633	17.58	.9038	.9507	.5875	.6500	870.2	1061.3	628.8
15000	5.5	465.2	−14.7	8.294	16.89	.8969	.9470	.5644	.6292	836.0	1057.3	626.4
16000	1.9	461.6	−16.7	7.965	16.22	.8900	.9434	.5420	.6089	802.9	1053.2	624.0
17000	−1.6	458.1	−18.7	7.647	15.57	.8831	.9398	.5203	.5892	770.8	1049.2	621.6
18000	−5.2	454.5	−20.7	7.339	14.94	.8763	.9361	.4994	.5699	739.8	1045.1	619.2
19000	−8.8	450.9	−22.6	7.041	14.34	.8694	.9324	.4791	.5511	709.8	1041.0	616.7
20000	−12.3	447.4	−24.6	6.754	13.75	.8625	.9287	.4596	.5328	680.8	1036.8	614.3
21000	−15.9	443.8	−26.6	6.475	13.18	.8556	.9250	.4406	.5150	652.7	1032.7	611.9
22000	−19.5	440.2	−28.6	6.207	12.64	.8488	.9213	.4223	.4976	625.6	1028.5	609.4
23000	−23.0	436.7	−30.6	5.947	12.11	.8419	.9175	.4047	.4806	599.4	1024.4	606.9
24000	−26.6	433.1	−32.5	5.696	11.60	.8350	.9138	.3876	.4642	574.1	1020.2	604.4
25000	−30.2	429.5	−34.5	5.454	11.10	.8281	.9100	.3711	.4481	549.7	1016.0	601.9
26000	−33.7	426.0	−36.5	5.220	10.63	.8213	.9062	.3552	.4325	526.2	1011.7	599.4
27000	−37.3	422.4	−38.5	4.994	10.17	.8144	.9024	.3398	.4173	503.4	1007.5	596.9
28000	−40.9	418.8	−40.5	4.777	9.725	.8075	.8986	.3250	.4025	481.5	1003.2	594.4
29000	−44.4	415.3	−42.4	4.567	9.298	.8006	.8948	.3107	.3881	460.3	988.9	591.9
30000	−48.0	411.7	−44.4	4.364	8.886	.7938	.8909	.2970	.3741	439.9	994.6	589.3
31000	−51.6	408.1	−46.4	4.169	8.489	.7869	.8871	.2837	.3605	420.3	990.3	586.8
32000	−55.1	404.6	−48.4	3.981	8.106	.7800	.8832	.2709	.3473	401.3	986.0	584.2
33000	−58.7	401.0	−50.4	3.800	7.737	.7731	.8793	.2586	.3345	383.1	981.6	581.6
34000	−62.3	397.4	−52.4	3.626	7.383	.7663	.8754	.2467	.3220	365.5	977.3	579.0
35000	−65.8	393.9	−54.3	3.458	7.041	.7594	.8714	.2353	.3099	348.6	972.9	576.4
36000	−69.4	390.3	−56.3	3.297	6.712	.7525	.8675	.2243	.2981	332.3	968.5	573.8
*36089	−69.7	390.0	−56.5	3.282	6.683	.7519	.8671	.2234	.2971	330.9	968.1	573.6
37000	−69.7	390.0	−56.5	3.142	6.397	.7519	.8671	.2138	.2843	316.7	968.1	573.6
38000	−69.7	390.0	−56.5	2.994	6.097	.7519	.8671	.2038	.2710	301.8	968.1	573.6
39000	−69.7	390.0	−56.5	2.854	5.811	.7519	.8671	.1942	.2583	287.7	968.1	573.6
40000	−69.7	390.0	−56.5	2.720	5.538	.7519	.8671	.1851	.2462	274.2	968.1	573.6
41000	−69.7	390.0	−56.5	2.592	5.278	.7519	.8671	.1764	.2346	261.3	968.1	573.6
42000	−69.7	390.0	−56.5	2.471	5.030	.7519	.8671	.1681	.2236	249.0	968.1	573.6
43000	−69.7	390.0	−56.5	2.355	4.794	.7519	.8671	.1602	.2131	237.4	968.1	573.6
44000	−69.7	390.0	−56.5	2.244	4.569	.7519	.8671	.1527	.2031	226.2	968.1	573.6
45000	−69.7	390.0	−56.5	2.139	4.355	.7519	.8671	.1455	.1936	215.6	968.1	573.6
46000	−69.7	390.0	−56.5	2.039	4.151	.7519	.8671	.1387	.1845	205.5	968.1	573.6
47000	−69.7	390.0	−56.5	1.943	3.956	.7519	.8671	.1322	.1758	195.8	968.1	573.6
48000	−69.7	390.0	−56.5	1.852	3.770	.7519	.8671	.1260	.1676	186.7	968.1	573.6
49000	−69.7	390.0	−56.5	1.765	3.593	.7519	.8671	.1201	.1597	177.9	968.1	573.6
50000	−69.7	390.0	−56.5	1.682	3.425	.7519	.8671	.1145	.1522	169.5	968.1	573.6
51000	−69.7	390.0	−56.5	1.603	3.264	.7519	.8671	.1091	.1451	161.6	968.1	573.6
52000	−69.7	390.0	−56.5	1.528	3.111	.7519	.8671	.1040	.1383	154.0	968.1	573.6
53000	−69.7	390.0	−56.5	1.456	2.965	.7519	.8671	.09909	.1318	146.8	968.1	573.6
54000	−69.7	390.0	−56.5	1.388	2.826	.7519	.8671	.09444	.1256	139.9	968.1	573.6
55000	−69.7	390.0	−56.5	1.323	2.693	.7519	.8671	.09000	.1197	133.3	968.1	573.6
56000	−69.7	390.0	−56.5	1.261	2.567	.7519	.8671	.08578	.1141	127.1	968.1	573.6
57000	−69.7	390.0	−56.5	1.201	2.446	.7519	.8671	.08175	.1087	121.1	968.1	573.6
58000	−69.7	390.0	−56.5	1.145	2.321	.7519	.8671	.07792	.1036	115.4	968.1	573.6
59000	−69.7	390.0	−56.5	1.091	2.222	.7519	.8671	.07426	.09877	110.0	968.1	573.6
60000	−69.7	390.0	−56.5	1.040	2.118	.7519	.8671	.07078	.09413	104.8	968.1	573.6
61000	−69.7	390.0	−56.5	.9913	2.018	.7519	.8671	.06746	.08971	99.93	968.1	573.6
62000	−69.7	390.0	−56.5	.9448	1.924	.7519	.8671	.06429	.08550	95.24	968.1	573.6
63000	−69.7	390.0	−56.5	.9005	1.833	.7519	.8671	.06127	.08149	90.77	968.1	573.6
64000	−69.7	390.0	−56.5	.8582	1.747	.7519	.8671	.05840	.07767	86.51	968.1	573.6
65000	−69.7	390.0	−56.5	.8179	1.665	.7519	.8671	.05566	.07402	82.45	968.1	573.6

U.S. Standard Atmosphere, 1962
(Geopotential Altitude)

British Units

Altitude feet	Temperature °F	°R	°C	Pressure psia	in. Hg	θ	$\sqrt{\theta}$	δ	σ	$\bar{q}/M^2$ lb/ft²	Sonic Velocity ft/sec	kts
* 65617	−69.7	390.0	−56.5	.7941	1.617	.7519	.8671	.05403	.07186	80.04	968.1	573.6
70000	−67.3	392.4	−55.2	.6437	1.311	.7565	.8698	.04380	.05789	64.88	971.0	575.3
75000	−64.6	395.1	−53.6	.5073	1.0333	.7618	.8728	.03452	.04532	51.14	974.4	577.3
80000	−61.8	397.9	−52.1	.4005	.8155	.7671	.8759	.02726	.03553	40.37	977.8	579.3
85000	−59.1	400.6	−50.6	.3167	.6449	.7724	.8789	.02155	.02790	31.93	981.2	581.3
90000	−56.3	403.4	−49.1	.2509	.5108	.7777	.8819	.01707	.02195	25.29	984.5	583.3
95000	−53.6	406.1	−47.5	.1990	.4052	.7830	.8849	.01354	.01730	20.06	987.9	585.3
100000	−50.8	408.9	−46.0	.1581	.3220	.7883	.8878	.01076	.01365	15.94	991.2	587.3
*104987	−48.1	411.6	−44.5	.1259	.2563	.7935	.8908	.008567	.010800	12.69	994.5	589.2
150000	21.0	480.7	−6.1	.01893	.03854	.9269	.9627	.001288	.001390	1.908	1074.8	636.8
*154199	27.5	487.2	−2.5	.01609	.03275	.9393	.9692	.001095	.001165	1.622	1082.0	641.1
*170604	27.5	487.2	−2.5	.00557	.01742	.9393	.9692	.0005823	.0006199	.8626	1082.0	641.1
200000	−4.8	454.9	−20.4	.002655	.005406	.8771	.9365	.0001807	.0002060	.2677	1045.5	619.5
*200131	−4.9	454.8	−20.5	.002641	.005377	.8768	.9364	.0001797	.0002050	.2662	1045.4	619.4

*Boundary between atmosphere layers of constant thermal gradient.

Note: The ICAO atmosphere is identical to the U.S. Standard Atmosphere for altitudes below 65,617 ft.

A2. Specific Weights of Liquids and Gases

Weights of Liquids

Liquid	Specific Gravity at °C		Specific Wt lb/U.S. gal	lb/cu ft
Acetylene tetrabromide ($AcBr_4$)	2.99	25	24.95	186.67
Alcohol (methyl)	0.810	0	6.75	50.5
Benzine	0.899	0	7.5	56.1
Carbon tetrachloride	1.595	20	13.32	99.6
Ethylene glycol	1.12		9.3	69.6
Gasoline	0.72		5.87	44.9
Glycerine	1.261	20	10.52	78.71
JP1 (MIL-L-5616)	0.80		6.65	49.7
JP3 (MIL-J-5624D)	0.775		6.45	48.2
JP4 (MIL-J-5624D)	0.785		6.55	49.0
JP5 (MIL-J-5624D)	0.817	15	6.82	51.1
Kerosene	0.82		6.7	51.2
Mercury	13.546	20	113.0	845.6
Oil (MIL-6082B Grade 1100)	0.89	15	7.4	55.3
Sea water	1.025	15	8.55	63.99
Synthetic oil (MIL-L-7808C-1)	0.928	15	7.74	57.9
Water	1.000	4	8.345	62.43
Jet A fuel (ASTM-D-1655)	.808	15	6.74	50.4

Weights of Gases

Gas	Specific Wt * lb/cu ft
Air	.07651 (at 59.0°F)
Air	.08071
Carbon dioxide	.12341
Carbon monoxide	.07806
Helium	.01114
Hydrogen	.005611
Nitrogen	.07807
Oxygen	.089212

*At atmospheric pressure and 0°C.

A3. Conversion Factors

Multiply	By			To obtain
acre	4.3560	X	10^{4}	square feet
	4.0469	X	10^{-1}	hectares
	4.0469	X	10^{3}	square meters
	1.5625	X	10^{-3}	square miles
	4.8400	X	10^{3}	square yards
atmosphere (atm)(1962)	7.6000	X	10	centimeters of mercury
	2.9921	X	10	inches of mercury
	1.0332	X	10^{4}	kilograms/square meter
	1.0133	X	10^{5}	newtons/square meter
	1.4696	X	10	pounds/square inch
bar	9.8692	X	10^{-1}	atmospheres
	1.0000	X	10^{6}	dynes/square centimeter
	7.5006	X	10^{2}	millimeters of mercury
	1.0000	X	10^{5}	newtons/square meter
	1.4504	X	10	pounds/square inch
barn	1.0000	X	10^{-24}	square centimeters (nuclear cross-section)
barrel, liquid (U.S.)	3.1500	X	10	gallons
	1.1924	X	10^{-1}	cubic meters
British thermal unit (Btu)	2.5180	X	10^{2}	calories(post-1956 IST)
	7.7817	X	10^{2}	foot-pounds
	1.0551	X	10^{10}	ergs
	3.9301	X	10^{-4}	horsepower-hours
	1.0551	X	10^{3}	joules
	1.0551	X	10^{3}	newton-meters
	2.9302	X	10^{-4}	kilowatt-hours
	1.0551	X	10^{3}	watt-seconds
British thermal unit/minute (Btu/min)	4.1999			calories/second
	1.7548	X	10^{8}	ergs/second
	1.2970	X	10	foot-pounds/second
	2.3581	X	10^{-2}	horsepower
	1.7548	X	10	joules/second
	1.7931			kilogram-meters/second
	1.7548	X	10	watts
calorie (cal)	3.9683	X	10^{-3}	British thermal units
	3.0880			foot-pounds
	4.1868	X	10^{7}	ergs
	4.1868			joules
	1.1630	X	10^{-6}	kilowatt-hours
	4.1868			watt-seconds
calorie/second (cal/sec)	2.3810	X	10^{-1}	British thermal units/minute
	4.1868	X	10^{7}	ergs/second
	3.0880			foot-pounds/second
	4.1868			joules/second
centimeter (cm)	3.2808	X	10^{-2}	feet
	3.9370	X	10^{-1}	inches
	1.0000	X	10^{-5}	kilometers
	1.0000	X	10^{-2}	meters
	1.0936	X	10^{-2}	yards
centimeter/second (cm/sec)	3.2808	X	10^{-2}	feet/second
	3.9370	X	10^{-1}	inches/second
	1.0000	X	10^{-2}	meters/second
centipoise	6.7197	X	10^{-4}	pounds(mass)/second-foot
	3.6000			kilograms/hour-meter
cubic centimeter (cm^3)	1.0000	X	10^{-3}	cubic decimeters
	3.5315	X	10^{-5}	cubic feet
	6.1024	X	10^{-2}	cubic inches
	1.0000	X	10^{-6}	cubic meters
	1.3080	X	10^{-6}	cubic yards
cubic decimeter (liter) (dm^3)	1.0000	X	10^{3}	cubic centimeters
	3.5315	X	10^{-2}	cubic feet
	6.1024	X	10	cubic inches
	1.0000	X	10^{-3}	cubic meters
	1.3080	X	10^{-3}	cubic yards
cubic foot (ft^3)	2.8317	X	10^{3}	cubic centimeters
	2.8317	X	10	cubic decimeters
	1.7280	X	10^{3}	cubic inches
	2.8317	X	10^{-2}	cubic meters
	3.7037	X	10^{-2}	cubic yards
cubic inch (in^3)	1.6387	X	10	cubic centimeters
	1.6387	X	10^{-2}	cubic decimeters
	5.7870	X	10^{-4}	cubic feet
	1.6387	X	10^{-5}	cubic meters
	2.1433	X	10^{-5}	cubic yards
cubic meter (m^3)	1.0000	X	10^{6}	cubic centimeters
	1.0000	X	10^{3}	cubic decimeters
	3.5315	X	10	cubic feet
	6.1024	X	10^{4}	cubic inches
	1.3080			cubic yards
curie	3.7000	X	10^{10}	disintegrations/second
degree (deg)	6.0000	X	10	minutes
	1.7453	X	10^{-2}	radians
	2.7778	X	10^{-3}	revolutions
	3.6000	X	10^{3}	seconds
dyne	1.0197	X	10^{-3}	grams
	1.0197	X	10^{-6}	kilograms
	1.0000	X	10^{-5}	newtons
	3.5970	X	10^{-5}	ounces
	2.2481	X	10^{-6}	pounds
dyne/square centimeter	2.9530	X	10^{-5}	inches of mercury
	1.0197	X	10^{-2}	kilograms/square meter
	7.5006	X	10^{-4}	millimeters of mercury
	1.0000	X	10	newtons/square meter
	1.4504	X	10^{-5}	pounds/square inch
electron volt (eV)	3.8268	X	10^{-20}	calories
	1.6022	X	10^{-12}	ergs
	1.0000	X	10^{-6}	MeV(mega electron volts)
erg	9.4782	X	10^{-11}	British thermal units
	2.3885	X	10^{-8}	calories
	1.0000			dyne-centimeters
	7.3756	X	10^{-8}	foot-pounds
	1.0000	X	10^{-7}	joules
erg/second	5.6869	X	10^{-9}	British thermal units/minute
	2.3885	X	10^{-8}	calories/second
	7.3756	X	10^{-8}	foot-pounds/second
	1.0000	X	10^{-7}	joules/second
	1.0000	X	10^{-7}	watts
flow rate, fuel (lb/hr)	4.5359	X	10^{-1}	kilograms/hour
foot (ft)	3.0480	X	10	centimeters
	1.2000	X	10	inches
	3.0480	X	10^{-4}	kilometers
	3.0480	X	10^{-1}	meters
	1.8939	X	10^{-4}	miles
	3.3333	X	10^{-1}	yards
foot-pound (ft-lb)	1.2851	X	10^{-3}	British thermal units
	1.3558	X	10^{7}	ergs
	5.0505	X	10^{-7}	horsepower-hours
	1.3558			joules
	3.7662	X	10^{-7}	kilowatt-hours
	1.3558			newton-meters
foot-pound/second (ft-lb/sec)	7.7104	X	10^{-2}	British thermal units/minute
	3.2383	X	10^{-1}	calories/second
	1.8182	X	10^{-3}	horsepower
	1.3558			joules/second
	1.3826	X	10^{-1}	kilogram-meters/second
	1.3558			watts
foot/second (fps)	3.0480	X	10	centimeters/second
	1.0973			kilometers/hour
	5.9248	X	10^{-1}	knots
	3.0480	X	10^{-1}	meters/second
	6.8182	X	10^{-1}	miles/hour

Conversion Factors (continued)

Multiply	By			To obtain
gallon (U.S.) (gal)	1.3368	X	10^{-1}	cubic feet
	3.7854			liters
	3.7854	X	10^{-3}	cubic meters
	8.0000			pints
	4.0000			quarts
gram (gm)	1.0000	X	10^{-3}	kilograms
	3.5274	X	10^{-2}	ounces
	2.2046	X	10^{-3}	pounds
	9.8067	X	10^{2}	dynes
	9.8067	X	10^{-3}	newtons
hectare	2.4711			acres
	1.0000	X	10^{2}	ares
	1.0000	X	10^{4}	square meters
	3.8610	X	10^{-3}	square miles
horsepower (hp)	4.2436	X	10	British thermal units/minute
	5.5000	X	10^{2}	foot-pounds/second
	3.3000	X	10^{4}	foot-pounds/minute
	7.4570	X	10^{2}	joules/second
	7.6040	X	10	kilogram-meters/second
	7.4570	X	10^{2}	watts
horsepower-hour (hp-hr)	2.5461	X	10^{3}	British thermal units
	1.9800	X	10^{6}	foot-pounds
	2.6845	X	10^{6}	joules
	7.4570	X	10^{-1}	kilowatt-hours
hour (hr)	6.0000	X	10	minutes
	3.6000	X	10^{3}	seconds
	4.1781	X	10^{-2}	sidereal days
	4.1667	X	10^{-2}	solar days
	1.1416	X	10^{-4}	solar years
imperial gallon	2.7742	X	10^{2}	cubic inches
	1.2009			gallons (U.S.)
	4.5460			liters
inch (in)	2.5400			centimeters
	8.3333	X	10^{-2}	feet
	2.5400	X	10^{-2}	meters
	2.7778	X	10^{-2}	yards
inch of mercury at 0°C (in Hg)	3.3421	X	10^{-2}	atmospheres
	3.3864	X	10^{-2}	bars
	3.3864	X	10^{4}	dynes/square centimeter
	1.3595	X	10	inches of water
	2.5400	X	10	millimeters of mercury
	3.3864	X	10^{3}	newtons/square meter
	7.0727	X	10	pounds/square feet
	4.9116	X	10^{-1}	pounds/square inch
inch/second (ips)	8.3333	X	10^{-2}	feet/second
	2.5400			centimeters/second
	2.5400	X	10^{-2}	meters/second
inch of water at 4°C (in H_2O)	2.4584	X	10^{-3}	atmospheres
	7.3556	X	10^{-2}	inches of mercury
	1.8683			millimeters of mercury
	2.4910	X	10^{2}	newtons/square meter
	3.6128	X	10^{-2}	pounds/square inch
joule (J)	9.4771	X	10^{-4}	British thermal units
	2.3889	X	10^{-1}	calories
	1.0000	X	10^{7}	dyne-centimeters
	1.0000	X	10^{7}	ergs
	7.3756	X	10^{-1}	foot-pounds
	1.0000			newton-meters
	1.0000			watt-seconds
kilogram (kg)	1.0000	X	10^{3}	grams
	3.5274	X	10	ounces
	2.2046			pounds
	6.8521	X	10^{-2}	slugs
	9.8067			newtons
	7.9290	X	10	poundals
kilogram/ square meter (kg/m^2)	9.6783	X	10^{-5}	atmospheres
	9.8067	X	10^{-5}	bars
	2.8959	X	10^{-3}	inches of mercury
	9.8067			newtons/ square meter
kilogram/ square meter (kg/m^2)	6.5895			poundals/square foot
	2.0482	X	10^{-1}	pounds/square foot
	1.4223	X	10^{-3}	pounds/square inch
kilogram-meter (kgm)	9.2938	X	10^{-3}	British thermal units
	7.2330			foot-pounds
	9.8067			joules
	9.8067			newton-meters
	2.7232	X	10^{-6}	kilowatt-hours
kilogram-meter/ second (kgm/sec)	3.3458	X	10	British thermal units/hour
	2.3423			calories/second
	7.2330			foot-pounds/second
	9.8067			joules/second
	1.3151	X	10^{-2}	horsepower
	9.8067	X	10^{-3}	kilowatts
kilometer (km)	3.2808	X	10^{3}	feet
	3.9370	X	10^{4}	inches
	1.0000	X	10^{3}	meters
	6.2137	X	10^{-1}	miles
	1.0936	X	10^{3}	yards
kilometer/hour (km/hr)	9.1130	X	10^{-1}	feet/second
	5.3960	X	10^{-1}	knots
	6.2137	X	10^{-1}	miles/hour
	2.7778	X	10^{-1}	meters/second
kilonewton (kN)	2.2481	X	10^{2}	pounds
kilowatt hour (kWh)	3.4128	X	10^{3}	British thermal units
	2.6560	X	10^{6}	foot-pounds
	1.3414			horsepower-hours
	3.6000	X	10^{6}	joules
	3.6721	X	10^{5}	kilogram-meters
	3.6000	X	10^{6}	watt-seconds
knot (kt)	1.6890			feet/second
	1.1516			miles/hour
	1.8532			kilometers/hour
	5.1480	X	10^{-1}	meters/second
light year	3.1040	X	10^{16}	feet
	5.8786	X	10^{12}	miles
	9.4608	X	10^{15}	meters
liter (l)	6.1024	X	10	cubic inches
	3.5315	X	10^{-2}	cubic feet
	2.6417	X	10^{-1}	gallons (U.S. liquid)
	1.0000	X	10^{-3}	cubic meters
	2.1134			pints (U.S. liquid)
	1.0567			quarts (U.S. liquid)
meter (m)	1.0000	X	10^{2}	centimeters
	3.2808			feet
	3.9370	X	10	inches
	1.0000	X	10^{-3}	kilometers
	6.2137	X	10^{-4}	miles
	1.0936			yards
meter/second (m/sec)	3.2808			feet/second
	3.6000			kilometers/hour
	1.9438			knots
	2.2369			miles/hour
metric horsepower	9.8632	X	10^{-1}	horsepower
	7.3550	X	10^{-1}	kilowatts
mile (mi)	5.2800	X	10^{3}	feet
	6.3360	X	10^{4}	inches
	1.6093			kilometers
	1.6093	X	10^{3}	meters
	3.2000	X	10^{2}	rods
	1.7600	X	10^{3}	yards
mile/hour (mph)	1.4667			feet/second
	1.6093			kilometers/hour
	8.6898	X	10^{-1}	knots
	4.4704	X	10^{-1}	meters/second
millimeter of mercury at 0°C (torr) (mm Hg)	1.3332	X	10^{3}	dynes/square centimeter
	3.9370	X	10^{-2}	inches of mercury (0°C)
	5.3526	X	10^{-1}	inches of water (4°C)
	1.3332	X	10^{2}	newtons/square meter
	1.9337	X	10^{-2}	pounds/square inch

Conversion Factors (continued)

Multiply	By			To obtain
minute (angle) (min)	1.6667	X	10^{-2}	degrees
	2.9089	X	10^{-4}	radians
	4.6296	X	10^{-5}	revolutions
	6.0000	X	10	seconds
minute (time) (min)	1.6667	X	10^{-2}	hours
	6.0000	X	10	seconds
	6.9444	X	10^{-4}	solar days
	1.9026	X	10^{-6}	solar years
nautical mile (international) (n mi)	6.0761	X	10^{3}	feet
	1.8520	X	10^{3}	meters
newton (N)	1.0000	X	10^{5}	dynes
	1.0197	X	10^{2}	grams
	1.0197	X	10^{-1}	kilograms
	2.2481	X	10^{-1}	pounds
	7.2330			poundals
newton/ square meter (pascal (Pa)) (N/m^2)	9.8692	X	10^{-6}	atmospheres
	1.0000	X	10	dynes/square centimeter
	2.9530	X	10^{-4}	inches of mercury (0°C)
	1.0197	X	10^{-1}	kilograms/square meter
	6.7200	X	10^{-1}	poundals/square foot
	2.0885	X	10^{-2}	pounds/square foot
	1.4504	X	10^{-4}	pounds/square inch
ounce (oz)	2.8349	X	10	grams
	2.8349	X	10^{-2}	kilograms
	6.2500	X	10^{-2}	pounds
	1.9428	X	10^{-3}	slugs
	2.7801	X	10^{4}	dynes
parsec	1.9163	X	10^{13}	miles
	3.0857	X	10^{16}	meters
pieze	1.0000	X	10^{3}	newtons/square meter
pound(mass) (lb)	4.5359	X	10^{2}	grams
	4.5359	X	10^{-1}	kilograms
	1.6000	X	10	ounces
pound (force) (lbf)	3.1081	X	10^{-2}	slugs
	4.4482			newtons
	4.4482	X	10^{-1}	dekanewtons
	4.4482	X	10^{-3}	kilonewtons
	3.2174	X	10	poundals
pound/ square foot (psf)	4.7254	X	10^{-4}	atmospheres
	4.7880	X	10^{-4}	bars
	4.7880	X	10^{2}	dynes/square centimeter
	1.4139	X	10^{-2}	inches of mercury (0°C)
	4.8824			kilograms/square meter
	4.7880	X	10	newtons/square meter
	3.2174	X	10	poundals/square foot
	6.9444	X	10^{-3}	pounds/square inch
pound/ square inch (psi)	6.8046	X	10^{-2}	atmospheres
	6.8948	X	10^{4}	dynes/square centimeter
	2.0360			inches of mercury (0°C)
	2.7681	X	10	inches of water (4°C)
	7.0307	X	10^{2}	kilograms/square meter
	6.8948	X	10^{3}	newtons/square meter
	4.6333	X	10^{3}	poundals/square foot
	1.4400	X	10^{2}	pounds/square foot
poundal	1.4098	X	10^{-2}	kilograms
	1.3825	X	10^{-1}	newtons
	3.1081	X	10^{-2}	pounds
poundal/ square foot	1.5174	X	10^{-1}	kilograms/square meter
	1.4882	X	10^{-1}	newtons/square meter
	3.1081	X	10^{-2}	pounds/square foot
	2.1583	X	10^{-4}	pounds/square inch
radian (rad)	5.7296	X	10	degrees
	3.4378	X	10^{3}	minutes
	1.5916	X	10^{-1}	revolutions
	2.0626	X	10^{5}	seconds
revolution (rev)	3.6000	X	10^{2}	degrees
	2.1600	X	10^{4}	minutes
	6.2832			radians
	1.2960	X	10^{6}	seconds
second (angle) (sec)	2.7778	X	10^{-4}	degrees
	1.6667	X	10^{-2}	minutes
	4.8481	X	10^{-6}	radians
	7.7160	X	10^{-7}	revolutions
second (time) (sec)	2.7778	X	10^{-4}	hours
	1.6667	X	10^{-2}	minutes
	1.1574	X	10^{-5}	solar days
slug	1.4594	X	10^{4}	grams
	1.4594	X	10	kilograms
	5.1478	X	10^{2}	ounces
	3.2174	X	10	pounds
square centimeter (cm^2)	1.0764	X	10^{-3}	square feet
	1.5500	X	10^{-1}	square inches
	1.0000	X	10^{-4}	square meters
	1.0000	X	10^{2}	square millimeters
square foot (ft^2)	2.2957	X	10^{-5}	acres
	9.2903	X	10^{2}	square centimeters
	1.4400	X	10^{2}	square inches
	9.2903	X	10^{-2}	square meters
	3.5870	X	10^{-8}	square miles
	1.1111	X	10^{-1}	square yards
square inch (in^2)	1.2732	X	10^{6}	circular mils
	6.4516			square centimeters
	6.9444	X	10^{-3}	square feet
	6.4516	X	10^{-4}	square meters
	6.4516	X	10^{2}	square millimeters
	1.0000	X	10^{6}	square mils
	7.7160	X	10^{-4}	square yards
square kilometers (km^2)	2.4711	X	10^{2}	acres
	1.0764	X	10^{7}	square feet
	1.0000	X	10^{6}	square meters
	3.8610	X	10^{-1}	square miles
square meter (m^2)	2.4711	X	10^{-4}	acres
	1.0000	X	10^{-4}	hectares
	1.0000	X	10^{4}	square centimeters
	1.0764	X	10	square feet
	1.5500	X	10^{3}	square inches
	3.8610	X	10^{-7}	square miles
	1.1960			square yards
square mile (mi^2)	6.4000	X	10^{2}	acres
	2.5900	X	10^{2}	hectares
	2.7878	X	10^{7}	square feet
	2.5900			square kilometers
	2.5900	X	10^{6}	square meters
	3.0976	X	10^{6}	square yards
thermie	4.1868	X	10^{6}	joules
thrust specific fuel consumption (TSFC) (lb/hr/lb Fn)	1.0197	X	10^{2}	kilograms/hour/ dekanewton
watt (joule/ second) (W)	3.4121			British thermal units/hour
	5.6869	X	10^{-2}	British thermal units/minute
	2.3900	X	10^{-1}	calories/second
	1.0000	X	10^{7}	ergs/second
	7.3756	X	10^{-1}	foot-pounds/second
	1.3410	X	10^{-3}	horsepower
	1.0197	X	10^{-1}	kilogram-meters/second
watt second (Wsec)	9.4782	X	10^{-4}	British thermal units
	7.3756	X	10^{-1}	foot-pounds
	1.0000			joule
	2.7778	X	10^{-7}	kilowatt-hours

APPENDIX B: METHODS FOR COMPUTING CIRCUMFERENCES, AREAS AND VOLUMES

In the process of airplane project design it is frequently necessary to compute the cross-section circumference, the surface area and/or the volume of components of the airplane such as: fuselages, fuselage boattails, wings, fuel tanks and nacelles.

Reference 58, by Professor E.Torenbeek of Delft University of Technology in Delft, The Netherlands is an excellent source of methods for computing such items. For that reason, Reference 58 has been copied and adapted for incorporation as Appendix B in this book.

Nomenclature

Most symbols are used only occasionaly. Therefore, the nomenclature is mentioned in the text or on the relevant figure or diagram.

Contents

B1. Introduction

In the calculation of mass properties and aerodynamic coefficients like profile drag coefficients and stability derivatives, reference is made to frontal areas, sideview areas, wetted areas and volumes. Once the detailed shape of the major aircraft components is accurately established by means of lofting processes (e.g. ref.B3), these characteristic areas and volumes can be computed numerically or by means of graphical methods. The present subject, however, is associated with project design studies, where the detailed shape and dimensions are not always accurately known or, in some cases, may have been chosen provisionally. An estimation, accurate within a few percent of the exact value, may be acceptable when emphasis is laid on time saving.

In the present memorandum methods are presented for the calculation of circumferences, areas and volumes, having different degrees of accuracy. The most exact procedure is based on a representation of the surface contour lines by a suitable polynomial with fractional exponents. Such a two-parameter method is explained in ch.B2 and is very simple to use when a three-view drawing of the component is available. Generalized results of the various integrations are presented in diagrams (ch.B3). These are useful not only for accurate computations, but they have been used for the derivation of simplified methods as well.

The reader who is interested in practical results only may omit the reading of chapters B2 and B3. Chapters B4, B5 and B6 deal with applications for fuselages, wings, tailplanes, fuel tanks and engine nacelles. In general, both accurate and simplified methods are presented. For fuselages a review of the various available methods is given on fig. 5.

B2. Approximation of contours by analytical functions

The rigid requirements in aeronautical design have led to the adoption of streamline shapes with smooth, continuous external lines, resulting in a smooth rate of change of curvature along the entire length of the body. For fuselages, the application of a pressurized cabin makes a circular cross section or a section built up from circular sections a very desirable, if not mandatory feature. Extensive areas of double curvature, like saddle surfaces, should be avoided because of the associated costly manufacturing processes. The design criteria for wings are entirely different as the external shape is dictated by aerodynamic requirements, viz. low drag, high maximum lift, favourable characteristics at high incidences and at Mach numbers where compressibility effects are dominant. For subsonic aircraft, leading and trailing edges of wings and tail surfaces are frequently straight lines. Aerofoils have neatly

rounded noses, while sharp trailing edges are used for good lifting properties. For ease of production, intermediate sections are often constructed from tip and root sections by assuming straight lines between corresponding points ("linear lofting").

In general, it will be necessary to subdivide the body, for which the characteristic areas and volumes must be calculated, into several sections. For example, the pressurized fuselage of a transport aircraft is logically split up into a nose section, a cylindrical mid section and a tail section. The more sections are used in non-cylindrical parts, the higher will be the accuracy of prediction. For project-design purposes, however, a method is required, resulting in an error of probably not more than a few percent, using a very limited amount of subdivisions to minimize the computational time.

The general shape of many curves and external lines can be represented in a most satisfactory way by the following two-dimensional convex polynomial:

$$(\frac{x}{a})^n + (\frac{y}{b})^m = 1 \qquad ; \text{ for } n, m \geq 1 \qquad (1)$$

For typical fuselage nose and tail sections examples of this function are plotted in fig. 1 for two combinations of the exponents n and m. Several special cases of eq. 1 are plotted in fig. 2 and discussed below.

The straight line ($n = m = 1$), used for cones.
Parabola 1 ($n = 2$ and $m = 1$) is representative to some degree for fuselage tail sections.
Parabola 2 ($n = 1$ and $m = 2$). Provided that the base area is not too large, this parabola may occasionally be used for blunt fuselage ends.
The ellipse ($n = m = 2$), appearing as a circle in fig. 2. Many fuselage and wing sections and nacelle noses have near-elliptic shapes.
Quartic 1 ($n = 4$; $m = 2$) and quartic 2 ($n = 2$; $m = 4$), representative for blunt noses and tails.
Lamé's quartic ($n = m = 4$). This curve is of particular interest for the representation of cross-sectional shapes of small aircraft with unpressurized cabins.

It is not suggested that for a particular body the sectional contour should be approximated by any of these special functions; errors of 5 - 10% in volumes and wetted areas may be introduced by doing so. However, several of these special cases can be treated analytically and are therefore useful to check the general solution, in which intermediate (fractional) values for n and m are treated as well.

For a specified contour shape, n and m can be determined readily from the geometric parameters φ and γ, defined in fig. 3. To this end, a suitable choice of the X- and Y-axes must be made.
For fuselages, the X-axis will usually be located in the plane of symmetry, the Y-axis may be on the intersection of the cylindrical part with the nose or tail section.
For wing sections, the effect of camber on the circumferential length of a section is negligible. On the corresponding symmetrical section, the X-axis is the chordline and the Y-axis will be taken at the point of maximum section thickness.

Point S in fig. 3 is determined graphically in the drawing as the intersection of the contourline and the diagonal of the rectangle which encloses the contour. The X-coordinate of S as a fraction of the projected contourlength (a) defines the parameter φ. The intersection of the tangent at S and the X-axis defines the parameter γ. The projected height of the contour is b. Although the graphical construction of a tangent is not always a very accurate procedure, it will be shown later on that the results are not affected to a great deal by errors in γ.

The equations relating combinations (n,m) and (φ,γ) to each other are derived in Ref. 58 ; the results are plotted in diagram 1. Once φ and γ are measured in the drawing, n and m can be found and, if desired, a check on the accuracy of the approximation by eq. 1 can be made by calculation of the contour. However, in ch.B3 it will be demonstrated that for the purpose of calculating volumes and areas, considerable deviations from the actual shape are acceptable, provided that the value of φ is accurate. For example, the parabolae 1 and 2 in fig. 2 have the same value $\varphi = \frac{1}{2}(\sqrt{5}-1)$. The sectional areas for both curves are exactly equal, the circumferential lengths are equal within a few tenths of a percent, while the volumes and wetted areas of corresponding bodies of revolution differ by one or two percent only.

B3. Diagrams for areas, circumferences and volumes

The choice of the polynomial given by eq. 1 provides the tool to calculate areas, circumferences and volumes of body sections. The suitability of the function is confirmed by the fact that all results can be plotted in two-dimensional diagrams, although 4 geometric parameters (φ, γ, a and b) are involved. The diagrams can be used for a very quick calculation, as no integrations are necessary.
For cross sections of pressure cabins a separate diagram is included.

B3.1 Sectional (projected) area - diagram 2

The area enclosed by the contour, the X-axis and the Y-axis is:

$$\text{SECTIONAL AREA} = \int_0^a y\,dx \qquad (2)$$

By substitution of y from eq. 1 and integration, the final result as derived in Ref. 58 is found and plotted in diagram 2. In terms of n and m, the area is determined by Γ-functions, which are symmetrical with respect to n and m. The simple representation in diagram 2 is possible, as the area is not affected by γ.

B3.2 Circumference of a section contour - diagram 3

The expression for the circumferential length is:

$$\text{CIRCUMFERENCE} = \int\sqrt{(dx)^2 + (dy)^2} = \int_0^a \sqrt{1 + \left(\frac{dy}{dx}\right)^2}\,dx \qquad (3)$$

For several special combinations of n and m, this integral can be solved analytically Ref. 58 , resulting in expressions with n, m and the ratio a/b as parameters. As in the case of the sectional area, it appears convenient to use φ and γ instead, but the effect of γ appears to be small. Hence, in diagram 3 only φ and a/b are used as parameters. Although the result is now no longer exact, the error introduced is quite small.
For example:

a) the difference between the exact results for the two parabolae 1 and 2 is indistinguishable in the diagram,
b) the two quartics (n = 4; m = 2 and n = 2; m = 4) are both represented by the dotted line $\varphi = \sqrt{(\sqrt{5}-1)/2} = 0.786$. For a given value of a/b, the error with respect to the exact result, as shown in the diagram, is less than one percent.

In some cases, the calculation of the circumferential length of a cross section is an intermediate step in the computation of wetted area. In those cases, the height/width ratio is always between 0.5 and 2 and, within the corresponding range $0.5 < a/b < 1.0$, the circumference is hardly affected by a/b as well. This property will be used for the simplified calculations of par. 4.2.

B3.3 Volume of bodies of revolution - diagram 4

By rotation of the contour, given by eq. 1, about the X-axis, a body of revolution is formed, with a volume equal to:

$$\text{VOLUME} = \int_0^a \pi y^2\,dx \qquad (4)$$

The complete solution is derived in Ref. 58 in terms of n and m and plotted in diagram 4. The parameters φ and γ may be used instead. The volume, expressed as a fraction of the cylinder volume (length a, radius b), is not affected by a/b. As in the previous cases, the parameter φ is most prominent, γ is of secondary importance. It can be shown that formulae for the sectional shape different from eq. 1 yield essentially the same results, provided that the same value of φ is used.

B3.4 Wetted area of bodies of revolution - diagram 5

The body of revolution as defined in the previous paragraph has the following wetted area:

$$\text{EXTERNAL AREA} = \int 2\pi y \sqrt{(dx)^2 + (dy)^2} = 2\pi \int_0^a y \sqrt{1 + \left(\frac{dy}{dx}\right)^2}\, dx \qquad (5)$$

For special combinations of n and m, analytical expressions for this integral can be derived (see Ref. 58). The wetted area, plotted in diagram 5 as a fraction of the cylinder external area ($2\pi ab$) plus one side area (πb^2), is affected primarily by φ and a/b. In analogy to the case for the circumference, the omission of γ results in errors of not more than 1 or 2%. This is illustrated in the diagram for the two parabolae, both represented by $\varphi = \frac{1}{2}(\sqrt{5} - 1)$ and the two quartics, with $\varphi = \sqrt{(\sqrt{5} - 1)/2}$.

B3.5 Correction factors for double bubble and flattened cross sections- diagram 6

For fuselages with "double bubble" cross sectional shapes, like the DC-8, DC-9, VC-10 and others, or a flattened belly below the cabin floor (e.g. F-27, C-5A), correction factors can be derived, relating the circumference and sectional area to those of a circle. The circle diameter is assumed equal to the max. width of the actual fuselage. The relevant equations are presented in fig. 4 and the results plotted in diagram 6. All parameters used can be measured on a drawing of the cross section or front view.

B4. Fuselages

The methods presented in this chapter refer to the gross wetted area of the streamline body by which most fuselage shapes can be approximated. Cockpit canopies, fillets, wing-fuselage attachments, air scoops, etc., are ignored and must be accounted for seperately.
A choice can be made between several methods. The most accurate of these is described in par.B4.1 and can be used when a complete three-view drawing is available. For substantially non-cylindrical fuselages, several cross sections must be available as well. The simplified methods discussed in par.B4.2 are useful when the fuselage shape or some dimensions are not completely known. A survey of the applicability of the various methods is given in fig. 5.

B4.1 "Accurate" calculations

a. Fuselages with circular cross sections

The nose and tail sections are usually nearly bodies of revolution as well. The planview is used to subdivide the fuselage into a nose section, a cylindrical mid section (if present) and a tail section and the parameters φ and γ are determined (fig. 3). Projected areas in sideview or planview can be derived from diagram 2. Volumes and wetted areas are computed with diagrams 4 and 5.

b. Fuselages with a blunt base or a beaver tail

The approximation for blunt and beaver tails, as presented in diagrams 7 and 8, can be used on the condition that the contour lines are not too different from a parabolic shape. Formulae for ogives can be found in ref.B6.

c. Fuselages with double-bubble or flattened cross sections

The volume and wetted area are computed, assuming that the fuselage is a body of revolution with diameter equal to the maximum width of the fuselage (fig. 4). Similarly to case a., the planview is used. The correction factors in diagram 6 are then applied to the frontal area, the volume and the wetted area.

d. Fuselages with non-circular cross sections

The following procedure is suggested:

1. A subdivision into a suitable number of segments is made.

2. The parallel end faces of the segments are local cross sections; their areas and circumference are calculated with diagrams 2 and 3.
3. The segments are approximated by bodies of type A or B in fig. 7. Their volumes are computed and added.
4. The circumferential lengths of the cross sections are plotted on the longitudinal axis and integrated numerically (e.g. Simpson's rule, ref.B6) or with diagram 3.
5. The integral is corrected by addition of an extra percentage:

$$\frac{\Delta(\text{wetted area})}{\text{wetted area}} = 75 \frac{\text{frontal area}}{(\text{fuselage length})^2} \ \% \qquad (6)$$

This approximate correction accounts for the fact that integration of the circumferential length should take place along the external contour instead of the longitudinal axis.

B4.2 Simplified methods

In many cases the fuselage contour is not completely defined and a certain amount of help from statistical data will be acceptable. The designer can make a choice between the following approximate methods:

a. Three-view drawing is available

In chapters 2 and 3 the parameters φ and γ were introduced to find the fractional exponents n and m. It was found that
- the effect of γ is very small or completely absent,
- for practical cross-sectional shapes the effect of the height/width ratio on the circumference is negligible.

Moreover, by application of the method to practical fuselages, it was concluded that for the most common nose and tail sections the wetted area as a fraction of the cilinder area ($2\pi ab$ in diagram 5) is approximately a function of φ only. Therefore, the procedure of ch.B4.1 can be simplified and the results are summarized in diagram 9.

b. Fuselage length, cross-sectional shape and length of mid section are known

Diagram 10 is composed from the results of calculations of volumes and wetted areas for several actual fuselages with near-circular cross sections, using diagrams 2-6. The dotted line is taken as the mean value and corrections are derived from diagram 2 and 3. This simple diagram may be of use when the actual shape of nose and tail sections are not specified.

c. Axisymmetric streamline bodies of given length and diameter

In fig. 6 the ratio:

$$\frac{\text{wetted area}}{2\sqrt[3]{2\pi\lambda}(\text{volume})^{2/3}}, \text{ where } \lambda = \frac{\text{length}}{\text{diameter}}$$

is plotted for cylinders, ellipsoids, paraboloids, double cones and typical streamline shapes with and without a cylindrical center section. This ratio is approximated by a simple function of λ for streamline bodies. Once the volume is known, the wetted area can be calculated in a straight forward manner. The expressions for the volume are based on typical nose and tail section shapes, according to fig. 1.

d. Volume and wetted area based on cabin dimensions

When observing actual fuselage shapes, it is noted that the fuselage length is considerably affected by the detailed shape of the nose and the tail extremities. On the contrary, the volume and wetted area are much less affected. In preliminary design the fuselage tail length may be subject to optimization at a later stage, when accurate data are available on structure weight and afterbody drag, in order to find the most favourable tailplane moment arm.

The dimensions of the passenger cabin and the freighthold volume, however, are established at a very early phase of the design, these being derived mainly from the design specifications. Hence, diagram 11 gives a statistical correlation of gross wetted areas and volumes with the principal dimensions of the pressurized section and with cabin plus freighthold volume. The diagram may be used in different ways:

for given pressure cabin outside dimensions, the volume and wetted area are found immediately;

if only the passenger cabin plus freighthold volume are known, the fuselage volume is read from the diagram and the wetted area is computed with the presented formula (based on fig. 6).

For payloads in excess of 30 passengers roughly, the correlation is remarkable in view of the simplicity of the method.

B5. Wings, tailplanes and fuel tanks

B5.1 Wetted area of wings and tailplanes

The wetted area is computed by spanwise integration of the sectional circumference. The net (exposed) area (S_{net}) to be used is the horizontal projection of the area exposed to the airflow.

The circumference of an arbitrary section can be computed from diagram 3, using a suitable subdivision of the contour. For most subsonic sections, the following simple expression is reasonably accurate:

$$\text{circumference} = 2 \times \text{chordlength} \; (1 + 0.25 \cdot t/c) \quad (7)$$

where t/c = thickness/chord ratio (fig. 8)

The wetted area of a linear lofted lifting surface is derived by integration:

$$\text{wetted area} = 2S_{net}\left\{1 + 0.25(t/c)_r \frac{1+\tau\lambda}{1+\lambda}\right\} \qquad (8)$$

λ = tipchord/root chord (taper ratio)

$\tau = (t/c)_t \;/\; (t/c)_r$

r = root; t = tip

In this particular case, the root and tip sections refer to the exposed part of the wing or tailplane.

B5.2 Fuel tank volume

a. Most internal bag-type tanks can be represented by a geometric body with parallel end faces of type A or B in fig. 7.

b. For integral tanks the external shape of the structure will be used to apply fig. 7. In this case, the volume of the structure * should be subtracted. In a completely filled tank roughly 5% of the volume must be available for expansion of the fuel (subsonic aircraft).

c. External fuel tanks can be treated in a similar fashion as the fuselage, e.g. with fig. 6 or diagram 10.

d. In project design a check on the available tank capacity must be made. A first estimate for the integral tank volume is given in fig. 8. Although statistical data were used to derive the constant 0.54, the method is not very accurate. Hence, when the available tank volume appears to be critical, a more precise calculation is necessary, to account for the actual section variation and the location of the spars.

B6. Engine nacelles and air ducts

In the most general case, the engine nacelle group may consist of a fan cowling, a gasgenerator cowling and a plug in the hot flow (fig. 9). The wetted areas of these components can be computed with the data on fig. 9 and diagram 7.

---

* to be derived from the structural weight.

References

B1. Schmidt, A.H. : "A simplified method for estimating the wetted area of aircraft fuselages". S.A.W.E. Technical Paper No. 308, 1962.

B2. Haase, H.H. : "The analytical development of curves and streamline shapes". Republic Aviation Corporation, 1948.

B3. Rehbinder, G. : "Analytical definition of aircraft shape". Journal of Aircraft, Vol. 4 No. 6, nov-dec. 1967, page 544-546.

B4. Granholm, J.W. : "The use of closed-curve equations of variable degree in airplane fuselage lofting". Aeronautical Engineering Review, july 1954, page 52-57.

B5. Abramowitz, M. and Stegun, I.A. : "Handbook of mathematical functions". Dover Publications, Inc., New York, 1965.

B6. An. : "Weight engineers handbook". Society of Aeronautical Weight Engineers Inc., revised ed. december 1968.

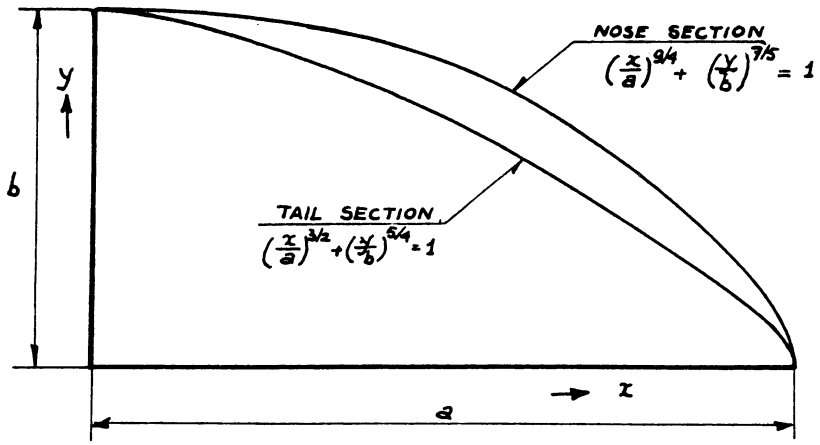

FIG. 1 REPRESENTATION OF TYPICAL NOSE AND TAIL SECTIONS OF STREAMLINE BODIES BY MATHEMATICAL FUNCTIONS

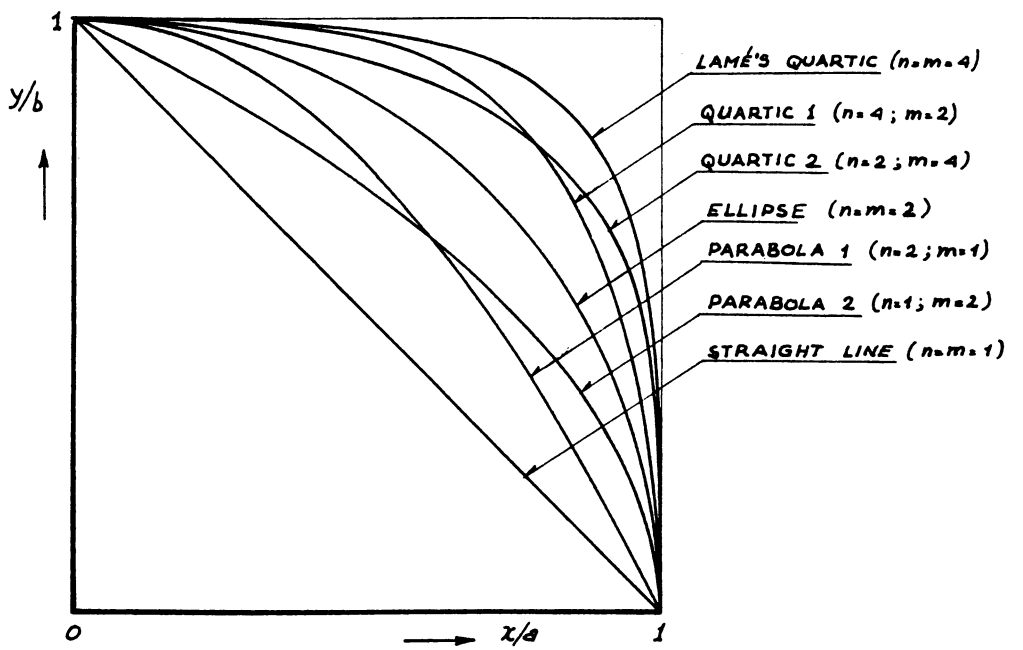

FIG. 2: SPECIAL CASES OF THE FUNCTION $\left(\frac{x}{a}\right)^n + \left(\frac{y}{b}\right)^m = 1$

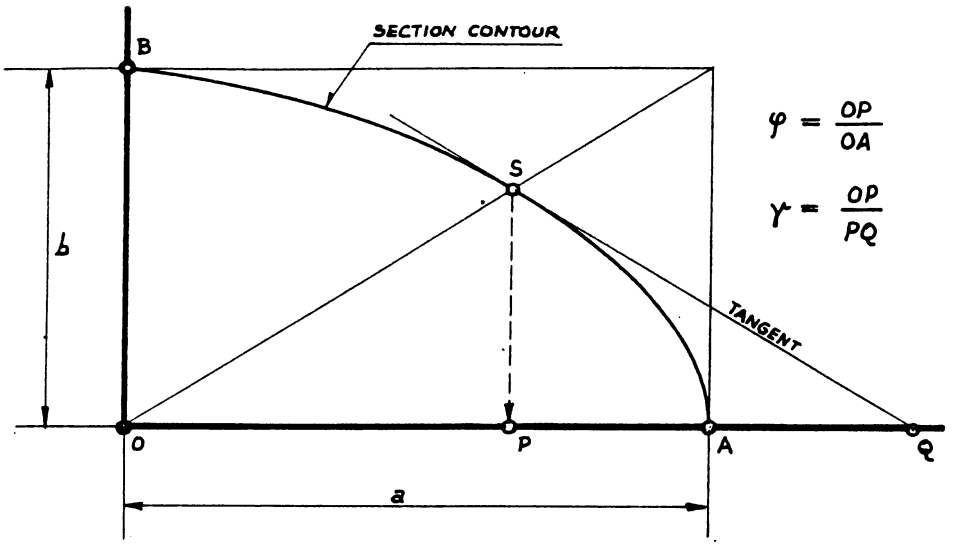

FIG. 3 : GRAPHICAL DETERMINATION OF THE PARAMETERS φ AND γ FROM THE DESIGN DRAWING

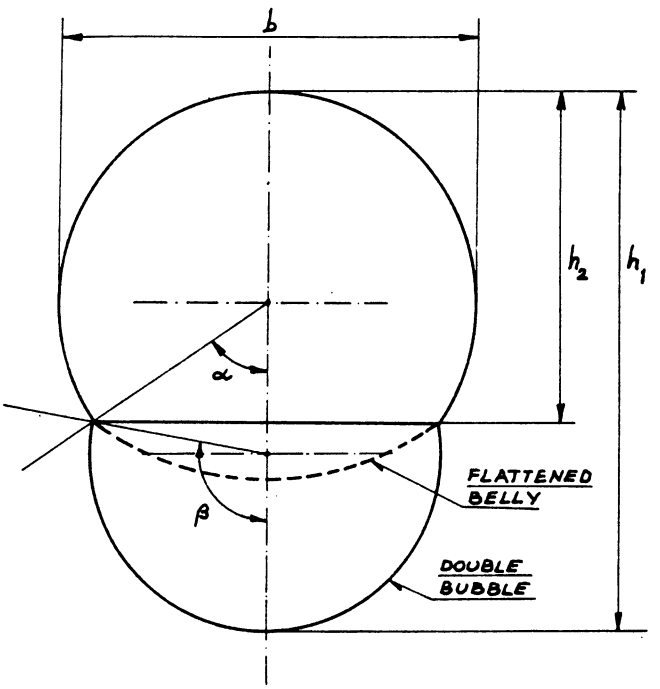

$$\cos\alpha = 2\frac{h_2}{b} - 1$$

$$\cos\beta = \frac{1 - b/h_2 + (h_1/h_2 - 1)^2}{1 - b/h_2 - (h_1/h_2 - 1)^2}$$

NOTE : CIRCUMFERENCE AND AREA ARE PLOTTED IN DIAGRAM 6 IN TERMS OF h_2/b AND h_2/h_1

$$\frac{\text{CIRCUMFERENCE}}{\pi b} = 1 - \frac{\alpha}{\pi} + \frac{\beta}{\pi}\frac{\sin\alpha}{\sin\beta}$$

$$\frac{\text{AREA}}{\frac{\pi}{4}b^2} = 1 - \left(\frac{\alpha}{\pi} - \frac{\sin 2\alpha}{2\pi}\right) + \left(\frac{\beta}{\pi} - \frac{\sin 2\beta}{2\pi}\right)\left(\frac{\sin\alpha}{\sin\beta}\right)^2$$

FIG. 4 . GEOMETRY OF CROSS SECTIONS COMPOSED OF TWO CIRCLE SECTORS

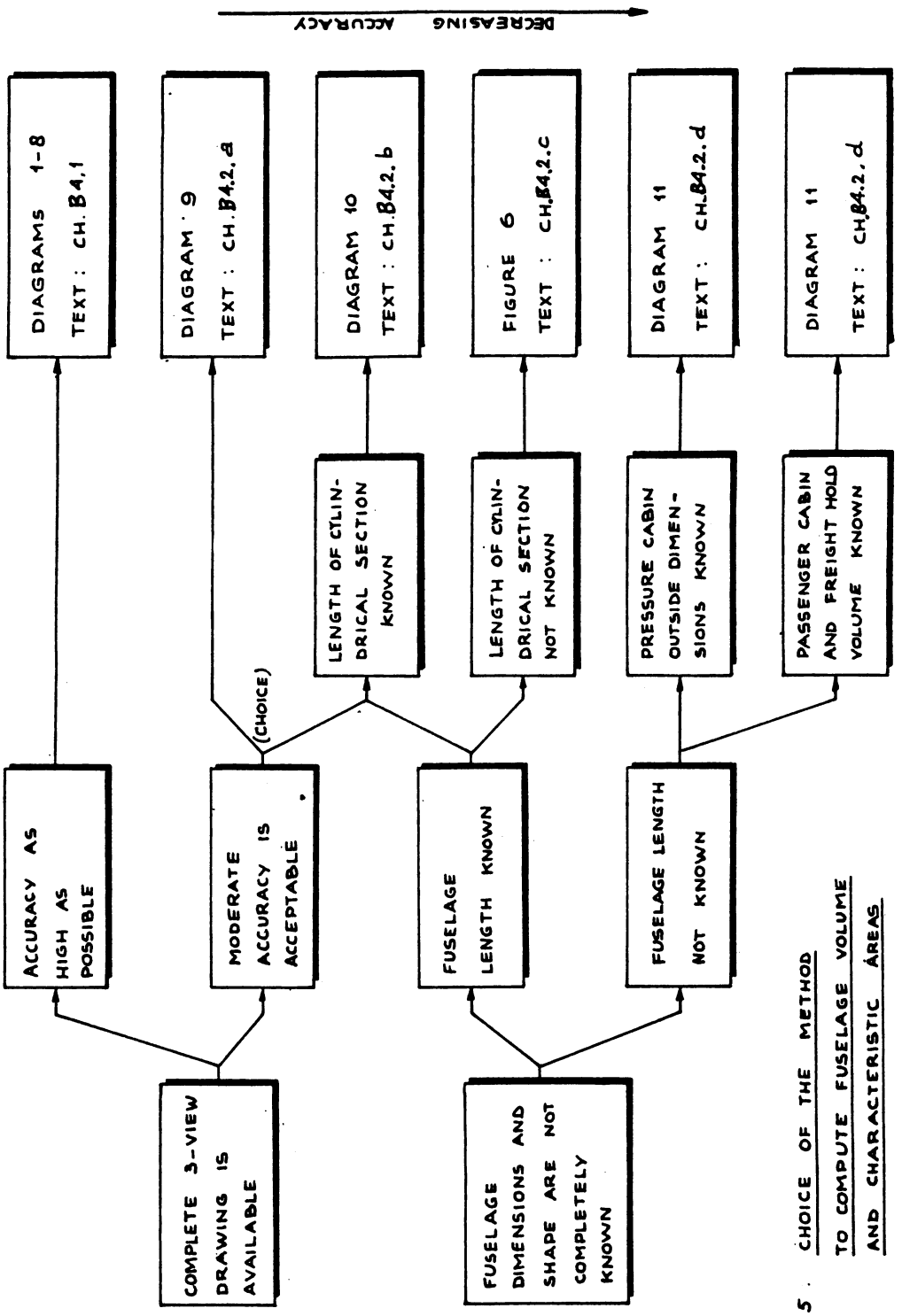

FIG. 5. CHOICE OF THE METHOD TO COMPUTE FUSELAGE VOLUME AND CHARACTERISTIC AREAS

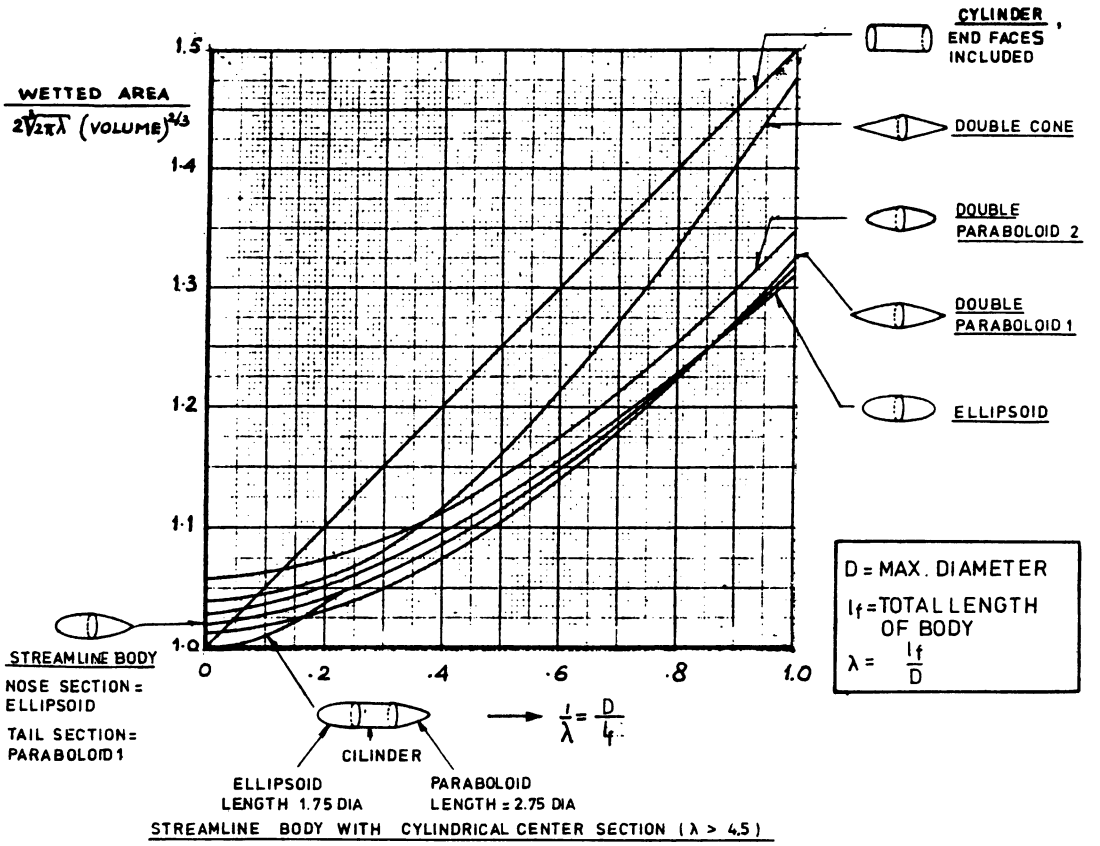

STREAMLINE BODY WITH CYLINDRICAL CENTER SECTION ($\lambda > 4.5$)

FOR FUSELAGES WITH CYLINDRICAL CENTER SECTION, NOSE AND TAIL SECTION SHAPES ACCORDING TO FIG. 1 AND LENGTH/DIAMETER RATIOS EQUAL TO 1.75 AND 2.75 RESP. :

$$\left.\begin{aligned} \text{VOLUME} &= \frac{\pi}{4} D^2 l_f \left(1 - \frac{2}{\lambda}\right) \\ \text{WETTED AREA} &= \pi D l_f \left(1 - \frac{2}{\lambda}\right)^{2/3} \left(1 + \frac{1}{\lambda^2}\right) \end{aligned}\right\} \quad \lambda \geq 4.5$$

FOR STREAMLINE BODIES WITHOUT CYLINDRICAL CENTER SECTION, NOSE AND TAIL SECTION SHAPES ACCORDING TO FIG. 1 :

$$\text{VOLUME} = \frac{\pi}{4} D^2 l_f \left(0.50 + 0.135 \frac{l_n}{l_f}\right) \qquad (l_n = \text{LENGTH OF BODY NOSE})$$

$$\text{WETTED AREA} = \pi D l_f \left(0.50 + 0.135 \frac{l_n}{l_f}\right)^{2/3} \left(1.015 + \frac{0.3}{\lambda^{3/2}}\right)$$

FIG. 6 : VOLUME AND WETTED AREA OF AXISYMMETRIC STREAMLINE BODIES.

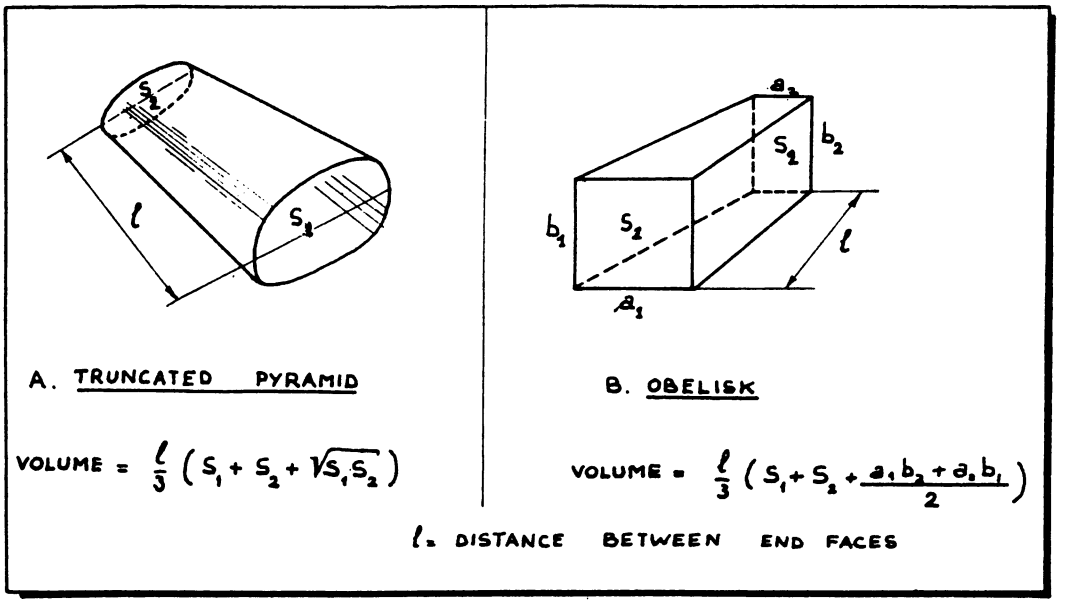

FIG. 7 : VOLUME OF GEOMETRIC BODIES WITH PARALLEL END FACES

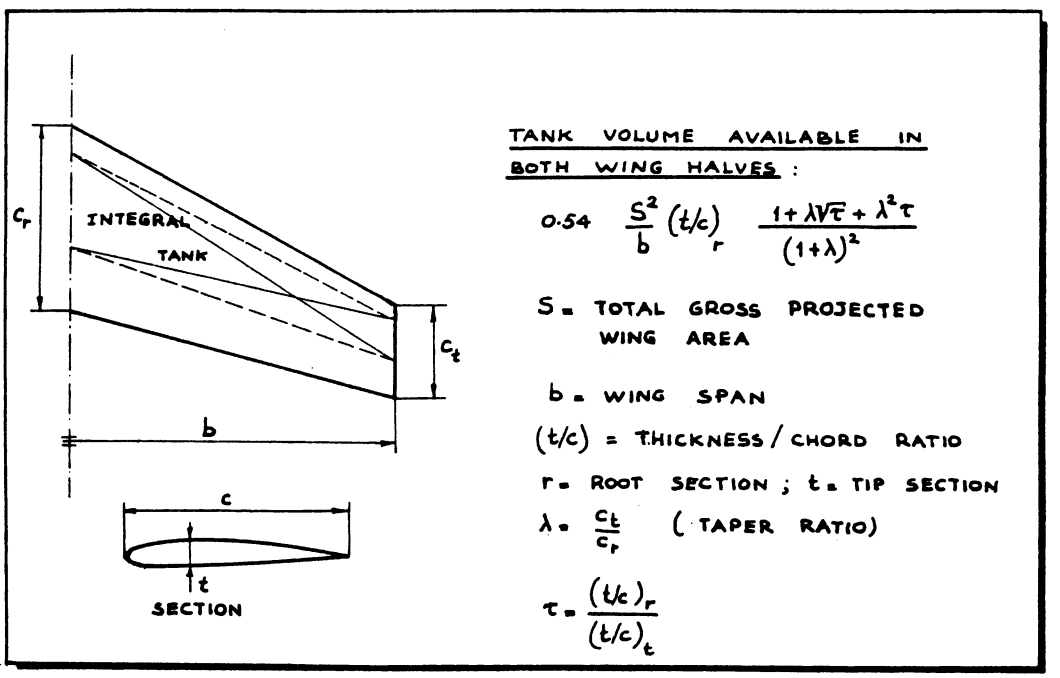

FIG. 8.: APPROXIMATION FOR INTEGRAL FUEL TANK VOLUME, AVAILABLE IN A LINEAR LOFTED WING

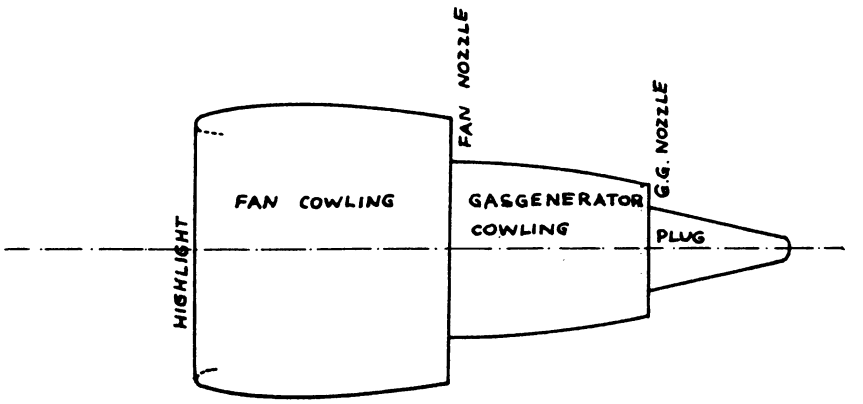

COMPONENTS OF AN ENGINE NACELLE GROUP

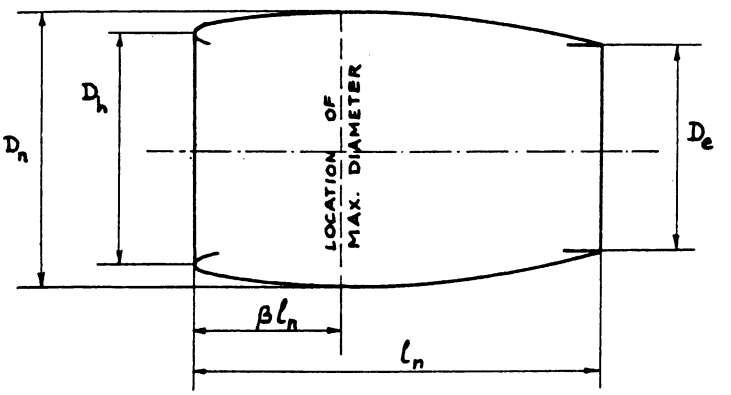

EXTERNAL WETTED AREA OF FAN COWLING :

$$l_n D_n \left\{ 2 + 0.35\beta + 0.80\beta \frac{D_h}{D_n} + 1.15(1-\beta) \frac{D_e}{D_n} \right\}$$

WETTED AREA OF GASGENERATOR COWLING : DIAGRAM 7

WETTED AREA OF PLUG :

2 * PLUG LENGTH * MAX. DIAMETER

FIG. 9 : WETTED AREA OF AN ENGINE NACELLE

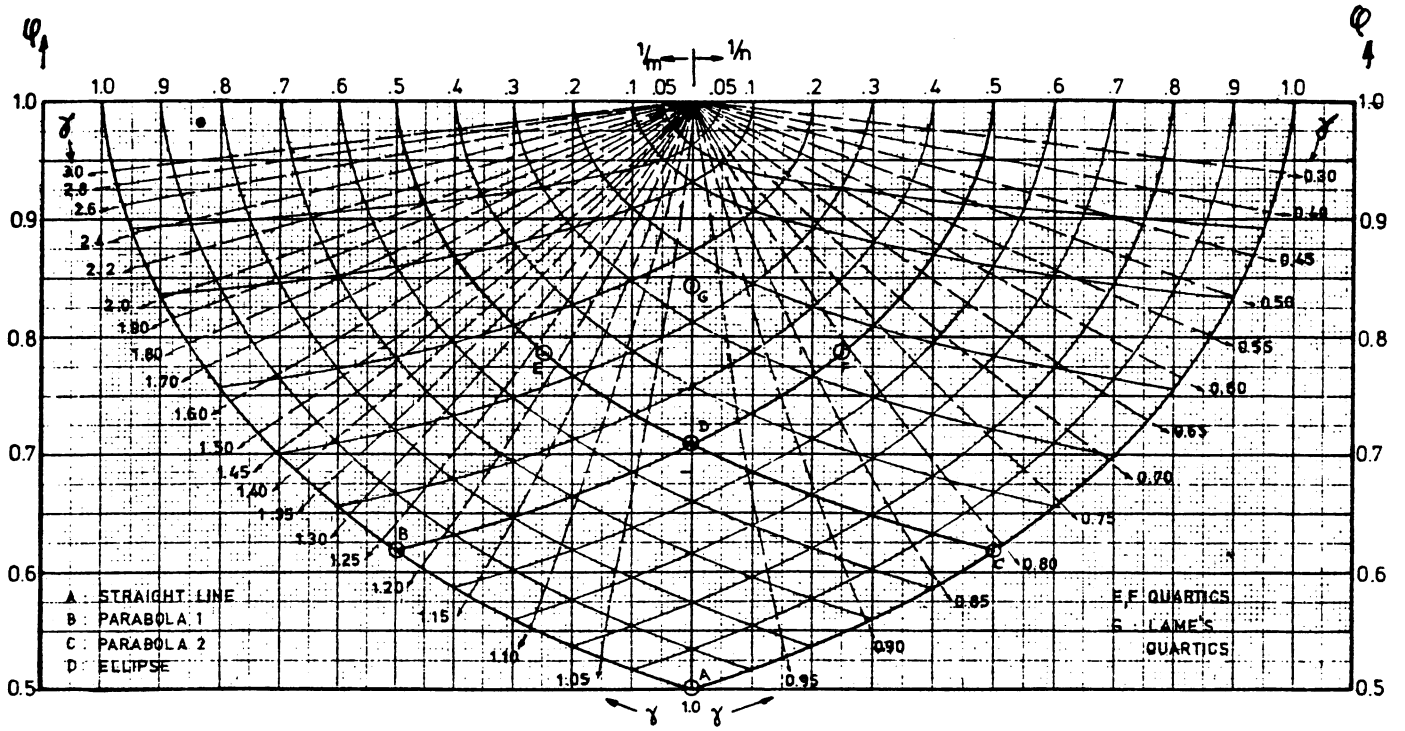

GENERAL EQUATION OF THE CONTOUR : $\left(\frac{x}{a}\right)^n + \left(\frac{y}{b}\right)^m = 1$

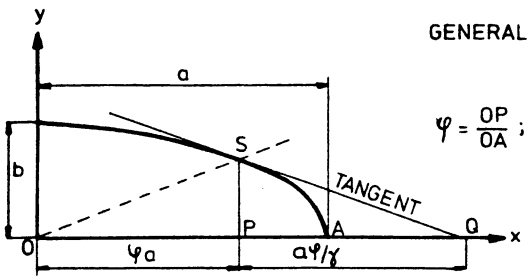

$\varphi = \frac{OP}{OA}$; $\gamma = \frac{OP}{PQ}$

RELATION BETWEEN (φ, γ) AND (n,m) :

$\varphi^n + \varphi^m = 1$; $\gamma = \frac{n}{m}\varphi^{n-m}$

DIAGRAM 1: DETERMINATION OF n AND m FROM KNOWN VALUES OF φ AND γ

AREA / a·b

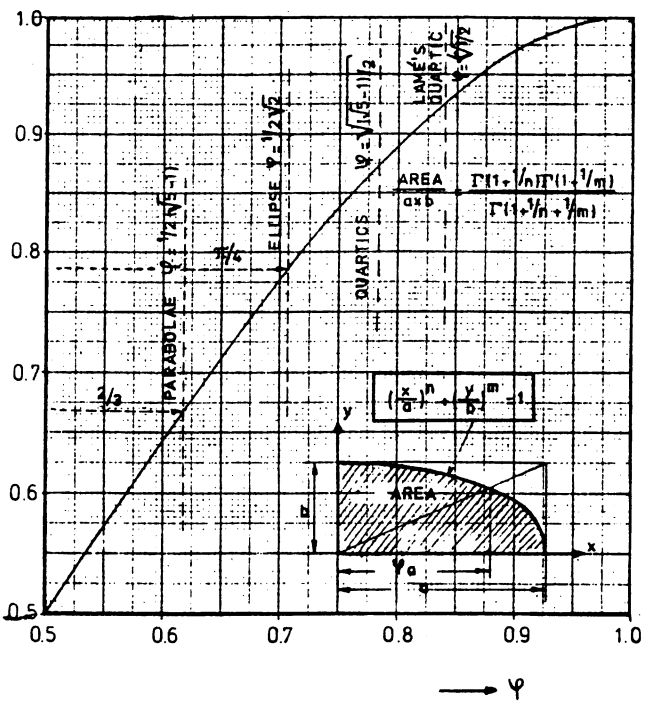

DIAGRAM 2: CROSS-SECTIONAL AREA

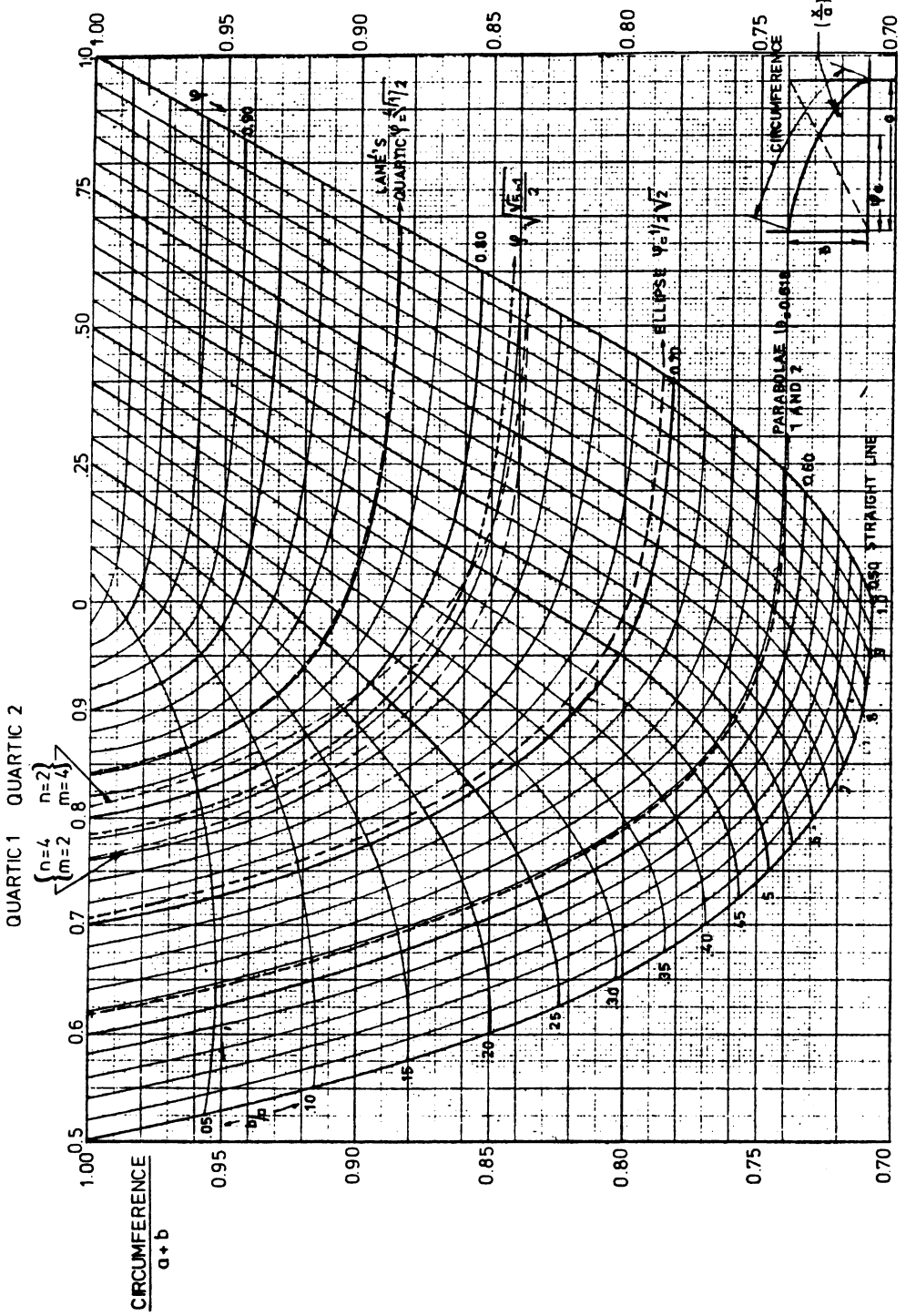

DIAGRAM 3: CIRCUMFERENCE OF A CONTOURLINE

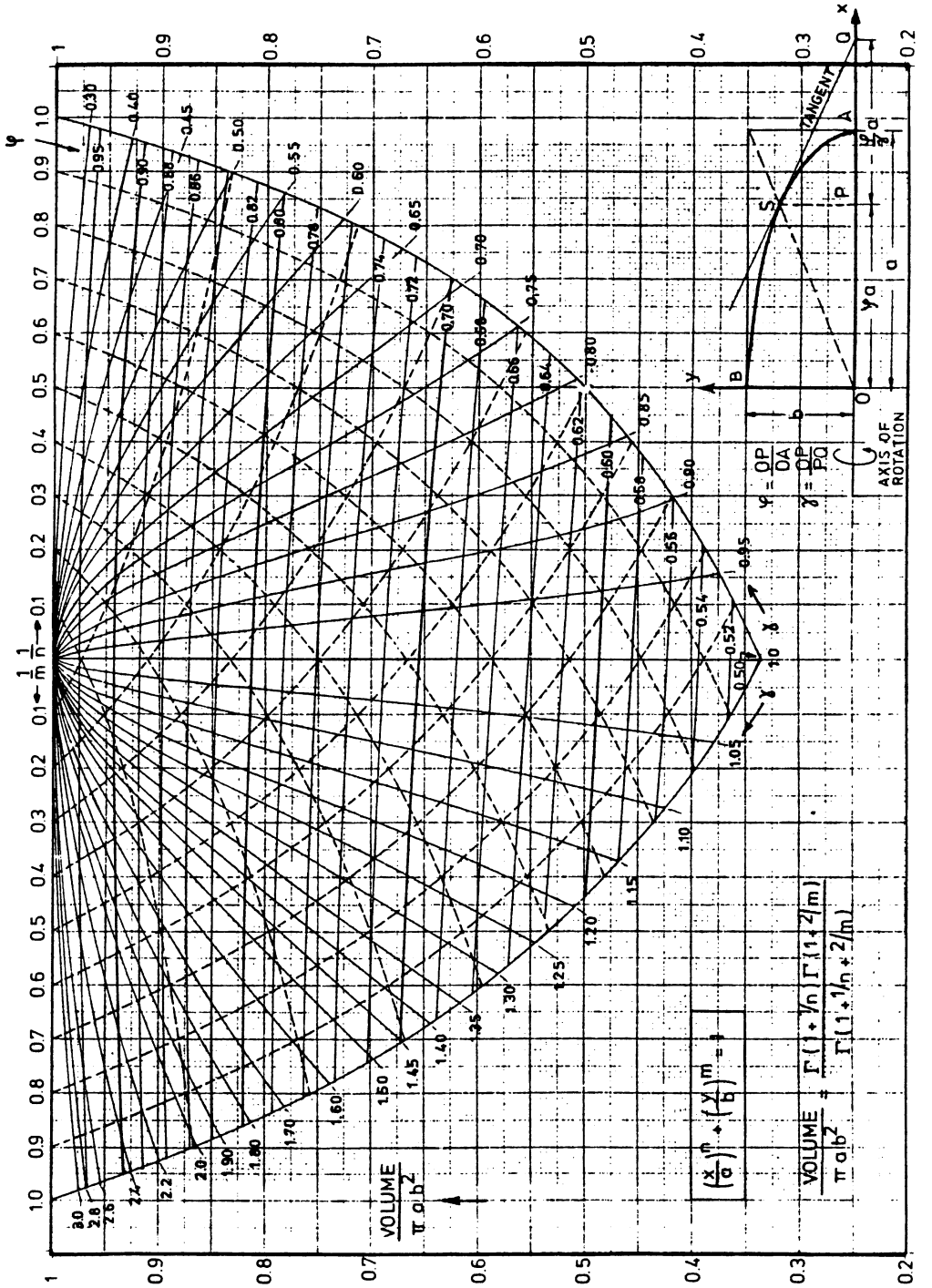

DIAGRAM 4: VOLUME OF A BODY OF REVOLUTION

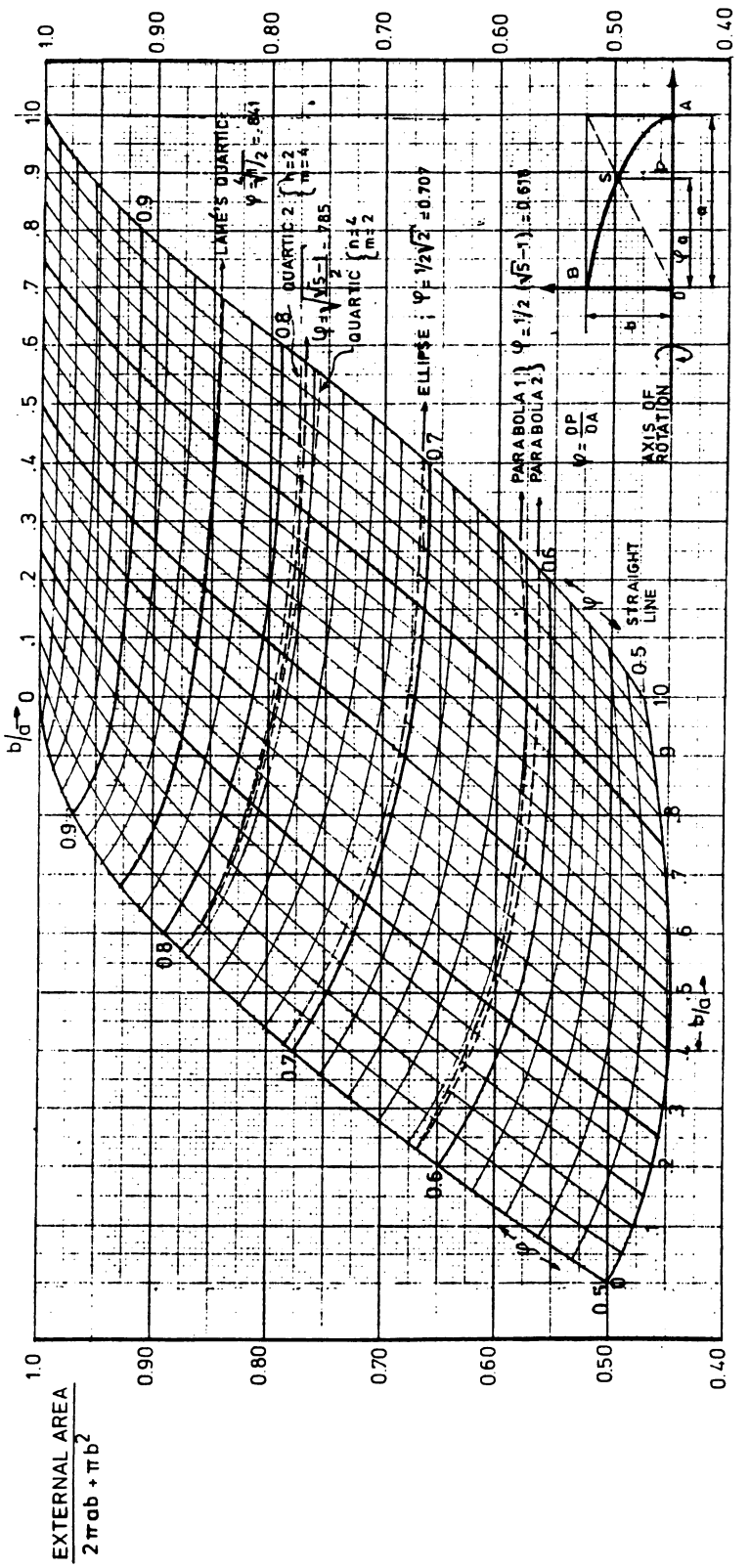

DIAGRAM 5: EXTERNAL AREA OF A BODY OF REVOLUTION.

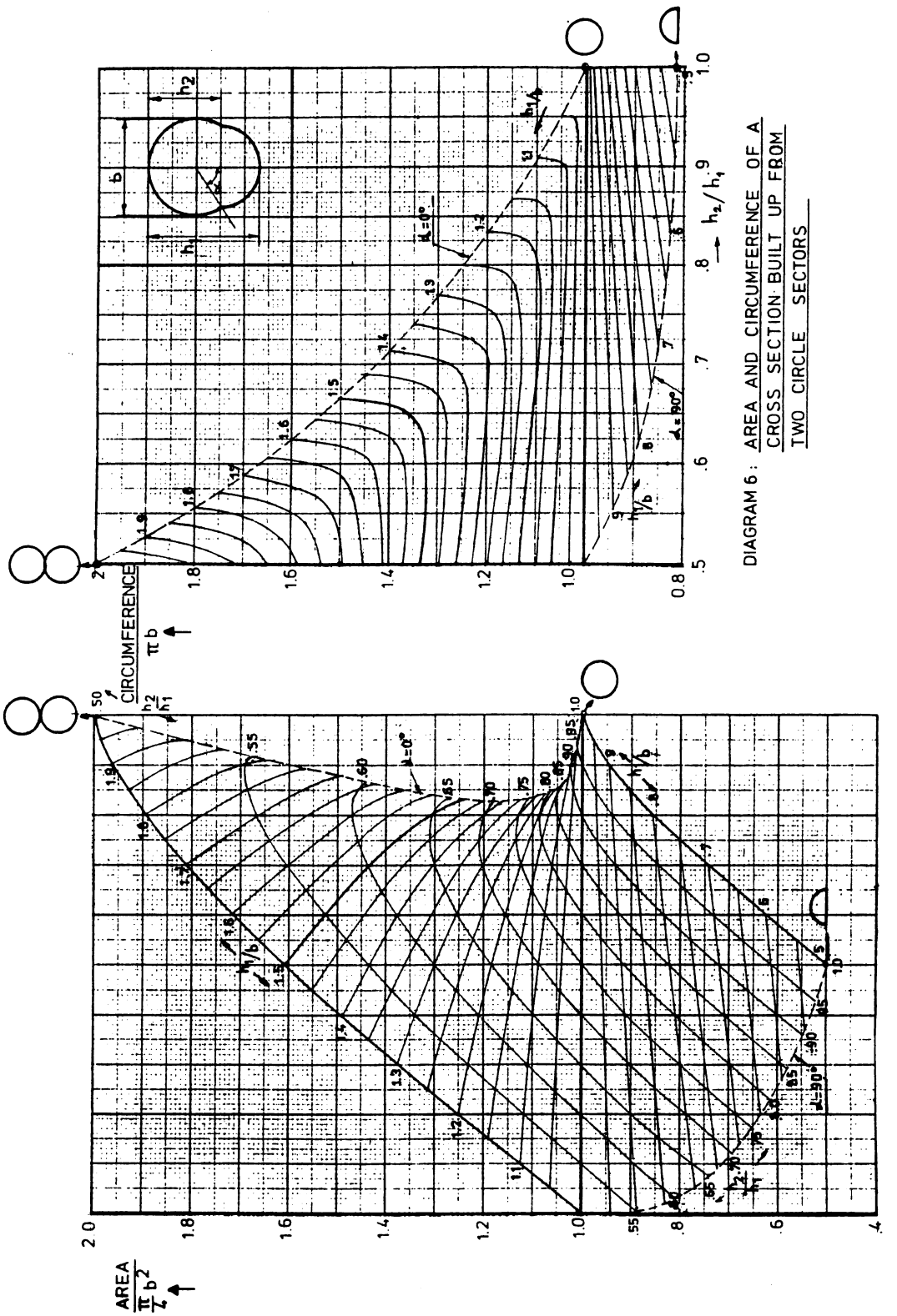

DIAGRAM 6: AREA AND CIRCUMFERENCE OF A CROSS SECTION BUILT UP FROM TWO CIRCLE SECTORS

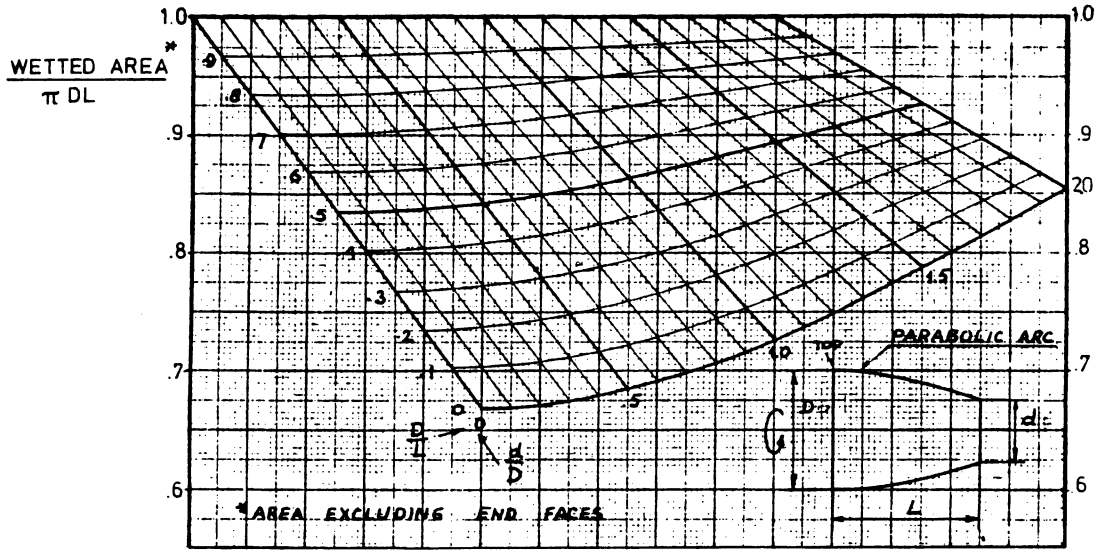

$$\frac{\text{VOLUME}}{\frac{\pi}{4}D^2 L} = \frac{1}{15}\left\{8 + 4\frac{d}{D} + 3\left(\frac{d}{D}\right)^2\right\}$$

DIAGRAM 7: GEOMETRIC PROPERTIES OF A FRUSTRUM OF A PARABOLOID

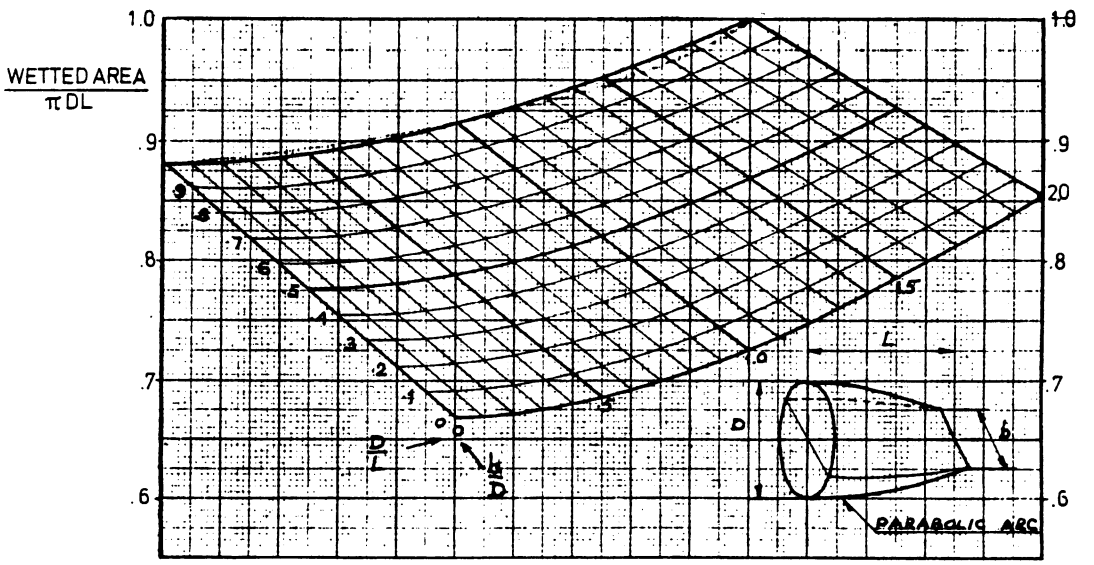

$$\frac{\text{VOLUME}}{\frac{\pi}{4}D^2 L} = \frac{1}{15}\left\{8 + 2\frac{b}{D}\right\}$$

DIAGRAM 8: APROXIMATE WETTED AREA AND VOLUME OF A "BEAVER TAIL"

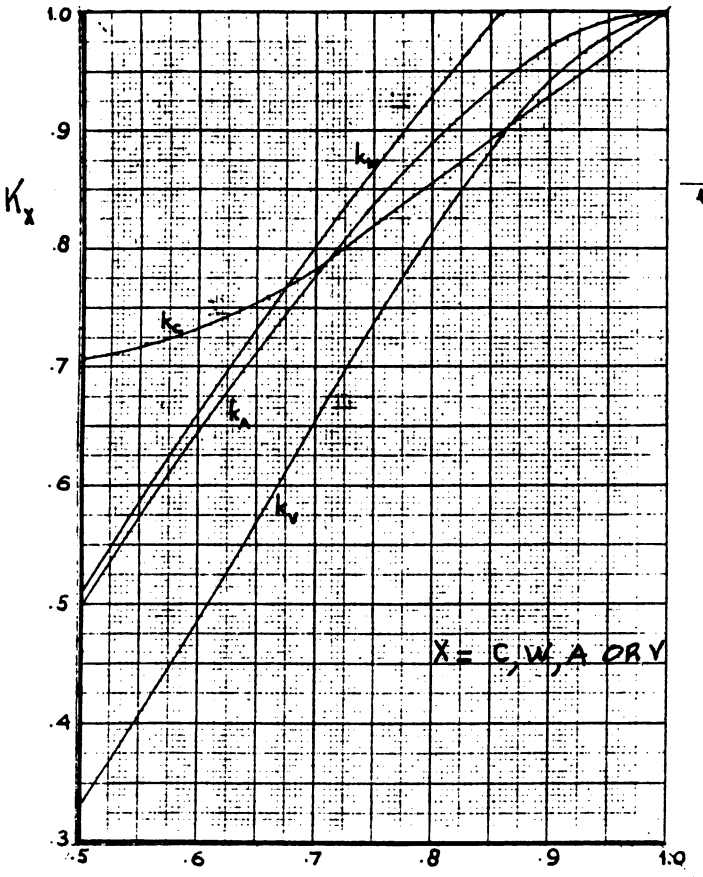

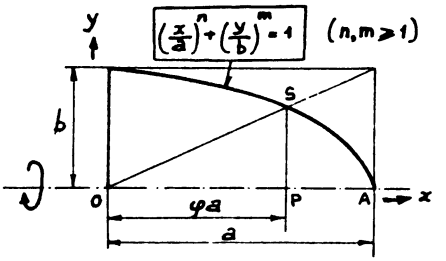

$k_A = \frac{\text{AREA OF SECTION}}{a \cdot b}$

$k_c = \frac{\text{CIRCUMFERENCE}}{a + b}$

$k_V = \frac{\text{VOLUME OF BODY OF REV.}}{\pi a b^2}$

$k_w = \frac{\text{WETTED AREA BODY OF REV.}}{2\pi a b}$

$\varphi = \frac{OP}{OA}$

DIAGRAM 9 :
SIMPLIFIED CALCULATION OF AREAS AND VOLUME

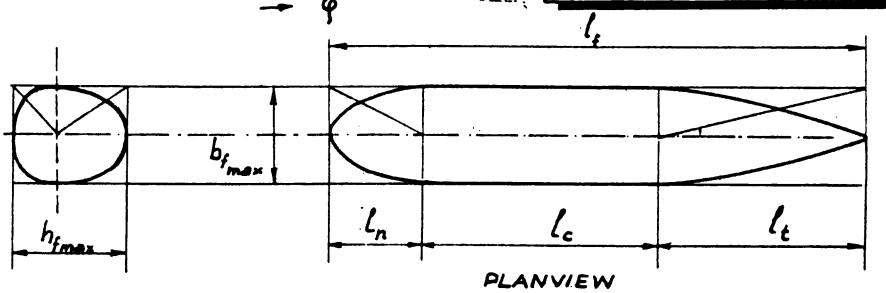

PLANVIEW

FRONT VIEW : AREA $S_f = k_A \cdot b_{f_{max}} \cdot h_{f_{max}}$

CIRCUMFERENCE $C_f = 2\, k_c \,(b_{f_{max}} + h_{f_{max}})$

(IF NECESSARY, THE FRONT VIEW IS SUBDIVIDED INTO SEVERAL PARTS)

VOLUME : $V_f = S_f (l_c + k_{V_n} l_n + k_{V_t} l_t)$

k_V IS DETERMINED FROM THE PLANVIEW FOR THE NOSE SECTION (k_{V_n}) AND THE TAIL SECTION (k_{V_t})

WETTED AREA : $S_{WET} = C_f (l_c + k_{W_n} l_n + k_{W_t} l_t)$

k_W - VALUES ARE DETERMINED FROM THE PLAN VIEW

PLANVIEW AND SIDEVIEW AREAS CAN BE COMPUTED IN SIMILAR FASHION

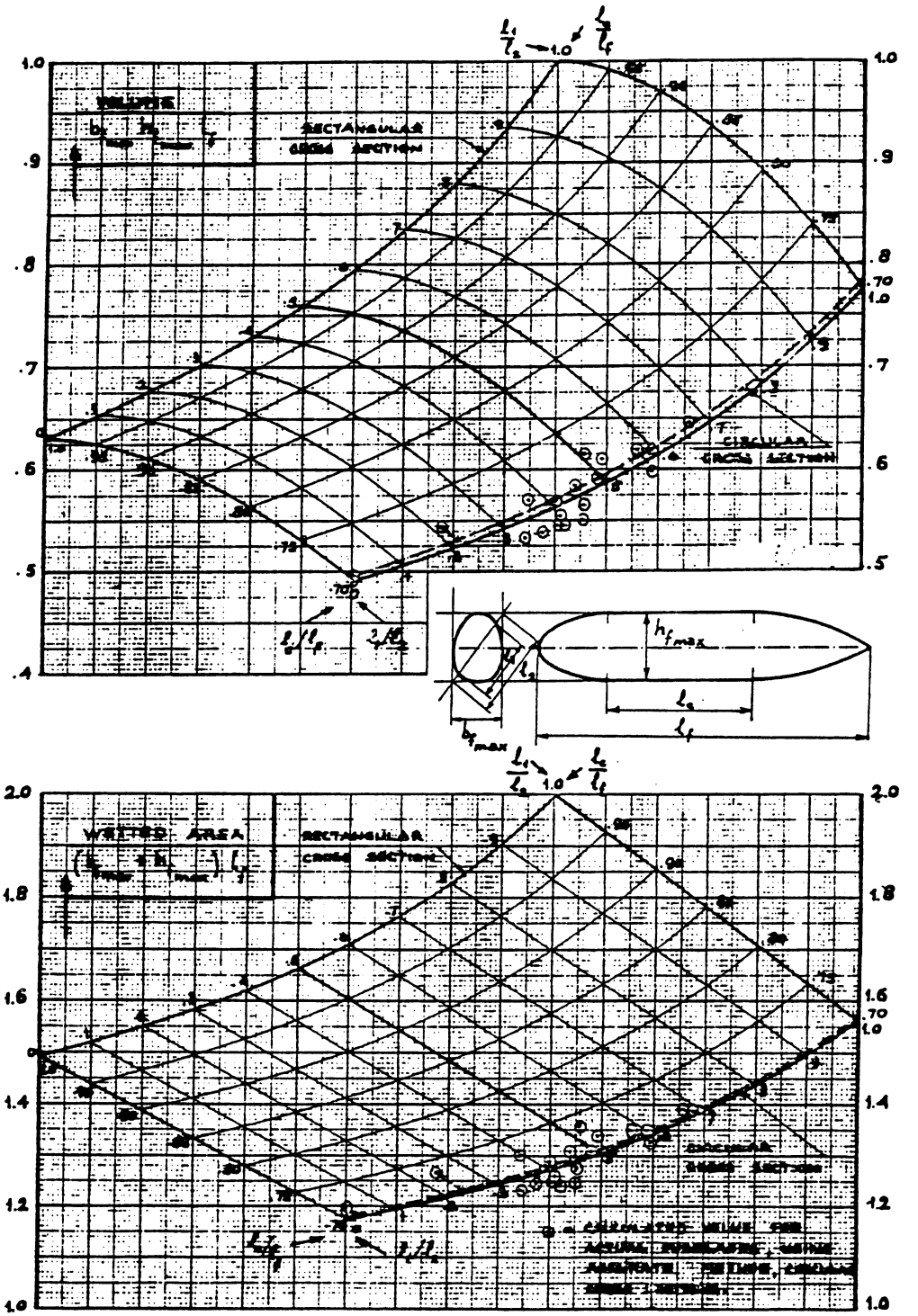

DIAGRAM 10: APPROXIMATE CALCULATION OF FUSELAGE VOLUME AND WETTED AREA (GIVEN: LENGTH OF CYL. SECTION)

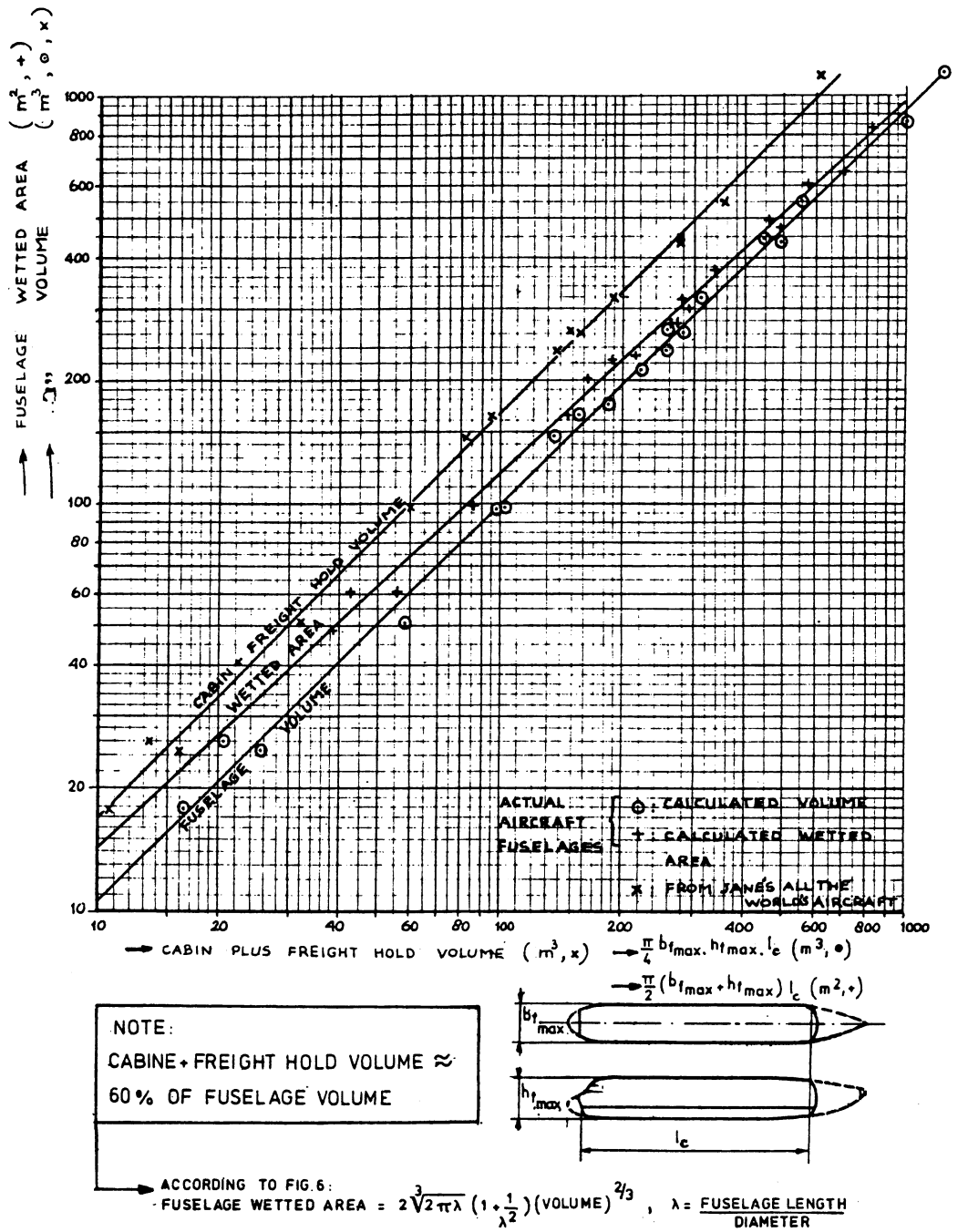

DIAGRAM 11 : STATISTICAL CORRELLATION OF VOLUME AND WETTED AREA BASED ON PRESSURE CABIN DIMENSIONS (VALID FOR FUSELAGES WITH CILINDRICAL SECTION)